Multiscale Thermohydrologic Model

Multiscale Thermohydrologic Model

ANL-EBS-MD-000049 REV 03

July 2005

2. Type of Mathematical Model

☒ Process Model   ☒ Abstraction Model   ☐ System Model

Describe Intended Use of Model

This model provides thermohydrologic information and data for other reports supporting License Application.

3. Title

Multiscale Thermohydrologic Model

4. DI (including Rev. No.):

ANL-EBS-MD-000049 REV 03

	Printed Name	Signature	Date
5. Originator	Tom Buscheck	*Thomas A. Buscheck*	7/7/05
6. Independent Technical Reviewer	Robert Andrews	*R.W.D*	7/7/05
7. Checker	Bruce Kirstein	*Bruce E. Kirstein*	7/7/05
8. QER	Darrell Svalstad	*Darrell Svalstad*	7/7/05
9. Responsible Manager/Lead	William Duffy	*William Duffy*	7/7/05
10. Responsible Manager	Ernest Hardin	*E Hardin*	7/7/05

11. Remarks

(ELH 6/15/05) This revision is supposed to discuss Danko's recent publication of an alternative model that describes ventilation and thermal-hydraulics. This addition has not yet been made.

Limitations of the model are that drift seepage during the post-boiling period is not predicted, and the predicted evaporation rate on the drip shield pertains to the case of no dripping on the drip shield.

Change History	
12. Revision No.	**13. Description of Change**
REV 00	Original issue. Supported TSPA-SR, Rev 00 for the Backfill Case. Used 1.54 kW/m line load.
REV 00 ICN 01	This ICN was developed to include the No Backfill Case supporting TSPA-SR Rev 00 ICN 01. The DTN:SN9908T0872799.004 references were removed. The data and inputs were referenced to updated DTNs and references, or entered as assumptions. Revised invert thermal conductivity values and an adjusted heat load of 1.45 kW/m were used for the no-backfill case.

| REV 00 ICN 02 | This ICN was developed to address the NRC KTI Agreement TEF 2.9 and show the influence of drift-scale fracture heterogeneity on TH behavior for the No Backfill Case. This was accomplished with the use of the 3-D heterogeneous Line-averaged heat-source Drift-scale TH (LDTH) model, which was developed for this ICN, and which is completely described in Section 6.14. The 3-D heterogeneous LDTH model is based on the 2-D homogeneous LDTH model. The data and inputs were referenced to updated DTNs and references, or entered as assumptions. Section 7 has also been updated to include the conclusions developed from the 3-D heterogeneous LDTH model. A postprocessor, XLDTH, was developed and used to address the influence of drift-scale heterogeneity of fracture properties as described above. This postprocessor is qualified in accordance with the currently approved version of AP-SI.1Q, Software Management.

Deficiency Report LVMO-00-D-039, Inaccurate Documentation and Validation of Software Routines and/or Macros, identified software issues that are addressed in MOL.20010910.0181 (Schreiner, R.L. 2001; Stand Alone DR-39 package for ANL-EBS-MD-000049, Rev. 00, ICN01, Multiscale Thermohydrologic Model). Attachment I contains a cross-walk between attachments in the Stand Alone Package and the attachments formerly included in this AMR. The Stand Alone package provides additional software documentation, e.g., source code listings, validation text files, input/output files and other corrections for routines formerly documented in Attachments I through XVII and XIX through XX of ICN 01 of this AMR.

Attachment II in this ICN 02 lists files supporting each version of this document, including the file lists previously documented in Attachment XVIII of ICN 01. ICN 02 also addresses in Section 2 the issues and concerns identified in Deficiency Report BSC-01-D-100, pertaining to control of electronic information. ICN 02 also addresses NRC KTI agreements pertinent to this AMR, in Section 1. The following sections have been affected by this ICN: Section 1, Section 2, Section 3, Section 4, Section 5, Section 6, Section 7, Section 8, Attachment I and Attachment II |
| REV 01 | Complete revision to support TSPA-LA. |
| REV 02 | Extensive revision to address comments on documentation from Regulatory Integration Team evaluation. Includes major revisions to the following sections: 4.1, 5.3.1.1, 5.3.1.7, 5.4, 6.1.4, and 6.2.1. Some material previously in Section 5 has been moved to Section 4.1. Section 4.1 has been extended to describe the minor modifications to the repository layout that resulted from updates to the related IEDs and to address the properties of the host-rock rubble for the low-probability-seismic collapsed-drift cases. Sections 6.2.9, 6.2.10, and 6.2.11 have been added to describe the submodels for the low-probability-seismic collapsed-drift cases. Section 6.3.3 has been added to discuss the mass influx in the invert. Section 6.3.4 has been added to address the influence of parametric uncertainty of percolation flux and host-rock thermal conductivity on near-field and in-drift thermal-hydrologic conditions. Section 6.3.5 is a revised summary of the range of predicted near-field and in-drift thermal-hydrologic conditions for the TSPA-LA base case. Section 6.3.6 has been added to describe the relationship between drip-shield/waste-package relative humidity and temperature at the drift wall. Section 6.3.7 has been added to describe the differences in the in-drift thermal-hydrologic conditions between the low-probability seismic collapsed-drift cases and the corresponding nominal intact-drift cases. Section 6.3.7 also includes a seepage analysis for the low-probability-seismic collapsed-drift |

	cases. Section 6.3.8 has been added to compare thermal-hydrologic condition predicted for the TSPA-LA with those predicted for the TSPA-SSPA. Section 6.3.9 has been added to describe the sensitivity (or lack thereof) of near-field and in-drift thermal-hydrologic conditions to host-rock hydrologic-property variability and uncertainty. Section 6.3.10 has been added to describe the sensitivity (or lack thereof) of in-drift thermal-hydrologic conditions to the value of in-drift pseudo permeability. Section 6.3.11 has been added to describe the sensitivity (or lack thereof) of near-field and in-drift thermal-hydrologic conditions to invert hydrologic-property variability and uncertainty. Section 6.3.12 has been added to investigate the sensitivity of in-drift thermal-hydrologic conditions to uncertainty in ventilation heat-removal efficiency. Section 6.3.13 has been added to describe the relationship between temperature and relative humidity on waste packages.
	Added Appendix X: Hydrological Properties for the Intragranular Porosity of the Invert; Appendix XI: Thermoconductivity of the Collapsed Drift Zone; and Appendix XII: Comparison of Percolation Fluxes; Appendix XIII: List of Data Sources for Figures and Tables; and Appendix XIV: Qualification of Unqualified Project Data.
	Revised Sections 7.4.3 and 7.4.4: Comparison of Simulated and Field-Measurement Temperatures, and Comparison of Simulated and Field-Measured Saturations in the Matrix; and Appendix VI: LDTH and DDT Submodel Thermal-Radiation Connection Calculation. Added Section 5.1.4: Timing of Climate Change Influence on Percolation Flux above Repository; Section 5.1.5: Water Table Rise; Section 5.3.1.10: Permeability of Host Rock at Emplacement Drift-Wall Surface; Section 5.3.2.7: Emissivity of Emplacement Drift Wall; Section 8.4: Yucca Mountain Review Plan Criteria Assessment; and Appendix XV: Prediction of Relative Humidity in the Invert.
	Brian Mitcheltree checked Sections 4, 5, and Appendix IV; Bruce Kirstein checked from the front through Section 3 and Sections 6.3 through 6.5, 7 and 8, and Appendices IX and XIII; John Case checked Sections 6 through 6.2, Section 9, and DIRS; Jim Kam checked Appendices I through III, V through VIII, X , XII and XV; Zane Walton checked Appendix XI; Bob Walsh checked Appendix XIV.
	Revision 02 addresses CR 79 (elimination of "Technical Information" as a DIRS Input Category), CR 1805 (adequacy of software) and CR 2049 (documentation of model validation). Table 4.1-1, changed equation number.
REV 03	This revision addresses CR-4961, CR-4675, and CR-4309.

INTENTIONALLY LEFT BLANK

CONTENTS

CONTENTS (Continued)

CONTENTS (Continued)

CONTENTS (Continued)

CONTENTS (Continued)

Page

INTENTIONALLY LEFT BLANK

FIGURES

FIGURES (Continued)

FIGURES (Continued)

FIGURES (Continued)

FIGURES (Continued)

FIGURES (Continued)

FIGURES (Continued)

INTENTIONALLY LEFT BLANK

TABLES

TABLES (Continued)

TABLES (Continued)

INTENTIONALLY LEFT BLANK

ACRONYMS AND ABBREVIATIONS

AP   absorber plate (in reference to a PWR waste package type)

AML   areal mass loading (mass of spent nuclear fuel and high-level waste per unit area of heated repository footprint MTU/acre)

BWR   boiling water reactor (in reference to a waste package type)

CR   control rod (in reference to a PWR waste package type)

CSNF   commercial spent nuclear fuel (in reference to a waste package type)

DDT   Discrete-heat-source, Drift-scale, Thermal-conduction submodel of the MSTHM (a three-dimensional NUFT submodel)

DHLW   defense high-level (radioactive) waste (in reference to a waste package type)

DKM   Dual Permeability Model

DMTH   Discrete-heat-source, Mountain-scale, Thermal-Hydrologic model (result of the MSTHM)

DOE   U.S. Department of Energy

D/LMTH   Discrete/Line-averaged-heat-source, Mountain-scale, Thermal-Hydrologic model (a monolithic three-dimensional NUFT model, using a nested mesh)

DST   Drift Scale Test

DTN   data tracking number

FEP   features, events, and processes

HLW   high-level radioactive waste (in reference to a waste package type)

IED   information exchange drawing

LBNL   Lawrence Berkeley National Laboratory

LLNL   Lawrence Livermore National Laboratory

LBT   Large Block (Thermal) Test

LDTH   Line-averaged-heat-source, Drift-scale, Thermal-Hydrologic submodel of the MSTHM; this submodel is a two-dimensional NUFT submodel

LMTH   Line-averaged-heat-source, Mountain-scale, Thermal-Hydrologic model (an intermediate result of the MSTHM)

LPD   Linear Power Density (kW/m)

MSTHAC   Multiscale Thermohydrologic Abstraction Code

MSTHM   Multiscale Thermohydrologic Model

MTU   metric tons of uranium (measure of mass of radioactive waste, which is also a measure of the thermal power loading)

PWR   pressurized water reactor (in reference to a waste package type)

RH   relative humidity

RTD   resistance temperature device (used in the field thermal tests, including the Large Block Test and Drift Scale Test)

SDT   Smeared-heat-source, Drift-scale, Thermal-conduction submodel
             (a one-dimensional NUFT submodel)
SMT   Smeared-heat-source, Mountain-scale, Thermal-conduction submodel
             (this submodel is a three-dimensional NUFT submodel)
SNF   spent nuclear fuel
SNL   Sandia National Laboratory

SSPA   Supplemental Science and Performance Analyses

TSPA   Total System Performance Assessment
TSPA-LA   Total System Performance Assessment for the License Application
TSPA-SR   Total System Performance Assessment for the Site Recommendation
TSPA-VA   Total System Performance Assessment for the Viability Assessment
TWP   technical work plan

UZ   unsaturated zone

WAPDEG   waste package degradation (analysis)

YMP   Yucca Mountain Project

1. PURPOSE

The intended purpose of the multiscale thermohydrologic model (MSTHM) is to predict the possible range of thermal-hydrologic conditions, resulting from uncertainty and variability, in the repository emplacement drifts, including the invert, and in the adjoining host rock for the repository at Yucca Mountain. The goal of the MSTHM is to predict a reasonable range of possible thermal-hydrologic conditions within the emplacement drift. To be reasonable, this range includes the influence of waste-package-to-waste-package heat output variability relevant to the license application design, as well as the influence of uncertainty and variability in the geologic and hydrologic conditions relevant to predicting the thermal-hydrologic response in emplacement drifts. This goal is quite different from the goal of a model to predict a single expected thermal-hydrologic response. As a result, the development and validation of the MSTHM and the associated analyses using this model are focused on the goal of predicting a reasonable range of thermal-hydrologic conditions resulting from parametric uncertainty and waste-package-to-waste-package heat-output variability.

Thermal-hydrologic conditions within emplacement drifts depend primarily on thermal-hydrologic conditions in the host rock at the drift wall and on the temperature difference between the drift wall and the drip-shield and waste-package surfaces. Thus, the ability to predict a reasonable range of relevant in-drift MSTHM output parameters (e.g., temperature and relative humidity) is based on valid predictions of thermal-hydrologic processes in the host rock, as well as valid predictions of heat-transfer processes between the drift wall and the drip-shield and waste-package surfaces. Because the invert contains crushed gravel derived from the host rock, the invert is, in effect, an extension of the host rock, with thermal and hydrologic properties that have been modified by virtue of the crushing (and the resulting geometry of the gravel grains). Thus, given that reasonable invert properties are applied, the ability to predict a reasonable range of relevant MSTHM output parameters for the invert are based on valid predictions of thermal-hydrologic processes in the host rock.

The MSTHM calculates the following thermal-hydrologic parameters: temperature, relative humidity, liquid-phase saturation, evaporation rate, air-mass fraction, gas-phase pressure, capillary pressure, and liquid- and gas-phase fluxes. The thermal-hydrologic parameters used to support *Total System Performance Assessment (TSPA) Model/Analysis for the License Application* are identified in Table 1-1. The thermal-hydrologic parameters are determined as a function of position along each of the emplacement drifts and as a function of waste package type. These parameters are determined at various reference locations within the emplacement drifts, including the waste package and drip-shield surfaces and in the invert. The parameters are also determined at various defined locations in the adjoining host rock.

The MSTHM uses data obtained from the data tracking numbers (DTNs) listed in Table 4.1-1. The majority of those DTNs were generated from the following analyses and model reports:

- *UZ Flow Model and Submodels* (BSC 2004 [DIRS 169861])

- *Development of Numerical Grids for UZ Flow and Transport Modeling* (BSC 2004 [DIRS 169855])

- *Calibrated Properties Model* (BSC 2004 [DIRS 169857])

- *Thermal Conductivity of the Potential Repository Horizon* (BSC 2004 [DIRS 169854])

- *Thermal Conductivity of the Non-Repository Lithostratigraphic Layers* (BSC 2004 [DIRS 170033])

- *Ventilation Model and Analysis Report* (BSC 2004 [DIRS 169862])

- *Heat Capacity Analysis Report* (BSC 2004 [DIRS 170003]).

The MSTHM simulations provide the total system performance assessment for the license application (TSPA-LA) with the thermal-hydrologic parameters (as a function of time) that influence the evolution of in-drift coupled flow and transport processes. The TSPA-LA then uses those thermal-hydrologic parameters as part of its integrated assessment of system performance.

Analysis and model reports that are directly downstream of this report include:

- *Drift Degradation Analysis*

- *Evaluation of Features, Events, and Processes (FEP) for the Biosphere Model*

- *Total System Performance Assessment (TSPA) Model/Analysis for the License Application*.

The limitations of the MSTHM include:

- Drift seepage prediction during the post-boiling period is beyond the scope of this report.

The MSTHM accounts for three-dimensional drift-scale and mountain-scale heat flow and captures the influence of the key engineering-design parameters and natural system factors affecting thermal-hydrologic conditions in the emplacement drifts and adjoining host rock. The natural system factors include:

- Repository-scale spatial variability of percolation flux above the repository

- Temporal variability of percolation flux (as influenced by climate change)

- Uncertainty in percolation flux (as addressed by the lower-bound, mean, and upper-bound infiltration-flux cases)

- Stratigraphic variation of thermal conductivity

- Stratigraphic variation of bulk rock density and specific heat

- Stratigraphic variation of hydrologic properties of the rock matrix

- Stratigraphic variation of hydrologic properties of fractures

- Variability in overburden thickness.

The engineering-design parameters include:

- Overall areal heat-generation density of the waste inventory, quantified by the average Areal Mass Loading (AML, expressed in metric tons of uranium (MTU) per acre)

- Line-averaged thermal load along emplacement drifts, quantified by the average Lineal Power Density (LPD, expressed in kW/m)

- Distance between emplacement drifts (also called drift spacing)

- Age of spent-nuclear fuel at time of emplacement

- Repository footprint shape, which influences the evolution of the edge-cooling effect that increases with proximity to the repository edges

- Dimensions of the in-drift design (waste packages, drip shield, and invert)

- Properties of the in-drift engineered barrier system components

- Waste package spacing along the drift (line-load versus point-load spacing)

- Waste package sequencing (particularly with respect to the heat output from the respective waste package types)

- Time- and distance-dependent heat-removal efficiency of preclosure drift ventilation.

The MSTHM (Figure 1-1, Tables 1-2 and 1-3) couples the Smeared-heat-source Drift-scale Thermal-conduction (SDT), Line-average-heat-source Drift-scale Thermal-Hydrologic (LDTH), Discrete-heat-source Drift-scale Thermal-conduction (DDT), and Smeared-heat-source Mountain-scale Thermal-conduction (SMT) submodels such that the flow of water, water vapor, air, and heat through partially saturated fractured porous rock are adequately represented. The relationships between the various submodel and model types are diagrammed in Figure 1-1. The submodel and model types are defined in Table 1-2. All submodels use the Nonisothermal Unsaturated-saturated Flow and Transport (NUFT) code (Nitao 1998 [DIRS 100474]). In addition to being used within the MSTHM itself, the two-dimensional LDTH submodel (Section 6.2.6) is also used as a stand-alone model to conduct sensitivity analyses in this report.

This report provides a description of the MSTHM concept and approach, detailing the software and the routines used in the MSTHM. It describes the inputs to the software and details the specific parameters of that data. It discusses the specific assumptions made in this modeling system and provides the rationale for each assumption. The report includes a description of the MSTHM and the specific submodel components, input-data-preparation and model-building steps, and the MSTHM calculation sequence. Finally, the report includes a discussion of the MSTHM validation in accordance with *Technical Work Plan For: Near-Field Environment and*

Transport In-Drift Heat and Mass Transfer Model and Analysis Reports Integration (BSC 2005 [DIRS 173377]). The purpose of the MSTHM, including how its output parameters are used in TSPA-LA, plays a key role in its validation and in its confidence building. Table 1-1 lists the MSTHM output parameters, indicating which parameters are used to support TSPA-LA, and references where validation and confidence building for prediction of the respective parameters is documented in this report. For the key MSTHM output parameters used in TSPA-LA (temperature, relative humidity, and liquid-phase saturation), model validation is documented in Sections 7.4 and 7.5. For other MSTHM output parameters (e.g., liquid-phase flux and evaporation rate), documentation in support of model confidence building is also supported by the analyses presented in Section 6.3.3. Because all of the MSTHM output parameters are interrelated (to varying degrees) it is useful to support confidence building for various parameters whether or not they are directly used in TSPA-LA or whether they support a FEP (see Section 6.5). The ensemble of MSTHM output parameters discussed in this report in reference to model validation is sufficient to build confidence in all aspects of the MSTHM that are useful to either TSPA-LA or to relevant FEPs.

For temperature and liquid-phase saturation, model confidence building is also supported in Section 7.3. As is shown in Table 1-1, all MSTHM output parameters used to support TSPA-LA are supported by model validation and by model confidence building, which are documented in this report.

Table 1-1.   List of Thermal-Hydrologic Parameters Predicted with the MSTHM

Thermal-Hydrologic Parameter	Drift-Scale Location	Used to Support TSPA-LA	Supported by Section(s)
Temperature	Near-field environment host rock (5 m above crown of drift)		7.3, 7.4
	Near-field environment host rock (mid-pillar at repository horizon)		7.3, 7.4
	Maximum lateral extent of boiling		7.3, 7.4
	Drift wall (perimeter average)	Yes	7.3, 7.4, 7.5, 7.7
	Drip shield (perimeter average)	Yes	7.3, 7.4, 7.5, 7.6, 7.7
	Drip shield (upper surface)		7.3, 7.4, 7.5
	Waste package (surface average)	Yes	7.3, 7.4, 7.5, 7.6, 7.7
	Invert (average)	Yes	7.3, 7.4, 7.5, 7.7
Relative humidity	Drift wall (perimeter average)		7.5
	Drip shield (perimeter average)		7.5
	Waste package	Yes	7.5, 7.7
	Invert (average)[a]	Yes	7.5, 7.7
Liquid-phase saturation (matrix)	Drift wall (perimeter average)		7.4, 7.5
	Drip shield (perimeter average)		
	Invert (average)	Yes	6.3.3, 7.3, 7.4, 7.5, 7.7

Table 1-1.   List of Thermal-Hydrologic Parameters Predicted with the MSTHM (Continued)

Thermal-Hydrologic Parameter	Drift-Scale Location	Used to Support TSPA-LA	Supported by Section(s)
Liquid-phase flux	Host rock (5 m above crown of drift)		
	Host rock (3 m above crown of drift)		
	Drift wall (upper surface)		
	Drift wall (lower surface below invert)		
	Drip shield (crown)		
	Drip shield (upper surface average)		
	Drip shield (lower side at the base)		
	Invert (average)[b]	Yes	6.3.3, 7.5, 7.7
Gas-phase air-mass fraction	Drip shield (perimeter average)		7.5
Gas-phase pressure	Drip shield (perimeter average)		
Capillary pressure	Drip shield (perimeter average)		
	Invert (average)		7.5
	Drift wall (crown, in matrix)		7.5
	Drift wall (crown, in fractures)		
Gas-phase (vapor) flux	Drift wall (perimeter average)		
Gas-phase (air) flux	Drift wall (perimeter average)		
Evaporation rate	Drip shield (crown)		
	Drip shield (perimeter total)		
	Drift wall (upper surface)		
	Drift wall (lower surface below invert)		
	Invert (total)[c]		6.3.3, 7.5

[a] The invert relative humidity is calculated by TSPA, using the MathCad spreadsheet described in Appendix XV, based on the MSTHM-predicted temperature and liquid-phase saturation in the invert.
[b] TSPA-LA only applies MSTHM result to the no-seep, no-condensation case.
[c] Directly related to liquid-phase saturation (see Section 6.3.3), which is validated in Section 7.5.

Appendix XIII presents a listing of data sources for figures and tables in this report. This includes the source DTN, the associated file name, and the software necessary to access the data. An example of accessing temperature and saturation time history data generated from the MSTHAC v7.0 (Section 3.1.5) using XTOOL v10.1 (Section 3.1.4) is presented in the flow chart in Figure XV-1 in Appendix XV. Note that in accessing the data, it is necessary to download from the YMP server using the Windows Operating System, and then to use File Transfer Protocol (FTP) to transfer the files to a Sun Workstation with the Sun OS 5.8 operating system with XTOOL v10.1 software installed.
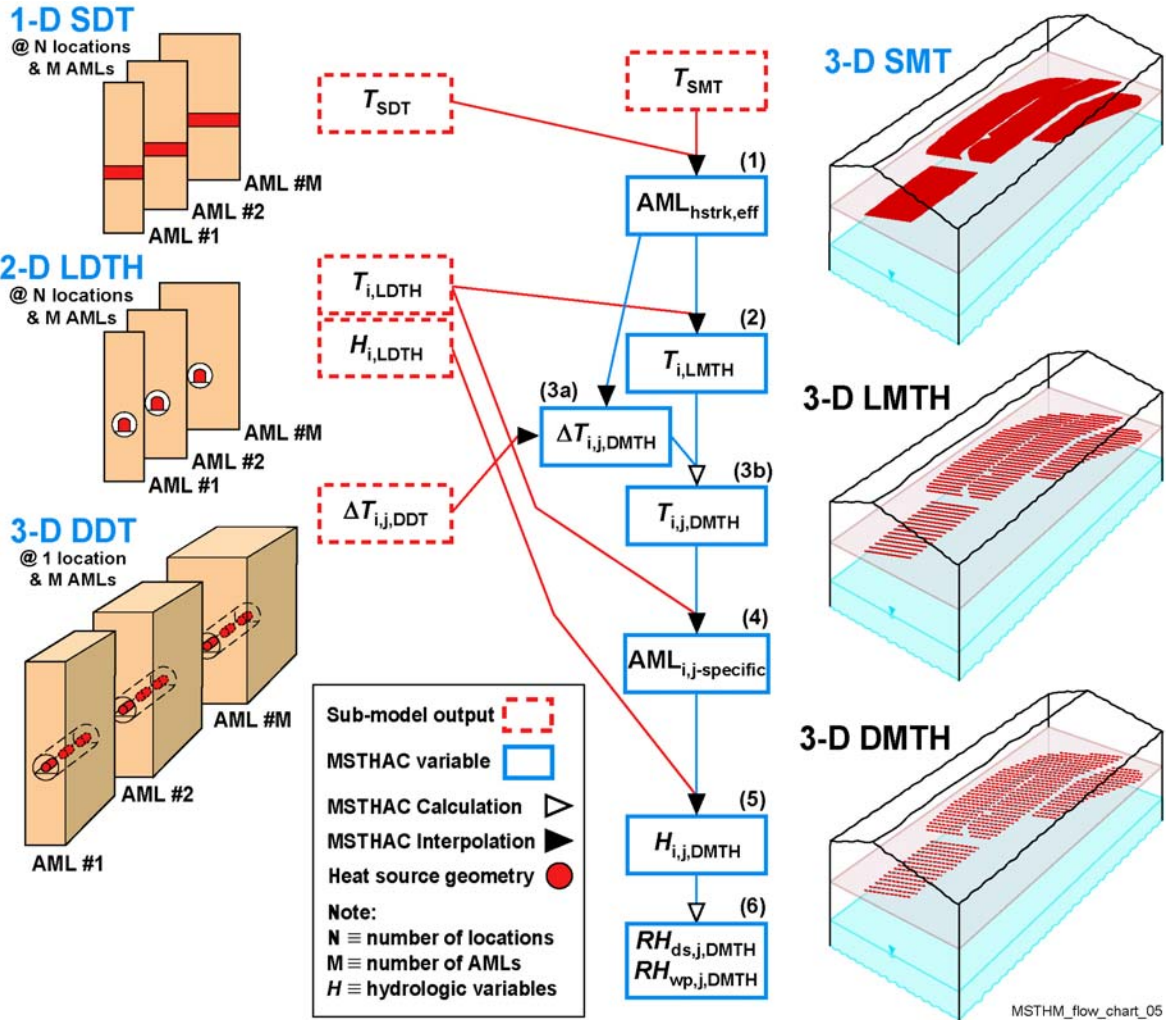
NOTE: SDT-, LDTH-, and DDT-submodel calculations are run with the NUFT code for different AMLs (left side). The SMT-submodel calculation is also run with the NUFT code. The SMT, LMTH and DMTH models are the series of 3-D mountain-scale models of increasing complexity (right side). The MSTHAC code assembles the results of the NUFT submodels in six stages, constructing intermediate parameters ($AML_{hstrk,eff}$, $\Delta T_{i,j,DMTH}$, $T_{i,LMTH}$ and $AML_{i,j\text{-specific}}$) and final MSTHM parameters ($T_{i,j,DMTH}$, $RH_{i,j,DMTH}$ and $H_{i,j,DMTH}$) from NUFT submodel output (T_{SDT}, T_{SMT}, $T_{i,LDTH}$, $H_{i,LDTH}$ and $\Delta T_{i,j,DDT}$). The submodel and model types are defined in Table 1-2. The parameters are defined in Table 1-3. Note that the four submodels of the MSTHM are the SDT, LDTH, DDT, and SMT submodels. The LMTH model is an intermediate result of the MSTHM and the DMTH model is the final result of the MSTHM.

Figure 1-1. Six Stage Flow Chart Diagram of the MSTHM

Table 1-2.   Submodel and Model Types Used in the MSTHM

Submodel / Model Type	Description
MSTHM	Multiscale thermohydrologic model
SMT	Smeared-heat-source, mountain-scale, thermal-conduction: three-dimensional NUFT submodel
SDT	Smeared-heat-source, drift-scale, thermal-conduction: one-dimensional NUFT submodel
LDTH	Line-averaged-heat-source, drift-scale, thermal-hydrologic: two-dimensional NUFT submodel
DDT	Discrete-heat-source, drift-scale, thermal-conduction: three-dimensional NUFT submodel
LMTH	Line-averaged-heat-source, mountain-scale, thermal-hydrologic model: three-dimensional MSTHM intermediate result
DMTH	Discrete-heat-source, mountain-scale, thermal-hydrologic model: three-dimensional MSTHM final result
D/LMTH	Discrete/line-averaged-heat-source, mountain-scale, thermal-hydrologic model: the nested-mesh monolithic three-dimensional NUFT model used in the MSTHM validation (Section 7.5)

NOTE: The four submodels of the MSTHM are the SDT, LDTH, DDT, and SMT submodels. The LMTH model is an intermediate result of the MSTHM and the DMTH model is the final result of the MSTHM.

Table 1-3.   Parameters Used in the MSTHM Methodology

Parameter Name	Description	Stage (see Figure 1-1)
T_{SDT}	Host-rock temperature output from the one-dimensional SDT submodel.	Stage 1 (NUFT output)
T_{SMT}	Host-rock temperature output from the three-dimensional mountain-scale SMT submodel.	Stage 1 (NUFT output)
$\Delta T_{i,j,DDT}$	Temperature deviation of individual waste package from averaged drift-wall temperature for reference location i and waste package j.	Stage 3a (NUFT output)
$\Delta T_{i,j,DMTH}$	Temperature deviation of individual waste package from averaged drift-wall temperature for reference location i and waste package j, adjusting for three-dimensional mountain-scale heat loss.	Stages 3a, 3b
$T_{i,LDTH}$	Temperature output from two-dimensional LDTH drift-scale submodel.	Stages 2, 4 (NUFT output)
$T_{i,LMTH}$	Temperature for reference location i adjusted for the three-dimensional mountain scale heat loss.	Stages 2, 3b
$T_{i,j,DMTH}$	Temperature for reference location i and waste package j adjusted for the three-dimensional mountain-scale heat loss and for waste package variation.	Stages 3b, 4
$H_{i,LDTH}$	Set of hydrologic parameters for reference location i. This set includes $RH_{i,LDTH}$ and $S_{i,LDTH}$.	Stage 5 (NUFT output)
$H_{i,j,DMTH}$	Set of hydrologic parameters for reference location i and waste package j adjusted for three-dimensional mountain-scale heat loss and for waste package variation. This set includes $RH_{i,j,DMTH}$ and $S_{i,j,DMTH}$.	Stages 5, 6
$RH_{i,j,DMTH}$	Relative humidity of the reference location i and waste package j for the DMTH model.	Stage 5, 6
$S_{i,j,DMTH}$	Liquid-phase saturation of the reference location i and waste package j for the DMTH model.	Stage 5, 6
$T_{dw,cav}$ $RH_{dw,cav}$	Perimeter averages of surfaces adjoining the open cavity outside of the drip shield only for the DMTH model.	Stage 6

Table 1-3.   Parameters Used in the MSTHM Methodology (Continued)

Parameter Name	Description	Stage (see Figure 1-1)
AML$_{hstrk,eff}$	A time-varying parameter that incorporates the influence of three-dimensional mountain-scale heat-loss (determined by the combined use of the SMT and SDT submodels) onto the LDTH submodel results.	Stages 1, 2, 3a
AML$_{i,j-specific}$	A time-varying parameter that combines the influences of waste package-to-waste package variation (determined by the DDT submodels) and three-dimensional mountain-scale heat loss (represented by the LMTH-modeled temperatures), resulting in DMTH-model results for reference location i and waste package j.	Stages 4, 5
P_{sat}	Saturated vapor pressure, which is a function of temperature.	Stage 6

NOTE: Subscript i refers to a reference location in the drift (or host rock); i = dw refers to drift wall, i = ds refers to drip shield, i = in refers to invert, and i = wp refers to waste package. Subscript j refers to the waste package type, such as j = DHLW, 21-PWR CSNF, or 44-BWR CSNF. The MSTHM calculation sequence is described in detail in Section 6.2.4.

2. QUALITY ASSURANCE

The Quality Assurance program applies to the development of this document (BSC 2005 [DIRS 173377], Section 8.1). This document was prepared in accordance with *Technical Work Plan for: Near-Field Environment and Transport In-Drift Heat and Mass Transfer Model and Analysis Reports Integration* (BSC 2005 [DIRS 173377]), which directs the work identified in work package ARTM02. The technical work plan (TWP) was prepared in accordance with LP-2.29Q-BSC, *Planning for Science Activities*. There were no variances from the planned activities. The methods used to control the electronic management of data are identified in the TWP (BSC 2005 [DIRS 173377], Section 8.4) and were implemented without variance. As directed in the TWP, this document was prepared in accordance with LP-SIII.10Q-BSC, *Models*; LP-SI.11Q-BSC, *Software Management*; LP-3.15Q-BSC, *Managing Technical Product Inputs*; and reviewed in accordance with LP-2.14Q-BSC, *Document Review*. As needed, unqualified project data is qualified in this document in accordance with LP-SIII.2Q-BSC, *Qualification of Unqualified Data*.

The work scope described in this report has been determined to be subject to the U.S. Department of Energy's (DOE's) *Quality Assurance Requirements and Description* (DOE 2004 [DIRS 171539]). The work scope of this report involves conducting investigations or analyses of Engineered Barrier System components contained in *Q-List* (BSC 2005 [DIRS 171190]). Safety Categories for the components are provided in Table 2-1.

Table 2-1. Engineered Barrier System Components Addressed in This Report, Listed with Corresponding Safety Category (SC) Criteria

Engineered Barrier System Component	Safety Category
Drip Shield	SC
Drift Invert (Steel)	SC
Emplacement Drift Excavated Opening	SC
DOE and Commercial Waste Packages	SC

Source: BSC 2005 [DIRS 171190].

Furthermore, this report provides analysis of model results supporting performance assessment activities for the Total Systems Performance Assessment for License Application.

This report documents the determination of in-drift thermal-hydrologic conditions that are required by TSPA-LA. It provides in-drift thermal-hydrologic parameters that are important to the performance of the engineered barriers classified in *Q-List* (BSC 2005 [DIRS 171190]) as "Safety Category" because they are important to waste isolation as defined in AP-2.22Q, *Classification Analyses and Maintenance of the Q-List*. The results of this report are important to the demonstration of compliance with the postclosure performance objectives prescribed in 10 CFR 63.113.

INTENTIONALLY LEFT BLANK

3. USE OF SOFTWARE

A complete list of the qualified software and the associated software tracking number is given in Table 3-1.

Table 3-1. Software Used

Software Name and Version	Software Tracking Number	Software Qualification Status	Computers Used to Run Software (DOE Property Number)	Sections Where Software Output Is Used[a]
NUFT v3.0s	10088-3.0s-02	Qualified	6549273, 6549266, 6700902, 6290847, 6426406, 6290830, 6877864, 6481320, 6290823, 6813251, 6877857, 6524867, 6878182, 6575968, 6274861, 6813244, 6877840, 6549297	6.2, 6.3, 6.4, 7.3, 7.5, 8.3
NUFT v3.0.1s	10130-3.0.1s-01	Qualified	6700902, 6426406, 6290830	7.4, 7.5
RADPRO v4.0	10204-4.0-00	Qualified	6877840, 6878182	6.2, 6.3, 8.3
XTOOL v10.1	10208-10.1-00	Qualified	6496843	6.2, 6.3, 6.4, 7.3, 7.4, 7.5
MSTHAC v7.0	10419-7.0-00	Qualified	6813251, 6290830, 6878182	6.2, 6.3, 7.5, 8.3
readsUnits v1.0	10602-1.0-00	Qualified	6371317	6.2, 6.3, 7.4, 7.5, 8.3
YMESH v1.54	10172-1.54-00	Qualified	6813251, 6813244, 6877864, 6878182	6.2, 6.3, 7.4, 7.5, 8.3
boundary_conditions v1.0	11042-1.0-00	Qualified	6877840	6.3, 7.4, 8.3
heatgen_ventTable_emplace v1.0	11039-1.0-00	Qualified	6813251	6.3, 8.3
rme6 v1.2	10617-1.2-00	Qualified	6813251	6.3, 8.3
xw v1.0	11035-1.0-00	Qualified	6813251	6.3, 8.3
colCen v1.0	11043-1.0-00	Qualified	6877840	6.3, 8.3
repository_percolation_calculator v1.0	11041-1.0-00	Qualified	6813251	6.3, 8.3
extractBlocks_EXT v1.0	11040-1.0-00	Qualified	6877857	6.3, 8.3
Chimney_interpolate v1.0	11038-1.0-00	Qualified	6813251, 6290830	6.3, 8.3
reformat_EXT_to_TSPA v1.0	11061-1.0-00	Qualified	6813251, 6290830, 6878182	6.3, 8.3

[a] These are the sections that directly or indirectly utilize the output from the listed software.

3.1 QUALIFIED SOFTWARE

The software described in this section is used in the data-flow diagrams (Figures 6-1 and 6-2) of Section 6. The computer software was qualified under procedure AP-SI.2Q, *Qualification of Level A Software*, before procedure LP-SI.11Q-BSC became effective and is therefore part of the established baseline in accordance with Section 2.0 of LP-SI.11Q-BSC. Because many of these items have to process or produce files consistent with NUFT formats and have been validated for this use, they are the only software appropriate for their tasks.

3.1.1   NUFT v3.0s

NUFT v3.0s (NUFT V3.0s, STN: 10088-3.0s-02 [DIRS 164541]) is baselined as qualified software per LP-SI.11Q-BSC, *Software Management*, and is used to conduct all of the submodel calculations required by the MSTHM. NUFT v3.0s was obtained from software configuration management and run on Sun workstations with the Sun OS 5.8 operating system. NUFT v3.0s was selected because it solves the governing equations of the mathematical model (Section 6.2), is supported by a suite of special-purpose software that completes implementation of the MSTHM, and imposes no limitations on outputs. As discussed below, the use of NUFT v3.0s for the submodel calculations was within the documented validation range of the software. Therefore, the use of this software was consistent with its intended use.

NUFT v3.0s (and v3.0.1s) is a general-purpose code for simulating mass and heat transport in fractured porous media. Because NUFT is based on the conservation of mass and energy, it is valid for any such calculation, provided the mass- and heat-transport parameters are used within their validation ranges. In other words, what limits the range of validation of NUFT are the mass- and heat-transport-phenomena-related parameters (or constitutive properties), such as thermal conductivity, which affects heat conduction, and permeability, which affects gas- and liquid-phase flow. Thus, if thermal conductivity and permeability are applicable for the range of predicted temperatures, the software (NUFT) is valid for this range. The validation range and limitation of applicability of NUFT is determined by the validation studies conducted in conjunction with the Drift Scale Test (Section 7.4). Comparisons of the NUFT-predicted temperatures with the measured temperatures in those tests show that NUFT meets the validation requirement described in *Technical Work Plan for: Near-Field Environment and Transport In-Drift Heat and Mass Transfer Model and Analysis Reports Integration* (BSC 2005 [DIRS 173377]). Because measured temperatures in the Drift Scale Test are as great as 280°C in the rock, the validation range of NUFT is up to 280°C in the host rock. In Section 6.3.4, which summarizes the range of thermal-hydrologic conditions predicted for the TSPA-LA, it is shown that the maximum peak drift-wall and waste package temperatures are 175.2°C and 203.1°C, respectively (Table 6.3-38). Therefore, NUFT was applied within its validation limits for the TSPA-LA.

3.1.2   NUFT v3.0.1s

NUFT v3.0.1s (NUFT V3.0.1s, STN: 10130-3.0.1s-01 [DIRS 166636]) is baselined as qualified software per LP-SI.11Q-BSC, and is used to conduct all of the nested-mesh model calculations in the model validation exercises for the MSTHM. NUFT v3.0.1s was obtained from software configuration management and run on Sun workstations with the Sun OS 5.8 operating system. NUFT v3.0.1s was selected because nested meshes are a feature of this newer version. Because its use was within the documented validation range of the software (see Section 3.1.1), it was consistent with its intended use.

3.1.3   RADPRO v4.0

RADPRO v4.0 (RADPRO V4.0, STN: 10204-4.0-00 [DIRS 164273]) is baselined as qualified software per LP-SI.11Q-BSC, and was obtained from software configuration management and run on a Sun workstation with a SunOS 5.8 (Solaris 8) operating system. RADPRO v4.0 was

selected because it calculates the radiative heat transfer coefficients in the emplacement drift in accordance with Equation 10 of Section 6.2.3.3 without limitations on its output. Its use was consistent with its intended use and within the documented validation range of the software. Because this software is only used to conduct simple arithmetic functions, it is not applicable to identify validation ranges or limitations of use.

3.1.4   XTOOL v10.1

XTOOL v10.1 (XTOOL V10.1, STN: 10208-10.1-00 [DIRS 148638]) is baselined as a qualified software routine per LP-SI.11Q-BSC, and was obtained from software configuration management and run on a Sun workstation with a SunOS 5.6.1 operating system. XTOOL v10.1 is used to generate graphical representations of the results given in the NUFT and MSTHAC v7.0 time-history files (which are files with the suffix: *.ext). XTOOL v10.1 is the only appropriate software for this task. Because this software is only used to generate graphical displays of data, it is not applicable to identify validation ranges or limitations of use.

3.1.5   MSTHAC v7.0

MSTHAC v7.0 (MSTHAC V7.0, STN: 10419-7.0-00 [DIRS 164274]) is baselined as qualified software per LP-SI.11Q-BSC, and was obtained from software configuration management and run on a Sun workstation with a SunOS 5.8 (Solaris 8) operating system. MSTHAC v7.0 integrates the results of NUFT submodel calculations to predict the multiscale thermal-hydrologic conditions in the emplacement drifts and adjoining host rock throughout the repository area. MSTHAC v7.0 is the only appropriate software for this task. Because MSTHAC integrates the results of NUFT submodel calculations, its validation range is the same as that described for NUFT v3.0s (Section 3.1.1).

3.1.6   readsUnits v1.0

Software routine readsUnits v1.0 (readsUnits V1.0, STN: 10602-1.0-00 [DIRS 164542]) is baselined as qualified software per LP-SI.11Q-BSC, and was obtained from software configuration management and run on a Sun workstation with a SunOS 5.5.1 operating system. This code reads YMESH-generated data describing a stratigraphic column and generates comment lines for NUFT input files that summarize the thicknesses of each of the hydrostratigraphic units (also called UZ model layers) in that column. Software routine readsUnits v1.0 is the only appropriate software for this task. Because this software is only used to generate comment lines in the NUFT input files, it does not influence any model predictions. Therefore, it is not applicable to identify validation ranges or limitations of use.

3.1.7   YMESH v1.54

YMESH v1.54 (YMESH v1.54, STN: 10172-1.54-00 [DIRS 163894]) is baselined as qualified software per LP-SI.11Q-BSC, and was obtained from software configuration management and run on a Sun workstation with a SunOS 5.8 (Solaris 8) operating system. YMESH v1.54 is used to generate the thicknesses of the hydrostratigraphic units (also called the UZ model layers) in the various MSTHM submodels based upon the grids from *Development of Numerical Grids for UZ Flow and Transport Modeling* (BSC 2004 [DIRS 169855]). YMESH v1.54 is the only appropriate software for this task. Because this software is only used to generate numerical grids

on the basis of geometric relationships, it is not applicable to identify validation ranges or limitations of use.

3.1.8   boundary_conditions v1.0

The software routine boundary_conditions v1.0 (boundary_conditions V 1.0, STN: 11042-1.0-00 [DIRS 164275]) is baselined as qualified software per LP-SI.11Q-BSC, and was obtained from software configuration management and run on a Sun workstation with a SunOS 5.8 (Solaris 8) operating system.   The purpose of this routine is to generate upper and lower boundary conditions for the LDTH, SMT, and SDT submodels of the MSTHM (Section 6.2), as well as for other models such as the three-dimensional thermal-hydrologic model for the Drift Scale Test (DST) (Section 7.4).   The software routine boundary_conditions v1.0 is the only appropriate software for this task.   Because this software is only used to conduct simple interpolations of data, it is not applicable to identify validation ranges or limitations of use.

3.1.9   heatgen_ventTable_emplace v1.0

The software routine heatgen_ventTable_emplace v1.0 (heatgen_ventTable_emplace V1.0, STN: 11039-1.0-00 [DIRS 164276]) is baselined as qualified software per LP-SI.11Q-BSC, and was obtained from software configuration management and run on a Sun workstation with a SunOS 5.8 (Solaris 8) operating system. The software routine heatgen_ventTable_emplace v1.0 modifies a heat-generation-rate-versus-time table in two ways.   First, it can "age" the heat-generation table by adding a specified number of years to the time entries. Second, it can account for the heat-removal efficiency of ventilation by multiplying the heat-generation-rate values by a specified fraction during the specified ventilation period.   The software routine heatgen_ventTable_emplace v1.0 also can incorporate the dependence of the heat-removal efficiency table on distance (along the emplacement drift) from the ventilation inlet.   The software routine heatgen_ventTable_emplace v1.0 is the only appropriate software for this task. Because this software is only used to conduct simple arithmetic functions, it is not applicable to identify validation ranges or limitations of use.

3.1.10   rme6 v1.2

The software routine rme6 v1.2 (rme6 v1.2, STN: 10617-1.2-00 [DIRS 163892]) is baselined as qualified software per LP-SI.11Q-BSC, and was obtained from software configuration management and run on a Sun workstation with a SunOS 5.8 (Solaris 8) operating system. This code converts the grid from *Development of Numerical Grids for UZ Flow and Transport Modeling* (BSC 2004 [DIRS 169855]) to a format that is readable by YMESH v1.54 (Section 3.1.7).   The software routine rme6 v1.2 is the only appropriate software for this task. Because this software is only used to reformat input data for YMESH v1.54, it is not applicable to identify validation ranges or limitations of use.

3.1.11   xw v1.0

The software routine xw v1.0 (xw V1.0, STN: 11035-1.0-00 [DIRS 164278]) is baselined as qualified software per LP-SI.11Q-BSC, and was obtained from software configuration management and run on a Sun workstation with a SunOS 5.8 (Solaris 8) operating system. The software routine xw v1.0 extends the grid from the three-dimensional unsaturated zone (UZ)

flow model in the horizontal direction for the purpose of building mountain-scale submodels that extend laterally beyond the grid of the three-dimensional UZ flow model. The software routine xw v1.0 is the only appropriate software for this task. Because this software is only used to horizontally extend the grid of the three-dimensional UZ flow model, it is not applicable to identify validation ranges or limitations of use.

3.1.12   colCen v1.0

The software routine colCen v1.0 (colCen V1.0, STN: 11043-1.0-00 [DIRS 164279]) is baselined as qualified software per LP-SI.11Q-BSC, and was obtained from software configuration management and was run on a Sun workstation with a SunOS 5.8 (Solaris 8) operating system. The purpose of colCen v1.0 grid is to determine the gridblock column in the three-dimensional UZ flow model in which a given gridblock column in a MSTHM submodel resides. The software routine colCen v1.0 is the only appropriate software for this task. Because this software is only used to identify the UZ flow-model gridblock column in which a MSTHM submodel resides, it is not applicable to identify validation ranges or limitations of use.

3.1.13   repository_percolation_calculator v1.0

The software routine repository_percolation_calculator v1.0 (repository_percolation_calculator V1.0, STN: 11041-1.0-00 [DIRS 164280]) is baselined as qualified software per LP-SI.11Q-BSC, and was obtained from software configuration management and run on a Sun workstation with a SunOS 5.8 (Solaris 8) operating system.   The purpose of repository_percolation_calculator v1.0 is to determine the value of percolation flux for each of the LDTH submodels based on the percolation flux map from the three-dimensional UZ flow model.   The software routine repository_percolation_calculator v1.0 is the only appropriate software for this task. Because this software is only used to conduct simple arithmetic functions, it is not applicable to identify validation ranges or limitations of use.

3.1.14   extractBlocks_EXT v1.0

The software routine extractBlocks_EXT v1.0 (extractBlocks_EXT V1.0, STN: 11040-1.0-00 [DIRS 164281]) is baselined as qualified software per LP-SI.11Q-BSC, and was obtained from software configuration management and run on a Sun workstation with a SunOS 5.8 (Solaris 8) operating system. The purpose of extractBlocks_EXT is to determine the effective thermal conductivity for the gridblocks in the drift cavity of an LDTH submodel based on a correlation accounting for the influence of natural convection (Francis et al. 2003 [DIRS 164602], Table 6). The software routine extractBlocks_EXT v1.0 is the only appropriate software for this task. Because this software is only used to conduct simple arithmetic functions, it is not applicable to identify validation ranges or limitations of use.

3.1.15   Chimney_interpolate v1.0

The software routine Chimney_interpolate v1.0 (Chimney_interpolate V1.0, STN: 11038-1.0-00 [DIRS 164271]) is baselined as qualified software per LP-SI.11Q-BSC, and was obtained from software configuration management and run on a Sun workstation with a SunOS 5.8 (Solaris 8) operating system. The purpose of Chimney_interpolate is to create a set of virtual SDT and LDTH "chimney" submodels from the 108 "real" chimney submodels (see Appendix VII) for

more details). The virtual chimney submodels are an input to the MSTHAC v7.0 micro-abstraction process (see Appendix VII for more details). The software routine Chimney_interpolate v1.0 is the only appropriate software for this task. Because this software is only used to conduct simple arithmetic functions, it is not applicable to identify validation ranges or limitations of use.

3.1.16   reformat_EXT_to_TSPA v1.0

The software routine reformat_EXT_to_TSPA v1.0 (reformat_EXT_to_TSPA V1.0, STN: 11061-1.0-00 [DIRS 164272]) is baselined as qualified software per LP-SI.11Q-BSC, and was obtained from software configuration management and run on a Sun workstation with a SunOS 5.8 (Solaris 8) operating system. The purpose of reformat_EXT_to_TSPA v1.0 is to post-process the micro-abstraction data produced by MSTHAC V7.0 (see Appendix VII for more details). The processing includes finding the typical waste package and location from a set of locations forming a bin and writing an output file in a format specified by the TSPA-LA organization. The software routine reformat_EXT_to_TSPA v1.0 is the only appropriate software for this task. Because this software is only used to reformat MSTHM output data, it is not applicable to identify validation ranges or limitations of use.

3.2   OTHER SOFTWARE

Commercial off-the-shelf software was used in the creation of tables and figures shown in this document as well as some data processing. This software was run on a Sun workstation with a SunOS 5.8 (Solaris 8) operating system, except Mathcad 11.2a, Excel 2003, Adobe Illustrator v8.0, and Microsoft Windows 2000 and 2003 operating systems, as described below.

The following discusses the use of this software on the SunOS 5.8 (Solaris 8) operating system. Figures presented in this report, with the exception of those in Appendices X, XII, and XV, were prepared using MatLab v6.1.0450 release 12.1. The figures can be divided into the following types: line plots showing time histories, contour plots showing the variation in some property at a particular point in time for a cross sectional area of interest, plots showing material properties for the repository plan view, and schematic drawings showing repository design parameters.

Contour plots of MSTHM output parameters (Figures 6.3-5, 6.3-6, and 6.3-7) were created using Tecplot v9.2-0-3 (09-16-2002).

Plots showing material properties at the repository horizon (Figure 6.3-1) or the locations of MSTHM submodels (Figures 4-1 and 6.2-3) for the repository plan view were created using MATLAB v6.1.0.450 release 12.1. MATLAB was used to create line plots of time histories of MSTHM output parameters (Figures 6.3-37 through 6.3-49; Figures 6.3-60, 6.3-61, 6.3-67, 6.3-68, and 6.3-69). MATLAB was used to generate the grid-block-weighted averages for the D/LMTH model in Section 7.5 (Figures 7.5-2 through 7.5-8). MATLAB was used to create the line plots of the histories of temperature, relative humidity, and liquid-phase saturation differences between the MSTHM and the D/LMTH model and the ranges of those parameters resulting from parametric uncertainty (Figures 7.5-9 through 7.5-14).

Mathcad 11.2a Professional was used to perform the calculations in Appendices X, XII and XV for developing the hydrologic properties of the invert; for comparing percolation fluxes, and for

prediction of RH in the invert, respectively. MathCad 11.2a Professional was used on the Microsoft Windows 2000 operating system.

Schematic drawings showing repository design information were created using Adobe Illustrator v8.0 on the Microsoft Windows 2003 operating system.

Microsoft Excel 2003 was used on the Microsoft Windows 2003 operating system to process data for the development of chimney percolation data as detailed in Appendix I.

Numerical results from the use of commercial off-the-shelf software in this report are not dependent on the software used. The documentation of each such use includes sufficient detail to allow an independent reviewer to reproduce or verify the results by visual inspection or hand calculation.

INTENTIONALLY LEFT BLANK

4. INPUTS

4.1 DIRECT INPUTS

Data, parameters, design information, and other model/analyses inputs are compiled and presented in Table 4.1-1. There are seven major sections of the table: (1) geometry of the engineered system, (2) geometry of the natural system, (3) properties of the engineered system inside the emplacement drift, (4) properties of the natural system, (5) boundary conditions of the natural system, (6) distribution of percolation flux just below the base of the PTn unit, and (7) waste package heat-generation data and ventilation heat-removal efficiency. The seven sections are further delineated to distinguish separate data, design information, and parameters. The majority of the information compiled in Table 4.1-1, which is direct input, falls into the parameter and design information categories.

In Table 4.1-1, most of the direct inputs to this report are traced to current qualified project data or to qualified data that have been superseded with small changes. One exception is the emissivity range for rock, which is from Incropera and DeWitt's (1996 [DIRS 108184]) advanced textbook for heat and mass transfer. Their range of 0.88 to 0.95 is adapted from sources for hemispherical emissivity of rock at 300 K and is corroborated by handbook values (Knudsen et al. 1984 [DIRS 170057], pp. 10-51 to 10-52, Table 10-17) for normal emissivity of rough silica and rough fused quartz, which range from 0.80 to 0.93. Therefore, the information is qualified for its use as emissivities of drift wall and crushed tuff in the MSTHM calculations.

The design of the repository continued to evolve during and after the calculations with the MSTHM. The effects of small changes in the design are discussed in Sections 4.1.2.1 through 4.1.2.8

4.1.1 Data, Parameters, and Parameter Uncertainty

The data and parameters required as input for the development of parameter values used in the models/analyses documented in this report are summarized in Table 4.1-1. The following sections of the table include information about parameters: geometry of natural system, invert thermal and hydrologic properties, hydrologic properties of all hydrostratigraphic units (also called UZ model layers), bulk thermal properties of the UZ model layers, and percolation flux below the base of the PTn unit. All of these data were obtained from studies specific to the Yucca Mountain site and are therefore appropriate for use in the MSTHM calculations reported in Section 6.3.

Sections 6.3.2, 6.3.4, and 6.3.0 provide analyses of the impact of uncertainty of key natural system parameters. Sections 6.3.11 and 6.3.12 provide analyses of the impact of uncertainty of key engineered system parameters.

4.1.2 Design Information

Other inputs required for the development of parameter values used in the models/analyses documented in this report take the form of design information, often from Interface Exchange Drawings (IEDs). The following sections of Table 4.1-1 include design information: geometry of the engineered system, waste package thermal properties, drip shield thermal properties,

drift-wall emissivity and waste package heat generation and ventilation heat-removal efficiency. Information from IEDs is appropriate for use in the MSTHM calculations reported in Section 6.3.

Table 4.1-1.   Summary of Input Data and Information Required by the MSTHM

Model Input	Value	Source
Geometry of the Engineered System: Design Information		
Repository emplacement-drift layout (elevations and end-point coordinates for each emplacement drift)	See IED	BSC 2003 [DIRS 161727]
Drift spacing	81 m	BSC 2004 [DIRS 168489], Table 1
End-to-end waste package spacing	0.1 m	BSC 2004 [DIRS 168489], Table 1
Drift diameter	5.5 m	BSC 2004 [DIRS 168489], Table 1
Location of 21-PWR AP WP centerline above invert	1018 mm	BSC 2004 [DIRS 167040]
Invert height from bottom of drift	0.806 m	BSC 2003 [DIRS 162444]
21-PWR AP WP length	5.165 m	BSC 2003 [DIRS 165406], Table 1
21-PWR AP WP diameter	1.644 m	BSC 2003 [DIRS 165406], Table 1
21-PWR CR WP diameter	1.644 m	BSC 2003 [DIRS 165406], Table 1
21-PWR AP WP inner-vessel thickness	0.0508 m	BSC 2005 [DIRS 173501], Table 1
21-PWR AP WP outer-barrier thickness	0.020 m	BSC 2005 [DIRS 173501], Table 1
Nominal quantity of 21-PWR AP waste packages in LA-design inventory	4299	BSC 2005 [DIRS 173501], Table 13
Nominal quantity of 21-PWR CR waste packages in LA-design inventory	95	BSC 2005 [DIRS 173501], Table 13
44-BWR WP length	5.165 m	BSC 2003 [DIRS 165406], Table 1
44-BWR WP diameter	1.674 m	BSC 2003 [DIRS 165406], Table 1
44-BWR WP inner-vessel thickness	0.0508 m	BSC 2005 [DIRS 173501], Table 1
44-BWR WP outer-barrier thickness	0.020 m	BSC 2005 [DIRS 173501], Table 1
Nominal quantity of 44-BWR AP waste packages in LA-design inventory	2831	BSC 2005 [DIRS 173501], Table 13
5 DHLW/DOE SNF-LONG WP length	5.217 m	BSC 2003 [DIRS 165406], Table 1
5 DHLW/DOE SNF-LONG WP diameter	2.110 m	BSC 2003 [DIRS 165406], Table 1
5 DHLW/DOE SNF-LONG WP inner-vessel thickness	0.0508 m	BSC 2005 [DIRS 173501], Table 1
5 DHLW/DOE SNF-LONG WP outer-barrier thickness	0.0254 m	BSC 2005 [DIRS 173501], Table 1
Nominal quantity of 5 DHLW/DOE SNF-LONG waste packages in LA-design inventory	1406	BSC 2005 [DIRS 173501] Table 13
5 DHLW/DOE SNF-SHORT WP length	3.590 m	BSC 2003 [DIRS 165406], Table 1
5 DHLW/DOE SNF-SHORT WP diameter	2.110 m	BSC 2003 [DIRS 165406], Table 1
5 DHLW/DOE SNF-SHORT WP inner-vessel thickness	0.0508 m	BSC 2005 [DIRS 173501], Table 1
5 DHLW/DOE SNF-SHORT WP outer-barrier thickness	0.0254 m	BSC 2005 [DIRS 173501], Table 1
Nominal quantity of 5 DHLW/DOE SNF-SHORT waste packages in LA-design inventory	1147	BSC 2005 [DIRS 173501], Table 13
Drip-shield length	6.105 m	BSC 2003 [DIRS 171024], Sheet 2
Drip-shield width	2.512 m	BSC 2003 [DIRS 171024], Sheet 2

Table 4.1-1. Summary of Input Data and Information Required by the MSTHM (Continued)

Model Input	Value	Source
Drip-shield thickness (plate-1 or plate-2)	0.015 m	BSC 2005 [DIRS 173303], Table 5
Intersection of drip-shield plate-1 with drip-shield plate-2 from base/top of invert	1875 mm	BSC 2003 [DIRS 171024], Sheet 2
Total nominal quantity of waste package in LA-design inventory	11,184	BSC 2005 [DIRS 173501], Table 13
Geometry of Natural System: Parameters		
Grid of three-dimensional Unsaturated-Zone Flow and Transport Model: element/connection file	File: Grid_LA_3D.mesh	DTN: LB03023DKMGRID.001 [DIRS 162354]
Grid of three-dimensional Unsaturated-Zone Flow and Transport Model: vertices file	File: grid2002.grd	DTN: LB03023DKMGRID.001 [DIRS 162354]
Properties of the Engineered System		
Invert Thermal and Hydrologic Properties: Parameters		
Intragranular permeability (tswM5, tsw35 matrix continuum for mean infiltration-flux property set)	4.48×10^{-18} m^2	DTN: LB0208UZDSCPMI.002 [DIRS 161243], File: drift-scale calibrated properties for mean infiltration2.xls; Worksheet: Drift-scale Cal. Hydro Props.
Porosity of crushed-tuff grains (tswM5, tsw35 matrix continuum for mean infiltration-flux property set)	0.131	DTN: LB0208UZDSCPMI.002 [DIRS 161243], File: drift-scale calibrated properties for mean infiltration2.xls; Worksheet: Drift-scale Cal. Hydro Props.
Intragranular van Genuchten α (tswM5, tsw35 matrix continuum for mean infiltration-flux property set)	1.08×10^{-5} 1/Pa	DTN: LB0208UZDSCPMI.002 [DIRS 161243], File: drift-scale calibrated properties for mean infiltration2.xls; Worksheet: Drift-scale Cal. Hydro Props.
Intragranular van Genuchten m (tswM5, tsw35 matrix continuum for mean infiltration-flux property set)	0.216	DTN: LB0208UZDSCPMI.002 [DIRS 161243], File: drift-scale calibrated properties for mean infiltration2.xls; Worksheet: Drift-scale Cal. Hydro Props.
Intragranular residual saturation (tswM5, tsw35 matrix continuum for mean infiltration-flux property set)	0.12	DTN: LB0208UZDSCPMI.002 [DIRS 161243], File: drift-scale calibrated properties for mean infiltration2.xls; Worksheet: Drift-scale Cal. Hydro Props.
Invert Thermal and Hydrologic Properties: Data		
Bulk Density of 4-10 crushed tuff	See Table IV-8 in Appendix IV	DTN: GS020183351030.001 [DIRS 163107], Table S02025_001; Rows 321 through 370
Specific heat of 4-10 crushed tuff	See Table IV-9 in Appendix IV	DTN: GS000483351030.003 [DIRS 152932], Table S01076_001; Rows 1 through 11
Thermal conductivity of 4-10 crushed tuff	See Table IV-9 in Appendix IV	DTN: GS000483351030.003 [DIRS 152932], Table S01076_001; Rows 1 through 11x
Emissivity (upper invert surface)	0.88 to 0.95	Incropera and DeWitt 1996 [DIRS 108184], Table A.11 for Rocks
Range in maximum void ratio for United Soils Classification type SP, which are poorly graded sands and gravelly sands.	0.67 to 0.94	Hilf 1975 [DIRS 169699], Table 7.3, p. 257
Waste Package Thermal Properties: Design Information		
Weight of 21-PWR AP WP	43,000 kg	BSC 2003 [DIRS 165406], Table 1
Weight of 44-BWR WP	43,000 kg	BSC 2003 [DIRS 165406], Table 1
Weight of 5 DHLW/DOE SNF-SHORT WP	39,000 kg	BSC 2003 [DIRS 165406], Table 1

Table 4.1-1. Summary of Input Data and Information Required by the MSTHM (Continued)

Model Input	Value	Source
Weight of 5 DHLW/DOE SNF-LONG	57,000 kg	BSC 2003 [DIRS 165406], Table 1
Emissivity of Alloy 22 (at T=650°C), which is the outer barrier of the following WPs: 21-PWR AP, 44-BWR, 5 DHLW/DOE SNF-SHORT, 5 DHLW/DOE SNF-LONG	0.87	DTN: MO0003RIB00071.000 [DIRS 148850], Table S04196_001
Mass density of Alloy 22 (N06022), which is the outer barrier of the following WPs: 21-PWR AP, 44-BWR, 5 DHLW/DOE SNF-SHORT, 5 DHLW/DOE SNF-LONG	8690 kg/m^3	DTN: MO0003RIB00071.000 [DIRS 148850], Table S04196_001
Mass density of Stainless Steel Type 316, which is the inner vessel of the following WPs: 21-PWR AP, 44-BWR, 5 DHLW/DOE SNF-SHORT, 5 DHLW/DOE SNF-LONG	7.98 g/cm^3	Table XI of ASTM G 1-90 [DIRS 103515]
Mass density of the internal cylinder of the 21-PWR AP WP	3495 kg/m^3	BSC 2005 [DIRS 173499], Table 2
Mass density of the internal cylinder of the 44-BWR WP	3342 kg/m^3	BSC 2005 [DIRS 173499], Table 2
Mass density of the internal cylinder of the 5 DHLW/DOE SNF-SHORT WP	2175 kg/m^3	BSC 2005 [DIRS 173499], Table 2
Mass density of the internal cylinder of the 5 DHLW/DOE SNF-LONG WP	2302 kg/m^3	BSC 2005 [DIRS 173499], Table 2
Thermal conductivity of Alloy 22 (at T = 373.15 K), which is the outer barrier of the following WPs: 21-PWR AP, 44-BWR, 5 DHLW/DOE SNF-SHORT, 5 DHLW/DOE SNF-LONG	11.1 W/m·K	DTN: MO0107TC239938.000 [DIRS 169995], p. 13
Thermal conductivity of Stainless Steel Type 316, which is the inner vessel of the following WPs: 21-PWR AP, 44-BWR, 5 DHLW/DOE SNF-SHORT, 5 DHLW/DOE SNF-LONG	8.4 BTU/hr-ft-°F at 200°F 8.7 BTU/hr-ft-°F at 250°F	ASME 1995 [DIRS 108417], Section II-D, Table TCD, p. 606
Thermal diffusivity of Stainless Steel Type 316, which is the inner vessel of the following WPs: 21-PWR AP, 44-BWR, 5 DHLW/DOE SNF-SHORT, 5 DHLW/DOE SNF-LONG	0.141 ft^2/hr at 200°F 0.143 ft^2/hr at 250°F	ASME 1995 [DIRS 108417], Section II-D, Table TCD, p. 606
Thermal conductivity of the internal cylinder of the following WPs: 21-PWR AP, 44-BWR, 5 DHLW/DOE SNF-SHORT, 5 DHLW/DOE SNF-LONG	1.5 W/m·K	BSC 2005 [DIRS 173499], Table 2
Specific heat of Alloy 22 (at T = 373.15 K, or 212°F), which is the outer barrier of the following WPs: 21-PWR AP, 44-BWR, 5 DHLW/DOE SNF-SHORT, 5 DHLW/DOE SNF-LONG	423.0 J/kg·K	DTN: MO0107TC239938.000 [DIRS 169995], p. 13
Specific heat of the internal cylinder of the 21-PWR AP WP	378.0 J/kg·K	BSC 2005 [DIRS 173499], Table 2
Specific heat of the internal cylinder of the 44-BWR WP	395.0 J/kg·K	BSC 2005 [DIRS 173499], Table 2
Specific heat of the internal cylinder of the 5 DHLW/DOE SNF-SHORT WP	718.0J/kg·K	BSC 2005 [DIRS 173499], Table 2
Specific heat of the internal cylinder of the 5 DHLW/DOE SNF-LONG WP	731.0 J/kg·K	BSC 2005 [DIRS 173499], Table 2

Table 4.1-1. Summary of Input Data and Information Required by the MSTHM (Continued)

Model Input	Value	Source
Drip-Shield Thermal Properties: Design Information		
Nominal weight of drip shield (for a nominal length of 5.805 m)	5000 kg	BSC 2005 [DIRS 173303], Table 1
Mass density of titanium	0.163 lb/in^3	ASME 1995 [DIRS 108417], Section II-D, Table NF-2, p. 620
Thermal conductivity of titanium	12.00 BTU/hr-ft-°F at 200°F; 11.85 BTU/hr-ft-°F at 250°F	ASME 1995 [DIRS 108417], Section II-D, Table TCD, p. 611
Thermal diffusivity of titanium	0.331 ft^2/hr at 200°F 0.322 ft^2/hr at 250°F	ASME 1995 [DIRS 108417], Section II-D, Table TCD, p. 611
Emissivity of titanium	0.63	Lide 1995 [DIRS 101876], p. 10-298
Drift-Wall Emissivity: Design Information		
Emissivity of rock	0.88 to 0.95	Incropera and DeWitt 1996 [DIRS 108184], Table A.11 for Rocks
Properties of the Natural System		
Hydrologic Properties of all Unsaturated-Zone Model Layers: Parameters		
Matrix and fracture properties of UZ Model Layers for mean infiltration-flux property set	See Table IV-4 in Appendix IV	DTN: LB0208UZDSCPMI.002 [DIRS 161243], File: drift-scale calibrated properties for mean infiltration2.xls; Worksheet: Drift-scale Cal. Hydro Props.
Matrix and fracture properties of UZ Model Layers for upper-bound infiltration-flux property set	See Table IV-6 in Appendix IV	DTN: LB0302UZDSCPUI.002 [DIRS 161787], File: drift-scale calibrated properties for upper infiltration2.xls; Worksheet: Drift-scale Cal. Hydro Props.
Matrix and fracture properties of UZ Model Layers for lower infiltration-flux property set	See Table IV-5 in Appendix IV	DTN: LB0208UZDSCPLI.002 [DIRS 161788], File: drift-scale calibrated properties for lower infiltration2.xls; Worksheet: Drift-scale Cal. Hydro Props.
Fracture frequency and fracture-matrix interfacial area of UZ Model Layers for lower-bound, mean, and upper-bound infiltration-flux property sets	See Table IV-7 in Appendix IV	DTN: LB0205REVUZPRP.001 [DIRS 159525], File: FRACTURE PROPERTY.xls; Worksheet: Table 1. Fracture Properties
Fracture-contact-length factor	0.0	DTN: LB03023DKMGRID.001 [DIRS 162354], File: mesh_3dn.dkm (found after the heading "CONNE" for all elements beginning with "F" in columns 31-40)
Bulk Thermal Properties of the Unsaturated-Zone Model Layers: Parameters		
Thermal conductivity and bulk density of the GFM2000 Layers of the nonrepository layers	See Table IV-3a in Appendix IV	DTN: SN0303T0503102.008 [DIRS 162401], File: NonrepositoryThermalConductivityModel 031403.xls; Worksheet: Sheet 1
Thermal conductivity and bulk density of the repository horizon GFM2000 layers	See Table IV-3a in Appendix IV	DTN: SN0404T0503102.011 [DIRS 169129], File: ReadMe Summary.doc, Table 7-10
Specific heat capacity of the Mineralogic Model Layers	See Table IV-3a in Appendix IV	DTN: SN0307T0510902.003 [DIRS 164196], File: rock_grain_heat_capacity (edited).xls; Worksheet: Cp grain 25-325; Column: Y Cp Rock Grain 25-325C round(cell,2)
Boundary Conditions of the Natural System: Parameters		
Temperatures at upper boundary (ground surface) of the three-dimensional Site-Scale UZ Flow Model	File: INCON_thm_s32.dat	DTN: LB991201233129.001 [DIRS 146894]
Gas-phase pressures at upper boundary (ground surface) of the three-dimensional Site-Scale UZ Flow Model	File: INCON_thm_s32.dat	DTN: LB991201233129.001 [DIRS 146894]

Table 4.1-1. Summary of Input Data and Information Required by the MSTHM (Continued)

Model Input	Value	Source
Temperatures at lower boundary (water table) of the three-dimensional Site-Scale UZ Flow Model	File: INCON_thm_s32.dat (pertains to an elevation of 730 m)	DTN: LB991201233129.001 [DIRS 146894]
Grid of the three-dimensional mountain-scale coupled processes (thermal-hydrologic) model; this grid is related to the file: INCON_thm_s32.dat, which is used to obtain temperatures and gas-phase pressures at the boundary for the three-dimensional Site-Scale UZ Flow Model (above)	File: MESH_rep.VF	DTN: LB991201233129.001 [DIRS 146894]
Distribution of Percolation Flux Below PTn Unit: Parameters		
Percolation Flux from PTn to TSw unit for mean infiltration-flux case (two-dimensional map of PTn-to-TSw percolation flux)	Files: preq_ma_ptn.q, monq_ma_ptn.q, glaq_ma_ptn.q	DTN: LB0302PTNTSW9I.001 [DIRS 162277]
Percolation Flux from PTn to TSw unit for upper-bound infiltration-flux case (two-dimensional map of PTn-to-TSw percolation flux)	Files: preq_ua_ptn.q, monq_ua_ptn.q, glaq_ua_ptn.q	DTN: LB0302PTNTSW9I.001 [DIRS 162277]
Percolation Flux from PTn to TSw unit for lower-bound infiltration-flux case (two-dimensional map of PTn-to-TSw percolation flux)	Files: preq_la_ptn.q, monq_la_ptn.q, glaq_la_ptn.q	DTN: LB0302PTNTSW9I.001 [DIRS 162277]
Probabilities of the three infiltration-flux cases (excluding contingency area)	See Table 6.3-35	BSC 2003 [DIRS 165991], Table 6-7
Waste Package Heat-Generation and Ventilation Heat-Removal Efficiency: Design Information		
Heat-generation rate history for entire repository	See IED	BSC 2005 [DIRS 173499], Table 1
Average initial heat-generation rate per meter	1.45 kW/m	BSC 2004 [DIRS 168489], Table 1
Ventilation-period duration	50 years after final emplacement	BSC 2004 [DIRS 168489], Table 1
Duration of waste package emplacement	23 years	BSC 2004 [DIRS 168489], Table 1
Heat-generation rates for each of the waste package types	See IED	BSC 2005 [DIRS 173705], Table 1
Ventilation heat-removal efficiency as a function of time and distance from the inlet of the emplacement drift	See Table III-1 in Appendix III	DTN: MO0304MWDALACV.000 [DIRS 164551], FILE: ANSYS-LA-Coarse_Efficiency.xls; Worksheet: sheet 1[a]

[a] DTN: MO0304MWDALACV.000 [DIRS 164551], which was superseded by DTN: MO0306MWDASLCV.001 [DIRS 165695], is justified for its use in this report, as documented in Appendix XIV.

During the preparation of this report, some of the design information was updated as several information exchange drawings (IEDs) were superseded. These revisions resulted in small changes to the dimensions of the waste packages and drip shield as summarized in Table 4.1-2. For the direct inputs to be justified as they appear in Table 4.1-1, these small changes to the dimensions must insignificantly affect the results of the MSTHM described in this report. The details of this justification are discussed in Sections 4.1.2.1 through 4.1.2.7.

Table 4.1-2.   Changes to the Waste Package and Drip Shield Design Information

Model Input	Superseded IED		Current IED		Relative Change in Value
	Value	Source	Value	Source	
21-PWR AP WP length	5.165 m	BSC 2003 [DIRS 165406], Table 1	5.024 m	BSC 2005 [DIRS 173501], Table 1	−2.7%
21-PWR AP WP diameter	1.644 m	BSC 2003 [DIRS 165406], Table 1	1.718 m	BSC 2005 [DIRS 173501], Table 1	+4.5%
21-PWR CR WP diameter	1.644 m	BSC 2003 [DIRS 165406], Table 1	1.718 m	BSC 2005 [DIRS 173501], Table 1	+4.5%
Weight of 21-PWR AP	43,000 kg	BSC 2003 [DIRS 165406], Table 1	41,100 kg	BSC 2005 [DIRS 173501], Table 1	−4.4%
44-BWR WP length	5.165 m	BSC 2003 [DIRS 165406], Table 1	5.024 m	BSC 2005 [DIRS 173501], Table 1	−2.7%
44-BWR WP diameter	1.674 m	BSC 2003 [DIRS 165406], Table 1	1.756 m	BSC 2005 [DIRS 173501], Table 1	+4.9%
Weight of 44-BWR WP	43,000 kg	BSC 2003 [DIRS 165406], Table 1	41,700 kg	BSC 2005 [DIRS 173501], Table 1	−3.0%
5 DHLW/DOE SNF-LONG WP length	5.217 m	BSC 2003 [DIRS 165406], Table 1	5.059 m	BSC 2005 [DIRS 173501], Table 1	−3.0%
5 DHLW/DOE SNF-LONG WP diameter	2.110 m	BSC 2003 [DIRS 165406], Table 1	2.126 m	BSC 2005 [DIRS 173501], Table 1	+0.8%
Weight of 5 DHLW/DOE SNF-LONG	57,000 kg	BSC 2003 [DIRS 165406], Table 1	53,100 kg	BSC 2005 [DIRS 173501], Table 1	−6.8%
5 DHLW/DOE SNF-SHORT length	3.590 m	BSC 2003 [DIRS 165406], Table 1	3.453 m	BSC 2005 [DIRS 173501], Table 1	−3.8%
5 DHLW/DOE SNF-SHORT diameter	2.110 m	BSC 2003 [DIRS 165406], Table 1	2.126 m	BSC 2005 [DIRS 173501], Table 1	+0.8%
Weight of 5 DHLW/DOE SNF-SHORT	39,000 kg	BSC 2003 [DIRS 165406], Table 1	36,100 kg	BSC 2005 [DIRS 173501], Table 1	−7.4%
Drip-shield length	6.105 m	BSC 2003 [DIRS 171024], Sheet 2	5.805 m	BSC 2005 [DIRS 173303], Table 1	−4.9%
Drip-shield width	2.512 m	BSC 2003 [DIRS 171024], Sheet 2	2.533 m	BSC 2005 [DIRS 173303], Table 1	+0.8%
Intersection of drip-shield plate-1 with drip-shield plate-2 from base/top of invert	1875 mm	BSC 2003 [DIRS 171024], Sheet 2	1891 mm	BSC 2004 [DIRS 168067]	+0.9%
Location of 21-PWR AP centerline above invert	1018 mm	BSC 2004 [DIRS 167040], Figure 1	1050.9 mm	BSC 2004 [DIRS 168489], Figure 1	+3.2%

AP = Absorber Plate, CR = Control Rods.

4.1.2.1   Waste Package Lengths

As summarized in Table 4.1-2, the differences in waste package lengths between those used in this report, which are obtained from the superseded IED (BSC 2003 [DIRS 165406]), and those listed in the current IED (BSC 2005 [DIRS 173501]) are small, ranging from −2.7 to −3.8 percent. Waste package lengths are used only in the DDT submodel. The DDT submodel is primarily used for two purposes: (1) calculating the temperature difference between the waste package and drip shield and (2) calculating the longitudinal temperature variations along the drift axis. If the slightly shorter waste package lengths given in the current IED (BSC 2005 [DIRS 173501]) were employed in the MSTHM calculations for this report, it would only result

in slightly less longitudinal temperature and relative humidity variation along the drift axis. This small reduction in longitudinal variability is insignificant compared to the range of temperature and relative humidity that results from the influence of parametric variability and uncertainty, which is discussed in Section 6.3. Therefore, the waste package lengths from the superseded IED are suitable for use in the MSTHM calculations reported in Section 6.3.

4.1.2.2   Waste Package Diameters

As summarized in Table 4.1-2, the differences in waste package diameters between those used in this report, which are obtained from the superseded IED (BSC 2003 [DIRS 165406]), and those listed in the current IED (BSC 2005 [DIRS 173501]) are small, ranging from +0.8 to +4.9 percent. Waste package diameters are used only in the DDT submodel. The DDT submodel is only used for two purposes: (1) calculating the temperature difference between the waste package and drip shield and (2) calculating the longitudinal temperature variations along the drift axis. If the slightly wider waste package diameters given in the current IED (BSC 2005 [DIRS 173501]) were employed in the MSTHM calculations for this report, it would only result in facilitating slightly better thermal-radiative heat transfer between the ends of the waste packages, thereby resulting in slightly less longitudinal temperature and relative humidity variations along the drift axis. If the slightly wider waste package diameters were employed in the MSTHM calculations for this report, it would also have the effect of slightly decreasing the temperature difference between the waste package and drip shield. The very small reductions in longitudinal temperature variability and in waste package-to-drip-shield temperature difference are insignificant compared to the range of temperature and relative humidity that results from the influence of parametric variability and uncertainty, which is discussed in Section 6.3. Therefore, the waste package diameters from the superseded IED are suitable for use in the MSTHM calculations reported in Section 6.3.

4.1.2.3   Waste Package Weights

As summarized in Table 4.1-2, the differences in waste package weights between those used in this report, which are obtained from the superseded IED (BSC 2003 [DIRS 165406]), and those listed in the current IED (BSC 2005 [DIRS 173501]) are small, ranging from –3.0 to –7.4 percent. Waste package weights are used only in the LDTH and DDT submodels. The weight of the waste package, multiplied by the waste package-specific heat capacity, is the heat capacity of the waste package. The only manner in which the waste package heat capacity affects the MSTHM results is by influencing the time required for heat transfer from the waste packages to the drift wall to reach a quasi-steady-state condition. Because this quasi-steady-state condition is established much earlier than when peak waste package, drip-shield, and drift-wall temperatures occur, it has an insignificant effect on peak temperatures. If the slightly lower waste package weights given in the current IED (BSC 2005 [DIRS 173501]) were employed in the MSTHM calculations for this report, they would only result in allowing heat transfer from the waste package to the drift wall reaching the quasi-steady-state condition slightly earlier. Furthermore, because the weight of the waste package is much less than that of the surrounding host rock, the waste package heat capacity per unit length of drift is much less than that of the surrounding host rock. As discussed in Section 6.3.2, parametric uncertainty of the host-rock heat capacity has an insignificant influence on MSTHM predictions of temperature and relative

humidity. Therefore, the waste package weights from the superseded IED are suitable for use in the MSTHM calculations reported in Section 6.3.

4.1.2.4 Drip Shield Length

As summarized in Table 4.1-2, the difference in drip-shield length between that used in this report, which is obtained from the superseded IED (BSC 2003 [DIRS 171024]), and that listed in the current IED (BSC 2005 [DIRS 173303]) is small (–4.9 percent). The only use of the drip-shield length, in conjunction with the drip-shield weight, is to determine the drip-shield weight per unit length of drift in the LDTH submodels and to determine the drip-shield mass density in the DDT submodels. The weight of the drip shield, multiplied by the specific heat capacity, affects the heat capacity of the drip shield. The only manner in which the drip-shield heat capacity affects the MSTHM results is by influencing the time required for heat transfer from the waste package to the drift wall to reach a quasi-steady-state condition. Because this quasi-steady-state condition is established much earlier than when peak waste package, drip-shield, and drift-wall temperatures occur, it has an insignificant effect on peak temperatures. If the slightly shorter drip-shield lengths given in the current IED (BSC 2005 [DIRS 173303]) were employed in the MSTHM calculations for this report, it would result in a slightly larger weight per unit length of drift, thereby causing a slight increase in heat capacity for the drip shield. The weight of the drip shield per unit length is much less than that of the waste packages. Therefore, the time required for heat transfer from the waste package to the drift wall reaching the quasi-steady-state condition would be insignificantly affected by this small change in drip-shield heat capacity. Furthermore, because the weight of the drip shield is much less than that of the surrounding host rock, the drip-shield heat capacity per unit length of drift is very much less than that of the surrounding host rock. As discussed in Section 6.3.2, parametric uncertainty of the host-rock heat capacity has an insignificant influence on MSTHM predictions of temperature and relative humidity. Therefore, the drip shield length from the superseded IED is suitable for use in the MSTHM calculations reported in Section 6.3.

4.1.2.5 Drip Shield Width

As summarized in Table 4.1-2, the difference in drip-shield width between that used in this report, which is obtained from the superseded IED (BSC 2003 [DIRS 171024]), and that listed in the current IED (BSC 2005 [DIRS 173303]) is extremely small (+0.8 percent). The only use of the drip-shield width is in the LDTH and DDT submodels, where it primarily affects the drip-shield surface area. In the LDTH submodels, it influences thermal-radiative heat transfer between the drip shield and other surfaces inside the drift cavity. In the DDT submodels (Figure 6.2-8) it influences thermal-radiative heat transfer between the waste package and underside of the drip shield and between the outside of the drip shield and the other surfaces inside the drift cavity. Thermal-radiative heat transfer is extremely efficient, driven by the difference of temperature to the fourth power of the respective surfaces. A very small (0.8 percent) difference in surface area of the drip-shield will have an insignificant effect on the temperature differences within the drift. Therefore, the difference in drip-shield width, which influences drip-shield surface area, has an insignificant effect on temperature or relative humidity predicted by the MSTHM, which is discussed in Section 6.3. Given the manner in which the DDT submodel approximates the geometry of the drip shield (Figure 6.2-8), the 0.8 percent change in drip-shield width is insignificant. Moreover, because the DDT submodel

representation of the drip shield was done to conserve the drip-shield weight per unit length of drift, any change in drip-shield width, however large or small, will not affect the heat capacity of the drip shield per unit length of drift. Therefore, the drip shield width from the superseded IED is suitable for use in the MSTHM calculations reported in Section 6.3.

4.1.2.6   Intersection of Drip-Shield Plate-1 with Drip-Shield Plate-2 from Base/Top of Invert

As summarized in Table 4.1-2, the difference in the intersection of drip shield plate-1 with drip shield plate-2 between that used in this report, which is obtained from the superseded IED (BSC 2003 [DIRS 171024]), and that listed in the current IED (BSC 2004 [DIRS 168067]) is extremely small (+0.9 percent). The only use of this value is in the LDTH submodels, where it affects the point at which the sloping portion of the drip shield meets the vertical sides of the drip shield (see Figure 6.2-6). Relative to the coarse approximation of the drip-shield shape in the LDTH submodel, this small change in where the sloping portion of the drip shield meets the vertical sides of the drip shield is insignificant. The primary manner in which the shape of the drip shield affects in-drift thermal-hydrologic behavior is by affecting the surface area from which thermal-radiative heat transfer occurs from the drip shield to the drift-wall and upper-invert surfaces. Changing where the sloping and vertical portions of the drip shield intersect does not change the surface area of the drip shield as it is represented in the LDTH submodel. Therefore, thermal-radiative heat transfer from the drip shield to the drift-wall and upper-invert surfaces is unaffected by this change. Consequently, the intersection location from the superseded IED is suitable for use in the MSTHM calculations reported in Section 6.3.

4.1.2.7   Location of 21-PWR AP Waste Package Centerline Above the Invert

As summarized in Table 4.1-2, the difference in the location of the 21-PWR AP WP centerline above the invert between that used in this report, which is obtained from the superseded IED (BSC 2004 [DIRS 167040]), and that given in the current IED (BSC 2004 [DIRS 168489]) is small (+3.2 percent). The only use of this dimension is in the DDT submodels, where it determines the position of the waste package above the invert (see Figures 6.2.7 through 6.2.10). Because the purpose of the MSTHM is to predict postclosure thermal-hydrologic conditions, the only manner in which this dimension affects results from the MSTHM is in how it influences radiative heat transfer between the waste package and drip shield. This radiative heat transfer is the primary factor influencing the temperature difference between the waste package and drip shield. Given the geometric approximation of the waste package and drip shield (see Figure 6.2.8) this small (3.2 percent) difference in the location of the waste package above the invert has an insignificant influence on the predicted temperature difference between the waste package and drip shield. Consequently, it also has an insignificant influence on the predicted thermal-hydrologic conditions within the emplacement drifts. Given the manner in which the DDT submodel approximates the geometry of the waste package and drip shield (Figure 6.2-8), this small change in vertical positioning of the waste package is insignificant. Therefore, the location of the centerline from the superseded IED is suitable for use in the MSTHM calculations reported in Section 6.3.

4.1.2.8 Repository Layout

During the preparation of this report, the repository layout information was updated as several IEDs were superseded (Table 4.1-3), causing small changes to the repository layout (Table 4.1-4 and Figure 4-1). Specifically, endpoint coordinates of emplacement drifts were updated in the current IED, resulting in the following changes:

1. Elimination of the northernmost drift in Panel P3W, formerly called Panel P2W.

2. Small reductions in the length of several emplacement drifts, particularly in the southern end of Panel 4, formerly called Panel 3 (Figure 4-1). Note that the minor reductions in drift length in Panel 1 and in Panel 3E, formerly called Panel 2E, are too small to appear in Figure 4-1.

3. Addition of two emplacement drifts in Panel P2, formerly called Panel P4.

As evident in Figure 4-1, the changes in the repository layout are small, justifying the use of the superseded IED in the MSTHM calculations reported in Section 6.3.

Table 4.1-3. Summary of Current and Superseded IEDs Providing Repository Layout Information

Model Input	Superseded IED	Current IED
Repository emplacement-drift layout (elevations and end-point coordinates for each emplacement drift)	BSC 2003 [DIRS 161727]	BSC 2004 [DIRS 172801]
Available emplacement drift lengths	Not Available[a]	BSC 2004 [DIRS 170202]
Invert height above drift	0.806 m (BSC 2003 [DIRS 162444])	2' 10'' (0.8636 m) (BSC 2004 [DIRS 169503])

[a] The footnote labeled ** in BSC 2004 [DIRS 170202] states that this information was not available for the superseded repository layout.

Table 4.1-4. Summary of Emplacement Panels and Drifts Represented in the SMT Submodel for the Layout in the Superseded IED and the Current IED

Panel		Number of drifts		Number of gridblocks	Modeled drift length (m)	Current drift length (m)
Old	New	Old	New			
1	1	8	8	206	4,120	4092
2E	3E	19	19	545	10,900	10,728
2W	3W	23	22	689	13,780	13,272
3	4	30	30	877	17,540	17,003
5	2	15[a]	17[a]	557	11,140	12,506
Total		95	96	2874	57,480	**57,601**

[a] Panel 5 (2) has a total of 27 drifts; the 15 (17) northernmost drifts are used in the TSPA-LA base case.

NOTES: The superseded (old) IED is presented in BSC 2003 [DIRS 161727]; the current (new) IED is presented in BSC 2004 [DIRS 170202]). Note that the layout for the superseded IED is also described in Table 6.2-1.

Each of the heated gridblocks represents a 20-m interval along the emplacement drift.
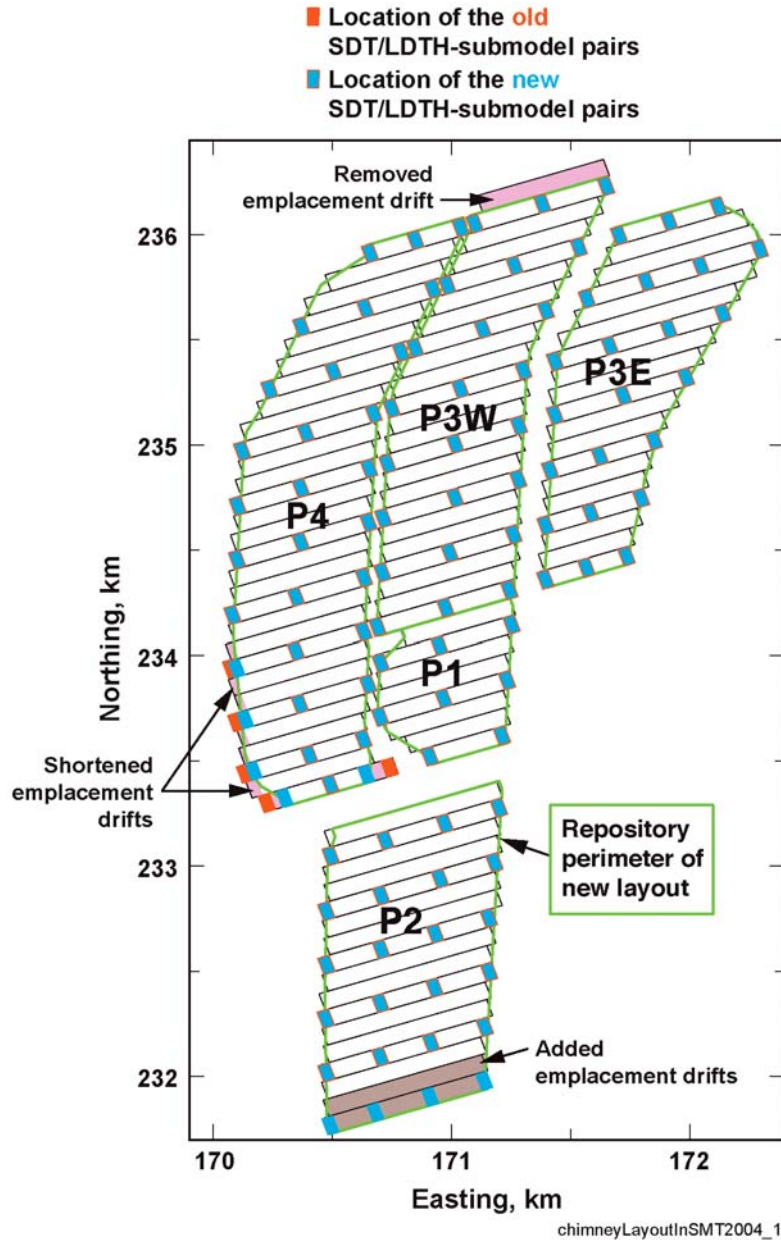
Source: See Table XIII-1.

NOTE: The repository layout incorporated in the MSTHM for the TSPA-LA (Figure 6.2-3) is based on the IED presented in *Repository Design, Repository/PA IED Subsurface Facilities* (BSC 2003 [DIRS 161727]). This IED has been superceded by the IED presented in *D&E/RIT IED Subsurface Facilities* (BSC 2004 [DIRS 172801]). The LDTH–SDT submodel locations shown in blue are those that have been either moved or added relative to Figure 6.2-3; those shown in orange are those used in the MSTHM for the TSPA-LA, and also correspond to those shown in Figure 6.2-3. Note that the minor reductions in drift length in Panel 1 and in Panel 3E, formerly called Panel 2E, are too small to be apparent at the scale of this diagram. The outline of the repository perimeter corresponds to the end-point coordinates of the heated portions of the emplacement drifts as given in *D&E/RIT IED Subsurface Facilities* (BSC 2004 [DIRS 172801]). There is one typographic error in *D&E/RIT IED Subsurface Facilities* (BSC 2004 [DIRS 172801] that was corrected to produce this figure. One of the endpoint easting coordinates for drift 2-27 was corrected from a value of 170018 to 171018.

Figure 4-1.   Differences Between the Repository Layout Incorporated in the MSTHM for the TSPA-LA, and the Repository Layout Given in the Current IED

Figure 4-1 clearly shows that the superseded and current repository layouts are very similar. The only areas where the two layouts do not coincide are (1) the northernmost drift of Panel P3W, which was formerly called Panel P2W, (2) the southwestern edge and southeastern corner of Panel 4, which was formerly called Panel 3, and (3) the two southernmost drifts in Panel 2, formerly called Panel P5, of the current repository layout (BSC 2004 [DIRS 172801]). These two southernmost drifts, which have a total length of 1400 m, were added to make up for the length of emplacement drifts that were removed from the superseded layout (BSC 2003 [DIRS 161727]). Dividing 1400 m by the total length of emplacement drift in the new repository layout (57,600 m) gives the percentage (2.4 percent) of the new repository area that lies outside of the superseded repository layout. Therefore, 97.6 percent of the new repository layout coincides with that of the superseded repository layout.

An important natural-system parameter influencing in-drift and near-field thermal-hydrologic conditions is the host-rock percolation flux. Figure 4-2 shows that the distribution of host-rock percolation flux over the repository area is very similar for the superseded and current repository layouts for all three climate states: (1) present-day, (2) monsoonal, and (3) glacial. Therefore, the repository layout from the superseded IEDs is suitable for use in the MSTHM calculations reported in Section 6.3.
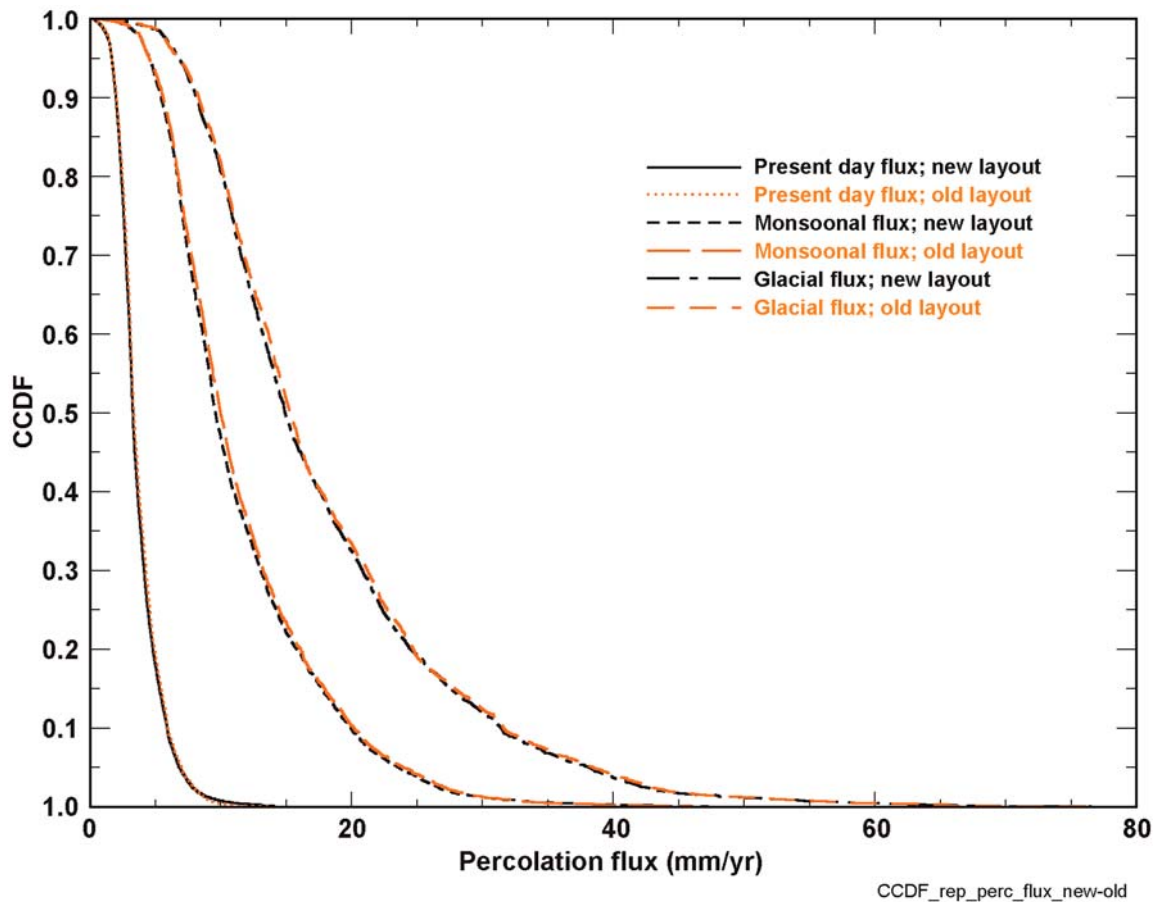
Source: See Table XIII-1.

NOTE: CCDF is given for the present-day, monsoonal, and glacial climates. The superceded repository layout is
         presented in *Repository Design, Repository/PA IED Subsurface Facilities* (BSC 2003 [DIRS 161727]).
         The current repository layout is presented in *D&E/RIT IED Subsurface Facilities* (BSC 2004
         [DIRS 172801]). There is one typographic error in *D&E/RIT IED Subsurface Facilities* (BSC 2004
         [DIRS 172801] that was corrected to produce this figure. One of the endpoint easting coordinates for
         drift 2-27 was corrected from a value of 170018 to 171018.

Figure 4-2. Complementary Cumulative Distribution Function (CCDF) for Distribution of Host-Rock
             Percolation Flux in the Superseded Repository Layout and the Current Repository Layout

4.1.3   Direct Inputs for Development of the Properties of Crushed Tuff in the Invert

Appendix X presents an analysis that produces retention and flow parameters for the invert. The
retention and hydraulic conductivity data used are obtained from Brooks and Corey (1964
[DIRS 156915]), and are qualified for their intended use within this report because of the
availability of corroborating data as prescribed by LP-SIII.l0Q-BSC, Section 5.2.1(1).   The
properties of interest (i.e., hydraulic conductivity, hydraulic head, saturation and water content of
crushed tuff in the invert) are considered adequate because of corroboration discussed below.
The input for the analysis in Appendix X includes the permeability, porosity, and retention data
for volcanic sand, fine sand, glass beads and Touchet Silt Loam.   Table 4.1-5 presents the

permeability data (k) and the porosity data (ϕ) of these unconsolidated materials. Table 4.1-6 presents the retention data for the same materials.

Table 4.1-5.   Summary of Permeability and Porosity of Various Unconsolidated Materials

Material [a]	Porosity	Value (-)	Intrinsic Permeability (m^2)	Value (m^2)
Volcanic Sand	ϕ_{vs}	0.351	k_{vs}	1.80E-11
Fine Sand	ϕ_{fs}	0.377	k_{fs}	2.50E-12
Glass Beads	ϕ_{gb}	0.37	k_{gb}	6.30E-12
Touchet Silt Loam	ϕ_{ts}	0.485	k_{ts}	6.00E-13

[a] See Appendix X for a description of these materials.

The development in Appendix X uses the following direct inputs:

- A value of 2 for the ratio of the capillary rise of water to the capillary rise of the hydrocarbon liquid used for the measurements (Brooks and Corey 1964 [DIRS 156915]).

- The Kozeny-Carman equation as Equation X.52 (Bear 1972 [DIRS 156269], p. 166).

- Porosity of poorly graded sands in the loose state (see below).

- Properties of water (see below).

These inputs are justified for this use in three ways. First, the data, and curve-fits to the data, for various size particles are corroborated by parallel calculations using the Campbell retention relation for the same size particles (BSC 2003 [DIRS 170881]).

The retention relationships developed by the Campbell method show the same characteristics as the nondimensionalized van Genuchten method based upon the Leverett Equation (Leverett 1941 [DIRS 100588]). The results show that as particle size is increased, water retention is reduced. Note that the NUFT dual continuum analyses presented in *Advection versus Diffusion in the Invert* (BSC 2003 [DIRS 170881]) were conducted over the range of moisture potentials anticipated for the repository using both the nondimensionalized van Genuchten and the Campbell retention constitutive relationships. In both instances, it was determined that intergranular porosity did not cause water retention. For this reason, the use of nondimensionalized van Genuchten parameters as direct input in this report is corroborated.

Table 4.1-6.   Retention Data for Various Materials

Volcanic Sand			Fine Sand			Glass Beads			Touchet Silt Loam		
Saturation	Capillary Rise(cm) Hydrocarbon	Capillary Rise(cm) Water	Saturation	Capillary Rise(cm) Hydrocarbon	Capillary Rise(cm) Water	Saturation	Capillary Rise(cm) Hydrocarbon	Capillary Rise(cm) Water	Saturation	Capillary Rise(cm) Hydrocarbon	Capillary Rise(cm) Water
0.99	12	24	0.99	12.8	25.6	0.995	5.9	11.8	0.998	32.8	65.6
0.986	13.5	27	0.98	27.8	55.6	0.989	11.8	23.6	0.995	42.8	85.6
0.98	14.5	29	0.962	30.8	61.6	0.985	17.8	35.6	0.992	52.8	105.6
0.974	15.5	31	0.95	31.8	63.6	0.98	23.8	47.6	0.984	62.8	125.6
0.948	16	32	0.926	34.8	69.6	0.971	26.9	53.8	0.978	67.8	135.6
0.895	17	34	0.901	36.8	73.6	0.938	28.8	57.6	0.967	72.5	145
0.875	17.2	34.4	0.855	39.8	79.6	0.912	29.3	58.6	0.946	77.8	155.6
0.638	21	42	0.788	42.8	85.6	0.764	30.4	60.8	0.892	82.3	164.6
0.479	24.8	49.6	0.716	45.8	91.6	0.681	31	62	0.821	87.7	175.4
0.277	36.9	73.8	0.627	48.8	97.6	0.579	32.1	64.2	0.719	97.8	195.6
0.188	67.7	135.4	0.503	52.8	105.6	0.465	32.7	65.4	0.641	107.6	215.2
0.158	136.6	273.2	0.393	57.7	115.4	0.337	33.9	67.8	0.562	123	246
—	—	—	0.314	64.8	129.6	0.269	35.7	71.4	0.492	142.6	285.2
—	—	—	0.273	71.7	143.4	0.19	39	78	0.424	177	354
—	—	—	0.262	74.4	148.8	0.13	43.8	87.6	0.383	207.2	414.4
—	—	—	0.217	92.1	184.2	0.099	53.5	107	—	—	—
—	—	—	0.174	150.1	300.2	0.097	150.4	300.8	—	—	—

NOTE: The conversion factor for capillary rise from hydrocarbon to water is two, as presented in Section X.1.   Data from Brooks and Corey 1964 [DIRS 156915], Table 1, Appendix III.

Second, the use of nondimensionalized constitutive relationships is corroborated by unsaturated flow measurements as reported in *Advection versus Diffusion in the Invert* (BSC 2003 [DIRS 170881], Section 6.8.3). The measurement results indicate that the intergranular porosity was free of water.

Finally, the sources of the inputs are individually justified. The value for the ratio of capillary rise of water to the capillary rise of the hydrocarbon is an estimate that is included in the Brooks and Corey report (1964 [DIRS 156915]) of the qualified data. Van Genuchten (1980 [DIRS 100610]) used the same factor in his analysis, thus corroborating the value for the ratio of the capillary rise. All three authors are prominent soil scientists whose work is widely recognized.

The Kozeny-Carman equation is corroborated by a similar form in a handbook (Winterkorn and Fang 1975 [DIRS 169700], p. 106, Eq. 2.19).

Porosity of Poorly Graded Sands in the Loose State

In a handbook, Hilf (1975 [DIRS 169699], Table 7.3, p. 257) reports a range in the maximum void ratio (*e*) of 0.67 to 0.94 for the Unified Soils Classification System type SP, which is for poorly graded sands and gravelly sands with little to no fines (Hilf 1975 [DIRS 169699], p. 84). The corresponding porosity (ϕ) can be calculated using the handbook formula that relates the void ratio to porosity (Kaviany 1998 [DIRS 170520], p. 9.76):

$$e = \frac{\phi}{1-\phi}$$

where

e = void ratio and
ϕ = porosity

Solving for ϕ in terms of *e*:

$$\phi = \frac{e}{1+e}$$

For the range of void ratios for SP materials, the corresponding range for intergranular porosity is 0.40 to 0.48. A value of 0.45 is selected for the intergranular porosity of the crushed tuff gravel in the invert because it is near the middle of this range.

Properties of Water

The properties of water at ambient temperature are given by Incropera and DeWitt (1996 [DIRS 108184]). The water density (ρ) equals approximately 1000 kg/m^3 and the absolute viscosity (μ) equals 8.935×10^{-4} N·s/(m^2). The surface tension of water equals 72 dynes/cm. These values are corroborated by handbook values from Liley et al. (1984 [DIRS 146851],

pp. 3-75 and 3-238) by interpolation to 25°C. Using MathCad 11.2a, the interpolation proceeds as follows:

Convert the temperature to Kelvin from Celsius:

25°C + 273.15 = 298.15 K

The density of water given by Liley et al. (1984 [DIRS 146851], Table 3-38) is 997.045 kg/m^3. Use 1,000 kg/m^3 for purposes of illustrating hydraulic conductivity versus moisture potential relationships, as in Attachment X. Liley et al. (1984 [DIRS 146851], Table 3-302) list the following values of viscosity and surface tension:

$$i := 0..1$$

$$\begin{pmatrix} Te \\ Vs \\ St \end{pmatrix} :=$$

Temperature (K)	Absolute Viscosity (N*sec/m²)	Surface Tension (N/m)
295	9.59E-04	0.0727
300	8.55E-04	0.0717

Add units for purposes of interpolation:

$$Temperature_i := Te_i \cdot K$$

$$Viscosity_i := Vs_i \cdot \left(N \cdot \frac{sec}{m^2} \right)$$

$$Surface\_Tension_i := St_i \cdot \frac{N}{m}$$

Perform a linear interpolation on this data for a temperature of 25°C or 298.15 K:

$$linterp(Temperature, Viscosity, 298.15 \cdot K) = 8.94 \times 10^{-4} \frac{N \cdot sec}{m^2}$$

$$linterp(Temperature, Surface\ Tension, 298.15 \cdot K) = 72.1 \frac{dyne}{cm}$$

The properties listed above are used for analysis of moisture retention and hydraulic conductivity relationships for the intergranular porosity of the invert in Appendix X. The ambient temperature of 25°C is consistent with the temperature used in the analysis of the Brooks and Corey moisture retention measurements presented in Appendix X. This analysis, which applies the ambient temperature value, is used only to illustrate the relationship of unsaturated hydraulic conductivity to moisture potential of the intergranular porosity of the invert. The NUFT code

uses van Genuchten moisture retention and relative permeability relationships that are independent of temperature; however, NUFT accounts for the temperature dependence of the fluid properties in the thermal-hydrologic simulations.

Adjustment for Fluid Density for the Height of Capillary Rise

The Brooks and Corey retention data presented in Appendix X used hydrocarbon as the fluid. The data in Appendix X are adjusted to account for the difference between water and the hydrocarbon fluid. According to Brooks and Corey (1964 [DIRS 156915], Equation 17, p. 9), the capillary rise of water was about twice that of the hydrocarbon used in the measurements. This relationship is justified for the intended use in that it is established fact that the capillary rise or retention equals the capillary pressure divided by the density of the fluid.

Qualification of the Use of Information from Fetter

The referenced source by Fetter (1993 [DIRS 102009]) on the topics of the theory supporting analytical equations for steady-state unsaturated flow in porous medium and the use of the van Genuchten relation was reviewed by the following individuals: J.M. Bahr at the University of Wisconsin – Madison; R.A. Griffin at the University of Alabama; J.I. Hoffman at Eastern Washington University; M. Th. van Genuchten at the U.S. Department of Agriculture Salinity Laboratory; S. Kornder at the James River Paper Company; G. Sposito at the University of California – Berkeley; N. Valkenburg at Geraghty and Miller, Inc.; and P. Wierenga at the University of Arizona. Noting that the information of interest from Fetter pertains to unsaturated flow and the van Genuchten relation, and the fact that this source was reviewed by Martinus Th. van Genuchten, among others, the source is considered reliable for its intended use. The extent to which this source of information addresses the supporting analytical equations for steady-state unsaturated flow in porous medium and the use of the van Genuchten relation is considered adequate because these topics were extensively reviewed, as documented here.

4.2 CRITERIA

Project Requirements Document (Canori and Leitner 2003 [DIRS 166275]) contains three criteria that are relevant to the work documented in this report. They are:

1. PRD-002/T-014 Performance Objectives for the Geologic Repository After Permanent Closure; see 10 CFR 63.113 [DIRS 156605] for compete requirement text.

2. PRD-002/T-015 Requirements for Performance Assessment; see 10 CFR 63.114 for compete requirement text.

3. PRD-002/T-016 Requirements for Multiple Barriers; see 10 CFR 63.115 for compete requirement text.

Work described in this document will support these requirements, but more specific criteria exist in *Yucca Mountain Review Plan, Final Report* (Yucca Mountain Review Plan) (NRC 2003 [DIRS 163274]). Selected Yucca Mountain Review Plan acceptance criteria are presented to supplement or clarify the *Project Requirements Document* citation.

Technical Work Plan for: Near-Field Environment In-Drift Heat and Mass Transfer Model and Analysis Reports Integration (BSC 2005 [DIRS 173377], Section 3.2) identifies the applicable acceptance criteria for this model report. Because this model report predicts results that directly or indirectly pertain to quantity of water contacting engineered barriers and waste forms, the following Yucca Mountain Review Plan acceptance criteria, based on meeting the requirements of 10 CFR 63.114(a)–(c) and (e)–(g) [DIRS 156605]), were identified as applicable to this technical product (NRC 2003 [DIRS 163274], Section 2.2.1.3.3.3). As discussed in Section 8.4, several parts of the criteria are not included because they are not relevant to this model report. Section 8.4 discusses the contents of this report as they relate to the acceptance criteria.

4.2.1 Acceptance Criterion 1 – System Description and Model Integration Are Adequate

(1) Total system performance assessment adequately incorporates important design features, physical phenomena, and couplings, and uses consistent and appropriate assumptions throughout the quantity and chemistry of water contacting engineered barriers and waste forms abstraction process;

(2) The abstraction of the quantity and chemistry of water contacting engineered barriers and waste forms uses assumptions, technical bases, data, and models, that are appropriate and consistent with other related U.S. Department of Energy abstractions. For example, the assumptions used for the quantity and chemistry of water contacting engineered barriers and waste forms are consistent with the abstractions of "Degradation of Engineered Barriers" (Section 2.2.1.3.1); "Mechanical Disruption of Engineered Barriers (Section 2.2.1.3.2); "Radionuclide Release Rates and Solubility Limits" (Section 2.2.1.3.4); "Climate and Infiltration" (Section 2.2.1.3.5); and "Flow Paths in the Unsaturated Zone" (Section 2.2.1.3.6). The descriptions and technical bases provide transparent and traceable support for the abstraction of quantity and chemistry of water contacting engineered barriers and waste forms;

(3) Important design features, such as waste package design and material selection, backfill, drip shield, ground support, thermal loading strategy, and degradation processes, are adequate to determine the initial and boundary conditions for calculations of the quantity and chemistry of water contacting engineered barriers and waste forms;

(4) Spatial and temporal abstractions appropriately address physical couplings (thermal-hydrologic-mechanical-chemical). For example, the U.S. Department of Energy evaluates the potential for focusing of water flow into drifts, caused by coupled thermal-hydrologic-mechanical-chemical processes;

(5) Sufficient technical bases and justification are provided for total system performance assessment assumptions and approximations for modeling coupled thermal-hydrologic-mechanical-chemical effects on seepage and flow, the waste package chemical environment, and the chemical environment for radionuclide release. The effects of distribution of flow on the amount of water contacting the engineered barriers and waste forms are consistently addressed, in all relevant abstractions;

(6) The expected ranges of environmental conditions within the waste package emplacement drifts, inside the breached waste packages, and contacting the waste forms and their evolution with time are identified. These ranges may be developed to include: (i) the effects of the drip shield and backfill on the quantity and chemistry of waster (e.g., the potential for condensate formation and dripping from the underside of the shield); (ii) conditions that promote corrosion of engineered barriers and degradation of waste forms; (iii) irregular wet and dry cycles; (iv) gamma-radiolysis; and (v) size and distribution of penetrations of engineered barriers;

(7) The model abstraction for quantity and chemistry of water contacting engineered barriers and waste forms is consistent with the detailed information on engineered barrier design and other engineered features. For example, consistency is demonstrated for: (i) dimensionality of the abstractions; (ii) various design features and site characteristics; and (iii) alternative conceptual approaches. Analyses are adequate to demonstrate that no deleterious effects are caused by design or site features that the U.S. Department of Energy does not take into account in this abstraction;

(8) Adequate technical bases are provided, including activities such as independent modeling, laboratory or field data, or sensitivity studies, for inclusion of any thermal-hydrologic-mechanical-chemical couplings and features, events, and processes;

(9) Performance-affecting processes that have been observed in thermal-hydrologic tests and experiments are included into the performance assessment. For example, the U.S. Department of Energy either demonstrates that liquid water will not reflux into the underground facility or incorporates refluxing water into the performance assessment calculation, and bounds the potential adverse effects of alteration of the hydraulic pathway that result from refluxing water;

(12) Guidance in NUREG–1297 (Altman et al. 1988 [DIRS 103597] and NUREG–1298 (Altman et al. 1988 [DIRS 103750]), or other acceptable approaches, is followed.

4.2.2 Acceptance Criterion 2 – Data Are Sufficient for Model Justification

(1) Geological, hydrological, and geochemical values used in the license application are adequately justified. Adequate description of how the data were used, interpreted, and appropriately synthesized into the parameters is provided;

(2) Sufficient data were collected on the characteristics of the natural system and engineered materials to establish initial and boundary conditions for conceptual models of thermal-hydrological-mechanical-chemical coupled processes, that affect seepage and flow and the engineered barriers chemical environment;

(3) Thermo-hydrologic tests were designed and conducted with the explicit objectives of observing thermal-hydrologic processes for the temperature ranges expected for repository conditions and making measurements for mathematical models. Data are sufficient to verify that thermal-hydrologic conceptual models address important thermal-hydrologic phenomena;

(4) Sufficient information to formulate the conceptual approach(es) for analyzing water contact with the drip shield, engineered barriers, and waste forms is provided.

4.2.3 Acceptance Criterion 3 – Data Uncertainty Is Characterized and Propagated Through the Model Abstraction

(1) Models use parameter values, assumed ranges, probability distributions, and bounding assumptions that are technically defensible, reasonably account for uncertainties and variabilities, and do not result in an under-representation of the risk estimate;

(2) Parameter values, assumed ranges, probability distributions, and bounding assumptions used in the total system performance assessment calculations of quantity and chemistry of water contacting engineered barriers and waste forms are technically defensible and reasonable, based on data from the Yucca Mountain region (e.g., results from large block and drift-scale heater and niche tests), and a combination of techniques that may include laboratory experiments, field measurements, natural analog research, and process-level modeling studies;

(3) Input values used in the total system performance assessment calculations of quantity and chemistry of water contacting engineered barriers (e.g., drip shield and waste package) are consistent with the initial and boundary conditions and the assumptions of the conceptual models and design concepts for the Yucca Mountain site. Correlations between input values are appropriately established in the U.S. Department of Energy total system performance assessment. Parameters used to define initial conditions, boundary conditions, and computational domain in sensitivity analyses involving coupled thermal-hydrologic-mechanical-chemical effects on seepage and flow, the waste package chemical environment, and the chemical environment for radionuclide release, are consistent with available data. Reasonable or conservative ranges of parameters or functional relations are established;

(4) Adequate representation of uncertainties in the characteristics of the natural system and engineered materials is provided in parameter development for conceptual models, process-level models, and alternative conceptual models. DOE may constrain these uncertainties using sensitivity analyses or conservative limits. For example, DOE demonstrates how parameters used to describe flow through the EBS bound the effects of backfill and excavation-induced changes;

4.2.4 Acceptance Criterion 4 – Model Uncertainty Is Characterized and Propagated Through the Model Abstraction

(1) Alternative modeling approaches of features, events, and processes are considered and are consistent with available data and current scientific understanding, and the results and limitations are appropriately considered in the abstraction;

(2) Alternative modeling approaches are considered and the selected modeling approach is consistent with available data and current scientific understanding. A description that includes a discussion of alternative modeling approaches not considered in the final analysis and the limitations and uncertainties of the chosen model is provided;

(3) Consideration of conceptual-model uncertainty is consistent with available site characterization data, laboratory experiments, field measurements, natural analog information and process-level modeling studies; and the treatment of conceptual-model uncertainty does not result in an under-representation of the risk estimate;

(4) Adequate consideration is given to effects of thermal-hydrologic-mechanical-chemical coupled processes in the assessment of alternative conceptual models. These effects may include: (i) thermal-hydrologic effects on gas, water, and mineral chemistry; (ii) effects of microbial processes on the engineered barrier chemical environment and the chemical environment for radionuclide release; (iii) changes in water chemistry that may result from the release of corrosion products from the engineered barriers and interactions between engineered materials and ground water; and (iv) changes in boundary conditions (e.g., drift shape and size) and hydrologic properties, relating to the response of the geomechanical system to thermal loading.

4.2.5 Acceptance Criterion 5 – Model Abstraction Output Is Supported by Objective Comparisons

No subcriteria are applicable to this report.

4.3 CODES, STANDARDS, AND REGULATIONS

This report was prepared to comply with 10 CFR Part 63 [DIRS 156605], the U.S. Nuclear Regulatory Commission rule on high-level radioactive waste. Subparts of this rule that are applicable to data include Subpart E, Section 114 (Requirements for Performance Assessment). The subpart applicable to models is also outlined in Subpart E Section 114. The subparts applicable to features, events, and processes (FEPs) are 10 CFR 63.114(d), (e), and (f) [DIRS 156605]. *Standard Practice for Preparing, Cleaning, and Evaluating Corrosion Test Specimens* (ASTM G 1-90 [DIRS 103515]) was also used in preparing this report, as was Section II of *1995 ASME Boiler and Pressure Vessel Code* (ASME 1995 [DIRS 108417]).

4.4 DATA FROM FIELD MEASUREMENTS IN THE LARGE BLOCK TEST AND DRIFT SCALE TEST

The source DTNs for the field measurements in the Large Block Test (LBT) are listed in Table 4.4-1. These DTNs are used for model validation purposes only and are not direct input to the MSTHM. The source DTNs for the field measurements in the Drift Scale Test (DST) are listed in Table 4.4-2.

Table 4.4-1. Source DTNs for Field Measurements Made in the Large Block Test (LBT)

Model Input	Value	Source
Heater power history	Heater power input for each of 5 heater boreholes; power history read from 7 tables; table name and time range as follows: • S98461_018 2/27/1997-4/30/1997 • S98461_019 5/1/1997-7/31/1997 • S98461_020 8/1/1997-10/31/1997 • S98461_021 11/1/1997-1/20/1998 • S98461_011 1/20/1998-3/31/1998 • S98461_012 4/1/1998-6/30/1998 • S98461_013 7/1/1998-9/16/1998	DTN: LL980918904244.074 [DIRS 135872]
Top surface boundary temperature controlled by heat exchanger	Temperature averaged from 4 RTDs, TNE-1, TNW-1,TSE1-1, and TSW-1; table name and time range as follows: • S98461_022 2/27/1997-4/30/1997 • S98461_023 5/1/1997-7/31/1997 • S98461_024 8/1/1997-10/24/1997 • S98461_025 10/25/1997-12/31/1997 • S98461_026 1/1/1998-3/31/1998 • S98461_027 4/1/1998-6/30/1998 • S98461_028 7/1/1998-9/16/1998	DTN: LL980918904244.074 [DIRS 135872]
Snapshots of rock temperature profile along Borehole TT1	Temperature profile along Borehole TT1 at five different times. Given below are table (or file) name, elapsed time in hours (h), and the range of row numbers that contain the data for each time. S98461_033 719.8 h 1 – 41136 S98461_034 2399.6 h 1 – 159235 S98461_ 035 4800.13 h 1 – 149893 S98461_029 7200.03 h 1 – 90950 S98461_031 9600.22 h 1 – 98329	DTN: LL980918904244.074 [DIRS 135872]
Initial volumetric water content from neutron measurements	Initial water content obtained from average of values measured along Borehole TN3 prior to heating; data from file at row numbers 1 -- 159	DTN: LL980919304244.075 [DIRS 145099]
Volumetric water content from neutron measurements	Rock water content profile along Borehole TN3 at 103 d, 361 d, and 501 d; data from file at row numbers 2200 – 2254 for 103 d, 2365 – 2419 for 361 d, and 2585 – 2639 for 501 d	DTN: LL980919304244.075 [DIRS 145099]
Air temperature: 1/1/1997 – 12/31/1997	Bureau of Land Management Site 8 temperature data used in boundary conditions. Data under table name S04010_001, and parameter name Temperature. Data in Microsoft Access folder Met1997t.mdb, in table S008_97t. The Julian day number is in Column 3 (1-365), time of day in Column 4 (hr, min) and temperature in Column 8 (ºC).	DTN: MO0312SEPQ1997.001 [DIRS 167116]
Air temperature: 1/1/1998 – 3/31/1998	Bureau of Land Management Site 8 temperature data used in boundary conditions. MOL.19990315.0065 Data file: 1q98b_sr.txt. The site number is in Column 1 (used only Site 8 data), Julian day number in Column 3 (1-365), time of day in Column 4 (hr) and temperature in Column 7 (K).	DTN: MO98METDATA114.000 [DIRS 165702]
Air temperature: 4/1/1998 – 6/30/1998	Bureau of Land Management Site 8 temperature data used in boundary conditions. Data file: 2q98a_sr.txt (MOL.19990323.0416). The site number is in Column 1 (used only Site 8 data), Julian day number in Column 3 (1-365), time of day in Column 4 (hr) and temperature in Column 7 (K).	DTN: MO98METDATA117.000 [DIRS 165705]

Table 4.4-1.   Source DTNs for Field Measurements Made in the Large Block Test (LBT) (Continued)

Model Input	Value	Source
Air temperature: 7/1/1998 – 9/30/1998	Bureau of Land Management Site 8 temperature data used in boundary conditions. Data file: 3q98_sr.txt (MOL.19990105.0204). The site number is in Column 1 (used only Site 8 data), Julian day number in Column 3 (1-365), time of day in Column 4 (hr) and temperature in Column 7 (K).	DTN: MO98METDATA120.000 [DIRS 165706]
Drift-scale calibrated one-dimensional property set, FY99: Base-case infiltration	Entire DTN.	DTN: LB990861233129.001 [DIRS 110226]

NOTE: Also listed is one of the data sets used in the thermal-hydrologic model calculations of the LBT. Note that these DTNs are used for validation purposes only.

Table 4.4-2.   Source DTNs for Field Measurements Made in the Drift Scale Test (DST)

Model Input	Value	Source
As-built locations of boreholes, sensors, and heaters	Location of temperature sensors in Table S00085_001; locations of temperature and neutron boreholes and heaters in Table S00085_002	DTN: MO0002ABBLSLDS.000 [DIRS 147304]
Heater power and sensor temperatures: November 7, 1997 – May 31, 1998	Floor heater and wing heater power in Table S98349_001; Table names and time intervals for temperatures are as follows: • S98349_004 11/7/1997 – 11/30/1997 • S98349_005 12/1/1997 – 12/31/1997 • S98349_006 1/1/1998 – 1/31/1998 • S98349_007 2/1/1998 – 2/28/1998 • S98349_008 3/1/1998 – 3/31/1998 • S98349_009 4/1/1998 – 4/30/1998 • S98349_010 5/1/1998 – 5/31/1998	DTN: MO9807DSTSET01.000 [DIRS 113644]
Heater power and sensor temperatures: June 1, 1998 – August 31, 1998	Floor heater and wing heater power in Table S99012_001; Table names and time intervals for temperatures are as follows: • S99012_004 6/1/1998 – 6/30/1998 • S99012_005 7/1/1998 – 7/31/1998 • S99012_006 8/1/1998 – 8/31/1998	DTN: MO9810DSTSET02.000 [DIRS 113662]
Heater power and sensor temperatures: September 1, 1998 – May 31, 1999	Floor heater and wing heater power in Table S99304_010; Table names and time intervals for temperatures are as follows: • S99304_001 9/1/1998 – 9/30/1998 • S99304_002 10/1/1998 – 10/31/1998 • S99304_003 11/1/1998 – 11/30/1998 • S99304_004 12/1/1998 – 12/30/1998 • S99304_005 1/1/1999 – 1/31/1999 • S99304_006 2/1/1999 – 2/28/1999 • S99304_007 3/1/1999 – 3/30/1999 • S99304_008 4/1/1999 – 4/29/1999 • S99304_009 5/1/1999 – 5/31/1999	DTN: MO9906DSTSET03.000 [DIRS 113673]

Table 4.4-2.   Source DTNs for Field Measurements Made in the Drift Scale Test (DST) (Continued)

Model Input	Value	Source
Heater power and sensor temperatures: June 1, 1999 – October 31, 1999	Floor heater and wing heater power in Table S00044_001; Table names and time intervals for temperatures are as follows: • S00044_004 6/1/1999 – 6/30/1999 • S00044_005 7/1/1999 – 7/31/1999 • S00044_006 8/1/1999 – 8/31/1999 • S00044_007 9/1/1999 – 9/30/1999 • S00044_008 10/1/1999 – 10/31/1999	DTN: MO0001SEPDSTPC.000 [DIRS 153836]
Heater power and sensor temperatures: November 1, 1999 – May 31, 2000	Floor heater and wing heater power in Table S00327_009; Table names and time intervals for temperatures are as follows: • S00327_002 1/1/2000 – 1/31/2000 • S00327_003 2/1/2000 – 2/29/2000 • S00327_004 3/1/2000 – 3/31/2000 • S00327_005 4/1/2000 – 4/30/2000 • S00327_006 5/1/2000 – 5/31/2000 • S00327_007 11/1/1999 – 11/30/1999 • S00327_008 12/1/1999 – 12/31/1999	DTN: MO0007SEPDSTPC.001 [DIRS 153707]
Sensor temperatures: January 15, 2002 – June 30, 2002	Data obtained from text files: TDIF_009_0201_2.txt, TDIF_009_0202.txt, TDIF_009_0203.txt, TDIF_009_0204.txt, TDIF_009_0205.txt, and TDIF_009_0206.txt	DTN: MO0208SEPDSTTD.001 [DIRS 161767]
Heater power and sensor temperatures: June 1, 2000 – November 30, 2000	Floor heater and wing heater power in Table S00468_002; Table names and time intervals for temperatures are as follows: • S00468_003 10/1/2000 – 10/31/2000 • S00468_004 6/1/2000 – 6/30/2000 • S00468_005 9/1/2000 – 9/30/2000 • S00468_006 8/1/2000 – 8/31/2000 • S00468_007 7/1/2000 – 7/31/2000 • S00468_008 11/1/2000 – 11/30/2000	DTN: MO0012SEPDSTPC.002 [DIRS 153708]
Heater power and sensor temperatures: December 1, 2000 – May 31, 2001	Floor heater and wing heater power in Table S01100_002; Table names and time intervals for temperatures are as follows: • S01100_004 12/1/2000 – 12/31/2000 • S01100_005 1/1/2001 – 1/31/2001 • S01100_006 2/1/2001 – 2/28/2001 • S01100_007 3/1/2001 – 3/31/2001 • S01100_008 4/1/2001 – 4/30/2001 • S01100_009 5/1/2001 – 5/31/2001	DTN: MO0107SEPDSTPC.003 [DIRS 158321]
Heater power and sensor temperatures: June 1, 2001 – January 14, 2002	Floor heater and wing heater power in Table S02060_010; Table names and time intervals for temperatures are as follows: • S02060_001 6/1/2001 – 6/30/2001 • S02060_002 7/1/2001 – 7/31/2001 • S02060_003 8/1/2001 – 8/31/2001 • S02060_004 9/1/2001 – 9/30/2001 • S02060_005 10/1/2001 – 10/31/2001 • S02060_006 11/1/2001 – 11/30/2001 • S02060_007 12/1/2001 – 12/31/2001 • S02060_008 1/1/2002 – 1/14/2002	DTN: MO0202SEPDSTTV.001 [DIRS 158320]

Table 4.4-2.   Source DTNs for Field Measurements Made in the Drift Scale Test (DST) (Continued)

Model Input	Value	Source
Sensor temperatures: July 1, 2002 – December 31, 2002	Data obtained from text files: TDIF_010_0207.txt, TDIF_010_0208.txt, TDIF_010_0209.txt, TDIF_010_0210.txt, TDIF_010_0211.txt, and TDIF_010_0212.txt	DTN: MO0303SEPDSTTM.000 [DIRS 165698]
Sensor temperatures: January 1, 2003 – June 30, 2003	Data obtained from text files: TDIF_011_0306.txt, TDIF_011_0302.txt, TDIF_011_0303.txt, TDIF_011_0304.txt, TDIF_011_0305.txt, and TDIF_011_0301.txt	DTN: MO0307SEPDST31.000 [DIRS 165699]
Water content in rock from neutron measurements: August 1997 – May 2002	Following are the neutron boreholes and files that supply the water content data: • Borehole 68 File N10hv.xls • Borehole 79 File N11hxv.xls • Borehole 80 File N12hxv.xls	DTN: LL020710223142.024 [DIRS 159551]
Water content in rock from neutron measurements: January 2003 – May 2003	Following are the neutron boreholes and files that supply the water content data: • Borehole 68 File TD100307.xls • Borehole 79 File TD110307.xls • Borehole 80 File TD120307.xls	DTN: LL030709023122.032 [DIRS 165701]
Temperatures and gas-phase pressures at upper boundary (ground surface) and lower boundary (water table) of the three-dimensional Site-Scale UZ Flow Model (Table 4.1-1)	Files: INCON_thm_s32.dat and MESH_rep.VF	DTN: LB991201233129.001 [DIRS 146894]

NOTE: These DTNs are used for validation purposes only.

INTENTIONALLY LEFT BLANK

5. ASSUMPTIONS

5.1 BOUNDARY CONDITIONS

5.1.1 Ground-Surface Relative Humidity

Assumption: The relative humidity at the ground surface above the repository is assumed to be 100 percent.

Rationale: The liquid-phase flux distribution applied at the upper boundary of the LDTH submodels of the MSTHM is the percolation-flux distribution (from the base of the PTn unit into the top of the TSw sequence of units) calculated by *UZ Flow Models and Submodels* (BSC 2004 [DIRS 169861]). Note that the three-dimensional UZ flow model accounts for the influence of evapotranspiration in the soil zone on net infiltration flux at Yucca Mountain by virtue of the fact that it is addressed in the net infiltration-flux distribution applied at the top of the three-dimensional UZ flow model. A relative humidity of 100 percent is applied at the atmosphere boundary at the top of the MSTHM to ensure that the PTn-to-TSw percolation flux is neither significantly diminished nor increased by virtue of gas-phase moisture flux at the top of the MSTHM. To verify that the PTn-to-TSw percolation flux is neither significantly diminished nor increased, the ambient present-day percolation flux above the repository horizon was compared to the PTn-to-TSw percolation flux, which is imposed at the upper boundary in the LDTH submodels (Section 6.2.6). It was found that the differences between the imposed PTn-to-TSw percolation flux at the upper boundary and the percolation flux above the repository horizon never exceed 3.61×10^{-4} mm/yr for the mean infiltration-flux case. For example, the percolation flux above the repository is 3.11×10^{-5} mm/yr greater than the imposed PTn-to-TSw percolation flux for the LDTH submodel location with the lowest present-day PTn-to-TSw percolation flux; because this difference is only 0.01 percent of the PTn-to-TSw percolation flux, which is 0.23 mm/yr, it is insignificant. The percolation flux above the repository is 3.61×10^{-4} mm/yr greater than the imposed PTn-to-TSw percolation flux for the LDTH submodel location with the highest present-day PTn-to-TSw percolation flux; because this difference is only 0.003 percent of the PTn-to-TSw percolation flux, which is 13.8 mm/yr, it is insignificant. Note that these small differences are positive; that is to say that imposing a relative humidity of 100 percent at the ground surface slightly increases the moisture flux above the repository horizon (by the very small quantities given above) compared to the imposed liquid-phase flux at the top of the LDTH submodel.

Confirmation Status: Because this assumption is justified, it does not require further confirmation.

Use in the Model: This assumption affects all LDTH submodels, and is used in Sections 6.2, 6.3, 6.4, 7.4, and 7.5.

5.1.2 Ambient Percolation Flux above Repository Horizon

Assumption: The ambient percolation-flux distribution above the repository horizon is assumed to be unaffected by mountain-scale repository-heat-driven thermal-hydrologic effects until it reaches the boiling condensation zones surrounding the emplacement drifts. Moreover, between

the base of the PTn UZ model layers and the repository horizon, ambient percolation flux is assumed to be one-dimensional vertically downward with no lateral diversion caused by layering or heterogeneity in the hydrologic-property distributions. Therefore, the percolation-flux distribution above the repository horizon is taken to be the percolation-flux distribution from the PTn to the upper TSw UZ model layer unit (also called the PTn-to-TSw percolation flux) that is predicted by *UZ Flow Models and Submodels* (BSC 2004 [DIRS 169861]).

Rationale: The influence of subboiling evaporation has an insignificant effect on the magnitude or direction of liquid-phase flux. Moreover, the LDTH submodels already account for the influence of subboiling evaporation within the confines of the two-dimensional LDTH-submodel geometry. Fracturing within the sequence of UZ model layer units between the PTn and the repository horizon is dense, which is not conducive to laterally diverting gravity-driven ambient percolation; thus, percolation within this interval is vertically downward. The denseness of the fracture spacing is evident in the data on fracture frequency (DTN: LB0205REVUZPRP.001 [DIRS 159525]). As is discussed in Section 6.1.4 of *Calibrated Properties Model* (BSC 2004 [DIRS 169857]), heterogeneity of hydrologic properties (including fracture spacing) is treated as a function of geologic layering; thus, any one geologic layer has homogeneous properties throughout the grid derived from *UZ Flow Models and Submodels* (BSC 2004 [DIRS 169861]), as well as throughout the MSTHM.

Confirmation Status: Because this assumption is justified, it does not require further confirmation.

Use in the Model: Section 6.2.6.6 describes the use of the PTn-to-TSw percolation flux in the MSTHM LDTH submodels. This assumption is used in Sections 6.2, 6.3, and 7.5.

5.1.3   Barometric Pressure Fluctuations at the Ground Surface

Assumption: Barometric (i.e., gas-phase) pressure fluctuations at the ground surface above the repository are assumed to be insignificant. Consequently, the gas-phase pressure at the ground surface is held constant (i.e., does not fluctuate with time) in all thermal-hydrologic models.

Rationale: The magnitude of gas-phase pressure fluctuations resulting from barometric pumping is small compared to the gas-phase pressure gradients resulting from (1) forced convective cooling of emplacement drifts during the preclosure ventilation period and (2) repository-heat-driven boiling during the postclosure period. Moreover, barometric pumping is not a significant contributor to the removal of water vapor from emplacement drifts and the adjoining host rock, compared to the effect of drift ventilation during the preclosure period and the effect of boiling during the postclosure period.

Confirmation Status: Because this assumption is justified, it does not require further confirmation.

Use in the Model: This assumption is used in Sections 6.3, 6.4, 7.3, 7.4, and 7.5.

5.1.4 Timing of Climate Change Influence on Percolation Flux above Repository

Assumption: For representing percolation flux above the repository, the transition from present-day to monsoonal climate is assumed to occur 600 years after emplacement and the transition from monsoonal to glacial transition climate is assumed to occur 2,000 years after emplacement.

Rationale: Section 6.6.1 and Table 6-1 of *Future Climate Analysis* (BSC 2004 [DIRS 170002]) give a range of duration for the transition from the present day to the monsoonal climate of 400 to 600 years, and a range of duration for the transition from the monsoonal to the glacial transition climate of 900 to 1,400 years. Thus, the minimum times for the timing of the climate transitions are 400 and 1,300 years, respectively. The maximum times for the timing of the climate transitions are 600 and 2,000 years, which is what is assumed in this report, as well as in all other thermal-hydrologic models supporting TSPA-LA, such as *Mountain-Scale Coupled Processes (TH/THC/THM) Models* (BSC 2004 [DIRS 169866] and *Drift-Scale Coupled Processes (DST and TH Seepage) Models* (BSC 2004 [DIRS 170338]). Because peak repository temperatures are predicted to occur within 15 to 20 years after closure (Section 6.3.2), the timing of the first climate transition (400 to 600 years) has no effect on peak temperatures. Because the majority of waste package locations in the repository are predicted to cool down below boiling (at the drift wall) prior to 1,300 years (Figure 6.3-52 and Table 6.3-37), the timing of the second climate transition (1,300 to 2,000 years) will have an insignificant effect on the majority of the waste package locations in the repository. The only locations potentially affected by this assumption are those in regions of low percolation flux, close to the center of the repository. Even for those situations, the influence of this assumption is not expected to be significant, compared to the influences of host-rock thermal conductivity uncertainty and percolation-flux uncertainty.

Confirmation Status: Because this assumption is justified, it does not require further confirmation.

Use in the Model: This assumption is used in Sections 6.3 and 7.5.

5.1.5 Water Table Rise

Assumption: The influence of water table rise, which results from future (wetter) climates, is assumed to have an insignificant effect on thermal-hydrologic conditions in the emplacement drifts and adjacent host rock. Thus, the influence of water table rise is assumed to have an insignificant effect on temperature and relative humidity in the emplacement drifts.

Rationale: As discussed in Section 6.6.3 of *UZ Flow Models and Submodels* (BSC 2004 [DIRS 169861]), paleohydrologic evidence suggests that at points downstream of Yucca Mountain, the water could have been on the order of 100 to 120 m higher during glacial climates (Forester et al. 1996 [DIRS 100148], p. 63). This change in water table elevation is small compared to the average distance between the repository horizon and the water table, which is on the order of 300 m. With regards to the thermal-hydrologic response in the repository, the primary potential influence of this change is to cause a small increase in liquid-phase saturation in the lower 100 to 120 m of the unsaturated zone, causing a small change in the thermal

conductivity in that vertical interval. Heat flow in that vertical interval, which is dominated by thermal conduction, will experience an insignificant change as a result of this small increase in liquid-phase saturation, causing an insignificant change in predicted repository temperatures. The other potential influence of water table rise is to increase the relative humidity in the host rock under ambient conditions. Because ambient relative humidity is already close to unity under the present-day climate, any increases resulting from a future (wetter) climate will be insignificant.

Confirmation Status: Because this assumption is justified, it does not require further confirmation.

Use in the Model: This assumption is used in Sections 6.3, 6.4, and 7.5.

5.2 HEAT FLOW PROCESSES

5.2.1 Mountain-Scale Heat Flow

Assumption: The following assumption only applies to the SMT submodels (Section 6.2.5). For the SMT submodels, differences in temperature that arise as a result of proximity to the repository edges are assumed to be governed by thermal conduction in the rock. This assumption is equivalent to saying that convective heat transfer mechanisms (notably, buoyant gas-phase convection and the heat-pipe effect) have an insignificant influence on lateral mountain-scale heat flow at Yucca Mountain. This assumption tends to preserve temperature differences that arise as a result of differences in proximity to the repository edges. This assumption allows mountain-scale heat flow to be represented using thermal-conduction models. This assumption is applied to the SMT submodels.

Rationale: The bulk permeability k_b of much of the unsaturated zone is much less than the threshold k_b value at which buoyant gas-phase convection begins to significantly influence heat flow (Buscheck and Nitao 1994 [DIRS 130561]); therefore, heat flow is dominated by heat conduction. *Mountain-Scale Coupled Processes (TH/THC/THM)* (BSC 2004 [DIRS 169866], Section 6.3) documents a three-dimensional mountain-scale thermal-hydrologic model that is similar in scale to the SMT submodel in the MSTHM. The vertical temperature profile of the mountain-scale thermal-hydrologic model (Figure 6.3.1-6 of BSC 2004 [DIRS 169866]) is indicative of conduction-dominated heat flow. Conduction dominates other heat transfer mechanisms (i.e., convection in fractures and lithophysae, and latent-heat transfer) in the host rock (Sass et al. 1988 [DIRS 100644], p. 35). This is also supported by the conclusions of data and modeling of the Drift Scale Test (Birkholzer and Tsang 2000 [DIRS 154608], p. 1439). Moreover, the primary role of the SMT submodel in the MSTHM methodology is to predict the rate at which the edge-cooling effect propagates inward from the repository edges toward the repository center. Mountain-scale buoyant gas-phase convection has an insignificant effect on controlling the rate at which the edge-cooling effect propagates in toward the center of the repository. This assumption is also justified because it tends to preserve temperature differences that arise as a result of differences in proximity to the repository edges.

Confirmation Status: Because this assumption is justified, it does not require further confirmation.

Use in the Model: This assumption is used in the MSTHM calculations in Sections 6.3, 6.4, and 7.5.

5.2.2   Drift-Scale Heat Flow

Assumption: The following assumption only applies to the DDT submodels. For the DDT submodels, the influence of repository-scale thermal conductivity variability and drift-scale buoyant gas-phase convection within the host rock are assumed to have an insignificant influence on waste package-to-waste package temperature deviations along the emplacement drifts. This assumption allows the MSTHM methodology to rely upon only one set of DDT submodel calculations conducted at a single LDTH–SDT submodel location.

Rationale: During the preclosure period, thermal radiation between the waste package and drift wall controls the longitudinal temperature deviations along the emplacement drift in the DDT submodels. During the postclosure period, thermal radiation between the waste package and drip shield and between the drip shield and drift wall control the temperature deviations along the emplacement drift. Heat flow in the longitudinal direction in the host rock (both by conduction and convection) plays a much smaller role in attenuating waste package-to-waste package temperature variations along the drift wall than does thermal radiation in the drift (Hardin 1998 [DIRS 100350], Section 3.7.5.4).

The DDT submodel is only used for two purposes: (1) calculating the temperature difference between the waste package and drip shield, and (2) calculating the longitudinal temperature variations along the drift axis. Neither of these quantities is significantly influenced by the thermal conductivity in the host rock (or in any of the other UZ model layers). Therefore, it is not necessary to run the DDT submodels at multiple locations because the only potential benefit would be to capture the influence of the local thermal conductivity values, which is relatively unimportant with regards to the two quantities that the DDT submodel is required to predict. Convective heat transfer driven by thermal-hydrologic behavior in the host rock has little effect on longitudinal temperature variation in the drift. In other words, thermal-hydrologic processes in the host rock do not contribute significantly to equalization of axial temperature variations in the drift. Therefore, the conduction-only DDT submodel adequately represents longitudinal temperature deviations in the drifts or adjoining host rock (relative to line-average-heat-source conditions). This assumption is also justified because it tends to preserve temperature variability along the drifts.

Drift-scale latent heat and convective heat transport by seeping water are included in the MSTHM methodology because these effects are fully addressed by the LDTH submodels. Section 6.2.1 outlines the MSTHM approach and the thermal-hydrologic processes accounted for by the model.

Confirmation Status: Because   this   assumption   is   justified,   it   does   not   require further confirmation.

Use in the Model: This assumption is used in the MSTHM calculations in Sections 6.2.8, 6.3, 6.4, and 7.5.

5.2.3   Waste Package Emplacement

Assumption: The assumption is made that the entire waste package inventory of the repository is emplaced at the same time.

Rationale: The heat-generation-rate-versus-time tables (BSC 2005 [DIRS 173499]) for the entire waste package inventory, as well as for the individual waste package types (BSC 2005 [DIRS 173705]), were effectively developed for a single time of emplacement and therefore, do not represent how the heat-generation-rate tables may vary for the inventory and respective waste package types during the 23-year emplacement period. Therefore, this assumption is consistent with the heat-generation-rate-versus-time tables. The 50-year ventilation duration is the minimum time that any waste package location in the repository will experience ventilation. For a sequential emplacement repository analysis with all waste packages assumed to be the same years out of reactor at the time of emplacement, packages emplaced at the beginning of the 23-year period would experience higher peak temperatures relative to those emplaced at the end of the emplacement period.   The assumption that all waste packages are emplaced simultaneously at 50 years results in an analysis that bounds peak temperatures compared to an analysis that accounts for sequential emplacement after a minimum 50-year ventilation period. Thus, this assumption requires a minimum 50-year ventilation period in order to bound peak temperatures.

Confirmation Status: Because this assumption is justified, it does not require further confirmation.

Use in the Model: This assumption is applied to all submodels, and is used in the MSTHM calculations in Sections 6.3, 6.4, and 7.5.

5.3   MATERIAL PROPERTIES

5.3.1   Hydrologic Properties

5.3.1.1   Permeability of the Drip Shield and Waste Package for the MSTHM

Assumption: The drip shield and waste packages are assumed to be impermeable to liquid-phase flow for the entire duration of the MSTHM simulation. The drip-shield is not impermeable to gas-phase flow.

Rationale: Because it is not the purpose of the MSTHM model to predict the consequences of seepage onto (or through) the waste package, the assumption that the drip-shield and waste package are impermeable to liquid-phase flow does not affect the intended purpose of the MSTHM. The drip shield will have joints where the drip-shield segments meet. The joints between the drip-shield segments allow the transport (by advection and binary diffusion) of gas (air plus water vapor) between the inside and outside of the drip shield. Note that the assumption of the continuity of P_v across the drip shield is also used in *In-Drift Natural Convection and Condensation* (BSC 2004 [DIRS 164327], Section 6.3.3.2.7), the calculations from which are used as bounding cases only for TSPA-LA.

Confirmation Status: Because this assumption is justified, it does not require further confirmation.

Use in the Model: This assumption is used in Section 6.3.

5.3.1.2   Hydrologic Properties of the Intragranular Porosity in the Invert Materials

Assumption: The hydrologic properties of the intragranular porosity of the invert materials are assumed to be the same as those of the matrix of the host rock. Because the Tptpll (tsw35) unit is the host-rock unit for 75.1 percent of the repository area as modeled in the MSTHM (Table 6.3-3), it is assumed that matrix properties of the tsw35 unit are applicable to the crushed-tuff invert for the entire repository area. The ratio of the surface area of the crushed tuff grains divided by the connection length into the grains is assumed to be 1×10^5 for the intragranular porosity.   These assumptions are used in all LDTH submodels (Sections 6.2.6 and 6.3).

Rationale: The invert is composed of crushed-tuff gravel, which is derived from the host rock. The dual-permeability model (DKM) is applied to represent flow in crushed-tuff gravel, with flow within the tuff grains (called the intragranular porosity) corresponding to flow in the matrix continuum of the DKM, and flow around the tuff grains (called the intergranular porosity) corresponding to flow in the fracture continuum of the DKM. Therefore, it is reasonable to assume that the hydrologic properties of the intragranular porosity are the same as those for the matrix of the predominant host-rock unit. Applying the *intact* host-rock matrix properties to the intragranular porosity of the invert implies that there is no reduction in the rewetting rate of the invert by virtue of limited rock-to-grain or grain-to-grain contact area. The limited contact area will not prevent the crushed-tuff grains from eventually attaining capillary-pressure equilibrium with the adjoining host rock. When the drift wall has rewet to ambient liquid-phase saturation, relative humidity at the drift wall will be very high (> 99 percent). The crushed-tuff grains in the invert cannot remain dry when exposed to a high-relative humidity environment. However, the limited rock-to-grain (and grain-to-grain) contact area may impede the rate at which rewetting allows the invert to attain capillary-pressure equilibrium with the adjoining host rock. Thus, there is some uncertainty about the time required for the invert to rewet to ambient liquid-phase saturation conditions. The fact that the crushed-tuff invert could be derived from material from the other three host-rock units (Tptpll, Tptpmn, and Tptpln) is also a source of uncertainty with respect to the time required for the invert to rewet to ambient liquid-phase saturation conditions.

The assumption that the ratio of the surface area of crushed-tuff grains divided by the connection length into the grains is equal to 1×10^5 affects the disequilibrium between the intergranular porosity and the intergranular porosity. For 3-mm-diameter grains and 45 percent intergranular porosity that apply to the invert (Table 4.1-2), this ratio is 7.33×10^5. Using a value of 1×10^5, which is a ratio smaller than 7.33×10^5, is appropriate because it is unlikely that all of the grain surfaces will be wetted as water drains through the intergranular porosity.

Section 6.3-11 discusses a sensitivity analysis of thermal-hydrological conditions in the invert to hydrologic properties of the intragranular porosity of the crushed-tuff gravel. Figure 6.3-63 plots the liquid-phase saturation for the intragranular porosity and the temperature averaged over the invert. Four different cases are considered, with each case utilizing the matrix properties from

each of the respective host-rock units: Tptpul (tsw33), Tptpmn (tsw34), Tptpll (tsw35), and Tptpln (tsw36). Invert temperature is insensitive to the hydrologic properties of the intragranular porosity (Figure 6.3-63b). Liquid-phase saturation is also insensitive to hydrologic properties of the intragranular porosity (Figure 6.3-63a). Figure 6.3-64 plots temperature and relative humidity at different locations in the drift, including the host rock at crown of the drift and below the invert, and at the top and bottom of the invert beneath the drip shield for crushed-tuff gravel derived from each of the host-rock units, respectively. Both temperature and relative humidity at those locations are insensitive to hydrologic properties of the intragranular porosity. This lack of sensitivity justifies this assumption.

Confirmation Status: Because these assumptions are considered to be adequate, they do not require further confirmation.

Use in the Model: This assumption is used in Section 6.3.

5.3.1.3 Hydrologic Properties for the Concrete Invert in the Drift Scale Test

Assumption: The hydrologic properties for the Tptpmn (tsw34) host rock in the Drift Scale Test (DST) are assumed to be applicable to the concrete invert in the Heated Drift of the DST.

Rationale: Hydrologic properties for the concrete invert were not measured and are not readily available from the literature. Because the invert comprises such a small volume relative to the thermally perturbed volume of the host rock in the DST, this assumption is justified.

Confirmation Status: Because this assumption is justified, it does not require further confirmation.

Use in the Model: This assumption is used in Section 7.4.

5.3.1.4 Fracture Permeability of the Host Rock in the Wing-Heater Array of the Drift Scale Test

Assumption: The boreholes that contain the wing heaters in the Drift Scale Test (DST) are not explicitly represented in the DST thermal-hydrologic models. The boreholes, which intersect the Heated Drift are not sealed and provide preferential conduits for gas flow. It is assumed that increasing the fracture permeability by a factor of 1,000, in the lateral (horizontal) direction, for the wing-heater array (Figures 7.4-2 and 7.4-16) adequately represents the influence of the wing-heater boreholes as preferential conduits to gas flow. Note that the lateral direction is parallel to the axis of the wing-heater boreholes. Note also that for the interval between the wing heaters and the Heated Drift the fracture permeability is also increased by a factor of 1,000 in the lateral (horizontal) direction.

Rationale: The wing-heater arrays consist of 50 open boreholes (with 25 boreholes located on each side of the Heated Drift) that function as preferential conduits (in the lateral direction) to gas flow within the boiling and dryout zones of the DST. The effect on thermal-hydrologic behavior is to provide a means of relieving gas-phase pressure buildup in the center of the boiling zone and to allow some of the water vapor generated in that zone to enter the Heated Drift and exit through the leaky bulkhead. A thousand-fold increase in lateral fracture

permeability effectively eliminates resistance to gas flow from the wing-heater array into the Heated Drift. In Section 7.4, it is found that modeled temperatures and liquid-phase saturations are weakly dependent on whether water vapor leaves the DST through the bulkhead. It should be noted that much of this water vapor entered in the Heated Drift from the wing-heater array. Therefore, the assumption for fracture permeability in the wing-heater array is justified in light of its small impact on modeled thermal-hydrologic behavior in the DST.

Confirmation Status: Because this assumption is justified, it does not require further confirmation.

Use in the Model: This assumption is used in Section 7.4.

5.3.1.5 Permeability of the Bulkhead in the Drift Scale Test

Assumption: The bulkhead in the Drift Scale Test (DST) is assumed to be extremely permeable, with a permeability one-tenth that of the open drift. This assumption is made because the bulkhead is not sealed and because it contains several openings between the hot and cold side of the bulkhead.

Rationale: *Drift-Scale Coupled Processes (DST and TH Seepage) Models* (BSC 2004 [DIRS 170338], Section 7.3.4) discusses how the bulkhead functions as an open boundary for gas-phase flow. In Section 7.4 of this report, it is found that modeled temperatures and liquid-phase saturations are weakly dependent on whether water vapor leaves the DST through the bulkhead. Therefore, the assumption for the permeability of the bulkhead is justified in light of its small impact on modeled thermal-hydrologic behavior in the DST.

Confirmation Status: Because this assumption is justified, it does not require further confirmation.

Use in the Model: This assumption is used in Section 7.4.

5.3.1.6 Permeability of the Bulkhead in the Three-Dimensional Monolithic Thermal-Hydrologic Model Used in the MSTHM Validation Test Case

Assumption: The nested-mesh three-dimensional monolithic thermal-hydrologic model, which is called the D/LMTH model and used in the MSTHM validation test case (Section 7.5), has a leaky bulkhead located just beyond the last waste package at the edge of the drift. It is assumed that this bulkhead is leaky, with the same bulk permeability as that of the adjoining fractured rock mass.

Rationale: The influence of an extremely leaky bulkhead on the DST thermal-hydrologic model results is investigated in Section 7.4, where it is found that modeled temperatures and liquid-phase saturations are weakly dependent on whether water vapor leaves the DST through the bulkhead. Therefore, the permeability of the bulkhead in the DST has a small impact on modeled thermal-hydrologic behavior in the DST. Because the thermally perturbed (boiling) zone of the DST is in closer proximity to the bulkhead than it will be for most of the interval of most emplacement drifts in the repository, the impact of the bulkhead on predicted thermal-hydrologic conditions along emplacement drifts will be no greater than that

demonstrated for the DST in Section 7.4. Therefore, the assumed permeability of the bulkhead in the three-dimensional monolithic D/LMTH model does not play a significant role in thermal-hydrologic behavior predicted in that model; thus, this assumption is justified.

Confirmation Status: Because this assumption is justified, it does not require further confirmation.

Use in the Model: This assumption is used in Section 7.5.

5.3.1.7 Pseudo Permeability of the Gas-Filled Cavities Inside the Emplacement Drifts in the LDTH Submodels

Assumption: The gas-filled cavity between the drip shield and drift wall is represented as a porous media with 100 percent porosity and a very large value of pseudo permeability of 1.0×10^{-8} m^2.

Rationale: The value for permeability (1.0×10^{-8} m^2) for the gas-filled cavity in the emplacement drifts is much larger than the bulk permeability (which is nearly the same as the fracture permeability in Table IV-4) of the four host-rock units (7.8×10^{-13}, 3.3×10^{-13}, 9.1×10^{-13}, and 1.3×10^{-12} m^2 for the tsw33, tsw34, tsw35, and tsw36, respectively). The effective permeability is large enough so that it does not impede advective gas-phase flow within the emplacement drifts. Because the LDTH submodel, in principle, allows natural convection to occur within the drift cavity, a possible concern is whether the in-drift convective cooling effect, together with the use of the effective thermal conductivity for the drift cavity, will over-account for the magnitude of in-drift convective cooling. Section 6.3.10 discusses a sensitivity analysis of in-drift pseudo permeability. Figure 6.3-62 plots drip-shield temperature and relative humidity for six different values of in-drift pseudo permeability, ranging over six orders of magnitude. Over this six order of magnitude range, the value of in-drift pseudo permeability has an insignificant influence on in-drift temperature and relative humidity. The range in peak drip-shield temperature is 150.9°C to 151.1°C for these cases. Clearly, there is no over-accounting of convective cooling in the LDTH submodels that support the MSTHM calculations in this report. Therefore, the approach of using an effective thermal conductivity for the drift cavity and a value of pseudo permeability of 1.0×10^{-8} m^2 is reasonable and appropriate in the LDTH submodels.

Confirmation Status: Because this assumption is considered to be adequate, it does not require further confirmation.

Use in the Model: This assumption is used in Sections 6.3, 6.4, 7.4, and 7.5.

5.3.1.8 Permeability of the Intergranular Porosity of the Invert Materials

Assumption: The permeability of the intergranular porosity of the crushed-tuff invert is 1.0×10^{-9} m^2, which is between the permeability values for the 0.317-mm particle size (1.681×10^{-10} m^2) and for the 3-mm particle size (1.511×10^{-8} m^2) from Table X-7 of Appendix X.

Rationale: The potential range of values for the permeability of the intergranular porosity of the crushed-tuff invert (Table X-7 of Appendix X) has little effect on thermal-hydrologic conditions in the invert for two reasons. The first reason relates to liquid-phase flow. An inspection of the LDTH submodel output related to the MSTHM base-case calculations for the TSPA-LA shows that the intergranular porosity remains dry for all but the initial one-to-two years of the postclosure period. During the first year or two following the end of the ventilation period, boiling and condensation within the invert results in a very small amount of condensate drainage at the base of the invert. After this condensate has drained and the invert has become dry as a result of boiling, the intergranular porosity is completely dry (i.e., 100 percent gas-filled). Therefore, liquid-phase flow in the intergranular porosity does not occur after the brief period of condensate drainage. The second reason relates to gas-phase flow. The value for permeability (of 1.0×10^{-9} m^2) for the intergranular porosity of the crushed-tuff invert is much larger than the bulk permeability (which is nearly the same as the fracture permeability in Table IV-4) of the four host-rock units (7.8×10^{-13}, 3.3×10^{-13}, 9.1×10^{-13}, and 1.3×10^{-12} m^2 for the tsw33, tsw34, tsw35, and tsw36, respectively). The effective permeability is large enough that it does not impede advective gas-phase flow within the emplacement drifts.

Section 6.3-11 discusses a sensitivity analysis of thermal-hydrological conditions in the invert to hydrologic properties of the intergranular porosity of the crushed-tuff gravel. Figure 6.3-65 plots the liquid-phase saturation for the intragranular porosity, temperature, and relative humidity at the top of the invert beneath the drip shield for five different sets of hydrologic properties for the intergranular porosity. Temperature, liquid-phase saturation, and relative humidity are all insensitive to the hydrologic properties of the intergranular porosity. This lack of sensitivity justifies this assumption.

Confirmation Status: Because this assumption is considered to be adequate, it does not require further confirmation.

Use in the Model: This assumption is used in Section 6.3.

5.3.1.9   Tortuosity Factor for Binary Gas-Phase Diffusion

Assumption: Appropriate values for the tortuosity factor are selected for the matrix and fracture continuum on the basis of the parameter range given by de Marsily (1986 [DIRS 100439], p. 233), which ranges from a value of 0.1 for clays to 0.7 for sands. A value of 0.2 is estimated for the matrix continuum because the pore sizes for the matrix are closer to that of clays than to that of sands. A value of 0.7 is assumed for the fracture continuum because the effective pore sizes for fractures are similar to those of sands.

Rationale: The tortuosity factor is used for determining the binary gas-phase diffusion of air and water vapor. Binary gas-phase diffusion is insignificant to the MSTHM results because its influence is primarily confined to being an insignificant impact on heat flow, compared to the impact of conductive and convective heat flow (Buscheck and Nitao 1994 [DIRS 130561], pp. 15 to 16). Therefore, exact quantification of the tortuosity factor is not required; instead appropriate values are taken from the literature, as discussed above. A value of tortuosity factor of 0.2 is selected for the rock matrix because the pore sizes of the matrix are similar to those of clay, which has a value for tortuosity factor of 0.1. The tortuosity factor is set to 0.7 for the

fractures, which corresponds to the highest value reported by de Marsily (1986 [DIRS 100439]), which corresponds to the value for sand. Binary gas-phase diffusion is further modified for the fracture-to-fracture connections by multiplication of the tortuosity factor by the fracture porosity of the bulk rock (Buscheck and Nitao 1994 [DIRS 130561], Equation 8). This operation yields the appropriate value for fracture-to-fracture interconnection area. Similarly, binary gas-phase diffusion is modified for the matrix-to-matrix connections by multiplication of the tortuosity factor by the matrix porosity of the bulk rock. This operation yields the appropriate value for the matrix-to-matrix interconnection area.

Confirmation Status: Because this assumption is considered to be adequate, it does not require further confirmation.

Use in the Model: This assumption is used in Sections 6.3, 7.3, 7.4, and 7.5.

5.3.1.10   Permeability of Host Rock at Emplacement Drift Wall

Assumption: The permeability of the host rock at the drift-wall surface is assumed to be unaffected by the presence of Bernold-style surface sheets, which are described by Michel (1999 [DIRS 163054]), *Ground Control for Emplacement Drifts for LA* (BSC 2004 [DIRS 170292]), and *Longevity of Emplacement Drift Ground Support Materials for LA* (BSC 2003 [DIRS 165425]). Thus, it is assumed that the drift wall can be treated as an uncovered surface, with unimpeded gas- and liquid-phase flow between the host rock and drift cavity.

Rationale: Bernold-style surface sheets (Michel 1999 [DIRS 163054]) are bolted tightly to the drift wall to provide ground control for emplacement drifts, as described in *Ground Control for Emplacement Drifts for LA* (BSC 2004 [DIRS 170292]) and *Longevity of Emplacement Drift Ground Support Materials for LA* (BSC 2003 [DIRS 165425]). The Bernold-style surface sheets are perforated and corrugated to provide air circulation with the drift cavity (BSC 2004 [DIRS 170292], Section 6.3.1.2; BSC 2003 [DIRS 165425], Section 6.3.2). Therefore, it is reasonable to assume that the Bernold surface sheets have an insignificant influence on the permeability of the host rock at the emplacement drift-wall surface.

Confirmation Status: Because this assumption is justified, it does not require further confirmation.

Use in the Model: This assumption is used in Sections 6.3, 6.4, and 7.5.

5.3.2   Thermal Properties

5.3.2.1   Thermal Conductivity in SDT, DDT, and SMT Submodels

Assumption: The thermal conductivity data is provided for both dry and wet conditions. The conduction-only submodels (SDT, DDT, and SMT submodels in Section 6.2) cannot explicitly represent the influence of liquid-phase saturation on thermal conductivity. Since the rock is generally much closer to being fully saturated than being completely dry, the wet value of thermal conductivity are applied to all conduction-only submodels. This assumption has an insignificant effect on the results of the MSTHM.

Rationale: This assumption must be judged in light of how the MSTHM combines the results of four families of submodels: SDT, DDT, SMT, and LDTH. The MSTHM methodology (see Figure 1-1, Table 1-1, Table 1-2, Table 1-3, Section 6.2.4, and Appendix IX) accounts for the influence of thermal-hydrologic processes (including liquid-phase saturation changes) on the temperature distribution around and inside the emplacement drifts. Thus the MSTHM fully accounts for the significant liquid-saturation dependence of thermal conductivity as it is affected by rock dryout and condensation buildup (if any). The LDTH submodels also represent the influence of the ambient liquid-phase saturation distribution, which is consistent with that of the three-dimensional UZ flow model, on drift-scale heat flow. It is also important to note that the zone for which the dry thermal conductivity is applicable is confined to a narrow cylindrically shaped dryout zone with a radius generally no greater than 10 m for the mean infiltration-flux case (Figure 6.3-4b).   The primary influence of the narrow zone of decreased thermal conductivity is on temperature buildup in the immediate vicinity of the emplacement drifts; this influence is fully captured in the finely gridded LDTH submodels of the MSTHM, which account for the liquid-phase saturation dependence of thermal conductivity. While significantly affecting the drift-scale temperature gradients around the drifts, this narrow region of reduced thermal conductivity has a no influence on mountain-scale heat flow. Because the volume of reduced thermal conductivity around the drifts is so small, compared to the scale at which mountain-scale heat flow occurs, it has an insignificant influence on mountain-scale heat flow. For the purposes of the SDT, SMT, and DDT submodels, the approximation is made that ambient liquid-phase saturation is 100 percent. The difference in thermal conductivity between a liquid-phase saturation of 90 percent (which is prevalent in the host-rock units) and 100 percent is small in comparison to parametric uncertainty of thermal conductivity (Section 6.3.2.2). Moreover, the LDTH submodel utilizes the ambient liquid-phase saturation values in determining thermal conductivity; thus, for drift-scale heat flow the MSTHM fully accounts for the ambient liquid-phase saturation conditions.

As for the validity of this assumption in the DDT submodel, it should be noted that the DDT submodel is only used for two purposes: (1) calculating the temperature difference between the waste package and drip shield and (2) calculating the longitudinal temperature variations along the drift axis.   Neither of these quantities is influenced by whether wet or dry thermal conductivity is applied in the host rock.

Section 7.5 describes the comparison between the MSTHM and a corresponding three-dimensional monolithic thermal-hydrologic model of the same three-drift system.   The good agreement between the MSTHM and the corresponding monolithic thermal-hydrologic model attests to the validity of this approach, as well as justifying the appropriateness of the assumption of the thermal conductivity used in the SDT, SMT, and DDT submodels.

Confirmation Status: Because this assumption is justified, it does not require further confirmation.

Use in the Model: This assumption is used in the MSTHM calculations in Sections 6.3 and 7.5.

5.3.2.2   SMT Submodel Saturated-Zone Thermal Properties

Assumption: The SMT submodel (Section 6.2.5) is the only submodel that explicitly represents the saturated zone. An assumption is made that the saturated zone is composed of a material with average thermal properties, including thermal conductivity, mass density, and specific heat capacity. The averaging is accomplished by determining area-weighting factors for each of the model layers from the UZ model that occur at the water table, which is the base of the grid from *UZ Flow Models and Submodels* (BSC 2004 [DIRS 169861]).

Rationale: The range in thermal properties of the units occurring at the water table is relatively narrow, and because the saturated zone is far enough away from the repository horizon (on the order of 300 m), the results of the MSTHM are insensitive to the averaging scheme selected for the thermal properties of the saturated zone.

Confirmation Status: Because the output of the MSTHM is not sensitive to this assumption, the assumption is justified and does not require further confirmation.

Use in the Model: This assumption is used in the MSTHM calculations in Sections 6.3 and 7.5.

5.3.2.3   Thermal Conductivity and Mass Density for the Dual-Permeability Model

Assumption: The dual-permeability model (DKM) is comprises a fracture and matrix continuum. It is necessary to apportion the bulk thermal property values to the fracture and matrix continua. The values of thermal conductivity K_{th} and mass density ρ are apportioned to the fracture and matrix from the values for the bulk rock mass, based on the fracture porosity ϕ_{frac} by the following relationships:

$$K_{th,frac} = K_{th,bulk} \times (\phi_{frac})$$

$$K_{th,mat} = K_{th,bulk} \times (1 - \phi_{frac})$$

$$\rho_{frac} = \rho_{bulk} \times (\phi_{frac})$$

$$\rho_{mat} = \rho_{bulk} \times (1 - \phi_{frac}).$$

The apportioning of fracture and matrix values of K_{th} and ρ is shown in Table IV-3b in Appendix IV. This assumption is used in the MSTHM calculations in Sections 6.3 and 7.5.

Rationale: This approach conserves the total value of thermal conductivity and the total value of mass density. Therefore, the total conductive heat flow is the same as a single continuum with the same total value of thermal conductivity. Similarly, during the transient (heat-up) period, the correct mass density of the rock mass is honored. This method is only used in the LDTH submodels.

Confirmation Status: Because   this   assumption   is   justified,   it   does   not   require further confirmation.

Use in the Model: This assumption is used in Sections 6.2.6, 6.3, and 7.5.

5.3.2.4   Thermal Properties of the Lumped Drip-Shield/Waste Package Heat Source in the LDTH Submodels

Assumption: The drip shield and waste package are represented as a lumped monolithic heat source in the LDTH submodels with thermal property values that are an average of the respective values for the waste package and drip shield. The mass density, specific heat, and thermal conductivity of the lumped monolithic heat source are a mass-weighted average of the respective waste package and drip-shield values.

Rationale: The purpose of the LDTH submodel within the context of the MSTHM (Section 6.2.4) does not require that the LDTH submodel provide a description of the temperature or hydrological effects inside the drip shield; thus, this assumption is justified.

Confirmation Status: Because this assumption is justified, it does not require further confirmation.

Use in the Model: This assumption is used in the MSTHM calculations in Sections 6.2.6, 6.3, and 7.5.

5.3.2.5   Thermal Properties for the Concrete Invert in the Drift Scale Test

Assumption: The thermal properties for the Tptpmn (tsw34) host rock in the Drift Scale Test (DST) are assumed to be applicable to the concrete invert in the Heated Drift of the DST. It is noted that the TSPA-LA design does not include a concrete liner.

Rationale: Because the invert comprises such a small volume relative to the thermally perturbed volume of the host rock in the DST (Figures 7.4-2 and 7.4-16) this assumption has an insignificant effect on thermal-hydrologic behavior in the DST; therefore, this assumption is justified. Moreover, the comparison between observed and simulated behavior in the DST is limited to the host rock, wherein the assumption about invert properties have an insignificant effect.

Confirmation Status: Because this assumption is justified, it does not require further confirmation.

Use in the Model: This assumption is used in Section 7.4.

5.3.2.6   Thermal Conductivity and Thickness of the Bulkhead in the Drift Scale Test

Assumption: The bulkhead in the Drift Scale Test is assumed to have a very large value of thermal conductivity (5.5 W/m°C) and a thickness of 0.12 m; thus, the thermal conductance of the bulkhead is assumed to be approximately 46 W/m²°C.

Rationale: As described in *Drift-Scale Test As-Built Report* (CRWMS M&O 1998 [DIRS 111115]), the bulkhead in the Drift Scale Test (DST) consists of a complex mix of steel, glass, and fiberglass. The thermal conductance of the bulkhead is assumed to be very large because portions of the bulkhead (such as the glass window) are not insulated and because the bulkhead is penetrated by a large array of metal conduit containing instrument cables and power

lines. Moreover, during the DST, the fiberglass insulation became extremely wet as a result of the condensation of water vapor that was passing through the bulkhead. The total effect of these conditions results in a large value of thermal conductance for the bulkhead that is very difficult to quantify. In Section 7.4, it is found that modeled temperatures and liquid-phase saturations are weakly dependent on whether water vapor leaves the DST through the bulkhead. In Section 7.4, it is also found that the heat loss through the bulkhead resulting from the convection of water vapor is much larger than the heat loss resulting from thermal conduction. Therefore, the assumption for the thermal conductance of the bulkhead is justified in light of its small impact on modeled thermal-hydrologic behavior in the DST.

Confirmation Status: Because this assumption is justified, it does not require further confirmation.

Use in the Model: This assumption is used in Section 7.4.

5.3.2.7 Emissivity of Emplacement Drift Wall

Assumption: The emissivity at the drift-wall surface is assumed to be unaffected by the presence of Bernold-style surface sheets, which are described by Michel (1999 [DIRS 163054]), *Ground Control for Emplacement Drifts for LA* (BSC 2004 [DIRS 170292]), and *Longevity of Emplacement Drift Ground Support Materials for LA* (BSC 2003 [DIRS 165425]). Thus, it is assumed that the drift wall can be treated as an uncovered surface, with an emissivity value of 0.9, which is the value for rock given by Incropera and DeWitt (1996 [DIRS 108184], Table A.11).

Rationale: Bernold-style surface sheets (Michel 1999 [DIRS 163054]) are rock bolted tightly to the drift wall to provide ground control for emplacement drifts, as described in *Ground Control for Emplacement Drifts for LA* (BSC 2004 [DIRS 170292]) and *Longevity of Emplacement Drift Ground Support Materials for LA* (BSC 2003 [DIRS 165425]). Because the Bernold surface sheets are in good mechanical contact with the surrounding rock, they are in reasonable thermal contact with the host rock as well. Thus, with respect to heat transfer in the drift, the influence of the Bernold surface sheets is to modify the value of emissivity at the drift-wall surface, compared to the value for exposed rock, as is described in Appendix VI. The Bernold-style surface sheets are a Type 316 stainless steel, which has an emissivity range of 0.52 to 0.66 (McAdams 1954 [DIRS 161435], p. 475). The value of effective emissivity ε_{eff} between the drip shield and drift-wall surface is affected by this change in emissivity at the drift wall surface. For the emissivity range of 0.52 to 0.66 for Type 316 stainless steel, the value of ε_{eff} between the drip shield and drift wall is reduced by 6.8 to 15.5 percent, compared to value of ε_{eff} used in the MSTHM predictions used in TSPA-LA (Appendix VI). Because thermal radiation depends on the difference of the respective temperatures each raised to the fourth power (Eq. VI-4), the influence of a 6.8 to 15.5 percent reduction in the value of ε_{eff} is small. When peak temperatures occur at the drift wall and drip shield (about 20 years after closure), reducing ε_{eff} by 6.8 to 15.5 percent results in a drip-shield temperature increase of 0.9 to 2.3°C, with an increase of 1.5°C for the average case (Appendix VI). The influence of reducing ε_{eff} by 6.8 to 15.5 percent on temperature decreases during cooldown after temperatures have peaked. These changes in temperature are insignificant compared to the influence of host-rock thermal conductivity

uncertainty and percolation-flux uncertainty. Therefore, it is reasonable to assume the Bernold surface sheets have an insignificant influence on heat transfer within the drift.

Confirmation Status: Because this assumption is justified, it does not require further confirmation.

Use in the Model: This assumption is used in Sections 6.3 and 6.4.

5.4 WASTE PACKAGE MODELING

5.4.1 Average Waste Package Diameter

Assumption: The waste package outer diameter is 1.644 meters, which is the diameter of the 21-PWR AP waste package (Table 4.1-2). This value is taken as the average diameter for the waste packages emplaced over the entire repository. This information is used only in the DDT submodels (Section 6.2.8).

Rationale: This assumption only influences two aspects of the MSTHM: (1) the temperature difference between the waste package and drip shield and (2) the waste package-to-waste package variation of this temperature difference. Note that this temperature difference depends on the waste package heat output. The 21-PWR AP waste packages, 21-PWR CR waste packages, and 44-BWR AP waste packages, comprising the majority of waste packages with an appreciable heat output, have diameters of 1.644, 1.644, and 1.674 meters, respectively (Table 4.1-2) which are very close to the value of 1.644 meters in the DDT submodels. Table 13 of *IED Waste Package Configuration [Sheet 1 of 1]* (BSC 2005 [DIRS 173501]) gives the nominal quantities of the various waste package types for the TSPA-LA design, including 4,299 21-PWR AP waste packages, 95 21-PWR CR waste packages, 2,831 44-BWR AP waste packages, and 11,184 total waste packages. Thus, these waste packages comprise a large portion (64.6 percent) of the waste package inventory in the TSPA-LA design. Waste packages that deviate more from a value of 1.644 meters, such as the 24-BWR 1.318-m-diameter AP waste packages and the 5-DHLW/DOE-SNF 2.110-m-diameter co-disposal waste packages (Table 4.1-2), generate much less heat and also comprise a relatively small portion of the overall waste package inventory (BSC 2005 [DIRS 173501], Table 13). Therefore, 1.644 meters is very close to the actual diameter for the majority of waste packages in the overall inventory and is also very close to the diameter of the waste packages generating an appreciable temperature difference between the waste package and drip shield.

Confirmation Status: On the basis of the rationale given above, this assumption is justified and does not require further confirmation.

Use in the Model: This assumption is used in Sections 6.2.8, 6.3, and 7.5.

5.4.2 Waste Package Sequence along Drifts

Assumption: The waste package sequence given in Figure 6.2-2 is assumed to be applicable over all emplacement drifts. Thus, this sequence is assumed to be representative of waste package-to-waste package heat output variability throughout the entire repository. The use of this sequence is equivalent to assuming that defense high-level waste (DHLW) waste packages, which produce

much less heat than commercial spent nuclear fuel (CSNF) waste packages, will not be grouped together. In other words, DHLW waste packages will always be placed adjacent to CSNF waste packages.

Rationale: Table 5.4-1 lists the nominal number of waste packages for the repository inventory. Table 5.4-1 also lists the waste packages of the assumed sequence in the MSTHM calculations. The waste packages in the assumed sequence in the MSTHM cover 86.7 percent of the total inventory. Moreover, the percentages of each of the respective waste package types in the MSTHM are similar to the corresponding percentages in the repository inventory. Therefore, the waste package sequence assumed in all of the MSTHM calculations is representative of the inventory of waste packages in the repository.

Table 5.4-1. Summary of Waste Package Types in the Repository Inventory and in the MSTHM

Waste Package Type	Nominal Number in Inventory[a]	Nominal Percentage of Inventory	Number Represented in MSTHM[b]	Percentage of Waste Packages Represented in MSTHM
21-PWR AP	4299	38.4%	2.5	35.7%
44-BWR AP	2831	25.4%	2.5	35.7%
5 DHLW/DOE SNF LONG	1406	12.6%	1	14.3%
5 DHLW/DOE SNF SHORT	1147	10.3%	1	14.3%
Total Number of 21-PWR AP, 44-BWR AP, 5 DHLW/DOE SNF LONG, 5 DHLW/DOE SNF-SHORT	9683	86.7%	7	100%
Total Inventory	11,184	100%	7	100%

[a] Source: BSC 2005 [DIRS 173501], Table 13.
[b] See Figure 6.2-2 and Table 6.3-13.

Confirmation Status: On the basis of the rationale given above, this assumption is justified and does not require further confirmation.

Use in the Model: This assumption is used in Sections 6.2.8 and 6.3.

5.5 RELATIVE HUMIDITY IN EMPLACEMENT DRIFTS

Assumption: For the purposes of calculating relative humidity (*RH*) on the drip shield and on the waste package the assumption is made that the partial pressure of water vapor P_v in the drift is uniform and the same as that on the drift-wall surface at a given location. This is the equivalent of saying that the absolute humidity in the drift is the same as that on the drift wall.

Rationale: This assumption recognizes that the gas in the drift (which consists of air and water vapor) is well mixed as a result turbulent mixing (driven by buoyant gas-phase convection) and binary vapor diffusion of air and water. This mixing causes the absolute humidity to be uniform inside the emplacement drift at a given location along the drift. This assumption is validated in Section 7.5 by virtue of the good agreement between the MSTHM predictions of relative humidity in the drift and those of the corresponding three-dimensional monolithic thermal-hydrologic model, which does not make this assumption about relative humidity in emplacement drifts.

Confirmation Status: Because this assumption is justified, it does not require further confirmation.

Use in the Model: This assumption is used in Sections 6.2.4, 6.3, 6.4, and 7.5.

5.6   CONDENSATE DRAINAGE AROUND EMPLACEMENT DRIFTS

Assumption: Condensate that drains around the boiling zone surrounding an individual drift is assumed not to cross the vertical midplanes, which lie between that drift and the adjoining emplacement drifts (note that these vertical midplanes are 40.5 m away (which is half the 81-m drift spacing) from the centerline of each drift). This assumption is implied with the use of the two-dimensional LDTH submodels (Section 6.2.6), which have adiabatic, no-fluid-flow boundaries on either side of the LDTH submodels.

Rationale: The boiling zones surrounding each emplacement drift are relatively narrow. As discussed in Section 6.3.1.1, the maximum lateral extent of boiling relative to the centerline of the emplacement drift is always much smaller than the half-drift spacing for the TSPA-LA design.   Therefore, the majority of the host rock between emplacement drifts always remains below the boiling point, thereby enabling condensate and percolation flux to continuously drain between emplacement drifts. Fracturing within the sequence of UZ model layer units at the repository horizon is dense, based on the fracture frequency data (DTN: LB0205REVUZPRP.001 [DIRS 159525]), which is not conducive to laterally diverting condensate drainage; thus, condensate drainage is extremely unlikely to cross the vertical midplane separating emplacement drifts.

Confirmation Status: Because this assumption is justified, it does not require further confirmation.

Use in the Model: This assumption is used in Sections 6.2.8, 6.3 and 7.5.

5.7   GAS- AND LIQUID-PHASE FLOW IN THE LONGITUDINAL DIRECTION ALONG EMPLACEMENT DRIFTS (THE COLD-TRAP EFFECT)

Assumption: Gas- and liquid-phase flow in the longitudinal direction along drifts is assumed to have an insignificant effect on all MSTHM predictions. This is equivalent to saying that the cold-trap effect does not play a significant role in the evolution of the temperature, relative humidity, and liquid-phase saturation histories within the emplacement drifts, as well as in the adjoining host rock. At the repository scale, the cold-trap effect involves the flow of water vapor from the hotter intervals of emplacement drifts (typically closer to the center of the repository) to cooler intervals (typically located closer to the edges of the repository) where this water vapor condenses. In principal, the cold-trap effect results in the transport of heat and moisture from hotter to cooler intervals of the emplacement drift. For all MSTHM predictions, it is assumed that heat and moisture transport in the longitudinal direction along emplacement drifts do not significantly affect thermal-hydrologic conditions along (and adjacent to) emplacement drifts. Thus, it is assumed that heat flow along the drifts is dominated by thermal radiation and that within the invert there is no capillary wicking of moisture in the longitudinal direction.

Rationale: This assumption is tested in Section 7.5, where the MSTHM is compared against a corresponding three-dimensional monolithic thermal-hydrologic model in which gas- and liquid-phase flow (i.e., the cold-trap effect) is allowed to occur along the emplacement drift, subject to limitations of porous media models. For the waste packages at the center of the repository, the MSTHM calculations are found to agree closely with those of the three-dimensional monolithic thermal-hydrologic model, with the differences between the two models being much smaller than the range of thermal-hydrologic conditions arising from parametric uncertainty. For the waste packages at the outer edge of the repository, the differences between the MSTHM predictions and those of the corresponding three-dimensional monolithic thermal-hydrologic model are larger than at the center of the repository. These differences, however, are still smaller than the range of thermal-hydrologic conditions arising from parametric uncertainty. The results of the validation study in Section 7.5 demonstrate that the MSTHM methodology (which includes the assumption of insignificant gas- and liquid-phase flow in the longitudinal direction along drifts) is validated for its intended purpose of predicting thermal-hydrologic conditions in emplacement drifts and in the adjoining host rock. Thus, this assumption is also justified.

Confirmation Status: Because this assumption is justified, it does not require further confirmation.

Use in the Model: This assumption is used in Sections 6.3 and 6.4, and is tested in Section 7.5.

5.8 PROPERTIES OF HOST-ROCK RUBBLE FOR LOW-PROBABILITY-SEISMIC COLLAPSED-DRIFT SCENARIO

5.8.1 Bulk Density of Host-Rock Rubble

In setting up the LDTH and DDT submodels (Sections 6.2.10 and 6.2.11) to represent the low-probability-seismic collapsed-drift scenario, a value of 1850 kg/m^3 was used for the rubble bulk density in the LDTH submodels (Table 6.2-3), while a rubble bulk density of 1608 kg/m^3 was used in the DDT submodels (Table 6.2-4). The bulk density of the intact Tptpll (tsw35) host rock is 1980 kg/m^3 (Tables IV-3b and IV-3c of Appendix IV). Using a bulk factor of 0.231 (Section 6.2.10.2) and a bulk density of 1980 kg/m^3 for the intact host rock, results in a rubble bulk density of 1608 kg/m^3. To assess whether this small difference in bulk density is significant, the LDTH submodel was rerun for the case where the rubble bulk density is 1608 kg/m^3, so that it could be compared to the case where the rubble bulk density is 1850 kg/m^3. As is evident in Figure 6.3-58, which plots the temperature and relative humidity at the crown of the drip shield for the low-K_{th} rubble, the influence of rubble bulk density is insignificant over the range of 1608 to 1850 kg/m^3. Therefore the following assumption can be made.

Assumption: The use of a bulk density value of 1850 kg/m^3 for the host-rock rubble in the LDTH submodels for the low-probability-seismic collapsed-drift scenario gives the same MSTHM results that would have been produced if a bulk density value of 1608 kg/m^3 had been used in the LDTH submodels for this scenario.

Rationale: Because steady-state heat flow conditions are quickly established within the rubble, temperature and relative humidity in the drift (Figure 6.3-58) are insensitive to the range in bulk rubble density (1680 to 1850 kg/m^3) considered in Section 6.3.7. Therefore, the MSTHM calculations for the low-probability-seismic collapsed-drift scenario are insensitive to the choice of rubble bulk density (1850 kg/m^3 versus 1608 kg/m^3).

Confirmation Status: Based on the rationale given above, this assumption is justified and does not require further confirmation.

Use in the Model: This assumption is used in Section 6.3.7.

INTENTIONALLY LEFT BLANK

6. MODEL DISCUSSION

This section of the model report describes the multiscale thermohydrologic model (MSTHM), including a discussion about its conceptual framework and how the MSTHM methodology implements that framework. The MSTHM is implemented in several input-data-processing and submodel-building steps (Figures 6-1 and 6-2). The four major steps are (1) submodel input-file preparation, (2) execution of the four submodel families with the use of the NUFT v3.0s code (Section 3.1.1), (3) execution of MSTHAC v7.0 (Section 3.1.5), and (4) binning and postprocessing (i.e., graphics preparation) of the output from MSTHAC v7.0. The overall organization of Section 6 is as follows:

- Section 6.1 presents the scientific framework for Yucca Mountain thermohydrology, beginning with an overview of the ambient hydrological system. This is followed by a discussion of radioactive-decay-heat-driven thermal-hydrologic behavior within the repository emplacement drifts and in the adjoining repository host rock.

- Section 6.2 describes the MSTHM approach. Before discussing the details of the MSTHM approach, this section presents the governing equations that are solved by the NUFT v3.0s and v3.0.1s codes to represent the coupled flow of water, water vapor, air, and heat at the drift scale and to represent heat flow at the mountain scale. This is followed by a detailed description of the four families of MSTHM submodels, which are run with the NUFT code, and the manner in which the Multiscale Thermohydrologic Model Abstraction Code (MSTHAC v7.0) integrates the results from those four families of submodels.

- Section 6.3 presents the results of the MSTHM for the lower-bound, mean, and upper-bound infiltration-flux cases with mean host-rock thermal conductivity; for the lower-bound infiltration-flux case with low host-rock thermal conductivity; and for the upper-bound infiltration-flux case with high host-rock thermal conductivity. This section also covers the sensitivity analysis of parameter uncertainty.

- Section 6.4 describes a study that compares the results of the MSTHM against those of a corresponding alternative conceptual model.

Before continuing, it is important to distinguish between the MSTHM and the Multiscale Thermohydrologic Abstraction Code (MSTHAC v7.0). The MSTHM is the process-level model itself, which consists of four families of submodel types (Section 6.2.4) that are run using the thermal-hydrologic simulation code NUFT v3.0s (Section 3.1.1) and the software that integrates the results of those submodel families. The integrating software used in this report is MSTHAC v7.0 (Section 3.1.5). There were no supporting and corroborating data or product outputs used in the development of this model.

The MSTHM predictions supporting the TSPA-LA utilize assumptions described in Sections 5.1.1, 5.1.2, 5.1.3, 5.1.4, 5.1.5, 5.2.1, 5.2.2, 5.2.3, 5.3.1.1, 5.3.1.2, 5.3.1.7, 5.3.1.8, 5.3.1.9, 5.3.1.10, 5.3.2.1, 5.3.2.2, 5.3.2.3, 5.3.2.4, 5.3.2.7, 5.4.1, 5.4.2, 5.5, 5.6, 5.7, and 5.8.1.
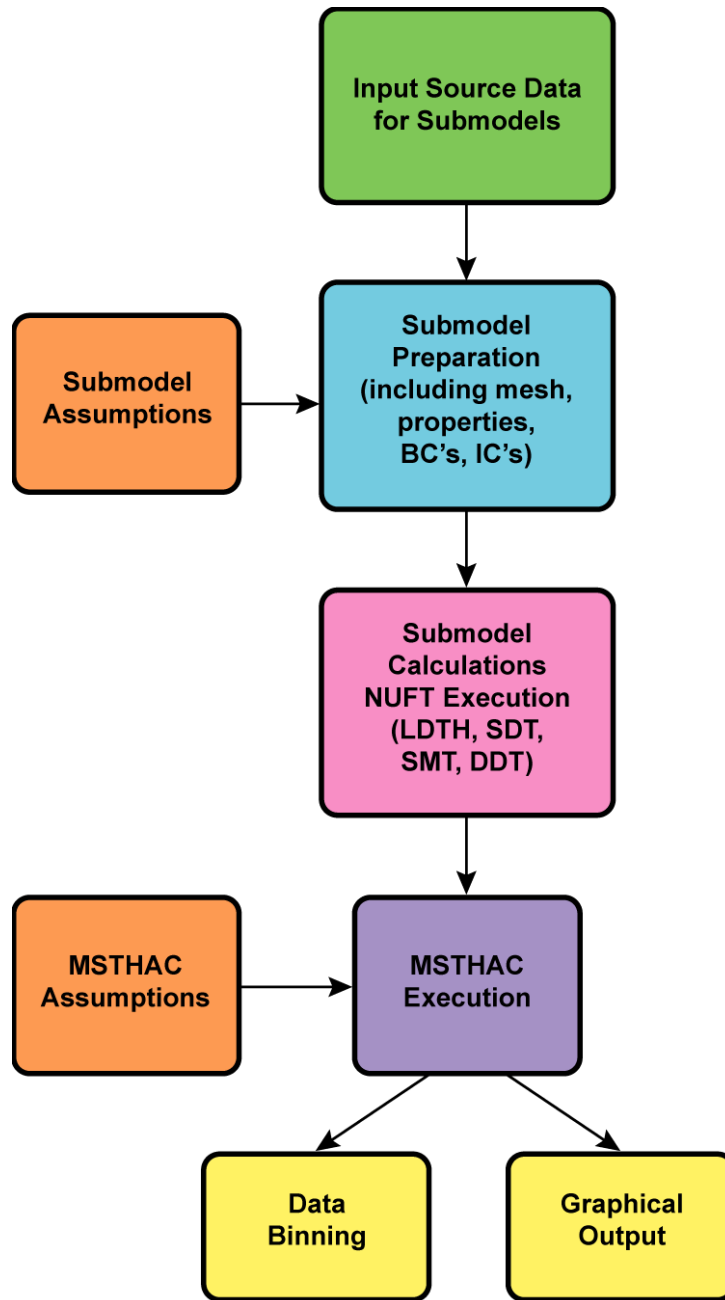
TB_AMR_fig1-2_MSTHM_flow

NOTE: BC = boundary conditions; IC = initial conditions.

Figure 6-1.   Overall Data Flow Diagram for the MSTHM
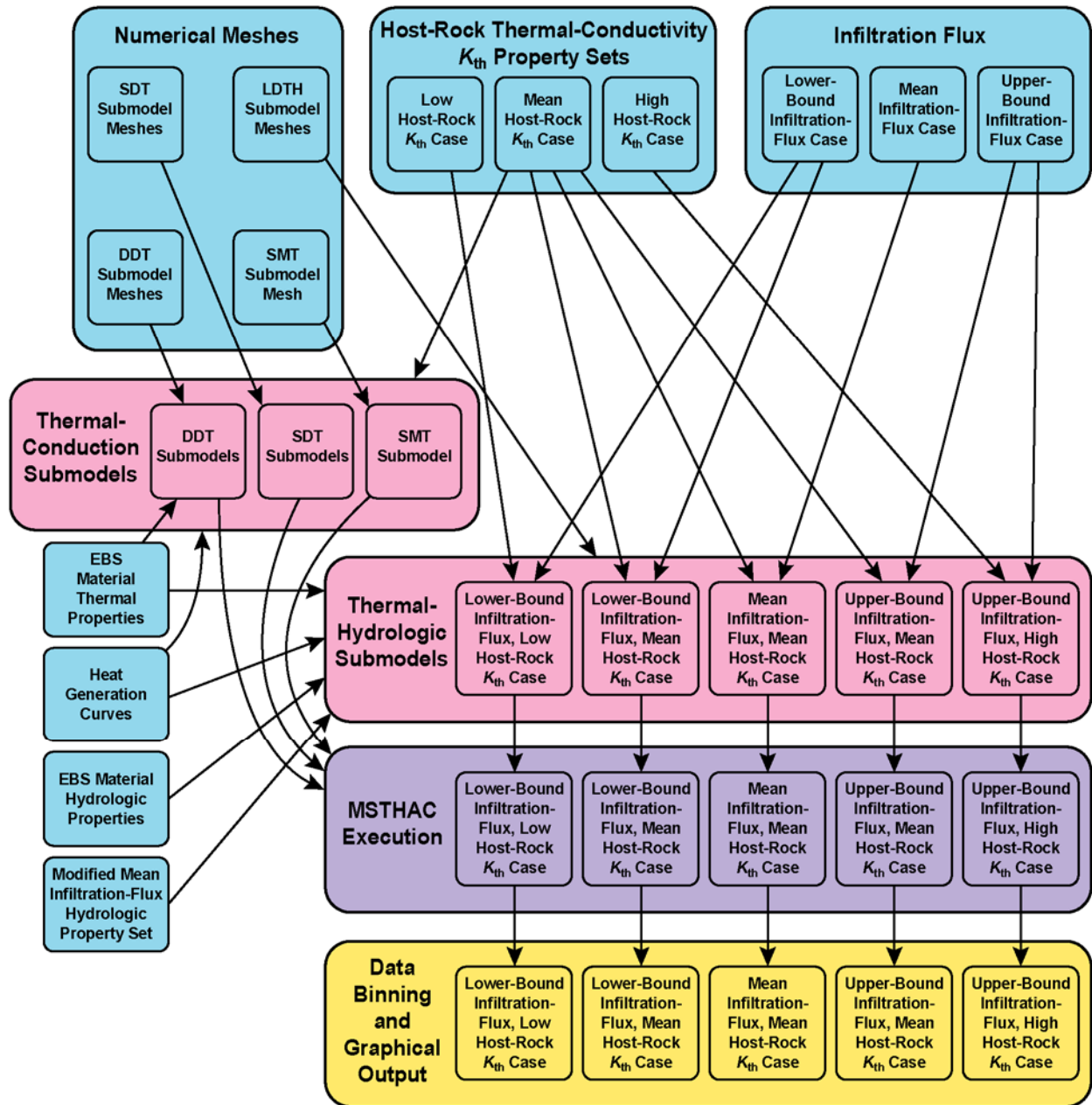
Figure 6-2. Relationship between Input Data and Submodels for Five Infiltration-Flux/Host-Rock Thermal-Conductivity K_{th} Cases

6.1 YUCCA MOUNTAIN THERMOHYDROLOGY CONCEPTUAL MODEL

The role of the movement of water and heat within the repository is treated by the study of thermohydrology, which combines the more traditional fields of hydrology and heat transfer. The physical domain that this model report is primarily concerned with is the unsaturated zone of Yucca Mountain that lies above the groundwater table. The geology of Yucca Mountain consists of several sequences of welded and nonwelded volcanic rocks, and the main hydrologic concern is with the movement of liquid water, originating from rainfall and snowmelt (Section 6.1.1). The thermal component of this model is concerned with the movement of liquid water driven by radioactive decay heat from emplaced waste and its effect on temperature and relative humidity (Section 6.1.2). When examining thermal-hydrologic phenomena, there are two distinct regions of concern: (1) the near-field host rock, and (2) within the repository emplacement drifts. The thermal-hydrologic phenomena associated with the host rock primarily involve boiling of water and re-wetting as heating diminishes with time (Section 6.1.3), while the thermal-hydrologic phenomena within the emplacement drift is associated with boiling, evaporation and condensation of water on the waste packages, drip shield, and drift wall (Section 6.1.4). Several factors can influence thermal-hydrologic phenomena, either through the design of the repository (e.g., the average areal-heat-density of the emplaced waste, as discussed in Section 6.1.5), or through the description of the natural system (e.g., percolation flux and thermal conductivity, as discussed in Section 6.1.5).

6.1.1 Ambient Hydrology and Geology

Yucca Mountain is composed of several sequences of volcanic tuffs deposited as ash flow sheets about 13 million years ago. Some units are completely devitrified and welded, while others are vitric or partially vitric with various degrees of welding. Some are also zeolitized to varying degrees. In general, the more welded units are more densely fractured. Hydrogeologic units, referred to as UZ-model layers in the grid developed by *UZ Flow Models and Submodels* (BSC 2004 [DIRS 169861], Section 6.1.1, Table 6.1-1), are defined primarily based on the degree of welding (Montazer and Wilson 1984 [DIRS 100161], p. 8). From the ground surface to the water table, these units are generally referred to as Tiva Canyon welded (TCw), Paintbrush nonwelded (PTn), Topopah Spring welded (TSw), Calico Hills nonwelded (CHn) and Crater Flat (Cfu). More details about the layering in the UZ are found in Table 6-5 of *Development of Numerical Grids for UZ Flow and Transport Modeling* (BSC 2004 [DIRS 169855]).

Most of the total fluid storage capacity of the welded units at Yucca Mountain is contained in the matrix pores of this rock. The permeability in the rock matrix in these units, however, is low, so fractures are the primary conduits for large-scale flow of water, air, and water vapor in these units. In some of the nonwelded units, fracturing is much less extensive, and the rock matrix is more permeable than in the welded units, causing gas and liquid-phase fluid flow to occur predominantly through the rock matrix.

The climate at Yucca Mountain is arid to semiarid, with infiltration from rainfall and snowmelt. Field data show that water that infiltrates at the ground surface percolates mostly vertically downward to the water table 700 m beneath the surface, with some degree of lateral diversion and the occasional occurrence of perched or semiperched aquifers (Flint et al. 2001 [DIRS 156351]). Note that under ambient conditions, the relative humidity (*RH*) in the

unsaturated zone at the elevation of the repository is very high with relative humidity generally above 99 percent (Buscheck et al. 2002 [DIRS 160749]).

6.1.2   Incorporating Radioactive Decay Heat

The repository is located in the unsaturated zone in the TSw hydrostratigraphic unit along a very gently dipping plane, approximately midway between the ground surface and the water table. The repository will accommodate the emplacement of spent nuclear fuel from commercial nuclear power plants and solidified high-level waste. The repository-wide thermal load declines exponentially with time, continuing for tens of thousands of years because of the very long half-life of many of the radionuclides (Figure 6.1-1).
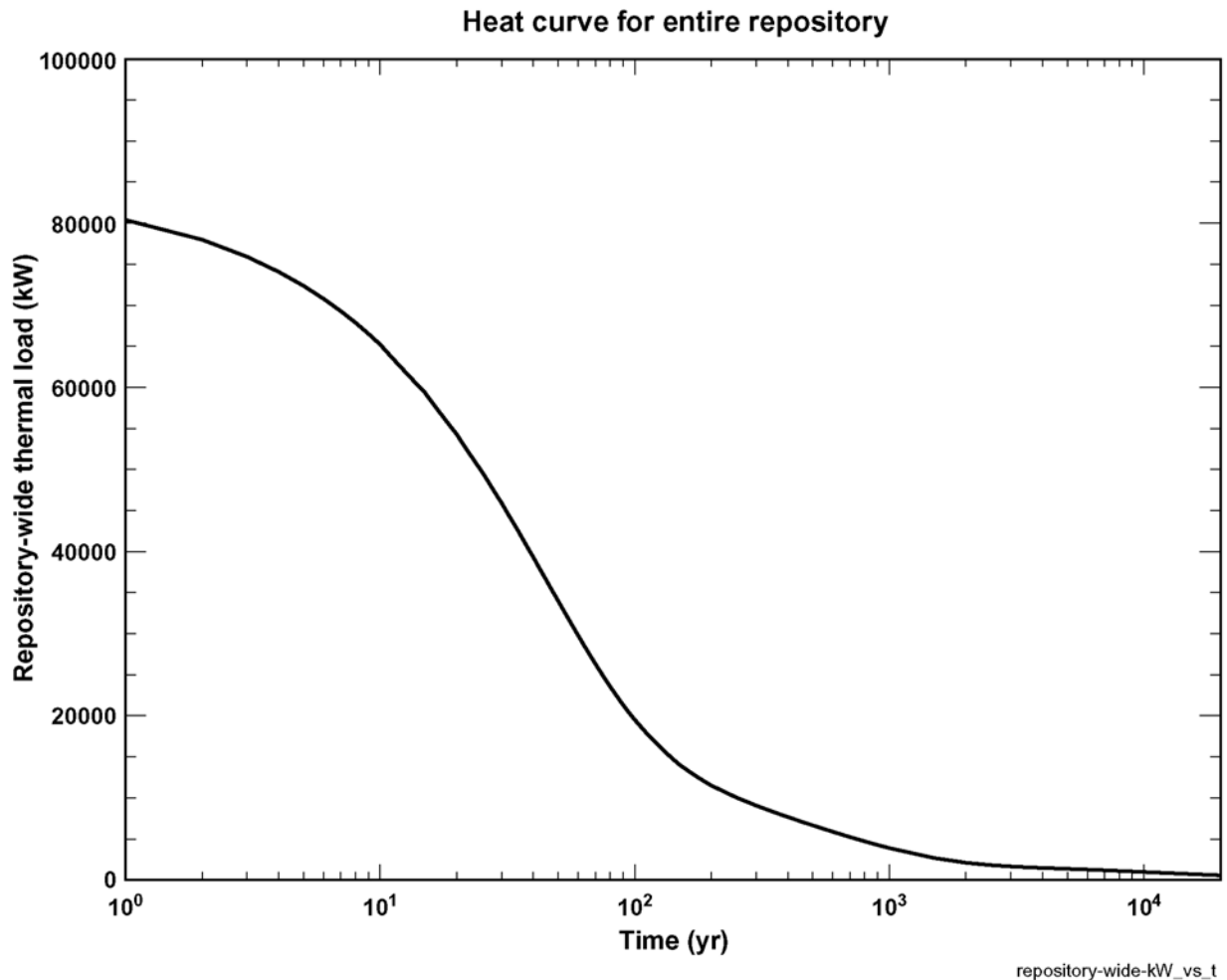
NOTE: The total repository heat load divided by the total length of emplacement drift in the repository (57.48 km) is equal to the line-averaged heat load. At the time of emplacement (0 yr) the total repository heat load is 83,300 kW, resulting in an initial line-averaged heat load of 1.45 kW/m. It is important to note that this is a semilog plot. At the time that this plot begins (1 year), the total repository heat load is 80,400 kW. This is the total thermal load represented in the SMT submodel (Section 6.2.5), using the information from BSC 2005 [DIRS 173499], Table 1.

Figure 6.1-1.   Repository-Wide Thermal Load Plotted as a Function of Time for the TSPA-LA Design

After the emplacement of heat-generating nuclear waste, the thermally driven flow of water vapor away from the heat source causes a redistribution of the pore fluids in the rock. Water in

the matrix pores evaporates, creating zones of rock dryout (with liquid-phase saturation substantially less than ambient values) around the emplacement drifts. This water vapor is driven (primarily in fractures) away from the heat source in the emplacement drifts to where cooler temperatures cause it to condense, forming condensation zones outside of the dryout zones. The reduction in liquid-phase saturation causes a reduction in relative humidity in both the near-field host rock as well as in the emplacement drifts. Heat pipes can result from the countercurrent flow of water vapor and liquid water between the dryout and condensation zones. The magnitude of the liquid flux in a heat pipe can greatly exceed the magnitude of ambient liquid-phase fluxes. As the heat pulse decays, the system gradually rewets, returning to ambient (humid) preheating conditions.

6.1.3 Thermohydrology in the Repository Host Rock

In the host rock, local thermal-hydrologic behavior is dominated by whether a location is inside or outside of the zone of boiling temperatures, 96°C (Buscheck et al. 2002 [DIRS 160749]) at the elevation of the repository horizon at Yucca Mountain approximately 1,100 m above mean sea level. Although evaporation, vapor flow (away from the heat source), and condensation occur at below-boiling temperatures, the thermally driven vaporization rates and vapor fluxes in the repository horizon are generally not great enough to result in significant dryout (and relative humidity reduction) in the rock unless temperatures are well above the boiling point.

The boiling zone evolves with time. Because most of the decay heat is removed with the ventilation air, temperatures are not high enough to allow boiling to occur during the preclosure (ventilation) period. However, because the ventilation air has a much lower relative humidity than ambient conditions in the host rock, some dryout will occur during the preclosure (ventilation) period. At the onset of the postclosure period when ventilation stops, a dryout zone caused by boiling-to-above-boiling temperatures forms in the rock immediately encircling each individual emplacement drift. Within this dryout zone, vaporization prevents liquid-phase flow. Moreover, capillary diversion will continue to divert liquid flow away from the drift opening, even after temperatures have dropped below the boiling point. As thermal output wanes, the dryout zones shrink, and the extent of dryout eventually retreats back to the drift wall (Section 6.2.2.1 of BSC 2004 [DIRS 170338]). Dryout zones around adjacent emplacement drifts never coalesce; they always remain distinct and separate.

Whether or not the boiling zones around adjacent drifts coalesce is important because it affects condensate drainage between drifts. If the repository (thermal) design does not result in coalescence of boiling zones, condensate drains continuously between the emplacement drifts. As discussed in Section 6.3.1.1, the maximum lateral extent of boiling relative to the centerline of the emplacement drift is always much smaller than the half-drift spacing for the TSPA-LA repository (thermal) design. Therefore, much of the host rock between emplacement drifts always remains below the boiling point, enabling condensate and percolation flux to continuously drain between emplacement drifts. Accordingly, the "cap" of accumulated condensate above the emplacement drifts is of very limited spatial extent. Variation in the spatial extent and duration of the boiling zone along the drift axis may also be important. Nonuniformity in boiling conditions along the drift axis (resulting from waste package-to-waste package variability in heat output) causes longitudinal variability in the radial extent and duration of boiling, and may promote seepage and/or condensation in the vicinity of cooler waste

packages. The end-to-end waste package spacing of 0.1 m (Table 4.1-2) used in the TSPA-LA repository design limits this longitudinal variability (Section 6.3.1.2).

6.1.4   Thermohydrology in Repository Emplacement Drifts

The TSPA-LA repository design includes 1.6-to 2.1-m-diameter (on average) waste packages constructed of corrosion-resistant materials, which are overlaid by upside down, U-shaped, corrosion-resistant metallic barriers called drip shields. Both the waste packages and drip shields are supported on an invert made of granular material on the floor of the drift. The configuration of these engineered components influences thermal-hydrologic behavior within the emplacement drifts.

Two important factors influence the local thermal-hydrologic conditions in the emplacement drifts. The first is whether temperature at the drift wall is above the boiling point, which controls the relative humidity in the near-field host rock and the potential for water seeping into the drift. The second is the temperature difference between the waste package and drift wall, which determines the relative humidity on the surfaces of the drip shield and waste package (Figure 6.1-2).   Specifically, the temperature difference between the waste package (or drip-shield) surface and the drift wall determines how much lower the relative humidity is on the waste package (or drip-shield) surface, compared to that on the drift wall. Note that the ratio of relative humidity on the waste package to relative humidity on the drift wall for a given temperature difference between these two surfaces decreases as the absolute temperature on the waste package increases during heating. Because of the edge-cooling effect, waste packages located closer to the repository edges cool down more quickly than those located closer to the repository center. Consequently, relative humidity reduction for waste packages located closer to the repository edges can be greater than for those located closer to the repository center.

Thermal-hydrologic behavior in and around emplacement drifts is easily described by three fundamental processes:

1. **Heat flow**–Occurs within emplacement drifts primarily by thermal radiation, and in the adjoining host rock, primarily by thermal conduction. Host-rock thermal conductivity is the key natural-system parameter determining the magnitude of temperature buildup in the host rock.

2. **Host-rock dryout**–Is driven by temperature buildup, resulting in evaporation (at the boiling point), which lowers the liquid-phase saturation in the host rock, thereby lowering the relative humidity in the host rock and in the emplacement drifts. The extent of dryout depends on the extent and duration of boiling conditions in the host rock, which depend on the magnitude of temperature buildup.

3. **Host-rock rewetting**–Primarily occurs as a result of gravity-driven percolation in fractures, with capillary-driven imbition into the adjoining matrix.   The rate of rewetting is controlled by the local percolation flux, except in regions of very low percolation flux (less than approximately 0.1 mm/yr), where modeling analyses show it is controlled by capillary-driven imbibition of water from the surrounding rock into the dryout zone, through the rock matrix (see Section 6.3.9).
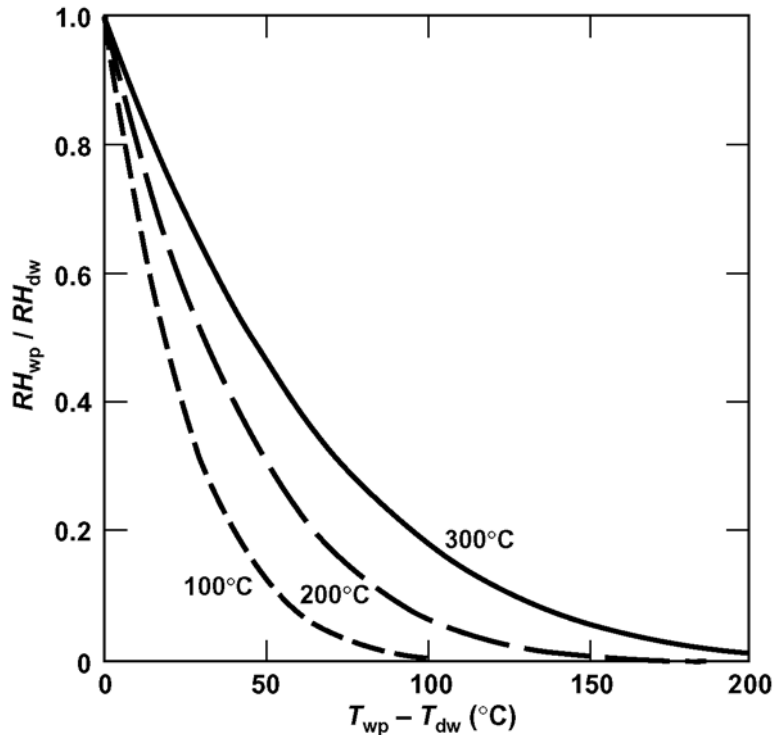
Source: See Table XIII-1.

NOTE: The ratio of relative humidity (RH) on the waste package surface to relative humidity on the drift-wall surface versus the temperature difference between these surfaces is plotted for three different temperatures (taken to be the average of the drift wall and waste package temperatures).

Figure 6.1-2. Ratio of Relative Humidity (RH) on the Waste Package Surface to Relative Humidity on the Drift-Wall Surface

The processes of dryout and rewetting are opposing. Net host-rock dryout, which is the balance between dryout and rewetting, is greatest in regions with a combination of low host-rock thermal conductivity (which facilitates greater temperature buildup) and low local percolation flux (which facilitates slower rewetting). Net host-rock dryout is least in regions with a combination of high host-rock thermal conductivity (which facilitates smaller temperature buildup) and high local percolation flux (which facilitates faster rewetting).

The temperature at the drift wall is controlled by the temperature buildup in the host rock, which is controlled by the local heating conditions and the host-rock thermal conductivity. The relative humidity at the drift wall is controlled by the reduction in liquid-phase saturation that results from boiling and rock dryout. The relative humidity at the drift wall controls relative humidity conditions within the drift; relative humidity in the drift can be no greater than it is at the drift wall. This is true because the absolute humidity within the drift is uniform or nearly so. Heat transfer between engineered components (such as the waste package and drip shield) and the drift wall determines the temperature difference between the waste package and drift wall. This temperature difference controls the reduction in relative humidity on the waste package, relative to that on the drift wall. The drip shield, which lies between the waste package and drift wall, functions as a thermal-radiation shield, which increases this temperature difference. The temperature difference between the waste package and the drift wall is greatest immediately after closure, and slowly decreases with time.

During the preclosure period (nominally 50 years), waste package heat output starts at the maximum, but the emplacement drifts are ventilated to remove most of the heat. As discussed in *Ventilation Model and Analysis Report* (BSC 2004 [DIRS 169862]), waste package temperatures are elevated, and some waste packages may approach 100°C immediately after emplacement (subject to control by ventilation). However, the warming of ventilation air ensures that preclosure conditions are dry, especially where in-drift temperatures are greatest.

At permanent closure, ventilation ceases and the drift-wall rock temperature is initially below boiling, but increases sharply, with temperature peaking within about 20 years. Waste package temperatures follow the evolution of the local drift-wall temperature, but are as much as 10 to 20°C warmer at the time when waste package temperatures peak, because of thermal resistance across the drip shield and the in-drift air spaces. This temperature difference approaches zero with time, as the heat output declines. The maximum postclosure temperature of a waste package at any location is determined by the history of heat output, the resistance to dissipation of heat in the host rock, heat transfer from the waste package to the drift wall, and the relationship to other nearby heat sources.

6.1.5   Design Factors Influencing Thermohydrology

There are many thermal design parameters that can affect thermal-hydrologic behavior in an underground nuclear waste repository (Table 6.1-1). These include the average areal-heat-generation density of the waste inventory over the heated repository footprint, and the average lineal-heat-generation density along the drifts (called the line-averaged thermal load). For a given waste inventory, these two parameters constrain the distance between drifts and the size of the required repository footprint.

Other engineering parameters include the placement of the repository horizon relative to the ground surface and the local hydrostratigraphy. The depth of the repository below the ground surface (overburden thickness) translates into the thickness of insulating rock between the repository and the ground surface, which acts like a heat sink. In-drift configuration, including most notably the presence or absence of backfill in the emplacement drifts, and the properties of any in-drift materials are also important to thermohydrology.

Waste package spacing affects the degree of nonuniformity of heating conditions along the axis of the drift. Individual waste packages are cylindrical in shape and 3.5 to 5.1 m long (Table 4.1-2). If waste packages are spaced far apart from each other along the drift ("point-load" waste package spacing), heating conditions along the drift are less uniform. For waste packages spaced nearly end-to-end ("line-load" waste package spacing), and which is the TSPA-LA repository design, adjacent waste packages couple and share their heat output more effectively, acting more like a uniform line source of heat. Line-load waste package spacing results in more uniform, and persistent rock dryout around the drifts and more efficient condensate shedding between drifts than does point-load waste package spacing with the same overall areal-heat-generation density. Point-load waste package spacing results in less uniform rock dryout around the drifts and less uniform thermal-hydrologic conditions along the drifts (Buscheck et al. 1999 [DIRS 145972]; Buscheck et al. (2002) [DIRS 160749]).

Table 6.1-1. Key Thermal Design Factors and Natural System Parameters Influencing Thermal-Hydrologic Conditions in the Emplacement Drifts and Near-Field Host Rock

Engineering Design Factors	Natural System Parameters
• Overall areal-heat-generation density of waste inventory • Line-averaged thermal load along drifts • Distance between emplacement drifts • Age of spent nuclear fuel at time of emplacement • Location of repository horizon with respect to stratigraphy • Overburden thickness (depth of repository below ground surface) • Repository footprint • Waste package spacing (line load versus point load) • Waste package sequencing • Duration and heat-removal efficiency of drift ventilation • In-drift design and materials	• Percolation flux above the repository horizon • Thermal conductivity (particularly for host-rock units) • Bulk rock density and specific heat • Matrix imbition • Capillary wicking in fractures

6.1.6 Natural System Factors Influencing Thermohydrology

Important natural system factors that affect the thermal-hydrologic environment include thermal properties of the repository host rock, hydrologic properties of the host rock, and the magnitude and spatial and temporal distribution of the percolation flux above the repository horizon (Table 6.1-1). Of these factors, the host-rock thermal conductivity and percolation flux above the repository horizon are the most important.

6.2 THE MULTISCALE THERMOHYDROLOGIC MODELING APPROACH

6.2.1 Overview of the MSTHM

The multiscale thermohydrologic model simulates nonisothermal, multiphase-flow in fractured porous rock of variable liquid-phase saturation and thermal radiation and convection in open cavities. The motivation behind the multiscale modeling approach is the need for a modeling tool that simultaneously accounts for relevant features, events, and processes (FEPs) that occur at a scale of a few tens of centimeters around individual waste packages and emplacement drifts and also at the scale of the mountain. A single numerical model is not used because it requires too large a computational cost to be a viable simulation tool. Note that performance assessment requires the ability to conduct multiple realizations. The multiscale modeling approach was used to model more than 20 different realizations for *Total System Performance Assessment-Viability Assessment (TSPA-VA) Analyses Technical Basis Document* (CRWMS M&O 1998 [DIRS 108000], Chapter 3). The approach was also used to model fourteen alternative repository designs during the license application design selection process (Buscheck 1999 [DIRS 130078]) and in six different realizations for *Total System Performance Assessment for the Site Recommendation* (CRWMS M&O 2000 [DIRS 153246], Section 3.3.3) and six different realizations for *FY 01 Supplemental Science and Performance Analyses, Volume 1: Scientific Bases and Analyses* (BSC 2001 [DIRS 155950], Section 5). The following description is a brief overview; a detailed description of the MSTHM is found in Section 6.2.4.

The multiscale approach breaks the solution of thermal-hydrologic modeling at Yucca Mountain into smaller pieces by varying dimensionality requirements (one-, two-, or three-dimensional) as needed for detail. The approach further subdivides the problem into thermal and thermal-hydrologic submodels. By subdividing the problem into more tractable pieces, the DOE can use efficient thermal-conduction/radiation submodels to address the three-dimensional nature of the heated repository footprint and mountain-scale heat flow as well as the three-dimensional geometric details of the in-drift engineered components, waste package-to-waste package heat-generation variability, and drift-scale heat flow. Two-dimensional thermal-hydrologic models, which are more efficient than three-dimensional thermal-hydrologic models, are used to model all thermal-hydrologic parameters in detail within the emplacement drifts and in the adjoining host rock.

Thermal-hydrologic behavior is directly simulated for an "average" waste package using a two-dimensional drift-scale cross section for a variety of areal-heat-generation densities at numerous locations throughout the repository footprint. In these simulations, the flow of liquid and gas (water vapor and air) through variably saturated fractured porous media is represented with a dual-permeability model of flow interaction between the fractures and rock matrix. This model accounts for two-phase behavior (i.e., evaporation, boiling, and condensation). Open drifts are modeled as porous media with very high permeability and porosity. The influence of buoyant gas-phase (natural) convection in the drift on heat flow is approximated with the use of an effective thermal conductivity for the gas-filled drift cavity that is based on a correlation (Francis et al. 2003 [DIRS 164602], Table 6). The model represents the processes of thermal conduction and convection in rock, and thermal conduction, convection, and radiation in the open cavities in the emplacement drifts.

The primary purpose of the multiscale thermohydrologic model is to predict the evolution of thermal-hydrologic conditions within emplacement drifts. To accomplish this it is necessary to predict thermal-hydrologic conditions in the adjoining host rock. As discussed in Section 6.1.4, thermal-hydrologic behavior in and around emplacement drifts can be simply broken down to three fundamental processes: (1) heat flow, (2) host-rock dryout, and (3) host-rock rewetting. A key principle utilized by the multiscale thermal-hydrologic model approach is that mountain-scale heat flow is dominated by thermal conduction. A second key principle is that heat flow within the drift is dominated by thermal radiation and that the influence of natural convection on heat flow within the drift can be approximated with an effective thermal conductivity. To summarize, the multiscale thermal-hydrologic model must represent the following processes:

1. **Heat flow within the drift**–The range of heat output generated by various waste package types and the delivery of that heat to the drift wall.

2. **Mountain-scale heat flow**–Conduction of heat throughout the mountain, from the ground surface down to a sufficient depth, which includes the entire unsaturated zone plus the upper portion (1000 m) of the saturated zone.

3. **Drift-scale heat flow in the host rock**–Heat flow (primarily by conduction, but also convection) occurring in variably saturated, fractured porous rock. Because thermal conductivity depends on liquid-phase saturation, it is necessary to capture the influence of host-rock dryout and rewetting.

4. **Host-rock dryout and rewetting**–Temperature buildup and cooldown in the host rock, as well as the magnitude of liquid-phase flux that enters the dryout zone (primarily resulting from gravity-driven percolation flux), influence the spatial and temporal extent of dryout.

The multiscale thermohydrologic model consists of four different submodel types, described in detail in Section 6.2.4, which collectively represent all four of these processes. Two of the submodel types (SMT and DDT) are three-dimensional in order to represent mountain-scale heat flow, which occurs by conduction, and to represent heat flow within the drifts, which occurs by conduction, radiation, and convection, and which is approximated with an effective thermal conductivity.

Two-dimensional drift-scale thermal-hydrologic submodels are used to predict drift-scale heat flow, dryout, and rewetting in the host rock; these models also predicts heat flow within the drift and how that heat flow influences relative humidity within the drift. One-dimensional drift-scale thermal-conduction models are used to relate the temperature predicted by the two-dimensional drift-scale thermal-hydrologic submodels with the temperatures predicted by the three-dimensional mountain-scale thermal-conduction submodel.

It is important to note that drift-scale thermal-hydrologic models are bounded on all four sides by insulated impermeable boundaries that prevent any heat or mass (gas- and liquid-phase) flow across these boundaries. As in the mountain-scale submodel, drift-scale submodels have an upper and lower boundary with specified boundary conditions. Thus, heat and mass flow can leave the drift-scale submodels at the upper and lower boundary. Because of the insulated lateral and longitudinal boundaries, drift-scale models cannot (directly) represent the influence of three-dimensional mountain-scale heat flow. There are several possible options for incorporating the influence of three-dimensional mountain-scale heat flow into the results of drift-scale submodels, including: (1) specifying time-dependent temperature boundary conditions, which are obtained from the three-dimensional mountain-scale submodel, at the sides of the drift-scale submodels, and (2) specifying time-dependent heat flux, which is determined from the three-dimensional mountain-scale submodel, out of the sides of the drift-scale submodels. Because it is computationally feasible, the multiscale thermal-hydrologic model uses the second approach, as is conceptually explained below, and which is described in detail in Section 6.2.4.

The multiscale thermal-hydrologic model implements the time-dependent heat flux at the lateral boundaries of the drift-scale thermal-hydrologic submodels in an empirical fashion. For a repository of theoretically infinite lateral and longitudinal extent, there would be no mountain-scale heat flow in the lateral and longitudinal directions. Consequently, drift-scale submodels could take advantage of symmetry by utilizing insulated lateral and longitudinal boundaries and closely predict the temperature evolution. These models could utilize an insulated boundary along the center axis of the drift and an insulated boundary at the mid-pillar location, which is 40.5 m from the drift centerline. Because the repository system is of finite lateral and longitudinal extent, three-dimensional mountain-scale heat flow causes heat to cross the lateral and longitudinal boundaries in the drift-scale submodels. The multiscale thermohydrologic model approximates this heat loss by allowing heat to leave the lateral boundary in the drift-scale submodels, which is 40.5 m away from the centerline of the drift, in a manner that is consistent with three-dimensional mountain-scale heat flow. This is accomplished by comparing temperatures predicted by the three-dimensional mountain-scale submodel with

those predicted by equivalent one-dimensional drift-scale submodels to adjust the lateral dimension of the drift-scale submodels so that the temperature predicted by the drift-scale submodel matches that of the mountain-scale submodel at each timestep. This adjustment process results in an effective drift spacing, which gradually increases with time, just as the lateral and longitudinal heat loss grows with time. Note that the description in Section 6.2.4 utilizes an effective areal mass loading, which has a one-to-one equivalence to the effective drift spacing. Thus, an effective drift spacing of 81 m corresponds to an effective areal mass loading of 55 MTU/acre, while an effective drift spacing of 162 m corresponds to an effective areal mass loading of about 27 MTU/acre. The gradually increasing drift spacing allows the appropriate quantity of heat to leave the physical lateral boundary (with time). This time-dependent drift spacing is then applied to the two-dimensional drift-scale thermal-hydrologic submodels, so that the influence of three-dimensional mountain-scale heat flow is appropriately represented in those submodels.

After the effective drift spacing is incorporated into the two-dimensional drift-scale thermal-hydrologic submodels, the intermediate results represent a repository that is uniformly heated with a repository-wide average thermal load per unit length. To incorporate the influence of nonuniform heating conditions along drifts (resulting from waste package-to-waste package variability in heat output), three-dimensional drift-scale submodels are used to determine the local temperature deviations relative to those arising from line-averaged heating conditions. These temperature deviations are added to the line-averaged results to determine temperature conditions that incorporate both the influence of three-dimensional mountain-scale heat flow and three-dimensional drift-scale heat flow. Thus, the effective drift spacing (and the corresponding equivalent effective areal mass loading) is adjusted to account for local temperature deviations, as well as for three-dimensional mountain-scale heat flow. The adjusted effective areal mass loading is applied to the two-dimensional drift-scale thermal-hydrologic submodels to determine all hydrologic parameters of interest throughout the repository.

The process of adding the results from three-dimensional thermal submodels to those from two-dimensional thermal-hydrologic submodels relies on the assumption (Section 5.2.1) that three-dimensional convective heat and mass transfer in the host rock do not influence longitudinal temperature variability along the drift axis. Moreover, the multiscale model approach assumes (Sections 5.2.2 and 5.6) that mountain-scale movement of water and water vapor along the drift axes or between drifts is insignificant. Thus, fluid flow and convection are mostly confined to a two-dimensional vertical cross section orthogonal to the drift axis, with insignificant fluid flow across the vertical midplane in the rock pillar between the drifts. These assumptions are justified by the model validation study documented in Section 7.5, where it was found that the influence of longitudinal vapor transport along the drift has an insignificant influence on in-drift thermal-hydrologic conditions compared to the influence of parametric uncertainty. The thermal-hydrologic multiscale model also neglects any changes in rock properties due to three-way or four-way coupled thermohydrologic-chemical-mechanical processes (Manteufel et al. 1993 [DIRS 100776]) and neglects the influence of dissolved solutes on the thermal-hydrologic properties of water.

The thermal-hydrologic multiscale modeling approach considers the influence of the following parameters as a function of geographic location in the repository: local stratigraphy, overburden thickness (i.e., distance between the repository and ground surface, which varies by approximately 150 m across the repository), thermal boundary conditions, and percolation flux.

It also considers the influence of the proximity to the edge of the repository, which is important because a waste package close to the repository edge will cool more quickly than one at the repository center. As discussed in Section 5.2.1, it is assumed that the differences in temperature that arise as a result of proximity to the repository edges are governed by thermal conduction in the rock. This assumption is equivalent to saying that convective heat transfer mechanisms have an insignificant influence on lateral mountain-scale heat flow at Yucca Mountain. These mechanisms (notably, buoyant gas-phase convection and the heat pipe effect) are included in the two-dimensional thermal-hydrologic (drift-scale) submodels of the MSTHM. The assumption of conduction dominance at the mountain scale bounds temperature differences that arise from differences in proximity to the repository edges, which captures the full range of boiling-period duration across the repository.

The MSTHM represents all possible waste packages emplaced in the repository by four major types: CSNF from pressurized-water reactors (PWRs), CSNF from boiling-water reactors (BWRs), high-level radioactive waste (HLW), and DOE-owned spent nuclear fuel. The relevant point here is that the heat-generation-rate-versus-time relationships for these four waste package types are different. The model considers a waste package sequence (Figure 6.2-2) that results in eight distinct local heating conditions for waste packages. For example, the model distinguishes between a BWR placed between a PWR and a HLW and a BWR placed between two PWRs. As discussed in Section 5.2.2, it is assumed that the differences in temperature between relatively hotter and cooler waste package locations are governed by thermal conduction in the host rock and emplacement drift and thermal radiation in the open cavities in the drift. This assumption is equivalent to saying that convective heat transfer mechanisms (notably, buoyant gas-phase convection) do not significantly contribute to the attenuation of temperature variations along the axis of the drift. However, the influence of buoyant gas-phase convection is represented in the vertical plane perpendicular to the drift axis. This assumption bounds temperature variability along the drifts.

To implement this multiscale approach, a modeling system has been developed that is called the MSTHM, which is described in detail in Section 6.2.4. The following discussion begins with the unsaturated zone hydrology model on which the natural system aspects of the MSTHM are based, followed by a detailed discussion of the governing equations that are used in all the MSTHM simulations.

6.2.2 Incorporating the Unsaturated-Zone Hydrology Model in the MSTHM

The MSTHM uses the representation of the unsaturated zone developed in *UZ Flow Models and Submodels* (BSC 2004 [DIRS 169861], Section 6.1.1). From *Development of Numerical Grids for UZ Flow and Transport Modeling* (BSC 2004 [DIRS 169855]), a three-dimensional definition of hydrostratigraphic units (called UZ-model layers) is incorporated in the MSTHM, including position of the water table and surface topography; thermal-hydrologic properties for these units; and model boundary conditions. The model includes 36 UZ-model layers, each of which is considered to be homogeneous with respect to thermal and hydrologic properties. These hydrologic properties are determined through an inverse modeling approach constrained by site hydrologic data; the assumption is made that important heterogeneity is captured by the detailed stratification (Bandurraga and Bodvarsson 1999 [DIRS 103949]). The thermal properties are determined based on laboratory and field measurements (BSC 2004 [DIRS 169854]; BSC 2004 [DIRS 170033]).

The MSTHM also incorporates the conceptualization for flow through unsaturated fractured porous rock at Yucca Mountain from the Lawrence Berkeley National Laboratory (LBNL) unsaturated-zone hydrology model. The current conceptual model is based on a dual-permeability representation of overlapping fracture and matrix continua, modified from the traditional approach such that only a portion of connected fractures actively conduct liquid water (Liu et al. 1998 [DIRS 105729]), a portion which depends on liquid-phase saturation in the fractures.

The next step in building the MSTHM involves the addition of the repository emplacement drifts and the engineered components inside those drifts to the unsaturated zone hydrology model discussed above. The geometric configuration of the engineered components inside the drifts used in the MSTHM calculations in support of the TSPA-LA base case is shown in Figures 6.2-1 and 6.2-2.
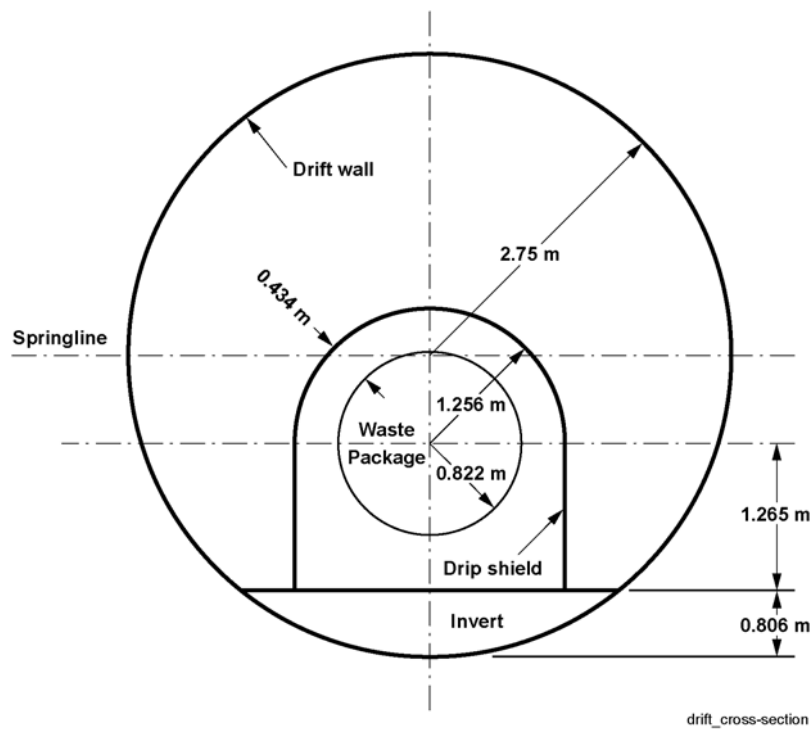
Source: BSC 2003 [DIRS 162444], Figure 2, for invert depth; BSC 2004 [DIRS 168489], Figure 1, for drift diameter.

NOTE: Average waste package diameter is obtained from assumption in Section 5.4.1. Drip-shield width is from BSC 2003 [DIRS 171024], Sheet 2. Location of waste package centerline above invert is from BSC 2004 [DIRS 167040].

Figure 6.2-1. Geometric Configuration of the Engineered Components Shown for an Average Cross-Section Inside the Emplacement Drifts as Represented in MSTHM
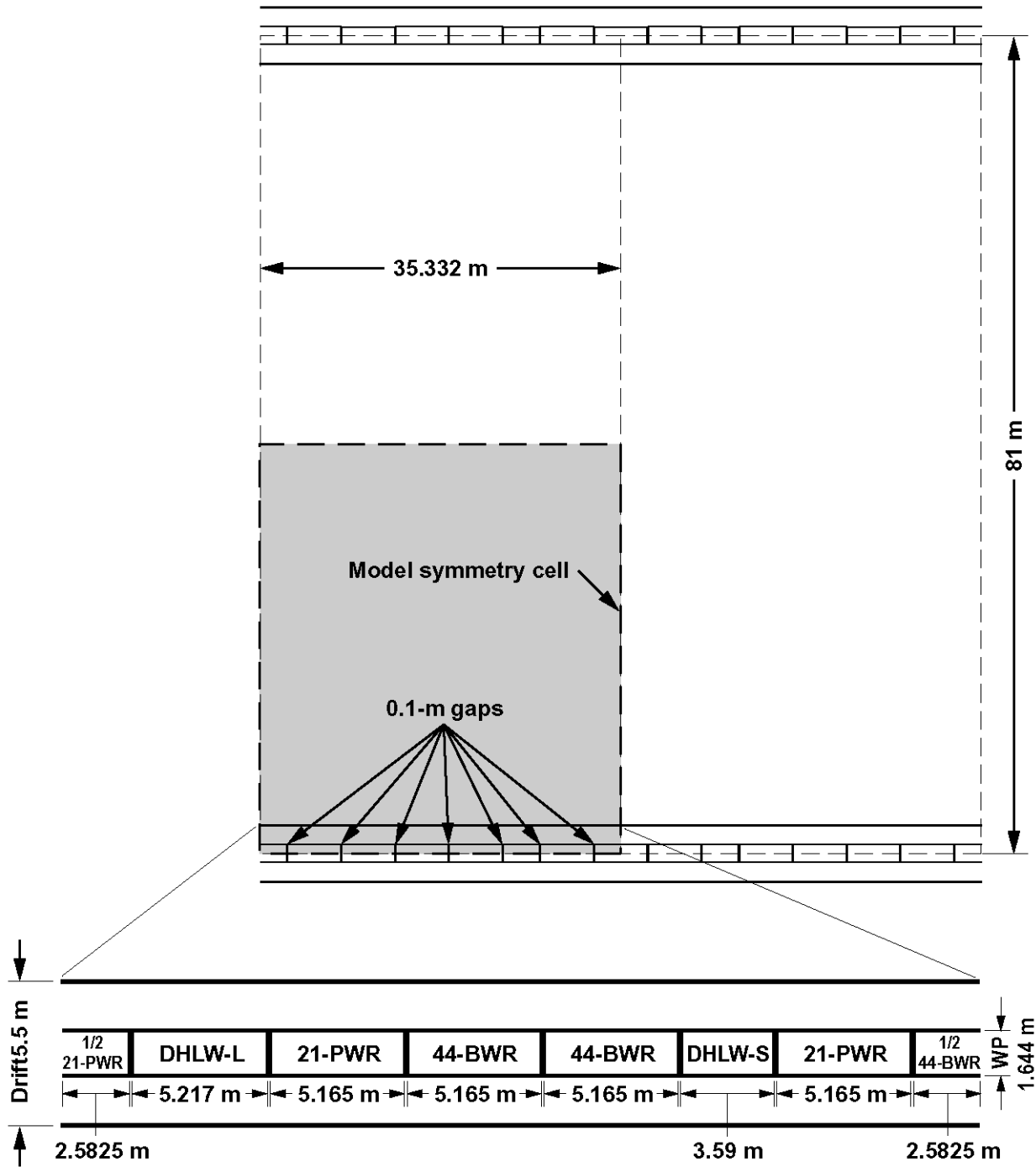
NOTE: Average waste package diameter is obtained from assumption in Section 5.4.1. Waste package lengths are obtained from BSC 2003 [DIRS 165406], Table 1. The names of the respective waste packages (21-PWR, 44-BWR, etc.) used in the DDT submodel are shown above for each waste package.

Figure 6.2-2. Diagram Showing Drift Spacing, Waste Package Lengths, and Waste Package Spacing in Plan View Considered in MSTHM Calculations for the TSPA-LA Base Case

6.2.3 Governing Equations for Unsaturated-Zone Thermohydrology

This section describes the theoretical basis for the NUFT software, which solves the governing equations. Section 3 lists versions of NUFT that are qualified software and are used in the MSTHM. The theoretical basis is repeated here for background.

6.2.3.1 Mass-Balance Equation for Thermal-Hydrologic Models

All thermal-hydrologic models in this report solve the mass-balance equation for air, water, and energy components for liquid- and gas-fluid phases and a nondeformable solid. The mass-balance equation for the air and water components is:

$$\frac{\partial}{\partial t} \sum_{\varsigma} \phi \rho_{\varsigma} S_{\varsigma} \omega_{\varsigma}^{\beta} = -\sum_{\varsigma} \nabla \cdot \phi \rho_{\varsigma} S_{\varsigma} \left(\omega_{\varsigma}^{\beta} \mathbf{V}_{\varsigma} + \mathbf{J}_{\varsigma}^{\beta} \right)$$

(Eq. 1)

where t is time, the superscript β denotes a component (e.g., air and water), the subscript ς denotes fluid phases (e.g., liquid and gas), ϕ is porosity, ρ_{ς} is density of phase ς, S_{ς} is saturation of a ς phase, $\omega_{\varsigma}^{\beta}$ denotes mass fraction of β component in phase ς, $\mathbf{V}_{\varsigma}$ is velocity vector for ς phase advection, and $\mathbf{J}_{\varsigma}^{\beta}$ is combined diffusive and dispersive flux tensor, which can be further given by Fick's law (Cho 1998 [DIRS 160802], p. 1.3, Equation 1-7):

$$\mathbf{J}_{\varsigma}^{\beta} = -D_{\varsigma}^{\beta} \nabla \omega_{\varsigma}^{\beta}$$

(Eq. 2)

D_{ς}^{β} is combined diffusion and dispersion coefficient for β component in ς phase. Darcy's law gives the advective flux vector (Nitao 2000 [DIRS 159883]):

$$S_{\varsigma} \phi \, \mathbf{V}_{\varsigma} = -\frac{k_{\varsigma}(S_{\varsigma})}{\mu_{\varsigma}} \left(\nabla p_{\varsigma} + \rho_{\varsigma} g \nabla z \right)$$

(Eq. 3)

where k_{ς} is the permeability function, μ_{ς} is phase viscosity, p_{ς} is phase pressure, g is gravitational acceleration, and z denotes distance in the vertical direction. The capillary pressure relationship is given by:

$$p_{\alpha} = p_g - p_c$$

(Eq. 4)

and p_c is the retention pressure function. In addition to the mass balance equation, there are the constraints:

$$\sum_{\beta} \omega_{\varsigma}^{\beta} = 1 \quad \text{and} \quad \sum_{\varsigma} S_{\varsigma} = 1$$

(Eq. 5)

Local thermodynamic equilibrium is assumed between all phases. Partitioning of components between phases is expressed in terms of partitioning coefficients:

$$n_\varsigma^\beta = K_{\varsigma,\xi}^\beta n_\xi^\beta \qquad \text{(Eq. 6)}$$

where n_ς^β is the mole fraction and $K_{\varsigma,\xi}^\beta$ is the partitioning coefficient between phase ς and phase ξ. For predicting the partitioning of water between the aqueous phases, the model includes the "vapor pressure lowering" effect based on the Kelvin law:

$$RH = \frac{P_v}{P_{sat}(T)} = \exp\left(\frac{MP_c}{\rho RT}\right) \qquad \text{(Eq. 7)}$$

where RH is relative humidity, P_v is partial pressure of water vapor, $P_{sat}(T)$ is the saturated vapor pressure from the steam tables, based on the local temperature T, M is the molecular weight of water, P_c is capillary pressure, ρ is the density of water R is the Gas Constant, and T is temperature.

6.2.3.2 Energy Balance Equation for Thermal-Hydrologic Models

For all thermal-hydrologic models and submodels in this report, the energy balance equation is:

$$\frac{\partial}{\partial t}\left[\sum_\varsigma \phi \rho_\varsigma u_\varsigma S_\varsigma + (1-\phi)\rho_s C_p (T - T_{\text{ref}})\right] = \sum_\beta \sum_\varsigma \left[\nabla \cdot \phi h_\varsigma^\beta \rho_\varsigma S_\varsigma \left(\omega_\varsigma^\beta \mathbf{V}_\varsigma + \mathbf{J}_\alpha^\gamma\right)\right] + \nabla \cdot K_H \nabla T \qquad \text{(Eq. 8)}$$

where T denotes temperature, T_{ref} is reference temperature, u_ς is specific internal energy, ρ_s is solid density, C_p is specific heat of solid, h_ς^β is partial specific enthalpy, and K_H is thermal conductivity. Note that thermal conductivity is a function of liquid-phase saturation S, varying linearly from a "dry" value of K_H ($S = 0.0$) to a "wet" value of K_H ($S = 1.0$). Where thermal radiation is included to couple grid blocks within the numerical model, a classical radiation term can be added to the right hand side of Equation 8, to represent the conceptual basis for radiative heat transfer.

It is noted that it is possible to use either a specific internal energy accumulation term or a specific enthalpy accumulation term for the fluid phases of Equation 8. *Transport Phenomena* (Bird et al. 1960 [DIRS 103524]) discusses the validity of either approach. The justification for the use of specific internal energy in the accumulation term of the fluid phases in the NUFT code is discussed in detail in Section 6.2.3.6.

The balance equations (1) and (8) are discretized in space using the integrated finite difference method and discretized in time using the fully implicit backward Euler method. The resulting nonlinear system of equations is solved at each time step using the Newton-Raphson method.

6.2.3.3 Radiative Heat Transfer

Where relevant, models, such as the LDTH and DDT submodels (Sections 6.2.6 and 6.2.8), include radiative heat transfer in the energy balance model for the open cavities within the

repository drifts in which waste packages are emplaced. In this case, the surfaces of the drift wall and waste package are subdivided into surface elements, each of which is mapped to a computational volume element. Radiative heat flux is calculated for connections between each pair of surface elements using temperatures from the corresponding volume element. The net radiative heat transferred between two model nodes is calculated from the Stefan-Boltzmann law (Cho 1998 [DIRS 160802]):

$$Q = c(T_1^4 - T_2^4) \tag{Eq. 9}$$

where T_1 is the absolute temperature of the radiator, T_2 is the absolute temperature of the receiver, and c is a coefficient defined by:

$$c = AF\varepsilon\sigma \tag{Eq. 10}$$

where A is the area of the radiating surface element, F is the radiative view factor (Holman 1990 [DIRS 106052]), ε is emissivity, and σ is the Stefan-Boltzmann constant.

6.2.3.4 Energy Balance Equations for Thermal-Conduction-Only Models

For all thermal-conduction models in this report, the energy balance is written:

$$(1-\phi)\rho_s C_p \frac{\partial T}{\partial t} = \nabla \cdot K_H \nabla T \tag{Eq. 11}$$

where ϕ is porosity, ρ_s is solid density, C_p is specific heat of solid, and K_H is thermal conductivity. For thermal-conduction-only models, thermal conductivity is not a function of liquid-phase saturation.

6.2.3.5 Dual-Permeability and Active-Fracture Models

All thermal-hydrologic models in this report utilize a dual-permeability approach in which the fracture and matrix systems are treated as two separate continua with a complete set of balance equations and computational grid for each continuum. Each continuum has coupling terms for mass and energy fluxes between the two continua. These terms have the general form:

$$q_{\text{exchange}} = a\kappa\Delta u / L, \tag{Eq. 12}$$

where q_{exchange} is flux of mass or energy per unit bulk volume, Δu is the difference in pressure or temperature between the continua, and κ is a transfer coefficient. The coefficient κ for advective flux is of the form Kk_r/μ, where K is saturated permeability, and k_r is relative permeability. For diffusive mass flux of a phase, κ is equal to the apparent diffusion coefficient $D_{app} = \phi S\tau D$, where τ is tortuosity factor, and D is the free diffusion coefficient. For energy flux, κ is the bulk thermal conductivity K_H. In the conventional dual-permeability approach, a is the surface area of the fracture walls per unit bulk volume, and L is the average distance between centers of the matrix elements, which is proportional to the fracture spacing. Also used is an active-fracture model modification to the traditional dual-permeability approach in which a and

L are modified to account for inactive fractures (or portions of fractures) as suggested by Liu et al. (1998 [DIRS 105729]).

Specifically, *a* is multiplied by S_e, and *L* is multiplied by $S_e^{-\gamma}$, where:

$$S_e = \frac{S_f - S_r}{S_{max} - S_r} \ , \tag{Eq. 13}$$

and S_r and S_{max} are residual and maximum liquid-phase fracture saturations, respectively, while S_f is the fracture saturation.

The relationships between permeability, saturation, and capillary pressure described in Equations 14 and 15 are described by the formulations of van Genuchten (1980 [DIRS 100610]) and Mualem (1976 [DIRS 100599]), modified to account for the active fracture model by the parameter γ which has a value between 0 and 1 (0 if all fractures are active).

The relative permeability for the liquid phase is given by:

$$k_{rl} = S_e^{(1+\gamma)/2} \left[1.0 - \left(1.0 - S_e^{(1-\gamma)/m} \right)^m \right]^2 \tag{Eq. 14}$$

It is assumed that $k_{rl} + k_{rg} = 1$; the subscripts "*l*" and "*g*" refer to the liquid and gas phases, respectively. The capillary pressure is given by:

$$p_c = \frac{1}{\alpha} \left(S_e^{\frac{\gamma-1}{m}} - 1 \right)^{\frac{1}{n}} \tag{Eq. 15}$$

where α is a curve-fitting parameter (units of inverse pressure), *n* is a dimensionless curve-fitting parameter, and *m = 1-1/n*.

The parameters used in this model are functions of pressure *p*, temperature *T*, mass fraction ω, and/or saturation *S* as follows: ρ_α (*p,T*, ω), D_α^γ (*p,T*), μ_α (*p,T*, ω), $K_{\alpha\beta}^\gamma$ (*p,T,S*), u_α(*p,T*, ω), h_α^γ (*p,T*), k_α(*S*), τ_α(*S*), and p_c (*S,T*).

6.2.3.6   Formulation of Energy Balance Equation for Thermal-Hydrologic Models

It is possible to formulate the energy balance equation (Equation 8) using either specific internal energy (u) or specific enthalpy (h) in the fluid-phase accumulation terms inside the time derivative. Numerical models for subsurface flow and transport have formulated the equation of energy for multicomponent systems both using enthalpy (e.g., Manteufel et al. 1993 [DIRS 100776]; Pollock 1986 [DIRS 164747]) and using specific internal energy (e.g., Lichtner and Walton 1994 [DIRS 152609]; Nitao 1998 [DIRS 100474]). Bird et al. (1960 [DIRS 103524], Table 18.3-1, p. 562) demonstrate that both formulations are valid, as follows:

$$\rho \frac{D}{Dt} h = -(\nabla \cdot q) + \frac{Dp}{Dt} - (\boldsymbol{\tau} : \nabla \mathbf{v}) + \sum_{i=1}^{n} (\mathbf{j}_i \cdot \mathbf{g}_i) \qquad \text{(Eq. 16)}$$

$$\rho \frac{D}{Dt} u = -(\nabla \cdot q) - (\boldsymbol{\pi} : \nabla \mathbf{v}) + \sum_{i=1}^{n} (\mathbf{j}_i \cdot \mathbf{g}_i) \qquad \text{(Eq. 17)}$$

One may note the fact that specific enthalpy of evaporation (h_{evap}) is greater than the specific internal energy of evaporation (u_{evap}) because the specific enthalpy includes a compressible work term. For example, at standard atmospheric pressure (101.3 kPa), h_{evap} = 2,257 kJ/kg while u_{evap} = 2088 kJ/kg, a difference of approximately 8 percent (Keenan et al. 1969 [DIRS 134666]). Such a difference is crucial when considering a simplified batch system (i.e., zero-dimensional reactor). In such simplified cases, one must consider different approaches to the system (i.e., approaching the problem as a closed system versus approaching the problem as an open system). The partial differential equation formulation as represented by Bird et al. (1960 [DIRS 103524], p. 566, Equation 18.4-2) in Equations 16 and 17 incorporates multidimensional transient processes, however. Both the enthalpy formulation (Equation 16) and the internal energy formulation (Equation 17) result in equivalent solutions.

The energy-balance equation in NUFT is based on the derivation of Equation 17, which is the internal energy formulation of the energy equation for n species. Expanding the total derivative on the left-hand side of Equation 17 and incorporating the continuity equation, Equation 17 can be rewritten as:

$$\frac{\partial}{\partial t}(\rho u) + \nabla \cdot (\rho u \mathbf{v}) = -(\nabla \cdot q) - (\boldsymbol{\pi} : \nabla \mathbf{v}) + \sum_{i=1}^{n} (\mathbf{j}_i \cdot \mathbf{g}_i) \qquad \text{(Eq. 18)}$$

The thermal energy flux q is composed of three terms (Bird et al. 1960 [DIRS 103524], Equation 18.4-2, p. 566):

$$q = -k\nabla T - \sum_{i=1}^{n} h_i \rho D_i \nabla \omega_i + q^{(\mathbf{x})} \qquad \text{(Eq. 19)}$$

representing, respectively, thermal conduction, species diffusion enthalpy transport, and the Dufour energy flux. Note that according to Bird et al. (1960 [DIRS 103524]), the Dufour energy flux is of minor importance and is therefore typically neglected. Incorporating Equation 19 (less the Dufour energy flux) into Equation 18 and noting that gravitational work (the last term in Equation 18) is zero (Nitao 2000 [DIRS 159883]), results in the simplified equation:

$$\frac{\partial}{\partial t}(\rho u) + \nabla \cdot (\rho u \mathbf{v}) = \left(\nabla \cdot \left[k\nabla T + \sum_{i=1}^{n} h_i \rho D_i \nabla \omega_i \right] \right) - (\boldsymbol{\pi} : \nabla \mathbf{v}) \qquad \text{(Eq. 20)}$$

The stress tensor π is related to the viscous shear tensor and pressure as follows:

$$\pi = \tau + p\boldsymbol{I} \qquad \text{(Eq. 21)}$$

Incorporating Equation 21 into the last term of Equation 20 and noting that $p\nabla \cdot \mathbf{v} = \nabla \cdot (p\mathbf{v}) - \mathbf{v} \cdot \nabla p$, Equation 20 can be rewritten as:

$$\frac{\partial}{\partial t}(\rho u) + \nabla \cdot (\rho u \mathbf{v}) = \left(\nabla \cdot \left[k\nabla T + \sum_{i=1}^{n} h_i \rho D_i \nabla \omega_i \right] \right) - (\tau : \nabla \mathbf{v}) - \nabla \cdot (p\mathbf{v}) + \mathbf{v} \cdot \nabla p$$

(Eq. 22)

As discussed by Nitao (2000 [DIRS 159883]), both the viscous dissipation term ($\tau : \nabla \mathbf{v}$) and the pressure gradient term ($\mathbf{v} \cdot \nabla p$) are typically neglected in Equation 22 because these terms are small compared to other terms. Estimates of the approximate potential error incurred by neglecting these two terms are discussed below. The third term on the right-hand side of Equation 22 can be incorporated into the second term on the left-hand side resulting in a convective enthalpy term. This results in the energy equation as it is employed in the NUFT code:

$$\frac{\partial}{\partial t}(\rho u) + \nabla \cdot (\rho h \mathbf{v}) = \left(\nabla \cdot \left[k\nabla T + \sum_{i=1}^{n} h_i \rho D_i \nabla \omega_i \right] \right)$$

(Eq. 23)

For a more rigorous mathematical development of Equation 23 from Equation 17, see *Documentation of the Thermal Energy Balance Equation Used in the USNT Module of the NUFT Flow and Transport Code* (Nitao 2000 [DIRS 159883]). Note that the above equations apply only at the "pore level" and not at the porous medium, or macroscopic, level. Nitao (2000 [DIRS 159883]) also discusses the method used to derive the porous medium energy balance equation by volume averaging the pore level equations.

It is possible to estimate the error incurred by neglecting the viscous dissipation term ($\tau : \nabla \mathbf{v}$) in Equation 22 by considering the maximum error that could occur for a thermal-hydrologic model calculation using the NUFT code. Nitao (2000 [DIRS 159883]) estimates that the maximum error caused by neglecting this term would occur during infiltration through the rock fractures. The maximum possible error in temperature at the repository for a high infiltration of 100 mm/yr would be $\Delta T \sim 0.3°C$.

The largest potential source of error lies in neglecting the pressure gradient term in Equation 22. Note that this assumption does not mean that a constant pressure is assumed—only that this particular term in the energy equation is neglected. In fact, pressure is a variable in all of the remaining terms in Equation 22 where it appears. It is possible to estimate the maximum potential error incurred by neglecting the heat gradient term ($\mathbf{v} \cdot \nabla p$) by comparing it to the convective enthalpy term ($\nabla \cdot (\rho h \mathbf{v})$). The greatest pressure would occur in the host rock immediately adjacent to the drift wall during a boiling event. As an example, consider a maximum drift-wall temperature of 140°C as estimated for the higher-temperature operating mode conditions analyzed in *FY 01 Supplemental Science and Performance Analyses, Volume 1: Scientific Bases and Analyses* (BSC 2001 [DIRS 155950], Figure 5.4.1-2). Such a temperature would result in a P_{sat} of 361 kPa. The results of the supplemental analyses indicate that such a drift-wall temperature incurs a relative humidity of 30 percent; thus, the pressure can be estimated as approximately 120 kPa. The extreme downstream temperature and pressure at the

repository level would be about 96°C and 84.5 kPa. If the ratio of $(\boldsymbol{v} \cdot \nabla p)/\nabla(\rho h \boldsymbol{v})$ is approximated as $\Delta p/\Delta(\rho_{sat} h_{sat})$ then the maximum difference is (120 kPa – 84.5 kPa)/(1.12 kg/m^3 × 2,706 kJ/kg – 0.353 kg/m^3 × 2,652 kJ/kg) or about 2 percent. Note that this is a conservative error estimate for this particular problem; the estimate neglects thermal conduction as an energy transport mechanism and thus exaggerates the potential error of this scenario where heat flow is dominated by thermal conduction. Hence, is concluded that neglecting the pressure gradient in Equation 22 would result in a maximum error of less than 2 percent for a short time over only the small region of host rock adjacent to drift wall, where boiling of pore water occurs. Neglecting the influence of viscous dissipation and the pressure gradient in the energy equation is therefore acceptable.

6.2.4   MSTHM Calculation Sequence

The MSTHM consists of four submodel types (Figure 1-1, Tables 1-2 and 1-3), all of which are run using the NUFT v3.0s code (Nitao 1998 [DIRS 100474], Section 3.1.1). For this report, the LDTH and SDT submodels (Sections 6.2.6 and 6.2.7) are run at 108 geographic locations distributed uniformly over the repository area (Figure 6.2-3); these submodels use the stratigraphy, overburden thickness, thermal-hydrologic boundary conditions, and percolation fluxes appropriate for each location. At each of those 108 geographic locations, the LDTH and SDT submodel calculations are conducted at different values of thermal loading, which can be quantified by the Areal Mass Loading (AML). Note that AML is expressed in terms of metric tons of uranium per acre. For the current repository design, the initial Lineal Power Density (LPD) is 1.45 kW/m (BSC 2004 [DIRS 168489], Table 1), which for a drift spacing of 81 m (BSC 2004 [DIRS 168489], Table 1) corresponds to an areal power density of 17.9 W/m^2. The repository has 57,480.2 m of emplacement drift (Table 6.2-1), which corresponds to a heated repository footprint of 4,655,896 m^2 (57,480.2 m of drift multiplied by an 81-m drift spacing, which is 1150 acres). From Table 6.2-1 it can be seen that the SMT submodel represents the repository as having 57,480 m of emplacement drift. For a 63,000 MTU inventory of commercial spent nuclear fuel (CSNF) waste packages, this corresponds to an AML of 54.76 MTU/acre (63,000 MTU divided by 1150 acres). Therefore, 1 MTU/acre is equivalent to 0.327 W/m^2 at the time of emplacement for the TSPA-LA design. The modeled AML is obtained by virtue of the selected drift spacing in the submodel.

Section 7.5 describes a MSTHM validation test case, also reported by Buscheck et al. (2003 [DIRS 164638]), in which the MSTHM and a corresponding monolithic thermal-hydrologic model are used to predict the thermal-hydrologic behavior of a three-drift repository test case, which is a scaled-down version of the repository. The following description of the MSTHM calculation sequence also pertains specifically to that test case, which utilizes six modeled AMLs: 66, 55, 37, 27, 14, and 7 MTU/acre. Because of the very small heated footprint of the three-drift repository test case, the influence of the edge-cooling effect occurs faster and with greater magnitude than is applicable to repository heating conditions, which requires that the LDTH-SDT submodel pairs be run at six different AMLs, rather than at just four (as is typically done for a full-scale repository example). An AML of 55 MTU/acre corresponds to 81-m drift spacing, while 27 MTU/acre corresponds to 162-m drift spacing. The emplaced AML for the repository is 55 MTU/acre for a total repository-wide heat load of 70,000 MTU (Canori and Leitner 2003 [DIRS 166275], p. 3-95). The modeled AMLs that are less than the emplaced AML account for the evolving influence of the edge-cooling effect (i.e., waste package locations close to the repository edges cool faster than those at the center). The modeled AML that is

higher than the emplaced AML accounts for hotter-than-average waste package thermal-loading conditions. The LDTH submodel domain is a two-dimensional drift-scale cross-section extending down from the ground surface to the water table. The LDTH submodels are the only submodels to include coupled thermal-hydrologic processes; these submodels assume a heat-generation history that is effectively that of the entire waste package inventory line-averaged over the total length of emplacement drifts in the repository.
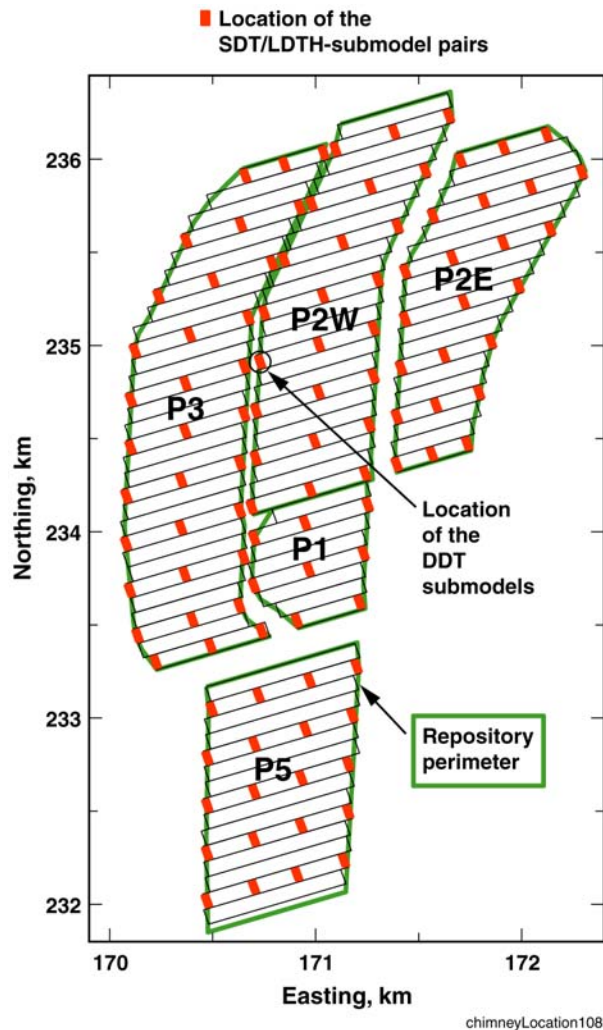
Source: See Table XIII-1.

NOTE: Nevada State Northing and Easting coordinates are given in kilometers. The subhorizontal lines depict the rows of gridblocks in the SMT submodel that represent each of the emplacement drifts. The rectangles correspond to the locations of LDTH–SDT submodel pairs. A total of 108 LDTH–SDT submodel locations are used in the TSPA-LA base case. The outline of the repository perimeter corresponds to the end-point coordinates of the heated portions of the emplacement drifts as given in the IED presented in *Repository Design, Repository/PA IED Subsurface Facilities* (BSC 2003 [DIRS 161727]). The MSTHM representation of the heated repository footprint closely matches the end-point coordinates of the repository layout. This layout has been slightly revised as shown in Figure 4-1, which is based on the end-point coordinates given in the IED presented in *D&E/RIT IED Subsurface Facilities* (BSC 2004 [DIRS 172801]). Note that the Panel numbers have changed in the revised layout, as shown in Figure 4-1.

Figure 6.2-3. Repository Layout Considered in MSTHM Calculations for the TSPA-LA Base Case

The three-dimensional SMT submodel, which simulates conductive heat flow from a heat source smeared over the repository area, represents the heated footprint of the repository and allows for consideration of edge-cooling effects and the influence of the varying overburden thickness above the repository. For this example, originally by Buscheck et al. (2003 [DIRS 164638]), the linear power density is 1.35 kW/m. Note that this linear power density is different from that being analyzed for the TSPA-LA (Section 6.3). The SMT submodel assumes a heat-generation history that is areally averaged for the entire waste package inventory over the entire heated footprint of the repository. The one-dimensional SDT submodels are run at the same 108 geographic locations as the two-dimensional LDTH submodels such that every LDTH submodel is paired to a corresponding SDT submodel. The SDT submodels utilize the same heat-generation history as the LDTH submodels except that heat is smeared over the repository plane in the SDT submodels.

The fundamental concept in the MSTHM is that the results from the two-dimensional LDTH submodels can be modified to account for the influence of three-dimensional mountain-scale heat flow as well as for local deviations arising from waste package-to-waste package variability in heat output. Output from the SMT submodel, together with the LDTH–SDT submodel pairs, is integrated to create the LMTH model (Figure 1-1). The DDT submodel is then used to further modify the LMTH model to account for waste package-specific deviations from average waste package behavior. For this report, the DDT submodels represent eight different waste packages, which fall in two major categories: commercial spent nuclear fuel (CSNF) waste packages, which include pressurized water reactor (PWR) and boiling water reactor (BWR) waste packages; and defense high-level waste (DHLW) waste packages. Four different waste package types are used in the model validation study: PWR1, PWR2, DHLW and BWR (Table 7.5-2). DDT submodel temperature variations are superimposed on LMTH model temperatures to generate the temperatures of the final discrete-heat-source mountain-scale thermal-hydrologic (DMTH) model (Figure 1-1, Tables 1-2 and 1-3).

For the MSTHM analysis of the repository, after all of the submodels have been run using the NUFT code, LDTH and SDT submodel results are spatially interpolated from the geographic locations (a total of 108 for the TSPA-LA MSTHM) to all of the repository subdomains in the SMT submodel (2,874 for the TSPA-LA MSTHM). This approximates running the LDTH–SDT submodel pairs at all repository subdomains in the SMT submodel.

The MSTHM calculation sequence to obtain temperature, relative humidity, and liquid-phase saturation is shown in Figures 6.2-4 and 6.2-5 and is divided into the six stages of Figure 1-1. While this analysis pertains to the three-drift repository model validation test case (Section 7.5), it also illustrates the MSTHM calculation sequence for each of the repository subdomains. The six calculation stages conceptually illustrated in Figure 1-1 are discussed in detail below.
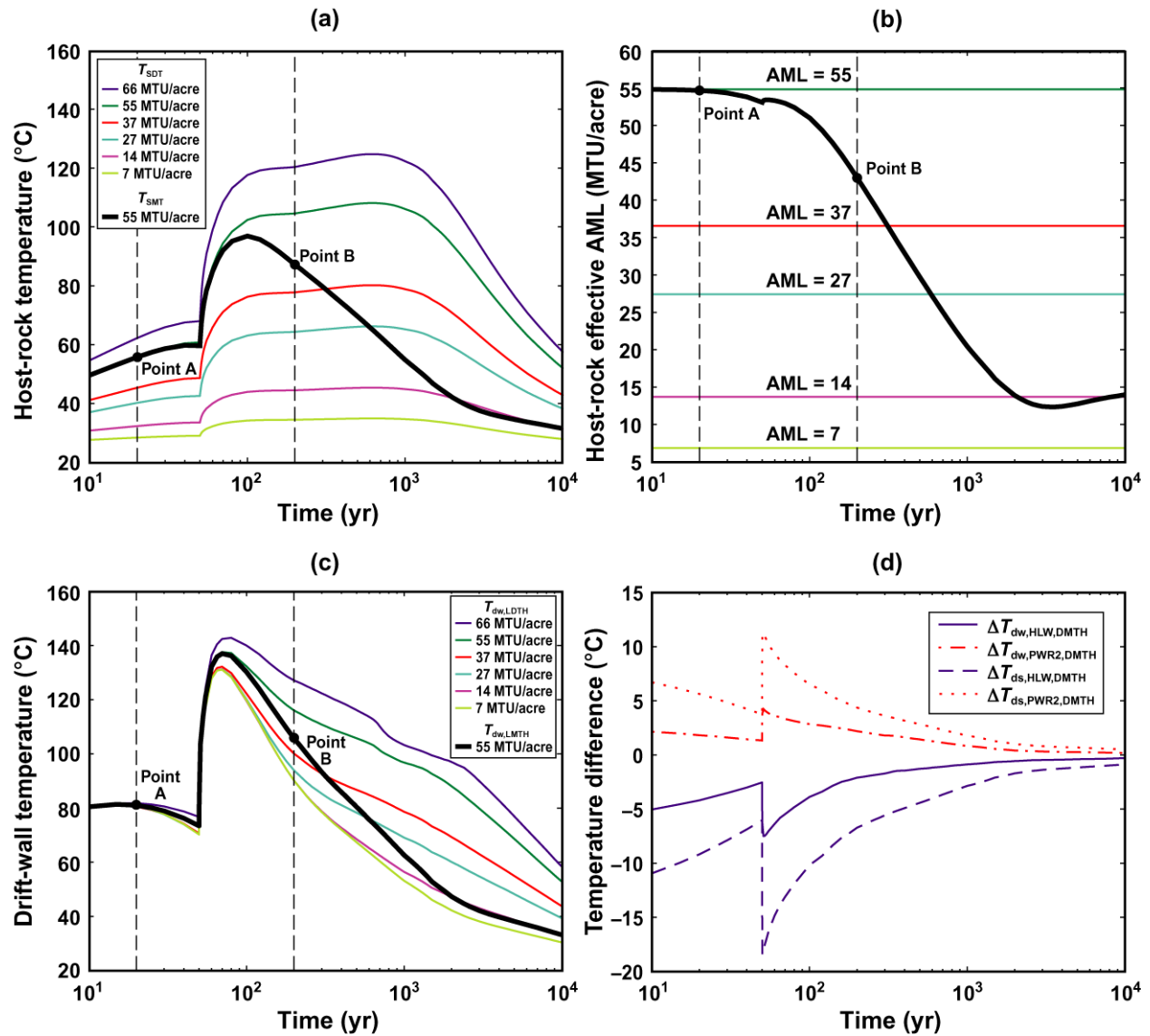
NOTE: (a) Host-rock temperature T_{SDT} vs. time calculated for the six listed AMLs; also plotted is T_{SMT} vs. time calculated at the repository center. Because the SDT and SMT submodels use smeared heat sources, the SDT and SMT host-rock temperatures are averaged temperatures for the repository horizon (from pillar mid-point to pillar mid-point) at a given drift location. (b) Host-rock effective AML (AML$_{hstrk,eff}$) vs. time calculated at the repository center. (c) Drift-wall temperature vs. time calculated for the six listed AMLs; also plotted is $T_{dw,LMTH}$ vs. time determined at the repository center. (d) Temperature difference $\Delta T_{dw,j,DMTH}$ between the local and the axially averaged $T_{dw,LMTH}$ calculated using the six DDT submodels and interpolated on the basis of AML$_{hstrk,eff}$ vs. time (Figure 6.2-4b) for the HLW and PWR2 waste packages; also plotted are the corresponding temperature deviations $\Delta T_{ds,j,DMTH}$ between the local drip-shield temperature and the axially averaged $T_{ds,LMTH}$.

Figure 6.2-4.   MSTHM Calculation Sequence for a Three-Drift 55-MTU/Acre-Repository Example
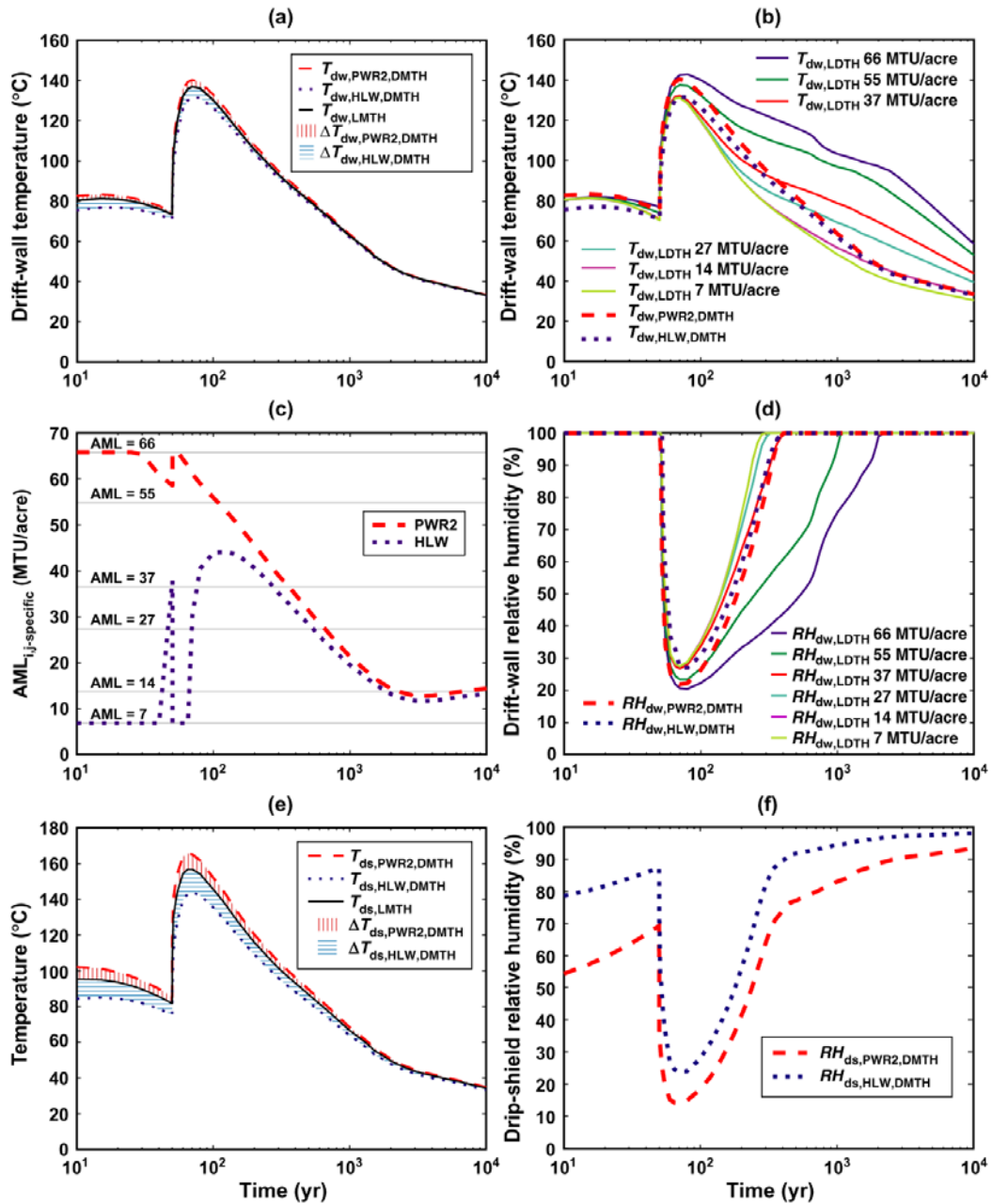
NOTE: (a) $T_{dw,j,DMTH}$ vs. time for the HLW and PWR2 waste packages at the repository center; also plotted is $T_{dw,LMTH}$ vs. time at the repository center (Figure 6.2-4c). (b) $T_{dw,LDTH}$ vs. time calculated for the six listed AMLs; also plotted is $T_{dw,j,DMTH}$ vs. time for the HLW and PWR2 waste packages at the repository center. (c) $AML_{i,j-specific}$ at the drift wall for the HLW and PWR2 waste packages at the repository center. (d) Drift-wall relative humidity $RH_{dw,LDTH}$ vs. time calculated for the six listed AMLs; also plotted is $RH_{dw,j,DMTH}$ vs. time for the HLW and PWR2 waste packages at the repository center, which is determined on the basis of $AML_{i,j-specific}$ vs. time for the respective waste packages. (e) $T_{ds,j,DMTH}$ vs. time for the HLW and PWR2 waste packages at the repository center; also plotted is $T_{ds,LMTH}$ vs. time at the repository center. (f) $RH_{ds,j,DMTH}$ vs. time for the HLW and PWR2 waste packages.

Figure 6.2-5.   MSTHM-Calculation Sequence (Continued)

STAGE 1–The first calculation stage generates the host-rock effective AML, referred to as $AML_{hstrk,eff}$. The $AML_{hstrk,eff}$ is generated at each repository subdomain in the following manner:

1. First, the repository subdomain's host-rock temperature history simulated by the three-dimensional SMT submodel is compared with temperature histories simulated by the one-dimensional SDT submodels for a range of heat loading conditions (e.g., for 55 MTU/acre, for 46 MTU/acre, etc.). Note that because the SDT and SMT submodels use smeared heat sources, the SDT and SMT host-rock temperatures are averaged temperatures for the repository horizon (from pillar centerline to pillar centerline) at a given location.

2. Second, the value of $AML_{hstrk,eff}$ at any given time is the AML that a one-dimensional SDT submodel would have to use in order to match the three-dimensional SMT modeled temperature at that location. By using the $AML_{hstrk,eff}$, the influence of three-dimensional mountain-scale heat flow is imposed on the two-dimensional LDTH submodels discussed in Stage 2. As an example, Figure 6.2-4a-c illustrates how the concept of the $AML_{hstrk,eff}$ is used to account for three-dimensional mountain-scale heat flow. The host-rock temperature T_{SMT} calculated by the three-dimensional SMT submodel is compared with temperatures T_{SDT} calculated by the family of AML-dependent SDT submodels (Figure 6.2-4a). For each timestep, $AML_{hstrk,eff}$ (Figure 6.2-4b) is obtained by interpolating for T_{SMT} among the family of AML-dependent T_{SDT} curves. For example, Point A, which is at 20 years, finds the T_{SMT} to be virtually the same as T_{SDT} for 55 MTU/acre, thus yielding an $AML_{hstrk,eff}$ of 55 MTU/acre at 20 years. Point B, which is at 200 years, finds T_{SMT} lying between T_{SDT} for 55 and 37 MTU/acre; linear interpolation between T_{SMT} and the two T_{SDT} curves straddling Point B results in an $AML_{hstrk,eff}$ of 43 MTU/acre at 200 years.

Initially, T_{SMT} at the center of this three-drift repository test case corresponds exactly to T_{SDT} calculated by the 55-MTU/acre SDT submodel because there has been no thermal communication between the center and edge of the repository. Thus, $AML_{hstrk,eff}$ is the emplaced AML of 55 MTU/acre for early time (Figure 6.2-4b). Because of the relatively small size of the repository in this example (which corresponds to the MSTHM validation test problem described in Section 7.5), it takes only 50 years to establish thermal communication between the center and edge of the repository. Thus, the edge-cooling effect begins to influence the repository center at about 50 years, causing T_{SMT} to begin a steady decline relative to the family of AML-dependent T_{SDT} curves. This relative decline in T_{SMT} (Figure 6.2-4a) results in a corresponding steady decline in host-rock effective AML (Figure 6.2-4b).

STAGE 2–This stage generates the three-dimensional LMTH-model (Table 1-2) temperatures at each of the repository subdomains; it does not address the influence of waste package-to-waste package variability in heat output. The LMTH-model drift-wall temperature $T_{dw,LMTH}$ is determined by linearly interpolating to the parameter $AML_{hstrk,eff}$ among the family of six AML-dependent LDTH submodel drift-wall temperature $T_{dw,LDTH}$ curves. Returning to the example discussed in Stage 1 and examining Figure 6.2-4c, the $AML_{hstrk,eff}$ is 55 MTU/acre at Point A ($t = 20$ years), and thus $T_{dw,LMTH}$ is equal to $T_{dw,LDTH}$ for 55 MTU/acre, which is about 81°C. At Point B ($t = 200$ years), the $AML_{hstrk,eff}$ is 43 MTU/acre, and thus an interpolated value of $T_{dw,LMTH}$ of 105°C is determined, which is between $T_{dw,LDTH}$ for 55 MTU/acre (115°C) and $T_{dw,LDTH}$ for 37 MTU/acre (100°C). The process of using $AML_{hstrk,eff}$ to generate LMTH-model

temperatures is repeated for invert temperatures $T_{in,LMTH}$, for drip-shield temperatures Tds, LMTH, and for temperatures at various reference locations in the host rock. LMTH-model temperatures are determined for each of the repository subdomains. It is important to note that the LDTH and DDT submodels include the mechanism of thermal-radiative heat transfer between the waste package, drip-shield, invert, and drift-wall surfaces. Because thermal-radiative heat transfer is proportional to the temperature difference between two surfaces raised to the fourth power (i.e., $T_1{}^4 - T_2{}^4$), it is dependent on temperature differences within the drifts, as well as on the absolute temperature (history) in the drifts. Consequently, a DDT submodel, which is run at only one AML, cannot address the manner in which thermal-radiative heat transfer is dependent on absolute temperature (history). To address this issue, DDT submodels are run at a variety of AMLs so that thermal-radiative heat transfer incorporates the influence of the temperature differences, as well as the influence of the absolute temperature in the drift, all as a function of time. Because the DDT submodels are run for at least four different AMLs that cover a wide range of temperature histories, interpolations between the respective DDT submodels are performed over small enough temperature-history ranges that piecewise linear interpolation adequately characterizes the underlying nonlinear process of thermal-radiative heat transfer.

STAGE 3–After LMTH-model temperatures have been determined at all reference locations (except for on the waste package) and for all repository subdomains, the next stage in the MSTHM process is to build the DMTH-model (Table 1-2) by incorporating the influence of waste package-to-waste package variability in heat output obtained from the family of DDT submodels. For each DDT submodel, the local deviation from an axially averaged temperature (i.e., averaged along the axis of the drift) is determined for each of the four waste package types (PWR1, PWR2, BWR, and HLW) for a variety of reference locations (e.g., drift wall, drip shield, invert, etc.). This local deviation is the difference between the local temperature of interest (e.g., the drift-wall temperature) and the corresponding axially averaged temperature. For example, local temperature deviations are computed for the drift wall ($\Delta T_{dw,j,DDT}$) and for the drip shield ($\Delta T_{ds,j,DDT}$). These temperature deviations are then interpolated as a function of the $AML_{hstrk,eff}$ in the same manner as $T_{i,LDTH}$ is interpolated to determine $T_{i,LMTH}$, as discussed in Stage 2. This is done to determine a temperature deviation accounting for the evolving influence of the edge-cooling effect at that repository subdomain. Computed temperature deviations for the drift wall and drip shield ($\Delta T_{dw,j,DMTH}$ and $\Delta T_{ds,j,DMTH}$) are illustrated in Figure 6.2-4d. The DMTH-model values of drift wall temperature ($T_{dw,j,DMTH}$, Figure 6.2-5a) are determined by adding $\Delta T_{dw,j,DMTH}$ (Figure 6.2-4d) to $T_{dw,LMTH}$ (Figure 6.2-4c). Note that the DMTH-model values of drip-shield temperature $T_{ds,j,DMTH}$ are similarly determined by adding $\Delta T_{ds,j,DMTH}$ to $T_{ds,LMTH}$ (Figure 6.2-5e).

STAGE 4–The parameter $AML_{i,j\text{-specific}}$ accounts for axial variations due to waste package sequencing and waste package-to-waste package variability in heat output and is necessary for the calculation of all hydrologic parameters in the DMTH-model. The parameter $AML_{i,j\text{-specific}}$ is generated in much the same manner as the parameter $AML_{hstrk,eff}$ in Stage 1. A number of values of $AML_{i,j\text{-specific}}$ are generated at each of the repository subdomains. For example, at the drift wall $AML_{dw,j\text{-specific}}$ is calculated in the following manner: (1) the local drift-wall temperature for a specific waste package $T_{dw,j,DMTH}$ is compared to the family of AML-dependent $T_{dw,LDTH}$ curves (Figure 6.2-5b); (2) the value of $AML_{dw,j\text{-specific}}$ at any given time is the AML that an LDTH submodel would have to be to match the three-dimensional DMTH-model result. Figure 6.2-5c illustrates the $AML_{dw,PWR2\text{-specific}}$ and $AML_{dw,HLW\text{-specific}}$ curves.

STAGE 5–Once the parameter AML$_{i,j\text{-specific}}$ is determined from the temperature at a particular repository subdomain and a reference/waste package-specific location, it is possible to determine the corresponding hydrologic parameters, using output from the family of AML-dependent LDTH submodels. Note that the hydrologic parameters from the LDTH submodels are collectively referred to as H$_{i,j,\text{LMTH}}$ in Figure 1-1 and Table 1-3. For example, $RH_{dw,j,\text{DMTH}}$ is obtained by linear interpolation for each timestep, using the AML$_{dw,j\text{-specific}}$ and the family of AML-dependent $RH_{dw,\text{LDTH}}$ curves (Figure 6.2-5d). The value of $RH_{dw,j,\text{DMTH}}$ accounts for both the reference/waste package-specific deviations in local temperature and for the influence of three-dimensional mountain-scale heat flow at that particular repository subdomain. With the exception of drip-shield relative humidity $RH_{ds,j,\text{DMTH}}$ and waste package relative humidity $RH_{wp,j,\text{DMTH}}$, all other hydrologic parameters are calculated in a similar manner to $RH_{dw,j,\text{DMTH}}$.

STAGE 6–The relative humidity on the drip shield and waste package ($RH_{ds,j,\text{DMTH}}$ and $RH_{wp,j,\text{DMTH}}$) is determined by relating thermal-hydrologic parameters that were determined by the DMTH model. The drip-shield relative humidity, $RH_{ds,j,\text{DMTH}}$ is obtained by the following relation:

$$RH_{ds,j,DMTH} = RH_{dw,cav} \frac{P_{sat}\left(T_{dw,cav}\right)}{P_{sat}\left(T_{ds,j,DMTH}\right)} \qquad \text{(Eq. 24)}$$

Here $RH_{ds,j,\text{DMTH}}$ and $T_{ds,j,\text{DMTH}}$ are the perimeter-averaged relative humidity and temperature on the drip shield, $RH_{dw,cav}$ and $T_{dw,cav}$ are the perimeter-averaged relative humidity and temperature on the drift wall and invert surfaces that adjoin the open drift cavity outside of the drip shield, and P_{sat} is the saturated vapor pressure. The waste package relative humidity $RH_{wp,j,\text{DMTH}}$ is calculated in an analogous manner. The relationship for the $RH_{wp,j,\text{DMTH}}$ utilizes the manner in which gas-phase mixing at the drip-shield joints allows the continuity of the partial pressure of water vapor P_v between the outside and inside of the drip shield. As discussed in Section 5.3.1.1, the joints in the drip shield allow the transport (by advection and binary diffusion) of gas (air plus water vapor) across the drip shield, which allows the continuity of P_v across the drip shield. Note that the assumption of the continuity of P_v across the drip shield is also used as a bounding case in *In-Drift Natural Convection and Condensation* (BSC 2004 [DIRS 164327], Section 6.3.3.2.7). From a heat-transfer perspective, the drip shield functions like a thermal-radiation shield (between the waste package and the drift wall) that causes the waste package to be hotter than it would have been without the presence of the drip shield. Figure 6.2-5f illustrates $RH_{ds,j,\text{DMTH}}$ at two waste package locations at the center of the repository.

6.2.5 SMT Submodels

The three-dimensional SMT submodel is used to determine the repository-scale variations in host-rock temperature (T) resulting from the heat output from the entire inventory of 70,000 MTU of waste, including 63,000 MTU of commercial spent nuclear fuel (CSNF) and 7,000 MTU of other nuclear waste (Canori and Leitner 2003 [DIRS 166275], p. 3-95). The SMT submodel includes the influence of mountain-scale thermal-property stratigraphic variation, the edge-cooling effect, which results from lateral heat loss at the repository edges, and the overburden-thickness distribution. Overburden thickness is defined to be the depth of the repository horizon below the ground surface. The SMT submodel domain extends from the ground surface to 1,000 m below the present-day water table and the lateral (adiabatic)

boundaries are far enough away from the repository that they do not affect repository temperatures. The temperature 1,000 m below the water table is estimated by extrapolation using the software routine boundary_conditions v1.0 (Section 3.1.8).

The primary purpose of the SMT submodel is to calculate the rate at which the edge-cooling effect propagates. As described in Section 6.2.4, taken together, the conduction-only SMT and SDT submodels (Section 6.2.7) provide relationships that describe the rate at which the edge-cooling effect gradually influences thermal-hydrologic conditions at given locations across the repository. The use of the SMT and SDT submodels requires the assumption that mountain-scale heat conduction controls the rate at which the edge-cooling effect proceeds. This assumption is justified in Section 5.2.1 and further validated in Section 7.5.

Given how the SMT submodel is used within the MSTHM methodology (Section 6.2.4), it does not require separate validation in this report. Moreover, the SMT submodels utilize standard scientific methods (e.g., Fourier's Law) to perform the calculations. Furthermore, validation testing of the NUFT v3.0s code included conduction-only test problems (bmrk002 and verif02), which are described in the Validation Test Plan for NUFT 3.0s (LLNL 2002 [DIRS 170259]; LLNL 2000 [DIRS 170258]).

The use of conduction-only SMT-submodel results at the mountain scale requires the assumption that mountain-scale heat flow is dominated by conductive heat flow, which is justified in Section 5.2.1. *Mountain-Scale Coupled Processes (TH/THC/THM)* (BSC 2004 [DIRS 169866], Section 6.3) documents a three-dimensional mountain-scale thermal-hydrologic model that is similar in scale to the SMT submodel in the MSTHM. The vertical temperature profile of the mountain-scale thermal-hydrologic model (Figure 6.3.1-6 of BSC 2004 [DIRS 169866]) is indicative of conduction-dominated heat flow. Conduction dominates other heat transfer mechanisms (i.e., convection in fractures and lithophysae, and latent heat) in the host rock (Sass et al. 1988 [DIRS 100644], p. 35). This is also supported by the conclusions of data and modeling of the Drift Scale Test (Birkholzer and Tsang 2000 [DIRS 154608], p. 1439). For the level of confidence required for the MSTHM (and its associated submodels), justifying the assumption that mountain-scale heat flow is dominated by conduction is equivalent to validating the conceptual model of the SMT submodel.

Given the above-mentioned observations supporting heat flow at various scales being dominated by conduction, NUFT-model results, regardless of dimensionality, can be validated by corroboration with results obtained from an alternate conduction-only mathematical model. Such a model-corroboration example is described in *Drift Degradation Analysis* (BSC 2004 [DIRS 166107], Section 6.2 and Figure 6-26). Figure 6-26 of that reference compares temperatures predicted by the NUFT code, for a two-dimensional line-averaged heat source, drift-scale, thermal-hydrologic (LDTH) submodel, with temperatures predicted by the FLAC3D code (FLAC3D V2.1, STN: 10502-2.1-00 [DIRS 161947]). The FLAC3D code is a thermal-mechanical simulator that does not consider hydrologic effects on heat transfer; thus, it assumes conduction-only heat flow (Itasca Consulting Group 2002 [DIRS 160331], Section 1). Figure 6-26 shows that the temperatures predicted by the two models are in good agreement. Since hydrologic effects on heat transfer are not important, as discussed in the preceding paragraph, the corroboration of NUFT-model results with those from FLA3D as illustrated in *Drift Degradation Analysis* (BSC 2004 [DIRS 166107], Section 6.2 and Figure 6-26) validates

the prediction of conductive heat flow in the NUFT model. Therefore, this model-corroboration example supports post-development validation of the NUFT SMT submodel.

6.2.5.1   SMT Submodel Mesh

The actual and modeled repository footprints (Figure 6.2-3) cover nearly identical areas of approximately 4.656 km^2, which is based on the modeled length of drifts (Table 6.2-1), multiplied by the 81-m drift spacing. The repository footprint corresponds to the area that is heated by the smeared-heat-source representation of heat generation from waste packages. The areal distribution of gridblocks in the repository area of the SMT submodel is shown in Figure 6.2-3. The SMT submodel discretely represents each emplacement panel (Panels 1, 2E, 2W, 3, and 5) as well as each emplacement drift by using rows of heated gridblocks that are 20 m in the longitudinal direction, 81 m perpendicular to the drift axis, and 6-m thick in the vertical direction. The 6-m-thickness of the smeared heat source in the SMT submodel is consistent with that of the SDT submodel discussed in Section 6.2.7. There are 2,874 20-m intervals along the 95 emplacement drifts in the SMT submodel. The actual total heated length of emplacement drift in the repository is 57,480.2 m; the modeled length of emplacement drifts is 57,480.0 m. Table 6.2-1 lists the actual and modeled lengths of heated emplacement drifts in each of the panels. The heated length of each emplacement drift is obtained from the end-point coordinates (BSC 2003 [DIRS 161727]).

The SMT submodel mesh is constructed so that boundary effects have an insignificant influence on the predicted temperatures near the repository. This is accomplished by extending the lateral boundaries at least 1,000 m beyond the repository edges and by extending the lower boundary 1,000 m below the water table.

The software routine YMESH v1.54 (Section 3.1.7) is used to generate the SMT submodel mesh file so that it is consistent with the three-dimensional distribution of UZ model layers in the site-scale UZ flow and transport model (DTN: LB03023DKMGRID.001 [DIRS 162354]), as described in Table 6-5 of *Development of Numerical Grids for UZ Flow and Transport Modeling* (BSC 2004 [DIRS 169855]). The process of building the SMT submodel mesh is described in Appendix I. Note that the lower boundary (corresponding to the water table) of the three-dimensional site-scale UZ flow model is a gently sloping surface. It is also noted that the output from the previous version of the site-scale UZ flow model (DTN: LB990701233129.001 [DIRS 106785]) had a horizontal lower boundary at an elevation of 730 m, which was based on an assumption that the water table was horizontal.

Table 6.2-1.   Summary of Emplacement Panels and Drifts Represented in the SMT Submodel

Panel	Total heated drift length (m)[a]	Number of emplacement drifts[a]	Number of heated gridblocks[b]	Total modeled length of drifts (m)[c]
1	4,100.4	8	206	4,120.0
2E	10,882.0	19	545	10,900.0
2W	13,845.1	23	689	13,780.0
3	17,493.6	30	877	17,540.0
5	11,159.1	15[d]	557	11,140.0
Entire repository	57,480.2	95	2874	57,480.0

[a] Total heated drift lengths for each panel and for the entire repository, as well as the number of emplacement drifts, are determined from the endpoint coordinates in BSC 2003 [DIRS 161727].
[b] Each of the heated gridblocks represents a 20-m interval along the emplacement drift.
[c] Total length of drifts as represented in the SMT submodel, as well as in the MSTHM.
[d] Panel 5 has a total of 27 drifts; the 15 northernmost drifts are emplaced in the TSPA-LA base case.

The 2,874 gridblocks in the SMT submodel are the 2,874 locations for which the MSTHM provides thermal-hydrologic output. Because each of these 2,874 locations is represented by a gridblock that is 20-m-long in the axial direction along the drift, they can each contain approximately four waste packages. The MSTHM uses the DDT submodel (Section 6.2.8) to discretely represent the thermal-hydrologic conditions for a wide range of waste packages, ranging from those that have low heat-generation rates (e.g., DHLW waste packages) to those that have high heat-generation rates (e.g., 21-PWR CSNF waste packages). The DDT submodel discretely represents eight waste packages, including three 21-PWR CSNF waste packages, three 44-BWR CSNF waste packages, and two DHLW waste packages. The MSTHM is constructed to provide thermal-hydrologic parameter histories (e.g., temperature and relative humidity) for each one of those eight waste packages at all 2,874 locations in the repository, which results in a total of 22,992 sets of thermal-hydrologic parameter histories. This number of sets is greater than the number of waste packages that could be emplaced in 57,480 m of emplacement drifts. The extra thermal-hydrologic parameter sets are provided to address uncertainty concerning the actual emplaced sequencing of waste packages. In other words, it cannot be known *a priori* what the actual emplaced waste package sequencing will be. The 22,992 sets of thermal-hydrologic parameter histories are provided for multiple scenarios, such as lower-bound, mean, and upper-bound infiltration-flux cases to allow downstream process models to sample from a broad set of thermal-hydrologic conditions that encompasses the influence of various sources of uncertainty.

6.2.5.2   SMT Submodel Boundary Conditions

The SMT submodel domain extends from the ground surface to 1,000 m below the present-day water table. The lateral boundaries, which are adiabatic boundaries, are at least 1,000 m from the repository edges, which is far enough away from the repository so that they do not affect thermal behavior in the repository. The average distances between the repository edges and the lateral boundaries are 1238, 2302, 1891, and 1893 m for the northern, eastern, southern, and western boundaries, respectively. The average distance between the northern repository edge and northern SMT-submodel boundary is 1238 m, ranging from 1081 to 1405 m. The average distance between the eastern repository edge and the eastern SMT-submodel boundary is 2302 m, ranging from 1000 to 3320 m. The average distance between the southernmost

repository edge and the southern SMT-submodel boundary is 1981 m, ranging from 1891 to 1891 m. The average distance from the western repository edge and the western SMT-submodel boundary is 1893 m, ranging from 1440 to 2400 m.

The ground surface, which is a fixed-temperature boundary, functions as a heat sink to mountain-scale heat flow, including both the geothermal heat flux and heating from the repository. Thus, evaluating the potential for the lateral boundaries affecting mountain-scale heat flow is best accomplished by comparing the distances between the repository edges and lateral SMT-submodel boundaries with the distance between the repository horizon and the ground surface (called overburden thickness). Over the heated footprint of the repository, the average overburden thickness is 329 m, which is substantially less (by about an order of magnitude) than the distances between the repository edges and the lateral SMT-submodel boundaries. Because the ground surface acts like a heat sink, heating from the repository reaches the ground surface long before it can reach any of the lateral boundaries. Therefore, the lateral boundaries have no influence on mountain-scale heat flow. Thus, the use of lateral adiabatic boundaries is justified.

The SMT submodel uses appropriate boundary conditions, which are location dependent. The temperature at the ground surface is based on ground-surface temperatures from the three-dimensional UZ flow model (DTN: LB991201233129.001 [DIRS 146894], File INCON_thm_s32.dat), which is based on a correlation of temperature versus elevation. The temperature at the lower boundary of the model domain is extrapolated vertically from the temperature gradient at the (sloping) water table of the current site-scale UZ flow model. The temperature at the sloping water table is interpolated, based on the temperature at an elevation of 730 m, which was the water table in the previous three-dimensional UZ flow model, and the ground-surface temperature. Both the ground-surface temperature distribution and the (730-m-elevation) water-table temperature distribution are found in DTN: LB991201233129.001 [DIRS 146894], File INCON_thm_s32.dat. Appendix II describes the process of generating boundary temperatures for the SMT submodels, as well as for the other submodels.

Note that since the boundary conditions were determined for the SMT submodel, a new source of boundary conditions has been made available in *Mountain-Scale Coupled Processes (TH/THC/THM) Models* (BSC 2004 [DIRS 169866]). The temperature boundary conditions can be extracted from the INCON block of file: th_v16.dat of DTN: LB0310MTSCLTH3.001 [DIRS 170270]. As discussed in Appendix I, these updated boundary conditions result in insignificant differences in temperatures at both the upper boundary (the ground surface) and the lower boundary (the water table), compared to those obtained in this report from file: INCON_thm_s32.dat of DTN: LB991201233129.001 [DIRS 146894].

6.2.5.3   SMT Submodel Heat-Generation Rates

The heat-generation rate for the SMT submodel is in the form of a heat-generation-rate-versus-time table, which is part of the SMT submodel NUFT-input file. For the TSPA-LA base case there is an assumption that all waste packages are simultaneously emplaced (Section 5.2.3). Thus, heating starts at the same time for the entire repository represented in the SMT submodel. The heat-removal efficiency of drift ventilation is represented by the reduction of the net heat-generation rate during the preclosure period. It is important to note that the

edge-cooling effects requires that most of the LDTH submodel runs use a modeled AML that is less than the actual AML of the repository.

In addition to their use as a submodel within the MSTHM methodology, the two-dimensional LDTH submodels are also used as stand-alone models to conduct sensitivity analyses in this report (e.g., Section 6.3.9). Thus, the LDTH submodel is validated against the Drift Scale Test in Section 7.4.

The NUFT code is used to model flow through a fractured porous media in the LDTH submodels. The key NUFT options that are required for LDTH simulations include the dual-permeability and the active-fracture concept. These NUFT options are required to be consistent with the hydrologic property set (DTN: LB0208UZDSCPMI.002 [DIRS 161243]) used in the MSTHM calculations supporting the TSPA-LA.

The DKM conceptualizes the fractured rock as having two interacting materials, one representing the matrix and one representing the fractures. The interaction between the fractures and the matrix is explicitly calculated from the local temperature and pressure differences, thus allowing disequilibrium behavior to be predicted between the fracture and matrix continua.

The active fracture concept accounts for the contact area between the fracture and the matrix, as well as the frequency of fractures. The concept is that fracture flow only occurs through some of the fractures. The flux through a fracture increases with liquid-phase saturation; thereby focusing flow through a portion of the fractures (i.e., through active fractures), which results in faster pathways for liquid-phase flux through the mountain.

The natural system hydrologic properties in the calibrated drift-scale hydrologic property set (DTN: LB0208UZDSCPMI.002 [DIRS 161243]) were calibrated in *Calibrated Properties Model* (BSC 2004 [DIRS 169857]), using an inverse modeling technique that assumes the use of the DKM and the active-fracture concept. Both the DKM and active-fracture concept are implemented in NUFT as options.

The LDTH submodels represent thermal radiation between the drip-shield, drift-wall, and upper invert (i.e., drift floor) surfaces. The LDTH submodels also utilize an effective thermal conductivity for air, which represents the influence of natural convection, on the basis of correlations from the FLUENT-code thermal model in *In-Drift Natural Convection and Condensation* (BSC 2004 [DIRS 164327], Appendix J). Section 7.6 provides the basis for validating that the influence of natural convection has been appropriately addressed in the MSTHM, which also requires that natural convection has been appropriately addressed in both the LDTH submodels.

6.2.6.1   LDTH Submodel Locations

The LDTH submodel locations are shown in Figure 6.2-3, and represent repository-scale variability of thermal properties, hydrologic properties, percolation flux, and overburden thickness.

6.2.6.2   LDTH Submodel Mesh

The cross-sectional (lateral) dimensions of the drift for the postclosure period are shown in Figure 6.2-1; these dimensions were used to build the numerical meshes of the LDTH submodels (Figure 6.2-6). The same mesh is used for the initialization submodel runs, which establish steady-state conditions for the time of emplacement and the submodel runs for the preclosure and postclosure periods. The process of building the LDTH submodel input files is described in Appendix V.

The numerical mesh for the LDTH submodel (Figure 6.2-6) assumes that the drip shield and waste package are lumped as a monolithic heat source. This lumped approximation of the drip shield and waste package allows for the representation of thermal-hydrologic behavior down to the surface of the drip shield. This lumped heat source is 1 m in the longitudinal direction along the drift axis (as it is in the smeared heat source in the SDT submodel discussed in Section 6.2.7). This lumped representation for the waste package and drip shield is applied during both the preclosure period and the postclosure period. Note that the drip shield is emplaced at the very end of the preclosure period. For the preclosure period, this lumped approximation of the drip shield and waste package in the LDTH submodel is corrected by the manner in which the preclosure DDT submodel (Figure 6.2-7), which accounts for the actual dimensions of the waste package (without the presence of the drip shield), is applied in the MSTHAC methodology (Section 6.2.4). The postclosure DDT submodel (Figure 6.2-8), which accounts for the actual waste package and drip-shield dimensions (including the correct dimensions of the gap between the waste package and drip shield), is applied in the MSTHAC methodology (Section 6.2.4) to represent thermal-hydrologic behavior between the drip shield and waste package.
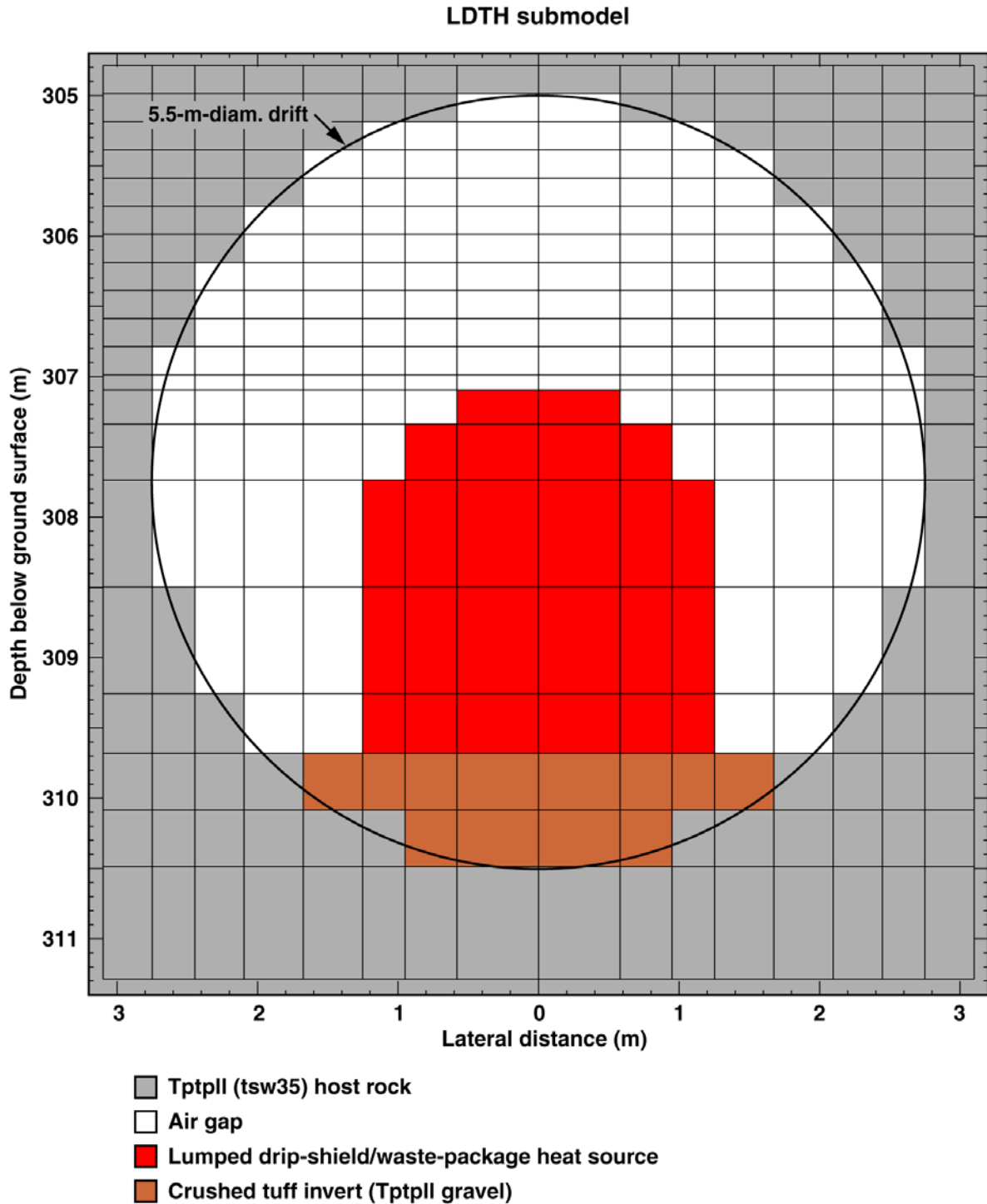
Source: See Table XIII-1.

NOTE: This illustrates just a portion of the mesh. The entire model extends laterally 40.5 m (the mid-pillar centerline) and extends from the ground surface to the water table.

Figure 6.2-6. Cross-Sectional (Lateral) View of the Numerical Mesh Used in the Vicinity of the Drift for All LDTH Submodels, Including Both the Initialization Runs and the Preclosure and Postclosure Runs

6.2.6.3   LDTH Submodel Boundary Conditions

Because the LDTH submodels are for a symmetry cell between the vertical plane down the center of the drift and the vertical midplane between drifts, the lateral boundaries are adiabatic and no-mass-flow boundaries. The LDTH submodels require temperature, pressure, and gas-phase air-mass fraction at the upper boundary, which represents the ground surface, and at the lower boundary, which represents the water table. The upper boundary also requires the enthalpy associated with the infiltration flux at the top of the model. Note that the enthalpy is determined from the temperature of the upper boundary.

Both the upper and lower boundaries have constant conditions with time. Note that the process of calculating air-mass fraction at the ground surface utilizes the assumption that the atmosphere is at 100 percent relative humidity (Section 5.1.1). The process of adding the boundary conditions to the LDTH submodels is described in Appendix II.

Note that since the boundary conditions were determined for the LDTH submodels, a new source of boundary condition has been made available in *Mountain-Scale Coupled Processes (TH/THC/THM) Models* (BSC 2004 [DIRS 169866]). The temperature and gas-phase-pressure boundary conditions can be extracted from the INCON block of file: th_v16.dat of DTN: LB0310MTSCLTH3.001 [DIRS 170270]. As discussed in Appendix I, these updated boundary conditions result in insignificant differences in temperatures and gas-phase pressures at both the upper boundary (the ground surface) and the lower boundary (the water table) compared to those obtained in this report from file: INCON_thm_s32.dat of DTN: LB991201233129.001 [DIRS 146894].

6.2.6.4   LDTH Submodel Heat-Generation Rates

The heat-generation rates for the LDTH submodels are in the form of heat-generation-rate-versus-time tables located in NUFT include files. Because any given LDTH submodel covers the same model domain (including the same area in plan view) as the corresponding SDT submodel, the LDTH and corresponding SDT submodel use the same heat-generation-rate-versus-time tables. The drip shield and waste package are lumped as a monolithic heat source. The heat-removal efficiency of drift ventilation is represented by the reduction of the net heat-generation rate during the preclosure period. The heat-removal efficiency depends on the distance from the ventilation inlet and also varies with time. Thus, the effective heat-generation rate along an emplacement drift depends on the distance from the edge of that drift during the preclosure period. The heat-removal effect of drift ventilation is incorporated into the heat-generation-rate-versus-time tables for a given LDTH–SDT submodel location, using the software routine heatgen_ventTable_emplace v1.0 (Section 3.1.9). For the postclosure period, the same heat-generation-rate-versus-time table is applied to all LDTH–SDT submodel locations because drift ventilation has ceased and the effective heat-generation rate is the full nominal rate at all locations. The input files for the LDTH submodels involve assumptions described in Sections 5.1.1, 5.1.2, 5.1.3, 5.1.4, 5.1.5, 5.3.1.1, 5.3.1.2, 5.3.1.7, 5.3.1.8, 5.3.1.9, 5.3.1.10, 5.3.2.3, 5.3.2.4, and 5.3.2.7. Appendix III describes the process of generating heat-generation-rate-versus-time tables for the LDTH submodels.

6.2.6.5 LDTH Submodel Material Properties

Material properties are read into the LDTH submodel NUFT-input files as "include" files for the natural system properties and for the engineered barrier system properties inside the emplacement drifts.

One hydrologic property set, called the modified-mean infiltration-flux hydrologic property set (dkm-afc-1Dds-mc-mi-04), is used to conduct the LDTH submodel calculations for lower-bound, mean, and upper-bound infiltration-flux cases. The modified-mean infiltration-flux property set is the same as the mean infiltration-flux property set (DTN: LB0208UZDSCPMI.002 [DIRS 161243]), with the one modification being that the van Genuchten fracture alpha in the Tptpul (tsw33) is set to be the same (1.02×10^{-4} Pa^{-1}) as that in the Tptpll (tsw35) unit (Table IV-4 in Appendix IV). The file dkm-afc-EBS-mi-03 gives the thermal and hydrologic properties of the materials inside the emplacement drift. The thermal properties inside the emplacement drifts, such as the drip shield composed of titanium and invert composed of crushed tuff, are given in Table 4.1-2. The thermal properties inside the drifts also include the emissivity values of the surfaces. Note that a value of 0.9 is used for the emissivity of the rock and invert surfaces in the drift, which is obtained from Incropera and DeWitt's (1996 [DIRS 108184]) advanced textbook for heat and mass transfer. The engineered barrier system thermal properties also include the use of an effective thermal conductivity for the gas-filled drift cavity that is based on a correlation (Francis et al. 2003 [DIRS 164602], Table 6) accounting for the influence of natural convection, which is described in Appendix I. It should be noted that the correlations for the in-drift effective thermal conductivity, which were obtained from Table 6 of Francis et al. (2003 [DIRS 164602]), have been updated in *In-Drift Natural Convection and Condensation* (BSC 2004 [DIRS 164327], Table 6.4.7-3), resulting in small changes to the coefficients. As evident in Figure I-1 of Appendix I, the small changes to the coefficients result in insignificant changes to the in-drift effective thermal conductivity. The gas-filled cavity between the drip shield and drift wall is represented as a porous medium with 100 percent porosity and a permeability of 1×10^{-8} m^2 (Section 5.3.1.7). Because the dual-permeability method is used, it is necessary to partition the gas-filled cavity into the matrix and fracture continua. This partitioning, which is taken to be 50 percent matrix continuum and 50 percent fracture continuum, has an insignificant on flow because of conditions in these respective continua are in equilibrium within the gas-filled drift. The input files are associated with the assumptions described in Sections 5.1.1, 5.1.2, 5.2.3, 5.3.1.1, 5.3.1.2, 5.3.1.7, 5.3.1.8, 5.3.2.3, and 5.3.2.4. The process of generating the LDTH submodel material properties files is described in Appendix IV. The input files require the assumptions described in Sections 5.1.1, 5.1.2, 5.2.3, 5.3.1.1, 5.3.1.2, 5.3.1.7, 5.3.1.8, 5.3.2.3, and 5.3.2.4. The process of generating the LDTH submodel material properties files is described in Appendix IV.

6.2.6.6 LDTH Submodel Percolation Flux

The liquid-phase flux is specified at the upper boundary of the LDTH submodels. For the TSPA-LA base case, the upper-boundary liquid-phase flux corresponds to the distribution of percolation flux just below the base of the PTn unit (also called the PTn-to-TSw percolation flux); these data are generated by the three-dimensional UZ flow model for the three climate states: present-day, monsoonal, and glacial-transition. Thus, the MSTHM includes the influence of lateral diversion in the PTn as represented in the three-dimensional UZ flow model.

The PTn-to-TSw percolation flux is provided for the present-day, monsoonal, and glacial-transition climates for lower-bound, mean, and upper-bound infiltration-flux cases (DTN: LB0302PTNTSW9I.001 [DIRS 162277]), resulting in nine files. The software routine repository_percolation_calculator v1.0 (Section 3.1.13) is used to determine the percolation flux at each of the 108 LDTH–SDT submodel locations (Figure 6.2-3) in Panels 1, 2E, 2W, 3, and 5. The process of generating LDTH submodel percolation-flux boundary conditions is described in Appendix I. Appendix XII describes a comparison of the percolation-flux distribution implemented in the MSTHM compared to the PTn-to-TSw percolation-flux distribution from DTN: LB0302PTNTSW9I.001 [DIRS 162277]. As is evident in Figures XII-3 through XII-11, the percolation flux implemented in the MSTHM corresponds closely with that from DTN: LB0302PTNTSW9I.001 [DIRS 162277] for all three climate states and for all three infiltration-flux cases.

6.2.6.7   LDTH Submodel Simulations

The LDTH submodel is the only submodel type that has to be run for each of the five infiltration-flux/host-rock thermal-conductivity cases (see Table 6.3-37). The simulations for the other three submodel types are applicable to all infiltration-flux cases.

Each LDTH submodel set for a given infiltration-flux case consists of 432 simulations, which comes from 108 drift-scale-submodel locations (Section 6.3.1) and 4 AML values run at each location ($108 \times 4 = 432$). The process of building the LDTH submodel input files is described in Appendix I. The NUFT code cannot complete a model simulation unless converged solutions are obtained for all calculational cycles (i.e., timesteps). Thus, numerical convergence is automatically assured in all LDTH-submodel simulations.

6.2.7   SDT Submodels

The one-dimensional smeared-heat-source drift-scale thermal-conduction (SDT) submodels are run in parallel with the LDTH submodels at the same 108 locations and for the same AMLs (14, 27, 55, and 66 MTU/acre). These submodels are required to obtain functional relationships between "line-averaged" temperatures predicted by the LDTH submodel and the "smeared" host-rock temperatures predicted by the SMT submodel.

The primary purpose of the SDT submodel is to work in conjunction with the SMT submodel (Section 6.2.5) to calculate the rate at which the edge-cooling effect propagates. As described in Section 6.2.4, taken together, the conduction-only SMT and SDT submodels provide relationships that describe the rate at which the edge-cooling effect gradually influences thermal-hydrologic conditions at given locations across the repository. As validated in Section 7.5, the rate at which the edge-cooling effect proceeds is taken to be dominated by heat conduction.

Given how the SDT submodels are used within the MSTHM methodology, they do not require separate validation in this report. Moreover, the conduction-only SDT submodels utilize standard scientific methods (e.g., Fourier's Law) to perform the calculations. Furthermore, validation testing of the NUFT v3.0s code included conduction-only test problems (bmrk002 and verif02), which are described in the Validation Test Plan for NUFT 3.0s (LLNL 2002 [DIRS 170259]; LLNL 2000 [DIRS 170258]).

Given the observations in Section 6.2.4 that support heat flow, at various scales, being dominated by conduction, NUFT-model results, regardless of dimensionality, can be validated by corroboration with results obtained from an alternate conduction-only mathematical model. Such a model-corroboration example is described in *Drift Degradation Analysis* (BSC 2004 [DIRS 166107], Section 6.2 and Figure 6-26). Figure 6-26 of that reference compares temperatures predicted by the NUFT code, for a two-dimensional line-averaged heat source, drift-scale, thermal-hydrologic (LDTH) submodel, with temperatures predicted by the FLAC3D code. The FLAC3D code is a thermal-mechanical simulator that does not consider hydrologic effects on heat transfer; thus, it assumes conduction-only heat flow (Itasca Consulting Group 2002 [DIRS 160331], Section 1). Figure 6-26 shows that the temperatures predicted by the two models are in good agreement. Since hydrologic effects on heat transfer are not important, as discussed in the preceding paragraph, the corroboration of NUFT-model results with those from FLA3D as illustrated in *Drift Degradation Analysis* (BSC 2004 [DIRS 166107], Section 6.2 and Figure 6-26) validates the prediction of conductive heat flow in the NUFT model. Therefore, this model-corroboration example supports post-development validation of the NUFT SDT submodels.

6.2.7.1 SDT Submodel Locations

The SDT submodels are run at the same 108 drift-scale-submodel locations (Figure 6.2-3) as the LDTH submodel (Section 6.2.6.1).

6.2.7.2 SDT Submodel Mesh

The SDT submodels use the same vertical discretization of gridblocks as is used in the SMT submodels (Section 6.2.5). The manner in which the LDTH–SDT temperature relationships are developed and used to modify SMT-predicted host-rock temperatures (Section 6.2.4) requires consistency between how vertical heat flow is modeled in the respective SDT and SMT submodels, including consistency in the vertical gridblock discretization in the respective submodels.

6.2.7.3 SDT Submodel Boundary Conditions

The SDT submodels use appropriate boundary conditions, which are location dependent, consistent with the LDTH submodels and the SMT submodel. Thus, the SDT submodel boundary temperature conditions are the same as the corresponding LDTH submodel (Section 6.2.6.3). Consistent upper and lower boundary temperatures ensure self-consistency with respect to how the LDTH and SDT submodels are used to generate LDTH-temperature versus SDT-temperature relationships and how these relationships are used in the MSTHAC v7.0 methodology to correct SMT-predicted temperatures to LMTH-model conditions (Section 6.2.4).

Because the SDT submodels are for a symmetry cell between the vertical plane down the center of the drift and the vertical midplane between drifts, the lateral boundaries are adiabatic and no-mass-flow boundaries. The SDT submodels require temperature at the upper boundary, which represents the ground surface, and the lower boundary, which represents the water table. Both boundaries have constant temperature conditions with time. The process for generating SDT submodel boundary conditions is described in Appendix II.

Note that since the boundary conditions were determined for the SDT submodels, a new source of boundary condition has been made available from the *Mountain-Scale Coupled Processes (TH/THC/THM) Models* (BSC 2004 [DIRS 169866). The temperature boundary conditions can be extracted from the INCON block of file: th_v16.dat of DTN: LB0310MTSCLTH3.001 [DIRS 170270]. As discussed in Appendix I, these updated boundary conditions result in insignificant differences in temperatures at both the upper boundary (the ground surface) and the lower boundary (the water table), compared to those obtained in this report from file: INCON_thm_s32.dat of DTN: LB991201233129.001 [DIRS 146894].

6.2.7.4   SDT Submodel Heat-Generation Rates

Because any given SDT submodel represents the same model domain (including the same area in plan view) as the corresponding LDTH submodel, the SDT and corresponding LDTH submodel use the same heat-generation rate-versus-time table (Section 6.2.6.4). Appendix III describes the process of generating heat-generation-rate-versus-time tables for the SDT submodels. The heat generation is smeared over a gridblock that is 6-m thick in the vertical direction (as it is in the SMT submodel, discussed in Section 6.2.5), 1 m in the longitudinal direction along the drift axis (as it is in the LDTH submodels, discussed in Section 6.2.6), and which extends from the drift centerline to the midpillar location between drifts.

6.2.7.5   SDT Submodel Material Properties

The SDT submodels are implemented with the appropriate stratigraphy, with respect to thermal properties; notably, thermal conductivity and heat capacity. The distribution of the thermal properties are location dependent, consistent with the three-dimensional distribution of UZ model layers in the site-scale UZ flow and transport model (DTN: LB03023DKMGRID.001 [DIRS 162354]), as described in Table 6-5 of *Development of Numerical Grids for UZ Flow and Transport Modeling* (BSC 2004 [DIRS 169855]).

Because the SDT submodel is a conduction-only model, the material properties only involve thermal properties. Material properties are read into the SDT submodel NUFT-input files as "include" files for the natural system thermal properties. The SDT submodel uses the same thermal properties (for the UZ model layers) that are used in the SMT submodel (Section 6.2.5.4). The material properties of the SDT submodels utilize assumptions described in Section 5.3.2.1. The process of building the SDT submodel material-property file is described in Appendix IV.

6.2.7.6   SDT Submodel Simulations

Each SDT submodel set consists of 432 simulations that come from 108 LDTH–SDT submodel locations (Figure 6.2-3) and 4 AML values run at each location ($108 \times 4 = 432$). The process of building the SDT submodel input files is described in Appendix V. The NUFT code cannot complete a model simulation unless converged solutions are obtained for all calculational cycles (i.e., timesteps). Thus, numerical convergence is automatically assured in all SDT-submodel simulations.

6.2.8   DDT Submodels

The three-dimensional DDT submodel is used to account for waste package-specific heat output and for thermal radiation between all waste package and drift surfaces to determine waste package-specific deviations (relative to line-averaged-heat-source conditions) in temperatures in the drift and adjoining host rock. For the preclosure and postclosure periods, thermal radiation between the waste package and drift surfaces controls the longitudinal temperature deviations along the drift. The values of thermal conductivity or convective heat-flow processes in the host rock play a minor role on the magnitude of longitudinal temperature deviations along the drift (Hardin 1998 [DIRS 100350], Section 3.7.5.4). This allows an MSTHM calculation to only require a set of DDT submodel calculations conducted at a single location in the repository. The P2WR5C10 LDTH–SDT submodel location is located in Panel 2W, which is located in the approximate center of the repository (Figures 6.2-3 and 6.3-1). The nomenclature R5C10 refers to the row and column of this drift-scale submodel location within the lattice of drift-scale submodel locations (Figure 6.2-3). This location was selected because the repository horizon at that location is in the middle of the Tptpll (tsw35 UZ model layer), which is the predominant host-rock type in the repository, and because the overburden thickness at that location is close to the average for the repository.   The DDT submodels utilize assumptions described in Sections 5.2.2, 5.2.3, 5.3.2.1, and 5.4.

Section 7.5 provides the primary basis for validating the temperature deviations along the drift $\Delta T_{i,j,DDT}$, which are calculated by the DDT submodels. Section 7.6 provides the basis for validating that the influence of natural convection has been appropriately addressed in the MSTHM, which also requires that natural convection has been appropriately addressed in both the DDT submodels.

The DDT submodels are conduction-only calculations that do not require separate validation in this report.   The reason they do not require validation is that they are conduction-only calculations that utilize standard scientific methods (e.g., Fourier's Law) to perform the calculations. Moreover, validation testing of the NUFT v3.0s code included conduction-only test problems (bmrk002 and verif02), which are described in the Validation Test Plan for NUFT 3.0s (LLNL 2002 [DIRS 170259]; LLNL 2000 [DIRS 170258]).   The DDT submodel represents thermal radiation inside the emplacement drifts and also represents the influence of natural convective heat flow in the drifts through the use of an equivalent thermal conductivity that is based on a correlation given by Francis et al. (2003 [DIRS 164602], Table 6) (Section 6.2.8.5). Thus, the DDT does not model natural convection in the drift; it only uses a correlation derived elsewhere as indicated. The software qualifications of NUFT v3.0s and NUFT v3.0.1s include test problems that demonstrate the validity of NUFT in modeling a one-dimensional thermal conduction problem (bmrk 002), a three-dimensional thermal conduction problem (verif02), and a three-dimensional thermal radiation problem (verif03) (LLNL 2002 [DIRS 170259]; LLNL 2000 [DIRS 170258]).

Given the observations in Section 6.2.4 that support heat flow, at various scales, being dominated by conduction, NUFT-model results, regardless of dimensionality, can be validated by corroboration with results obtained from an alternate conduction-only mathematical model. Such a model-corroboration example is described in *Drift Degradation Analysis* (BSC 2004 [DIRS 166107], Section 6.2 and Figure 6-26).   Figure 6-26 of that reference compares temperatures predicted by the NUFT code, for a two-dimensional line-averaged heat source,

drift-scale, thermal-hydrologic (LDTH) submodel, with temperatures predicted by the FLAC3D code. The FLAC3D code is a thermal-mechanical simulator that does not consider hydrologic effects on heat transfer; thus, it assumes conduction-only heat flow (Itasca Consulting Group 2002 [DIRS 160331], Section 1). Figure 6-26 shows that the temperatures predicted by the two models are in good agreement. Since hydrologic effects on heat transfer are not important, as discussed in the preceding paragraph, the corroboration of NUFT-model results with those from FLA3D as illustrated in *Drift Degradation Analysis* (BSC 2004 [DIRS 166107], Section 6.2 and Figure 6-26) validates the prediction of conductive heat flow in the NUFT model. Therefore, this model-corroboration example supports post-development validation of the NUFT DDT submodels.

6.2.8.1   DDT Submodel Locations

The P2WR5C10 LDTH–SDT submodel location, which is in the center of the repository, located in Panel 2W (Figures 6.2-3 and 6.3-1), is used for all DDT submodel calculations.

6.2.8.2   DDT Submodel Mesh

The lateral and longitudinal dimensions of the drift for the preclosure and postclosure periods are shown in Figures 6.2-1 and 6.2-2, respectively. Note that the drip shield (Figure 6.2-1) is not present during the preclosure ventilation period. These dimensions were used to build the numerical meshes of the DDT submodels. The cross-section view of the mesh is shown in Figures 6.2-7 and 6.2-8 for the preclosure and postclosure periods, respectively. The longitudinal view of the mesh is shown in Figures 6.2-9 and 6.2-10 for the preclosure and postclosure periods, respectively. The DDT submodel utilizes symmetry in all four directions: (1) about the vertical midplane down the center of the drift, (2) the vertical midplane down the center of the rock pillar between drifts, (3) the vertical plane that is orthogonal to and intersects the "one-half" 21-PWR waste package, and (4) the vertical plane that is orthogonal to and intersects the "one-half" 44-BWR waste package (Figure 6.2-2). Thermal radiation is represented between all surfaces in the drift. From a heat-transfer perspective, the drip shield functions like a thermal-radiation shield (between the waste package and the drift wall) that causes the waste package to be hotter than it would have been without the presence of the drip shield. The increased temperature difference between the waste package and the drift wall reduces the relative humidity on the waste package in a fashion that is analogous to that given in Equation 24 (Section 6.2.4) for the drip shield itself.

6.2.8.3   DDT Submodel Boundary Conditions

The DDT submodels use appropriate boundary conditions, which are location dependent, consistent with the SDT and LDTH submodels, as well as the SMT submodel. The temperature boundary conditions for the DDT submodels are the same as those for the SDT submodel at the P2WR5C10 LDTH–SDT submodel location (Figures 6.2-3 and 6.3-1), which is in the center of the repository, located in Panel 2W. The DDT submodel temperature boundary conditions are the same as the corresponding LDTH submodel.

Because the DDT submodels are for a symmetry cell between the vertical plane down the center of the drift and the vertical midplane between drifts, the lateral boundaries are adiabatic and no-mass-flow boundaries. The DDT submodels require temperature at the upper boundary,

which represents the ground surface, and at the lower boundary, which represents the water table. Both boundaries have constant temperature conditions with time. The process for generating DDT submodel boundary conditions is described in Appendix II.

6.2.8.4   DDT Submodel Heat-Generation Rates

Heat-generation-rate-versus-time tables are required for the 8 different waste packages represented in the DDT submodels (Figure 6.2-2), which are read into the DDT submodel NUFT-input files as "include" files. The heat-generation-rate-versus-time tables utilize the assumption described in Section 5.2.3. During the preclosure period, the DDT submodel has the same heat-removal-efficiency-versus-time table that is applicable to the P2WR5C10 LDTH-SDT submodel location (Figures 6.2-3 and 6.3-1). Note that the heat-removal-efficiency-versus-time tables are derived from DTN: MO0304MWDALACV.000 [DIRS 164551]. Appendix III describes the process of generating heat-generation-rate-versus-time tables for the DDT submodel, as well as for the other submodels.
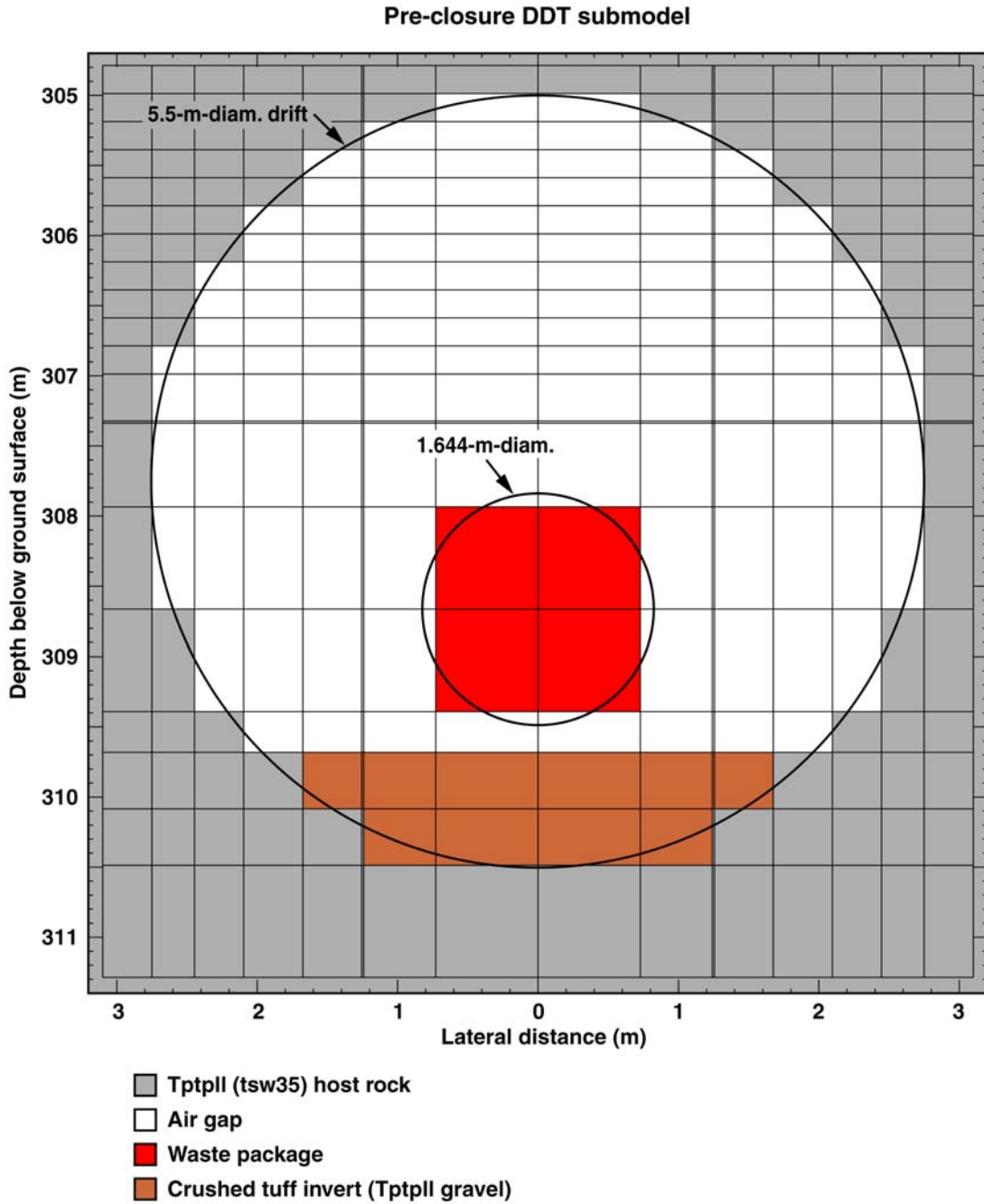
Source: See Table XIII-1.

NOTE: This illustrates just a portion of the mesh. The entire model extends laterally 40.5 m (the mid-pillar centerline) and extends from the ground surface to the water table.

Figure 6.2-7. Cross-Sectional (Lateral) View, Perpendicular to Drift Axis, of the Mesh Used in the Preclosure DDT Submodels
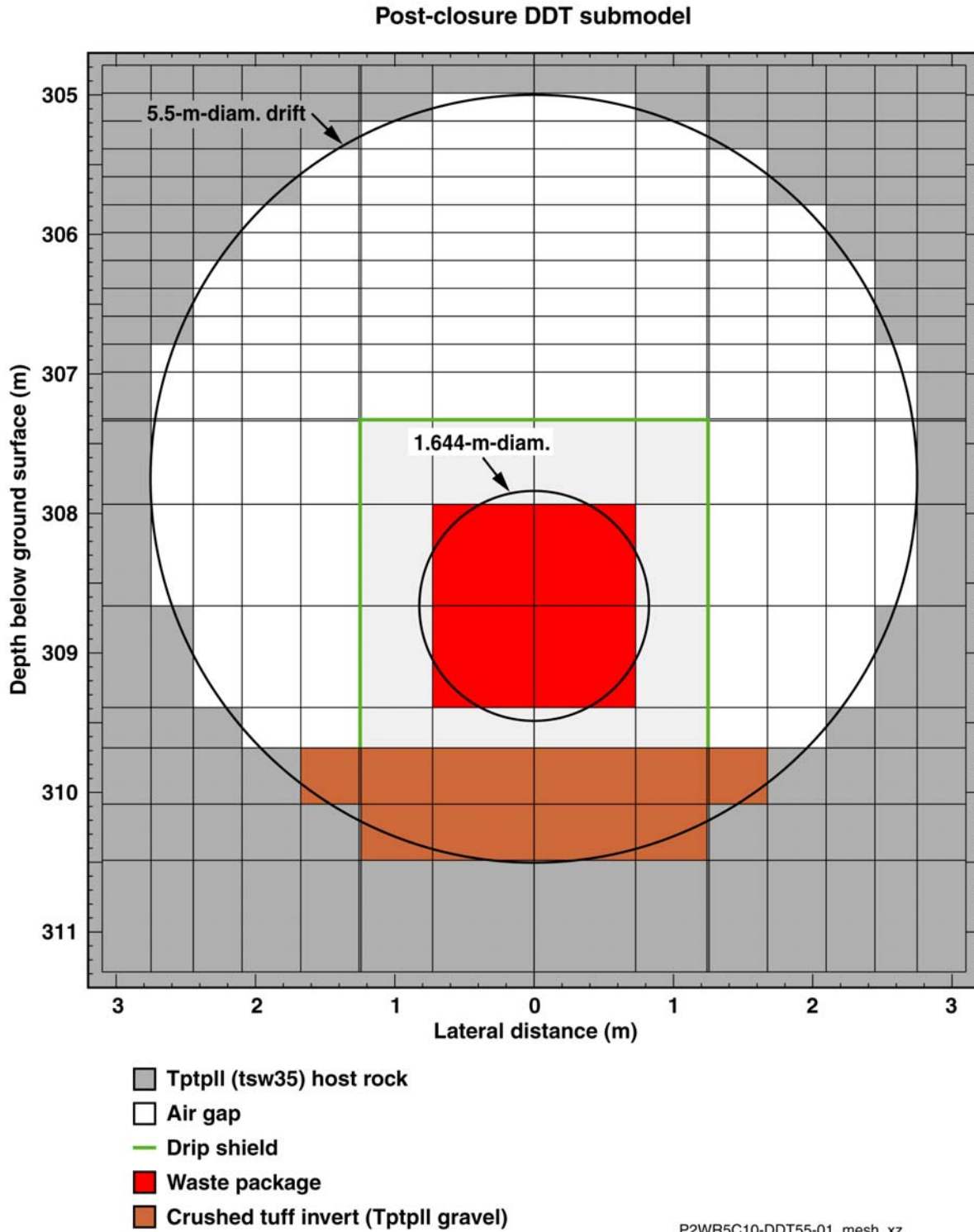
Source: See Table XIII-1.

NOTE: This illustrates just a portion of the mesh. The entire model extends laterally 40.5 m (the mid-pillar
         centerline) and extends from the ground surface to the water table.

Figure 6.2-8. Cross-Sectional (Lateral) View, Perpendicular to Drift Axis, of the Mesh Used in the
               Postclosure DDT Submodels
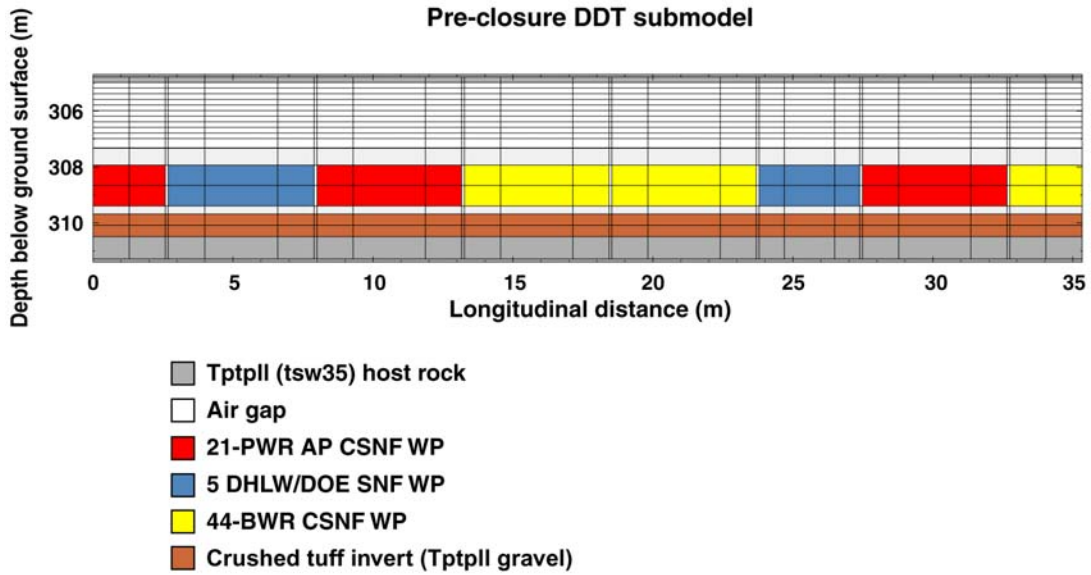
Source: See Table XIII-1.

NOTE: WP = waste package. This illustrates just a portion of the mesh. The entire model extends laterally 40.5 m (the mid-pillar centerline) and extends from the ground surface to the water table.

Figure 6.2-9. Cross-Sectional (Longitudinal) View, Parallel to Drift Axis, of the Mesh Used in the Preclosure DDT Submodels
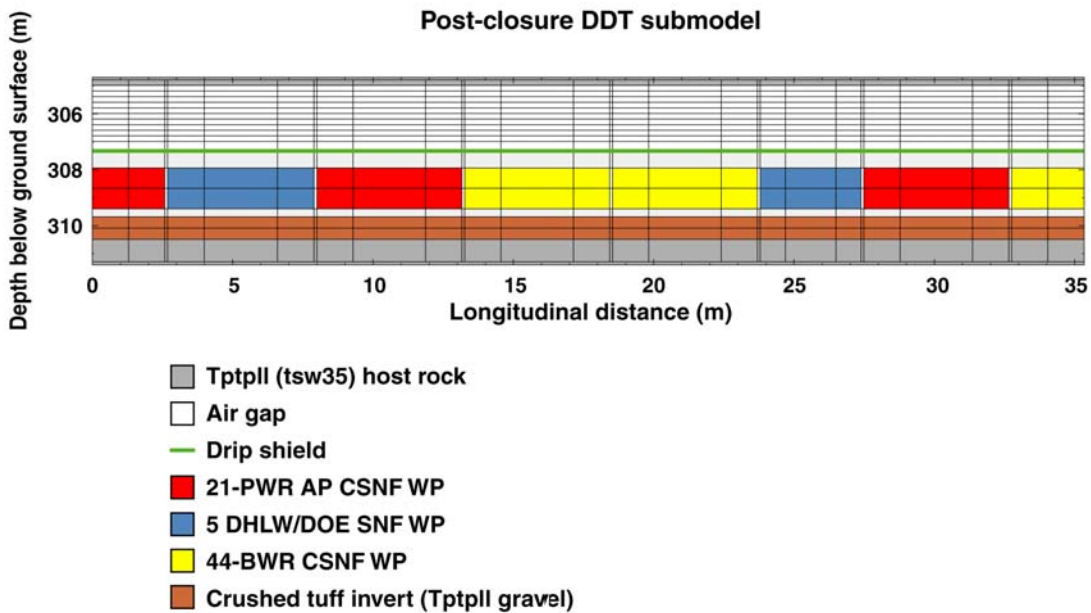
Source: See Table XIII-1.

NOTE: WP = waste package. This illustrates just a portion of the mesh. The entire model extends laterally 40.5 m (the mid-pillar centerline) and extends from the ground surface to the water table.

Figure 6.2-10. Cross-Sectional (Longitudinal) View, Parallel to Drift Axis, of the Mesh used in the Postclosure DDT Submodels

6.2.8.5 DDT Submodel Material Properties

The DDT submodels are implemented with the appropriate stratigraphy, with respect to thermal properties; notably, thermal conductivity and heat capacity. The distribution of the thermal properties are location dependent, consistent with the three-dimensional distribution of UZ model layers in the site-scale UZ flow and transport model (DTN: LB03023DKMGRID.001 [DIRS 162354]), as described in Table 6-5 of *Development of Numerical Grids for UZ Flow and Transport Modeling* (BSC 2004 [DIRS 169855]).

Because the DDT submodel is a thermal-conduction/radiation-only model (i.e., does not represent hydrologic processes), the material properties only involve thermal properties. Material properties are read into the SDT submodel NUFT-input files as "include" files for the natural system thermal properties. The DDT submodel uses the same thermal properties (for the UZ model layers) that are used in the SMT and SDT submodels (Sections 6.2.5.4 and 6.2.7.5). The DDT submodels also use thermal properties of the engineered barrier system components, such as the drip shield, invert, and respective waste packages (Table 4.1-2). The thermal properties of the engineered barrier system components include the emissivity values of the surfaces within the emplacement drifts. The engineered barrier system thermal properties also include the use of an effective thermal conductivity for the air in the drift cavity that is based on a correlation (Francis et al. 2003 [DIRS 164602], Table 6) accounting for the influence of natural convection, which is described in Appendix I. It should be noted that the correlations for the in-drift effective thermal conductivity, which were obtained from Table 6 of Francis et al (2003 [DIRS 164602]), have been updated in *In-Drift Natural Convection and Condensation* (BSC 2004 [DIRS 164327], Table 6.4.7-3), resulting in very small changes to the coefficients. As evident in Figure I-1 of Appendix I, the small changes to the coefficients result in insignificant changes to the in-drift effective thermal conductivity. The material properties of the DDT submodels utilize assumptions described in Section 5.3.2.1. The process of building the DDT submodel material-property file is described in Appendix IV.

6.2.8.6 DDT Submodel Simulations

A single set of DDT submodel simulations (for modeled AMLs of 14, 27, 55, and 66 MTU/acre) was conducted for this report at the P2WR5C10 LDTH–SDT submodel location (Figures 6.2-3 and 6.3-1). This set of DDT submodel simulations is used in all three (lower-bound, mean, and upper-bound) infiltration-flux cases. The process of building the DDT submodel NUFT-input files is described in Appendix V. The NUFT code cannot complete a model simulation unless converged solutions are obtained for all calculational cycles (i.e., timesteps). Thus, numerical convergence is automatically assured in all DDT-submodel simulations.

6.2.9 SMT and SDT Submodels for the Low-Probability-Seismic Collapsed-Drift Scenario

For the low-probability-seismic collapsed-drift scenario, no changes are required for the SMT submodel. Therefore, the description of the SMT submodel (Section 6.2.5) is applicable. For the collapsed-drift scenario, no changes are required for the SDT submodels. Therefore, the description of the SDT submodels (Section 6.2.7) is applicable. The SDT submodel location is the P2WR5C10 LDTH–SDT submodel location (Figures 6.2-3 and 6.3-1). A single set of SDT submodel simulations (for modeled AMLs of 14, 27, 55, and 66 MTU/acre) was utilized.

6.2.10   LDTH Submodels for the Low-Probability-Seismic Collapsed-Drift Scenario

For the low-probability-seismic collapsed-drift scenario, two changes need to be implemented in the LDTH submodels. First, the geometry of the drift is changed to account for the host-rock rubble that fills the drift from the outer surface of the drip shield to the intact host-rock. Second, thermal-hydrologic properties are required for the host-rock rubble. The implementation of these changes is described in the following sections. The boundary conditions, heat-generation rates, and percolation-flux values are the same as those used in the corresponding MSTHM calculations for the intact drift (i.e., nominal) case. Two thermal conductivity K_{th} cases are considered: (1) high- K_{th} host-rock rubble and (2) low- K_{th} host-rock rubble.

6.2.10.1   LDTH Submodel Location

The LDTH submodel location is the P2WR5C10 LDTH–SDT submodel location (Figures 6.2-3 and 6.3-1). Two sets of LDTH submodel simulations (for modeled AMLs of 14, 27, 55, and 66 MTU/acre) are conducted for two different host-rock rubble thermal conductivity cases. This location was selected because it is representative of a typical location in the predominant host-rock unit (Tptpll), close to the center of the repository area, and because the local percolation-flux values (Table 6.3-9) are close to the repository-wide averages for the present-day, monsoonal, and glacial climates (Table 6.3-4).

6.2.10.2   LDTH Submodel Mesh

The low-probability-seismic scenario causes collapse of the drift opening, which is represented by a circular profile with a diameter of 11 m. The resulting host-rock rubble completely fills the modified drift opening, from the outer surface of the drip shield out to the modified "drift wall," as shown in Figures 6.2-11 and 6.2-12 of this report, and in Section 6.4.3.4 of *Abstraction of Drift Seepage* (BSC 2004 [DIRS 169131]). A schematic of the collapsed-drift scenario is also given in Figure 6.4-16 of *Abstraction of Drift Seepage* (BSC 2004 [DIRS 169131]). The cross-sectional (lateral) geometry of the drift for the collapsed drift is represented in the LDTH submodel mesh, which is shown in Figure 6.2-11. Note that the cross-sectional geometries of the drip shield and invert remain the same. Note that this mesh is used for both the preclosure and postclosure periods.

The bulking factor is obtained from the LDTH submodel mesh (Figure 6.2-11) as follows. The bulking factor is a measure of the additional volume that the host-rock rubble occupies (after it collapses into and completely fills the previously open drift cavity) compared to the volume it occupied while it was intact host rock. Thus, the bulking factor is a relative measure of how much "bulkier" the host-rock rubble is (when it falls into and fills the drift cavity) than the original intact host rock that it was derived from. Note that the host-rock rubble also completely fills the volume that the intact host rock originally occupied. The bulking factor is equal to the cross-sectional area of the previously open drift cavity, which is the area of the blue region that lies inside of the dashed line in Figure 6.2-11 (and which is shown in white in Figure 6.2-6), divided by the cross-sectional area of the host-rock rubble zone outside of the original 5.5-m-diameter drift (which is the area of the blue region that lies outside of the dashed line in Figure 6.2-11). On the basis of the LDTH submodel mesh (Figure 6.2-11), the bulking factor is equal to 0.231. Thus, the volume of host-rock rubble zone is 23.1 percent larger than the original volume of the intact host rock from which the rubble was derived.
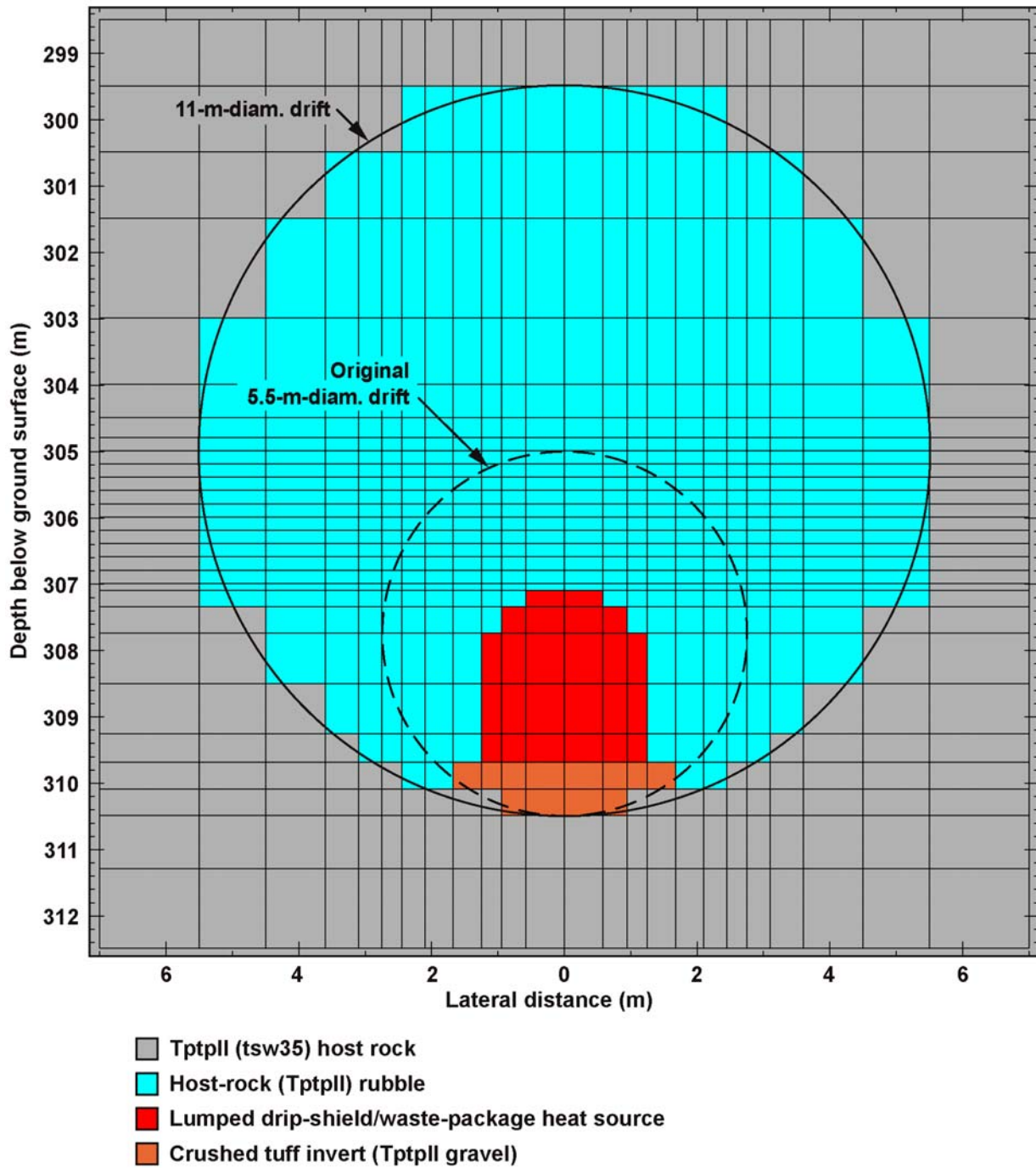
Source: See Table XIII-1.

NOTE: This mesh is used for the preclosure and postclosure periods. The figure illustrates just a portion of the mesh. The entire model extends laterally 40.5 m (the mid-pillar centerline) and extends from the ground surface to the water table.

Figure 6.2-11. Cross-sectional (Lateral) View of the LDTH Submodel Mesh Used for the Low-Probability-Seismic Collapsed-Drift Scenario
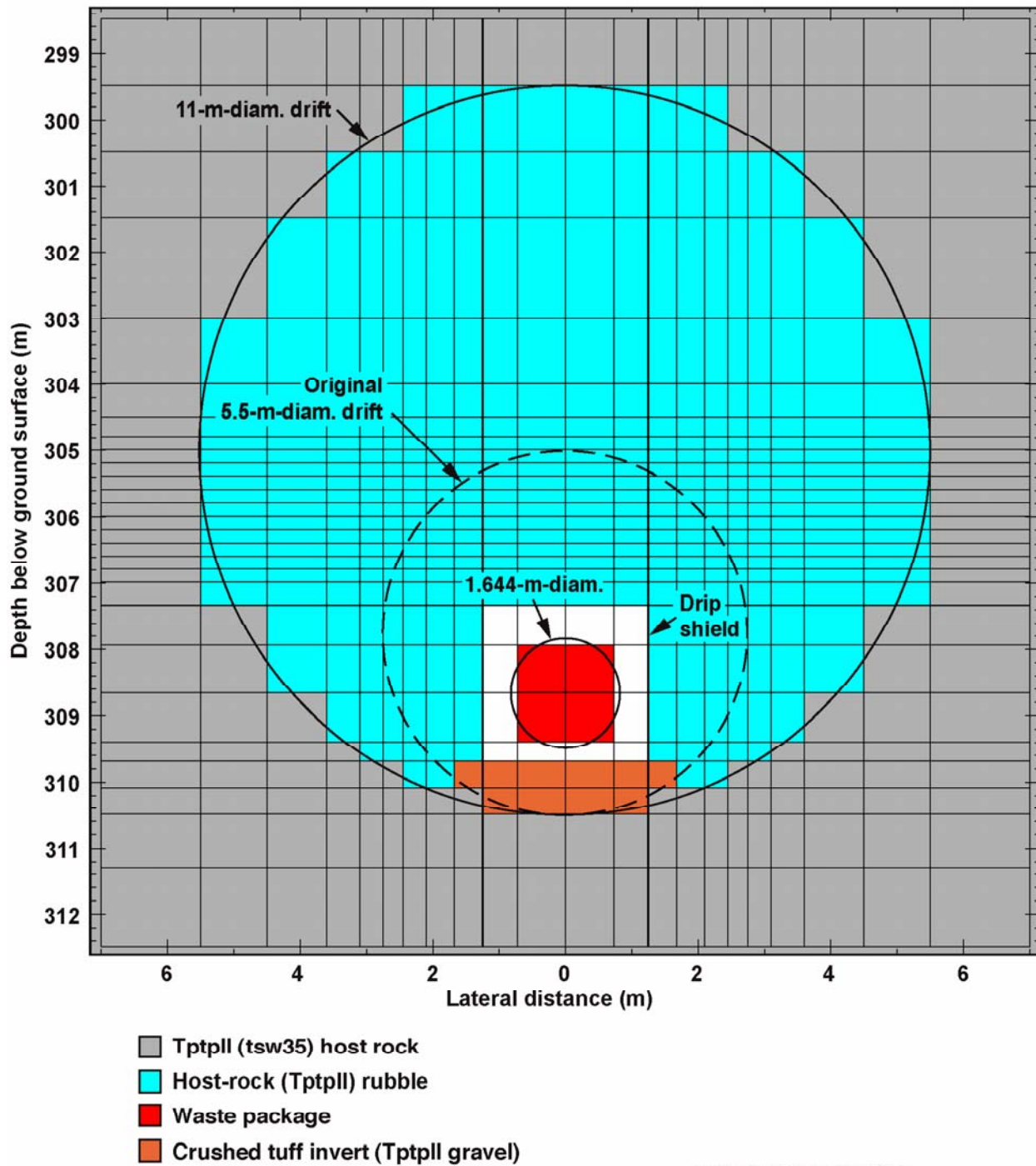
Source: See Table XIII-1.

NOTE: This mesh is used for the preclosure and postclosure periods.

Figure 6.2-12. Cross-Sectional (Lateral) View of the DDT Submodel Mesh Used for the Low-Probability-
Seismic Collapsed-Drift Scenario

6.2.10.3   LDTH Submodel Host-Rock Rubble Thermal-Hydrologic Properties

The thermal-hydrologic properties of the host-rock rubble are derived from those of the Tptpll (tsw35) unit, which is the host-rock unit at the P2WR5C10 LDTH–SDT submodel location (Figures 6.2-3 and 6.3-1). The hydrologic properties of the host-rock rubble are modified from those of the intact host rock (Table 6.2-2) in a manner that is analogous to what is done to the crushed-tuff invert. The only matrix-continuum hydrologic parameters that are modified from the intact host-rock values are the matrix porosity and matrix permeability; these two parameters are reduced to account for the decreased density of the host-rock rubble by multiplying the intact-host-rock values by $1/(1 + BF)$, where BF is the bulking factor. The bulk grain density and bulk thermal conductivity (Table 6.2-3) are also reduced to account for the decreased density of the host-rock rubble by multiplying the intact-host-rock values by $1/(1 + BF)$. This value of bulk thermal conductivity K_{th} is applied to the high-K_{th} case because it implicitly incorporates parallel thermal conductors (versus series thermal conductors). Thus, the solid portion of the host-rock rubble is effectively lined up in parallel with the void portion of the rubble.

The low-K_{th} case is intended to account for the thermal-contact resistance between blocks of the rubble. Because the thermal conductivity of the solid portion of the rubble is much greater than that of the air-filled voids, the vast majority of thermal conduction occurs in the solid portion. The geometry of the rubble causes a "bottle-necking" effect at the point where the rock blocks contact each other. The values of K_{th} for the low-K_{th} case are half of those of the high-K_{th} case to account for thermal-contact resistance at the bottlenecks. Thermal radiative heat transfer also contributes to heat transfer within the air-filled voids. The relative contribution of radiative heat transfer depends on the size of the rock blocks and voids, with larger voids facilitating more efficient thermal-radiative heat transfer than smaller voids. For large block (and void) sizes, thermal-radiative heat transfer will mitigate the influence of the bottlenecking effect, which will make the high-K_{th} case applicable. For small block (and void) sizes, the low-K_{th} case will be applicable. Neither the high-K_{th} case nor low-K_{th} case is more or less likely to be the appropriate value to be applied for effective thermal conductivity of the host-rock rubble. As a result of this argument, each alternative, the high- and low-K_{th} cases, can be assigned the same probability (of 50 percent).

Table 6.2-2. Hydrologic Property Values for the "Intact" Tptpll (tsw35) Host-Rock Unit and for the Host-Rock Rubble Derived from the Tptpll (tsw35) Unit.

Property	Intact Host-Rock Property Value	Host-Rock Rubble Property Value	Basis for Rubble Property Value
Matrix porosity	0.131	0.1065	Intact Value $\times$ 1/(1 + BF)
Fracture porosity	9.6×10^{-3}	0.187	1 − 1/(1 + BF)
Matrix permeability	$4.48 \times 10^{-18}\,m^2$	$3.6393 \times 10^{-18}\,m^2$	Intact Value $\times$ 1/(1 + BF)
Fracture permeability	$9.10 \times 10^{-13}\,m^2$	$1.0 \times 10^{-10}\,m^2$	Assumption 7 of Section 5 of BSC 2004 [DIRS 170338]
Fracture van Genuchten alpha	$1.02 \times 10^{-4}\,Pa^{-1}$	$0.01\,Pa^{-1}$	Assumption 6 of Section 5 of BSC 2004 [DIRS 170338]

NOTES: Intact host-rock property values for the Tptpll (tsw35) unit are obtained from Table IV-4 and IV-5 in Appendix IV.

The only property values listed are those for which the intact and rubble values differ. All other property values for the intact host rock and host-rock rubble are the same.

Table 6.2-3. Thermal Property Values for the "Intact" Tptpll (tsw35) Host-Rock Unit and for the Host-Rock Rubble Derived from the Tptpll (tsw35) Unit

Property	Intact Host-Rock Property Value	Host-Rock Rubble Property Value	Basis for Rubble Property Value
Bulk density	1980 kg/m[a]	1850.0 kg/m[a]	Assumption, Section 5.8.1
Bulk density of matrix continuum	Not used or determined	1831.5 kg/m[a]	99 percent of bulk rubble value
Bulk density of fracture continuum	Not used or determined	18.5 kg/m[a]	1 percent of bulk rubble value
Grain density of matrix continuum	2258.11 kg/m[a]	2049.8 kg/m[a]	Bulk matrix density/$(1 - \phi_m)$, where $\phi_m = 0.1065$ (Table 6.2-2)
Grain density of fracture continuum	21.89 kg/m[a]	22.76 kg/m[a]	Bulk fracture density/$(1 - \phi_f)$, where $\phi_f = 0.187$ (Table 6.2-2)
Bulk dry thermal conductivity	1.28 W/m-K	1.0 W/m-K (High-K_{th} case)[b] 0.5 W/m-K (Low-K_{th} case)	Intact Value $\times$ 1/(1 + BF) (High-K_{th} rubble value)/2
Bulk wet thermal conductivity	1.89 W/m-K	1.515 W/m-K (High-K_{th} case)[a] 0.7575 W/m-K (Low-K_{th} case)	Intact Value $\times$ 1/(1 + BF) (High-K_{th} rubble value)/2
Dry thermal conductivity of matrix continuum	1.268 W/m-K	0.99 W/m-K (High-K_{th} case) 0.495 W/m-K (Low-K_{th} case)	99 percent of bulk rubble value
Dry thermal conductivity of fracture continuum	1.23×10^{-2} W/m-K	0.01 W/m-K (High-K_{th} case) 0.005 W/m-K (Low-K_{th} case)	1 percent of bulk rubble value
Wet thermal conductivity of matrix continuum	1.872 W/m-K	1.5 W/m-K (High-K_{th} case) 0.75 W/m-K (Low-K_{th} case)	99 percent of bulk rubble value
Wet thermal conductivity of fracture continuum	1.81×10^{-2} W/m-K	0.015 W/m-K (High-K_{th} case) 0.0075 W/m-K (Low-K_{th} case)	1 percent of bulk rubble value
Bulk density	1980.0 kg/m[a]	1608.0 kg/m[a] (sensitivity case: Figure 6.3-58)	Intact Value $\times$ 1/(1 + BF)
Bulk density of matrix continuum	Not used or determined	1591.9 kg/m[a] (sensitivity case: Figure 6.3-58)	99 percent of bulk rubble value
Bulk density of fracture continuum	Not used or determined	16.1 kg/m[a] (sensitivity case: Figure 6.3-58)	1 percent of bulk rubble value
Grain density of matrix continuum	2258.11 kg/m[a]	1781.6 kg/m[a] (sensitivity case: Figure 6.3-58)	Bulk matrix density/$(1 - \phi_m)$, where $\phi_m = 0.1065$ (Table 6.2-2)
Grain density of fracture continuum	21.89 kg/m[a]	19.8 kg/m[a] (sensitivity case: Figure 6.3-58)	Bulk fracture density/$(1 - \phi_f)$, where $\phi_f = 0.187$ (Table 6.2-2)

[a] Value is close to, but slightly less than, the value obtained from the Intact Value $\times$ 1/(1 + BF), in order to be consistent with the slight reduction made to the dry K_{th} value, which was rounded down.
[b] This value is rounded down slightly.

NOTE: Intact host-rock property values are obtained from Table IV-3b in Appendix IV. The only property values listed are those for which the intact and rubble values differ. All other property values for the intact host rock and host-rock rubble are the same. Note that ϕ_m and ϕ_f are matrix-continuum and fracture-continuum porosity, respectively.

Appendix XI corroborates estimates of the effective dry bulk thermal conductivity of the host-rock rubble in the collapsed drift on the basis of the Kunii and Smith relationship (Kunii and Smith 1960 [DIRS 153166], Equation 8). On the basis of that assessment, a mean value of 0.81 W/m°C is determined for the dry bulk thermal conductivity, with a range of 0.57 to 1.05 W/m°C. The low end of this range (0.57 W/m°C) is very close to the dry bulk thermal conductivity value of 0.5 W/m°C used in low- K_{th} case. The high end of this range

(1.05 W/m°C) is very close to the dry bulk thermal conductivity value of 1.0 W/m°C used in the high- K_{th} case.

The fracture-continuum porosity of the rubble does not include the small contribution of the fracture porosity, which is 9.6×10^{-3} for the Tptpll (tsw35) unit (Table IV-4 of Appendix IV), that was present in the intact rock (prior to its collapse into the drift). The fracture-continuum permeability and van Genuchten alpha parameter are taken from assumptions 6 and 7 of Section 5 of *Drift-Scale Coupled Processes (DST and TH Seepage) Models* (BSC 2004 [DIRS 170338]). The fracture-continuum permeability is 10^{-10} m^2 (about two orders of magnitude larger than that of the intact Tptpll host rock). The fracture-continuum van Genuchten alpha is 0.01 Pa^{-1}. The bulk density and bulk thermal conductivity of the host-rock rubble are partitioned between the fracture and matrix continuum in the exactly same fashion, and for the same reasons, as is done for the crushed-tuff invert material (see Appendix IV). Thus, 99 percent of the bulk density and bulk thermal conductivity are partitioned to the matrix continuum and 1 percent is partitioned to the fracture continuum. This partitioning is done because the majority of the thermal mass in the rubble resides in the matrix continuum.

6.2.11   DDT Submodels for the Low-Probability-Seismic Collapsed-Drift Scenario

For the collapsed-drift scenario, two changes need to be implemented in the DDT submodels. First, the geometry of the drift is changed to account for the host-rock rubble that fills the drift from the outer surface of the drip shield to the intact host-rock. Second, thermal properties are required for the host-rock rubble. The implementation of these changes is described in the following sections. The boundary conditions and heat-generation rates are the same as those used in the corresponding MSTHM calculations for the intact drift (i.e., nominal) case. Two thermal conductivity K_{th} cases are considered: (1) high-K_{th} host-rock rubble and (2) low-K_{th} host-rock rubble.

6.2.11.1   DDT Submodel Location

The DDT submodel location is the P2WR5C10 LDTH–SDT submodel location (Figures 6.2-3 and 6.3-1). Two sets of LDTH submodel simulations (for modeled AMLs of 14, 27, 55, and 66 MTU/acre) are conducted for two different host-rock rubble thermal conductivity cases.

6.2.11.2   DDT Submodel Mesh

The low-probability-seismic scenario causes collapse of the drift opening, which is represented by a circular profile with a diameter of 11 m (see Section 6.2.10.2). The resulting host-rock rubble completely fills the modified drift opening, from the outer surface of the drip shield out to the modified "drift wall," which now has a diameter of 11 m. The cross-sectional (lateral) geometry of the drift for the collapsed drift is represented in the DDT submodel mesh as is shown in Figure 6.2-12. Note that the cross-sectional geometries of the drip shield, waste package, and invert remain the same.

6.2.11.3   DDT Submodel Host-Rock Rubble Thermal Properties

The thermal properties of the host-rock rubble (Table 6.2-4) are derived from those of the Tptpll (tsw35) unit, which is the host-rock unit at the P2WR5C10 LDTH–SDT submodel location

(Figures 6.2-3 and 6.3-1). Just as is done for the LDTH submodels, the bulk grain density and bulk thermal conductivity are reduced to account for the decreased density of the host-rock rubble by multiplying the intact-host-rock values by $1/(1 + BF)$. The DDT submodels use the same bulk grain density as is used in the LDTH submodels for the high-K_{th} and low-K_{th} host-rock rubble cases. For thermal conductivity, the DDT submodels use the bulk dry thermal conductivity that is used in the LDTH submodels for the high-K_{th} and low-K_{th} host-rock rubble cases, respectively. The dry value of bulk thermal conductivity is used because the DDT submodels are primarily used to predict longitudinal variability in temperature along the axis of the drift. The longitudinal variability is greatest when peak temperatures occur, which is when the majority of the rubble is dry as a result of boiling. Much of the rubble remains relatively dry throughout the majority of the simulation period of 20,050 years; therefore, the dry value of thermal conductivity for the rubble is a reasonable choice.

Table 6.2-4. Thermal Property Values for the "Intact" Tptpll (tsw35) Host-Rock Unit and for the Host-Rock Rubble Derived from the Tptpll (tsw35) Unit.

Property	Intact Host-Rock Property Value	Host-Rock Rubble Property Value	Basis for Rubble Property Value
Bulk density	1980 kg/m^3	1608 kg/m^3	Intact Value $\times$ 1/(1 + BF)
Bulk grain density	2280 kg/m^3	1850 kg/m^3	Bulk density/(1 − ϕ_m), where ϕ_m = 0.131[a]
Bulk dry thermal conductivity	1.28 W/m-K	1.0 W/m-K (High-K_{th} case) 0.5 W/m-K (Low-K_{th} case)	Intact Value $\times$ 1/(1 + BF) (High-K_{th} rubble value)/2

[a] A porosity value of 0.131 only affects the relationship between bulk density and bulk grain density applied to the DDT submodel. It has no other influence on the DDT submodel.

NOTE: Intact host-rock property values are obtained from Table IV-3b in Appendix IV. The only property values listed are those for which the intact and rubble values differ. All other property values for the intact host rock and host-rock rubble are the same.

6.3   MSTHM RESULTS

6.3.1   TSPA-LA Base Case

This section discusses the MSTHM calculations that were conducted for the TSPA-LA base case. As was done for the Total System Performance Assessment for the Site Recommendation (called the TSPA-SR), the base case consists of three infiltration-flux cases: lower-bound, mean, and upper-bound infiltration-flux cases for three climate states: present-day, monsoonal, and glacial-transition. Past MSTHM calculations directly used the infiltration maps for these three cases with the underlying assumption being that there is no lateral attenuation of infiltration in the PTn unit (or in any other unit above the repository); thus, percolation above the repository occurs strictly as one-dimensional vertical downward flow. For the TSPA-LA base case, the upper-boundary liquid-phase flux in the MSTHM corresponds to the distribution of percolation flux just below the base of the PTn unit; these data (Table 4.1-1) are generated for the three climate states: present-day, monsoonal, and glacial-transition. Thus, the TSPA-LA base-case MSTHM accounts for the influence of lateral diversion in the PTn as represented in the three-dimensional UZ flow model.

Previous MSTHM calculations (such as those in support of the TSPA-SR) used different hydrologic property sets for each of the infiltration-flux cases; thus, lower-bound, mean, and

upper-bound one-dimensional drift-scale hydrologic property sets were applied to their respective infiltration-flux cases. For this study it was found that only one hydrologic property set (called the modified-mean infiltration-flux property set) is needed for conducting MSTHM calculations for the three infiltration-flux cases. *Abstraction of Drift Seepage* (BSC 2004 [DIRS 169131], Section 6.6.4) addresses the van Genuchten fracture alpha and permeability distributions for the Tptpul (tsw33) and Tptpln (tsw36) units. It is recommended by this reference that the same alpha and permeability distributions be used in the Tptpul (tsw33) unit as was derived for the Tptpll (tsw35) unit. The modified-mean infiltration-flux property set is the same as the mean infiltration-flux property set (DTN: LB0208UZDSCPMI.002 [DIRS 161243]) with the one modification being that the van Genuchten fracture alpha in the Tptpul (tsw33) is set to be the same (1.021×10^{-4} Pa^{-1}) as that in the Tptpll (tsw35) unit (see Table IV-4, Appendix IV). This is consistent with the recommendation made in *Abstraction of Drift Seepage* (BSC 2004 [DIRS 169131], Section 6.6.4). As discussed below, this one modification also produces a consistent contrast in capillary pressure between the matrix and fracture continuum for all four host-rock units.

For this study, it was found that the application of the modified-mean infiltration-flux property set to lower-bound, mean, and upper-bound infiltration-flux cases produces uniform calculated host-rock liquid-phase saturation for the three infiltration-flux cases. It was also found that host-rock liquid-phase saturation consistently increases (slightly) with increasing percolation flux. The purpose for conducting lower-bound, mean, and upper-bound infiltration-flux cases with the MSTHM is to address the influence of percolation-flux uncertainty on thermal-hydrologic conditions within emplacement drifts and in the adjoining host rock. In conducting a sensitivity study to a particular parameter (in this case, percolation flux), it is preferred to vary only one parameter at a time. Table 6.3-1 lists the initial (ambient) liquid-phase saturation in the host rock (immediately above the crown of the emplacement drift) for lower-bound, mean, and upper-bound infiltration-flux cases when the modified-mean drift-scale hydrologic property set is applied to the MSTHM. Table 6.3-1 shows that the use of the modified-mean infiltration-flux property set results in similar initial liquid-phase saturation at a given location for lower-bound, mean, and upper-bound infiltration-flux cases.

Table 6.3-2 lists the initial (ambient) capillary pressure in the fracture and matrix continuum of the host rock for the same locations given in Table 6.3-1. The mean infiltration-flux property set produces very small values of capillary pressures in the fracture continuum for locations where the host rock is the Tptpul (tsw33) unit; these small values of fracture capillary pressure are much smaller than they are for regions of the repository where the host rock is not the Tptpul (tsw33) unit (i.e., where the local host-rock unit is either Tptpmn (tsw34), Tptpll (tsw35), or Tptpln (tsw36)). Moreover, the mean infiltration-flux property set produces a large (order of magnitude) contrast in capillary pressure between the matrix and fracture continuum in the Tptpul (tsw33) unit, whereas the contrast in capillary pressure is much smaller for the other three host-rock units: Tptpmn, Tptpll, and Tptpln. The modified-mean infiltration-flux property set produces fracture capillary pressures in the Tptpul unit that are consistent with those in the rest of the repository (i.e., in regions where the host rock is either Tptpmn, Tptpll, or Tptpln). Moreover, for all four host-rock units, the modified-mean infiltration-flux property set produces a consistent contrast in capillary pressure between the matrix and fracture continuum, which is generally on the order of a factor of two throughout most of the repository area, with the only exception being in the Tptpln unit where the contrast is larger (about a factor of six).

Table 6.3-3 and Figure 6.3-1 show the distribution of host-rock units over the repository area. The majority of the repository area (81.1 percent) is in the two units (Tptpll and Tptpul) with lithophysal cavities. Most of the remainder of the repository area (where waste is to be emplaced) is in the nonlithophysal units (Tptpmn and Tptpln) with a small percentage (1.6 percent) being in fault zones. These areas are based on *Development of Numerical Grids for UZ Flow and Transport Modeling* (BSC 2004 [DIRS 169855]).

Table 6.3-1. Initial Liquid-Phase Saturation in the Host Rock at Several Locations in the Repository for Three Infiltration-Flux Cases

LDTH–SDT submodel location	Host-Rock unit	Nevada State Coordinates		Initial Liquid-Phase Saturation in the Host Rock (%)		
		Easting (m)	Northing (m)	Lower-Bound Infiltration-Flux Case	Mean Infiltration-Flux Case	Upper-Bound Infiltration-Flux Case
P2ER4C4	Tptpul (tsw33)	172138.9	235625.9	96.4	96.4	96.9
P2ER5C5	Tptpul (tsw33)	171985.7	235320.6	95.5	95.6	95.8
P2ER6C6	Tptpul (tsw33)	171623.3	234947.4	95.4	95.5	95.7
P2ER8C7	Tptpul (tsw33)	171393.1	234361.5	94.0	97.2	97.3
P2ER8C6	Tptpul (tsw33)	171564.3	234417.2	90.5	95.6	95.7
P2ER8C5	Tptpul (tsw33)	171735.5	234472.8	93.6	97.4	97.3[a]
P2ER7C6	Tptpul (tsw33)	171584.3	234679.2	93.0	96.5	96.3[a]
P2ER7C5	Tptpul (tsw33)	171793.5	234747.2	95.1	95.2	95.3
P2ER6C5	Tptpul (tsw33)	171851.6	235021.5	93.6	95.5	95.6
P2ER3C4	Tptpmn (tsw34)	172292.1	235931.1	97.5	97.8	98.0
P2ER2C5	Tptpll (tsw35)	172121.9	236131.4	92.0	92.0	92.1
P2WR1C8	Tptpll (tsw35)	171647.4	236232.7	94.0	94.0	94.1
P3R1C11	Tptpll (tsw35)	171038.7	236034.9	94.6	94.6	94.7
P3R8C13	Tptpln (tsw36)	170080.6	233935.1	98.6	98.7	98.7

Source: See Table XIII-2.

[a] The value of percolation flux for the upper-bound infiltration-flux case is less than that for the mean infiltration-flux case at this particular location.

NOTE: The initial (ambient) liquid-phase saturation in the host rock (prior to waste emplacement) is obtained by applying the modified-mean infiltration-flux property set to the MSTHM.

Table 6.3-2. Initial Capillary Pressure for the Fracture and Matrix Continuum in the Host Rock

LDTH–SDT submodel location	Host-Rock Unit	Fracture capillary pressure (Pa)		Matrix capillary pressure (Pa)	
		Mean Infiltration-Flux Property Set	Modified-Mean Infiltration-Flux Property Set	Mean Infiltration-Flux Property Set	Modified-Mean Infiltration-Flux Property set
P2ER4C4	Tptpul (tsw33)	1.46×10^3	2.28×10^4	3.23×10^4	4.27×10^4
P2ER5C5	Tptpul (tsw33)	1.46×10^3	2.28×10^4	4.51×10^4	5.06×10^4
P2ER6C6	Tptpul (tsw33)	1.46×10^3	2.27×10^4	4.38×10^4	5.18×10^4
P2ER8C7	Tptpul (tsw33)	1.45×10^3	2.27×10^4	2.03×10^4	3.50×10^4
P2ER8C6	Tptpul (tsw33)	1.45×10^3	2.26×10^4	4.51×10^4	5.09×10^4
P2ER8C5	Tptpul (tsw33)	1.47×10^3	2.29×10^4	3.14×10^4	3.34×10^4
P2ER7C6	Tptpul (tsw33)	1.43×10^3	2.22×10^4	3.46×10^4	4.25×10^4
P2ER7C5	Tptpul (tsw33)	1.46×10^3	2.28×10^4	5.34×10^4	5.43×10^4
P2ER6C5	Tptpul (tsw33)	1.47×10^3	2.30×10^4	4.55×10^4	5.13×10^4
P2ER3C4	Tptpmn (tsw34)	2.22×10^4	2.22×10^4	2.32×10^4	2.32×10^4
P2ER2C5	Tptpll (tsw35)	2.40×10^4	2.40×10^4	5.78×10^4	5.78×10^4
P2WR1C8	Tptpll (tsw35)	2.44×10^4	2.44×10^4	4.37×10^4	4.37×10^4
P3R1C11	Tptpll (tsw35)	2.44×10^4	2.44×10^4	3.95×10^4	3.95×10^4
P3R8C13	Tptpln (tsw36)	3.32×10^3	3.32×10^3	1.94×10^4	1.94×10^4

Source: See Table XIII-2.

NOTE: The initial (ambient) capillary pressure for the fracture and matrix continuum in the host rock (prior to waste emplacement) is obtained by applying the mean and the modified-mean infiltration-flux property set to the MSTHM. Note that values are listed for the same locations given in Table 6.3-1.

Table 6.3-3. Distribution of the Host-Rock Units as Represented in SMT Submodel for the Emplaced Repository Area (Figure 6.3-1)

GFM2000 Lithostratigraphic Unit	UZ Model Layer Unit	Length of Emplacement Drift (m)	Area (km^2)	Percentage of Repository Area
Tptpul	tsw33	3,460	0.2803	6.0%
Tptpmn	tsw34	9,260	0.7501	16.1%
Tptpll	tsw35	43,160	3.4960	75.1%
Tptpln	tsw36	660	0.0535	1.2%
Fault zone	tswfl	940	0.0761	1.6%
Total	N/A	57,480	4.6559	100%

NOTE: The values of emplacement-drift length and area are as they are represented in the SMT submodel (Section 6.2.5). In the SMT submodel, the represented lengths of the emplacement drifts are based on information from BSC 2003 [DIRS 161727]; the distribution of host-rock units (with respect to the UZ model layers) is consistent with the grid in DTN: LB03023DKMGRID.001 [DIRS 162354].
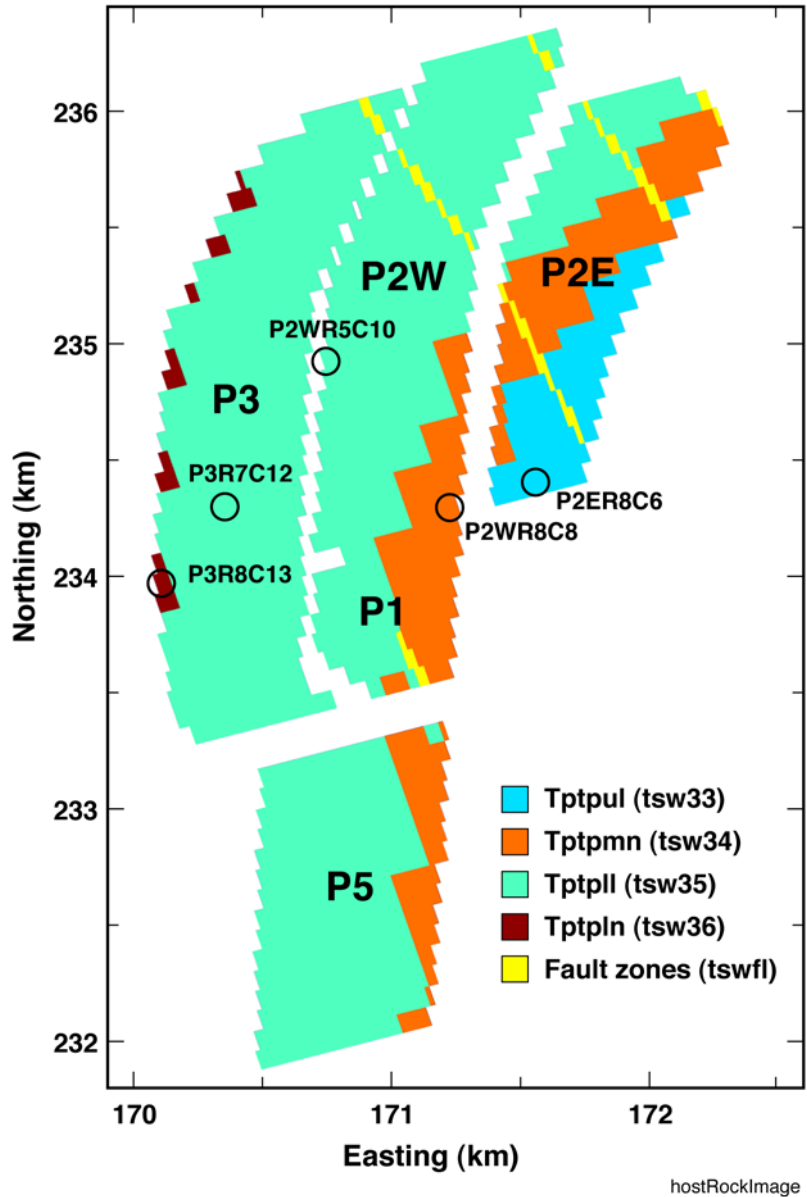
Source: See Table XIII-1.

NOTE: Note that tswfl stands for fault zone. Also shown are the five representative locations that were selected to examine thermal-hydrologic conditions in the four primary host-rock units.

Figure 6.3-1. Distribution of the Four Primary Host-Rock Units Shown for the Repository Layout Considered in MSTHM Calculations for the TSPA-LA Base Case

6.3.1.1   Lower-Bound, Mean, and Upper-Bound Infiltration-Flux Cases

The repository-wide averaged percolation flux for the three climate states (present-day, monsoonal, and glacial-transition) is summarized in Table 6.3-4 for the lower-bound, mean, and upper-bound infiltration-flux cases. Table 6.3-5 summarizes the range of percolation flux for the present-day climate for the lower-bound, mean, and upper-bound infiltration-flux cases. Figure 6.3-2 gives the complementary cumulative distribution function for the peak temperature on the drift wall and on waste packages; these complementary cumulative distribution functions

are for all waste packages over the entire repository area. Table 6.3-6 gives the coolest, median, and hottest peak drift-wall and waste package temperatures for the three infiltration-flux cases. The spatial extent and duration of dryout of the host rock increase with decreasing percolation flux. Because the thermal conductivity of dry rock is less than that of wet rock, peak temperatures increase with decreasing percolation flux. The sensitivity of peak temperature to percolation flux is strongest at either end of the complementary cumulative distribution function distributions. The differences between the mean and lower-bound infiltration-flux cases are greatest for the hottest waste package locations. The differences between the mean and upper-bound infiltration-flux cases are greatest for the coolest waste package locations. In general, the sensitivity of peak temperature to percolation flux is stronger for the hottest waste package locations.

Table 6.3-4. Repository-Wide Averaged Percolation Flux Summarized for Lower-Bound, Mean, and Upper-Bound Infiltration-Flux Cases

Infiltration-Flux Case	Repository-Wide Averaged Percolation Flux (mm/yr)		
	Present-Day (0 years $< t <$ 600 years)	Monsoonal (600 years $< t <$ 2,000 years)	Glacial-Transition (2,000 years $< t$)
Lower	0.41	4.23	1.95
Mean	3.77	11.15	17.29
Upper	10.84	19.48	34.35

NOTE: These averages are based on averaging the percolation data from DTN: LB0302PTNTSW9I.001 [DIRS 162277] over the heated repository footprint represented in the SMT submodel, as described in Appendix I.

Table 6.3-5. Range of Percolation Fluxes for the MSTHM for the Lower-Bound, Mean, and Upper-Bound Infiltration-Flux Cases for the Present-Day Climate

	Percolation flux (mm/yr)		
	Lower infiltration-flux case	Mean infiltration-flux case	Upper infiltration-flux case
Lowest value	2.8×10^{-5}	0.24	1.12
Mean value	0.41	3.77	10.84
Highest value	2.20	13.74	36.18

DTN: LL030808623122.036.

Table 6.3-6. Peak Drift-Wall and Waste Package Temperatures for Lower-Bound, Mean, and Upper-Bound Infiltration-Flux Cases

Infiltration-Flux Case	Peak Drift-Wall Temperature (°C)			Peak Waste Package Temperature (°C)		
	Coolest	Median	Hottest	Coolest	Median	Hottest
Lower	105.7	135.4	154.8	116.3	156.0	182.9
Mean	105.0	133.0	144.2	115.6	153.3	172.0
Upper	98.6	131.6	142.5	108.6	152.1	170.8

NOTE: These values are based on Figure 6.3-2.

CCDF-Tpeak-dw-wp_li_mi_ui
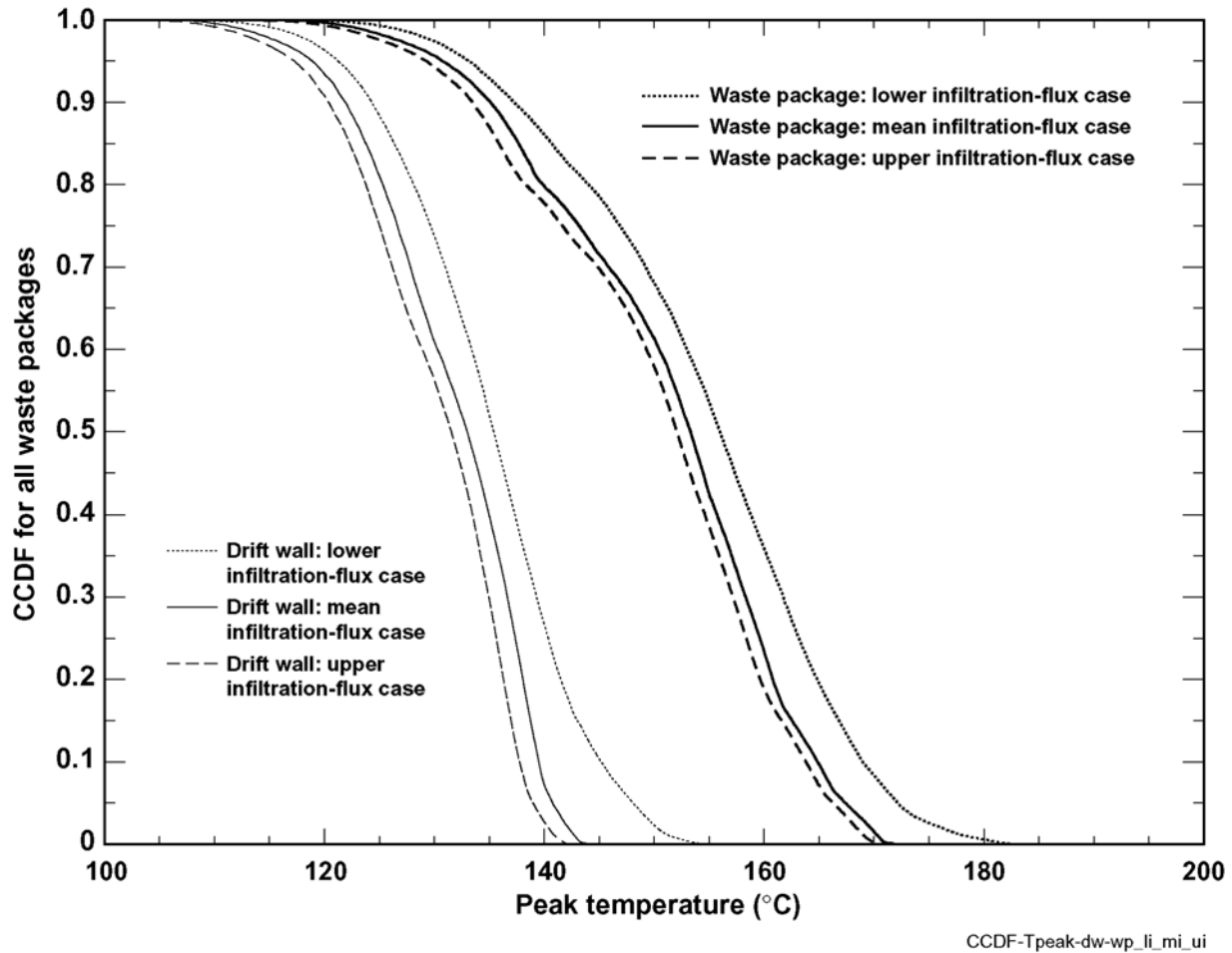
Source: See Table XIII-1.

NOTE: CCDF is plotted for lower-bound, mean, and upper-bound infiltration-flux cases.

Figure 6.3-2. Complementary Cumulative Distribution Function (CCDF) for Peak Temperature on the Drift Wall and Waste Packages

Figure 6.3-3, which is the contour map of peak waste package temperature for PWR waste packages, illustrates how peak temperatures increase with distance from the repository edges. There are two reasons for this relationship. First, the edge-cooling effect, which results from lateral heat loss at the repository edges, is strongest for locations close to the edge of the repository. Second, the direction of the ventilation-air flow is from the ventilation inlets located at the repository edges in towards the ventilation outlets, which are generally located close to the center of the repository. Table III-1 of Appendix III, which lists the net available heat-generation fraction as a function of time and distance from the ventilation inlet (DTN: MO0304MWDALACV.000 [DIRS 164551]), shows that heat-removal efficiency (resulting from ventilation of emplacement drifts) decreases with distance from the ventilation inlet. Thus, locations closer to the repository edge receive more of the ventilation cooling effect than locations closer to the repository center. One slight variation of this trend is in Panel 5 where the ventilation inlet is on the eastern edge and the ventilation outlet is on the western edge. Figure 6.3-3 shows that peak temperatures on the eastern side of Panel 5 (where the heat-removal efficiency is greatest) are slightly lower than on the western side (where the heat-removal efficiency is least).
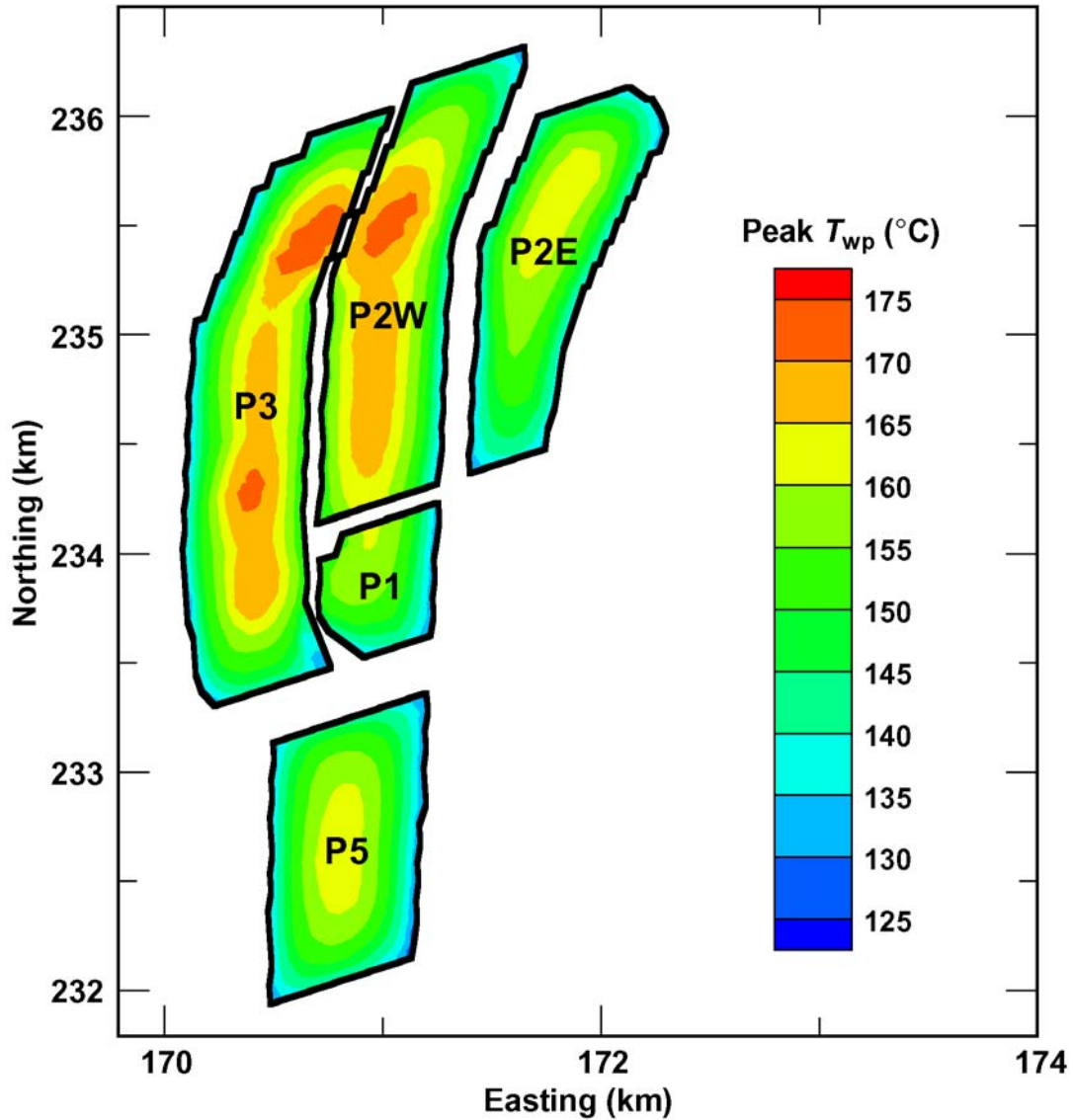
Source: See Table XIII-1.

NOTE: This contour map is plotted over the repository area for the mean infiltration-flux case. The pwr1-2 (21-PWR AP CSNF) waste package is the hottest package in the sequence (Table 6.3-13).

Figure 6.3-3. Contour Map of Peak Waste Package Temperature for the pwr1-2 Waste Package

Figure 6.3-4a and Table 6.3-7 give the complementary cumulative distribution function for the time when boiling at the drift wall ceases for lower-bound, mean, and upper-bound infiltration-flux cases; these complementary cumulative distribution functions are for all waste package locations throughout the repository area. Note that at the repository horizon, which ranges in elevation ranging from about 1038 to 1092 m, the boiling temperature is approximately 96°C. The boiling-period duration is a useful thermal-hydrologic parameter because seepage into the drift is predicted not to occur during this period in Section 6.3.2 of *Abstraction of Drift Seepage* (BSC 2004 [DIRS 169131]). As was the case for peak temperatures, the boiling-period duration increases with decreasing percolation flux. Figure 6.3-5, which is a contour map of the time when boiling at the drift wall ceases for a PWR CSNF waste package for the mean infiltration-flux case, clearly shows that the boiling-period duration increases strongly with distance from the repository edges. The sensitivity of boiling-period duration to percolation flux is greatest for those locations with the longest boiling-period duration, which correspond to locations furthest away from the repository edges where differences in the spatial (and temporal) extent of rock dryout (resulting from differences in percolation flux) have more time to develop. There is a strong relationship between boiling-period duration and the spatial (and temporal) extent of rock dryout. Areas with low percolation flux will have a greater spatial extent of dryout, increasing the volume of rock in which the dry (low) value of thermal conductivity pertains, which enhances the temperature rise around the drifts. The enhanced temperature rise around the drift has the effect of extending the duration of boiling. Areas with high percolation flux will have a smaller spatial (and temporal) extent of rock dryout, decreasing the volume of rock in which the dry (low) value of thermal conductivity pertains, which reduces the temperature rise around the drifts. This reduced temperature rise around the drifts has the effect of shortening the duration of boiling.

Figure 6.3-4b and Table 6.3-8 give the complementary cumulative distribution function for the maximum lateral extent of the boiling-point isotherm for lower-bound, mean, and upper-bound infiltration-flux cases. Note that the lateral extent of the boiling-point isotherm approximately corresponds to the lateral extent of the dryout zone. As was the case for the peak temperatures and boiling-period duration, the maximum lateral extent of boiling increases with decreasing percolation flux. Figure 6.3-6 is a contour map of the maximum lateral extent of boiling (and dryout) for a PWR CSNF waste package. It is apparent that the maximum lateral extent of boiling increases with distance from the repository edges. Areas with low percolation flux will have a greater spatial extent of dryout, increasing the volume of rock in which the dry (low) value of thermal conductivity pertains, which enhances the temperature rise around the drifts. This enhanced temperature rise has the effect of increasing the volume of rock dryout around the drifts. Areas with high percolation flux will have a smaller spatial (and temporal) extent of rock dryout, decreasing the volume of rock to which the dry (low) value of thermal conductivity pertains, which reduces the temperature rise around the drifts. This reduced temperature rise around the drifts has the effect of limiting the volume of rock dryout around the drifts.

It is important to note that the lateral extent of boiling is always much smaller than the half spacing between emplacement drifts. Therefore, the majority of the host rock between emplacement drifts always remains below the boiling point, thereby enabling condensate and percolation flux to continuously drain between emplacement drifts.

Table 6.3-7. Time When Boiling Ceases at the Drift Wall Summarized for Lower-Bound, Mean, and Upper-Bound Infiltration-Flux Cases

Infiltration-flux case	Time when boiling at the drift wall ceases (years)						
	Shortest	10th Percentile	30th Percentile	Median	70th Percentile	90th Percentile	Longest
Lower	130.2	349.9	630.9	859.6	1,122.5	1,453.3	1,734.6
Mean	127.2	297.5	535.8	721.0	870.6	1,006.5	1,356.0
Upper	97.7	267.7	471.6	643.7	768.6	887.2	1,162.9

NOTE: These values are based on data plotted in Figure 6.3-4a.

Table 6.3-8. Maximum Lateral Extent of the Boiling-Point Isotherm (96 °C) Summarized for Lower-Bound, Mean, and Upper-Bound Infiltration-Flux Cases

Infiltration-flux case	Maximum Lateral Extent of Boiling (T > 96°C) (m)						
	Least	10th Percentile	30th Percentile	Median	70th Percentile	90th Percentile	Greatest
Lower	5.6	7.1	7.9	8.4	9.4	12.3	17.8
Mean	5.3	6.7	7.5	7.9	8.2	8.7	9.9
Upper	5.1	6.5	7.3	7.7	7.9	8.1	9.0

NOTE: These values are based on data plotted in Figure 6.3-4b. The maximum lateral extent of the boiling-point isotherm, which is measured from the center of the emplacement drift, approximately corresponds to the maximum lateral extent of dryout.
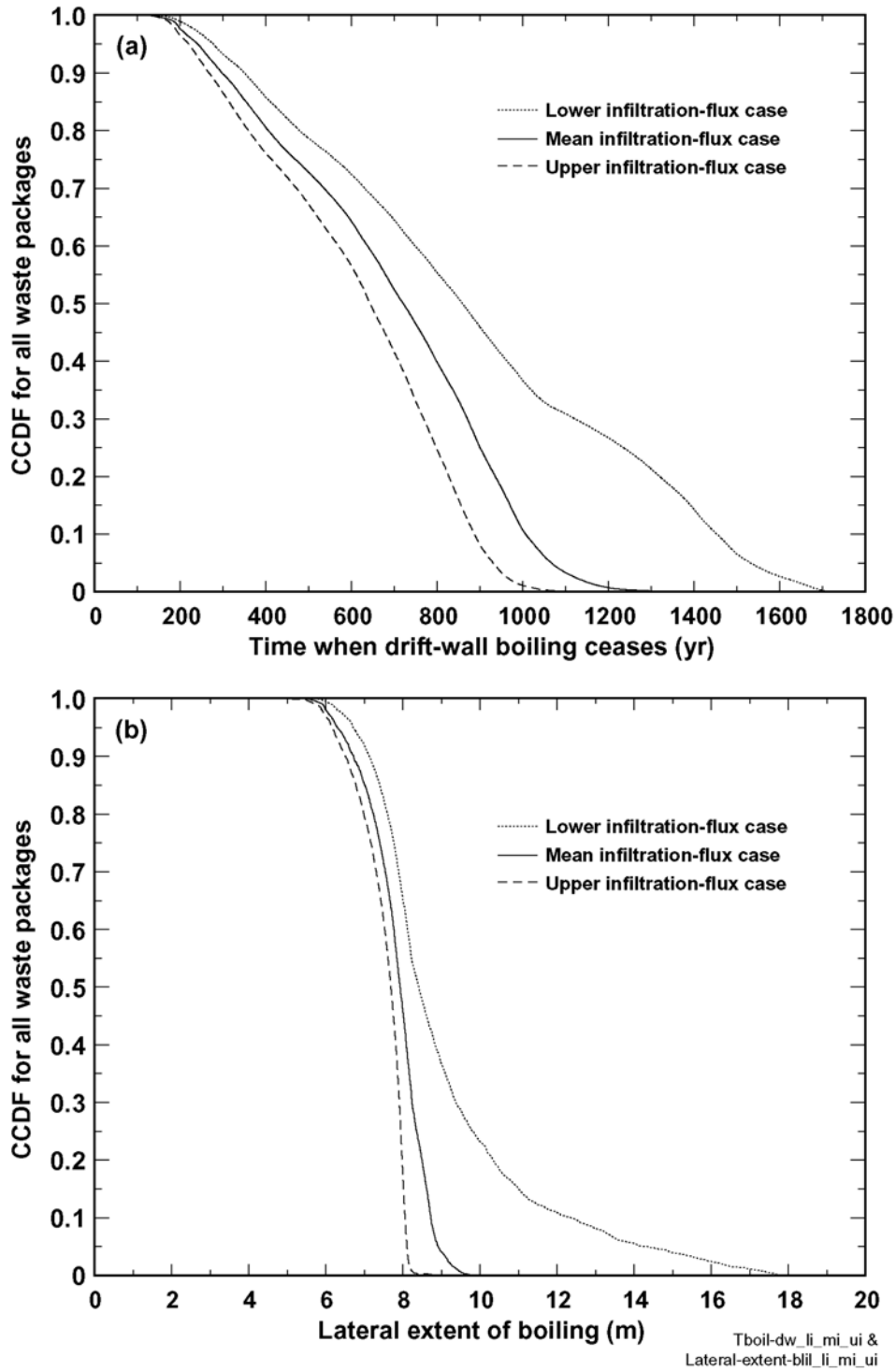
Source: See Table XIII-1.

NOTE: CCDFs are plotted for the lower-bound, mean, and upper-bound infiltration-flux cases. The maximum lateral extent of the boiling-point isotherm, which is measured from the center of the emplacement drift, approximately corresponds to the maximum lateral extent of the dryout zone.

Figure 6.3-4. Complementary Cumulative Distribution Functions (CCDFs) for (a) the Time When Boiling at the Drift Wall Ceases and (b) the Maximum Lateral Extent of the Boiling-Point Isotherm (96°C)

Figure 6.3-5. Contour Map of the Time When Boiling at the Drift Wall Ceases for the pwr1-2 Waste Package
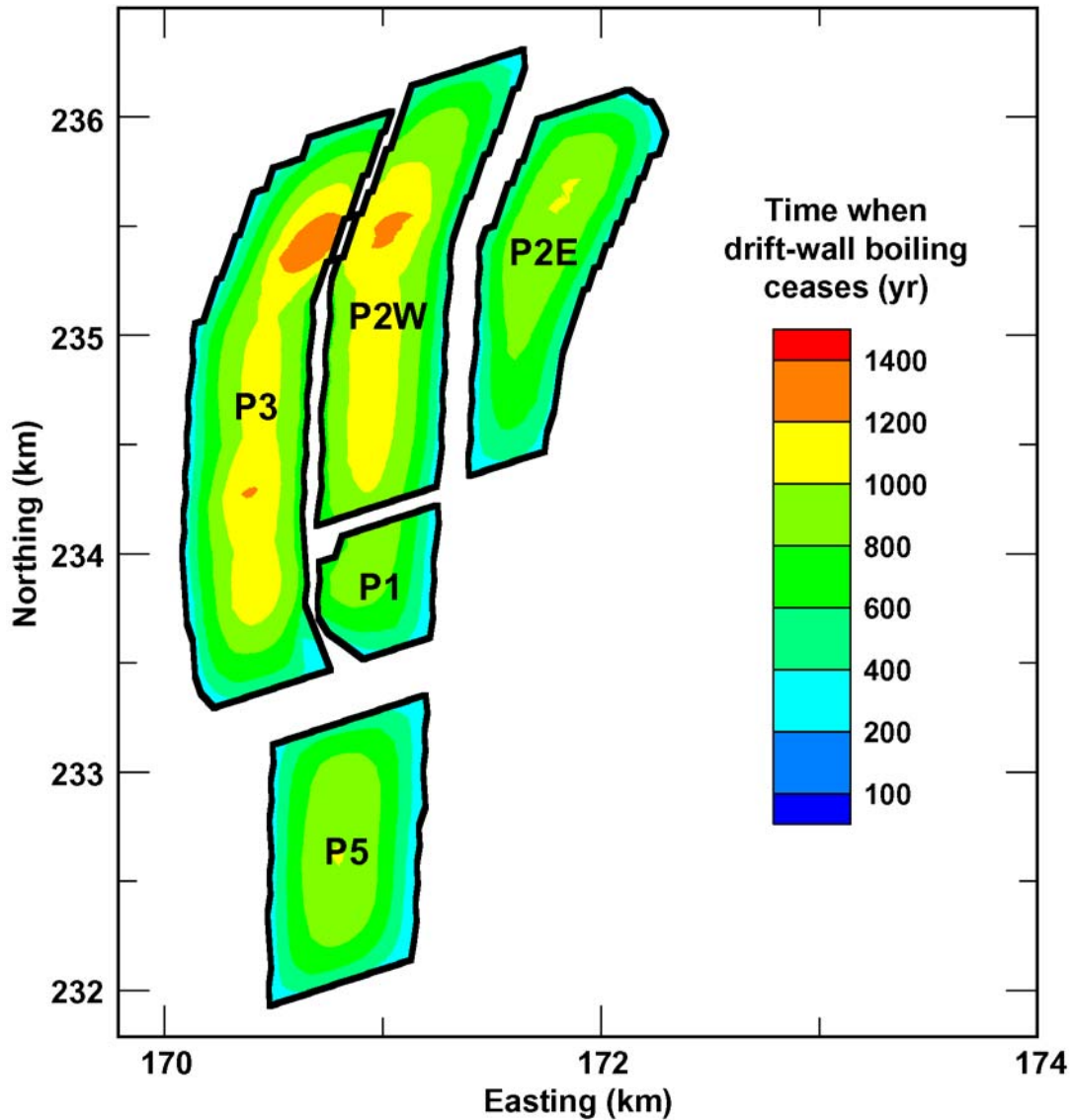
Source: See Table XIII-1.

NOTE: This contour map is plotted over the repository area for the mean infiltration-flux case. The pwr1-2 (21-PWR AP CSNF) waste package is the hottest package in the sequence (Figure 6.2-2).

Figure 6.3-5. Contour Map of the Time When Boiling at the Drift Wall Ceases for the pwr1-2 Waste Package
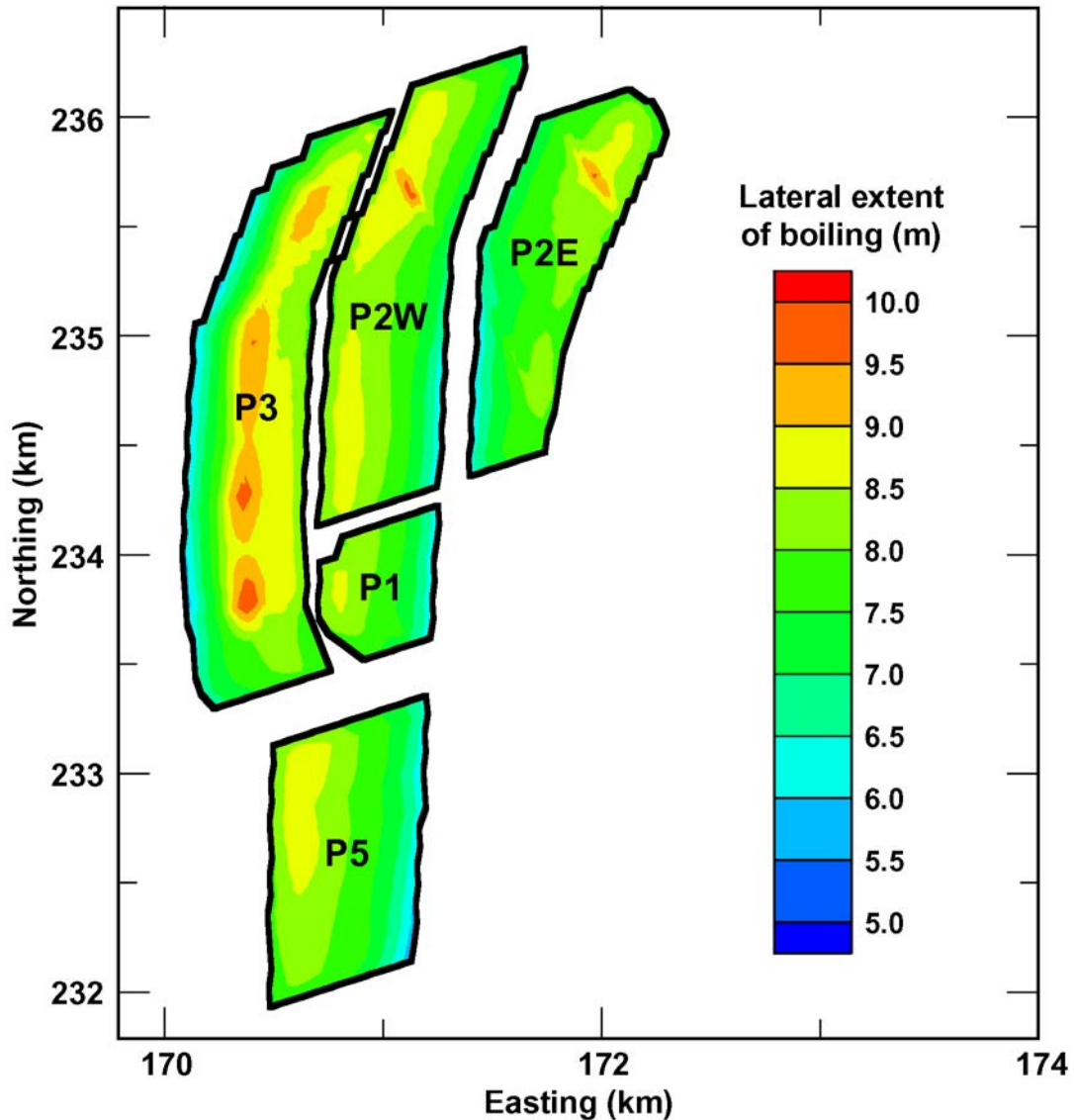
Source: See Table XIII-1.

NOTE   This contour map is plotted over the repository area for the mean infiltration-flux case. The pwr1-2 (21-PWR AP CSNF) waste package is the hottest package in the sequence (Table 6.3-13). The maximum lateral extent of the boiling-point isotherm, which is measured from the center of the emplacement drift, approximately corresponds to the maximum lateral extent of dryout.

Figure 6.3-6. Contour Map of the Maximum Lateral Extent of the Boiling-Point Isotherm (96°C) from the Drift Centerline for the pwr1-2 Waste Package

For the purpose of examining the details of thermal-hydrologic behavior in emplacement drifts, five locations were chosen that cover all four of the host-rock units (Tables 6.3-9, 6.3-10 and Figure 6.3-1). Four of these locations (P2ER8C6, P2WR8C8, P2WR5C10, and P3R8C13) were chosen because their respective values of percolation flux are close to the repository-wide averages (Table 6.3-4). The fifth location (P3R7C12) was chosen because it has close to the longest boiling-period duration over the entire repository area; note that this location is in a region of low percolation flux, which is a major contributing factor to its very long boiling-period duration. Time histories of drift-wall temperature and liquid-phase saturation, waste package temperature and relative humidity, and invert liquid-phase saturation are plotted (Figures 6.3-7 through 6.3-11) for these five locations (Figure 6.3-1). Tables 6.3-9 and 6.3-10 summarize the relationship between percolation flux and infiltration-flux case for the five locations and three climate states. Using Tables 6.3-9 and 6.3-10 as a guide, the influence of percolation flux on peak temperatures is summarized in Table 6.3-11 for the five locations. The influence of percolation flux on the duration of boiling is summarized in Table 6.3-12, which gives the time when boiling at the drift wall ceases.

Table 6.3-9. Percolation Flux for Mean Infiltration-Flux Case for Five Locations Used to Examine Thermal-Hydrologic Conditions in the Repository

LDTH–SDT submodel location	Host-rock unit	Nevada State Coordinates		Percolation flux for the mean infiltration-flux case (mm/yr)		
		Easting (m)	Northing (m)	Present-day	Monsoonal	Glacial-transition
P2ER8C6	Tptpul (tsw33)	171564.3	234417.3	5.41	11.70	23.03
P2WR8C8	Tptpmn (tsw34)	171240.9	234312.1	4.47	10.45	15.65
P2WR5C10	Tptpll (tsw35)	170730.3	234912.7	4.71	14.60	22.07
P3R7C12	Tptpll (tsw35)	170347.9	234277.5	0.86	3.43	6.32
P3R8C13	Tptpln (tsw36)	170080.6	233935.1	7.07	21.95	31.66

NOTE: See Figure 6.3-1 for locations. The percolation flux is obtained from DTN: LB0302PTNTSW9I.001 [DIRS 162277], as discussed in Appendix I of this report.

Table 6.3-10. Percolation Flux for the Lower and Upper Infiltration-Flux Cases for Five Locations Used to Examine Thermal-Hydrologic Conditions in the Repository

LDTH–SDT submodel location	Percolation Flux for the Lower-Bound Infiltration-Flux Case (mm/yr)			Percolation Flux for the Upper-Bound Infiltration-Flux Case (mm/yr)		
	Present-day	Monsoonal	Glacial-transition	Present-day	Monsoonal	Glacial-transition
P2ER8C6	6.331×10^{-2}	3.57	1.79	7.22	14.11	34.53
P2WR8C8	2.621×10^{-3}	3.44	1.31	7.31	12.51	22.14
P2WR5C10	2.261×10^{-3}	5.58	2.02	15.22	26.12	43.60
P3R7C12	1.081×10^{-4}	0.91	0.12	6.76	12.82	24.28
P3R8C13	0.36	6.66	3.69	16.57	33.64	54.99

NOTE: See Figure 6.3-1 for locations. The percolation flux is obtained from DTN: LB0302PTNTSW9I.001 [DIRS 162277], as discussed in Appendix I of this report.

Table 6.3-11. Range of Peak Temperatures over the Three Infiltration-Flux Cases for the pwr1-2 Waste Package for Five Locations in the Repository

LDTH–SDT submodel location	Host-rock unit	Peak Drift-Wall Temperature (°C)				Peak Waste Package Temperature (°C)			
		Lower	Mean	Upper	Range	Lower	Mean	Upper	Range
P2ER8C6	Tptpul (tsw33)	138.2	135.5	135.2	3.0	165.8	163.2	163.5	2.3
P2WR8C8	Tptpmn (tsw34)	127.4	123.0	122.3	5.1	154.8	150.6	150.8	4.0
P2WR5C10	Tptpll (tsw35)	149.3	141.5	139.6	9.7	177.8	169.4	168.2	9.6
P3R7C12	Tptpll (tsw35)	148.9	140.0	138.7	10.2	176.6	167.3	166.5	10.1
P3R8C13	Tptpln (tsw36)	121.4	120.5	118.8	2.6	149.2	148.2	147.4	1.8

NOTE: See Figure 6.3-1 for locations. These values are based on data plotted in Figures 6.3-7 through 6.3-11.

Table 6.3-12. Range of Time When Boiling at the Drift Wall Ceases over the Three Infiltration-Flux Cases for the pwr1-2 Waste Package for Five Locations in the Repository

LDTH–SDT submodel location	Host-rock unit	Time When Boiling at the Drift Wall Ceases for Three Infiltration-flux cases (years)				
		Lower	Mean	Upper	Range	Range[a]
P2ER8C6	Tptpul (tsw33)	425.3	365.6	359.8	65.5	16.7%
P2WR8C8	Tptpmn (tsw34)	298.8	221.0	213.1	85.7	33.5%
P2WR5C10	Tptpll (tsw35)	1,230.7	686.1	540.4	690.3	78.0%
P3R7C12	Tptpll (tsw35)	1,592.3	1,200.1	1,030.9	561.4	42.8%
P3R8C13	Tptpln (tsw36)	242.3	218.8	199.2	43.1	19.5%

[a] The range (%) is the range (years) divided by the average time when drift-wall boiling ceases [(shortest + longest)/2].

NOTE: See Figure 6.3-1 for locations. These values are based on data plotted in Figures 6.3-7 through 6.3-11.
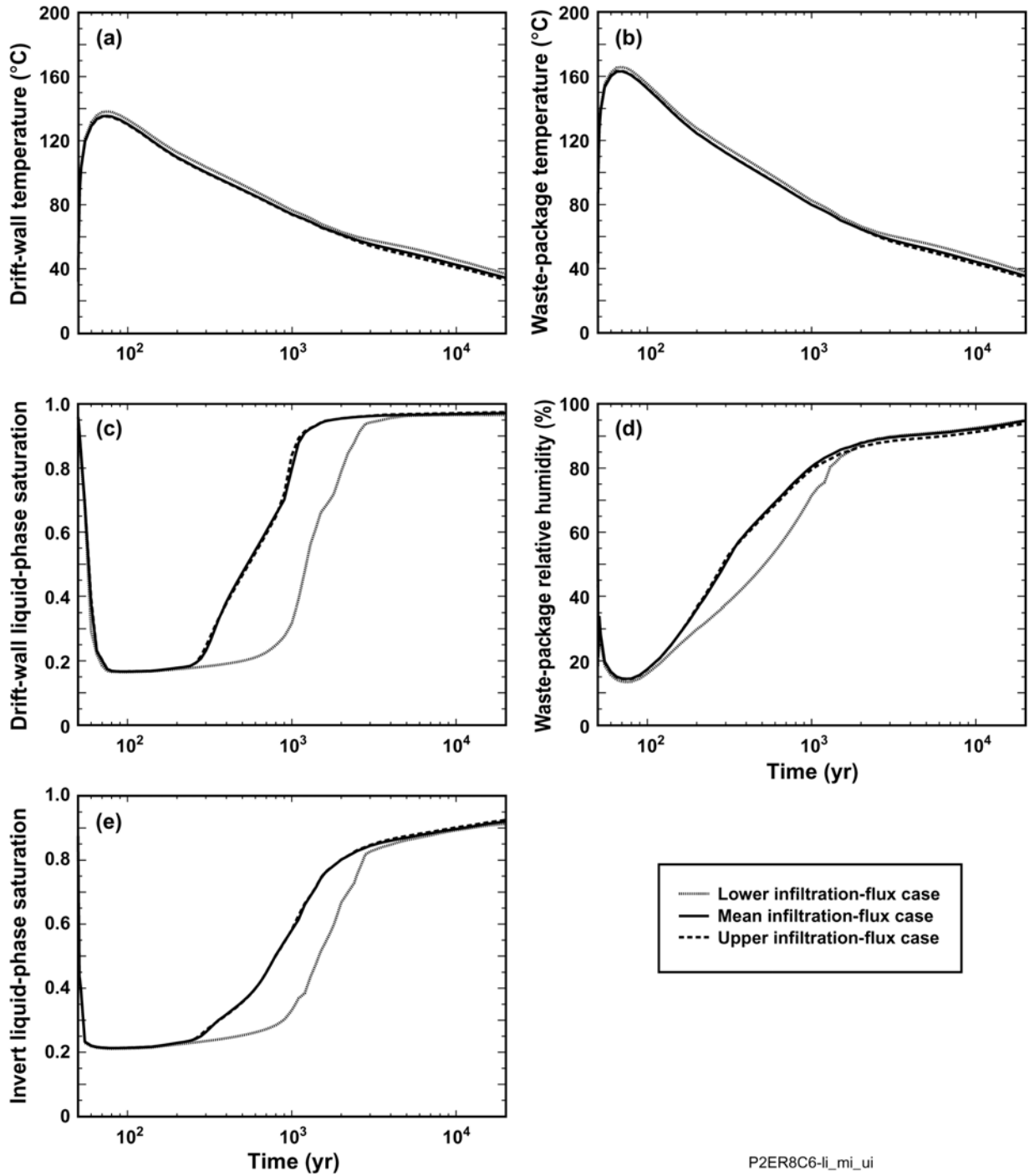
Source: See Table XIII-1.

NOTE: See Figure 6.3-1 for location. The plotted thermal-hydrologic parameters are (a) drift-wall temperature, (b) waste package temperature, (c) drift-wall liquid-phase saturation, (d) waste package relative humidity, and (e) invert liquid-phase saturation. The pwr1-2 (21-PWR AP CSNF) waste package is the hottest waste package in the sequence (Figure 6.2-2).

Figure 6.3-7. Thermal-Hydrologic Conditions for the pwr1-2 Waste Package Plotted for Lower-Bound, Mean, and Upper-Bound Infiltration-Flux Cases at the P2ER8C6 Location in the Tptpul (tsw33) Unit
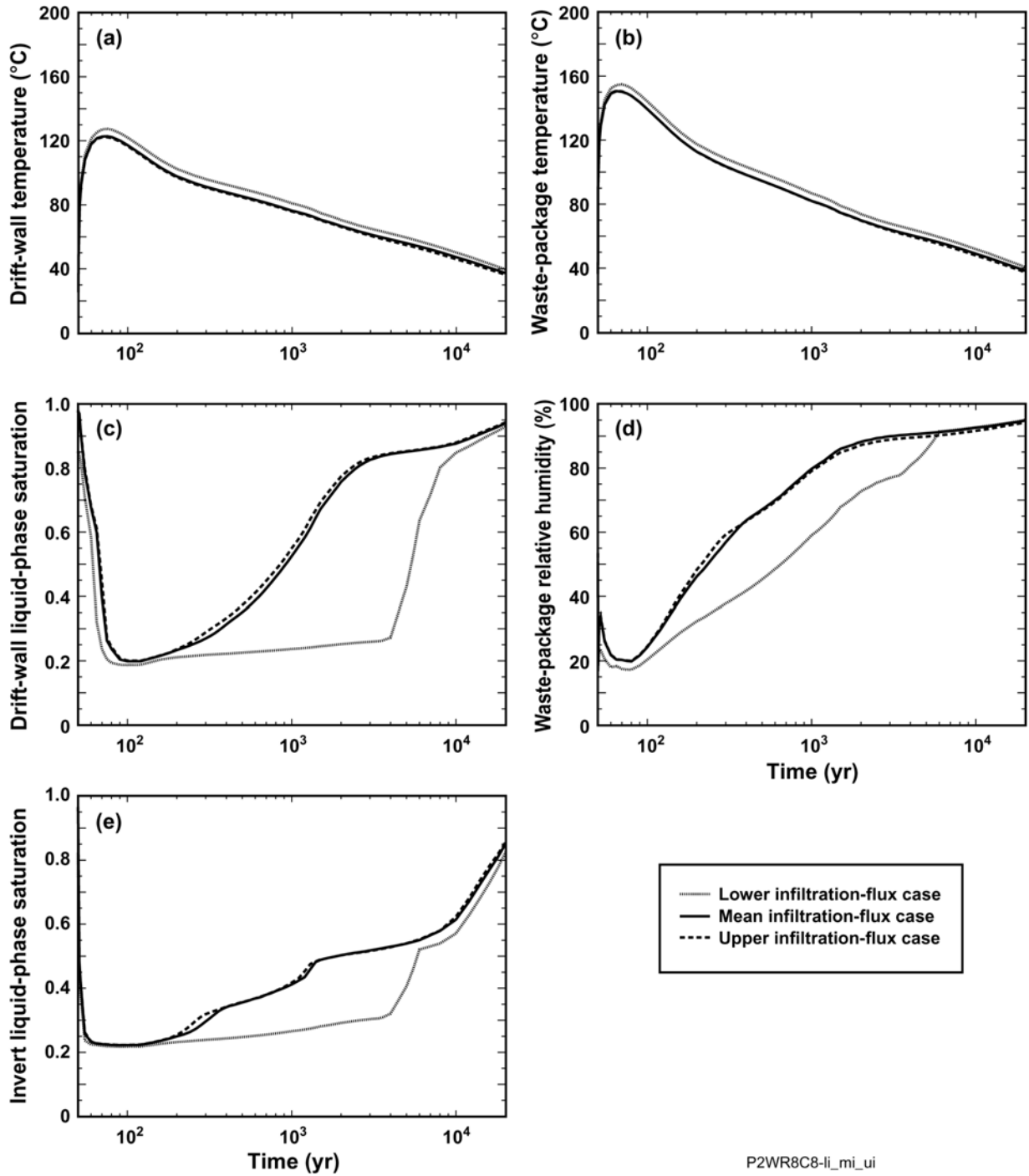
Source: See Table XIII-1.

NOTE: See Figure 6.3-1 for location. The plotted thermal-hydrologic parameters are (a) drift-wall temperature, (b) waste package temperature, (c) drift-wall liquid-phase saturation, (d) waste package relative humidity, and (e) invert liquid-phase saturation. The pwr1-2 (21-PWR AP CSNF) waste package is the hottest waste package in the sequence (Figure 6.2-2).

Figure 6.3-8. Thermal-Hydrologic Conditions for the pwr1-2 Waste Package Plotted for Lower-Bound, Mean, and Upper-Bound Infiltration-Flux Cases at the P2WR8C8 Location in the Tptpmn (tsw34) Unit
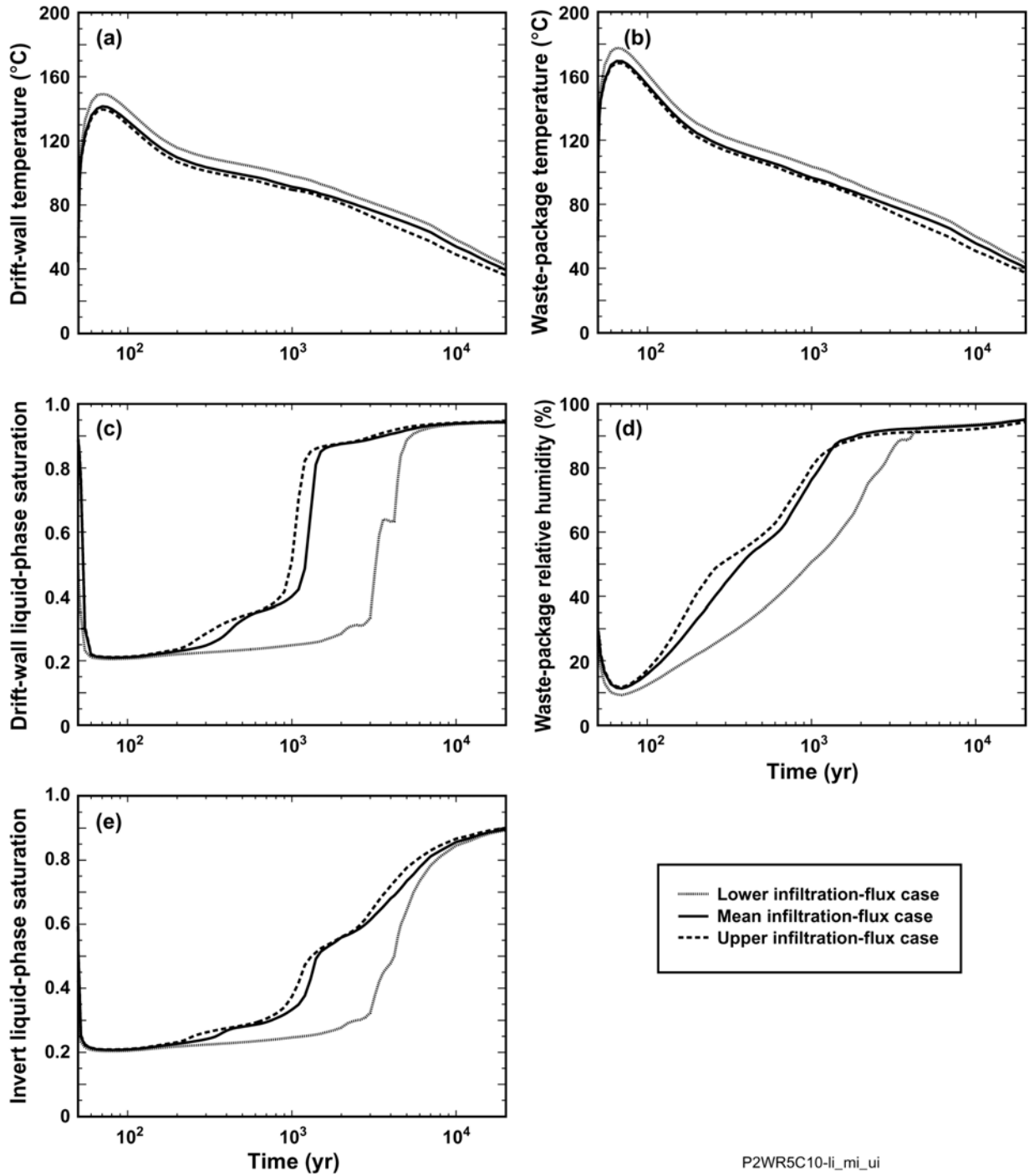
Source: See Table XIII-1.

NOTE: See Figure 6.3-1 for location. The plotted thermal-hydrologic parameters are (a) drift-wall temperature, (b) waste package temperature, (c) drift-wall liquid-phase saturation, (d) waste package relative humidity, and (e) invert liquid-phase saturation. The pwr1-2 (21-PWR AP CSNF) waste package is the hottest waste package in the sequence (Figure 6.2-2).

Figure 6.3-9. Thermal-Hydrologic Conditions for the pwr1-2 Waste Package Plotted for Lower-Bound, Mean, and Upper-Bound Infiltration-Flux Cases at the P2WR5C10 Location in the Tptpll (tsw35) Unit
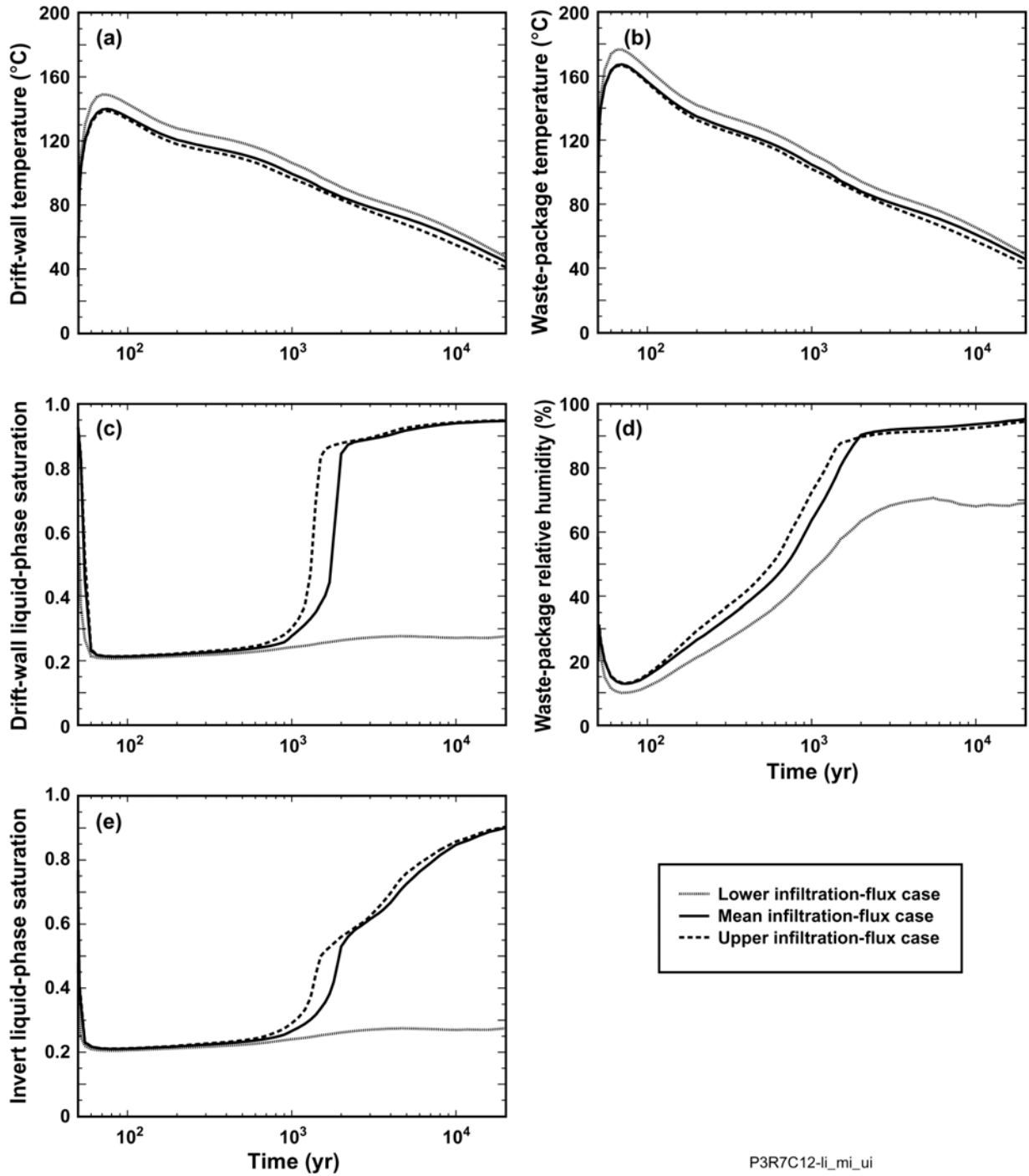
Source: See Table XIII-1.

NOTE: See Figure 6.3-1 for location. The plotted thermal-hydrologic parameters are (a) drift-wall temperature, (b) waste package temperature, (c) drift-wall liquid-phase saturation, (d) waste package relative humidity, and (e) invert liquid-phase saturation. The pwr1-2 (21-PWR AP CSNF) waste package is the hottest waste package in the sequence (Figure 6.2-2).

Figure 6.3-10. Thermal-Hydrologic Conditions for the pwr1-2 Waste Package Plotted for Lower-Bound, Mean, and Upper-Bound Infiltration-Flux Cases at the P3R7C12 Location in the Tptpll (tsw35) Unit

Source: See Table XIII-1.

NOTE: See Figure 6.3-1 for location. The plotted thermal-hydrologic parameters are (a) drift-wall temperature, (b) waste package temperature, (c) drift-wall liquid-phase saturation, (d) waste package relative humidity, and (e) invert liquid-phase saturation. The pwr1-2 (21-PWR AP CSNF) waste package is the hottest waste package in the sequence (Figure 6.2-2).

Figure 6.3-11. Thermal-Hydrologic Conditions for the pwr1-2 Waste Package Plotted for Lower-Bound, Mean, and Upper-Bound Infiltration-Flux Cases at the P3R8C13 Location in the Tptpln (tsw36) Unit

The influence of percolation flux on peak temperature is about the same for the waste package as it is for the drift wall (Table 6.3-11). The range of peak temperatures (from lower-bound to upper-bound infiltration-flux case) is slightly less for the waste package than it is for the drift wall. The reason for this relationship is that the effectiveness of thermal radiation increases slightly with temperature; consequently, the difference in peak temperature between the waste package and drift wall decreases slightly with increasing peak drift-wall temperature. Because the thermal conductivity of the rock is less for the lithophysal units (Tptpul and Tptpll) than it is for the nonlithophysal units (Tptpmn and Tptpln), peak temperatures are greater in the lithophysal units than in the nonlithophysal units.

The influence of percolation flux on the duration of boiling at the drift wall is greater for the locations (P2WR5C10 and P3R7C12) further from the repository edges than for those closer to the repository edges (P2ER8C6, P2WR8C8, and P3R8C13). Because location P2WR8C8 (located on the eastern edge of Panel 2W) receives some heat from the southern portion of Panel 2E, its boiling duration is somewhat greater than it is for the other two "edge" locations (P2ER8C6 and P3R8C13). Locations away from the repository edges have longer boiling durations that allow more time for the differences in rock dryout between lower and higher percolation fluxes to develop. There is a strong relationship between boiling-period duration and the spatial (and temporal) extent of rock dryout. Areas with low percolation flux will have a greater spatial extent of dryout, increasing the volume of rock in which the dry (low) value of thermal conductivity pertains, which enhances the temperature rise around the drifts. The enhanced temperature rise around the drift has the effect of extending the duration of boiling. Areas with high percolation flux will have a smaller spatial (and temporal) extent of rock dryout, decreasing the volume of rock in which the dry (low) value of thermal conductivity pertains, which reduces the temperature rise around the drifts. This reduced temperature rise around the drifts has the effect of shortening the duration of boiling.

The influence of percolation flux on dryout/rewetting is illustrated by the drift-wall and invert liquid-phase saturation histories (Figures 6.3-7c, 6.3-7e, 6.3-8c, 6.3-8e, 6.3-9c, 6.3-9e, 6.3-10c, 6.3-10e, 6.3-11c, and 6.3-11e). Locations P2ER8C6 and P2WR8C8 have small differences in dryout/rewetting between the upper-bound and mean infiltration-flux cases (Figures 6.3-7c, 6.3-7e, 6.3-8c, and 6.3-8e), while having larger differences between the lower-bound and mean infiltration-flux cases. Location P2WR5C10 has moderate differences in dryout/rewetting between the upper-bound and mean infiltration-flux cases (Figures 6.3-9c and 6.3-9e), while having larger differences between the lower-bound and mean infiltration-flux cases. Tables 6.3-9 and 6.3-10 show that location P2WR5C10 has larger differences in percolation flux between the lower-bound, mean, and upper-bound infiltration cases than do locations P2ER8C6 and P2WR8C8; consequently, location P2WR5C10 shows a greater sensitivity to the infiltration-flux case. Tables 6.3-9 and 6.3-10 show that location P3R7C12 has larger differences in percolation flux between the lower-bound, mean, and upper-bound infiltration-flux cases than does location P2WR5C10; thus, location P3R7C12 (Figures 6.3-10c and 6.3-10e) has larger differences in dryout/rewetting between the upper-bound and mean infiltration-flux cases than does location P2WR5C10 (Figures 6.3-9c and 6.3-9e). Location P3R7C12 has substantial differences in dryout/rewetting between the lower-bound and mean infiltration-flux cases, with the lower-bound infiltration-flux case remaining at low liquid-phase saturation beyond 20,000 years (Figures 6.3-10c and 6.3-10e). Location P3R8C13 has larger differences in dryout/rewetting between the upper-bound and mean infiltration-flux cases (Figures 6.3-11c and 6.3-11e) and between the lower-bound and mean infiltration-flux cases.

The influence of percolation flux on waste package relative humidity histories is similar to its influence on dryout/rewetting (Figures 6.3-7d, 6.3-8d, 6.3-9d, 6.3-10d, and 6.3-11d). Locations P2ER8C6 and P2WR8C8 have small differences in waste package relative humidity history between the upper-bound and mean infiltration-flux cases (Figures 6.3-7d and 6.3-8d), while having larger differences between the lower-bound and mean infiltration-flux cases. Location P2WR5C10 has moderate differences in waste package relative humidity history between the upper-bound and mean infiltration-flux cases (Figure 6.3-9d), while having larger differences between the lower-bound and mean infiltration-flux cases. Location P3R7C12 has moderate differences in waste package relative humidity history between the upper-bound and mean infiltration-flux cases (Figure 6.3-10d), while having substantial differences between the lower-bound and mean infiltration-flux cases. Location P3R8C13 has small differences in waste package relative humidity history between the upper-bound and mean infiltration-flux case (Figure 6.3-11d); moderate differences between the lower-bound and mean infiltration-flux cases persist for about 700 years. With the exception of location P3R7C12, differences in waste package relative humidity history among the infiltration-flux cases generally diminish within one to several thousand years.

6.3.1.2   Influence of Waste Package-to-Waste Package Heat-Generation Variability

This section investigates the influence of waste package-to-waste package heat-generation variability on thermal-hydrologic conditions in the emplacement drifts. The eight different waste packages considered in all of the MSTHM calculations (Figure 6.2-2) are summarized in Table 6.3-13. Time histories of drift-wall temperature and liquid-phase saturation, waste package temperature and relative humidity, and invert liquid-phase saturation are plotted (Figures 6.3-12 through 6.3-16) for three of these waste packages (dhlw-l1, bwr1-1, and pwr1-2) for the five locations discussed in the previous section (see Figure 6.3-1 for locations). Note that these three waste packages include the coolest and hottest in the waste package sequence considered. The influence of waste package-to-waste package heat-generation variability on peak temperatures is summarized in Table 6.3-14 for the five locations. The influence of waste package-to-waste package heat-generation variability on the duration of boiling is summarized in Table 6.3-15, which gives the time when boiling at the drift wall ceases.

Table 6.3-13. Summary of Waste Packages Included in the MSTHM Calculations (Figure 6.2-2)

Waste Package Name in MSTHM	Waste Package type	Length in Model (m)	Initial Heat-Generation Rate (kW)	Notes (based on MSTHM output temperatures and heat output)
pwr1-1	21-PWR AP CSNF *½ 21-PWR AP*	2.5825	5.764[a]	Half waste package in model; coolest PWR waste package in sequence, but "average" PWR waste package with respect to heat output
dhlw-l1	5 DHLW/DOE SNF-LONG *5-HLW LONG*	5.217	0.990	Coolest waste package in sequence with the lowest heat output
pwr2-1	21-PWR AP CSNF *21-PWR AP (HOT)*	5.165	11.800	"Average" PWR waste package in sequence with respect to temperatures, but highest heat output in sequence
bwr1-1	44-BWR CSNF *44-BWR AP*	5.165	7.377	Hottest BWR waste package in sequence, but "average" BWR waste package with respect to heat output
bwr2-1	44-BWR CSNF *44-BWR ADJUSTED*	5.165	7.100	"Oldest" BWR waste package in sequence
dhlw-s1	5 DHLW/DOE SNF-SHORT *5-HLW SHORT*	3.59	2.983	Hottest DHLW waste package in sequence
pwr1-2	21-PWR AP CSNF *21-PWR AP*	5.165	11.528	"Hottest" waste package in sequence, but average PWR waste package with respect to heat output
bwr1-2	44-BWR CSNF *½ 44-BWR AP*	2.5825	3.689[a]	Half waste package in model; coolest BWR waste package in sequence, but "average" BWR waste package with respect to heat output

[a] These values represent the heat-generation rate for a half waste package.

NOTES: Waste packages included in Figures 6.3-12 through 6.3-16 are shown in bold. Names of waste package types as they appear in BSC 2005 [DIRS 173705] are shown in italics.

Waste package lengths are based on information from BSC 2003 [DIRS 165406], Table 1. Heat generation rates are based on information from BSC 2005 [DIRS 173705], Table 1. The heat generation rates used in the MSTHM calculations are based on the first 25,000 years of entries in Table 1 of BSC 2005 [DIRS 173705]. Heat generation values for 20,050 years, which corresponds to the end of the MSTHM simulations, are linearly interpolated between the values for 20,000 years and 25,000 years from Table 1 of BSC 2005 [DIRS 173705].

Table 6.3-14. Range of Peak Temperatures from Variability in Waste Package-to-Waste Package Heat Generation for the Mean Infiltration-Flux Case, Summarized for Five Locations in the Repository

LDTH–SDT Submodel Location	Host-Rock Unit	Peak Drift-Wall Temperature (°C)			Peak Waste Package Temperature (°C)		
		Lowest	Highest	Range	Lowest	Highest	Range
P2ER8C6	Tptpul (tsw33)	122.3	135.5	13.2	132.0	163.2	31.2
P2WR8C8	Tptpmn (tsw34)	109.7	123.0	13.3	118.9	150.6	31.7
P2WR5C10	Tptpll (tsw35)	126.8	140.8	14.0	136.7	168.8	32.1
P3R7C12	Tptpll (tsw35)	126.8	140.0	13.2	136.3	167.3	31.0
P3R8C13	Tptpln (tsw36)	106.6	120.2	13.6	116.1	148.2	32.1

NOTE: See Figure 6.3-1 for locations. These values are based on data plotted in Figures 6.3-7 through 6.3-16.

Table 6.3-15. Range of Time When Boiling at the Drift Wall Ceases (Resulting from Variability in Waste Package-to-Waste Package Heat Generation) for the Mean Infiltration-Flux Case, Summarized for Five Locations in the Repository

LDTH–SDT Submodel Location	Host-Rock Unit	Time When Boiling at the Drift Wall Ceases (years)			
		Shortest	Longest	Range	Range[a]
P2ER8C6	Tptpul (tsw33)	284.2	364.8	80.6	24.8%
P2WR8C8	Tptpmn (tsw34)	166.1	242.8	76.7	37.5%
P2WR5C10	Tptpll (tsw35)	340.7	623.0	282.3	58.6%
P3R7C12	Tptpll (tsw35)	1,072.3	1,200.1	127.8	11.3%
P3R8C13	Tptpln (tsw36)	140.4	195.2	54.8	32.7%

[a] The range (%) is the range (years) divided by the average time when drift-wall boiling ceases [(shortest + longest)/2].

NOTE: See Figure 6.3-1 for locations.

The influence of waste package-to-waste package heat-generation variability on peak drift-wall temperatures is virtually the same for all five locations (Table 6.3-14); similarly, the influence of heat-generation variability on peak waste package temperatures is virtually the same for all five locations. The range of peak drift-wall temperatures is less than the range of peak waste package temperatures. Thermal radiation in the drift is an efficient heat-transfer mechanism for limiting the extent of temperature variability along the axis of the drift. The influence of heat-generation variability on boiling duration varies among the five locations (Table 6.3-15). The greatest degree of boiling-duration variability is at location P2WR5C10, while location P3R7C12 has the least degree of boiling-duration variability.

The influence of heat-generation variability on dryout/rewetting is illustrated by the drift-wall and invert liquid-phase saturation histories (Figures 6.3-12c, 6.3-12e, 6.3-13c, 6.3-13e, 6.3-14c, 6.3-14e, 6.3-15c, 6.3-15e, 6.3-16c, and 6.3-16e). Dryout/rewetting at locations P2ER8C6, P2WR8C8, and P3R8C13 (Figures 6.3-12c 6.3-12e, 6.3-13c, 6.3-13e, 6.3-16c, and 6.3-16e), which are close to the repository edges, exhibit more sensitivity to heat-generation variability than at locations P2WR5C10 and P3R7C12 (Figures 6.3-14c, 6.3-14e, 6.3-15c, and 6.3-15e), which are farther away from the repository edges. Note that location P3R7C12 has by far the least degree of dryout/rewetting variability. For all locations, the invert exhibits less dryout/rewetting variability than the drift wall.
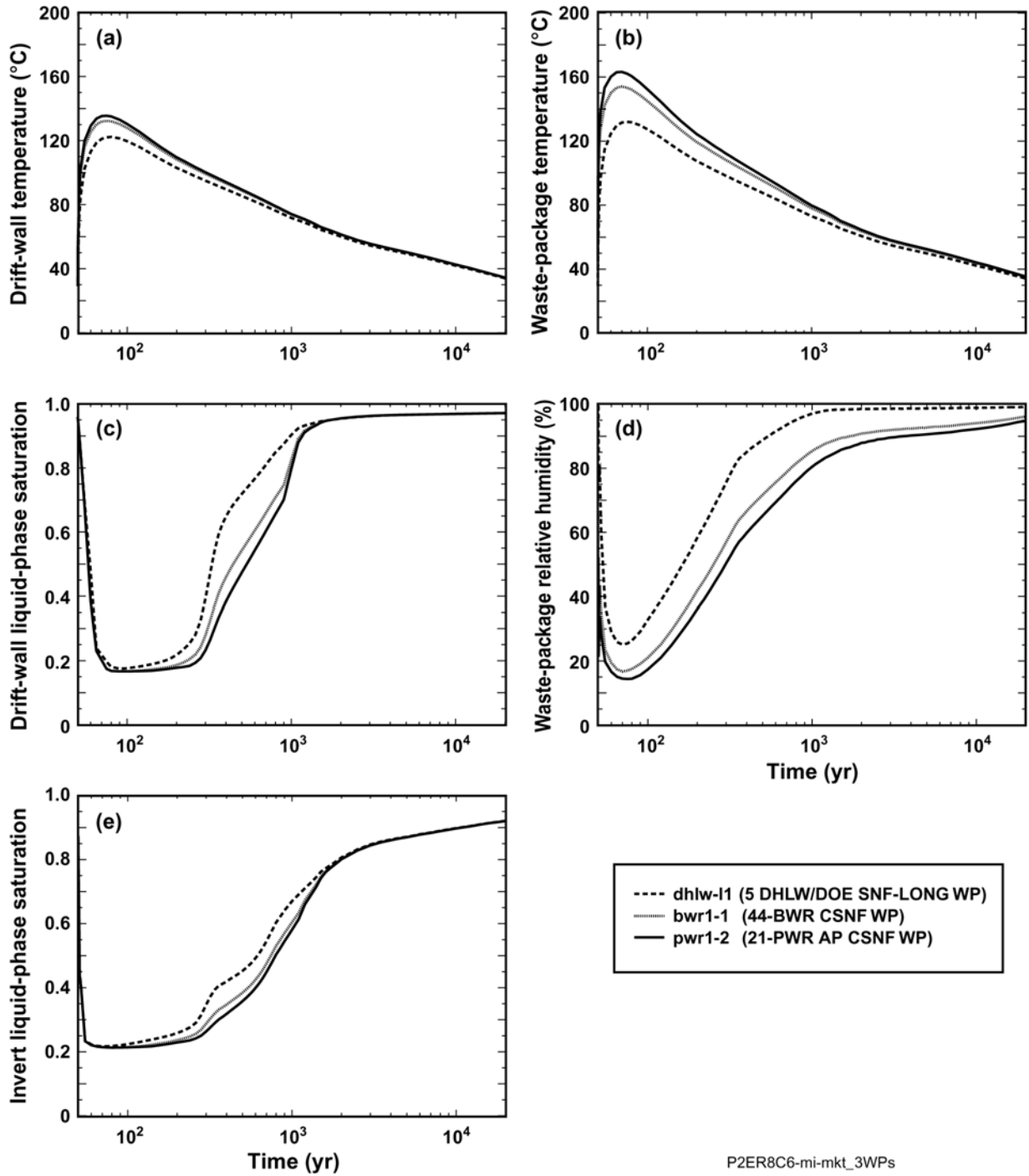
Source: See Table XIII-1.

NOTE: See Figure 6.3-1 for location. The plotted thermal-hydrologic parameters are (a) drift-wall temperature, (b) waste package temperature, (c) drift-wall liquid-phase saturation, (d) waste package relative humidity, and (e) invert liquid-phase saturation. These waste packages bracket the entire range of temperature at this location.

Figure 6.3-12. Thermal-Hydrologic Conditions for the Mean Infiltration-Flux Case Plotted for a Range of Waste Packages at the P2ER8C6 Location in the Tptpul (tsw33) Unit
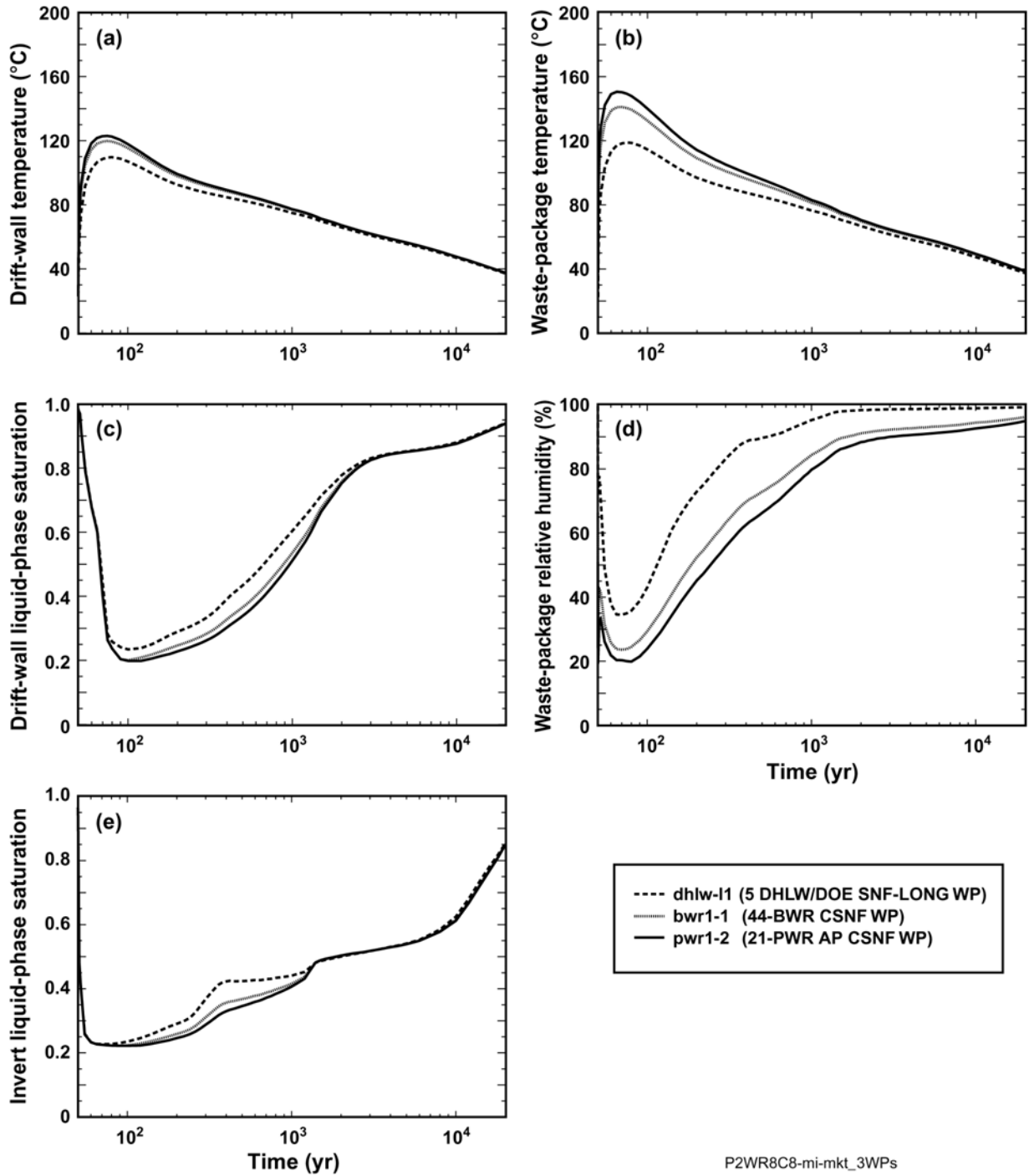
Source: See Table XIII-1.

NOTE: WP = waste package. See Figure 6.3-1 for location. The plotted thermal-hydrologic parameters are
         (a) drift-wall temperature, (b) waste package temperature, (c) drift-wall liquid-phase saturation, (d) waste
         package relative humidity, and (e) invert liquid-phase saturation. These waste packages bracket the entire
         range of temperature at this location.

Figure 6.3-13. Thermal-Hydrologic Conditions for the Mean Infiltration-Flux Case Plotted for a Range of
                Waste Packages at the P2WR8C8 Location in the Tptpmn (tsw34) Unit
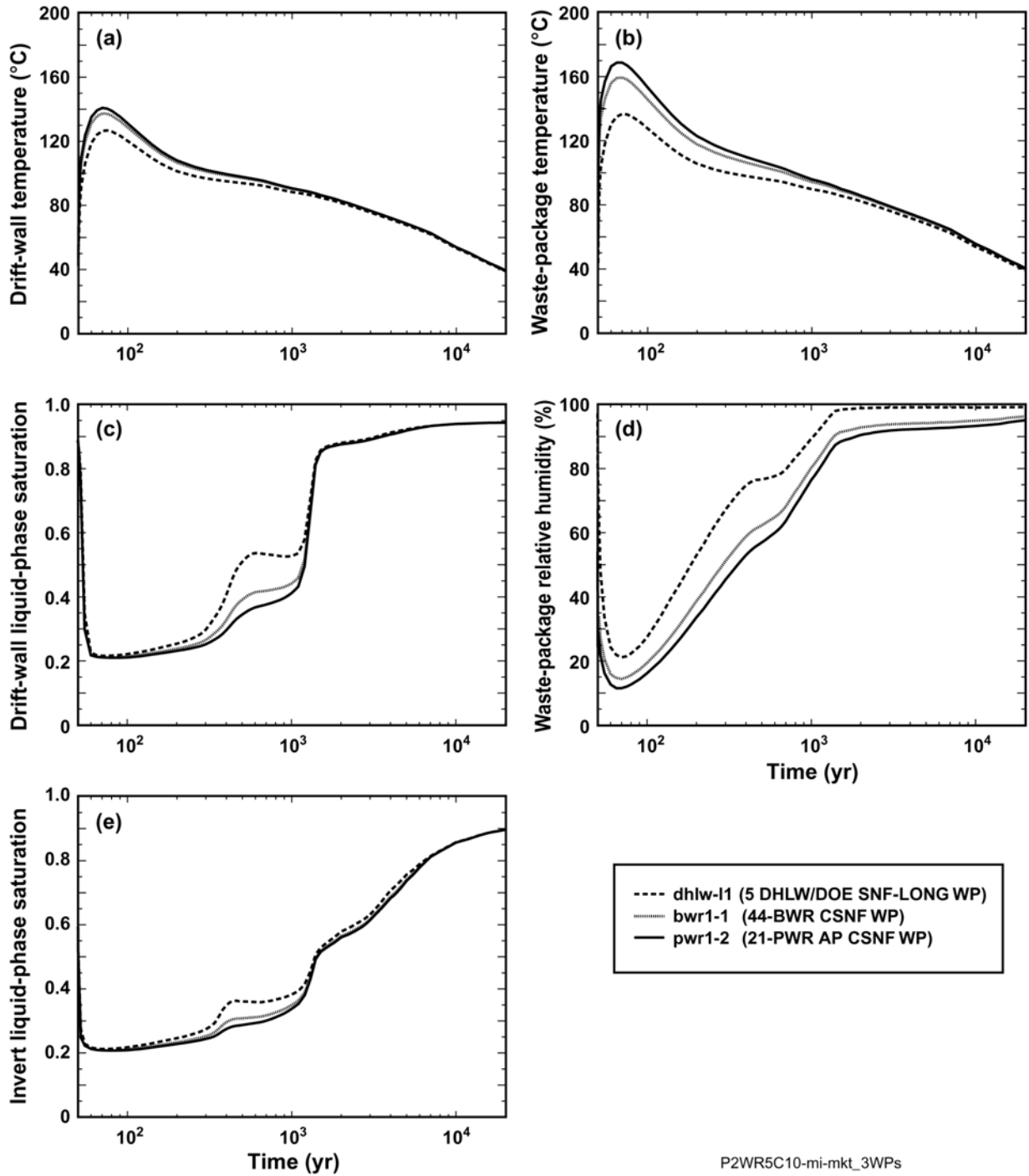
Source: See Table XIII-1.

NOTE: WP = waste package. See Figure 6.3-1 for location. The plotted thermal-hydrologic parameters are (a) drift-wall temperature, (b) waste package temperature, (c) drift-wall liquid-phase saturation, (d) waste package relative humidity, and (e) invert liquid-phase saturation. These waste packages bracket the entire range of temperature at this location.

Figure 6.3-14. Thermal-Hydrologic Conditions for the Mean Infiltration-Flux Case Plotted for a Range of Waste Packages at the P2WR5C10 Location in the Tptpll (tsw35) Unit
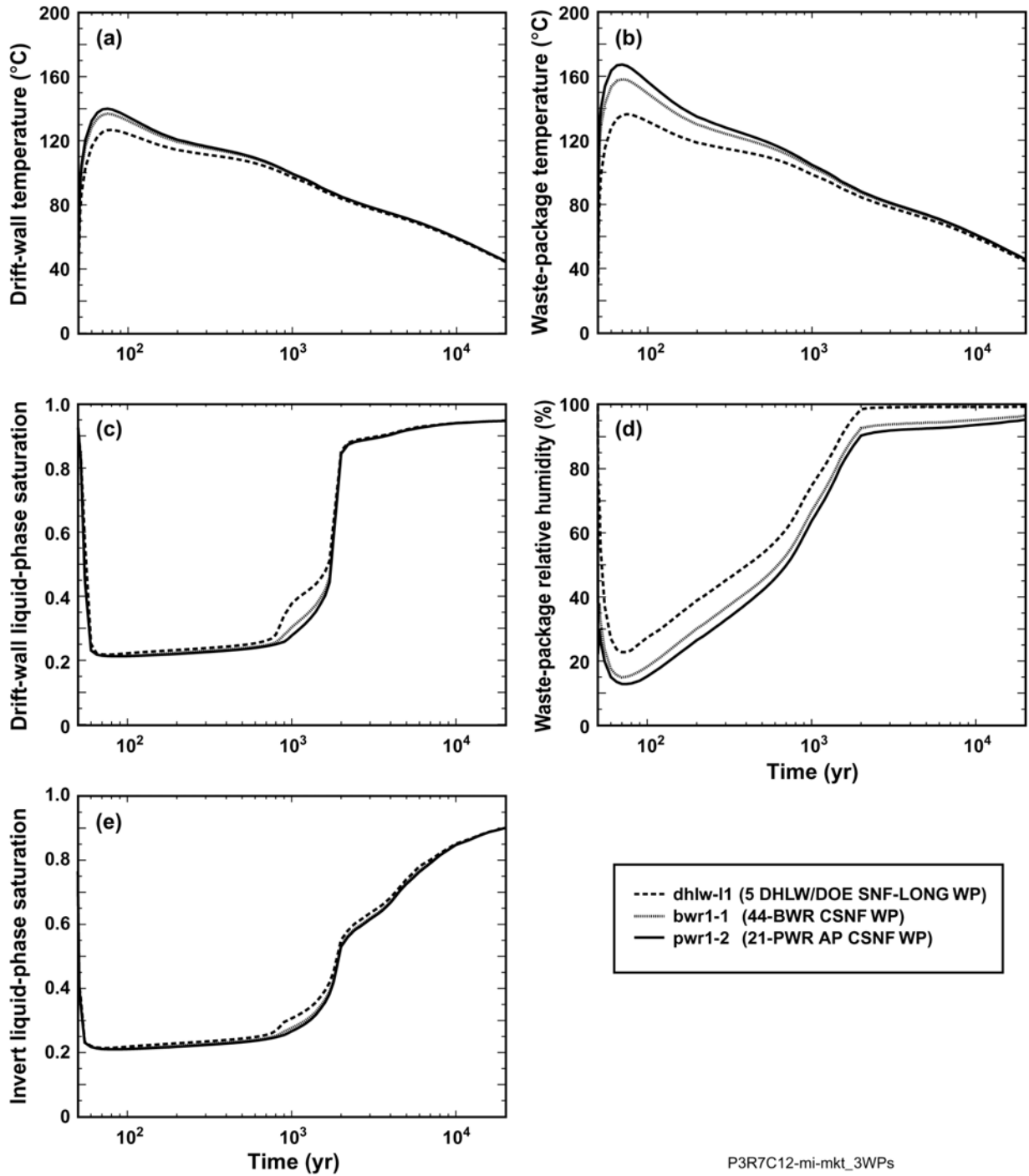
Source: See Table XIII-1.

NOTE: WP = waste package. See Figure 6.3-1 for location. The plotted thermal-hydrologic parameters are (a) drift-wall temperature, (b) waste package temperature, (c) drift-wall liquid-phase saturation, (d) waste package relative humidity, and (e) invert liquid-phase saturation. These waste packages bracket the entire range of temperature at this location.

Figure 6.3-15. Thermal-Hydrologic Conditions for the Mean Infiltration-Flux Case Plotted for a Range of Waste Packages at the P3R7C12 Location in the Tptpll (tsw35) Unit
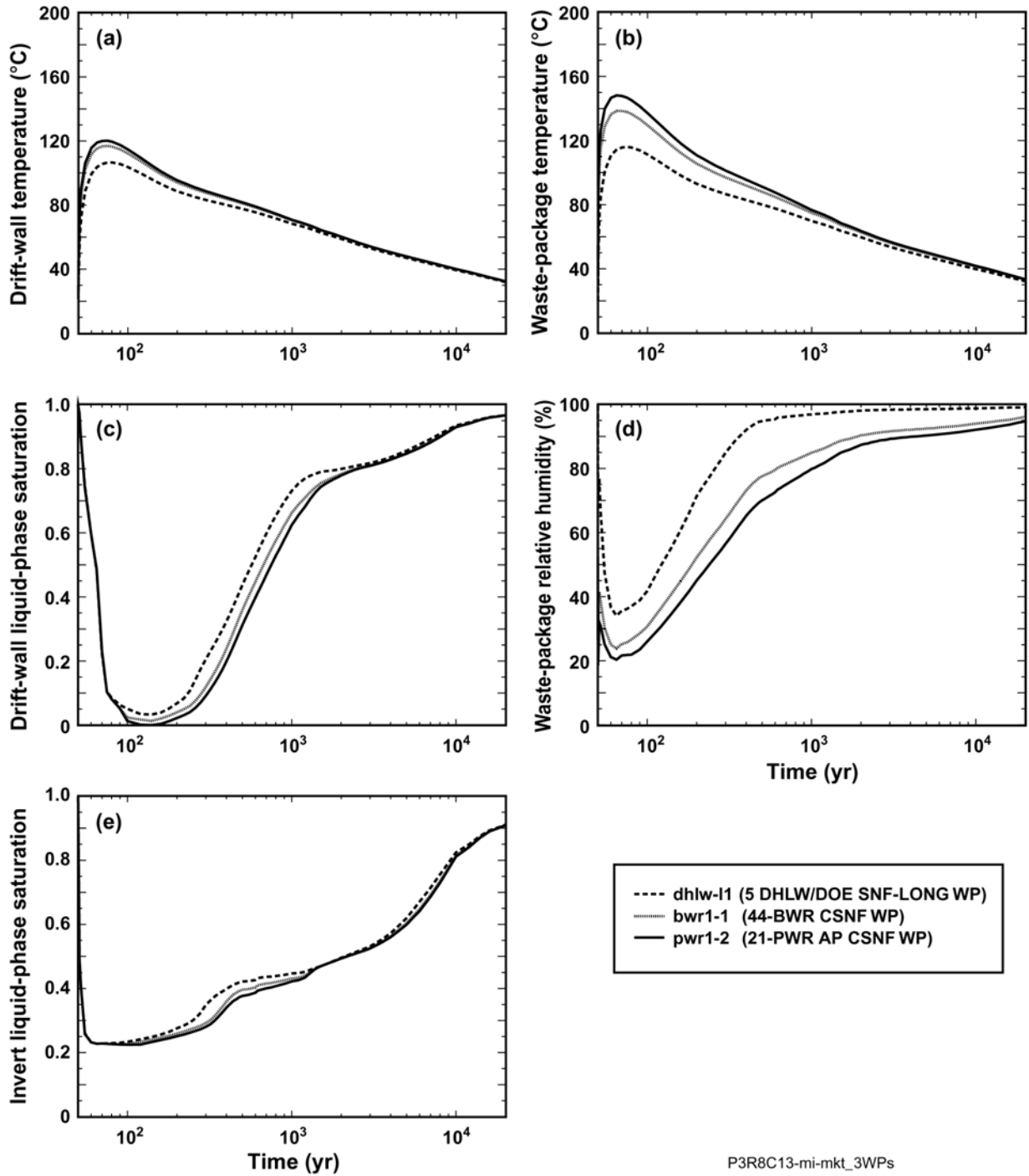
Source: See Table XIII-1.

NOTE: WP = waste package. See Figure 6.3-1 for location. The plotted thermal-hydrologic parameters are
         (a) drift-wall temperature, (b) waste package temperature, (c) drift-wall liquid-phase saturation, (d) waste
         package relative humidity, and (e) invert liquid-phase saturation. These waste packages bracket the entire
         range of temperature at this location.

Figure 6.3-16. Thermal-Hydrologic Conditions for the Mean Infiltration-Flux Case Plotted for a Range of
          Waste Packages at the P3R8C13 Location in the Tptpln (tsw36) Unit

The influence of heat-generation variability on waste package relative humidity variability is similar to the influence on dryout/rewetting. Because the relative humidity at the drift wall depends on the liquid-phase saturation and temperature, the variability of drift-wall relative humidity is similar to that of drift-wall liquid-phase saturation. Relative humidity at a given waste package depends on two factors. The first is the adjacent drift-wall relative humidity. The second factor is the temperature difference between the waste package and adjoining drift-wall surface; relative humidity reduction (relative to the adjacent drift wall) depends on this temperature difference (Section 6.1.4). Waste packages with higher heat-generation rates result in a greater relative humidity reduction, for longer times, than those with lower heat-generation rates. The large difference in heat-generation rate between the coolest and hottest waste packages results in a large difference in the respective relative humidity histories.

From a heat-transfer perspective, the drip shield functions like a thermal-radiation shield (between the waste package and the drift wall) that causes the waste package to be hotter than it would without the presence of the drip shield. The increased temperature difference between the waste package and the drift wall reduces the relative humidity on the waste package. For waste packages with higher heat-generation rates (i.e., the pwr1-2 waste package in Figure 6.3-16), the influence of the thermal-radiation shield on waste package temperature and relative humidity is much greater than it is for waste packages with lower heat-generation rates (i.e., the dhlw-ll waste package in Figure 6.3-16). This effect is exhibited by comparing the range in drift-wall temperatures (Figure 6.3-16a) with the range in waste package temperatures (Figure 6.3-16b). The larger range in waste package temperatures, compared to the corresponding range in drift-wall temperatures, results in a wide range in waste package relative humidities (Figure 6.3-16d).

6.3.1.3 Alternative MSTHM with Vertically Extended LDTH/SDT Submodels

The standard MSTHM utilizes LDTH and SDT submodels that have a constant-temperature boundary at the water table. To test an alternative approach, MSTHM calculations were conducted with vertically extended LDTH and SDT submodels. In these submodels, the lower boundary of the LDTH and SDT submodels is set 1,000 m below the water table (as is done in the SMT submodel). A series of initialization runs are conducted with the SDT submodel where the lower boundary temperature is iteratively adjusted until the temperature at the water table is equal to that of the SDT submodel with the lower boundary at the water table. The vertically extended SDT submodel is then run with the appropriate heat-generation-rate-versus-time table and the temperature at the water table is saved as output. The water-table temperature history is then applied as the lower boundary temperature (at the water table) in the corresponding LDTH submodel. Applying the SDT submodel water-table temperature history to the lower (water-table) boundary of the LDTH submodel is equivalent to having extended the LDTH submodel 1,000 m below the water table. This alternative MSTHM approach, with vertically extended LDTH and SDT submodels, was applied to four of the five locations (Figure 6.3-1) discussed in previous sections. The alternative MSTHM approach is compared to the standard MSTHM approach in Figures 6.3-17 through 6.3-20. Overall, the two approaches predict nearly the same thermal-hydrologic conditions at the four locations. The small differences between the two approaches occur only at later time (e.g., Figures 6.3-19a, 6.3-19b, 6.3-20a, 6.3-20b, 6.3-20c, and 6.3-20e). At early time, the two approaches predict virtually identical thermal-hydrologic conditions. Peak temperatures (Table 6.3-16) are exactly the same for the two approaches and the duration of boiling (Table 6.3-17) is nearly the same for the two

approaches. Waste package relative humidity is virtually the same for all time (Figures 6.3-17d, 6.3-18d, 6.3-19d, and 6.3-20d). The alternative MSTHM approach is applied to the low percolation-flux cases described in Sections 6.3.2.1 and 6.3.2.3.

Table 6.3-16. Peak Temperatures in an Alternative MSTHM with Vertically Extended LDTH and SDT Submodels, as Compared with Standard MSTHM Results, for the pwr1-2 at Four Locations in the Repository

LDTH–SDT Submodel Location	Host-Rock Unit	Peak Drift-Wall Temperature (°C)			Peak Waste Package Temperature (°C)		
		Standard MSTHM	Alternative MSTHM	Difference	Standard MSTHM	Alternative MSTHM	Difference
P2ER8C6	Tptpul (tsw33)	135.5	135.5	0.0	163.2	163.2	0.0
P2WR8C8	Tptpmn (tsw34)	123.0	123.0	0.0	150.6	150.6	0.0
P2WR5C10	Tptpll (tsw35)	140.8	140.8	0.0	168.8	168.8	0.0
P3R8C13	Tptpln (tsw36)	120.2	120.2	0.0	148.2	148.2	0.0

NOTE: See Figure 6.3-1 for locations. These values are based on data plotted in Figures 6.3-17 through 6.3-20.

Table 6.3-17. Time When Boiling at the Drift Wall Ceases in an Alternative MSTHM with Vertically Extended LDTH and SDT Submodels, as Compared to the Standard MSTHM Results, for the pwr1-2 at Four Locations in the Repository

LDTH–SDT Submodel Location	Host-Rock Unit	Time When Boiling at the Drift Wall Ceases (years)			
		Standard MSTHM	Alternative MSTHM	Difference	Range[a]
P2ER8C6	Tptpul (tsw33)	364.8	364.9	0.1	0.027%
P2WR8C8	Tptpmn (tsw34)	242.8	242.6	-0.2	0.082%
P2WR5C10	Tptpll (tsw35)	623.0	622.0	-1.0	0.161%
P3R8C13	Tptpln (tsw36)	195.2	195.1	-0.1	0.051%

[a] The range (%) is the range (years) divided by the average time when drift-wall boiling ceases [(shortest + longest)/2].

NOTE: See Figure 6.3-1 for locations. These values are based on data plotted in Figures 6.3-17 through 6.3-20.

Source: See Table XIII-1.

NOTE: SZ = saturated zone. See Figure 6.3-1 for location. The plotted thermal-hydrologic parameters are (a) drift-wall temperature, (b) waste package temperature, (c) drift-wall liquid-phase saturation, (d) waste package relative humidity, and (e) invert liquid-phase saturation. The standard MSTHM calculation is compared with an alternative MSTHM calculation in which the LDTH and SDT submodels are vertically extended to include the upper 1 km of the saturated zone.

Figure 6.3-17. Thermal-Hydrologic Conditions for the Mean Infiltration-Flux Case Plotted for the pwr1-2 Waste Package at the P2ER8C6 Location in the Tptpul (tsw33) Unit
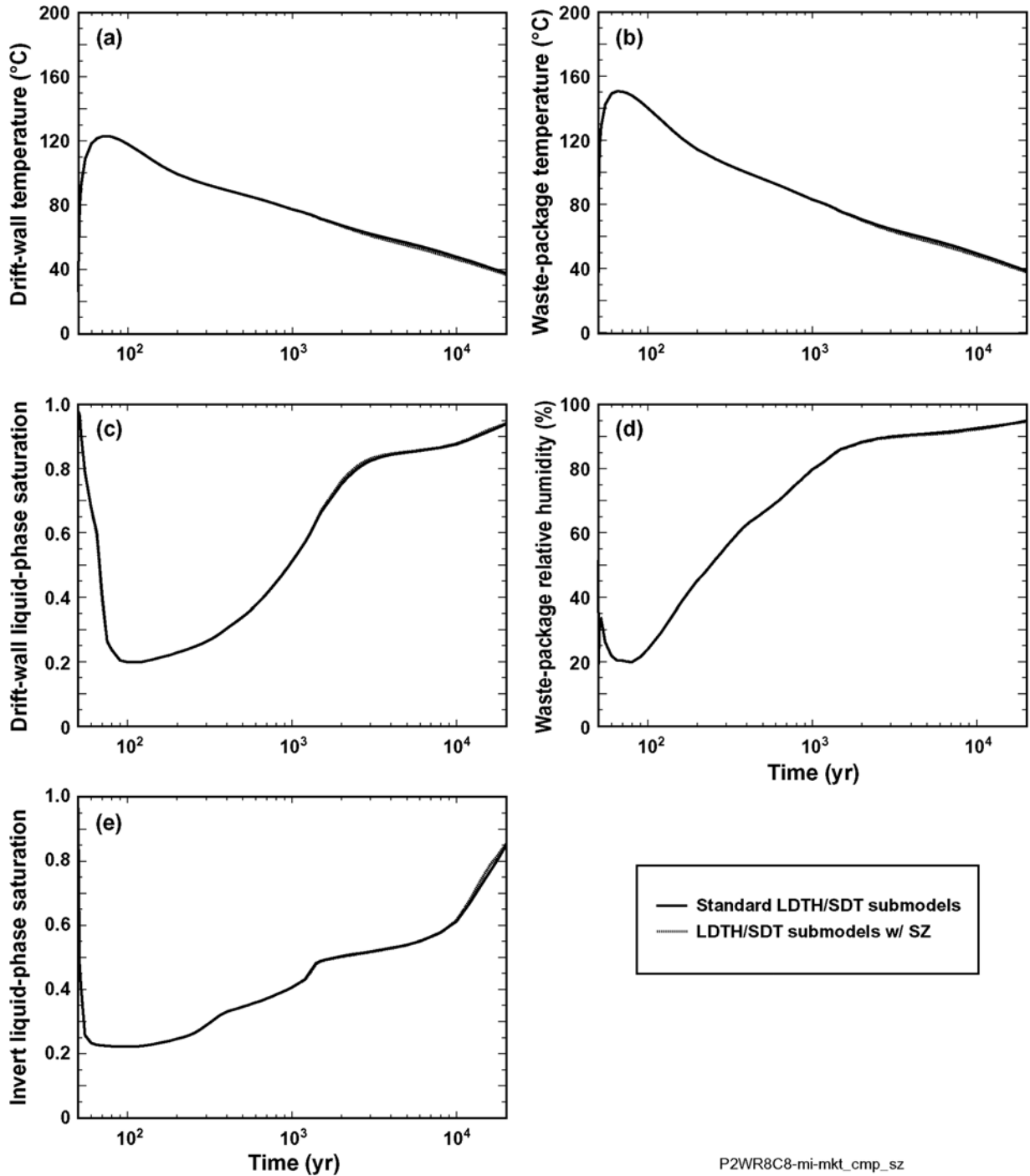
Source: See Table XIII-1.

NOTE: SZ = saturated zone. See Figure 6.3-1 for location. The plotted thermal-hydrologic parameters are (a) drift-wall temperature, (b) waste package temperature, (c) drift-wall liquid-phase saturation, (d) waste package relative humidity, and (e) invert liquid-phase saturation. The standard MSTHM calculation is compared with an alternative MSTHM calculation in which the LDTH and SDT submodels are vertically extended to include the upper 1 km of the saturated zone.

Figure 6.3-18. Thermal-Hydrologic Conditions for the Mean Infiltration-Flux Case Plotted for the pwr1-2 Waste Package at the P2WR8C8 Location in the Tptpmn (tsw34) Unit
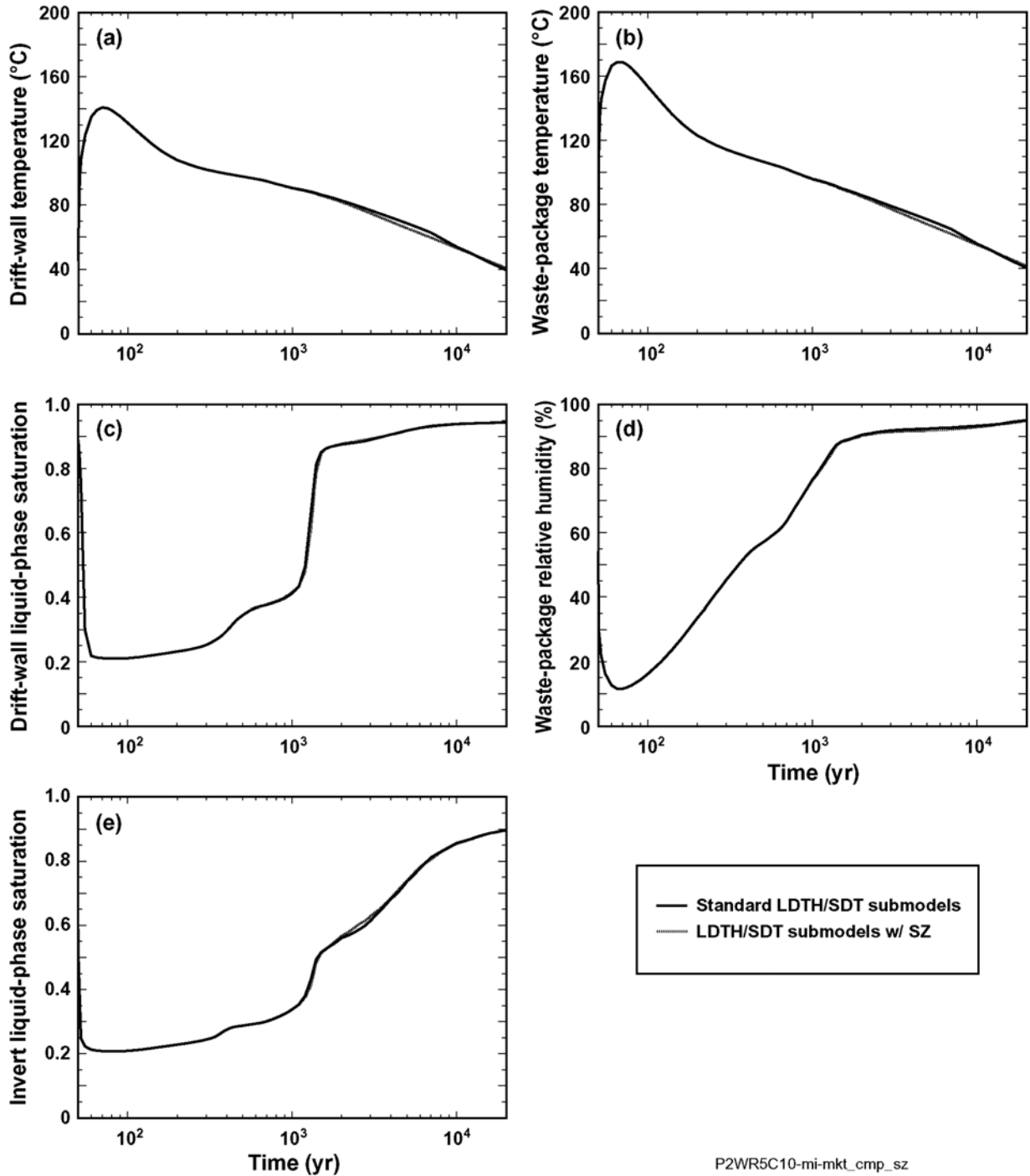
Source: See Table XIII-1.

NOTE: SZ = saturated zone. See Figure 6.3-1 for location. The plotted thermal-hydrologic parameters are (a) drift-wall temperature, (b) waste package temperature, (c) drift-wall liquid-phase saturation, (d) waste package relative humidity, and (e) invert liquid-phase saturation. The standard MSTHM calculation is compared with an alternative MSTHM calculation in which the LDTH and SDT submodels are vertically extended to include the upper 1 km of the saturated zone.

Figure 6.3-19. Thermal-Hydrologic Conditions for the Mean Infiltration-Flux Case Plotted for the pwr1-2 Waste Package at the P2WR5C10 Location in the Tptpll (tsw35) Unit
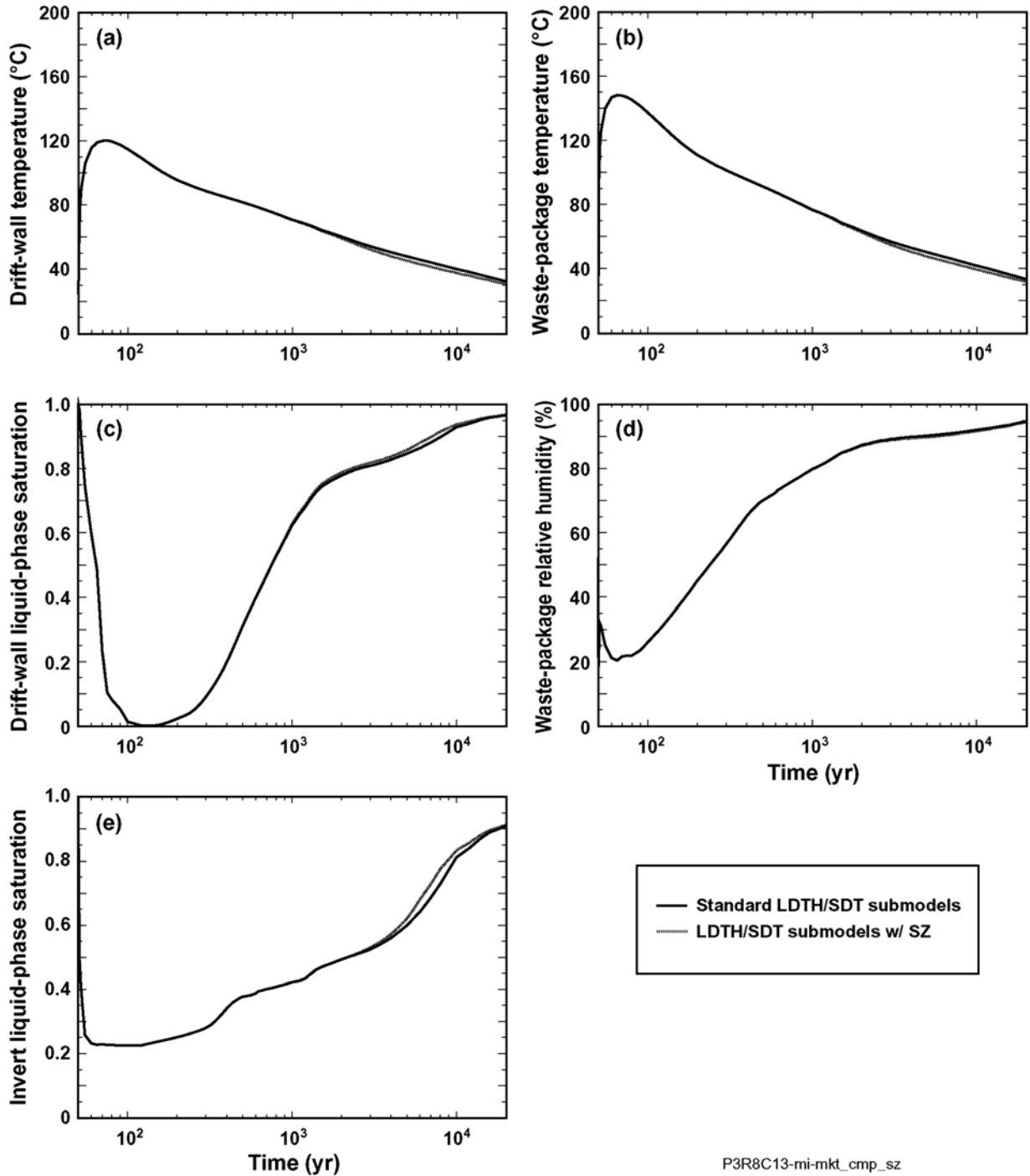
Source: See Table XIII-1.

NOTE: SZ = saturated zone. See Figure 6.3-1 for location). The plotted thermal-hydrologic parameters are (a) drift-wall temperature, (b) waste package temperature, (c) drift-wall liquid-phase saturation, (d) waste package relative humidity, and (e) invert liquid-phase saturation. The standard MSTHM calculation is compared with an alternative MSTHM calculation in which the LDTH and SDT submodels are vertically extended to include the upper 1 km of the saturated zone.

Figure 6.3-20. Thermal-Hydrologic Conditions for the Mean Infiltration-Flux Case Plotted for a Range of Waste Packages at the P3R8C13 Location in the Tptpln (tsw36) Unit

6.3.2 Parameter-Uncertainty Sensitivity Analyses

For MSTHM predictions of thermal-hydrologic conditions within the emplacement drifts and in the adjoining host rock, the key uncertainty parameters (Table 6.3-18) fall into three categories: (1) thermal properties, (2) hydrologic properties, and (3) percolation flux. For thermal and hydrologic properties, the primary focus is the properties of the host rock and of the materials within the emplacement drifts and the ambient percolation flux at the repository horizon.

The primary thermal properties are heat capacity and thermal conductivity. From past analyses, it is known that host-rock heat capacity has an insignificant effect on the thermal-hydrologic response in the drifts and adjacent host rock. This is corroborated by Section 5.3.1.4.10 of *FY 01 Supplemental Science and Performance Analyses, Volume 1: Scientific Bases and Analyses* (BSC 2001 [DIRS 155950]). Similarly, the insensitivity to invert thermal conductivity, within its range of uncertainty, is corroborated by Section 5.3.1.4.10 of that report. Note that the host-rock thermal conductivity was found to be a significant parameter (BSC 2001 [DIRS 155950], Section 5.3.1.4.8); consequently, it is addressed in Sections 6.3.2.2 and 6.3.2.3 of this report.

The primary hydrologic property of interest is the bulk permeability of the host rock, which is primarily affected by the permeability of the fracture network. A sensitivity study of host-rock bulk permeability (BSC 2001 [DIRS 155950], Section 5.3.1.4.7) found the influence to be primarily confined to temperature. Host-rock bulk permeability was found to modestly influence peak temperatures and boiling-period duration. In Section 6.3.9 of this report, temperature and relative humidity were found to be insensitive to a range of host-rock bulk permeability. The influence of coupled thermal-hydrologic-mechanical coupling on permeability is investigated for the Tptpmn (tsw34) and Tptpll (tsw35) host-rock units in *Drift Scale THM Model* (BSC 2004 [DIRS 169864]). There it was found that thermal stresses alter the host-rock permeability in the vertical and horizontal directions. However, these thermal-stress-induced changes in host-rock permeability were concluded to have a small influence on dryout and rewetting (BSC 2004 [DIRS 169864], Section 8.1). Because the effect of host-rock bulk permeability on temperature and relative humidity is insignificant, compared to that of host-rock thermal conductivity uncertainty (which is addressed in Sections 6.3.2.2 and 6.3.2.3), it is unnecessary to further investigate the influence of bulk-permeability uncertainty in this report.

Percolation-flux uncertainty at the repository horizon can result from at least two sources. The first source is the uncertainty concerning the magnitude of infiltration flux, which is addressed by way of lower-bound, mean, and upper-bound infiltration flux cases in Section 6.3.1.1.

The second source of percolation-flux uncertainty concerns the possibility of flow focusing in the UZ model layers between the base of the PTn sequence of units and the repository horizon. The liquid-phase flux distribution applied at the upper boundary of the LDTH submodels of the MSTHM is the percolation-flux distribution (from the base of the PTn unit into the top of the TSw sequence of units) calculated by *UZ Flow Models and Submodels* (BSC 2004 [DIRS 169861]). Flow focusing is the term used to denote the potential concentration of percolation flux from the large-scale average distribution of percolation flux, as simulated by the relatively coarsely gridded three-dimensional UZ flow model, to the drift scale, as simulated by the MSTHM and by *Drift-Scale Coupled Processes (DST and TH Seepage) Models* (BSC 2004 [DIRS 170338]). The impact of flow focusing of ambient percolation flux at the repository horizon is addressed in Sections 6.3.2.1 and 6.3.2.3.

Table 6.3-18. Potentially Important Parameters to Thermal-Hydrologic Conditions in Emplacement Drifts, Listed for Consideration in the Parameter-Uncertainty Sensitivity Analysis.

Parameter	Previous Parameter-Uncertainty Sensitivity Analyses	Importance to In-drift Thermal-Hydrologic Conditions	Parameter-Uncertainty Sensitivity Analyses in This Report
Host-rock heat capacity (which includes influence of specific heat and bulk density)	BSC 2001 [DIRS 155950], Section 5.3.1.4.10	Insignificant	None
Host-rock thermal conductivity	BSC 2001 [DIRS 155950], Section 5.3.1.4.8	Important	Sections 6.3.2.2 and 6.3.2.3
Invert thermal conductivity	BSC 2001 [DIRS 155950], Section 5.3.1.4.10	Insignificant	None
Host-rock bulk permeability	BSC 2001 [DIRS 155950], Section 5.3.1.4.7	Minor influence on temperature, small compared to that of host rock thermal conductivity uncertainty (Sections 6.3.2.2 and 6.3.2.3)	None
Percolation flux	BSC 2001 [DIRS 158204], Sections 6.11 and 6.12	Important	Sections 6.3.1.1, 6.3.2.1, and 6.3.2.3

6.3.2.1 Percolation-Flux Uncertainty at the Repository Horizon, Including the Influence of Flow Focusing

Between the base of the PTn unit and the repository horizon, ambient percolation flux is assumed to be vertically downward with neither lateral diversion nor flow focusing caused by layering or heterogeneity in the hydrologic-property distributions. Section 6.2.1.4 of *Drift-Scale Coupled Processes (DST and TH Seepage) Models* (BSC 2004 [DIRS 170338]) discusses the need to address the potential for flow focusing of percolation flux in the hydrogeologic units above the repository horizon. Flow focusing is the term used to denote the potential concentration of percolation flux from the large-scale distribution of percolation flux, as simulated by the relatively coarsely gridded three-dimensional UZ flow model, to the drift scale, as simulated by the MSTHM and by *Drift-Scale Coupled Processes (DST and TH Seepage) Models* (BSC 2004 [DIRS 170338]). Stochastic modeling analyses discussed in Section 4.3.2 of *FY 01 Supplemental Science and Performance Analyses, Volume 1: Scientific Bases and Analyses* (BSC 2001 [DIRS 155950]), using a two-dimensional, finely gridded vertical cross section of the unsaturated zone, resulted in maximum flow-focusing factors between 5 and 6. In Section 6.2.2.2.4 of *Drift-Scale Coupled Processes (DST and TH Seepage) Models* (BSC 2004 [DIRS 170338]) flow-focusing factors of 5 and 10 were considered in the sensitivity study to percolation flux, resulting in percolation fluxes of 30, 80, and 125 mm/yr for the present-day, monsoonal, and glacial-transition climate states, respectively.

Table 6.3-19 summarizes the percolation fluxes for the low and high percolation-flux cases considered in this study. To better discern the influence of the local host-rock unit on thermal-hydrologic behavior, it was decided to use the same value of present-day percolation flux (25 mm/yr) for the high percolation-flux case at all four locations, thus resulting in an effective flow focusing factor of close to 5 at all locations. To obtain the monsoonal and glacial-transition high percolation-flux values at a given location (Table 6.3-19), the

corresponding percolation flux values in Table 6.3-9 are multiplied by the corresponding factor. Note that the present-day, monsoonal, and glacial-transition high percolation-flux values are similar to those used in Section 6.2.2.2.4 of *Drift-Scale Coupled Processes (DST and TH Seepage) Models* (BSC 2004 [DIRS 170338]) for the case with a factor of 5 (that case used percolation flux values of 30, 80, and 125 mm/yr for the three climate states, respectively).

The low percolation-flux case in Table 6.3-19 corresponds to the possibility of a region of the repository experiencing "flow defocusing," which is the opposite of "flow focusing." Thus, for flow focusing to be able to occur in one region of the repository, it is necessary for adjoining regions to receive less percolation flux than would have occurred without flow focusing. To discern the influence of the local host-rock unit on thermal-hydrologic behavior, it was decided to apply the same value (0.025 mm/yr) to all four locations. Because the low percolation-flux cases are meant to correspond to regions that are, in effect, shielded from significant percolation flux, regardless of the magnitude of repository-wide percolation flux, it was decided to use the same small value of percolation flux for all (three) climate states. Thus, this "defocusing" effect persists during all (three) climate states. It is noted that the low percolation-flux cases considered in this section correspond to persistently small flux values, thereby allowing the dryout and temperature effects of low percolation flux to develop. Note that values of present-day percolation flux vary by a factor of 1,000 between the low and high percolation-flux cases.

Table 6.3-19. Percolation Flux for the Low, Mean, and High Percolation-Flux Cases Summarized for Four Locations Used to Examine Thermal-Hydrologic Conditions in the Repository

LDTH–SDT Submodel Location	Percolation Flux for the Low Percolation-Flux (defocused flow) Case (mm/yr)			Percolation Flux for the High Percolation-Flux (focused flow) Case (mm/yr)			
	Present-Day	Monsoonal	Glacial-Transition	Present-Day	Monsoonal[a]	Glacial-Transition[a]	Effective Focus Factor[b]
P2ER8C6	0.025	0.025	0.025	25.00	54.04	106.3	4.62
P2WR8C8	0.025	0.025	0.025	25.00	58.41	87.47	5.59
P2WR5C10	0.025	0.025	0.025	25.00	77.49	117.18	5.31
P3R8C13	0.025	0.025	0.025	25.00	77.57	111.89	3.54

[a] The monsoonal and glacial-transition percolation flux values for the high percolation-flux case are obtained by multiplying the corresponding percolation flux values in Table 6.3-9 by the effective focus factor for that location.
[b] The effective focus factor is obtained by dividing 25.00 mm/yr by the present-day percolation flux listed for the given location in Table 6.3-9.

NOTE: See Figure 6.2-2 for locations. Values for the mean percolation-flux case are given in Table 6.3-9.

The influence of percolation-flux uncertainty on thermal-hydrologic behavior at four locations (P2ER8C6, P2WR8C8, P2WR5C10, and P3R8C13) in the repository (see Figure 6.3-1 for locations) is shown in time histories of drift-wall temperature and liquid-phase saturation, waste package temperature and relative humidity, and invert liquid-phase saturation (Figures 6.3-21 through 6.3-24) for a 21-PWR AP CSNF waste package. Percolation-flux uncertainty is seen to have a small influence on peak drift-wall temperature (Table 6.3-20) and on peak waste package temperature (Table 6.3-21). Peak drift-wall temperatures only vary by 3.7 to 5.2 percent and peak waste package temperatures only vary by 2.9 to 4.3 percent for a 1,000-fold range of percolation flux. Compared to its influence on peak temperatures, percolation-flux uncertainty has a much stronger influence on the duration of boiling (Table 6.3-22). The sensitivity of

boiling-period duration to percolation-flux uncertainty is greatest for those locations with the longest boiling-period duration, which correspond to locations near the center of the repository where the extent of rock dryout has more time to develop. Thus locations P2ER8C6 and P3R8C13, which are at the repository edges have the smallest sensitivity to percolation-flux uncertainty, while location P2WR5C10, which is close to the center of the repository, has the greatest sensitivity.

Percolation-flux uncertainty has a strong influence on dryout/rewetting behavior, as shown in the drift-wall and invert liquid-phase saturation histories (Figures 6.3-21c, 6.3-21e, 6.3.22c, 6.3.22e, 6.3-23c, 6.3-23e, 6.3-24c, and 6.3-24e). Similarly, it also has a strong influence on the waste package relative humidity histories (Figures 6.3-21d, 6.3-22d, 6.3-23d, and 6.3-24d). Because the relative humidity at the drift wall depends on the liquid-phase saturation (as well as on temperature) at the drift wall, the variability of drift-wall relative humidity is similar to that of drift-wall liquid-phase saturation. Relative humidity on a given waste package depends on relative humidity at the adjacent drift wall. The large differences in drift-wall liquid-phase saturation histories (between the low and high percolation-flux cases) result in large differences in waste package relative humidity histories between the flux cases.

Table 6.3-20. Range of Peak Drift-Wall Temperatures for the pwr1-2 Waste Package (Resulting from Percolation-Flux Uncertainty) Summarized for Four Locations in the Repository

LDTH–SDT Submodel Location	Host-Rock Unit	Peak Drift-Wall Temperature (°C)				
		Low Percolation Flux	Mean Percolation Flux	High Percolation Flux	Low to High Range	Low to High Range[a]
P2ER8C6	Tptpul (tsw33)	138.9	135.5	131.9	7.0	5.2%
P2WR8C8	Tptpmn (tsw34)	124.5	123.0	119.4	5.1	4.2%
P2WR5C10	Tptpll (tsw35)	144.1	140.8	137.2	6.9	4.9%
P3R8C13	Tptpln (tsw36)	121.9	120.2	117.5	4.4	3.7%

[a] The range (%) is the range (°C) divided by the peak drift-wall temperature [(low + high)/2].

NOTE: See Figure 6.3-1 for locations. The pwr1-2 (21-PWR AP CSNF) waste package is the hottest waste package in the sequence (Figure 6.2-2). These values are based on data plotted in Figures 6.3-21 through 6.3-29.

Table 6.3-21. Range of Peak Waste Package Temperatures for the pwr1-2 Waste Package (Resulting from Percolation-Flux Uncertainty) Summarized for Four Locations in the Repository

LDTH–SDT Submodel Location	Host-Rock Unit	Peak Waste Package Temperature (°C)				
		Low Percolation Flux	Mean Percolation Flux	High Percolation Flux	Low to High Range	Low to High Range[a]
P2ER8C6	Tptpul (tsw33)	166.5	163.2	159.5	7.0	4.3%
P2WR8C8	Tptpmn (tsw34)	151.7	150.6	147.4	4.3	2.9%
P2WR5C10	Tptpll (tsw35)	172.4	168.8	165.4	7.0	4.1%
P3R8C13	Tptpln (tsw36)	149.9	148.2	145.9	4.0	2.7%

[a] The range (%) is the range (°C) divided by the peak drift-wall temperature [(low + high)/2].

NOTE: See Figure 6.3-1 for locations. The pwr1-2 (21-PWR AP CSNF) waste package is the hottest waste package in the sequence (Figure 6.2-2). These values are based on data plotted in Figures 6.3-21 through 6.3-29.

Table 6.3-22. Range of Time When Boiling at the Drift Wall Ceases for the pwr1-2 Waste Package (Resulting from Percolation-Flux Uncertainty) Summarized for Four Locations in the Repository

LDTH–SDT Submodel Location	Host-Rock Unit	Time When Boiling at the Drift Wall Ceases (years)				
		Low Percolation Flux	Mean Percolation Flux	High Percolation Flux	Low to High Range	Low to High Range[a]
P2ER8C6	Tptpul (tsw33)	438.1	364.8	313.3	124.8	33.2%
P2WR8C8	Tptpmn (tsw34)	286.1	242.8	197.7	88.4	36.5%
P2WR5C10	Tptpll (tsw35)	896.9	623.0	385.4	484.5	75.6%
P3R8C13	Tptpln (tsw36)	224.2	195.2	175.2	49.0	24.5%

[a] The range (%) is the range (years) divided by the average time when drift-wall boiling ceases [(shortest + longest)/2].

NOTE: See Figure 6.3-1 for locations. The pwr1-2 (21-PWR AP CSNF) waste package is the hottest waste package in the sequence (Figure 6.2-2). These values are based on data plotted in Figures 6.3-21 through 6.3-29.
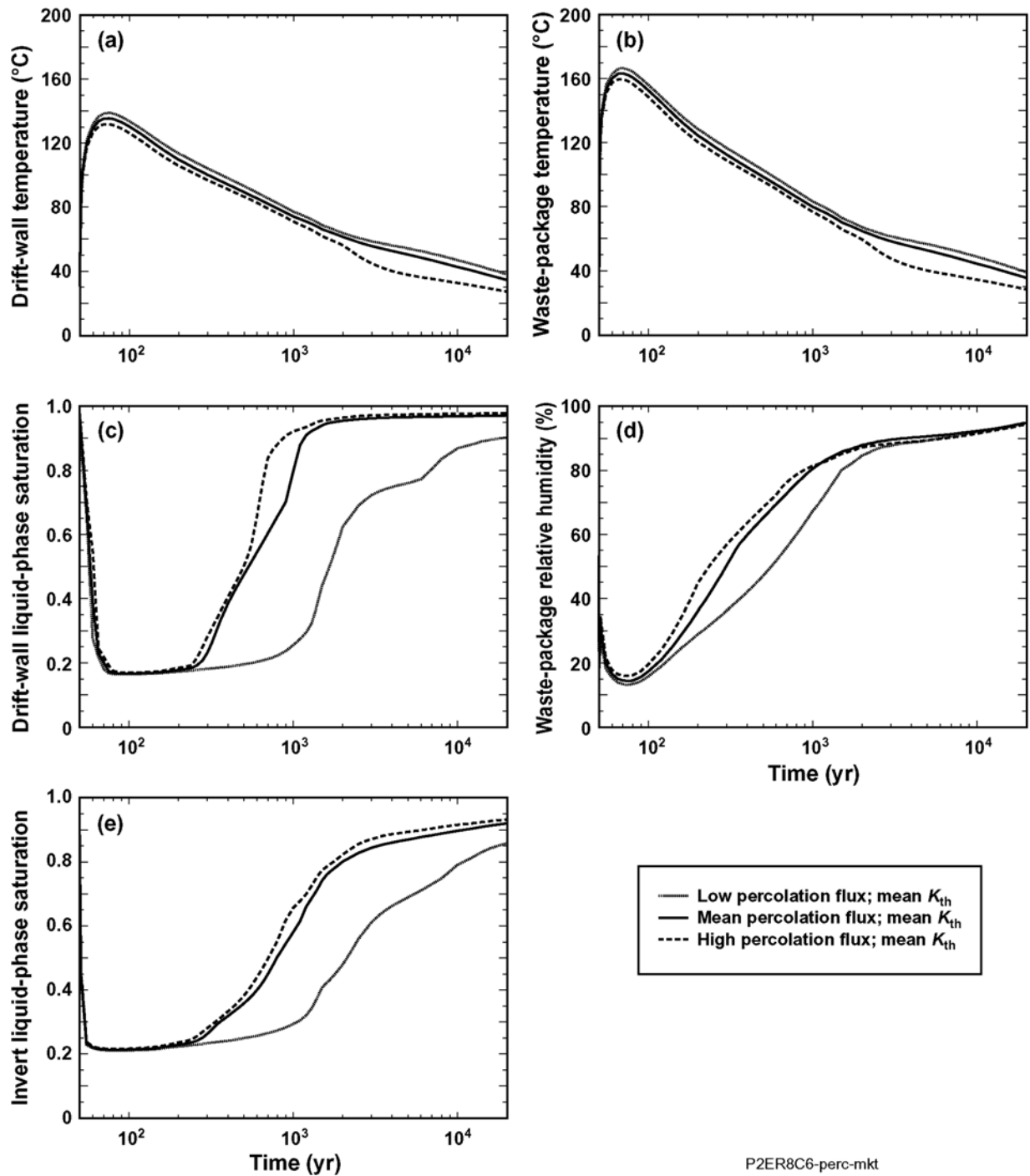
Source: See Table XIII-1.

NOTE: See Figure 6.3-1 for location. The plotted thermal-hydrologic parameters are (a) drift-wall temperature, (b) waste package temperature, (c) drift-wall liquid-phase saturation, (d) waste package relative humidity, and (e) invert liquid-phase saturation. The pwr1-2 (21-PWR AP CSNF) waste package is the hottest waste package in the sequence (Figure 6.2-2).

Figure 6.3-21. Thermal-Hydrologic Conditions for the pwr1-2 Waste Package Plotted for the Low, Mean, and High Percolation-Flux Cases at the P2ER8C6 Location in the Tptpul (tsw33) Unit
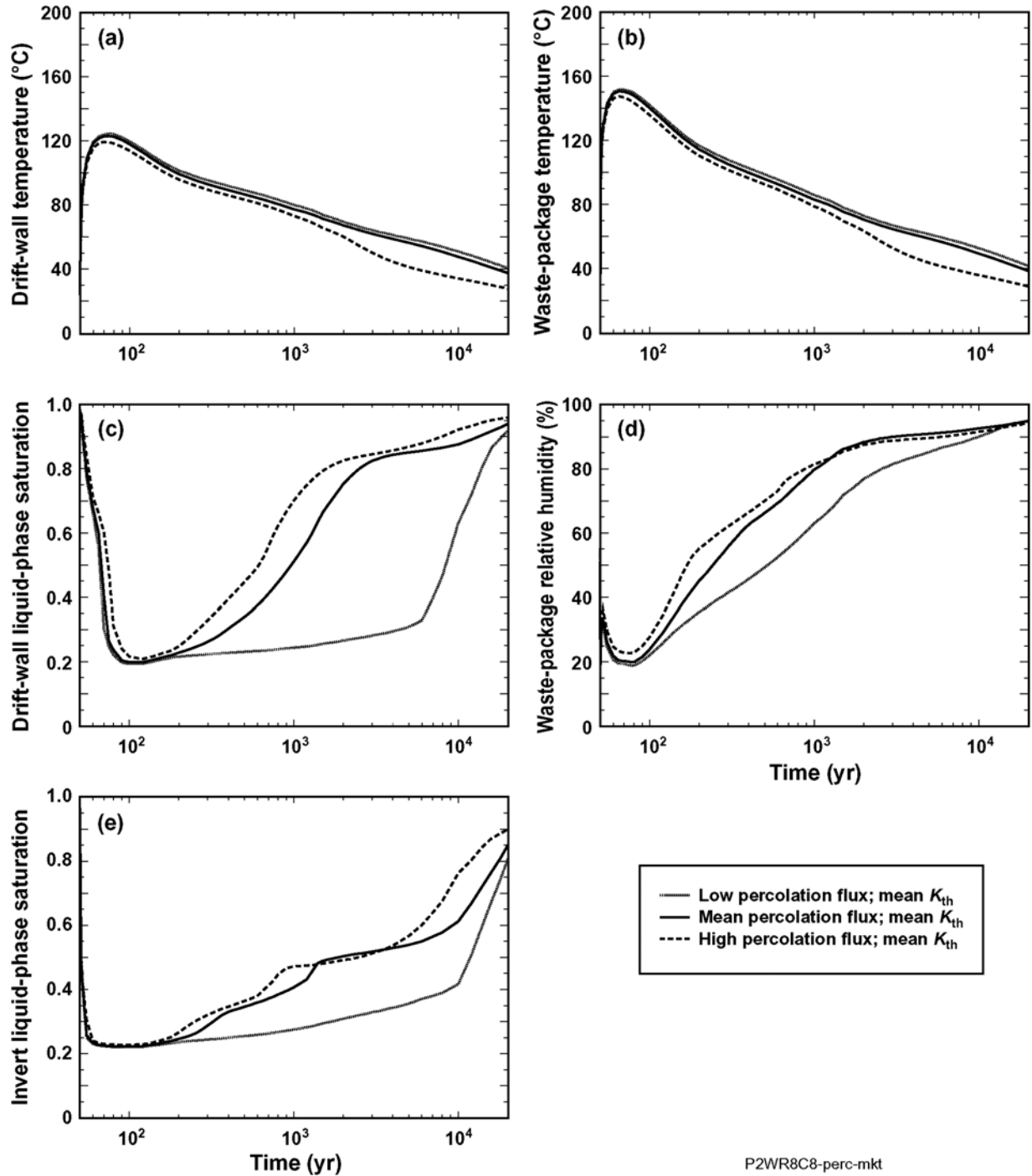
Source: See Table XIII-1.

NOTE: See Figure 6.3-1 for location. The plotted thermal-hydrologic parameters are (a) drift-wall temperature, (b) waste package temperature, (c) drift-wall liquid-phase saturation, (d) waste package relative humidity, and (e) invert liquid-phase saturation. The pwr1-2 (21-PWR AP CSNF) waste package is the hottest waste package in the sequence (Figure 6.2-2).

Figure 6.3-22. Thermal-Hydrologic Conditions for the pwr1-2 Waste Package Plotted for the Low, Mean, and High Percolation-Flux Cases at the P2WR8C8 Location in the Tptpmn (tsw34) Unit
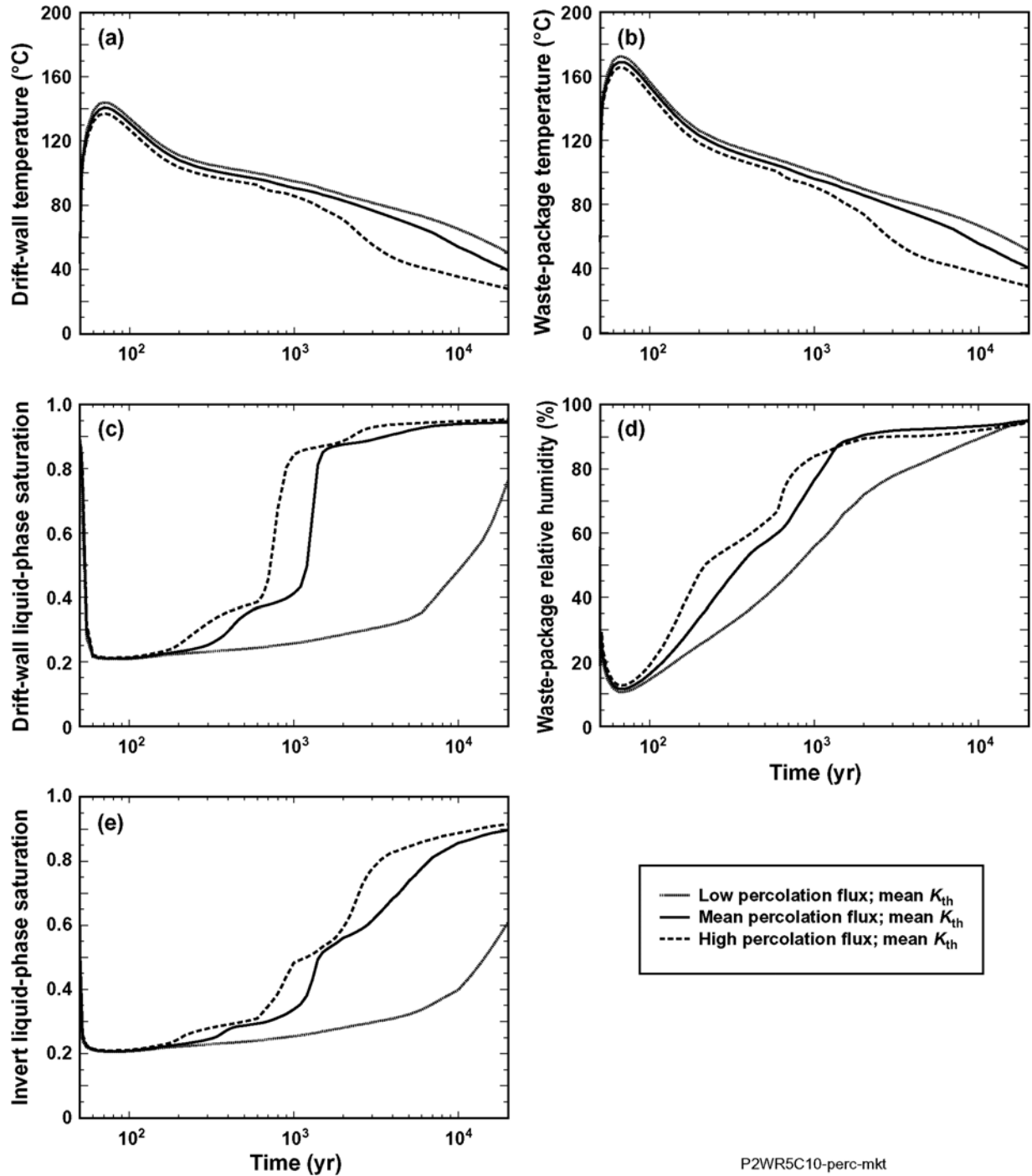
Source: See Table XIII-1.

NOTE: See Figure 6.3-1 for location. The plotted thermal-hydrologic parameters are (a) drift-wall temperature, (b) waste package temperature, (c) drift-wall liquid-phase saturation, (d) waste package relative humidity, and (e) invert liquid-phase saturation. The pwr1-2 (21-PWR AP CSNF) waste package is the hottest waste package in the sequence (Figure 6.2-2).

Figure 6.3-23. Thermal-Hydrologic Conditions for the pwr1-2 Waste Package Plotted for the Low, Mean, and High Percolation-Flux Cases at the P2WR5C10 Location in the Tptpll (tsw35) Unit
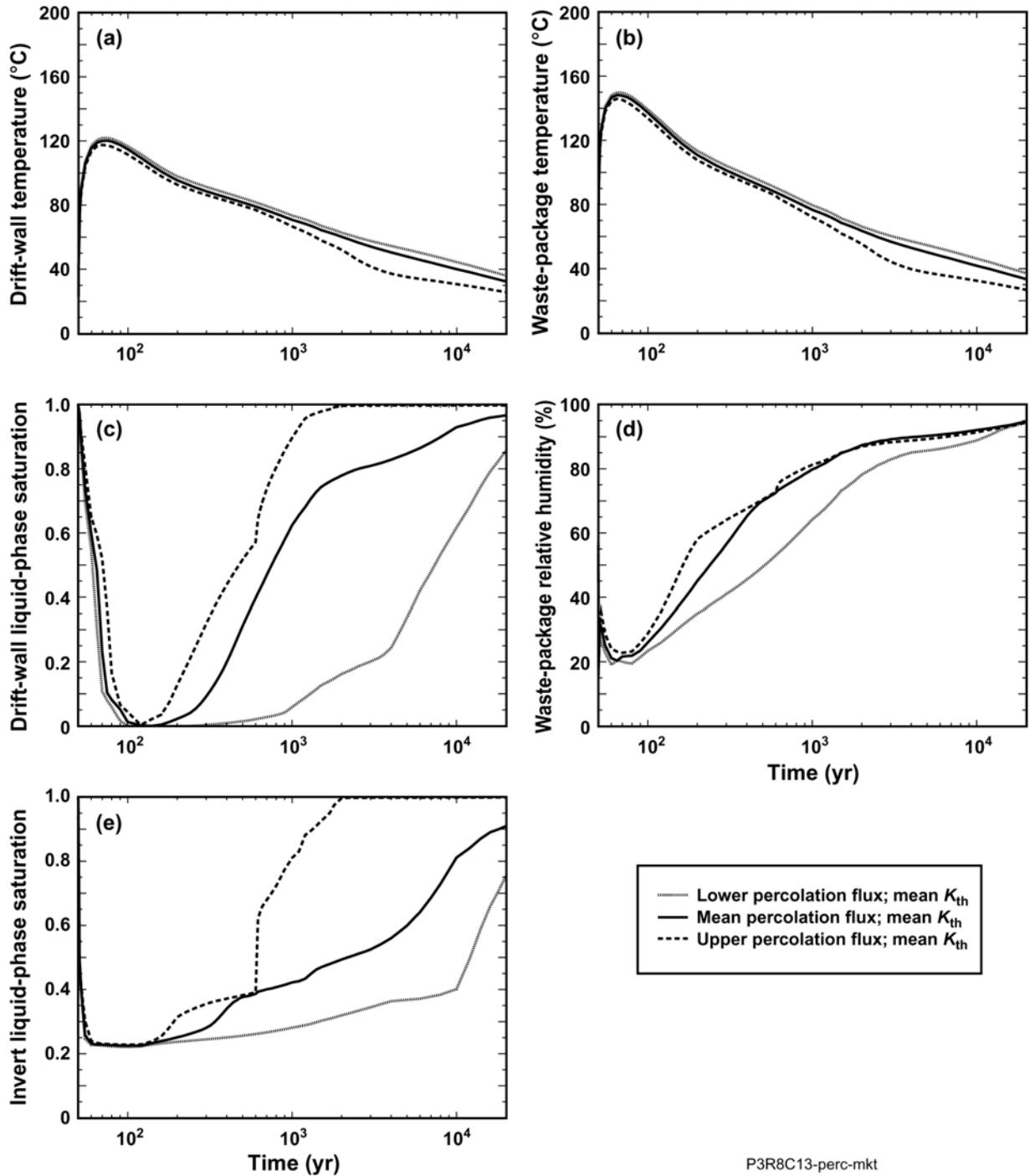
Source: See Table XIII-1.

NOTE: See Figure 6.3-1 for location. The plotted thermal-hydrologic parameters are (a) drift-wall temperature, (b) waste package temperature, (c) drift-wall liquid-phase saturation, (d) waste package relative humidity, and (e) invert liquid-phase saturation. The pwr1-2 (21-PWR AP CSNF) waste package is the hottest waste package in the sequence (Figure 6.2-2).

Figure 6.3-24. Thermal-Hydrologic Conditions for the pwr1-2 Waste Package Plotted for the Low, Mean, and High Percolation-Flux Cases at the P3R8C13 Location in the Tptpln (tsw36) Unit

6.3.2.2 Host-Rock Thermal Conductivity Uncertainty

The sensitivity of thermal-hydrologic behavior to host-rock thermal conductivity uncertainty is addressed for ranges that extend approximately ±1 standard deviation about the mean value (Table 6.3-23). The thermal conductivity data from Table 7-10 of DTN: SN0404T0503102.011 [DIRS 169129] (File: ReadMeSummary.doc) are used to determine the ranges for the wet and dry thermal conductivity values for the four host-rock units. Note that the mean values of K_{th} of the Tptpul (tsw33) unit are slightly different from those in Table 7-10 of DTN: SN0404T0503102.011 [DIRS 169129] (File: ReadMeSummary.doc). To be consistent with the other thermal-hydrologic models, such as those in *Drift-Scale Coupled Processes (DST and TH Seepage) Models* (BSC 2004 [DIRS 170338]), K_{th} for the Tptpul (tsw33) unit is computed as a straight arithmetic average of K_{th} for the Tptpul from Table 7-10 of DTN: SN0404T0503102.011 [DIRS 169129] (File: ReadMeSummary.doc) and the K_{th} of the Tptrl from DTN: SN0303T0503102.008 [DIRS 162401] (row 66). This averaging for the Tptpul (tsw33) unit is also applied to the other thermal properties to be consistent with *Drift-Scale Coupled Processes (DST and TH Seepage) Models* (BSC 2004 [DIRS 170338]), which computes the thermal properties (including K_{th}) of the Tptpul (tsw33) unit to be the average of the thermal properties of the Tptpul from Table 7-10 of DTN: SN0404T0503102.011 [DIRS 169129] (File: ReadMeSummary.doc) and the thermal properties of the Tptrl unit from DTN: SN0303T0503102.008 [DIRS 162401] (row 66).

For all locations, host-rock thermal conductivity uncertainty has a strong influence on peak temperatures (Table 6.3-25) and on boiling duration (Table 6.3-26), with the influence being stronger for locations closer to the repository center. Thus, the P2WR5C10 location, which is located close to the center of the repository, has the widest range (114.3 percent) of the time when boiling at the drift wall ceases. Locations P2ER8C6 and P3R8C13, which are at the edge of the repository, have somewhat smaller ranges (65.2 percent and 75.4 percent, respectively) of the time when boiling ceases at the drift wall.

Host-rock thermal conductivity uncertainty has a strong influence on dryout/rewetting behavior for the first 1,000 to 2,000 years, as shown in the drift-wall and invert liquid-phase saturation histories (Figures 6.3-25c, 6.3-25e, 6.3.26c, 6.3.26e, 6.3-27c, 6.3-27e, 6.3-28c, and 6.3-28e). Similarly, host-rock thermal conductivity uncertainty also has a strong influence on the waste package relative humidity histories for the first one- to two-thousand years (Figures 6.3-21d, 6.3-22d, 6.3-23d, and 6.3-24d).

Table 6.3-23. Wet and Dry Thermal Conductivity Values Used in the Host-Rock Thermal Conductivity Uncertainty Study

Host-Rock Unit	Dry Thermal Conductivity (W/m °C)			Wet Thermal Conductivity (W/m °C)		
	Low	Mean	High	Low	Mean	High
Tptpul (tsw33)	0.9842	1.24	1.4958	1.5405	1.79	2.0395
Tptpmn (tsw34)	1.1544	1.42	1.6856	1.8188	2.07	2.3212
Tptpll (tsw35)	1.0286	1.28	1.5314	1.6415	1.89	2.1385
Tptpln (tsw36)	1.2056	1.49	1.7744	1.8624	2.13	2.3976

NOTE: Low, mean, and high thermal conductivity cases are considered for ranges that extend approximately ±1 standard deviation about the mean value. With the exception of the mean values of K_{th} for the Tptpul (tsw33) unit, these values are taken from Table 7-10 of DTN: SN0404T0503102.011 [DIRS 169129] (File: ReadMeSummary.doc). The mean values of K_{th} for the Tptpul (tsw33) unit are a straight arithmetic averages of the mean K_{th} values for the Tptpul from Table 7-10 of DTN: SN0404T0503102.011 [DIRS 169129] (File: ReadMeSummary.doc) and the mean K_{th} of the Tptrl from DTN: SN0303T0503102.008 [DIRS 162401] (row 66). Also note that Table IV-3a in Appendix IV lists K_{th} for the Tptpul unit from Table 7-10 of DTN: SN0404T0503102.011 [DIRS 169129] (File: ReadMeSummary.doc) and K_{th} for the Tptrl unit from DTN: SN0303T0503102.008 [DIRS 162401]. The standard deviations for the Tptpul (tsw33) in Table 7-10 of DTN: SN0404T0503102.011 [DIRS 169129] (File: ReadMeSummary.doc) are divided by the corresponding mean K_{th} values to obtain the percentage differences for plus and minus one standard deviation. These percentages are then applied to the arithmetic-averaged mean K_{th} for the Tptpul (tsw33) unit to obtain the plus and minus one-standard-deviation values of K_{th} for the Tptpul (tsw33) unit.

Table 6.3-24. Range of Peak Drift-Wall Temperatures for the pwr1-2 Waste Package (Resulting from Thermal Conductivity Uncertainty) Summarized for Four Locations in the Repository

LDTH–SDT Submodel Location	Host-Rock Unit	Peak Drift-Wall Temperature (°C)				
		Low Thermal Conductivity	Mean Thermal Conductivity	High Thermal Conductivity	Low to High Range	Low to High Range[a]
P2ER8C6	Tptpul (tsw33)	153.3	135.5	123.2	30.1	21.8%
P2WR8C8	Tptpmn (tsw34)	136.5	123.0	113.8	22.7	18.1%
P2WR5C10	Tptpll (tsw35)	158.9	140.8	127.4	31.5	22.0%
P3R8C13	Tptpln (tsw36)	132.7	120.2	110.8	21.9	18.0%

[a] The range (%) is the range (°C) divided by the peak drift-wall temperature [(low + high)/2].

NOTE: See Figure 6.3-1 for locations. The pwr1-2 (21-PWR AP CSNF) waste package is the hottest waste package in the sequence (Figure 6.2-2). Low, mean, and high thermal conductivity cases are considered for a range of plus and minus one standard deviation about the mean value. These values are based on data plotted in Figures 6.3-25 through 6.3-28.

Table 6.3-25. Range of Peak Waste Package Temperatures for the pwr1-2 Waste Package (Resulting from Thermal Conductivity Uncertainty) Summarized for Four Locations in the Repository

LDTH–SDT Submodel Location	Host-Rock Unit	Peak Waste Package Temperature (°C)				
		Low Thermal Conductivity	Mean Thermal Conductivity	High Thermal Conductivity	Low to High Range	Low to High Range[a]
P2ER8C6	Tptpul (tsw33)	181.2	163.2	151.4	29.8	17.9%
P2WR8C8	Tptpmn (tsw34)	163.8	150.6	141.9	21.9	14.3%
P2WR5C10	Tptpll (tsw35)	187.2	168.8	155.8	31.4	18.3%
P3R8C13	Tptpln (tsw36)	160.6	148.2	139.2	21.4	14.3%

[a] The range (%) is the range (°C) divided by the peak drift-wall temperature [(low + high)/2].

NOTE: See Figure 6.3-1 for locations. The pwr1-2 (21-PWR AP CSNF) waste package is the hottest waste package in the sequence (Figure 6.2-2). Low, mean, and high thermal conductivity cases are considered for a range of plus and minus one standard deviation about the mean value. These values are based on data plotted in Figures 6.3-25 through 6.3-28.

Table 6.3-26. Range of Time When Boiling at the Drift Wall Ceases for the pwr1-2 Waste Package (Resulting from Host-Rock Thermal Conductivity Uncertainty) Summarized for Four Locations in the Repository

LDTH–SDT Submodel Location	Host-Rock Unit	Time When Boiling at the Drift Wall Ceases (years)				
		Low Thermal Conductivity	Mean Thermal Conductivity	High Thermal Conductivity	Low to High Range	Low to High Range[a]
P2ER8C6	Tptpul (tsw33)	508.9	364.8	258.9	250.0	65.2%
P2WR8C8	Tptpmn (tsw34)	412.8	242.8	163.8	249.0	86.4%
P2WR5C10	Tptpll (tsw35)	963.8	623.0	263.0	700.8	114.3%
P3R8C13	Tptpln (tsw36)	309.0	195.2	139.8	169.2	75.4%

[a] The range (%) is the range (years) divided by the average time when drift-wall boiling ceases [(shortest + longest)/2].

NOTE: See Figure 6.3-1 for locations. The pwr1-2 (21-PWR AP CSNF) waste package is the hottest waste package in the sequence (Figure 6.2-2). Low, mean, and high thermal conductivity cases are considered for a range of plus and minus one standard deviation about the mean value. These values are based on data plotted in Figures 6.3-25 through 6.3-28.

Source: See Table XIII-1.

NOTE: See Figure 6.3-1 for location. Low, mean, and high thermal conductivity cases are considered for a range of plus and minus one standard deviation about the mean value. The plotted thermal-hydrologic parameters are (a) drift-wall temperature, (b) waste package temperature, (c) drift-wall liquid-phase saturation, (d) waste package relative humidity, and (e) invert liquid-phase saturation. The pwr1-2 (21-PWR AP CSNF) waste package is the hottest waste package in the sequence (Figure 6.2-2).

Figure 6.3-25. Thermal-Hydrologic Conditions for the pwr1-2 Waste Package Plotted for the Mean Infiltration-Flux Case at the P2ER8C6 Location in the Tptpul (tsw33) Unit
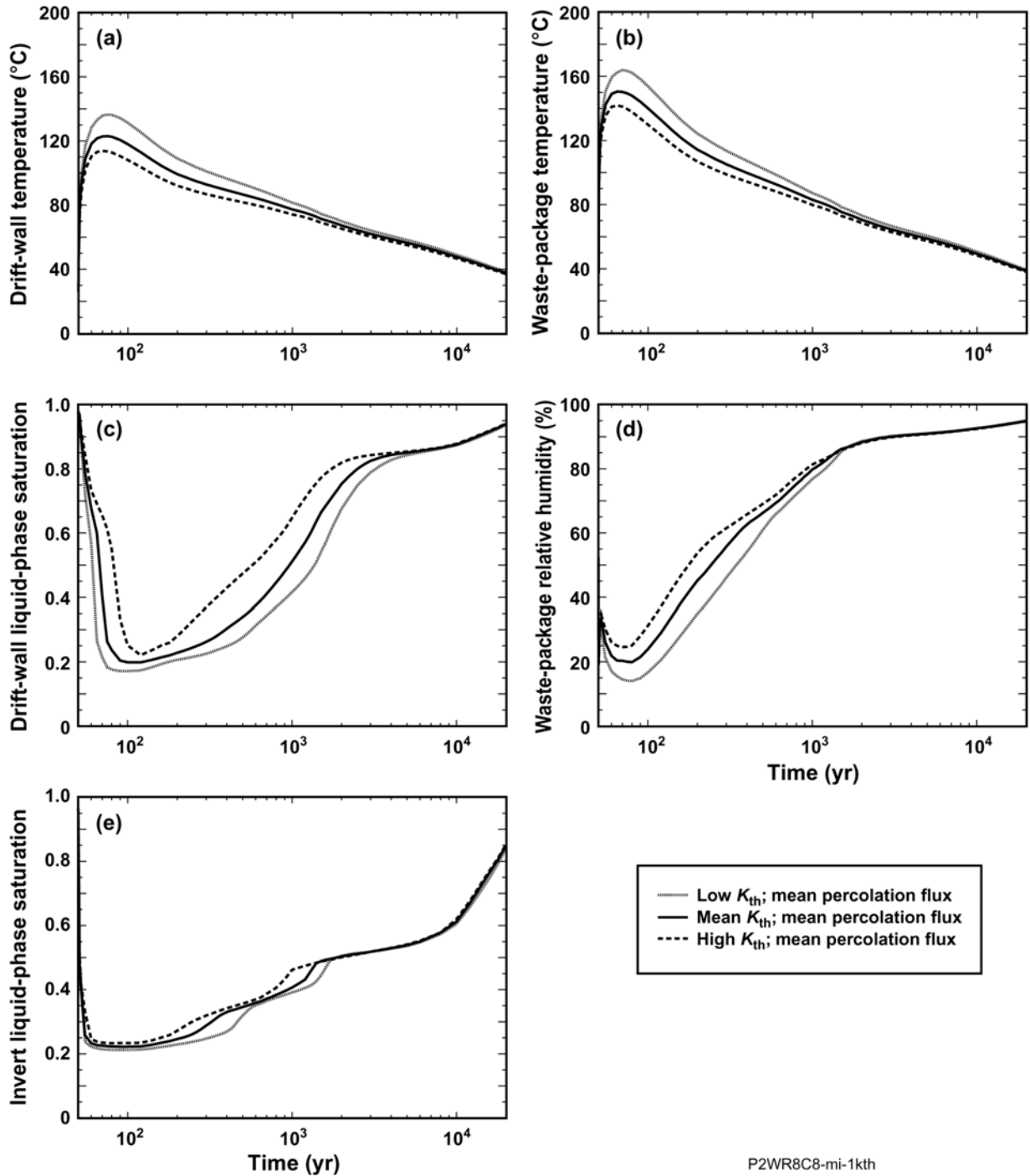
Source: See Table XIII-1.

NOTE: See Figure 6.3-1 for location. Low, mean, and high thermal conductivity cases are considered range of plus and minus one standard deviation about the mean value. The plotted thermal-hydrologic parameters are (a) drift-wall temperature, (b) waste package temperature, (c) drift-wall liquid-phase saturation, (d) waste package relative humidity, and (e) invert liquid-phase saturation. The pwr1-2 (21-PWR AP CSNF) waste package is the hottest waste package in the sequence (Figure 6.2-2).

Figure 6.3-26. Thermal-Hydrologic Conditions for the pwr1-2 Waste Package Plotted for the Mean Infiltration-Flux Case at the P2WR8C8 Location in the Tptpmn (tsw34) Unit
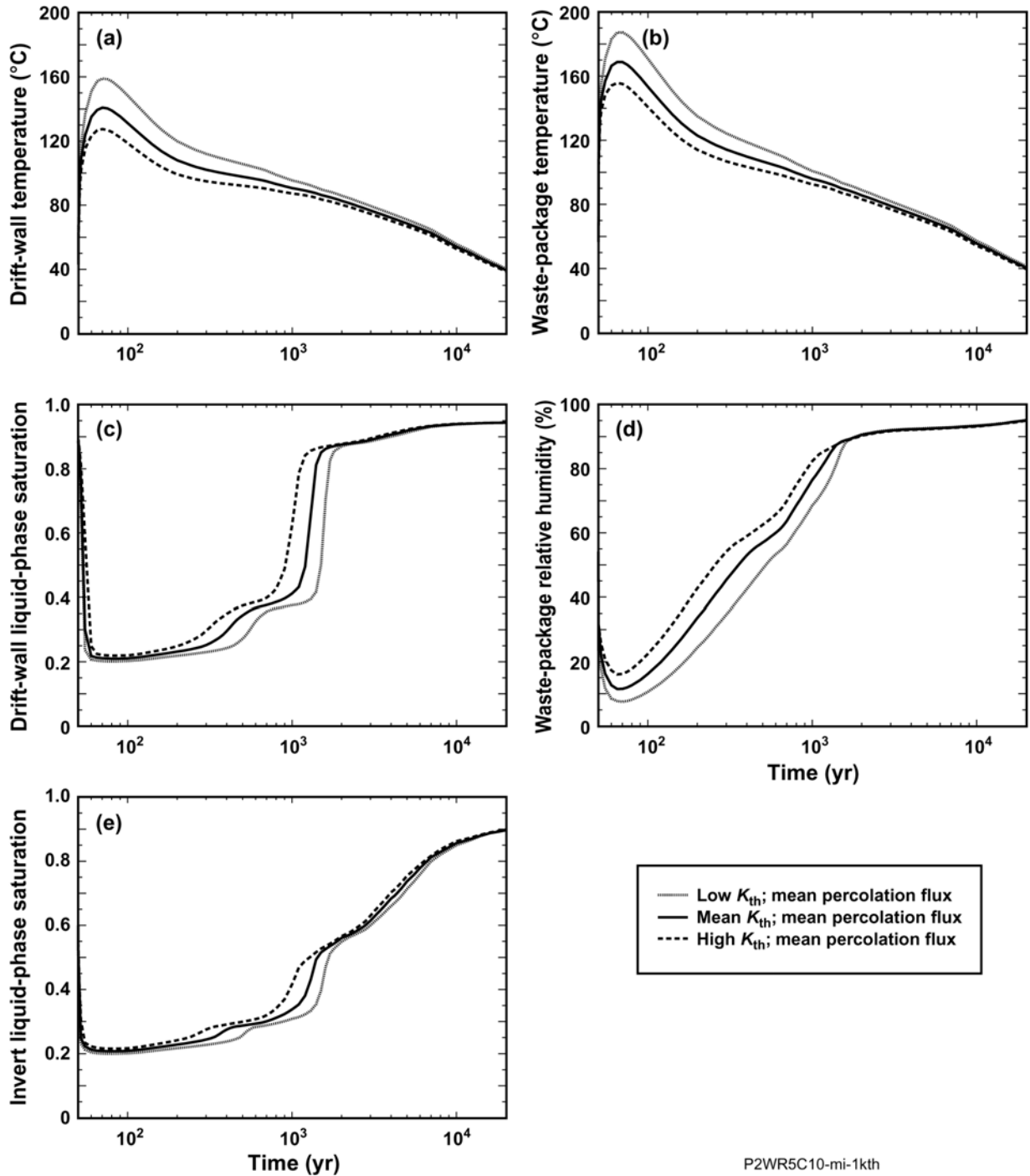
Source: See Table XIII-1.

NOTE: See Figure 6.3-1 for location. Low, mean, and high thermal conductivity cases are considered for a range of plus and minus one standard deviation about the mean value. The plotted thermal-hydrologic parameters are (a) drift-wall temperature, (b) waste package temperature, (c) drift-wall liquid-phase saturation, (d) waste package relative humidity, and (e) invert liquid-phase saturation. The pwr1-2 (21-PWR AP CSNF) waste package is the hottest waste package in the sequence (Figure 6.2-2).

Figure 6.3-27. Thermal-Hydrologic Conditions for the pwr1-2 Waste Package Plotted for the Mean Infiltration-Flux Case at the P2WR5C10 Location in the Tptpll (tsw35) Unit
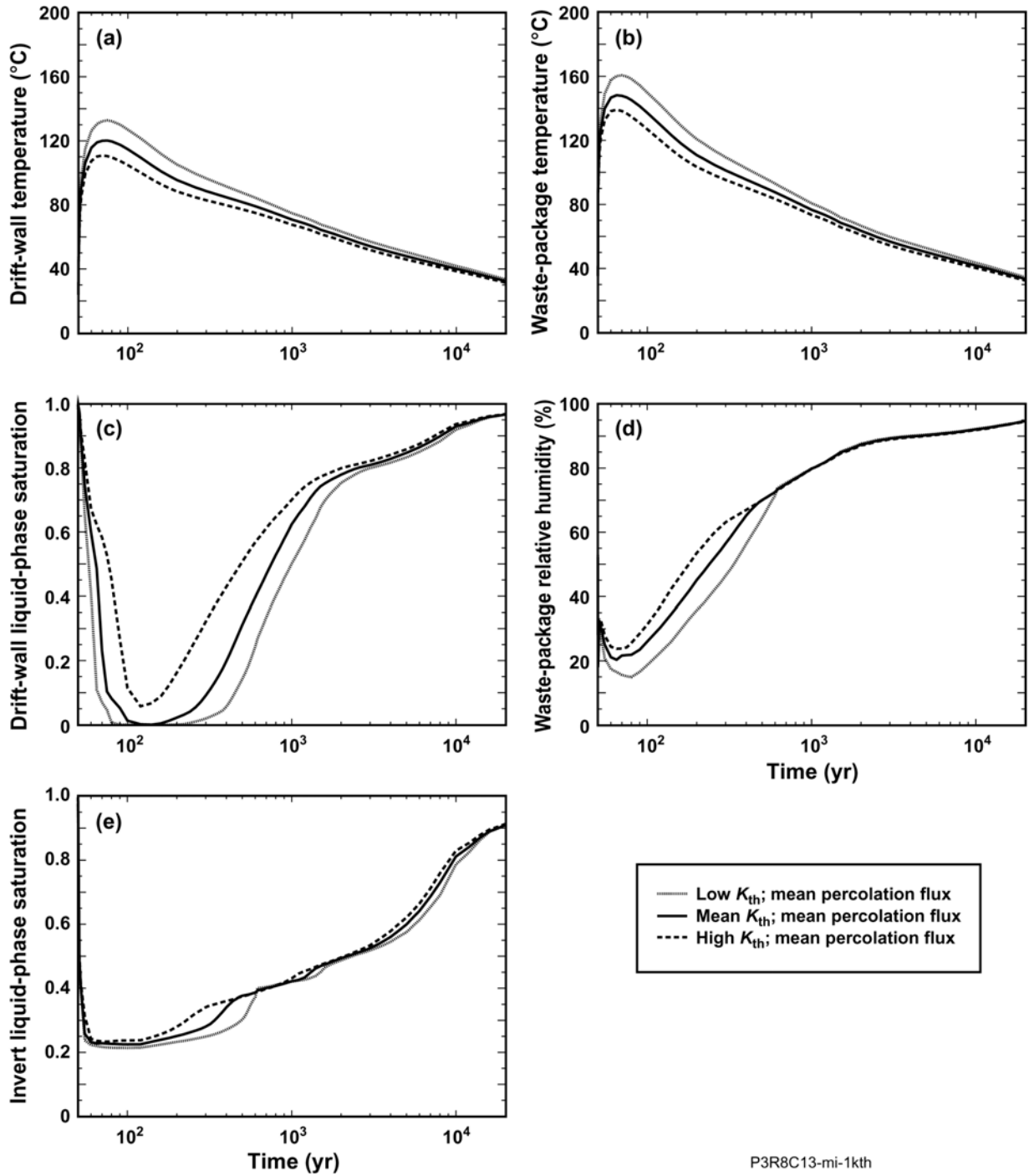
Source: See Table XIII-1.

NOTE: See Figure 6.3-1 for location. Low, mean, and high thermal conductivity cases are considered for a range
         of plus and minus one standard deviation about the mean value. The plotted thermal-hydrologic
         parameters are (a) drift-wall temperature, (b) waste package temperature, (c) drift-wall liquid-phase
         saturation, (d) waste package relative humidity, and (e) invert liquid-phase saturation. The pwr1-2
         (21-PWR AP CSNF) waste package is the hottest waste package in the sequence (Figure 6.2-2).

Figure 6.3-28. Thermal-Hydrologic Conditions for the pwr1-2 Waste Package Plotted for the Mean
               Infiltration-Flux Case at the P3R8C13 Location in the Tptpln (tsw36) Unit

6.3.2.3 Combined Influence of Percolation Flux and Host-Rock Thermal Conductivity Uncertainty, Including the Influence of Flow Focusing

In this section, the combined influence of percolation-flux uncertainty and host-rock thermal conductivity uncertainty on thermal-hydrologic behavior at four locations (P2ER8C6, P2WR8C8, P2WR5C10, and P3R8C13) in the repository (Figure 6.3-1) is shown in time histories of drift-wall temperature and liquid-phase saturation, waste package temperature and relative humidity, and invert liquid-phase saturation (Figures 6.3-29 through 6.3-32) for a 21-PWR AP CSNF waste package. Three cases are considered: (1) low percolation flux and low host-rock thermal conductivity, (2) mean percolation flux and mean host rock thermal conductivity, and (3) high percolation flux and high host-rock thermal conductivity. The values of present-day, monsoonal, and glacial-transition percolation flux values for the low and high percolation-flux cases are summarized in Table 6.3-19; the mean percolation flux values are summarized in Table 6.3-9. The values of dry and wet host-rock thermal conductivity for the low, mean, and high thermal conductivity cases are summarized in Table 6.3-23. Note that the values of percolation flux for these cases are the same as those considered in Section 6.3.2.1 and that the values of host-rock thermal conductivity are the same as those considered in Section 6.3.2.2. Low percolation flux and low host-rock thermal conductivity both result in higher peak temperatures and longer boiling durations. High percolation flux and high host-rock thermal conductivity both result in lower peak temperatures and shorter boiling durations. The range of peak drift-wall and waste package temperatures that result from the two extreme combinations of percolation flux and thermal conductivity are summarized in Tables 6.3-27 and 6.3-28, respectively; the range of the time when boiling on the drift wall ceases is summarized in Table 6.3-29.

Table 6.3-27. Range of Peak Drift-Wall Temperatures for the pwr1-2 Waste Package (Resulting from a Combination of Percolation Flux Q_{perc} and Thermal Conductivity K_{th} Uncertainty) Summarized for Four Locations in the Repository

LDTH–SDT Submodel Location	Host-Rock Unit	Peak Drift-Wall Temperature (°C)				
		Low Q_{perc} Low K_{th}	Mean Q_{perc} Mean K_{th}	High Q_{perc} High K_{th}	Low to High Range	Low to High Range[a]
P2ER8C6	Tptpul (tsw33)	156.9	135.5	120.4	36.5	26.3%
P2WR8C8	Tptpmn (tsw34)	138.0	123.0	111.4	26.6	21.3%
P2WR5C10	Tptpll (tsw35)	162.8	140.8	124.5	38.3	26.7%
P3R8C13	Tptpln (tsw36)	136.1	120.2	108.8	27.3	22.3%

[a] The range (%) is the range (°C) divided by the peak drift-wall temperature [(low + high)/2].

NOTE: See Figure 6.3-1 for locations. The pwr1-2 (21-PWR AP CSNF) waste package is the hottest waste package in the sequence (Figure 6.2-2). Low, mean, and high thermal conductivity cases are considered for a range of plus and minus one standard deviation about the mean.

Table 6.3-28. Range of Peak Waste Package Temperatures for the pwr1-2 Waste Package (Resulting from a Combination of Percolation Flux Q_{perc} and Thermal Conductivity K_{th} Uncertainty) Summarized for Four Locations in the Repository

LDTH–SDT Submodel Location	Host-Rock Unit	Peak Waste Package Temperature (°C)				
		Low Q_{perc} Low K_{th}	Mean Q_{perc} Mean K_{th}	High Q_{perc} High K_{th}	Low to High Range	Low to High Range[a]
P2ER8C6	Tptpul (tsw33)	185.1	163.2	148.7	36.4	21.8%
P2WR8C8	Tptpmn (tsw34)	165.4	150.6	139.5	25.9	17.0%
P2WR5C10	Tptpll (tsw35)	191.0	168.8	152.7	38.3	22.3%
P3R8C13	Tptpln (tsw36)	163.9	148.2	137.3	26.6	17.7%

[a] The range (%) is the range (°C) divided by the peak drift-wall temperature [(low + high)/2].

NOTE: See Figure 6.3-1 for locations. The pwr1-2 (21-PWR AP CSNF) waste package is the hottest waste package in the sequence (Figure 6.2-2). Low, mean, and high thermal conductivity cases are considered for a range of plus and minus one standard deviation about the mean.

Table 6.3-29. Range of Time When Boiling at the Drift Wall Ceases for the pwr1-2 Waste Package (Resulting from a Combination of Percolation Flux Q_{perc} and Thermal Conductivity K_{th} Uncertainty) Summarized for Four Locations in the Repository

LDTH–SDT Submodel Location	Host-Rock Unit	Time When Boiling at the Drift Wall Ceases (years)				
		Low Q_{perc} Low K_{th}	Mean Q_{perc} Mean K_{th}	High Q_{perc} High K_{th}	Low to High Range	Low to High Range*
P2ER8C6	Tptpul (tsw33)	615.5	364.8	222.5	393.0	93.8%
P2WR8C8	Tptpmn (tsw34)	514.1	242.8	144.7	369.4	112.1%
P2WR5C10	Tptpll (tsw35)	1,415.8	623.0	207.4	1,208.4	148.9%
P3R8C13	Tptpln (tsw36)	377.2	195.2	129.8	247.4	97.6%

[a] The range (%) is the range (years) divided by the average time when drift-wall boiling ceases [(shortest + longest)/2].

NOTE: See Figure 6.3-1 for location. The pwr1-2 (21-PWR AP CSNF) waste package is the hottest waste package in the sequence (Figure 6.2-2). Low, mean, and high thermal conductivity cases are considered for a range of plus and minus one standard deviation about the mean.

Source: See Table XIII-1.

NOTE: See Figure 6.3-1 for location. These cases are: (1) low percolation flux and low thermal conductivity, (2) mean percolation flux and mean thermal conductivity, and (3) high percolation flux and high thermal conductivity, where the thermal conductivity is varied by plus and minus one standard deviation about the mean. The plotted thermal-hydrologic parameters are (a) drift-wall temperature, (b) waste package temperature, (c) drift-wall liquid-phase saturation, (d) waste package relative humidity, and (e) invert liquid-phase saturation. The pwr1-2 (21-PWR AP CSNF) waste package is the hottest waste package in the sequence (Figure 6.2-2).

Figure 6.3-29. Thermal-Hydrologic Conditions for the pwr1-2 Waste Package Plotted for Three Cases at the P2ER8C6 Location in the Tptpul (tsw33) Unit

Source: See Table XIII-1.

NOTE: See Figure 6.3-1 for location. These cases are: (1) low percolation flux and low thermal conductivity, (2) mean percolation flux and mean thermal conductivity, and (3) high percolation flux and high thermal conductivity, where the thermal conductivity is varied by plus and minus one standard deviation about the mean. The plotted thermal-hydrologic parameters are (a) drift-wall temperature, (b) waste package temperature, (c) drift-wall liquid-phase saturation, (d) waste package relative humidity, and (e) invert liquid-phase saturation. The pwr1-2 (21-PWR AP CSNF) waste package is the hottest waste package in the sequence (Figure 6.2-2).

Figure 6.3-30. Thermal-Hydrologic Conditions for the pwr1-2 Waste Package Plotted for Three Cases at the P2WR8C8 Location in the Tptpmn (tsw34) Unit
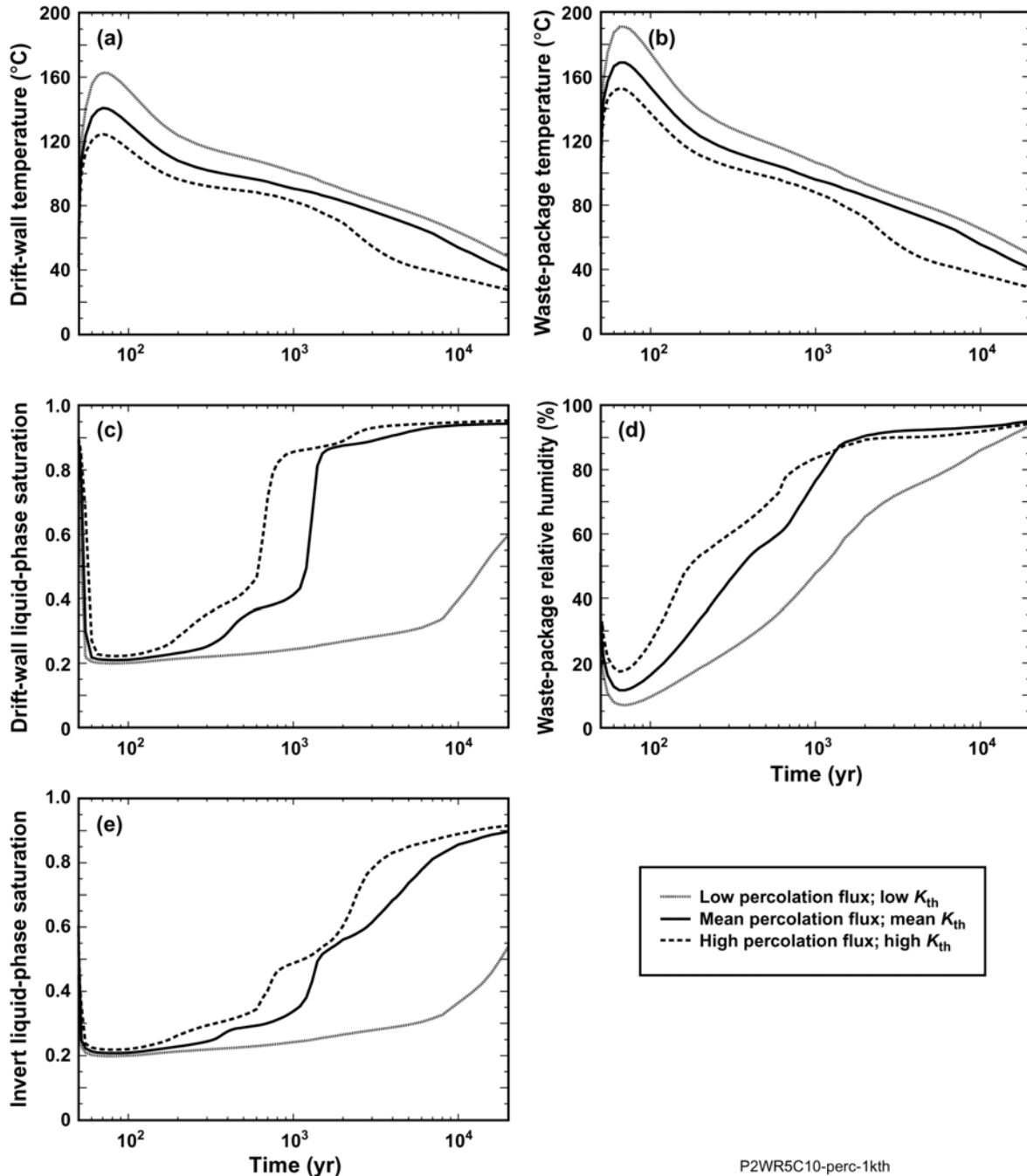
Source: See Table XIII-1.

NOTE: See Figure 6.3-1 for location. These cases are: (1) low percolation flux and low thermal conductivity, (2) mean percolation flux and mean thermal conductivity, and (3) high percolation flux and high thermal conductivity, where the thermal conductivity is varied by plus and minus one standard deviation about the mean. The plotted thermal-hydrologic parameters are (a) drift-wall temperature, (b) waste package temperature, (c) drift-wall liquid-phase saturation, (d) waste package relative humidity, and (e) invert liquid-phase saturation. The pwr1-2 (21-PWR AP CSNF) waste package is the hottest waste package in the sequence (Figure 6.2-2).

Figure 6.3-31. Thermal-Hydrologic Conditions for the pwr1-2 Waste Package Plotted for Three Cases at the P2WR5C10 Location in the Tptpll (tsw35) Unit

Source: See Table XIII-1.

NOTE: See Figure 6.3-1 for location. These cases are: (1) low percolation flux and low thermal conductivity, (2) mean percolation flux and mean thermal conductivity, and (3) high percolation flux and high thermal conductivity, where the thermal conductivity is varied by plus and minus one standard deviation about the mean. The plotted thermal-hydrologic parameters are (a) drift-wall temperature, (b) waste package temperature, (c) drift-wall liquid-phase saturation, (d) waste package relative humidity, and (e) invert liquid-phase saturation. The pwr1-2 (21-PWR AP CSNF) waste package is the hottest waste package in the sequence (Figure 6.2-2).

Figure 6.3-32. Thermal-Hydrologic Conditions for the pwr1-2 Waste Package Plotted for Three Cases at the P3R8C13 Location in the Tptpln (tsw36) Unit

An important question to ask is whether the combined influence of percolation-flux uncertainty and host-rock thermal conductivity on peak temperatures is simply the sum of the individual contributions to peak-temperature uncertainty. Table 6.3-30 compares the ranges of peak temperatures resulting from (1) percolation-flux uncertainty, (2) host-rock thermal conductivity uncertainty, and (3) a combination of percolation flux and host-rock thermal conductivity uncertainty; Table 6.3-31 makes the same comparison for peak waste package temperatures. Adding the range of peak temperatures resulting from percolation-flux uncertainty to those from host-rock thermal conductivity uncertainty, the results are nearly identical to the range of peak temperatures resulting from the combination of percolation-flux uncertainty and host-rock thermal conductivity. Taking location P2WR5C10 in Table 6.3-30 as an example: adding the peak-temperature range resulting from percolation-flux uncertainty (6.9°C) to that resulting from host-rock thermal conductivity uncertainty (31.5°C) yields a total of 38.4°C, which is close to the peak-temperature range (38.3°C) that results when the influences of percolation flux and host-rock thermal conductivity uncertainty are combined.

A related question is whether the combined influence of percolation-flux uncertainty and host-rock thermal conductivity on boiling duration is simply the sum of the individual contributions to boiling-duration uncertainty. Table 6.3-32 compares the ranges of the time when boiling at the drift wall ceases resulting from (1) percolation-flux uncertainty, (2) host-rock thermal conductivity uncertainty, and (3) the combination of percolation flux and host-rock thermal conductivity uncertainty. Adding the range of time when drift-wall boiling ends resulting from percolation-flux uncertainty to that from host-rock thermal conductivity uncertainty is nearly equal to the range of boiling duration resulting from the combination of percolation-flux uncertainty and host-rock thermal conductivity uncertainty. Taking location P2WR5C10 in Table 6.3-32 as an example, adding the range of the time when boiling at the drift wall ceases resulting from percolation-flux uncertainty (484.5 years) to that resulting from host-rock thermal conductivity uncertainty (700.8 years), yields 1,185.3 years, which is similar to the range (1,208.4 years) that results when the influences of percolation flux and host-rock thermal conductivity uncertainty are combined. In general, the range resulting from the combined uncertainties is always slightly greater than the sum of the individual contributions to boiling-duration uncertainty.

Table 6.3-30. Range of Peak Drift-Wall Temperatures for the pwr1-2 Waste Package Resulting from Various Combinations of Percolation Flux Q_{perc} and Thermal Conductivity K_{th} Uncertainty, Summarized for Four Locations in the Repository

LDTH–SDT Submodel Location	Host-Rock Unit	Influence of Percolation-Flux Uncertainty on Peak Drift-Wall Temperature		Influence of Host-Rock Thermal Conductivity Uncertainty on Peak Drift-Wall Temperature		Influence of Combined Percolation Flux and Host-Rock Thermal Conductivity Uncertainty on Peak Drift-Wall Temperature	
		Range (°C)	Range (%)	Range (°C)	Range (%)	Range (°C)	Range (%)
P2ER8C6	Tptpul (tsw33)	7.0	5.2%	30.1	21.8%	36.5	26.3%
P2WR8C8	Tptpmn (tsw34)	5.1	4.2%	22.7	18.1%	26.6	21.3%
P2WR5C10	Tptpll (tsw35)	6.9	4.9%	31.5	22.0%	38.3	26.7%
P3R8C13	Tptpln (tsw36)	4.4	3.7%	21.9	18.0%	27.3	22.3%

NOTE: See Figure 6.3-1 for locations. The pwr1-2 (21-PWR AP CSNF) waste package is the hottest waste package in the sequence (Figure 6.2-2). These values summarize Tables 6.3-20 through 6.3-29.

Table 6.3-31. Range of Peak Waste Package Temperatures for the pwr1-2 Waste Package Resulting from Various Combinations of Percolation Flux Q_{perc} and Thermal Conductivity K_{th} Uncertainty, Summarized for Four Locations in the Repository

LDTH–SDT Submodel Location	Host-Rock Unit	Influence of Percolation-Flux Uncertainty on Peak Waste Package Temperature		Influence of Host-Rock Thermal Conductivity Uncertainty on Peak Waste Package Temperature		Influence of Combined Percolation Flux and Host-Rock Thermal Conductivity Uncertainty on Peak Waste Package Temperature	
		Range (°C)	Range (%)	Range (°C)	Range (%)	Range (°C)	Range (%)
P2ER8C6	Tptpul (tsw33)	7.0	4.3%	29.8	17.9%	36.4	21.8%
P2WR8C8	Tptpmn (tsw34)	4.3	2.9%	21.9	14.3%	25.9	17.0%
P2WR5C10	Tptpll (tsw35)	7.0	4.1%	31.4	18.3%	38.3	22.3%
P3R8C13	Tptpln (tsw36)	4.0	2.7%	21.4	14.3%	26.6	17.7%

NOTE: See Figure 6.3-1 for locations. The pwr1-2 (21-PWR AP CSNF) waste package is the hottest waste package in the sequence (Figure 6.2-2).

The combined influence of percolation-flux uncertainty and host-rock thermal conductivity uncertainty on dryout/rewetting is illustrated by the drift-wall and invert liquid-phase saturation histories (Figures 6.3-29c, 6.3-29e, 6.3-30c, 6.3-30e, 6.3-31c, 6.3-31e, 6.3-32c, and 6.3-32e). The time for liquid-phase saturation to rewet back to ambient values ranges by two orders of magnitude for these cases. The combined influence of percolation-flux uncertainty and host-rock thermal conductivity uncertainty on waste package relative humidity histories is shown in Figures 6.3-29d, 6.3-30d, 6.3-31d, and 6.3-32d. Because of the contribution of the temperature difference between the waste package and the drift wall on relative humidity reduction on waste packages, the combined influence of percolation flux and host-rock thermal conductivity uncertainty on waste package relative humidity, while evident, is not as strong as for liquid-phase saturation histories.

Table 6.3-32. Range of Time When Boiling at the Drift Wall Ceases for the pwr1-2 Waste Package Resulting from Various Combinations of Percolation Flux Q_{perc} and Thermal Conductivity K_{th} Uncertainty, Summarized for Four Locations in the Repository

LDTH–SDT Submodel Location	Host-Rock Unit	Influence of Percolation-Flux Uncertainty on Time When Boiling at the Drift Wall Ceases		Influence of Host-Rock Thermal Conductivity Uncertainty on Time When Boiling at the Drift Wall Ceases		Influence of Combined Percolation Flux and Host-Rock Thermal Conductivity Uncertainty on Time When Boiling at the Drift Wall Ceases	
		Range (years)	Range (%)	Range (years)	Range (%)	Range (years)	Range (%)
P2ER8C6	Tptpul (tsw33)	124.8	33.2%	250.0	65.2%	393.0	93.8%
P2WR8C8	Tptpmn (tsw34)	88.4	36.5%	249.0	86.4%	369.4	112.1%
P2WR5C10	Tptpll (tsw35)	484.5	75.6%	700.8	114.3%	1,208.4	148.9%
P3R8C13	Tptpln (tsw36)	49.0	24.5%	169.2	75.4%	247.4	97.6%

NOTE: See Figure 6.3-1 for locations. The pwr1-2 (21-PWR AP CSNF) waste package is the hottest waste package in the sequence (Figure 6.2-2).

6.3.2.4   Influence of Hydrologic-Property Uncertainty on In-Drift Temperature and Relative Humidity

The primary purpose of this section is to help determine whether it is necessary to propagate hydrologic-property uncertainty in the MSTHM calculations for TSPA-LA. The primary hydrologic property of interest is the bulk permeability of the host rock; this parameter is primarily affected by the permeability of the fracture network. As discussed in Section 6.3.2, a sensitivity study (BSC 2001 [DIRS 155950], Section 5.3.1.4.7) found that host-rock bulk permeability has a minor influence on peak temperatures and boiling-period duration. Therefore, host-rock bulk permeability uncertainty does not need to be propagated in the MSTHM calculations for TSPA-LA. In this section, the influence of hydrologic-property uncertainty is further addressed by investigating the impact of utilizing various hydrologic-property sets that have differing values of matrix and fracture properties in the four host-rock units (Tptpul, Tptpmn, Tptpll, and Tptpln).

The influence of hydrologic-property uncertainty on in-drift temperature and relative humidity at four locations (P2ER8C6, P2WR8C8, P2WR5C10, and P3R8C13) in the repository (Figure 6.3-1) is illustrated in time histories of drip-shield temperature and relative humidity (Figures 6.3-33 through 6.3-36). These time histories were generated with the use of the LDTH submodel (Section 6.2.6), which is the primary thermal-hydrologic submodel in the MSTHM family of submodels. Because the LDTH submodel is the only MSTHM submodel that uses hydrologic-property information as input, it is reasonable to use the results of the LDTH submodel to investigate the degree of sensitivity of in-drift temperature and relative humidity to hydrologic-property uncertainty.   The LDTH submodel calculations in this section were conducted for an Areal Mass Loading (AML) of 55 MTU/acre. Thus, these results correspond to line-average heat-generation conditions for a repository location far enough away from the repository edges not to be influenced by the edge-cooling effect. For these four locations in the repository, four different cases are investigated: (1) lower-bound infiltration-flux case with lower-bound infiltration-flux property set, (DTN: LB0208UZDSCPLI.002 [DIRS 161788]), (2) lower-bound infiltration-flux case with modified-mean infiltration-flux property set, (3) upper-bound infiltration-flux case with upper-bound infiltration-flux property set

(DTN: LB0302UZDSCPUI.002 [DIRS 161787]), and (4) upper-bound infiltration-flux case with modified-mean infiltration-flux property set. The modified-mean infiltration-flux property set is used in all of the MSTHM calculations discussed in Sections 6.3.2.1 through 6.3.2.3 and in Section 6.3.3. These pairs of cases were chosen to be able to discern the influence of hydrologic properties on in-drift temperature and relative humidity. Because temperature and relative humidity on the drip shield are key measures of in-drift thermal-hydrologic conditions, this section focuses on those parameters.
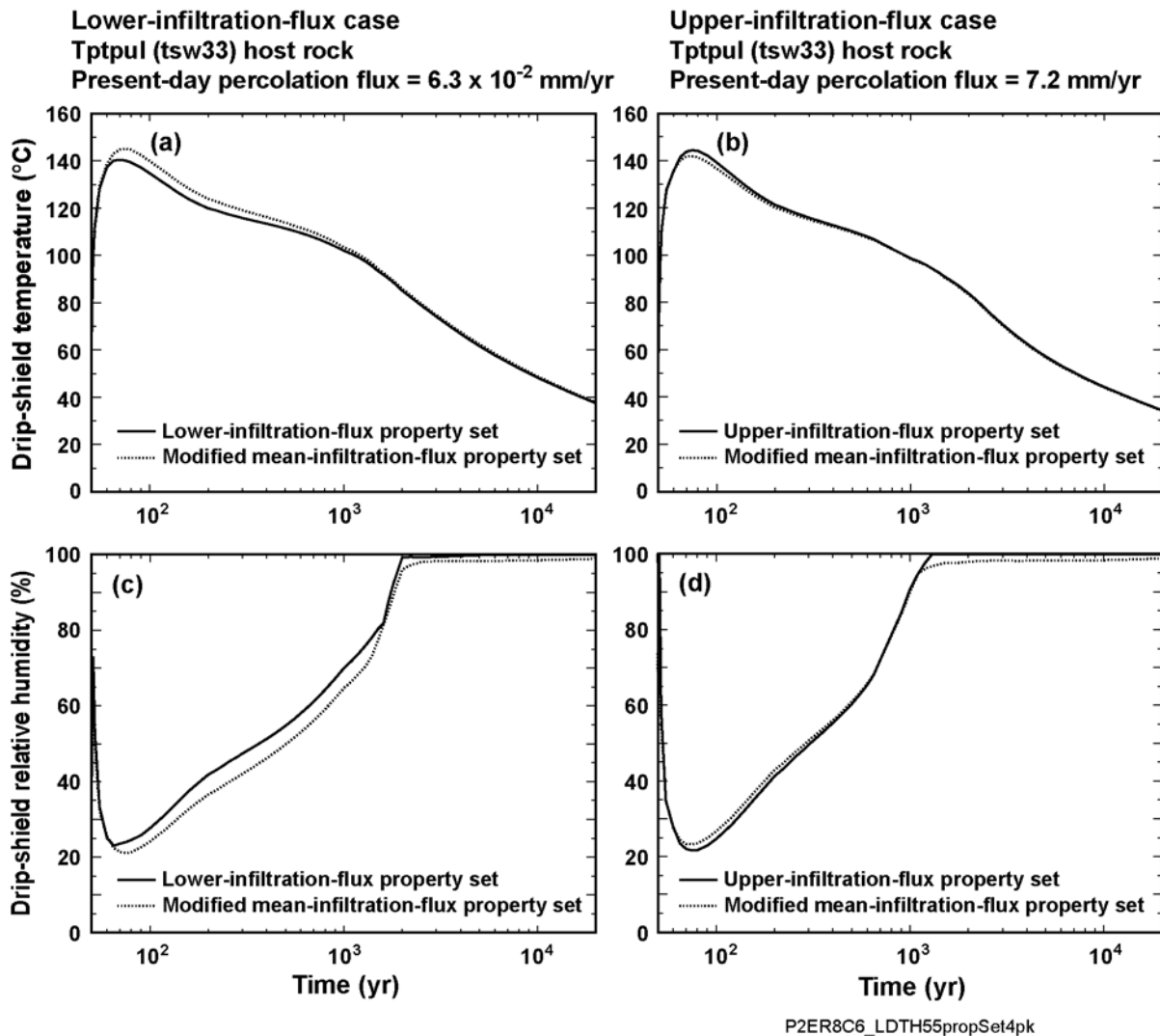
Source: See Table XIII-1.

NOTE: See Figure 6.3-1 for location. The four cases are: (1) lower-bound infiltration-flux case with lower-bound infiltration-flux property set, (2) lower-bound infiltration-flux case with modified-mean infiltration-flux property set, (3) upper-bound infiltration-flux case with upper-bound infiltration-flux property set, and (4) upper-bound infiltration-flux case with modified-mean infiltration-flux property set.

Figure 6.3-33. Drip-Shield Temperature (a,b) and Relative Humidity (c,d) for Line-Averaged Heating Conditions Plotted for Four Cases at the P2ER8C6 Location in the Tptpul (tsw33) Unit
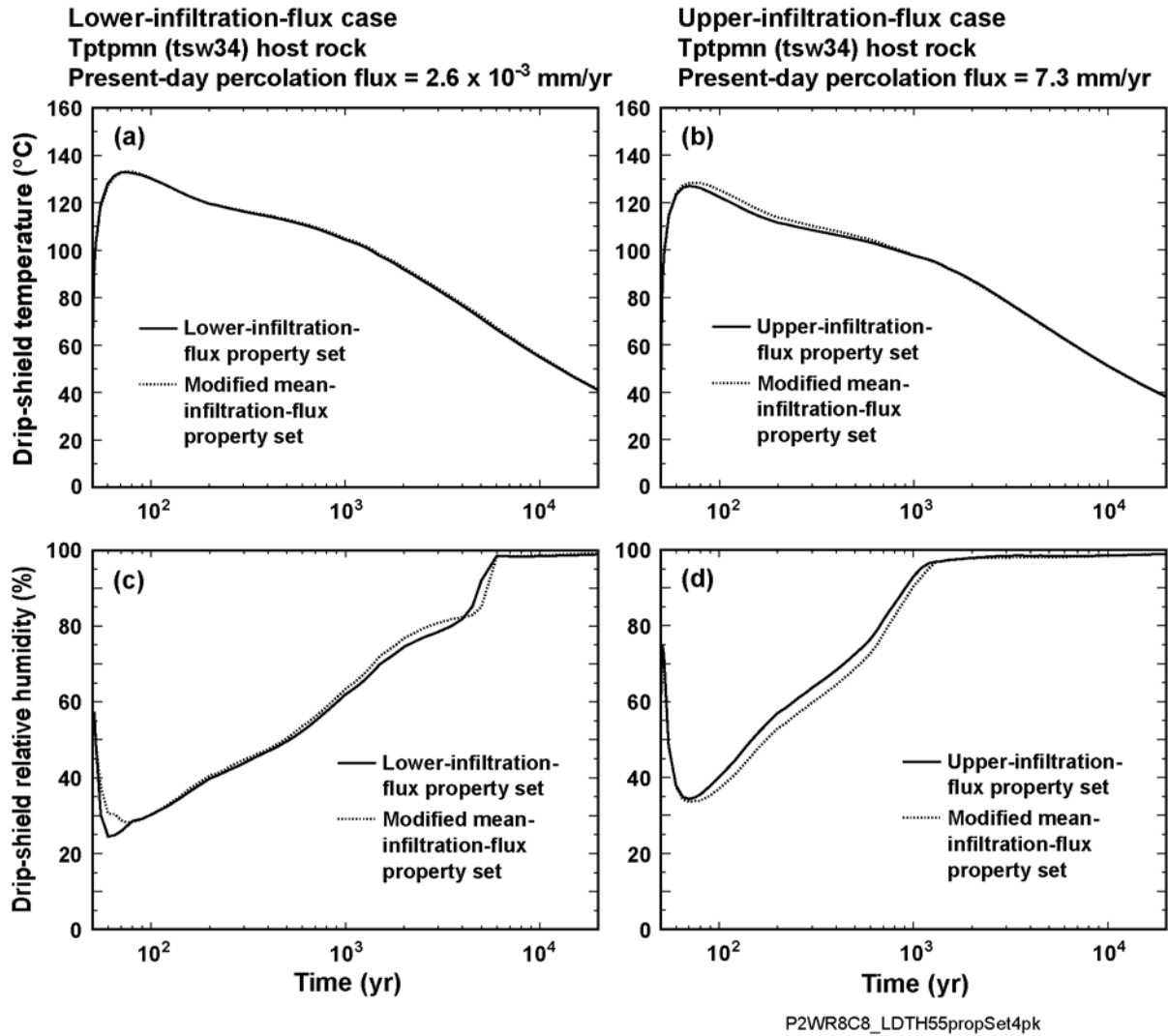
Source: See Table XIII-1.

NOTE: See Figure 6.3-1 for location. The four cases are: (1) lower-bound infiltration-flux case with lower-bound infiltration-flux property set, (2) lower-bound infiltration-flux case with modified-mean infiltration-flux property set, (3) upper-bound infiltration-flux case with upper-bound infiltration-flux property set, and (4) upper-bound infiltration-flux case with modified-mean infiltration-flux property set.

Figure 6.3-34. Drip-Shield Temperature (a,b) and Relative Humidity (c,d) for Line-Averaged Heating Conditions Plotted for Four Cases at the P2WR8C8 Location in the Tptpmn (tsw34) Unit
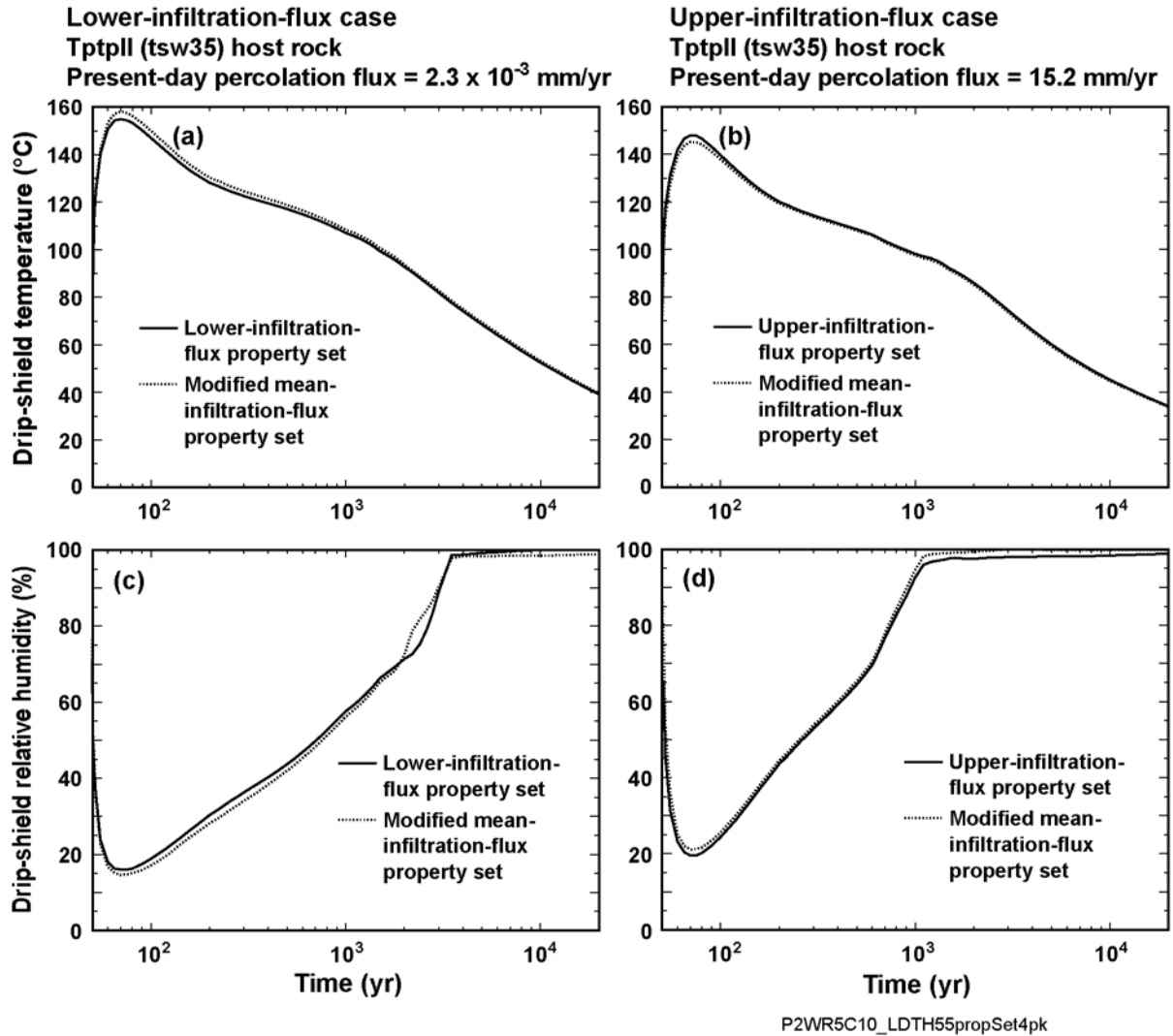
Source: See Table XIII-1.

NOTE: See Figure 6.3-1 for location. The four cases are: (1) lower-bound infiltration-flux case with lower-bound infiltration-flux property set, (2) lower-bound infiltration-flux case with modified-mean infiltration-flux property set, (3) upper-bound infiltration-flux case with upper-bound infiltration-flux property set, and (4) upper-bound infiltration-flux case with modified-mean infiltration-flux property set.

Figure 6.3-35. Drip-Shield Temperature (a,b) and Relative Humidity (c,d) for Line-Averaged Heating Conditions Plotted for Four Cases at the P2WR5C10 Location in the Tptpll (tsw35) Unit
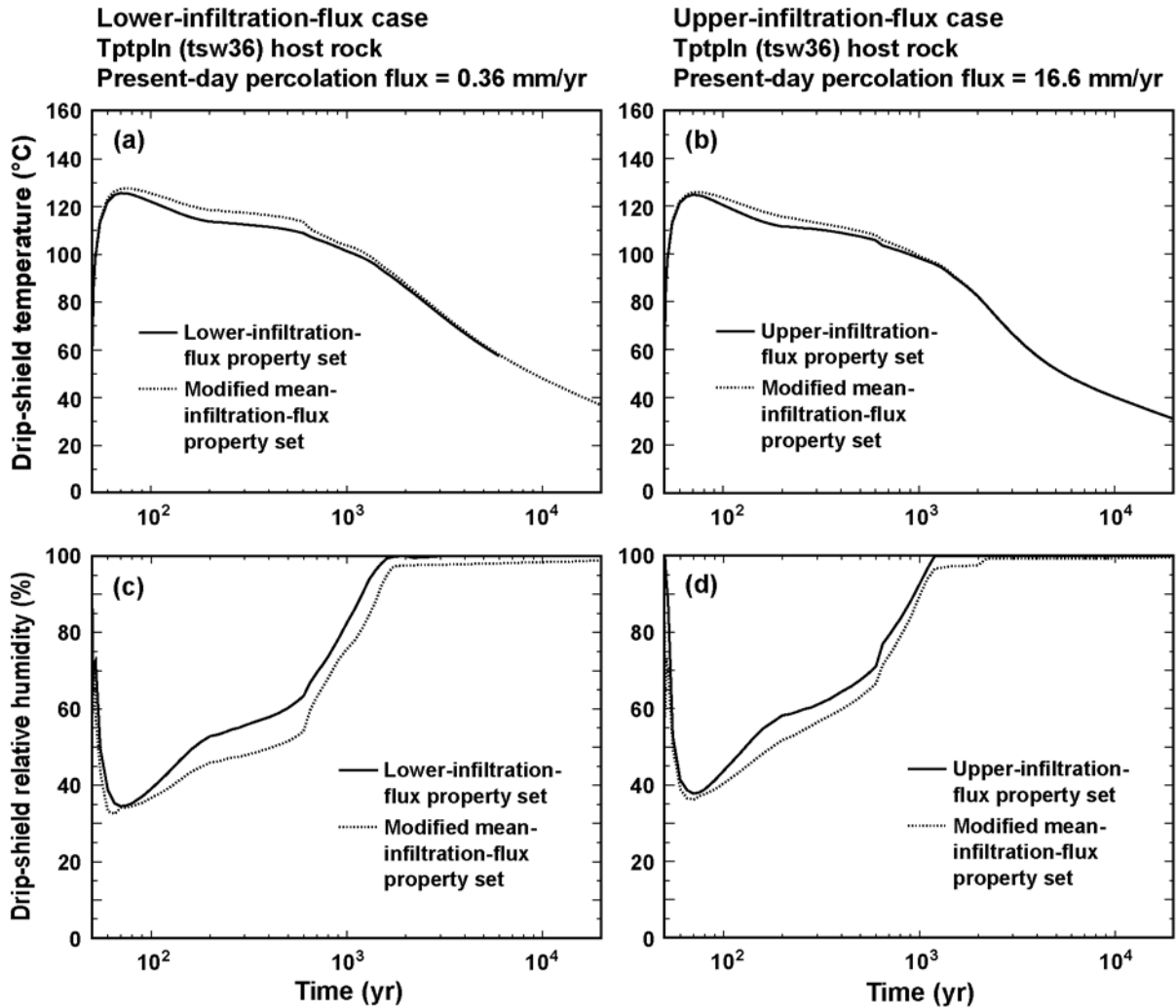
Source: See Table XIII-1.

NOTE: See Figure 6.3-1 for location. The four cases are: (1) lower-bound infiltration-flux case with lower-bound infiltration-flux property set, (2) lower-bound infiltration-flux case with modified-mean infiltration-flux property set, (3) upper-bound infiltration-flux case with upper-bound infiltration-flux property set, and (4) upper-bound infiltration-flux case with modified mean infiltration-flux property set.

Figure 6.3-36. Drip-Shield Temperature (a,b) and Relative Humidity (c,d) for Line-Averaged Heating Conditions Plotted for Four Cases at the P3R8C13 Location in the Tptpln (tsw36) Unit

Figures 6.3-33 through 6.3-36 indicate that in-drift temperature and relative humidity are insensitive to hydrologic-property uncertainty. For drifts located in the Tptpul (tsw33) unit (Figure 6.3-33) and the Tptpmn (tsw34) unit (Figure 6.3-34), which comprise 6.0 percent and 16.1 percent of the repository area, respectively (Table 6.3-3), drip-shield temperature and relative humidity are weakly sensitive to hydrologic properties. For drifts located in the Tptpll (tsw35) unit (Figure 6.3-35), which comprise 75.1 percent of the repository area (Table 6.3-3), drip-shield temperature and relative humidity are insensitive to hydrologic properties. For drifts located in the Tptpln (tsw36) unit (Figure 6.3-36), which comprise only 1.6 percent of the repository area (Table 6.3-3), drip-shield temperature and relative humidity are relatively insensitive to hydrologic properties. The results support the conclusion that hydrologic-property uncertainty does not need to be propagated in the MSTHM calculations of in-drift temperature and relative humidity. This conclusion is corroborated by the findings and conclusions of Section 6.3.4, where it is demonstrated that hydrologic-property uncertainty/variability has an insignificant influence on thermal-hydrologic conditions within the drifts and in the adjoining host rock.

6.3.3 Mass Flux in the Invert

The primary purpose of this section is to present a detailed examination of gas- and liquid-phase mass fluxes in the invert, including fluxes into and out of the invert, as well as fluxes within the invert. This detailed examination illustrates the relationship between MSTHM output parameters that pertain to the invert, such as liquid-phase saturation, liquid-phase flux, gas-phase flux, and evaporation rate. An important outcome of this detailed examination is demonstrating that the MSTHM provides a mass balance (of water) in the invert and thereby builds confidence in the model itself. This model confidence building discussion, in conjunction with the MSTHM model-validation discussion presented in Section 7.5, provides the basis for predicting a reasonable range of several MSTHM output parameters that pertain to the invert, such as liquid-phase flux and evaporation rate.

Time histories of gas- and liquid-phase flux and of liquid-phase saturation are provided in Figures 6.3-37 through 6.3-44 for four locations (P2ER8C6, P2WR8C8, P2WR5C10, and P3R8C13) in the repository (Figure 6.3-1). Figure 6.3-45 plots the phase change (with positive and negative phase change corresponding to evaporation and condensation, respectively) and the liquid-phase flux for the lower half of the invert. These four locations were chosen because they cover all four of the host-rock units in the repository and because their respective values of percolation flux are relatively close to the repository-wide averages (Tables 6.3-4, 6.3-5, and 6.3-9). These time histories were generated with the use of the LDTH submodel (Section 6.2.6), which is the primary thermal-hydrologic submodel in the MSTHM family of submodels. The LDTH submodel calculations in this section were conducted for an Areal Mass Loading (AML) of 55 MTU/acre. Thus, these results correspond to line-average heat-generation conditions for a repository location far enough away from the repository edges not to be influenced by the edge-cooling effect.

Figure 6.3-37 plots liquid-phase and gas-phase fluxes between the invert and the adjoining drift and host rock, as well as plotting the liquid-phase saturation in the invert, for the P2ER8C6 location, which is in the Tptpul (tsw33) unit. Figure 6.3-38 plots liquid- and gas-phase fluxes between the upper and lower halves of the invert. Table 6.3-33 provides the peak values of liquid-phase and gas-phase fluxes after 50 years, while Table 6.3-34 provides the peak values

after 100 years. These figures and tables show there are three distinctive time periods with respect to mass flux, dryout, and rewetting of the invert, which are:

1. Initial period of *strong dryout*, when the strong gas-phase flux of water vapor (in the fracture continuum) out of the invert dominates the return capillary-driven liquid-phase flux (in the matrix continuum). Thus, refluxing (i.e., the countercurrent flow of water vapor and liquid water) is quite pronounced during this period. Gas- and liquid-phase fluxes rapidly increase and decrease during this period. At the very beginning of the initial dryout period, condensation is strong in the lower half of the invert (Figure 6.3-45), which lasts until the boiling front passes through the bottom of the invert and into the underlying host rock. Liquid-phase flux (in the fracture continuum) drains from the bottom of the invert to the underlying host rock. Thus, liquid-phase drainage in the fracture continuum contributes significantly to the initial dryout of the invert. The source of this liquid-phase drainage is condensation of water vapor that boiled in the upper portion of the invert and was driven downward to the lower portion of the invert. By the end of the initial dryout period the liquid-phase saturation in the invert has attained its minimum value.

2. Period of *sustained dryout*, when the dryout front is in the host rock beyond the drift wall. During this period, the liquid-phase saturation remains close to its minimum value and mass fluxes within the invert, as well as at its interface with the adjoining drift and with the host rock, are essentially zero.

3. Period of *rewetting*, when the return capillary-driven liquid-phase flux (in the matrix continuum) dominates the outward flux of water vapor (in the fracture continuum). Gas- and liquid-phase fluxes gradually increase and decrease during this period. Liquid-phase flux (in the fracture continuum) drains from the bottom of the invert to the underlying host rock. The source of this liquid-phase drainage flux (which is of a much smaller magnitude than during the initial dryout period) is the condensation of water vapor that boiled in the upper portion of the invert and was driven downward to the lower portion of the invert (Figures 6.3-45a and 6.3-45b). Refluxing, both within the invert as well as at the interface with the host rock, is strong during this period.

Figures 6.3-39 and 6.3-40 for the P2WR8C8 location, which is in the Tptpmn (tsw34) host-rock unit, are qualitatively similar to Figures 6.3-37 and 6.3-38; however, the magnitudes of the gas- and liquid-phase fluxes associated with refluxing are much less during the rewetting period (Table 6.3-34). Moreover, the P2WR8C8 location experiences no liquid-phase drainage in the fracture continuum during the rewetting period (Figure 6.3-45d).

Figures 6.3-41 and 6.3-42 for the P2WR5C10 location, which is in the Tptpll (tsw35) host-rock unit, are also qualitatively similar to Figures 6.3-37 and 6.3-38; however, the magnitude of the gas- and liquid-phase fluxes associated with refluxing is somewhat less during the rewetting period (Table 6.3-34). Moreover, the P2WR5C10 location experiences a much smaller liquid-phase drainage flux in the fracture continuum during the rewetting than the P2ER8C6 location (compare Figure 6.3-45f with Figure 6.3-45b).

Figures 6.3-43 and 6.3-44 for the P3R8C13 location, which is in the Tptpln (tsw36) host-rock unit, are qualitatively similar to Figures 6.3-37 and 6.3-38; however, the magnitude of the gas-

and liquid-phase fluxes associated with refluxing is much less during the rewetting period (Table 6.3-34). Moreover, the P3R8C13 location experiences no liquid-phase drainage in the fracture continuum during the rewetting period (Figure 6.3-45h).
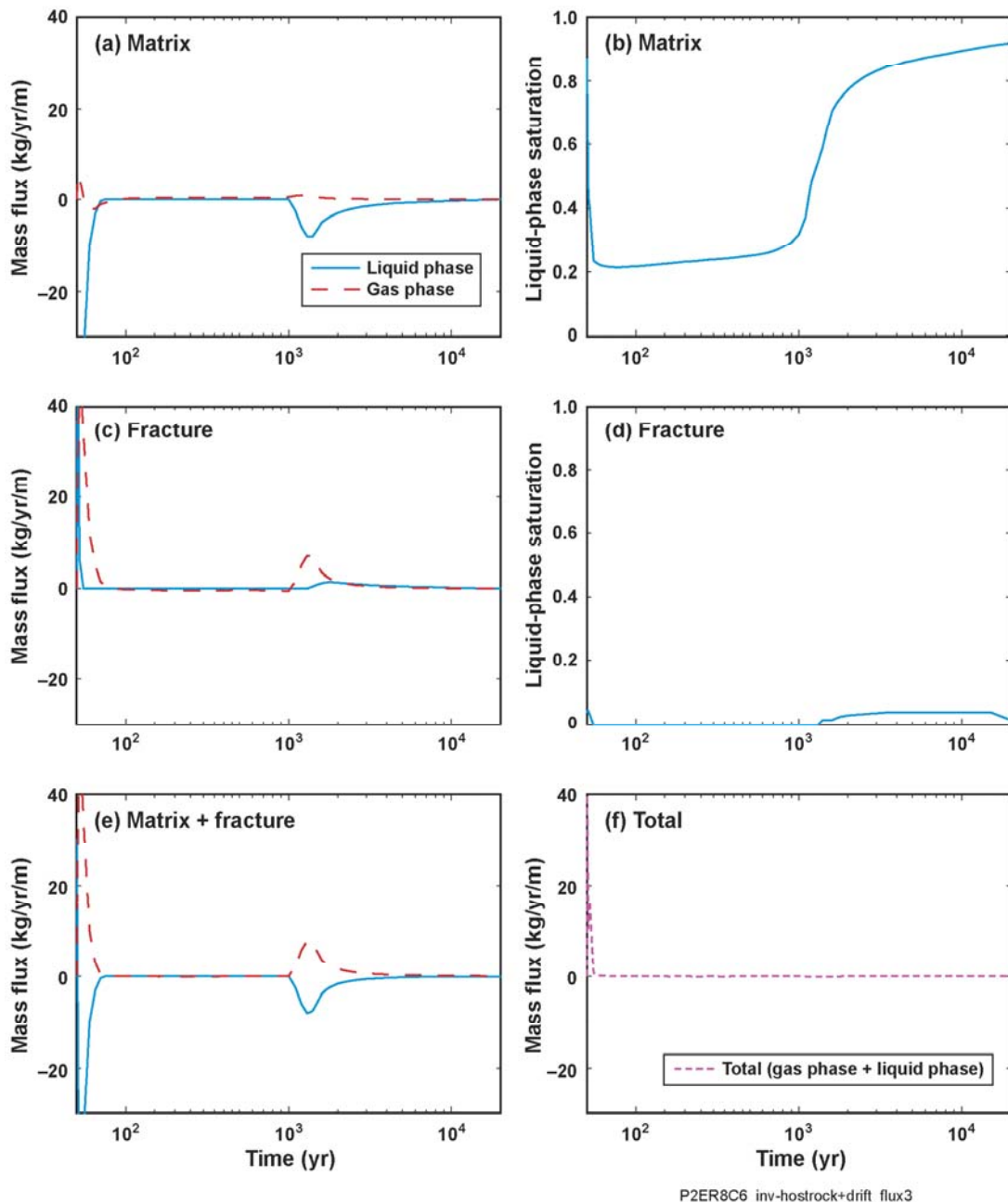
P2ER8C6 inv-hostrock+drift flux3

Source: See Table XIII-1.

NOTE: See Figure 6.3-1 for location. Also plotted is (f) the total (gas-phase + liquid-phase) mass flux for the matrix + fracture continua. A positive value of mass flux corresponds to flux out of the invert. Also plotted is the liquid-phase saturation for the (b) matrix and (d) fracture continuum. These fluxes are the result of line-averaged heating conditions.

Figure 6.3-37. Liquid-Phase and Gas-Phase Flux Between the Invert and Adjoining Drift and Host Rock Plotted for the (a) Matrix, (c) Fracture, and (e) Matrix + Fracture Continuum at the P2ER8C6 Location in the Tptpul (tsw33) Unit
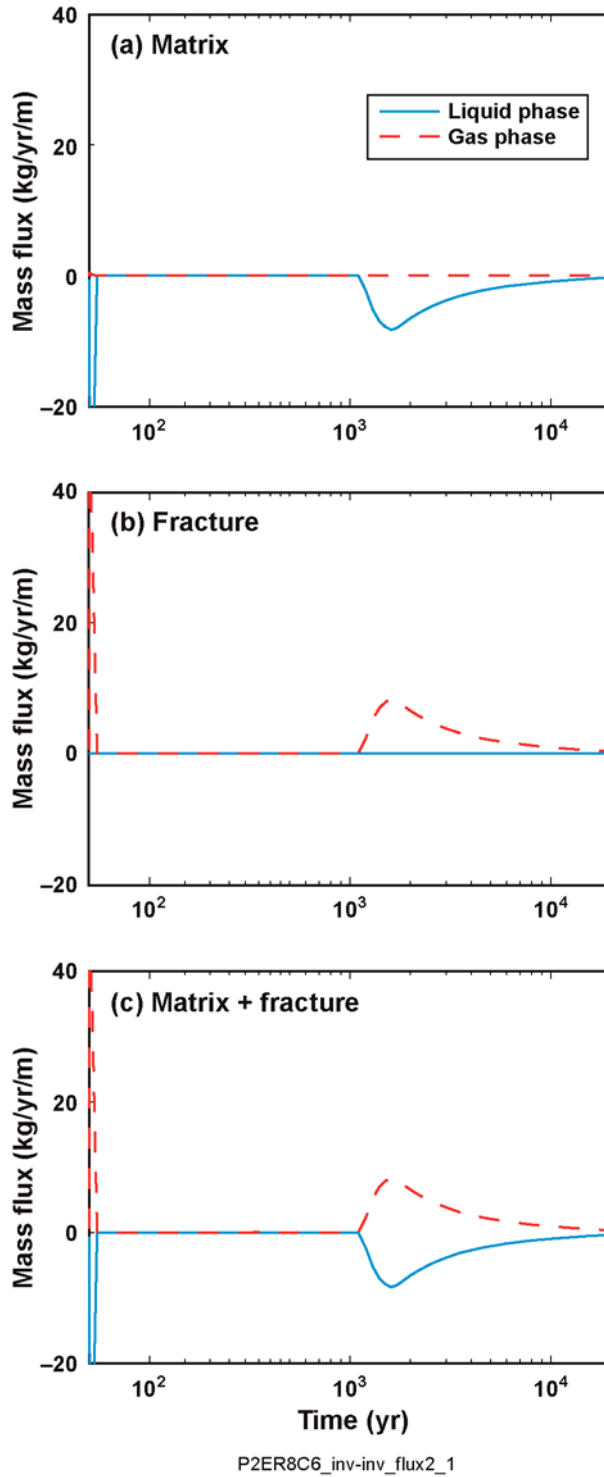
Source: See Table XIII-1.

NOTE: See Figure 6.3-1 for location. A positive value of mass flux corresponds to vertically downward flow.
        These fluxes are the result of line-averaged heating conditions.

Figure 6.3-38. Liquid-Phase and Gas-Phase Flux Between the Upper and Lower Half of the Invert Plotted for the (a) Matrix, (b) Fracture, and (c) Matrix + Fracture Continuum at the P2ER8C6 Location in the Tptpul (tsw33) Unit

P2WR8C8_inv-hostrock+drift_flux3
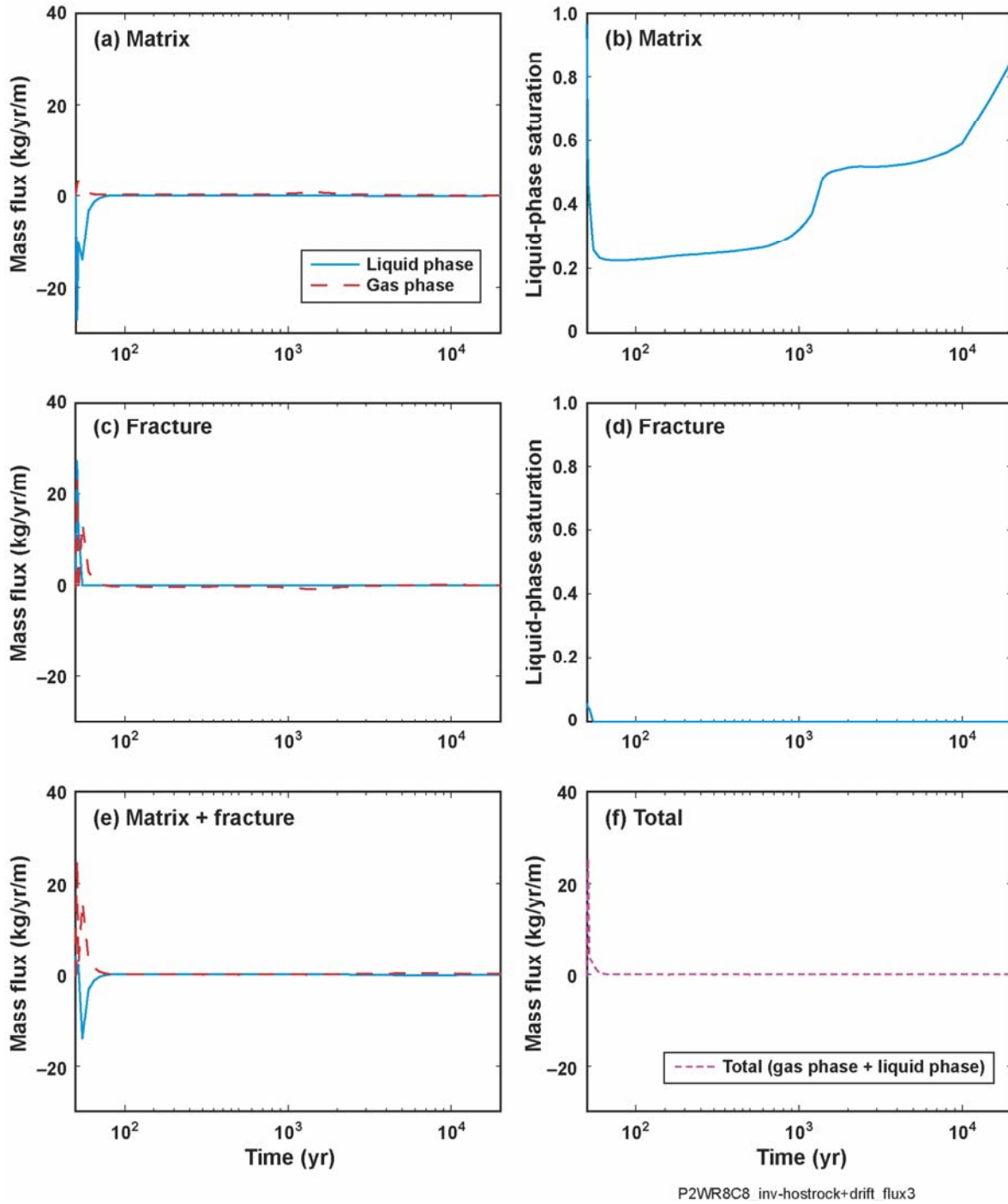
Source: See Table XIII-1.

NOTE: See Figure 6.3-1 for location. Also plotted is (f) the total (gas-phase + liquid-phase) mass flux for the
         matrix + fracture continua. A positive value of mass flux corresponds to flux out of the invert. Also plotted
         is the liquid-phase saturation for the (b) matrix and (d) fracture continuum. These fluxes are the result of
         line-averaged heating conditions.

Figure 6.3-39. Liquid-Phase and Gas-Phase Flux Between the Invert and Adjoining Drift and Host Rock
                Plotted for the (a) Matrix, (c) Fracture, and (e) Matrix + Fracture Continuum at the
                P2WR8C8 Location in the Tptpmn (tsw34) Unit

P2WR8C8_inv-inv_flux2_1
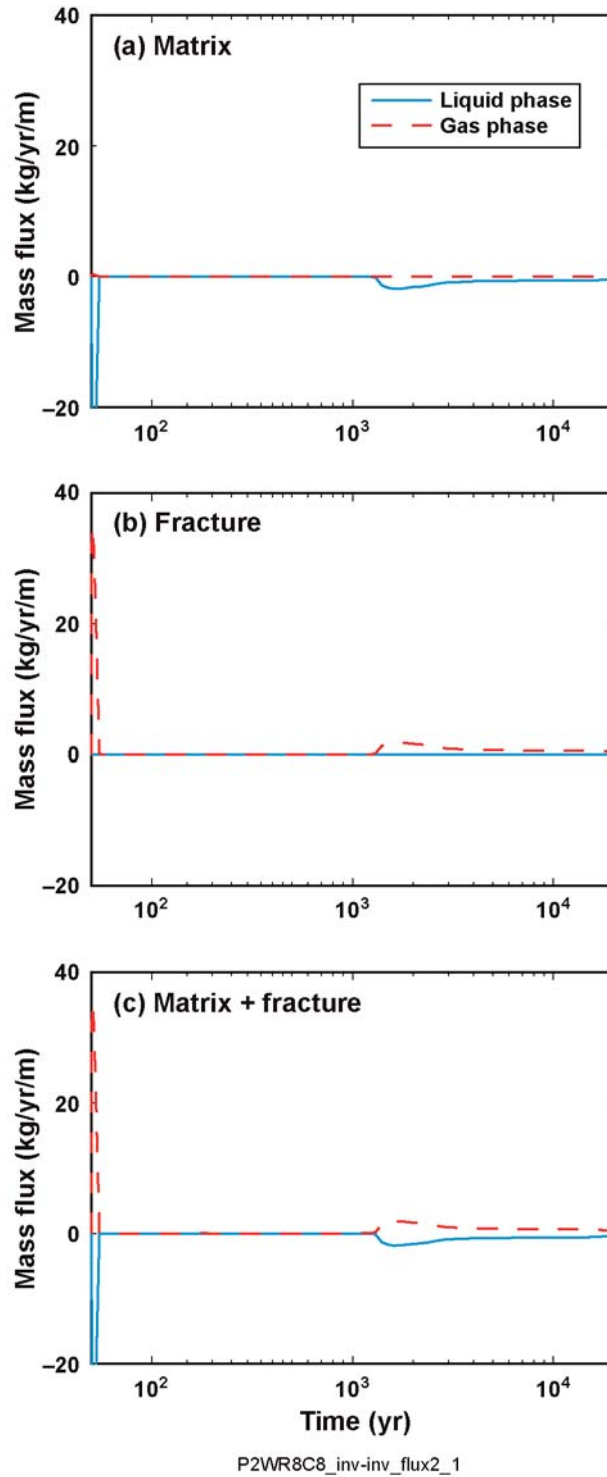
Source: See Table XIII-1.

NOTE: See Figure 6.3-1 for location. A positive value of mass flux corresponds to vertically downward flow.
         These fluxes are the result of line-averaged heating conditions.

Figure 6.3-40. Liquid-Phase and Gas-Phase Flux Between the Upper and Lower Half of the Invert
              Plotted for the (a) Matrix, (b) Fracture, and (c) Matrix + Fracture Continuum at the
              P2WR8C8 Location in the Tptpmn (tsw34) Unit

Source: See Table XIII-1.

NOTE: See Figure 6.3-1 for location. Also plotted is (f) the total (gas-phase + liquid-phase) mass flux for the matrix + fracture continua. A positive value of mass flux corresponds to flux out of the invert. Also plotted is the liquid-phase saturation for the (b) matrix and (d) fracture continuum. These fluxes are the result of line-averaged heating conditions.

Figure 6.3-41. Liquid-Phase and Gas-Phase Flux Between the Invert and Adjoining Drift and Host Rock Plotted for the (a) Matrix, (c) Fracture, and (e) Matrix + Fracture Continuum at the P2WR5C10 Location in the Tptpll (tsw35) Unit

P2WR5C10_inv-inv_flux2_1
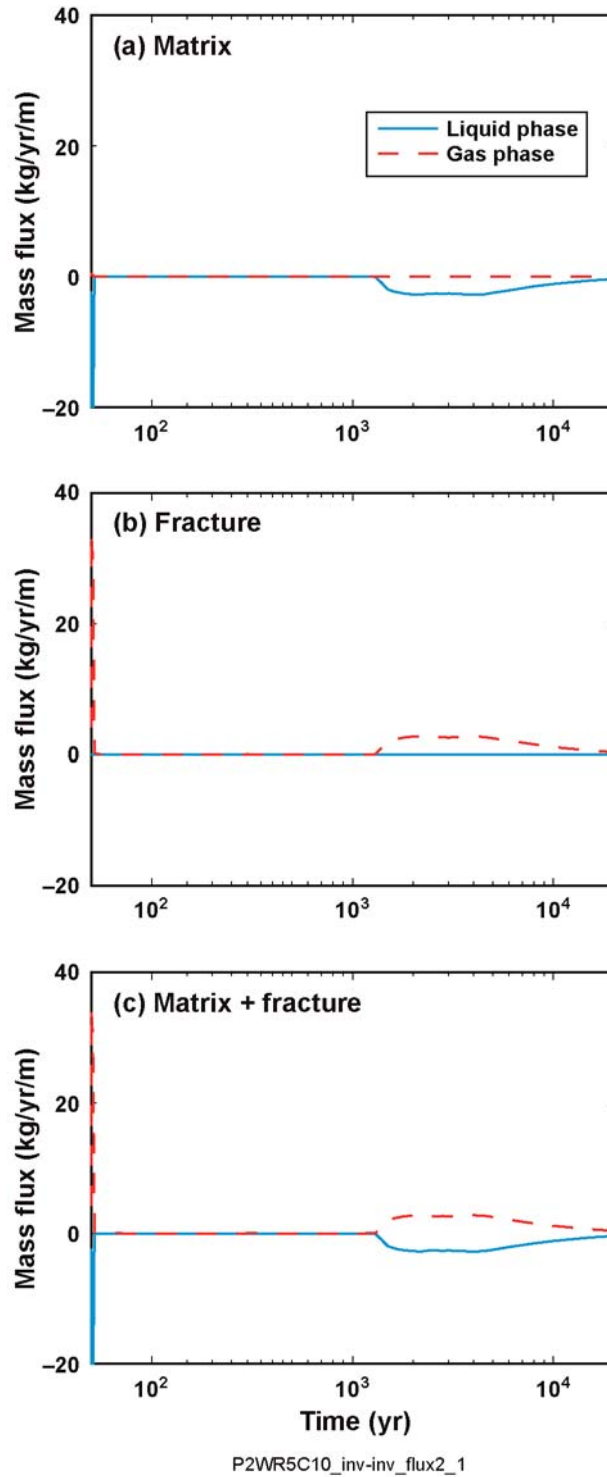
Source: See Table XIII-1.

NOTE: See Figure 6.3-1 for location. A positive value of mass flux corresponds to vertically downward flow. These fluxes are the result of line-averaged heating conditions.

Figure 6.3-42. Liquid-Phase and Gas-Phase Flux Between the Upper and Lower Half of the Invert Plotted for the (a) Matrix, (b) Fracture, and (c) Matrix + Fracture Continuum at the P2WR5C10 Location in the Tptpll (tsw35) Unit

P3R8C13_inv-hostrock+drift_flux3
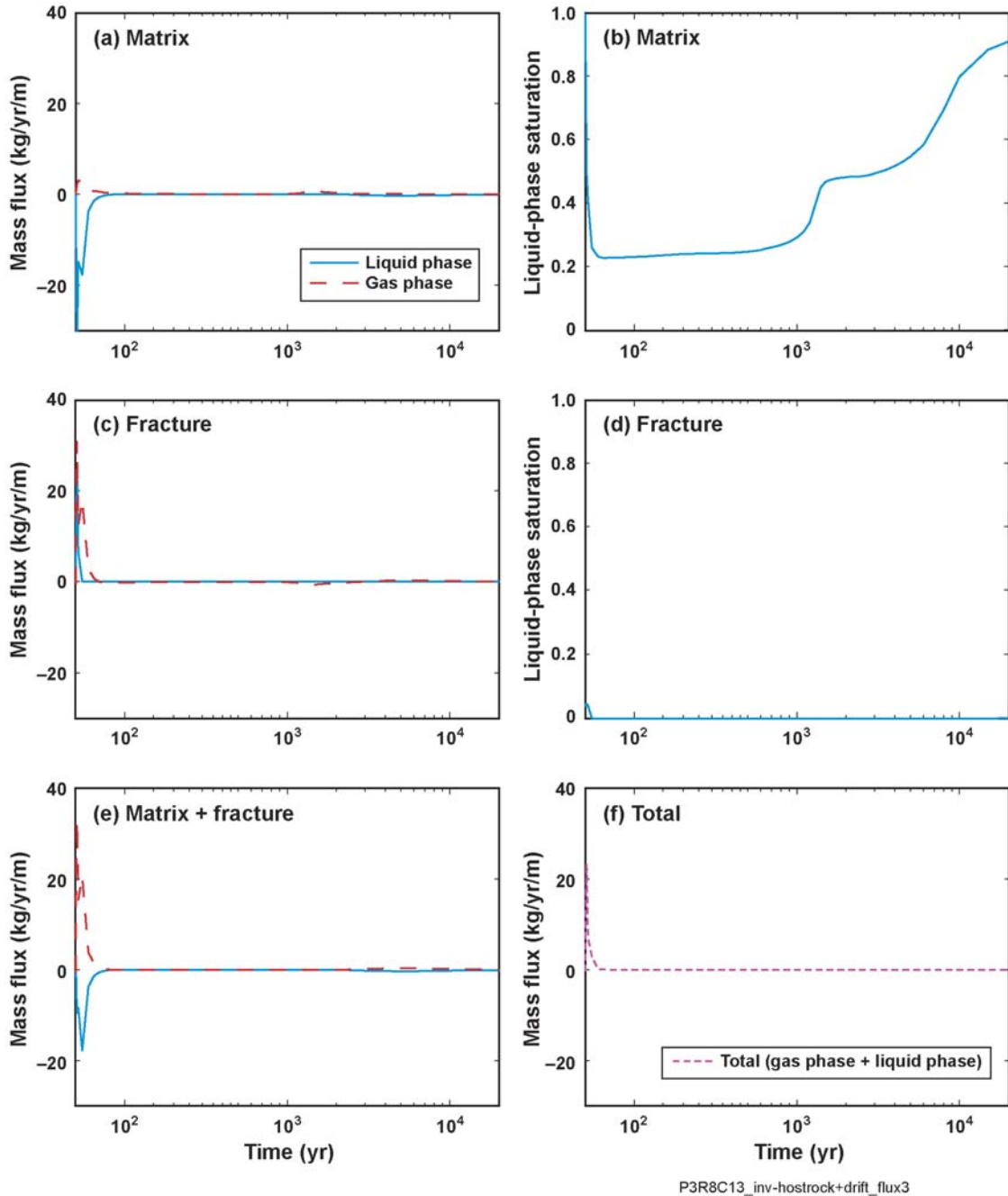
Source: See Table XIII-1.

NOTE: See Figure 6.3-1 for location. Also plotted is (f) the total (gas-phase + liquid-phase) mass flux for the matrix + fracture continua. A positive value of mass flux corresponds to flux out of the invert. Liquid-phase saturation for the (b) matrix and (d) fracture continuum is also plotted. These fluxes are the result of line-averaged heating conditions.

Figure 6.3-43. Liquid-Phase and Gas-Phase Flux Between the Invert and Adjoining Drift and Host Rock Plotted for the (a) Matrix, (c) Fracture, and (e) Matrix + Fracture Continuum at the P3R8C13 Location in the Tptpln (tsw36) Unit

P3R8C13_inv-inv_flux2_1
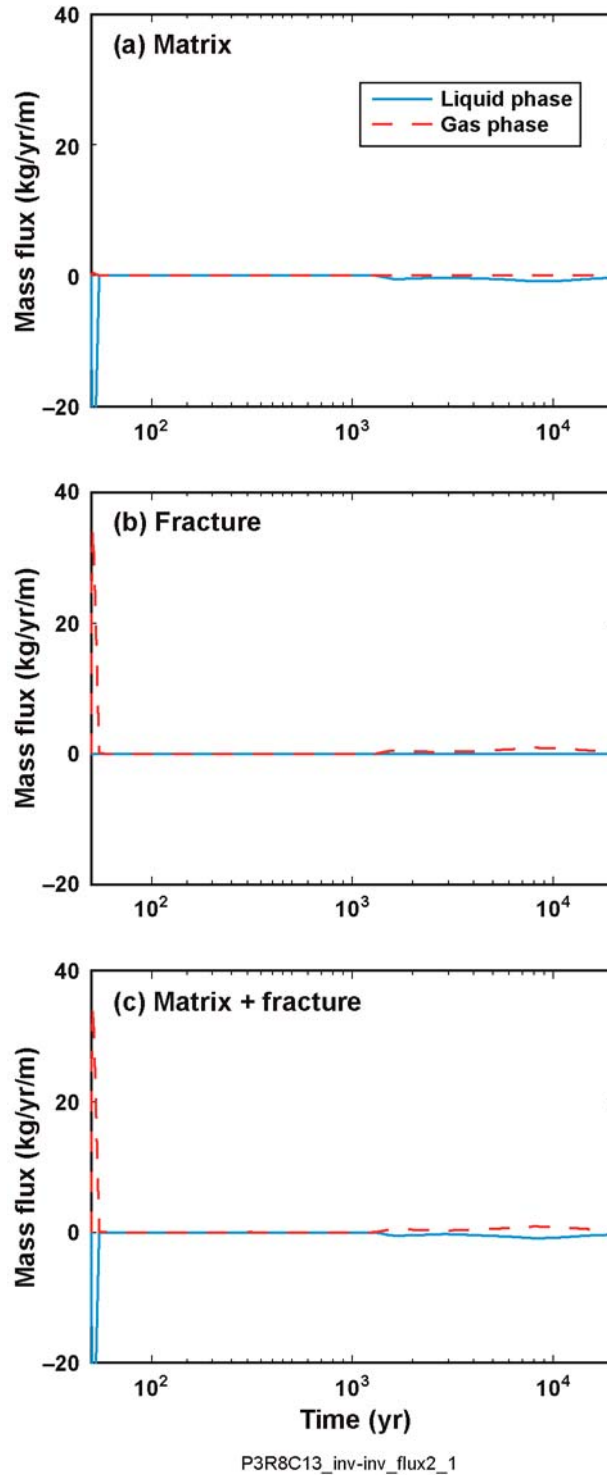
Source: See Table XIII-1.

NOTE: See Figure 6.3-1 for location. A positive value of mass flux corresponds to vertically downward flow. These fluxes are the result of line-averaged heating conditions.

Figure 6.3-44. Liquid-Phase and Gas-Phase Flux Between the Upper and Lower Half of the Invert Plotted for the (a) Matrix, (b) Fracture, and (c) Matrix + Fracture Continuum at the P3R8C13 Location in the Tptpln (tsw36) Unit

Table 6.3-33. Peak Values of Liquid-Phase and Gas-Phase Flux for the Matrix and Fracture Continuum Given for *t* > 50 Years at Two Different Interfaces

LDTH Submodel Location (Host-Rock Unit)	Interface	Mass Flux (kg/yr/m)					
		Matrix		Fracture		Matrix + Fracture	
		Liquid-Phase	Gas-Phase	Liquid-Phase	Gas-Phase	Liquid-Phase	Gas-Phase
P2ER8C6 Tptpul (tsw33)	Invert to drift + host rock	-74.18	5.57	49.92	48.95	-37.15	53.73
	Upper to lower invert	-40.77	0.33	0.00	47.96	-40.77	48.29
P2WR8C8 Tptpmn (tsw34)	Invert to drift + host rock	-27.25	3.25	27.29	23.19	-14.11	25.36
	Upper to lower invert	-35.06	0.40	0.00	35.02	-35.06	35.41
P2WR5C10 Tptpll (tsw35)	Invert to drift + host rock	-28.07	4.47	3.93	30.57	-28.07	33.09
	Upper to lower invert	-30.05	0.46	0.00	33.94	-30.05	34.41
P3R8C13 Tptpln (tsw36)	Invert to drift + host rock	-34.31	3.09	24.78	30.87	-17.77	32.92
	Upper to lower invert	-34.66	0.42	0.00	34.42	-34.66	34.84

NOTE: Values are given for *t* > 50 years at two different interfaces, including (1) between the invert and the adjoining drift and host rock and (2) between the upper and lower halves of the invert. The mass fluxes are given for four typical locations in the repository. These fluxes, which are the result of line-averaged heating conditions, are given in kg/yr per meter of drift. Because peak mass fluxes can occur at different times for the matrix and fracture, the sum of the peak matrix and fracture fluxes may not be equal to the peak matrix + fracture flux. These values are based on data plotted in Figures 6.3-37, 6.3-39, 6.3-41 and 6.3-43.

Table 6.3-34. Peak Values of Liquid-Phase and Gas-Phase Flux for the Matrix and Fracture Continuum Given for *t* > 100 Years at Two Different Interfaces

| LDTH Submodel Location (Host-Rock Unit) | Interface | Mass Flux (kg/yr/m) | | | | | |
| | | Matrix | | Fracture | | Matrix + Fracture | |
		Liquid-Phase	Gas-Phase	Liquid-Phase	Gas-Phase	Liquid-Phase	Gas-Phase
P2ER8C6 Tptpul (tsw33)	Invert to drift + host rock	-8.04	0.88	1.39	7.08	-7.97	7.91
	Upper to lower invert	-8.34	0.04	0.00	8.30	-8.34	8.33
P2WR8C8 Tptpmn (tsw34)	Invert to drift + host rock	-0.18	0.76	0.00	-0.79	-0.18	0.18
	Upper to lower invert	-1.89	-0.03	0.00	1.89	-1.89	1.89
P2WR5C10 Tptpll (tsw35)	Invert to drift + host rock	-1.87	0.62	0.02	1.42	-1.87	1.84
	Upper to lower invert	-2.77	0.03	0.00	2.75	-2.77	2.77
P3R8C13 Tptpln (tsw36)	Invert to drift + host rock	-0.31	0.66	0.00	-0.69	-0.31	0.31
	Upper to lower invert	-0.91	0.02	0.00	0.90	-0.91	0.91

NOTE: Values are given for *t* > 100 years at two different interfaces, including (1) between the invert and the adjoining drift and host rock and (2) between the upper and lower halves of the invert. The mass fluxes are given for four typical locations in the repository. These fluxes, which are the result of line-averaged heating conditions, are given in kg/yr per meter of drift. Because the peak mass fluxes can occur at different times for the matrix and fracture, the sum of the peak matrix and fracture fluxes may not be equal to the peak matrix + fracture flux. These values are based on data plotted in Figures 6.3-37, 6.3-39, 6.3-41 and 6.3-43.
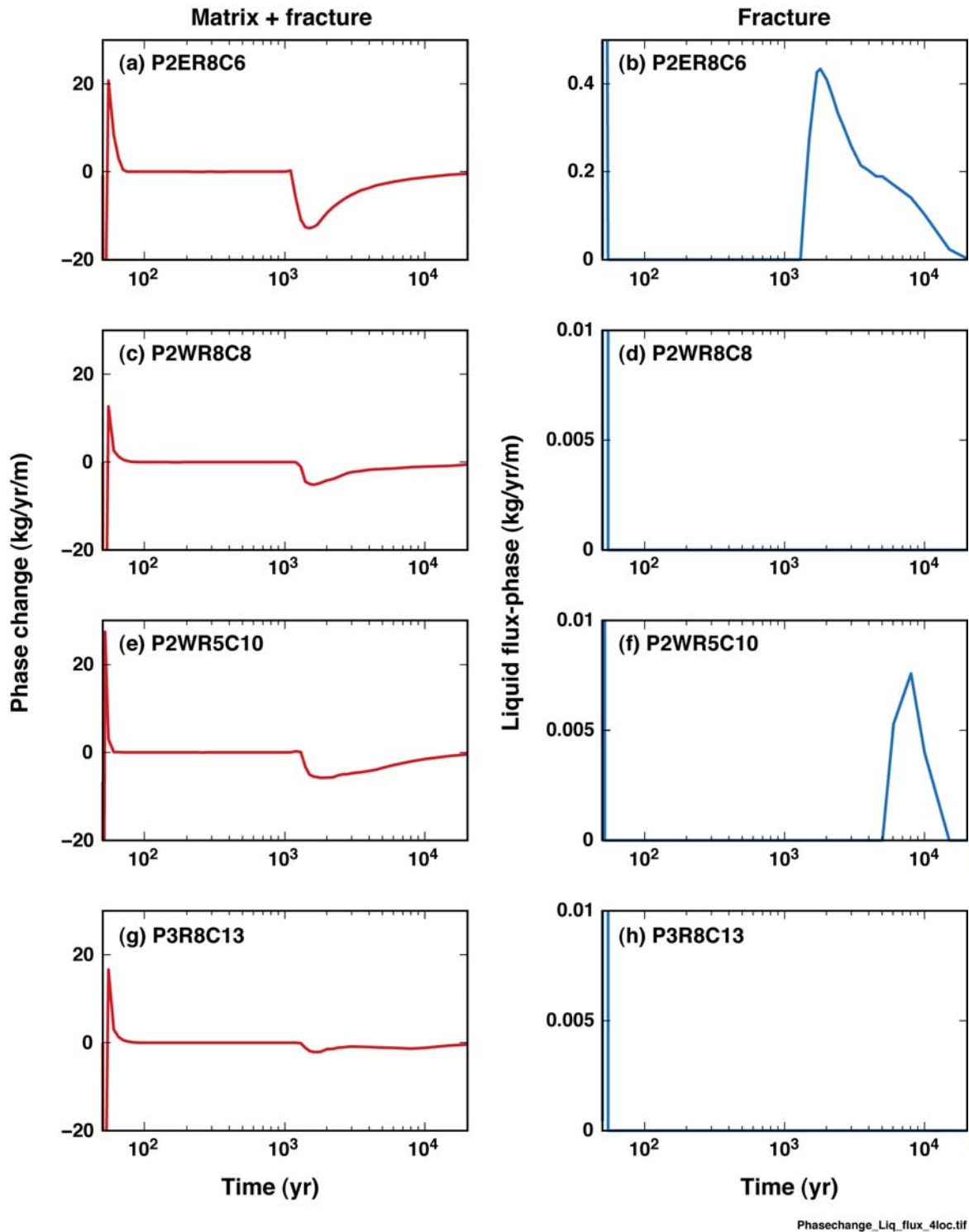
Source: See Table XIII-1.

NOTE: The locations (P2ER8C6, P2WR8C8, P2WR5C10, and P3R8C13) are shown in Figure 6.3-1. Positive values of phase change correspond to evaporation, while negative values correspond to condensation.

Figure 6.3-45. Phase Change (a, c, e, and g) in the Matrix and Fracture Continuum and Liquid-Phase Flux (b, d, f, h) in the Fracture Continuum Plotted for the Lower Two Gridblocks in the Invert at Four Locations in the Repository

As discussed above, during the rewetting period the return capillary-driven liquid-phase flux (in the matrix continuum) is greater than the outward gas-phase flux of water vapor (in the matrix and fracture continuum) leaving the invert. The total (or net) mass flux of water (liquid-phase plus gas-phase) is plotted in Figures 6.3-37f, 6.3-39f, 6.3-41f, and 6.3-43f. During the rewetting period, the magnitude of this net mass flux is a small negative value (which is too small to be readily apparent in these figures), indicating that mass is returning to the invert. To clearly demonstrate that water is returning to the invert during the rewetting period, and that a mass balance of water is achieved in the invert, the net accumulated mass flux of water out of the invert is plotted in Figures 6.3-46 through 6.3-49; these figures also plot the liquid-phase saturation history in the invert. Note that this rewetting process occurs over a very long period, while the initial dryout process occurred over a very short period at the beginning of the postclosure period ($t > 50$ yr). Note also that all time histories are plotted with a logarithmic time scale. During the *initial dryout* period, the liquid-phase saturation (very quickly) reaches its minimum value just as the net accumulated mass flux out of the invert has reached its maximum value. During the *sustained dryout* period, the liquid-phase saturation in the invert remains nearly constant, just as the net accumulated mass flux out of the invert remains nearly constant. During the *rewetting* period, the liquid-phase saturation in the invert gradually rises, just as the net accumulated mass flux out of the invert gradually declines.
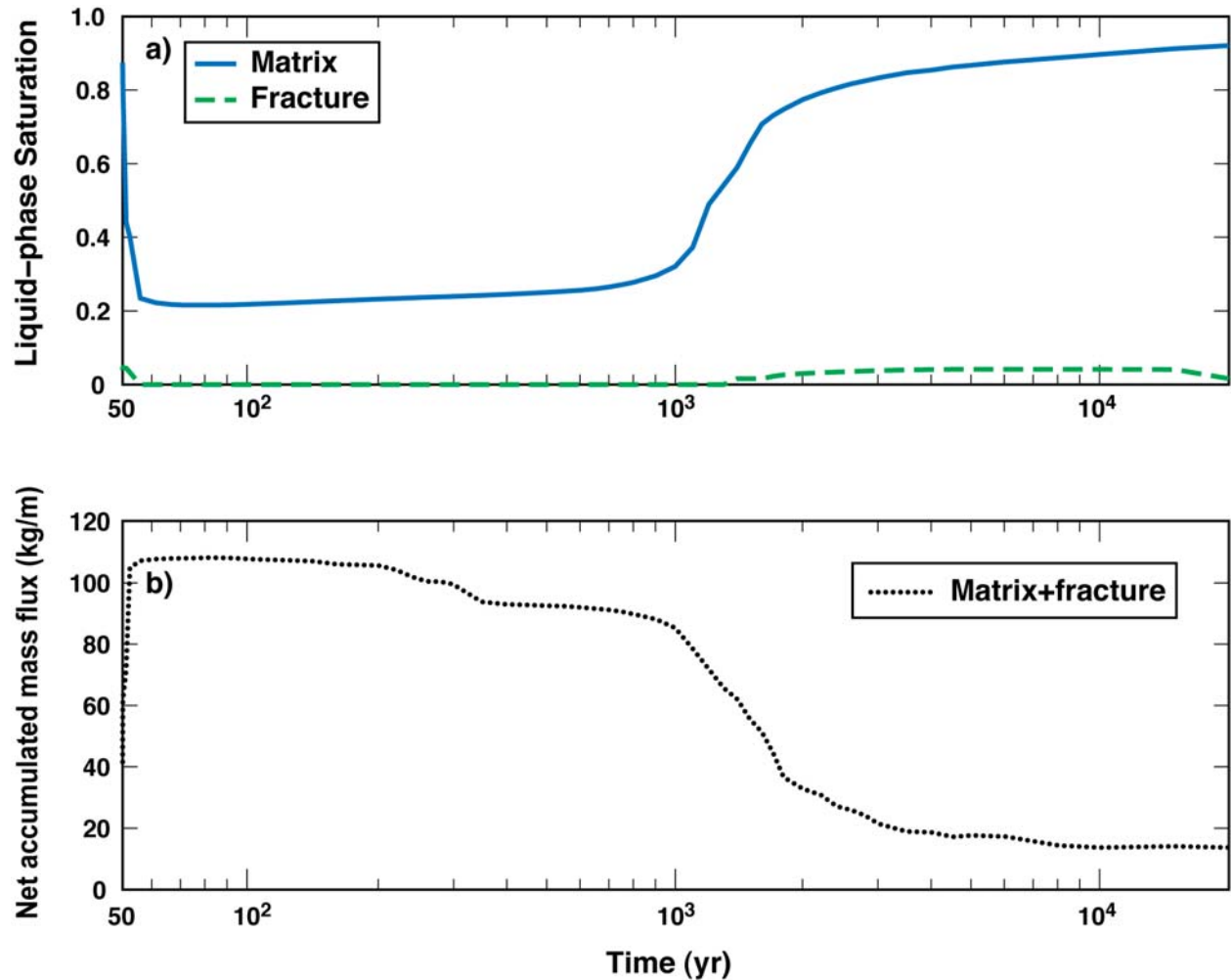
P2ER8C6-accumulatedFlux.tif

Source: See Table XIII-1.

NOTE: See Figure 6.3-1 for location. Increasing net accumulated mass flux indicates drying, while decreasing net accumulated mass flux indicates rewetting.

Figure 6.3-46. Mass Balance in the Invert Shown by Plotting (a) Liquid-Phase Saturation in the Fracture and Matrix Continuum in the Invert and (b) the Net Accumulated Mass Flux out of the Invert at the P2ER8C6 Location in the Tptpul (tsw33) Unit
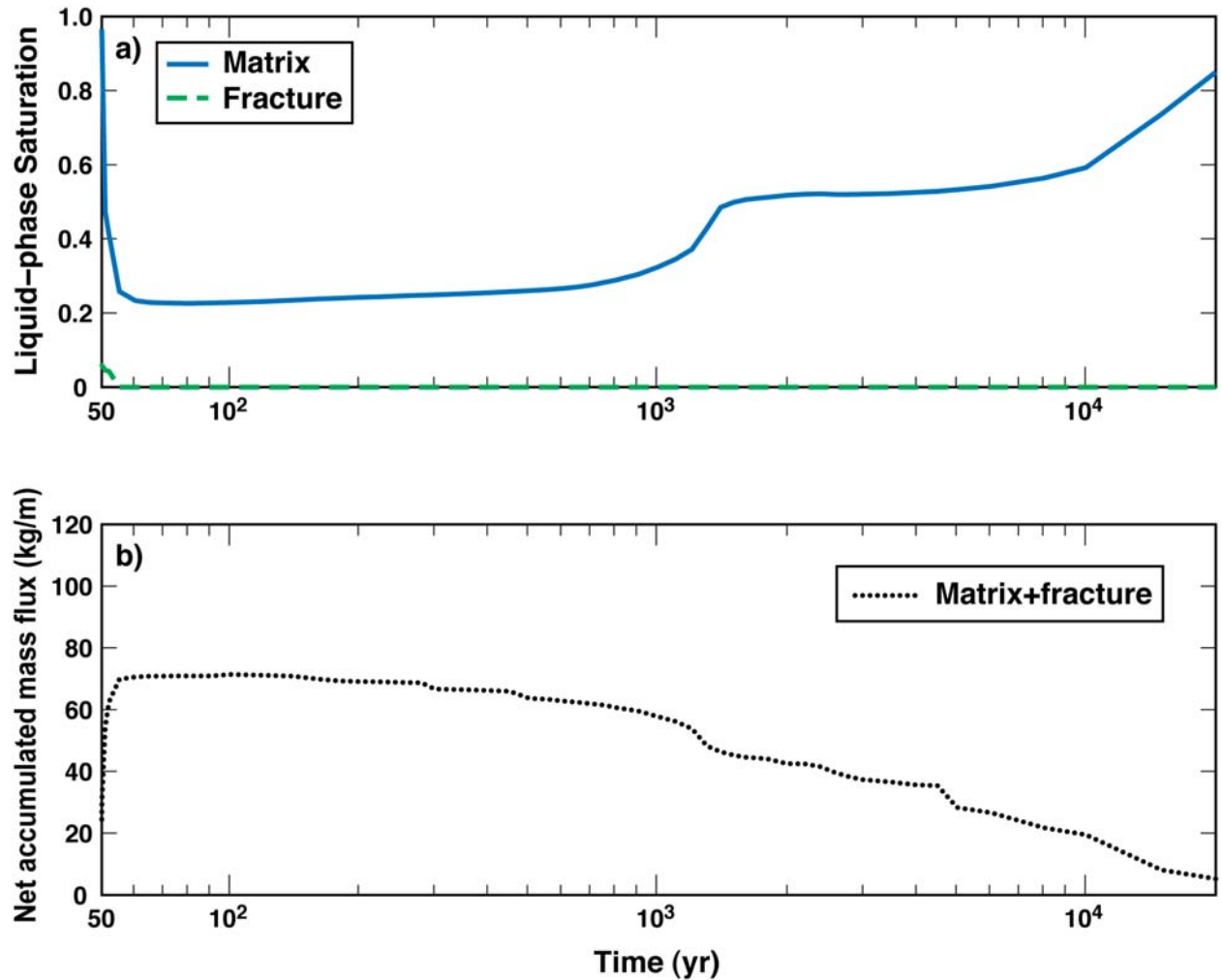
P2WR8C8-accumulatedFlux.tif

Source: See Table XIII-1.

NOTE: See Figure 6.3-1 for location. Increasing net accumulated mass flux indicates drying, while decreasing net accumulated mass flux indicates rewetting.

Figure 6.3-47. Mass Balance in the Invert Shown by Plotting (a) Liquid-Phase Saturation in the Fracture and Matrix Continuum in the Invert and (b) the Net Accumulated Mass Flux out of the Invert at the P2WR8C8 Location in the Tptpmn (tsw34) Unit
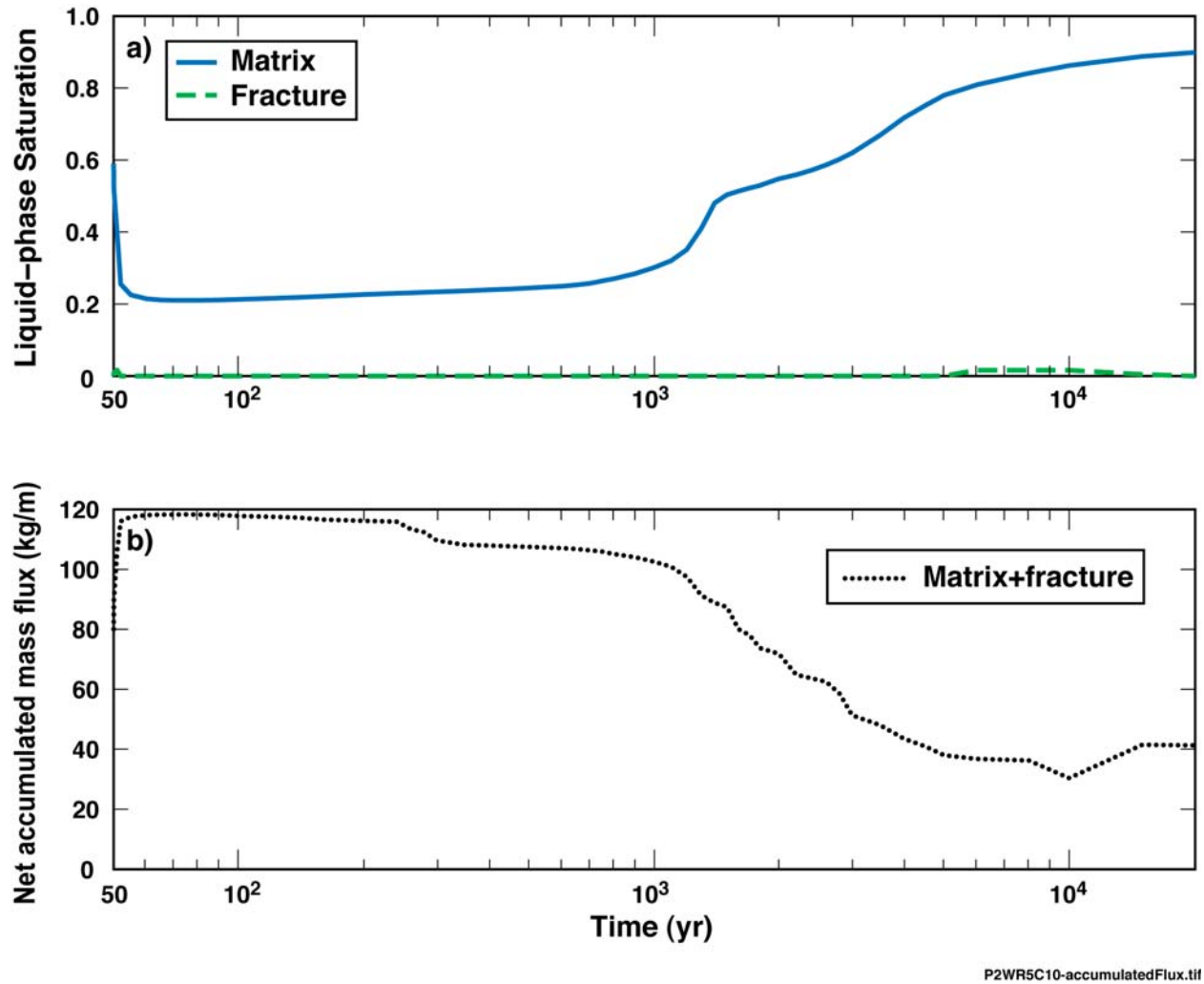
P2WR5C10-accumulatedFlux.tif

Source: See Table XIII-1.

NOTE: See Figure 6.3-1 for location. Increasing net accumulated mass flux indicates drying, while decreasing net accumulated mass flux indicates rewetting.

Figure 6.3-48. Mass Balance in the Invert Shown by Plotting (a) Liquid-Phase Saturation in the Fracture and Matrix Continuum in the Invert and (b) the Net Accumulated Mass Flux out of the Invert at the P2WR5C10 Location in the Tptpll (tsw35) Unit
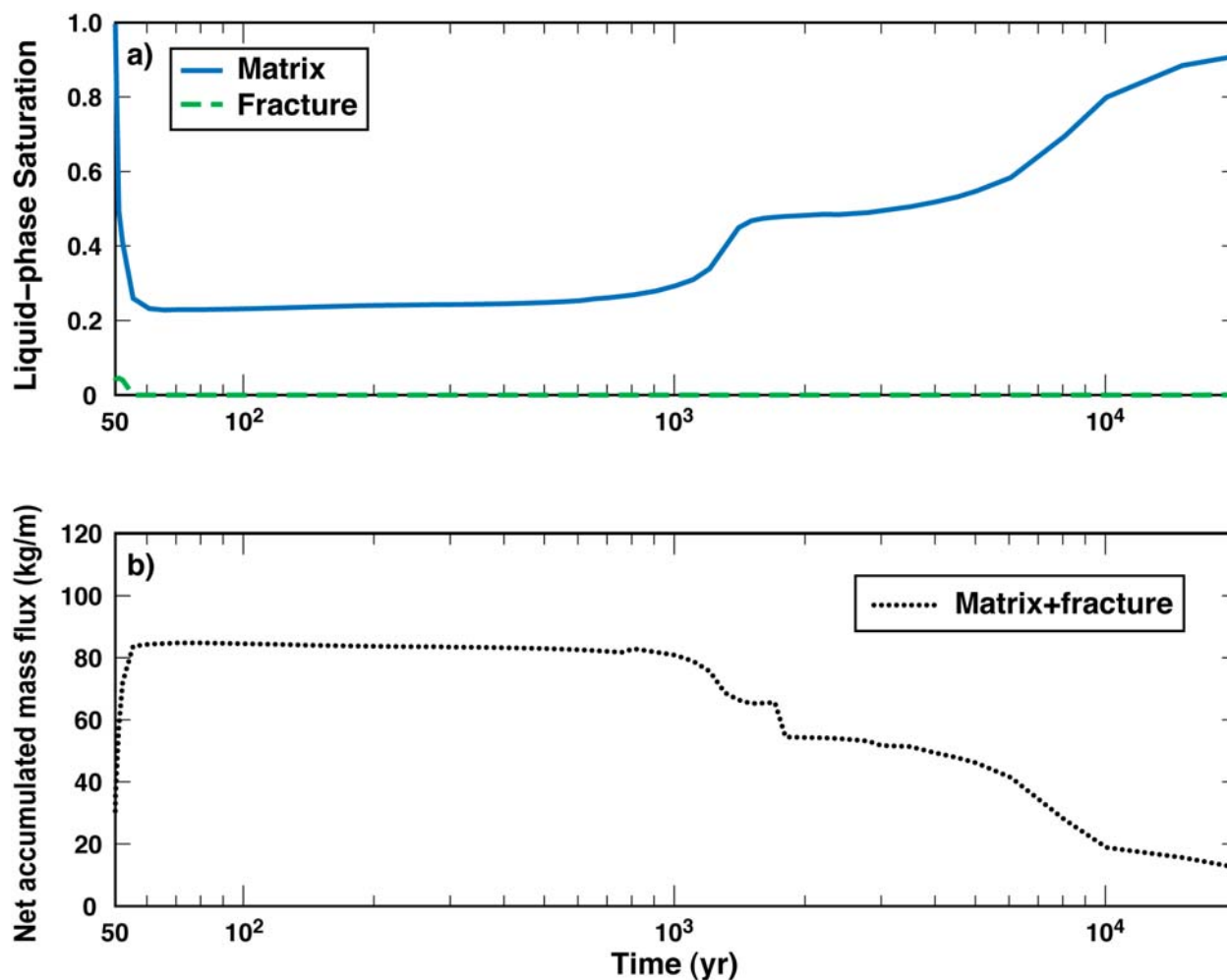
Source: See Table XIII-1.

NOTE: See Figure 6.3-1 for location. Increasing net accumulated mass flux indicates drying, while decreasing net accumulated mass flux indicates rewetting.

Figure 6.3-49. Mass Balance in the Invert Shown by Plotting (a) Liquid-Phase Saturation in the Fracture and Matrix Continuum in the Invert and (b) the Net Accumulated Mass Flux out of the Invert at the P3R8C13 Location in the Tptpln (tsw36) Unit

6.3.4   Combined Influences of Percolation-Flux and Host-Rock Thermal Conductivity Uncertainty on the TSPA-LA Base Case

The purpose of this section is to combine the analyses discussed in Sections 6.3.1.1 and 6.3.2.2. Section 6.3.2.2 describes a sensitivity analysis of the influence of host-rock thermal conductivity uncertainty on thermal-hydrologic behavior in the repository. The analysis in Section 6.3.2.2 was conducted at four locations in the repository (Figure 6.3-1), which cover all four of the host-rock units (Table 6.3-3). This analysis does not explicitly address thermal-hydrologic behavior across the entire repository. These four repository locations (P2ER8C6, P2WR8C8, P2WR5C10, and P3R8C13) were selected because their respective values of percolation flux are relatively close to the repository-wide averages for the mean infiltration-flux case (Tables 6.3-4, 6.3-5, and 6.3-9). Section 6.3.1.1 describes the MSTHM TSPA-LA base-case calculations of the

entire repository for the three infiltration-flux cases (lower, mean, and upper). Thus, Section 6.3.1.1 addresses the influence of percolation-flux uncertainty on the MSTHM TSPA-LA base-case calculations for the entire repository. The purpose of this subsection (Section 6.3.4) is to address the combined influences of percolation-flux and host-rock thermal conductivity uncertainty on the MSTHM TSPA-LA base-case calculations for the entire repository.

As discussed in Section 6.3.2, the two most significant sources of uncertainty for the output of the MSTHM are host-rock thermal conductivity and percolation flux. Percolation-flux uncertainty is addressed in Section 6.3.1.1 of this report with the use of the three infiltration-flux cases, which are called the lower-, mean, and upper-bound infiltration-flux cases (Table 6.3-4). The three cases in Section 6.3.1.1 use the mean thermal conductivity values (Table 6.3-23) for the four host-rock units (also called repository units), as well as for all of the non-repository units. The probabilities of the three infiltration-flux cases are provided in Table 6.3-35, which is based on Table 6-7 of Section 6.3.2 of *Analysis of Infiltration Uncertainty* (BSC 2003 [DIRS 165991]), excluding the contingency area. The sensitivity of thermal-hydrologic behavior to host-rock thermal conductivity uncertainty is addressed for approximately ±1 standard deviation about the mean values (Table 6.3-23).

Table 6.3-35. Probabilities of the Three Infiltration-Flux Cases

Infiltration-Flux Case	Probability
Lower	0.24
Mean	0.41
Upper	0.35
Total	1.00

Source: Table 6-7 of BSC 2003 [DIRS 165991].

The three host-rock thermal conductivity cases, which are called the low-, mean, and high-thermal conductivity cases, are used to address parametric uncertainty. The guidelines for TSPA-LA define certain types of uncertainty (BSC 2002 [DIRS 158794], Section 4.1). Variability, also referred to as aleatory uncertainty, arises due to natural randomness or heterogeneity. This first type of uncertainty cannot be reduced through further testing and data collection; it can only be better characterized. Thus, aleatory uncertainty is also referred to as irreducible uncertainty. The second type of uncertainty, which is referred to as epistemic uncertainty, arises from lack of knowledge about a parameter because the data are limited or there are alternative interpretations of the available data. This second type of uncertainty is also called reducible uncertainty because the state of knowledge can be improved with further testing or data collection.

Section 6.2.4 describes the manner in which the MSTHM combines the results from the four submodel types. The SMT submodel (Section 6.2.5) is used to determine the repository-scale variations in host-rock temperature as affected by the mountain-scale thermal-property distribution, the overburden-thickness distribution, and the edge-cooling effect, which is strongly affected by the overall shape of the repository area. The LDTH submodels (Section 6.2.6) are used to determine the influence of local conditions on thermal-hydrologic behavior, including percolation flux and the thermal and hydrologic properties of the local host-rock unit. Percolation-flux uncertainty is incorporated in only the LDTH submodels. In the same fashion,

host-rock thermal conductivity uncertainty is also incorporated in only the LDTH submodels. The SMT submodel does not incorporate host-rock thermal conductivity uncertainty because it would only potentially influence the rate at which the edge-cooling effect propagates from the edges towards the central region of the repository. At the scale at which the edge-cooling effect propagates, the natural randomness of host-rock thermal conductivity distribution tends to average out, allowing, in effect, the mean thermal conductivity values to control the rate at which the edge-cooling effective propagates in those respective units. Note that for the low-thermal conductivity case, K_{th} is equal to the mean minus one standard deviation for all of the host-rock units. Similarly, for the high-thermal conductivity case, K_{th} is equal to the mean plus one standard deviation for all of the host-rock units: (1) Tptpul (tsw33), (2) Tptpmn (tsw34), (3) Tptpll (tsw35), and (4) Tptpln (tsw36 and tsw37).

In *Thermal Conductivity of the Potential Repository Horizon* (BSC 2004 [DIRS 169854]), fifty equally likely sets of three-dimensional thermal conductivity fields (or realizations) are generated for the four host-rock units. Each field has a mean thermal conductivity, μ_{ij}, and a standard deviation, σ_{ij}, for local variability in thermal conductivity (e.g., see Figure 6-31 of BSC 2004 [DIRS 169854]), where $i = 1, 2, 3, 4$ corresponds to the four host-rock units and $j = 1, 2,\ldots, 50$ corresponds to the fifty fields (or realizations). Values for

$$\mu_i = \frac{1}{50}\sum_{j=1}^{50}\mu_{ij}$$

and

$$\sigma_i = \frac{\sigma_{i,15} + \sigma_{i,30} + \sigma_{i,45}}{3}$$

are reported in Table 7-10 of DTN: SN0404T0503102.011 [DIRS 169129] (File: ReadMeSummary.doc). The quantity σ_i is a reasonable estimator of drift-scale variability and uncertainty, and is appropriate for use in the LDTH submodels.

Calculations performed using $\mu_i - \sigma_i$, μ_i, and $\mu_i + \sigma_i$ (Table 6.3-20) raise the question concerning how much weight (i.e., probability in the epistemic sense) should be applied to these three host-rock thermal conductivity cases. Probability distributions for μ_{ij} for the fifty fields are presented in *Thermal Conductivity of the Potential Repository Horizon* (e.g., see lower right plot in Figure 6-31 of BSC 2004 [DIRS 169854]). These distributions are very narrow, with $\mu_i \pm \sigma_i$ tending to be close to the extremes of the presented distributions. As presented by *Thermal Conductivity of the Potential Repository Horizon* (BSC 2004 [DIRS 169854]), the distributions for μ_i, probably underestimate the uncertainty in μ_i (i.e., the value for a single effective thermal conductivity to be used over an entire host-rock unit) because they are based only on the fifty fields generated without including potential epistemic uncertainties, such as (1) those associated with the quality of the observational data underlying the generation of the fields, (2) those associated with the model used in determining thermal conductivity values, and (3) the appropriateness of the geostatistical model used in the generation of the thermal conductivity fields.

Therefore, neither $\mu_i - \sigma_i$ nor $\mu_i + \sigma_i$ represents extreme or unlikely values for the appropriate effective (i.e., spatially averaged) thermal conductivity values to be applied to the respective host-rock units in the LDTH submodels. Furthermore, neither $\mu_i - \sigma_i$ nor $\mu_i + \sigma_i$ is more or less likely than μ_i to be the appropriate value to be applied for effective thermal conductivity in the host-rock units in the LDTH submodels. As a result of this argument, each alternative ($\mu_i - \sigma_i$, μ_i, and $\mu_i + \sigma_i$) can be assigned the same probability (i.e., one in three), which is shown in Table 6.3-36.

Combining the probabilities of the three infiltration-flux cases (Table 6.3-35) and the equal (one in three) probabilities of the three host-rock thermal conductivity cases results in a three-by-three matrix of nine percolation-flux host-rock thermal conductivity cases provided in Table 6.3-36. Repository-wide MSTHM calculations were conducted for five of these nine cases, including the three infiltration-flux cases conducted with the mean thermal conductivity values (Section 6.3.1.1), as well as the two cases with the extreme combinations of percolation flux and host-rock thermal conductivity: (1) the lower-bound infiltration-flux, low host-rock thermal conductivity case, and (2) the upper-bound infiltration-flux, high host-rock thermal conductivity case. The four cases for which repository-wide calculations were not conducted are shown in italics in Table 6.3-36.

Table 6.3-36. Probabilities of the Combinations of the Three Infiltration-Flux Cases and the Three Host-Rock Thermal Conductivity Cases

| | Probability | | | |
| | Host-Rock Thermal Conductivity Case | | | |
Infiltration-Flux Case	All	Low (Mean – 1 SD)	Mean	High (Mean + 1 SD)
All	1.0000	0.33333	0.33333	0.33333
Lower	0.2400	0.08000	0.08000	*0.08000*
Mean	0.4100	*0.13667*	0.13667	*0.13667*
Upper	0.3500	*0.11666*	0.11666	0.11666

NOTE: SD stands for standard deviation. Repository-wide MSTHM calculations were not conducted for the four cases shown in italics.

Figure 6.3-50 outlines how the four cases for which repository-wide MSTHM calculations were not made (shown in italics in Table 6.3-36) are addressed by the other five cases. First, as was shown in Sections 6.3.2.1 and 6.3.2.2, low percolation flux and low host-rock thermal conductivity affect thermal-hydrologic behavior in a similar fashion, which is to create hotter drier conditions in the adjoining host rock, and high percolation flux and high host-rock thermal conductivity affect thermal-hydrologic behavior similarly, by creating cooler, less dry conditions in the adjoining host rock. Accordingly, there are two cases for which percolation flux and host-rock thermal conductivity have opposing effects: (1) the lower-bound infiltration-flux case with high host-rock thermal conductivity and (2) the upper-bound infiltration-flux case with low host-rock thermal conductivity. For both of these cases, the effects of percolation flux and host-rock thermal conductivity tend to be mutually canceling and the net effect is equivalent to having the mean infiltration-flux case with mean host-rock thermal conductivity. These two cases appear in the upper right and lower left corners of Figure 6.3-50. The arrows from the upper right and lower left corners that point to the center of Figure 6.3-50 are depicting how the mean infiltration-flux case with mean host-rock thermal conductivity is the "surrogate" case for these two "corner" cases. Thus, the probabilities (Table 6.3-36) for the lower-bound

infiltration-flux case with high host-rock thermal conductivity (0.08000) and for the upper-bound infiltration flux with low thermal conductivity (0.11666) are added to that of the mean infiltration-flux case with mean host-rock thermal conductivity (0.13667), resulting in a combined probability of 0.33333, as shown in Table 6.3-37.
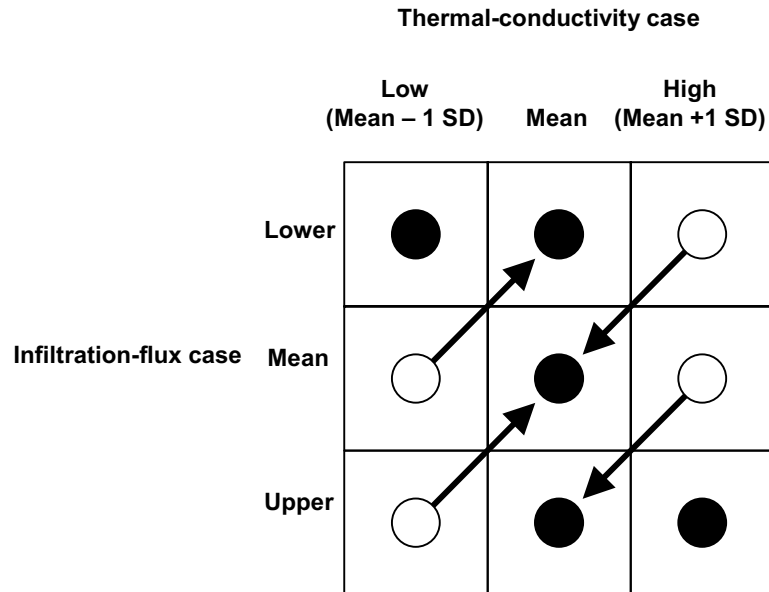
NOTES: The open circles correspond to the cases for which repository-wide MSTHM calculations were not conducted. The filled circles correspond to the cases for which repository-wide MSTHM calculations have been conducted.

Figure 6.3-50. Regrouping of the Three-by-Three Matrix of Infiltration Flux and Host-Rock Thermal Conductivity Cases

Table 6.3-37. Probabilities of the Combinations of the Three Infiltration-Flux Cases and the Three Host-Rock Thermal Conductivity Cases after the Regrouping Shown in Figure 6.3-50

	Probability			
		Host-Rock Thermal Conductivity Case		
Infiltration-Flux Case	All	Low (Mean – 1 SD)	Mean	High (Mean + 1 SD)
All	1.0000	0.33333	0.33333	0.33333
Lower	0.2400	0.08000	0.21667	
Mean	0.4100		0.33333	
Upper	0.3500		0.25334	0.11666

NOTE: SD stands for standard deviation.

As discussed above, low percolation flux and low host-rock thermal conductivity affect thermal-hydrologic behavior in a similar fashion, which is to promote hotter drier conditions in the adjoining host rock. Accordingly, the lower-bound infiltration-flux case with mean host-rock thermal conductivity is the "surrogate" case for the mean infiltration-flux case with low host-rock thermal conductivity. This substitution is depicted in Figure 6.3-50 by the arrow pointing from the left column in the middle row to the middle column in the upper row. Thus, the probability (Table 6.3-36) for the mean infiltration-flux case with low host-rock thermal conductivity (0.13667) is added to that of the lower-bound infiltration-flux case with mean

host-rock thermal conductivity (0.08000), resulting in a combined probability of 0.21667, as shown in Table 6.3-37.

As discussed above, high percolation flux and high host-rock thermal conductivity affect thermal-hydrologic behavior in a similar fashion, which is to promote cooler, less dry conditions in the adjoining host rock. Accordingly, the upper-bound infiltration-flux case with mean host-rock thermal conductivity is the "surrogate" case for the mean infiltration-flux case with high host-rock thermal conductivity. This substitution is depicted in Figure 6.3-50 by the arrow pointing from the right column in the middle row to the middle column in the lower row. Thus, the probability (Table 6.3-36) for the mean infiltration-flux case with high host-rock thermal conductivity (0.13667) is added to that of the upper-bound infiltration-flux case with mean host-rock thermal conductivity (0.11666), resulting in a combined probability of 0.25334, as shown in Table 6.3-37.

Figure 6.3-51 gives the complementary cumulative distribution function (CCDF) for the peak temperature on the drift wall and on waste packages for the five infiltration-flux/host-rock thermal conductivity cases; these CCDFs are for all waste packages over the entire repository area. Table 6.3-38 gives the coolest, median, and hottest peak drift-wall and waste package temperatures for these five cases. Because there are 2874 locations in the MSTHM (Table 6.2-1) and eight different waste packages that are represented at each location, there are a total of 22,992 waste package histories provided in each of the five cases for which repository-wide MSTHM calculations were conducted. For the upper-bound infiltration-flux case with high host-rock thermal conductivity, there are 22 waste package histories for which the peak drift-wall temperature is less than the boiling point (96°C). These 22 histories represent 0.10 percent of the 22,992 histories in that case. Because that case has a probability of 0.11666 (Table 6.3-37), these 22 waste package histories are representative of only 0.01 percent of all waste packages in the repository. Thus, for a total of 11,184 waste packages in the repository (Table 4.1-2), there is a probability of 1.0 that a single waste package will never experience boiling at the drift wall. For the lower-bound infiltration-flux case with low host-rock thermal conductivity, there are 106 waste package histories for which the peak waste package temperature is greater than 200°C. Because the probability of this case is 0.08000, these 106 histories are representative of only 0.04 percent of all waste packages in the repository. Thus, for a total of 11,184 waste packages in the repository (Table 4.1-2), only four waste packages are predicted to have a peak temperature in excess of 200°C.
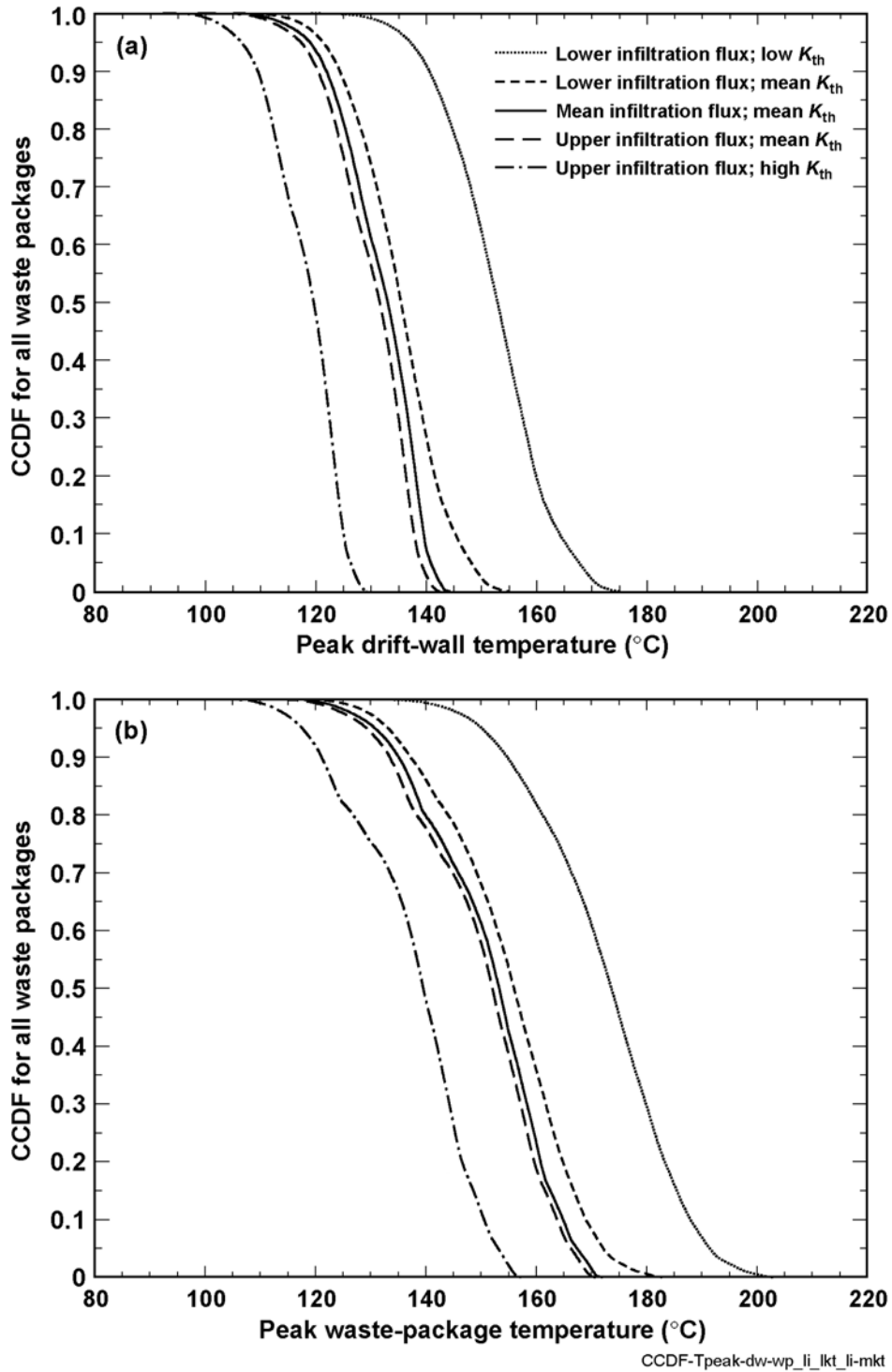
Source: See Table XIII-1.

NOTE: These five cases cover the range of percolation-flux and host-rock thermal conductivity uncertainty addressed in this report.

Figure 6.3-51. Complementary Cumulative Distribution Function (CCDF) for Peak Temperature on the (a) Drift Wall and on the (b) Waste Packages Plotted for Five Cases

Table 6.3-38. Peak Drift-Wall and Waste Package Temperatures Summarized for Five Cases

Case	Peak Drift-Wall Temperature (°C)			Peak Waste Package Temperature (°C)		
	Coolest	Median	Hottest	Coolest	Median	Hottest
Lower-bound infiltration-flux, low thermal conductivity	119.1	152.9	175.2	130.1	173.6	203.1
Lower-bound infiltration-flux, mean thermal conductivity	105.7	135.4	154.8	116.3	156.0	182.9
Mean infiltration-flux, mean thermal conductivity	105.0	133.0	144.2	115.6	153.3	172.0
Upper-bound infiltration-flux, mean thermal conductivity	98.6	131.6	142.5	108.6	152.1	170.8
Upper-bound infiltration-flux, high thermal conductivity	92.3	119.6	129.3	102.0	139.5	157.2

NOTE: These cases cover the range of percolation-flux and host-rock thermal conductivity uncertainty addressed in this report. This table is based on Figure 6.3-51. These values are data plotted in Figure 6.3-51.

Figure 6.3-52a and Table 6.3-39 give the complementary cumulative distribution function (CCDF) for the time when boiling at the drift wall ceases for the five infiltration-flux host-rock thermal conductivity cases; these CCDFs are for all waste package locations throughout the repository area. As was the case for peak temperatures, the boiling period duration increases with decreasing percolation flux and with decreasing host-rock thermal conductivity. The median waste package experiences boiling at the drift wall for 721 years, and there is a broad range of duration of boiling at the drift wall. There is a probability of less than 1.0 that a single waste package will never experience boiling at the drift, while the waste package at the hottest, driest location in the repository may experience boiling at the drift wall for up to 2,176 years. Figure 6.3-52b and Table 6.3-40 provide the complementary cumulative distribution function (CCDF) for the maximum lateral extent of the boiling point isotherm for the five cases. As was the case for the peak temperatures and boiling period duration, the maximum lateral extent of boiling increases with decreasing percolation flux and with decreasing host-rock thermal conductivity. The median waste package has a maximum lateral extent of boiling of 7.9 m, which is 5.15 m beyond the springline of the drift. There is a probability of less than 1.0 that a single waste package will never experience boiling in the host rock, while the waste package at the hottest, driest location in the repository may have a maximum lateral extent of boiling of 27.9 m, which represents 69 percent of the lateral extent between the emplacement drift centerline and the midplane in the center of the rock pillar between drifts. For the lower-bound infiltration-flux, low host-rock-thermal conductivity case, 10 percent of the waste package histories have a maximum lateral extent of boiling that exceeds 19 m. Because the probability of this case is 0.08000 (Table 6.3-37), this is representative of 0.8 percent of the waste packages in the repository. Thus, for a total of 11,184 waste packages in the repository (Table 4.1-2), 89 waste packages are expected to have a maximum lateral extent of boiling that exceeds 19 m.
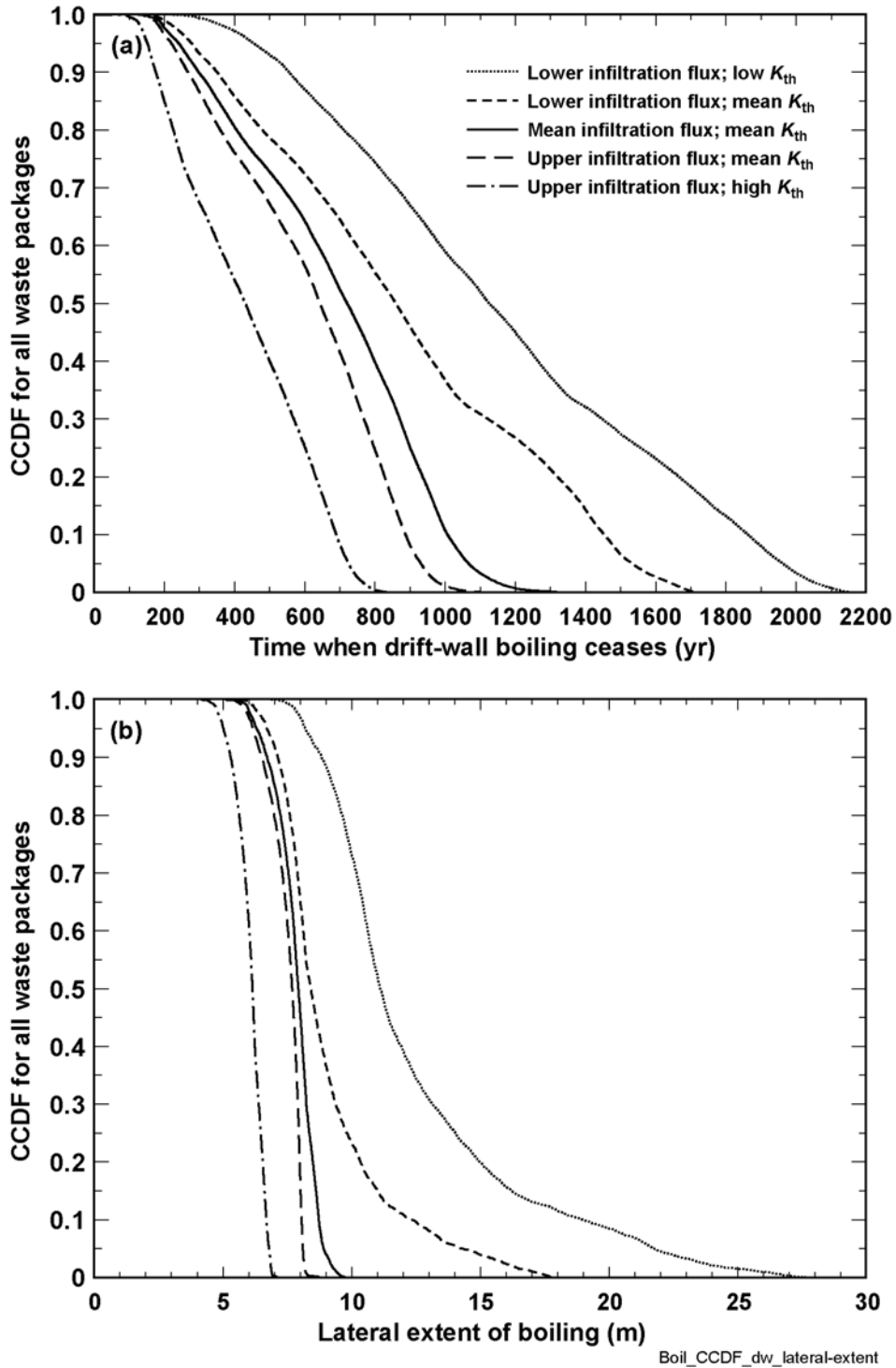
Source: See Table XIII-1.

NOTE: These five cases cover the range of percolation-flux and host-rock thermal conductivity uncertainty addressed in this report.

Figure 6.3-52. Complementary Cumulative Distribution Functions (CCDF) for (a) the Time When Boiling at the Drift Wall Ceases and (b) the Maximum Lateral Extent of the Boiling-Point Isotherm (96°C) from the Drift Centerline, Plotted for Five Cases

Table 6.3-39. Time When Boiling Ceases at the Drift Wall Summarized for Five Cases

Infiltration-Flux, Host-Rock Thermal Conductivity Case	Time When Boiling at the Drift Wall Ceases (years)						
	Shortest	10 Percentile	30 Percentile	Median	70 Percentile	90 Percentile	Longest
Lower-bound infiltration-flux, low thermal conductivity	192.6	555.3	861.6	1125.4	1447.4	1862.7	2176.5
Lower-bound infiltration-flux, mean thermal conductivity	130.2	349.9	630.9	859.6	1122.5	1453.3	1734.6
Mean infiltration-flux, mean thermal conductivity	127.2	297.5	535.8	721.0	870.6	1006.5	1356.0
Upper-bound infiltration-flux, mean thermal conductivity	97.7	267.7	471.6	643.7	768.6	887.2	1162.9
Upper-bound infiltration-flux, high thermal conductivity	NA[a]	175.7	281.6	430.4	568.9	689.5	859.5

[a] 22 out of 22,992 waste package/location combinations (or 0.1 percent of the total) never experience boiling at the drift wall.

NOTE: These cases cover the range of percolation-flux and host-rock thermal conductivity uncertainty addressed in this report. This table is based on data plotted in Figure 6.3-52a.

Table 6.3-40. Maximum Lateral Extent of the Boiling-Point Isotherm (96°C) Measured from the Drift Centerline, Summarized for Five Cases

Infiltration-Flux, Host-Rock Thermal Conductivity Case	Maximum Lateral Extent of Boiling (T > 96°C) (m)						
	Least	10 Percentile	30 Percentile	Median	70 Percentile	90 Percentile	Greatest
Lower-bound infiltration-flux, low thermal conductivity	6.9	8.8	10.2	11.1	13.2	19.0	27.9
Lower-bound infiltration-flux, mean thermal conductivity	5.6	7.1	7.9	8.4	9.4	12.3	17.8
Mean infiltration-flux, mean thermal conductivity	5.3	6.7	7.5	7.9	8.2	8.7	9.9
Upper-bound infiltration-flux, mean thermal conductivity	5.1	6.5	7.3	7.7	7.9	8.1	9.0
Upper-bound infiltration-flux, high thermal conductivity	4.1[a]	5.3	5.9	6.1	6.4	6.7	7.2

[a] 22 out of 22,992 waste package/location combinations (or 0.1 percent of the total) never experience boiling at the drift wall; therefore, for those locations, the lateral extent of boiling is inside the emplacement drift.

NOTE: These cases cover the range of percolation-flux and host-rock thermal conductivity uncertainty addressed in this report. This table is based on data plotted in Figure 6.3-52b.

6.3.5 Summary of the Range of Thermal-Hydrologic Conditions for the TSPA-LA Base Case

In Section 6.3, the ranges of thermal-hydrologic conditions across the repository are described for the five infiltration-flux host-rock thermal conductivity cases addressed in this report (Table 6.3-37). Figure 6.3-53 gives the corresponding ranges of temperature and relative–humidity histories for all waste packages. The plots in Figure 6.3-53, sometimes referred to as "horsetail" plots, also break down the ranges in temperature and relative–humidity histories into CSNF and DHLW groupings. The peak temperatures are predicted to be 203.1°C and 189.4°C for the hottest CSNF and DHLW waste packages, respectively. The peak temperatures are predicted to be 107.7°C and 102.0°C for the coolest CSNF and DHLW waste packages, respectively. Table 6.3-39 shows that the predicted range in the time when boiling at the drift wall ceases ranges from no boiling to 2176.5 years. The ranges in thermal-hydrologic conditions shown in Figure 6.3-53 incorporate the influence of percolation-flux uncertainty, as it is represented in the lower, mean, and upper infiltration-flux cases. The ranges in thermal-hydrologic conditions shown in Figure 6.3-53 also incorporate the influence of host-rock thermal conductivity uncertainty.
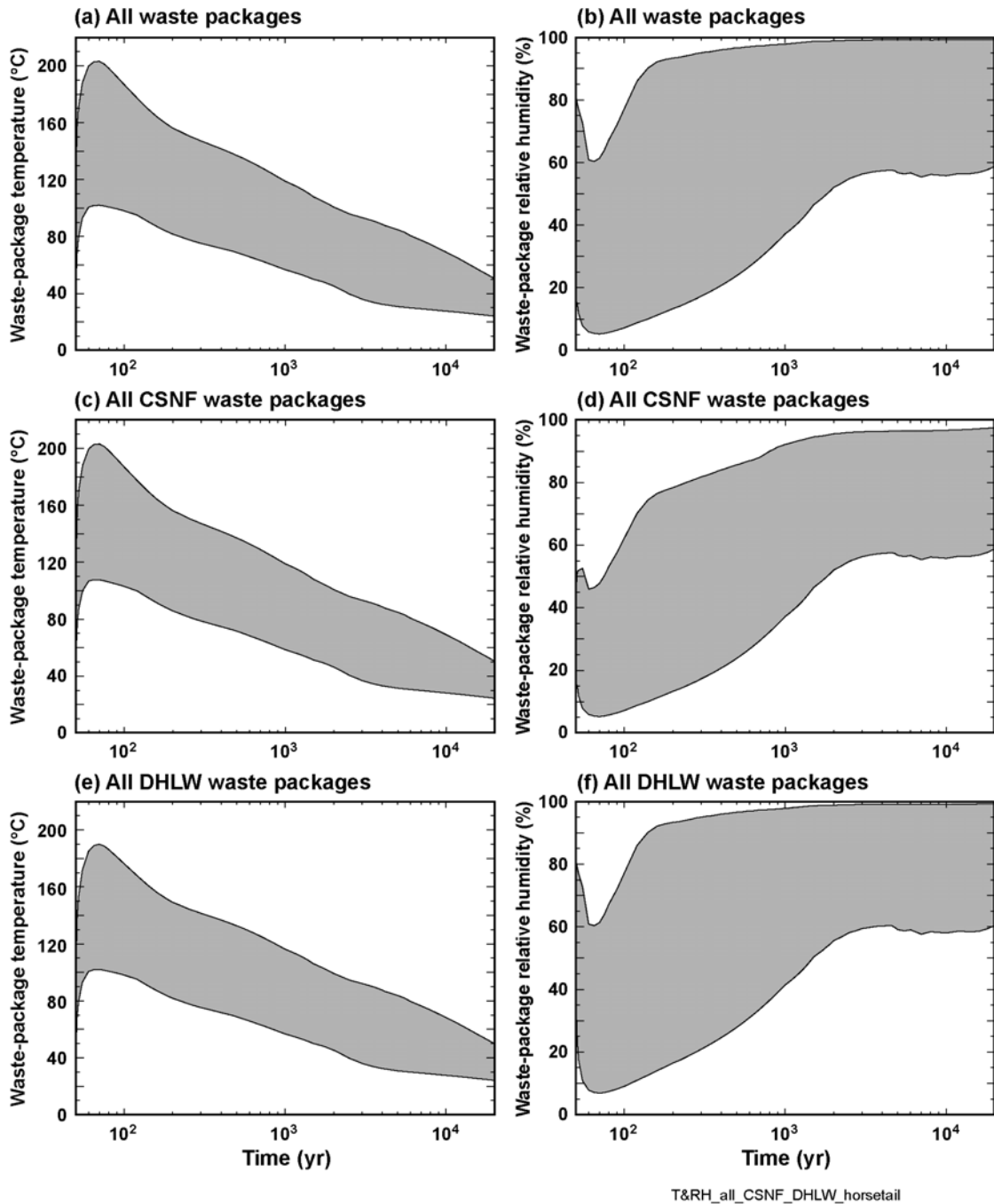
Source: See Table XIII-1.

NOTE: The ranges include the five cases listed in Table 6.3-37: (1) lower infiltration-flux, low thermal conductivity case, (2) lower infiltration-flux, mean thermal conductivity case, (3) mean infiltration-flux, mean thermal conductivity case, (4) upper infiltration-flux, mean thermal conductivity case, and (5) upper infiltration-flux, high thermal conductivity case.

Figure 6.3-53. Range of Waste Package Temperature and Relative Humidity Histories for all Waste Packages (a, b), for All CSNF Waste Packages (c, d), and for All DHLW Waste Packages (e, f)

6.3.6 Relationship Between Relative Humidity on the Waste Package and Drip Shield and Temperature on the Drift Wall

For the purpose of conducting in-drift geochemical analyses, it is useful to extract thermal-hydrologic output that quantifies the relationship between when boiling conditions cease at the drift wall (and when seepage can potentially commence) and the corresponding relative humidity on the drip-shield and waste package surfaces. Note that the boiling temperature at the repository horizon is 96°C. Figure 6.3-54 is a plot of the complementary cumulative distribution function (CCDF) of the relative humidity on the drip shield and waste package that corresponds to when the drift-wall temperature is 96°C. Figure 6.3-54 also plots the CCDF of drip-shield and waste package relative humidity that corresponds to when the drift-wall temperature is 100°C. Note that in Section 6.5.2.2 of *Abstraction of Drift Seepage* (BSC 2004 [DIRS 169131]), it is recommended that a threshold temperature of 100°C, which is higher than the nominal boiling point of 96°C, be used to define the duration of boiling for abstraction of drift seepage for intact drifts. Note also that the CCDF plots in Figure 6.3-54 account for the influence of parametric uncertainty of host-rock thermal conductivity and percolation flux as is discussed in Section 6.3.4. The probabilities of the five infiltration-flux/host-rock thermal conductivity cases, summarized in Table 6.3-37, were utilized as weighting factors for those respective cases. Table 6.3-41 summarizes the data given in Figure 6.3-54.
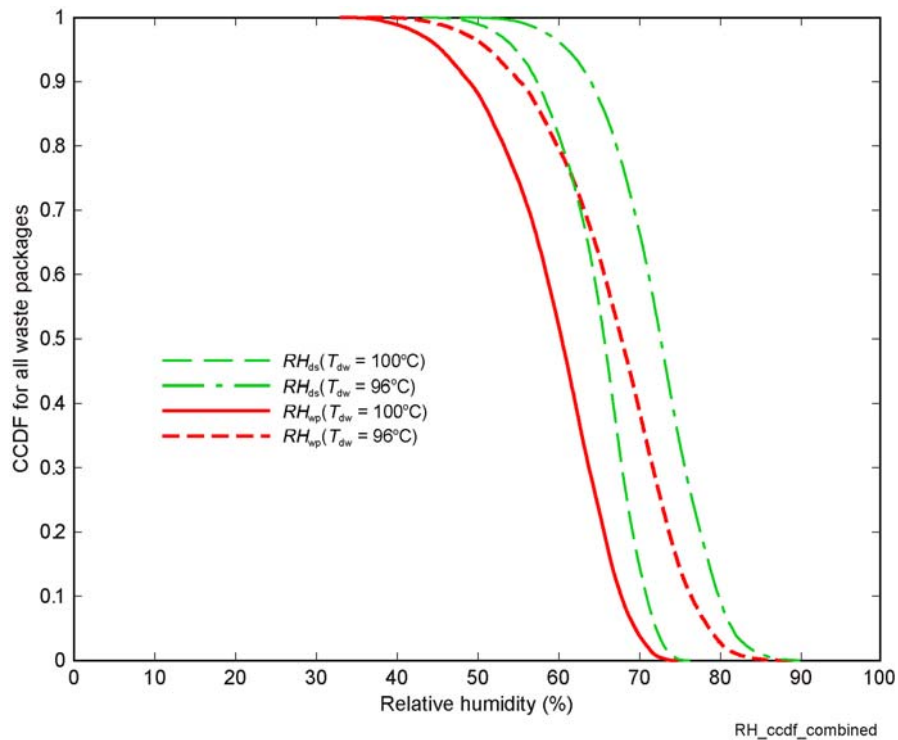
Source: See Table XIII-1.

NOTE: The CCDF corresponds to when the drift-wall temperature is 96°C and 100°C. These plots account for the five infiltration-flux/host-rock thermal conductivity cases discussed in Section 6.3.4, using the probabilities summarized in Table 6.3-37.

Figure 6.3-54. The Complementary Cumulative Distribution Function (CCDF) for Relative Humidity on the Drip Shield and Waste Package

Table 6.3-41. Relative Humidity on the Drip Shield and Waste Package Corresponding to When the Drift-Wall Temperature is 96°C and 100°C, Summarized for Figure 6.3-54.

Drift-wall temperature (°C)	Drip-shield relative humidity (%)			Waste package relative humidity (%)		
	Lowest	Median	Highest	Lowest	Median	Highest
96	47.76	72.61	89.76	36.19	67.32	88.62
100	43.08	65.62	76.20	32.92	60.36	74.60

6.3.7 Influence of a Low-Probability-Seismic Collapsed-Drift Scenario on In-Drift Thermal-Hydrologic Conditions

The influence of a low-probability-seismic collapsed-drift scenario on in-drift thermal-hydrologic conditions is considered for the P2WR5C10 location, which is a typical location at the center of the repository. Throughout Section 6.3, the P2WR5C10 location (see Figure 6.3-1 for location) is used for examining the sensitivity of thermal-hydrologic conditions in emplacement drifts to various sources of uncertainty and variability. This location is representative of a typical location in the predominant host-rock unit, which is the Tptpll (tsw35) unit, close to the center of the repository area, and because the local percolation-flux values (Table 6.3-9) are close to the repository averages for the present-day, monsoonal, and glacial climates (Table 6.3-4) for the mean infiltration-flux case.

Sections 6.2.9, 6.2.10, and 6.2.11 describe the changes to the MSTHM submodels that are required to model the influence of drift collapse. Although a full MSTHM calculation involves submodels located at 108 locations spread across the entire repository (Figure 6.2-3), it is only necessary to conduct a MSTHM calculation at a single repository location for the purpose of analyzing the influence of drift collapse on in-drift thermal-hydrologic conditions. The reasoning for this is that the purpose of this section (Section 6.3.7) is to generate tables of "deltas," which are the differences between the thermal-hydrologic results for the case with drift collapse and those for the intact (nominal) case with no drift collapse. These differences, such as the temperature difference (or delta), are entirely dependent on the modified material properties within the emplacement drifts. In other words, the differences are insensitive to the local host-rock unit or local percolation flux. Because of this lack of sensitivity to conditions outside of the drift, these calculated differences (or deltas) can then be applied to the MSTHM results of the five nominal cases with no drift collapse, which are summarized in Table 6.3-37. These differences (deltas) are determined for the eight different waste packages addressed by the MSTHM (Figure 6.2-2 and Table 6.3-13).

The low-probability-seismic scenario causes severe shaking that fails the host rock (breaking it into rubbelized blocks) out to a diameter of 11 m. This scenario is shown in Figure 139f of *Drift Degradation Analysis* (BSC 2004 [DIRS 166107]). The result of this is a host-rock rubble zone that extends from the outer surface of the drip shield out to the "modified" drift wall, which is the interface between rubbelized host rock and intact host rock. A schematic of this case is given in Figure 6.4-16 of *Abstraction of Drift Seepage* (BSC 2004 [DIRS 169131]). The key uncertainty influencing in-drift thermal-hydrologic conditions is the effective thermal conductivity K_{th} of the host-rock rubble. Two K_{th} cases are considered to address this uncertainty: (1) high-K_{th} case and (2) low-K_{th} case. On the basis of the discussion in Section 6.2.10.3, the high- and low-K_{th} cases are assigned the same probability (of 50 percent).

6.3.7.1 In-Drift Thermal-Hydrologic Conditions for the High and Low Thermal Conductivity Rubble Cases with Total Drift Collapse

Figures 6.3-55, 6.3-56, and 6.3-57 show the influence of drift collapse, out to a diameter of 11 m, on in-drift thermal-hydrologic conditions for the coolest, average, and hottest waste packages, respectively. These three waste packages are the dhlw-l1, bwr1-1, and pwr1-2 waste packages in Table 6.3-13 and in Figure 6.2-2. Table 6.3-42 summarizes the peak waste package temperatures for the same three waste packages, while Table 6.3-43 summarizes the time when boiling on the waste package ceases for these waste packages. For both the high- and low-K_{th} cases, the host-rock rubble functions as an insulator that increases the temperature rise on the drip shield (not shown in the figures) and on the waste packages (Figure 6.3-55a, Figure 6.3-56a, and Figure 6.3-57a), as well as in the invert (Figure 6.3-55b, Figure 6.3-56b, and Figure 6.3-57b). The increase in temperature rise, compared to the intact (nominal) case, resulting from drift collapse is about twice as great for the low-K_{th} case as it is for the high-K_{th}, which is consistent with K_{th} for the low-K_{th} case being half of that for the high-K_{th} case (Table 6.3-23).

The insulating effect of the host-rock rubble substantially extends the duration of boiling conditions on the waste packages (Table 6.3-43). The increase in waste package boiling duration is about twice as great for the low-K_{th} case as it is for the high-K_{th} case. Higher temperatures and extended boiling duration in the drift have the effect of substantially extending the period of reduced liquid-phase saturation in the invert (Figure 6.3-55d, Figure 6.3-56d, and Figure 6.3-57d). The liquid-phase saturation in the matrix continuum of the host-rock rubble also remains low for a greatly extended period (Figure 6.3-55e, Figure 6.3-56e, and Figure 6.3-57e). Higher temperatures and extended boiling duration in the drift also substantially extend the period of reduced relative humidity on the drip-shield humidity (not shown in figure) and on the waste package (Figure 6.3-55c, Figure 6.3-56c, and Figure 6.3-57c).
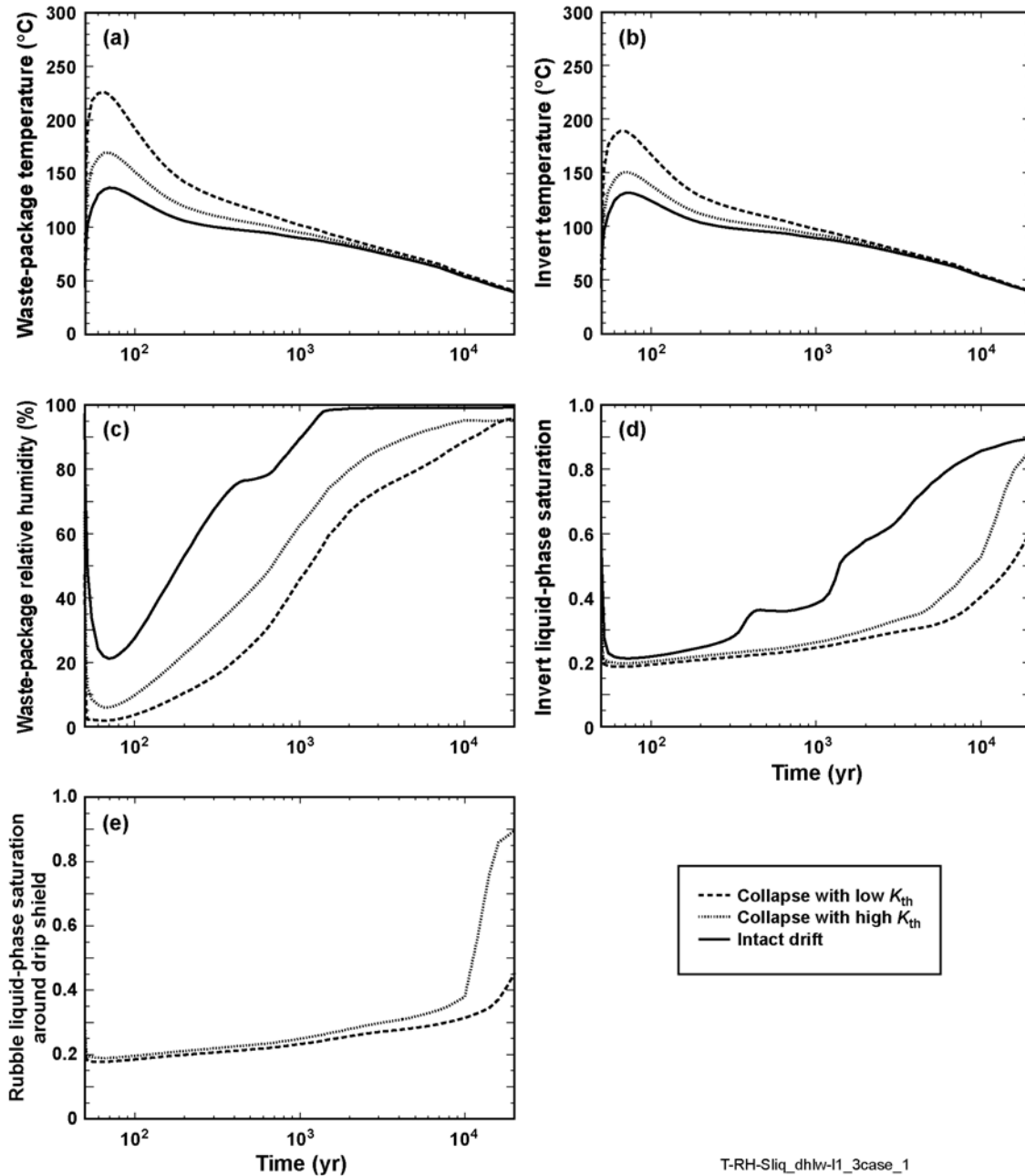
T-RH-Sliq_dhlw-l1_3case_1

Source: See Table XIII-1.

NOTE: See Figure 6.3-1 for location. The cases are: (1) intact-drift (nominal) case, (2) low-probability-seismic collapsed drift with high- K_{th} host-rock rubble, and (3) low-probability-seismic collapsed drift with low-K_{th} rubble. The plotted parameters are (a) waste package temperature, (b) invert temperature, (c) waste package relative humidity, (d) invert liquid-phase saturation, and (e) matrix liquid-phase saturation of the rubble surrounding the drip shield.

Figure 6.3-55. Thermal-Hydrologic Parameters for the "Coolest" Waste Package, the 5 DHLW/DOE SNF-Long (dhlw-l1), Plotted for the Mean Infiltration Flux at the P2WR5C10 Location in the Tptpll (tsw35) Unit
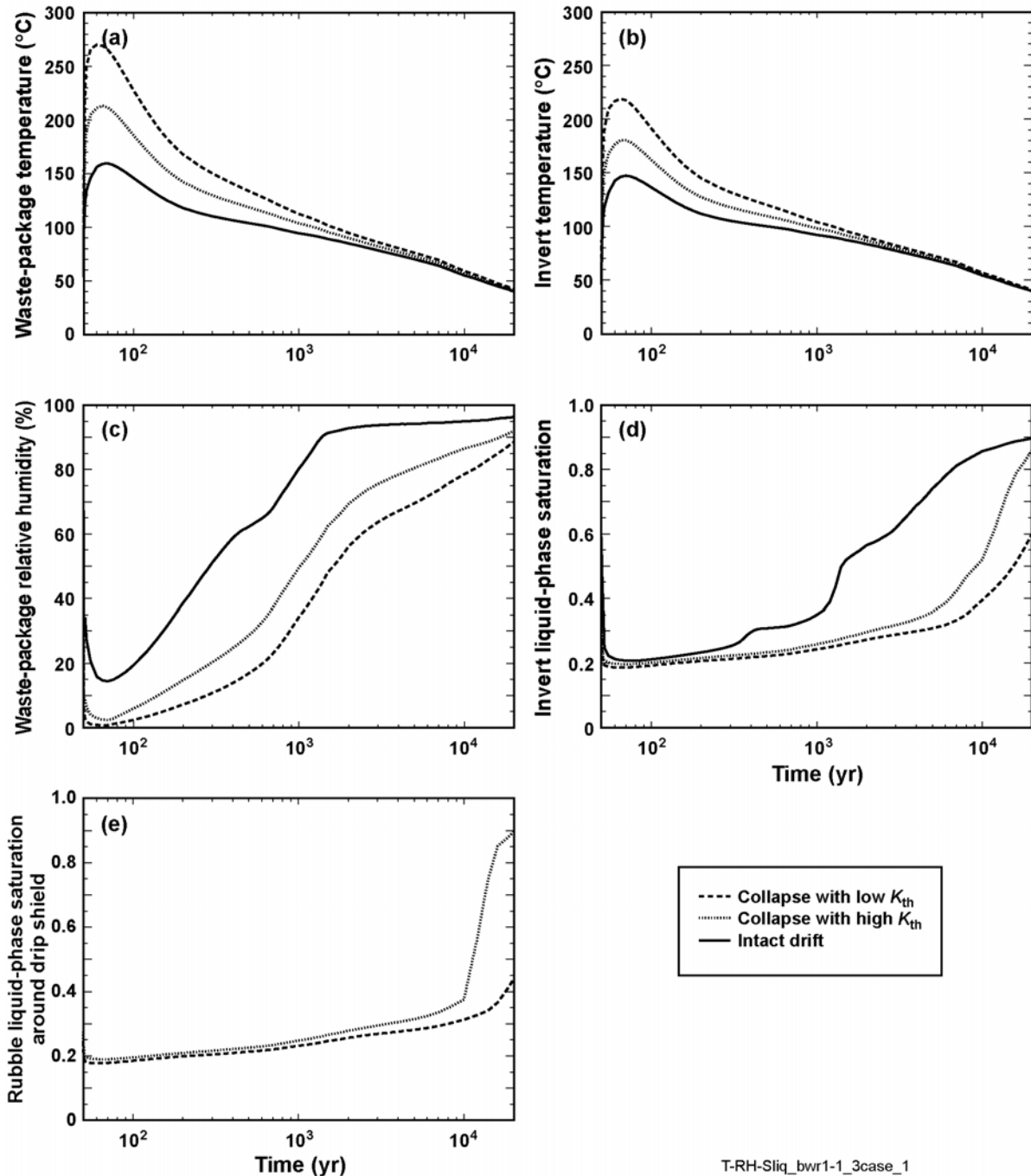
Source: See Table XIII-1.

NOTE: See Figure 6.3-1 for location. The cases are: (1) intact-drift (nominal) case, (2) low-probability-seismic collapsed drift with high- K_{th} host-rock rubble, and (3) low-probability-seismic collapsed drift with low-K_{th} rubble. The plotted parameters are (a) waste package temperature, (b) invert temperature, (c) waste package relative humidity, (d) invert liquid-phase saturation, and (e) matrix liquid-phase saturation of the rubble surrounding the drip shield.

Figure 6.3-56. Thermal-Hydrologic Parameters for the "Average" Waste Package, the 44-BWR CSNF (bwr1-1), Plotted for the Mean Infiltration Flux at the P2WR5C10 Location in the Tptpll (tsw35) Unit
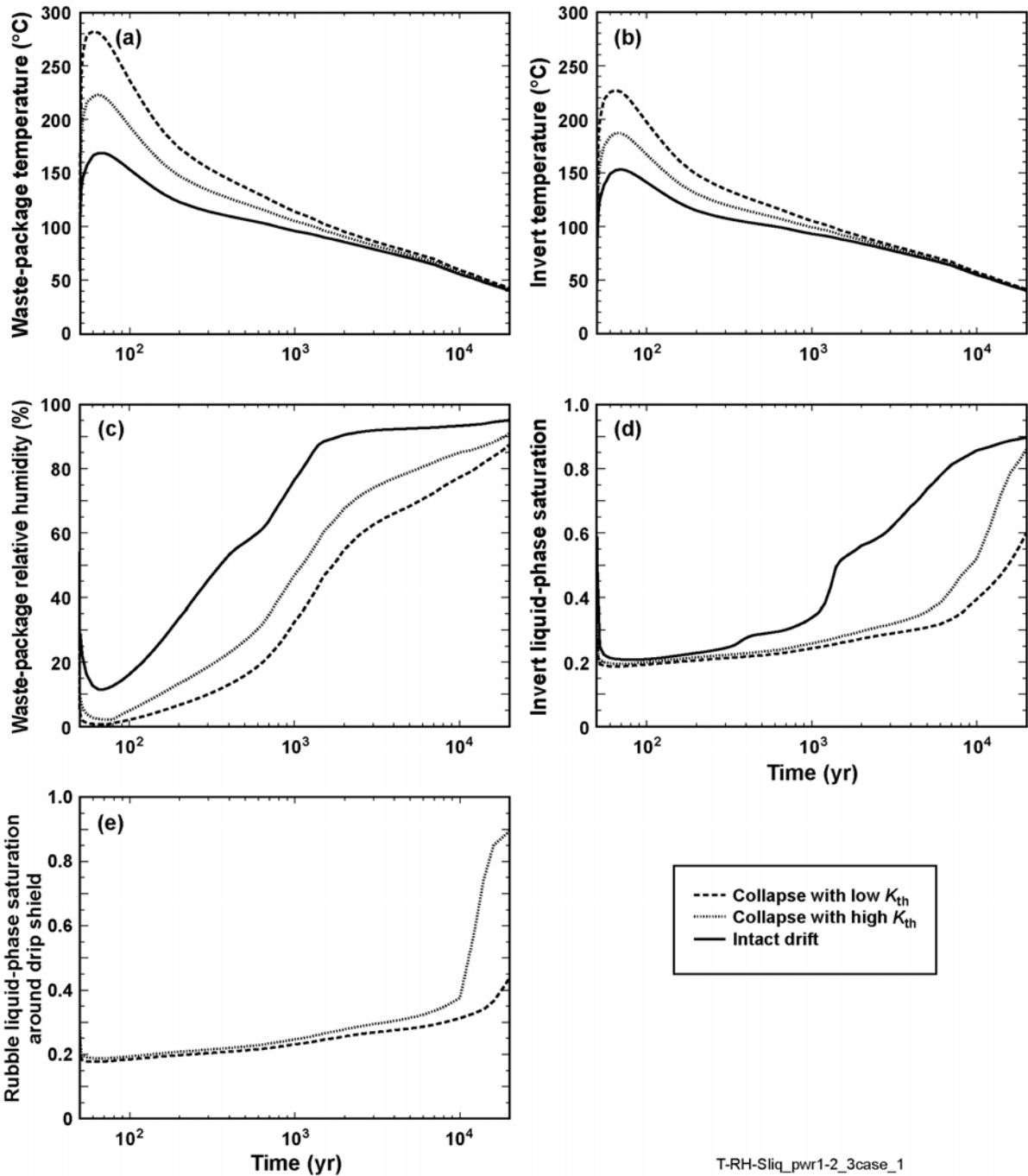
Source: See Table XIII-1.

NOTE: See Figure 6.3-1 for location. The cases are: (1) intact-drift (nominal) case, (2) low-probability-seismic collapsed drift with high-K_{th} host-rock rubble, and (3) low-probability-seismic collapsed drift with low-K_{th} rubble. The plotted parameters are (a) waste package temperature, (b) invert temperature, (c) waste package relative humidity, (d) invert liquid-phase saturation, and (e) matrix liquid-phase saturation of the rubble surrounding the drip shield.

Figure 6.3-57. Thermal-Hydrologic Parameters for the "Hottest" Waste Package, the 21-PWR AP CSNF (pwr1-2), Plotted for the Mean Infiltration Flux at the P2WR5C10 Location in the Tptpll (tsw35) Unit.

Table 6.3-42. Peak Waste Package Temperature for the "Coolest," "Average," and "Hottest" Package for Three Cases at the P2WR5C10 Location in the Tptpll (tsw35) Unit

Waste Package Type	Peak Waste Package Temperature (°C)		
	Intact-drift (nominal) case	Collapsed Drift with High-K_{th} Rubble	Collapsed Drift with Low-K_{th} Rubble
Coolest Waste Package 5 DHLW/DOE SNF-Long (dhlw-l1) WP	136.7	169.3	225.9
Average Waste Package 44-BWR CSNF (bwr1-1) WP	159.5	213.2	270.0
Hottest Waste Package 21-PWR AP CSNF (pwr1-2) WP	168.8	223.4	282.2

NOTES: See Figure 6.3-1 for location of the Tptpll. The location of the waste packages is given in Figure 6.2-2 and their characteristics listed in Table 6.3-13.

Cases are evaluated for the mean infiltration flux. The cases are: (1) intact-drift (nominal) case, (2) low-probability-seismic collapsed drift with high- K_{th} host-rock rubble, and (3) low-probability-seismic collapsed drift with low-K_{th} host-rock rubble.

Table 6.3-43. Time When Boiling on the Waste Package Ceases for the "Coolest," "Average," and "Hottest" Package for Three Cases at the P2WR5C10 Location in the Tptpll (tsw35) Unit

Waste Package Type	Time When Boiling on the Waste Package Ceases (yr)		
	Intact Drift (Nominal) Case	Collapsed Drift with High-K_{th} Rubble	Collapsed Drift with Low-K_{th} Rubble
Coolest Waste Package 5 DHLW/DOE SNF-Long (dhlw-l1) WP	527.8	912.6	1368.9
Average Waste Package 44-BWR CSNF (bwr1-1) WP	888.2	1466.0	1898.7
Hottest Waste Package 21-PWR AP CSNF (pwr1-2) WP	995.0	1527.1	1947.2

NOTES: See Figure 6.3-1 for location of the Tptpll. The location of the waste packages is given in Figure 6.2-2 and their characteristics listed in Table 6.3-13.

Cases are evaluated for the mean infiltration flux. The cases are: (1) intact-drift (nominal) case, (2) low-probability-seismic collapsed drift with high- K_{th} host-rock rubble, and (3) low-probability-seismic collapsed drift with low-K_{th} rubble.

6.3.7.2   Influence of Bulk Density of Rubble on Thermal-Hydrologic Conditions for Low-Probability-Seismic Collapsed-Drift Scenario

As is discussed in Section 6.2.10.3, the rubble bulk density value used in the LDTH submodels (1850 kg/m^3) is greater than the value used in the DDT submodels (1608 kg/m^3). Note that a rubble bulk density value of 1608 kg/m^3 is the value that corresponds to a bulking factor of 0.231 and a bulk density of 1980 kg/m^3 (see Table IV-3b and IV-3c of Appendix IV) for the intact Tptpll (tsw35) host-rock unit. To assess whether this difference in bulk density is significant, the LDTH submodel was rerun for the case where the rubble bulk density is 1608 kg/m^3, so that it could be compared to the case where the rubble bulk density is 1850 kg/m^3. As is evident in Figure 6.3-58, which plots the temperature and relative humidity at the crown of the drip shield for the low-K_{th} rubble, the influence of rubble bulk density over this range of 1608 to 1850 kg/m^3 is insignificant. Because steady-state heat flow conditions are quickly established within the

rubble, temperature and relative humidity in the drift are insensitive to the bulk density value of the rubble. Therefore, the MSTHM calculations are insensitive to the choice of rubble bulk density (1850 kg/m^3 versus 1608 kg/m^3).
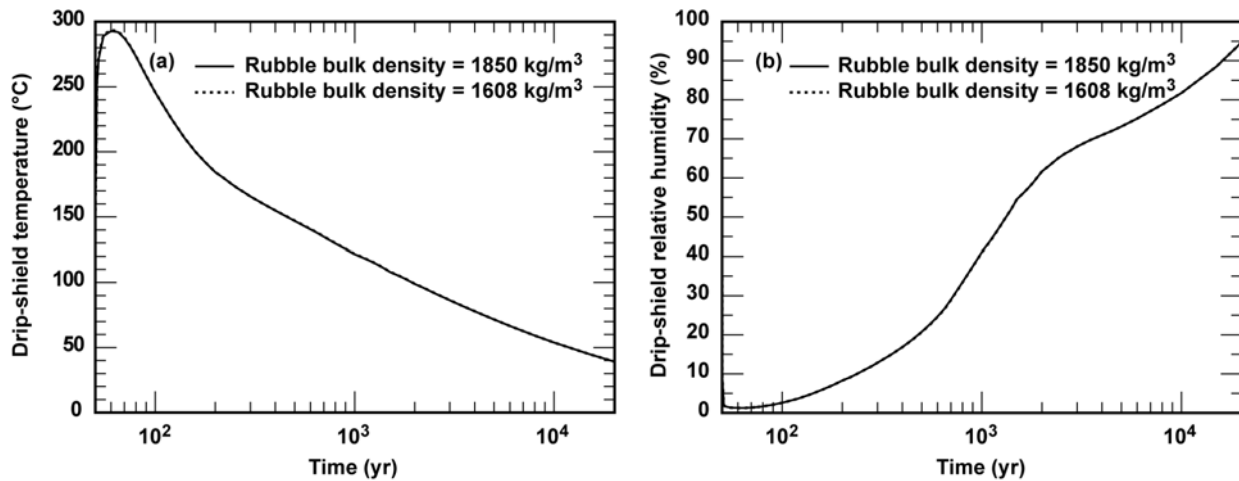
Source: See Table XIII-1.

NOTE: See Figure 6.3-1 for location. Two cases for bulk density of the host-rock rubble are considered, including: (1) bulk density = 1850 kg/m^3 and (2) bulk density = 1608 kg/m^3. Because these plots are from an LDTH submodel, they are representative of line-averaged heating conditions.

Figure 6.3-58. Temperature and Relative Humidity at the Drip Shield Crown for the P2WR5C10 Location in the Tptpll (tsw35) Unit, Plotted for the Mean Infiltration Flux and the Low-Probability-Seismic Collapsed Drift with Low-K_{th} Rubble

6.3.7.3   Influence of Seepage on the High and Low Thermal Conductivity Rubble Cases with Total Drift Collapse

This section describes a sensitivity study of the potential influence of seepage on the high- and low-K_{th} rubble cases that are discussed in Section 6.3.7.1. Note that the results presented in Section 6.3.7.1 are obtained by executing the full MSTHM methodology executed at a specific location in the repository (location P2WR5C10 in Figure 6.3-1). The seepage analysis in this section (Section 6.3.7.3) is conducted using the LDTH submodel at the P2WR5C10 location conducted for an AML of 55 MTU/acre. Thus, the results in this section are not full MSTHM results. However, the results of the seepage analysis in this section are representative of line-averaged heating conditions at the P2WR5C10 location, which is close to the repository center (i.e., relatively distant from the repository edges).

The seepage analysis is conducted by specifying a seep at the top of the rubble for selected seep magnitudes of 10, 30, 100, and 1,000 liter/yr/WP, which represents a broad range of possible conditions. In order not to artificially heat or cool the model by virtue of this specified seepage flux, the seep has a specified enthalpy history, which causes the seep temperature history to be consistent with the local temperature history that would have occurred in the absence of the seep. To account for the residual dryout effects resulting from drift ventilation, the seep is turned on at 65 years, which is 15 years after closure.

Table 6.3-44 summarizes the time that the seep arrives at the crown of the drip shield for the high- and low-K_{th} rubble cases and for four seep magnitudes. Also summarized is the range in waste package temperatures that occur at the time that the seep arrives at the drip-shield crown based upon the corresponding MSTHM calculations conducted in Section 6.3.7.1. Note that the range of temperatures corresponds to the eight different waste packages that are represented by the MSTHM (see Table 6.3-13). Because the temperatures are taken from the MSTHM calculations that did not incorporate the seeps, the cooling effect of the seep is not included in the waste package temperature ranges in Table 6.3-44. Thus, the listed waste package temperatures are somewhat higher than would occur if the cooling effect of the seep had been included.

Table 6.3-44. Summary of Arrival Time at Drip-Shield Crown for Seeps of Varying Magnitude for Low-Probability-Seismic Collapsed-Drift Scenario for the High-K_{th} and Low-K_{th} Rubble Cases

Seep Magnitude (liter/yr/WP)	High-K_{th} Rubble		Low-K_{th} Rubble	
	Arrival Time at Drip-Shield Crown (yr)	Waste Package Temperature Range ($^\circ$C)	Arrival Time at Drip-Shield Crown (yr)	Waste Package Temperature Range ($^\circ$C)
10	10,000	54.1 to 57.2	15,000	46.7 to 49.5
30	5000	69.3 to 73.4	8000	61.7 to 65.7
100	2800	79.1 to 84.0	4000	75.6 to 80.8
1,000	1400	90.3 to 98.3	1500	93.7 to 102.4

DTN: LL040404423122.045.

NOTE: Waste package temperature ranges are obtained from full MSTHM results at the P2WR5C10 location (see Figure 6.3-1 for location).

As discussed in Section 6.3.7.1, because the rubble has a lower thermal conductivity than the adjoining host rock, and because the nominal case of no drift collapse involves thermal radiation, which is a highly efficient mode of heat transfer, the introduction of rubble has a strong insulating effect. The insulating effect of the rubble substantially extends the duration of the boiling period on the waste packages (Table 6.3-43). The increase in waste package boiling duration is about twice as great for the low-K_{th} case as it is for the high-K_{th} case. The liquid-phase saturation in the matrix continuum of the host-rock rubble remains low for a greatly extended period (Figure 6.3-55e, Figure 6.3-56e, and Figure 6.3-57e). The low liquid-phase saturation substantially reduces the relative humidity in the rubble.

The extended boiling duration and extended duration of reduced relative humidity in the rubble greatly extend the time that seeps can be completely evaporated in the rubble. Thus, a seep of 10 liter/yr/WP requires 10,000 and 15,000 years to reach the crown of the drip shield for the high- and low-K_{th} rubble cases, respectively. Waste package temperatures have declined substantially by the time that a 10-liter/yr/WP seep reaches the drip shield. A seep of 100 liter/yr/WP requires 2800 and 4000 yr to reach the crown of the drip shield for the high- and low-K_{th} rubble cases, respectively. Waste package temperatures have declined to well below the boiling point by the time a 100-liter/yr/WP seep reaches the crown of the drip shield. It requires a seep of 1,000 liter/yr/WP to reach the crown of the drip shield while some (but not all) of the waste packages are above the boiling point. Had the cooling effect of the seep on the waste package temperatures been included, it is likely that all of waste package temperatures for the 1,000-liter/yr/WP seep would also have been below the boiling point.

6.3.8   Comparison of Results for the TSPA-LA Base Case with Those for the FY01 Supplemental Science and Performance Analyses (SSPA)

This section gives a brief comparison between the thermal-hydrologic conditions predicted for the TSPA-LA base case with those predicted for the *FY 01 Supplemental Science and Performance Analyses, Volume 1: Scientific Bases and Analyses* (Section 5.4.1 of BSC 2001 [DIRS 155950]). Figure 6.3-59 plots the thermal-hydrologic parameters for all eight waste packages considered in both the TSPA-LA and the SSPA. The LDTH submodel location P3R7C12 was chosen because it is very close to the location used to plot the thermal-hydrologic parameters in Figure 5.4.1-7 of the *FY 01 Supplemental Science and Performance Analyses, Volume 1: Scientific Bases and Analyses* (Section 5.4.1 of BSC 2001 [DIRS 155950]). This location was chosen because it is close to the geographic center of the repository and because it is the Tptpll (tsw35), which is the host-rock unit for 75.1 percent of the repository area (Table 6.3-2). Note that this comparison is for the mean infiltration-flux case. Note also that the MSTHM calculations for the SSPA were for a period of 1,000,000 years, while the MSTHM calculations for the TSPA-LA are for a period of 20,050 years. The same time axis is used in Figure 6.3-59 as in Figure 5.4.1-7 (Section 5.4.1 of BSC 2001 [DIRS 155950]) to provide a more consistent basis for comparing the history plots of thermal-hydrologic conditions. The legend in Figure 6.3-59 utilizes the same waste package names used in Figure 5.4.1-7 (Section 5.4.1 of BSC 2001 [DIRS 155950]), as well as providing the waste package names (e.g., pwr1-1) used in the TSPA-LA (see Table 6.3-13).

Peak waste package temperatures at the repository center in the MSTHM calculations for the SSPA, as given in Figure 5.4.1-7 (Section 5.4.1 of BSC 2001 [DIRS 155950]), range from 152.3 to 180.1°C. Peak waste package temperatures at the repository center in the MSTHM calculations for the TSPA-LA base case, as given in Figure 6.3-59, range from 136.3 to 167.3°C. Thus, for this location in the repository, and for the mean infiltration-flux case, peak waste package temperatures are 12 to 16°C lower for the TSPA-LA than for the SSPA. There are two primary causes for the TSPA-LA temperatures being lower than they are in the SSPA. The first is differences in the heat-removal efficiency that was applied to the respective models during the preclosure ventilation period. The MSTHM calculations for the SSPA used a constant heat-removal efficiency of 70 percent (Section 5.3.2.4.1 of BSC 2001 [DIRS 155950]). The MSTHM calculations for the TSPA-LA use a time-varying heat-removal efficiency (DTN: MO0304MWDALACV.000 [DIRS 164551]). Thus, in-drift temperatures are lower at the onset of the postclosure period for the TSPA-LA MSTHM calculations than they are for the SSPA MSTHM calculations. The second reason for the lower TSPA-LA temperatures is the approximation of the influence of natural convection on heat transfer in the drift. The TSPA-LA MSTHM calculations use an effective thermal conductivity for the gas-filled drift cavity that is based on a correlation (Francis et al. 2003 [DIRS 164602], Table 6) that more realistically accounts for the in-drift geometry than the approximation used in the SSPA MSTHM calculations (CRWMS M&O 2001 [DIRS 153410]). It should be noted that the correlations for the in-drift effective thermal conductivity, which were obtained from Table 6 of Francis et al (2003 [DIRS 164602]), have been updated in *In-Drift Natural Convection and Condensation* (BSC 2004 [DIRS 164327], Table 6.4.7-3), resulting in very small changes to the coefficients. As evident in Figure I-1 of Appendix I, the small changes to the coefficients result in insignificant changes to the in-drift effective thermal conductivity. The in-drift convective heat transfer approximation for the TSPA-LA MSTHM results in more efficient heat transfer (by

natural convection), which lowers the temperature difference between the waste package and drift wall; the lower temperature difference results in lower waste package temperatures.
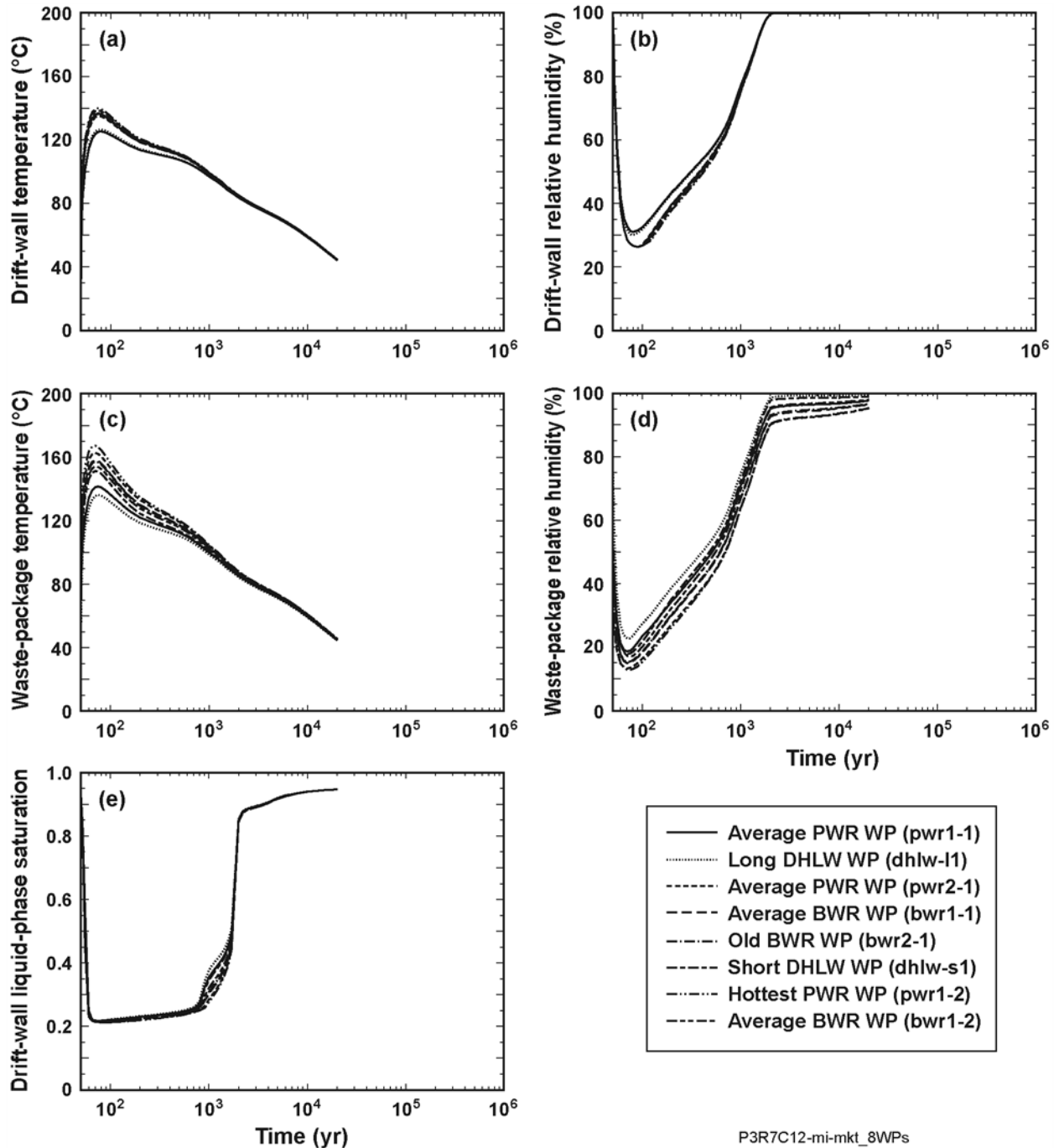
Source: See Table XIII-1.

NOTE: The plotted thermal-hydrologic parameters are (a) drift-wall temperature, (b) drift-wall relative humidity, (c) waste package temperature, (d) waste package relative humidity, and (e) drift-wall liquid-phase saturation. The waste package names (in parentheses) are given in Figure 6.2-2 and in Table 6.3-13.

Figure 6.3-59. Thermal-Hydrologic Parameters for the Eight Waste Packages Considered in this Report, Plotted for the Mean Infiltration-Flux Cases at the P3R7C12 Location in the Tptpll (tsw35) Unit, Close to the Repository Center

6.3.9 Influence of Host-Rock Hydrologic-Property Variability and Uncertainty

The multiscale thermal-hydrologic model addresses repository-scale variability of hydrologic properties. A sensitivity study of hydrologic-property variability, described below, for the four host-rock types (Tptpul, Tptpmn, Tptpll, and Tptpln) demonstrates that multiscale thermohydrologic model-simulated in-drift and near-field thermal-hydrologic conditions are insensitive to differences in the hydrologic property values for these respective host-rock units. The reason for this lack of sensitivity is provided at the end of this section (6.3.9).

Figure 6.3-60 gives the drift-wall and drip-shield temperature histories at a typical location at the center of the repository for percolation flux values ranging from 0.1 to 10 mm/yr. Figure 6.3-61 gives the corresponding drift-wall and drip-shield relative humidity histories for this location. This location (P2WR5C10 in Figure 6.3-1) happens to be in the Tptpll host-rock unit, which is the predominant host-rock type in the repository (Table 6.3-3). For the purpose of showing the influence of hydrologic-property variability, model calculations were made using the line-averaged-heat-source drift-scale thermal-hydrologic (LDTH) submodel (Section 6.2.6) applying the hydrologic property values for each of the host-rock types (Tptpul, Tptpmn, Tptpll, and Tptpln), respectively. For a percolation flux of 0.1 mm/yr or greater, temperature is insensitive to hydrologic properties (Figures 6.3-60a to 6.3-60f). For a percolation flux of 0.01 mm/yr, hydrologic properties exert a minor influence on temperature (Figures 6.3-60g and 6.3-60h). For a percolation flux of 1 mm/yr or greater, relative humidity is insensitive to hydrologic properties (Figures 6.3-61a to 6.3-61d). For a percolation flux of 0.1 mm/yr or less, hydrologic properties exert a minor influence on relative humidity (Figures 6.3-61e to 6.3-61h).

The influence that hydrologic properties exert on temperature and relative humidity is insignificant for two reasons. First, it is insignificant compared to the influence of host-rock thermal conductivity and percolation flux, as evident in Figures 6.3-51 and 6.3-61. Second, the percolation flux range for which hydrologic properties exert some influence (equal to or less than 0.1 mm/yr) constitutes a small portion of the repository for the three climate states (present-day, monsoonal, and glacial), as is evident in Figure 4-2.

The lack of sensitivity of in-drift and near-field temperature and relative humidity to hydrologic properties can be understood by considering the key processes and factors governing thermal-hydrologic behavior in and around emplacement drifts. Thermal-hydrologic behavior in and around emplacement drifts consists of three fundamental processes:

1. **Heat Flow**–Occurs in emplacement drifts, primarily by thermal radiation, and in the adjoining host rock, primarily by thermal conduction. Consequently, host-rock thermal conductivity is the key natural-system parameter determining the magnitude of temperature buildup in the host rock.

2. **Host-Rock Dryout**–Is driven by temperature buildup, resulting in evaporation (boiling), which lowers the liquid-phase saturation in the host rock, thereby lowering the relative humidity in the host rock and in the emplacement drifts.

3. **Host-Rock Rewetting**–Primarily occurs as a result of gravity-driven percolation in fractures, with capillary-driven imbition into the adjoining matrix. The rate of rewetting is controlled by the local percolation flux except in regions of very low

percolation flux (less than approximately 0.1 mm/yr), where it is controlled by capillary-driven imbibition in the matrix. The approximate percolation-flux threshold of 0.1 mm/yr is obtained by observing the sensitivity of temperature (Figure 6.3-60) and relative humidity (Figure 6.3-61) to percolation flux, which is discussed above
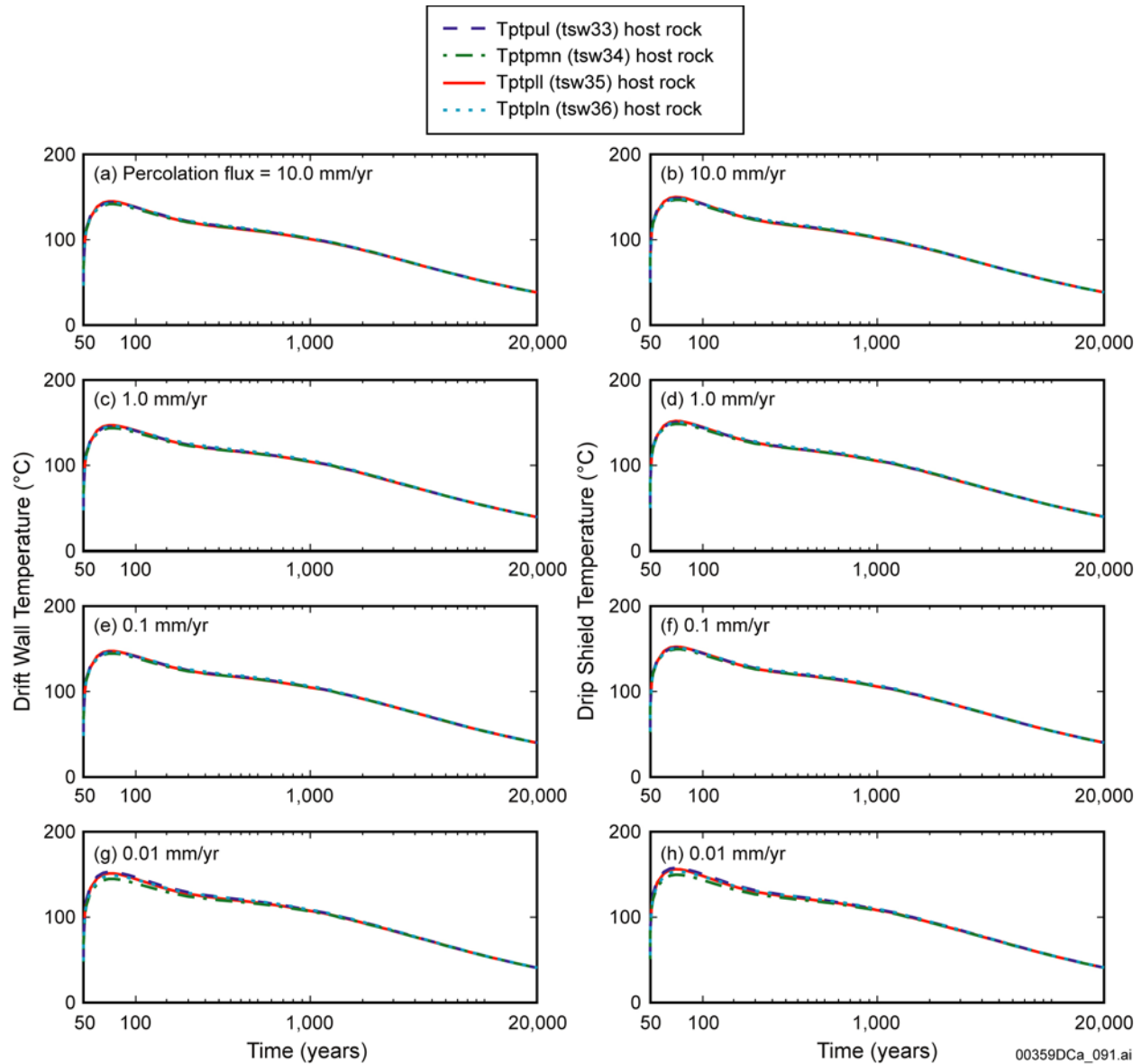
Source: See Table XIII-1.

NOTE: The temperature histories are calculated by the LDTH submodel of the multiscale thermohydrologic model (Section 6.2.6). These temperature histories are calculated for a location close to the center of the repository (the P2WR5C10 location shown Figure 6.3-1). All cases use the thermal properties, including the mean thermal conductivity, of the Tptpll host-rock unit (Table 6.3-23).

Figure 6.3-60. Drift-Wall and Drip-Shield Temperature History at the Repository Center for Four Values of Percolation Flux and for the Hydrologic Properties of Each of the Host-Rock Types
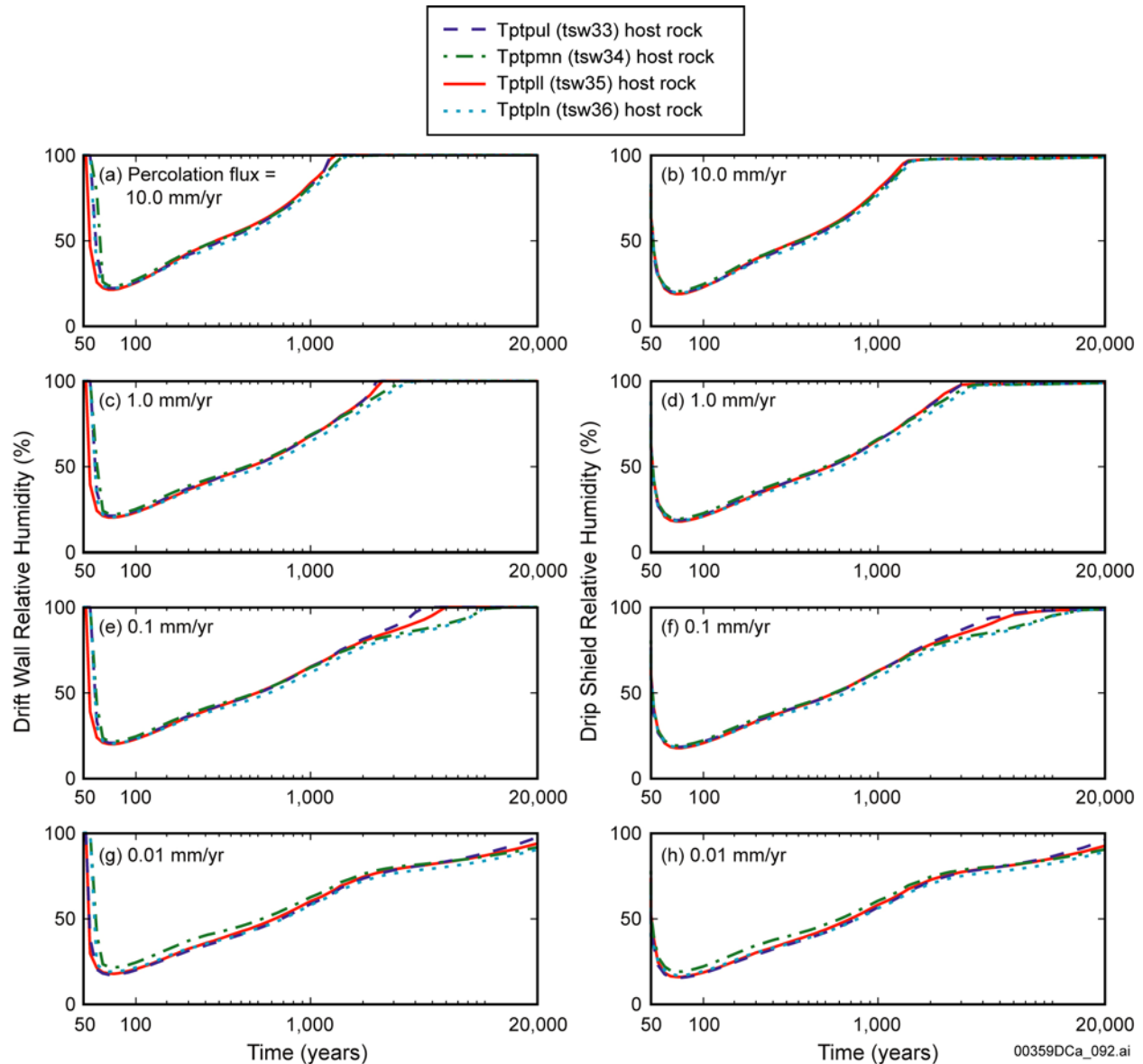
Source: See Table XIII-1.

NOTE: The relative-humidity histories are calculated by the LDTH submodel of the multiscale thermal-hydrologic model (Section 6.2.6). These relative-humidity histories are calculated for a location close to the center of the repository (the P2WR5C10 location shown Figure 6.3-1). All cases use the thermal properties, including the mean thermal conductivity, of the Tptpll host-rock unit (Table 6.3-23).

Figure 6.3-61. Drift-Wall and Drip-Shield Relative-Humidity History at the Repository Center for Four Values of Percolation Flux and for the Hydrologic Properties of Each of the Host-Rock Types

For the range of host-rock hydrologic properties of the four host-rock units, vapor flow from the boiling to the condensation zone essentially occurs in an unthrottled (i.e., unrestricted) fashion. Permeability in the fractures and matrix and fracture spacing is always sufficiently large to result in a (insignificantly) small gas-phase pressure buildup with respect to boiling. Consequently, the gas-phase pressure buildup is small enough to not throttle (i.e., restrict) the rate at which boiling occurs and the resulting vapor flux from the boiling zone to the condensation zone. Thus, the

range in hydrologic properties for the host rock does not result in differences in the rate at which boiling occurs in the host rock.

For the range of host-rock hydrologic properties of the four host-rock units, the contribution of buoyant gas-phase convection to overall heat flow is small compared to that of thermal convection. Thus, the range in host-rock thermal-hydrologic properties of the four host-rock types does not result in differences in the temperature buildup in the host rock, as is evident in Figure 6.3-60.

For the range of hydrologic properties of the four host-rock units, fracture permeability is sufficiently large and fractures are sufficiently well connected to allow gravity-driven drainage of percolation to occur in an unrestricted fashion. Thus, percolation flux, not fracture permeability, is the rate-limiting quantity governing the magnitude of gravity-driven liquid-phase flow to the boiling–dryout zone. One important caveat to this generalization relates to flow focusing, which arises due to heterogeneity in fracture permeability. The influence of flow focusing is addressed by including areal variability of percolation flux, which results in a broad range of percolation flux over the repository footprint (Table 6.3-5), and by including uncertainty, as is addressed in the lower, mean, and upper infiltration-flux cases (Table 6.3-4). Thus, the manner in which hydrologic properties primarily affect rewetting (and, thus, net dryout) behavior is related to the manner in which those properties affect capillary-driven flow, which primarily occurs as imbibition in the matrix.

For the range of host-rock hydrologic properties of the four host-rock units, capillary-driven imbibition always results in a rewetting magnitude that is effectively less than approximately 0.1 mm/yr. Accordingly, only in regions with very low percolation flux (less than 0.1 mm/yr) do the hydrologic properties exert a small but insignificant influence on dryout and rewetting behavior in the host rock, as is evident in Figure 6.3-61. For areas of the repository with a local percolation flux greater than 0.1 mm/yr (which is the vast majority of the repository area for all three climate states, as shown in Figure 4-2), differences in host-rock hydrologic properties exert an insignificant influence on dryout and rewetting behavior. Even in areas with low percolation flux, the influence of hydrologic properties on dryout and rewetting behavior is small compared to that of host-rock thermal conductivity and percolation flux, as is evident in Figures 6.3-50 and 6.3-51.

6.3.10 Influence of Pseudo Permeability on In-Drift Temperature and Relative Humidity

Although the emplacement drift is an open cavity rather than a porous media, the vast majority of simulations of in-drift and near-field thermal-hydrologic conditions use porous-media flow and transport simulators, such as NUFT (Nitao 1998 [DIRS 100474]) and TOUGH2 (Pruess et al. 1999 [DIRS 160778]), which necessitates treating the drift cavity as a porous media with a large permeability and 100 percent porosity. Because the drift cavity is not a porous medium, the permeability of the drift cavity is called *pseudo permeability*. A value of pseudo permeability of 1×10^{-8} m^2 is used in all of the LDTH submodels used to support all MSTHM calculations in this report. It is important that the value of pseudo permeability is at least as large as that of the bulk permeability of the fractured host rock. In that way, the value of pseudo permeability will not impede advective gas-phase flow within the drift cavity, particularly as it relates to buoyant gas-phase convection (also called natural convection) cells that develop in the adjoining host rock.

As demonstrated below, the porous medium approach with pseudo permeability does not represent the influence of buoyant gas-phase convection (also called natural convection) on heat transfer within the emplacement drift. To represent the influence of natural convection on heat transfer within the drift, an effective thermal conductivity for the gas-filled drift cavity is used. This effective thermal conductivity is based on a correlation (Francis et al. 2003 [DIRS 164602], Table 6) accounting for the influence of natural convection, which is described in Appendix I. It should be noted that the correlations for the in-drift effective thermal conductivity, which were obtained from Table 6 of Francis et al. (2003 [DIRS 164602]), have been updated in *In-Drift Natural Convection and Condensation* (BSC 2004 [DIRS 164327], Table 6.4.7-3), resulting in small changes to the coefficients. As evident in Figure I-1 of Appendix I, the small changes to the coefficients result in insignificant changes to the in-drift effective thermal conductivity. The effective conductivity approach is used both in the DDT submodels (Section 6.2.8) and in the LDTH submodels (Section 6.2.6). Because the LDTH submodel allows natural convection to occur within the drift cavity, a concern is whether the in-drift convective cooling effect, together with the use of the effective thermal conductivity for the drift cavity, will over-account for the magnitude of in-drift convective cooling.

Figure 6.3-62 plots drip-shield temperature and relative humidity for six different values of in-drift pseudo permeability, ranging over six orders of magnitude. The largest value of in-drift pseudo permeability considered is 1×10^{-6} m^2, which is two orders of magnitude larger than the value used in all MSTHM calculations. The smallest value of in-drift pseudo permeability is 1×10^{-12} m^2, which is four orders of magnitude smaller than the value used in all MSTHM calculations; it is also of the same order of the fracture permeability of the host rock. Over this range, the value of in-drift pseudo permeability has an insignificant effect on in-drift temperature and relative humidity. The range in peak drip-shield temperature is 150.9°C to 151.1°C for these cases. Clearly, there is no over-accounting of convective cooling in the LDTH submodels that support the MSTHM calculations in this report. Therefore, the approach of using an effective thermal conductivity for the drift cavity is reasonable and appropriate in the LDTH submodels.
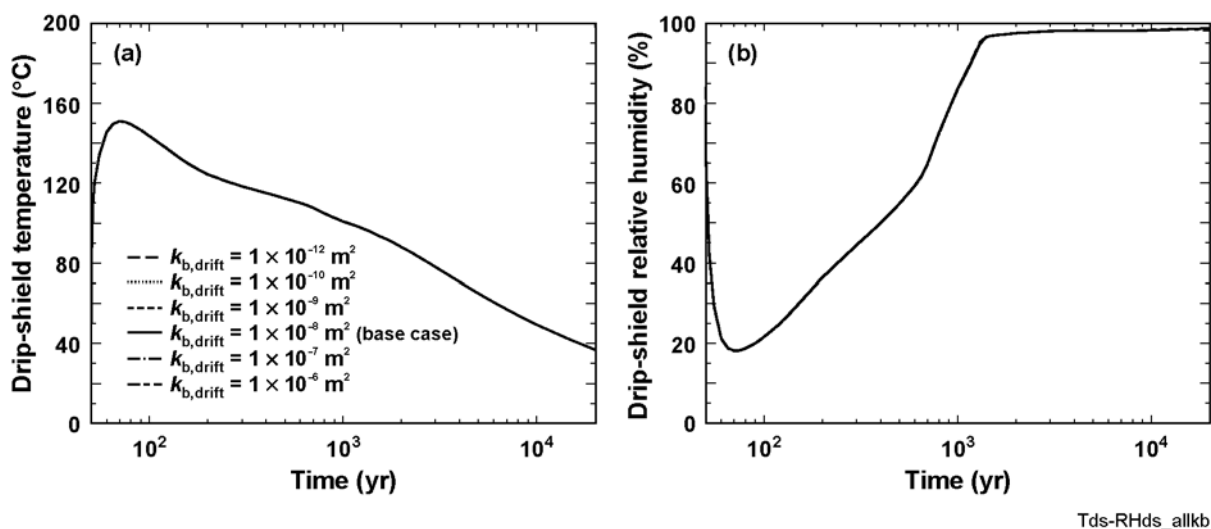
Source: See Table XIII-1.

NOTE: Temperature and relative-humidity histories are calculated by the LDTH submodel (Section 6.2.6) for an AML of 55 MTU/acre and for a location close to the center of the repository (the P2WR5C10 location shown Figure 6.3-1) for the mean infiltration-flux case with mean host-rock thermal conductivity.

Figure 6.3-62. Drip-Shield Temperature (a) and Relative Humidity (b) at the Repository Center for Different Values of Pseudo Permeability of the Gas-Filled Emplacement Drift Cavity

6.3.11 Influence of Invert Hydrologic-Property Variability and Uncertainty

All of the MSTHM calculations in this report utilized a single hydrologic property set for the crushed-tuff gravel invert. The dual-permeability model (DKM) is applied to represent flow in crushed-tuff gravel, with flow within the tuff grains (called the intragranular porosity) corresponding to flow in the matrix continuum of the DKM and flow around the tuff grains (called the intergranular porosity) corresponding to flow in the fracture continuum of the DKM. As discussed in Section 5.3.1.2, the hydrologic properties of the intragranular porosity are assumed to be the same as the intact properties for the Tptpll (tsw35) host-rock unit. As discussed in Section 5.3.1.8, the hydrologic properties of the intergranular porosity are taken from case 2 (3-mm particle size) from Table X-7 of Appendix X, with the one modification that the permeability is taken to be $1.0 \times 10^{-9}\,\text{m}^2$, which is between the values for case 1, which has a 0.317-mm particle size ($1.681 \times 10^{-10}\,\text{m}^2$) and for case 2, which has a 3-mm particle size ($1.511 \times 10^{-8}\,\text{m}^2$) from Table X-7 of Appendix X. Thus, the base case MSTHM calculations used a *modified* case 2 intergranular-porosity hydrologic property set. The purpose of this section (Section 6.3-11) is to demonstrate the sensitivity (or lack thereof) of thermal-hydrologic conditions in the invert to intragranular properties (as represented by the matrix properties of the four host-rock units) and to intergranular properties (as represented by the cases 1 through 4 in Table X-7 of Appendix X, as well as the modified case 2).

Figure 6.3-63 plots the liquid-phase saturation for the intragranular porosity and the temperature averaged over the invert. Four different cases are considered, with each case utilizing the matrix properties from each of the respective host-rock units: Tptpul (tsw33), Tptpmn (tsw34), Tptpll (tsw35), and Tptpln (tsw36). All four cases utilize the modified case 2 intergranular properties discussed above. Invert temperature is insensitive to the hydrologic properties of the intragranular porosity (Figure 6.3-63b). Liquid-phase saturation is also insensitive to hydrologic

properties of the intragranular porosity (Figure 6.3-63a), and also justifies not propagating invert hydrologic-property through the MSTHM calculations supporting TSPA-LA. Rewetting proceeds similarly in the two lithophysal units (Tptpul and Tptpll), and also in the two nonlithophysal units (Tptpmn and Tptpln). Because the matrix permeability is smaller in the nonlithophysal units than in the lithophysal units, rewetting proceeds somewhat more slowly in the nonlithophysal units than in the lithophysal units.
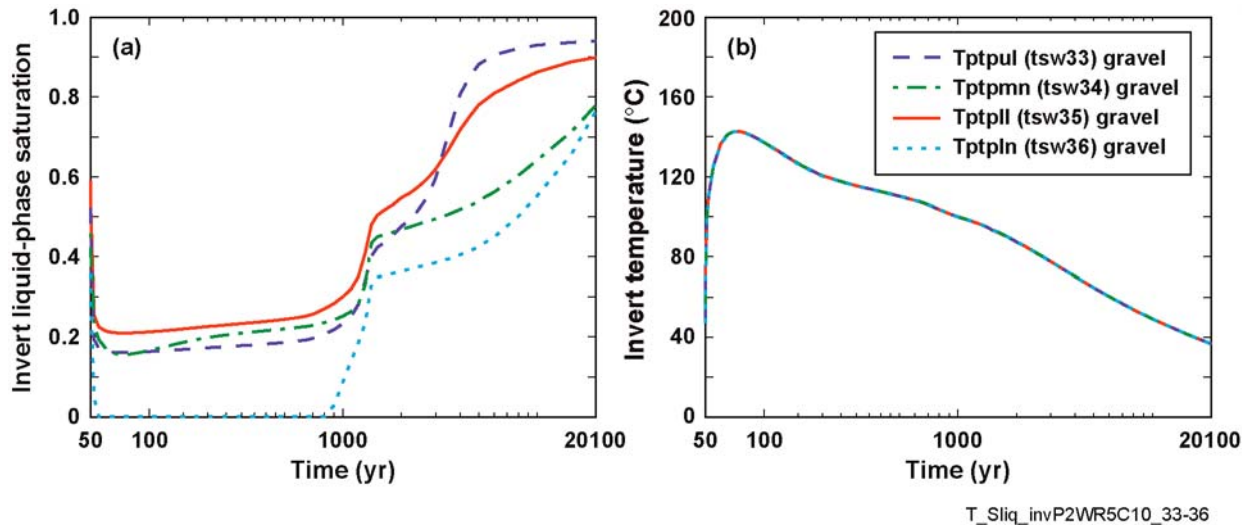
Source: See Table XIII-1.

NOTE: Invert liquid-phase saturation and temperature histories are calculated by the LDTH submodel (Section 6.2.6) for an AML of 55 MTU/acre and for a location close to the center of the repository (the P2WR5C10 location shown Figure 6.3-1) for the mean infiltration-flux case with mean host-rock thermal conductivity.

Figure 6.3-63. Invert Liquid-Phase Saturation for the Intragranular Porosity (a) and Temperature (b) at the Repository Center for Invert Gravel Derived from Each of the Indicated Host-Rock Units

Figure 6.3-64 plots temperature and relative humidity at different locations in the drift, including the host rock at the crown of the drift and below the invert, and at the top and bottom of the invert beneath the drip shield for crushed-tuff gravel derived from each of the host-rock units, respectively. Both temperature and relative humidity at those locations are insensitive to hydrologic properties of the intragranular porosity. This lack of sensitivity justifies the assumption discussed in Section 5.3.1.2. The small thermal conductivity in the invert results in a large vertical temperature gradient in the invert. This large temperature gradient results in a large relative-humidity gradient in the invert. Consequently, the top of the invert beneath the drip shield always has a much lower relative humidity than any location around the drift wall. As seen in Figure 6.3-64, this relationship (that relative humidity is always less at the top of the invert than at the drift wall) holds for all four of the crushed-tuff gravels (Tptpul, Tptpmn, Tptpll, and Tptpln).
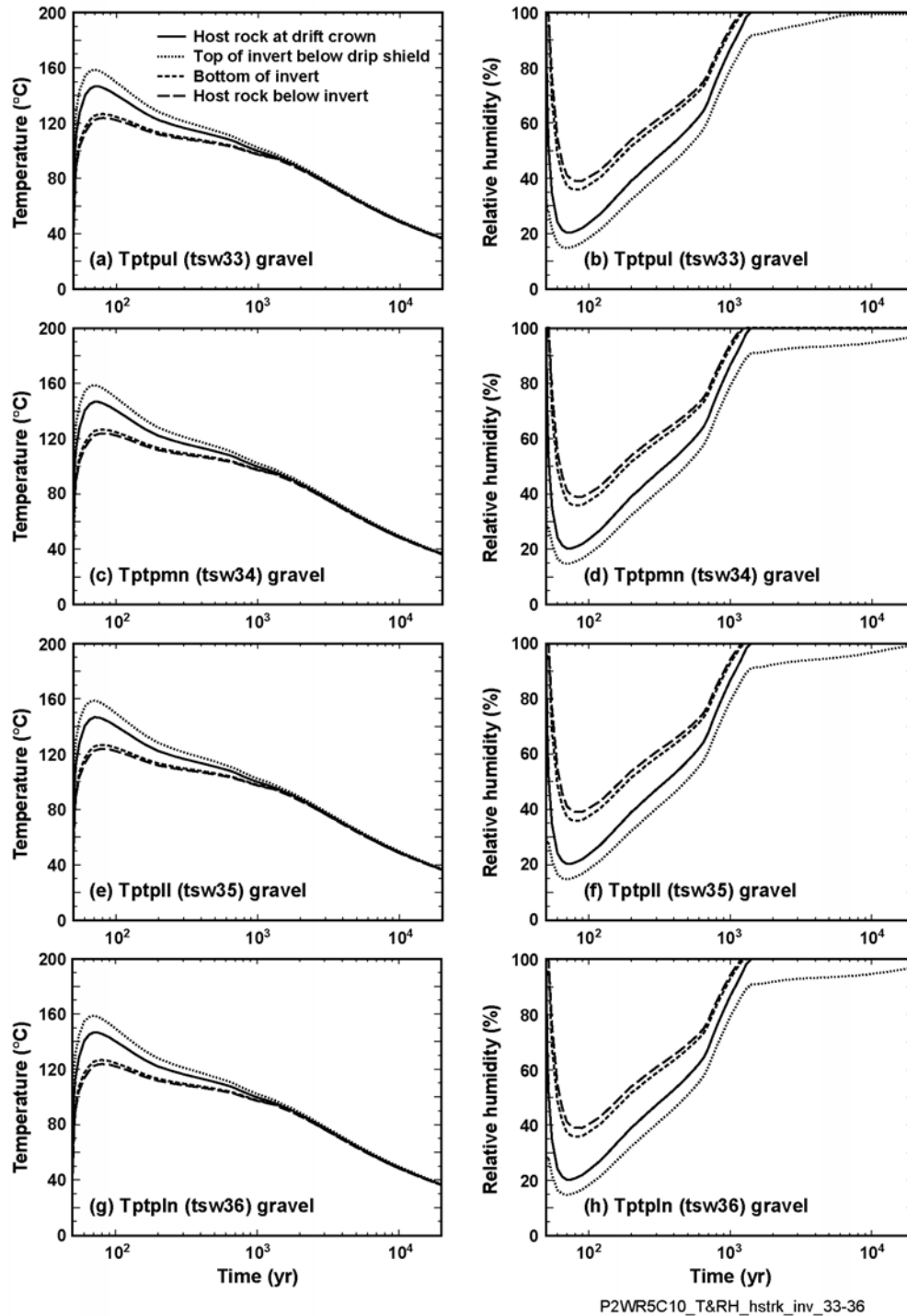
Source: See Table XIII-1.

NOTE: Temperature and relative humidity histories are calculated by the LDTH submodel (Section 6.2.6) for an
         AML of 55 MTU/acre and for a location close to the center of the repository (the P2WR5C10 location
         shown Figure 6.3-1) for the mean infiltration-flux case with mean host-rock thermal conductivity.

Figure 6.3-64. Temperature (a,c,e,g) and Relative Humidity (b,d,f,h) for Various Locations in the Drift at
                the Repository Center for Invert Gravel Derived from Each of the Indicated Host-Rock
                Units

Table 6.3-45 lists the temperatures at the drift crown, drip-shield crown, top and bottom of the invert beneath the drip shield, and in the host rock below the invert. It is important to note that the temperature difference between the top and bottom of the invert is always greater than the temperature difference between the top of the invert and drip-shield crown. This observation has important implications for the consequences of the flux of water vapor longitudinally along the drift axis from hotter to cooler locations where it will condense. For any given drift cross section, the coolest and most humid location is always at the bottom of the invert. Therefore, water vapor that is transported longitudinally along the drift axis will have a greater tendency to condense at the bottom of the invert, where it is coolest and most humid. Moreover, much of the water vapor created by virtue of evaporation at the top of the invert will move downward by advection and binary gas-phase diffusion to the bottom of the invert (or into the host rock below), where it will condense.

Table 6.3-45. Summary of Temperature at Various Locations in Drift Cross Section, Including Host Rock at Drift Crown, Top and Bottom of Invert Beneath Drip Shield, and Host Rock Below Invert

Time (yr)	Temperature ($^\circ$C)				
	Host Rock at Drift Crown[a]	Crown of Drip Shield[b]	Top of Invert Beneath Drip Shield[a]	Bottom of Invert Beneath Drip Shield[a]	Host Rock Below Invert[a]
70.	146.6	152.2	158.7	125.5	122.3
100.	140.1	144.2	149.3	124.4	122.1
1000.	99.7	100.9	102.1	97.7	97.2
2000.	87.3	88.0	88.7	86.5	86.2
5000.	64.5	64.9	65.4	63.9	63.8
10,000.	49.0	49.3	49.7	48.6	48.5
20,050.	36.5	36.7	37.0	36.3	36.2

[a] Temperatures correspond to Figure 6.3-64e.
[b] Temperatures obtained by applying the temperature difference between top of invert and crown of invert calculated using the DDT submodel.

Figure 6.3-65 plots the liquid-phase saturation for the intragranular porosity, temperature, and relative humidity at the top of the invert beneath the drip shield for five different sets of hydrologic properties for the intergranular porosity discussed above. Temperature, liquid-phase saturation, and relative humidity are all insensitive to the hydrologic properties of the intergranular porosity. This lack of sensitivity justifies the assumption discussed in Section 5.3.1.8. This lack of sensitivity also justifies not propagating invert hydrologic-property uncertainty through the MSTHM calculations supporting TSPA-LA.
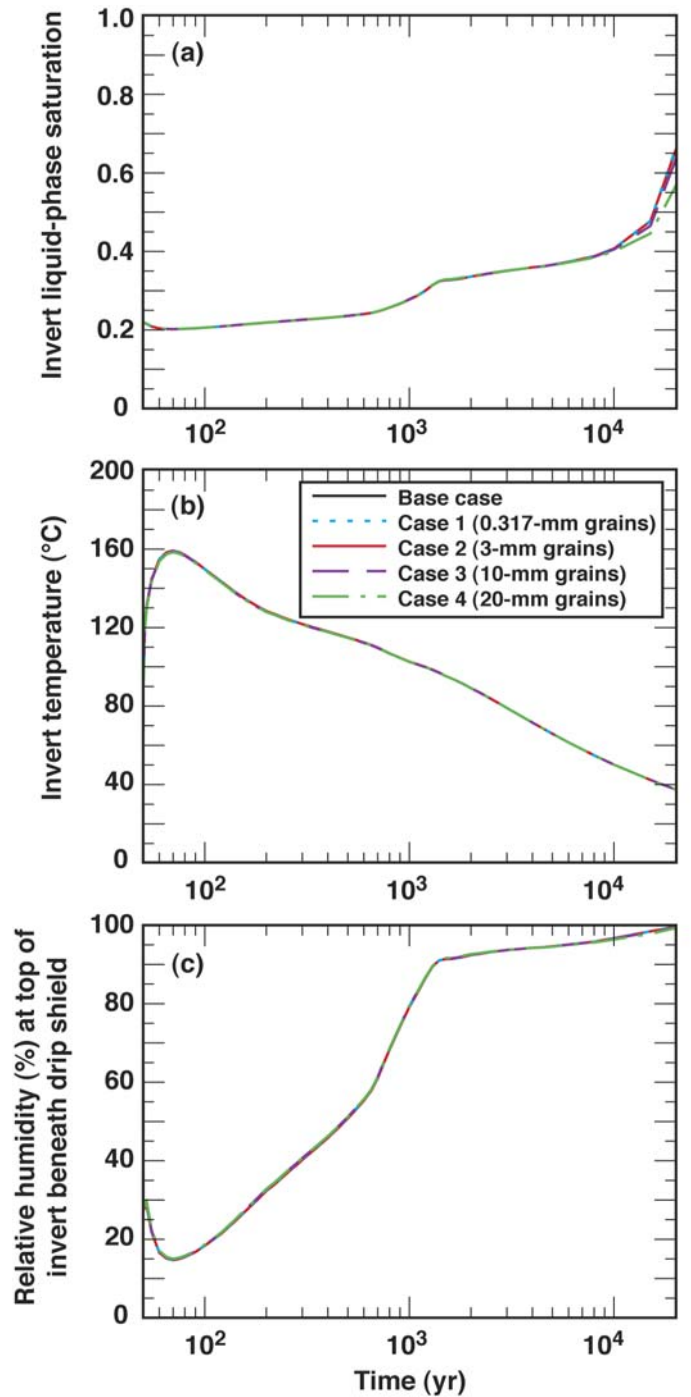
T-S-RH_inv_P2WR5C10_all-intergran

Source: See Table XIII-1.

NOTE: Liquid-phase saturation, temperature and relative humidity histories are calculated by the LDTH submodel (Section 6.2.6) for an AML of 55 MTU/acre and for a location close to the center of the repository (the P2WR5C10 location shown Figure 6.3-1) for the mean infiltration-flux case with mean host-rock thermal conductivity.

Figure 6.3-65. Invert Liquid-Phase Saturation (a) for the Intragranular Porosity, Temperature (b), and Relative Humidity (c) at the Top of the Invert Beneath the Drip Shield at the Repository Center for Different Sets of Hydrologic Parameters for the Intergranular Porosity

6.3.12 Influence of Ventilation Heat-Removal Efficiency Uncertainty

All MSTHM calculations in this report utilize the distance- and time-dependent ventilation heat-removal efficiency tables from DTN: MO0304MWDALACV.000 [DIRS 164551]. This section (Section 6.3-12) investigates the potential impact of uncertainty in ventilation heat-removal efficiency on in-drift thermal-hydrologic conditions. Five heat-removal efficiency cases are considered for a location close to the center of the repository, which is the P2WR5C10 location (see Figure 6.3-3 for location). These calculations use the LDTH submodel (Section 6.2.6) for an AML of 55 MTU/acre. The five cases include the base case, which applied a time-dependent heat-removal efficiency table from DTN: MO0304MWDALACV.000 [DIRS 164551]. The other four cases apply a constant heat-removal efficiency (i.e., constant during the 50-year ventilation period) for values of 70, 80, 90, and 100 percent efficiency. Note that the case with 100 percent efficiency is a hypothetical limiting case, which is equivalent to the surface storage of waste packages during the entire 50-year preclosure period. Figure 6.3-66 plots drip-shield temperature and relative humidity for these five cases. Note that the drip-shield temperature and relative-humidity temperatures for the base case lie between those of the 80- and 90-percent efficiency cases. Based on linear interpolation of peak drip-shield temperature (Table 6.3-45), the base case has an effective constant heat-removal efficiency of 83 percent.
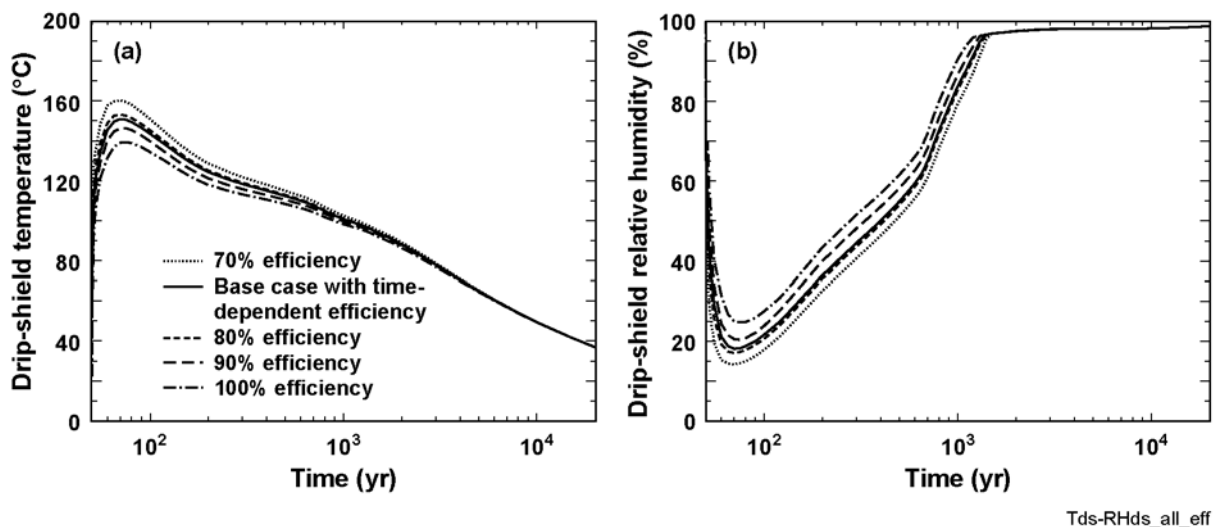
Source: See Table XIII-1.

NOTE: Temperature and relative humidity histories are calculated by the LDTH submodel (Section 6.2.6) for an AML of 55 MTU/acre and for a location close to the center of the repository (the P2WR5C10 location shown Figure 6.3-1) for the mean infiltration-flux case with mean host-rock thermal conductivity.

Figure 6.3-66. Drip-Shield Temperature (a) and Relative Humidity (b) at the Repository Center for Different Values of Ventilation Heat-Removal Efficiency

Table 6.3-46. Peak Drip-Shield Temperature for Different Values of Ventilation Heat-Removal Efficiency

Ventilation Heat-Removal Efficiency (%)	Peak Drip-Shield Temperature (C°)	Peak Drip-Shield Temperature Compared to Base Case (C°)
70	160.4	9.4
80	153.2	2.2
Base Case	151.0	0.0
90	146.3	–4.7
100	139.3	–11.7

NOTE: Drip-shield temperatures correspond to Figure 6.3-66.

Over the range of heat-removal efficiency of 70 to 100 percent, the range in the in-drift temperature and relative humidity conditions is less than that resulting from parametric uncertainty of percolation flux and host-rock thermal conductivity (Tables 6.3-27 through 6.3-29 and Figure 6.3-31). Moreover, the impact of the differences arising as a result of proximity to the repository edge, together with the impact of parametric uncertainty (Figure 6.3-53) is much greater than that arising from uncertainty in ventilation heat-removal efficiency. Therefore, uncertainty in ventilation heat-removal efficiency does not need to be propagated through the MSTHM results supporting the TSPA-LA.

6.3.13   Relationship Between Temperature and Relative Humidity on Waste Packages

Figure 6.3-67 plots the range of temperature histories for all waste packages across the repository, accounting for the influence of parametric uncertainty of host-rock thermal conductivity and percolation flux above the repository. Note that a comprehensive discussion of the influence of parametric uncertainty on in-drift and near-field thermal-hydrologic conditions is given in Section 6.2.4. Figure 6.3-68 plots the corresponding range of waste package relative humidity histories across the repository. Figure 6.3-69 plots the corresponding range of temperature versus relative humidity trajectories, during cooldown (i.e., after the waste package temperature has peaked). Also plotted on these three figures are histories and trajectories for three distinct waste packages, including (1) a cool DHLW waste package close to the edge of the repository, (2) an average BWR waste package at the center of the repository, and (3) a hot PWR waste package at the edge of the repository. The temperature versus relative humidity trajectories are important to the evolution of the chemical environment on waste packages.
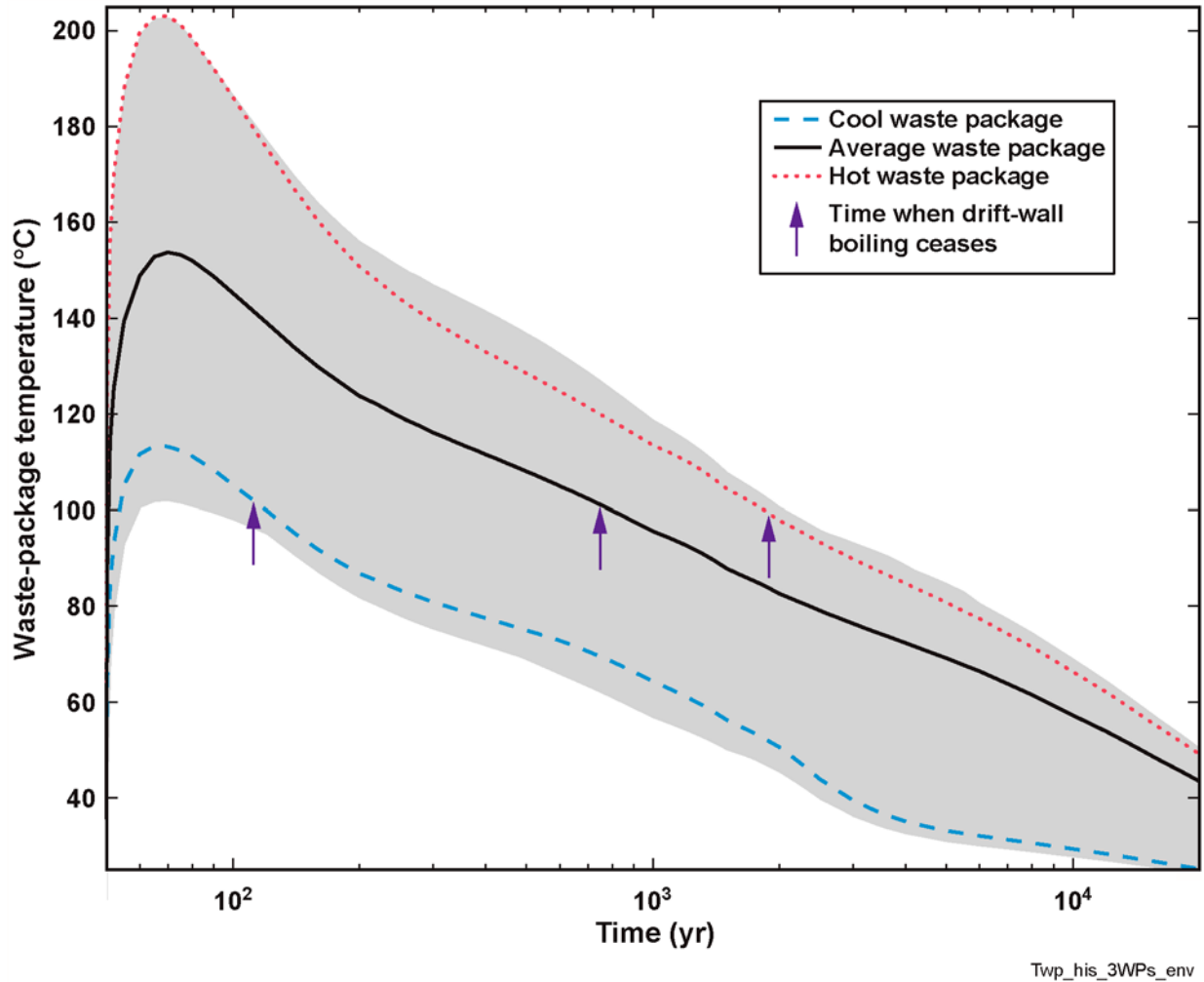
Source: See Table XIII-1.

NOTE: Also plotted are the temperature histories of three distinct waste packages, including (1) a cool DHLW
         waste package at the edge of the repository, (2) an average BWR waste package at the center of the
         repository, and (3) a hot PWR waste package at the center of the repository. The upward arrows indicate
         the time when boiling ceases at the drift wall. The range of waste package temperature histories is the
         same as that given in Figure 6.3-53a.

Figure 6.3-67. Range of Temperature Histories for All Waste Packages, Accounting for Uncertainty of
               Host-Rock Thermal Conductivity and Percolation Flux
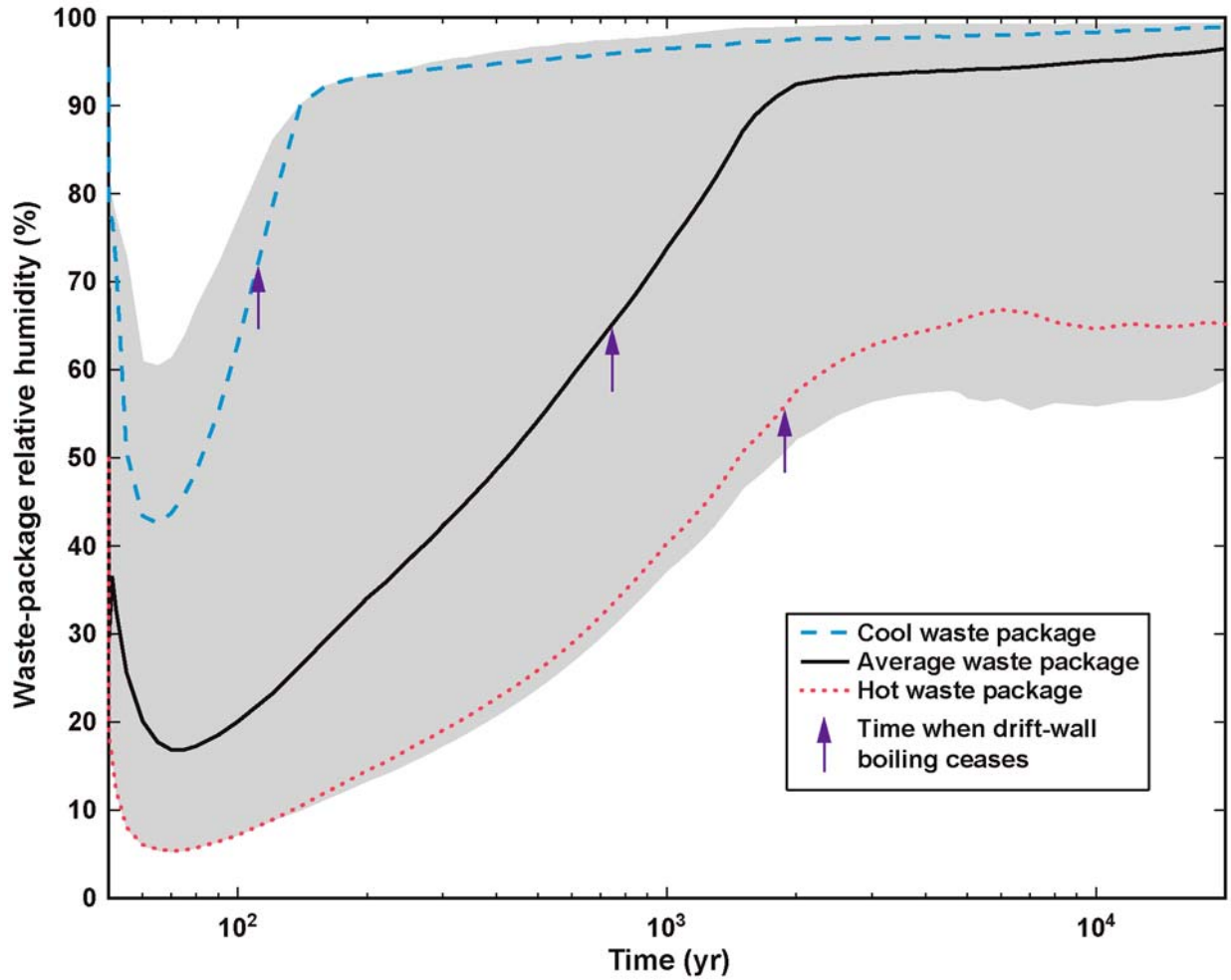
RHwp_his_3WPs_env

Source: See Table XIII-1.

NOTE: Also plotted are the relative-humidity histories of three distinct waste packages, including (1) a cool DHLW waste package at the edge of the repository, (2) an average BWR waste package at the center of the repository, and (3) a hot PWR waste package at the center of the repository. The upward arrows indicate the time when boiling ceases at the drift wall. The range in waste package relative-humidity histories is the same as that given in Figure 6.3-53b.

Figure 6.3-68. Range of Relative Humidity Histories for All Waste Packages, Accounting for Uncertainty of Host-Rock Thermal Conductivity and Percolation Flux
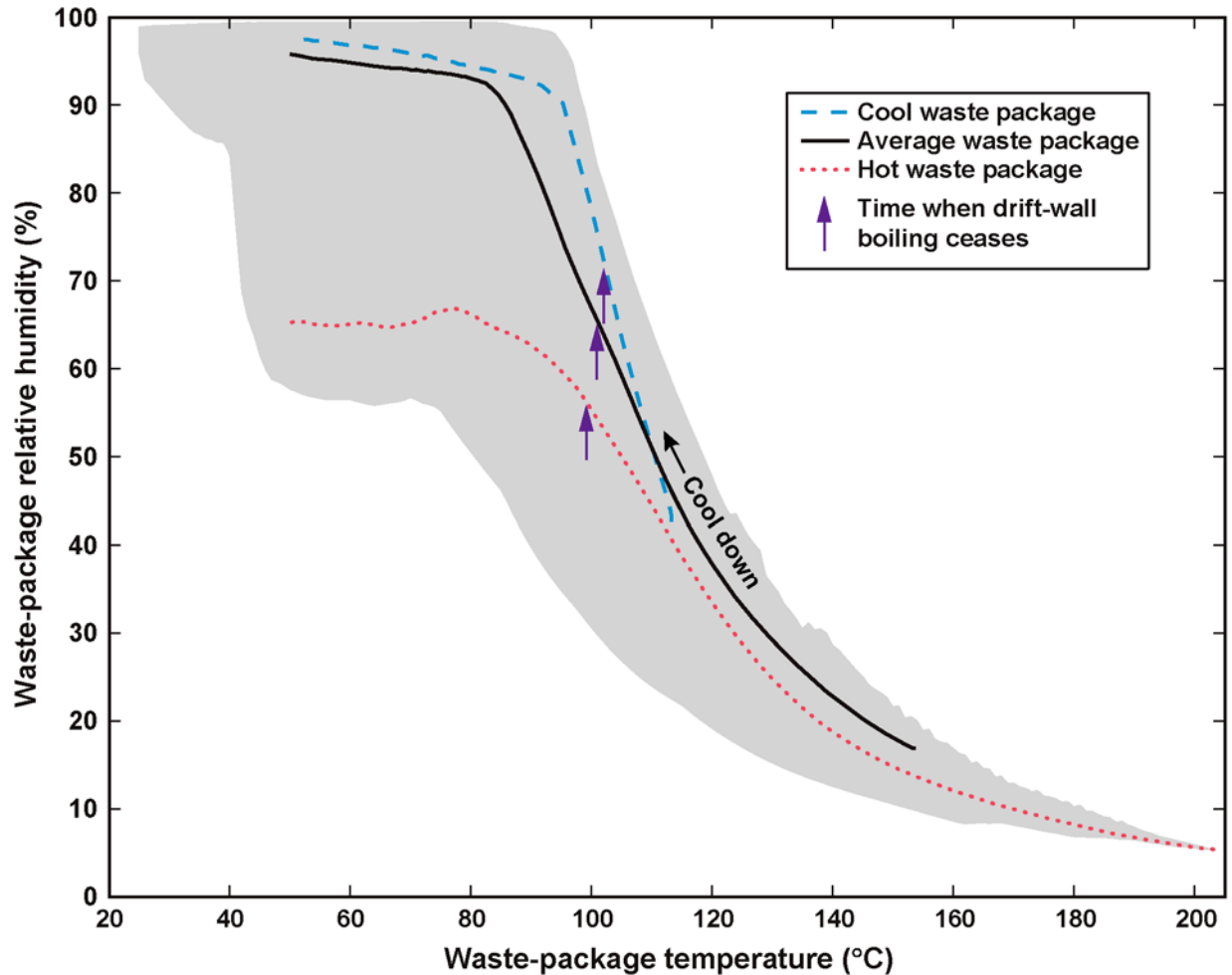
RHvsT_cool_3WPs_env

Source: See Table XIII-1.

NOTE: Also plotted are the temperature versus relative-humidity trajectories, during cooldown, of three distinct waste packages, including (1) a cool DHLW waste package at the edge of the repository, (2) an average BWR waste package at the center of the repository, and (3) a hot PWR waste package at the center of the repository. The upward arrows indicate the time when boiling ceases at the drift wall.

Figure 6.3-69. Range of Temperature vs. Relative Humidity Trajectories for All Waste Packages, During Cooldown, Accounting for Uncertainty in Host-Rock Thermal Conductivity and Percolation Flux

6.4   COMPARISON AGAINST AN ALTERNATIVE CONCEPTUAL MODEL

An alternative conceptual model to the MSTHM is a mountain-scale thermal-hydrologic model developed by LBNL (Haukwa et al. 1998 [DIRS 117826]). The LBNL model is a monolithic thermal-hydrologic model. Note that the three-drift repository MSTHM model validation test case (Section 7.5) also used a monolithic thermal-hydrologic model to compare against the MSTHM. There is an important distinction between how the monolithic thermal-hydrologic model was used in Section 7.5 and how the LBNL monolithic thermal-hydrologic model is being used in this section (Section 6.4). In Section 7.5, the MSTHM and monolithic thermal-hydrologic model representation of the model validation test problem are essentially equivalent in a number of important respects, including (1) gridblock discretization at the drift

scale, (2) heat-generation-rate-versus-time tables, (3) representation of in-drift heat-flow processes, and (4) hydrologic and thermal properties used in the respective models. In Section 6.4, the MSTHM and corresponding LBNL thermal-hydrologic model were similar, but not identical in any of these aspects. As discussed below, the LBNL thermal-hydrologic model used (1) coarser grid discretization at the drift scale than the MSTHM, (2) a line-averaged approximation of the heat-generation-rate-versus-time table (whereas the MSTHM represented the waste packages as discrete heat sources), and (3) a lumped heat source that filled the entire cross section of the emplacement drift.

Before discussing the comparison study between the MSTHM and an alternative conceptual model, it is noted that there are several differences between the version of the MSTHM used at the time of this comparison study (Buscheck et al. 1998 [DIRS 148521]) and the version of the MSTHM used to support TSPA-LA (as described in this report). These differences fall under the following categories.

1. **Repository layout**: As seen in comparing Figure 6.2-3 with Figures 5.1, 5.2, and 6.1 of BSC 2001 [DIRS 158204], both the repository layout and the MSTHM representation of the layout have changed. The current version of the MSTHM utilizes 108 drift-scale submodel locations, while the previous version of the MSTHM utilizes 31 locations. The current version explicitly represents each emplacement drift, while the previous version does not.

2. **Drift ventilation:** The current version of the MSTHM represents how heat-removal efficiency from drift ventilation varies as a function of time and distance along each of the emplacement drifts, given in DTN: MO0304MWDALACV.000 [DIRS 164551], while the previous version used a single value of heat-removal efficiency for the entire repository, which is held constant during the preclosure ventilation period.

3. **Percolation flux:** The current version of the MSTHM represents the influence of lateral diversion in the PTn by using the percolation-flux distribution (from the base of the PTn unit into the top of the TSw sequence of units) calculated by *UZ Flow Models and Submodels* (BSC 2004 [DIRS 169861]). Because the previous version used the infiltration maps at the ground surface from DTN: GS000308311221.005 [DIRS 147613], it did not represent the influence of lateral diversion in the PTn.

Because these differences also pertain to the alternative conceptual model, they do not affect the usefulness of the comparison between the MSTHM and that model.

Figure 6.4-1 compares the drift-wall temperature predicted by the MSTHM (Buscheck et al. 1998 [DIRS 148521]) with those predicted by an east-west cross-sectional mountain-scale thermal-hydrologic model (Haukwa et al. 1998 [DIRS 117826]). Because the east-west thermal-hydrologic model does not predict in-drift thermal-hydrologic conditions and because relative humidity and liquid-phase saturation was not provided from that model, the comparison is restricted to predictions of drift-wall temperatures by the respective modeling approaches.
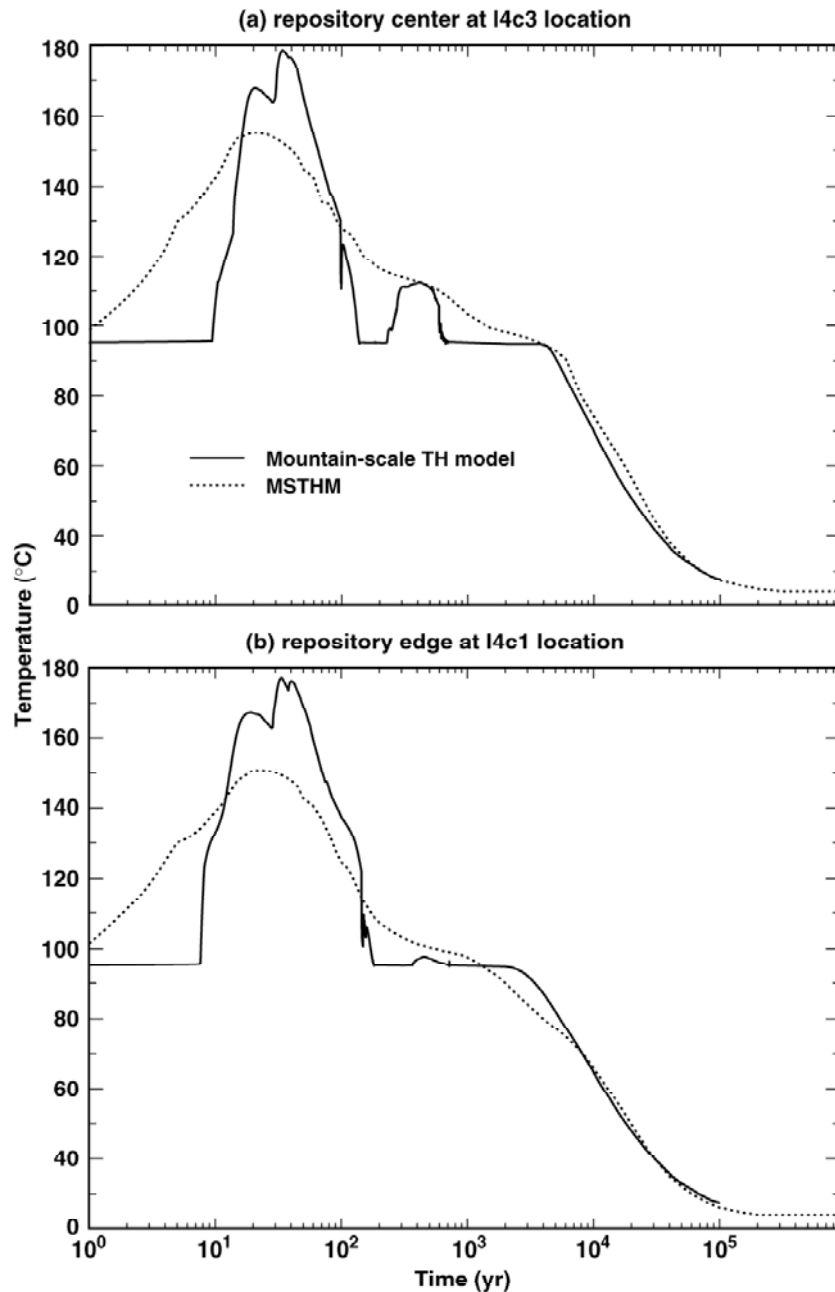
NOTE: This comparison of predicted temperatures at (a) center of the repository (l4c3 location in Buscheck et al. 1998 [DIRS 148521], Table 2-2) and (b) 100 m from the edge of the repository (l4c1 location) is run for the 12/97 TSPA-VA base-case I1 × 1 $\alpha_{f,mean}$ parameter set, where the symbol I stands for the nominal infiltration flux q_{inf} map (average q_{inf} = 7.8 mm/yr) for the present-day climate and the parameter α_f is the van Genuchten "alpha" parameter for fractures. The MSTHM is used to predict drift-wall temperature adjacent to an "average" 21-PWR medium-heat CSNF waste package. The east-west cross-sectional mountain-scale thermal-hydrologic model (Haukwa et al. 1998 [DIRS 117826]) is used to predict the drift temperature, which is averaged over the cross section of the drift, arising from a line-averaged heat-source representation of waste package decay heat.

Figure 6.4-1. Comparison of Predicted Temperatures at (a) the Center of the Repository and (b) 100 m from the Edge of the Repository

Before discussing the differences in the temperatures predicted by the two approaches (Figure 6.4-1), it is important to discuss the differences in the models. The temperature predicted by the MSTHM is the perimeter-averaged drift-wall temperature adjacent to an "average" 21-PWR medium-heat CSNF waste package. MSTHM discretely represents the decay-heat source from individual waste packages; therefore, some of the drift-wall locations are hotter than that shown in Figure 6.4-1, while some are considerably cooler. The drift-wall gridblocks over which the temperature is averaged extend 0.5 m into the host rock surrounding the drift. The temperature prediction in the east-west cross-sectional mountain-scale thermal-hydrologic model is for a gridblock that occupies the entire cross section of the drift; therefore, it is a lumped representation of the drift temperature. Moreover, because the east-west cross-sectional mountain-scale model uses a line-averaged heat source, it axially smears out the differences between "hot" and "cold" waste package locations along the drift.

Another difference between the modeling approaches concerns the mountain-scale dimensionality. The MSTHM represents three-dimensional mountain-scale heat flow for the entire extent of the heated repository footprint, while the east-west cross-sectional mountain-scale thermal-hydrologic model has a reflected boundary at the east-west midpoint of the repository. Thus, the east-west model assumes that the overburden thickness of the entire repository area can be approximated with the overburden thickness between the western repository boundary and the midpoint of the repository. Because the eastern half of the repository has much less overburden thickness than the western half, this east-west symmetry approximation effectively over represents the effective overburden thickness for the eastern half of the repository. The cross-sectional geometry of the east-west mountain-scale model implicitly assumes that mountain-scale heat loss in the north-south dimension is insignificant, which is a reasonable assumption given the large north-south dimension of the repository.

Another difference between the two modeling approaches concerns the areal power density applied in the respective models. The initial areal power density in the MSTHM is 92.3 kW/acre, while it is 99.4 kW/acre in the east-west cross-sectional mountain-scale model. Thus, the east-west model has a 7.7 percent larger areal power density than does the MSTHM (Buscheck et al. 1998 [DIRS 148521], p. 3-10).

At the center of the repository (the l4c3 location in Buscheck et al. 1998 [DIRS 148521], Table 2-2) the respective modeling approaches predict almost an identical duration of boiling (Figure 6.4-1a). At the edge repository location, which is 100 m from the western edge of the repository in the MSTHM (the l4c1 location in Buscheck et al. 1998 [DIRS 148521], Table 2-2), the east-west cross-sectional mountain-scale model predicts a longer duration of boiling than does the MSTHM (Figure 6.4-1b). One reason for this difference is that the east-west model representation of the heated repository footprint extends slightly further to the west than in the MSTHM.

During the postboiling period, the temperatures predicted by the respective modeling approaches are in good agreement. During the early time heat-up period, the coarse (lateral and axial) grid-block spacing in the east-west cross-sectional mountain-scale model does not capture the rapid drift-wall temperature rise that the more finely gridded MSTHM predicts. Because of the coarse lateral grid-block spacing in the east-west model, it smears out the lateral temperature gradient between the drift and the mid-pillar location. Therefore, it tends to overpredict the temperature at the mid-pillar location and thereby prevent condensate from shedding between

drifts. The fine lateral grid-block spacing in the MSTHM captures the influence that the lateral temperature gradient has on allowing condensate to shed between drifts. The tendency for the east-west cross-sectional mountain-scale model to underrepresent condensate shedding results in a more substantial condensate buildup above the repository horizon. Also, the line-averaged heat-source approximation smears out differences in temperature between otherwise "hot" and "cold" waste package locations and thereby preventing condensate from breaking through "cold" waste package locations along the drift. Altogether, the underprediction of condensate shedding between drifts and condensate breakthrough at "cold" waste package locations causes the east-west cross-sectional mountain-scale model to build up more condensate above the repository horizon that leads to episodic heat-pipe behavior. This episodic behavior is exhibited by the rapid decline from superheated conditions to heat-pipe conditions (Figure 6.4-1a) and the rapid rise once again to superheated conditions at about 400 years. Notice that during the second superheated period predicted by the east-west model, the temperature climbs to be almost exactly that predicted by the MSTHM.

Given the differences between the MSTHM and the east-west cross-sectional mountain-scale model, the agreement between the two models is adequate. Moreover, the differences in predicted temperatures between the MSTHM and the east-west cross-sectional mountain-scale model are within the range of temperature differences resulting from parametric uncertainty (Tables 6.3-30 and 6.3-31). Therefore, the impact of conceptual-model uncertainty is no larger than that of parametric uncertainty. On the basis of this comparison, it is determined that the MSTHM is validated for its intended use.

6.5 FEPS

The development of a comprehensive list of features, events, and processes (FEPs) potentially relevant to postclosure performance of the Yucca Mountain repository is an ongoing, iterative process based on site-specific information, design, and regulations. The approach for developing an initial list of FEPs in support of TSPA-SR (CRWMS M&O 2000 [DIRS 153246]) was documented in *The Development of Information Catalogued in REV00 of the YMP FEP Database* (BSC 2001 [DIRS 154365]). The initial FEP list contained 328 FEPs, of which 176 were included in the TSPA-SR models (CRWMS M&O 2000 [DIRS 153246], Tables B-9 to B-17). To support TSPA-LA, the FEP list was re-evaluated in accordance with *The Enhanced Plan for Features, Events, and Processes (FEPs) at Yucca Mountain* (BSC 2002 [DIRS 158966], Section 3.2). Table 6.5-1 provides a listing of FEPs.

Table 6.5-1. FEPs Addressed by This Report

FEP	Name	Section Where Disposition is Addressed
2.1.06.06.0A	Effects of drip shield on flow	6.3
2.1.08.03.0A	Repository dry-out due to waste heat	6.3
2.1.08.04.0A	Condensation forms on roofs of drifts (drift-scale cold traps)	7.5[a] and 6.3
2.1.08.04.0B	Condensation forms at repository edges (repository-scale cold traps)	7.5[b]
2.1.08.05.0A	Flow through invert	6.3
2.1.08.06.0A	Capillary effects (wicking) in EBS	6.3
2.1.08.11.0A	Repository resaturation due to waste cooling	6.3
2.1.11.01.0A	Heat generation in EBS	6.3
2.1.11.02.0A	Non-uniform heat distribution in EBS	6.3
2.1.11.09.0A	Thermal effects on flow in the EBS	6.3 and 7.5

[a] In Section 7.5, the drift-scale cold-trap effect is found to be insignificant. Therefore, condensation on the roofs of the drifts (from the drift-scale cold-trap effect) is found to have an insignificant impact on the MSTHM output parameters.

[b] In Section 7.5, condensation at the repository edge (from the repository-scale cold-trap effect) is found to have an insignificant impact on the MSTHM output parameters.

documented in *Mountain-Scale Coupled Processes (TH/THC/THM)* (BSC 2004 [DIRS 169866]). Percolation fluxes are documented in *UZ Flow Models and Submodels* (BSC 2004 [DIRS 169861]). These inputs were sufficient to define complete initial and boundary conditions for the MSTHM submodels which can be found in Sections 6.2.5, 6.2.6, 6.2.7, and 6.2.8. Additional simulation cases were developed and run to cover the low probability seismic collapsed-drift scenario in Sections 6.2.9, 6.2.10, and 6.2.11. Results are presented in Section 6.3. The MSTHM addresses the three-dimensional spatial and temporal (e.g., percolation flux and ventilation heat-removal efficiency) distribution of natural-system parameters, boundary conditions, and design information that influence the thermal-hydrologic response throughout the repository, which assures consistency of the MSTHM outputs. The MSTHM predictions have been thoroughly inspected, as displayed in plots and tables throughout Section 6.3, and thoroughly tested, by way of sensitivity analyses documented in Section 6.3, to assure the reasonableness and appropriateness of the MSTHM outputs. There were no calibration activities associated with the MSTHM. The NUFT code cannot complete a model simulation unless converged solutions are obtained for all calculational cycles (i.e., timesteps). Thus, numerical convergence is automatically addressed in all NUFT-submodel results that are utilized by the MSTHM. Thus, convergence is addressed in all MSTHM results.

3. *Discussion of the impacts of uncertainties to the model results including how the model results represent the range of possible outcomes consistent with important uncertainties [LP-SIII.10Q-BSC, Section 5.3.2(b)(3) and LP-2.29Q-BSC, Attachment 3 Level 1 (d) and (f)].*

Discussion of model uncertainties and their impacts on model results are provided in Section 6.3.1 which discusses the TSPA-LA base case, Section 6.3.4 which discusses the combined influences of percolation-flux and host-rock thermal conductivity uncertainty, and Section 6.3.7 which discusses the influence of a low-probability-seismic collapsed-drift scenario on in-drift thermal-hydrologic conditions relative to the TSPA-LA base case.

4. *Formulation of defensible assumptions and simplifications [LP-2.29Q-BSC, Attachment 3 Level I (b)].*

Discussion of assumptions and simplifications are provided in Sections 5, 6.1, and 6.2. Additional discussion of simplifications can be found in Appendix IX.

5. *Consistency with physical principles, such as conservation of mass, energy, and momentum [LP-2.29Q-BSC, Attachment 3 Level I (c)].*

Consistency with physical principles is demonstrated by the conceptual and mathematical formulations for the mass and energy balance equations in Section 6.2.3 and the selection and use of the NUFT code based on those physical principles.

The purpose of the MSTHM, which is to predict a reasonable range of relevant thermal-hydrologic parameters in the emplacement drifts and adjoining host rock, plays a key role in its validation and in confidence building. Table 1-1 lists all MSTHM output parameters used to support TSPA-LA. Table 1-1 also references where validation and confidence building

for the prediction of a reasonable range of these parameters is documented in this report. The purpose of the MSTHM is to predict a reasonable range of thermal-hydrologic conditions, resulting from parametric uncertainty and variability, and from the influence of waste-package heat-output variability. Thus, the goal is to predict the range of possible thermal-hydrologic responses across the repository; this is quite different from predicting a single expected thermal-hydrologic response. This range in thermal-hydrologic conditions must capture the influence of the key processes and conditions, including the uncertainty and variability associated with those processes and conditions. Thus, the influence of conceptual-model uncertainty must be judged relative to the influence of parametric uncertainty on the range of predicted thermal-hydrologic responses. The comparison of the influence of conceptual-model uncertainty with the influence of parametric uncertainty and waste-package heat-output variability is presented in Section 7.5.4.

The propagation of parametric uncertainty in the MSTHM addresses the two key natural system parameters: host-rock thermal conductivity and percolation flux. A sensitivity study of the influence of hydrologic-property uncertainty supports the conclusion that hydrologic-property uncertainty does not need to be propagated in the MSTHM calculations of in-drift temperature and relative humidity. The propagation of percolation-flux uncertainty and host-rock thermal conductivity uncertainty on repository-wide MSTHM output is captured with five infiltration-flux host-rock thermal conductivity cases (Table 6.3-37). For these five data sets, the range in peak drift-wall temperature is from 92.3°C to 175.2°C, with a median drift-wall temperature of 133.0°C; the range in peak waste package temperature is from 102.0°C to 203.1°C, with a median waste package temperature of 153.3°C (Table 6.3-38). These five cases also result in a wide range of waste package relative-humidity histories as is shown in Figure 6.3-53. For the five infiltration-flux host-rock thermal conductivity cases, the time when drift-wall boiling ceases ranges from no boiling to 2,176.5 years, with a median time of 721.0 years (Table 6.3-39). The percentage of waste packages that may experience no boiling at the drift wall is extremely low (0.01% of all waste packages in the repository).

The validation of the MSTHM involves the validation of both the MSTHM methodology and the submodels, or components, used in the MSTHM. Note that all MSTHM submodels (called the SDT, SMT, and DDT submodels) are executed with the NUFT v3.0s code (Section 3.1.1). Because the SDT, SMT, and DDT submodels are conduction-only calculations, which utilize standard scientific methods (e.g., Fourier's Law) to perform the calculations, they do not require separate validation in this report in the manner that is applied to the LDTH submodel. Moreover, the SDT, SMT, and DDT submodels are never applied as "stand-alone" models for analysis, as is the case for the LDTH submodel (e.g., Section 6.3.9). It should be noted that validation testing of the NUFT v3.0s code included conduction-only test problems (bmrk002 and verif02), which are described in the Validation Test Plan for NUFT 3.0s (LLNL 2002 [DIRS 170259]; LLNL 2000 [DIRS 170258]). These conduction-only test problems are sufficient to validate the usage of the conduction-only submodels in the MSTHM. However, an additional post-development model-validation activity, involving corroboration with results obtained from an alternate conduction-only mathematical model is described in Sections 6.2.5, 6.2.7, and 6.2.9, pertaining to the SMT, SDT, and DDT submodels, respectively. This model-corroboration example is found in *Drift Degradation Analysis* (BSC 2004 [DIRS 166107], Section 6.2 and Figure 6-26).

In Section 7.5, the MSTHM is validated as a whole. However, it would be inappropriate to validate the individual components (or submodels) of the MSTHM as independent entities in Section 7.5 because they do not function as independent entities within the MSTHM methodology. Within the context of the MSTHM methodology, these submodels do not provide "intermediate" model results; rather they provide relationships that are utilized in the calculational sequence in the MSTHM, as described in Section 6.2.4. Taken together, the SDT and SMT submodels, provide relationships that describe the rate at which the edge-cooling effect gradually influences thermal-hydrologic conditions at given locations across the repository. As discussed in Section 6.2.5, the rate at which the edge-cooling effect proceeds is taken to be governed by conduction, which is validated in Section 7.5. As discussed in Section 6.2.9, the DDT submodels provide the relationship (called deviations) between temperatures at discrete waste-package locations and line-averaged temperatures. These deviations are taken to be dominated by heat-transfer processes within the drift (namely thermal radiation and convection), as well as being influenced by conduction in the host rock, which is validated in Sections 7.5 and 7.6. The LDTH submodel is validated in Section 7.4 against the Drift Scale Test, because it is sometimes applied in this report as a "stand-alone" model to conduct sensitivity analyses (e.g., see Section 6.3.9).

The manner in which the MSTHM utilizes the SDT, SMT, and DDT submodels is justified and further described in Sections 5.3.2.1 and 6.2.4. The DDT submodel represents thermal radiation inside the emplacement drifts and also represents the influence of natural convective heat flow in the drifts through the use of an equivalent thermal conductivity that is based on a correlation given by Francis et al. (2003 [DIRS 164602], Table 6) (Section 6.2.8.5). Thus, the DDT does not model natural convection in the drift; it uses a correlation derived elsewhere as indicated. The software qualifications of NUFT v3.0s and NUFT v3.0.1s include test problems that demonstrate the validity of NUFT in modeling a one-dimensional thermal-conduction problem (bmrk 002), a three-dimensional thermal-conduction problem (verif02), and a three-dimensional thermal-radiation problem (verif03) (LLNL 2002 [DIRS 170259]; LLNL 2000 [DIRS 170258]). The NUFT code uses an industry-standard finite-difference method that solves the mass balance of water and air and an energy balance.

7.2 CONFIDENCE BUILDING AFTER MODEL DEVELOPMENT TO SUPPORT THE SCIENTIFIC BASIS OF THE MODEL

The purpose of the MSTHM, which is to predict a reasonable range of thermal-hydrologic conditions in emplacement drifts and in the adjoining host rock, plays a key role in its validation and in confidence building. Table 1-1 lists all MSTHM output parameters used to support TSPA-LA, and references where validation and confidence building for the prediction of a reasonable range of these output parameters is documented in this report. For predicting a reasonable range of the key MSTHM output parameters used in TSPA-LA (temperature, relative humidity, and liquid-phase saturation), model validation is documented in Sections 7.4 and 7.5. For predicting a reasonable range of other MSTHM output parameters (e.g., liquid-phase flux and evaporation rate), documentation in support of model confidence building is also supported by the analyses presented in Section 6.3. For predicting a reasonable range of temperature, model confidence building is also supported in Section 7.3. As is shown in Table 1-1, all MSTHM output parameters used to support TSPA-LA are supported by the model validation and model confidence building documented in this report.

Level I validation must include at least one postdevelopment method described in Paragraph 5.3.2(c) of LP-SIII.10Q-BSC. The governing TWP (BSC 2005 [DIRS 173377], Section 2.3.3) describes two such activities. One is a corroboration of model results with data acquired from the Drift Scale Test (DST).

The other validation method is a comparison against an alternative thermal-hydrologic model for a three-drift validation test case, described in Section 7.5, which is a scaled-down version of the repository. The validation test case utilizes an alternative model, which is a monolithic three-dimensional thermal-hydrologic model. The results from the alternative model are compared with those from an implementation of the MSTHM methodology specifically pertaining to the validation test case. The locations for comparison include the repository center and the repository edge. The comparison of magnitude of the differences between the MSTHM and the alternative model with the magnitude of the influence of parametric uncertainty is presented in Section 7.5.4.

In addition to the postdevelopment validation activities listed in the TWP, this section reports two other confidence-building comparisons. One is a comparison of results against the Large Block Test (LBT). The other is a comparison of MSTHM results against alternative numerical models. All of these comparisons are summarized in the following list and described in greater detail throughout the remainder of this section:

- **Comparison of NUFT LDTH submodel results against the Large Block Test**–*Thermal Tests Thermal-Hydrological Analyses/Model Report* (CRWMS M&O 2000 [DIRS 146921], Section 6.2.4) documents the comparison of NUFT thermal-hydrologic model calculations against measurements made in the Large Block Test. This confidence-building activity supplements the activities required by the TWP and therefore has no specific validation criterion. The difference between the modeled and field-measured thermal-hydrologic behavior is compared with the impact of parameter uncertainty on thermal-hydrologic behavior. A summary of this comparison is given in Section 7.3. The NUFT thermal-hydrologic model used in this confidence-building study is a three-dimensional equivalent to the two-dimensional LDTH submodels (Section 6.2.6) used in the MSTHM. These thermal-hydrologic calculations used NUFT v3.0s (Section 3.1.1). The sources of the test data are listed in Table 4.4-1.

- **Comparison of NUFT LDTH submodel results against the Drift Scale Test**–Section 7.4 documents the comparison of NUFT thermal-hydrologic model calculations against measurements made in the Drift Scale Test. The adequacy of the agreement between the modeled and field-measured thermal-hydrologic behavior is judged in light of the impact of parameter uncertainty on thermal-hydrologic behavior. The NUFT thermal-hydrologic model used in this validation study is a three-dimensional equivalent to the two-dimensional LDTH submodels (Section 6.2.6) used in the MSTHM. These thermal-hydrologic calculations used NUFT v3.0.1s (Section 3.1.2), which is essentially identical to NUFT v3.0s except that NUFT v3.0.1s is able to address nested-mesh problems having a large number of nests, while NUFT v3.0s can handle nested meshes with two nests. One validation criterion for this comparison is that temperature changes should agree within 30 percent for the heating phase (BSC 2005 [DIRS 173377], Section 2.3.4). The 30-percent validation criterion for temperature rise (above ambient) is consistent with the magnitude of the influence of

the parametric uncertainty of host-rock thermal conductivity and percolation flux on temperature. As indicated by comparing the lower bound-infiltration-flux low K_{th} case with the upper-bound infiltration-flux high K_{th} case in Table 6.3-38, the combined influence of host-rock thermal conductivity uncertainty and percolation-flux uncertainty causes the rise in peak drift-wall temperature (above ambient) to vary by about 30 percent. Differences greater than 30 percent may be accepted if they resulted from short-term or localized transients in the test conditions, or from instrument response. Another criterion is that matrix liquid saturation trends should be qualitatively the same with respect to location and direction. Table 4-9 lists the sources for results of the Drift Scale Test.

- **Comparison of the MSTHM results against a monolithic three-dimensional thermal-hydrologic model**–Using a three-drift repository test case (which is a scaled-down version of the repository), the validity of the MSTHM approach is demonstrated by comparing the results of the MSTHM against a corresponding monolithic three-dimensional thermal-hydrologic model (called the D/LMTH model) that uses a nested mesh. This validation test case is similar to that reported by Buscheck et al. (2003 [DIRS 164638]). A summary of this comparison is given in Section 7.5. For this comparison, NUFT v3.0s is used for the MSTHM calculations, while NUFT v3.0.1s is used in the corresponding D/LMTH model. The model validation criterion applicable to Section 7.5 is specified in the governing TWP (BSC 2005 [DIRS 173377], Section 2.3.4). The model validation criterion compares the magnitude of the MSTHM-to-D/LMTH-model differences in a particular output parameter (e.g., temperature or relative humidity) to the range in that parameter arising from parametric uncertainty (of percolation flux and host-rock thermal conductivity). Therefore, the model-validation criterion in the governing TWP is based on a comparison of the influence of conceptual-model uncertainty with that of parametric uncertainty. The MSTHM-to-D/LMTH model differences for changes in temperature, liquid-phase saturation, or relative humidity at either of the two representative locations (representing the repository center and edge), at any time during the simulation must be reasonably comparable to the range of the relevant parameter arising from parametric uncertainty. The pertinent range of uncertainty is the range in the results generated by the MSTHM for ranges of percolation flux and host rock thermal conductivity in full-repository simulations (BSC 2005 [DIRS 173377], Section 2.3.4). These results are propagated to TSPA.

- **Comparison of MSTHM results against alternative numerical models**–Buscheck et al. (1998 [DIRS 148521]) document a comparison between the results of the MSTHM against a three-dimensional east-west cross-sectional mountain-scale thermal-hydrologic model developed at Lawrence Berkeley National Laboratory (Haukwa et al. 1998 [DIRS 117826]). This confidence-building activity is another supplement to the activities required by the TWP; there are no specific validation criteria for this comparison. The difference between the model results is compared with the impact of parameter uncertainty on thermal-hydrologic behavior. A brief summary of this comparison is given in Section 6.4.

7.3 COMPARISON OF NUFT THERMAL-HYDROLOGIC MODEL AGAINST THE LARGE BLOCK TEST

The NUFT thermal-hydrologic model used to model the Large Block Test (LBT) is described in Section 6.1.4 of *Thermal Tests Thermal-Hydrological Analyses/Model Report* (CRWMS M&O 2000 [DIRS 146921]). The NUFT thermal-hydrologic model used in this confidence-building study is a three-dimensional equivalent to the two-dimensional LDTH submodels (Section 6.2.6) used in the MSTHM. As in the case of the Drift-Scale Test (DST), the LBT was located in the Tptpmn (tsw34) unit. In the LBT, a block of excavated rock (3 m by 3 m by 4.5 m) was heated for one year with five heaters placed in an array of horizontal boreholes 2.75 m from the top of the block. Temperatures were constantly monitored during the test, while liquid-phase saturations were measured on a regular basis. The source DTN for the heater power history is listed in Table 4.4-1. Note that location-specific thermal or hydrologic property data were not available for the LBT. As described below, two different data sets were used to model the LBT, including that used in the TSPA-SR base-case MSTHM calculations and that used in the TSPA-LA base-case MSTHM calculations (which are described in this report).

7.3.1 Comparison of Simulated and Field-Measured Temperatures

Figure 7.3-1 shows the NUFT-simulated versus measured temperature profile along Borehole TT1 at five times from 30 to 400 days. The source DTNs for all field measurements of temperatures are listed in Table 4.4-1. Because the LBT is in the Tptpmn (tsw34) unit, the NUFT thermal-hydrologic models apply the thermal and hydrologic properties for that unit. Two cases are considered: (1) the mean infiltration-flux hydrologic property set used in the TSPA-SR base-case MSTHM calculations (BSC 2001 [DIRS 158204]) and (2) the modified-mean infiltration-flux hydrologic property set used in the TSPA-LA base-case MSTHM calculations. The source of the mean infiltration-flux hydrologic property set used in the TSPA-SR base-case MSTHM calculations is DTN: LB990861233129.001 [DIRS 110226], Table 4.4-1. For the Tptpmn (tsw34) unit, the modified-mean infiltration-flux property set used in the TSPA-LA base-case MSTHM calculations is the same mean infiltration-flux property set (DTN: LB0208UZDSCPMI.002 [DIRS 161243]). Both the TSPA-SR and TSPA-LA cases are in good agreement with the field-measured temperature data. However, both cases predict slightly higher temperatures than the field-measured values, with the TSPA-LA case resulting in the highest temperatures. As is discussed below, the primary cause for the higher simulated temperatures for the TSPA-LA case is the large gas-phase pressure buildup in the matrix (Figure 7.3-2b, d, and f).
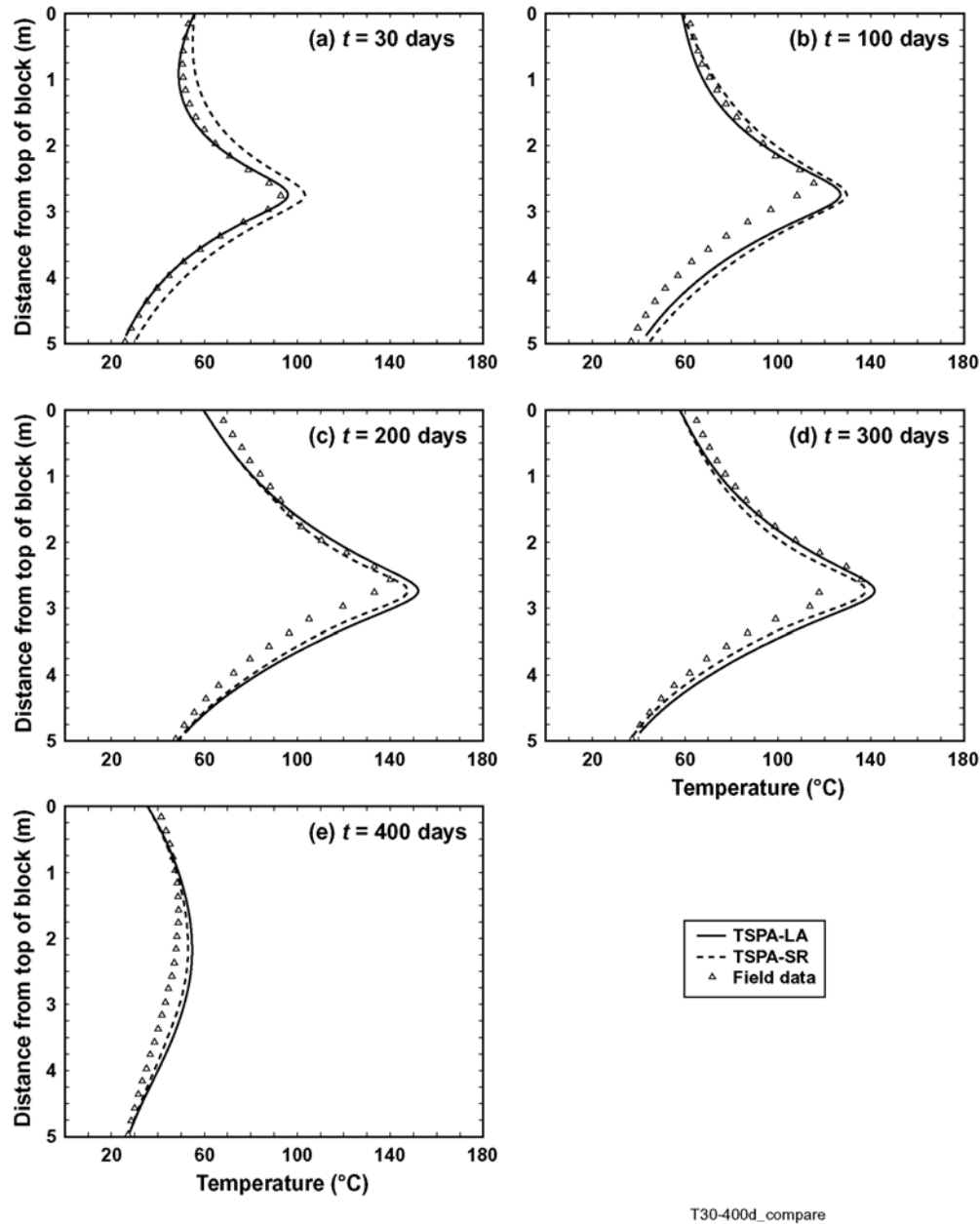
Source: See Table XIII-1.

NOTE: The NUFT simulations include two cases. The TSPA-LA case uses the modified-mean infiltration-flux hydrologic property values for the Tptpmn (tsw34) unit that are used in the MSTHM calculations for the TSPA-LA base case (Section 6.3). Note that for the Tptpmn (tsw34) unit, the mean and modified-mean property sets (discussed in Section 6.3.1) are the same. The TSPA-SR case uses the mean infiltration-flux property values for the Tptpmn (tsw34) unit that are used in the MSTHM calculations for the TSPA-SR base case (BSC 2001 [DIRS 158204]).

Figure 7.3-1. Comparison of the NUFT-Simulated and Measured Temperatures along Borehole TT1 in the Large Block Test, Given at (a) 30 Days, (b) 100 Days, (c) 200 Days, (d) 300 Days, and (e) 400 Days
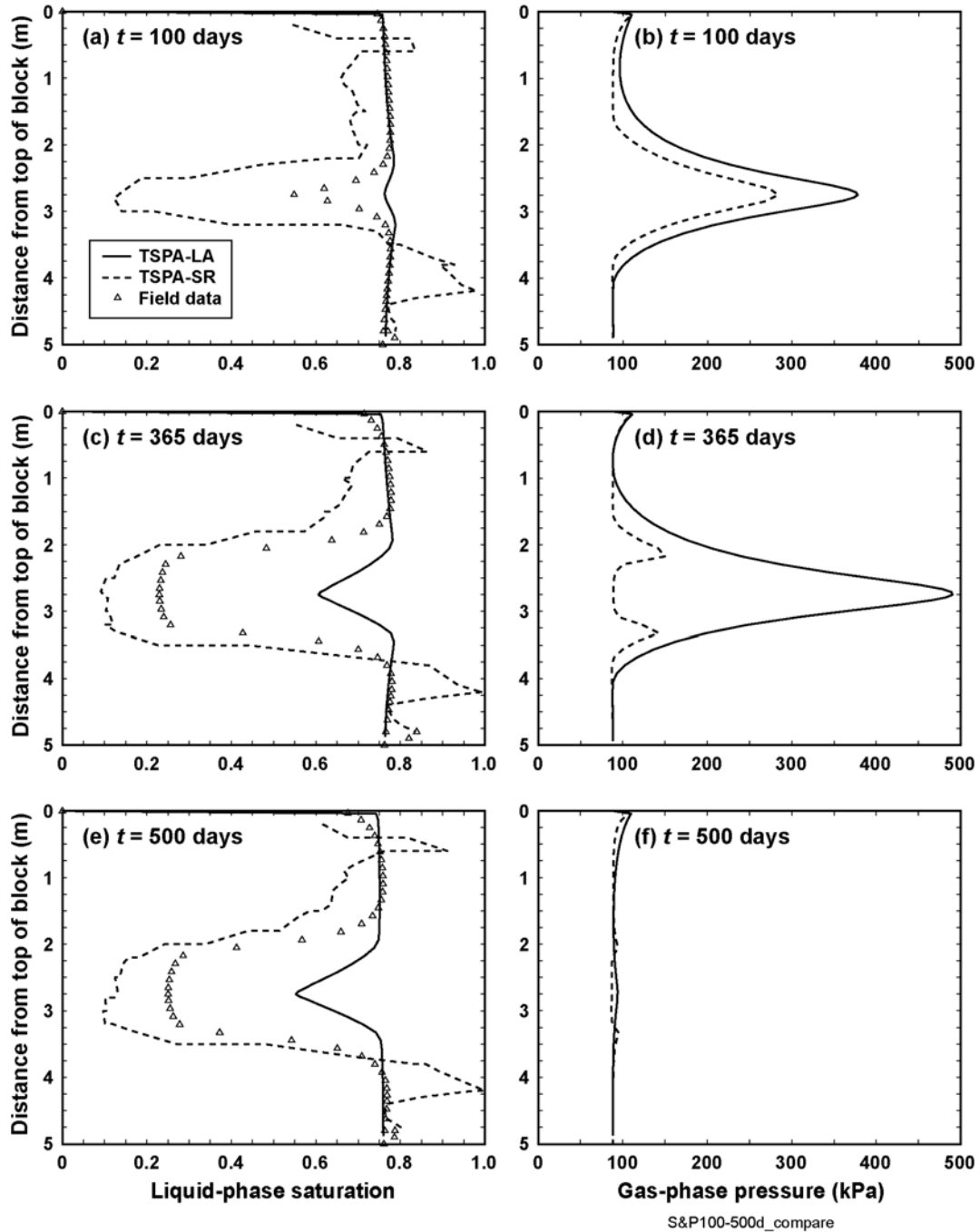
Source: See Table XIII-1.

NOTE: The NUFT-simulated gas-phase pressures in the matrix are also plotted at (b) 100 days, (d) 365 days, and (f) 500 days. Note that there are no field measurements of gas-phase pressure in the matrix. The NUFT simulations include two cases. The TSPA-LA case uses the modified-mean infiltration-flux hydrologic property values for the Tptpmn (tsw34) unit that are used in the MSTHM calculations for the TSPA-LA base case (Section 6.3). Note that for the Tptpmn (tsw34) unit, the mean and modified-mean property sets (discussed in Section 6.3.1) are the same. The TSPA-SR case uses the mean infiltration-flux property values for the Tptpmn (tsw34) unit that are used in the MSTHM calculations for the TSPA-SR base case.

Figure 7.3-2. Comparison of the NUFT-Simulated and Measured Liquid-Phase Saturations in the Matrix along Borehole TN3, Given at (a) 100 Days, (c) 365 Days, and (e) 500 Days

7.3.2 Comparison of Simulated and Field-Measured Liquid-Phase Saturations in the Matrix

Figure 7.3-2 shows the NUFT-simulated and measured liquid-phase saturation profile along TN3, which is a vertical borehole used for neutron probe measurements of water content. Note that the liquid-phase saturations discussed in this section apply to the matrix, rather than to the fractures. The source DTNs for all liquid-phase saturation measurements are listed in Table 4.4-1. Figure 7.3-2 also shows the NUFT-simulated gas-phase pressures in the matrix; note that there are no field measurements of gas-phase pressure in the matrix. At 100 days, the NUFT simulation for the TSPA-SR case shows a well-developed dryout zone, while the TSPA-LA case shows almost no dryout. An important distinction between these two cases is that the matrix permeability for the TSPA-SR case is 23 times greater than it is for the TSPA-LA case. The small matrix permeability in the TSPA-LA case causes more gas-phase pressure buildup, which drives the saturation (or boiling) temperature to be higher, thereby throttling the rate of vaporization and rock dryout. The difference in gas-phase pressure buildup is pronounced at 365 days (Figure 7.3-2d), which causes a large difference in the dryout zones for these two cases (Figure 7.3-2c). The simulated dryout zone for the TSPA-SR case is in close agreement with the measured dryout zone, which in the TSPA-LA case results in little dryout. At 365 days the gas-phase pressure nearly reaches 5 atm for the TSPA-LA case, while for the TSPA-SR case it is less than 1.5 atm (Figure 7.3-2d). Notice that the TSPA-SR case produces two zones of increased gas-phase pressure with each zone corresponding to the boiling zones above and below the heater horizon.

Although the NUFT-simulated dryout lags behind the LBT-observed dryout for the TSPA-LA case, this is not adverse to model confidence. The reason this is not adverse to model confidence is that rock dryout predicted for repository heating conditions is much slower, occurring over much longer time frames than that applicable to the LBT. Consequently, although there may be some lag in predicting dryout under repository conditions in regions of the repository where the Tptpmn (tsw34) unit is the local host-rock unit, it cannot be nearly as great as that illustrated for the LBT conditions, and the long-term MSTHM-predicted saturation histories should closely correspond to those applicable to repository heating conditions.

A comparison of the field-measured liquid-phase saturations at 365 days (when heating ceased) and at 500 days (Figure 7.3-2c and e) indicate that rewetting of the dryout zone in the LBT progresses at a slow rate. Similarly, a comparison of the NUFT-simulated liquid-phase saturations for 365 and 500 days indicates that rewetting progresses at a slow rate. Therefore, this comparison builds confidence that the NUFT thermal-hydrologic model, for both the TSPA-SR and TSPA-LA hydrologic property sets, provides a valid representation of rewetting behavior observed in the LBT.

7.3.3 Summary of Model Confidence Building Using LBT Data

The good agreement between the NUFT-simulated and measured temperatures demonstrates that the thermal conductivity values in the TSPA-SR and TSPA-LA property sets are appropriate. Moreover, this agreement builds confidence that the NUFT thermal-hydrologic model provides a valid representation of heat flow in the LBT. The differences between the predicted and field-measured temperatures are well within the relative impact of parametric uncertainty (Section 7.5.4). The agreement between the simulated and measured dryout behavior builds

confidence that the NUFT thermal-hydrologic model provides a valid representation of dryout behavior for the TSPA-SR hydrologic property set. The NUFT thermal-hydrologic model, using both the TSPA-SR and TSPA-LA hydrologic property sets, builds confidence that the NUFT thermal-hydrologic model provides a valid representation of rewetting behavior observed in the LBT. The cause for the differences between the NUFT-simulated dryout (using the TSPA-LA hydrologic property set) and the measured dryout data is well understood and does not affect the conclusion that the NUFT thermal-hydrologic model of the LBT provides a valid representation of dryout behavior.

7.4   VALIDATION OF THE LDTH SUBMODEL USING THE DRIFT SCALE TEST

The three-dimensional thermal-hydrologic model of the Drift-Scale Test (DST) is a three-dimensional equivalent of the two-dimensional LDTH submodels (Section 6.2.6) used in the MSTHM. Both the three-dimensional thermal-hydrologic model of the DST and the two-dimensional LDTH submodel use the NUFT code. Both models use the same (lateral) cross-sectional approximation of the emplacement (or heater) drift and both use the same grid refinement within the drift and in the near-field host rock. Both models use the same representation of thermal-radiative heat transfer in the drift. They both use the same effective thermal conductivity approach to representing the influence of natural convective heat flow in the drifts, which is based on a correlation by Francis et al. (2003 [DIRS 164602], Table 6) (Section 6.2.8.5). Both models use the same thermal and hydrologic property set. Both models use the same boundary conditions at the ground surface and at the water table. The only difference between the three-dimensional thermal-hydrologic model of the DST and the two-dimensional LDTH submodel is the dimensionality of the respective models. Therefore, the validation of the three-dimensional thermal-hydrologic model of the DST is equivalent to validating the two-dimensional LDTH submodels in the MSTHM.

7.4.1   Design and Geometry of the DST

The DST is the largest (and longest duration) in situ heater test of its kind (Figure 7.4-1). At the center of the DST is the Heated Drift, which is 47.5-m long with a 5.0-m diameter (similar to the 5.5-m-diameter emplacement drifts in the repository). The thermal load comes from two kinds of heat sources. The Heated Drift has nine waste package-sized heat sources. Emanating from either side of the Heated Drift are 50 horizontal boreholes (25 on each side), containing "wing heaters" that provide additional heating to simulate (in an accelerated fashion) the influence of heating from neighboring emplacement drifts. Each wing heater is composed of two 4.44-m-long segments separated by a 0.66-m gap. The outside of each wing heater is 14 m from the centerline of the heater drift, while the inside of each wing heater is 4.46 m from the centerline. The "hot" side of the Heated Drift is separated from the cold side with a thermally insulated bulkhead. The DST heating began on December 3, 1997 and continued for 1,503 days (4.1 years) until January 14, 2002. The DST is now in the cooldown phase and continues to be monitored. The source DTN for the heater power history is listed in Table 4.4-2.

The purpose of large-scale thermal testing at Yucca Mountain is discussed in Section II.E of *Thermal-Hydrological Analysis of Large-Scale Thermal Tests in the Exploratory Studies Facility at Yucca Mountain* (Buscheck and Nitao 1995 [DIRS 100657]). Sections II.F and II.G of that report discuss the rationale and criteria for the design of large-scale thermal tests. A thermal-hydrologic modeling study (Buscheck and Nitao 1995 [DIRS 100657], Section IV)

helped determine the recommended size and duration of the DST. A comprehensive description of the design and geometry of the DST is documented in Sections 7.2.1 and 7.2.2 of *Drift-Scale Coupled Processes (DST and TH Seepage) Models* (BSC 2004 [DIRS 170338]). Section 7.4 of that report gives a detailed and discussion of a thermal-hydrologic model validation study, similar to the results presented below.
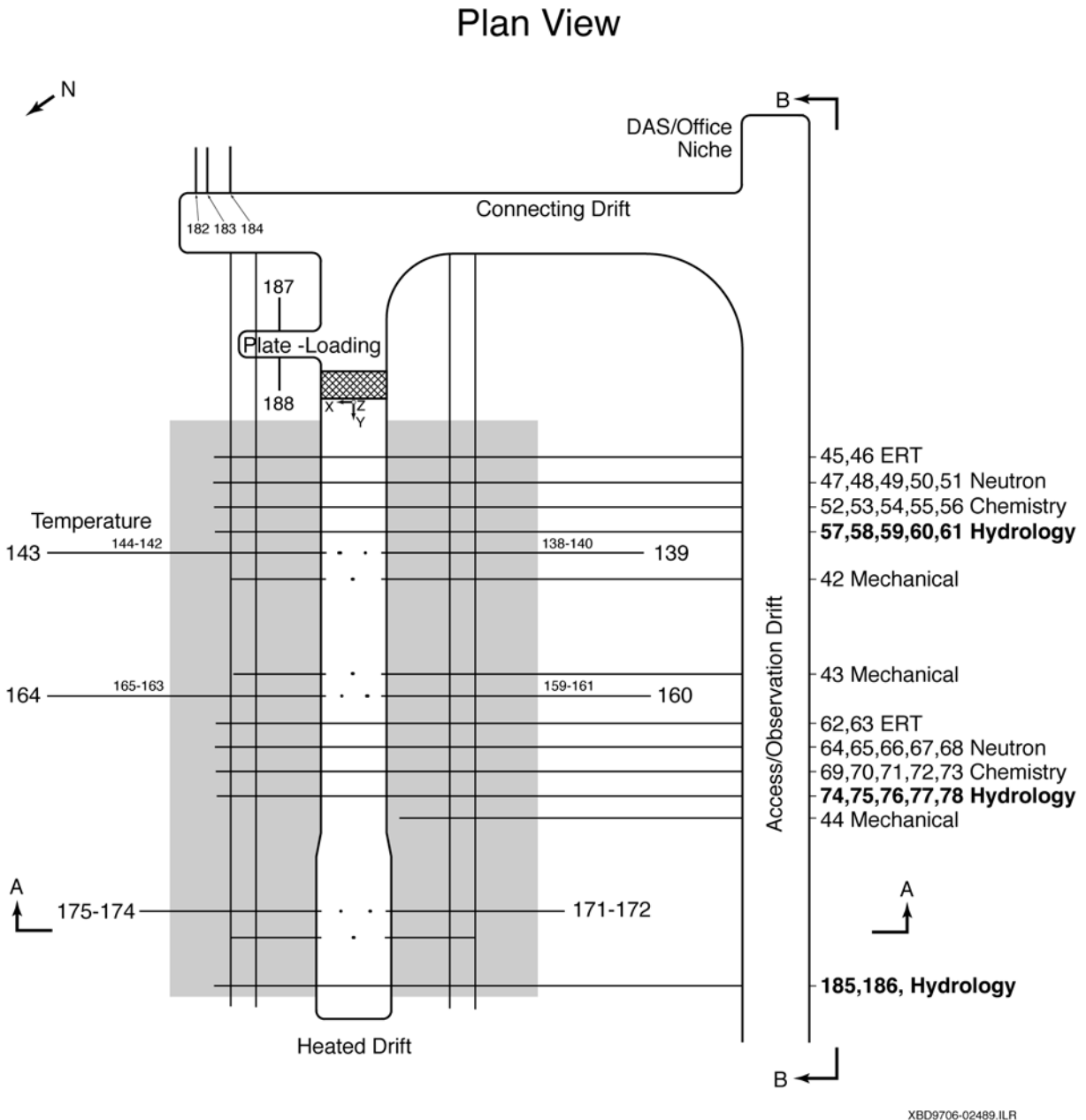
Source: BSC 2004 [DIRS 170338], Figure 7.2.1-1.

NOTE: The bulkhead is shown as the cross-hatched region, adjacent to the Plate-Loading Niche.

Figure 7.4-1. Plan View of the Drift Scale Test Area

7.4.2   Description of Three-Dimensional Thermal-Hydrologic Model of the DST

The model is designed to accurately represent the test domain and the processes governing heat and mass transport in the system. The test geometry, including the dimensions of the stratigraphic units from the water table to the ground surface, is adequately represented in this full three-dimensional model. Fracture and matrix interaction is handled using the dual-permeability model employing the active-fracture concept. The thermal-hydrologic simulation code NUFT v3.0.1s (Section 3.1.2) is used because of its ability to handle nested meshes containing many levels of nesting. The model handles heat transfer by conduction, convection, and radiation. The simulation time is 6 years, which includes the 4.1-year heating phase, and 1.9 years of the ongoing cooldown phase.

The thicknesses of hydrogeologic units in the model were obtained by using the software routine YMESH v1.54 (Section 3.1.7) to extract a profile of the units located at the origin of the DST field coordinate system, E171432, N234060 (CRWMS M&O 1998 [DIRS 111115]). The model extends from the ground surface to the water table 576 m below the surface, 278 m in the x-direction, and 478 m in the y-direction. The center of the bulkhead is located at elevation 1,053 m, 253 m below the ground surface, and 323 m above the water table. The test configuration geometry allows use of a half-symmetry model since the test is approximately symmetrical about the axis of the Heated Drift. The Connecting Drift, Access Observation Drift, and Plate-Loading Niche are not included in the model. Field data show that these structures have limited effect on the thermal-hydrologic response of the system within a radius of about 25 m from the Heated Drift.

The half-symmetry model has x-coordinate origin at the center of the bulkhead, and x positive in the direction away from the access drift (Northward). The y-coordinate axis is parallel to the axis of the Heated Drift with origin 215.9 m from the bulkhead, and positive in a general westerly direction. The z-direction is positive downward, with origin at the ground surface 252.9 m above the center of the bulkhead. The root mesh contains four levels of nesting, permitting sufficiently fine discretization in the Heated Drift and wing heater areas, while limiting memory requirements and computation time for the relatively large model. Element dimension varies from 6 cm in the bulkhead to tens of meters away from the heated areas of the test. The model has a total of 58,258 active elements, 29,129 elements in each of the two continua.

The origin of field coordinates is located at the center of the cold side of the bulkhead that separates the Heated Drift from an unheated and ventilated section of the drift. The y-axis extends from the origin through the bulkhead towards the back end of the Heated Drift (positive to west). X is positive in a direction away from the access drift (approximately north) and z is positive downward. The origin of field coordinates is located at approximately (0, 216, 253) with respect to the computational mesh.

The Heated Drift section in the x-z plane is stair-stepped to approximate the 5-m diameter circular drift using a rectangular Cartesian coordinate system. The surface of the invert is 1.3 m below the center of the drift. Since no thermal and hydrologic properties are available for the invert, material properties of the host rock, Tptpmn (tsw34), are assumed to be applicable to the invert for the DST thermal-hydrologic calculation (Sections 5.3.1.3 and 5.3.2.5).

The nine cylindrical heaters along the Heated Drift are modeled as having a square cross section with area equal to that of the 1.7-m diameter of the cylinder. There are no gaps between the heaters in the model; however, the thermal influence of the gaps is represented by removing conductive heat transfer between the ends of the heaters and by adding thermal-radiative heat transfer between the ends of the heaters. Thermal-radiative heat transfer between heater and rock wall elements and across rock wall elements is handled in the model. No fluid flow between canisters is permitted. Wing heater arrays are treated as a separate smeared heat sources.

7.4.2.1 Wing-Heater Arrays

Because the wing-heater boreholes are open to the Heated Drift and because they reside in the area of intensive boiling they are preferential conduits for the flow of water vapor into the Heated Drift. Once the water vapor enters the Heated Drift it then tends to flow towards and through the leaky bulkhead. The NUFT thermal-hydrologic model of the DST does not discretely represent the wing-heater boreholes. However, it is important to include the influence of the wing-heater boreholes on the preferential flow of water vapor. To include the influence of these conduits, the fracture permeability is treated as being anisotropic over the volume of rock occupied by the wing-heater boreholes. The fracture permeability in the x-direction (which is lateral to the Heated Drift axis) is increased by a factor of 1,000 relative to the value of fracture permeability for the Tptpmn (tsw34) unit (Section 5.3.1.4).

7.4.2.2 Bulkhead

The bulkhead, which separates the hot and cold sides of the Heated Drift, is treated as being highly permeable (Section 5.3.1.5). This was necessary because gas-phase pressure measurements across the bulkhead suggest that the structure acts as a partially open boundary that allows substantial vapor loss from the Heated Drift. As described in *Drift Scale Test As-Built Report* (CRWMS M&O 1998 [DIRS 111115]), the bulkhead consists of a complex mix of steel, glass, and fiberglass insulation. As described in Section 5.3.2.6, the bulkhead in the Drift Scale Test is assumed to have a very large value of thermal conductivity (5.5 W/m°C) and a thickness of 0.12 m; thus, the thermal conductance of the bulkhead is equal to 45.83 W/m^2°C. This assumption is made because portions of the bulkhead (such as the glass window) are not insulated and because the bulkhead is penetrated by a large array of metal conduit containing instrument cables and power lines.

7.4.2.3 Initial and Boundary Conditions

One-dimensional initialization models with the stratigraphic profile developed from the software routine YMESH v1.54 (Section 3.1.7) were used to establish initial conditions for the full three-dimensional models. Boundary conditions were obtained using the software routine boundary_conditions v1.0 (Section 3.1.8), a code developed for calculating boundary conditions for multiscale submodels based on location. For the present-day climate of the mean infiltration-flux case the local percolation flux is 5.922 mm/yr at location of the bulkhead. This percolation flux is obtained for the P1-UB26@r#83:43:1 location in the MSTHM. Note that this nomenclature is related to the naming convection in the SMT submodel, with P1 standing for Panel 1, UB26 pertaining to the 26th drift in the SMT submodel, and r#83:43:1 corresponding to the numerical mesh in the SMT submodel. The ground surface and water table boundary

conditions at this location were obtained from the software routine boundary_conditions v1.0 (Section 3.1.8). Surface boundary parameters calculated were temperature, pressure, air mass fraction, and specific enthalpy of water. Water table parameters were temperature and pressure. The simulation time used for one-dimensional initialization run is 1.0×10^9 years, which is more than enough time for the model to reach steady state. The initialization process is equivalent to that of the LDTH submodels.

7.4.3   Comparison of Simulated and Field-Measured Temperatures

Temperatures are monitored in the DST area on a continuous basis by resistance temperature device (RTD) sensors along 28 boreholes; thus, the boreholes containing the thermocouples are called RTD boreholes. The source DTNs for all field measurements of temperatures in the DST are listed in Table 4.4-2. The spatial layout of the 28 RTD boreholes is shown in Figure 7.2.2-1 of *Drift-Scale Coupled Processes (DST and TH Seepage) Models* (BSC 2004 [DIRS 170338]). For the purpose of comparison with the simulated temperatures, a daily temperature value is taken at 00:00 Greenwich Mean Time. Table 7.4-1 summarizes the RTD boreholes that were used to compare against the NUFT-simulated temperatures. The RTD boreholes fall into four categories. The first three categories consist of RTD boreholes that lie within vertical planes that are orthogonal to the HD axis, including those oriented (1) vertically, (2) laterally, and (3) at a 45° angle. The fourth category consists of RTD boreholes oriented in the longitudinal direction, which is parallel to the HD axis. The NUFT simulations considered three cases. The base case represents the bulkhead as being thermally insulated and permeable, thereby being leaky to gas flow. The sealed bulkhead case represents the bulkhead as being thermally insulated and impermeable, thereby allowing no gas flow across it. The high thermal conductivity K_{th} case is the same as the base case with K_{th} being one standard deviation above the mean, based on Table 7-10 of DTN: SN0404T0503102.011 [DIRS 169129] (File: ReadMe Summary.doc).

Table 7.4-1. Summary of Thermocouple (RTD) Boreholes Used to Compare Field-Measured Temperatures with NUFT-Simulated Temperatures.

Borehole Number	Figure	Orientation	Collar X Coordinate	Collar Y Coordinate	Collar Z Coordinate
137	7.4-3, 7.4-4	Vertical above HD (+Z)	0.775	11.918	2.510
141	7.4-3, 7.4-4	Vertical below HD (-Z)	0.764	11.893	−1.637
168	7.4-5, 7.4-6	Vertical above HD (+Z)	−0.071	31.952	2.451
169	7.4-5, 7.4-6	Vertical below HD (-Z)	−0.003	32.007	−1.629
170	7.4-7, 7.4-8	Vertical above HD (+Z)	0.751	39.306	2.488
173	7.4-7, 7.4-8	Vertical below HD (-Z)	0.758	39.324	−1.623
139	7.4-9, 7.4-10	Lateral (-X)	−2.569	11.891	−0.017
143	7.4-9, 7.4-10	Lateral (+X)	2.665	11.890	−0.008
79	7.4-11, 7.4-12	Longitudinal (+Y)	9.460	−11.022	3.752
80	7.4-11, 7.4-12	Longitudinal (+Y)	−9.486	−11.059	3.228

NOTE: HD = Heated Drift. The indicated orientation is relative to the Heated Drift. The source of the coordinates is given in Tables S00085_001 and S00085_002 of DTN: MO0002ABBLSLDS.000 [DIRS 147304].

Figure 7.4-2 shows the temperature contours just prior to the end of the heating phase (1,500 days) in plan view through a plane at the elevation of the wing-heater array and for a vertical cross-section midway along the length of the Heated Drift. Note that the heaters are

turned off at 1,503 days. Notice also that the highest temperatures are located close to the wing heaters and that the temperature contours are vertically symmetrical about the heater horizon, which indicates that heat flow there is dominated by heat conduction. Because the bulk permeability k_b of the DST area is less than the threshold k_b value at which buoyant gas-phase convection begins to significantly influence heat flow (Buscheck and Nitao 1994 [DIRS 130561], pp. 8 to 12), heat flow in the subboiling region is dominated by heat conduction.

Figures 7.4-3 through 7.4-8 compare NUFT-simulated temperatures (for three cases) with measured temperatures along vertically oriented RTD boreholes. Figures 7.4-9 and 7.4-10 compare NUFT-simulated temperatures (for the three cases) with measured temperatures along horizontal (lateral) RTD boreholes. Figures 7.4-13 through 7.4-16 compare NUFT-simulated temperature histories (for the three cases) with measured temperature histories. Table 7.4-2 summarizes the information for the thermocouple sensors used to compare NUFT-simulated and field-measured temperature histories.

Table 7.4-2. Coordinates of Thermocouple Sensors Used in Figures 7.4-13, 7.4-14, and 7.4-15

Borehole	Sensor	Figure	X Coordinate	Y Coordinate	Z Coordinate
133	52	7.4-13	0.85	2.81	17.85
133	23	7.4-13	0.79	2.77	9.12
141	20	7.4-13	0.70	11.94	-8.87
138	23	7.4-13	-6.39	11.77	6.36
134	8	7.4-14	0.73	2.74	-3.13
144	21	7.4-14	6.31	11.96	6.27
162	26	7.4-14	0.79	22.9	-8.85
163	24	7.4-14	6.39	22.72	-6.49
138	3	7.4-15	-2.15	11.88	2.12
139	23	7.4-15	-8.9	11.91	0.04
144	1	7.4-15	2.07	11.92	2.04
164	24	7.4-15	9.01	22.77	0.11

Source: CRWMS M&O 1998 [DIRS 111115].

NOTE: The source of the coordinates is given in the top of Table 4.4-2.

It is noted that these comparisons are made for the NUFT simulations that applied the modified-mean infiltration-flux hydrologic-property set (Section 6.3.1). In Section 7.4.4 of *Drift-Scale Coupled Processes (DST and TH Seepage) Models* (BSC 2004 [DIRS 170338]), comparisons are made for thermal-hydrologic simulations for two property sets. The first set is the DS/AFM-UZ02-MEAN property set (BSC 2004 [DIRS 170338]), also known as the *calibrated* hydrologic property set, which is equivalent to the modified-mean infiltration-flux hydrologic-property set in the Tptpmn (tsw34), Tptpll (tsw35), and Tptpln (tsw36) units, as discussed in Section 6.3.1. The second set is the site-specific DKM-TT99 property set that was developed specifically for the DST (BSC 2001 [DIRS 157330]). An important difference between these two property sets is that the value of matrix permeability of the Tptpmn (tsw34) unit in the site-specific property set is 70 times larger than that of the calibrated property set. Another difference is that the calibrated property uses the Active Fracture Model (AFM), described in Liu et al. (1998 [DIRS 105729]), while the site-specific set does not use the AFM. As evident in Section 7.4.4 of *Drift-Scale Coupled Processes (DST and TH Seepage) Models* (BSC 2004 [DIRS 170338]), differences between these respective property sets affect

above-boiling temperatures and rock dryout, which are discussed below. Several general observations are made about the temperature comparisons in the vertical RTD boreholes.

- NUFT-simulated temperatures are higher than the measured temperatures in the zone where temperatures exceed 96°C. In Section 7.4.4.1 of *Drift-Scale Coupled Processes (DST and TH Seepage) Models* (BSC 2004 [DIRS 170338]), it was found that the site-specific property set resulted in lower simulated temperatures for the above-boiling region than those resulting from the calibrated hydrologic property set (which is the same as that used in NUFT DST TH simulations). Figures 7.4.4.1-1 and 7.4.4.1-2 of *Drift-Scale Coupled Processes (DST and TH Seepage) Models* (2004 [DIRS 170338]) show differences in simulated temperature of up to 20°C in the above-boiling region between these two property sets. Results from Section 7.4.4.1 of *Drift-Scale Coupled Processes (DST and TH Seepage) Models* (BSC 2004 [DIRS 170338]) show that better agreement is obtained between simulated and measured temperatures in the above-boiling region when the site-specific property set is used.

- NUFT-simulated temperatures agree fairly well with measured temperatures for the lower temperature range (less than 80°C) during the heating phase. This is consistent with Figures 7.4.4.1-1 and 7.4.4.1-2 of *Drift-Scale Coupled Processes (DST and TH Seepage) Models* (2004 [DIRS 170338]), which show small differences in simulated temperatures in the below-boiling region between the calibrated and site-specific property sets, together with Figures 7.4.3.1-1, 7.4.3.1-2, and 7.4.3.1-3 of *Drift-Scale Coupled Processes (DST and TH Seepage) Models* (2004 [DIRS 170338]), which show close agreement between measured and simulated temperatures, with the use of the site-specific property set.

- The high-K_{th} case, which results in the lowest NUFT-simulated temperatures, is in best agreement with the measured temperatures during both the heating and cooldown phases.

- The sealed-bulkhead case results in slightly higher NUFT-simulated temperatures than the base case (which had a leaky bulkhead). The influence of the leaky bulkhead on simulated temperatures is less than that resulting from a one standard-deviation range in thermal conductivity (which is evident in the temperature differences between the high-K_{th} case and the base case).

- For the vertical RTD boreholes (Figures 7.4-3 through 7.4-8), "plateau" behavior in temperature close to 96°C develops in virtually all of the measured temperature profiles. However, it appears in only a few of the NUFT-simulated temperature profiles, occurring at times later than observed in the field. This effect is associated with the use of the calibrated hydrologic property set and the low value of matrix permeability, which results in a large gas-phase pressure buildup in the matrix that increases the saturation (boiling) temperature. This is consistent with Figure 7.4.4.1-2 of *Drift-Scale Coupled Processes (DST and TH Seepage) Models* (BSC 2004 [DIRS 170338]). The impact of the large gas-phase pressure buildup is discussed in more detail in Section 7.4.4 of this report.

- At early time (175, 365, and 730 days) for the lateral RTD boreholes (Figure 7.4-9), the NUFT-simulated temperature profiles exhibit more plateau behavior than the measured temperature profiles within the zone of likely condensate shedding.

- At later time (1,096 and 1,500 days) for the lateral RTD boreholes (Figure 7.4-10), the plateau behavior in temperature close to 96°C appears in measured temperature profiles. The NUFT-temperature profiles exhibit plateau behavior at much higher temperatures. This effect is associated with the use of the calibrated hydrologic property set and the low value of matrix permeability, which results in a large gas-phase pressure buildup in the matrix that increases the saturation (boiling) temperature. High gas-phase pressures in the matrix throttle (i.e., restrict) both vaporization and rock dryout rates. This is consistent with Section 7.4.4 of *Drift-Scale Coupled Processes (DST and TH Seepage) Models* (BSC 2004 [DIRS 170338]). The impact of the large gas-phase pressure buildup is discussed in more detail in Section 7.4.4 in this report.

- For all boreholes, measured temperatures indicate a more rapid cooldown than NUFT-simulated cooldown. This effect is associated with the use of the calibrated hydrologic properties and the low value of matrix permeability.

- For distances greater than 12 m from the borehole collar for the lateral RTD boreholes (Figures 7.4-10e and 7.4-10f), there is a pronounced "scattering" of the measured temperature profile during the cooldown phase, which is indicative of either RTD failure or of preferential condensate drainage down fractures into the boreholes, resulting in local convective cooling. Note that the outer portions of Boreholes 139 and 143 are located in the intervals where condensate shedding is most likely to occur.

- At early time (175 and 365 days) for (longitudinal) Boreholes 79 and 80 (Figures 7.4-11 and 7.4-12), NUFT-simulated temperatures agree closely with the measured temperatures. Good temperature agreement persists in Borehole 79 throughout the heating phase.

- At later time (730, 1,096, and 1,500 days) for (longitudinal) Borehole 80 (Figures 7.4-11 and 7.4-12), NUFT-simulated temperatures are higher than measured temperatures for the interval of 15 to 50 m from the borehole collar. For the interval of 0 to 15 m from the borehole collar, measured temperatures are higher than NUFT-simulated temperatures. The measured-temperature profile suggests vapor migration towards the borehole collar, where it condenses, with associated heat transfer along the borehole. This effect removes the latent heat of evaporation from the interval of 15 to 50 m from the borehole collar and deposits this latent heat along the interval 0 to 15 m.

- For (longitudinal) Boreholes 79 and 80 (Figures 7.4-11 and 7.4-12), scattering of the measured temperature profile during the cooldown phase is indicative of either RTD failures or of preferential condensate drainage down fractures into the boreholes, resulting in local convective cooling. Note that Boreholes 79 and 80 are located in a region where condensate shedding is more likely to occur.

It is important to note that the simulated large gas-phase pressure rise in the rock matrix, as discussed above, is transient and that temperature rise and dryout in the DST are accelerated, compared to those predicted for repository heating conditions. Peak temperatures in the DST occurred within 4 years, while peak temperatures require approximately 15 years to occur for repository heating conditions (e.g., Figure 6.3-23). In Section 6.3.9, which describes a sensitivity analysis of the influence of hydrologic properties on the in-drift thermal-hydrologic

response, it is found that temperature (peak temperatures and boiling-period duration) and relative humidity are insensitive to the differences in the hydrologic properties for the four host-rock units. Although matrix permeability varies by a factor of 37 over the four host-rock units, there is an insignificant influence on predicted thermal-hydrologic responses. Differences in simulated temperatures for the DST arising from differences in the value of matrix permeability are therefore not applicable to temperatures predicted by the MSTHM for repository heating conditions. Thus, although matrix permeability is seen to have a noticeable affect on temperatures simulated for the DST, it does not significantly affect repository temperature evolution predicted by thermal-hydrologic models supporting TSPA-LA.
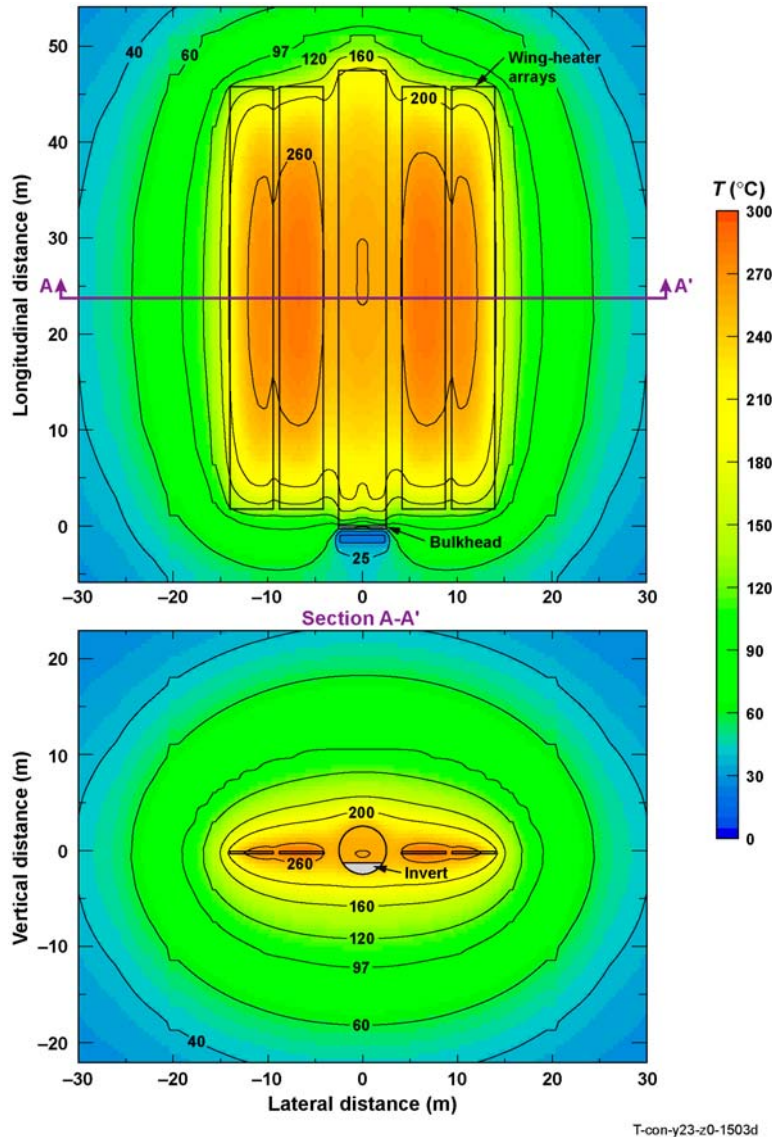
Source: See Table XIII-1.

NOTE: Heaters are turned off at 1,503 days, ending the heating phase.

Figure 7.4-2. Contours of Temperature (for the Base Case) at the End of the Heating Phase, Plotted in (a) Plan View Through a Horizontal Plane at the Elevation of the Wing-Heater Array and (b) for a Vertical Cross-Section Midway along the Heated Drift (y = 22.9 m)

Source: See Table XIII-1.

NOTE: The NUFT simulations are for the three indicated cases. The base case represents gas leakage through the bulkhead, while the sealed-bulkhead case does not allow gas leakage through the bulkhead. The high-K_{th} case is the same as the base case except with the host-rock thermal conductivity K_{th} being one standard deviation higher than the mean.

Figure 7.4-3. NUFT-Simulated and Measured Temperatures Compared along Borehole 137 (a, c, e) and Borehole 141 (b, d, f) at 175, 365, and 730 Days
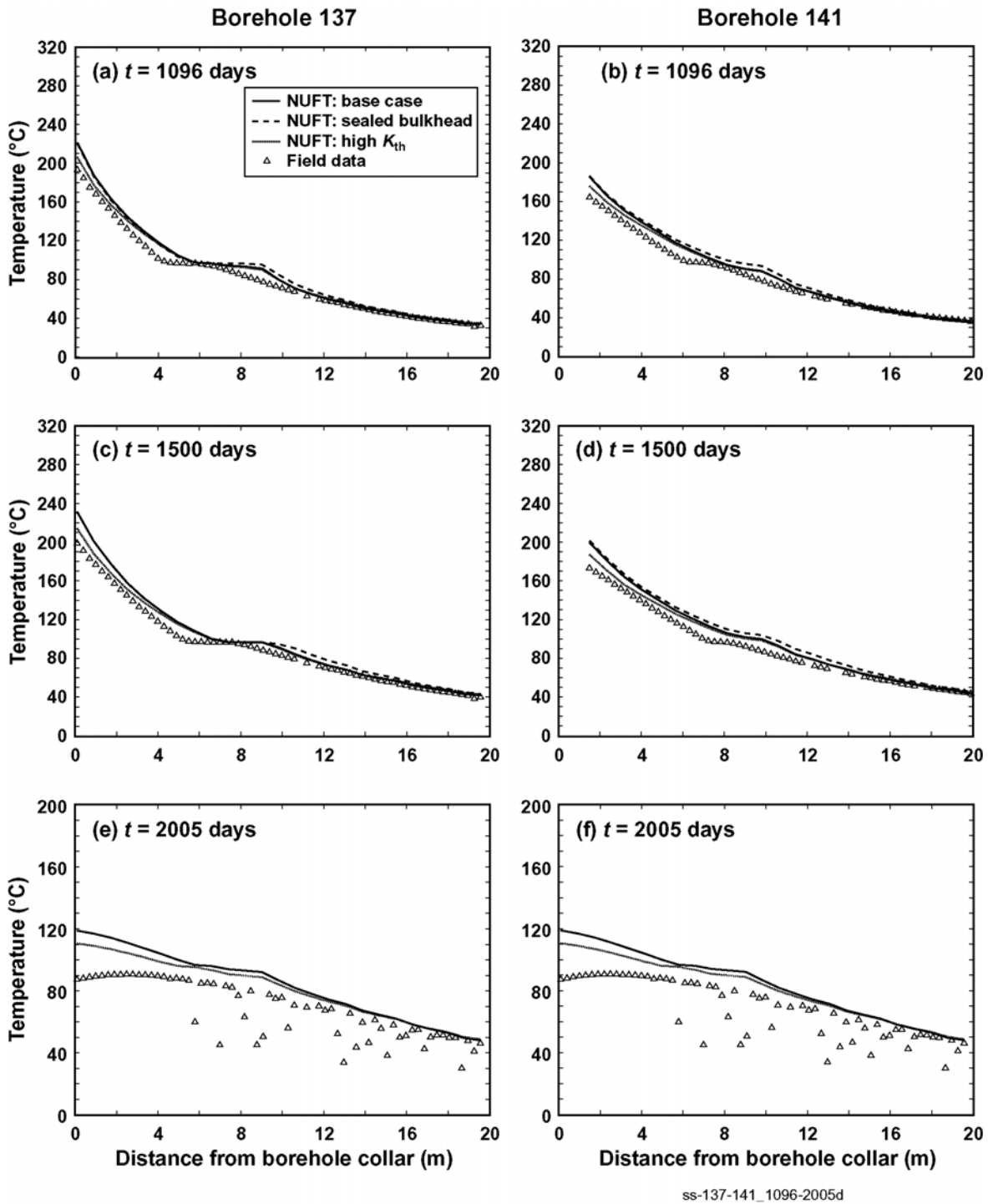
Source: See Table XIII-1.

NOTE: The NUFT simulations are for the three indicated cases. The base case represents gas leakage through the bulkhead, while the sealed-bulkhead case does not allow gas leakage through the bulkhead. The high-K_{th} case is the same as the base case except with the host-rock thermal conductivity K_{th} being one standard deviation higher than the mean. Note that the heaters are turned off at 1,503 days.

Figure 7.4-4. NUFT-Simulated and Measured Temperatures Compared along Borehole 137 (a, c, e) and Borehole 141 (b, d, f) at 1,096, 1,500, and 2,005 Days
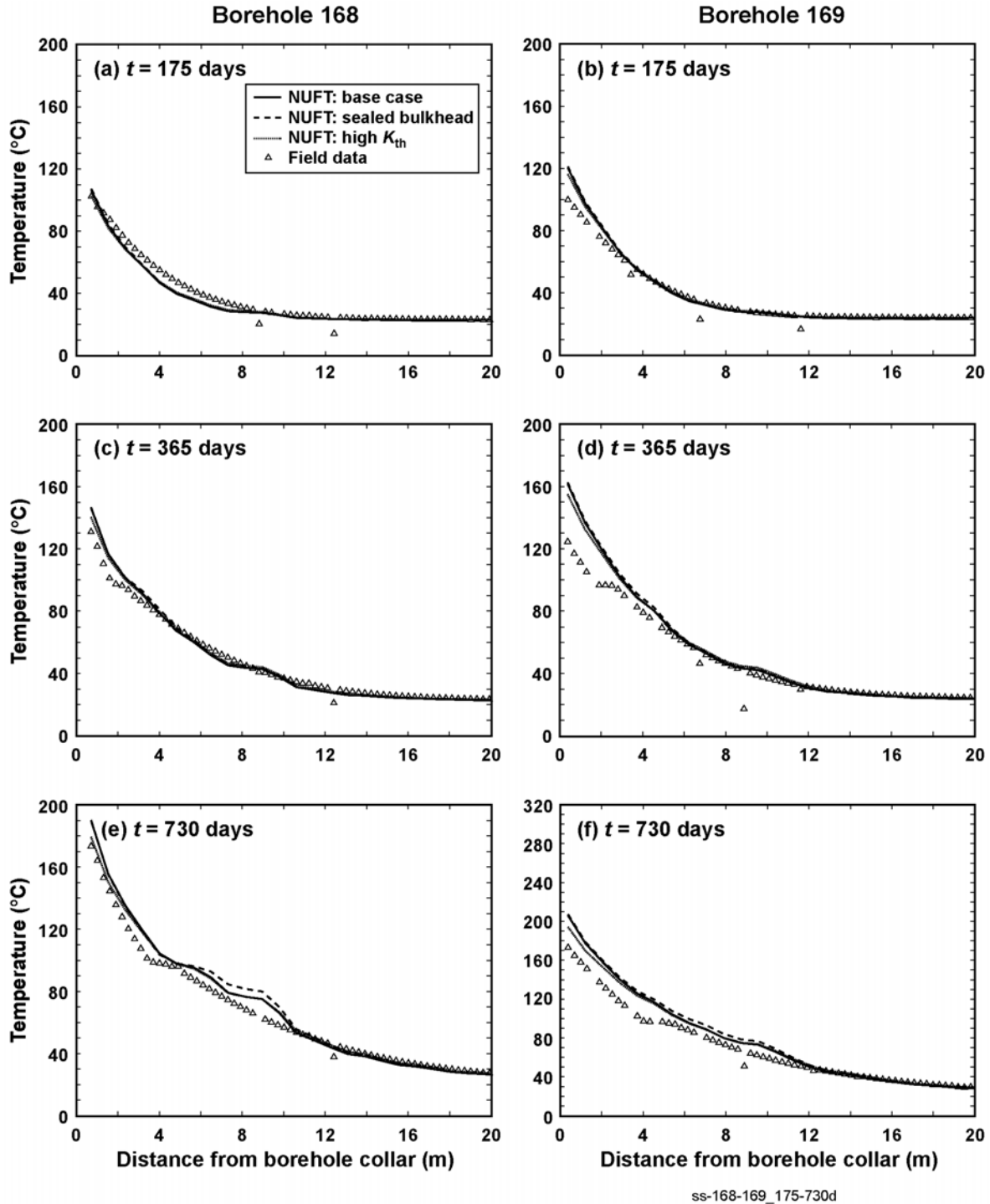
Source: See Table XIII-1.

NOTE: The NUFT simulations are for the three indicated cases. The base case represents gas leakage through the bulkhead, while the sealed-bulkhead case does not allow gas leakage through the bulkhead. The high-K_{th} case is the same as the base case except with the host-rock thermal conductivity K_{th} being one standard deviation higher than the mean.

Figure 7.4-5. NUFT-Simulated and Measured Temperatures Compared along Borehole 168 (a, c, e) and Borehole 169 (b, d, f) at 175, 365, and 730 Days
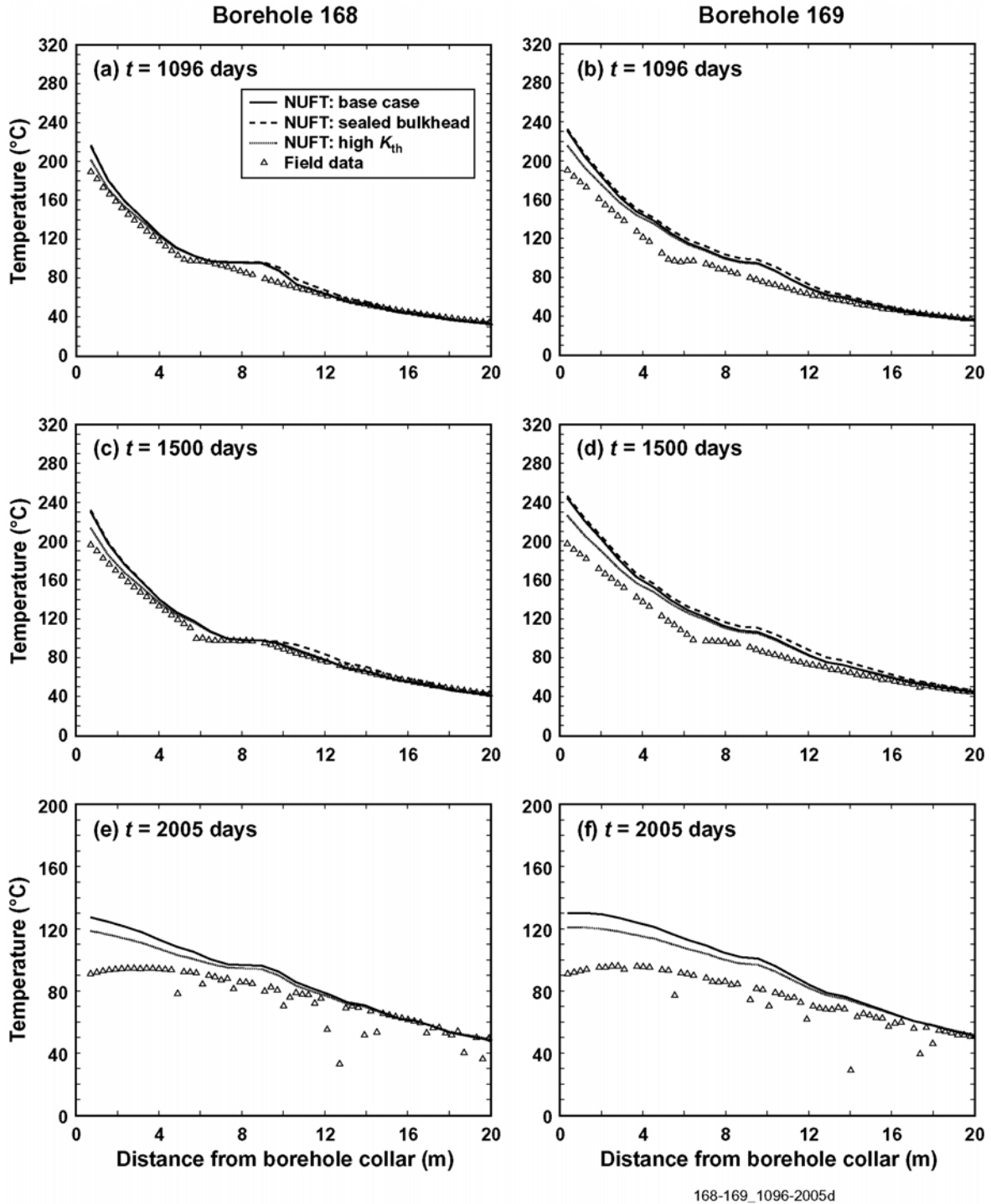
Source: See Table XIII-1.

NOTE: The NUFT simulations are for the three cases. The base case represents gas leakage through the bulkhead, while the sealed-bulkhead case does not allow gas leakage through the bulkhead. The high-Kth case is the same as the base case except with the host-rock thermal conductivity K_{th} being one standard deviation higher than the mean. Note that the heaters are turned off at 1,503 days.

Figure 7.4-6. NUFT-Simulated and Measured Temperatures Compared along Borehole 168 (a, c, e) and Borehole 169 (b, d, f) at 1,096, 1,500, and 2,005 Days
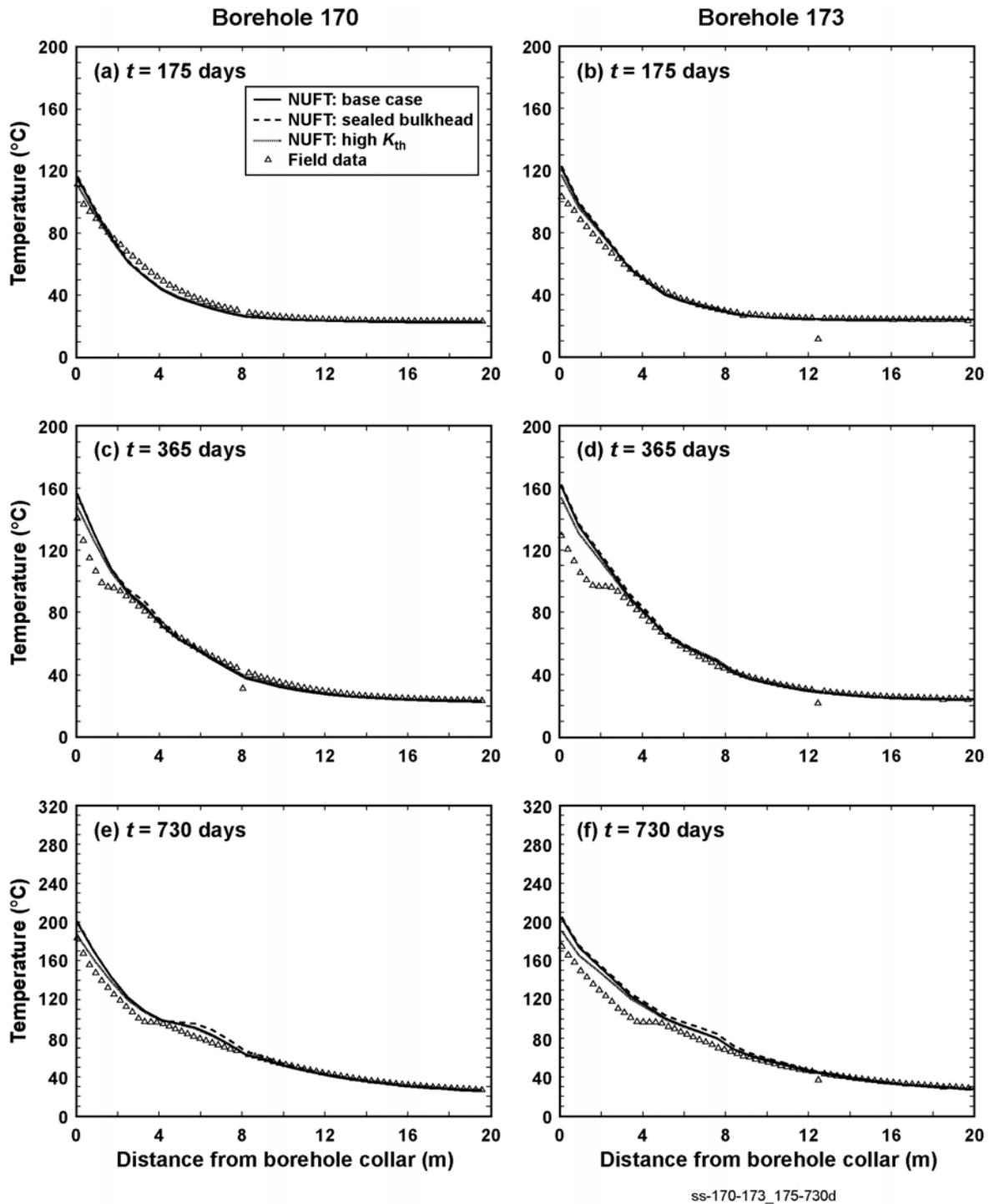
Source: See Table XIII-1.

NOTE: The NUFT simulations are for the three indicated cases. The base case represents gas leakage through the bulkhead, while the sealed-bulkhead case does not allow gas leakage through the bulkhead. The high-K_{th} case is the same as the base case except with the host-rock thermal conductivity K_{th} being one standard deviation higher than the mean.

Figure 7.4-7. NUFT-Simulated and Measured Temperatures Compared along Borehole 170 (a, c, e) and Borehole 173 (b, d, f) at 175, 365, and 730 Days
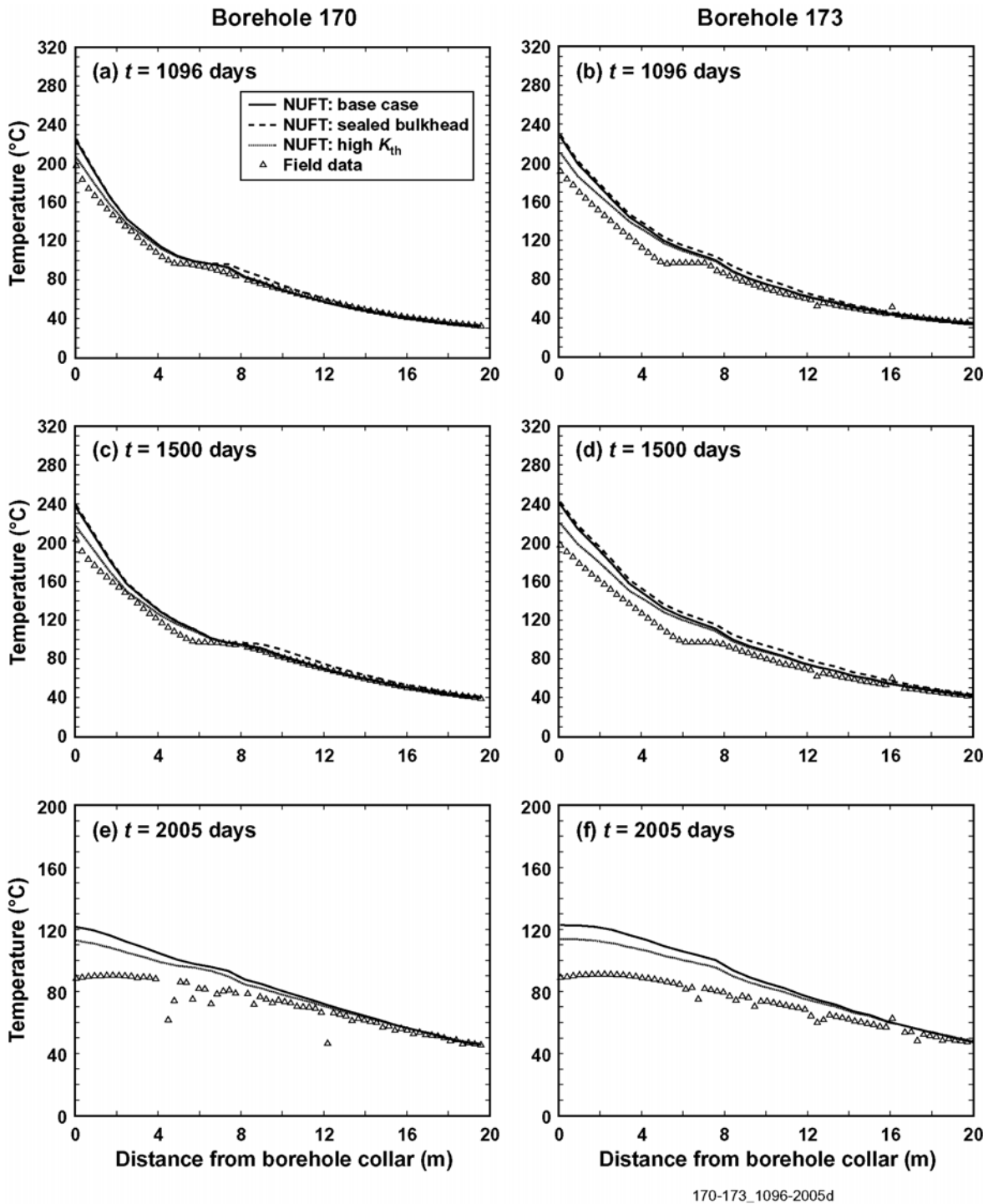
Source: See Table XIII-1.

NOTE: The NUFT simulations are for the three indicated cases. The base case represents gas leakage through the bulkhead, while the sealed bulkhead case does not allow gas leakage through the bulkhead. The high-K_{th} case is the same as the base case except with the host-rock thermal conductivity K_{th} being one standard deviation higher than the mean. Note that the heaters are turned off at 1,503 days.

Figure 7.4-8. NUFT-Simulated and Measured Temperatures Compared along Borehole 170 (a, c, e) and Borehole 173 (b, d, f) at 1,096, 1,500, and 2,005 Days
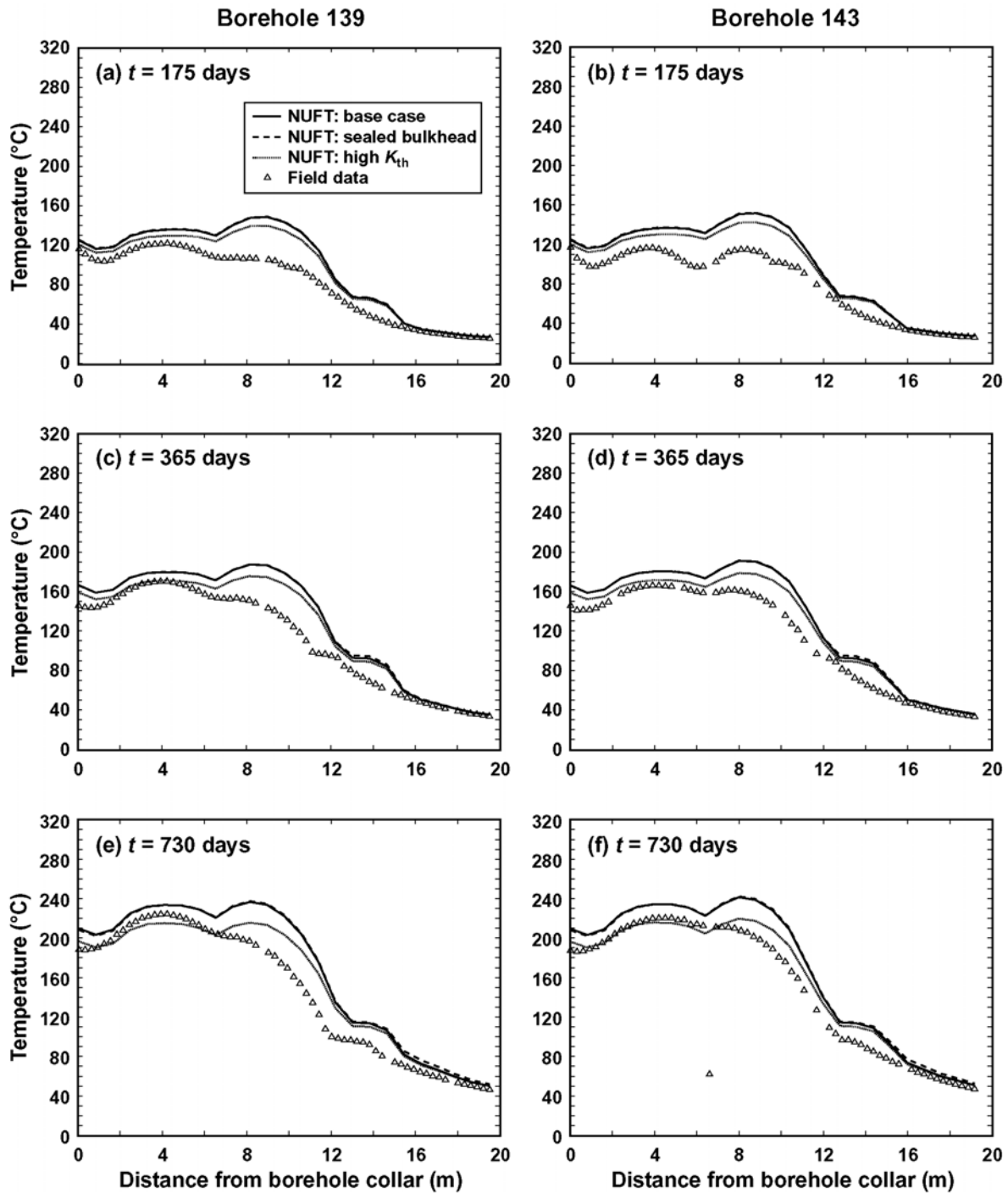
Source: See Table XIII-1.

NOTE: The NUFT simulations are for the three indicated cases. The base case represents gas leakage through the bulkhead, while the sealed-bulkhead case does not allow gas leakage through the bulkhead. The high-K_{th} case is the same as the base case except with the host-rock thermal conductivity K_{th} being one standard deviation higher than the mean.

Figure 7.4-9. NUFT-Simulated and Measured Temperatures Compared along Borehole 139 (a, c, e) and Borehole 143 (b, d, f) at 175, 365, and 730 Days
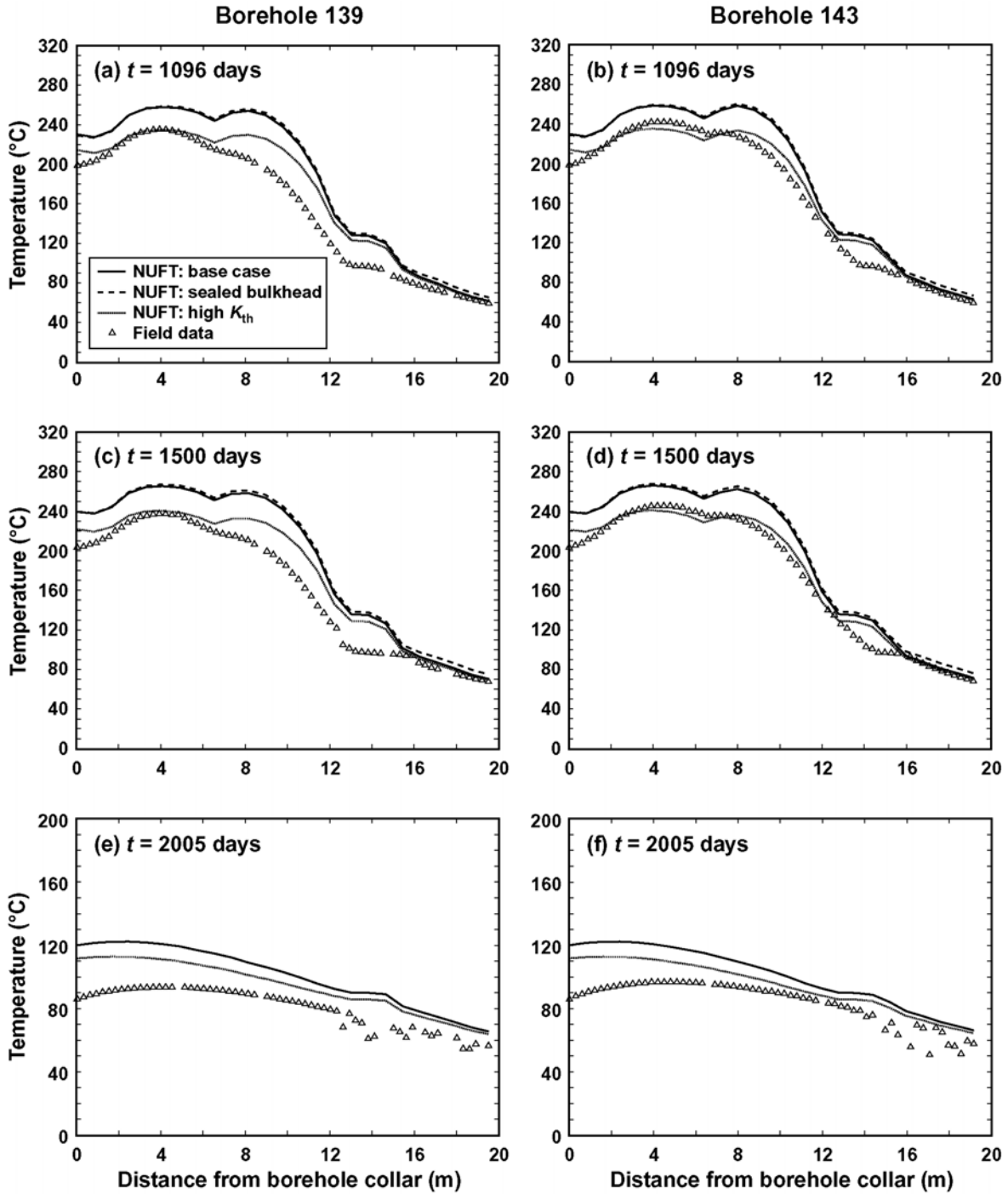
Source: See Table XIII-1.

NOTE: The NUFT simulations are for the three indicated cases. The base case represents gas leakage through the bulkhead, while the sealed-bulkhead case does not allow gas leakage through the bulkhead. The high-K_{th} case is the same as the base case except with the host-rock thermal conductivity K_{th} being one standard deviation higher than the mean. Note that the heaters are turned off at 1,503 days.

Figure 7.4-10. NUFT-Simulated and Measured Temperatures Compared along Borehole 139 (a, c, e) and Borehole 143 (b, d, f) at 1,096, 1,500, and 2,005 Days
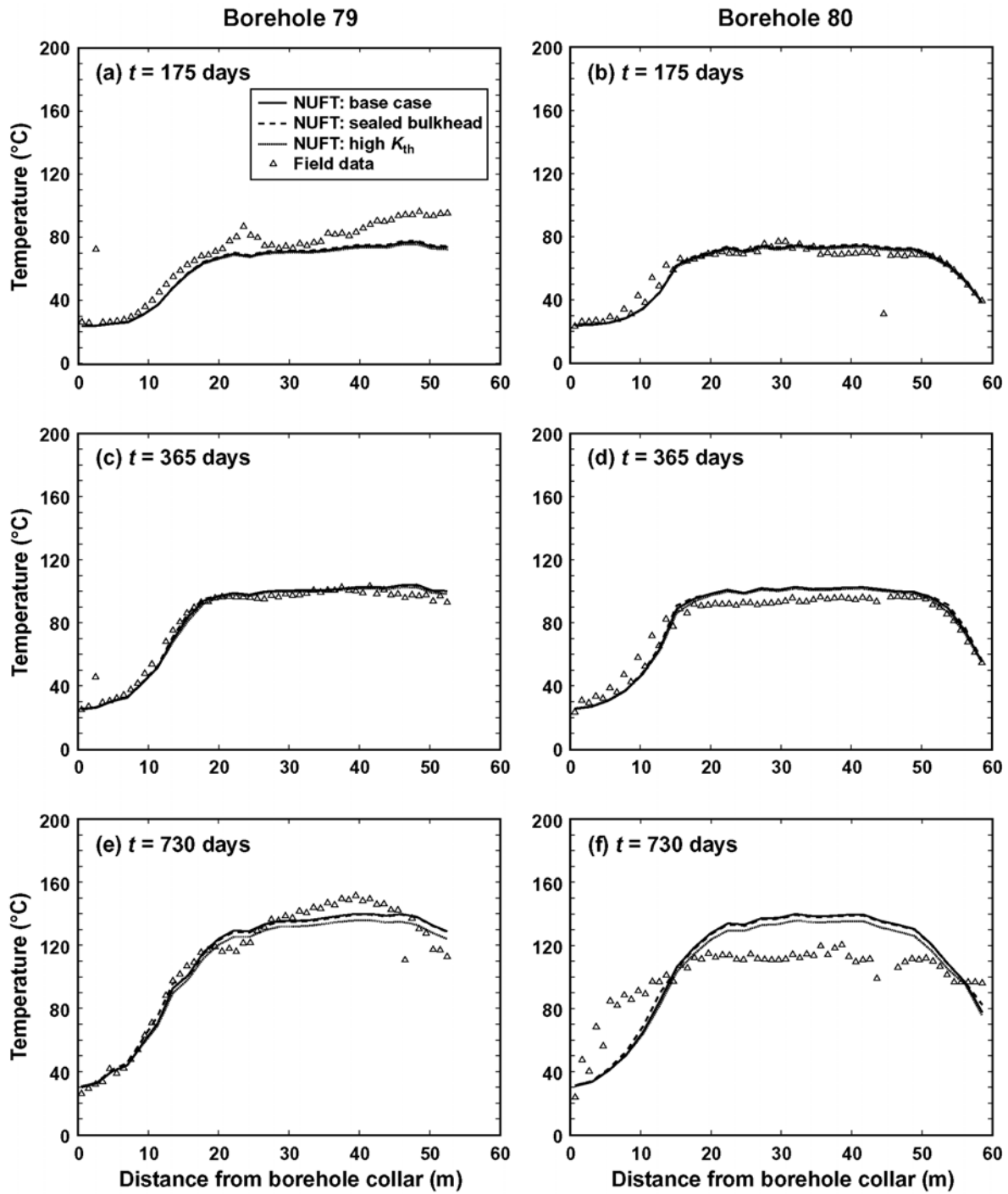
Source: See Table XIII-1.

NOTE: The NUFT simulations are for the three indicated cases. The base case represents gas leakage through the bulkhead, while the sealed-bulkhead case does not allow gas leakage through the bulkhead. The high-K_{th} case is the same as the base case except with the host-rock thermal conductivity K_{th} being one standard deviation higher than the mean.

Figure 7.4-11. NUFT-Simulated and Measured Temperatures Compared along Borehole 79 (a, c, e) and Borehole 80 (b, d, f) at 175, 365, and 730 Days
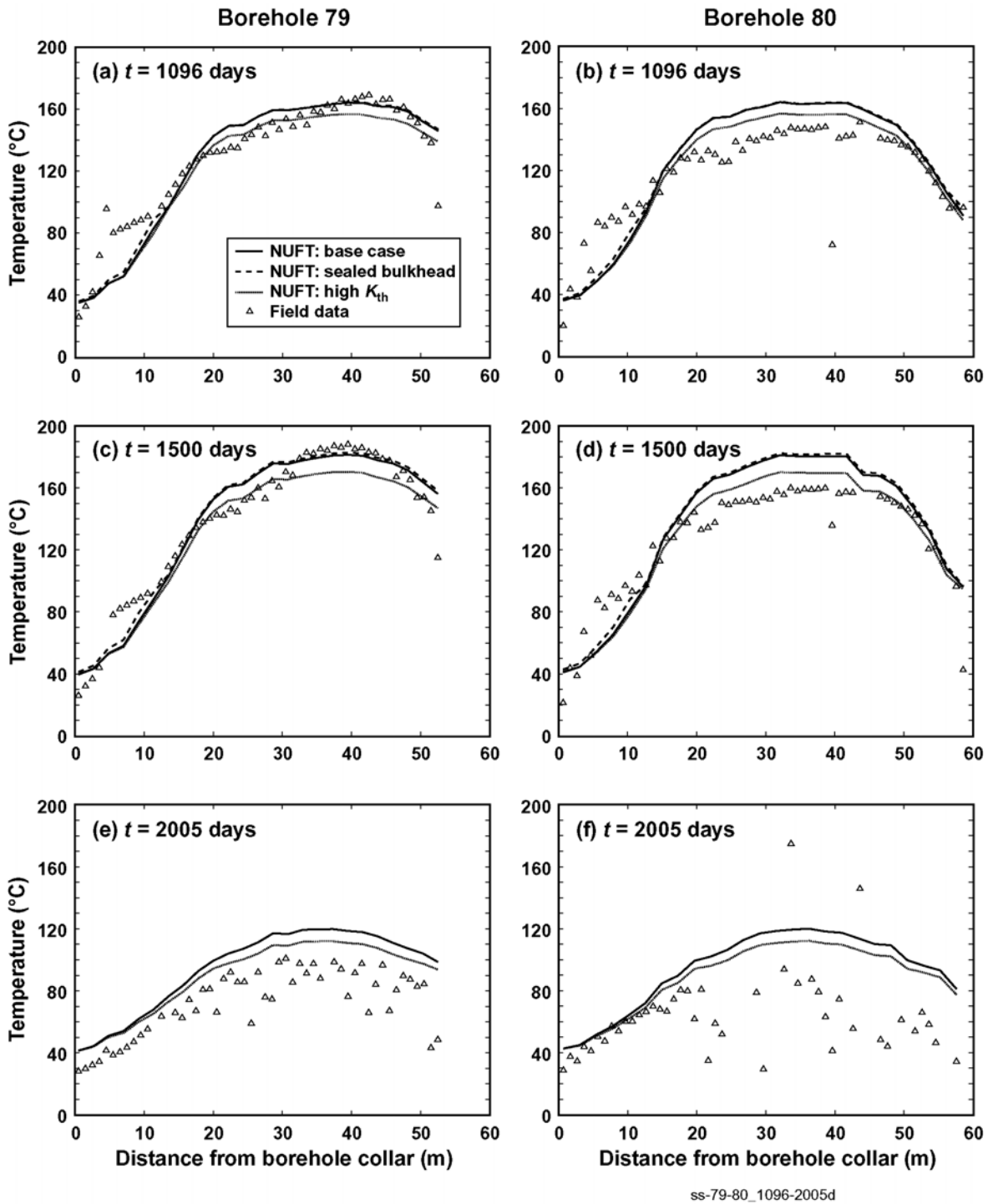
Source: See Table XIII-1.

NOTE: The NUFT simulations are for the three indicated cases. The base case represents gas leakage through the bulkhead, while the sealed-bulkhead case does not allow gas leakage through the bulkhead. The high-K_{th} case is the same as the base case except with the host-rock thermal conductivity K_{th} being one standard deviation higher than the mean. Note that the heaters are turned off at 1,503 days.

Figure 7.4-12. NUFT-Simulated and Measured Temperatures Compared along Borehole 79 (a, c, e) and Borehole 80 (b, d, f) at 1,096, 1,500, and 2,005 Days
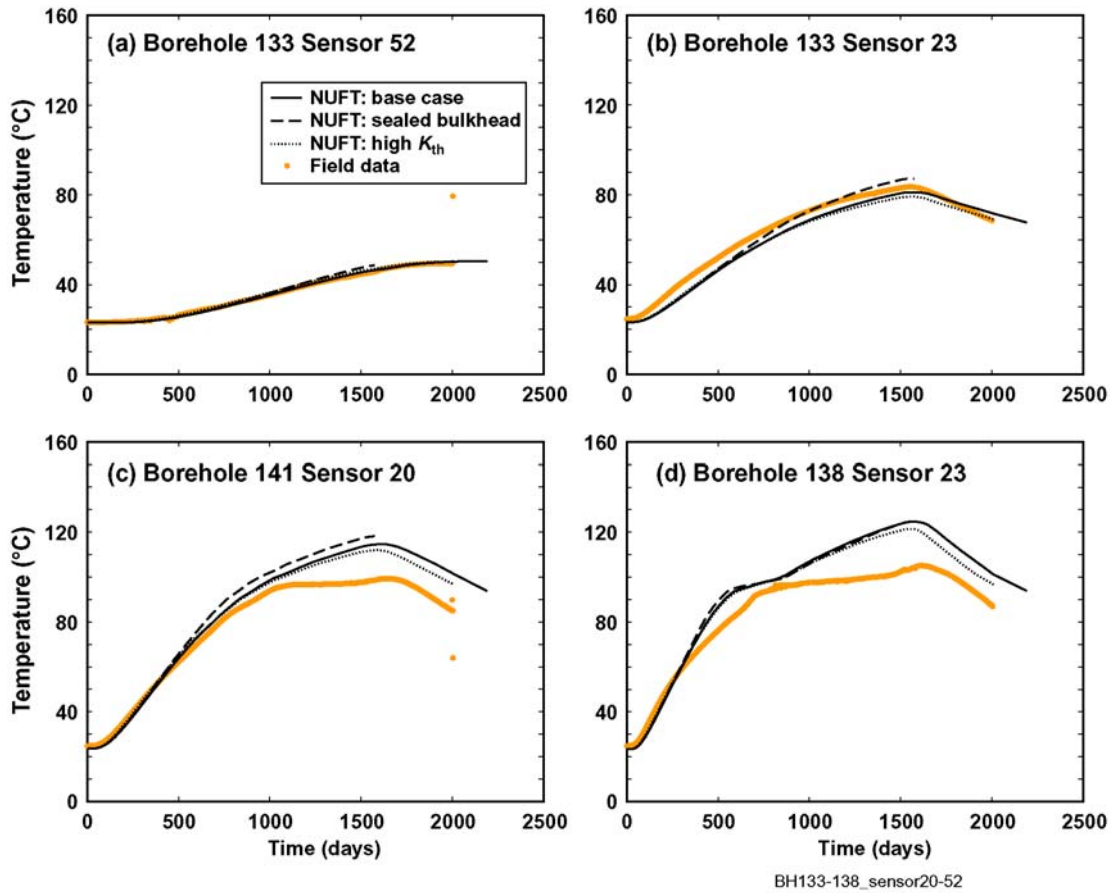
BH133-138_sensor20-52

Source: See Table XIII-1.

NOTE: The NUFT simulations are for the three indicated cases. The base case represents gas leakage through the bulkhead, while the sealed-bulkhead case does not allow gas leakage through the bulkhead. The high-K_{th} case is the same as the base case except with the host-rock thermal conductivity K_{th} being one standard deviation higher than the mean. Note that the heaters are turned off at 1,503 days.

Figure 7.4-13. NUFT-Simulated and Measured Temperature Histories Compared at Borehole 133: Sensor 52 (a) and Sensor 23 (b), Borehole 141: Sensor 20 (c), and Borehole 138: Sensor 23 (d)
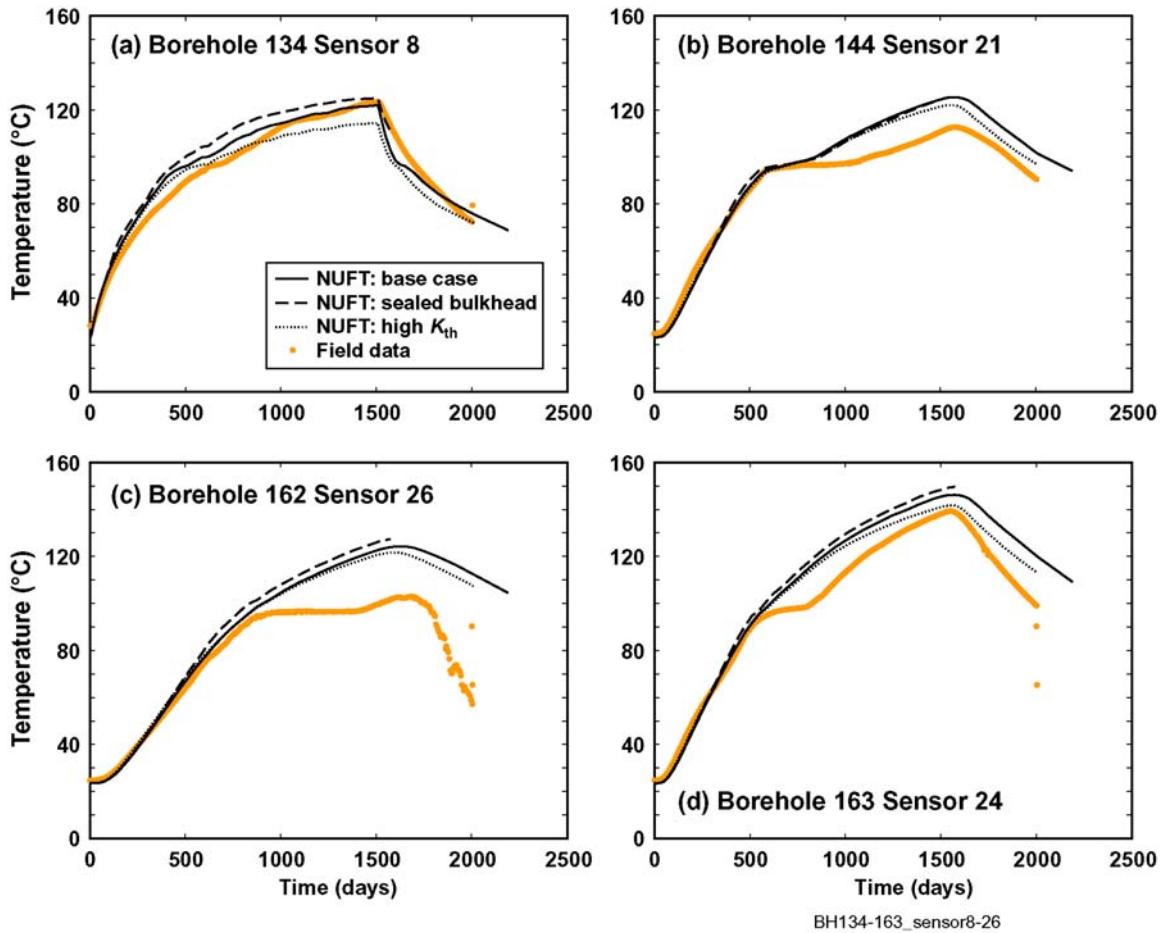
Source: See Table XIII-1.

NOTE: The NUFT simulations are for the three indicated cases. The base case represents gas leakage through the bulkhead, while the sealed-bulkhead case does not allow gas leakage through the bulkhead. The high-K_{th} case is the same as the base case except with the host-rock thermal conductivity K_{th} being one standard deviation higher than the mean. Note that the heaters are turned off at 1,503 days.

Figure 7.4-14. NUFT-Simulated and Measured Temperature Histories Compared at Borehole 134: Sensor 8 (a), Borehole 144: Sensor 21 (b), Borehole 162: Sensor 26 (c), and Borehole 163: Sensor 24 (d)
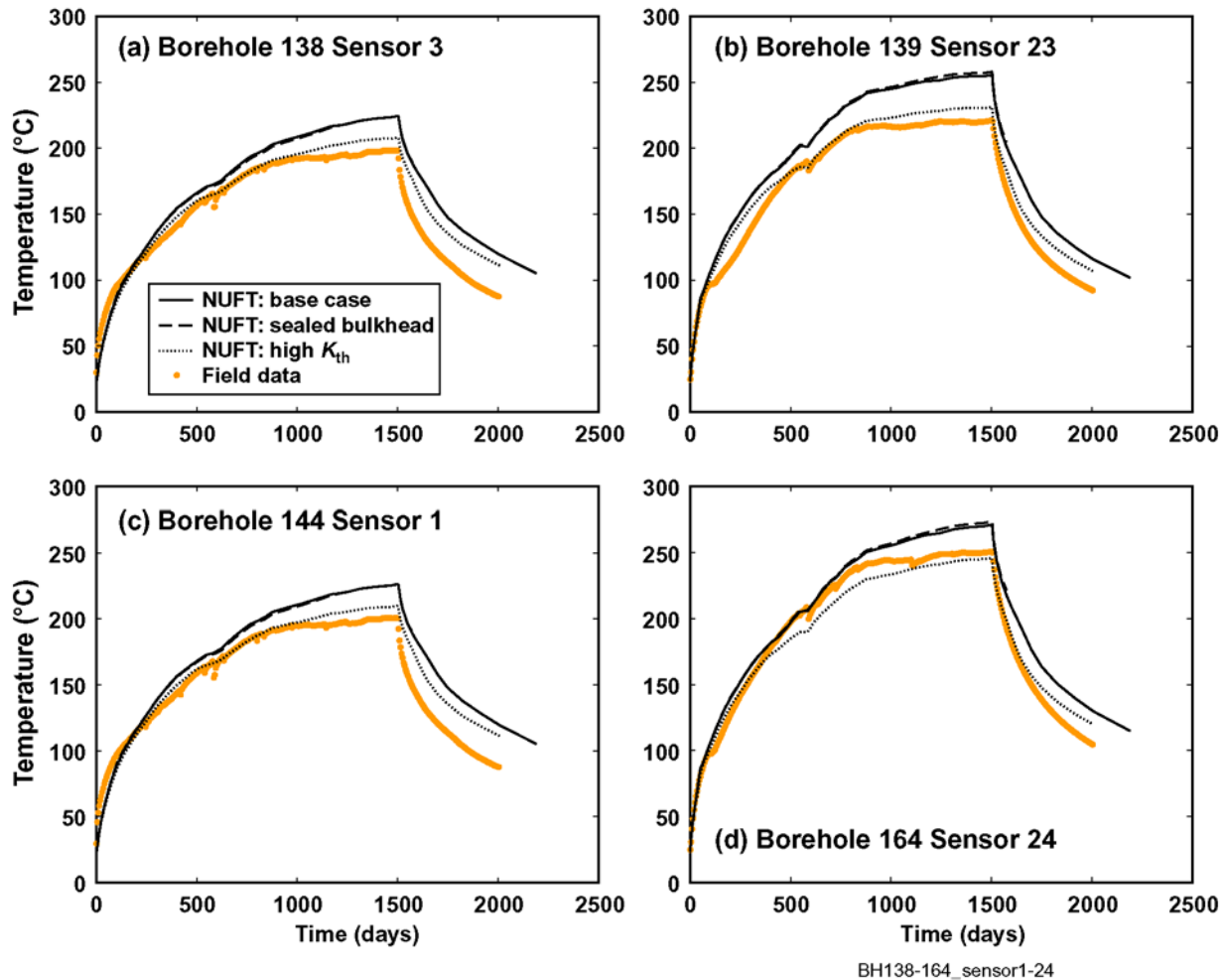
Source: See Table XIII-1.

NOTE: The NUFT simulations are for the three indicated cases. The base case represents gas leakage through the bulkhead, while the sealed-bulkhead case does not allow gas leakage through the bulkhead. The high-K_{th} case is the same as the base case except with the host-rock thermal conductivity K_{th} being one standard deviation higher than the mean. Note that the heaters are turned off at 1,503 days.

Figure 7.4-15. NUFT-Simulated and Measured Temperature Histories Compared at Borehole 138: Sensor 3 (a), Borehole 139: Sensor 23 (b), Borehole 144: Sensor 1 (c), and Borehole 164: Sensor 24 (d)

7.4.4 Comparison of Simulated and Field-Measured Liquid-Phase Saturations in the Matrix

The source DTNs for all field measurements of liquid-phase saturations in the DST are listed in Table 4.4-2. Note that all of the liquid-phase saturations discussed in this section apply to the matrix, rather than to the fractures; thus, they are called matrix liquid-phase saturations. Figure 7.4-16 shows the matrix liquid-phase saturation contours near the end of the heating phase (1,500 days) in plan view through a plane at the elevation of the wing-heater array and for a vertical cross-section midway along the length of the Heated Drift. Note that the heaters are turned off at 1,503 days. The maximum spatial extent of rock dryout occurs at the end of the heating phase. The dryout zones have coalesced between the wing-heater arrays and the Heated

Drift. Also, rock dryout is vertically symmetrical about the heater horizon, indicating that condensate shedding is occurring efficiently around the edges of the boiling/rock-dryout zone.
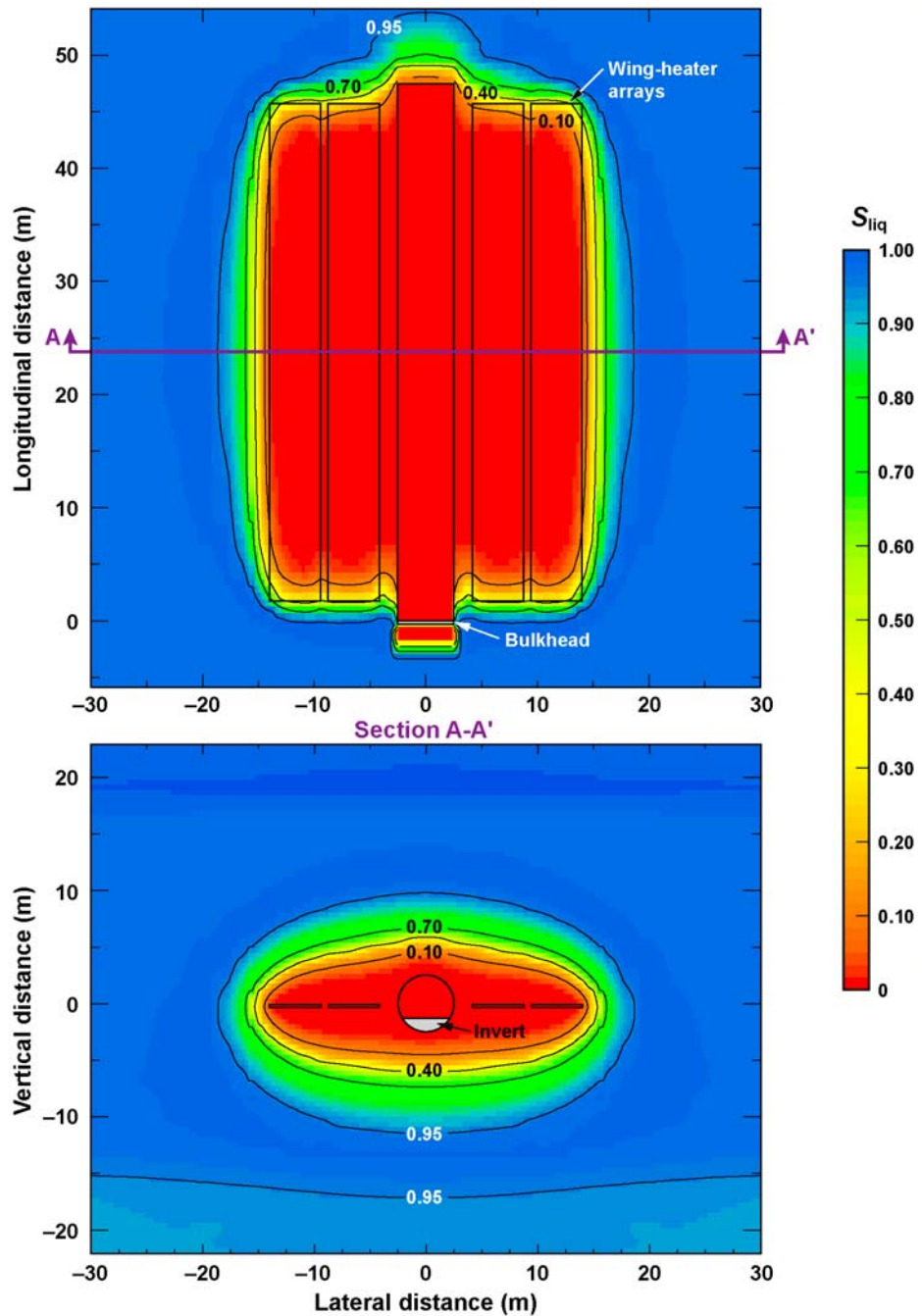
Source: See Table XIII-1.

NOTE: Heaters are turned off at 1,503 days, ending the heating phase.

Figure 7.4-16   Contours of Liquid-Phase Saturation (for the Base Case) in the Matrix at the End of the Heating Phase, Plotted in (a) Plan View Through a Horizontal Plane at the Elevation of the Wing-Heater Array and (b) for a Vertical Cross-Section Midway along the Heated Drift (y = 22.9 m)

Figures 7.4-17 through 7.4-19 compare NUFT-simulated and measured matrix liquid-phase saturation profiles along the Neutron Probe boreholes. Boreholes 79 and 80 are described in Table 7.4-1, while Borehole 68 is an inclined borehole passing below the Heated Drift, as is shown in Figure 7.2.2-3 of *Drift-Scale Coupled Processes (DST and TH Seepage) Models* (BSC 2004 [DIRS 170338]). All of the comparisons of matrix liquid-phase saturation profiles clearly indicate that the NUFT-simulated rock dryout lags far behind the dryout measured in the field. Figure 7.4-20 shows the NUFT-simulated time histories of temperature, liquid-phase saturation, and gas-phase pressure in the matrix at two locations: 20 and 27 m from the collar in Borehole 68. An inspection of Table 7.4-3, which summarizes NUFT-simulated temperature, liquid-phase saturation, and gas-phase pressure in the matrix at those locations, indicates that high gas-phase pressure is throttling vaporization and delaying rock dryout (indicated by the NUFT-simulated matrix liquid-phase saturation) compared to the observed dryout rate in the DST (indicated by field measurements of matrix liquid-phase saturation). The implication is that the use of a larger value of matrix permeability in the NUFT thermal-hydrologic model would result in less of a delay in NUFT-simulated rock dryout compared to the observed dryout rate in the DST. This conclusion is supported by the comparison of NUFT-simulated and observed rock dryout for the Large Block Test (Figure 7.3-2), which showed that the use of a larger value of matrix permeability resulted in a larger dryout zone. As discussed earlier, this is also consistent with the discussion in Section 7.4.4 of *Drift-Scale Coupled Processes (DST and TH Seepage) Models* (BSC 2004 [DIRS 170338]).

Table 7.4-3. NUFT-Simulated (Base-Case) Temperature, Liquid-Phase Saturation, and Gas-Phase Pressure in the Matrix Summarized at 20 and 27 m from the Collar of Borehole 68.

Distance (m) From Collar of Borehole 68	Time (days)	Temperature (°C)	Liquid-Phase Saturation	Gas-Phase Pressure in Matrix (atm)	Saturation Temperature from Steam Tables (°C)
20	877	128.7	0.806	2.600	128.7
20	1,242	143.9	0.684	4.032	143.9
20	1,500	150.9	0.560	4.864	150.9
20	1,917	118.2	0.376	1.946	118.2
27	877	121.8	0.847	2.100	121.8
27	1,242	139.7	0.721	3.582	139.7
27	1,500	147.8	0.632	4.476	147.8
27	1,917	128.0	0.462	2.562	128.0

NOTE: These values are based on data plotted in Figure 6.3-20.

The underlying cause for the NUFT-simulated dryout behavior lagging behind the dryout behavior observed in the DST is the low value of matrix permeability in the Tptpmn (tsw34) in the modified-mean infiltration-flux hydrologic property set, which results in a large gas-phase pressure buildup in the matrix. This gas-phase pressure buildup throttles (i.e., restricts) the rate of vaporization and delays dryout of the host rock in the DST. Eventually, the spatial extent of the NUFT-simulated dryout zones approaches that of the measured dryout zones. The cause of the throttled dryout is consistent with the discussion in Section 7.4.4.2 of *Drift-Scale Coupled Processes (DST and TH Seepage) Models* (BSC 2004 [DIRS 170338]). The influence of matrix permeability on dryout is evident by comparing Figure 7.4.4.2-1a (which used the calibrated hydrologic property set, which is the same as the modified-mean infiltration-flux hydrologic property set in the Tptpmn, Tptpll, and Tptpln units) with Figure 7.4.4.2-1b (which used the site-specific property set), both of which are from BSC (2004 [DIRS 170338]). The site-specific

property set, which has a larger value of matrix permeability, results in a larger simulated rock dryout zone than that simulated with a smaller value of matrix permeability (Figures 7.4.4.2-1a and 7.4.4.2-1b from BSC 2004 [DIRS 170338]).

A comparison of the measured matrix liquid-phase saturation profiles at 1,510 days (approximately when heating ceased) and 1,917 days shows that the dryout zone continues to expand during the cooldown phase. Thus, the DST measurements indicate that no rewetting has commenced prior to 1,917 days. Similarly, the NUFT-simulated matrix liquid-phase saturations continue to decrease during the cooldown phase. Thus, the NUFT thermal-hydrologic model agrees with the field measurements of rewetting behavior in the DST.

The lag in simulated dryout for the DST is a transient effect. As noted earlier, heating conditions for the DST result in an accelerated temperature rise and rock dryout, compared to those predicted for repository heating conditions. Although the comparison of NUFT-simulated dryout with the DST-observed dryout shows that NUFT-simulated dryout lags behind the DST-observed dryout, this is not important to the application of the MSTHM for post-closure repository predictions. This is because rock dryout predicted for repository heating conditions is much slower, occurring over much longer time frames than occurred during the DST. Within four years, the DST-observed rock dryout approaches the NUFT-simulated dryout. Under repository heating conditions, predicted rock dryout occurs over a much longer timeframe (hundreds to thousands of years as shown in Figure 6.3-22c) than was applicable to the DST. This conclusion is consistent with the discussion in Section 7.4.4.2 of *Drift-Scale Coupled Processes (DST and TH Seepage) Models* (BSC 2004 [DIRS 170338]). Summarizing, compared to the typical duration of rock dryout predicted for repository heating conditions, the duration of the DST-observed lag in rock dryout is insignificant.
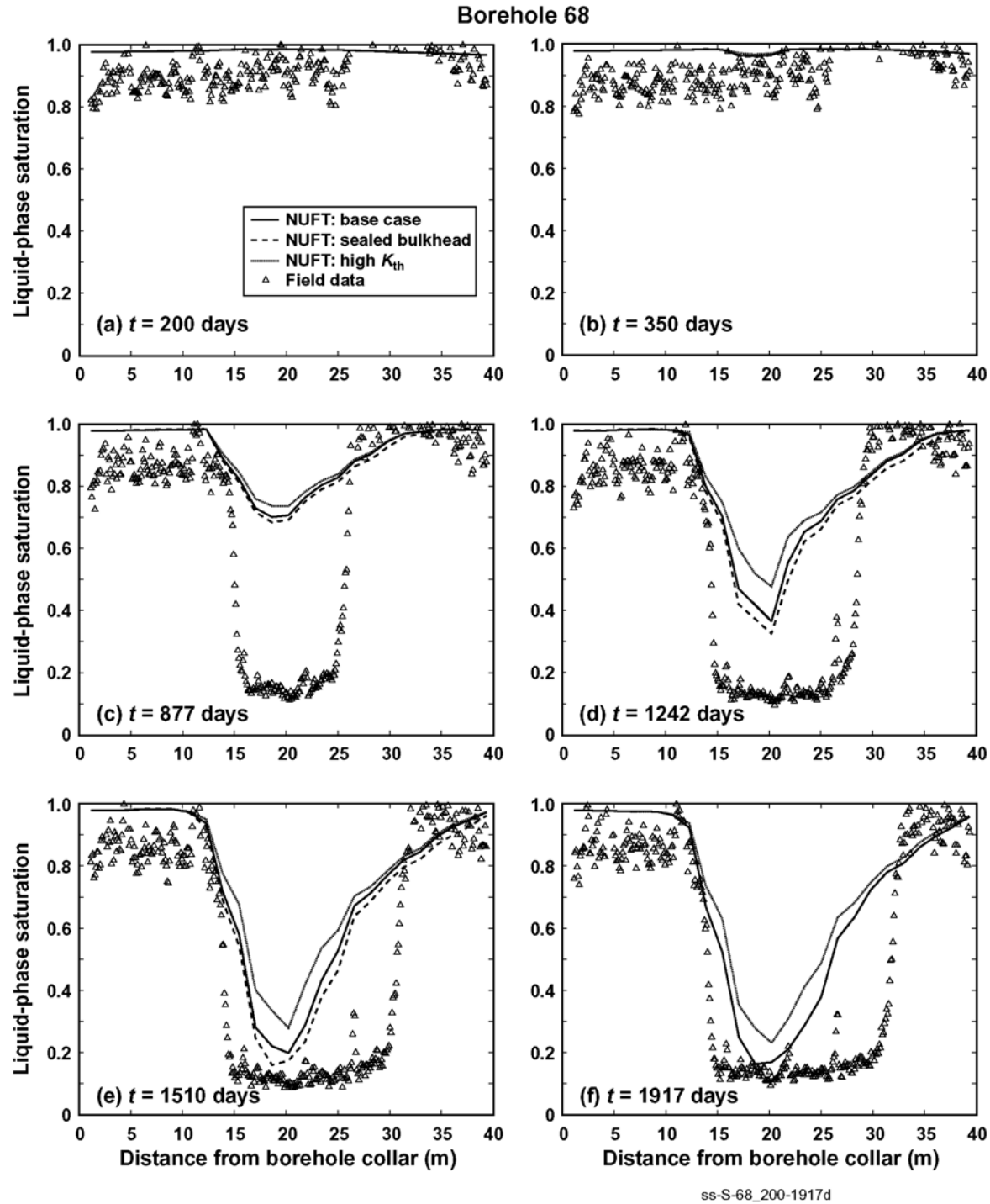
Source: See Table XIII-1.

NOTE: The NUFT simulations are for the three indicated cases. The base case represents gas leakage through the bulkhead, while the sealed-bulkhead case does not allow gas leakage through the bulkhead. The high-K_{th} case is the same as the base case except with the host-rock thermal conductivity K_{th} being one standard deviation higher than the mean. Note that the heaters are turned off at 1,503 days.

Figure 7.4-17. NUFT-Simulated and Measured Liquid-Phase Saturations in the Matrix Compared along Borehole 68 at (a) 200 Days, (b) 350 Days, (c) 877 Days, (d) 1,242 Days, (e) 1,510 Days, and (f) 1,917 Days
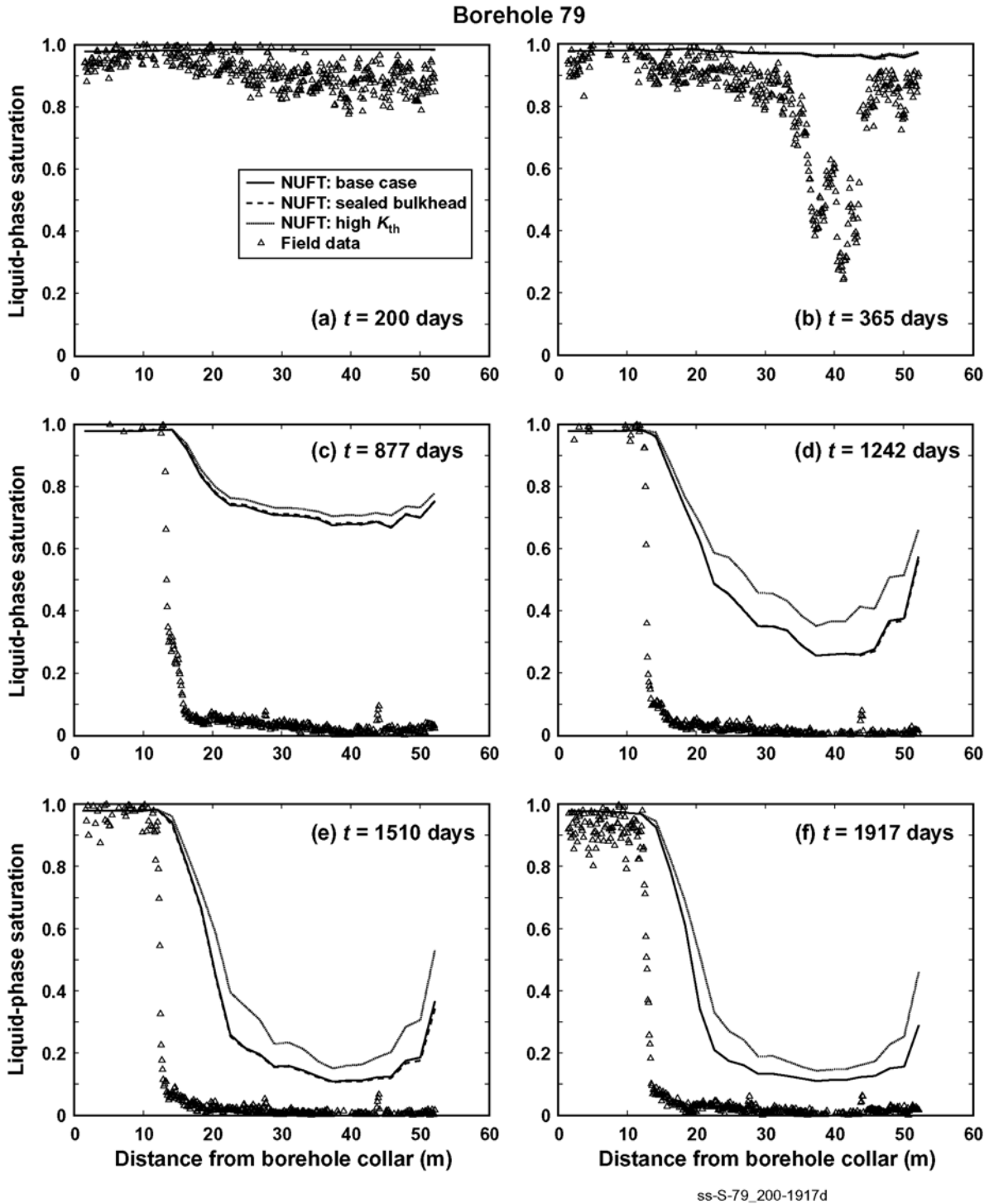
Source: See Table XIII-1.

NOTE: The NUFT simulations are for the three indicated cases. The base case represents gas leakage through the bulkhead, while the sealed-bulkhead case does not allow gas leakage through the bulkhead. The high-K_{th} case is the same as the base case except with the host-rock thermal conductivity K_{th} being one standard deviation higher than the mean. Note that the heaters are turned off at 1,503 days.

Figure 7.4-18. NUFT-Simulated and Measured Liquid-Phase Saturations in the Matrix Compared along Borehole 79 at (a) 200 Days, (b) 365 Days, (c) 877 Days, (d) 1,242 Days, (e) 1,510 Days, and (f) 1,917 Days
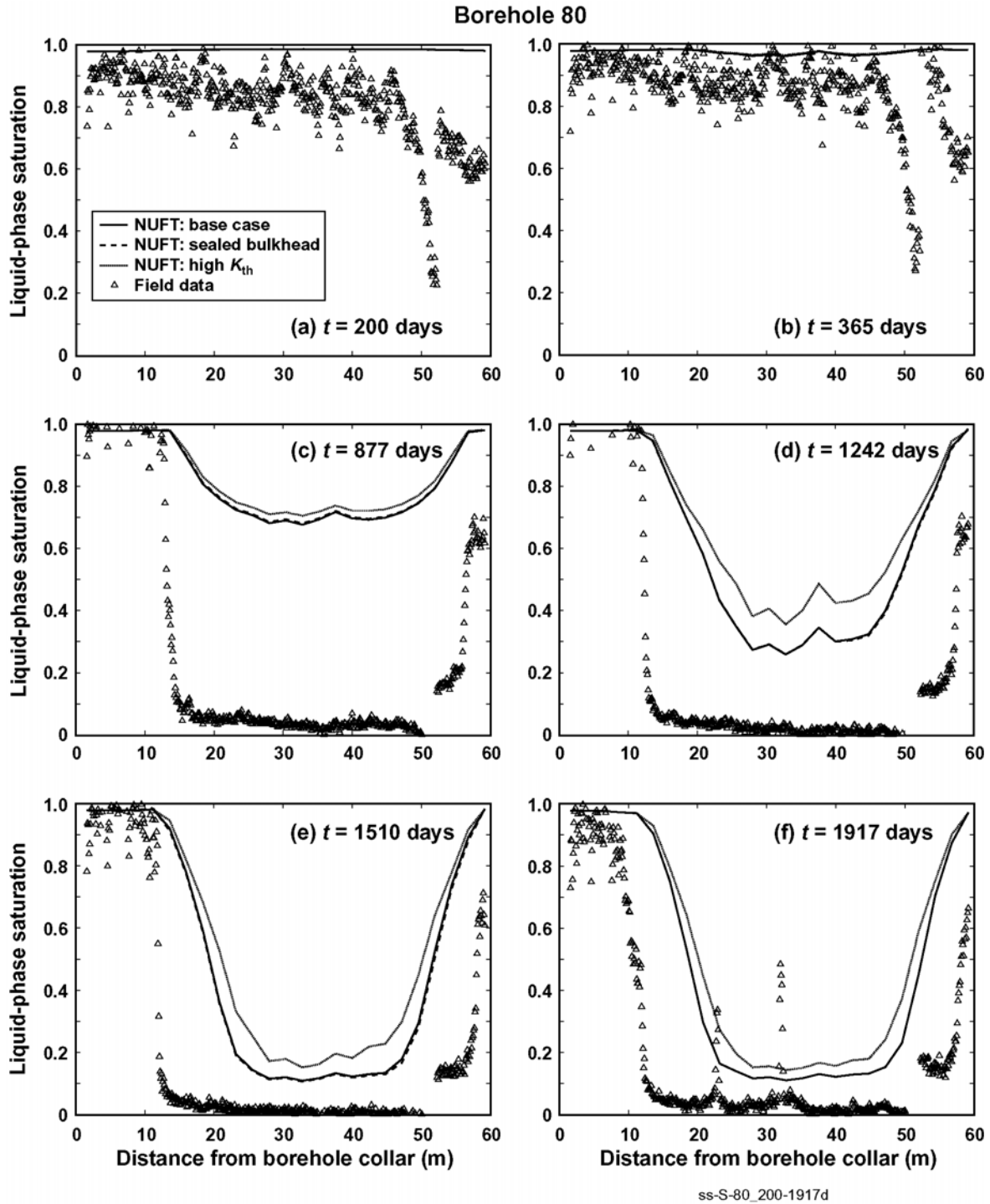
Source: See Table XIII-1.

NOTE: The NUFT simulations are for the three indicated cases. The base case represents gas leakage through the bulkhead, while the sealed-bulkhead case does not allow gas leakage through the bulkhead. The high-K_{th} case is the same as the base case except with the host-rock thermal conductivity K_{th} being one standard deviation higher than the mean. Note that the heaters are turned off at 1,503 days.

Figure 7.4-19. NUFT-Simulated and Measured Liquid-Phase Saturations in the Matrix Compared along Borehole 80 at (a) 200 Days, (b) 365 Days, (c) 877 Days, (d) 1,242 Days, (e) 1,510 Days, and (f) 1,917 Days
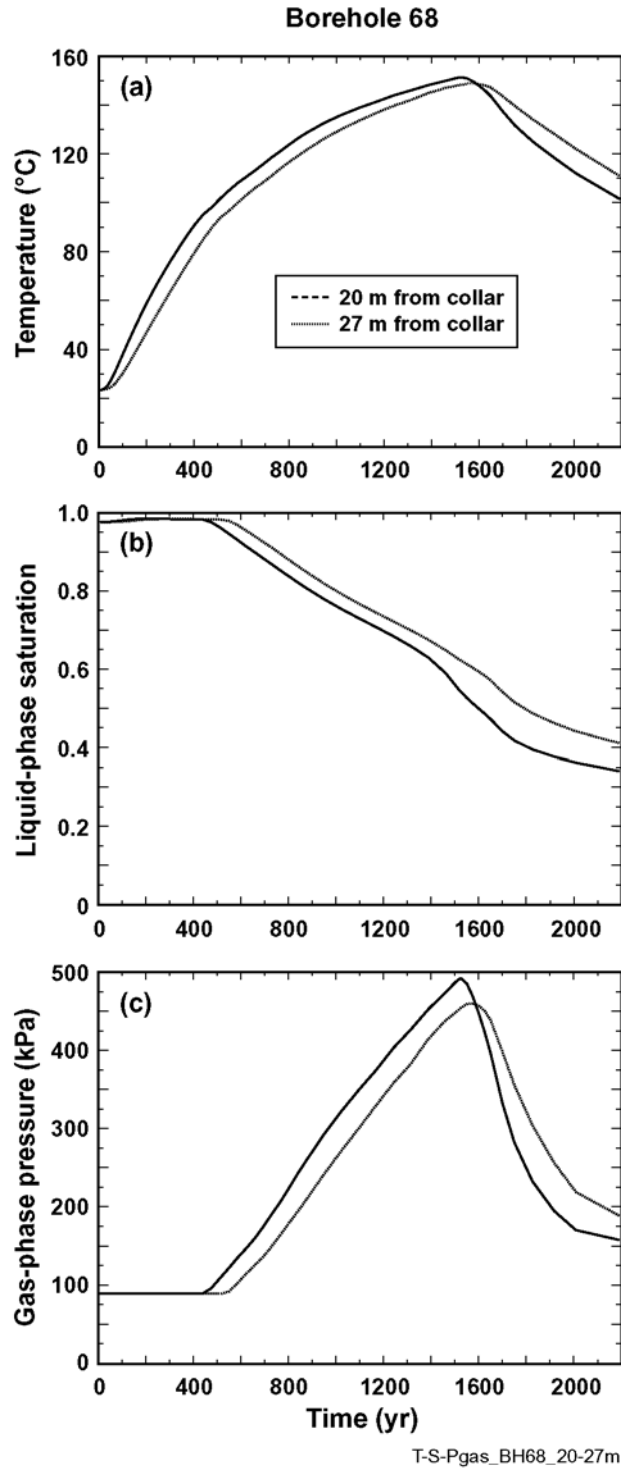
Source: See Table XIII-1.

Figure 7.4-20. NUFT-Simulated Time Histories of (a) Temperature, (b) Liquid-Phase Saturation, and (c) Gas-Phase Pressure in the Matrix, Plotted at Distances of 20 m and 27 m from the Collar of Borehole 68.

7.4.5 Summary of Model Validation Using DST Data

The underlying cause for the absence of a NUFT-simulated temperature plateau (at 96°C) is the low value of matrix permeability in the Tptpmn (tsw34) in the modified-mean infiltration-flux hydrologic property set, which results in a large gas-phase pressure buildup in the matrix, causing an increase in the saturation (boiling) temperature. The absence of a temperature plateau at 96°C causes the NUFT-simulated temperatures to be generally higher than field-measured temperatures for temperatures exceeding 96°C. These observations are consistent with the discussion in Sections 7.4.3 and 7.4.4 of *Drift-Scale Coupled Processes (DST and TH Seepage) Models* (BSC 2004 [DIRS 170338]).

Another reason for NUFT-simulated temperatures being higher than measured temperatures is the uncertainty in host-rock thermal conductivity K_{th} in the DST area. For the high-K_{th} case (one standard deviation above the mean), NUFT-simulated temperatures were in better agreement with measured temperatures than the cases that used the mean K_{th} values. Because percolation fluxes cannot be directly measured, uncertainty in local percolation flux in the DST area also contributes to differences between NUFT-simulated and measured temperatures. Section 6.3.4 discusses the influence of key parametric uncertainties on predicted thermal-hydrologic conditions in the repository. As indicated by the temperature ranges plotted in Figures 7.5-9 and 7.5-12, the combined influence of host-rock percolation-flux and thermal conductivity uncertainties results in peak drift-wall temperatures varying by 35 to 43°C. Note that the 30-percent validation criterion for temperature rise (above ambient), which is given in the TWP, is consistent with the magnitude of the influence of the parametric uncertainty of host-rock thermal conductivity and percolation flux on temperature. As indicated by comparing the lower bound-infiltration-flux low K_{th} case with the upper-bound infiltration-flux high K_{th} case in Table 6.3-38, the combined influence of host-rock thermal conductivity uncertainty and percolation-flux uncertainty causes the rise in peak drift-wall temperature (above ambient) to vary by about 30 percent.

For temperatures less than about 80°C, NUFT-simulated and measured temperatures are in good agreement (and the temperature rise is within 30 percent as required by the TWP) for all three cases: (1) base case, (2) sealed bulkhead, and (3) high K_{th}. Overall, the comparison of NUFT-simulated and measured temperatures demonstrate that the NUFT thermal-hydrologic model provides a valid representation of heat flow in the DST. These observations are consistent with the discussion in Sections 7.4.3 and 7.4.4 of *Drift-Scale Coupled Processes (DST and TH Seepage) Models* (BSC 2004 [DIRS 170338]).

The underlying cause for the NUFT-simulated throttled (i.e., restricted) vaporization and delayed dryout (compared to dryout observed in the DST) is the large gas-phase pressure buildup in the matrix, which is caused by the low matrix permeability in the Tptpmn (tsw34) in the calibrated hydrologic property set. Thus, the cause of the difference between the NUFT-simulated and observed rock-dryout rate is well understood. Eventually, the spatial extent of the NUFT-simulated dryout zone approaches that of the dryout zone observed in the DST. Therefore, the ultimate spatial extent of rock dryout simulated by the NUFT thermal-hydrologic model agrees with that measured in the DST. From this it is concluded that the NUFT thermal-hydrologic model provides a valid representation of rock dryout in the DST. This conclusion is consistent with the discussion in Sections 7.4.3 and 7.4.4 of *Drift-Scale Coupled Processes (DST and TH Seepage) Models* (BSC 2004 [DIRS 170338]). To the extent that the

observations of cooldown in the DST presently allow, the NUFT thermal-hydrologic model provides a valid representation of rewetting behavior in the DST.

With a few exceptions, the differences between the NUFT-simulated and measured temperature changes from ambient temperatures are less than 30 percent. The exceptions are related to the above-mentioned large gas-phase pressure buildup that temporarily throttles (i.e., restricts) vaporization and rock dryout. It is important to note that this effect is transient that dissipates as the NUFT-simulated gas-phase pressure buildup declines. With the decline of the NUFT-simulated gas-phase pressure buildup, agreement between the NUFT-simulated and measured temperatures improves, and the differences between the NUFT-simulated and measured temperature changes from ambient temperatures are less than 30 percent. The NUFT-simulated rock dryout behavior (as measured by liquid-phase saturation in the matrix continuum versus time) agrees qualitatively with the measured dryout behavior. For the ultimate spatial extent of rock dryout, there is very good agreement between the NUFT-simulated and measured dryout. Overall, the comparisons of NUFT-simulated and measured temperatures and matrix liquid-phase saturations demonstrate that the NUFT thermal-hydrologic model provides a valid representation of heat flow, as well as dryout and rewetting of the host rock in the DST. These conclusions are consistent with the discussion in Sections 7.4.3 and 7.4.4 of *Drift-Scale Coupled Processes (DST and TH Seepage) Models* (BSC 2004 [DIRS 170338]).

Another conclusion from the DST model validation study is that the sealed-bulkhead case results in slightly higher NUFT-simulated temperatures than the base case (which had a leaky bulkhead). The influence of the leaky bulkhead on simulated temperatures is much less than that resulting from a one standard-deviation range in thermal conductivity. This conclusion is useful with respect to the potential significance of whether the ends of the emplacement drifts are sealed with bulkheads or simply backfilled with highly permeable crushed tuff. The conclusion of the insensitivity of the DST thermal-hydrologic simulations to the treatment of the bulkhead (leaky versus sealed) suggests that the MSTHM representation of thermal-hydrologic behavior in the emplacement drifts will not be significantly affected by whether the ends of the emplacement drifts are sealed.

7.5   COMPARISON OF THE MSTHM RESULTS AGAINST A MONOLITHIC THREE-DIMENSIONAL THERMAL-HYDROLOGIC MODEL

This model validation test case is similar to that conducted by Buscheck et al. (2003 [DIRS 164638]). Using a scaled-down three-drift repository as a model validation test case, the MSTHM is applied along with a corresponding monolithic three-dimensional thermal-hydrologic model for calculating drift-scale thermal-hydrologic conditions. The monolithic thermal-hydrologic model, which is called a Discrete-/Line-Averaged-Heat-Source Mountain-Scale Thermal-Hydrologic (D/LMTH) model (Table 1-2), uses a nested mesh to represent detailed thermal-hydrologic behavior in the vicinity of the emplacement drifts as well as mountain-scale thermal-hydrologic behavior. Both the MSTHM and the corresponding monolithic three-dimensional thermal-hydrologic model discretely represent eight individual waste packages down to the surface of the drip shield. Results from these two models are compared at the drift wall, drip shield, and invert. This comparison is the basis for the validation of the MSTHM methodology.

The model validation criterion applicable to Section 7.5 is specified in the governing TWP (BSC 2005 [DIRS 173377], Section 2.3.4). The model validation criterion compares the magnitude of the MSTHM-to-D/LMTH-model differences of a particular output parameter (e.g., temperature or relative humidity) to the range in that parameter arising from parametric uncertainty (of percolation flux and host-rock thermal conductivity). Therefore, the model-validation criterion in the governing TWP is based on a comparison of the influence of conceptual-model uncertainty with that of parametric uncertainty.

As is shown in Table 1-1, this section (Section 7.5) provides direct validation for predicting a reasonable range of the three key MSTHM output parameters (temperature, relative humidity, and liquid-phase saturation) used in TSPA-LA. These MSTHM output parameters were chosen because they provide sufficient coverage for demonstrating that the MSTHM provides a valid representation of thermal-hydrologic processes in the porous portion of the system, which includes the host rock and invert. Section 7.6 of this report is complementary to Section 7.5 in that it demonstrates that the MSTHM provides a valid representation of heat-transfer within the emplacement drifts. As discussed in Sections 7.6 and 7.7, a reasonable representation of temperature and relative humidity on the waste package (or drip shield) depends on two things: (1) a reasonable representation of temperature and relative humidity at the drift wall and (2) a reasonable representation of the temperature difference between the waste package (or drip shield) and the drift wall.

This section also supports model confidence building for liquid-phase flux in the invert, which is also used in TSPA-LA. Note that for TSPA-LA, the MSTHM-predicted invert liquid-phase flux is only applied to waste packages that experience no seepage and no condensation. This section also supports model confidence building for MSTHM output parameters that are not used in TPSA-LA, such as gas-phase air-mass fraction, capillary pressure, and evaporation rate.

7.5.1 Description of the MSTHM Validation Test Case

The test case used to validate the MSTHM approach represents a scaled-down repository, consisting of three 243-m long drifts (Figure 7.5-1 and Table 7.5-1). The total heat output from these three drifts is 986.6 kW, representing approximately 143 average waste packages (Buscheck et al. 2003 [DIRS 164638]). This heat output is modeled in the three drifts as a line-averaged heat source everywhere except at the center of Drift #2 where 15 discrete waste packages are modeled: 7 at the center of Drift #2 and 4 at either end of Drift #2. Because the test case is symmetric, the 15 discrete waste packages can be modeled as the 7.5 discrete waste packages described in Table 7.5-2. The thermal-operating parameters of the three-drift repository test case are equivalent to those being considered for the TSPA-LA except for the total inventory of waste packages. The waste packages are spaced end to end along the drift with a gap of 10.6 cm, which is similar to 0.1-m end-to-end waste-package spacing that is being considered for the TSPA-LA (Table 4.1-2). Preclosure ventilation of the drifts is assumed to remove 70 percent of the heat generated during the 50-year ventilation period. Note that at the time this validation test case was developed, a heat-removal efficiency of 70 percent was being used in the MSTHM calculations in support of *FY 01 Supplemental Science and Performance Analyses, Volume 1: Scientific Bases and Analyses* (BSC 2001 [DIRS 155950]). The initial heat output is 986.6 kW for the entire three-drift system, which is equivalent to about 1.18 percent of the 63,000-MTU thermal load (83,346 kW) for the repository (Canori and Leitner 2003 [DIRS 166275], p. 3-95). Note that the total repository thermal load is obtained by multiplying

the initial linear power density of 1.45 kW/m (Table 4.1-1) by 57,480 m of heated emplacement drift (Table 6.2-1). Four different types of waste packages are represented in the test case and are described in Table 7.5-2.

Table 7.5-1. Design and Operating Parameters Used in MSTHM Validation Test Case

Parameter	Parameter Value
Drift spacing	81 m
Drift length	243 m
Drift diameter	5.5 m
Drip-shield diameter	2.512 m
Areal Mass Loading (AML)	54.5 MTU/acre[a]
Heated repository footprint	59,049 m^2
Lineal Power Density	1.3534 kW/m
Total heat output	986.6 kW
Approximate number of waste packages represented in entire three-drift model	143
Heat removal by ventilation	70% for 50 years
Waste package configuration and spacing	Line load with 10.6-cm end-to-end waste-package spacing

Source: Buscheck et al. 2003 [DIRS 164638], Table 4.

[a] Note that this value is rounded to 55 MTU/acre elsewhere in Section 7.5.

Table 7.5-2. Waste Package Types Used in the MSTHM Validation Test Case

Waste Package Type	Waste Package Description	Number of Waste Packages[a]	Length (m)	Initial Heat Output (kW)
PWR1	Average 21-PWR CSNF	1.5	5.17	11.53
DHLW	Long DHLW	2	5.22	0.282
PWR2	Design-Basis 21-PWR CSNF	2	5.17	11.80
BWR	Average 44-BWR CSNF	2	5.17	7.377

Source: Buscheck et al. 2003 [DIRS 164638].

[a] The number of discrete waste packages in the quarter-symmetry element test case (Figure 7.5-1).
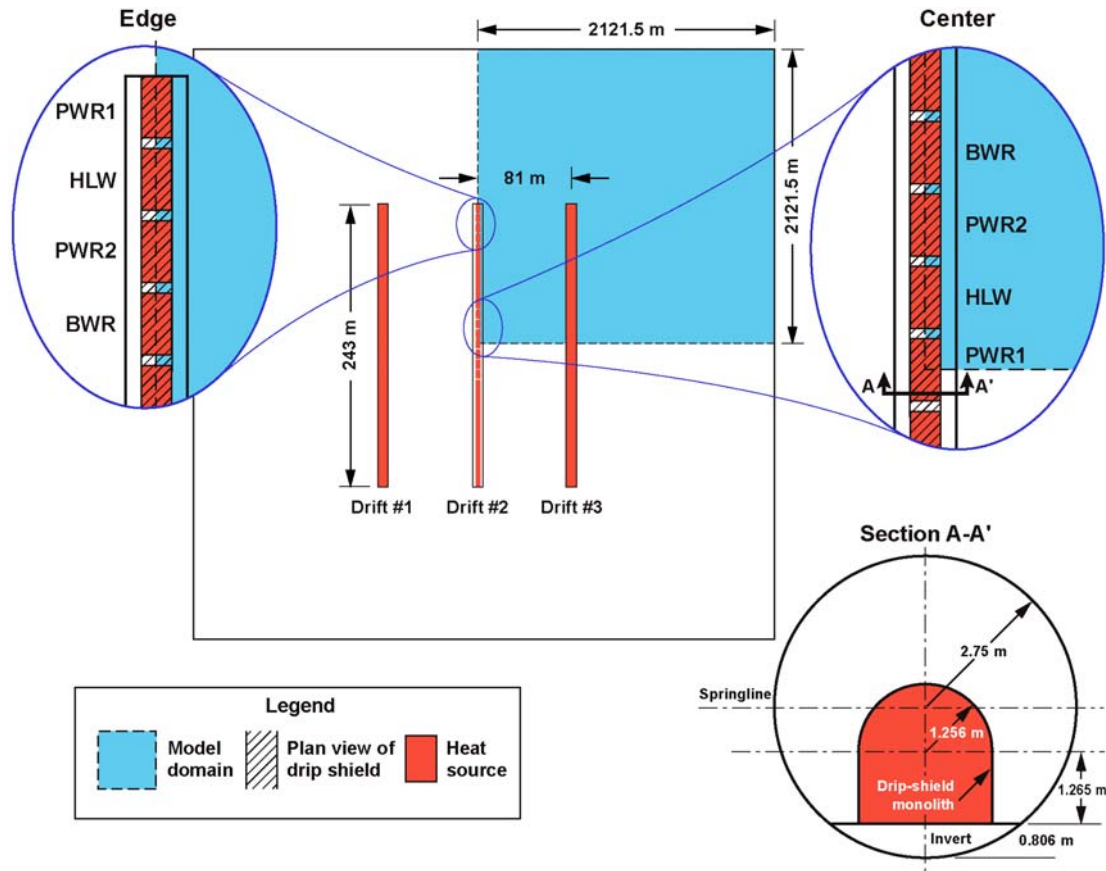
NOTE: To the upper left is the plan view of the three-drift repository test case; highlighted in blue is the zone of symmetry. To the upper right is a close-up of the Drift #2 waste package sequencing. To the bottom right is the vertical cross-section of the modeled drift with the drip shield and waste package lumped together as a heat source.

Figure 7.5-1. Drift-Scale Conceptual Schematic Shown for the Model Validation Test Case

The validation test case focuses on two locations: at the center and edge of the repository. At the center of the repository, four waste package types are discretely represented (Figure 7.5-1) in Drift #2, which is the central drift. At the edge of the repository, the same four waste package types are discretely represented; these four waste packages are also in Drift #2. In this test case, the waste packages are not represented distinctly from the drip shield. Instead, the waste package and drip shield are lumped together and treated as a monolithic heat source. Moreover, the validation of heat-transfer between the waste-package, drip-shield and drift-wall surfaces is validated in Section 7.6 of this report. The remainder of Drift #2, beyond the discretely represented waste package locations, has a line-averaged heat source within the drip-shield/waste package monolith (Figure 7.5-1). For Drifts #1 and #3, the heat-source representation is a line-averaged heat source distributed over the entire 5.5-m diameter cross section of the drift. Within Drift #2, thermal radiation and natural convection are approximated with a time-dependent effective thermal conductivity for the drift cavity between the drip shield and the drift wall (CRWMS M&O 2001 [DIRS 153410]). Note that this approximation is different from that being used in the MSTHM calculations in support of the TSPA-LA (Section 6.3). However, for the purpose of the MSTHM validation problem it is only necessary that the MSTHM and the corresponding D/LMTH model both use the same approximation for thermal radiation and convection in the drift. Permeability in the drift cavity of Drift #2 (which is the central drift in

Figure 7.5-1) is 1.0×10^{-8} m^2 in all three principal directions. Because advective and diffusive transport of gas can occur in the longitudinal direction along the drift axis (also called the axial direction), this model allows the cold-trap effect to occur. This D/LMTH model also allows liquid-phase flow in the invert to occur in the longitudinal direction along the drift axis. Note that in the MSTHM calculations in support of the TSPA-LA (Section 6.3) the permeability in the drift is 1.0×10^{-8} m^2 in the vertical and lateral directions. However, the MSTHM calculations in support of the TSPA-LA assume that gas- and liquid-phase transport in the axial direction along the drift is insignificant (Section 5.7). This assumption is equivalent to assuming that the cold-trap effect is insignificant. A sealed bulkhead is placed at the very end of the heated portion of Drift #2 in the D/LMTH model. However, this sealed bulkhead is not impermeable, because it is assigned the same bulk permeability as that of the adjoining host rock (Section 5.3.1.6).

A second set of D/LMTH model calculations was conducted in which the permeability in the drift cavity and in the invert of Drift #2 is set to zero in the axial direction. Because this D/LMTH model prevents the cold-trap effect from occurring, it corresponds to the assumption in the MSTHM calculations in support of the TSPA-LA. The differences in thermal-hydrologic behavior in the drift between the D/LMTH model, which allows gas-phase and liquid-phase transport in the axial direction along the drift, and the D/LMTH model, which does not allow this axial transport, quantify the relative influence of the cold-trap effect in this three-drift repository test case.

The D/LMTH model assumes the stratigraphy and boundary conditions, including infiltration flux, that pertain to the center of the repository modeled in supplemental analyses (BSC 2001 [DIRS 155950]; BSC 2001 [DIRS 158204]) in the MSTHM. The stratigraphic information and boundary conditions are derived from DTN: LB991201233129.001 [DIRS 146894], while the percolation fluxes for the present-day, monsoonal, and glacial climates are derived from DTN: GS000308311221.005 [DIRS 147613], according to Section 4.1.12 of *Multiscale Thermohydrologic Model* (BSC 2001 [DIRS 158204]). The assumption in this test case is that the conditions at this location apply to the entire model domain, that is, there is no lateral variation of stratigraphy in the test model. At this location, the repository is 372.9 m below the ground surface and 344.7 m above the water table. The host-rock unit at this location is the Tptpll (tsw35) unit. The Tptpll unit, which is the host-rock unit for the majority of the repository area, is modeled with a matrix porosity of 0.131, a matrix permeability of 3.04×10^{-17} m^2, a fracture porosity of 0.018 and a fracture permeability of 2.38×10^{-11} m^2. Thermal parameters for the Tptpll unit are modeled using 900 J/kg°C for specific heat capacity, and 1.84 and 1.25 W/m°C for wet and dry thermal conductivity, respectively. The time-dependent infiltration rates at this location, the "L5C3" location, are 5.7 mm/yr for the present-day climate (0 to 600 years), 15.1 mm/yr for the monsoonal climate (600 to 2,000 years), and 23.2 mm/yr for the glacial-transition climate (beyond 2,000 years) (Flint et al. 2001 [DIRS 156351]; BSC 2001 [DIRS 158204]). Parameter values used here are the same as those used for *FY 01 Supplemental Science and Performance Analyses, Volume 1: Scientific Bases and Analyses* (BSC 2001 [DIRS 155950]).

The numerical mesh in the D/LMTH model includes four nested regions: (1) the very-fine-gridded inner nest surrounding Drift #2 with grid-block dimensions of approximately 0.2 m in the horizontal and the vertical directions; (2) the fine-gridded intermediate mesh, surrounding the inner nest, with grid-block dimensions of approximately 1 m in the horizontal and the vertical directions; (3) the medium-gridded intermediate nest

surrounding the fine-gridded intermediate nest, as well as Drifts #1 and #3, with grid-block dimensions of approximately 5 m in the horizontal and the vertical directions; and (4) the coarse-gridded mountain-scale mesh, surrounding the medium-gridded intermediate nest with grid-block dimensions of approximately 50 m in the horizontal direction and approximately 20 m in the vertical direction, and which extends 2 km laterally to the model boundaries. Because of symmetry, it is only necessary to explicitly model one-quarter of the model domain (Figure 7.5-1).

All of the MSTHM submodels used in the model validation test case used the same stratigraphy and boundary conditions as in the D/LMTH model. The SMT submodel has a heated repository footprint of 59,049 m^2 and the same total initial heat output (986.6 kW or 829 MTU) as in the D/LMTH model (Buscheck et al. 2003 [DIRS 164638], p. 434, Table 4). MSTHM calculations for TSPA-LA involved running the LDTH and SDT submodels at four different AMLs. Because of the smaller heated footprint in this example, the influence of the edge-cooling effect occurs faster and with greater magnitude so that the LDTH–SDT submodel pairs are run at six different AMLs, rather than four. The DDT submodels are also run for the same six AMLs.

An important distinction between the MSTHM and the D/LMTH model concerns the treatment of air and vapor transport along the emplacement drift. The MSTHM effectively sets the axial permeability along the emplacement drift to zero, preventing axial air and vapor transport along the drift. For the D/LMTH model, the axial permeability is the same as that in the lateral and vertical directions (1×10^{-8} m^2, which is about three orders of magnitude greater than the bulk permeability of the host rock). Consequently, axial vapor transport (and the resulting moisture redistribution or cold-trap effect) occurs in the D/LMTH model, but does not occur in the MSTHM. The comparison of the MSTHM-simulated thermal-hydrologic behavior with that of the D/LMTH model is useful in determining the relative importance of axial vapor transport on thermal-hydrologic behavior in the emplacement drifts.

7.5.2 Results of the MSTHM Validation Test Case

The results of the nested-mesh D/LMTH model and the MSTHM are compared at the four waste package locations at the center and at the edge of the three-drift repository test case. For the center of the repository (Sections 7.5.2.1, 7.5.2.2, and 7.5.2.3), the results from the D/LMTH model are shown for two cases: (1) the case with axial gas- and liquid-phase transport along the drift, a sealed bulkhead at the edge of the drift, and low gas-phase dispersivity in the drift and (2) the case without that axial transport. Note that the low gas-phase dispersion coefficient accounts for binary diffusion of water vapor, but does not account for the influence of natural-convective mixing. The binary diffusion coefficient for water vapor varies as a function of temperature and pressure (Nitao 1998 [DIRS 100474], Equation 8). For the in-drift gas-phase pressure (which is nearly constant at about 8.845×10^4 Pa) and in-drift temperature range (25 to 150°C) applicable to the three-drift repository test case, the binary diffusion coefficient varies from 2.82×10^{-5} to 4.22×10^{-5} m^2/sec. Thus, for the low dispersion case, the gas-phase dispersion coefficient corresponds to this range.

For the repository edge (Sections 7.5.2.4, 7.5.2.5, 7.5.2.6, and 7.5.2.7), D/LMTH-model results are given for three cases, including one case without axial gas- and liquid-phase transport along the drift and two with axial transport along the drift. The two cases with axial transport include one with a sealed bulkhead at the end of the drift and low gas-phase dispersivity in the drift and a

case with no bulkhead and high gas-phase dispersivity in the drift. The high gas-phase dispersion coefficient in the second case with axial moisture transport is used to account for the influence of turbulent natural-convection mixing. For the temperature range of 25 to 150°C, the dispersion coefficient in the high-dispersion case varies between 0.011 and 0.021, which is within a factor of two of the value used (0.008 m^2/sec) in the high-dispersion case in *In-Drift Natural Convection and Condensation* (BSC 2004 [DIRS 164327], Section 6.2.7). The second case with axial transport (and high gas-phase dispersion) also accounts for the open unheated section of drift (called the turnout area) beyond the last outermost waste package, and it includes the effects of rock dryout during the ventilation period. Of the D/LMTH-model cases, the case with no bulkhead and a high gas-phase dispersion coefficient in the drift is most representative of the cold-trap effect at the repository edge. Differences between that case and the D/LMTH case with no axial gas- and liquid-phase transport quantify the influence of the cold-trap effect. For the waste packages at the repository center, the differences between these respective cases quantify the influence of the drift-scale cold-trap effect. For the waste packages at the repository edge, the differences between these respective cases quantify (primarily) the influence of the repository-scale cold-trap effect.

7.5.2.1 Temperature at the Center of the Three-Drift Repository Test Case

Drift-wall and drip-shield temperatures that are predicted by the D/LMTH model and the MSTHM are in good agreement at all four waste package locations at the center of Drift #2 (Figure 7.5-2). Axial gas- and liquid-phase transport along the drift is seen to have an insignificant influence on temperatures at the center of the three-drift repository test case. Table-7.5-3 summarizes the peak drift-wall and drip-shield temperatures predicted by the MSTHM and the D/LMTH model at the center of the three-drift repository test case. Differences in peak drift-wall temperature between the MSTHM and the D/LMTH model with axial gas- and liquid-phase transport along the drift axis range from 0.5°C to 2.3°C; differences in peak drip-shield temperature range from −1.7°C to 2.7°C. Table 7.5-4 summarizes the time when boiling at the drift wall ceases; differences between the two models are insignificant (generally 3% or less).

There is similar good agreement in temperature at other reference locations, such as in the invert. The D/LMTH-predicted temperatures tend to be slightly lower than the MSTHM-predicted temperatures. This is most likely because the MSTHM does not consider mountain-scale buoyant gas-phase convection, nor does it consider vapor (and latent heat) transport along the axis of the drift from the center to the edge of the repository and beyond. The D/LMTH model considers both of these cooling mechanisms and therefore predicts slightly cooler temperature histories than the MSTHM.

Table 7.5-3. Summary of Peak Temperatures for the Four Waste Package Locations at the Center of the Three-Drift Repository Test Case

Waste package	Peak Drift-Wall Temperature (°C)			Peak Drip Shield Temperature (°C)		
	MSTHM	D/LMTH model	Difference	MSTHM	D/LMTH model	Difference
PWR1	140.4	138.8 (139.3)	1.6 (1.1)	160.0	160.5 (160.9)	-0.5 (-0.9)
DHLW	135.5	133.2 (133.7)	2.3 (1.8)	145.1	142.4 (142.9)	2.7 (2.2)
PWR2	146.4	145.9 (146.3)	0.5 (0.1)	168.0	169.7 (170.1)	-1.7 (-2.1)
BWR	145.5	144.9 (145.3)	0.6 (0.2)	163.1	164.0 (164.4)	-0.9 (-1.3)

NOTE: The D/LMTH-model results are for the cases with and without axial gas- and liquid-phase transport along the drift; the latter case is given in the parentheses. These values are based on data plotted in Figure 7.5-2.

In general, the small differences in predicted temperatures between the D/LMTH-model case with axial gas- and liquid-phase transport and the D/LMTH-model case without axial transport indicate that the influence of the drift-scale cold-trap effect on temperature is insignificant.

7.5.2.2 Relative Humidity at the Center of the Three-Drift Repository Test Case

Drift-wall relative humidity predicted by the D/LMTH model and the MSTHM are in good agreement at all four center waste package locations. Figure 7.5-3 shows drift-wall relative humidity for the four waste packages. The agreement is closest up until the very end of the rock dryout period when the MSTHM predicts slightly lower relative humidity at the drift wall. The agreement in the predicted drip-shield relative humidity between the two models is best for the PWR2 and BWR waste package (Figure 7.5-3f and h). The MSTHM predicts slightly lower relative humidity than the D/LMTH model for the relatively cool DHLW waste package (Figure 7.5-3d). It is noted that the DHLW waste package location has temperature and relative humidity gradients within the drip shield in the axial direction (not shown). The DHLW waste package is warmer (and drier) at its end than at its center because it is being heated by its neighboring waste packages that generate more heat (Table 7.5-2). Axial gas- and liquid-phase transport along the drift is seen to have an insignificant influence on relative humidity at the center of the three-drift repository test case. Therefore, the influence of the drift-scale cold-trap effect on relative humidity is insignificant.

Table 7.5-4. Summary of Time When Boiling Ceases at the Drift Wall for the Four Waste Package Locations at the Center of the Three-Drift Repository Test Case

Waste package	Time When Boiling at Drift Wall Ceases (years)			
	MSTHM	D/LMTH model	Difference	Difference[a]
PWR1	291.2	283.1	8.1	2.82%
DHLW	269.7	259.5	10.2	3.85%
PWR2	312.0	303.2	8.8	2.86%
BWR	304.0	294.4	9.6	3.21%

[a] The difference (%) is the difference (years) divided by the average time when drift-wall boiling ceases [(shortest + longest)/2]. The D/LMTH-model results are for the case with axial gas- and liquid-phase transport along the drift. These values are based on data plotted in Figure 7.5-2.

7.5.2.3 Liquid-Phase Saturation at the Center of the Three-Drift Repository Test Case

Drift-wall liquid-phase saturation $S_{dw,j,DMTH}$ predicted by the D/LMTH model and MSTHM are in good agreement at all four center waste package locations (Figure 7.5-4a, c, e, and g). This

good agreement is obtained regardless of whether axial gas- and liquid-phase transport is allowed to occur along the drift in the D/LMTH model. The minimum $S_{dw,j,DMTH}$, which occurs during the boiling period, is virtually identical for the two models. The MSTHM predicts a slightly longer duration of dryout for the PWR1, PWR2, and BWR waste packages; for the DHLW waste package, the two models predict virtually the same dryout duration (Figure 7.5-4c). Axial gas- and liquid-phase transport along the drift is seen to have an insignificant influence on drift-wall liquid-phase saturation. The agreement between the MSTHM and the D/LMTH model for the invert liquid-phase saturation, $S_{inv,j,DMTH}$, is good for the CSNF waste packages (Figure 7.5-4b, f, and h) and it is adequate for the relatively cool DHLW waste package (Figure 7.5-4d). The influence of the cold-trap effect is exhibited by the slightly higher values of $S_{inv,j,DMTH}$ for the DHLW waste package in the D/LMTH model with axial gas- and liquid-phase transport along the drift, compared to the D/LMTH model that does not allow that axial transport. The cold-trap effect causes the advection of water vapor from the relatively hot CNSF waste package locations to the relatively cool DHLW waste package location, where it condenses, causing an increase in $S_{in,j,DMTH}$. The two hot CSNF waste packages next to the DHLW waste package have slightly reduced $S_{in,j,DMTH}$ for the D/LMTH model with axial gas- and liquid-phase transport along the drift compared to the D/LMTH model that does not allow that axial transport.

In general, small differences in predicted liquid-phase saturation between the D/LMTH-model case with axial gas- and liquid-phase transport and the D/LMTH-model case without axial transport indicate that the influence of the drift-scale cold-trap effect on liquid-phase saturation is insignificant.

Source: See Table XIII-1.

NOTE: Drift-wall temperature ($T_{dw,j,DMTH}$) vs. time (a, c, e, g) and drip-shield temperature ($T_{ds,j,DMTH}$) vs. time (b, d, f, h) are determined by the MSTHM and the D/LMTH model. The D/LMTH-model results are given for the cases with and without axial gas- and liquid-phase transport along the drift.

Figure 7.5-2. Drift-Wall and Drip-Shield Temperature vs. Time for the (a,b) PWR1, (c,d) DHLW, (e, f) PWR2, and (g, h) BWR Waste Packages at the Center of the Three-Drift Repository Test Case
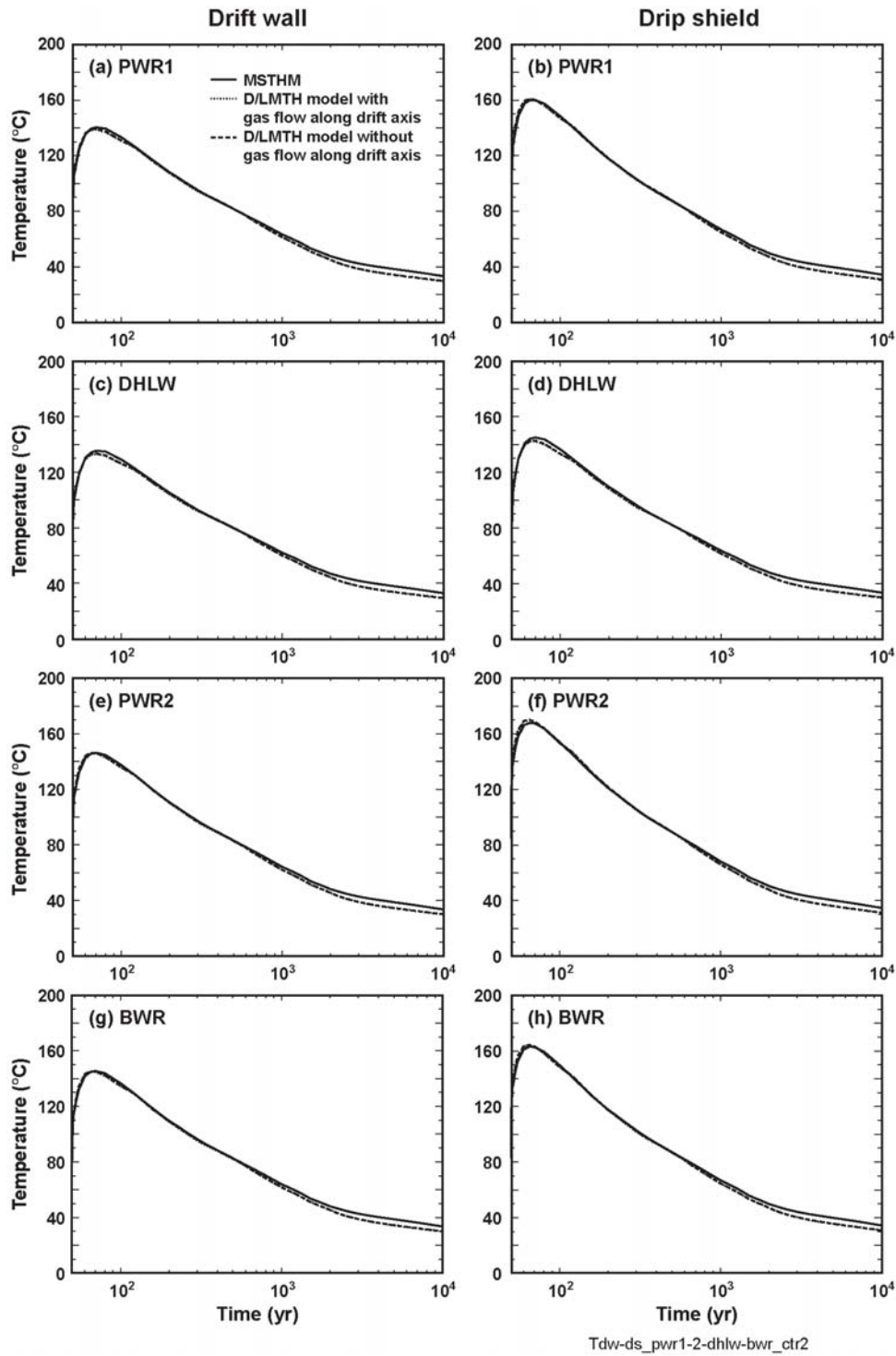
RHdw-ds_pwr1-2-dhlw-bwr_ctr2
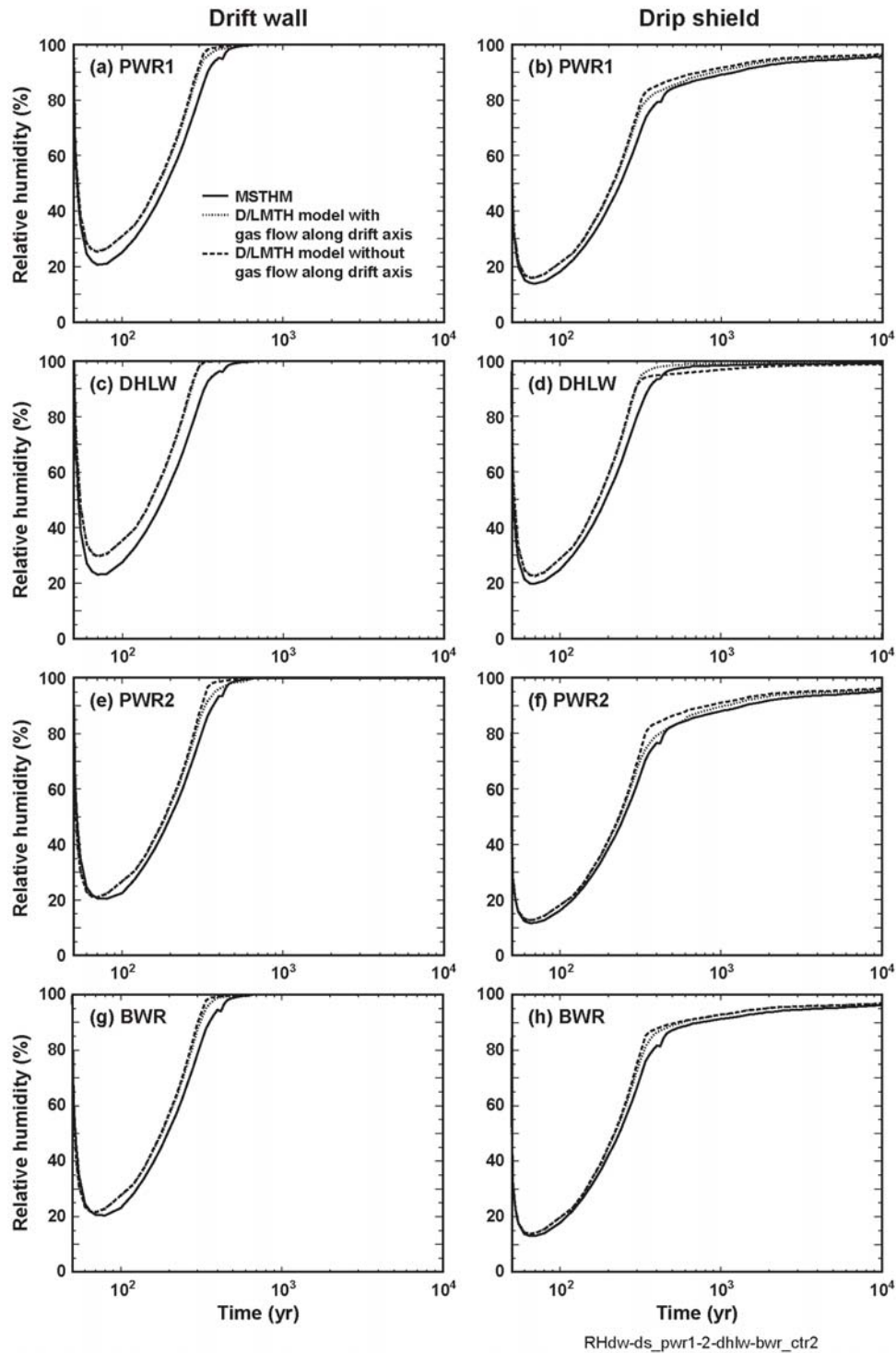
Source: See Table XIII-1.

NOTE: Drift-wall relative humidity ($RH_{dw,j,DMTH}$) vs. time (a, c, e, g) and drip-shield relative humidity ($RH_{ds,j,DMTH}$) vs. time (b, d, f, h) are determined by the MSTHM and the D/LMTH model. The D/LMTH-model results are given for the cases with and without axial gas- and liquid-phase transport along the drift.

Figure 7.5-3. Drift-Wall and Drip-Shield Relative Humidity vs. Time for the (a,b) PWR1, (c,d) DHLW, (e, f) PWR2, and (g, h) BWR Waste Packages at the Center of the Three-Drift Repository Test Case
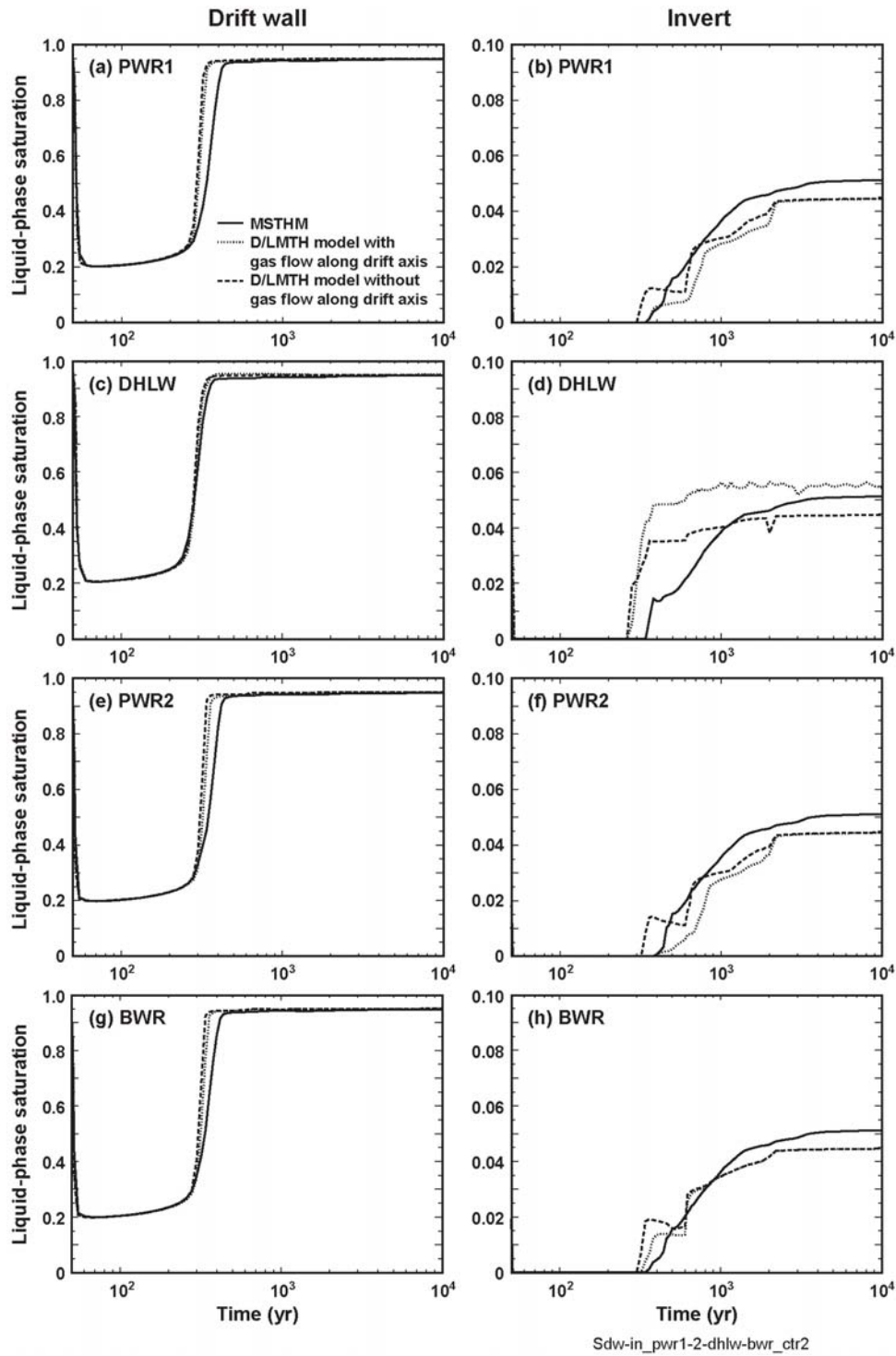
Source: See Table XIII-1.

NOTE: Drift-wall liquid-phase saturation ($S_{dw,j,DMTH}$) vs. time (a, c, e, g) and invert liquid-phase saturation ($S_{in,j,DMTH}$) vs. time (b, d, f, h) are determined by the MSTHM and the D/LMTH model. The D/LMTH-model results are given for the cases with and without axial gas- and liquid-phase transport along the drift.

Figure 7.5-4. Drift-Wall Liquid-Phase and Invert Liquid-Phase Saturation vs. Time for the (a, b) PWR1, (c, d) DHLW, (e, f) PWR2, and (g, h) BWR Waste Packages at the Center of the Three-Drift Repository Test Case

7.5.2.4   Temperature at the Edge of the Three-Drift Repository

At the edge of the three-drift repository test case, the longitudinal waste package order from the end of the drift is the following: PWR1, DHLW, PWR2, BWR. The drift-wall temperatures predicted by the D/LMTH model and the MSTHM are in reasonably good agreement at the four waste package locations at the edge of Drift #2 (Figure 7.5-5). This agreement is achieved regardless of whether axial gas- and liquid-phase transport along the drift is allowed to occur in the D/LMTH model. Tables 7.5-5 and 7.5-6 summarize the peak drift-wall and drip-shield temperatures predicted by the MSTHM and the D/LMTH model at the edge of the three-drift repository test case. A comparison of the D/LMTH-model temperatures (Figure 7.5-5 and Tables 7.5-5 and 7.5-6) clearly shows that the effect of axial transport of vapor and condensation on temperatures is small. Therefore, the influence of the repository-scale cold-trap effect on temperature is insignificant. When the MSTHM is compared with the D/LMTH model that allows axial gas- and liquid-phase transport along the drift (with no bulkhead and high gas-phase dispersivity in the drift), differences in peak drip-shield temperature range from 6.5°C for BWR package to 17.1°C for the DHLW package (Table 7.5-6). The outermost two waste package locations, which have a peak temperature bias of about 17°C, are representative of waste package locations that occupy only 1.6 percent of the repository area. The third and fourth waste package locations in from the repository edge, which have a peak temperature bias of about 7°C (Table 7.5-6), are representative of waste packages that occupy only 1.6 percent of the repository area. These results indicate that for waste packages located more than 20 m from the repository edge, which encompasses about 97 percent of the repository area, the peak temperature overprediction by the MSTHM is less than about 7°C.
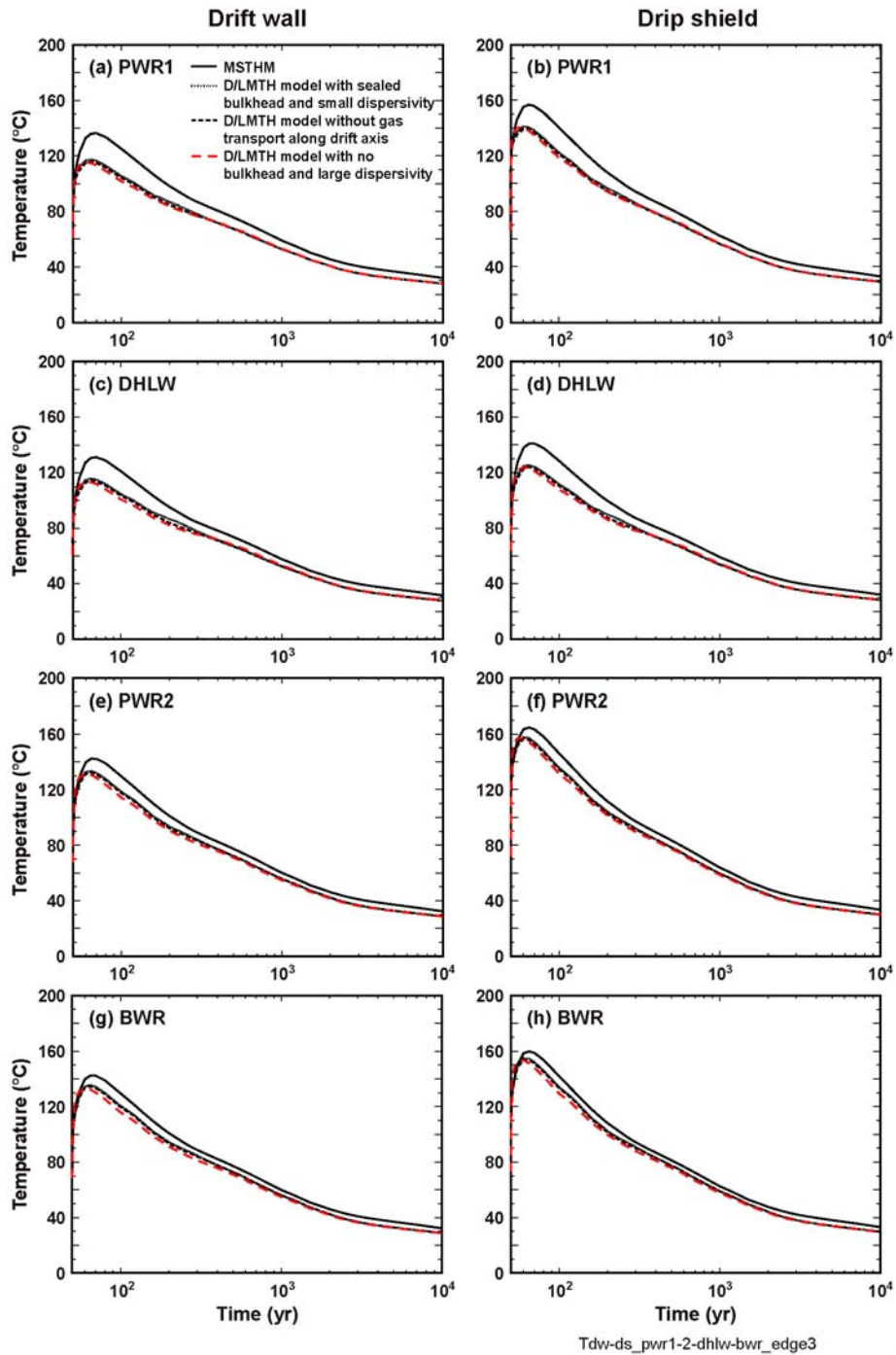
Source: See Table XIII-1.

NOTE: Drift-wall temperature ($T_{dw,j,DMTH}$) vs. time (a, c, e, g) and drip-shield temperature ($T_{ds,j,DMTH}$) vs. time (b, d, f, h) are determined by the MSTHM and the D/LMTH model. The D/LMTH-model results are given for a case without axial gas- and liquid-phase transport along the drift and for two cases with axial transport along the drift, including one with a sealed bulkhead and low gas-phase dispersivity in the drift and one with no bulkhead and high gas-phase dispersivity.

Figure 7.5-5. Drift-Wall and Drip-Shield Temperature vs. Time for the (a, b) PWR1, (c, d) DHLW, (e, f) PWR2, and (g, h) BWR Waste Packages at the Edge of the Three-Drift Repository Test Case

Table 7.5-5.   Peak Drift-Wall Temperatures Summarized for the Four Waste Package Locations at the Edge of the Three-Drift Repository Test Case

Waste Package	Peak Drift-Wall Temperature (°C)						
	MSTHM	D/LMTH Model			Difference (MSTHM – D/LMTH Model)		
		Axial gas- and liquid-phase transport in drift		No axial gas- & liquid-phase transport in drift	Axial gas- and liquid-phase transport in drift		No axial gas- and liquid-phase transport in drift
		No bulkhead & large dispersivity	With bulkhead & small dispersivity		No bulkhead & large dispersivity	With bulkhead & small dispersivity	
PWR1	136.3	115.4	117.4	115.7	20.9	18.9	20.6
DHLW	131.3	113.5	115.9	114.3	17.8	15.4	17.0
PWR2	142.3	131.6	133.4	132.2	10.7	8.9	10.1
BWR	141.4	133.0	135.5	134.5	8.4	5.9	6.9

NOTE: These values are based on data plotted in Figure 7.5-5.

Table 7.5-6.   Peak Drip-Shield Temperatures Summarized for the Four Waste Package Locations at the Edge of the Three-Drift Repository Test Case

Waste Package	Peak Drip-Shield Temperature (°C)						
	MSTHM	D/LMTH Model			Difference (MSTHM – D/LMTH Model)		
		Axial gas- and liquid-phase transport in drift		No axial gas- & liquid-phase transport in drift	Axial gas- and liquid-phase transport in drift		No axial gas- and liquid-phase transport in drift
		No bulkhead & large dispersivity	With bulkhead & small dispersivity		No bulkhead & large dispersivity	With bulkhead & small dispersivity	
PWR1	156.7	140.2	141.0	139.2	16.5	15.7	17.5
DHLW	141.0	123.9	125.5	124.0	17.1	15.5	17.0
PWR2	164.7	156.9	158.0	156.6	7.8	6.7	8.1
BWR	159.9	153.4	154.9	153.9	6.5	5.0	6.0

NOTE: These values are based on data plotted in Figure 7.5-5.

As discussed above, the agreement between the two models improves with distance from the edge of the repository. There are two reasons for the increasing disagreement in temperature with proximity to the edge. The first is related to the gridblock discretization in the SMT submodel and the second is related to the dimensionality of the DDT submodel.

The current implementation of the MSTHM has an SMT submodel that discretizes the emplacement drifts into 20-m intervals (Section 6.2.5.1). Thus, the edge of the repository is represented by an SMT submodel temperature history that is 10 m from the repository edge. Finer gridding in the axial direction would result in finer representation of the rate of cooling for the outermost waste packages in the drift.

As discussed in Section 6.2.1, an underlying principle in the MSTHM concept is that the influence of three-dimensional mountain-scale heat flow on drift-scale thermal-hydrologic behavior can be approximated with the use of an effective drift spacing that is implemented in the LDTH submodels. This effective drift spacing gradually increases with time to approximate the increasing influence of the edge-cooling effect, which allows heat to migrate away from the heated footprint of the repository area. The principle of the effective drift spacing relies on heat flow immediately away from the emplacement drift (and into the adjoining host rock) occurring

in a predominantly radial fashion. However, for the outermost two to three waste packages at the repository edge, heat flow can also have a substantial axial component. The use of a DDT submodel (Section 6.2.8) with an unheated portion in the axial direction (i.e., beyond the outermost waste package) would capture the influence of axial heat flow for the outermost two to three waste packages. The implementation of such a DDT submodel in the MSTHM methodology would likely result in closer agreement in temperatures predicted by the MSTHM and the D/LMTH model, and thereby reduce the small disagreement in temperatures for the outermost waste packages.

It is important to point out that even while the MSTHM overpredicts temperatures for packages near the end of the drift, these temperature differences between the MSTHM and D/LMTH model are well within the range of temperature differences resulting from parametric uncertainty (Section 7.5.4). A comparison of the magnitude of the influence of conceptual-model uncertainty with the magnitude of the influence of parametric uncertainty is presented in Section 7.5.4 (see Figure 7.5-9). When the D/LMTH model that allows axial transport along the drift is compared with the D/LMTH model that does not, the small (insignificant) influence of the cold-trap effect on temperatures is evident (Tables 7.5-5 and 7.5-6).

A useful way of examining the differences between the MSTHM and D/LMTH models is to consider the center-to-edge temperature differences predicted by the two models (Table 7.5-7). Note that the MSTHM represents all four waste packages as having the same center-to-edge distance, whereas the D/LMTH-model representation has a progressively smaller center-to-edge distance with increasing distance from the repository edge. The MSTHM utilizes an SMT submodel that discretizes the emplacement drifts into 20-m intervals; thus, the outer 20 m of the MSTHM is treated in the same fashion insofar as the influence of the edge-cooling effect is concerned. Similarly, the four waste packages at the center of the three-drift repository are treated in the same fashion insofar as their proximity to the repository edge is concerned. In a sense, the MSTHM does not distinguish which of the four waste packages is actually the outermost waste package over the outermost 20 m of the emplacement drift. All four waste packages are treated as though their respective centers are located 10 m from the edge of the heated footprint of the repository. Similarly, all four waste packages at the center of the three-drift repository are treated as though their centers are located 111.5 m from the edge of the heated repository footprint. Consequently, all four waste packages have virtually the same center-to-edge temperature difference. Conversely, the D/LMTH model does distinguish the respective distances from the repository edge for each of the four waste packages.

Table 7.5-7. Drip-Shield Temperature Difference Between the Center and Edge of the Three-Drift Repository Test Case, Compared for the D/LMTH Model and MSTHM

Waste Package	Center-to-Edge Distance (m)		Center-to-Edge Drip Shield Temperature Difference (°C)	
	MSTHM	D/LMTH model	MSTHM	D/LMTH model
PWR1	101.5	118.862	3.3	19.5
DHLW	101.5	108.260	4.1	16.9
PWR2	101.5	97.658	3.3	11.7
BWR	101.5	87.106	3.2	8.2

NOTE: Temperature differences are based upon Tables 7.5-6 and 7.5-5. The center-to-edge distances are based upon Figure 7.5-1. The D/LMTH-model results are for the case with longitudinal gas- and liquid-phase transport along the drift axis and with a bulkhead and low gas-phase dispersivity. These values are based on data plotted in Figure 7.5-5.

Table 7.5-7 indicates that the center-to-edge temperature difference in the D/LMTH model approaches that of the MSTHM for increasing distance from the repository edge. The reasons for the increasing agreement with increasing distance from the edge are discussed above. Tables 7.5-5 and 7.5-6 indicate that for waste packages located 20 m or more from the repository edge, the differences in temperature predicted by the MSTHM and D/LMTH model are small (less than 7°C for peak drip-shield temperatures). The MSTHM discretizes thermal-hydrologic behavior for 2,874 20-m intervals (Figure 6.2-3); of these intervals, only 92 are potentially affected by the axial vapor (and latent heat) loss at the edge of the repository, constituting only 3.2 percent of the repository area. Consequently, 96.8 percent of the repository should not be influenced by this effect at the outermost edge of the repository. For the outermost 3.2 percent of the repository, the small overprediction of MSTHM temperatures is well within the range of temperature differences resulting from parametric uncertainty (Section 7.5.4). A comparison of the magnitude of the influence of conceptual-model uncertainty with the magnitude of the influence of parametric uncertainty is presented in Section 7.5.4 (see Figure 7.5-12).

Table 7.5-8 summarizes the time when boiling at the drift wall ceases; differences between the two models range from 26.7 to 52.7 percent. Again, the agreement between the two models improves with distance from the edge of the repository. Because the differences between the two models are within the range of differences arising from parametric uncertainty (Figure 7.5-12), the impact of conceptual-model uncertainty is less than that of parametric uncertainty.

Table 7.5-8. Summary of Time When Boiling Ceases at the Drift Wall for the Four Waste Package Locations at the Edge of the Three-Drift Repository Test Case

Waste Package	Time When Boiling at Drift Wall Ceases (years)			
	MSTHM	D/LMTH Model	Difference	Difference[a]
PWR1	215.0	125.3	89.7	52.7%
DHLW	195.9	121.4	74.5	47.0%
PWR2	233.2	167.3	65.9	32.9%
BWR	226.6	173.3	53.3	26.7%

[a] The difference (%) is the difference (years) divided by the average time when drift-wall boiling ceases [(shortest + longest)/2]. The D/LMTH model results are for the case with longitudinal gas- and liquid-phase transport along the drift axis, and with no bulkhead and high gas-phase dispersivity.

NOTE: These values are based on data plotted in Figure 7.5-5.

7.5.2.5 Relative Humidity at the Edge of the Three-Drift Repository Test Case

Figure 7.5-6 gives the drift-wall relative humidity for the four waste packages at the edge of the repository. Drift-wall relative humidity predicted by the D/LMTH model and the MSTHM are in reasonable agreement at the four "edge" waste package locations. This agreement is achieved regardless of whether axial gas- and liquid-phase transport along the drift is allowed to occur in the D/LMTH model. However, the inclusion of axial vapor transport and the unheated part of the drift in the D/LMTH model (with no bulkhead and high gas-phase dispersivity) improves the agreement of predicted relative humidity (Figure 7.5-6) between the MSTHM and the D/LMTH model. Note also that the agreement between the two models improves with distance from the repository edge. The agreement in the predicted drift-wall relative humidity between the two models is best for the PWR2 and BWR waste package (Figure 7.5-6e and g). The agreement between the two models is better for drip-shield relative humidity (Figure 7.5-6b, d, f, and h) than it is for drift-wall relative humidity (Figure 7.5-6a, c, e, and g). The agreement is best during the postboiling period when relative humidity reduction resulting from rock dryout no longer plays a significant role in relative humidity reduction on the drip shield. During the boiling period, the agreement in drip-shield relative humidity improves with distance from the edge of the repository. The differences between the two models in drip-shield relative humidity are within the range of differences arising from parametric uncertainty (Section 7.5.4). A comparison of the magnitude of the influence of conceptual-model uncertainty with the magnitude of the influence of parametric uncertainty is presented in Section 7.5.4 (see Figure 7.5-13).

The influence of the cold-trap effect can be observed in Figure 7.5-6 by comparing the results from the D/LMTH model that allows axial gas- and liquid-phase transport along the drift with those from the D/LMTH model that does not allow that axial transport. The influence of the cold-trap effect is to reduce the drift-wall relative humidity, with the reduction being stronger for the three CSNF waste packages than it is for the DHLW waste package. This reduction results because some of the water vapor generated in the host rock flows radially inward into the drift and then axially along the drift beyond the outermost waste package, where it condenses and is imbibed into the host rock. This process results in a net reduction in moisture in the host rock, particularly adjacent to the CSNF waste packages. The drift-wall temperature adjacent to the DHLW waste package drops below the boiling point earlier than at the (relatively hotter) CSNF waste package locations. The earlier return to sub-boiling temperatures causes preferential condensation and imbibition into the host rock adjoining the DHLW waste package. The

preferential condensation in the host rock adjacent to the DHLW waste package offsets some of the ongoing moisture loss from the host rock, decreasing the net reduction in liquid-phase saturation in the host rock. This smaller net reduction in liquid-phase saturation at the (relatively cooler) DHLW waste package location results in a smaller reduction in relative humidity than occurs for the (relatively hotter) CSNF waste packages.

In general, the small differences in predicted relative humidity between the D/LMTH-model case with axial gas- and liquid-phase transport and the D/LMTH-model case without axial transport indicate that the influence of drift-scale cold-trap effect on relative humidity is insignificant.

RHdw-ds_pwr1-2-dhlw-bwr_edge3

Source: See Table XIII-1.

NOTE: Drift-wall relative humidity ($RH_{dw,j,DMTH}$) vs. time (a, c, e, g) and drip-shield relative humidity ($RH_{ds,j,DMTH}$) vs. time (b, d, f, h) are determined by the MSTHM and the D/LMTH model. The D/LMTH-model results are given for a case without axial gas- and liquid-phase transport along the drift and for two cases with transport along the drift, including one with a sealed bulkhead and low gas-phase dispersivity in the drift and one with no bulkhead and high gas-phase dispersivity.

Figure 7.5-6. Drift-Wall and Drip-Shield Relative Humidity vs. Time for the (a, b) PWR1, (c, d) DHLW, (e, f) PWR2, and (g, h) BWR Waste Packages at the Edge of the Three-Drift Repository Test Case

7.5.2.6   Liquid-Phase Saturation at the Edge of the Three-Drift Repository Test Case

Drift-wall liquid-phase saturation $S_{dw,j,DMTH}$ predicted by the D/LMTH model and MSTHM are in reasonable agreement at the four "edge" center waste package locations (Figure 7.5-7a, c, e, and g). This agreement is achieved regardless of whether axial gas- and liquid-phase transport along the drift is allowed to occur in the D/LMTH model. However, the inclusion of axial vapor transport and the unheated part of the drift in the D/LMTH model (with no bulkhead and high gas-phase dispersivity) improves the agreement of predicted liquid-phase saturation (Figure 7.5-7) between the MSTHM and the D/LMTH model, with one exception, which is the invert liquid-phase saturation for the DHLW waste package (Figure 7.5-7d). Preferential condensation at the cold (DHLW waste package) location increases the invert liquid-phase saturation beneath that waste package. The cold-trap effect also results in a loss of moisture from the host rock adjoining all waste package locations (the hot CSNF waste packages in particular), which decreases the drift-wall liquid-phase saturation at those locations. The net reduction in liquid-phase saturation in the host rock at the cooler DHLW waste package location is reduced by virtue of preferential condensation occurring there after boiling ceases. The cold-trap effect also removes moisture from the invert liquid-phase saturation beneath the hot CSNF waste packages, which reduces the invert liquid-phase saturation at those locations. Preferential condensation beneath the (relatively cooler) DHLW waste package results in an increase in liquid-phase saturation in the invert (Figure 7.5-7d).

In general, the small differences in predicted liquid-phase saturation between the D/LMTH-model case with axial gas- and liquid-phase transport and the D/LMTH-model case without axial transport indicate that the influence of drift-scale cold-trap effect on liquid-phase saturation is insignificant.

7.5.2.7   Vapor and Condensate Fluxes at the Edge of the Three-Drift Repository Test Case

Figure 7.5-8 shows the axial mass flux of water vapor in the gas phase along the central drift in the model, plotted for the upstream end of each of the four waste packages (the end closer to the repository center), and also at the repository edge (the downstream end of the outermost waste package, PWR1). Note that Figure 7.5-1 shows the waste package sequence. These results are for the most realistic D/LMTH case, which has no bulkhead and high gas-phase dispersivity in the drift. The curves are parallel, with the upstream value being less than the downstream value at a given waste package location, with the exception of the last two curves labeled PWR1 (the outermost waste package) and Repository Edge. The last two curves drop below the value of the respective upstream curves at approximately 300 years, signifying that condensation is occurring in the vicinity of the cooler DHLW waste package after about 300 years.
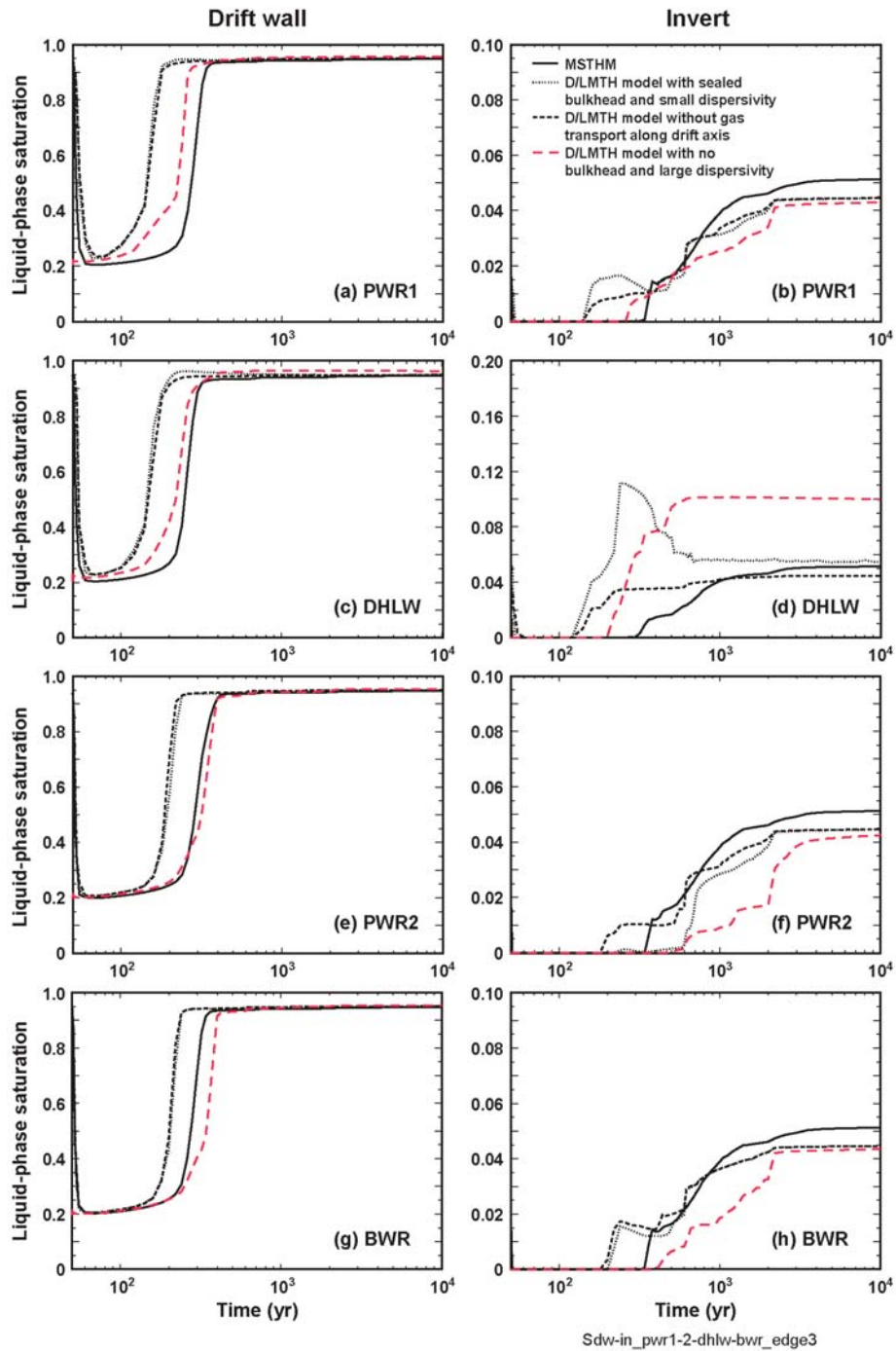
Source: See Table XIII-1.

NOTE: Drift-wall liquid-phase saturation ($S_{dw,j,DMTH}$) vs. time (a, c, e, g) and invert liquid-phase saturation
         ($S_{in,j,DMTH}$) vs. time (b, d, f, h) are determined by the MSTHM and the D/LMTH model. The D/LMTH-model
         results are given for a case without axial gas- and liquid-phase transport along the drift and for two cases
         with transport along the drift, including one with a sealed bulkhead and low gas-phase dispersivity in the
         drift and one with no bulkhead and high gas-phase dispersivity.

Figure 7.5-7. Drift-Wall Liquid-Phase and Invert Liquid-Phase Saturation vs. Time for the (a, b) PWR1,
             (c, d) DHLW, (e, f) PWR2, and (g, h) BWR Waste Packages at the Edge of the Three-Drift
             Repository Test Case
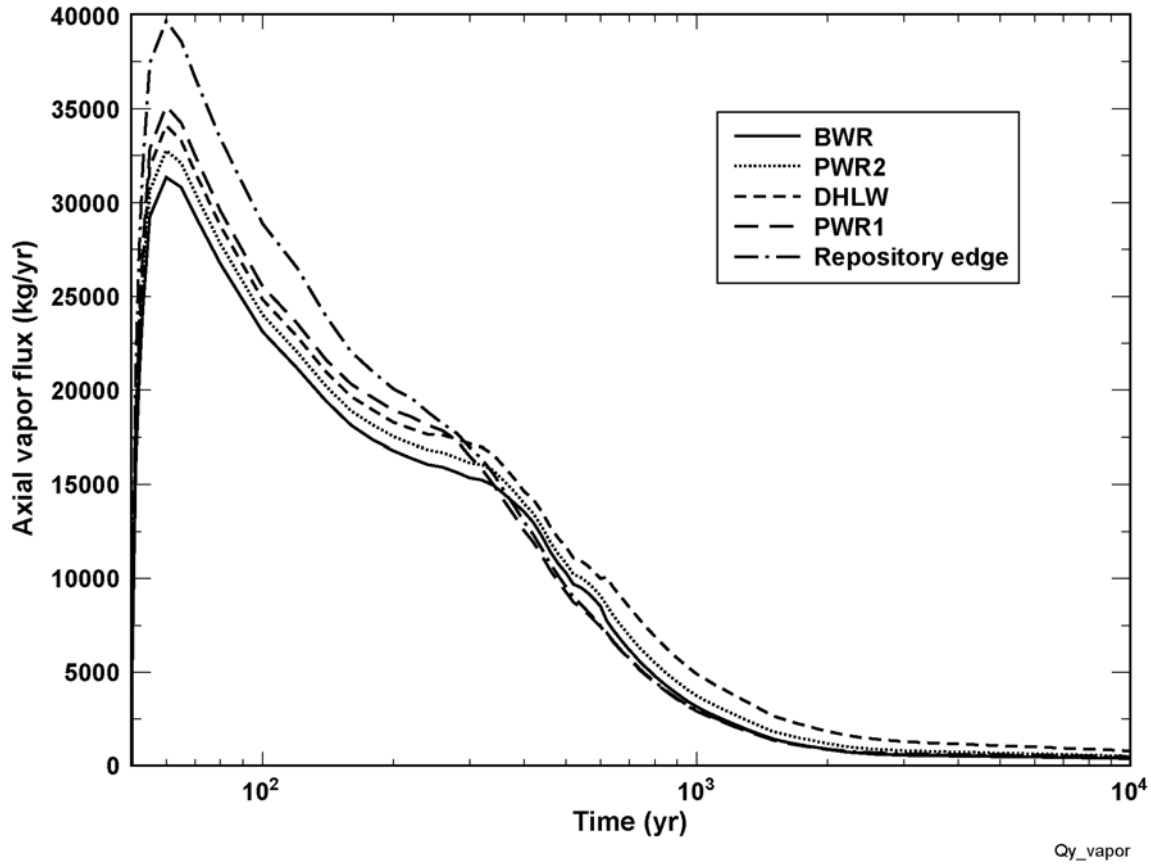
Source: See Table XIII-1.

NOTE: This figure corresponds to the D/LMTH-model case with no bulkhead and high gas-phase dispersivity. This case also includes the influence of host-rock dryout during the ventilation period. The waste package sequencing, starting from the edge, is PWR1, DHLW, PWR2, and BWR, as is shown in Figure 7.5-1. The upstream side of the waste package is the side closer to the repository center. The curve listed "repository edge" corresponds to the downstream side of the PWR1 waste package. The curve listed "PWR1" corresponds to the upstream side of the PWR 1 waste package, and to the downstream side of the DHLW waste package. The curve listed "DHLW" corresponds to the upstream side of the DHLW waste package and to the downstream site of the PWR2 waste package. The curve listed "PWR2" corresponds to the upstream side of the PWR2 waste package and to the downstream side of the BWR waste package. The curve listed "BWR" corresponds to the upstream side of the BWR waste package.

Figure 7.5-8. Axial Vapor Flux on the Upstream Side of the Listed Waste Packages at the Edge of the Three-Drift Repository Test Case

Tables 7.5-9 to 7.5-12 show moisture balance results for each of the four outermost waste packages at the repository edge, from the D/LMTH model case with no bulkhead and large dispersivity (case 3). The phase change columns show where evaporation (positive values) and condensation (negative values) are occurring at each waste package location for several discrete times distributed over the regulatory period. Note that the delta axial vapor flux, which is the difference in axial vapor flux between the upstream and downstream sides of a waste package (see Figure 7.5-8), corresponds to the net condensation or evaporation occurring at a waste package location. The radial vapor flux corresponds to the phase change that occurs in the host rock. Thus, the sum of the radial vapor flux, the invert phase change, and the drift phase change is equal to the delta axial vapor flux. Of the four waste packages, the DHLW waste package (Table 7.5-10) is the coolest, and condensation occurs mainly there. A comparison of the delta axial vapor flux with the radial vapor flux shows that most of the condensation at the cooler

waste package results from water vapor migration outward into cooler rock, where it condenses. This water is then diverted around the drift opening along with the ambient percolation flux.

Table 7.5-9. Summary of Moisture Balance for PWR1 Waste Package in Multiscale Thermal-Hydrologic Model Validation Test Case

Time (years)	Vapor Flux (kg/yr)				Phase Change (kg/yr)	
	Axial (upstream)	Axial (downstream)	Delta Axial	Radial	Invert	Drift
60	35,137.7	39,680.5	4,542.8	4,300.3	242.8	0.0
100	25,530.0	28,876.8	3,346.8	3,113.4	233.3	0.0
500	9,273.2	9,554.1	280.9	51.9	229.5	−0.4
1,000	2,928.7	2,978.4	49.7	−59.4	109.1	0.0
2,000	878.3	904.4	26.1	−17.6	51.6	−7.9
5,000	547.5	603.6	56.1	19.3	36.8	0.0
10,000	448.7	499.4	50.7	21.5	29.1	0.0

Source: DTNs: LL040703223122.050 and LL050500323122.060.

NOTE: The PWR1 waste package is located at the outer edge of the three-drift validation test case Figure 7.5-1) for the D/LMTH model with no bulkhead and a high gas-phase dispersion coefficient along the drift. Positive values of radial vapor flux correspond to vapor leaving the host rock and entering the drift (and invert); negative values correspond to vapor leaving the drift (and invert) and entering the host rock. Positive values of phase change correspond to evaporation; negative values correspond to condensation. The delta axial vapor flux, which is the difference in axial vapor flux between the upstream and downstream sides of a waste package (see Figure 7.5-8), corresponds to the net condensation or evaporation occurring at a waste package location. The radial vapor flux corresponds to the phase change that occurs in the host rock. Thus, the sum of the radial vapor flux, the invert phase change, and the drift phase change is equal to the delta axial vapor flux.

Table 7.5-10. Summary of Moisture Balance for DHLW Waste Package in Multiscale Thermal-Hydrologic Model Validation Test Case

Time (years)	Vapor Flux (kg/yr)				Phase Change (kg/yr)	
	Axial (upstream)	Axial (downstream)	Delta Axial	Radial	Invert	Drift
60	34,102.0	35,137.7	1,035.7	1,036.0	0.0	0.0
100	24,834.9	25,530.0	695.1	695.0	0.0	0.0
500	11,679.4	9,273.2	−2,406.2	−2,381.4	−12.5	−12.4
1,000	4,902.1	2,928.7	−1,973.4	−1,920.2	−30.4	−22.8
2,000	1,851.1	878.3	−972.8	−925.7	−19.1	−28.0
5,000	1,076.4	547.5	−528.9	−495.0	−10.4	−23.4
10,000	800.6	448.7	−351.9	−332.2	−6.6	−13.1

Source: DTNs: LL040703223122.050 and LL050500323122.060.

NOTE: The DHLW waste package is the second to the last waste package located at the outer edge of the three-drift validation test case (Figure 7.5-1) for the D/LMTH model with no bulkhead and a high gas-phase dispersion coefficient along the drift. Positive values of radial vapor flux correspond to vapor leaving the host rock and entering the drift (and invert); negative values correspond to vapor leaving the drift (and invert) and entering the host rock. Positive values of phase change correspond to evaporation; negative values correspond to condensation. The delta axial vapor flux, which is the difference in axial vapor flux between the upstream and downstream sides of a waste package (see Figure 7.5-8), corresponds to the net condensation or evaporation occurring at a waste package location. The radial vapor flux corresponds to the phase change that occurs in the host rock. Thus, the sum of the radial vapor flux, the invert phase change, and the drift phase change is equal to the delta axial vapor flux.

Table 7.5-11. Summary of Moisture Balance for PWR2 Waste Package in Multiscale Thermal-Hydrologic Model Validation Test Case

Time (years)	Vapor Flux (kg/yr)				Phase Change (kg/yr)	
	Axial (upstream)	Axial (downstream)	Delta Axial	Radial	Invert	Drift
60	32,775.4	34,102.0	1,326.6	1,326.9	0.0	0.0
100	24,013.9	24,834.9	821.0	821.0	0.0	0.0
500	10,813.1	11,679.4	866.3	711.8	153.7	0.8
1,000	3,744.8	4,902.1	1,157.3	1,062.5	94.8	0.0
2,000	1,202.0	1,851.1	649.1	592.5	56.6	0.0
5,000	678.6	1,076.4	397.8	348.9	48.8	0.0
10,000	524.7	800.6	275.9	238.2	37.7	0.0

Source: DTNs: LL040703223122.050 and LL050500323122.060.

NOTE: The PWR2 waste package is the third to the last waste package located at the outer edge of the three-drift validation test case (Figure 7.5-1) for the D/LMTH model with no bulkhead and a high gas-phase dispersion coefficient along the drift. Positive values of radial vapor flux correspond to vapor leaving the host rock and entering the drift (and invert); negative values correspond to vapor leaving the drift (and invert) and entering the host rock. Positive values of phase change correspond to evaporation; negative values correspond to condensation. The delta axial vapor flux, which is the difference in axial vapor flux between the upstream and downstream sides of a waste package (see Figure 7.5-8), corresponds to the net condensation or evaporation occurring at a waste package location. The radial vapor flux corresponds to the phase change that occurs in the host rock. Thus, the sum of the radial vapor flux, the invert phase change, and the drift phase change is equal to the delta axial vapor flux.

Table 7.5-12. Summary of Moisture Balance for BWR Waste Package in Multiscale Thermal-Hydrologic Model Validation Test Case

Time (years)	Vapor Flux (kg/yr)				Phase Change (kg/yr)	
	Axial (upstream)	Axial (downstream)	Delta Axial	Radial	Invert	Drift
60	31,340.3	32,775.4	1,435.1	1,435.3	0.0	0.0
100	23,118.2	24,013.9	895.7	895.7	0.0	0.0
500	10,292.6	10,813.1	520.5	389.3	130.2	1.0
1,000	3,161.5	3,744.8	583.3	500.9	82.4	0.0
2,000	889.2	1,202.0	312.8	264.5	48.4	0.0
5,000	489.6	678.6	189.0	155.7	33.4	−0.1
10,000	400.8	524.7	123.9	98.7	26.3	−1.1

Source: DTNs: LL040703223122.050 and LL050500323122.060.

NOTE: The BWR waste package is the fourth to the last waste package located at the outer edge of the three-drift validation test case (Figure 7.5-1) for the D/LMTH model with no bulkhead and a high gas-phase dispersion coefficient along the drift. Positive values of radial vapor flux correspond to vapor leaving the host rock and entering the drift (and invert); negative values correspond to vapor leaving the drift (and invert) and entering the host rock. Positive values of phase change correspond to evaporation; negative values correspond to condensation. The delta axial vapor flux, which is the difference in axial vapor flux between the upstream and downstream sides of a waste package (see Figure 7.5-8), corresponds to the net condensation or evaporation occurring at a waste package location. The radial vapor flux corresponds to the phase change that occurs in the host rock. Thus, the sum of the radial vapor flux, the invert phase change, and the drift phase change is equal to the delta axial vapor flux.

7.5.3   Summary of Three-Drift Repository Validation Test Case

The MSTHM is validated against a monolithic three-dimensional porous-medium model implemented using the NUFT code (Nitao 1998 [DIRS 100474]) for a three-drift test case, representing a scaled-down repository. Each simulated drift is 243 m long and uses a combination of line-averaged and discrete heat sources to represent the waste packages. The central drift uses a combination of a line-averaged heat source for most of the drift and four discrete sources (representing individual waste packages) at the center of the drift and four discrete sources at the outer end of the drift (Figure 7.5-1). The monolithic three-dimensional thermal-hydrologic model is called the discrete/line-averaged mountain-scale thermal-hydrologic (D/LMTH) model.

The D/LMTH model was run in three ways:

- Case 1:   This case allows no axial vapor (or gas) transport along the drifts, corresponding to the MSTHM, which does not include vapor transport along the drift axis. Case 1 was run for both the center and edge waste packages.

- Case 2: This case allows axial vapor transport, using a small value for the gas-phase dispersion coefficient to account for binary diffusion of water vapor but not for the influence of convective mixing. In addition, a bulkhead was located just beyond the outermost waste package at the end of each drift. Case 2 was run for both the center and edge waste packages.

- Case 3: This case allows axial vapor transport, using the high value of the gas-phase dispersion coefficient to account for the influence of turbulent convective mixing. The third case has no bulkhead at the end of the drift, and includes the unheated section of the drift beyond the outermost waste package. The third case includes the effects of rock dryout during the ventilation period.   Case 3 was only run for the edge waste packages.

Of the three cases, the third is most realistic and is emphasized in the discussion below. Differences in the predicted thermal-hydrologic conditions for the drift and the adjoining host rock between cases 1 and 3 are used as quantitative indicators of the importance of the cold-trap effect, and moisture transport to the unheated part of each drift, with respect to MSTHM predictions. D/LMTH-model calculations were conducted for cases 1 and 2 for the four waste packages at the repository center. D/LMTH-model calculations were conducted for cases 1, 2, and 3 for the four waste packages at the repository edge.

For comparison, the MSTHM was configured for this same three-drift configuration and boundary conditions, so that results are directly comparable to the D/LMTH-model cases. The locations selected for direct comparisons are at the center and edge of the simplified three-drift repository.

Temperature differences between the MSTHM results and cases 1 through 3 are dominated by how the MSTHM methodology addresses three-dimensional heat losses. For waste packages located more than 20 m from the repository edge, which represents approximately 97% of the emplaced repository area, overprediction of peak drip shield temperature by the MSTHM is less

than 7°C. At the edge, comparison of the MSTHM with case 3 shows relatively small differences (6.5 to 17.1°C) in peak drip-shield temperature (Figure 7.5-6). These differences are smaller than the overall effect of parametric uncertainty of host-rock thermal conductivity and percolation flux (Section 7.5.4). A comparison of the magnitude of the influence of conceptual model uncertainty with the magnitude of the influence of parametric uncertainty is presented in Section 7.5.4 (see Figure 7.5-12). Temperature differences are greatest for the last two waste packages at the edge, and are caused by the coarse spatial grid resolution of the SMT submodel used in the MSTHM framework.

The small differences in temperatures between cases 1 and 3 show the lack of influence of the cold-trap effect on temperatures for waste package locations at the repository edge. This result supports use of the MSTHM for predicting thermal-hydrologic conditions in the drifts and in the adjoining host rock for waste package locations near the repository edge.

For case 3, which includes axial vapor transport and the resulting cold-trap effect, the predicted in-drift relative humidity and host-rock liquid saturation conditions (Figures 7.5-6 and 7.5-7) agree more closely with the MSTHM results than the other cases. Importantly, the cold-trap effect causes net reduction in moisture (matrix liquid-phase saturation) in the host rock at all waste package locations, because water is evaporated and transported to unheated regions of the drift. The greatest moisture losses occur at the hotter spent-fuel waste packages, and smallest losses occur at the cooler DHLW waste packages that receive condensation when they cool below boiling (96°C). Condensation at the drift wall, and within the near-field host rock adjacent to the DHLW waste package, offsets some (but not all) of the initial moisture loss. The smaller net moisture reduction at the cooler waste package locations results in smaller reduction in relative humidity than occurs for at hotter waste packages. Axial vapor transport is also predicted to cause net moisture reduction in the invert beneath the hotter waste package locations (Figure 7.5-7). Condensation in the invert beneath cooler waste packages increases the liquid-phase saturation there (Figure 7.5-7d).

Because the MSTHM does not include axial vapor transport along the drift, it does not represent the net moisture reduction discussed above. However, the differences in predicted relative humidity and host-rock liquid saturation between the MSTHM results and case 3 are smaller than the overall effect of parametric uncertainty of host-rock thermal conductivity and percolation flux for the MSTHM of the repository (Section 7.5.4). A comparison of the magnitude of the influence of conceptual-model uncertainty with the magnitude of the influence of parametric uncertainty is presented in Section 7.5.4 (Figures 7.5-13 and 7.5-14). Although the MSTHM does not directly account for the influences of the cold-trap effect or of rock dryout during the ventilation period, it does compare well with case 3, which includes both of these influences. Therefore, it is unnecessary to incorporate axial vapor transport and the resulting cold-trap effect into the MSTHM for TSPA-LA.

7.5.4 Comparison of the Influence of Conceptual-Model Uncertainty with the Influences of Parametric Uncertainty and Waste-Package Heat Output Variability

The difference between the MSTHM and the alternative (D/LMTH) model for the three-drift validation test case is a measure of the influence of conceptual-model uncertainty for the MSTHM. A comparison of the magnitude of the influence of conceptual-model uncertainty against that of parametric uncertainty determines the relative significance of conceptual-model

uncertainty for the MSTHM. The magnitude of conceptual-model uncertainty is also compared with the combined influences of parametric uncertainty and waste-package heat-output variability. The model validation criterion applicable to Section 7.5 is specified in the governing TWP (BSC 2005 [DIRS 173377], Section 2.3.4). The model validation criterion compares the magnitude of the MSTHM-to-D/LMTH-model differences of a particular output parameter (e.g., temperature or relative humidity) to the range in that parameter arising from parametric uncertainty (of percolation flux and host-rock thermal conductivity). Therefore, the model-validation criterion in the governing TWP is based on a comparison of the influence of conceptual-model uncertainty with that of parametric uncertainty.

For the purpose of determining the relative significance of conceptual model uncertainty at the center (Figures 7.5-2 through 7.5-4) and at the edge (Figure 7.5-5 through 7.5-7) of the three-drift repository validation test case, two locations were selected from the MSTHM representation of the entire repository emplacement area (Figure 6.3-1). The P2WR5C10 location was selected because it is representative of a typical center location in the repository, while the P2ER8C6 location was selected because it is representative of a typical edge location (see Figure 6.3-1 for locations). For the nominal intact-drift case, parametric uncertainty represented in the MSTHM comes from the two (primary) sources:

- **Host-rock thermal conductivity uncertainty:** represented by the high, mean, and low host-rock thermal-conductivity cases

- **Percolation-flux uncertainty:** represented by the lower-bound, mean, and upper-bound infiltration-flux cases

In addition to parametric uncertainty, waste-package heat-output variability also contributes to a range of predicted thermal-hydrological conditions at a given location in the repository. Waste package heat-output variability in the MSTHM is represented by eight distinct waste packages in the DDT submodel (Section 6.2.8.4).

The influence of host-rock thermal conductivity and percolation-flux uncertainty is addressed by conducting repository-wide MSTHM calculations for the five cases described in Section 6.3.4 (Table 6.3-37). To obtain the range resulting from parametric uncertainty, two of those five cases are used:

1. **Lower-bound infiltration-flux, low host-rock thermal conductivity case:** Of the five cases, this results in the hottest and driest conditions in the host rock and in the emplacement drift.

2. **Upper-bound infiltration-flux, high host-rock thermal conductivity case:** Of the five cases, this results in the coolest and wettest conditions in the host rock and in the emplacement drift.

For both of these cases, three waste packages out of the eight distinct waste packages in the DDT submodel are considered, including:

1. **Hottest waste package**: This waste package corresponds to the pwr1-2 waste package from Table 6.3-13. The range of thermal-hydrologic conditions for this waste package is compared with the differences between the MSTHM and the alternative

(D/LMTH) model for the PWR1 and PWR2 waste packages in the three-drift validation test case (Table 7.5-2). The pwr1-2 waste package is also used, in conjunction with the dhlw-l1 waste package (which is the coolest waste package), to determine the total range in MSTHM-predicted thermal-hydrologic conditions at a given location.

2. **Average waste package:** This waste package corresponds to the bwr1-1 waste package in Table 6.3-13. The range of thermal-hydrologic conditions for this waste package is compared with the differences between the MSTHM and the alternative (D/LMTH) model for the BWR waste package in the three-drift validation test case (Table 7.5-2).

3. **Coolest waste package:** This waste package corresponds to the dhlw-l1 waste package in Table 6.3-13. The range of thermal-hydrologic conditions for this waste package is compared with the differences between the MSTHM and the alternative (D/LMTH) model for the DHLW waste package in the three-drift validation test case (Table 7.5-2). The dhlw-l1 waste package is also used, in conjunction with the pwr1-2 (which is the hottest waste package), to determine the total range in MSTHM-predicted thermal-hydrologic conditions at a given location.

The difference in temperature for a given waste package (e.g., the pwr1-1 waste package) between the first (lower-bound infiltration, low host-rock K_{th}) case and the second (upper-bound infiltration, high host-rock K_{th}) case at the P2WR5C10 location represents the range in that parameter resulting from parametric uncertainty at that location. The difference in temperature between the hottest (pwr1-2) waste package in the first case and the coolest (dhlw-l1) waste package in the second case represents the entire range in temperature predicted by the MSTHM at that location. For Figures 7.5-9 through 7.5-14, this range is designated to be the *total* range. Thus, the *total* temperature range predicted by the MSTHM at a particular location includes both the influences of parametric uncertainty and waste-package heat-output variability. The total temperature range, as well as the temperature range resulting from parametric uncertainty (alone), is determined for both the waste package and drift wall, respectively, as a function of time, and plotted in Figure 7.5-9. Also plotted in Figure 7.5-9 is the absolute difference in temperature between the MSTHM and the D/LMTH model for the waste packages at the repository center for case 2 (axial vapor transport along the drift, with a bulkhead at the end of the drift, and low gas-phase dispersivity along the drift). Figure 7.5-9 shows that both the total temperature range and the range in temperature resulting from parametric uncertainty (alone) are much greater than the temperature difference between the MSTHM and the D/LMTH model. Therefore, with respect to temperature predicted at the center of the repository, conceptual model uncertainty is insignificant.

The difference in relative humidity for a given waste package (e.g., the pwr1-1 waste package) between the second (upper-bound infiltration, high host-rock K_{th}) case and the first (lower-bound infiltration, low host-rock K_{th}) case at the P2WR5C10 location represents the range in that parameter resulting from parametric uncertainty at that location. The difference in relative humidity between the coolest (dhlw-l1) waste package in the second case and the hottest (pwr1-2) waste package in the first case represents the *total* range in relative humidity predicted by the MSTHM at that location. The total relative-humidity range, as well as the range resulting from parametric uncertainty (alone), is determined for the waste package and drift wall,

respectively, as a function of time, and plotted in Figure 7.5-10. Also plotted in Figure 7.5-10 is the absolute difference in relative humidity between the MSTHM and the D/LMTH model for the waste packages at the repository center for case 2 (axial vapor transport along the drift, with a bulkhead at the end of the drift, and low gas-phase dispersivity along the drift). Figure 7.5-10 shows that both the total relative-humidity range and the range in relative humidity resulting from parametric uncertainty (alone) are much greater than the relative-humidity difference between the MSTHM and the D/LMTH model. Therefore, with respect to relative humidity predicted at the center of the repository, conceptual model uncertainty is insignificant.

The difference in liquid-phase saturation for a given waste package (e.g., the pwr1-1 waste package) between the second (upper-bound infiltration, high host-rock K_{th}) case and the first (lower-bound infiltration, low host-rock K_{th}) case at the P2WR5C10 location represents the range in that parameter resulting from parametric uncertainty at that location. The difference in liquid-phase saturation between the coolest (dhlw-l1) waste package in the second case and the hottest (pwr1-2) waste package in the first case at the P2WR5C10 location represents the *total* range of liquid-phase saturation predicted by the MSTHM at that location. The total liquid-phase saturation range, as well as the range resulting from parametric uncertainty (alone), is determined for the drift wall and invert, respectively, as a function of time, and plotted in Figure 7.5-11. Also plotted in Figure 7.5-11 is the absolute difference in liquid-phase saturation between the MSTHM and the D/LMTH model for the waste packages at the repository center for case 2 (axial vapor transport along the drift, with a bulkhead at the end of the drift, and low gas-phase dispersivity along the drift). Figure 7.5-11 shows that the total liquid-phase saturation range is greater than the liquid-phase saturation difference between the MSTHM and the D/LMTH model.

The range in liquid-phase saturation resulting from parametric uncertainty (alone) is greater than the liquid-phase saturation difference between the MSTHM and the D/LMTH model for the majority of the 10,000-yr simulation period. The minor exception to this trend occurs during the brief period that liquid-phase saturation increases steeply with time (e.g., Figure 7.5-4a). Consequently, a small difference in the predicted time required to reach the steep portion of the rewetting curve results in a relatively large difference in liquid-phase. Table 7.5-13 summarizes the time required to attain a liquid-phase saturation value of 0.5 at the drift wall. Table 7.5-13 also lists the range of times (arising from parametric uncertainty) required to attain a liquid-phase saturation value of 0.5 at the drift wall for the P2WR5C10 location. With respect to time to attain a liquid-phase saturation of 0.5, the differences between the MSTHM and the D/LMTH model are much smaller than the range arising from parametric uncertainty. Therefore, the differences between the MSTHM and the D/LMTH model are insignificant compared to the influence of parametric uncertainty. Therefore, with respect to liquid-phase saturation predicted at the center of the repository, conceptual model uncertainty is insignificant. The differences between the MSTHM and the D/LMTH model in the prediction of liquid-phase saturation are further discussed later in this section.
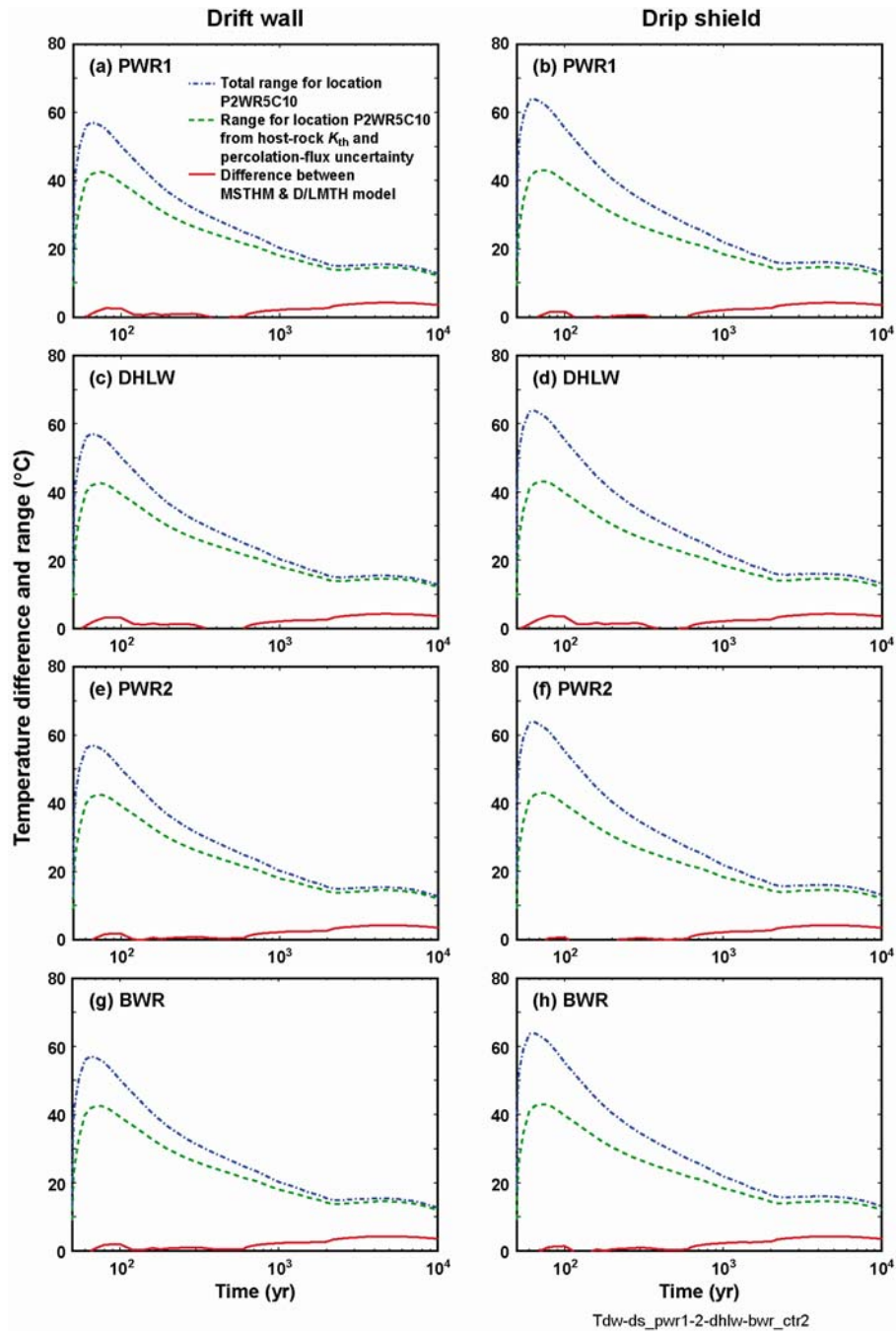
Source: See Table XIII-1.

NOTE: The absolute difference in temperature between the MSTHM and the D/LMTH model is for the case with axial gas- and liquid-phase transport along the drift and low gas-phase dispersivity (see Figure 7.5-2). The total temperature range includes the influences of parametric uncertainty and waste package heat-output variability.

Figure 7.5-9. Absolute Difference (vs. Time) in Drift-Wall and Drip-Shield Temperature between the MSTHM and D/LMTH Model for the (a,b) PWR1, (c,d) DHLW, (e, f) PWR2, and (g, h) BWR Waste Packages at the Center of the Three-Drift Repository Test Case, as Compared with the Range of Temperature Resulting from Parametric Uncertainty, with and without the Influence of Waste-Package Heat-Output Variability, at the P2WR5C10 Location (Figure 6.3-1)

Source: See Table XIII-1.

NOTE: The absolute difference in relative humidity between the MSTHM and the D/LMTH model is for the case with axial gas- and liquid-phase transport along the drift and low gas-phase dispersivity (see Figure 7.5-3). The total relative-humidity range includes the influences of parametric uncertainty and waste package heat-output variability.

Figure 7.5-10. Absolute Difference (vs. Time) in Drift-Wall and Drip-Shield Relative Humidity between the MSTHM and D/LMTH Model for the (a,b) PWR1, (c,d) DHLW, (e, f) PWR2, and (g, h) BWR Waste Packages at the Center of the Three-Drift Repository Test Case, as Compared with the Range of Temperature Resulting from Parametric Uncertainty, with and without the Influence of Waste-Package Heat-Output Variability, at the P2WR5C10 Location (Figure 6.3-1)

Source: See Table XIII-1.

NOTE: The absolute difference in liquid-phase saturation between the MSTHM and the D/LMTH model is for the case with axial gas- and liquid-phase transport along the drift and low gas-phase dispersivity (see Figure 7.5-4). The total relative-humidity range includes the influences of parametric uncertainty and waste package heat-output variability.

Figure 7.5-11. Absolute Difference (vs. Time) in Drift-Wall and Invert Liquid-Phase Saturation between the MSTHM and D/LMTH Model for the (a,b) PWR1, (c,d) DHLW, (e, f) PWR2, and (g, h) BWR Waste Packages at the Center of the Three-Drift Repository Test Case, as Compared with the Range of Temperature Resulting from Parametric Uncertainty, with and without the Influence of Waste-Package Heat-Output Variability, at the P2WR5C10 Location (Figure 6.3-1)

Table 7.5-13. Summary of Time Required to Attain a Liquid-Phase Saturation Value of 0.5 at the Drift Wall for the Waste Packages at the Center of the Three-Drift Repository Test Case, as Compared with the Range Arising from Parametric Uncertainty at the P2WR5C10 Location (Figure 6.3-1)

Waste Package	Time to Attain a Liquid-Phase Saturation of 0.5 for the Three-Drift-Repository Test Case (yr)			Range in Time to Attain a Liquid-Phase Saturation of 0.5 for the P2WR5C10 Location Arising from Parametric Uncertainty (yr)		
	MSTHM	D/LMTH Model	Difference	Minimum	Maximum	Range
PWR1	336.9	300.6	36.3	760.7	3740.4	2979.7
DHLW	283.5	284.2	0.7	203.6	3621.9	3537.0
PWR2	348.1	321.8	26.3	760.7	3740.4	2979.7
BWR	337.7	317.2	20.5	724.1	3708.8	2984.7

Source: DTNs: LL040703223122.050 and LL050500323122.060.

The difference in temperature for a given waste package (e.g., the pwr1-1 waste package) between the first (lower-bound infiltration, low host-rock K_{th}) case and the second (upper-bound infiltration, high host-rock K_{th}) case at the P2ER8C6 location represents the range in that parameter resulting from parametric uncertainty at that location. The difference in temperature between the hottest (pwr1-2) waste package in the first case and coolest (dhlw-l1) waste package in the second case represents the entire range in temperature predicted by the MSTHM at that location. The total temperature range and the range resulting from parametric uncertainty (alone) is determined for the waste package and drift wall, respectively, as a function of time, and plotted in Figure 7.5-12. Also plotted in Figure 7.5-12 is the absolute difference in temperature between the MSTHM and the D/LMTH model for the waste packages at the repository edge for case 3 (axial vapor transport along the drift, with no bulkhead at the end of the drift, and high gas-phase dispersivity along the drift). Figure 7.5-12 shows that the total temperature range and the range in temperature resulting from parametric uncertainty (alone) are much greater than the temperature difference between the MSTHM and the D/LMTH model. Therefore, with respect to temperature predicted at the edge of the repository, conceptual-model uncertainty is insignificant.

The difference in relative humidity for a given waste package (e.g., the pwr1-1 waste package) between the second (upper-bound infiltration, high host-rock K_{th}) case and the first (lower-bound infiltration, low host-rock K_{th}) case at the P2ER8C6 location represents the range in that parameter resulting from parametric uncertainty at that location. The difference in relative humidity between the coolest (dhlw-l1) waste package in the second case and the hottest (pwr1-2) waste package in the first case represents the *total* range in relative humidity predicted by the MSTHM at that location. The total relative-humidity range, as well as the range resulting from parametric uncertainty (alone), is determined for the waste package and drift wall, respectively, as a function of time, and plotted in Figure 7.5-13. Also plotted in Figure 7.5-13 is the absolute difference in relative humidity between the MSTHM and the D/LMTH model for the waste packages at the repository edge for case 3 (axial vapor transport along the drift, with no bulkhead at the end of the drift, and high gas-phase dispersivity along the drift). Figure 7.5-13 shows that the total relative-humidity range and the range in relative humidity resulting from parametric uncertainty are much greater than the relative humidity difference between the

MSTHM and the D/LMTH model. Therefore, with respect to relative humidity predicted at the edge of the repository, conceptual-model uncertainty is insignificant.

The ability of the MSTHM to predict a reasonable range of capillary pressure is supported by virtue of the fact that it is related to relative humidity by the Kelvin law (Equation 7 in Section 6.2.3.1) and because the ability of the MSTHM to predict a reasonable range of relative humidity has been demonstrated.

The difference in liquid-phase saturation for a given waste package (e.g., the pwr1-1 waste package) between the second (upper-bound infiltration, high host-rock K_{th}) case and the first (lower-bound infiltration, low host-rock K_{th}) case at the P2ER8C6 location represents the range in that parameter resulting from parametric uncertainty at that location. The difference in liquid-phase saturation between the coolest (dhlw-l1) waste package in the second case and the hottest (pwr1-2) waste package in the first case at the P2ER8C6 location represents the *total* range of liquid-phase saturation predicted by the MSTHM at that location. The total liquid-phase-saturation range, as well as the range resulting from parametric uncertainty (alone), is determined for both the drift wall and invert, respectively, as a function of time, and plotted in Figure 7.5-14. Also plotted in Figure 7.5-14 is the absolute difference in liquid-phase-saturation between the MSTHM and the D/LMTH model for the waste packages at the repository edge for case 3 (axial vapor transport along the drift, with no bulkhead at the end of the drift, and high gas-phase dispersivity along the drift). With the exception of the cool DHLW waste package, which is where preferential condensation resulting from the cold-trap effect occurs, the total liquid-phase saturation range is greater than the liquid-phase saturation difference between the MSTHM and the D/LMTH model (Figure 7.5-14). With the exception of the cool DHLW waste package, the range in liquid-phase saturation resulting from parametric uncertainty (alone) is greater than the liquid-phase saturation difference between the MSTHM and the D/LMTH model for the majority of the 10,000-year simulation period.

The above-mentioned exception for the cool DHLW waste package occurs during the brief period that liquid-phase saturation increases steeply with time (e.g., Figure 7.5-7a). Consequently, a small difference in the predicted time required to reach the steep portion of the rewetting curve results in a relatively large difference in liquid-phase saturation. The model validation criterion applicable to Section 7.5 is specified in the governing TWP (BSC 2005 [DIRS 173377], Section 2.3.4). The model validation criterion compares the magnitude of the MSTHM-to-D/LMTH-model differences of a particular output parameter (e.g., temperature or relative humidity) to the range in that parameter arising from parametric uncertainty (of percolation flux and host-rock thermal conductivity). For abruptly varying output parameters it is also reasonable to compare the predicted time to a given value of that parameter, as is done in Table 7.5-14, which summarizes the time required to attain a liquid-phase saturation value of 0.5 at the drift wall. Table 7.5-14 also lists the range of times (arising from parametric uncertainty) required to attain a liquid-phase saturation value of 0.5 at the drift wall for the P2ER8C6 location. With respect to time to attain a liquid-phase saturation of 0.5, the differences between the MSTHM and the D/LMTH model are much smaller than the range arising from parametric uncertainty. Therefore, the differences between the MSTHM and the D/LMTH model are insignificant compared to the influence of parametric uncertainty. Therefore, with respect to liquid-phase saturation predicted at the edge of the repository, conceptual-model uncertainty is insignificant.

The above-mentioned exception for the DHLW waste package (Figure 7.5-14d) occurs because water vapor transported from the hotter portion of the drift (closer to the repository center) towards the repository edge preferentially condenses in the invert below this relatively cool waste package. Condensation in the invert causes an increase in liquid-phase saturation, compared to the situation where condensation does not occur. Because this effect occurs at later times when the invert liquid-phase saturation is approaching ambient values (see, for example, Figure 6.3-12), the model-to-model differences in invert liquid-phase saturation are relatively small compared to the magnitude of invert liquid-phase saturation. Therefore, the model-to-model difference in liquid-phase saturation is insignificant.
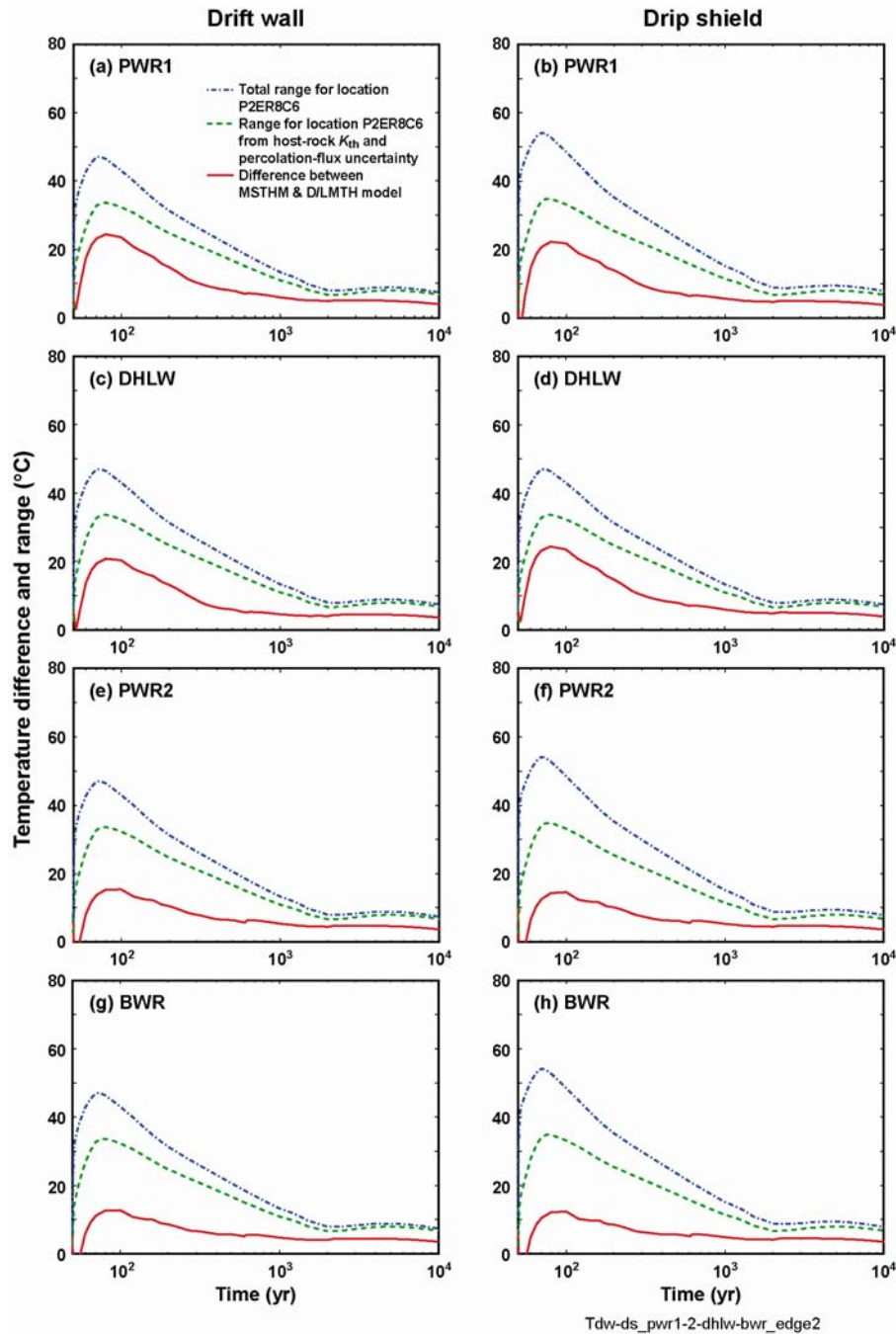
Source: See Table XIII-1.

NOTE: The absolute difference in temperature between the MSTHM and the D/LMTH model is for the case with axial gas- and liquid-phase transport along the drift, no bulkhead, and high gas-phase dispersivity (see Figure 7.5-5). The total temperature range includes the influences of parametric uncertainty and waste package heat-output variability.

Figure 7.5-12. Absolute Difference (vs. Time) in Drift-Wall and Drip-Shield Temperature between the MSTHM and D/LMTH Model for the (a,b) PWR1, (c,d) DHLW, (e, f) PWR2, and (g, h) BWR Waste Packages at the Edge of the Three-Drift Repository Test Case, as Compared with the Range of Temperature Resulting from Parametric Uncertainty, with and without the Influence of Waste Package Heat-Output Variability, at the P2ER8C6 Location (Figure 6.3-1)

Source: See Table XIII-1.

NOTE: The absolute difference in relative humidity between the MSTHM and the D/LMTH model is for the case with axial gas- and liquid-phase transport along the drift, no bulkhead, and high gas-phase dispersivity (see Figure 7.5-6). The total relative-humidity range includes the influences of parametric uncertainty and waste package heat-output variability.

Figure 7.5-13. Absolute Difference (vs. Time) in Drift-Wall and Drip-Shield Relative Humidity between the MSTHM and D/LMTH model for the (a,b) PWR1, (c,d) DHLW, (e, f) PWR2, and (g, h) BWR Waste Packages at the Edge of the Three-Drift Repository Test Case, as Compared with the Range of Temperature Resulting from Parametric Uncertainty, with and without the Influence of Waste Package Heat-Output Variability, at the P2ER8C6 Location (Figure 6.3-1)

Source: See Table XIII-1.

NOTE: The absolute difference in liquid-phase saturation between the MSTHM and the D/LMTH model is for the case with axial gas- and liquid-phase transport along the drift, no bulkhead, and high gas-phase dispersivity (see Figure 7.5-7). The total liquid-phase saturation range includes the influences of parametric uncertainty and waste package heat-output variability.

Figure 7.5-14. Absolute Difference (vs. Time) in Drift-Wall and Invert Liquid-Phase Saturation between the MSTHM and D/LMTH Model for the (a,b) PWR1, (c,d) DHLW, (e, f) PWR2, and (g, h) BWR Waste Packages at the Edge of the Three-Drift Repository Test Case, as Compared with the Range of Temperature Resulting from Parametric Uncertainty, with and without the Influence of Waste Package Heat-Output Variability, at the P2ER8C6 Location (Figure 6.3-1)

Table 7.5-14. Summary of Time Required to Attain a Liquid-Phase Saturation Value of 0.5 at the Drift Wall for the Waste Packages at the Edge of the Three-Drift Repository Test Case, as Compared with the Range Arising from Parametric Uncertainty at the P2ER8C6 Location (Figure 6.3-1)

Waste Package	Time to Attain a Liquid-Phase Saturation of 0.5 for the Three-Drift-Repository Test Case (yr)			Range in Time to Attain a Liquid-Phase Saturation of 0.5 for the P2WR5C10 Location Arising from Parametric Uncertainty (yr)		
	MSTHM	D/LMTH Model	Difference	Minimum	Maximum	Range
PWR1	273.8	225.0	48.8	471.0	1560.4	1089.4
DHLW	249.2	219.9	29.3	184.5	1480.4	1295.9
PWR2	287.9	316.8	28.9	471.0	1560.4	1089.4
BWR	274.2	342.4	68.2	384.8	1529.7	1144.9

Source: DTNs:LL040703223122.050 and LL050500323122.060.

As, discussed earlier, Figures 7.5-11 and 7.5-14 exhibit a brief period when the absolute difference in drift-wall liquid-phase saturation between the MSTHM and D/LMTH model abruptly increases and decreases. This abrupt rise and fall in the absolute difference in drift-wall liquid-phase saturation corresponds to the period of time that the drift-wall liquid-phase saturation is abruptly increasing (Figures 7.5-4 and 7.5-7). All of the other thermal-hydrologic variables experience more gradual changes and therefore do not show an abrupt increase in absolute differences between the MSTHM and D/LMTH model. For example, relative humidity (Figures 7.5-3 and 7.5-6) experiences a more gradual increase during the rewetting period; consequently, the absolute difference in relative humidity (Figures 7.5-10 and 7.5-13) exhibit a gradual increase and decrease.

To further illustrate why the absolute difference (between the MSTHM and D/LMTH model) in drift–wall relative humidity does not (qualitatively) exhibit the same behavior as the absolute difference in drift-wall liquid-phase saturation, it is useful to plot relative humidity as a function of liquid-phase saturation in the rock matrix at the crown of the drift, as is done in Figure 7.5-15. Over the liquid-phase saturation range of 0.2 to 0.3, drift-wall relative humidity increases steeply (from about 20 to 90 percent) as a function of drift-wall liquid-phase saturation in the matrix. Above a liquid-phase saturation value of about 0.3, relative humidity increases more gradually as a function of liquid-phase saturation, with relative humidity reaching 99 percent at a liquid-phase saturation of 0.5. Drift-wall relative humidity increases gradually during the dryout period (which is the period when drift-wall saturation slowly increases over the range of 0.2 to 0.3). Drift-wall relative humidity reaches a value of about 90 percent prior to the period when drift-wall liquid-phase saturation increases abruptly as a function of time. Consequently, the small difference (between the MSTHM and D/LMTH model) in the predicted time required to reach the period of abrupt drift-wall liquid-phase saturation increase has little affect on the corresponding drift-wall relative humidity history.

Also of interest is onset of the post-closure period when the drift-wall liquid-phase saturation and relative humidity for case 3 in the D/LMTH model is briefly lower than in the MSTHM model for the waste packages at the repository edge (Figures 7.5-6 and 7.5-7). Recall that in the D/LMTH model, case 3 includes the influence of rock dryout during the ventilation period. Consequently, drift-wall liquid-phase saturation is about 0.2 at the onset of the post-closure

period. Recall also that the MSTHM does not include the influence of rock dryout during the ventilation period. Consequently, the MSTHM-predicted drift-wall liquid-phase saturation is above 0.9 at the onset of the post-closure period. After ventilation ceases and host-rock temperatures rapidly increase to above the boiling point, rock dryout causes a rapid decrease in drift-wall liquid-phase saturation, causing the absolute difference in drift-wall liquid-phase saturation (between the MSTHM and D/LMTH model) to abruptly decrease to a small value (Figure 7.5-14). Because the drift-wall relative humidity is directly related to the drift-wall liquid-phase saturation, the MSTHM-predicted drift-wall relative humidity is greater than that predicted by the D/LMTH model (Figure 7.5-6). Consequently, this causes the absolute difference in drift-wall relative humidity (between the MSTHM and D/LMTH model) to be large at the onset of the post-closure period and then abruptly decrease to a small value (Figure 7.5-13), just as occurs for the drift-wall liquid-phase saturation (Figure 7.5-14).
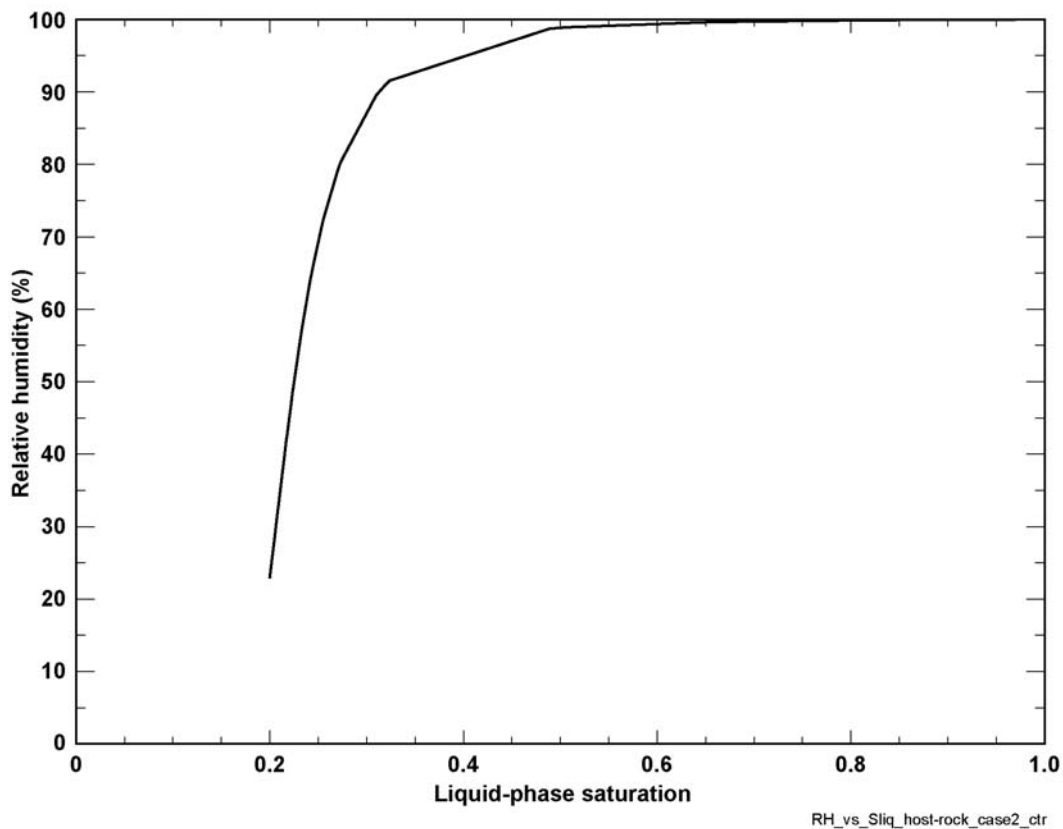
Source: See Table XIII-1.

NOTE: The relative humidity versus liquid-phase saturation relationship is plotted in the host rock at the drift crown above the PWR1 waste package for case 2, which has gas- and liquid-phase transport along the drift and low gas-phase dispersivity. This plot corresponds to Figures 7.5-3a and 7.5-4a.

Figure 7.5-15. Relative Humidity versus Liquid-Phase Saturation in the Matrix in the Host Rock at the Crown of the Drift for the P2W5C10 Location (Figure 6.3-1)

7.6 COMPARISON OF THE MSTHM-PREDICTED IN-DRIFT TEMPERATURE DIFFERENCES AGAINST THOSE PREDICTED BY THE FLUENT CODE

Thermal-hydrologic conditions within emplacement drifts depend primarily on thermal-hydrologic conditions in the host rock at the drift wall and on the temperature difference between the drift wall and the drip-shield and waste-package surfaces. Thus, the ability to predict a reasonable range of relevant in-drift MSTHM output parameters (e.g., temperature and relative humidity) are based on valid predictions of thermal-hydrologic processes in the host rock, as well as valid predictions of heat-transfer processes between the drift wall, drip-shield, and waste-package surfaces. The purpose of this section is to demonstrate that MSTHM-predicted in-drift temperature differences are based upon a valid representation of heat-transfer processes between the drift wall, drip-shield, and waste-package surfaces. To support this validation effort, MSTHM-predicted in-drift temperature differences are compared against those predicted by a two-dimensional FLUENT-code model of a waste package, drip shield, and emplacement drift, which are used to support model validation for In-Drift Natural Convection and Condensation (BSC 2004 [DIRS 164327], Appendix J). The two-dimensional FLUENT calculations apply line-averaged lineal power densities of 157.8, 67.7, 28.7, and 17.1 W/m at 300, 1000, 3000, and 10,000 years, respectively. For comparison purposes, the bwr1-1 waste package in the MSTHM is chosen because its heat output, averaged over its length, results in lineal power densities of 152, 67.7, 30.5, and 17.9 W/m at 300, 1000, 3000, and 10,000 years, respectively, which corresponds closely with the values applied in the two-dimensional FLUENT model. The MSTHM results pertain to the P2WR5C10 location (Figure 6.3-1) for the mean infiltration case with mean host-rock thermal conductivity (Figure 6.3-14 and Table 6.3-14). Table 7.6-1 summarizes the comparison between the bwr1-1 waste package in the MSTHM and the FLUENT calculations.

Table 7.6-1. Comparison of MSTHM-Predicted and FLUENT-Model-Predicted In-Drift Temperature Differences between the Drift Wall, Drip Shield, and Waste-Package Surfaces

Time (years)	Waste-Package-to-Drift-Wall Temperature Difference $\Delta T_{\text{wp-dw}}$ (°C)		Waste-Package-to-Drip-Shield Temperature Difference $\Delta T_{\text{wp-ds}}$ (°C)		Drip-Shield-to-Drift-Wall Temperature Difference $\Delta T_{\text{ds-dw}}$ (°C)	
	MSTHM	FLUENT	MSTHM	FLUENT	MSTHM	FLUENT
300	9.0	7.2	4.0	4.2	5.0	3.0
1000	4.0	3.4	1.9	2.0	2.1	1.4
3000	1.9	1.5	1.0	0.9	0.9	0.6
10,000	1.3	0.9	0.7	0.5	0.6	0.4

Source: See Table XIII-2.

NOTE: The MSTHM-predicted temperature differences are for the bwr1-1 waste package (Table 6.3-13) at the P2WR5C10 location (Figure 6.3-1) and are for the mean infiltration-flux case with mean host-rock thermal conductivity. The FLUENT-model-predicted temperature differences are for a line-averaged lineal power density.

As shown in Table 7.6-1, the MSTHM- and FLUENT-predicted in-drift temperature differences compare reasonably well. The differences between the two models primarily are related to the differences in their respective dimensionality. Although the bwr1-1 waste package in the MSTHM has an average lineal power density (averaged over its own length) that is similar to that used in the FLUENT model, its local heating conditions are also influenced by its neighboring waste packages, which are the pwr2-1 and bwr2-1 waste packages listed in Table

6.3-13. Taking a three-waste-package average, the local initial lineal power density for the bwr1-1 waste package is 1.66 kW/m, which is 15 percent greater than the value used in the two-dimensional FLUENT model. Accordingly, the drip-shield-to-drift-wall temperature differences (and the waste-package-to-drift-wall temperature differences) predicted by the MSTHM are greater than those predicted by the FLUENT model (Table 7.6-1). It is worth noting that the waste-package-to-drip-shield temperature differences predicted by the respective models are in close agreement. This close agreement is related to small gap between the waste package and drip shield, compared to the larger gap between the drip shield and drift wall (see Figure 6.2-1). Thermal radiation between two surfaces depends on the incidence angle, with the efficiency of thermal-radiative heat transfer decreasing with increasing incidence angle. Consequently, below the drip shield it is more difficult for waste packages to share heat in the longitudinal direction than it is above the drip shield. Thus, the drip-shield-to-drift-wall temperature difference is influenced by a given waste package and its two neighboring waste packages, while the waste-package-to-drip-shield temperature difference is primarily influenced by the heating from a given waste package, with little influence from its neighboring waste packages.

It is useful to compare the FLUENT-predicted in-drift temperature differences to the range of in-drift temperature differences predicted for all waste packages in the MSTHM, which is summarized in Table 7.6-2. The minimum in-drift temperature differences pertain to the coolest (dhlw-l1) waste package, while the maximum in-drift temperature differences pertain to the hottest (pwr1-2) waste package. A comparison of the FLUENT-predicted values in Table 7.6-1 to the range of MSTHM-predicted values in Table 7.6-2 shows that the FLUENT-predicted values are close to the middle of the range for the MSTHM-predicted values. Therefore, the in-drift temperature differences predicted by the MSTHM are in reasonable agreement with those predicted by the FLUENT model, demonstrating the MSTHM provides a valid representation of in-drift heat transfer, and thereby predicts a reasonable range of in-drift temperature differences.

Table 7.6-2. Range of MSTHM-Predicted In-Drift Temperature Differences between the Drift Wall, Drip Shield, and Waste-Package Surfaces

Time (years)	Waste-Package-to-Drift-Wall Temperature Difference ΔT_{wp-dw} (°C)		Waste-Package-to-Drip-Shield Temperature Difference ΔT_{wp-ds} (°C)		Drip-Shield-to-Drift-Wall Temperature Difference ΔT_{ds-dw} (°C)	
	Minimum	Maximum	Minimum	Maximum	Minimum	Maximum
300	3.4	12.1	0.4	6.3	3.0	5.8
1000	1.4	5.3	0.2	2.9	1.2	2.4
3000	0.5	2.4	0.1	1.4	0.4	1.0
10,000	0.4	1.6	0.1	0.9	0.3	0.7

Source: See Table XIII-2.

NOTE: The MSTHM-predicted temperature differences pertain to the P2WR5C10 location (Figure 6.3-1) and are for the mean infiltration-flux case with mean host-rock thermal conductivity. The minimum and maximum values of ΔT are for the dhlw-l1 and pwr1-2 waste packages, respectively.

7.7 VALIDATION SUMMARY

The intended purpose of the MSTHM, including how its output parameters are used in TSPA-LA, plays a key role in its validation, and in its confidence building. The intended purpose of the MSTHM is to predict a reasonable range of possible thermal-hydrologic conditions within the emplacement drift. To be reasonable, this range includes the influence of waste-package-to-waste-package heat output variability relevant to the license application design, as well as the influence of uncertainty and variability in the geologic and hydrologic conditions relevant to predicting the thermal-hydrologic response in emplacement drifts. This goal is quite different from the goal of a model to predict a single expected thermal-hydrologic response. As a result, the development and validation of the MSTHM and the associated analyses using this model are focused on the goal of predicting a reasonable range of thermal-hydrologic conditions resulting from parametric uncertainty and waste-package-to-waste-package heat-output variability. The governing technical work plan (BSC 2005 [DIRS 173377], Section 2.3.2) identifies Level I as the appropriate level of validation for the MSTHM.

The validation activities documented in Sections 7.4 and 7.5 are satisfactory for the intended purpose of the MSTHM and for the required level of confidence. For predicting a reasonable range of temperature and liquid-phase saturation, model confidence building is also supported in Section 7.3. Table 1-1 lists all relevant MSTHM output parameters used to support TSPA-LA. Table 1-1 also references where model validation and confidence building in support of the prediction of a reasonable range of relevant MSTHRM output parameters is documented in this report.

Thermal-hydrologic conditions within emplacement drifts depend primarily on thermal-hydrologic conditions in the host rock at the drift wall and on the temperature difference between the drift wall and the drip-shield and waste-package surfaces. Thus, the ability to predict a reasonable range of relevant in-drift MSTHM output parameters (e.g., temperature and relative humidity) are based on valid predictions of thermal-hydrologic processes in the host rock, as well as valid predictions of heat-transfer processes between the drift wall and the drip-shield and waste-package surfaces. Because the invert contains crushed gravel derived from the host rock, the invert is, in effect, an extension of the host rock, with thermal and hydrologic properties that have been modified by virtue of the crushing (and the resulting geometry of the gravel grains). Thus, given reasonable invert properties are applied, the ability to predict a reasonable range of relevant MSTHM output parameters for the invert are based on valid predictions of thermal-hydrologic processes in the host rock. Section 6.3.11 discusses the sensitivity analyses of the influence of intergranular and intragranular invert hydrologic properties on predicted thermal-hydrologic conditions in the invert. Thermal-hydrologic conditions in the invert are found to be insensitive to a wide range of hydrologic property values (as shown in Figures 6.3-63 and 6.3-65), demonstrating that uncertainty and variability of invert hydrologic properties have an insignificant influence on MSTHM output parameters for the invert. Therefore, reasonable invert hydrologic properties are applied to the MSTHM, resulting in a reasonable range of relevant MSTHM output parameters for the invert.

The following is a list of the eight different MSTHM output parameters used in TSPA-LA:

1. Drift-wall temperature

2. Drip-shield temperature

3. Waste-package temperature

4. Invert temperature

5. Waste-package relative humidity

6. Invert relative humidity

7. Invert liquid-phase saturation

8. Invert liquid-phase flux.

The ability of the MSTHM to predict a reasonable range of temperatures for the drift wall, drip shield, waste package, and invert (items 1, 2, 3, and 4) is supported in Section 7.5 by virtue of direct comparisons between temperatures predicted by the MSTHM and those predicted by a corresponding three-dimensional monolithic thermal-hydrologic model for a three-drift validation test case. Section 7.4, which documents the comparison of NUFT-predicted temperatures against those measured in the Drift Scale Test, supports the ability of the MSTHM to predict a reasonable range of temperatures in the host rock. Section 7.6, which documents a comparison of the MSTHM-predicted in-drift temperature differences against those predicted by the FLUENT model, supports the ability of the MSTHM to predict temperature differences between the drift wall and the drip-shield and waste-package surfaces. Model confidence building for the ability of the MSTHM to predict a reasonable range of temperatures in the host rock is supported in Section 7.3, which documents the comparison of NUFT-predicted temperatures against those measured in the Large Block Test.

The ability of the MSTHM to predict a reasonable range of relative-humidity values for the waste package and invert (items 5 and 6) is supported in Section 7.5 by virtue of direct comparisons between values predicted by the MSTHM and those predicted by a corresponding three-dimensional monolithic thermal-hydrologic model for a three-drift validation test case. Section 7.4, which documents the comparison of NUFT-predicted liquid-phase saturations against those measured in the Drift Scale Test, along with the relationship between liquid-phase saturation and relative humidity, also supports the ability of the MSTHM to predict a reasonable range of relative humidity values in the host rock. Section 7.6, which supports the ability of the MSTHM to predict temperature differences between the drift wall and the drip-shield and waste package surfaces, along with the relationship between in-drift temperature-differences and in-drift relative-humidity differences (Eq. 24), supports the ability of the MSTHM to predict a reasonable range of relative humidity on the drip-shield and waste-package surfaces.

The ability of the MSTHM to predict a reasonable range of liquid-phase saturation values for the invert (item 7) is supported in Section 7.5 by virtue of a direct comparison between values predicted by the MSTHM and those predicted by a corresponding three-dimensional monolithic thermal-hydrologic model for a three-drift validation test case. Section 7.4, which documents the

comparison of NUFT-predicted liquid-phase saturations against those measured in the Drift Scale Test also supports the ability of the MSTHM to predict a reasonable range of liquid-phase saturation in the invert.

The ability of the MSTHM to predict a reasonable range of liquid-phase flux values for the invert (item 8) is supported by virtue of the relationship between liquid-phase flux and liquid-phase saturation, which is documented in Section 6.3.3, in conjunction with demonstrated ability of the MSTHM to predict a reasonable range of liquid-phase saturation, which is documented in Section 7.5. (Note that for TSPA-LA, the MSTHM-predicted liquid-phase flux is only applied to waste packages that experience no seepage and no condensation.)

Thus, as is shown in Table 1-1, all MSTHM output parameters used by TSPA-LA are supported by model validation and by model confidence building, which are documented in this report. The ability to predict a reasonable range of other MSTHM output parameters that are not used in TSPA-LA is also supported by model validation and confidence building activities in this report. For example, the ability of the MSTHM to predict a reasonable range of capillary-pressure values is supported by virtue of the fact that it is related to relative humidity by the Kelvin law (Equation 7 in Section 6.2.3.1) and because the demonstrated ability of the MSTHM to predict a reasonable range of relative-humidity values, which is documented in Sections 7.4 and 7.5. The ability of the MSTHM to predict a reasonable range of gas-phase air-mass fraction values in the drift is supported by virtue of the relationship between gas-phase air-mass fraction and relative humidity and temperature (through the ideal gas law), which are both supported by model validation activities documented in Sections 7.4 and 7.5.

The MSTHM has been validated by applying acceptance criteria, which are based on evaluation of the model's relative importance to the performance of the repository system. All validation requirements defined in the governing TWP (BSC 2005 [DIRS 173377], Section 2.3.4) have been fulfilled, including corroboration of model results with experimental data (Section 7.4) and corroboration with an alternative mathematical model (Section 7.5). Requirements for confidence building during model development have also been satisfied. The model development activities and post-development validation activities described in Section 7.1 of this report establish the scientific bases for the MSTHM. Based on this, the MSTHM is sufficiently accurate and adequate for the intended purpose, consistent with the level of confidence required by the model's relative importance to the performance of the repository system.

8. CONCLUSIONS

8.1 ANALYSIS AND MODELING CONCLUSIONS

This model report documents the multiscale thermohydrologic model (MSTHM). An important phenomenological consideration for the licensing of the repository at Yucca Mountain is the generation of decay heat by the emplaced waste and the thermal-hydrologic consequences of this decay heat. A thermal-hydrologic modeling tool is developed and used to support the performance assessment of the engineered barrier system of the repository. This modeling tool simultaneously accounts for processes occurring at a scale of a few tens of centimeters around individual waste packages, for processes occurring around the emplacement drifts themselves, and for processes occurring at the mountain scale. Additionally, many other features are considered including nonisothermal, multiphase-flow in fractured porous rock of variable liquid-phase saturation and thermal radiation and convection in open cavities.

The MSTHM calculates the following thermal-hydrologic parameters: temperature, relative humidity, liquid-phase saturation, evaporation rate, air-mass fraction, gas-phase pressure, capillary pressure, and liquid- and gas-phase fluxes. The thermal-hydrologic parameters are determined as functions of position along each of the emplacement drifts in the repository and as functions of waste package type. These parameters are determined at various reference locations within the emplacement drifts, including the waste package and drip-shield surfaces and in the invert. They are also determined at various reference locations in the adjoining host rock; these parameters are determined every 20 m for each emplacement drift in the repository. Each emplacement drift is represented with its precise coordinate location, as well as each of the emplacement panels in the repository area (Figure 4-1). The MSTHM also accounts for ventilation during the preclosure period, including how heat-removal efficiency from drift ventilation varies as a function of time and distance along each of the emplacement drifts. The MSTHM accounts for three-dimensional drift-scale and mountain-scale heat flow. The MSTHM captures the influence of the key engineering-design parameters and natural system factors affecting thermal-hydrologic conditions in the emplacement drifts and adjoining host rock, including:

- Repository-scale variability of percolation flux above the repository
- Temporal variability of percolation flux (as influenced by climate change)
- Uncertainty in percolation flux (as addressed by the lower-bound, mean, and upper-bound infiltration-flux cases)
- Uncertainty in percolation flux (associated with infiltration estimates, flow focusing, and flow diversion by the rock layers overlying the repository)
- Stratigraphic variation of thermal conductivity
- Uncertainty in host-rock thermal conductivity of the host rock
- Stratigraphic variation of bulk rock density and specific heat
- Stratigraphic variation of hydrologic properties of the rock matrix
- Stratigraphic variation of hydrologic properties of fractures

- Variability in overburden thickness

- Overall areal heat-generation density of the waste inventory, quantified by the Areal Mass Loading (AML, expressed in MTU/acre)

- Line-averaged thermal load along emplacement drifts, quantified by the Lineal Power Density (LPD, expressed in kW/m)

- Distance between emplacement drifts (also called drift spacing)

- Age of spent-nuclear fuel at time of emplacement

- Repository footprint shape, which influences the evolution of the edge-cooling effect that increases with proximity to the repository edges

- Dimensions of the in-drift design (waste packages, drip shield, and invert)

- Properties of the in-drift engineered barrier system components

- Waste package spacing along the drift (line-load versus point-load spacing)

- Waste package sequencing (particularly with respect to the heat output from the respective waste package types)

- Time- and distance-dependent heat-removal efficiency of preclosure drift ventilation.

This report describes MSTHM calculations conducted to support the Total System Performance Assessment for the License Application (TSPA-LA). The MSTHM simulations are conducted for three infiltration-flux cases (lower-bound, mean, and upper-bound). The impact of parametric uncertainty of the key input parameters, percolation flux and host-rock thermal conductivity, is also addressed. Percolation flux and host-rock thermal conductivity are the two most important natural system parameters influencing peak temperatures and the time that the drift wall remains above the boiling point. It is found that the combined influence of percolation-flux uncertainty and host-rock thermal conductivity uncertainty on peak temperatures is represented by the sum of the individual contributions to peak-temperature uncertainty. It is also found that the combined influence of percolation-flux uncertainty and host-rock thermal conductivity on the duration of boiling at the drift wall is represented by the sum of the individual contributions to drift-wall-boiling-duration uncertainty. These conclusions are consistent with the approach used for abstraction of MSTHM results, with uncertainty, for TSPA-LA.

8.2 MODEL VALIDATION, UNCERTAINTIES, AND LIMITATIONS

This report documents decisions implemented during model development that build confidence and verify that a reasonable, credible technical approach using scientific and engineering principles was taken in order to:

- Evaluate and select inputs

- Formulate defensible assumptions

- Ensure consistency with physical principles

- Represent important uncertainties

- Ensure that MSTHM predictions represent the range of possible outcomes, consistent with important processes, variabilities, and uncertainties.

The intended purpose of the MSTHM, including how its output parameters are used in TSPA-LA, plays a key role in its validation, and in its confidence building. The governing technical work plan (BSC 2005 [DIRS 173377], Section 2.3.2) identifies Level I as the appropriate level of validation for the MSTHM. The validation activities documented in Sections 7.4 and 7.5 are satisfactory for the intended purpose of the MSTHM and for the required level of confidence. Sections 6.3.3 and 7.3 also support model confidence building.

For the purpose of confidence building and model validation, results from the MSTHM are compared against those from a mountain-scale thermal-hydrologic model, which is an alternative conceptual model (Section 6.4). Validation of the MSTHM is also supported by using results from field-scale thermal tests and using a monolithic thermal-hydrologic model of a three-drift repository test case, which is a scaled-down example of the actual repository (Section 7.5). The following discussion summarizes results using the Large Block Test (LBT) and Drift Scale Test (DST), and the three-drift repository test case.

Three-dimensional NUFT thermohydrologic-model simulations are compared with temperatures and liquid-phase saturations measured in the Large Block Test (LBT). The NUFT thermal-hydrologic model used in this confidence-building study is a three-dimensional equivalent to the two-dimensional LDTH submodels (Section 6.2.6) used in the MSTHM. The good agreement between the simulated and measured temperatures in the LBT builds confidence that the NUFT model provides a valid representation of heat flow in partially saturated fractured porous rock. Good agreement between the simulated and measured dryout and rewetting behavior in the LBT demonstrates that the NUFT thermal-hydrologic simulations provide valid representation of dryout and rewetting behavior in partially saturated fractured porous rock.

Three-dimensional NUFT thermal-hydrologic simulations are also compared with temperatures and liquid-phase saturations measured in the Drift Scale Test (DST). Note that the thermal-hydrologic model of the DST is a three-dimensional equivalent to the two-dimensional LDTH submodels (Section 6.2.6) used in the MSTHM. Overall agreement was achieved between simulated and measured temperatures. Simulated temperatures exhibit less of a distinctive plateau close to 96°C than the measured temperatures. This effect is associated with the use of the calibrated hydrologic property set and the low value of matrix permeability, which causes a large gas-phase pressure buildup in the matrix that increases the saturation (boiling) temperature and temporarily throttles (i.e., restricts) vaporization and delays rock dryout. Higher saturation (boiling) temperatures and lack of a temperature plateau close to 96°C cause simulated temperatures to be higher than measured temperatures for the above-boiling region. Results from Section 7.4.4 of *Drift-Scale Coupled Processes (DST and TH Seepage) Models* (BSC 2004 [DIRS 170338]) show that when the site-specific property set is used, this transient throttling effect does not occur and better agreement is obtained between simulated and measured temperatures in the above-boiling region.

Another reason for the NUFT-simulated temperatures being higher than measured temperatures is the uncertainty in host-rock thermal conductivity K_{th} at the DST location. For the high-K_{th}

case (one standard deviation above the mean), simulated temperatures are in better agreement with the measured temperatures than the cases that used the mean K_{th} values. Because percolation fluxes cannot be directly measured, uncertainty in the local percolation flux in the DST area also contributes to differences between simulated and measured temperatures. Section 6.3.4 discusses the influence of key parametric uncertainties on predicted thermal-hydrologic conditions in the repository. Figures 7.5-9 and 7.5-12 show that the combined influence of host-rock percolation-flux and thermal conductivity uncertainties results in peak drift-wall temperatures varying by 35 to 43°C. The 30-percent validation criterion for temperature rise (above ambient), which is given in the TWP, is consistent with the magnitude of the influence of the parametric uncertainty of host-rock thermal conductivity and percolation flux on temperature. As indicated by comparing the lower bound-infiltration-flux low K_{th} case with the upper-bound infiltration-flux high K_{th} case in Table 6.3-38, the combined influence of host-rock thermal conductivity uncertainty and percolation-flux uncertainty causes the rise in peak drift-wall temperature (above ambient) to vary by about 30 percent. For temperatures less than about 80°C, simulated and measured temperatures are in good agreement for all three cases considered: (1) base case, (2) sealed bulkhead, and (3) high K_{th}.

With a few exceptions, the differences between the NUFT-simulated and measured temperature increases above ambient temperatures are less than 30 percent, thereby satisfying one part of the validation criterion for the DST comparison. The few exceptions are associated with the use of the calibrated hydrologic property set and the low value of matrix permeability, which results in a large gas-phase pressure buildup in the matrix that increases the saturation (boiling) temperature. It is important to note that this transient throttling effect dissipates as the NUFT-simulated gas-phase pressure buildup declines. Heating conditions for the DST result in an accelerated temperature increase, compared to that predicted for repository heating conditions. Thus, although matrix permeability is seen to have a noticeable affect on temperatures simulated for the DST, it does not significantly affect repository temperature evolution predicted by thermal-hydrologic models supporting TSPA-LA. Overall, the comparison of NUFT-simulated and measured temperatures demonstrates that the NUFT thermal-hydrologic model provides a valid representation of heat flow in the DST.

Although the NUFT-simulated dryout behavior (as measured by the liquid-phase saturation in the matrix continuum) lagged behind that observed in the DST, this is a transient effect. Heating conditions for the DST result in an accelerated temperature rise and dryout, compared to those predicted for repository heating conditions. Although the NUFT-simulated dryout lags behind the DST-observed dryout, this is not important to the application of the MSTHM for post-closure repository predictions. This is because predicted rock dryout for repository heating conditions is slower, occurring over much longer time frames than applicable to the DST. Within four years, the DST-observed rock dryout approaches the NUFT-simulated dryout, which satisfies the validation criterion for the DST comparison. Therefore, it can be concluded that the NUFT thermal-hydrologic model provides a valid representation of rock dryout in the DST and that the MSTHM provides valid predictions of post-closure dryout. To the extent that the observations in the DST allow, the NUFT thermal-hydrologic model provides a valid representation of rewetting behavior in the DST.

Another conclusion from the DST model validation study is that the sealed-bulkhead case results in slightly higher NUFT-simulated temperatures than the base case (which had a leaky bulkhead). The influence of the leaky bulkhead on simulated temperatures is less than that

resulting from a one standard-deviation estimated range in thermal conductivity. This conclusion is useful with respect to the potential significance of whether the ends of the emplacement drifts are sealed with bulkheads or simply backfilled with highly permeable crushed tuff. The lack of sensitivity of the DST thermal-hydrologic simulations to the treatment of the bulkhead (leaky versus sealed) suggests that the MSTHM predictions of thermal-hydrologic response in the emplacement drifts is not significantly affected by whether the ends of the emplacement drifts are sealed.

Validation of the MSTHM methodology itself involves a three-drift repository test case. This test case represents a scaled-down repository, consisting of three 243-m long drifts. A monolithic three-dimensional thermal-hydrologic model of this three-drift repository test case discretely represents 15 waste packages: 7 at the center of the central drift and 4 at either end of the central drift. The MSTHM and the monolithic thermal-hydrologic model predict almost identical thermal-hydrologic conditions at all waste package locations at the center of the three-drift repository test case. At the edge of the three-drift repository test case, the MSTHM and monolithic thermal-hydrologic model also predict similar conditions. Differences between the two models are largest for the last two waste packages at the edge, where the MSTHM predicts peak temperatures that are about 17°C higher than predicted in the monolithic thermal-hydrologic model. Note that the outermost two waste packages cover only 1.6 percent of the repository area. For the third and fourth waste package in from the repository edge, the MSTHM predicts peak temperatures that are about 6 to 8°C higher than predicted in the monolithic thermal-hydrologic model. For waste packages located more than 20 m from the repository edge, which encompasses 96.8 percent of the repository area, the bias in peak temperatures predicted by the MSTHM is less than about 6°C. However, because all of the differences are within the range of those caused by parametric uncertainty (see Figure 7.5-12), the MSTHM satisfies the validation criterion for this comparison and is suitable for predicting thermal-hydrologic conditions for all waste package locations.

The propagation of parametric uncertainty in the MSTHM addresses the two key natural system parameters: host-rock thermal conductivity and percolation flux. A sensitivity study of the influence of hydrologic-property uncertainty supports the conclusion that hydrologic-property uncertainty does not need to be propagated in the MSTHM calculations of in-drift temperature and relative humidity. Propagation of percolation-flux and host-rock thermal conductivity uncertainty in repository-wide MSTHM output is addressed with the following five (infiltration-flux host-rock thermal conductivity) cases:

- Lower-bound infiltration-flux case with low (mean minus one standard deviation) host-rock thermal conductivity

- Lower-bound infiltration-flux case with mean host-rock thermal conductivity

- Mean infiltration-flux case with mean host-rock thermal conductivity

- Upper-bound infiltration-flux case with mean host-rock thermal conductivity

- Upper-bound infiltration-flux case with high (mean plus one standard deviation) host-rock thermal conductivity

For these five cases, the range in peak drift-wall temperature is from 92°C to 175°C, with a median drift-wall temperature of 133°C; the range in peak waste package temperature is from 102°C to 203°C, with a median waste package temperature of 153°C (Table 6.3-38). These five cases also result in a wide range of waste package relative-humidity histories as is shown in Figure 6.3-53.

Another thermal-hydrologic parameter is the time when boiling ceases at the drift wall. For the five infiltration-flux host-rock thermal conductivity cases, the time when drift-wall boiling ceases ranges from no boiling to 2,177 years, with a median time of 721 years (Table 6.3-39). The percentage of waste packages that may experience no boiling at the drift wall is low (0.1% of all waste packages).

Another thermal-hydrologic parameter of interest is the maximum lateral extent of the boiling zone relative to the centerline of the emplacement drifts because this indicates the likelihood of condensate and percolation flux drainage around emplacement drifts during the dryout period. For the five infiltration-flux host-rock thermal conductivity cases, the maximum lateral extent of boiling ranges from 4.1 to 27.9 m, with a median maximum lateral extent of 7.9 m (Table 6.3-40). The lowest end of this range (4.1 m) pertains to the situation where boiling only occurs within the emplacement drift (i.e., not at the drift wall). For the majority of cases the lateral extent of boiling is much smaller than the half spacing between emplacement drifts. Therefore, the majority of the host rock between emplacement drifts always remains below the boiling point, thereby enabling condensate and percolation flux to continuously drain between emplacement drifts. Because of the continuous drainage of condensate around a dryout zone of limited extent, condensate above the emplacement drifts is limited.

8.3   MODEL OUTPUTS

The MSTHM output parameters supplied to TSPA are summarized in Table 1-1. For each SMT submodel location (2,874 locations distributed over the repository area, which is shown in Figure 6.2-3), bin indices are calculated based on the rank order of the percolation flux associated with the location. Bin 1 includes the 5 percent of locations with the smallest percolation flux. Bin 2 includes locations with percolation fluxes in the 5th to 30th percentile. Bin 3 includes locations with percolation fluxes in the 30th to 70th percentile. Bin 4 includes locations with percolation fluxes in the 70th to 95th percentile. Bin 5 includes locations with percolation fluxes above the 95th percentile. Note that the binning is based solely on the percolation fluxes for the glacial-transition climate of the mean infiltration-flux case. Moreover, the lower- and upper-bound infiltration-flux cases share the same areal binning as that determined for the mean infiltration-flux case.

MSTHAC v7.0 calculations are performed at all 2,874 SMT submodel locations, and the output from these calculations are postprocessed and written in a format required to satisfy TSPA parameter requirements. Two sets of information are generated for the MSTHM output-parameter DTNs. The first set, which is called the "WAPDEG binning" set (BSC 2004 [DIRS 169996]), includes limited output parameters at every SMT submodel location and for each of the two waste package groups, including commercial spent nuclear fuel (CSNF) and defense high-level waste (DHLW). The second set, which is called the "TSPA binning" set, includes complete output variable information for only typical bin locations and for typical waste packages (with respect to temperature and relative humidity histories) for each of the two waste

package groups (CSNF and DHLW). Note that the waste package degradation (WAPDEG) analysis is downstream of the MSTHM (with respect to model-to-model parameter flow) and directly uses MSTHM output parameters.

For seepage modeling and engineered barrier system performance assessment (Seepage model and WAPDEG analysis), all SMT submodel locations and each of the eight waste package types (Table 6.3-13) are considered; therefore, there are 2,874 locations multiplied by 8 waste package types, which results in 22,992 waste package histories that are reported. For each SMT submodel location and waste package type, a single file is produced that reports T_{wp}, RH_{wp}, T_{dw}, T_{ds}, and RH_{ds}, where T and RH are temperature and relative humidity and wp, dw, and ds stand for waste package, drift wall, and drip shield, respectively. Two waste package groups–DHLW and CSNF–are also defined, and for each SMT submodel location, the most typical waste package in the grouping is selected and the same five parameters reported. The DHLW group includes waste packages dhlw-l1 and dhlw-s1. The CSNF group includes waste packages pwr1-1, pwr2-1, bwr1-1, bwr2-1, pwr1-2 and bwr1-2. Details of the determination of the typical waste package can be found in Appendix VIII.

Since the WAPDEG binning produces a large number of output files, the first set of files are concatenated using a UNIX shell script so that all locations falling within a bin and all waste packages of a given type (CSNF or DHLW) are included in a single file. This process creates 5 (the number of bins) multiplied by 2 (the number of waste package groups), which results in 10 output files. The second set of typical files is also concatenated so that there is one file for each bin and each waste package group. This produces another $5 \times 2 = 10$ files. Hence a total of 20 WAPDEG files are provided for each infiltration-flux case.

The second process (TSPA binning) involves determining the most typical location given a set of locations that define a "bin." For TSPA purposes, the focus is the most typical waste package (see below) in a group or bin; therefore, there are 5 bins × 2 groups = 10 typical waste packages reported. TSPA binning uses the same waste package group definitions used in WAPDEG binning. For each bin, two output files are created, one for the most typical CSNF package and one for the most typical DHLW package. There are 5 (the number of bins) multiplied by 2 (the number of waste package groups) files created for this type of processing. The process of determining the typical waste packages is described in Appendix VIII. The TSPA files include all MSTHM output parameters that are relevant to the modeled repository (43 in all) covering temperature, relative humidity, liquid-phase saturation, liquid-phase flux and other thermal-hydrologic parameters at reference locations within and adjacent to the emplacement drifts.

Table 8-1 is a list of data tracking numbers (DTNs) associated with the output produced by this report.

8.4   YUCCA MOUNTAIN REVIEW PLAN CRITERIA ASSESSMENT

This model report predicts results that directly pertain to the abstraction of the quantity and chemistry of water contacting engineered barriers and waste forms. This section summarizes the contents of this report as they apply to U.S. Nuclear Regulatory Commission's criteria for a detailed review of that abstraction. These are the relevant criteria from the *Yucca Mountain*

Review Plan, Final Report (NRC 2003, Section 2.2.1.3.3.3 [DIRS 163274] which is from 10 CFR 63.114(a)–(c) and (e)–(g) [DIRS 156605]).

This report provides predictions of the evolution of thermal-hydrologic conditions in the repository emplacement drifts and in the adjoining host rock, but not predictions of seepage, in-drift condensation, or in-drift chemistry. These predictions provide the downstream process models and model abstraction with the thermal-hydrologic parameters (as functions of time) that influence the evolution of in-drift coupled flow and transport processes. Some aspects of the acceptance criteria (chemistry, seepage) are not addressed by this report.

8.4.1 Acceptance Criterion 1 – System Description and Model Integration Are Adequate

(1) Total system performance assessment adequately incorporates important design features, physical phenomena, and couplings, and uses consistent and appropriate assumptions throughout the quantity and chemistry of water contacting engineered barriers and waste forms abstraction process;

Table 4.1-1 lists the sources of input for design features and physical features. The design features that are inputs to the MSTHM calculations (including drip shield, invert, waste packages, drift design, and thermal loading) are in accordance with Interface Exchange Drawings (IEDs) (Section 4.1.1). Section 4.1.2 discusses the effects of small changes to the IEDs subsequent to the calculations documented in this report. Supplementary properties of the planned components are inputs from ASME standards and other justified sources (Section 4.1.1 and Appendix X). Simplifying assumptions about material properties are stated and justified (Section 5.3). The ventilation efficiency as a function of drift location and time is input from *Ventilation Model and Analysis Report* (BSC 2004 [DIRS 169862]).

Physical features of the unsaturated zone (stratigraphy) and some properties of the materials are input from *Development of Numerical Grids for UZ Flow and Transport Modeling* (BSC 2004 [DIRS 169855]). Other properties of the natural materials are input from *Calibrated Properties Model* (BSC 2004 [DIRS 169857]), *Analysis of Hydrologic Properties Data* (BSC 2004 [DIRS 170038]), *Thermal Conductivity of Non-Repository Lithostratigraphic Layers* (BSC 2004 [DIRS 170033]), *Thermal Conductivity of the Potential Repository Horizon* (BSC 2004 [DIRS 169854]), and other justified sources (Section 4.1). These sources assure consistency throughout the abstractions affecting the representation of the quantity and chemistry of water contacting engineered barriers and waste forms. Simplifying assumptions about material properties are stated and justified (Section 5.3).

The MSTHM represents the design features, physical phenomena, and couplings at the appropriate spatial scales. It incorporates a conceptual model for flow through unsaturated fractured porous rock at Yucca Mountain that is based on a dual-permeability representation of overlapping fracture and matrix continua (Section 6.2.2), which is consistent with all other hydrologic models, such as *UZ Flow Models and Submodels* (BSC 2004 [DIRS 169861], *Drift-Scale Coupled Processes (DST and TH Seepage) Models* (BSC 2004 [DIRS 170338]) and *Mountain-Scale Coupled Processes (TH/THC/THM)* (BSC 2004 [DIRS 169866]). These models employ the same general conceptual model for unsaturated-zone flow, which is described in Section 6.2.1.1 of *Drift-Scale Coupled Processes (DST and TH Seepage) Models* (BSC 2004 [DIRS 170338]) and in Sections 6.2.2 and 6.2.3 of this report. The differences among these

models, which are primarily related to the dimensionality, scale, and grid resolution employed in the respective computational domains, are justified by virtue of differences in the intended purpose for these respective models. The conceptual model for unsaturated-zone thermohydrology is implemented from standard form mass- and energy-balance equations (Sections 6.2.3.1, 6.2.3.2, and 6.2.3.6), including treatments of radiative heat transfer (Section 6.2.3.3) and thermal conduction (Section 6.2.3.4), with an active-fracture modification to the traditional dual-permeability approach (Section 6.2.3.5). The model does not address the chemistry of the water, but provides input to process models and abstractions that address chemical environments, waste package corrosion, and waste-form degradation.

Results from the FLUENT thermal model, which is the thermal model in *In-Drift Natural Convection and Condensation* (BSC 2004 [DIRS 164327]), are applied in the MSTHM to generate an in-drift effective thermal conductivity versus time relationship that captures the time-dependent influence of in-drift natural convection on the MSTHM results. Consequently, as documented in Section 7.6, there is excellent agreement between the MSTHM and FLUENT thermal model in predicting temperature differences between the waste-package, drip-shield, and drift-wall surfaces. Therefore, there is consistency in predicting in-drift heat transfer between the MSTHM and the thermal model used in *In-Drift Natural Convection and Condensation* (BSC 2004 [DIRS 164327]). Differences between the MSTHM and *In-Drift Natural Convection and Condensation* (BSC 2004 [DIRS 164327]) are consistent with the intended purpose of the respective models. The primary difference in the intended purpose is related to the fact that the *In-Drift Natural Convection and Condensation* (BSC 2004 [DIRS 164327]) is intended to predict bounds in the in-drift condensation rates, resulting from the cold-trap effect, while the MSTHM is not.

The coupling of thermal and hydrologic processes is at the heart of the model presented in this report. The MSTHM couples the effects of processes at various spatial scales, from a few tens of centimeters around individual waste packages and emplacement drifts to the scale of the mountain (Section 6.2.1). The MSTHM accomplishes this with four submodel types of varying dimensionality (Section 6.2.4), using simplified assumptions that are stated and justified (Sections 5.2, 5.5, 5.6, and 5.7). The MSTHM is validated by comparing predictions from its key thermal-hydrological submodel (called the LDTH submodel) against field-test data (Section 7.4) and by comparing MSTHM predictions with predictions from a monolithic three-dimensional thermal-hydrological model (Section 7.5). For temperature and liquid-phase saturation, model confidence building is also supported in Section 7.3. Coupled processes that are not addressed in this report are considered, and their rationale for exclusion presented, in *Engineered Barrier System Features, Events, And Processes* (BSC 2004 [DIRS 169898]).

(2) The abstraction of the quantity and chemistry of water contacting engineered barriers and waste forms uses assumptions, technical bases, data, and models, that are appropriate and consistent with other related U.S. Department of Energy abstractions. For example, the assumptions used for the quantity and chemistry of water contacting engineered barriers and waste forms are consistent with the abstractions of "Degradation of Engineered Barriers" (Section 2.2.1.3.1); "Mechanical Disruption of Engineered Barriers (Section 2.2.1.3.2); "Radionuclide Release Rates and Solubility Limits" (Section 2.2.1.3.4); "Climate and Infiltration" (Section 2.2.1.3.5); and "Flow Paths in the Unsaturated Zone" (Section 2.2.1.3.6). The descriptions and technical

bases provide transparent and traceable support for the abstraction of quantity and chemistry of water contacting engineered barriers and waste forms;

The MSTHM provides the basis for how long boiling conditions in the host rock adjacent to the drift wall prevent water from seeping into drifts. The MSTHM also determines temperature and relative humidity on the engineered barriers, quantities required for determining in-drift chemistry. The MSTHM has been validated for its intended purpose (Sections 7.1 and 7.2), using the results from a field test (Section 7.4), and by comparing the MSTHM against an alternative model for the three-drift repository test case (Section 7.5). For temperature and liquid-phase saturation, model confidence building is also supported in Section 7.3. The magnitude of seepage during the post-boiling period and the chemistry of that seepage are not determined by the MSTHM or in this report.

(3) Important design features, such as waste package design and material selection, backfill, drip shield, ground support, thermal loading strategy, and degradation processes, are adequate to determine the initial and boundary conditions for calculations of the quantity and chemistry of water contacting engineered barriers and waste forms;

Initial and boundary conditions for the MSTHM calculations of repository performance are based on inputs from other project documents (Section 4.1). Descriptions of design features are documented in IEDs (Section 4.1). Predicted heat-removal efficiency of the ventilation system is documented in *Ventilation Model and Analysis Report* (BSC 2004 [DIRS 169862]). The rationale for not directly representing ground support in the MSTHM is documented in Sections 5.3.1.10 and 5.3.2.7, and in Appendix VI. These inputs were sufficient to completely define the initial and boundary conditions for the MSTHM calculations.

(4) Spatial and temporal abstractions appropriately address physical couplings (thermal-hydrologic-mechanical-chemical). For example, the U.S. Department of Energy evaluates the potential for focusing of water flow into drifts, caused by coupled thermal-hydrologic-mechanical-chemical processes;

The physics of coupled thermal-hydrological processes (Sections 6.1 and 6.2) are adequately incorporated into the MSTHM methodology (Section 6.2.4) and its submodels (Sections 6.2.5 through 6.2.11). Sensitivity analyses (Sections 6.3.9) on the influence of hydrologic property variability and uncertainty, demonstrate that the potential impact of mechanical and chemical coupling on the thermal-hydrological response in repository drifts (and in the adjacent host rock) are insignificant, compared to the influences of parametric uncertainty (Sections 6.3.2 and 6.3.4), which are addressed by the MSTHM and this report.

(5) Sufficient technical bases and justification are provided for total system performance assessment assumptions and approximations for modeling coupled thermal-hydrologic-mechanical-chemical effects on seepage and flow, the waste package chemical environment, and the chemical environment for radionuclide release. The effects of distribution of flow on the amount of water contacting the engineered barriers and waste forms are consistently addressed, in all relevant abstractions;

The MSTHM addresses repository-scale variability and uncertainty of percolation flux that is based on the output (DTN: LB0302PTNTSW9I.001 [DIRS 162277]) from the *UZ Flow Models and Submodels* (BSC 2004 [DIRS 169861]). The MSTHM provides the basis for how long boiling conditions in the host rock adjacent to the drift wall prevent water from seeping into drifts. The magnitude of seepage during the post-boiling period and the chemistry of that seepage are not determined by the MSTHM nor in this report. However, the MSTHM determines temperature and relative humidity on the engineered barriers, quantities required for determining in-drift chemistry. The physics of coupled thermal-hydrological processes (Sections 6.1 and 6.2) are adequately incorporated into the MSTHM methodology (Section 6.2.4) and its submodels (Sections 6.2.5 through 6.2.11). Sensitivity analyses (Sections 6.3.9) on the influence of hydrologic property variability and uncertainty, demonstrate that the potential impact of mechanical and chemical coupling on the thermal-hydrological response in repository drifts (and in the adjacent host rock) is insignificant, compared to the influences of parametric uncertainty (Sections 6.3.2 and 6.3.4), which are addressed by the MSTHM and this report.

(6) The expected ranges of environmental conditions within the waste package emplacement drifts, inside the breached waste packages, and contacting the waste forms and their evolution with time are identified. These ranges may be developed to include: (i) the effects of the drip shield and backfill on the quantity and chemistry of water (e.g., the potential for condensate formation and dripping from the underside of the shield); (ii) conditions that promote corrosion of engineered barriers and degradation of waste forms; (iii) irregular wet and dry cycles; (iv) gamma-radiolysis; and (v) size and distribution of penetrations of engineered barriers;

The MSTHM provides the basis for how long boiling conditions in the host rock adjacent to the drift wall prevent water from seeping into drifts. The magnitude of seepage during the postboiling period and the chemistry of that seepage are not determined by the MSTHM or in this report. However, the MSTHM determines temperature and relative humidity on the engineered barriers, quantities required for determining in-drift chemistry.

(7) The model abstraction for quantity and chemistry of water contacting engineered barriers and waste forms is consistent with the detailed information on engineered barrier design and other engineered features. For example, consistency is demonstrated for: (i) dimensionality of the abstractions; (ii) various design features and site characteristics; and (iii) alternative conceptual approaches. Analyses are adequate to demonstrate that no deleterious effects are caused by design or site features that the U.S. Department of Energy does not take into account in this abstraction;

The MSTHM accounts for the three-dimensional geometry of the emplacement drift, drip shield, and invert (Section 6.2), including a discrete representation of each emplacement drift (Figure 6.2-3). The MSTHM also addresses the distribution of hydrostratigraphic units (and their respective thermal-hydrologic properties), based on *Development of Numerical Grids for UZ Flow and Transport Modeling* (BSC 2004 [DIRS 169855]), *Calibrated Properties Model* (BSC 2004 [DIRS 169857]), *Thermal Conductivity of the Potential Repository Horizon* (BSC 2004 [DIRS 169854]), *Thermal Conductivity of Non-Repository Lithostratigraphic Layers* (BSC 2004 [DIRS 170033]), and *Heat Capacity Analysis Report* (BSC 2004 [DIRS 170003]).

The MSTHM also addresses the distribution of percolation flux above the repository, based on *UZ Flow Models and Submodels* (BSC 2004 [DIRS 169861]).

(8) Adequate technical bases are provided, including activities such as independent modeling, laboratory or field data, or sensitivity studies, for inclusion of any thermal-hydrologic-mechanical-chemical couplings and features, events, and processes;

This report lists ten features, events and processes (FEPs) that are included in the MSTHM model (Section 6.5). Table 6.5-1 provides, for each FEP, a cross-reference to the section that describes its disposition. Coupled processes that are not addressed in this report are considered, and their rationale for exclusion or inclusion elsewhere, is presented in *Engineered Barrier System Features, Events, And Processes* (BSC 2004 [DIRS 169898]).

(9) Performance-affecting processes that have been observed in thermal-hydrologic tests and experiments are included into the performance assessment. For example, the U.S. Department of Energy either demonstrates that liquid water will not reflux into the underground facility or incorporates refluxing water into the performance assessment calculation, and bounds the potential adverse effects of alteration of the hydraulic pathway that result from refluxing water;

The LDTH submodel of the MSTHM has been validated against the Drift Scale Test (Section 7.4). For temperature and liquid-phase saturation, model confidence building is also supported in Section 7.3, which documents a thermal-hydrologic model study of the Large Block Test. The LDTH submodel includes the influence of refluxing water in the host rock on the predicted thermal-hydrologic response in the drift and adjacent host rock. However, the LDTH-submodel results have never suggested the possibility of that refluxing water entering the emplacement drifts. Neither the results of the thermal-hydrological model simulations nor the measurements associated with the DST suggest the possibility of refluxing water entering emplacement drifts. Section 8.1 of *Drift-Scale Coupled Processes (DST and TH Seepage) Models* (BSC 2004 [DIRS 170338]) includes the following key conclusions:

- For cases where thermal seepage takes place, it is predicted to begin several hundred to a few thousand years after rock temperature has returned below boiling, the delay caused by the slow saturation buildup in fractures; there is no seepage during the time period of above-boiling temperatures in the rock.

- Thermal-seepage percentages are always smaller than the respective ambient reference values, indicating that there is no enhanced seepage as a result of reflux of water.

Based on these conclusions, it is unnecessary to incorporate refluxing water in performance assessment calculations.

(12) Guidance in NUREG–1297 (Altman et al. 1988 [DIRS 103597]) and NUREG–1298 (Altman et al. 1988 [DIRS 103750]), or other acceptable approaches, is followed.

Inputs were selected and documented, and documents were checked and reviewed according to applicable BSC procedures, which comply with NUREG-1297 and 1298 (see Section 2).

8.4.2   Acceptance Criterion 2 – Data Are Sufficient for Model Justification

(1)   Geological, hydrological, and geochemical values used in the license application are adequately justified. Adequate description of how the data were used, interpreted, and appropriately synthesized into the parameters is provided;

Geological and hydrological parameters and related information are input from *Development of Numerical Grids for UZ Flow and Transport Modeling* (BSC 2004 [DIRS 169855]), *Calibrated Properties Model* (BSC 2004 [DIRS 169857]), *Analysis of Hydrologic Properties Data* (BSC 2004 [DIRS 170038]), *Thermal Conductivity of Non-Repository Lithostratigraphic Layers* (BSC 2004 [DIRS 170033]), *Thermal Conductivity of the Potential Repository Horizon* (BSC 2004 [DIRS 169854], Section 4.1), and other justified sources. Descriptions of how the data were used, interpreted, and appropriately synthesized are provided in those documents.

(2)   Sufficient data were collected on the characteristics of the natural system and engineered materials to establish initial and boundary conditions for conceptual models of thermal-hydrological-mechanical-chemical coupled processes, that affect seepage and flow and the engineered barrier chemical environment;

Initial and boundary conditions for the MSTHM calculations are documented in *Mountain-Scale Coupled Processes (TH/THC/THM)* (BSC 2004 [DIRS 169866]) and *UZ Flow Models and Submodels* (BSC 2004 [DIRS 169861]). Those reports describe the technical basis for establishing the initial and boundary conditions.

(3)   Thermo-hydrologic tests were designed and conducted with the explicit objectives of observing thermal-hydrologic processes for the temperature ranges expected for repository conditions and making measurements for mathematical models. Data are sufficient to verify that thermal-hydrologic conceptual models address important thermal-hydrologic phenomena;

The Large Block Test and the Drift Scale Test provided data for processes in the expected temperature range. The Drift Scale Test was used to validate the conceptual model underlying the LDTH submodels used in the MSTHM (Section 7.4). The Large Block Test (Section 7.3) was used to build confidence in the ability of the model to predict thermal-hydrologic processes in the host rock.

(4)   Sufficient information to formulate the conceptual approach(es) for analyzing water contact with the drip shield, engineered barriers, and waste forms is provided.

The MSTHM provides the basis for how long boiling conditions in the host rock adjacent to the drift wall prevents water from seeping into drifts. The magnitude of seepage during the postboiling period and the chemistry of that seepage are not determined by the MSTHM or in this report. However, the MSTHM determines temperature and relative humidity on the engineered barriers, quantities required for determining in-drift chemistry. The MSTHM is validated by comparing predictions from its key thermal-hydrological submodel (called the LDTH submodel) against field-test data (Section 7.4) and by comparing MSTHM predictions with predictions from a monolithic three-dimensional thermal-hydrological model (Section 7.5), which is an alternative model. For ability to predict reasonable ranges of temperature and liquid-

phase saturation in the host rock, model confidence building is also supported in Section 7.3, which documents a thermal-hydrologic model study of the Large Block Test.

8.4.3   Acceptance Criterion 3 – Data Uncertainty Is Characterized and Propagated Through the Model Abstraction

(1) Models use parameter values, assumed ranges, probability distributions, and bounding assumptions that are technically defensible, reasonably account for uncertainties and variabilities, and do not result in an under-representation of the risk estimate;

The model parameter values were selected based on the characteristics of the input and are considered representative of the natural and engineered systems (Section 4.1). Design information is taken from Interface Exchange Drawings and qualified analyses. Boundary conditions, stratigraphy, and percolation fluxes are from UZ flow models, including uncertainties. Properties of the natural and engineered materials are based on measurements taken and documented in accordance with DOE quality requirements (Section 4.1 and Appendices IV and X). When modeling decisions were necessary, the choices were made to preserve the variability of thermal-hydrologic responses (Sections 5.2.1, 5.2.2, and 6.2.1), thereby avoiding an under-representation of the risk estimate.

(2) Parameter values, assumed ranges, probability distributions, and bounding assumptions used in the total system performance assessment calculations of quantity and chemistry of water contacting engineered barriers and waste forms are technically defensible and reasonable, based on data from the Yucca Mountain region (e.g., results from large block and drift-scale heater and niche tests), and a combination of techniques that may include laboratory experiments, field measurements, natural analog research, and process-level modeling studies;

Sufficiently wide ranges of the key natural-system parameters are addressed to reasonably account for uncertainty (Section 6.3), and therefore do not result in an under-representation of the risk estimate. A sensitivity study (Section 6.3.9) justifies the decision not to propagate hydrologic-property uncertainty in the MSTHM. Sensitivity studies (Sections 6.3.10, 6.3.11, and 6.3.12) justify assumptions made in Section 5 concerning engineered-system parameter values.

(3) Input values used in the total system performance assessment calculations of quantity and chemistry of water contacting engineered barriers (e.g., drip shield and waste package) are consistent with the initial and boundary conditions and the assumptions of the conceptual models and design concepts for the Yucca Mountain site. Correlations between input values are appropriately established in the U.S. Department of Energy total system performance assessment. Parameters used to define initial conditions, boundary conditions, and computational domain in sensitivity analyses involving coupled thermal-hydrologic-mechanical-chemical effects on seepage and flow, the waste package chemical environment, and the chemical environment for radionuclide release, are consistent with available data. Reasonable or conservative ranges of parameters or functional relations are established;

Parameters used to define initial conditions, boundary conditions, and computational domain of the MSTHM are consistent with available data. The MSTHM addresses the distribution of hydrostratigraphic units (and their respective thermal-hydrologic properties), based on *Development of Numerical Grids for UZ Flow and Transport Modeling* (BSC 2004 [DIRS 169855]), *Calibrated Properties Model* (BSC 2004 [DIRS 169857]), *Thermal Conductivity of the Potential Repository Horizon* (BSC 2004 [DIRS 169854]), *Thermal Conductivity of Non-Repository Lithostratigraphic Layers* (BSC 2004 [DIRS 170033]), and *Heat Capacity Analysis Report* (BSC 2004 [DIRS 170003]). The MSTHM addresses the distribution of percolation flux above the repository, based on *UZ Flow Models and Submodels* (BSC 2004 [DIRS 169861]).

(4) Adequate representation of uncertainties in the characteristics of the natural system and engineered materials is provided in parameter development for conceptual models, process-level models, and alternative conceptual models. The U.S. Department of Energy may constrain these uncertainties using sensitivity analyses or conservative limits. For example, the U.S. Department of Energy demonstrates how parameters used to describe flow through the engineered barrier system bound the effects of backfill and excavation-induced changes;

Previous studies have found that uncertainty in calculated thermal-hydrologic response is dominated by the uncertainty in host-rock thermal conductivity (Section 6.3.2). The sensitivity of thermal-hydrologic response to host-rock thermal conductivity uncertainty is addressed for plus and minus one standard deviation about the mean value (Section 6.3.2.2). Measurement statistics are used to determine the standard deviation for the wet and dry thermal conductivity values for each of the four host-rock units. Section 6.3.9 demonstrates that host-rock hydrologic property uncertainty has an insignificant influence on the thermal-hydrologic response. Section 6.3.11 demonstrates that invert hydrologic-property uncertainty has an insignificant influence on the thermal-hydrologic response. Sections 5.3.1.10 and 5.3.2.7 justify the assumption that ground support does not need to be incorporated in the MSTHM.

Previous studies have found that the contribution to uncertainty in calculated thermal-hydrologic conditions from the uncertainties in boundary values is dominated by the uncertainty in percolation flux (Section 6.3.2). The uncertainty in percolation flux at the repository horizon is addressed by way of lower-bound, mean, and upper-bound infiltration-flux cases, generated by *UZ Flow Models and Submodels* (BSC 2004 [DIRS 169861]) for each of three climate states: present-day, monsoonal, and glacial-transition (Section 6.3.2.1). The percolation-flux range from lower bound to upper bound for the present-day climate covers five orders of magnitude. Similar ranges apply to the monsoonal and glacial-transition climates.

In summary, the influence of parametric uncertainty of host-rock thermal conductivity and percolation flux on the predicted thermal-hydrologic response, which is represented in the MSTHM, is greater than differences in the predicted thermal-hydrologic response between the MSTHM and alternative conceptual models (Section 7.5).

8.4.4 Acceptance Criterion 4 – Model Uncertainty Is Characterized and Propagated Through the Model Abstraction

(1) Alternative modeling approaches of features, events, and processes are considered and are consistent with available data and current scientific understanding, and the results and limitations are appropriately considered in the abstraction;

The validation of the MSTHM involved comparison with the results from a three-dimensional monolithic thermal-hydrologic model (Section 7.5), which is an alternative model. The differences in predicted thermal-hydrologic responses between the MSTHM and the alternative model are smaller than differences resulting from parametric uncertainty. Therefore, model uncertainty does not need to be propagated through the model abstraction.

(2) Alternative modeling approaches are considered and the selected modeling approach is consistent with available data and current scientific understanding. A description that includes a discussion of alternative modeling approaches not considered in the final analysis and the limitations and uncertainties of the chosen model is provided;

The validation of the MSTHM involved comparison with the results from a three-dimensional monolithic thermal-hydrologic model (Section 7.5), which is an alternative model. The differences in predicted thermal-hydrologic responses between the MSTHM and the alternative model are smaller than differences resulting from parametric uncertainty. Therefore, model uncertainty does not need to be propagated through the model abstraction. This report also considers a mountain-scale thermal-hydrologic model as an alternative to the MSTHM (Section 6.4). A calculation with the alternative model used (1) coarser grid discretization at the drift scale than the MSTHM, (2) a line-averaged approximation of the heat-generation-rate-versus-time table (whereas the MSTHM represented the waste packages as discrete heat sources), and (3) a lumped heat source that filled the entire cross section of the emplacement drift. Because of limitations in the predictions provided from the alternative model, comparison is restricted to predictions of drift-wall temperatures. The differences are within the range of temperature differences resulting from parametric uncertainty. This report also contains a discussion of the limitations of the MSTHM (Section 1) and its uncertainties (Sections 6.3.9 through 6.3.13).

(3) Consideration of conceptual-model uncertainty is consistent with available site characterization data, laboratory experiments, field measurements, natural analog information and process-level modeling studies; and the treatment of conceptual-model uncertainty does not result in an under-representation of the risk estimate;

Comparison of the MSTHM with field-test data (Section 7.4) finds that the model uncertainty is within the range of parameter uncertainty. Comparison between the MSTHM and the three-drift monolithic TH model for the three-drift repository test case (Section 7.5), finds that the model uncertainty is within the range of parameter uncertainty. For temperature and liquid-phase saturation, model confidence building is also supported in Section 7.3, which documents a thermal-hydrologic model study of the Large Block Test.

(4) Adequate consideration is given to effects of thermal-hydrologic-mechanical-chemical coupled processes in the assessment of alternative conceptual models. These effects may include: (i) thermal-hydrologic effects on gas, water, and mineral chemistry; (ii) effects of microbial processes on the engineered barrier chemical environment and the chemical environment for radionuclide release; (iii) changes in water chemistry that may result from the release of corrosion products from the engineered barriers and interactions between engineered materials and ground water; and (iv) changes in boundary conditions (e.g., drift shape and size) and hydrologic properties, relating to the response of the geomechanical system to thermal loading.

Sensitivity analyses (Sections 6.3.9) on the influence of hydrologic property variability and uncertainty, demonstrate that the potential impact of mechanical and chemical coupling on the thermal-hydrological response in repository drifts (and in the adjacent host rock) are insignificant, compared to the influences of parametric uncertainty (Sections 6.3.2 and 6.3.4), which are addressed by the MSTHM and this report. The influence of drift collapse on thermal-hydrologic response is addressed in Section 6.3.7.

Table 8-1.   Data Tracking Numbers Associated with the Output Produced by This Report

DTN	Title
LL030602723122.027	Multiscale Thermohydrologic Model Output to TSPA and WAGDEG for Upper Infiltration Case
LL030608723122.028	Multiscale Thermohydrologic Model Output to TSPA and WAPDEG for the Lower Infiltration Case
LL030610323122.029	Multiscale Thermohydrologic Model Output to TSPA and WAPDEG for the Mean Infiltration Case
LL030704523122.030	NUFT Input File Data Development to Support LA Multi-Scale Analyses
LL030704623122.031	NUFT Input File Data Development to Support LA Multi-Scale Analyses
LL030804023122.034	Sensitivity Studies for Evaluating the Impact of Thermal Conductivity and Percolation Rate on LA Multi-Scale Analyses
LL030808523122.035	Input and Output Files Supporting MSTHM Micro-Abstractions for LA Multi-Scale Analyses
LL030808623122.036	Input and Output Files for NUFT MSTHM Submodels Supporting LA Multi-Scale Analyses
LL030808723122.037	Input and Output Files for the Creation of NUFT MSTHM Submodel Input Files Supporting LA Multi-Scale Analyses
LL030808823122.038	Input and Output Files for Building SMT, SDT, and LDTH Submodel Mesh Files in Support of LA Multi-Scale Analyses
LL030808923122.039	Input and Output Files Associated with the Large-Block and Drift Scale Tests in Support of LA Multi-Scale Analyses
LL030905931032.001	Sensitivity Studies for Evaluating the Impact of Thermal Conductivity and Percolation Rate on LA Multi-Scale Analyses. Lower Percolation Case, Low Thermal Conductivity in Host Rock
LL030906131032.002	Output from the Multi-Scale AMR for the Lower Percolation Mean Thermal Conductivity Case including Drift Wall Temperatures
LL030906331032.004	Sensitivity Studies for Evaluating the Impact of Thermal Conductivity and Percolation Rate on LA Multi-Scale Analyses. Upper Percolation Case, High Thermal Conductivity in Host Rock
LL030906531032.005	Output from the Multi-Scale AMR for the Upper Percolation Mean Thermal Conductivity Case including Drift Wall Temperatures
LL031206723122.041	WAPDEG Output from the Multi-Scale AMR for the Mean Percolation Mean Thermal Conductivity Case including Drift Wall Temperatures

Table 8-1.   Data Tracking Numbers Associated with the Output Produced by This Report (Continued)

DTN	Title
LL040102223122.042	Evaluation of the Sensitivity of In-Drift Temperature and Relative Humidity to Hydrologic-Property Uncertainty
LL040310323122.044	Input and Output files of the MSTHM Micro-Abstractions for the Collapsed-Drift cases for the TSPA-LA Low-Probability-Seismic Scenario
LL040404423122.045	Input and Output Files of the LDTH-Model Runs for the Focused-Seepage Sensitivity Analysis for the Collapsed-Drift Cases Conducted in ANL-EBS-MD-000049 Rev 1 ICN1
LL040501323122.046	Input and Output Files for the Sensitivity Studies for (1) Host-Rock Hydrologic Properties, (2) Invert Intragranular Hydrologic Properties, and (3) Rubble Heat Capacity for the Low-Probability-Seismic, Collapsed-Drift Cases
LL040604823122.047	Input and Output Files for the Creation of NUFT MSTHM Submodel Input Files Supporting LA Multi-Scale Analyses
LL040703023122.048	Input and Output Files Associated with the Large-Block and Drift Scale Tests in Support of LA Multi-Scale Analyses
LL040703123122.049	Input and Output Files for the Sensitivity Studies for (1) Invert Intergranular Hydrologic Properties, (2) Pseudo Permeability of the Gas-Filled Drift Cavity, and (3) Ventilation Heat-Removal Efficiency
LL040703223122.050	Validation of the Multiscale Thermal-Hydrologic Model Against a Corresponding Three-Dimensional Monolithic Thermal-Hydrologic Model
LL040704323122.051	Input and Output Files for the Comparison Study of Initial Liquid-Phase Saturation and Capillary Pressure for the Mean and Modified-Mean Infiltration-Flux Property Sets for the Lower-Bound, Mean, and Upper-Bound Infiltration-Flux Cases
LL050204723122.053	Multiscale Thermohydrologic Model Output of Fourteen TH Variables from AMR ANL-EBS-MD-000049 (Rev03) for the Upper-Bound Infiltration Case with Mean Host-Rock Thermal Conductivity
LL050204823122.054	Multiscale Thermohydrologic Model Output of Fourteen TH Variables from AMR ANL-EBS-MD-000049 (Rev03) for the Lower-Bound Infiltration Case with Mean Host-Rock Thermal Conductivity
LL050204923122.055	Multiscale Thermohydrologic Model Output of Fourteen TH Variables from AMR ANL-EBS-MD-000049 (Rev03) for the Upper-Bound Infiltration Case with High Host-Rock Thermal Conductivity
LL050205023122.056	Multiscale Thermohydrologic Model Output of Fourteen TH Variables from AMR ANL-EBS-MD-000049 (Rev03) for the Lower-Bound Infiltration Case with Low Host-Rock Thermal Conductivity
LL050401723122.058	Multiscale Thermohydrologic Model Output of Fourteen TH Variables from AMR ANL-EBS-MD-000049 (Rev03) for the Mean Infiltration Flux Case with Mean Host-Rock Thermal Conductivity
LL050500323122.060	Comparison of the Differences Between the Multiscale Thermohydrologic Model and a Corresponding Three-Dimensional Monolithic Thermal-Hydrologic Model with the Range of Conditions Resulting from Parametric Uncertainty
MO0307SPAVGSUM.000	van Genuchten hydrologic parameters
MO0406CDFINSMT.000	Area Weighted Cumulative Distribution Function (CDF) for PTN/TSW Infiltration Rates Within SMT Area
MO0505SPAROCKM.000	Rock Mass and Invert Properties for TSPA-LA

9.   INPUTS AND REFERENCES

9.1   DOCUMENTS CITED

Altman, W.D.; Donnelly, J.P.; and Kennedy, J.E. 1988. *Qualification of Existing Data for High-Level Nuclear Waste Repositories: Generic Technical Position*. NUREG-1298. Washington, D.C.: U.S. Nuclear Regulatory Commission. TIC: 200652.   103750

Altman, W.D.; Donnelly, J.P.; and Kennedy, J.E. 1988. *Peer Review for High-Level Nuclear Waste Repositories*: *Generic Technical Position*. NUREG-1297. Washington, D.C.: U.S. Nuclear Regulatory Commission. TIC: 200651.   103597

Bandurraga, T.M. and Bodvarsson, G.S. 1999. "Calibrating Hydrogeologic Parameters for the 3-D Site-Scale Unsaturated Zone Model of Yucca Mountain, Nevada." *Journal of Contaminant Hydrology, 38,* (1-3), 25-46. New York, New York: Elsevier. TIC: 244160.   103949

Bear, J. 1972. *Dynamics of Fluids in Porous Media*. Environmental Science Series. Biswas, A.K., ed. New York, New York: Elsevier. TIC: 217356.   156269

Bird, R.B.; Stewart, W.E.; and Lightfoot, E.N. 1960. *Transport Phenomena*. New York, New York: John Wiley & Sons. TIC: 208957.   103524

Brooks, R.H. and Corey, A.T. 1964. *Hydraulic Properties of Porous Media*. Hydrology Paper No. 3. Fort Collins, Colorado: Colorado State University. TIC: 217453.   156915

Birkholzer, J.T. and Tsang, Y.W. 2000. "Modeling the Thermal-Hydrologic Processes in a Large-Scale Underground Heater Test in Partially Saturated Fractured Tuff." *Water Resources Research, 36,* (6), 1431-1447. Washington, D.C.: American Geophysical Union. TIC: 248278.   154608

BSC 2001. *FY 01 Supplemental Science and Performance Analyses, Volume 1*: *Scientific Bases and Analyses*. TDR-MGR-MD-000007 REV 00 ICN 01. Las Vegas, Nevada: Bechtel SAIC Company. ACC: MOL.20010801.0404; MOL.20010712.0062; MOL.20010815.0001.   155950

BSC 2001. *Multiscale Thermohydrologic Model*. ANL-EBS-MD-000049 REV 00 ICN 02. Las Vegas, Nevada: Bechtel SAIC Company. ACC: MOL.20020123.0279.   158204

BSC 2001. *Thermal Tests Thermal-Hydrological Analyses/Model Report.* ANL-NBS-TH-000001 REV 00 ICN 02. Las Vegas, Nevada: Bechtel SAIC Company. ACC: MOL.20011116.0025.   157330

BSC 2002. *The Enhanced Plan for Features, Events, and Processes (FEPs) at Yucca Mountain*. TDR-WIS-PA-000005 REV 00. Las Vegas, Nevada: Bechtel SAIC Company. ACC: MOL.20020417.0385.   158966

BSC 2002. *Guidelines for Developing and Documenting Alternative Conceptual Models, Model Abstractions, and Parameter Uncertainty in the Total System Performance Assessment for the License Application*. TDR-WIS-PA-000008 REV 00, ICN 01. Las Vegas, Nevada: Bechtel SAIC Company. ACC: MOL.20020904.0002.   158794

BSC 2003. *Advection Versus Diffusion in the Invert*. ANL-EBS-MD-000063. Las Vegas, Nevada: Bechtel SAIC Company. ACC: DOC.20040217.0004.   170881

BSC 2003. *Analysis of Infiltration Uncertainty*. ANL-NBS-HS-000027 REV 01. Las Vegas, Nevada: Bechtel SAIC Company. ACC: DOC.20031030.0003.   165991

BSC 2003. *Design and Engineering, D&E/PA/C IED Typical Waste Package Components Assembly 1 of 9*. 800-IED-WIS0-00201-000-00C. Las Vegas, Nevada: Bechtel SAIC Company. ACC: ENG.20030917.0002.   165406

BSC 2003. *Interlocking Drip Shield.* 000-MW0-TED0-00102-000-00A. Las Vegas, Nevada: Bechtel SAIC Company. ACC: ENG.20030205.0002.   171024

BSC 2003. *Longevity of Emplacement Drift Ground Support Materials for LA.* 800-K0C-TEG0-01200-000-00A. Las Vegas, Nevada: Bechtel SAIC Company. ACC: ENG.20030922.0004.   165425

BSC 2003. *Repository Design Project, Repository/PA IED Emplacement Drift Committed Materials.* 800-IED-EBS0-00301-000-00A. Las Vegas, Nevada: Bechtel SAIC Company. ACC: ENG.20030311.0022.   162444

BSC 2003. *Repository Design, Repository/PA IED Subsurface Facilities*. 800-IED-EBS0-00402-000-00B. Las Vegas, Nevada: Bechtel SAIC Company. ACC: MOL.20030109.0146.   161727

BSC 2004. *Abstraction of Drift Seepage.* MDL-NBS-HS-000019, Rev. 01. Las Vegas, Nevada: Bechtel SAIC Company. ACC: DOC.20041103.0003.   169131

BSC 2004. *Analysis of Hydrologic Properties Data.* ANL-NBS-HS-000042, Rev. 00. Las Vegas, Nevada: Bechtel SAIC Company. ACC: DOC.20041005.0004.   170038

BSC 2004. *Calibrated Properties Model.* MDL-NBS-HS-000003, Rev. 02. Las Vegas, Nevada: Bechtel SAIC Company. ACC: DOC.20041006.0004.   169857

BSC 2004. *D&E / PA/C IED Emplacement Drift Configuration.* 800-IED-MGR0-00201-000-00A. Las Vegas, Nevada: Bechtel SAIC Company. ACC: ENG.20040113.0011.   167040

BSC 2004. *D&E / PA/C IED Emplacement Drift Configuration and Environment*. 800-IED-MGR0-00201-000-00B. Las Vegas, Nevada: Bechtel SAIC Company. ACC: ENG.20040326.0001.   168489

BSC 2004. *D&E / PA/C IED Subsurface Facilities*. 800-IED-WIS0-00102-000-00A. Las Vegas, Nevada: Bechtel SAIC Company. ACC: ENG.20040309.0027.   170202

BSC 2004. *D&E/RIT IED Subsurface Facilities [Sheet 1 of 4]*. 800-IED-WIS0-00101-000-00B. Las Vegas, Nevada: Bechtel SAIC Company. ACC: ENG.20041130.0002.   172801

BSC 2004. *Design and Engineering, Interlocking Drip Shield Configuration*. 000-M00-SSE0-00102-000-00B. Las Vegas, Nevada: Bechtel SAIC Company. ACC: ENG.20040305.0021.   168067

BSC 2004. *Development of Numerical Grids for UZ Flow and Transport Modeling.* ANL-NBS-HS-000015 REV 02. Las Vegas, Nevada: Bechtel SAIC Company. ACC: DOC.20040901.0001.   169855

BSC 2004. *Drift Degradation Analysis*. ANL-EBS-MD-000027 REV. 03. Las Vegas, Nevada: Bechtel SAIC Company. ACC: MOL.20040915.0010.   166107

BSC 2004. *Drift-Scale Coupled Processes (DST and TH Seepage) Models.* MDL-NBS-HS-000015, Rev. 01. Las Vegas, Nevada: Bechtel SAIC Company. ACC: DOC.20040930.0003.   170338

BSC 2004. *Drift Scale THM Model.* MDL-NBS-HS-000017, Rev. 01. Las Vegas, Nevada: Bechtel SAIC Company. ACC: DOC.20041012.0001.   169864

BSC 2004. *Engineered Barrier System Features, Events, and Processes.* ANL-WIS-PA-000002, Rev. 03. Las Vegas, Nevada: Bechtel SAIC Company. ACC: DOC.20041122.0008.   169898

BSC 2004. *Evaluation of Features, Events, and Processes (FEP) for the Biosphere Model*. ANL-MGR-MD-000011 Rev. 04. Las Vegas, Nevada: Bechtel SAIC Company. ACC: DOC.20041028.0002.   169826

BSC 2004. *Future Climate Analysis.* ANL-NBS-GS-000008 REV 01. Las Vegas, Nevada: Bechtel SAIC Company. ACC: DOC.20040908.0005.   170002

BSC 2004. *Ground Control for Emplacement Drifts for LA*. 800-K0C-SSE0-00100-000-00A. Las Vegas, Nevada: Bechtel SAIC Company. ACC: ENG.20040712.0019.   170292

BSC 2004. *Heat Capacity Analysis Report*. ANL-NBS-GS-000013, Rev. 01. Las Vegas, Nevada: Bechtel SAIC Company. ACC: DOC.20041101.0003.   170003

BSC 2004. *In-Drift Natural Convection and Condensation.*
MDL-EBS-MD-000001, Rev. 00. Las Vegas, Nevada: Bechtel SAIC Company.
ACC: DOC.20041025.0006.

164327

BSC 2004. *Mountain-Scale Coupled Processes (TH/THC/THM).*
MDL-NBS-HS-000007 REV 02. Las Vegas, Nevada: Bechtel SAIC Company.
ACC: DOC.20041108.0001.

169866

BSC 2004. *Repository Subsurface Emplacement Drifts Steel Invert Structure Plan
& Elevation.* 800-SS0-SSE0-00101-000-00B. Las Vegas, Nevada: Bechtel SAIC
Company. ACC: ENG.20040520.0004.

169503

BSC 2004. *Thermal Conductivity of Non-Repository Lithostratigraphic Layers.*
MDL-NBS-GS-000006, Rev. 01. Las Vegas, Nevada: Bechtel SAIC Company.
ACC: DOC.20041022.0004.

170033

BSC 2004. *Thermal Conductivity of the Potential Repository Horizon.*
MDL-NBS-GS-000005 REV 01. Las Vegas, Nevada: Bechtel SAIC Company.
ACC: DOC.20040928.0006.

169854

BSC 2004. *UZ Flow Models and Submodels.* MDL-NBS-HS-000006, Rev. 02.
Las Vegas, Nevada: Bechtel SAIC Company. ACC: DOC.20041101.0004.

169861

BSC 2004. *Ventilation Model and Analysis Report.* ANL-EBS-MD-000030,
Rev. 04. Las Vegas, Nevada: Bechtel SAIC Company.
ACC: DOC.20041025.0002.

169862

BSC 2004. *WAPDEG Analysis of Waste Package and Drip Shield Degradation.*
ANL-EBS-PA-000001 REV 02. Las Vegas, Nevada: Bechtel SAIC Company.
ACC: DOC.20041004.0005.

169996

BSC 2005. *Data Qualification Plan - Qualification of DTN
MO0304MWDALACV.000 for Use in the Multiscale Thermohydrologic Model.*
Las Vegas, Nevada: Bechtel SAIC Company, LLC. ACC: MOL.20050412.0107.

173404

BSC 2005. *IED Interlocking Drip Shield and Emplacement Pallet [Sheet 1 of 1].*
800-IED-WIS0-00401-000-00E. Las Vegas, Nevada: Bechtel SAIC Company.
ACC: ENG.20050301.0007.

173303

BSC 2005. *IED Waste Package Configuration [Sheet 1 of 1].*
800-IED-WIS0-00601-000-00A. Las Vegas, Nevada: Bechtel SAIC Company.
ACC: ENG.20050406.0005.

173501

BSC 2005. *IED Waste Package Decay Heat Generation [Sheet 1 of 1].*
800-IED-WIS0-00701-000-00A. Las Vegas, Nevada: Bechtel SAIC Company.
ACC: ENG.20050406.0006.

173705

BSC 2005. *IED Waste Package Decay Heat Generation Design Basis and Thermal Information [Sheet 1 of 1].* 800-IED-WIS0-00801-000-00A. Las Vegas, Nevada: Bechtel SAIC Company. ACC: ENG.20050406.0007.

173499

BSC 2005. *Q-List.* 000-30R-MGR0-00500-000-001. Las Vegas, Nevada: Bechtel SAIC Company. ACC: ENG.20050217.0010.

171190

BSC 2005. *Technical Work Plan for: Near-Field Environment and Transport In-Drift Heat and Mass Transfer Model and Analysis Reports Integration.* TWP-MGR-PA-000018 REV 02. Las Vegas, Nevada: Bechtel SAIC Company, LLC. ACC: DOC.20050413.0003.

173377

Buscheck, T.A. 1999. *Thermohydrologic Calculations for the Site Recommendation/License Application Design Selection, Phase 2.* UCRL-ID-133988. BB0000000-01717-0210-00009 REV 00. Livermore, California: Lawrence Livermore National Laboratory. ACC: MOL.20000606.0193.

130078

Buscheck, T.A. and Nitao, J.J. 1994. *The Impact of Buoyant, Gas-Phase Flow and Heterogeneity on Thermo-Hydrological Behavior at Yucca Mountain.* UCRL-JC-115351. Livermore, California: Lawrence Livermore National Laboratory. ACC: NNA.19940524.0012.

130561

Buscheck, T.A. and Nitao, J.J. 1995. *Thermal-Hydrological Analysis of Large-Scale Thermal Tests in the Exploratory Studies Facility at Yucca Mountain.* UCRL-ID-121791. Livermore, California: Lawrence Livermore National Laboratory. ACC: MOL.19960501.0392.

100657

Buscheck, T.A.; Gansemer, J.; DeLorenzo, T.H.; Nitao, J.J.; and Shaffer, R.J. 1998. *Multiscale Thermohydrologic Model Sensitivity Analysis.* UCRL-ID-131489. Livermore, California: Lawrence Livermore National Laboratory. ACC: MOL.19980901.0245.

148521

Buscheck, T.A.; Gansemer, J.; Nitao, J.J.; and Delorenzo, T.H. 1999. "Multi-Scale Near-Field Thermohydrologic Analysis of Alternative Designs for the Potential Repository at Yucca Mountain." *Scientific Basis for Nuclear Waste Management XXII, Symposium held November 30-December 4, 1998, Boston, Massachusetts, U.S.A.* Wronkiewicz, D.J. and Lee, J.H., eds. *556,* 615-622. Warrendale, Pennsylvania: Materials Research Society. TIC: 246426.

145972

Buscheck, T.A.; Glascoe, L.G.; Lee, K.H.; Gansemer, J.; Sun, Y.; and Mansoor, K. 2003. "Validation of the Multiscale Thermohydrologic Model Used for Analysis of a Proposed Repository at Yucca Mountain." *Journal of Contaminant Hydrology, 62-63,* 421-440. New York, New York: Elsevier. TIC: 254205.

164638

Buscheck, T.A.; Rosenberg, N.D.; Gansemer, J.; and Sun, Y. 2002. "Thermohydrologic Behavior at an Underground Nuclear Waste Repository." *Water Resources Research, 38,* (3), 10-1 through 10-19. Washington, D.C.: American Geophysical Union. TIC: 253566.

160749

Canori, G.F. and Leitner, M.M. 2003. *Project Requirements Document*. TER-MGR-MD-000001 REV 02. Las Vegas, Nevada: Bechtel SAIC Company. ACC: DOC.20031222.0006.

166275

Cho, Y.I.; Ganic, E.N.; Hartnett, J.P.; and Rohsenow, W.M. 1998. "Basic Concepts of Heat Transfer." Chapter 1 of *Handbook of Heat Transfer*. 3rd Edition. Rohsenow, W.M.; Hartnett, J.P.; and Cho, Y.I., eds. New York, New York: McGraw-Hill. TIC: 253612.

160802

Crane, R.A.; Vachon, R.I.; and Khader, M.S. 1977. "Thermal Conductivity of Granular Materials - A Review." *Proceedings of the Seventh Symposium on Thermophysical Properties, held at National Bureau of Standards, Gaithersburg, Maryland, May 10-12, 1977*. Cezairliyan, A., ed. Pages 109-123. New York, New York: American Society of Mechanical Engineers. TIC: 246057.

113426

CRWMS (Civilian Radioactive Waste Management System) M&O (Management and Operating Contractor) 1998. *Drift Scale Test As-Built Report*. BAB000000-01717-5700-00003 REV 01. Las Vegas, Nevada: CRWMS M&O. ACC: MOL.19990107.0223.

111115

CRWMS M&O 1998. *Total System Performance Assessment-Viability Assessment (TSPA-VA) Analyses Technical Basis Document*. Las Vegas, Nevada: CRWMS M&O. ACC: MOL.19981008.0001; MOL.19981008.0002; MOL.19981008.0003; MOL.19981008.0004; MOL.19981008.0005; MOL.19981008.0006; MOL.19981008.0007; MOL.19981008.0008; MOL.19981008.0009; MOL.19981008.0010; MOL.19981008.0011.

108000

CRWMS M&O 2000. *Thermal Tests Thermal-Hydrological Analyses/Model Report*. ANL-NBS-TH-000001 REV 00. Las Vegas, Nevada: CRWMS M&O. ACC: MOL.20000505.0231.

146921

CRWMS M&O 2000. *Total System Performance Assessment for the Site Recommendation*. TDR-WIS-PA-000001 REV 00 ICN 01. Las Vegas, Nevada: CRWMS M&O. ACC: MOL.20001220.0045.

153246

CRWMS M&O 2001. *Effective Thermal Conductivity for Drift-Scale Models Used in TSPA-SR*. CAL-EBS-HS-000001 REV 00. Las Vegas, Nevada: CRWMS M&O. ACC: MOL.20010301.0252.

153410

de Marsily, G. 1986. *Quantitative Hydrogeology*: *Groundwater Hydrology for Engineers*. San Diego, California: Academic Press. TIC: 208450.

100439

DOE (U.S. Department of Energy) 2004. *Quality Assurance Requirements and Description.* DOE/RW-0333P, Rev. 16. Washington, D.C.: U.S. Department of Energy, Office of Civilian Radioactive Waste Management. ACC: DOC.20040907.0002.   171539

Fetter, C.W. 1993. *Contaminant Hydrogeology.* Upper Saddle River, New Jersey: Prentice Hall. TIC: 240691.   102009

Flint, A.L.; Flint, L.E.; Bodvarsson, G.S.; Kwicklis, E.M.; and Fabryka-Martin, J. 2001. "Evolution of the Conceptual Model of Unsaturated Zone Hydrology at Yucca Mountain, Nevada." *Journal of Hydrology, 247,* ([1-2]), 1-30. New York, New York: Elsevier. TIC: 250932.   156351

Forester, R.M.; Bradbury, J.P.; Carter, C.; Elvidge, A.B.; Hemphill, M.L.; Lundstrom, S.C.; Mahan, S.A.; Marshall, B.D.; Neymark, L.A.; Paces, J.B.; Sharpe, S.E.; Whelan, J.F.; and Wigand, P.E. 1996. *Synthesis of Quaternary Response of the Yucca Mountain Unsaturated and Saturated Zone Hydrology to Climate Change.* Milestone 3GCA102M. Las Vegas, Nevada: U.S. Geological Survey. ACC: MOL.19970211.0026.   100148

Francis, N.D., Jr.; Webb, S.W.; Itamura, M.T.; and James, D.L. 2003. *CFD Modeling of Natural Convection Heat Transfer and Fluid Flow in Yucca Mountain Project (YMP) Enclosures.* SAND2002-4179. Albuquerque, New Mexico: Sandia National Laboratories. ACC: MOL.20030906.0165.   164602

Freeze, G.A.; Brodsky, N.S.; and Swift, P.N. 2001. *The Development of Information Catalogued in REV00 of the YMP FEP Database.* TDR-WIS-MD-000003 REV 00 ICN 01. Las Vegas, Nevada: Bechtel SAIC Company. ACC: MOL.20010301.0237.   154365

Freeze, R.A. and Cherry, J.A. 1979. *Groundwater.* Englewood Cliffs, New Jersey: Prentice-Hall. TIC: 217571.   101173

Hardin, E.L. 1998. *Near-Field/Altered-Zone Models Report.* UCRL-ID-129179 DR. Livermore, California: Lawrence Livermore National Laboratory. ACC: MOL.19980504.0577.   100350

Haukwa, C.; Wu, Y.S.; Hinds, J.J.; Zhang, W.; Ritcey, A.C.; Pan, L.H.; Simmons, A.M.; and Bodvarsson, G.S. 1998. *Results of Sensitivity Studies of Thermo-Hydrologic Behavior Conducted on Hydrologic Parameter Sets.* Milestone SP3CK5M4. Berkeley, California: Lawrence Berkeley National Laboratory. ACC: MOL.19980918.0001.   117826

Hilf, J.W. 1975. "Compacted Fill." Chapter 7 of *Foundation Engineering Handbook.* Winterkorn, H.F. and Fang, H.-Y., eds. New York, New York: Van Nostrand Reinhold. TIC: 248400.   169699

Hillel, D. 1998. *Environmental Soil Physics*. San Diego, California: Academic Press. TIC: 254422.

165404

Holman, J.P. 1990. *Heat Transfer*. 7th Edition. New York, New York: McGraw-Hill. TIC: 242477.

106052

Incropera, F.P. and DeWitt, D.P. 1996. *Fundamentals of Heat and Mass Transfer*. 4th Edition. New York, New York: John Wiley & Sons. TIC: 243950.

108184

Incropera, F.P. and DeWitt, D.P. 2002. *Fundamentals of Heat and Mass Transfer*. 5th Edition. New York, New York: John Wiley & Sons. TIC: 254280.

163337

Irvine, T.F., Jr. 1998. "Thermophysical Properties." Chapter 2 of *Handbook of Heat Transfer*. 3rd Edition. Rohsenow, W.M.; Hartnett, J.P.; and Cho, Y.I., eds. New York, New York: McGraw-Hill. TIC: 253612.

170361

Itasca Consulting Group 2002. *Itasca Software–Cutting Edge Tools for Computational Mechanics*. Minneapolis, Minnesota: Itasca Consulting Group. TIC: 252592.

160331

Jury, W.A.; Gardner, W.R.; and Gardner, W.H. 1991. *Soil Physics*. 5th Edition. New York, New York: John Wiley & Sons. TIC: 241000.

102010

Kaviany, M. 1998. "Heat Transfer in Porous Media." Chapter 9 of *Handbook of Heat Transfer*. 3rd Edition. Rohsenow, W.M.; Hartnett, J.P.; and Cho, Y.I., eds. New York, New York: McGraw-Hill. TIC: 253612.

170520

Keenan, J.H.; Keyes, F.G.; Hill, P.G.; and Moore, J.G. 1969. *Steam Tables, Thermodynamic Properties of Water Including Vapor, Liquid, and Solid Phases (English Units)*. New York, New York: John Wiley & Sons. TIC: 246766.

134666

Knudsen, J.G.; Bell, K.J.; Holt, A.D.; Hottel, H.C.; Sarofim, A.F.; Standiford, F.C.; Stuhlbarg, D.; and Uhl, V.W. 1984. "Heat Transmission." Section 10 of *Perry's Chemical Engineers' Handbook*. 6th Edition. Perry, R.H.; Green, D.W.; and Maloney, J.O., eds. New York, New York: McGraw-Hill. TIC: 246473.

170057

Kunii, D. and Smith, J.M. 1960. "Heat Transfer Characteristics of Porous Rocks." *American Institute of Chemical Engineers Journal, 6,* (1), 71-78. New York, New York: American Institute of Chemical Engineers. TIC: 249321.

153166

Leverett, M.C. 1941. "Capillary Behavior in Porous Solids." *AIME Transactions, Petroleum Development and Technology, Tulsa Meeting, October 1940. 142,* 152-169. New York, New York: American Institute of Mining and Metallurgical Engineers. TIC: 240680.

100588

Lichtner, P.C. and Walton, J.C. 1994. *Near-Field Liquid-Vapor Transport in a Partially Saturated High-Level Nuclear Waste Repository*. CNWRA 94-022. San Antonio, Texas: Center for Nuclear Waste Regulatory Analyses. TIC: 216007.

152609

Lide, D.R., ed. 1995. *CRC Handbook of Chemistry and Physics*. 76th Edition. Boca Raton, Florida: CRC Press. TIC: 216194.   101876

Liley, P.E.; Reid, R.C.; and Buck, E. 1984. "Physical and Chemical Data." Section 3 of *Perry's Chemical Engineers' Handbook*. 6th Edition. Perry, R.H.; Green, D.W.; and Maloney, J.O., eds. New York, New York: McGraw-Hill. TIC: 246473.   146851

Liu, H.H.; Doughty, C.; and Bodvarsson, G.S. 1998. "An Active Fracture Model for Unsaturated Flow and Transport in Fractured Rocks." *Water Resources Research, 34,* (10), 2633-2646. Washington, D.C.: American Geophysical Union. TIC: 243012.   105729

LLNL (Lawrence Livermore National Laboratory) 2000. *Validation Test Plan, The Prediction of Thermohydrologic Behavior—NUFT 3.0.1s*. Document Number: 10130-VTP-3.0.1s-00. North Las Vegas, Nevada: U.S. Department of Energy, Yucca Mountain Site Characterization Office. ACC: MOL.20010905.0180.   170258

LLNL (Lawrence Livermore National Laboratory) 2002. *Validation Test Plan, The Prediction of Thermohydrologic Behavior—NUFT 3.0s, Rev 02*. Software Document Number: 10088-VTP-3.0s-02. North Las Vegas, Nevada: U.S. Department of Energy, Yucca Mountain Site Characterization Office. ACC: MOL.20031024.0397.   170259

Manteufel, R.D.; Ahola, M.P.; Turner, D.R.; and Chowdhury, A.H. 1993. *A Literature Review of Coupled Thermal-Hydrologic-Mechanical-Chemical Processes Pertinent to the Proposed High-Level Nuclear Waste Repository at Yucca Mountain*. NUREG/CR-6021. Washington, D.C.: U.S. Nuclear Regulatory Commission. TIC: 207771.   100776

McAdams, W.H. 1954. *Heat Transmission.* 3rd Edition. New York, New York: McGraw-Hill. TIC: 242359.   161435

Michel, H. 1999. "Bernold Sheets." Letter from H. Michel (Bernold AG) to M. Grigore (MK), July 2, 1999, with enclosures. ACC: MOL.20030506.0321.   163054

Montazer, P. and Wilson, W.E. 1984. *Conceptual Hydrologic Model of Flow in the Unsaturated Zone, Yucca Mountain, Nevada*. Water-Resources Investigations Report 84-4345. Lakewood, Colorado: U.S. Geological Survey. ACC: NNA.19890327.0051.   100161

Mualem, Y. 1976. "A New Model for Predicting the Hydraulic Conductivity of Unsaturated Porous Media." *Water Resources Research, 12,* (3), 513-522. Washington, D.C.: American Geophysical Union. TIC: 217339.   100599

Nitao, J.J. 1998. *Reference Manual for the NUFT Flow and Transport Code, Version 2.0*. UCRL-MA-130651. Livermore, California: Lawrence Livermore National Laboratory. ACC: MOL.19980810.0391.   100474

Nitao, J.J. 2000. *Documentation of the Thermal Energy Balance Equation Used in the USNT Module of the NUFT Flow and Transport Code*. UCRL-ID-139836. Livermore, California: Lawrence Livermore National Laboratory. ACC: MOL.20020711.0161. 159883

NRC (U.S. Nuclear Regulatory Commission) 2003. *Yucca Mountain Review Plan, Final Report*. NUREG-1804, Rev. 2. Washington, D.C.: U.S. Nuclear Regulatory Commission, Office of Nuclear Material Safety and Safeguards. TIC: 254568. 163274

Perry, R.H.; Green, D.W.; and Maloney, J.O., eds. 1984. *Perry's Chemical Engineers' Handbook*. 6th Edition. New York, New York: McGraw-Hill. TIC: 246473. 125806

Pollock, D.W. 1986. "Simulation of Fluid Flow and Energy Transport Processes Associated with High-Level Radioactive Waste Disposal in Unsaturated Alluvium." *Water Resources Research, 22,* (5), 765-775. Washington, D.C.: American Geophysical Union. TIC: 253791. 164747

Pruess, K.; Oldenburg, C.; and Moridis, G. 1999. *TOUGH2 User's Guide, Version 2.0*. LBNL-43134. Berkeley, California: Lawrence Berkeley National Laboratory. TIC: 253038. 160778

Sass, J.H.; Lachenbruch, A.H.; Dudley, W.W., Jr.; Priest, S.S.; and Munroe, R.J. 1988. *Temperature, Thermal Conductivity, and Heat Flow Near Yucca Mountain, Nevada: Some Tectonic and Hydrologic Implications.* Open-File Report 87-649. Denver, Colorado: U.S. Geological Survey. TIC: 203195. 100644

van Genuchten, M.T. 1980. "A Closed-Form Equation for Predicting the Hydraulic Conductivity of Unsaturated Soils." *Soil Science Society of America Journal, 44,* (5), 892-898. Madison, Wisconsin: Soil Science Society of America. TIC: 217327. 100610

Winterkorn, H.F. and Fang, H.-Y. 1975. "Soil Technology and Engineering Properties of Soils." Chapter 2 of *Foundation Engineering Handbook.* Winterkorn, H.F. and Fang, H.-Y., eds. New York, New York: Van Nostrand Reinhold. TIC: 248400. 169700

Yagi, S. and Kunii, D. 1957. "Studies on Effective Thermal Conductivities in Packed Beds." *AIChE Journal, 3,* (3), 373-381. New York, New York: American Institute of Chemical Engineers. TIC: 255847. 170330

9.2   CODES, STANDARDS, REGULATIONS, AND PROCEDURES

10 CFR 63. 2005 Energy: Disposal of High-Level Radioactive Wastes in a Geologic Repository at Yucca Mountain, Nevada. ACC: MOL.20050405.0118. 173273

AP-2.22Q, Rev. 1, ICN 1. *Classification Analyses and Maintenance of the Q-List*. Washington, D.C.: U.S. Department of Energy, Office of Civilian Radioactive

Waste Management. ACC: DOC.20040714.0002

AP-SI.2Q, Rev. 0. *Qualification of Level A Developed or Modified Software*.
Washington, D.C.: U.S. Department of Energy, Office of Civilian Radioactive
Waste Management. ACC: MOL.20030113.0150.

ASME (American Society of Mechanical Engineers) 1995. "Materials." Section II   108417
of *1995 ASME Boiler and Pressure Vessel Code*. New York, New York:
American Society of Mechanical Engineers. TIC: 245287.

ASTM G 1-90 (Reapproved 1999). 1999. *Standard Practice for Preparing,*   103515
Cleaning, and Evaluating Corrosion Test Specimens. West Conshohocken,
Pennsylvania: American Society for Testing and Materials. TIC: 238771.

LP-2.14Q-BSC, Rev. 0, ICN 0. *Document Review*. Washington, D.C.:
U.S. Department of Energy, Office of Civilian Radioactive Waste Management.
ACC: DOC.20050113.0007.

LP-2.29Q-BSC, Rev. 0, ICN 0. *Planning for Science Activities*. Washington,
D.C.: U.S. Department of Energy, Office of Civilian Radioactive Waste
Management. ACC: DOC.20050114.0001.

LP-3.15Q-BSC, Rev. 0, ICN 1. *Managing Technical Product Inputs*. Washington,
D.C.: U.S. Department of Energy, Office of Civilian Radioactive Waste
Management. ACC: DOC.20050622.0003.

LP-SIII.2Q-BSC, Rev. 0, ICN 0. *Qualification of Unqualified Data*. Washington,
D.C.: U.S. Department of Energy, Office of Civilian Radioactive Waste
Management. ACC: DOC.20050119.0002.

LP-SIII.10Q-BSC, Rev. 0, ICN 1. *Models*. Washington, D.C.: U.S. Department
of Energy, Office of Civilian Radioactive Waste Management.
ACC: DOC.20050623.0001.

LP-SI.11Q-BSC, Rev. 0, ICN 1. *Software Management.* Washington, D.C.: U.S.
Department of Energy, Office of Civilian Radioactive Waste Management.
ACC: DOC.20041005.0008.

9.3   SOURCE DATA, LISTED BY DATA TRACKING NUMBER

GS000308311221.005. Net Infiltration Modeling Results for 3 Climate Scenarios for   147613
FY99. Submittal date: 03/01/2000.

GS000483351030.003. Thermal Properties Measured 12/01/99 to 12/02/99 Using the   152932
Thermolink Soil Multimeter and Thermal Properties Sensor on Selected Potential
Candidate Backfill Materials Used in the Engineered Barrier System. Submittal date:
11/09/2000.

GS020183351030.001. Uncompacted Bulk Density for Analyses Performed 02/02/00 to 05/23/00 on Potential Backfill Materials Used in the Engineered Barrier System. Submittal date: 01/22/2002.   163107

GS980808312242.015. Water Retention and Unsaturated Hydraulic Conductivity Measurements for Various Size Fractions of Crushed, Sieved, Welded Tuff Samples Measured Using a Centrifuge. Submittal date: 08/21/1998.   119916

LB0205REVUZPRP.001. Fracture Properties for UZ Model Layers Developed from Field Data. Submittal date: 05/14/2002.   159525

LB0208UZDSCPLI.002. Drift-Scale Calibrated Property Sets: Lower Infiltration Data Summary. Submittal date: 08/26/2002.   161788

LB0208UZDSCPMI.002. Drift-Scale Calibrated Property Sets: Mean Infiltration Data Summary. Submittal date: 08/26/2002.   161243

LB03023DKMGRID.001. UZ 3-D Site Scale Model Grids. Submittal date: 02/26/2003.   162354

LB03023DSSCP9I.001. 3-D Site Scale UZ Flow Field Simulations for 9 Infiltration Scenarios. Submittal date: 02/28/2003.   163044

LB0302PTNTSW9I.001. PTN/TSW Interface Percolation Flux Maps for 9 Infiltration Scenarios. Submittal date: 02/28/2003.   162277

LB0302UZDSCPUI.002. Drift-Scale Calibrated Property Sets: Upper Infiltration Data Summary. Submittal date: 02/05/2003.   161787

LB0310MTSCLTH3.001. Mountain Scale 3D TH Predictions: Simulations. Submittal date: 10/21/2003.   170270

LB990701233129.001. 3-D UZ Model Grids for Calculation of Flow Fields for PA for AMR U0000, "Development of Numerical Grids for UZ Flow and Transport Modeling". Submittal date: 09/24/1999.   106785

LB990861233129.001. Drift Scale Calibrated 1-D Property Set, FY99. Submittal date: 08/06/1999.   110226

LB991201233129.001. The Mountain-Scale Thermal-Hydrologic Model Simulations for AMR U0105, "Mountain-Scale Coupled Processes (TH) Models". Submittal date: 03/11/2000.   146894

LL020710223142.024. Moisture Content of Rock from Neutron Logging Activities in the Drift Scale Test (DST): August 1997 through May 2002. Submittal date: 08/20/2002.   159551

LL030709023122.032. Moisture Content of Rock from Neutron Logging Activities in the Drift Scale Test (DST): January 2003 through May 2003. Submittal date: 07/24/2003.   165701

LL980918904244.074. Temperature, Relative Humidity and Gas Pressure Results During the Large Block Test FY 98. Submittal date: 09/29/1998.   135872

LL980919304244.075. Neutron Logging Activities at the Large Block Test (LBT). Submittal date: 09/30/1998.   145099

MO0001SEPDSTPC.000. Drift Scale Test (DST) Temperature, Power, Current, and Voltage Data for June 1, 1999 through October 31, 1999. Submittal date: 01/12/2000.   153836

MO0002ABBLSLDS.000. As-Built Borehole Locations and Sensor Locations for the Drift Scale Test Given in Local (DST) Coordinates. Submittal date: 02/01/2000.   147304

MO0003RIB00071.000. Physical and Chemical Characteristics of Alloy 22. Submittal date: 03/13/2000.   148850

MO0007SEPDSTPC.001. Drift Scale Test (DST) Temperature, Power, Current, and Voltage Data for November 1, 1999 through May 31, 2000. Submittal date: 07/13/2000.   153707

MO0012SEPDSTPC.002. Drift Scale Test (DST) Temperature, Power, Current, and Voltage Data for June 1, 2000 through November 30, 2000. Submittal date: 12/19/2000.   153708

MO0107SEPDSTPC.003. Drift Scale Test (DST) Temperature, Power, Current, and Voltage Data for December 1, 2000 through May 31, 2001. Submittal date: 07/06/2001.   158321

MO0107TC239938.000. Hastelloy Alloy C-22, the Most Versatile Nickel-Chromium-Molybdenum Alloy Available Today with Improved Resistance to Both Uniform and Localized Corrosion as Well as a Variety of Mixed Industrial Chemicals. Submittal date: 07/23/2001.   169995

MO0202SEPDSTTV.001. Drift Scale Test (DST) Temperature, Power, Current, and Voltage Data for June 1, 2001 through January 14, 2002. Submittal date: 02/28/2002.   158320

MO0208SEPDSTTD.001. Drift Scale Test (DST) Temperature Data for January 15, 2002 through June 30, 2002. Submittal date: 08/29/2002.   161767

MO0303SEPDSTTM.000. Drift Scale Test (DST) Temperature Data for July 1, 2002 through December 31, 2002. Submittal date: 03/17/2003.   165698

MO0304MWDALACV.000. ANSYS-LA-Coarse Ventilation. Submittal date: 04/09/2003.	164551
MO0306MWDASLCV.001. ANSYS-LA-Coarse Ventilation. Submittal date: 07/01/2003.	165695
MO0307SEPDST31.000. Drift Scale Test (DST) Temperature Data for 01/01/2003 through 06/30/2003. Submittal date: 07/07/2003.	165699
MO0312SEPQ1997.001. Meteorological Monitoring Data for 1997. Submittal date: 12/24/2003.	167116
MO9807DSTSET01.000. Drift Scale Test (DST) Temperature, Power, Current, Voltage Data for November 7, 1997 through May 31, 1998. Submittal date: 07/09/1998.	113644
MO9810DSTSET02.000. Drift Scale Test (DST) Temperature, Power, Current, Voltage Data for June 1 through August 31, 1998. Submittal date: 10/09/1998.	113662
MO98METDATA114.000. Validated Meteorological Data for Ambient Air Monitoring Report Period 27, January - March 1998. Submittal date: 04/30/1998.	165702
MO98METDATA117.000. Validated Meteorological Data for Ambient Air Monitoring Report Period 28, April - June 1998. Submittal date: 08/11/1998.	165705
MO98METDATA120.000. Validated Meteorological Data for Ambient Air Monitoring Report Period 29, July - September 1998. Submittal date: 10/30/1998.	165706
MO9906DSTSET03.000. Drift Scale Test (DST) Temperature, Power, Current, Voltage Data for September 1, 1998 through May 31, 1999. Submittal date: 06/08/1999.	113673
SN0303T0503102.008. Revised Thermal Conductivity of the Non-Repository Layers of Yucca Mountain. Submittal date: 03/19/2003.	162401
SN0307T0510902.003. Updated Heat Capacity of Yucca Mountain Stratigraphic Units. Submittal date: 07/15/2003.	164196
SN0404T0503102.011. Thermal Conductivity of the Potential Repository Horizon Rev 3. Submittal date: 04/27/2004.	169129

9.4   OUTPUT DATA, LISTED BY DATA TRACKING NUMBER

LL030602723122.027. Multiscale Thermohydrologic Model Output to TSPA and WAGDEG for Upper Infiltration Case. Submittal date: 06/25/2003.

LL030608723122.028. Multiscale Thermohydrologic Model Output to TSPA and WAPDEG for the Lower Infiltration Case. Submittal date: 06/27/2003.

LL030610323122.029. Multiscale Thermohydrologic Model Output to TSPA and WAPDEG for the Mean Infiltration Case. Submittal date: 06/27/2003.

LL030704523122.030. NUFT Input File Data Development to Support LA Multi-Scale Analyses. Submittal date: 07/17/2003.

LL030704623122.031. NUFT Input File Data Development to Support LA Multi-Scale Analyses. Submittal date: 07/23/2003.

LL030804023122.034. Sensitivity Studies for Evaluating the Impact of Thermal Conductivity and Percolation Rate on LA Multi-Scale Analyses. Submittal date: 09/11/2003.

LL030808523122.035. Input and Output Files Supporting MSTHM Micro-Abstractions for LA Multi-Scale Analyses. Submittal date: 09/11/2003.

LL030808623122.036. Input and Output Files for NUFT MSTHM Submodels Supporting LA Multi-Scale Analyses. Submittal date: 09/11/2003.

LL030808723122.037. Input and Output Files for the Creation of NUFT MSTHM Submodel Input Files Supporting LA Multi-Scale Analyses. Submittal date: 09/11/03.

LL030808823122.038. Input and Output Files for Building SMT, SDT, and LDTH Submodel Mesh Files in Support of LA Multi-Scale Analyses. Submittal date: 09/11/03.

LL030808923122.039. Input and Output Files Associated with the Large-Block and Drift Scale Tests in Support of LA Multi-Scale Analyses. Submittal date: 09/11/2003.

LL030906131032.002. Output from the Multi-Scale AMR for the Lower Percolation Mean Thermal Conductivity Case including Drift Wall Temperatures. Submittal date: 09/16/2003.

LL040102223122.042. Evaluation of the Sensitivity of In-Drift Temperature and Relative Humidity to Hydrologic-Property Uncertainty. Submittal date: 01/12/2004.

LL031206723122.041. WAPDEG Output from the Multi-Scale AMR for the Mean Percolation Mean Thermal Conductivity Case including Drift Wall Temperatures. Submittal date: 12/22/2003.

LL030906531032.005. Output from the Multi-Scale AMR for the Upper Percolation Mean Thermal Conductivity Case including Drift Wall Temperatures. Submittal date: 09/16/2003.

LL030905931032.001. Sensitivity Studies for Evaluating the Impact of Thermal Conductivity and Percolation Rate on LA Multi-Scale Analyses. Lower Percolation Case, Low Thermal Conductivity in Host Rock. Submittal date: 09/16/2003.

LL030906331032.004. Sensitivity Studies for Evaluating the Impact of Thermal Conductivity and Percolation Rate on LA Multi-Scale Analyses. Upper Percolation Case, High Thermal Conductivity in Host Rock. Submittal date: 09/16/2003.

LL040310323122.044. Input and Output files of the MSTHM Micro-Abstractions for the Collapsed-Drift cases for the TSPA-LA Low-Probability Seismic Scenario. Submittal date: 03/26/2004.

LL040404423122.045. Input and Output Files of the LDTH-Model Runs for the Focused-Seepage Sensitivity Analysis for the Collapsed-Drift Cases Conducted in ANL-EBS-MD-000049 Rev 1 ICN1. Submittal date: 04/21/2004.

LL040501323122.046. Input and Output Files for the Sensitivity Studies for (1) Host-Rock Hydrologic Properties, (2) Invert Intragranular Hydrologic Properties, and (3) Rubble Heat Capacity for the Low-Probability-Seismic, Collapsed-Drift Cases. Submittal date: 05/19/2004.

LL040604823122.047. Input and Output Files for the Creation of NUFT MSTHM Submodel Input Files Supporting LA Multi-Scale Analyses. Submittal date: 07/12/2004.

LL040703023122.048. Input and Output Files Associated with the Large-Block and Drift Scale Tests in Support of LA Multi-Scale Analyses. Submittal date: 07/15/2004.

LL040703123122.049. Input and Output Files for the Sensitivity Studies for (1) Invert Intergranular Hydrologic Properties, (2) Pseudo Permeability of the Gas-Filled Drift Cavity, and (3) Ventilation Heat-Removal Efficiency. Submittal date: 07/14/2004.

LL040703223122.050. Validation of the Multiscale Thermal-Hydrologic Model Against a Corresponding Three-Dimensional Monolithic Thermal-Hydrologic Model. Submittal date: 07/14/2004.

LL040704323122.051. Input and Output Files for the Comparison Study of Initial Liquid-Phase Saturation and Capillary Pressure for the Mean and Modified-Mean Infiltration-Flux Property Sets for the Lower-Bound, Mean, and Upper-Bound Infiltration-Flux Cases. Submittal date: 07/16/2004.

LL050204723122.053. Multiscale Thermohydrologic Model Output of Fourteen TH Variables from AMR ANL-EBS-MD-000049 (Rev03) for the Upper-Bound Infiltration Case with Mean Host-Rock Thermal Conductivity. Submittal date: 03/03/2005.

LL050204823122.054. Multiscale Thermohydrologic Model Output of Fourteen TH Variables from AMR ANL-EBS-MD-000049 (Rev03) for the Lower-Bound Infiltration Case with Mean Host-Rock Thermal Conductivity. Submittal date: 03/03/2005.

LL050204923122.055. Multiscale Thermohydrologic Model Output of Fourteen TH Variables from AMR ANL-EBS-MD-000049 (Rev03) for the Upper-Bound Infiltration Case with High Host-Rock Thermal Conductivity. Submittal date: 03/03/2005.

LL050205023122.056. Multiscale Thermohydrologic Model Output of Fourteen TH Variables from AMR ANL-EBS-MD-000049 (Rev03) for the Lower-Bound Infiltration Case with Low Host-Rock Thermal Conductivity. Submittal date: 03/03/2005.

LL050401723122.058. Multiscale Thermohydrologic Model Output of Fourteen TH Variables from AMR ANL-EBS-MD-000049 (Rev03) for the Mean Infiltration Flux Case with Mean Host-Rock Thermal Conductivity. Submittal date: 04/12/2005.

LL050500323122.060. Comparison of the Differences Between the Multiscale Thermohydrologic Model (MSTHM) and a Corresponding Three-Dimensional Monolithic Thermal-Hydrologic Model (THM) with the Range of Conditions Resulting from Parametric Uncertainty. Submittal date: 05/25/2005.

MO0307SPAVGSUM.000. van Genuchten hydrologic parameters. Submittal date: 07/26/2003.

MO0406CDFINSMT.000. Area Weighted Cumulative Distribution Function (CDF) for PTN/TSW Infiltration Rates Within SMT Area. Submittal date: 07/01/2004.

MO0505SPAROCKM.000. Rock Mass and Invert Properties for TSPA-LA. Submittal date: 05/23/2005.

9.5   SOFTWARE CODES

boundary_conditions. V1.0. Sun, Sun OS 5.8. 11042-1.0-00.   164275

Chimney_interpolate. V1.0. Sun, Solaris 8. 11038-1.0-00.   164271

colCen. V1.0. Sun, Solaris 8. 11043-1.0-00.   164279

extractBlocks_EXT. V1.0. Sun, SUN O.S. 5.8. 11040-1.0-00.   164281

FLAC3D. V2.1. PC WINDOWS 2000/NT 4.0. 10502-2.1-00.   161947

heatgen_ventTable_emplace. V1.0. Sun, Solaris 8. 11039-1.0-00.   164276

MSTHAC. V7.0. Sun, SUN O.S. 5.8. 10419-7.0-00.   164274

NUFT. V3.0.1s. Sun, SUN O.S. 5.8. 10130-3.0.1s-01.   166636

NUFT. V3.0s. SUN, Sun O.S. 5.8. 10088-3.0s-02.   164541

RADPRO. V4.0. Sun, SUN O.S. 5.8. 10204-4.0-00.   164273

readsUnits. V1.0. Sun, O.S. 5.5.1. 10602-1.0-00.   164542

reformat_EXT_to_TSPA. V1.0. Sun, Sun OS 5.8. 11061-1.0-00.   164272

repository_percolation_calculator. V1.0. Sun, SUN O.S. 5.8. 11041-1.0-00.   164280

rme6. v1.2. SUN, SOLARIS 8. 10617-1.2-00.   163892

XTOOL V10.1. V10.1. Sun Ultra10. 10208-10.1-00.   148638

xw. V1.0. Sun, Solaris 8. 11035-1.0-00.   164278

YMESH. v1.54. SUN, SOLARIS 8. 10172-1.54-00.   163894

APPENDIX I

BUILDING NUFT SUBMODELS

To build the NUFT submodels, the following 14 steps must be completed:

Step –Reformat the mesh from* UZ Flow Models and Submodels** (BSC 2004 [DIRS *169861*]) ***using rme6 v1.2.

The mesh of the three-dimensional site-scale UZ flow model requires some minor modifications in order to be usable as input to YMESH v1.54. Note that the term "World Grid," which is used in the following description, refers to the three-dimensional mountain-scale mesh that is required as input to YMESH v1.54. The software code rme6 v1.2 is used to read the element and vertices files in DTN: LB03023DKMGRID.001 [DIRS 162354] and to then create a single output file (called the World Grid), which contains the three-dimensional mountain-scale mesh in a format that can be read by YMESH v1.54. The software code rme6 v1.2 renames the UZ blocks such that the substring "Ze" in the block name is replaced by "z". Likewise, "VI" is replaced by "v", and all trailing "_" characters are removed.

The three-dimensional mountain-scale mesh (called the World Grid) is built by taking the element/connection and vertices files in DTN: LB03023DKMGRID.001 [DIRS 162354] and reformatting them into a YMESH-readable format using software code rme6 v1.2. Rename "*__" to "*", rename "*Ze" to "*z", and rename "*VI" to "*v".

software code:
　　rme6

inputs:
　　1) Element/connection file (from DTN: LB03023DKMGRID.001 [DIRS 162354])
　　　　Grid_LA_3D.mesh
　　2) Vertices file (from DTN: LB03023DKMGRID.001 [DIRS 162354])
　　　　grid2002.grd

output:
　　1) World Grid
　　　　LBL2003-LA-YMESH (DTN: LL030808823122.038)

command line:
　　rme6 Grid_LA_3D.mesh grid2002.grd LBL2003-LA-YMESH

Step 2 – Expand the reformatted mountain-scale mesh using xw v1.0.

The three-dimensional mountain-scale mesh (file LBL2003-LA-YMESH, which is called the World Grid) created in the previous step needs to be expanded since it is not large enough to encompass the required SMT submodel mesh. The software code xw v1.0 reads the three-dimensional mountain-scale mesh (LBL2003-LA-YMESH) and expands it in the easting direction such that the grid begins at 166,000 m easting and ends at 177,000 m easting in the Nevada Central coordinate system.

software code:
　　xw v1.0

inputs:
    LBL2003-LA-YMESH (output from rme6 v1.2)

outputs:
    1) Expanded World Grid
       LBL2003-LA-YMESH-expand (DTN: LL030808823122.038)

command line:
    xw LBL2003-LA-YMESH LBL2003-LA-YMESH-expand (DTN: LL030808823122.038)

Step 3 – Create the SDT, LDTH, DDT submodel ".dat" files.

The first step in building the NUFT LDTH, SDT, and DDT submodel (also called chimney submodels) input files is to create the files containing the vertical grid dimensions and associated UZ model layers at each LDTH/SDT submodel location. This process begins with a file that gives the easting, northing, and repository elevation in Nevada Central coordinates for each LDTH/SDT submodel location. There are two additional reference files (one for LDTH submodels and one for SDT submodels) that detail how the UZ model layers should be vertically discretized by YMESH v1.54. These files serve as a template for the ".dat" files, which are constructed by taking the relevant template (SDT or LDTH) and inserting the Nevada Central coordinates for the specified LDTH/SDT submodel locations. These files are in the format specified by the YMESH v1.54 user's manual for extracting LDTH/SDT submodel (chimney-submodel) stratigraphies from the expanded World Grid.

inputs:
    a. *SDT and LDTH submodel inputs:*
        chimneyLocation.dat (DTN: LL030808823122.038)
            Contains name, easting, northing, and repository elevation for each "chimney" LDTH/SDT submodel location.

    b. *SDT submodel inputs:*
        SDT_column_template_2003: Template for the SDT submodel .dat files. The template gives instructions to YMESH v1.54 about how to discretize the grid vertically by defining the vertical gridblock dimensions. This is essentially a complete .dat file, except the easting, northing, and repository elevation for each LDTH/SDT submodel (i.e., chimney-submodel) location (e.g., P1R10C5) defined in the file "chimneyLocation.dat" have been inserted (by copying and pasting), which creates ".dat" files for each of the respective SDT submodel locations (DTN: LL030808823122.038).

    c. *LDTH submodel inputs:*
        LDTH_column_template_2003: Template for the LDTH .dat files. The template gives instructions to YMESH v1.54 about how to discretize the grid vertically by defining the vertical gridblock dimensions. This is essentially a complete .dat file, except the easting, northing, and repository elevation for each chimney-submodel location (e.g., P1R10C5) defined in the file "chimneyLocation.dat" have been inserted (by copying and pasting), which creates ".dat" files for each of the respective LDTH submodel locations (DTN: LL030808823122.038).

***Step 4 – Create the SDT, LDTH, DDT submodel ".col" and ".nft" files (software code
YMESH v1.54).***

Once the ".dat" files have been created, YMESH v1.54 is used to create the "User Column
Description" files that contain the vertical dimensions of the grid, along with the vertical
distribution of UZ model layers. This file contains the definition of each gridblock layer
including its thickness and material type (i.e., UZ model layer). To create these files,
YMESH v1.54 is started and the expanded World Mesh is read. Next, a ".dat" file is opened and
a ".col" file is saved by selecting the "User Column Description" save option in the YMESH
File/Save menu. This process is repeated at each chimney-submodel location and for each of the
SDT, LDTH, and DDT submodels.

The output ".nft" file is a NUFT genmsh table as defined in the NUFT user's manual
(Nitao 1998 [DIRS 100474]). To create these files, YMESH v1.54 is started and the expanded
World Mesh is read as input (using the "Open data file" command). Next, a ".dat" file is opened
and a ".nft" file is saved by selecting the "User NUFT genmsh" save option in the YMESH
v1.54 File/Save menu. This process is repeated at each chimney-submodel location and for each
of the SDT, LDTH, and DDT submodels.

software code:
    YMESH v1.54

inputs:
        LBL2003-LA-YMESH-expand (output from xw v1.0) (DTN: LL030808823122.038)
    ".dat" files for each SDT submodel (chimney-submodel) location
(DTN: LL030808823122.038)
    ".dat" files for each LDTH submodel (chimney-submodel) location
(DTN: LL030808823122.038)

outputs:
        ".col" file for each SDT submodel (chimney-submodel) location
(DTN: LL030808823122.038)
        ".nft" file for each SDT submodel (chimney-submodel) location
(DTN: LL030808823122.038)

        ".col" file for each LDTH submodel (chimney-submodel) location
(DTN: LL030808823122.038)
        ".nft" file for each LDTH submodel (chimney-submodel) location
(DTN: LL030808823122.038)

methodology:
    1) Start YMESH v1.54
    2) Open data file: World Grid (/LBL2003-LA-YMESH-expand)
    3) Open data file: chimney.dat file ("*.dat")
    4) Save data file: User NUFT genmsh file ("*.nft")
    5) Save data file: User Column Description file ("*.col")
    6) Repeat Substeps 3 to 5 for all chimney-submodel locations and for each of the SDT,
        LDTH, and DDT submodels.

Step 5 – Create the SDT submodel files.

Once the ".nft" files have been created for the SDT submodel "chimney-submodel" files (Step 4), the following substeps are carried out. For each chimney-submodel location, two output files are created. The first output file is a ".nft.dkm" file that adds the atm, wt, and wp blocks (for atmosphere, water table boundaries, and waste package, respectively) to the input NUFT gensmsh ".nft" file; this file is used for the SDT submodel runs with repository heating. A second file is also created that is a duplicate of the ".nft.dkm" file except there is no wp block present. The second file is called ".nft.dkm0"; this file is used for the SDT submodel initialization runs that have no repository heating. Note that because the file-naming convention is parallel with that used for the LDTH submodels (discussed below), the suffix "dkm" is used for the SDT submodels, as well as for the LDTH submodels. This naming convention does not mean that the SDT submodels use the DKM.

inputs (DTN: LL030808823122.038)
    ".nft" file for each SDT submodel (chimney-submodel) location

output files: (DTN: LL030808823122.038)
    ".nft.dkm" file: adds the atm, wt boundary gridblocks and wp gridblocks to the input ".nft" file for each chimney-submodel location

    ".nft.dkm0" file: adds the atm and wt blocks to the input ".nft" file for each chimney-submodel location

Step 6 – Create the LDTH submodel DKM files.

Once the ".nft" files have been created, the DKM version of these files are created for each LDTH submodel (chimney-submodel) location. There are five output files created for each chimney-submodel location. The input files are modified to include the atmosphere and water table boundary gridblocks, to define the gridblocks within the emplacement drifts that represent the engineered barrier system components (e.g., invert), and to define the matrix and fracture continua. The specific elements added to each of the five types of output files are detailed below. Note that the files with the string "dkm" are used in the LDTH submodel runs with repository heating. The files with the string "dkm0" are used in the LDTH submodel initialization runs that have no repository heating.

inputs: (DTN: LL030808823122.038)
    ".nft" file for each LDTH submodel (chimney-submodel) location

output files (a total of 5: for each chimney-submodel location): (DTN: LL030808823122.038)
    "*.nft.msh.dkm0":   adds the atm and wt boundary gridblocks to the input ".nft" file
    "*.nft.msh.dkm0.f": adds the atm and wt fracture boundary gridblocks to the input ".nft" file. All blocks are prepended with "f-" to represent the fractures.
    "*.nft.msh.dkm.f":   adds the atm, wt, drift, wp, invert, and hstrk fracture gridblocks to the input ".nft" file. All blocks are prepended with "f-" to represent the fractures.

"*.nft.msh.dkm0.m": adds the atm and wt matrix boundary gridblocks to the input .nft file. All blocks are prepended with "m-" to represent the matrix.

"*.nft.msh.dkm.m": adds the atm, wt, drift, wp, invert, and hstrk matrix gridblocks to the input .nft file. All blocks are prepended with "m-" to represent the matrix.

Step 7 – Create DDTand LDTH submodel thermal-radiation connections.

Radiative heat transfer is an important component in the DDT and LDTH heat transfer models. To accommodate this mechanism, NUFT requires a list of all thermal-radiation connections between surfaces inside the drifts that are separated by air. Typical thermal-radiation connections are found between the waste package and the drift wall, the waste package and the drip shield, the drip shield and the drift wall, and the drift wall and other drift wall elements. These connections are generated by hand and verified visually using RADPRO v4.0.

Step 8 – Calculate LDTH submodel percolation flux values.

1. **Determine the "raw" percolation flux value for each LDTH submodel (chimney-submodel) location**

   The LDTH submodel ".col" files created in Step 4 include the name of the grid column (e.g., g_9) from the three-dimensional site-scale UZ model grid (DTN: LB03023DKMGRID.001 [DIRS 162354]) that a given LDTH submodel resides within. For each of the respective LDTH submodel locations, the identity of the three-dimensional site-scale UZ model grid column is recorded; note that this grid column is called the "World Column" by YMESH v1.54). Note that the identity of the World Column is given after the string "WORLD COLUMN" in the LDTH submodel input file. For each LDTH submodel location, the identity of the World Column is used to find the corresponding the present-day-, monsoonal- and glacial-transition-climate PTn-to-TSw percolation fluxes calculated by the three-dimensional site-scale UZ flow model (DTN: LB0302PTNTSW9I.001 [DIRS 162277]). This is repeated for the lower-bound, mean, and upper-bound infiltration flux cases. Note that there are nine percolation flux maps produced by the three-dimensional site-scale UZ flow model, corresponding to the three climate states and three infiltration flux cases.

   i. For each LDTH submodel ".col" file generated above, grep for the string "WORLD COLUMN" and record the name of the World Column that the LDTH submodel resides within.

   ii. From the three-dimensional site-scale UZ flow model (DTN: LB0302PTNTSW9I.001 [DIRS 162277]) and on the basis of the World Column that a given LDTH submodel resides within, find the PTn-to-TSw percolation flux values for the present-day, monsoonal, and glacial-transition climates and for the lower-bound, mean, and upper-bound infiltration flux cases.

2. Determine the average percolation flux value for each repository panel

The software code repository_percolation_calculator v1.0 is used, along with two input files to determine the repository-panel-averaged percolation flux for each repository panel (Panels 1, 2E, 2W, 3, and 5 in Figure 6.3-1). The first input file gives the coordinates of the vertices (i.e., corners) of a given repository panel. The second file is one of nine PTn-to-TSw percolation flux maps calculated by the three-dimensional site-scale UZ flow model (DTN: LB0302PTNTSW9I.001 [DIRS 162277]). The output from repository_percolation_calculator v1.0 is a file that contains the percolation flux values for each of the World Columns (i.e., grid columns from the three-dimensional site-scale UZ flow model) that fall within the given repository panel footprint. The output file also contains the average percolation flux for that repository panel. This averaged panel flux is a simple arithmetic average of the percolation flux values falling within the repository-panel footprint. Because Panel 1 is relatively small, it was decided to group it with Panel 2W and to treat Panels 1 and 2W as a contiguous repository panel. Panels 2E, 3, and 5 are treated individually according to the procedure described above.

> *software code:*
> repository_percolation_calculator v1.0: given a set of coordinates defining the footprint of a repository panel and a PTn-to-TSw percolation flux map from the three-dimensional site-scale UZ flow model (DTN: LB0302PTNTSW9I.001 [DIRS 162277]), determine which World Columns lie within the polygon and do a simple average of the corresponding percolation values to determine the average panel percolation.

> *input files:* (DTN: LL030808723122.037)
> frameData1.dat: define the polygon for panel 1
> frameData2e.dat: define the polygon for panel 2E
> frameData2w.dat:define the polygon for panel 2W
> frameData3.dat: define the polygon for panel 3
> frameData5.dat: define the polygon for panel 5
>
> preq_la_ptn.dat: the present-day-climate lower-bound infiltration flux case PTn-to-TSw percolation flux map (DTN: LB0302PTNTSW9I.001 [DIRS 162277])
> preq _ma_ptn.dat: the present-day-climate mean infiltration flux case PTn-to-TSw percolation flux map (DTN: LB0302PTNTSW9I.001 [DIRS 162277])
> preq _ua_ptn.dat: the present-day-climate upper-bound infiltration flux case PTn-to-TSW percolation flux map (DTN: LB0302PTNTSW9I.001 [DIRS 162277])
>
> monq_la_ptn.dat: the monsoonal-climate lower-bound infiltration flux case PTn-to-TSw percolation flux map (DTN: LB0302PTNTSW9I.001 [DIRS 162277])

monq _ma_ptn.dat: the monsoonal-climate mean infiltration flux case PTn-to-TSw percolation flux map (DTN: LB0302PTNTSW9I.001 [DIRS 162277])

monq _ua_ptn.dat: the monsoonal-climate upper-bound infiltration flux case PTn-to-TSw percolation flux map (DTN: LB0302PTNTSW9I.001 [DIRS 162277])

glaq_la_ptn.dat: the glacial-transition-climate lower-bound infiltration flux case PTn-to-TSw percolation flux map (DTN: LB0302PTNTSW9I.001 [DIRS 162277])

glaq _ma_ptn.dat: the glacial-transition-climate mean infiltration flux case PTn-to-TSw percolation flux map (DTN: LB0302PTNTSW9I.001)

glaq _ua_ptn.dat: the glacial-transition-climate upper-bound infiltration flux case PTn-to-TSw percolation flux map (DTN: LB0302PTNTSW9I.001 [DIRS 162277])

command line

 repository_percolation_calculator <percolation map> <panel outline> <output file>

output files: (DTN: LL030808723122.037)

 glacial_la_frameData1.dat
 glacial_la_frameData2e.dat
 glacial_la_frameData2w.dat
 glacial_la_frameData3.dat
 glacial_la_frameData5.dat
 modern_la_frameData1.dat
 modern_la_frameData2e.dat
 modern_la_frameData2w.dat
 modern_la_frameData3.dat
 modern_la_frameData5.dat
 monsoon_la_frameData1.dat
 monsoon_la_frameData2e.dat
 monsoon_la_frameData2w.dat
 monsoon_la_frameData3.dat
 monsoon_la_frameData5.dat

 glacial_ma_frameData1.dat
 glacial_ma_frameData2e.dat
 glacial_ma_frameData2w.dat
 glacial_ma_frameData3.dat
 glacial_ma_frameData5.dat
 modern_ma_frameData1.dat
 modern_ma_frameData2e.dat
 modern_ma_frameData2w.dat
 modern_ma_frameData3.dat
 modern_ma_frameData5.dat
 monsoon_ma_frameData1.dat
 monsoon_ma_frameData2e.dat

> monsoon_ma_frameData2w.dat
> monsoon_ma_frameData3.dat
> monsoon_ma_frameData5.dat
>
> glacial_ua_frameData1.dat
> glacial_ua_frameData2e.dat
> glacial_ua_frameData2w.dat
> glacial_ua_frameData3.dat
> glacial_ua_frameData5.dat
> modern_ua_frameData1.dat
> modern_ua_frameData2e.dat
> modern_ua_frameData2w.dat
> modern_ua_frameData3.dat
> modern_ua_frameData5.dat
> monsoon_ua_frameData1.dat
> monsoon_ua_frameData2e.dat
> monsoon_ua_frameData2w.dat
> monsoon_ua_frameData3.dat
> monsoon_ua_frameData5.dat
>
> Note: These files contain the PTn-to-TSw percolation flux values falling within a given repository panel footprint and average value for that repository panel.

3. **Calculate panel averages for panels 1 and 2w**

Panels 1 and 2W are grouped for the purpose of computing the LDTH submodel percolation fluxes. This is an area-weighted average, using the respective areas of Panels 1 and 2W.

4. **Calculate average percolation of all LDTH submodels falling within a repository panel**

A weighted average of the percolation flux values (Substep 2) for all LDTH submodel locations that fall inside of a particular panel footprint is calculated. The weighting factors, found in DTN: LL030808723122.037 (Microsoft Excel spreadsheets: scaled chimney percolation (base PTn)_la.xls, scaled chimney percolation (base PTn)_ma.xls, and scaled chimney percolation (base PTn)_ua.xls), are determined by the following simple process. First, each of the SMT gridblocks in a given Panel is assigned to the closest LDTH submodel location. The weighting factors are equal to the number of SMT gridblocks assigned to a given LDTH submodel location divided by the total number of SMT gridblocks in that panel.

5. **Determine the scaled LDTH submodel percolation flux values from the "raw" LDTH submodel "chimney" percolation flux values**

The "raw" LDTH submodel (chimney-submodel) percolation values determined in Step 8, Substep 1 above are scaled so that the average "scaled" percolation flux of all LDTH submodels falling within a given repository panel is the same as the average

percolation flux for that panel determined in Step 8, Substep 2 above. First, a simple arithmetic average of the "raw" LDTH submodel percolation flux values is calculated for a given repository panel. Then a scaling factor is computed for that panel, which is equal to the average percolation flux for that panel (determined in Step 8, Substep 2 above) divided by the average "raw" percolation flux of all LDTH submodels (determined in Step 8, Substep 4) within that panel. Finally, for each of the LDTH submodels within a repository panel, the "raw" percolation flux values are multiplied by the scaling factor for that panel to obtain the scaled percolation flux values for each of the LDTH submodels. This process is repeated for each repository panel, for each of the three climate states and for each of the three infiltration flux cases. These calculations are performed using Microsoft Excel spreadsheets in DTN: LL030808723122.037:

> scaled chimney percolation (base PTn)_la.xls
> scaled chimney percolation (base PTn)_ma.xls
> scaled chimney percolation (base PTn)_ua.xls

6. Create scaled SMT submodel repository-gridblock percolation-flux values

Once the scaled percolation flux values have been calculated for each of the LDTH submodel locations, the corresponding percolation flux values for each of the SMT submodel gridblock locations can be calculated by interpolating the percolation fluxes between each of the LDTH submodel locations. Note that each of the LDTH/SDT submodel locations lies at the centers of SMT submodel repository gridblocks (see Figure 6.2-3). The LDTH and SDT submodel pairs are more or less equally spaced along drifts in the SMT submodel, and are always located at the ends of the emplacement drifts, and typically at one or two other locations along the central portion of the drift. Also, LDTH and SDT submodel pairs are typically located along every third drift. It is important to note that the gridblocks representing the emplacement drifts in the SMT submodel are regularly spaced, with 20-m gridblock spacing along each drift and each drift being represented by a gridblock row that is 81-m wide (which represents the drift spacing). Thus, intermediate locations along a drift (between LDTH/SDT submodel locations) can be linearly interpolated simply on the basis of the number of gridblocks separating that particular location from the pair of LDTH/SDT submodel locations that straddle it, and upon which the simple linear interpolation is based. Once the drifts that contain LDTH and SDT submodel pairs have been filled in with interpolated values, the drifts lying between these interpolated drifts can also be interpolated as well. The interpolation methodology interpolates linearly between drifts (north/south) such that the previously interpolated SMT submodel gridblock pairs are the same distance from the ventilation inlet as the target SMT submodel gridblock location. Again, because of the uniform gridblock spacing, the interpolation process is simply based upon the number of drifts between the drift for which the interpolation is being conducted and the previously interpolated emplacement drifts (which contain the LDTH-SDT submodel locations) that straddle the target drift.

Step 9 – Determine the identity of the world column (from the three-dimensional site-scale UZ flow model) for each LDTH-SDT submodel pair.

The ".col" files created in Step 4 include the name of the world column into which an LDTH/SDT submodel pair falls. These world column names are recorded from the ".col" files for the LDTH and SDT submodels.

Step 10 – Compute SMT, SDT, and LDTH submodel boundary conditions.

The software code boundary_conditions v1.0 generates upper and lower boundary conditions for the LDTH, SMT, and SDT submodels of the MSTHM. The boundary conditions are derived from the three-dimensional site-scale UZ flow model. Data are extracted from the three-dimensional site-scale UZ flow model grid (DTN: LB03023DKMGRID.001 [DIRS 162354]) and from a file (DTN: LB991201233129.001 [DIRS 146894]) containing boundary conditions at the ground surface and at an elevation of 730 m, which was the location of the (horizontal) water table in the three-dimensional site-scale UZ flow model grid used in the TSPA-SR (DTN: LB990701233129.001 [DIRS 106785]). Interpolation is used to determine the boundary conditions at the sloping water table in the three-dimensional site-scale UZ flow model. The software code boundary_conditions v1.0 reads input files containing the following information, respectively: (1) the SMT submodel grid, (2) the UZ model grid (File: MESH_rep.VF of DTN: LB991201233129.001 [DIRS 146894]) and (3) the initial conditions (File: INCON_thm_s32.dat of DTN: LB991201233129.001 [DIRS 146894]) from *Mountain-Scale Coupled Processes (TH/THC/THM) Models* (BSC 2004 [DIRS 169866]), (4) the grid centers and ground-surface and water-table elevations of the World Columns in the three-dimensional site-scale UZ flow model, (5) coordinates of the LDTH/SDT submodel locations, and (6) the values of wet thermal conductivity of the UZ model layers. Boundary conditions are generated at all World Columns (from the three-dimensional site-scale UZ flow model) and at all LDTH/SDT submodel locations. For the LDTH submodels, boundary_conditions v1.0 generates a table of boundary conditions at the ground surface, including temperature, gas-phase pressure, air mass fraction, and specific enthalpy of water at the ground-surface conditions in NUFT-input format. Also generated for LDTH submodels are boundary conditions at the water table, including temperature and gas-phase pressure in NUFT-input format. For the SMT and SDT submodels, boundary_conditions v1.0 generates ground-surface and water table temperatures in NUFT-input format. See Appendix II for details on the SMT submodel boundary condition construction.

Note that since the boundary conditions were determined for the SMT, SDT, and LDTH submodels, a new source of boundary condition has been made available from the *Mountain-Scale Coupled Processes (TH/THC/THM) Models* (BSC 2004 [DIRS 169866]). The temperature and gas-phase-pressure boundary conditions can be extracted from the INCON block of file: th_v16.dat of DTN: LB0310MTSCLTH3.001 [DIRS 170270]. Compared to the use of file: INCON_thm_s32.dat of DTN: LB991201233129.001 [DIRS 146894], these updated boundary conditions result in negligible differences in temperatures and gas-phase pressures at both the upper boundary (the ground surface) and the lower boundary (the water table). Table I-1 gives the repository-wide averaged temperature at the upper and lower boundaries for the mountain-scale TH model from *Mountain-Scale Coupled Processes (TH/THC/THM) Models* (BSC 2004 [DIRS 169866]) and for the MSTHM. Table I-2 gives the corresponding

repository-wide averaged gas-phase pressure at the upper and lower boundaries for the respective models.

Table I-1. Repository-Wide Averaged Temperature at the Upper and Lower Boundaries of the Mountain-Scale TH Model and the MSTHM

	Temperature (°C)			
	Mountain-Scale TH Model[a]	MSTHM[b]	Mean Difference	Root Mean Squared Error
Upper Boundary	17.098	17.061	-0.037	0.170
Lower Boundary	30.097	30.117	0.021	0.157

[a] Mountain Scale TH values based on DTN: LB0310MTSCLTH3.001 [DIRS 170270], INCON block of file: th_v16.dat.
[b] MSTHM based on DTN: LB991201233129.001 [DIRS 146894], file INCON_thm_s32.dat.

NOTE: Repository-wide temperature and gas-phase pressures are determined for the heated repository footprint, plus the contingency area in the southern portion of Panel 2 (previously called Panel 5 in Figure 6.2.3).

Table I-2. Repository-Wide Averaged Gas-Phase Pressure at the Upper and Lower Boundaries of the Mountain-Scale TH Model and the MSTHM

	Gas-Phase Pressure (Pa)			
	Mountain-Scale TH Model[a]	MSTHM[b]	Mean Difference	Root Mean Squared Error
Upper Boundary	85,787	85,782	-5	172
Lower Boundary	91,810	91,805	-5	18

[a] Mountain Scale TH values based on DTN: LB0310MTSCLTH3.001 [DIRS 170270], INCON block of file: th_v16.dat.
[b] MSTHM based on DTN: LB991201233129.001 [DIRS 146894], file INCON_thm_s32.dat.

NOTE: Repository-wide temperature and gas-phase pressures are determined for the heated repository footprint, plus the contingency area in the southern portion of Panel 2 (previously called Panel 5 in Figure 6.2.3).

Tables I-1 and I-2 also give the root mean square error in temperature and gas-phase pressure boundary conditions between the Mountain-Scale TH and the MSTHM. The differences between the two models are negligible. Therefore, obtaining the boundary conditions from DTN: LB991201233129.001 [DIRS 146894], file INCON_thm_s32.dat is reasonable and appropriate.

Step 11 – Compute SMT, SDT, LDTH and DDT submodel heat-generation curves.

Using a reference heat-generation-versus-time table, as well as a table of ventilation-heat-removal-efficiency as a function of time and distance from the ventilation inlet, heatgen_ventTable_emplace v1.0 produces files of heat-generation-versus-time tables in NUFT-heatgen format. These heat-generation files have the influence of reduced heat-generation rates during the 50-year ventilation preclosure period and full-power heating during the postventilation postclosure period. See Appendix III for details on building the heat generation curves. See Appendix V for the assembly of NUFT input files.

Step 12 – Compile natural- and engineered-system properties.

Using several DTNs containing material-property values of the natural system and several Information Exchange Drawings containing material-property values of the engineered system,

material-property files (called NUFT rocktab files) are constructed. These files are in the NUFT rocktab format; these files are read in as "include" file in the SMT, SDT, LDTH and DDT submodel NUFT input files. See Appendix IV for details on assembling the rocktab files that contain the material property values for the respective submodels.

Step 13 – Compute effective thermal conductivity.

To account for heat transfer by natural convection in the emplacement drift, correlations have been developed (Francis et al. 2003 [DIRS 164602], Table 6) for the relationship between drift wall, waste package, and drift air temperatures and an effective thermal conductivity K_{eff} of the air in the emplacement drift cavity that represents the influence of heat transfer by natural convection. This process is conducted for the cavity between the drip shield and drift wall in the LDTH submodels and DDT submodels. This process is also conducted for the cavity between the waste package and drip shield in the DDT submodels.

It should be noted that the correlations for the in-drift effective thermal conductivity, which were obtained from Table 6 of Francis et al (2003 [DIRS 164602]), have been updated in *In-Drift Natural Convection and Condensation* (BSC 2004 [DIRS 164327], Table 6.4.7-3), resulting in very small changes to the coefficients. The small changes to the coefficients in the correlations are negligible, as shown in Figure I-1 for the effective thermal conductivity between the drip shield and drift wall at an average fluid temperature of 95°C.
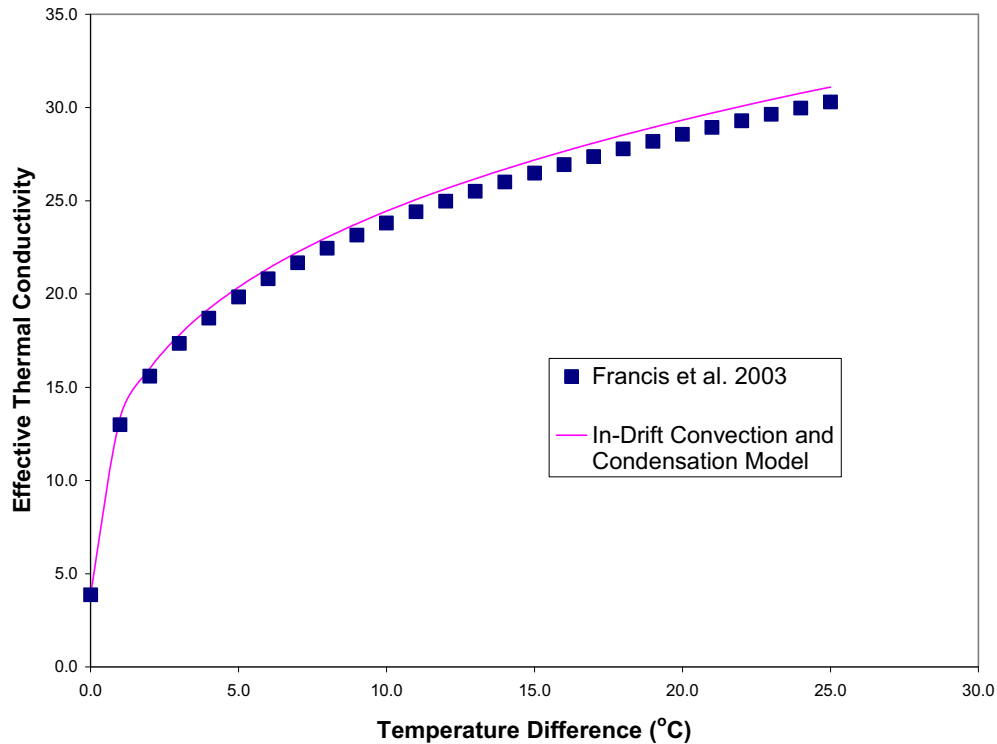
NOTE: The in-drift effective thermal conductivity between the drip shield and drift wall as a function of the temperature difference between those surfaces is plotted from the correlation in Table 6 of Francis et al. (2003 [DIRS 164602]) and in Table 6.4.7-3 of *In-Drift Natural Convection and Condensation* (BSC 2004 [DIRS 164327]).

Figure I-1.   Plot of In-Drift Effective Thermal Conductivity Between the Drip Shield and Drift Wall as a Function of Temperature Difference

The effective thermal conductivity K_{eff} is determined by running a NUFT submodel (either LDTH or DDT) starting with an initial guess for K_{eff} for the gas-filled cavities in the drift. The appropriate formula from Table 6 of *CFD Modeling of Natural Convection Heat Transfer and Fluid Flow in Yucca Mountain Project (YMP) Enclosures* (Francis et al. 2003 [DIRS 164602]) is used to compute K_{eff} in the gas-filled cavities and the NUFT submodel is rerun with the new value of K_{eff}. Each time a new NUFT-submodel run is completed, the value of K_{eff} is computed and compared with the previous iteration. After the value of K_{eff} has converged (between successive iterations), the iterative process is completed. The effective thermal conductivity K_{eff} is a time-varying parameter and the formula in Table 6 of Frances et al. (2003 [DIRS 164602]) involves computing temperatures averaged over the gridblocks representing the gas-filled cavities in the emplacement drift. To carry out this iterative process, extractBlocks_EXT v1.0 is used. This software code takes a list of gridblocks, extracts the required information from the NUFT-submodel output, applies the appropriate formula from Table 6 of Frances et al. (2003 [DIRS 164602]), and produces a time history of calculated K_{eff}.

software code:
    extractBlocks_EXT v1.0

inputs:
    The name of an input file that defines how to apply the formula from Table 6 of
    Frances et al. (2003 [DIRS 164602]) (DTN: LL030808723122.037)

```
DDT_Keff_postclose_inside_0_wp1
DDT_Keff_postclose_inside_0_wp2
DDT_Keff_postclose_inside_0_wp3
DDT_Keff_postclose_inside_0_wp4
DDT_Keff_postclose_inside_0_wp5
DDT_Keff_postclose_inside_0_wp6
DDT_Keff_postclose_inside_0_wp7
DDT_Keff_postclose_inside_0_wp8
DDT_Keff_preclose_0_wp1
DDT_Keff_preclose_0_wp2
DDT_Keff_preclose_0_wp3
DDT_Keff_preclose_0_wp4
DDT_Keff_preclose_0_wp5
DDT_Keff_preclose_0_wp6
DDT_Keff_preclose_0_wp7
DDT_Keff_preclose_0_wp8
```

outputs:
    A file with a time history of K_{eff} calculated from the NUFT input
    (DTN: LL030808723122.037)

```
DDT_Keff_postclose_inside_0_wp1.out
DDT_Keff_postclose_inside_0_wp2.out
DDT_Keff_postclose_inside_0_wp3.out
DDT_Keff_postclose_inside_0_wp4.out
DDT_Keff_postclose_inside_0_wp5.out
DDT_Keff_postclose_inside_0_wp6.out
DDT_Keff_postclose_inside_0_wp7.out
DDT_Keff_postclose_inside_0_wp8.out
DDT_Keff_preclose_0_wp1.out
DDT_Keff_preclose_0_wp2.out
DDT_Keff_preclose_0_wp3.out
DDT_Keff_preclose_0_wp4.out
DDT_Keff_preclose_0_wp5.out
DDT_Keff_preclose_0_wp6.out
DDT_Keff_preclose_0_wp7.out
DDT_Keff_preclose_0_wp8.out
```

Step 14 – Create SMT submodel mesh.

To create the SMT submodel mesh used for the MSTHM calculations in this report, one must
carefully perform the following steps. Note that one must be using the qualified version of
YMESH v1.54 and Solaris OS 5.8 UNIX operating system.

   a. Execute YMESH v1.54
       ymesh

b. Pull down *File* tab on YMESH v1.54 to and *Open* the data file. In the *Select Input File* popup highlight the file "LBL2003-LA-YMESH-expand_qualified" (from NUFT-submodel Building Step 2) and click *OK*

c. Pull down *Edit* tab and highlight *Extend World Columns*. Make certain the *Above* tab is active. Enter the following:

Material   atm
Thickness   200.
click *OK* button

d. Remain in the *Extended World Columns* but now make the *Below* tab active. Enter the following:

Material   sz1
Thickness   30.
click *OK* button

Material   sz2
Thickness   60.
click *OK* button

Material   sz3
Thickness   70.
click *OK* button

Material   sz4
Thickness   120.
click *OK* button

Material   sz5
Thickness   240.
click *OK* button

Material   sz6
Thickness   480.
click *OK* button

Material   bsmnt
Thickness   0.1
click *OK* button

e. Click *CLOSE* button on *Extend World Columns* popup

f. Open *File* pulldown from YMESH v1.54 menu and select *Open data file*

g. In the *Select Input File* popup, select file "tspa03.grid03-150w" and click *OK* button

h. Highlight *Options* pulldown from YMESH v1.54 menu and select *Trim Top Boundary*

i. In *Ending Conditions* popup menu, enter the following:

   Material   atm
   Thickness   0.1
   click *Apply* button
   click *Close* button

j. Highlight *Edit* pulldown from YMESH v1.54 menu and select *Element Names*

k. In *Rename Elements* popup window, follow these steps:

   i. Select *Material* button and enter

      Prefix   atm
      Material   atm
      Click *Apply* button

      Prefix   bsm

      Material   bsmnt

      Click *Apply* button

   ii. Select *PrefixIndexFile* button

      In the PrefixIndexRangeFile space enter
      heatBlockIndicesPanel1_2e_2w_3_5.data
      Click Apply button
      Click *Close* button

l. Highlight the *File* pulldown menu and select *Save data file*

   In the Save File popup window type the *Selection* space enter "tspa03.mesh03-150w"
   Click *OK* button
   (Note that this saves the mesh)

m. Return to a UNIX command prompt and type the following UNIX commands

   ```
   rm P1-UB_list P2E-UB_list P2W-UB_list P3-UB_listP5-UB_list
   grep P1 tspa03.mesh03-150w > P1-UB_list
   grep P2E tspa03.mesh03-150w > P2E-UB_list
   grep P2W tspa03.mesh03-150w > P2W-UB_list
   grep P3 tspa03.mesh03-150w > P3-UB_list
   grep P5 tspa03.mesh03-150w > P5-UB_list
   ```

n. Using a text editor, open the five files just created: P1-UB_list, P2E-UB_list, P2W-UB_list, P3-UB_list, and P5-UB_list (DTN: LL030808823122.038)

o. Edit the five files by removing all gridblock connections information (which is the last 70 percent of the file), saving only the element information (which is the first 30 percent of the file)

     p.   Save the five files with the above names

Note that any mistake made by the user in executing the YMESH v1.54 steps forces the user to return to the beginning and redo the YMESH v1.54 steps.

INTENTIONALLY LEFT BLANK

APPENDIX II

BUILDING BOUNDARY CONDITIONS FOR SUBMODELS

The software code boundary_conditions v1.0 generates upper and lower boundary conditions for the LDTH, SMT, and SDT submodels (see Step 10 of Appendix I). The boundary conditions are derived from *Mountain-Scale Coupled Processes (TH/THC/THM) Models* (BSC 2004 [DIRS 169866]) (DTN: LB991201233129.001 [DIRS 146894]). Data are extracted from the three-dimensional site-scale UZ flow model grid being used in the TSPA-LA (DTN: LB03023DKMGRID.001 [DIRS 162354]), as well as from *Mountain-Scale Coupled Processes (TH/THC/THM) Models* (BSC 2004 [DIRS 169866]), including the boundary conditions (file INCON_thm_s32.dat in DTN: LB991201233129.001 [DIRS 146894]) and the corresponding three-dimensional mountain-scale grid (file MESH_rep.VF in DTN: LB991201233129.001 [DIRS 146894]). It should be noted that the three-dimensional mountain-scale grid used in *Mountain-Scale Coupled Processes (TH/THC/THM) Models* (BSC 2004 [DIRS 169866]) has a horizontal water table at an elevation of 730 m, while the three-dimensional site-scale UZ flow model grid used in the TSPA-LA (DTN: LB03023DKMGRID.001 [DIRS 162354]) has a sloping water table. The software code boundary_conditions v1.0 uses linear interpolation to determine the water-table boundary conditions at the sloping water-table surface in the three-dimensional site-scale UZ flow model grid used in the TSPA-LA (DTN: LB03023DKMGRID.001 [DIRS 162354]). The software code boundary_conditions v1.0 reads input files containing the following information, respectively: (1) the SMT submodel grid, (2) the UZ model grid and (3) initial conditions from *Mountain-Scale Coupled Processes (TH/THC/THM) Models* (BSC 2004 [DIRS 169866]), (4) the grid centers and ground-surface and water-table elevations of the World Columns in the three-dimensional site-scale UZ flow model, (5) coordinates of the LDTH/SDT submodel locations, and (6) the values of wet thermal conductivity of the UZ model layers.

For item (4) above, colCen v1.0 is used to determine the grid centers for all World Columns in the three-dimensional site-scale UZ flow model.

Boundary conditions are generated by boundary_conditions v1.0 at all World Columns (from the three-dimensional site-scale UZ flow model) and at all LDTH/SDT submodel locations. For the LDTH submodels, boundary_conditions v1.0 generates a table of boundary conditions at the ground surface, including temperature, gas-phase pressure, air mass fraction, and specific enthalpy of water at the ground-surface conditions in NUFT-input format. Also generated for LDTH submodels are boundary conditions at the water table, including temperature and gas-phase pressure in NUFT-input format. For the SMT and SDT submodels, boundary_conditions generates ground-surface and water-table temperatures in NUFT-input format.

Prior to determining the boundary conditions, Steps 1 and 2 of Appendix I, which result in an expanded three-dimensional mountain-scale mesh (called the expanded World Grid for YMESH v1.54), must be executed. This expanded three-dimensional mountain-scale mesh (also called the expanded World Grid) is used as an input to boundary_conditions v1.0, which subsequently outputs all of the boundary condition files to be used for all of the submodels (see Appendix V for the assembly of NUFT input files).

Create boundary condition files for all submodels.

The software code boundary_conditions v1.0 was used to create the boundary conditions for all submodels.

software code:

boundary_conditions

input files (DTN: LL030808723122.037)

smtMesh (SMT submodel mesh file in NUFT meshfile input format)

MESH_rep.VF of DTN: LB991201233129.001 [DIRS 146894] (Mesh file for *Mountain-Scale Coupled Processes (TH/THC/THM) Models* (BSC 2004 [DIRS 169866]))

INCON_thm_s32.dat of DTN: LB991201233129.001 (Initial conditions for *Mountain-Scale Coupled Processes (TH/THC/THM) Models* (BSC 2004 [DIRS 169866]))

grid_column_centers (Ground-surface and water-table elevations and coordinates of World Columns of the three-dimensional site-scale UZ flow model grid, which is the LBL2002-YMESH Expanded World Grid; this information is generated as output from colCen v1.0—see above**)**

chimneyLocation (For each LDTH-SDT submodel pair this file locates the corresponding World Column in the LBL2002-YMESH Expanded World Grid)

tcond.dat (Thermal conductivity of UZ model layers)

output files (DTN: LL030808723122.037)

chimSurfBC.out (LDTH submodel surface boundary conditions: temperature, gas pressure, air mass fraction in gas phase, and specific enthalpy of water)

chimLowerBC.out (LDTH submodel water table boundary conditions: temperature and gas pressure)

smtUpperBC.out (Surface boundary temperature for SMT submodel in NUFT input format)

smtLowerBC.out (Lower boundary temperature for SMT submodel in NUFT input format)

worldColBC.out (LDTH/SDT submodel-type boundary conditions for all World Columns in the LBL2002-YMESH Expanded World Grid)

smtWorldBC (Summary of SMT submodel boundary conditions for columns in the LBL2002-YMESH Expanded World Grid)

execution process

To start, type:
boundary_conditions

Enter output file extension:

`out`

Enter thermal cond. of material below water table, SMT submodel:

`1.2`

Enter value of added thickness below water table, SMT submodel:

`1000`

Enter name of SMT submodel mesh file:

Hit return with no entry to use default file, smtMesh

`SMTMESHTEST`

Enter name of the Mountain-Scale Coupled Process (TH/THC/THM) Models (BSC 2004 [DIRS 169866]) mesh file:

Hit return with no entry to use default file, MESH_rep.VF

MESH_rep.VF
Enter name of the Mountain-Scale Coupled Process (TH/THC/THM) Models (BSC 2004 [DIRS 169866]) file with init.cond.:

Hit return with no entry to use default file, INCON_thm_s32.dat

INCON_thm_s32.dat
Enter name of file with World Column data from the 3-D site-scale UZ flow model:

Hit return with no entry to use default file, grid_column_centers

`GRID_COLUMN_CENTERS`

Enter name of file with LDTH-/SDT submodel "chimney" locations:

Hit return with no entry to use default file, chimneyLocation

`CHIMNEYLOCATION`

Enter name of file with thermal cond. data:
Hit return with no entry to use default file, tcond.dat

`TCOND.DAT`

INTENTIONALLY LEFT BLANK

APPENDIX III

HEAT GENERATION FOR SUBMODELS

To produce the heat generation for the SMT, SDT, DDT, and LDTH submodels (Step 11 in Appendix I) the following instructions must be followed. The software code heatgen_ventTable_emplace v1.0 is used for this purpose.

The software code heatgen_ventTable_emplace v1.0 is used to incorporate the influence of ventilation heat-removal efficiency on the net heat generation available for heating the host rock. This is accomplished using a net-available-heat-generation fraction (Table III-1), which is equal to 1 minus the heat-removal-efficiency fraction, and which is given as a function of time and distance from the ventilation inlet. This code requires a control file that provides names of the locations (within the repository) at which heat generation files should be created along with the distance of that location from the ventilation inlet. The output of heatgen_ventTable_emplace v1.0 is a series of files of heat-generation-rate-versus-time tables that account for the heat-removal efficiency of forced-convection ventilation of the emplacement drifts during the preclosure period. The output files from heatgen_ventTable_emplace v1.0 are in NUFT heatgen format.

Table III-1. Net Available Heat-Generation Fraction as a Function of Time and Distance from the Ventilation Inlet Used in this Report

Time	Distance from Ventilation Inlet (m)										
(yr)	0	1	10	100	200	300	400	500	600	700	800
0.000001	1	1	1	1	1	1	1	1	1	1	1
0.00001	0.146308	0.142676	0.142563	0.140993	0.140799	0.140799	0.140799	0.140799	0.140799	0.140799	0.140799
0.0001	0.217303	0.216986	0.227705	0.228043	0.227014	0.226996	0.226996	0.226996	0.226996	0.226996	0.226996
0.001	0.476088	0.473018	0.481063	0.53203	0.523485	0.52025	0.520202	0.520168	0.520168	0.520168	0.520168
0.002	0.292264	0.316736	0.339064	0.639182	0.629461	0.623959	0.623759	0.623744	0.623744	0.623744	0.623744
0.005	0.280038	0.285626	0.299503	0.623057	0.63828	0.632743	0.625883	0.625394	0.625413	0.625413	0.625413
0.01	0.193758	0.208711	0.222313	0.342672	0.618228	0.62856	0.609709	0.607226	0.607041	0.607041	0.607041
0.02	0.13269	0.147196	0.158759	0.269033	0.281053	0.620632	0.614217	0.601249	0.599502	0.599277	0.599301
0.05	0.098427	0.107858	0.117531	0.207132	0.270728	0.592514	0.600299	0.609218	0.624081	0.640142	0.621325
0.1	0.081837	0.090038	0.098317	0.179413	0.242904	0.301132	0.38071	0.447719	0.48086	0.561239	0.641619
0.167	0.071587	0.07973	0.087446	0.161575	0.219363	0.276089	0.328697	0.372876	0.398714	0.457227	0.51574
0.5	0.054689	0.061099	0.067563	0.12848	0.173734	0.216918	0.259313	0.300316	0.333768	0.364466	0.395163
1	0.046744	0.051877	0.057946	0.111957	0.152629	0.191916	0.230384	0.269126	0.306335	0.340477	0.372663
2	0.040779	0.043124	0.048668	0.098252	0.133631	0.168209	0.203015	0.237214	0.27068	0.30221	0.333407
5	0.034946	0.028339	0.034312	0.07884	0.109622	0.139492	0.170165	0.20001	0.229961	0.257114	0.285117
7	0.034075	0.032974	0.039111	0.07985	0.107428	0.135075	0.163945	0.191241	0.218936	0.245204	0.271005
10	0.031507	0.027718	0.034033	0.072152	0.098795	0.124889	0.151777	0.178159	0.204479	0.229816	0.253769
20	0.027692	0	0.008322	0.04327	0.068591	0.093648	0.117834	0.142747	0.166506	0.191557	0.213319
30	0.026128	0.001645	0.010748	0.038894	0.060805	0.083288	0.103578	0.125227	0.145393	0.166498	0.186734
50	0.021768	0	0	0.008813	0.026882	0.044891	0.064152	0.080771	0.099534	0.11707	0.134762

Source: These values are equal to 1 minus the heat-removal-efficiency fraction, which is given in
DTN: MO0304MWDALACV.000 [DIRS 164551], FILE: ANSYS-LA-Coarse_Efficiency.xls, Worksheet: sheet 1.

It is important to note that the source of the heat-removal efficiency versus time and distance table (DTN: MO0304MWDALACV.000 [DIRS 164551], FILE: ANSYS-LA-Coarse_Efficiency.xls; Worksheet: sheet 1, "Efficiency Data" Worksheet) was superseded by DTN: MO0306MWDASLCV.001 [DIRS 165695], FILE: ANSYS-LA_Coarse.xls, Worksheet: Efficiency Data. Table III-2 gives the net available heat-generation fraction as a function of time and distance from the ventilation inlet, which is obtained from DTN: MO0306MWDASLCV.001 [DIRS 165695]. Appendix XIV documents the qualification of DTN: MO0304MWDALACV.000 for use in the MSTHM calculations reported in Section 6.3.

Table III-2. Net Available Heat-Generation Fraction as a Function of Time and Distance from the Ventilation Inlet from Updated Data Source

Time (yr)	Distance from Ventilation Inlet (m)										
	0	1	10	100	200	300	400	500	600	700	800
0.000001	1	1	1	1	1	1	1	1	1	1	1
0.00001	0.135066	0.135098	0.134942	0.133348	0.133147	0.133147	0.133147	0.133147	0.133147	0.133147	0.133147
0.0001	0.214621	0.215113	0.225830	0.219550	0.218889	0.218889	0.218889	0.218889	0.218889	0.218889	0.218889
0.001	0.478338	0.475022	0.483168	0.524651	0.511303	0.509651	0.509610	0.509610	0.509610	0.509610	0.509610
0.002	0.357323	0.341228	0.359332	0.637949	0.615778	0.613866	0.613771	0.613771	0.613771	0.613771	0.613771
0.005	0.295914	0.298644	0.311384	0.626357	0.638665	0.618744	0.617352	0.617309	0.617309	0.617309	0.617309
0.01	0.211570	0.220611	0.234199	0.344166	0.623465	0.608533	0.600455	0.599997	0.599962	0.599927	0.599927
0.02	0.148423	0.156541	0.167830	0.277095	0.588253	0.597282	0.616473	0.596000	0.592972	0.592701	0.592664
0.05	0.111385	0.113755	0.123993	0.213644	0.274106	0.347422	0.619900	0.623108	0.623445	0.612159	0.609106
0.1	0.093342	0.094252	0.103040	0.184760	0.248296	0.300246	0.305689	0.627862	0.637413	0.647127	0.656842
0.167	0.082390	0.083169	0.090779	0.165763	0.224567	0.282320	0.334485	0.365615	0.431550	0.553138	0.674726
0.5	0.064291	0.063075	0.069602	0.130512	0.175606	0.219324	0.262088	0.302489	0.331269	0.309213	0.287158
1	0.055766	0.053096	0.059301	0.113254	0.153850	0.192711	0.231531	0.269038	0.306778	0.340002	0.371565
2	0.049463	0.043804	0.050139	0.098439	0.133850	0.167701	0.201723	0.235521	0.269083	0.300283	0.331118
5	0.043663	0.028618	0.035436	0.078572	0.108016	0.138321	0.167566	0.197426	0.225970	0.252974	0.280183
7	0.042880	0.033521	0.038796	0.078778	0.105996	0.133101	0.160787	0.188093	0.214863	0.240398	0.265608
10	0.040675	0.028033	0.034276	0.071455	0.097638	0.123108	0.149386	0.174865	0.199773	0.224872	0.248124
20	0.038559	-0.001342	0.009525	0.042960	0.067913	0.092815	0.116884	0.140830	0.164491	0.187746	0.209693
30	0.038599	0.003452	0.011231	0.040311	0.062029	0.083344	0.104132	0.125229	0.145945	0.166299	0.186499
50	0.037744	-0.022832	-0.011204	0.010284	0.029428	0.048125	0.067176	0.085635	0.103205	0.120745	0.139413

Source: These values are equal to 1 minus the heat-removal-efficiency fraction, which is given in DTN: MO0306MWDASLCV.001 [DIRS 165695], FILE: ANSYS-LA-Coarse.xls, Worksheet: Efficiency data.

Creating Heat Generation Curves for the SDT and LDTH submodels
software code
  heatgen_ventTable_emplace v1.0

inputs: (DTN: LL030808723122.037)
  SDT: string indicating to the software code that this is an SDT/LDTH submodel heatgen
    file
  multi-package_7WP_Segment_Info_SDT_LDTH_TSPA03: default SDT/LDTH
  submodel heat-generation table with nominal loading and no ventilation

  LA_ventilation_table_50yr.rfm: ventilation table with ventilation efficiency as a function
  of time and distance from the ventilation inlet.

  ventilation_time.reform: file giving the name and distance from the ventilation inlet
  for each LDTH-/SDT submodel "chimney" location.

outputs: (heatgen file) (DTN: LL030808723122.037)
  P*_LDTH-SDT output heatgen file for each LDTH-/SDT submodel "chimney" location

Creating Heat Generation Curves for the DDT submodels
software code
  heatgen_ventTable_emplace

inputs: (DTN: LL030808723122.037)
  DDT: string indicating to the software code that this is a DDT heatgen file
  DDT_TSPA03: default DDT heat generation table with nominal loading and no
  ventilation

  LA_ventilation_table_50yr.rfm: ventilation table with ventilation efficiency as a function
  of time and distance from the ventilation inlet.

  ventilation_time.reform: file giving the name and distance from the ventilation inlet
  for each LDTH-/SDTsubmodel "chimney" location.

outputs: (heatgen file) (DTN: LL030808723122.037)
  P*_DDT output heatgen file for each LDTH-/SDT-submodel "chimney" location

Creating Heat Generation Curves for the SMT submodel
software code
  heatgen_ventTable_emplace

inputs: (DTN: LL030808723122.037)
  SMT: string indicating to the software code that this is an SMT submodel heatgen file
  SMT_TSPA03: default SMT submodel heat-generation-versus-time table with
  nominal loading and no ventilation

  LA_ventilation_table_50yr.rfm: ventilation table with ventilation efficiency as a function
  of time and distance from the ventilation inlet.

ventilation_time.rfm: file giving the name and distance from the ventilation inlet for each LDTH-/SDT submodel "chimney" location.

outputs: (heatgen file) (DTN: LL030808723122.037)
SMT_TSPA03_P*   output heatgen file for each SMT submodel location

The heatgen files are then used as inputs to the NUFT input files; see Appendix V for details on the assembly of NUFT input files.

APPENDIX IV

BUILDING SUBMODEL MATERIAL PROPERTY FILES

LDTH - Submodel DKM Properties

Hydrologic properties from DTN: LB0208UZDSCPMI.002 [DIRS 161243] are used for all three infiltration flux cases (Table IV-4), which are documented in Sections 6.3.1, 6.3.2, 6.3.3. Hydrologic properties from DTN: LB0208UZDSCPLI.002 [DIRS 161788] (Table IV-5) and from DTN: LB0302UZDSCPUI.002 [DIRS 161787] (Table IV-6) are used for the sensitivity study to hydrologic-property uncertainty, which is discussed in Section 6.3.2.4. From each of the three Microsoft Excel spreadsheet files contained in the respective DTNs, the following parameters are obtained: permeability (matrix and fracture), porosity (matrix and fracture), van Genuchten properties (matrix and fracture) and residual saturation (matrix and fracture).

The thermal properties are taken from files of the following sources: DTN: SN0303T0503102.008 [DIRS 162401], DTN: SN0307T0510902.003 [DIRS 164196], and Table 7-10 of DTN: SN0404T0503102.011 [DIRS 169129] (File: readme.doc). Bulk thermal conductivity K_{th} (for both wet and dry conditions) and bulk density (average and 1 standard deviation above and below) of the nonrepository GFM2000 layers are contained in DTN: SN0303T0503102.008 [DIRS 162401]. The bulk thermal conductivity (for both wet and dry conditions) and bulk density ρ_b of the repository UZ model layers was obtained from Table 7-10 of DTN: SN0404T0503102.011 [DIRS 169129] (File: readme.doc); these data include mean values as well as one standard deviation above and below the mean. The specific heat capacity of the mineralogical model layers is taken from DTN: SN0307T0510902.003 [DIRS 164196]. The source input data for bulk density and bulk thermal-conductivity is summarized in Table IV-3a.

The following parameters were calculated by hand using parameters obtained in the files listed above: (1) grain density, (2) matrix density and fracture density, (3) matrix and fracture contact length factors, and (4) thermal conductivity relations for matrix and fracture. Table IV-3b shows the results of calculating the density and thermal conductivity for the matrix and fracture continua. It should be noted that the vitric units have no fractures, but in order for the DKM to work, values must be assigned to a pseudo-fracture continuum for vitric units. This is accomplished by simply assigning matrix properties to the fracture continuum for the vitric units (tsw9v, ch1v, ch2v, ch3v, ch4v, ch5v, and ch6v). The specific details of the hand calculations are listed below.

1. The grain density ρ_g is calculated as:

$$\rho_g = \frac{\rho_b}{1 - \phi_m}$$

    where ϕ_m is matrix porosity and ρ_b is bulk density.

2. The grain density ρ_g is partitioned to the matrix and fracture continuum according to the fracture porosity, ϕ_f. The matrix and fracture densities, $\rho_{g,m}$ and $\rho_{g,f}$, are calculated as:

$$\rho_{g,m} = \rho_g \left(1 - \phi_f\right)$$

$$\rho_{g,f} = \rho_g \, \phi_f$$

Because the vitric units do not have fractures, the grain density for the fracture and matrix continuum is calculated slightly differently. The matrix porosity is portioned 50 percent to the matrix continuum and 50 percent to the "pseudo-fracture" continuum. The bulk density is portioned 50 percent to the matrix continuum and 50 percent to the pseudo-fracture continuum. Thus, the grain densities for the fracture and matrix continuum are calculated as:

$$\rho_{g,m} = \rho_{g,f} = \frac{\rho_b}{2\left(1 - \dfrac{\phi_m}{2}\right)}$$

where ϕ_m is the total matrix porosity and ρ_b is the total bulk density. Table IV-3b shows the result of this hand calculation for the vitric units.

3. The matrix-contact-length factor is calculated as $1/(6N)$ where N is the fracture frequency from DTN: LB0205REVUZPRP.001 [DIRS 159525] (Table IV-7) and 6 accounts for the distance between the center of the matrix block and the fractures for Type #1 fractures as described in *Development of Numerical Grids for UZ Flow and Transport Modeling* (BSC 2004 [DIRS 169855], Equation 6-4). The fracture-contact-length factor is always 0, which is obtained from Equation 6-3 of *Development of Numerical Grids for UZ Flow and Transport Modeling* (BSC 2004 [DIRS 169855], Section 6.7). The matrix-contact-length factor and the fracture-contact-length factor affect disequilibrium between the matrix and fracture continuum in the LDTH submodels.

4. The thermal conductivity for the matrix $K_{th,m}$ and fracture $K_{th,f}$ (both dry and wet) are calculated as a function of fracture porosity ϕ_f for the given wet and dry bulk thermal conductivities K_{th}:

$$K_{th,m}^{dry} = K_{th}^{dry} \left(1 - \phi_f\right)$$

$$K_{th,f}^{dry} = K_{th}^{dry} \phi_f$$

$$K_{th,m}^{wet} = K_{th}^{wet} \left(1 - \phi_f\right)$$

$$K_{th,f}^{wet} = K_{th}^{wet} \phi_f$$

These properties are written into a "rocktab" file (an example of which is listed at the bottom of this Appendix) for the NUFT input file (see Appendix V). All transport and partitioning parameters (e.g., Kd and Kd$_{Factor}$) are set to zero because sorption is not considered for any of the calculations of this report.

The uncertainty of the wet and dry thermal conductivity values of the repository UZ model layers was addressed with values from DTN: SN0303T0503102.008 [DIRS 162401] and from Table 7-10 of DTN: SN0404T0503102.011 [DIRS 169129] (File: readme.doc).

Note that de Marsily (1986 [DIRS 100439], p. 233) gives a range from 0.1 for clays to 0.7 for sands. The value of 0.2 for the matrix continuum is used because the pore sizes for matrix are closer to that of clays than to that of sands. A value of 0.7 is assumed for the fracture.

LDTH Submodel In-Drift, DKM Properties

Invert Properties

The invert properties for the matrix continuum (i.e., the intragranular porosity) are obtained from DTN: LB0208UZDSCPMI.002 [DIRS 161243] and for the fracture continuum (i.e., the intergranular porosity) are from Appendix X. Section 5.3.1.8 discusses the assumption about the intergranular permeability of the crushed-tuff invert material. The van Genuchten alpha for the fracture continuum from Table X-7 of Appendix X is 624 bar^{-1}, which converted to SI units, is equal to 6.24×10^{-3} Pa^{-1}. The input parameters that require hand calculations are: (1) intragranular porosity (ϕ_m), (2) the thermal conductivity for the fracture and matrix continuum, and (3) the grain density of the matrix and of the fracture continuum. The thermal properties of the crushed-tuff invert are given in Tables IV-8 and IV-9.

Invert Porosity

The matrix porosity or intergranular porosity of the crushed-tuff grains in the invert, ϕ_m, is taken from DTN: LB0208UZDSCPMI.002 [DIRS 161243] and is equal to 0.131, which is the matrix porosity of the Tptpll (tsw35) unit. The intergranular porosity of the crushed-tuff invert material is obtained from Table X-7 of Appendix X and is equal to 0.45. The porosity of the fracture continuum in the invert, ϕ_f, which is called the intergranular porosity, is a bulk quantity. Because the porosity of the matrix continuum in the invert, which is called the intragranular porosity, $\phi_\mathrm{g,m}$, is also a bulk quantity, the intragranular porosity of the crushed-tuff invert material is given by:

$$\phi_\mathrm{g,m} = \phi_\mathrm{m} \, (1 - \phi_\mathrm{f})$$

Thus, the intragranular porosity (or matrix-continuum porosity) of the crushed-tuff invert material used in the LDTH submodels is equal to 0.0721.

Invert Thermal Conductivity

The bulk thermal conductivity of the crushed-tuff invert material is partitioned 99 percent to the matrix continuum and 1 percent to the fracture continuum, as follows:

$$K_\mathrm{th,f} = K_\mathrm{th} \, (0.01)$$
$$K_\mathrm{th,m} = K_\mathrm{th} \, (0.99)$$

This partitioning is done because the majority of the thermal mass in the invert resides in the matrix continuum.

Invert Grain Density

The bulk grain density of the crushed-tuff invert material is partitioned 99 percent to the matrix continuum and 1 percent to the fracture continuum, as follows:

$$\rho_{g,m} = (0.99)\rho_b/(1-\phi_m)$$
$$\rho_{g,f} = (0.01)\rho_b/(1-\phi_f)$$

where $\rho_{g,m}$ is the grain density of the matrix continuum, $\rho_{g,f}$ is the grain density of the fracture continuum, ρ_b is the bulk density of the crushed-tuff invert material obtained from DTN: GS020183351030.001 [DIRS 163107] (rows 321-370) and given in Table IV-8, ϕ_m is the matrix-continuum porosity of the crushed-tuff invert material, and ϕ_f is the fracture-continuum porosity of the crushed-tuff invert. This partitioning is done because the majority of the thermal mass in the invert resides in the matrix continuum.

Waste Package and Drip Shield Properties

Due to grid resolution limitations in the drift, the geometry of the waste package and drip shield are lumped into a monolithic heat source in the LDTH submodels (see Figure 6.2-6). Waste package density, drip shield density, and thermal conductivity should be averaged into this lumped approximation. The half-area (called $A_{1/2}$) of the waste package and drip shield as represented in the LDTH submodel as a group of finite difference blocks with an area calculated as:

$$A_{1/2} = 0.242 \times 0.58 + 0.40 \times (0.58+0.37) + (0.759+0.760+0.425) \times (0.58+0.37+0.3025) = 2.9552 \text{ m}^2$$

These dimensions are obtained from the gridblock spacings in the LDTH submodels (see Figure 6.2-6). Table 4-1 gives the nominal number of waste packages in the repository: (1) 4,299 21-PWR AP waste packages, (2) 2,831 44-BWR AP waste packages, and (3) 11,184 total waste packages. Therefore, the majority of waste packages (64 percent) will be either 21-PWR AP waste packages or 44-BWR AP waste packages; both of these waste packages weigh 43,000 kg and are 5.165 m in length (Table 4-1). After adding 0.1 m for the waste-package spacing (Table 4-1) to the length of the waste package, the weight per unit length of the majority of waste packages is 43,000 kg divided by 5.265 m (5.165 m + 0.1 m), or 8,200 kg/m. This is taken to be representative of the average waste package in the repository. The lineal weight per unit length of drip shield is equal to the weight of the drip shield (5,000 kg, given in Table 4-1) divided by the drip-shield length (6.105 m, given in Table 4-1), which is equal to 820 kg/m.

The lineal weight per unit length of the average waste package and drip shield is 8,200 kg/m and 820 kg/m, respectively, yielding a total lineal weight of 9,020 kg/m. The equivalent density, ρ_{equiv}, of the LDTH waste package and drip shield is calculated as:

$$\rho_{equiv} = (9,020 \text{ kg/m})/(2 \times A_{1/2}) = 1,526.1 \text{ kg/m}^3$$

The thermal conductivity of the waste package and drip shield is the sum of the thermal conductivity values weighted by the relative weight of the respective materials:

$$K_{th,equiv} = K_{th,ds} \times (820/9,020) + K_{th,wp} \times (8,200/9,020)$$

SDT/DDT Submodel Thermal Properties

The thermal properties are taken from files of the following sources: DTN: SN0303T0503102.008 [DIRS 162401], DTN: SN0307T0510902.003 [DIRS 164196], and DTN: SN0404T0503102.011 [DIRS 169129] (Table 7-10, File: readme.doc). Bulk thermal conductivity and bulk density (average and 1 standard deviation above and below) of the GFM2000 nonrepository layers are contained in DTN: SN0303T0503102.008 [DIRS 162401]. Bulk thermal conductivity and bulk density variation (mean, and 1 standard deviation above and below) of the repository horizon UZ model layers are contained in Table 7-10 of DTN: SN0404T0503102.011 [DIRS 169129] (File: readme.doc). The specific heat capacity of the mineralogical model units was taken from DTN: SN0307T0510902.003 [DIRS 164196]. The input data from these DTNs are summarized in Table IV-3a. As discussed in the footnotes of Table IV-3a there are minor differences between the specific heat capacity used for several mineralogical model units and those given in the source DTN: SN0307T0510902.003 [DIRS 164196]. These differences are much smaller than the range of uncertainty for the affected layers (see column Z of the excel spreadsheet for DTN: SN0307T0510902.003 [DIRS 164196]). The affected mineralogical model units are well removed from the repository horizon; consequently, these small differences have no effect on thermal-hydrologic conditions within and adjacent to emplacement drifts. The SDT, DDT, and SMT submodels use the bulk density and bulk thermal conductivity values and do not require that these values be partitioned into the fracture and matrix continuum. Note that because NUFT uses the grain density (also called solid density), the matrix porosity, which is obtained from DTN: LB0208UZDSCPMI.002 [DIRS 161243], is also required as input to the input files for the SDT, DDT, and SMT submodels.

The only parameter requiring a hand calculation for the SDT and DDT submodel near-field properties is the grain density (or solid density) ρ_g, which is calculated as:

$$\rho_g = \frac{\rho_b}{1 - \phi_m}$$

DDT Submodel In-drift Thermal Properties

The material properties for the DDT submodel are the same as the corresponding bulk thermal properties in the drift for the LDTH submodel. There is a difference with how the waste package and drip shield are accounted for in the DDT submodel, however, as the DDT submodel represents each waste package separately and discretizes the drip shield.

Waste Package and Drip Shield Thermal Properties

For the DDT submodel the weights of each individual waste package are discretely represented, not lumped, into an average representation of the drip shield and waste package, as was done for the LDTH submodel. The mass density of each waste package type (21-PWR, 44-BWR, 5DHLW-long, and 5DHLW-short) is determined by taking volumetric average of the materials (outer barrier, inner vessel, internal cylinder):

$$\rho_{WP} = [\rho_{outer}\,(d_3{}^2 - d_2{}^2) + \rho_{inner}\,(d_2{}^2 - d_1{}^2) + \rho_{internal}\,(d_1{}^2)] / d_3{}^2$$

where d_3 is the outermost diameter of the waste package, d_2 is the inner diameter of the "outer barrier," and d_1 is the diameter of the internal cylinder obtained. The mass densities, ρ_{WP}, ρ_{outer}, ρ_{inner}, and $\rho_{internal}$ are, respectively, the weighted waste package mass density, the outer-barrier mass density, the inner-vessel mass density, and the internal cylinder density. These diameters were obtained from *Design and Engineering, D&E/PA/C IED Typical Waste Package Components Assembly 1 of 9* (BSC 2003 [DIRS 165406], Table 1). The density of the outer barrier (Alloy 22) was obtained from DTN: MO0003RIB00071.000 [DIRS 148850]; the density of the inner vessel (Stainless Steel Type 316) was obtained from Table XI of ASTM G 1-90; the density of the internal cylinder was obtained from Table 2 of *IED Waste Package Decay Heat Generation Design Basis and Thermal Information [Sheet 1 of 1]* (BSC 2005 [DIRS 173499]).

The effective waste package specific heat, Cp_{WP}, of the DDT submodel are calculated for each waste package using a volumetric average of the corresponding materials:

$$Cp_{WP} = [Cp_{outer}\,(d_3{}^2 - d_2{}^2) + Cp_{inner}\,(d_2{}^2 - d_1{}^2) + Cp_{internal}\,(d_1{}^2)] / d_3{}^2$$

where d_3 is the outer diameter of the outer barrier, d_2 is the outer diameter of the inner vessel, and d_1 is the inner diameter of the inner vessel; Cp_{outer} is the specific heat of the outer barrier, Cp_{inner} is the specific heat of the inner vessel, and $Cp_{internal}$ is the specific heat of the internal cylinder.

The effective waste package thermal conductivity, $K_{th,WP}$, also uses a volumetric average:

$$K_{th,WP} = [K_{th,outer}\,(d_3{}^2 - d_2{}^2) + K_{th,inner}\,(d_2{}^2 - d_1{}^2) + K_{th,internal}\,(d_1{}^2)] / d_3{}^2$$

The waste package thermal conductivity only influences longitudinal heat flow along the axis of the drift in the DDT submodel. In other words, radial heat flow (from the center of the waste package to the outer surface) is not predicted in the DDT submodel. Therefore, only the axial component of $K_{th,WP}$ is required in the DDT submodel. Because the materials in the waste package are concentrically arranged, the volumetric average of $K_{th,WP}$ of the respective components of the waste package is the appropriate manner in which to determine the effective waste package thermal conductivity.

The thermal parameters for the drip shield (Table 4-1) were taken directly from Table TCD of *1995 ASME Boiler and Pressure Vessel Code* (ASME 1995, Section II). The thermal parameters required in the NUFT submodels necessitate the calculations described below for titanium.

Due to limitations of grid resolution in the drift of the DDT submodels, all waste packages are modeled as though they have the same diameter even though the actual diameters are not the same (Table 4-1). An effective density ρ_{eff} is calculated for each of the respective waste

packages so that the mass of each waste package is properly represented in the DDT submodels. The effective density ρ_{eff} is equal to the mass of the waste package (Table 4-1) divided by volume of the waste package as it is represented in the DDT submodel.

Thermal Properties for Stainless Steel Type 316 and Titanium

Several of the direct inputs available for determining waste package and drip shield thermal properties require interpolation (to a reference temperature) and/or require simple calculations to the input parameters required by the DDT submodel. The thermal conductivity of Stainless Steel Type 316, which is used in the inner cylinder of the waste packages, requires interpolation to 100°C. Furthermore, the specific heat for Stainless Steel Type 316 should be calculated on the basis of thermal diffusivity and thermal conductivity, which are direct inputs. Similarly, the thermal conductivity of titanium, which is used in the drip shield, require interpolation to a temperature of 100°C. Furthermore, the specific heat for titanium should be calculated on the basis of thermal diffusivity and thermal conductivity, which are direct inputs. The following steps were used to obtain the required parameter values.

1. Mass density of Stainless Steel Type 316

    7.98 g/cm^3 = 7,980 kg/m^3 = 498.175 lb/ft^3

    The bold value above is taken from Table XI of ASTM G 1-90.

2. Thermal conductivity of Stainless Steel Type 316 ($T = 100$°C)

Table IV-1. Interpolation of Thermal Diffusivity and Thermal Conductivity Outlined for Stainless Steel Type 316

Temperature (°F)	Temperature (°C)	Thermal Diffusivity (ft^2/hr)	Thermal Conductivity (BTU/hr-ft-°F)	Thermal Conductivity (W/m·K)
200	93.33	**0.141**	**8.4**	14.54
250	121.11	**0.143**	**8.7**	15.06
212	100.00	*0.1415*	*8.472*	*14.665*
Conversion Factor			1.0	1.730734666

NOTE: The conversion of these parameters from English units to SI units is also shown. The bold values are from Table TCD of *1995 ASME Boiler and Pressure Vessel Code* (ASME 1995).

$$0.1415 = \mathbf{0.141} + \left(\mathbf{0.143} - \mathbf{0.141}\right) \times \frac{212 - 200}{250 - 200}$$

$$8.472 = \mathbf{8.4} + \left(\mathbf{8.7} - \mathbf{8.4}\right) \times \frac{212 - 200}{250 - 200}$$

$$14.665 = 14.54 + \left(15.06 - 14.54\right) \times \frac{212 - 200}{250 - 200}$$

$$14.663 = 1.730734666 \times 8.472$$

3. Specific heat of Stainless Steel Type 316 ($T = 100°C$)

$$\text{Specific Heat (BTU/lb-}^{\circ}\text{F)} = \frac{\text{Thermal Conductivity (BTU/hr-ft-}^{\circ}\text{F)}}{\text{Density (lb/ft}^{3}\text{) Thermal Diffusivity(ft}^{2}\text{/hr)}}$$

$$= \frac{8.472}{498.175 \times 0.1415} = 0.1202 \, (\text{BTU/lb-}^{\circ}\text{F})$$

$$= 503.19 \, (\text{J/kg-}^{\circ}\text{K}).$$

4. Density of titanium

    0.163 lb/in^3 = *4521* kg/m^3 = *281.675* lb/ft^3

    The bold value above is taken from Section II, Table NF-2 of *1995 ASME Boiler and Pressure Vessel Code* (ASME 1995).

5. Thermal conductivity of titanium ($T = 100°C$)

Table IV-2.   Interpolation of Thermal Diffusivity and Thermal Conductivity Outlined for Titanium

Temperature (°F)	Temperature (°C)	Thermal Diffusivity (ft^2/hr)	Thermal Conductivity (BTU/h-ft-°F)	Thermal Conductivity (W/m·K)
200	93.33	**0.331**	**12.00**	20.7688
250	121.11	**0.322**	**11.85**	20.5092
212	100.00	0.3288	11.964	20.7065

NOTE: The conversion of these parameters from English units to SI units is also shown. The bold values are taken from Section II, Table NF-2 of *1995 ASME Boiler and Pressure Vessel Code* (ASME 1995).

$$0.3288 = \mathbf{0.331} + (\mathbf{0.322} - \mathbf{0.331}) \times \frac{212 - 200}{250 - 200}$$

$$11.964 = \mathbf{12.0} + (\mathbf{11.8}5 - \mathbf{12.0}) \times \frac{212 - 200}{250 - 200}$$

6. Specific heat of titanium ($T = 100°C$)

$$\text{Specific Heat (BTU/lb-}^{\circ}\text{F)} = \frac{\text{Thermal Conductivity (BTU/h-ft-}^{\circ}\text{F)}}{\text{Density (lb/ft}^{3}\text{) Thermal Diffusivity(ft}^{2}\text{/h)}}$$

$$= \frac{11.964}{281.675 \times 0.3288} = 0.1292 \, (\text{BTU/lb-}^{\circ}\text{F})$$

$$= 540.85 \, (\text{J/kg-K}).$$

These simple calculations used the following conversion factors:

1. Heat Capacity: 1.0 Btu/(lb-°F) = 4186.8 J/(kg·K)
2. Thermal Conductivity 1.0 Btu/(h-ft-°F) = 1.730734666 W/(m·K)
3. Density 1.0 g/cm^3 = 62.427960576 lb/ft^3
4. 1.0 lb/in^3 = 27,679.904710203 kg/m^3

Invert Thermal Properties

For the DDT submodels, the invert has the same bulk thermal properties as the bulk thermal properties in the LDTH submodels. That is to say that the thermal conductivity, specific heat, and mass density in the DDT submodels are the same as the bulk thermal conductivity, specific heat capacity, and bulk mass density of the invert in the LDTH submodels.

SMT–Submodel thermal properties

Only fault and saturated zone thermal properties need to be specifically calculated for the SMT submodel thermal properties. Otherwise, the SMT submodel uses the same thermal properties as the SDT submodels.

Fault-Zone Thermal Properties

The density of the fault zone is simply the average of all of the units that make up the fault zone:

$$\rho_{tcwfl} = (\rho_{tcwl1} + \rho_{tcwl2} + \rho_{tcwl3})/3$$
$$\rho_{ptnfl} = (\rho_{ptn21} + \rho_{ptn22} + \rho_{ptn23} + \rho_{ptn24} + \rho_{ptn25} + \rho_{ptn26})/6$$
$$\rho_{tsw} = (\rho_{tsw31} + \rho_{tsw32} + \rho_{tsw33} + \rho_{tsw34} + \rho_{tsw35} + \rho_{tsw36} + \rho_{tsw37} + \rho_{tsw38} + \rho_{tsw9v} + \rho_{tsw9z})/10$$
$$\rho_{ch1fl} = (\rho_{ch1v} + \rho_{ch1z})/2 \text{ (similar for ch2fl, ch3fl, ch4fl, ch5fl, ch6fl)}$$
$$\rho_{pp4fl} = \rho_{pp4} \text{ (similar for pp3, pp2, pp1, bf3, bf2, tr3, tr2)}$$

The same process is used to determine the fault-zone properties for thermal conductivity, specific heat and porosity.

Saturated Zone Thermal Properties

The saturated zone intersects 14 UZ model layers (ch1z, ch2z, ch3z ch4z, ch5z, ch6z, pp4, pp3, pp2, pp1, bf3, bf2, tr3, and tr2). The saturated-zone density, thermal conductivity, specific heat, and porosity are simply calculated as the sum of the properties for those units divided by 14.

Rocktab File Example

Listed below is a part of an example rocktab file (dkm-afc-1Dds-mc-mi-03) that would be called in a NUFT input file (see Appendix V). Of note is that several material properties are listed each delineated by the line ";; End of the material". Specific details of the rocktab file properties are found in the NUFT user's manual (Nitao 1998 [DIRS 100474], p. 41).

```
;; dkm-afc-1Dds-mc-mi-03
;;  4/11/2003 @16:23:21
;; 0.50 Shared in matrix & 0.50 shared in fracture
;; atm
(atm
```

```
  (cont-len-fac 1.00e+00) (cont-area-fac 2.00e+00)
  (exfac-adv (liquid 1.00e+00) (gas 1.00e+00))
  (solid-density 1.00e+08) (porosity 0.99)
  (Kd        (water 0.0) (air 0.0))
  (KdFactor  (water 0.0) (air 0.0))
  (Cp 1.00e+08)
  (tcond tcondLin (solid 1.00e+02) (liquid 1.00e+02) (gas 1.00e+02))
  (K0 1.00e-08) (K1 1.00e-08) (K2 1.00e-08)
  (tort (gas 1.00e+00) (liquid 0.00e+00))
  (kr (liquid krlLinear (Sr 0.00e+00) (Smax 1.0))
      (gas krgLinear    (Sr 0.00e+00) (Smax 1.0)))
  (pc (liquid  0.0))
  (krMC (liquid  krMCintrinsic) (gas  krMCintrinsic))
) ;;End of the material
;;Matrix materials
(m-tcw11
  (cont-len-fac 1.81e-01) (cont-area-fac 1.56e+00)
  (exfac-adv (liquid 1.00e+00) (gas 1.00e+00))
  (solid-density 2820.64) (porosity 0.241)
  (Kd        (water 0.0) (air 0.0))
  (KdFactor  (water 0.0) (air 0.0))
  (Cp 9.30e+02)
  (tcond tcondLin (solid 1.26880) (liquid 1.76656) (gas 1.26880))
  (K0 3.74e-15) (K1 3.74e-15) (K2 3.74e-15)
  (tort (gas 2.00e-01) (liquid 0.00e+00))
  (kr (liquid krlVanGen (Sr 2.00e-02) (m 3.88e-01) (Smax 1.0))
      (gas krgModCorey (Srl 2.00e-02) (m 3.88e-01) (Slmax 1.0)))
  (pc (liquid pcVanGen (Sr 2.00e-02) (m 3.88e-01) (alpha 1.01e-05) (Smax 1.0)))
  (krMC (liquid  krMCintrinsic) (gas  krMCintrinsic))
) ;;End of the material
```

[SECTION SKIP]

```
(f-ptn24
  (cont-len-fac 0.00e+00) (cont-area-fac 1.00e+00)
  (exfac-adv (liquid 1.00e+00) (gas 1.00e+00))
  (solid-density 24.90) (porosity 1.00e-02)
  (Kd        (water 0.0) (air 0.0))
  (KdFactor  (water 0.0) (air 0.0))
  (Cp 9.60e+02)
  (tcond tcondLin (solid 0.00490) (liquid 0.01060) (gas 0.00490))
  (K0 3.00e-12) (K1 3.00e-12) (K2 3.00e-12)
  (tort (gas 7.00e-01) (liquid 0.00e+00))
  (kr (liquid krlVanGen (Sr 1.00e-02) (m 6.33e-01) (Smax 1.0) (gamma 2.32e-01))
      (gas krgModCorey (Srl 1.00e-02) (m 6.33e-01) (Slmax 1.0)))
  (pc (liquid pcVanGen (Sr 1.00e-02) (m 6.33e-01)(alpha 1.86e-03)
                       (Smax 1.0) (gamma 2.32e-01)))
  (krMC (liquid  krMCactiveFrac (gamma 2.32e-01) (Sr 1.00e-02))
        (gas      krMCactiveFrac (gamma 2.32e-01) (Sr 0.0)))
) ;;End of the material
(f-ptn25
  (cont-len-fac 0.00e+00) (cont-area-fac 1.00e+00)
  (exfac-adv (liquid 1.00e+00) (gas 1.00e+00))
  (solid-density 16.00) (porosity 5.50e-03)
  (Kd        (water 0.0) (air 0.0))
  (KdFactor  (water 0.0) (air 0.0))
  (Cp 9.60e+02)
  (tcond tcondLin (solid 0.00269) (liquid 0.00583) (gas 0.00269))
  (K0 1.70e-13) (K1 1.70e-13) (K2 1.70e-13)
  (tort (gas 7.00e-01) (liquid 0.00e+00))
  (kr (liquid krlVanGen (Sr 1.00e-02) (m 6.33e-01) (Smax 1.0) (gamma 2.32e-01))
      (gas krgModCorey (Srl 1.00e-02) (m 6.33e-01) (Slmax 1.0)))
```

```
   (pc (liquid pcVanGen (Sr 1.00e-02) (m 6.33e-01)(alpha 1.33e-03)
                        (Smax 1.0) (gamma 2.32e-01)))
   (krMC (liquid  krMCactiveFrac (gamma 2.32e-01) (Sr 1.00e-02))
         (gas     krMCactiveFrac (gamma 2.32e-01) (Sr 0.0)))
) ;;End of the material
```

[SECTION SKIP]

```
(f-tr2
   (cont-len-fac 0.00e+00) (cont-area-fac 1.00e+00)
   (exfac-adv (liquid 1.00e+00) (gas 1.00e+00))
   (solid-density 0.85) (porosity 3.70e-04)
   (Kd        (water 0.0) (air 0.0))
   (KdFactor  (water 0.0) (air 0.0))
   (Cp 9.40e+02)
   (tcond tcondLin (solid 0.00020) (liquid 0.00041) (gas 0.00020))
   (K0 2.50e-14) (K1 2.50e-14) (K2 2.50e-14)
   (tort (gas 7.00e-01) (liquid 0.00e+00))
   (kr (liquid krlVanGen (Sr 1.00e-02) (m 6.33e-01) (Smax 1.0) (gamma 3.70e-01))
       (gas krgModCorey (Srl 1.00e-02) (m 6.33e-01) (Slmax 1.0)))
   (pc (liquid pcVanGen (Sr 1.00e-02) (m 6.33e-01)(alpha 8.90e-04)
                        (Smax 1.0) (gamma 3.70e-01)))
   (krMC (liquid  krMCactiveFrac (gamma 3.70e-01) (Sr 1.00e-02))
         (gas     krMCactiveFrac (gamma 3.70e-01) (Sr 0.0)))
) ;;End of the material
```

Table IV-3a. Specific Heat Capacity, Thermal Conductivity (Dry and Wet) and Bulk Density for the GFM2000 Units

Material Name Used in LDTH Submodels	GFM2000 Layer	Mineralogic Model Unit	Bulk Density kg/m3	Thermal Conductivity, Dry W/m K	Thermal Conductivity, Wet W/m K	Specific Heat Capacity J/g·K
tcw11	Tpcp	Tpc_un	2,190	1.30	1.81	0.93
tcw12	Tpcp		2,190	1.30	1.81	0.93
	TpcLD		2,190	1.30	1.81	0.93
tcw13	Tpcpv3	Tcppv3 -	2,310	0.688	0.796	0.95
	Tpcpv2	Tpcpv2	1,460	0.490	1.06	0.95
ptn21	Tpcpv1	PTn[f]	1,460	0.490	1.06	0.96
ptn22	Tpbt4		1,460	0.490	1.06	0.96
	Tpy (Yucca)		1,460	0.490	1.06	0.96
ptn23	Tpbt3		1,460	0.490	1.06	0.96
ptn24	Tpy		1,460	0.490	1.06	0.96
	Tpbt3		1,460	0.490	1.06	0.96
ptn25	Tpp (Pah)		1,460	0.490	1.06	0.96
ptn26	Tpbt2		1,460	0.490	1.06	0.96
	Tptrv3		1,460	0.490	1.06	0.96
	Tptrv2		1,460	0.490	1.06	0.96
tsw31	Tptrv1	Tptrv1	2,310	0.688	0.796	0.95
	Tptrn	Tptrn -	2,190	1.30	1.81	0.93
tsw32	Tptrn	Tptrl -	2,190	1.30	1.81	0.93
tsw33	Tptrl	Tptf	2,190	1.30	1.81	0.93
	Tptpul	Tptul	1,830	1.1829	1.7749	0.93
tsw34	Tptpmn	Tptpmn	2,150	1.4189	2.0741	0.93
tsw35	Tptpll	Tptpll	1,980	1.2784	1.8895	0.93
tsw36	Tptpln	Tptpln	2,210	1.4900	2.1303	0.93
tsw37	Tptpln		2,210	1.4900	2.1303	0.93
tsw38	Tptpv3	Tptpv3	2,310	0.688	0.796	0.98
tsw9v	Tptpv2	Tptpv2	1,460	0.490	1.06	0.98[a]
tsw9z	Tptpv2		1,460	0.490	1.06	0.98
ch1v	Tptpv1	Tptpv1 -	1,460	0.490	1.06	1.08[b]
	Tpbt1	Tpbt1	1,460	0.490	1.06	1.08[b]
ch1z	Tptpv1		1,460	0.490	1.06	1.08
	Tpbt1		1,460	0.490	1.06	1.08
ch2v	Tac (Calico)	Tac	1,670	0.595	1.26	1.07[c]
ch3v	Tac (Calico)	(4 layers)	1,670	0.595	1.26	1.07[c]
ch4v	Tac (Calico)		1,670	0.595	1.26	1.07[c]
ch5v	Tac (Calico)		1,670	0.595	1.26	1.07[c]
ch2z	Tac (Calico)		1,670	0.595	1.26	1.07
ch3z	Tac (Calico)		1,670	0.595	1.26	1.07
ch4z	Tac (Calico)		1,670	0.595	1.26	1.07

Table IV-3a. Specific Heat Capacity, Thermal Conductivity (Dry and Wet) and Bulk Density for the GFM2000 Units (Continued)

Material Name Used in LDTH Submodels	GFM2000 Layer	Mineralogic Model Unit	Bulk Density kg/m3	Thermal Conductivity, Dry W/m K	Thermal Conductivity, Wet W/m K	Specific Heat Capacity J/g·K
ch5z	Tac (Calico)	Tac (Cont.)	1,670	0.595	1.26	1.07
ch6v	Tacbt (Calicobt)	Tacbt	1,670	0.595	1.26	1.02 d
ch6z	Tacbt (Calicobt)		1,670	0.595	1.26	1.02
pp4	Tcpuv (Prowuv)	Tcpuv	1,790	0.569	1.13	1.04
pp3	Tcpuc (Prowuc)	Tcpuc -	1,790	0.569	1.13	0.93
pp2	Tcpmd (Prowmd)	Tcplc	2,070	1.06	1.63	0.93
	Tcplc (Prowlc)		1,790	0.569	1.13	0.93
pp1	Tcplv (Prowlv)	Tcplv -	1,790	0.569	1.13	1.05 e
	Tcpbt (Prowbt)	Tcbuv	1,790	0.569	1.13	1.05 e
	Tcbuv (Bullfroguv)		1,880	0.658	1.19	1.05 e
bf3	Tcbuc (Bullfroguc)	Tcbuc -	1,880	0.658	1.19	0.93
	Tcbmd (Bullfrogmd)	Tcblc	2,260	1.30	1.81	0.93
	Tcblc (Bullfroglc)		1,880	0.658	1.19	0.93
bf2	Tcblv (Bullfroglv)	Tcblv -	1,880	0.658	1.19	1.05
	Tcbbt (Bullfrogbt)	Tctuv	1,880	0.658	1.19	1.05
	Tctuv (Tramuv)		1,760	0.535	1.10	1.05
tr3	Tctuc (Tramuc)	Tctuc -	1,760	0.535	1.10	0.94
	Tctmd (Trammd)	Tctlc	2,140	1.06	1.63	0.94
	Tctlc (Tramlc)		1,760	0.535	1.10	0.94
tr2	Tctlv (Tramlv)	Tctlv -	1,760	0.535	1.10	0.94
	Tctbt (Trambt)	Tctbt	1,760	0.535	1.10	0.94

[a] Zeolitic value of specific heat capacity (0.98 J/g·K) is used rather than the vitric value (0.96 J/g·K).

[b] Zeolitic value of specific heat capacity (1.08 J/g·K) is used rather than the vitric value (0.96 J/g·K).

[c] Zeolitic value of specific heat capacity (1.07 J/g·K) is used rather than the vitric value (0.96 J/g·K).

[d] Zeolitic value of specific heat capacity (1.02 J/g·K) is used rather than the vitric value (0.97 J/g·K).

[e] Specific heat capacity value for the Tcblv-Tctuv (1.05 J/g·K) is used rather than for the Tcplv-Tcbuv (1.10 J/g·K).

[f] Ptn = Tpcpv1, Tpbt4, Tpy, Tpbt3, Tpp, Tpbt2, Tptrv3, Tptrv2

NOTE: The values for the nonrepository layers are from DTN: SN0303T0503102.008 [DIRS 162401]. The thermal conductivity and bulk density values for the repository layers (tsw33, tsw34, tsw35, tsw36, and tsw37) are from Table 7-10 of DTN: SN0404T0503102.011 [DIRS 169129] (File: readme.doc), with the density values rounded. The GFM2000 layers shown in italics pertain to data obtained from Table 7-10 of DTN: SN0404T0503102.011 [DIRS 169129] (File: readme.doc). The bulk density values from DTN: SN0404T0503102.011 [DIRS 169129] (File: readme.doc) have been slightly rounded to be consistent with the bulk density values from DTN: SN0303T0503102.008 [DIRS 162401]. Mineralogic model units are from *Heat Capacity Analysis Report* (BSC 2004 [DIRS 170003], Tables 6-1 and 6-7). The specific heat capacity for all layers is from DTN: SN0307T0510902.003 [DIRS 164196] for the temperature range of 25 to 325°C. The values of specific heat capacity, thermal conductivity, and bulk density for the layers with multiple GFM2000 layers (e.g., pp1) are the arithmetic average of the corresponding GFM2000-layer values. Table IV-3b gives the result of this averaging for bulk density and bulk thermal conductivity.

Table IV-3b. Thermal Properties for the UZ Model Layers

Material Name	Porosity		Density				Thermal Conductivity					
	ϕ_m	ϕ_f	ρ_b kg/m^3	ρ_G kg/m^3	$\rho_{G,m}$ kg/m^3	$\rho_{G,f}$ kg/m^3	$K_{th,b}$ wet W/m°C	$K_{th,m}$ wet W/m°C	$K_{th,f}$ wet W/m°C	$K_{th,b}$ dry W/m°C	$K_{th,m}$ dry W/m°C	$K_{th,f}$ dry W/m°C
tcw11	0.241	2.40E-02	2190	2890	2820.64	69.36	1.81	1.767	4.34E-02	1.30	1.269	3.12E-02
tcw12	0.088	1.70E-02	2190	2400	2359.20	40.80	1.81	1.779	3.08E-02	1.30	1.278	2.21E-02
tcw13	0.200	1.30E-02	1890	2360	2329.32	30.68	0.93	0.918	1.21E-02	0.59	0.582	7.67E-03
ptn21	0.387	9.20E-03	1460	2380	2358.10	21.90	1.06	1.050	9.75E-03	0.49	0.485	4.51E-03
ptn22	0.428	1.00E-02	1460	2550	2524.50	25.50	1.06	1.049	1.06E-02	0.49	0.485	4.90E-03
ptn23	0.233	2.10E-03	1460	1900	1896.01	3.99	1.06	1.058	2.23E-03	0.49	0.489	1.03E-03
ptn24	0.413	1.00E-02	1460	2490	2465.10	24.90	1.06	1.049	1.06E-02	0.49	0.485	4.90E-03
ptn25	0.498	5.50E-03	1460	2910	2894.00	16.00	1.06	1.054	5.83E-03	0.49	0.487	2.69E-03
ptn26	0.490	3.10E-03	1460	2860	2851.13	8.87	1.06	1.057	3.29E-03	0.49	0.488	1.52E-03
tsw31	0.054	5.00E-03	2250	2380	2368.10	11.90	1.30	1.294	6.50E-03	0.99	0.985	4.95E-03
tsw32	0.157	8.30E-03	2190	2600	2578.42	21.58	1.81	1.795	1.50E-02	1.30	1.289	1.08E-02
tsw33	0.155	5.80E-03	2010	2380	2366.20	13.80	1.79	1.780	1.04E-02	1.24	1.233	7.19E-03
tsw34	0.111	8.50E-03	2150	2420	2399.43	20.57	2.07	2.052	1.76E-02	1.42	1.408	1.21E-02
tsw35	0.131	9.60E-03	1980	2280	2258.11	21.89	1.89	1.872	1.81E-02	1.28	1.268	1.23E-02
tsw36	0.103	1.30E-02	2210	2460	2428.02	31.98	2.13	2.102	2.77E-02	1.49	1.471	1.94E-02
tsw37	0.103	1.30E-02	2210	2460	2428.02	31.98	2.13	2.102	2.77E-02	1.49	1.471	1.94E-02
tsw38	0.043	1.10E-02	2310	2410	2383.49	26.51	0.80	0.791	8.80E-03	0.69	0.682	7.59E-03
tsw9v	0.115[a]	0.115[a]	1460	1890[b]	824.39[c]	824.39[c]	1.06	1.060	N/A	0.49	0.490	N/A
tsw9z	0.275	4.30E-03	1460	2010	2001.36	8.64	1.06	1.055	4.56E-03	0.49	0.488	2.11E-03
ch1v	0.166[a]	0.166[a]	1460	2180[b]	874.78[c]	874.78[c]	1.06	1.060	N/A	0.49	0.490	N/A
ch1z	0.285	1.60E-04	1460	2040	2039.67	0.33	1.06	1.060	1.70E-04	0.49	0.490	8.00E-05
ch2v	0.173[a]	0.173[a]	1670	2550[b]	1009.67[c]	1009.67[c]	1.26	1.260	N/A	0.60	0.600	N/A
ch3v	0.173[a]	0.173[a]	1670	2550[b]	1009.67[c]	1009.67[c]	1.26	1.260	N/A	0.60	0.600	N/A
ch4v	0.173[a]	0.173[a]	1670	2550[b]	1009.67[c]	1009.67[c]	1.26	1.260	N/A	0.60	0.600	N/A
ch5v	0.173[a]	0.173[a]	1670	2550[b]	1009.67[c]	1009.67[c]	1.26	1.260	N/A	0.60	0.600	N/A
ch2z	0.322	3.70E-04	1670	2460	2459.09	0.91	1.26	1.260	4.70E-04	0.60	0.600	2.20E-04
ch3z	0.322	3.70E-04	1670	2460	2459.09	0.91	1.26	1.260	4.70E-04	0.60	0.600	2.20E-04
ch4z	0.322	3.70E-04	1670	2460	2459.09	0.91	1.26	1.260	4.70E-04	0.60	0.600	2.20E-04
ch5z	0.322	3.70E-04	1670	2460	2459.09	0.91	1.26	1.260	4.70E-04	0.60	0.600	2.20E-04
ch6v	0.166[a]	0.166[a]	1670	2550[b]	1000.60[c]	1000.60[c]	1.26	1.260	N/A	0.60	0.600	N/A
ch6z	0.271	1.60E-04	1670	2290	2289.63	0.37	1.26	1.260	2.00E-04	0.60	0.600	1.00E-04
pp4	0.321	3.70E-04	1790	2640	2639.02	0.98	1.13	1.130	4.20E-04	0.57	0.570	2.10E-04
pp3	0.318	9.70E-04	1790	2620	2617.46	2.54	1.13	1.129	1.10E-03	0.57	0.569	5.50E-04
pp2	0.221	9.70E-04	1930	2480	2477.59	2.41	1.38	1.379	1.34E-03	0.81	0.809	7.90E-04
pp1	0.297	3.70E-04	1820	2590	2589.04	0.96	1.15	1.150	4.30E-04	0.60	0.600	2.20E-04
bf3	0.175	9.70E-04	2010	2440	2437.63	2.37	1.40	1.399	1.36E-03	0.87	0.869	8.40E-04
bf2	0.234	3.70E-04	1840	2400	2399.11	0.89	1.16	1.160	4.30E-04	0.62	0.620	2.30E-04
tr3	0.175	9.70E-04	1890	2290	2287.78	2.22	1.28	1.279	1.24E-03	0.71	0.709	6.90E-04
tr2	0.234	3.70E-04	1760	2300	2299.15	0.85	1.10	1.100	4.10E-04	0.54	0.540	2.00E-04

[a] Vitric units have matrix porosity partitioned 50% to the matrix continuum and 50% to the pseudo-fracture continuum.
[b] Value not used in LDTH submodel.
[c] Vitric units have grain density partitioned 50% to the matrix continuum and 50% to the pseudo-fracture continuum.

NOTES: The subscripts m, f, b, and g stand for matrix, fracture, bulk, and grain, respectively. The bulk density ρ_β and bulk thermal conductivity $K_{th,b}$ (wet and dry) are obtained from Table IV-3a, with averaging applied to UZ model layers with multiple GFM2000 layers. The density and thermal-conductivity for the matrix and fracture continua are calculated by hand on the basis of fracture porosity.

Porosity values are derived from Table IV-4.

Table IV-4. Matrix and Fracture Properties for the Mean Infiltration Flux One-Dimensional Drift-Scale Hydrologic Property Set

Material name from DTN source	Material name used in LDTH submodels	Permeability [m²]	Porosity [-]	Residual saturation [-]	α (alpha) [1/Pa]	m [-]	γ (gamma) [-]
tcwM1	m-tcw11	3.74E-15	0.241	0.02	1.01E-05	0.388	N/A[a]
tcwM2	m-tcw12	5.52E-20	0.088	0.20	3.11E-06	0.280	N/A[a]
tcwM3	m-tcw13	5.65E-17	0.200	0.31	3.26E-06	0.259	N/A[a]
ptnM1	m-ptn21	4.60E-15	0.387	0.24	1.62E-04	0.245	N/A[a]
ptnM2	m-ptn22	4.43E-12	0.428	0.13	1.46E-04	0.219	N/A[a]
ptnM3	m-ptn23	9.20E-15	0.233	0.07	2.47E-05	0.247	N/A[a]
ptnM4	m-ptn24	2.35E-12	0.413	0.14	7.90E-04	0.182	N/A[a]
ptnM5	m-ptn25	2.15E-13	0.498	0.06	1.04E-04	0.300	N/A[a]
ptnM6	m-ptn26	1.00E-11	0.490	0.05	9.83E-04	0.126	N/A[a]
tswM1	m-tsw31	2.95E-17	0.054	0.21	8.70E-05	0.218	N/A[a]
tswM2	m-tsw32	2.23E-16	0.157	0.07	1.14E-05	0.290	N/A[a]
tswM3	m-tsw33	6.57E-18	0.155	0.12	6.17E-06	0.283	N/A[a]
tswM4	m-tsw34	1.77E-19	0.111	0.19	8.45E-06	0.317	N/A[a]
tswM5	m-tsw35	4.48E-18	0.131	0.12	1.08E-05	0.216	N/A[a]
tswM6	m-tsw36	2.00E-19	0.103	0.20	8.32E-06	0.442	N/A[a]
tswM7	m-tsw37	2.00E-19	0.103	0.20	8.32E-06	0.442	N/A[a]
tswM8	m-tsw38	2.00E-18	0.043	0.42	6.23E-06	0.286	N/A[a]
tswMv	m-tsw9v	1.49E-13	0.229	0.13	4.86E-05	0.293	N/A[a]
tswMz	m-tsw9z	3.5E-17	0.275	0.36	4.61E-06	0.059	N/A[a]
ch1Mv	m-ch1v	6.65E-13	0.331	0.06	8.73E-05	0.240	N/A[a]
ch1Mz	m-ch1z	3.5E-17	0.285	0.38	2.12E-07	0.349	N/A[a]
ch2Mv	m-ch2v	2.97E-11	0.346	0.06	2.59E-04	0.158	N/A[a]
ch3Mv	m-ch3v	2.97E-11	0.346	0.06	2.59E-04	0.158	N/A[a]
ch4Mv	m-ch4v	2.97E-11	0.346	0.06	2.59E-04	0.158	N/A[a]
ch5Mv	m-ch5v	2.97E-11	0.346	0.06	2.59E-04	0.158	N/A[a]
ch2Mz	m-ch2z	5.2E-18	0.322	0.26	2.25E-06	0.257	N/A[a]
ch3Mz	m-ch3z	5.2E-18	0.322	0.26	2.25E-06	0.257	N/A[a]
ch4Mz	m-ch4z	5.2E-18	0.322	0.26	2.25E-06	0.257	N/A[a]
ch5Mz	m-ch5z	5.2E-18	0.322	0.26	2.25E-06	0.257	N/A[a]
ch6Mv	m-ch6v	2.35E-13	0.331	0.06	1.57E-05	0.147	N/A[a]
ch6Mz	m-ch6z	8.2E-19	0.271	0.36	1.56E-07	0.499	N/A[a]
pp4Mz	m-pp4	8.77E-17	0.321	0.29	4.49E-07	0.474	N/A[a]
pp3Md	m-pp3	7.14E-14	0.318	0.08	8.83E-06	0.407	N/A[a]
pp2Md	m-pp2	1.68E-15	0.221	0.10	2.39E-06	0.309	N/A[a]
pp1Mz	m-pp1	2.35E-15	0.297	0.30	9.19E-07	0.272	N/A[a]
bf3Md	m-bf3	4.34E-13	0.175	0.11	1.26E-05	0.193	N/A[a]
bf2Mz	m-bf2	8.1E-17	0.234	0.21	1.18E-07	0.617	N/A[a]
tr3Md	m-tr3	1.1E-15	0.175	0.11	1.12E-05	0.193	N/A[a]

Table IV-4. Matrix and Fracture Properties for the Mean Infiltration Flux One-Dimensional Drift-Scale Hydrologic Property Set (Continued)

Material name from DTN source	Material name used in LDTH submodels	Permeability [m²]	Porosity [-]	Residual saturation [-]	α (alpha) [1/Pa]	m [-]	γ (gamma) [-]
tr2Mz	m-tr2	8.1E-17	0.234	0.21	1.18E-07	0.617	N/A[a]
tcwF1	f-tcw11	3.0E-11	2.4E-02	0.01	5.27E-03	0.633	0.587
tcwF2	f-tcw12	5.3E-12	1.7E-02	0.01	1.57E-03	0.633	0.587
tcwF3	f-tcw13	4.5E-12	1.3E-02	0.01	1.24E-03	0.633	0.587
ptnF1	f-ptn21	3.2E-12	9.2E-03	0.01	8.70E-04	0.633	0.232
ptnF2	f-ptn22	3.0E-13	1.0E-02	0.01	1.57E-03	0.633	0.232
ptnF3	f-ptn23	3.0E-13	2.1E-03	0.01	5.18E-03	0.633	0.232
ptnF4	f-ptn24	3.0E-12	1.0E-02	0.01	1.86E-03	0.633	0.232
ptnF5	f-ptn25	1.7E-13	5.5E-03	0.01	1.33E-03	0.633	0.232
ptnF6	f-ptn26	2.2E-13	3.1E-03	0.01	1.34E-03	0.633	0.232
tswF1	f-tsw31	8.1E-13	5.0E-03	0.01	1.60E-05	0.633	0.129
tswF2	f-tsw32	7.1E-13	8.3E-03	0.01	1.00E-04	0.633	0.600
tswF3	f-tsw33	7.8E-13	5.8E-03	0.01	1.59E-03	0.633	0.600
tswF4	f-tsw34	3.3E-13	8.5E-03	0.01	1.04E-04	0.633	0.569
tswF5	f-tsw35	9.1E-13	9.6E-03	0.01	1.02E-04	0.633	0.569
tswF6	f-tsw36	1.3E-12	1.3E-02	0.01	7.44E-04	0.633	0.569
tswF7	f-tsw37	1.3E-12	1.3E-02	0.01	7.44E-04	0.633	0.569
tswF8	f-tsw38	8.1E-13	1.1E-02	0.01	2.12E-03	0.633	0.569
tswFv	f-tsw9v	N/A[b]	N/A[b]	N/A[b]	N/A[b]	N/A[b]	N/A[b]
tswFz	f-tsw9z	8.1E-13	4.3E-03	0.01	1.5E-03	0.633	0.370
ch1Fv	f-ch1v	N/A[b]	N/A[b]	N/A[b]	N/A[b]	N/A[b]	N/A[b]
ch1Fz	f-ch1z	2.5E-14	1.6E-04	0.01	1.4E-03	0.633	0.370
ch2Fv	f-ch2v	N/A[b]	N/A[b]	N/A[b]	N/A[b]	N/A[b]	N/A[b]
ch3Fv	f-ch3v	N/A[b]	N/A[b]	N/A[b]	N/A[b]	N/A[b]	N/A[b]
ch4Fv	f-ch4v	N/A[b]	N/A[b]	N/A[b]	N/A[b]	N/A[b]	N/A[b]
ch5Fv	f-ch5v	N/A[b]	N/A[b]	N/A[b]	N/A[b]	N/A[b]	N/A[b]
ch2Fz	f-ch2z	2.5E-14	3.7E-04	0.01	8.9E-04	0.633	0.370
ch3Fz	f-ch3z	2.5E-14	3.7E-04	0.01	8.9E-04	0.633	0.370
ch4Fz	f-ch4z	2.5E-14	3.7E-04	0.01	8.9E-04	0.633	0.370
ch5Fz	f-ch5z	2.5E-14	3.7E-04	0.01	8.9E-04	0.633	0.370
ch6Fv	f-ch6v	N/A[b]	N/A[b]	N/A[b]	N/A[b]	N/A[b]	N/A[b]
ch6Fz	f-ch6z	2.5E-14	1.6E-04	0.01	1.4E-03	0.633	0.370
pp4Fz	f-pp4	2.5E-14	3.7E-04	0.01	1.83E-03	0.633	0.370
pp3Fd	f-pp3	2.2E-13	9.7E-04	0.01	2.47E-03	0.633	0.199
pp2Fd	f-pp2	2.2E-13	9.7E-04	0.01	3.17E-03	0.633	0.199
pp1Fz	f-pp1	2.5E-14	3.7E-04	0.01	1.83E-03	0.633	0.370
bf3Fd	f-bf3	2.2E-13	9.7E-04	0.01	2.93E-03	0.633	0.199

Table IV-4.   Matrix and Fracture Properties for the Mean Infiltration Flux One-Dimensional Drift-Scale Hydrologic Property Set (Continued)

Material name from DTN source	Material name used in LDTH submodels	Permeability [m²]	Porosity [-]	Residual saturation [-]	α (alpha) [1/Pa]	m [-]	γ (gamma) [-]
bf2Fz	f-bf2	2.5E-14	3.7E-04	0.01	8.9E-04	0.633	0.370
tr3Fd	f-tr3	2.2E-13	9.7E-04	0.01	1.6E-03	0.633	0.199
tr2Fz	f-tr2	2.5E-14	3.7E-04	0.01	8.9E-04	0.633	0.370

DTN: LB0208UZDSCPMI.002 [DIRS 161243], File: drift-scale calibrated properties for mean infiltration2.xls; Worksheet: Drift-scale Cal. Hydro Props.

[a] Gamma value does not apply to matrix continuum.
[b] Vitric units (those units ending with a "v") do not have fractures. The fracture continuum properties are the same as those of the matrix continuum for these units.

NOTE: The prefix "m-" stands for matrix and "f-" stands for fracture.

Table IV-5.   Matrix and Fracture Properties for the Lower-Bound Infiltration Flux One-Dimensional Drift-Scale Hydrologic Property Set

Material name from DTN source	Material name used in LDTH submodels	Permeability [m²]	Porosity [-]	Residual saturation [-]	α (alpha) [1/Pa]	m [-]	γ (gamma) [-]
tcwM1	m-tcw11	3.44E-15	0.241	0.02	1.16E-05	0.388	N/A[a]
tcwM2	m-tcw12	3.00E-20	0.088	0.20	2.67E-06	0.280	N/A[a]
tcwM3	m-tcw13	3.96E-17	0.200	0.31	1.64E-06	0.259	N/A[a]
ptnM1	m-ptn21	5.55E-15	0.387	0.24	6.38E-05	0.245	N/A[a]
ptnM2	m-ptn22	8.40E-12	0.428	0.13	1.67E-04	0.219	N/A[a]
ptnM3	m-ptn23	1.92E-14	0.233	0.07	4.51E-05	0.247	N/A[a]
ptnM4	m-ptn24	6.66E-13	0.413	0.14	2.52E-03	0.182	N/A[a]
ptnM5	m-ptn25	1.96E-14	0.498	0.06	1.24E-04	0.300	N/A[a]
ptnM6	m-ptn26	1.00E-11	0.490	0.05	1.63E-03	0.126	N/A[a]
tswM1	m-tsw31	1.42E-17	0.054	0.21	8.02E-05	0.218	N/A[a]
tswM2	m-tsw32	3.96E-16	0.157	0.07	9.46E-06	0.290	N/A[a]
tswM3	m-tsw33	1.60E-18	0.155	0.12	4.25E-06	0.283	N/A[a]
tswM4	m-tsw34	1.38E-19	0.111	0.19	1.19E-06	0.317	N/A[a]
tswM5	m-tsw35	2.33E-18	0.131	0.12	1.97E-06	0.216	N/A[a]
tswM6	m-tsw36	5.58E-19	0.103	0.20	4.22E-07	0.442	N/A[a]
tswM7	m-tsw37	5.58E-19	0.103	0.20	4.22E-07	0.442	N/A[a]
tswM8	m-tsw38	2.93E-18	0.043	0.42	1.43E-06	0.286	N/A[a]
tswMv	m-tsw9v	3.15E-13	0.229	0.13	1.86E-05	0.293	N/A[a]
tswMz	m-tsw9z	3.5E-17	0.275	0.36	4.61E-06	0.059	N/A[a]
ch1Mv	m-ch1v	3.15E-14	0.331	0.06	4.50E-05	0.240	N/A[a]
ch1Mz	m-ch1z	3.5E-17	0.285	0.38	2.12E-07	0.349	N/A[a]
ch2Mv	m-ch2v	1.13E-11	0.346	0.06	1.22E-04	0.158	N/A[a]
ch3Mv	m-ch3v	1.13E-11	0.346	0.06	1.22E-04	0.158	N/A[a]
ch4Mv	m-ch4v	1.13E-11	0.346	0.06	1.22E-04	0.158	N/A[a]
ch5Mv	m-ch5v	1.13E-11	0.346	0.06	1.22E-04	0.158	N/A[a]

Table IV-5. Matrix and Fracture Properties for the Lower-Bound Infiltration Flux One-Dimensional Drift-Scale Hydrologic Property Set (Continued)

Material name from DTN source	Material name used in LDTH submodels	Permeability [m²]	Porosity [-]	Residual saturation [-]	α (alpha) [1/Pa]	m [-]	γ (gamma) [-]
ch2Mz	m-ch2z	5.2E-18	0.322	0.26	2.25E-06	0.257	N/A[a]
ch3Mz	m-ch3z	5.2E-18	0.322	0.26	2.25E-06	0.257	N/A[a]
ch4Mz	m-ch4z	5.2E-18	0.322	0.26	2.25E-06	0.257	N/A[a]
ch5Mz	m-ch5z	5.2E-18	0.322	0.26	2.25E-06	0.257	N/A[a]
ch6Mv	m-ch6v	2.54E-13	0.331	0.06	9.05E-06	0.147	N/A[a]
ch6Mz	m-ch6z	8.2E-19	0.271	0.36	1.56E-07	0.499	N/A[a]
pp4Mz	m-pp4	2.98E-16	0.321	0.29	2.88E-07	0.474	N/A[a]
pp3Md	m-pp3	5.37E-14	0.318	0.08	7.97E-06	0.407	N/A[a]
pp2Md	m-pp2	4.24E-16	0.221	0.10	2.41E-06	0.309	N/A[a]
pp1Mz	m-pp1	7.02E-16	0.297	0.30	1.36E-06	0.272	N/A[a]
bf3Md	m-bf3	2.97E-14	0.175	0.11	1.32E-05	0.193	N/A[a]
bf2Mz	m-bf2	8.1E-17	0.234	0.21	1.18E-07	0.617	N/A[a]
tr3Md	m-tr3	1.1E-15	0.175	0.11	1.12E-05	0.193	N/A[a]
tr2Mz	m-tr2	8.1E-17	0.234	0.21	1.18E-07	0.617	N/A[a]
tcwF1	f-tcw11	3.0E-11	2.4E-02	0.01	4.68E-03	0.633	0.483
tcwF2	f-tcw12	5.3E-12	1.7E-02	0.01	3.20E-03	0.633	0.483
tcwF3	f-tcw13	4.5E-12	1.3E-02	0.01	2.13E-03	0.633	0.483
ptnF1	f-ptn21	3.2E-12	9.2E-03	0.01	2.93E-03	0.633	0.065
ptnF2	f-ptn22	3.0E-13	1.0E-02	0.01	6.76E-04	0.633	0.065
ptnF3	f-ptn23	3.0E-13	2.1E-03	0.01	3.96E-03	0.633	0.065
ptnF4	f-ptn24	3.0E-12	1.0E-02	0.01	2.51E-03	0.633	0.065
ptnF5	f-ptn25	1.7E-13	5.5E-03	0.01	1.53E-03	0.633	0.065
ptnF6	f-ptn26	2.2E-13	3.1E-03	0.01	1.52E-03	0.633	0.065
tswF1	f-tsw31	8.1E-13	5.0E-03	0.01	1.58E-05	0.633	0.037
tswF2	f-tsw32	7.1E-13	8.3E-03	0.01	1.31E-04	0.633	0.528
tswF3	f-tsw33	7.8E-13	5.8E-03	0.01	1.94E-03	0.633	0.528
tswF4	f-tsw34	3.3E-13	8.5E-03	0.01	6.55E-04	0.633	0.476
tswF5	f-tsw35	9.1E-13	9.6E-03	0.01	1.35E-03	0.633	0.476
tswF6	f-tsw36	1.3E-12	1.3E-02	0.01	1.31E-03	0.633	0.476
tswF7	f-tsw37	1.3E-12	1.3E-02	0.01	1.31E-03	0.633	0.476
tswF8	f-tsw38	8.1E-13	1.1E-02	0.01	1.75E-03	0.633	0.476
tswFv	f-tsw9v	N/A[b]	N/A[b]	N/A[b]	N/A[b]	N/A[b]	N/A[b]
tswFz	f-tsw9z	8.1E-13	4.3E-03	0.01	1.5E-03	0.633	0.276
ch1Fv	f-ch1v	N/A[b]	N/A[b]	N/A[b]	N/A[b]	N/A[b]	N/A[b]
ch1Fz	f-ch1z	2.5E-14	1.6E-04	0.01	1.4E-03	0.633	0.276
ch2Fv	f-ch2v	N/A[b]	N/A[b]	N/A[b]	N/A[b]	N/A[b]	N/A[b]
ch3Fv	f-ch3v	N/A[b]	N/A[b]	N/A[b]	N/A[b]	N/A[b]	N/A[b]
ch4Fv	f-ch4v	N/A[b]	N/A[b]	N/A[b]	N/A[b]	N/A[b]	N/A[b]
ch5Fv	f-ch5v	N/A[b]	N/A[b]	N/A[b]	N/A[b]	N/A[b]	N/A[b]
ch2Fz	f-ch2z	2.5E-14	3.7E-04	0.01	8.9E-04	0.633	0.276
ch3Fz	f-ch3z	2.5E-14	3.7E-04	0.01	8.9E-04	0.633	0.276

Table IV-5. Matrix and Fracture Properties for the Lower-Bound Infiltration Flux One-Dimensional Drift-Scale Hydrologic Property Set (Continued)

Material name from DTN source	Material name used in LDTH submodels	Permeability [m²]	Porosity [-]	Residual saturation [-]	α (alpha) [1/Pa]	m [-]	γ (gamma) [-]
ch4Fz	f-ch4z	2.5E-14	3.7E-04	0.01	8.9E-04	0.633	0.276
ch5Fz	f-ch5z	2.5E-14	3.7E-04	0.01	8.9E-04	0.633	0.276
ch6Fv	f-ch6v	N/A[b]	N/A[b]	N/A[b]	N/A[b]	N/A[b]	N/A[b]
ch6Fz	f-ch6z	2.5E-14	1.6E-04	0.01	1.4E-03	0.633	0.276
pp4Fz	f-pp4	2.5E-14	3.7E-04	0.01	1.88E-03	0.633	0.276
pp3Fd	f-pp3	2.2E-13	9.7E-04	0.01	1.32E-03	0.633	0.248
pp2Fd	f-pp2	2.2E-13	9.7E-04	0.01	2.80E-03	0.633	0.248
pp1Fz	f-pp1	2.5E-14	3.7E-04	0.01	6.39E-04	0.633	0.276
bf3Fd	f-bf3	2.2E-13	9.7E-04	0.01	1.91E-03	0.633	0.248
bf2Fz	f-bf2	2.5E-14	3.7E-04	0.01	8.9E-04	0.633	0.276
tr3Fd	f-tr3	2.2E-13	9.7E-04	0.01	1.6E-03	0.633	0.248
tr2Fz	f-tr2	2.5E-14	3.7E-04	0.01	8.9E-04	0.633	0.276

DTN: LB0208UZDSCPLI.002 [DIRS 161788]. File: drift-scale calibrated properties for lower infiltration2.xls; Worksheet: Drift-scale Cal. Hydro Props.

[a] Gamma value does not apply to matrix continuum.
[b] Vitric units (those units ending with a "v") do not have fractures. The fracture continuum properties are the same as those of the matrix continuum for these units.

NOTE: The prefix "m-" stands for matrix and "f-" stands for fracture.

Table IV-6. Matrix and Fracture Properties for the Upper-Bound Infiltration Flux One-Dimensional Drift-Scale Hydrologic Property Set

Material name from DTN source	Material name used in LDTH submodels	Permeability [m²]	Porosity [-]	Residual saturation [-]	α (alpha) [1/Pa]	m [-]	γ (gamma) [-]
tcwM1	m-tcw11	3.90E-15	0.241	0.02	1.23E-05	0.388	N/A[a]
tcwM2	m-tcw12	1.16E-19	0.088	0.20	3.39E-06	0.280	N/A[a]
tcwM3	m-tcw13	4.41E-16	0.200	0.31	3.25E-06	0.259	N/A[a]
ptnM1	m-ptn21	2.14E-14	0.387	0.24	1.56E-04	0.245	N/A[a]
ptnM2	m-ptn22	1.29E-11	0.428	0.13	1.33E-04	0.219	N/A[a]
ptnM3	m-ptn23	4.07E-14	0.233	0.07	2.39E-05	0.247	N/A[a]
ptnM4	m-ptn24	4.27E-12	0.413	0.14	5.62E-04	0.182	N/A[a]
ptnM5	m-ptn25	1.01E-12	0.498	0.06	9.48E-05	0.300	N/A[a]
ptnM6	m-ptn26	1.00E-11	0.490	0.05	5.23E-04	0.126	N/A[a]
tswM1	m-tsw31	1.77E-17	0.054	0.21	4.85E-05	0.218	N/A[a]
tswM2	m-tsw32	2.13E-16	0.157	0.07	1.96E-05	0.290	N/A[a]
tswM3	m-tsw33	2.39E-17	0.155	0.12	5.22E-06	0.283	N/A[a]
tswM4	m-tsw34	2.96E-19	0.111	0.19	1.65E-06	0.317	N/A[a]
tswM5	m-tsw35	8.55E-18	0.131	0.12	5.03E-06	0.216	N/A[a]
tswM6	m-tsw36	7.41E-19	0.103	0.20	1.08E-06	0.442	N/A[a]
tswM7	m-tsw37	7.41E-19	0.103	0.20	1.08E-06	0.442	N/A[a]
tswM8	m-tsw38	7.40E-18	0.043	0.42	5.58E-06	0.286	N/A[a]

Table IV-6. Matrix and Fracture Properties for the Upper-Bound Infiltration Flux One-Dimensional Drift-Scale Hydrologic Property Set (Continued)

Material name from DTN source	Material name used in LDTH submodels	Permeability [m²]	Porosity [-]	Residual saturation [-]	α (alpha) [1/Pa]	m [-]	γ (gamma) [-]
tswMv	m-tsw9v	2.24E-13	0.229	0.13	4.86E-05	0.293	N/A[a]
tswMz	m-tsw9z	3.5E-17	0.275	0.36	4.61E-06	0.059	N/A[a]
ch1Mv	m-ch1v	1.39E-12	0.331	0.06	8.82E-05	0.240	N/A[a]
ch1Mz	m-ch1z	3.5E-17	0.285	0.38	2.12E-07	0.349	N/A[a]
ch2Mv	m-ch2v	4.90E-11	0.346	0.06	2.73E-04	0.158	N/A[a]
ch3Mv	m-ch3v	4.90E-11	0.346	0.06	2.73E-04	0.158	N/A[a]
ch4Mv	m-ch4v	4.90E-11	0.346	0.06	2.73E-04	0.158	N/A[a]
ch5Mv	m-ch5v	4.90E-11	0.346	0.06	2.73E-04	0.158	N/A[a]
ch2Mz	m-ch2z	5.2E-18	0.322	0.26	2.25E-06	0.257	N/A[a]
ch3Mz	m-ch3z	5.2E-18	0.322	0.26	2.25E-06	0.257	N/A[a]
ch4Mz	m-ch4z	5.2E-18	0.322	0.26	2.25E-06	0.257	N/A[a]
ch5Mz	m-ch5z	5.2E-18	0.322	0.26	2.25E-06	0.257	N/A[a]
ch6Mv	m-ch6v	2.72E-13	0.331	0.06	1.67E-05	0.147	N/A[a]
ch6Mz	m-ch6z	8.2E-19	0.271	0.36	1.56E-07	0.499	N/A[a]
pp4Mz	m-pp4	1.02E-15	0.321	0.29	4.57E-07	0.474	N/A[a]
pp3Md	m-pp3	1.26E-13	0.318	0.08	9.50E-06	0.407	N/A[a]
pp2Md	m-pp2	1.70E-15	0.221	0.10	2.25E-06	0.309	N/A[a]
pp1Mz	m-pp1	2.57E-15	0.297	0.30	8.77E-07	0.272	N/A[a]
bf3Md	m-bf3	3.55E-14	0.175	0.11	3.48E-05	0.193	N/A[a]
bf2Mz	m-bf2	8.1E-17	0.234	0.21	1.18E-07	0.617	N/A[a]
tr3Md	m-tr3	1.1E-15	0.175	0.11	1.12E-05	0.193	N/A[a]
tr2Mz	m-tr2	8.1E-17	0.234	0.21	1.18E-07	0.617	N/A[a]
tcwF1	f-tcw11	3.0E-11	2.4E-02	0.01	5.01E-03	0.633	5.00E-01
tcwF2	f-tcw12	5.3E-12	1.7E-02	0.01	2.19E-03	0.633	5.00E-01
tcwF3	f-tcw13	4.5E-12	1.3E-02	0.01	1.86E-03	0.633	5.00E-01
ptnF1	f-ptn21	3.2E-12	9.2E-03	0.01	2.69E-03	0.633	1.00E-01
ptnF2	f-ptn22	3.0E-13	1.0E-02	0.01	1.38E-03	0.633	1.00E-01
ptnF3	f-ptn23	3.0E-13	2.1E-03	0.01	1.23E-03	0.633	1.00E-01
ptnF4	f-ptn24	3.0E-12	1.0E-02	0.01	2.95E-03	0.633	1.00E-01
ptnF5	f-ptn25	1.7E-13	5.5E-03	0.01	1.10E-03	0.633	1.00E-01
ptnF6	f-ptn26	2.2E-13	3.1E-03	0.01	9.55E-04	0.633	1.00E-01
tswF1	f-tsw31	8.1E-13	5.0E-03	0.01	1.58E-05	0.633	1.00E-01
tswF2	f-tsw32	7.1E-13	8.3E-03	0.01	1.00E-04	0.633	5.61E-01
tswF3	f-tsw33	7.8E-13	5.8E-03	0.01	1.58E-03	0.633	5.61E-01
tswF4	f-tsw34	3.3E-13	8.5E-03	0.01	1.00E-04	0.633	5.70E-01
tswF5	f-tsw35	9.1E-13	9.6E-03	0.01	5.78E-04	0.633	5.70E-01
tswF6	f-tsw36	1.3E-12	1.3E-02	0.01	1.10E-03	0.633	5.70E-01
tswF7	f-tsw37	1.3E-12	1.3E-02	0.01	1.10E-03	0.633	5.70E-01
tswF8	f-tsw38	8.1E-13	1.1E-02	0.01	8.91E-04	0.633	5.70E-01
tswFv	f-tsw9v	N/A[b]	N/A[b]	N/A[b]	N/A[b]	N/A[b]	N/A[b]
tswFz	f-tsw9z	8.1E-13	4.3E-03	0.01	1.5E-03	0.633	5.00E-01
ch1Fv	f-ch1v	N/A[b]	N/A[b]	N/A[b]	N/A[b]	N/A[b]	N/A[b]

Multiscale Thermohydrologic Model

Table IV-6. Matrix and Fracture Properties for the Upper-Bound Infiltration Flux One-Dimensional Drift-Scale Hydrologic Property Set (Continued)

Material name from DTN source	Material name used in LDTH submodels	Permeability [m²]	Porosity [-]	Residual saturation [-]	α (alpha) [1/Pa]	m [-]	γ (gamma) [-]
ch1Fz	f-ch1z	2.5E-14	1.6E-04	0.01	1.4E-03	0.633	5.00E-01
ch2Fv	f-ch2v	N/A[b]	N/A[b]	N/A[b]	N/A[b]	N/A[b]	N/A[b]
ch3Fv	f-ch3v	N/A[b]	N/A[b]	N/A[b]	N/A[b]	N/A[b]	N/A[b]
ch4Fv	f-ch4v	N/A[b]	N/A[b]	N/A[b]	N/A[b]	N/A[b]	N/A[b]
ch5Fv	f-ch5v	N/A[b]	N/A[b]	N/A[b]	N/A[b]	N/A[b]	N/A[b]
ch2Fz	f-ch2z	2.5E-14	3.7E-04	0.01	8.9E-04	0.633	5.00E-01
ch3Fz	f-ch3z	2.5E-14	3.7E-04	0.01	8.9E-04	0.633	5.00E-01
ch4Fz	f-ch4z	2.5E-14	3.7E-04	0.01	8.9E-04	0.633	5.00E-01
ch5Fz	f-ch5z	2.5E-14	3.7E-04	0.01	8.9E-04	0.633	5.00E-01
ch6Fv	f-ch6v	N/A[b]	N/A[b]	N/A[b]	N/A[b]	N/A[b]	N/A[b]
ch6Fz	f-ch6z	2.5E-14	1.6E-04	0.01	1.4E-03	0.633	5.00E-01
pp4Fz	f-pp4	2.5E-12	3.7E-04	0.01	8.91E-04	0.633	5.00E-01
pp3Fd	f-pp3	2.2E-12	9.7E-04	0.01	1.66E-03	0.633	5.00E-01
pp2Fd	f-pp2	2.2E-13	9.7E-04	0.01	1.66E-03	0.633	5.00E-01
pp1Fz	f-pp1	2.5E-14	3.7E-04	0.01	8.91E-04	0.633	5.00E-01
bf3Fd	f-bf3	2.2E-13	9.7E-04	0.01	1.66E-03	0.633	5.00E-01
bf2Fz	f-bf2	2.5E-14	3.7E-04	0.01	8.9E-04	0.633	5.00E-01
tr3Fd	f-tr3	2.2E-13	9.7E-04	0.01	1.6E-03	0.633	5.00E-01
tr2Fz	f-tr2	2.5E-14	3.7E-04	0.01	8.9E-04	0.633	5.00E-01

DTN: LB0302UZDSCPUI.002 [DIRS 161787], File: drift-scale calibrated properties for upper infiltration2.xls; Worksheet: Drift-scale Cal. Hydro Props.

[a] Gamma value does not apply to matrix continuum.
[b] Vitric units (those units ending with a "v") do not have fractures. The fracture continuum properties are the same as those of the matrix continuum for these units.

NOTE: The prefix "m-" stands for matrix and "f-" stands for fracture.

Table IV-7. Fracture Frequency and Fracture-to-Matrix Interface Area

Material Name	Fracture Frequency (m⁻¹)	Interface Area [m²/m³]
tcw11	0.92	1.56
tcw12	1.91	13.39
tcw13	2.79	3.77
ptn21	0.67	1.00
ptn22	0.46	1.41
ptn23	0.57	1.75
ptn24	0.46	0.34
ptn25	0.52	1.09
ptn26	0.97	3.56
tsw31	2.17	3.86
tsw32	1.12	3.21
tsw33	0.81	4.44

Table IV-7. Fracture Frequency and Fracture-to-Matrix Interface Area (Continued)

Material Name	Fracture Frequency (m^{-1})	Interface Area $[m^2/m^3]$
tsw34	4.32	13.54
tsw35	3.16	9.68
tsw36	4.02	12.31
tsw37	4.02	12.31
tsw38	4.36	13.34
tsw39 (tsw9v)	NA[a]	NA[a]
tsw39 (tsw9z)	0.96	2.95
ch1VI (ch1v)	NA[a]	NA[a]
ch1Ze (ch1z)	0.04	0.11
ch2VI (ch2v)	NA[a]	NA[a]
ch3VI (ch3v)	NA[a]	NA[a]
ch4VI (ch4v)	NA[a]	NA[a]
ch5VI (ch5v)	NA[a]	NA[a]
ch2Ze (ch2z)	0.14	0.43
ch3Ze (ch3z)	0.14	0.43
ch4Ze (ch4z)	0.14	0.43
ch5Ze (ch5z)	0.14	0.43
ch6VI (ch6v)	NA[a]	NA[a]
ch6 (ch6z)	0.04	0.11
pp4	0.14	0.43
pp3	0.20	0.61
pp2	0.20	0.61
pp1	0.14	0.43
bf3	0.20	0.61
bf2	0.14	0.43
tr3	0.20	0.61
tr2	0.14	0.43

DTN: LB0205REVUZPRP.001 [DIRS 159525] FRACTURE
PROPERTY.xls; Worksheet: Table 1. Fracture Properties.

[a] Vitric units (those units ending with a "VI" or a "v") do not have
fractures; therefore, fracture properties do not pertain to those units.

NOTE: In parentheses are the material names used in the LDTH
submodels of this report.

Table IV-8.   Bulk Density of 4-10 Crushed Tuff

Row number	Mass density (gm/cm^3)
321	1.3
322	1.2
323	1.3
324	1.3
325	1.3
326	1.2
327	1.3
328	1.2
329	1.3
330	1.2
331	1.2
332	1.2
333	1.3
334	1.3
335	1.3
336	1.3
337	1.3
338	1.2
339	1.2
340	1.2
341	1.3
342	1.3
343	1.3
344	1.3
345	1.3
346	1.3
347	1.3
348	1.3
349	1.3
350	1.2
351	1.3
352	1.3
353	1.3
354	1.2
355	1.3
356	1.3
357	1.2
358	1.2
359	1.2
360	1.3
361	1.3
362	1.3
363	1.3
364	1.2
365	1.2
366	1.2
367	1.3
368	1.3
369	1.3
370	1.3

DTN: GS020183351030.001 [DIRS 163107], rows 321-370.

NOTE: The average mass density for the 50 samples is
1.27 gm/cm^3, which is the value used for the
crushed-tuff invert.

Table IV-9.   Specific heat and thermal conductivity of 4-10 crushed tuff

Row number	Specific heat (J/cm^3-°C)	Thermal conductivity (W/m °C)
1	0.82	0.17
2	0.84	0.14
3	0.98	0.17
4	0.98	0.17
5	0.99	0.17
6	0.92	0.16
7	0.96	0.17
8	0.86	0.15
9	0.88	0.16
10	1.06	0.17
11	0.94	0.17

DTN: GS000483351030.003 [DIRS 152932], rows 1 to 11.

NOTE: The average specific heat for the 11 samples is 0.93 J/cm^3-°C, which is the value used for the crushed-tuff invert. The average thermal conductivity for the 11 samples is 0.2 W/m-°C, which is the averaged valued rounded up to the nearest "tenths"; this rounded averaged value is used for the crushed-tuff invert.

APPENDIX V

BUILDING SUBMODEL INPUT FILES

SMT Submodel

The SMT submodel has the following information in this order:

1. Time information (starttime, stoptime, timestepsize)
2. Material properties (in the form of a rocktab file; see Appendix IV)
3. Output information (for ".ext" time-history output; this is readable by XTOOL v10.1)
4. Heat generation information (in the form of a heatgen file; see Appendix III)
5. Restart file information
6. Boundary-conditions
7. Initial conditions
8. SMT submodel mesh file (in the form of an SMT submodel mesh file; see Appendix I)
9. Run control parameters.

All parameter values are taken directly from inputs or calculations described in other Appendices. An example of an SMT submodel NUFT usnt-option input file follows below. For more information, see the NUFT documentation (Nitao 1998 [DIRS 100474]).

```
 (usnt
  (title "* YMP Site-Scale 3D Model, Conduction-Only Post-Emplacement Run")
;; AML = 55 MTU/acre
;; ventilation + post-closure run for MSTHM for the License Application
;; rotated mesh explicitly representing emplacement drifts
;; Western Model representing Panels 1, 2E, 2W, 3, and 5
;; conduction only
  (modelname usnt)
  (include-pkg "thermcon.pkg")
  ;; single-comp (air), single-phase (gas) pkg for cond-only run
  (tstop 20100y)
  (time 0)
  (stepmax 1000000)
  (dtmax 1.0e25)
  (dt 1e2)
;; include thermal properties
 (rocktab
    (include "/data34/TSPA03/physical_properties/SDT-1Dds-03") ;; read rocktab data
    (include "/data34/TSPA03/physical_properties/SMT-1Dds-fl-03") ;; read rocktab data
    (include "/data34/TSPA03/physical_properties/SMT-1Dds-sz-03") ;; read rocktab data
 )  ;; end rocktab
;;
;; **********************************************************************
(output
    (extool (variables T )  ;; repository node temperatures
            (file-ext ".lvl.ext")(range "*#*:*:1")
            (outtimes
                (include "/data34/TSPA03/outputTimes/outputTimes-SMT-55-01")
            )
    )
)  ;; end output
;; **********************************************************************
;;  include heat curves in srctab
;;   (srctab
          (include
"/data34/TSPA03/heatgen/SMT_blocks/preliminary_DTN2/SMT_LA_includes01")
;;   ) ;; end srctab
;; **********************************************************************
;; read restart file
```

```
   (read-restart
    (file  "/data34/TSPA03/SMT/SMT55/03-150w-i/SMT55-03-150w-i.rst")
    (time 1.0e6y))
;; ***********************************************************************
   (bctab
    (top
        (range "at*")
        (clamped))
    (bottom
        (range "bs*")
        (clamped))
   )  ;; end bctab
;; ***********************************************************************
;; set initial conditions
;; (state
;;  P by-key  ("*"  1.0e5))
;;  (T by-key
;;     (include "/data34/TSPA03/BoundaryConditions/preliminary_DTN/smtUpperBC.out")
;;     (include "/data34/TSPA03/BoundaryConditions/preliminary_DTN/smtLowerBC.out")
;;  )
;; )  ;; end state
;; ***********************************************************************
   (mesh-file  "/data34/TSPA03/smt_mesh/preliminary_DTN/tspa03.mesh03-150w")
;; read mesh and connection data
;; ***********************************************************************

(include "/data30/TSPA01/run_control_param/run_control_param_SMT-v01"))
;; end of model
```

LDTH submodel

For the LDTH submodel input files, a calculation (in addition to those described in other Appendices) must be made to convert the percolation flux from mm/yr to kg/m^2/sec. An example of this calculation is:

$$J = 4.1884 \text{ mm/yr } (1 \text{ day}/86{,}400 \text{ sec})(1 \text{ yr}/365.25 \text{ days})(m/1{,}000 \text{ mm})(1{,}000 \text{ kg/m}^3) = 1.3274 \times 10^{-7} \text{ kg/m}^2/\text{sec}$$

The LDTH submodel has the following information in this order:

1. Header information (lines preceded by a semicolon)
2. Time information (start time, stop time, timestepsize)
3. Convergence tolerance information
4. Output file (for ".ext" time-history output; this is readable by XTOOL v10.1)
5. Material properties (in the form of rocktab files; see Appendix IV)
6. Percolation flux information (see the flux conversion mm/yr to kg/m^2/sec noted above)
7. Heat generation information (in the form of a heatgen file; see Appendix III)
8. Boundary-conditions
9. Restart conditions (optional)
10. Initial conditions (optional)
11. Mesh information for matrix continuum
12. Radcon information for matrix continuum (in the form of a file for doing thermal-radiation connections, see Appendix VI)
13. Mesh information for fracture continuum
14. Run control parameters.

All parameter values are taken directly from inputs or calculations described in other appendices. An example of an DDT submodel NUFT usnt-option input file (P1R10C8-LDTH14-1Dds_mc-mi-02.in) follows below. For more information, see the NUFT documentation (Nitao 1998 [DIRS 100474]). LDTH submodel input files follow the naming convention P(x)R(y)C(z)-LDTH(aml)-1Dds_mc-(percolation)i-0(property set).in. For the three infiltration flux cases, there are 2,592 input files including 1,296 initialization runs and 1,296 postemplacement runs. These files are found in DTN: LL030808623122.036.

```
;; This Model was produced on
;; Thu May 22 18:12:31 PDT 2003
;; Implicit DKM with active fracture concept (AFC)
;; NBS material properties from 1D drift-scale infiltration flux property set
;; AML = 13.705 MTU/acre; half drift spacing = 162.0 m

;;  P1R10C8.col.units

;;  COLUMN INFORMATION (x,y =   171232.891,   233883.719) WORLD COLUMN h44

;;  unitthickness (m)
;;  _____

;;  tcw11        0.059
;;  tcw12       77.988
;;  tcw13        5.771
;;  ptn21        3.867
;;  ptn22        5.303
;;  ptn23        1.670
;;  ptn24        8.643
;;  ptn25       18.486
;;  ptn26       12.832
;;  tsw31        1.904
;;  tsw32       52.070
;;  tsw33       85.734
;;  tsw34       33.656
;;  tsw35      101.756
;;  tsw36       36.992
;;  tsw37       18.486
;;  tsw38       16.699
;;  tsw9v        1.904
;;  tsw9z        0.000
;;  ch1v         0.000
;;  ch1z        16.787
;;  ch2v         0.000
;;  ch3v         0.000
;;  ch4v         0.000
;;  ch5v         0.000
;;  ch2z        21.299
;;  ch3z        21.299
;;  ch4z        21.299
;;  ch5z        21.299
;;  ch6v         0.000
;;  ch6z        17.461
;;  pp4         12.949
;;  pp3          8.320
;;  pp2          0.000
;;  pp1          0.000
;;  bf3          0.000
;;  bf2          0.000
;;  tr3          0.000
;;  tr2          0.000

;;  repository elevation (m):                    1069.300
;;  host rock:                          tsw34

;;  meters of host rock (tsw34) above repository:        12.001
;;  meters of host rock (tsw34) below repository:        21.656

;;  overburden thickness (m):               286.329
;;  distance from repository plane to top of chn (m):    197.494
```

```
;;  distance from repository plane to top of water table (m):     338.206

(usnt
  (title "4.1883590e+00mm_yr,line-load,AML=14mtu_acre,LDTH14_1Dds_mc-mi")
  (modelname usnt)

  (tstop  20100y)
  (time 0y)
  (stepmax 1000000)
  (dtmax 1.000e+25)
  (dt 1e2)

  (tolerconv (P 5000.)(S 0.005)(X 0.005)(T 0.5))
  ;; absolute NR conv. tolerance
  (reltolerconv (P 0.005)(S 0.0)(X 0.0)(T 1.e-3))

  (tolerdt (P 2.e4)(S 0.35)(X 0.25)(T 10.))
  (reltolerdt (P 0.1)(S 0.0)(X 0.0)(T 0.0))

  ;; trying with harmonic mean everywhere which means
  ;; turning off the geometric before vtough.pkg gets called.
  (diffusion-geo-mean off)
  ;; for imp-DKM do not have this so that it will default to
  ;; harmonic for fract-matrix interaction
  ;;(mult-cont-diff-harmonic off)
  ;; following has to come after tolerances
  (rmstolerconv 1e-4)
  (include-pkg "vtough.pkg")
  (check-mult-con off )

;;
*****************************************************************************
*************
  (output
        (extool (continuum f)
                (variables T S.liquid X.air.gas RH Pc.liquid P.gas qPhChg.water.gas
                           QPhChg.water.gas q.liquid q.water.gas q.air.gas)
                (file-ext ".f.EBS.ext")(range "*hstrk*.f*" "dr*.f*" "*in*.f*"
                                              "*wp*.f*")
             (outtimes
               (include "/data34/TSPA03/outputTimes/outputTimes-LDTH-SDT-DDT-14-01")
             )
        )
        (extool (continuum m)
                (variables T S.liquid X.air.gas RH Pc.liquid P.gas qPhChg.water.gas
                           QPhChg.water.gas q.liquid q.water.gas q.air.gas)
                (file-ext ".m.EBS.ext")(range "*hstrk*.m*" "dr*.m*" "*in*.m*"
                                              "*wp*.m*")
             (outtimes
               (include "/data34/TSPA03/outputTimes/outputTimes-LDTH-SDT-DDT-14-01")
             )
        )

    ) ;; end output

;; ********************************************************************************
(rocktab
        (include "/data34/TSPA03/physical_properties/dkm-afc-1Dds-mc-mi-04")
        (include "/data34/TSPA03/physical_properties/dkm-afc-EBS-mi-03")
) ;; close rocktab
        (include "/data34/TSPA03/physical_properties/modpropTSPA03_01_14")
;; ********************************************************************************

;;  This srctab is adjusted to allocate percolation to just the fracture.
  (srctab
        (compflux
            (comp water)
            (name infil)
            (range "*.f*:*:2")
            (mult-by-area z)
            (allocate-by-element ("*" 1.0))
            (table 0.0    1.3274464e-07  600.00y 1.3274464e-07 ;;4.1883590e+00 mm/yr
                   600.001y 2.4720940e-07  2000.00y 2.4720940e-07 ;;7.7999510e+00 mm/yr
```

```
                    2000.001y 3.6606447e-07  1.0e30   3.6606447e-07);;1.1550066e+01 mm/yr
                (enthalpy  0.0    7.1314900e+04   1E+30    7.1314900e+04 )
        )

    (include "/data34/TSPA03/heatgen/SDT_LDTH_blocks/preliminary_DTN/P1R10C8_LDTH-SDT")
   ) ;; end srctab

     ;; set boundary conditions
    (bctab
    (atmos
        (range   "at*")
        (basephase gas)
        (tables
            (T        0.0  1.6984000e+01   1.0e30  1.6984000e+01 )
            (S.liquid 0.0  0.0      1.0e30   0.0  )
            (P        0.0  8.5705180e+04   1.0e30  8.5705180e+04 )
            (X.air    0.0  9.8582710e-01   1.0e30  9.8582710e-01 )
        )
    )

    (gwater
        (range   "wt*")
        (basephase liquid)
        (tables
            (T        0  3.2083000e+01     1.0e30   3.2083000e+01)
            (S.liquid  0  1.0       1.0e30    1.0)
            (P        0  9.1988930e+04     1.0e30   9.1988930e+04)
            (X.air    0  1.0e-6   1.0e30  1.0e-6)
        )
;;   SET PHASEFACTOR GAS TO 0, AND LIQUID TO 1
        (phasefactor
            (gas    0  0.0   1.0e30   0.0)
            (liquid  0  1.0   1.0e30   1.0)
        )

    )
    ) ;; end bctab

;; set initial conditions.
    (read-restart (time 3.15576e20)
    (file "/data33/TSPA03/LDTH/LDTH14/1Dds_mc-mi/02i/P1R10C8-LDTH14-1Dds_mc-mi-02i.res"))
    (overwrite-restart
        (X.air by-key      ("dr*" 1.0)("*wp*" 1.0)("*in*" 1.0))
        (S.liquid  by-key ("dr*" 0.0)("*wp*" 0.0)("*in.m*" 0.9)("*in.f*" 0.1))
    ) ;; end overwrite

;;This is for a unit symmetry cell with a half drift and half pillar
;;between drifts.
  (genmsh
    (anisotropic)
    (down 0. 0. 1.0)
    (coord rect)
    (multi-continua
        (type rocktab)
        (continuum  (name m)
        ;; 13.705 MTU/acre
            (dx 0.580 0.370 0.3025 0.4222 0.4222 0.350  0.3031  0.35  0.5 0.9
                1.0   1.5   2.5    4.0    7.0   13.0   24.00   42.0 62.5)
            (dy 1.0)
    (dz
    1.0e-30    0.059   17.988   30.000   30.000 ;; 1- 5:     atm   tcw11  tcw12  tcw12  tcw12
    5.771    3.867    5.303    1.670    8.643 ;; 6- 10:   tcw13  ptn21  ptn22  ptn23  ptn24
   18.486   12.832    1.904   17.070   15.000 ;; 11- 15:  ptn25  ptn26  tsw31  tsw32  tsw32
   10.000   10.000    7.734    6.000    6.000 ;; 16- 20:  tsw32  tsw32  tsw33  tsw33  tsw33
    6.000    6.000    6.000    6.000    6.000 ;; 21- 25:  tsw33  tsw33  tsw33  tsw33  tsw33
    6.000    6.000    6.000    6.000    3.000 ;; 26- 30:  tsw33  tsw33  tsw33  tsw33  tsw33
    3.000    3.000    3.000    1.500    2.000 ;; 31- 35:  tsw33  tsw33  tsw33  tsw34  tsw34
    1.000    1.000    0.500    0.300    0.200 ;; 36- 40:  tsw34  tsw34  tsw34  tsw34  tsw34
    0.200    0.200    0.200    0.200    0.200 ;; 41- 45:  tsw34  tsw34  tsw34  tsw34  tsw34
    0.200    0.200    0.200    0.200    0.200 ;; 46- 50:  tsw34  tsw34  tsw34  tsw34  tsw34
    0.108    0.242    0.400    0.759    0.760 ;; 51- 55:  tsw34  tsw34  tsw34  tsw34  tsw34
    0.425    0.403    0.403    0.800    1.200 ;; 56- 60:  tsw34  tsw34  tsw34  tsw34  tsw34
    1.500    2.500    3.000    3.000    6.000 ;; 61- 65:  tsw34  tsw34  tsw34  tsw34  tsw34
    3.656    6.000    6.000    6.000    6.000 ;; 66- 70:  tsw34  tsw35  tsw35  tsw35  tsw35
    6.000    6.000    6.000    6.000    6.000 ;; 71- 75:  tsw35  tsw35  tsw35  tsw35  tsw35
    6.000    6.000    6.000   10.000   10.000 ;; 76- 80:  tsw35  tsw35  tsw35  tsw35  tsw35
    9.756   15.000   20.000    1.992   18.486 ;; 81- 85:  tsw36  tsw36  tsw36  tsw36  tsw37
   16.699    1.904   16.787   21.299   21.299 ;; 86- 90:  tsw38  tsw9v  ch1z   ch2z   ch3z
   21.299   21.299   17.461   12.949    8.320 ;; 91- 95:   ch4z   ch5z   ch6z   pp4    pp3
```

```
        1.0e-30                            ;; 96- 96:      wt
        )
       (mat
          (atm            atm          1  nx  1  ny   1   1)
          (tcw11          m-tcw11      1  nx  1  ny   2   2)
          (tcw12          m-tcw12      1  nx  1  ny   3   5)
          (tcw13          m-tcw13      1  nx  1  ny   6   6)
          (ptn21          m-ptn21      1  nx  1  ny   7   7)
          (ptn22          m-ptn22      1  nx  1  ny   8   8)
          (ptn23          m-ptn23      1  nx  1  ny   9   9)
          (ptn24          m-ptn24      1  nx  1  ny  10  10)
          (ptn25          m-ptn25      1  nx  1  ny  11  11)
          (ptn26          m-ptn26      1  nx  1  ny  12  12)
          (tsw31          m-tsw31      1  nx  1  ny  13  13)
          (tsw32          m-tsw32      1  nx  1  ny  14  17)
          (tsw33          m-tsw33      1  nx  1  ny  18  33)
          (tsw34          m-tsw34      1  nx  1  ny  34  66)
          (tsw35          m-tsw35      1  nx  1  ny  67  81)
          (tsw36          m-tsw36      1  nx  1  ny  82  84)
          (tsw37          m-tsw37      1  nx  1  ny  85  85)
          (tsw38          m-tsw38      1  nx  1  ny  86  86)
          (tsw9v          m-tsw9v      1  nx  1  ny  87  87)
          (ch1z           m-ch1z       1  nx  1  ny  88  88)
          (ch2z           m-ch2z       1  nx  1  ny  89  89)
          (ch3z           m-ch3z       1  nx  1  ny  90  90)
          (ch4z           m-ch4z       1  nx  1  ny  91  91)
          (ch5z           m-ch5z       1  nx  1  ny  92  92)
          (ch6z           m-ch6z       1  nx  1  ny  93  93)
          (pp4            m-pp4        1  nx  1  ny  94  94)
          (pp3            m-pp3        1  nx  1  ny  95  95)
          (wt             m-pp3        1  nx  1  ny  96  96)
          (hstrk          m-tsw34      1  nx  1  ny  34  61)
          (dr             m-dr         1   1  1  ny  41  41)
          (dr             m-dr         1   3  1  ny  42  42)
          (dr             m-dr         1   4  1  ny  43  44)
          (dr             m-dr         1   5  1  ny  45  46)
          (dr             m-dr         1   6  1  ny  47  49)
          (dr             m-dr         1   7  1  ny  50  54)
          (dr             m-dr         1   6  1  ny  55  55)
          (dr             m-dr         1   5  1  ny  56  56)
          (wp             lsnf         1   1  1  ny  52  52)
          (wp             lsnf         1   2  1  ny  53  53)
          (wp             lsnf         1   3  1  ny  54  56)
          ;; invert
          (in             m-invert1    1   4  1  ny  57  57)
          (in             m-invert2    1   2  1  ny  58  58) ;; bottom of invert
       )

  (radcon
       (surface-offset 0 0  -3)
       (include "/data34/TSPA03/radcon/LDTH/preliminary_DTN/ldth0_300m.radcon")
) ;; close radcon

) ;; end continuum
      (continuum  (name f)
          (flow-area-density ("*.f*" 1.0))
          (LenFirst  ("*.f*" 1.0))    ;; same as y-direction
                                      ;; half-width of matrix block
          (Len  ("*.f*" 1.0))         ;; same as y-direction
                                      ;; half-width of fracture
                      ;; LenFirst and Len values are doubled here since 50% of cont-
len-fac
                      ;; is used in rocktab file
        ;; 13.705 MTU/acre
      (dx 0.580 0.370 0.3025 0.4222 0.4222 0.350  0.3031  0.35  0.5 0.9
          1.0   1.5   2.5     4.0    7.0    13.0   24.00   42.0 62.5)
      dy  1.0)
    (dz
    1.0e-30     0.059   17.988   30.000   30.000 ;; 1- 5:    atm    tcw11   tcw12   tcw12   tcw12
    5.771       3.867    5.303    1.670    8.643 ;; 6- 10:   tcw13  ptn21   ptn22   ptn23   ptn24
    18.486     12.832    1.904   17.070   15.000 ;; 11- 15:  ptn25  ptn26   tsw31   tsw32   tsw32
    10.000     10.000    7.734    6.000    6.000 ;; 16- 20:  tsw32  tsw32   tsw33   tsw33   tsw33
    6.000       6.000    6.000    6.000    6.000 ;; 21- 25:  tsw33  tsw33   tsw33   tsw33   tsw33
    6.000       6.000    6.000    6.000    3.000 ;; 26- 30:  tsw33  tsw33   tsw33   tsw33   tsw33
    3.000       3.000    3.000    1.500    2.000 ;; 31- 35:  tsw33  tsw33   tsw33   tsw34   tsw34
    1.000       1.000    0.500    0.300    0.200 ;; 36- 40:  tsw34  tsw34   tsw34   tsw34   tsw34
    0.200       0.200    0.200    0.200    0.200 ;; 41- 45:  tsw34  tsw34   tsw34   tsw34   tsw34
```

```
          0.200     0.200     0.200     0.200     0.200 ;; 46- 50:    tsw34     tsw34     tsw34     tsw34     tsw34
          0.108     0.242     0.400     0.759     0.760 ;; 51- 55:    tsw34     tsw34     tsw34     tsw34     tsw34
          0.425     0.403     0.403     0.800     1.200 ;; 56- 60:    tsw34     tsw34     tsw34     tsw34     tsw34
          1.500     2.500     3.000     3.000     6.000 ;; 61- 65:    tsw34     tsw34     tsw34     tsw34     tsw34
          3.656     6.000     6.000     6.000     6.000 ;; 66- 70:    tsw34     tsw35     tsw35     tsw35     tsw35
          6.000     6.000     6.000     6.000     6.000 ;; 71- 75:    tsw35     tsw35     tsw35     tsw35     tsw35
          6.000     6.000     6.000    10.000    10.000 ;; 76- 80:    tsw35     tsw35     tsw35     tsw35     tsw35
          9.756    15.000    20.000     1.992    18.486 ;; 81- 85:    tsw35     tsw36     tsw36     tsw36     tsw37
         16.699     1.904    16.787    21.299    21.299 ;; 86- 90:    tsw38     tsw9v     ch1z      ch2z      ch3z
         21.299    21.299    17.461    12.949     8.320 ;; 91- 95:    ch4z      ch5z      ch6z      pp4       pp3
          1.0e-30                                       ;; 96- 96:    wt
        )
        (mat
          (atm          atm        1  nx  1  ny  1   1)
          (tcw11        f-tcw11     1  nx  1  ny  2   2)
          (tcw12        f-tcw12     1  nx  1  ny  3   5)
          (tcw13        f-tcw13     1  nx  1  ny  6   6)
          (ptn21        f-ptn21     1  nx  1  ny  7   7)
          (ptn22        f-ptn22     1  nx  1  ny  8   8)
          (ptn23        f-ptn23     1  nx  1  ny  9   9)
          (ptn24        f-ptn24     1  nx  1  ny  10  10)
          (ptn25        f-ptn25     1  nx  1  ny  11  11)
          (ptn26        f-ptn26     1  nx  1  ny  12  12)
          (tsw31        f-tsw31     1  nx  1  ny  13  13)
          (tsw32        f-tsw32     1  nx  1  ny  14  17)
          (tsw33        f-tsw33     1  nx  1  ny  18  33)
          (tsw34        f-tsw34     1  nx  1  ny  34  66)
          (tsw35        f-tsw35     1  nx  1  ny  67  81)
          (tsw36        f-tsw36     1  nx  1  ny  82  84)
          (tsw37        f-tsw37     1  nx  1  ny  85  85)
          (tsw38        f-tsw38     1  nx  1  ny  86  86)
          (tsw9v        f-tsw9v     1  nx  1  ny  87  87)
          (ch1z         f-ch1z      1  nx  1  ny  88  88)
          (ch2z         f-ch2z      1  nx  1  ny  89  89)
          (ch3z         f-ch3z      1  nx  1  ny  90  90)
          (ch4z         f-ch4z      1  nx  1  ny  91  91)
          (ch5z         f-ch5z      1  nx  1  ny  92  92)
          (ch6z         f-ch6z      1  nx  1  ny  93  93)
          (pp4          f-pp4       1  nx  1  ny  94  94)
          (pp3          f-pp3       1  nx  1  ny  95  95)
          (wt           f-pp3       1  nx  1  ny  96  96)
          (hstrk        f-tsw34     1  nx  1  ny  34  61)
          (dr           f-dr        1   1  1  ny  41  41)
          (dr           f-dr        1   3  1  ny  42  42)
          (dr           f-dr        1   4  1  ny  43  44)
          (dr           f-dr        1   5  1  ny  45  46)
          (dr           f-dr        1   6  1  ny  47  49)
          (dr           f-dr        1   7  1  ny  50  54)
          (dr           f-dr        1   6  1  ny  55  55)
          (dr           f-dr        1   5  1  ny  56  56)
          (wp           lsnf        1   1  1  ny  52  52)
          (wp           lsnf        1   2  1  ny  53  53)
          (wp           lsnf        1   3  1  ny  54  56)
          ;; invert
          (in           f-invert1   1   4  1  ny  57  57)
          (in           f-invert2   1   2  1  ny  58  58) ;; bottom of invert
        )
      ) ;; end continuum
    ) ;; end multi-continua
  ) ;; end genmsh

;; *********************** Solver options ***************************
(include "/data30/TSPA01/run_control_param/run_control_param_LDTH-v09")

);; end of model input

;; ********************** Done ***********************************
```

SDT submodel

The SDT submodel has the following information in this order:

1. Header information (lines preceded by a semicolon)
2. Time information (start time, stop time, timestepsize)
3. Output information (for ".ext" time-history output; this is a readable by XTOOL v10.1)
4. Material properties (in the form of a rocktab file, see Appendix IV)
5. Heat generation information (in the form of a heatgen file, see Appendix III)
6. Boundary-conditions
7. Initial conditions ("state" command)
8. SDT submodel mesh file (in the form of an SDT submodel mesh file, see Appendix I).

All parameter values are taken directly from inputs or calculations described in other appendices. An example of an SDT submodel NUFT input file (P5415C8-SDT27-00-01.in) follows. For more information, see the NUFT documentation (Nitao 1998 [DIRS 100474]). SDT submodel input files follow the naming convention P(x)R(y)C(z)-SDT(aml)-00-01.in. Note that only one set of SDT submodels to cover all three infiltration flux cases (lower-bound, mean, and upper-bound), thus, there are 540 input files, which includes 108 initialization runs and 324 postemplacement runs. These files are found in DTN: LL030808623122.036.

```
;; /data34/TSPA03/chimney_mesh/SDT/preliminary_DTN/P5R16C8-SDT27-00-01.in
;; was produced on
;; Wed Apr 23 09:48:11 PDT 2003
;; Conduction-only for smeared-heat-source cases
;; AML = 27 MTU/acre; half drift spacing = 81.00 m
;; use tcond_wet for both solid and gas pgases.


;;  P5R16C8.col.units

;;  COLUMN INFORMATION (x,y =   171137.797,   232234.609) WORLD COLUMN q47

;;  unitthickness (m)
;;  _____

;; tcw11        0.000
;; tcw12       68.320
;; tcw13        5.039
;; ptn21        3.105
;; ptn22        0.000
;; ptn23        0.000
;; ptn24        3.809
;; ptn25        3.867
;; ptn26       10.195
;; tsw31        1.992
;; tsw32       32.041
;; tsw33       69.281
;; tsw34       35.906
;; tsw35       86.696
;; tsw36       43.164
;; tsw37       21.553
;; tsw38        9.082
;; tsw9v        9.023
;; tsw9z        0.000
;; ch1v    22.529
;; ch1z     0.000
```

```
;;  ch2v    14.326
;;  ch3v    14.326
;;  ch4v     0.000
;;  ch5v    14.326
;;  ch2z     0.000
;;  ch3z     0.000
;;  ch4z    14.355
;;  ch5z     0.000
;;  ch6v     0.000
;;  ch6z    14.971
;;  pp4      8.643
;;  pp3     33.545
;;  pp2     23.760
;;  pp1     25.049
;;  bf3      0.000
;;  bf2      0.000
;;  tr3      0.000
;;  tr2      0.000

;;  repository elevation (m):                        1091.500
;;  host rock:                              tsw34

;;  meters of host rock (tsw34) above repository:          29.906
;;  meters of host rock (tsw34) below repository:           6.000

;;  overburden thickness (m):                       227.556
;;  distance from repository plane to top of chn (m):       175.518
;;  distance from repository plane to top of water table (m):     361.347

 (usnt
  (title "AML=27mtu_acre,SDT27,00")
  (modelname usnt)

(include-pkg "thermcon.pkg")
;; single-comp (air), single-phase (gas) pkg for cond-only run
  (tstop 20100y)
  (time 0)
  (stepmax 1000000)
  (dtmax 1.728e+18)
  (dt 1e2)

;; *****************************************************************************

(output
    (extool (variables T)
            (file-ext ".ext")(range "*")
        (outtimes
            (include "/data34/TSPA03/outputTimes/outputTimes-LDTH-SDT-DDT-27-01")
        )
    )

)

;;********************** *******************************************************
  (rocktab
       (include "/data34/TSPA03/physical_properties/SDT-1Dds-03")
) ;; close rocktab
;;***************************************************** *************************

;;   There is no percolation for the conduction-only case
 (srctab
   (include "/data34/TSPA03/heatgen/SDT_LDTH_blocks/preliminary_DTN/P5R16C8_LDTH-SDT")
 ) ;; end srctab
;;***************************************************** *************************

;; set boundary conditions
```

```
  (bctab
    (atmos
        (range  "at*")
                (clamped)
    )
    (gwater
        (range  "wt*")
                (clamped)
    )
    ) ;; end bctab

;;********************************************************************************
   (state
        (include "/data34/TSPA03/SDT/SDT66/00/00i/P5R16C8-SDT-00i.ztable")
   )  ;; end state
;;********************************************************************************
   (genmsh
      (down 0. 0. 1.0)
      (coord rect)
      (dx    81.00)
      (dy    1.0)
     (dz
   1.0e-30       8.320      30.000      30.000       5.039 ;; 1 - 5:   atm  tcw12tcw12tcw12tcw13
      3.105       3.809       3.867      10.195       1.992 ;; 6 - 10:  ptn21ptn24ptn25ptn26tsw31
     12.041      10.000      10.000       3.281       6.000 ;; 11 - 15: tsw32tsw32tsw32tsw33tsw33
      6.000       6.000       6.000       6.000       6.000 ;; 16 - 20: tsw33tsw33tsw33tsw33tsw33
      6.000       6.000       6.000       6.000       6.000 ;; 21 - 25: tsw33tsw33tsw33tsw33tsw33
      5.906       6.000       6.000       6.010       5.990 ;; 26 - 30: tsw34tsw34tsw34tsw34tsw34
      6.000       6.000       6.000       6.000       6.000 ;; 31 - 35: tsw34tsw35tsw35tsw35tsw35
      6.000       6.000       6.000       6.000       6.000 ;; 36 - 40: tsw35tsw35tsw35tsw35tsw35
      6.000       6.000       6.000       6.000       4.348 ;; 41 - 45: tsw35tsw35tsw35tsw35tsw35
      4.348      10.000      10.000      15.000       8.164 ;; 46 - 50: tsw35tsw36tsw36tsw36tsw36
     20.000       1.553       9.082       9.023      22.529 ;; 51 - 55: tsw37tsw37tsw38tsw9vch1v
     14.326      14.326      14.355      14.326      14.971 ;; 56 - 60: ch2v ch3v ch4z ch5v ch6z
      8.643      30.000      30.000      30.000      30.000 ;; 61 - 65: pp4  pp3  pp3  pp2  pp1
      1.0e-30                                              ;; 66 - 66: wt
)
(mat
    (    atm    atm 1   nx  1   ny  1    1)
    ( tcw12  tcw12 1   nx  1   ny  2    4)
    ( tcw13  tcw13 1   nx  1   ny  5    5)
    ( ptn21  ptn21 1   nx  1   ny  6    6)
    ( ptn24  ptn24 1   nx  1   ny  7    7)
    ( ptn25  ptn25 1   nx  1   ny  8    8)
    ( ptn26  ptn26 1   nx  1   ny  9    9)
    ( tsw31  tsw31 1   nx  1   ny 10   10)
    ( tsw32  tsw32 1   nx  1   ny 11   13)
    ( tsw33  tsw33 1   nx  1   ny 14   25)
    ( tsw34  tsw34 1   nx  1   ny 26   31)
    ( tsw35  tsw35 1   nx  1   ny 32   46)
    ( tsw36  tsw36 1   nx  1   ny 47   50)
    ( tsw37  tsw37 1   nx  1   ny 51   52)
    ( tsw38  tsw38 1   nx  1   ny 53   53)
    ( tsw9v  tsw9v 1   nx  1   ny 54   54)
    (  ch1v   ch1v 1   nx  1   ny 55   55)
    (  ch2v   ch2v 1   nx  1   ny 56   56)
    (  ch3v   ch3v 1   nx  1   ny 57   57)
    (  ch4z   ch4z 1   nx  1   ny 58   58)
    (  ch5v   ch5v 1   nx  1   ny 59   59)
    (  ch6z   ch6z 1   nx  1   ny 60   60)
    (   pp4    pp4 1   nx  1   ny 61   61)
    (   pp3    pp3 1   nx  1   ny 62   63)
    (   pp2    pp2 1   nx  1   ny 64   64)
    (   pp1    pp1 1   nx  1   ny 65   65)
    (    wt    pp1 1   nx  1   ny 66   66)
    (wp      tsw34 1   nx  1   ny 30   30)
  )
   ) ;; end genmsh
```

```
;;    Use this for the 1-D, 2-D cases
         (linear-solver d4vband)

);; end of model input
```

DDT submodel

The DDT submodel has the following information in this order:

1. header information (lines preceded by a semicolon)
2. time information (start time, stop time, timestepsize)
3. output information (for ".ext" time-history output this is a readable by XTOOL v10.1)
4. material properties (in the form of a rocktab file, see Appendix IV)
5. heat generation information (in the form of a heatgen file, see Appendix III)
6. boundary-conditions
7. restart file information
8. initial conditions
9. DDT mesh file
10. radcon information (in the form of a file for doing thermal-radiation connections, see Appendix VI)
11. run control parameters.

All parameter values are taken directly from inputs or calculations described in other appendices. An example of an DDT submodel NUFT input file (P2WR5C10-DDT55-01-1e11.in) follows below. The interested reader is referred to the NUFT documentation (Nitao 1998 [DIRS 100474]) for specific details of this input file.

DDT submodel input files are found in DTN: LL030808623122.036. The names of these files are:

```
P2WR5C10-DDT14-01v.in
P2WR5C10-DDT27-01v.in
P2WR5C10-DDT55-01v.in
P2WR5C10-DDT66-01v.in
P2WR5C10-DDT66-03.in
P2WR5C10-DDT55-03.in
P2WR5C10-DDT27-03.in
P2WR5C10-DDT14-03.in

;; Implicit DKM with active fracture concept (AFC)
;; NBS material properties from 1D drift-scale mean infiltration flux property set
;; AML = 54.82 MTU/acre; half drift spacing = 40.5 m
;; represents 8 WPs: 6 full WPs and 2 half WPs

;;  P2WR5C10.col.units

;;  COLUMN INFORMATION (x,y =   170730.297,   234912.719) WORLD COLUMN g_9

;;  unitthickness (m)
;;  _____

;;  tcw11        0.000
;;  tcw12       20.244
;;  tcw13        4.014
;;  ptn21        7.207
;;  ptn22        5.596
;;  ptn23        2.021
;;  ptn24       12.510
```

```
;;  ptn25       36.504
;;  ptn26       11.279
;;  tsw31        1.992
;;  tsw32       45.586
;;  tsw33       85.252
;;  tsw34       32.954
;;  tsw35      104.719
;;  tsw36       25.828
;;  tsw37       12.914
;;  tsw38       21.904
;;  tsw9v        0.000
;;  tsw9z        6.592
;;  ch1v         0.000
;;  ch1z        15.039
;;  ch2v         0.000
;;  ch3v         0.000
;;  ch4v         0.000
;;  ch5v         0.000
;;  ch2z        20.293
;;  ch3z        20.303
;;  ch4z        20.273
;;  ch5z        20.303
;;  ch6v         0.000
;;  ch6z        17.578
;;  pp4         19.688
;;  pp3         14.326
;;  pp2          4.102
;;  pp1          0.000
;;  bf3          0.000
;;  bf2          0.000
;;  tr3          0.000
;;  tr2          0.000

;;  repository elevation (m):                        1052.901
;;  host rock:                            tsw35

;;  meters of host rock (tsw35) above repository:         45.328
;;  meters of host rock (tsw35) below repository:         59.391

;;  overburden thickness (m):                310.485
;;  distance from repository plane to top of chn (m):     126.629
;;  distance from repository plane to top of water table (m):   278.533

 (usnt
  (title "line-load,AML=55mtu_acre,P2WR5C10-DDT55-01")
  (modelname usnt)

(include-pkg "thermcon.pkg")

;; single-comp (air), single-phase (gas) pkg for cond-only run

  (tstop  20100y)
  (time 50y)
  (stepmax 1000000)
  (dtmax 1.000e+25)
  (dt 1e2)
  (check-mult-con off)

;; *****************************************************************************
  (output
     (extool (variables T )
        (file-ext ".EBS.ext")(range "hstrk*" "dr*" "dhlw*" "bwr*" "pwr*" "in*" "ds*")
            (outtimes
                (include "/data34/TSPA03/outputTimes/outputTimes-LDTH-SDT-DDT-55-01")
            )
        )
    ) ;; end output

;; *****************************************************************************
(rocktab
      (include "/data34/TSPA03/physical_properties/SDT-1Dds-03")
      (include "/data34/TSPA03/physical_properties/DDT-EBS_Rev500")
) ;; close rocktab
```

```
;; *****************************************************************************

;;   There is no percolation for the conduction-only case
  (srctab
     (include "/data34/TSPA03/heatgen/DDT_blocks/preliminary_DTN/P2WR5C10_DDT")
  ) ;; end srctab

;;*****************************************************************************

;; set boundary conditions
  (bctab
    (atmos
        (range  "at*")
               (clamped)
    )
    (gwater
        (range  "wt*")
               (clamped)
    )
    ) ;; end bctab

;;*****************************************************************************
   ;; set initial conditions.
    (read-restart (time 50y)
    (file "/data34/TSPA03/DDT/DDTlab/01v/P2WR5C10-DDT55-01v.res"))

;;*****************************************************************************
;;This is for a unit symmetry cell with a half drift and half pillar
;;between drifts.
  (genmsh
    (down 0. 0. 1.0)
    (coord rect)
       ;; 54.82 MTU/acre
          (dx 0.7285 0.5125 0.015 0.4187 0.4222 0.350 0.3031 0.35 0.5 0.9
             1.0 1.5 2.5 3.0 5.0  7.0  9.250)
          ;; the WP cross-sectional area is the same as
          ;; for a 21-PWR AP WP with a diameter of 1.644 m
          ;; the drip-shield width is 2.512 m
          ;; the drip-shield half-width is 1.256 m
          (dy    1.29125 1.29125  ;; 1/2 21-PWR AP    2.5825 m  j = 1-2
                            0.1  ;; gap              0.1 m     j = 3
          1.30425 2.60850 1.30425  ;; 5-DHLW Long      5.217 m  j = 4-6
                            0.1  ;; gap              0.1 m     j = 7
          1.29125 2.58250 1.29125  ;; 21-PWR AP Hot    5.165 m  j = 8-10
                            0.1  ;; gap              0.1 m     j = 11
          1.29125 2.58250 1.29125  ;; 44-BWR AP        5.165 m  j = 12-14
                            0.1  ;; gap              0.1 m     j = 15
          1.29125 2.58250 1.29125  ;; 44-BWR AP        5.165 m  j = 16-18
                            0.1  ;; gap              0.1 m     j = 19
          0.89750 1.79500 0.89750  ;; 5-DHLW Short     3.59 m   j = 20-22
                            0.1  ;; gap              0.1 m     j = 23
          1.29125 2.58250 1.29125  ;; 21-PWR AP        5.165 m  j = 24-26
                            0.1  ;; gap              0.1 m     j = 27
          1.29125 1.29125          ;; 1/2 44-BWR AP    2.5825 m j = 28-29
          ) ;; total length of drift = 35.3320 m
    (dz
    1.0e-30    20.244     4.014     7.207     5.596  ;;  1- 5:    atm    tcw12   tcw13   ptn21   ptn22
    2.021     12.510     6.504    30.000    11.279  ;;  6- 10:   ptn23  ptn24   ptn25   ptn25   ptn26
    1.992     15.586    30.000    18.252    20.000  ;; 11- 15:   tsw31  tsw32   tsw32   tsw33   tsw33
    15.000    10.000    10.000     6.000     6.000  ;; 16- 20:   tsw33  tsw33   tsw33   tsw33   tsw33
    4.477      4.477     6.000     6.000     6.000  ;; 21- 25:   tsw34  tsw34   tsw34   tsw34   tsw34
    6.000      3.328     6.000     6.000     6.000  ;; 26- 30:   tsw34  tsw35   tsw35   tsw35   tsw35
    3.000      3.000     3.000     3.000     1.500  ;; 31- 35:   tsw35  tsw35   tsw35   tsw35   tsw35
    2.000      1.000     1.000     0.500     0.300  ;; 36- 40:   tsw35  tsw35   tsw35   tsw35   tsw35
    0.200      0.200     0.200     0.200     0.200  ;; 41- 45:   tsw35  tsw35   tsw35   tsw35   tsw35
    0.200      0.200     0.200     0.200     0.200  ;; 46- 50:   tsw35  tsw35   tsw35   tsw35   tsw35
    0.200      0.335     0.015     0.5975    0.7285 ;; 51- 55:   tsw35  tsw35   tsw35   tsw35   tsw35
    0.7285     0.2895    0.403     0.403     0.800  ;; 56- 60:   tsw35  tsw35   tsw35   tsw35   tsw35
    1.200      1.500     2.500     3.000     3.000  ;; 61- 65:   tsw35  tsw35   tsw35   tsw35   tsw35
    6.000      6.000     6.000     6.000     6.000  ;; 66- 70:   tsw35  tsw35   tsw35   tsw35   tsw35
    6.000      6.000     5.391     6.000     6.000  ;; 71- 75:   tsw35  tsw35   tsw35   tsw36   tsw36
    6.000      3.914     3.914     6.000     6.914  ;; 76- 80:   tsw36  tsw36   tsw36   tsw37   tsw37
    10.000    10.000     1.904     6.592    15.039  ;; 81- 85:   tsw38  tsw38   tsw38   tsw9z   ch1z
    20.000     0.293    20.303    20.273    20.303  ;; 86- 90:   ch2z   ch2z    ch3z    ch4z    ch5z
    17.578    19.688    14.326     4.102    1.0e-30 ;; 91- 95:   ch6z   pp4     pp3     pp2     wt
    )
      (mat
         (atm        atm      1  nx  1  ny   1   1)
         (tcw12      tcw12    1  nx  1  ny   2   2)
         (tcw13      tcw13    1  nx  1  ny   3   3)
```

```
            (ptn21      ptn21    1  nx  1  ny    4    4)
            (ptn22      ptn22    1  nx  1  ny    5    5)
            (ptn23      ptn23    1  nx  1  ny    6    6)
            (ptn24      ptn24    1  nx  1  ny    7    7)
            (ptn25      ptn25    1  nx  1  ny    8    9)
            (ptn26      ptn26    1  nx  1  ny   10   10)
            (tsw31      tsw31    1  nx  1  ny   11   11)
            (tsw32      tsw32    1  nx  1  ny   12   13)
            (tsw33      tsw33    1  nx  1  ny   14   20)
            (tsw34      tsw34    1  nx  1  ny   21   26)
            (tsw35      tsw35    1  nx  1  ny   27   73)
            (tsw36      tsw36    1  nx  1  ny   74   78)
            (tsw37      tsw37    1  nx  1  ny   79   80)
            (tsw38      tsw38    1  nx  1  ny   81   83)
            (tsw9z      tsw9z    1  nx  1  ny   84   84)
            ( ch1z       ch1z    1  nx  1  ny   85   85)
            ( ch2z       ch2z    1  nx  1  ny   86   87)
            ( ch3z       ch3z    1  nx  1  ny   88   88)
            ( ch4z       ch4z    1  nx  1  ny   89   89)
            ( ch5z       ch5z    1  nx  1  ny   90   90)
            ( ch6z       ch6z    1  nx  1  ny   91   91)
            (  pp4        pp4    1  nx  1  ny   92   92)
            (  pp3        pp3    1  nx  1  ny   93   93)
            (  pp2        pp2    1  nx  1  ny   94   94)
            (wt           pp2    1  nx  1  ny   95   95)
            (hstrk      tsw35    1  nx  1  ny   35   62)
            (dr         drift    1   1  1  ny   42   42)
            (dr         drift    1   3  1  ny   43   43)
            (dr         drift    1   4  1  ny   44   45)
            (dr         drift    1   5  1  ny   46   47)
            (dr         drift    1   6  1  ny   48   50)
            (dr         drift    1   7  1  ny   51   55)
            (dr         drift    1   6  1  ny   56   56)
            (dr         drift    1   5  1  ny   57   57)
;; WP1 half 21-PWR PWR AP WP
        (dro_wp1    dro_wp1     1   1  1   3   42   42)
        (dro_wp1    dro_wp1     1   3  1   3   43   43)
        (dro_wp1    dro_wp1     1   4  1   3   44   45)
        (dro_wp1    dro_wp1     1   5  1   3   46   47)
        (dro_wp1    dro_wp1     1   6  1   3   48   50)
        (dro_wp1    dro_wp1     1   7  1   3   51   55)
        (dro_wp1    dro_wp1     1   6  1   3   56   56)
        (dro_wp1    dro_wp1     1   5  1   3   57   57)
        (dri_wp1    dri_wp1     1   2  1   3   54   57)
        (ds_pwr1-1  drpshld 1   3  1   2   53   53)
        (ds_pwr1-1  drpshld 3   3  1   2   54   57)
        (pwr1-1     pwr     1   1  1   2   55   56)
        (dr     drift       1   1  3   3   55   56)
;; Gap1
        (dr     drift       1   1  3   3   55   56)
        (ds_gap1    drpshld 1   3  3   3   53   53)
        (ds_gap1    drpshld 3   3  3   3   54   57)
;; WP2 full 5-DHLW Long WP
        (dro_wp2    dro_wp2     1   1  4   7   42   42)
        (dro_wp2    dro_wp2     1   3  4   7   43   43)
        (dro_wp2    dro_wp2     1   4  4   7   44   45)
        (dro_wp2    dro_wp2     1   5  4   7   46   47)
        (dro_wp2    dro_wp2     1   6  4   7   48   50)
        (dro_wp2    dro_wp2     1   7  4   7   51   55)
        (dro_wp2    dro_wp2     1   6  4   7   56   56)
        (dro_wp2    dro_wp2     1   5  4   7   57   57)
        (dri_wp2    dri_wp2     1   2  4   7   54   57)
        (ds_dhlw-l1    drpshld 1   3  4   6   53   53)
        (ds_dhlw-l1    drpshld 3   3  4   6   54   57)
        (dhlw-l1    dhlw-l      1   1  4   6   55   56)
;; Gap2
        (dr     drift       1   1  7   7   55   56)
        (ds_gap2    drpshld 1   3  7   7   53   53)
        (ds_gap2    drpshld 3   3  7   7   54   57)
;; WP3 full 21-PWR AP Hot WP
        (dro_wp3    dro_wp3     1   1  8  11   42   42)
        (dro_wp3    dro_wp3     1   3  8  11   43   43)
        (dro_wp3    dro_wp3     1   4  8  11   44   45)
```

```
        (dro_wp3   dro_wp3    1    5    8   11   46   47)
        (dro_wp3   dro_wp3    1    6    8   11   48   50)
        (dro_wp3   dro_wp3    1    7    8   11   51   55)
        (dro_wp3   dro_wp3    1    6    8   11   56   56)
        (dro_wp3   dro_wp3    1    5    8   11   57   57)
        (dri_wp3   dri_wp3    1    2    8   11   54   57)
        (ds_pwr2-1 drpshld 1   3    8   10   53   53)
        (ds_pwr2-1 drpshld 3   3    8   10   54   57)
        (pwr2-1    pwr        1    1    8   10   55   56)
;; Gap3
        (dr     drift        1    1   11   11   55   56)
        (ds_gap3   drpshld 1    3   11   11   53   53)
        (ds_gap3   drpshld 3    3   11   11   54   57)
;; WP4 full 44-BWR AP WP
        (dro_wp4   dro_wp4    1    1   12   15   42   42)
        (dro_wp4   dro_wp4    1    3   12   15   43   43)
        (dro_wp4   dro_wp4    1    4   12   15   44   45)
        (dro_wp4   dro_wp4    1    5   12   15   46   47)
        (dro_wp4   dro_wp4    1    6   12   15   48   50)
        (dro_wp4   dro_wp4    1    7   12   15   51   55)
        (dro_wp4   dro_wp4    1    6   12   15   56   56)
        (dro_wp4   dro_wp4    1    5   12   15   57   57)
        (dri_wp4   dri_wp4    1    2   12   15   54   57)
        (ds_bwr1-1 drpshld 1   3   12   14   53   53)
        (ds_bwr1-1 drpshld 3   3   12   14   54   57)
        (bwr1-1    bwr        1    1   12   14   55   56)
;; Gap4
        (dr     drift        1    1   15   15   55   56)
        (ds_gap4   drpshld 1    3   15   15   53   53)
        (ds_gap4   drpshld 3    3   15   15   54   57)
;; WP5 full 44-BWR AP Adjusted WP
        (dro_wp5   dro_wp5    1    1   16   19   42   42)
        (dro_wp5   dro_wp5    1    3   16   19   43   43)
        (dro_wp5   dro_wp5    1    4   16   19   44   45)
        (dro_wp5   dro_wp5    1    5   16   19   46   47)
        (dro_wp5   dro_wp5    1    6   16   19   48   50)
        (dro_wp5   dro_wp5    1    7   16   19   51   55)
        (dro_wp5   dro_wp5    1    6   16   19   56   56)
        (dro_wp5   dro_wp5    1    5   16   19   57   57)
        (dri_wp5   dri_wp5    1    2   16   19   54   57)
        (ds_bwr2-1 drpshld 1   3   16   18   53   53)
        (ds_bwr2-1 drpshld 3   3   16   18   54   57)
        (bwr2-1    bwr        1    1   16   18   55   56)
;; Gap5
        (dr     drift        1    1   19   19   55   56)
        (ds_gap5   drpshld 1    3   19   19   53   53)
        (ds_gap5   drpshld 3    3   19   19   54   57)
;; WP6 full 5-DHLW Short WP
        (dro_wp6   dro_wp6    1    1   20   23   42   42)
        (dro_wp6   dro_wp6    1    3   20   23   43   43)
        (dro_wp6   dro_wp6    1    4   20   23   44   45)
        (dro_wp6   dro_wp6    1    5   20   23   46   47)
        (dro_wp6   dro_wp6    1    6   20   23   48   50)
        (dro_wp6   dro_wp6    1    7   20   23   51   55)
        (dro_wp6   dro_wp6    1    6   20   23   56   56)
        (dro_wp6   dro_wp6    1    5   20   23   57   57)
        (dri_wp6   dri_wp6    1    2   20   23   54   57)
        (ds_dhlw-s1    drpshld 1   3   20   22   53   53)
        (ds_dhlw-s1    drpshld 3   3   20   22   54   57)
        (dhlw-s1   dhlw-s     1    1   20   22   55   56)
;; Gap6
        (dr     drift        1    1   23   23   55   56)
        (ds_gap6   drpshld 1    3   23   23   53   53)
        (ds_gap6   drpshld 3    3   23   23   54   57)
;; WP7 full 21-PWR AP WP
        (dro_wp7   dro_wp7    1    1   24   27   42   42)
        (dro_wp7   dro_wp7    1    3   24   27   43   43)
        (dro_wp7   dro_wp7    1    4   24   27   44   45)
        (dro_wp7   dro_wp7    1    5   24   27   46   47)
        (dro_wp7   dro_wp7    1    6   24   27   48   50)
        (dro_wp7   dro_wp7    1    7   24   27   51   55)
        (dro_wp7   dro_wp7    1    6   24   27   56   56)
        (dro_wp7   dro_wp7    1    5   24   27   57   57)
```

```
        (dri_wp7   dri_wp7    1   2   24  27  54  57)
        (ds_pwr1-2 drpshld 1  3   24  26  53  53)
        (ds_pwr1-2 drpshld 3  3   24  26  54  57)
        (pwr1-2    pwr     1   1   24  26  55  56)
;; Gap7
        (dr    drift       1   1   27  27  55  56)
        (ds_gap7   drpshld 1  3   27  27  53  53)
        (ds_gap7   drpshld 3  3   27  27  54  57)
;; WP8 half 44-BWR AP WP
        (dro_wp8   dro_wp8    1   1   28  29  42  42)
        (dro_wp8   dro_wp8    1   3   28  29  43  43)
        (dro_wp8   dro_wp8    1   4   28  29  44  45)
        (dro_wp8   dro_wp8    1   5   28  29  46  47)
        (dro_wp8   dro_wp8    1   6   28  29  48  50)
        (dro_wp8   dro_wp8    1   7   28  29  51  55)
        (dro_wp8   dro_wp8    1   6   28  29  56  56)
        (dro_wp8   dro_wp8    1   5   28  29  57  57)
        (dri_wp8   dri_wp8    1   2   28  29  54  57)
        (ds_bwr1-2 drpshld 1  3   28  29  53  53)
        (ds_bwr1-2 drpshld 3  3   28  29  54  57)
        (bwr1-2    bwr     1   1   28  29  55  56)
        (in        invert  1   4   1   ny  58  58)
        (in        invert  1   2   1   ny  59  59)
        ) ;; end of material assignment

 (radcon
      (surface-offset 0 0  0)
      (include
       "/data34/TSPA03/radcon/DDT/preliminary_DTN/P2WR5C10-DDT55-01_1e-11.radcon")
 ) ;; close radcon
) ;; end genmsh

;; *********************** Solver options ************************************
(include "/data30/TSPA01/run_control_param/run_control_param_SMT-v02")

);; end of model input

;; ******************** Done ************************************************
```

APPENDIX VI

LDTH AND DDT SUBMODEL THERMAL-RADIATION CONNECTION CALCULATION

The LDTH and DDT submodels include heat transfer by thermal radiation inside the drift. The LDTH and DDT submodels represent thermal-radiative heat transfer between the drip shield, drift wall, and invert surfaces. The DDT submodels also represent thermal-radiative heat transfer between the waste package, drip shield, and invert surfaces beneath the drip shield. The determination of the thermal-radiation coefficients requires one direct input, which is the emissivity of the surfaces. The emissivity of the drift wall and invert surfaces is taken to be 0.9, which is near the middle of the range given for rocks (0.88 to 0.95) in Table A.11 of *Fundamentals of Heat and Mass Transfer* (Incropera and DeWitt 1996 [DIRS 108184]). The process of determining thermal-radiation connections for the LDTH and the DDT submodels is done by hand following these steps:

1. Compile a list of model gridblocks that have at least 1 face contacting air within the drift

2. For each pair of gridblocks in this list

    a. Determine if there is a clear path (line of sight between face centers) between the air contacting face of each block

    b. If a clear path exists, calculate the thermal-radiation coefficient for that connection and write a "radcon" entry in NUFT format, which is given in *Reference Manual for the NUFT Flow and Transport Code, Version 2.0* (Nitao 1998 [100474]). The coefficient c used in Equations 9 and 10 of Section 6.2.3.3, and which is calculated by RADPRO v4.0 (Section 3.1.3), is determined as follows:

$$c = (\ \sigma \varepsilon \, (\text{N1} \times \text{R})(-\text{N2} \times \text{R}) \, A_1 \, A_2) / \pi \, | \, \text{R} \, |^4 \qquad \text{(Eq. VI-1)}$$

where:

σ = Stefans Constant
π = pi
ε = emissivity
A_1 = area of grid block face 1 (radiating)
A_2 = area of grid block face 2 (connecting)
N1 = unit vector normal to face 1
N2 = unit vector normal to face 2
R = distance from center of face 1 to center of face 2

grid block 1

N1

R

N2

grid block 2
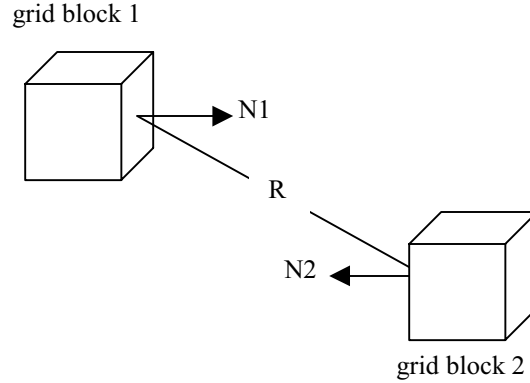
Radcon files are located in DTN: LL030808623122.036. The file names are:

```
P2WR5C10-DDT55-01_full.radcon
ldth0_300m.radcon
P2WR5C10-DDT55-01v.radcon
```

Determining Effective Emissivity for RADPRO Radcon Files

Equations 9 and 10 in Section 6.2.3.3 apply to gray-body-to-black-body thermal radiation, where the heat receiving surface (A_2) is a perfect black body (i.e., ε equal to 1). The software routine RADPRO v4.0 (Section 3.1.3), which calculates the coefficient c in Eq. VI-1, also pertains to gray-body-to-black-body thermal radiation. However, all surfaces within the emplacement drifts are gray bodies, with values of emissivity less than 1. Therefore, the value of emissivity ε taken as input for RADPRO v4.0 is actually an *effective* emissivity $\varepsilon_{\mathrm{eff}}$, for the heat emitting surface, which accounts for the fact that the heat receiving surface is a gray body, rather than a black body. The value of effective emissivity $\varepsilon_{\mathrm{eff}}$ is determined by applying the solution of Bird et al. (1960 [DIRS 103524]) for radiative heat transfer between two long, gray coaxial cylinders by considering multiple reflections from the two sources:

$$Q_{12} = \sigma(T_1^4 - T_2^4)/[1/A_1\varepsilon_1 + (1/A_2)(1/\varepsilon_2 - 1)] \qquad \text{(Eq. VI-2)}$$

Multiplying the numerator and denominator by $A_1\varepsilon_1$ results in the following expression:

$$Q_{12} = A_1\varepsilon_1\sigma(T_1^4 - T_2^4)/[1 + (A_1\varepsilon_1/A_2)(1/\varepsilon_2 - 1)] \qquad \text{(Eq. VI-3)}$$

Using an *effective* emissivity $\varepsilon_{\mathrm{eff}}$ results in the following expression:

$$Q_{12} = A_1\ \varepsilon_{\mathrm{eff}}\ \sigma(T_1^4 - T_2^4) \qquad \text{(Eq. VI-4)}$$

where $\varepsilon_{\mathrm{eff}}$ is given by:

$$\varepsilon_{\mathrm{eff}} = \varepsilon_1/[1 + (A_1/A_2)\ \varepsilon_1\ (1/\varepsilon_2 - 1\ )] \qquad \text{(Eq. VI-5)}$$

The effective emissivity $\varepsilon_{\mathrm{eff}}$ is simply ε_1, multiplied by a coefficient C:

$$\varepsilon_{\mathrm{eff}} = C\varepsilon_1 \qquad \text{(Eq. VI-6)}$$

where the coefficient C is given by:

$$C = 1/[1 + (A_1/A_2)\, \varepsilon_1\, (1/\varepsilon_2 - 1\,)]$$ (Eq. VI-7)

For the LDTH submodels (Section 6.2.6) and DDT submodels (6.2.9), A_1 is taken to be equal to A_2, resulting in the following expression:

$$C = 1/[1 + \varepsilon_1\, (1/\varepsilon_2 - 1\,)]$$ (Eq. VI-8)

Section 5.3.2.7 discusses the assumption concerning the emissivity at the drift-wall surface of emplacement drifts. The value of ε_{eff} between the drip shield and drift-wall surface is determined for the LDTH and DDT submodels, using Equations VI-6 and VI-8 and the following values for emissivity on the drip shield (ε_1) and for emissivity on the drift-wall (rock) surface (ε_2):

$$\varepsilon_1 = 0.63 \text{ (titanium from Lide 1995 [DIRS 101876], p. 10-298)}$$

$$\varepsilon_2 = 0.9 \text{ (rock, in the range of 0.88 to 0.95 from Incropera and DeWitt 1996 [DIRS 108184])}$$

This results in a value of 0.935 for the coefficient C. As discussed in Section 5.3.2.7, the drift-wall surface is covered with Type 316 stainless steel liner, which has an emissivity of 0.52 to 0.66 (McAdams, Heat Transmission, 1954 [DIRS 161435]). Table VI-1 summarizes the value of the coefficient C for different values of emissivity (ε_2) at the drift wall.

Table VI-1. The Value of the Coefficient C from Equation VI-7 Calculated for Different Values of Emissivity at the Drift Wall

Emissivity at Drift Wall (ε_2)	C	C/C_{orig}[b]
0.90	0.935[a]	1.000
0.90	0.969	1.037
0.52	0.790	0.845
0.59	0.833	0.892
0.66	0.871	0.932

NOTE: These values pertain to radiation between the drip shield and drift wall, where emissivity on the drip shield (ε_1) is equal to 0.63. [a]C is calculated using Eq. VI-8. [b]C_{orig} is the value of C that was applied to determine ε_{eff} from the drip shield to the drift wall for the LDTH and DDT submodels, which was calculated using Equation VI-8, and is equal to 0.935.

For emissivity (ε_1) on the drip shield equal to 0.63, and emissivity (ε_2) at the drift wall ranging from 0.52 to 0.66, Eq. VI-7 gives values of C ranging from 0.790 to 0.871. As discussed above, for the LDTH and DDT submodels, a value of 0.935 was calculated (using Eq. VI-8) for the coefficient C (called C_{orig} in Table VI-1), which was used to determine the value ε_{eff} from the drip shield to drift wall. The ratio C/C_{orig} is listed in Table VI-1 to illustrate the relative change in ε_{eff} that would occur if this range of ε_2 were applied, compared to the value of ε_{eff} used in the LDTH and DDT submodels. Thus, the value of ε_{eff} would be reduced by 6.8 to 15.5 percent for the range of emissivities reported for Type 316 stainless steel.

Because thermal radiation depends on the difference of the respective temperatures each raised to the fourth power (Eq. VI-4), the influence of a 6.8 to 15.5 percent reduction in the value of ε_{eff} is small. An example illustrating this point is taken from Figure 6.3-23 in Section 6.3.2.1 of this report. At 70 years (20 years after closure), the temperature on the drip shield attains its peak value of 155.3^{o}C. (Note that the drip-shield temperature is not plotted in Figure 6.3-23.) At 70 years, the drift wall attains a peak temperature of 140.8^{o}C. When ε_{eff} is reduced by 6.8 percent, the peak drip-shield temperature from Eq. VI-6 is calculated to be 156.2^{o}C. When ε_{eff} is reduced by 10.8 percent (the average case in Table VI-1), the peak drip-shield temperature is calculated to be 156.8^{o}C. When ε_{eff} is reduced by 15.5 percent, the peak drip-shield temperature is calculated to be 157.6^{o}C. Thus, reducing the value of ε_{eff} by 6.8 to 15.5 percent results in a drip-shield temperature increase of 0.9 to 2.3^{o}C, with an increase of 1.5^{o}C for the average case.

APPENDIX VII

**EXTRACTION/MICRO-ABSTRACTION PROCESS FOR MSTHAC (BUILDING
VIRTUAL LDTH AND SDT "CHIMNEY" SUBMODELS)**

Extract MSTHAC v7.0 information from real LDTH and SDT "chimney" submodel output

For the first stage of the multiscale thermohydrologic model abstraction process, MSTHAC v7.0 reads the NUFT output files for the SMT, SDT, LDTH, and DDT submodels, extracts the requested time histories, and saves them to a MSTHAC v7.0 "extraction" file. In order to perform the extraction, a MSTHAC v7.0 input file is created using the format defined in the MSTHAC 7.0 user's manual. A set of input files is created for each LDTH-/SDT submodel "chimney" location, with input files corresponding to each of the AMLs for which the LDTH and SDT submodels are run (e.g., AMLs of 66, 55, 27, and 14 MTU/acre). The resulting input files are run using MSTHAC 7.0.

Interpolate extracted real LDTH and SDT "chimney" submodel output to the SMT submodel locations (virtual LDTH and SDT "chimney" submodel extraction files)

Note that 108 out of 2874 of the SMT submodel repository-gridblock locations correspond to actual LDTH/SDT submodel locations. As discussed in Appendix I, these 108 locations generally occur for every third emplacement drift (see Figure 6.2-3). LDTH/SDT submodels are always placed at the ends of drifts and are usually placed at one or two locations along the central portion of those drifts. For the other locations that lie in between the 108 LDTH/SDT submodel locations, it is necessary to interpolate LDTH and SDT submodel results. These interpolated LDTH and SDT submodels are called "virtual" LDTH and SDT submodels.

The process of creating virtual LDTH and SDT "chimney" submodel extraction files is carried out with the use of chimney_interpolate v1.0. The software code chimney_interpolate v1.0 reads a control file that defines the following information: (1) name of a "real" chimney-submodel extraction file, (2) fractional weighting for this real chimney-submodel file (note that these weighting factors are the same as those used to interpolate percolation flux, as described in substep 6 of step 8 in Appendix I), (3) name of a second real chimney-submodel extraction file, (4) fractional weighting for this file and (5) the name of the virtual chimney-submodel extraction that will be created. Note that the two "real" chimney submodels straddle the target location where the interpolation occurs. The software code chimney_interpolate v1.0 does a simple linear interpolation between the two input files using the specified weights for each of the real chimney submodels.

The interpolation process is the same as that carried out for percolation flux (see substep 6 of step 8 of Appendix I). The interpolation process is two step: (1) "row-wise" interpolation along the drifts containing real chimney submodels and (2) "column-wise" interpolation to obtain virtual chimney submodels for the drifts lying between the drifts containing the real chimney submodels. First, "virtual" LDTH and SDT submodels are interpolated for all intermediate locations along the emplacement drifts that contain "real" LDTH and SDT submodels. Once these drifts have all of the virtual LDTH and SDT submodels created for the entire row of SMT submodel repository gridblocks, the "column-wise" interpolation process is conducted to create the virtual chimney submodels for the repository drifts lying between those with the real chimney submodels. The specified weighting factors for this linear interpolation process are the same as those used in interpolating the percolation flux for the SMT submodel repository gridblocks, as is described in Appendix I (see Substep 6 of Step 8). The output is a virtual chimney-submodel extraction file at each SMT submodel location and for each AML (e.g., 66, 55, 27, and 14 MTU/acre). This process is only conducted for the SDT and LDTH submodels.

There are approximately 69,000 such files created. These files are found in DTN: LL030808523122.035. File names follow the conventions:

LDTH submodels: (panel #)(i index):(j index)-LDTH(AML)-1Dds_mc-(percolation case)I-0(parameter case).m-f.EBS.ext.extract_LDTH_rev_14
SDT submodels: (panel #)(i index):(j index)-SDT(AML)-00-01.ext.extract_SDT_rev_0

Create *.in files for each virtual NUFT LDTH "chimney" submodel

For the purposes of micro-abstraction, MSTHAC v7.0 requires the following: (1) the coordinates of the LDTH "chimney" submodels, (2) the real number for the AML (e.g., the real number for an AML of 66 MTU/acre is 65.784 MTU/acre), and (3) the present-day-, monsoonal-, and glacial-transition-climate percolation fluxes for that LDTH submodel location. Note that 108 out of 2874 of the SMT submodel repository-gridblock locations correspond to actual LDTH submodel locations. For the other locations, interpolated LDTH and SDT submodel results are obtained; these interpolated LDTH and SDT submodels are called "virtual" LDTH and SDT submodels. To obtain this information, MSTHAC v7.0 reads a *.in file associated with each LDTH submodel. The format of the *.in file is specified by the NUFT user's manual (Nitao 1998 [DIRS 100474]) (see Appendix V), and the MSTHAC 7.0 user's manual specifies the required information for this file. A "virtual" LDTH submodel *.in file is created for each SMT submodel repository-gridblock location. Note that the only purpose for the virtual LDTH submodel *.in files is to supply MSTHAC v7.0 with the percolation flux for the glacial-transition climate for each of the SMT submodel repository gridblock locations. Although it is not required, the virtual LDTH submodel *.in files also contain the percolation-flux values for the present-day and monsoonal climates as well. The percolation-flux values that were interpolated for each of the SMT submodel repository gridblock locations (see substep 6 of step 8 in Appendix I), along with the coordinates of that location, are edited into each of the virtual LDTH submodel *.in files with the use of scripts containing standard UNIX commands. There is a script for each of the three infiltration-flux cases: (1) create_virtual_in_SCRIPT_ma for the mean-infiltration-flux case, (2) create_virtual_in_SCRIPT_la for the lower-infiltration-flux case, and (3) create_virtual_in_SCRIPT_ua for the upper-infiltration-flux case. These three scripts, along with the instructions and control files for running these scripts, are found in DTN: LL030808523122.035 [DIRS 166419]. The names of these virtual LDTH submodel *.in files use the following convention:

(panel #)(i index):(j index)-LDTH(AML)-1Dds_mc-(infiltration-flux case)i-0(parameter case).in

Note that the infiltration-flux-case labels are:

1. mi, which stands for mean infiltration flux

2. ui, which stands for upper infiltration flux

3. li, which stands for lower infiltration flux.

Note also that the i and j indices are those from the SMT submodel and that the Panel numbers are P1, P2E, P2W, P3, and P5 (see Figure 6.2-3). The parameter case is 2, which is for the modified-mean-infiltration-flux property set.

Run MSTHAC v7.0 at all SMT submodel locations using virtual SDT and LDTH "chimney" submodel extraction files, in conjunction with DDT and SMT submodel extraction files

Once the virtual SDT and LDTH submodel extraction files have been created and the virtual LDTH submodel *.in files have been created, MSTHAC v7.0 is run to generate the micro-abstraction output file at each SMT submodel location. This process also requires DDT submodel extraction files, as well as the SMT submodel extraction file. This process is carried out by first creating an abstraction MSTHAC v7.0 input file, as defined in the MSTHAC 7.0 user's manual. Once the input files are created, MSTHAC 7.0 is run with these files as input and the micro-abstraction output files are generated at each SMT submodel location.

INTENTIONALLY LEFT BLANK

APPENDIX VIII

BINNING CALCULATIONS

Bin Indexes

Bin indexes were calculated for each SMT submodel location based on the rank of the percolation flux associated with the location. The general calculation procedure is as follows:

1. Sort SMT submodel locations by ascending values of percolation flux

2. Calculate quantile values for each sorted point according to the rank of the point in the sorted data set

3. Assign bin indexes according to quantile intervals.

Binning was performed according to specifications provided by the Performance Assessment Department. Glacial-transition climate state (median case) was specified as the percolation flux source. Binning quantiles were as follows:

Bin Index	Quantile Range
Bin 1	less than 5 percent
Bin 2	greater than or equal to 5 percent less than 30 percent
Bin 3	greater than or equal to 30 percent less than 70 percent
Bin 4	greater than or equal to 70 percent less than 95 percent
Bin 5	greater than or equal to 95 percent

Bin indexes were calculated for each of the 2,874 SMT submodel locations.

Bin the MSTHAC v7.0 output and reformat it for TSPA

After all 2,874 MSTHAC v7.0 microabstractions have been created for a particular percolation case, the output is processed to produce the set of information required by TSPA. To facilitate their work, TSPA requires the micro-abstraction to be processed two different ways: "WAPDEG" binning and "TSPA" binning. Note that WAPDEG is an analysis that uses MSTHM output. Because the WAPDEG is downstream of the MSTHM (with respect to model-to-model parameter flow), WAPDEG does not produce any output required by the MSTHM. The total binned files are:

$$22,992 \text{ (from WAPDEG)} + 5,748 \text{ (from TSPA)} = 28,740$$

WAPDEG Binning

The first processing (WAPDEG binning) involves reporting the T_wp, RH_wp, T_ds and RH_ds for each SMT submodel location and each waste package type. There are 8 waste package types which form two waste package groups:

Group1 : DHLW : dhlw-l1, dhlw-s1

Group2 : CSNF : pwr1-1, pwr2-1, bwr1-1, bwr2-1, pwr1-2, bwr1-2

For WAPDEG purposes, we are interested in each repository location and each waste package type, therefore, there are 2,874 locations × 8 waste package type = 22,992 typical waste packages reported.

Since the WAPDEG binning produces a large number of output files, the files are concatenated using a UNIX shell script so that all locations falling within a bin and all waste packages of a given type (CSNF or DHLW) are included in a single file. This process creates 5 (# of bins) × 2 (number of waste package groups) = 10 output files for delivery. A second set of 10 files is provided in the WAPDEG format that only uses the "typical waste package" as explained below. Hence a total of 20 WAPDEG files are provided for each infiltration flux case.

TSPA Binning

The second process (TSPA binning) involves determining the most typical location given a set of locations that define a "bin." For TSPA purposes, this process is interested in the most typical waste package (see below) in a group / bin; therefore, there are 5 bins × 2 groups = 10 typical waste packages reported. A bin is a set of SMT submodel locations that have similar percolation values and is defined by the TSPA organization. For the purposes of processing, the waste packages are grouped into two waste package type groups (CSNF and DHLW). For each bin, two output files are created, one for the most typical CSNF package and one for the most typical DHLW package. There are 5 (# of bins) × 2 (waste package groups) files created for this type of processing. This results in an additional 2,874 locations × 2 waste package groups = 5,748 files.

The TSPA binning results of typical waste packages are concatenated using a UNIX shell so that all locations falling within a bin and all waste packages of a given type (CSNF or DHLW) are included in a single file. This process creates 5 (# of bins) × 2 (number of waste package groups) = 10 output files for delivery.

Typical Waste Package Determination

The most typical package is selected by compiling for each waste package type and bin member, peak waste package temperature, and duration of boiling at the drift wall. These data are sorted from low to high, and a percentile assigned to each. For each waste package type and location in the list, the typical package is the one that is most median on the two parameter spaces.

To do this processing, reformat_EXT_to_TSPA v1.0 is used. The software code reformat_EXT_to_TSPA v1.0 takes the name of an input file as its only input. The format of this file is defined in the software code reformat_EXT_to_TSPA v1.0 user's manual.

Binning files are delivered as output from reformat_EXT_to_TSPA v1.0.

Binning Algorithm

For each location in a bin and waste package in a waste package group:

   1.   Calculate peak waste package temperature
   2.   Calculate boiling duration at the waste package

3. Sort peak waste package temperature from high to low
4. Sort boiling duration from low to high
5. Assign percentile rank to each waste package temperature
6. Assign percentile rank to each boiling duration.

For each included waste package type / location in the bin:

1. Calculate deviation of percentile rank from median (50 percent) for peak waste package temperature
   a. if current loc/waste package type is ranked 47 percent, deviation = 0.50 − 0.47 = 0.03
2. Calculate deviation of percentile rank from median (50 percent) for boiling duration
   b. if current loc/waste package type is ranked 54 percent, deviation = 0.50 − 0.54 = −0.04
3. Calculate sum of squared deviations from Step 1 and 2
   c. $0.03^2 + 0.04^2 = 0.0025$.

For the current bin / waste package group, select the waste package/location with the smallest squared deviation (this is the most typical package).

INTENTIONALLY LEFT BLANK

APPENDIX IX

MULTISCALE MODEL APPROACH TO THERMOHYDROLOGY AT YUCCA MOUNTAIN

MSTHM Concept

The MSTHM approach breaks the solution of thermal-hydrologic modeling at Yucca Mountain into smaller pieces by varying dimensionality requirements (one-, two-, or three-dimensional) as needed for detail. The MSTHM approach subdivides the problem into thermal and thermal-hydrologic submodels. By subdividing the problem into more tractable pieces, more efficient thermal-conduction and thermal-radiation submodels are used to address the three-dimensional nature of the heated repository footprint and mountain-scale heat flow and the three-dimensional geometric details of the engineered components in the emplacement drifts, waste-package-to-waste-package heat-generation variability, and drift-scale heat flow. Two-dimensional thermal-hydrologic models, which are much more efficient than three-dimensional thermal-hydrologic models, are used to model all thermal-hydrologic variables in detail, within the emplacement drifts and in the adjoining host rock.

MSTHM Spatial Scales

Two spatial scales are considered for the MSTHM: (1) mountain scale (on the order of hundreds to thousands of meters) and (2) drift scale (on the order of fraction of meters). Drift-scale modeling includes the coupling of drift-scale processes both within the engineered barrier system and within the near field environment. Mountain-scale processes are needed to account for the influence of the ground surface, the water table, and most importantly, the influence of repository edge cooling effects. In addition to coupling the drift scale and mountain scale, the MSTHM also allows for consideration of the effect of different waste package types (e.g., different CSNF waste packages, co-disposal of DHLW) on the various performance measures.

MSTHM Submodels

The MSTHM simulates processes under a range of heat loading conditions to capture the edge effects within the repository and the discrete nature of waste packages. MSTHM simulates the TH response at various locations within the domain to account for variations in stratigraphy and infiltration. This is accomplished by simultaneously solving four "submodels" at different spatial scales. These four submodels comprising the MSTHM are categorized into four NUFT submodel types (SMT, SDT, DDT, and LDTH). The MSTHM also results in two MSTHAC v7.0 models (LMDH and DMTH). A consistent naming convention is used for these submodels. The first letter applies to the thermal loading where S is the "smeared" area averaged heat loading, L is the "line" heat loading, and D is the "discrete" point heat loading. The second letter applies to the spatial scaling where M is the "mountain" scale and D is the "drift" scale. The last letters refer to the variables considered where T indicates that only "thermal conduction" variables are considered and where TH indicates that all "thermal-hydrologic" variables are considered.

The four different NUFT submodels (listed below) are solved simultaneously at different spatial scales:

- **SMT Submodel** – The three-dimensional smeared-source mountain-scale thermal-only submodel

- **LDTH Submodel** – The two-dimensional line-source drift-scale thermal-hydrology submodel

- **SDT Submodel** – The one-dimensional smeared-source drift-scale thermal-only submodel

- **DDT Submodel** – The three-dimensional discrete-source drift-scale thermal-only submodel.

The MSTHM processes the four NUFT submodels using MSTHAC v7.0 to produce the two following models:

- **LMTH Model** – The intermediary three-dimensional line-source mountain-scale thermal-hydrologic model.

- **DMTH Model** – The final three-dimensional discrete-source mountain-scale thermohydrology model.

Figure IX-1 illustrates the general conceptual relation between the four NUFT submodels (identified by red text) and the two MSTHAC v7.0 submodels (identified by blue text). The successive nature of the NUFT submodel execution followed by the MSTHAC v7.0 calculation for final output is illustrated in the flowchart of Figure IX-2.

The fundamental concept behind MSTHM is that two-dimensional representations of drift-scale thermal-hydrology (the LDTH submodels) can account for mountain-scale edge cooling processes by changing the horizontal distance of the adiabatic boundary in the drift-scale model. For locations within an infinite (x and y) expansive repository, the drift-scale model adiabatic boundary distance would be the half-way point between drifts. Edge effects within the model are accommodated by allowing the adiabatic boundaries to extend in time to mimic the cooling process. The distance to the adiabatic boundary is measured using the areal mass loading (AML) factor, which reports the heat input per unit area (reported in metric tonnes of uranium/acre, MTU/acre). As the distance to the adiabatic boundary increases, the AML decreases.

The relation between the time-varying AML at any given point in the repository is determined by interpolating the necessary width to the adiabatic boundary needed for an SDT submodel at the point to match the SMT submodel-predicted temperature. This is merely a superposition process justified by the linear nature of the conduction-only energy equation. Once this AML history is established, it is applied to the LDTH submodel, which introduces the dimensionality of the heat source (a waste package) and the hydrology of the system. The final component of MSTHM is the inclusion of thermal-radiative heat transfer with the DDT submodel. Here the temperature redistribution due to the variation between hotter waste packages, colder waste packages, and gaps between waste packages for one location in the repository is determined. This temperature difference is then applied to the two-dimensional thermal-hydrologic results to give complete thermal-hydrologic histories for all locations and all waste packages within the repository.

MSTHM Model Process

The MSTHM methodology can be subdivided into the two specific "steps" illustrated in Figure IX-2. Step 1 is the simultaneous execution of the four NUFT submodels. Step 2 is the assembly of the NUFT submodel results into final MSTHM results through the use of MSTHAC v7.0. These processes are discussed in detail below.

STEP 1: NUFT Submodel Execution

A three-dimensional SMT submodel simulation determines the temperature history for a specific simulated repository life-cycle event. This three-dimensional conduction-only submodel has the total energy of the repository delivered over a smeared heat-source. Taking advantage of the fact that the transient conduction equation is linear and therefore super-positional, the temperature generated at any given location of the 3D SMT submodel at any given point in time can be simulated by a one-dimensional SDT conduction-only submodel of a certain heat input. This heat input can be characterized as the "emplaced heat input" divided by the lateral "width" of drift that the SDT submodel heating occurs, resulting in an areal mass loading AML. By superposing SDT submodels to create an SMT submodel temperature, an AML-varying history referred to as an $AML_{hstrk,eff}$ is used to describe the heat-up and cool-down of that particular location of the repository. The MSTHM represents thermal-hydrologic processes, which includes the influences of hydrologic properties and percolation flux, by incorporating the results of two-dimensional LDTH submodels at each of the drift-scale-submodel locations. At each location, an AML curve is generated which describes the temperature history due to a specified heat input to the LDTH submodel.

The three-dimensional SMT and the one-dimensional SDT submodels solve for thermal conduction only and both share the same smeared-heat-source approximation and thermal-conduction representation of heat flow. The one-dimensional SDT submodels are executed at the same 108 locations and for the same AMLs as are the LDTH submodels providing a linkage between the SMT and the LDTH submodels. The common repository location of the SDT submodel and LDTH submodel drift wall temperatures allows for the SMT submodel temperature to be corrected for both the influence of thermal-hydrologic processes on temperature and for the influence of two-dimensional drift-scale dimensionality (orthogonal to the axis of the drift). This is accomplished by interpolating between AML histories. The SMT, SDT, and LDTH submodels share a blended heat-generation history of the entire waste package repository; hence, the heat-generation history is effectively that of an average waste package.

The three-dimensional DDT submodel is a drift-scale submodel, which includes individual waste packages with distinct heat-generation histories. The DDT submodel solves for thermal conduction and accounts for thermal radiation in addition to thermal conduction between the waste package and drift surfaces. The drift wall temperatures for an average waste package, calculated with the combined use of the LDTH, SMT, and SDT submodels, are then further modified to account for waste-package-specific deviations using the DDT submodel.

One complete MSTHM simulation requires multiple NUFT submodel executions to simulate the entire repository. Each MSTHM simulation includes the following NUFT submodel executions:

- 1 SMT submodel execution for the mountain

- 1 DDT submodel × 4 AMLs execution at one location in the repository
- N SDT submodel locations × 4 AMLs
- N LDTH submodel locations × 4 AMLs.

STEP 2: MSTHM assembly process

The use of MSTHAC v7.0 to assemble the execution results of the NUFT submodels into final output is the second part of MSTHM process (see Figure IX-2). MSTHAC v7.0 assembles the execution results from the submodels at the N locations within the repository creating time-varying AML curves.

The MSTHM assembly process can be broken into six calculation stages which center on the construction of two time-varying AMLs: an effective AML for the host rock ($AML_{hstrk,eff}$) and a specific AML ($AML_{specific}$) for specific waste package locations along the drift. The $AML_{hstrk,eff}$ varies spatially and temporally and is the interpolated AML that would be prescribed for an insulated heat submodel (SDT) to predict the temperature produced by a mountain-scale submodel (SMT). The $AML_{specific}$ incorporates the discrete nature of the waste packages using the DDT submodel. Both AMLs are used to interpret LDTH submodel results to the LMTH and DMTH models. The six-stage process of MSTHM assembly is illustrated as an overview in Figure IX-2. Each stage is explained in detail below in conjunction with Figures IX-3 through IX-7.

Assembly Stage 1: Assemble $AML_{hstrk,eff}$ (Figure IX-3)

The SDT submodel temperature histories are plotted for each of the N spatial locations for a "family" of four AMLs (66, 55, 27, and 14 MTU/acre for this model report). For each spatial location, the plotted family of SDT submodel temperature histories is plotted against the time history of the temperature from the SMT submodel. The $AML_{hstrk,eff}$ is interpolated by determining the AML needed for the SDT submodel to generate the SMT temperature at any given time.

Assembly Stage 2: Interpolate LMTH (Figure IX-4)

The LMTH results are determined by taking the thermal-hydrologic output from the LDTH submodels and plotting the time-history of the variables for each of the family of AMLs. First for each of the N locations, the thermal-hydrologic output history from the LDTH submodel is plotted for each of the four AMLs. Second, the thermal-hydrologic history for the LMTH at any given time t* is determined by interpolating the thermal-hydrologic value at $AML_{hstrk,eff}$(t*) from the LDTH histories (note that the LDTH and DDT submodels include radiative heat transfer between the waste package, drip shield, and drift wall surfaces). As radiative heat transfer is proportional to the temperature difference between two surfaces raised to the fourth power, i.e., ΔT^4, linear interpolation between two bounding AML curves is not sufficient to accurately calculate a result. To address this issue, MSTHM submodels are run at a variety of AMLs. Hence, interpolations are performed over a small enough range that piecewise linear interpolation adequately characterizes the underlying nonlinear process of radiative heat transfer.

Assembly Stage 3: Calculate DMTH (Figure IX-5)

The discrete thermal-hydrologic values are calculated from the LMTH submodel by incorporating the DDT submodel temperature results. Here, the temperature variation along the average temperature of the LMTH submodel accounts for differences in waste package loading. The temperature difference is calculated using the $AML_{hstrk,eff}$ and the temperature from the DDT submodel. This difference is then superimposed on the LMTH submodel to yield DMTH submodel results.

Assembly Stage 4: Assembling AMLspecific (Figure IX-6)

The procedure for assembling $AML_{specific}$ is very similar to that of assembling $AML_{hstrk,eff}$. The temperature history from the LDTH submodel is plotted for each of the N spatial locations for a "family" of four AMLs (66, 55, 27, and 14 MTU/acre). Along with the family of LDTH submodel temperature histories at each spatial location is plotted the time history of the temperature from the DMTH model. The $AML_{specific}$ is interpolated by determining the AML needed for the LDTH submodel to generate the DMTH- model temperature at any given time.

Assembly Stage 5: Interpolate Thermal-Hydrologic Variables for DMTH (Figure IX-7)

The DMTH results are determined by taking the thermal-hydrologic output from the LDTH submodels and plotting the time-history of the variables for each of the family of AMLs. First for each of the N locations, the thermal-hydrologic output history from the LDTH submodel is plotted for each of the four AMLs. The thermal-hydrologic history for the DMTH at any given time t* is determined by interpolating the thermal-hydrologic value at $AML_{specific}(t^*)$ from the LDTH histories.

Assembly Stage 6: Determine Relative Humidity for the Waste Package and Drip Shield

The relative humidity on top of the drip shield and on the waste package is calculated as a function of the saturated pressures in the drift.
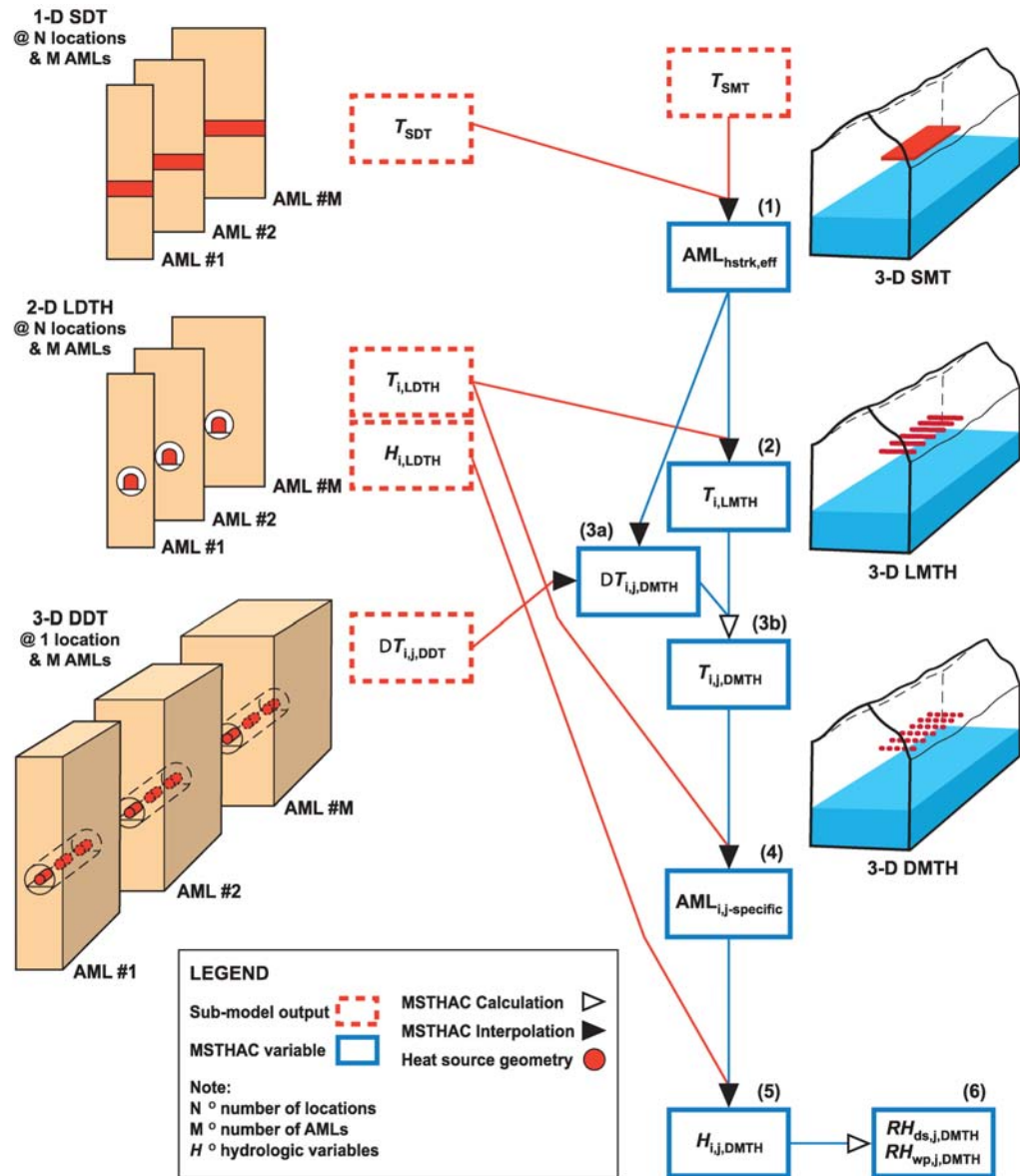
NOTE: SDT, LDTH, and DDT submodels are run a different AMLs (left side). SMT, LMTH, and DMTH models are the series of three-dimensional mountain-scale models of increasing complexity (right side). The six stages illustrate the process of constructing intermediate variables.

Figure IX-1. Six-Stage Flow Chart Diagram of the Multiscale Thermohydrologic Model (MSTHM)
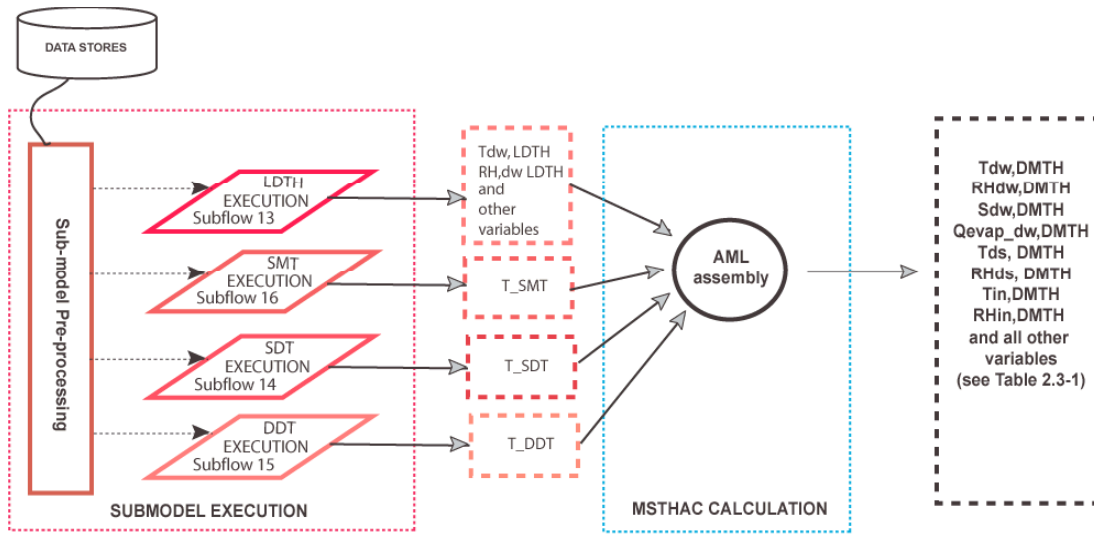
Figure IX-2.   MSTHM Flowchart Shown in Two Steps: (1) NUFT Submodel Execution in Red, and (2) MSTHM Processing of Final Output Using MSTHAC v7.0 (Blue)
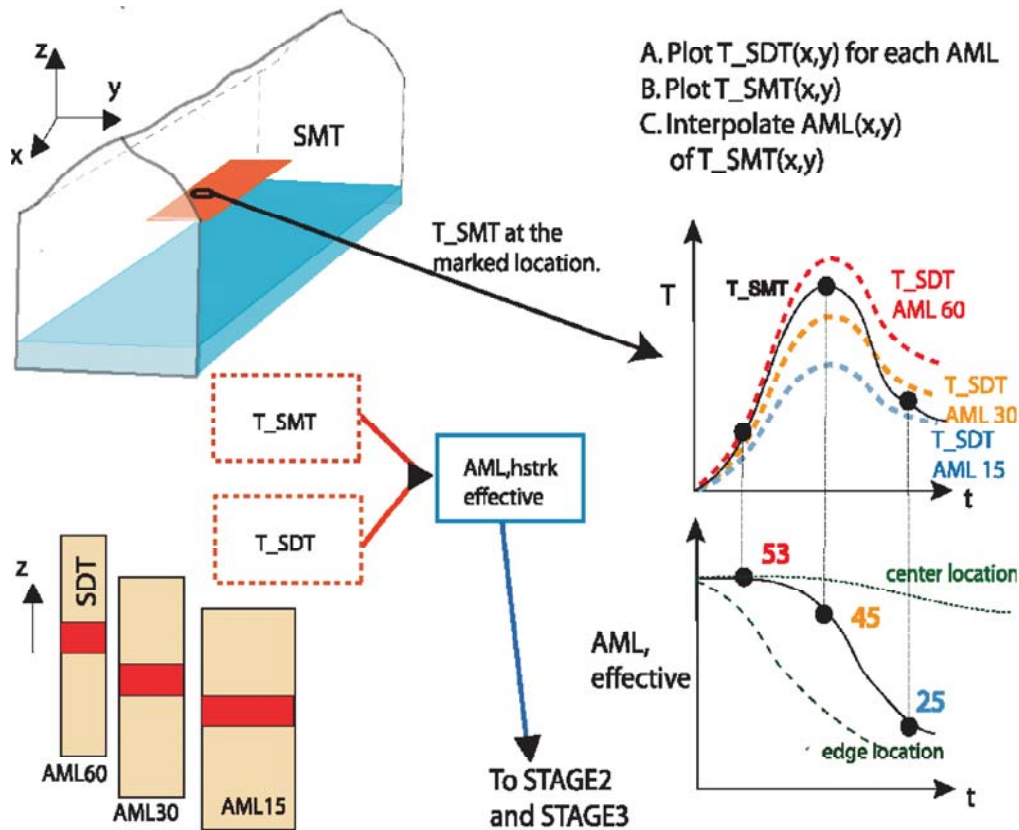
NOTE: Stage 1 involves the interpolation of the variable AML,effective from the SMT submodel temperature T_SMT and the family of SDT submodel temperatures T_SDT at three different AMLs.

Figure IX-3.   MSTHM Stage 1
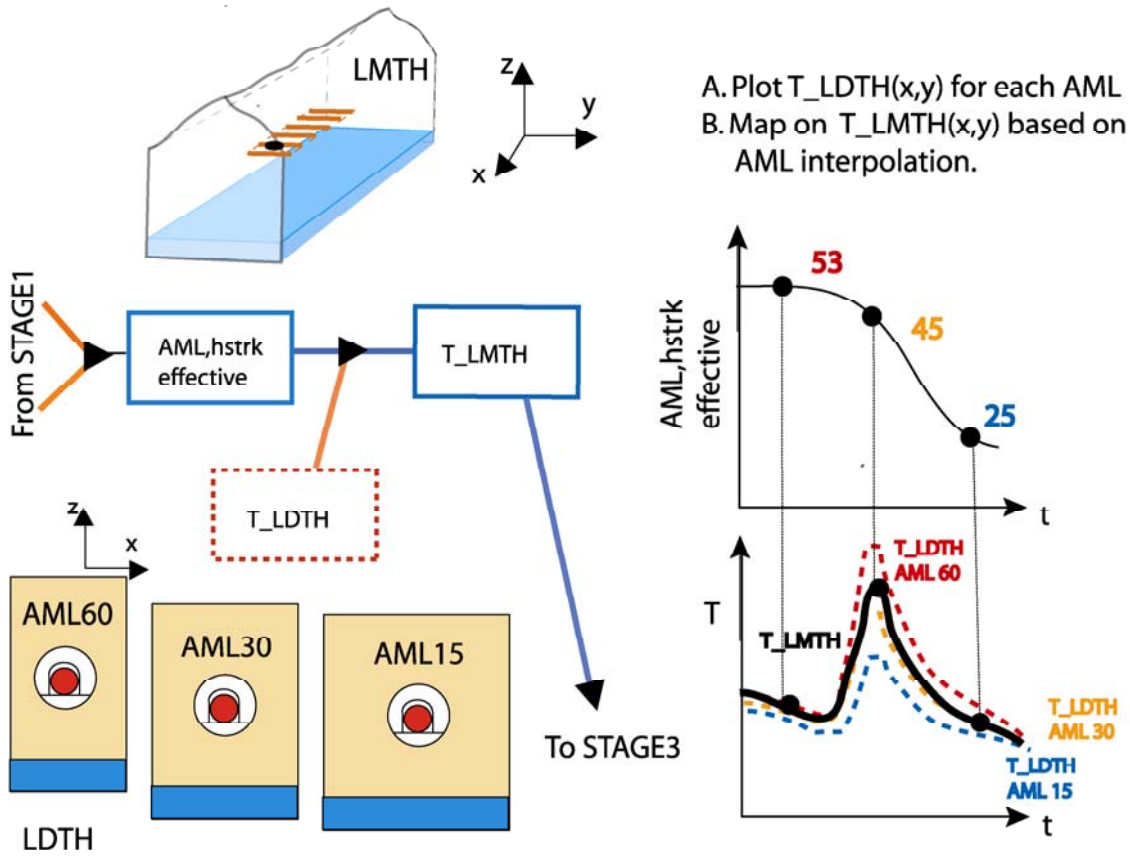
NOTE: Stage 2 involves the interpolation of the LMTH-model temperature T_LMTH from the variable AML,hstrk,effective and the family of LDTH submodel temperatures T_LDTH.

Figure IX-4.   MSTHM Stage 2
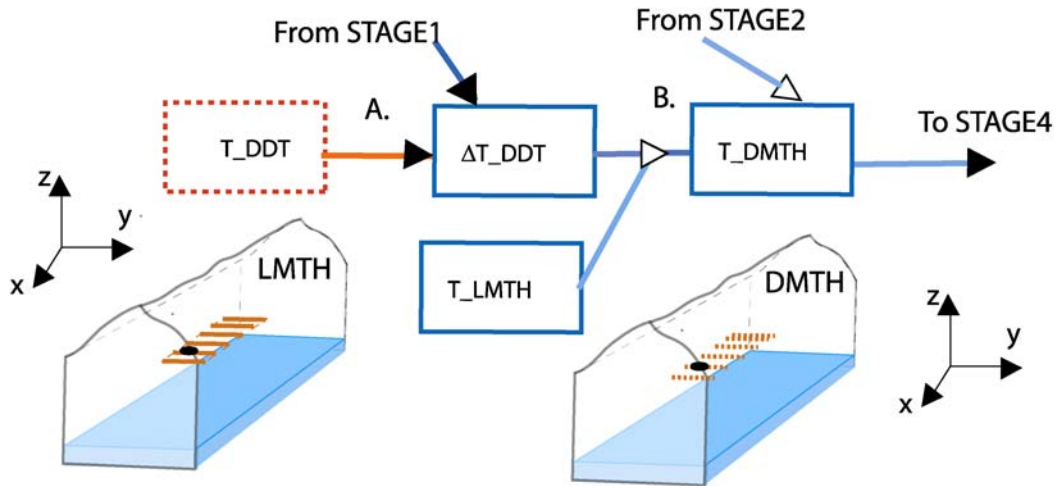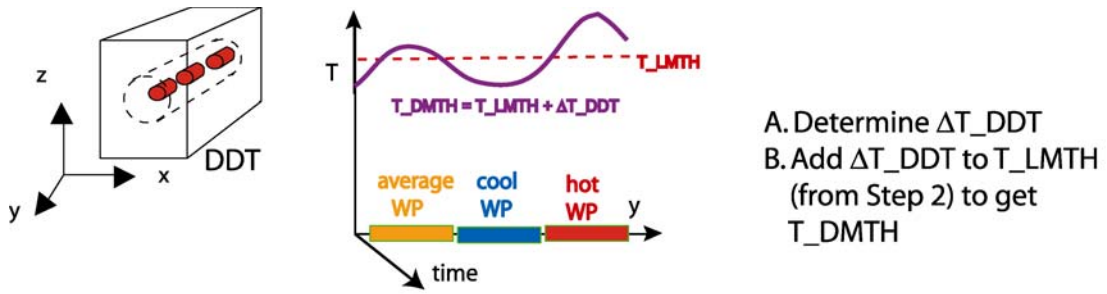
NOTE: Stage 3 involves the calculation of the DMTH-model temperature T_DMTH from the LMTH-model
         temperature T_LMTH and DDT submodel temperature T_DDT.

Figure IX-5.   MSTHM Stage 3
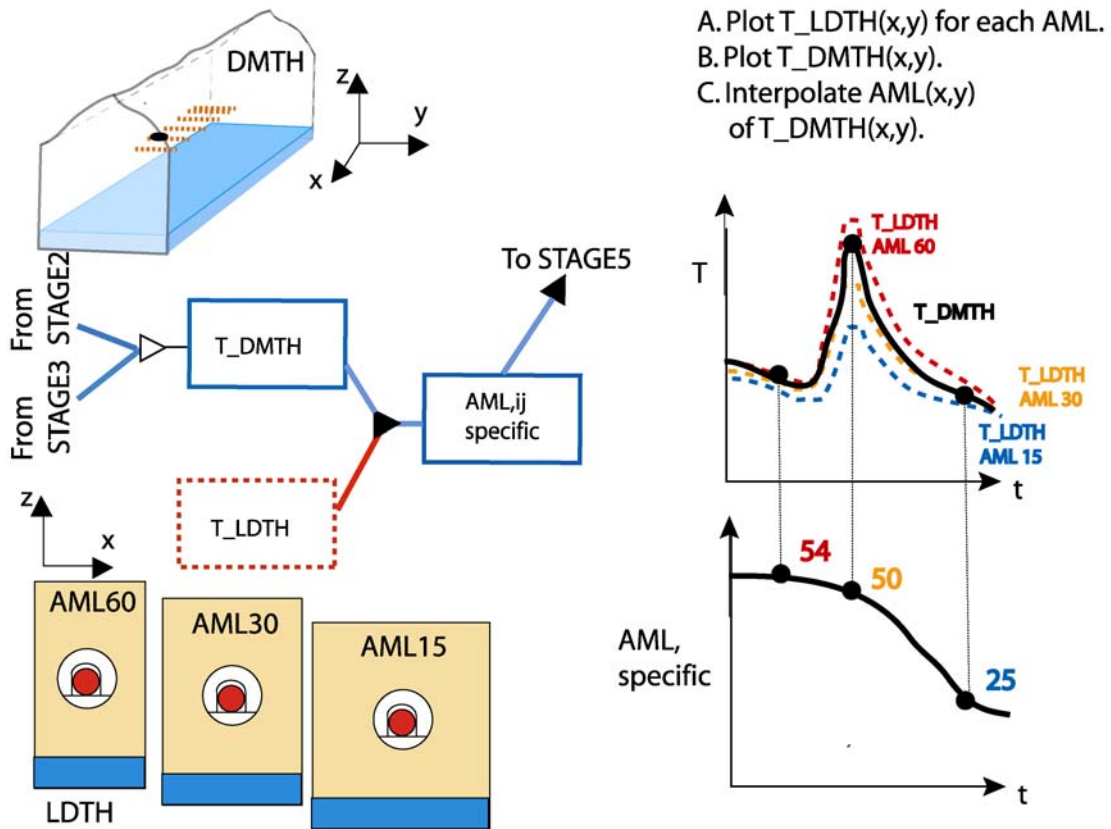
NOTE: Stage 4 involves the interpolation of the variable AMLspecific from the DMTH-model temperature T_DMTH and the family of LDTH submodel temperatures T_LDTH.

Figure IX-6. MSTHM Stage 4
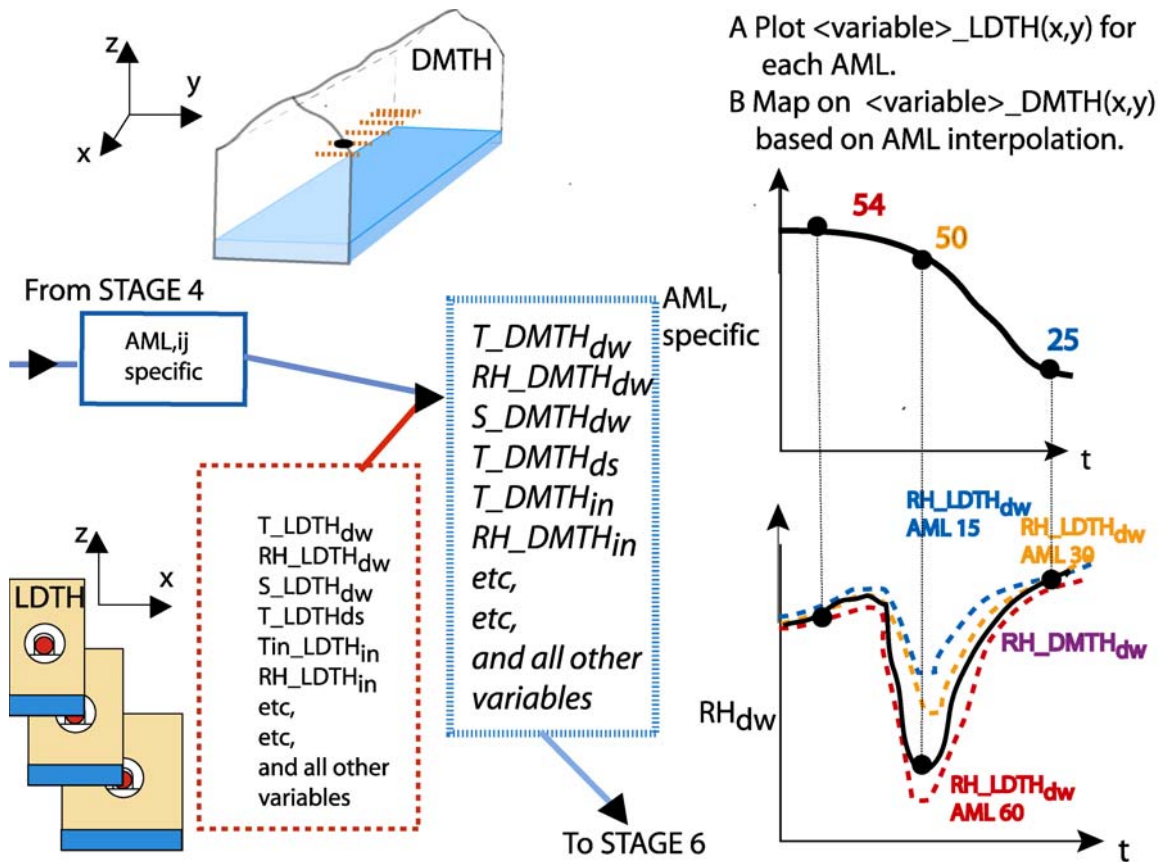
NOTE: Stage 5 involves the determination of each hydrologic variable (e.g., *RH*) using the variable AML,specific and the corresponding family of LDTH submodel hydrologic variable values.

Figure IX-7.   MSTHM Stage 5

INTENTIONALLY LEFT BLANK

APPENDIX X

HYDROLOGIC PROPERTIES FOR THE INTERGRANULAR POROSITY OF THE INVERT

The multiscale thermohydrologic model requires an evaluation of the retention and hydraulic properties of the crushed tuff that comprises the invert. In this appendix, retention and hydraulic properties are estimated for the coarse pore space of the crushed tuff invert.

This appendix initially develops a nondimensionalized curve fit to the two-parameter van Genuchten retention relation for several materials that cover a wide range of particle sizes. The nondimensional curve fit is then applied to crushed tuff to develop moisture potential retention relations for various size particles ranging from 0.3 mm to 20 mm. The relationship of unsaturated hydraulic conductivity to moisture potential is then developed on the basis of the van Genuchten curve-fit parameters. A summary of the hydrologic properties for the intergranular porosity of the invert is then presented.

Sections X.1 and X.2 develop water retention relationships for four unconsolidated materials, each representing a particular particle size. First, Section X.1 converts the retention data for a hydrocarbon fluid into water retention data, using an estimate from Brooks and Corey (1964 [DIRS 156915]). Section X.1 also provides constants from Incropera and DeWitt (1996 [DIRS 108184]) that are needed to make relations nondimensional.

Next, for each of the four unconsolidated materials, Section X.2 demonstrates the development of a best-fit formula for the water retention relation, using the functional form of van Genuchten (1980 [DIRS 100610]). These are only examples; for further analysis, the appendix needs a form that incorporates information about particle size. To this end, and following a procedure suggested by Leverett (1941 [DIRS 100588], p. 159), Section X.2.5 develops a best fit to a formula that contains a nondimensional form of the intrinsic permeability (van Genuchten alpha), using the capillary rise as a surrogate for the particle size.

Sections X.3 and X.4 develop estimates of intrinsic permeability for possible crushed tuffs of differing particle size. Section X.3 begins by estimating an intergranular porosity applicable to all four crushed tuffs, taking the central value from a handbook range. Section X.4 determines the intrinsic permeability (as $(cm)^{-1}$ or $(bars)^{-1}$) for each of the crushed tuffs, using the Kozeny-Carman equation (Bear 1972 [DIRS 156269], p. 166).

Unsaturated hydraulic conductivity is calculated within the qualified NUFT software, based on a relationship given by Fetter (1993 [DIRS 102009], p. 182). Section X.5 provides example results for each of the crushed tuffs.

X.1 NON-DIMENSIONALIZED VAN GENUCHTEN RETENTION RELATION

Measured data on retention of a hydrocarbon fluid by four different particulate materials are reported by Brooks and Corey (1964 [DIRS 156915]), as presented in *Advection versus Diffusion in the Invert* (BSC 2003 [DIRS 170881]). Figure X-1 presents the capillary rise of these unconsolidated samples. The Brooks and Corey moisture potential measurements include a range of particle sizes. A description of these data sets follows:

- **Volcanic Sand**—This material originates from a wind-blown deposit along Crab Creek in Washington State. It consists of dark-colored aggregates that can be broken down into finer particles by applying pressure. It is not known to what degree these

aggregates are themselves permeable, but they undoubtedly have some permeability. This sand has a degree of structure and has both primary and secondary porosity.

- **Fine Sand**—This sand was supplied by the Hanford Laboratories of General Electric Company at Richland, Washington, and apparently contains some volcanic minerals. This material contains a wide range of particle sizes, ranging down to silt size. Most of the particles are angular and not as rounded as most river bed sands.

- **Glass Beads**—This material is an example of media having a very narrow range of pore sizes. It is not much different in this respect, however, from many clean river sands.

- **Touchet Silt Loam**—This soil comes from the Columbia River basin and is also supplied by the Hanford Laboratory. It is extremely fine textured in that it contains practically no coarse sand, but it is somewhat unusual in that it contains a smaller amount of clay than would be expected in such a fine-textured soil. It is, in fact, nearly pure silt mixed with some extremely fine sand. It contains enough clay, however, to create a structure with secondary porosity.
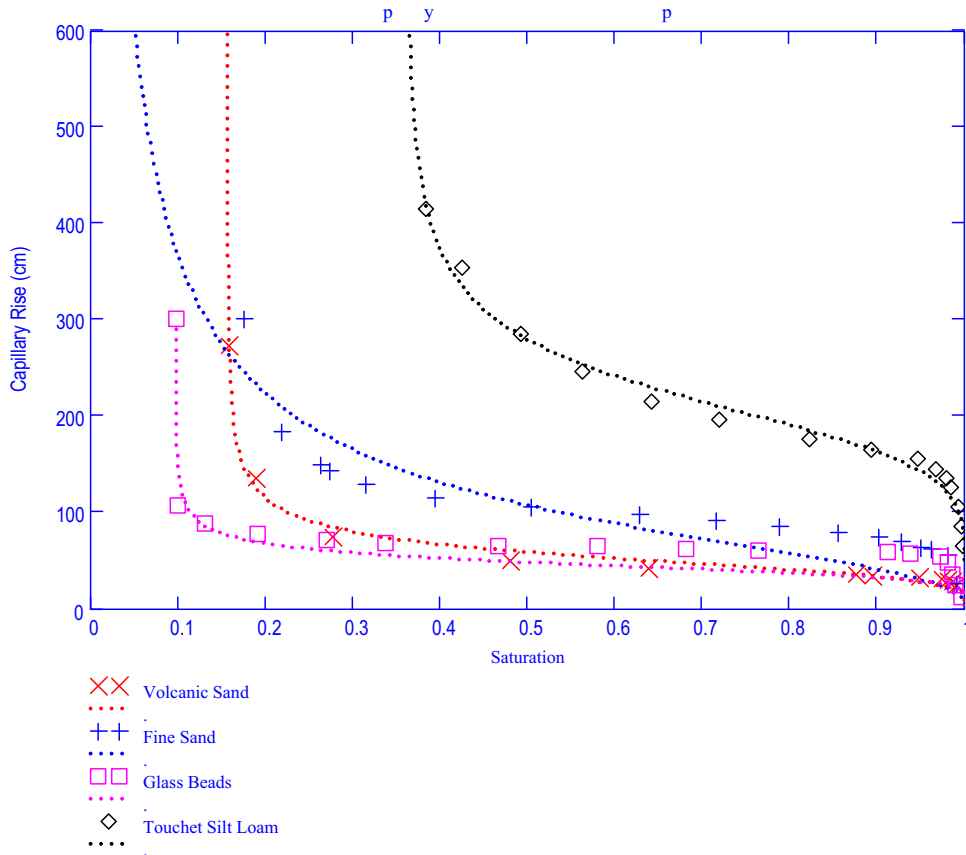
Source: Brooks and Corey 1964 [DIRS 156915].

Figure X-1. Capillary Rise of Unconsolidated Samples

The dependence of the capillary pressure curve on particle diameter and porosity is analyzed in the same manner as Leverett (1941 [DIRS 100588], p.159). Leverett showed that capillary

pressure data for various sands could be correlated using a non-dimensional group that included the mean particle diameter and the porosity. This approach is applied to the data provided by Brooks and Corey (1964 [DIRS 156915]) to produce a non-dimensional capillary pressure/saturation curve. This non-dimensional data is then fitted with the functional form posed by van Genuchten (1980 [DIRS 100610], Equation 21).

The relative permeability is based upon the work of Mualem, as reported by van Genuchten (1980 [DIRS 100610]). Mualem developed a semi-empirical relationship between the capillary pressure curve and the relative permeability curve. Mualem's correlation coefficient is combined with the fit of the non-dimensional capillary pressure to produce a liquid relative permeability curve appropriate for the invert interparticle porosity. The relative permeability of the gas phase is set to unity in anticipation of the very low interparticle saturation anticipated in the invert.

The Brooks and Corey data (1964 [DIRS 156915]) for unconsolidated particulate media are appropriate for the proposed invert configuration. Like the invert, all materials are composed of unconsolidated particles. Angularity of the particulate will be reflected in the data for sands. This, of course, presumes that the invert "rock" is "roughly" spherical, as opposed to a plate-like shape.

Input the properties for the four materials from Brooks and Corey (1964 [DIRS 156915]):

VS :=

	0	1
0	12.000	0.990
1	13.500	0.986
2	14.500	0.980
3	15.500	0.974
4	16.000	0.948
5	17.000	0.895
6	17.200	0.875

FS :=

	0	1
0	12.800	0.990
1	27.800	0.980
2	30.800	0.962
3	31.800	0.950
4	34.800	0.926
5	36.800	0.901
6	39.800	0.855

GB :=

	0	1
0	5.900	0.995
1	11.800	0.989
2	17.800	0.985
3	23.800	0.980
4	26.900	0.971
5	28.800	0.938

TSL :=

	0	1
0	32.800	0.998
1	42.800	0.995
2	52.800	0.992
3	62.800	0.984
4	67.800	0.978
5	72.500	0.967

Note that only the first few values are printed out in the MathCad format. For a complete listing of the properties, the data are presented by Brooks and Corey (1964 [DIRS 156915]).

Input the intrinsic permeability and porosity (Brooks and Corey 1964 [DIRS 156915]).

$$
\begin{pmatrix} k_{VS} \\ k_{FS} \\ k_{FM} \\ k_{GB} \\ k_{TSL} \\ k_{FFH} \end{pmatrix} := \begin{pmatrix} 18 \\ 2.5 \\ 11.3 \\ 6.3 \\ 0.6 \\ 30 \end{pmatrix} \cdot \left(10^{-6} \cdot m\right)^2 \qquad \text{(Eq. X.1)}
$$

The data have to be adjusted to account for the difference between water and the hydrocarbon fluid. According to Brooks and Corey (1964 [DIRS 156915], Equation 17, p. 9), the capillary rise of water was about twice that of the hydrocarbon used in the measurements. Van Genuchten (1980 [DIRS 100610]) used the same factor in his analysis.

$$
\begin{pmatrix} VS^{\langle 1 \rangle} \\ FS^{\langle 1 \rangle} \\ FM^{\langle 1 \rangle} \\ GB^{\langle 1 \rangle} \\ TSL^{\langle 1 \rangle} \\ FFH^{\langle 1 \rangle} \end{pmatrix} := \begin{pmatrix} VS^{\langle 1 \rangle} \cdot 2 \\ FS^{\langle 1 \rangle} \cdot 2 \\ FM^{\langle 1 \rangle} \cdot 2 \\ GB^{\langle 1 \rangle} \cdot 2 \\ TSL^{\langle 1 \rangle} \cdot 2 \\ FFH^{\langle 1 \rangle} \cdot 2 \end{pmatrix} \qquad \text{(Eq. X.2)}
$$

Because Brooks and Corey (1964 [DIRS 156915]) do not specify surface tension or temperature, they assume an ambient temperature to represent laboratory conditions. The surface tension of water equals 72 dynes/cm at 25°C. The water surface tension and density are (Incropera and DeWitt 1996 [DIRS 108184], p. 846):

$$
\sigma_w := 72 \cdot \frac{dyne}{cm}
$$

$$
\rho := 998 \cdot \frac{kg}{m^3}
$$

In accordance with the Brooks-Corey estimate of capillary rise,

$$
\sigma_{HC} := \frac{\sigma_w}{2}
$$

X.2 DATA FITTING

In the following analysis, curve fits are developed for the four materials separately for comparison to the measured retention data. A function representing the van Genuchten function is defined. Error functions are defined that for a set of van Genuchten parameters (α, n, S_r) provide a summation of the residuals squared between the predicted value for capillary pressure, and the measured capillary pressure. After defining the error function, the MathCad Minerr function is used to calculate the set of van Genuchten parameters (α, n, S_r) that minimizes the sum of the residuals squared. Define a vector of points for plotting purposes in MathCad. Note that the following function in MathCad defines a set of saturations that are then used to calculate corresponding capillary pressure or moisture potential that can then be used to generate a plot of moisture retention.

$$f_{plot} := \begin{vmatrix} \text{for} & i \in 1..9999 \\ & s_i \leftarrow \dfrac{i}{10000} \\ s \end{vmatrix}$$

(Eq. X.3)

The van Genuchten's fitting function (van Genuchten 1980 [DIRS 100610], Equation 21) is:

$$\theta = \theta_r + \frac{\left(\theta_s - \theta_r\right)}{\left[1 + (\psi \cdot \alpha)^n\right]^m}$$

(Eq. X.4)

Van Genuchten includes the residual saturation in the fit. The van Genuchten m parameter is defined in terms of n (van Genuchten 1980 [DIRS 100610], Equation 22):

$$m = 1 - \frac{1}{n}$$

(Eq. X.5)

Rewriting this Equation X.5 to solve for the exponent:

$$\frac{1}{m} = \frac{n}{n-1}$$

(Eq. X.6)

$$\frac{-1}{m} = \frac{n}{1-n}$$

(Eq. X.7)

Substituting in the value of m into Equation X.4:

$$\theta = \theta_r + \frac{\left(\theta_s - \theta_r\right)}{\left[1 + (\psi \cdot \alpha)^n\right]^{1 - \frac{1}{n}}}$$

(Eq. X.8)

Define the values for saturation:

$$S_s = \frac{\theta_s}{\theta_s}$$

$$S_s = 1$$

By definition, the value of Ss at saturation is one.

$$\theta = S \cdot \theta_s$$

$$\theta_r = S_r \cdot \theta_s$$

Substitute these definitions into Equation X.8:

$$S \cdot \theta_s = S_r \cdot \theta_s + \frac{\left[-\theta_s \cdot \left(-1 + S_r \right) \right]}{\left[\left[1 + (\psi \cdot \alpha)^n \right]^{\left(1 - \frac{1}{n} \right)} \right]}$$ (Eq. X.9)

Factor out θ_s from both sides of the equation:

$$S = S_r + \frac{\left[-1 \cdot \left(-1 + S_r \right) \right]}{\left[\left[1 + (\psi \cdot \alpha)^n \right]^{\left(1 - \frac{1}{n} \right)} \right]}$$ (Eq. X.10)

Restating the equation:

$$\frac{S - S_r}{1 - S_r} = \frac{1}{\left[\left[1 + (\psi \cdot \alpha)^n \right]^{\left(1 - \frac{1}{n} \right)} \right]}$$ (Eq. X.11)

Solve for the value of moisture potential as a function of saturation (S):

$$\left[\left[1 + (\psi \cdot \alpha)^n \right]^{\left(1 - \frac{1}{n} \right)} \right] = \frac{\left(1 - S_r \right)}{S - S_r}$$ (Eq. X.12)

$$\left[\left[1 + (\psi \cdot \alpha)^n \right]^{\frac{n-1}{n}} \right] = \frac{\left(1 - S_r \right)}{S - S_r}$$ (Eq. X.13)

$$\left[1 + (\psi \cdot \alpha)^n \right] = \left[\frac{(S - S_r)}{1 - S_r} \right]^{\frac{n}{n-1}} \qquad \text{(Eq. X.14)}$$

$$(\psi \cdot \alpha)^n = \left[\frac{(S - S_r)}{1 - S_r} \right]^{\frac{n}{n-1}} - 1$$

Solving for the moisture potential in terms of the saturation, and defining a function for the moisture potential:

$$G(S, S_r, \alpha, n) := \frac{1}{\alpha} \cdot \left[\left(\frac{S - S_r}{1 - S_r} \right)^{\frac{n}{1-n}} - 1 \right]^{\frac{1}{n}} \qquad \text{(Eq. X.15)}$$

X.2.1   Volcanic Sand

Define a function, in terms of the van Genuchten, parameters that represents the sum of the residuals squared between the measured capillary pressure and the predicted capillary pressure for the volcanic sand:

$$\text{error}(Sr, \alpha, n) := \sum_{i=1}^{\text{rows}(VS)} \left[\left(G(VS_{i,2}, Sr, \alpha, n) - VS_{i,1} \right)^2 \right] \qquad \text{(Eq. X.16)}$$

Define an initial estimate of the parameters:

$$\begin{pmatrix} Sr \\ \alpha \\ n \end{pmatrix} := \begin{pmatrix} 0.1 \\ 0.02 \\ 6 \end{pmatrix} \qquad \text{(Eq. X.17)}$$

Use the Minerr function to obtain the lease squares fit to the volcanic sand data:

Given

$$\text{error}(Sr, \alpha, n) = 0 \qquad \text{(Eq. X.18)}$$

$$\begin{pmatrix} Sr_{VS} \\ \alpha_{VS} \\ n_{VS} \end{pmatrix} := Minerr(Sr, \alpha, n)$$ (Eq. X.19)

$$\begin{pmatrix} Sr_{VS} \\ \alpha_{VS} \\ n_{VS} \end{pmatrix} = \begin{pmatrix} 0.156 \\ 0.021 \\ 4.413 \end{pmatrix}$$ (Eq. X.20)

Output the sum of the residuals squared:

$$error\left(Sr_{VS}, \alpha_{VS}, n_{VS}\right) = 536.779$$ (Eq. X.21)

Define a function for plotting purposes:

$$Splot_{VS} := Sr_{VS} + \left(1 - Sr_{VS}\right) \cdot f_{plot}$$ (Eq. X.22)

X.2.2   Fine Sand

Define a function, in terms of the van Genuchten parameters, that represents the sum of the residuals squared between the measured capillary pressure and the predicted capillary pressure for the fine sand:

$$error(Sr, \alpha, n) := \sum_{i=1}^{rows(FS)} \left[\left(G\left(FS_{i,2}, Sr, \alpha, n\right) - FS_{i,1}\right)^2\right]$$ (Eq. X.23)

Define an initial estimate of the parameters:

$$\begin{pmatrix} Sr \\ \alpha \\ n \end{pmatrix} := \begin{pmatrix} 0.01 \\ 0.1 \\ 2 \end{pmatrix}$$

Use the Minerr function to obtain the lease squares fit to the fine sand data:

$$Given$$

$$error(Sr, \alpha, n) = 0$$ (Eq. X.24)

$$\begin{pmatrix} Sr_{FS} \\ \alpha_{FS} \\ n_{FS} \end{pmatrix} := Minerr(Sr, \alpha, n)$$

(Eq. X.25)

$$\begin{pmatrix} Sr_{FS} \\ \alpha_{FS} \\ n_{FS} \end{pmatrix} = \begin{pmatrix} 0.170 \\ 0.010 \\ 5.664 \end{pmatrix}$$

(Eq. X.26)

Output the sum of the residuals squared:

$$error(Sr_{FS}, \alpha_{FS}, n_{FS}) = 675.283$$

(Eq. X.27)

Define a function for plotting purposes:

$$Splot_{FS} := Sr_{FS} + (1 - Sr_{FS}) \cdot f_{plot}$$

(Eq. X.28)

X.2.3 Glass Beads

Define a function, in terms of the van Genuchten parameters, that represents the sum of the residuals squared between the measured capillary pressure and the predicted capillary pressure for the glass beads:

$$error(Sr, \alpha, n) := \sum_{i=1}^{rows(GB)} \left[\left(G(GB_{i,2}, Sr, \alpha, n) - GB_{i,1} \right)^2 \right]$$

(Eq. X.29)

Define an initial estimate of the parameters:

$$\begin{pmatrix} Sr \\ \alpha \\ n \end{pmatrix} := \begin{pmatrix} 0.01 \\ 0.03 \\ 7 \end{pmatrix}$$

(Eq. X.30)

Use the Minerr function to obtain the lease squares fit to the glass beads data:

$$Given$$

$$error(Sr, \alpha, n) = 0$$

$$\begin{pmatrix} Sr_{GB} \\ \alpha_{GB} \\ n_{GB} \end{pmatrix} := Minerr(Sr, \alpha, n) \qquad \text{(Eq. X.31)}$$

$$\begin{pmatrix} Sr_{GB} \\ \alpha_{GB} \\ n_{GB} \end{pmatrix} = \begin{pmatrix} 0.096991 \\ 0.016780 \\ 8.122966 \end{pmatrix} \qquad \text{(Eq. X.32)}$$

Output the sum of the residuals squared:

$$error(Sr_{GB}, \alpha_{GB}, n_{GB}) = 2.472 \times 10^3 \qquad \text{(Eq. X.33)}$$

Define a function for plotting purposes:

$$Splot_{GB} := Sr_{GB} + (1 - Sr_{GB}) \cdot f_{plot} \qquad \text{(Eq. X.34)}$$

X.2.4   Touchet Silt Loam

Define a function, in terms of the van Genuchten parameters, that represents the sum of the residuals squared between the measured capillary pressure and the predicted capillary pressure for the Touchet Silt Loam:

$$error(Sr, \alpha, n) := \sum_{i=1}^{rows(TSL)} \left[\left(G(TSL_{i,2}, Sr, \alpha, n) - TSL_{i,1} \right)^2 \right] \qquad \text{(Eq. X.35)}$$

Define an initial estimate of the parameters:

$$\begin{pmatrix} Sr \\ \alpha \\ n \end{pmatrix} := \begin{pmatrix} 0.001 \\ 0.01 \\ 3 \end{pmatrix} \qquad \text{(Eq. X.36)}$$

Use the Minerr function to obtain the lease squares fit to the Touchet Silt Loam data:

$$Given$$

$$error(Sr, \alpha, n) = 0$$

$$\text{(Eq. X.37)}$$

$$\begin{pmatrix} Sr_{TSL} \\ \alpha_{TSL} \\ n_{TSL} \end{pmatrix} := Minerr(Sr, \alpha, n) \qquad \text{(Eq. X.38)}$$

$$\begin{pmatrix} Sr_{TSL} \\ \alpha_{TSL} \\ n_{TSL} \end{pmatrix} = \begin{pmatrix} 0.360 \\ 4.775 \times 10^{-3} \\ 5.808 \end{pmatrix} \qquad \text{(Eq. X.39)}$$

Output the sum of the residuals squared:

$$error(Sr_{TSL}, \alpha_{TSL}, n_{TSL}) = 1.872 \times 10^3 \qquad \text{(Eq. X.40)}$$

Define a function for plotting purposes:

$$Splot_{TSL} := Sr_{TSL} + (1 - Sr_{TSL}) \cdot f_{plot} \qquad \text{(Eq. X.41)}$$

The data sets have now been fitted individually. The residual saturation (Sr) for each set is inferred from the data. The results of the analysis are presented in Figure X-1.

X.2.5   Nondimensional Capillary Pressure Correlation Using Leverett's Non-Dimensional Group

The next analysis applies Leverett's nondimensional group (Leverett 1941 [DIRS 100588], p. 159) to the four data sets. It collapses the data reasonably well, with the volcanic sand providing the major deviation from the group. It compares favorably with Leverett's drainage curve for clean unconsolidated sands (Leverett 1941[DIRS 100588], Figure 4).

Composite Set

Define the function using the := notation for assigning a function.

$$G2(S_{eff}, \alpha, n) := \frac{1}{\alpha} \cdot \left(S_{eff}^{\frac{n}{1-n}} - 1 \right)^{\frac{1}{n}} \qquad \text{(Eq. X.42)}$$

Define the nondimensional parameter for analysis (Leverett 1941 [DIRS 100588], p. 159).

$$G2 = \frac{P_C}{\sigma_w} \cdot \sqrt{\frac{k}{\phi}} \qquad \text{(Eq. X.43)}$$

Define a function in terms of the dimensionless capillary pressure and the nondimensional van Genuchten parameters that represents the sum of the residuals squared between the measured dimensionless capillary pressure and the predicted dimensionless capillary pressure for all data sets:

$$\text{error}(\alpha, n) := \sum_{i=1}^{\text{rows(VS)}} \left[\left[G2\left(\frac{VS_{i,2} - Sr_{VS}}{1 - Sr_{VS}}, \alpha, n \right) - \left(\frac{VS_{i,1} \cdot cm \cdot \rho \cdot g}{\sigma_w} \cdot \sqrt{\frac{k_{VS}}{\phi_{VS}}} \right) \right]^2 \right] \ldots$$ (Eq. X.44)

$$+ \sum_{i=1}^{\text{rows(FS)}} \left[\left[G2\left(\frac{FS_{i,2} - Sr_{FS}}{1 - Sr_{FS}}, \alpha, n \right) - \left(\frac{FS_{i,1} \cdot cm \cdot \rho \cdot g}{\sigma_w} \cdot \sqrt{\frac{k_{FS}}{\phi_{FS}}} \right) \right]^2 \right] \ldots$$

$$+ \sum_{i=1}^{\text{rows(GB)}} \left[\left[G2\left(\frac{GB_{i,2} - Sr_{GB}}{1 - Sr_{GB}}, \alpha, n \right) - \left(\frac{GB_{i,1} \cdot cm \cdot \rho \cdot g}{\sigma_w} \cdot \sqrt{\frac{k_{GB}}{\phi_{GB}}} \right) \right]^2 \right] \ldots$$

$$+ \sum_{i=1}^{\text{rows(TSL)}} \left[\left[G2\left(\frac{TSL_{i,2} - Sr_{TSL}}{1 - Sr_{TSL}}, \alpha, n \right) - \left(\frac{TSL_{i,1} \cdot cm \cdot \rho \cdot g}{\sigma_w} \cdot \sqrt{\frac{k_{TSL}}{\phi_{TSL}}} \right) \right]^2 \right]$$

$$i := 1 .. \text{rows}(VS)$$

Define an initial estimate of the parameters:

$$\begin{pmatrix} \alpha \\ n \end{pmatrix} := \begin{pmatrix} 4 \\ 2.3 \end{pmatrix}$$ (Eq. X.45)

Use the Minerr function to obtain the lease squares fit to the volcanic sand data:

$$\text{Given}$$

$$\text{error}(\alpha, n) = 0$$ (Eq. X.46)

$$\begin{pmatrix} \alpha_{comp} \\ n_{comp} \end{pmatrix} := \text{Minerr}(\alpha, n)$$ (Eq. X.47)

$$\begin{pmatrix} \alpha_{comp} \\ n_{comp} \end{pmatrix} = \begin{pmatrix} 2.455 \\ 8.013 \end{pmatrix}$$ (Eq. X.48)

Output the sum of the residuals squared:

$$j := 1 .. \text{rows}(FS)$$

$$k := 1 .. \text{rows}(GB)$$

$$\text{error}\left(\alpha_{comp}, n_{comp}\right) = 4.054 \tag{Eq. X.49}$$

Define a function for plotting purposes:

$$Splot_{comp} := f_{plot}$$

$$l := 1 .. \text{rows}(TSL) \tag{Eq. X.50}$$

The results of the analysis for normalized capillary rise for various materials are presented in Figure X-2.

Advection versus Diffusion in the Invert (BSC 2003 [DIRS 170881], Appendix VII) presents an independent verification using the Microsoft EXCEL equation solver. The analysis uses the same curve fitting procedure for volcanic sand, fine sand, glass beads, and Touchet Silt Loam individually, and then collectively by transforming the capillary rise data to a nondimensional capillary rise. Microsoft EXCEL is used to perform curve fitting to the van Genuchten retention relationship. The Solver is an add-in function in EXCEL. The Solver can minimize a target cell that involves multiple cell variables that might be subject to multiple constraints. The Solver is used specifically to solve for several variables under the constraint for a target value. In this case, the minimization of the least squares of the capillary rise is the target value for curve fitting.
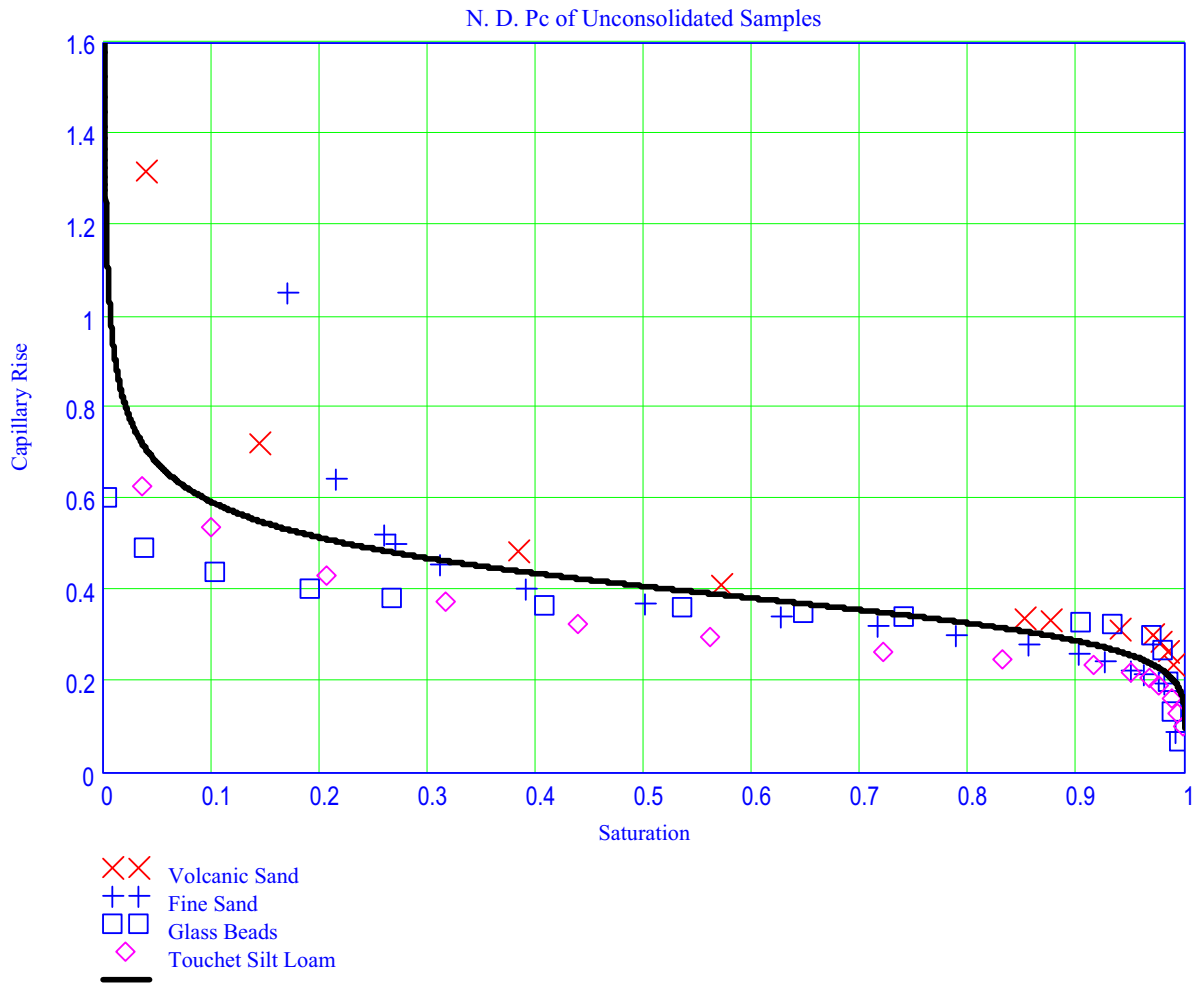
DTN: MO0307SPAVGHYD.000.

Figure X-2. Normalized Capillary Rise for Various Materials

X.3 ASSESSMENT OF INTERGRANULAR POROSITY

Hilf evaluated uniformly graded or poorly sorted sands and measured intergranular porosity (ϕ_{matrix}) ranges from 0.40 to about 0.48 when considering the maximum void ratio or porosity (Hilf 1975 [DIRS 169699], p. 257). For purposes of analysis, considering that crushed tuff may settle over time, a median value of 0.45 is adopted for the intergranular porosity ($\phi_{intergrain}$).

Prior analyses reported in *Advection versus Diffusion in the Invert* (BSC 2003 [DIRS 170881], Section 6.3) have estimated the intragranular porosity ($\phi_{inatrix}$) of crushed tuff to be 0.112 (BSC 2003 [DIRS 170881], Table 4-3). However, the total porosity includes both the intergranular porosity ($\phi_{intergrain}$), related to the voids between the crushed tuff particles, as well as the intragranular porosity, related to the voids within the crushed tuff particles (ϕ_{matrix}). A total

porosity of 0.545 has been calculated in *Advection versus Diffusion in the Invert* (BSC 2003 [DIRS 170881], Appendix XI) for sieved samples of crushed tuff ranging from 2 to 4.75 mm.

Previous analysis in *Advection versus Diffusion in the Invert* (BSC 2003 [DIRS 170881], Section 6.3) estimated the intergranular porosity ($\phi_{intergrain}$) that pertains to this coarse void space is equal to 0.49.

Because the intergranular porosity value of 0.49 exceeds the range 0.40 to 0.48, it suggests that the USGS values for measured bulk porosity (DTN GS980808312242.015 [DIRS 119916]) are consistent with a poorly graded sand in a loose state.

X.4 MOISTURE POTENTIAL RETENTION RELATION FOR VARIOUS SIZE PARTICLES

This section presents the calculations and plots of the retention curves for the non-dimensionalized van Genuchten moisture potential retention relation for various size particles ranging from 0.317 mm to 20 mm. The summary of the calculations of the air entry parameters is presented in Table X-1. The van Genuchten (n) value is 8.013 as discussed below.

Equation X.51 defines a nondimensional moisture potential parameter (Ψ_{ND}) for analysis, as suggested by Leverett (1941[DIRS 100588], p.159).

$$\psi_{ND} = \psi \cdot \frac{\rho \cdot g}{\sigma_W} \cdot \sqrt{\frac{k}{\phi}} \qquad \text{(Eq. X.51)}$$

where

Ψ_{ND} = nondimensionalized moisture potential
Ψ = moisture potential
ρ = mass density of water (kg/m^3)
g = acceleration due to gravity
k = intrinsic permeability
σ_w = interfacial tension between the pore water and mineral surface (dyne/cm)
ϕ = porosity

The van Genuchten non-dimensional parameter (n) is calculated, where the van Genuchten dimensionless air entry parameter, $\alpha_{ND} = 2.455$, such that n = 8.01 as presented above. For specific sized grains, the Kozeny-Carman equation expresses the relationship of the intrinsic permeability (k) to the porosity (ϕ) (Bear 1972 [DIRS 156269], p. 166):

$$\text{Intrinsic permeability} = k = \frac{d_m^2}{180} \cdot \frac{\phi^3}{(1-\phi)^2} \qquad \text{(Eq. X.52)}$$

where

d_m = mean particle diameter
ϕ = porosity

This equation is rearranged to obtain:

$$\sqrt{\frac{k}{\phi}} = \frac{d_m}{\sqrt{180}} \cdot \frac{\phi}{(1-\phi)}$$

(Eq. X.53)

The Leverett Equation as presented in Equation X.51 expresses the relationship of the nondimensional moisture potential (Ψ_{ND}) to the dimensional moisture potential (Ψ). Since the air-entry parameter α is inversely proportional to the moisture potential (See Equation X.4), the relationship of the nondimensional air-entry parameter as determined from the regression analysis for Equation X.4 is given by:

$$\frac{1}{\alpha_{ND}} = \frac{1}{\alpha} \cdot \frac{\rho \cdot g}{\sigma_w} \cdot \sqrt{\frac{k}{\phi}}$$

(Eq. X.54)

Solving for the air-entry parameter α in terms of the nondimensional air-entry parameter:

$$\alpha = \alpha_{ND} \cdot \frac{\rho \cdot g}{\sigma_w} \cdot \sqrt{\frac{k}{\phi}}$$

(Eq. X.55)

Substituting in Equation X.53 into Equation X.55 to express the air-entry parameter α in terms of the particle diameter (d_m); the fluid density (ρ); the surface tension (σ_w); the porosity (ϕ), the gravitational constant (g); and the dimensionless air entry parameter (α_{ND}) as determined from the curve-fitting analysis:

$$\alpha = \alpha_{ND} \cdot \frac{\rho \cdot g}{\sigma_w} \cdot \frac{d_m}{\sqrt{180}} \cdot \frac{\phi}{(1-\phi)} = 2.455 \cdot \frac{\rho \cdot g}{\sigma_w} \cdot \frac{d_m}{\sqrt{180}} \cdot \frac{\phi}{(1-\phi)}$$

(Eq. X.56)

Substituting in the value of 0.317 mm as a particle size with an intergranular porosity ($\phi_{intergrain}$) of 0.45, the calculated value for the van Genuchten air-entry parameter (α) in cm^{-1} for this size material is given in Equation X.55:

$$\frac{\rho \cdot g}{\sigma_w} \sqrt{\frac{k}{\phi}} 2.455 = \frac{\rho \cdot g}{\sigma_w} \frac{0.0317 \cdot cm}{\sqrt{180}} \cdot \frac{0.45}{(1-0.45)} 2.455 = 0.0646 \cdot cm^{-1}$$

(Eq. X.57)

This analysis uses the following referenced properties for water: mass density, ρ= 1000 kg/m^3, σ_g, geometric standard deviation, an interfacial tension between the pore water and mineral

surface, σ_w = 72 dynes/cm at ambient temperature, and gravity, g = 9.81 m/sec^2 (Incropera and DeWitt 1996 [DIRS 108184], p. 846). Equation X.58 is used to calculate the value of the air-entry parameter (α) in terms of (bars)$^{-1}$ for a particle size of 0.3173 mm:

$$\alpha = \frac{0.06466 \cdot cm^{-1}}{1000 \cdot \dfrac{kg}{m^3} \cdot 9.81 \cdot \dfrac{m}{sec^2}} = 65.9(bars)^{-1} \tag{Eq. X.58}$$

Now consider the particle size of 3 mm. The van Genuchten air-entry parameter (α) for this grain size from Equations X.55, is given as:

$$\frac{\rho \cdot g}{\sigma_w} \sqrt{\frac{k}{\phi}} \cdot 2.455 = \frac{\rho \cdot g}{\sigma_w} \frac{0.3 \cdot cm}{\sqrt{180}} \cdot \frac{0.45}{(1-0.45)} \cdot 2.455 = 0.612 \cdot cm^{-1} \tag{Eq. X.59}$$

The value of the van Genuchten air-entry parameter (α) for the 3 mm diameter grain size in terms of bars^{-1} is calculated using Equation X.58 (bars)$^{-1}$:

$$\alpha = \frac{0.611 \cdot cm^{-1}}{1000 \cdot \dfrac{kg}{m^3} \cdot 9.81 \cdot \dfrac{m}{sec^2}} = 624. \cdot bars^{-1} \tag{Eq. X.60}$$

The van Genuchten air entry parameter calculations are presented in Table X-1. The individual retention curves with curve fits are presented in Tables X-2 through X-5 and are illustrated in Figures X-3 through X-6.

Table X-1. van Genuchten Air Entry Parameter (α) Calculations.

Parameter	Particle Diameter (d_m)			
	0.317 mm	3 mm	10 mm	20 mm
van Genuchten air-entry parameter(α) (cm)$^{-1}$	0.0646[a]	0.612[c]	2.05	4.09
van Genuchten air entry parameter(bars)$^{-1}$	65.9[b]	624[d]	2080	4160

[a] See the calculation presented in Equation X.57.
[b] See the calculation presented in Equation X.58.
[c] See the calculation presented in Equation X.59.
[d] See the calculation presented in Equation X.60.

Table X-2.   Moisture Retention Data for 0.317 mm Crushed Tuff

Van Genuchten Curve Parameters				
Moisture Content at Saturation (θs)	0.45			
Residual Moisture Content (θr)	0.05			
Alpha (α)	65.9	bars^-1	0.0646	cm^-1
n	8.01			
m	0.88			

Retention Analysis	
Moisture Potential ψ**(bars)**	**Predicted Moisture Content** **(θ)**
0.0001	0.450
0.0002	0.450
0.0005	0.450
0.001	0.450
0.002	0.450
0.005	0.450
0.01	0.438
0.02	0.103
0.05	0.050
0.1	0.050
0.2	0.050
0.5	0.050
1	0.050
2	0.050
5	0.050
10	0.050
20	0.050
50	0.050
100	0.050
200	0.050
500	0.050
1000	0.050

Predicted Moisture content obtained from Equation X.4

Table X-3. Moisture Retention Data for 3.0 mm Crushed Tuff

Van Genuchten Curve Parameters					
Moisture Content at Saturation (θs)	0.45				
Residual Moisture Content (θr)	0.05				
Alpha (α)	624	bars^-1	0.612	cm^-1	
n	8.01				
m	0.88				

Retention Analysis	
Moisture Potential ψ(bars)	Predicted Moisture Content (θ)
0.0001	0.450
0.0002	0.450
0.0005	0.450
0.001	0.442
0.002	0.124
0.005	0.050
0.01	0.050
0.02	0.050
0.05	0.050
0.1	0.050
0.2	0.050
0.5	0.050
1	0.050
2	0.050
5	0.050
10	0.050
20	0.050
50	0.050
100	0.050
200	0.050
500	0.050
1000	0.050

Predicted Moisture content obtained from Equation X.4

Table X-4. Moisture Retention Data for 10.0 mm Crushed Tuff

Van Genuchten Curve Parameters				
Moisture Content at Saturation (θs)	0.45			
Residual Moisture Content (θr)	0.05			
Alpha (α)	2080	bars^-1	2.05	cm^-1
n	8.01			
m	0.88			

Retention Analysis	
Moisture Potential ψ(bars)	Predicted Moisture Content (θ)
0.0001	0.450
0.0002	0.450
0.0005	0.238
0.001	0.052
0.002	0.050
0.005	0.050
0.01	0.050
0.02	0.050
0.05	0.050
0.1	0.050
0.2	0.050
0.5	0.050
1	0.050
2	0.050
5	0.050
10	0.050
20	0.050
50	0.050
100	0.050
200	0.050
500	0.050
1000	0.050

Predicted Moisture content obtained from Equation X.4

Table X-5. Moisture Retention Data for 20.0 mm Crushed Tuff

van Genuchten Curve Parameters				
Moisture Content at Saturation (θs)	0.45			
Residual Moisture Content (θr)	0.05			
Alpha (α)	4160	bars^-1	4.09	cm^-1
n	8.01			
m	0.88			

Retention Analysis	
Moisture Potential ψ(bars)	Predicted Moisture Content (θ)
0.00001	0.450
0.0002	0.384
0.0005	0.052
0.001	0.050
0.002	0.050
0.005	0.050
0.01	0.050
0.02	0.050
0.05	0.050
0.1	0.050
0.2	0.050
0.5	0.050
1	0.050
2	0.050
5	0.050
10	0.050
20	0.050
50	0.050
100	0.050
200	0.050
500	0.050
1000	0.050

Predicted Moisture content obtained from Equation X.4

Figure X-3. Nondimensionalized Relationship for Mean Particle Diameter of 0.317 mm
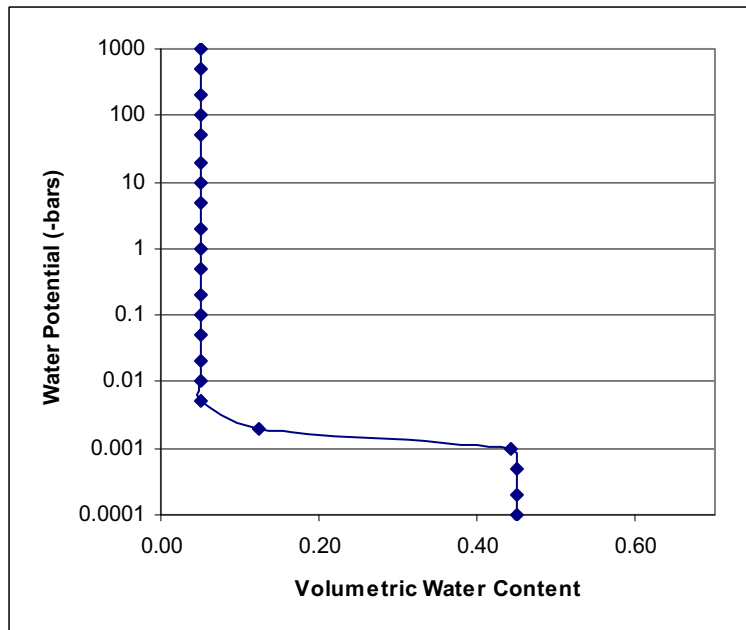
Figure X-4. Nondimensionalized Relationship for Mean Particle Diameter of 3.0 mm
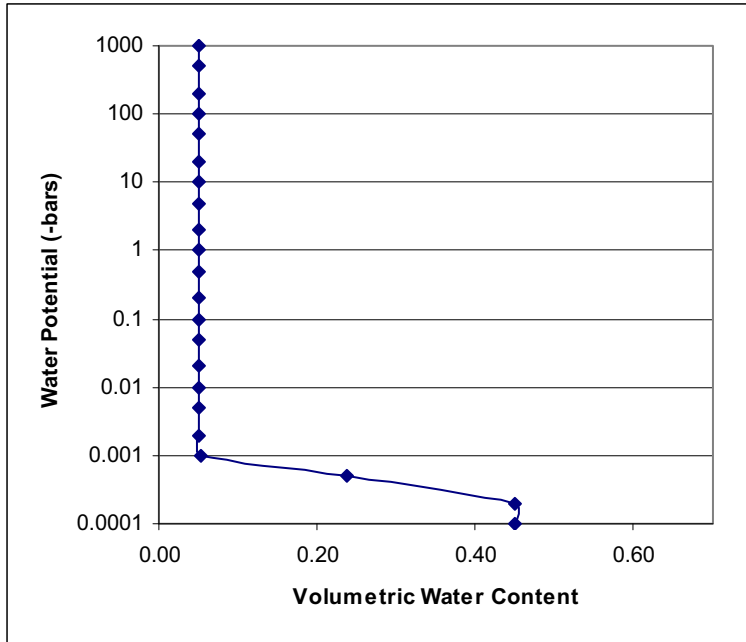
Figure X-5.   Nondimensionalized Relationship for Mean Particle Diameter of 10.0 mm
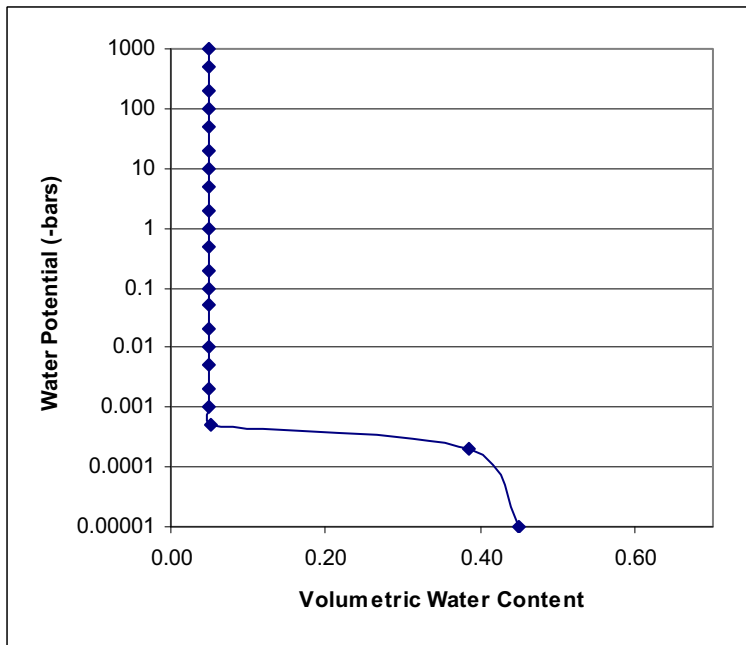
Figure X-6.   Nondimensionalized Relationship for Mean Particle Diameter of 20.0 mm

X.5 UNSATURATED HYDRAULIC CONDUCTIVITY AND CAPILLARY PRESSURE FOR THE CRUSHED TUFF INVERT

The following discussion presents the methodology and the analysis for determining the relationship between unsaturated hydraulic conductivity (K_{us}) and capillary pressure from the retention curve using the two-parameter nondimensional van Genuchten relationship and the size of the crushed tuff. The basis for the nondimensional retention relationship is a least squares curve fit for a series of retention measurements made on the materials presented above. The nondimensional van Genuchten air-entry parameter (α) is determined from a scaling relationship while the nondimensional (n) parameter is constant. The intrinsic permeability (k) is determined from the Kozeny-Carman formula shown by Equation X.62 (Bear 1972 [DIRS 156269], p. 166) that relates intrinsic permeability (k) to the grain size or pore diameter (d_m) and porosity (ϕ). On the basis of the selected grain size, the saturated hydraulic conductivity (K_s) and the van Genuchten relationship for relative permeability, the relationship of unsaturated hydraulic conductivity (K_{us}) relationship to moisture potential (ψ) is determined.

A qualitative assessment is made over the range of moisture potentials (ψ) of interest (0.01 to 0.1 bars) as to whether significant intergranular liquid-phase advection in the coarse fraction of the crushed tuff would occur for a range of particle diameters. The analysis presented below is performed for grain size diameters of 0.317 mm, 3 mm, 10 mm and 20 mm for the intergranular porosity ($\phi_{intergrain}$) respectively to cover a broad range of particle diameters.

The wetting-phase relative permeability as a function of moisture potential (ψ) for van Genuchten curve fit is restated from Fetter (1993 [DIRS 102009], p. 182). The unsaturated hydraulic conductivity (K_{us}) (wetting-phase relative permeability times saturated hydraulic conductivity) as a function of moisture potential (ψ) is derived using Equation X.61 (same as Equation 4.17 of Fetter 1993 [DIRS 102009], with n=1/(1-m)).

$$K_{us} = K\left(\alpha, n, \psi, K_s\right) = K_s \frac{\left[1 - \left(|\alpha\psi|\right)^{(n-1)}\left[1 + \left(|\alpha\psi|\right)^n\right]^{\left(-1+\frac{1}{n}\right)}\right]^2}{\left[\left[1 + \left(|\alpha\psi|\right)^n\right]^{\left[\frac{1}{2} - \frac{1}{(2n)}\right]}\right]} \qquad \text{(Eq. X.61)}$$

The intrinsic permeability (k) corresponding to a grain size of 3 mm is calculated from Equation X.52 as 1.51×10^{-8} m^2:

$$k = \frac{d_m^2}{180} \cdot \frac{\phi^3}{(1-\phi)^2} = 1.51 \cdot 10^{-8} \cdot m^2 \qquad \text{(Eq. X.62)}$$

Noting a conversion to saturated hydraulic conductivity from intrinsic permeability, the value for saturated conductivity is calculated for each of the particle sizes from 0.3 to 20 mm in diameter.

The unsaturated hydraulic conductivity relationships are determined from the van Genuchten properties presented in Table X-1, and the saturated hydraulic conductivity. The calculations over a range of moisture potentials are presented in Table X-6, and are plotted in Figure X-7.

Comparison of Conductivity Relationships
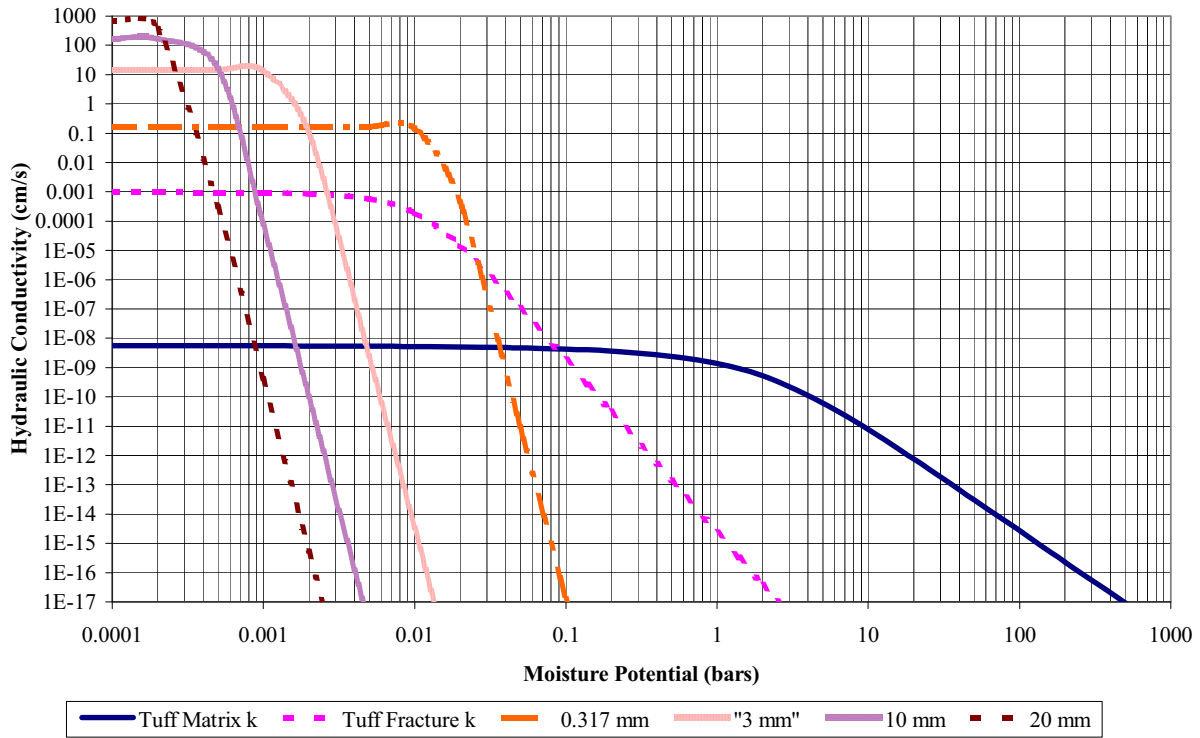
Figure X-7.   Unsaturated Hydraulic Conductivity Relationships

Table X-6. Unsaturated Hydraulic Conductivity (Kus) Calculations for the Non-Dimensionalized Moisture Potential (ψ) Retention Relation

Moisture Potential (ψ)(bars)	Unsaturated Hydraulic Conductivity (K$_{us}$) (cm/sec)				
	Particle Size (d$_m$)				
	Welded Tuff Matrix	0.317 mm	3 mm	10 mm	20 mm
0.0001	6.23E-09	1.84E-01	1.65E+01	1.83E+02	7.29E+02
0.0002	6.21E-09	1.84E-01	1.65E+01	1.82E+02	3.97E+02
0.001	6.15E-09	1.84E-01	1.52E+01	8.60E-05	4.56E-10
0.0015	6.13E-09	1.84E-01	4.54E+00	3.15E-08	1.66E-13
0.002	6.10E-09	1.84E-01	1.16E-01	1.14E-10	6.01E-16
0.005	5.99E-09	1.84E-01	2.81E-09	1.93E-18	1.01E-23
0.01	5.86E-09	1.63E-01	3.71E-15	2.54E-24	1.36E-29
0.02	5.66E-09	5.02E-04	4.89E-21	3.41E-30	2.02E-34
0.05	5.24E-09	1.08E-11	8.27E-29	1.22E-35	5.45E-36
0.1	4.74E-09	1.42E-17	1.57E-34	1.36E-36	5.92E-37
0.2	4.02E-09	1.86E-23	7.34E-37	1.48E-37	6.30E-38

DTN: MO0307SPAVGSUM.000

NOTE: The values for the saturated hydraulic conductivity (K$_s$) (cm/sec) as a function of the moisture potential (ψ) are obtained by calculating the intrinsic permeability (k) for a given set of van Genuchten parameters from Equation X.62 and then applying the conversion from intrinsic permeability (k) to saturated hydraulic conductivity (K$_s$) (Freeze and Cherry 1979 [DIRS 101173], p. 27):

$$K_s = \frac{\rho \cdot g}{\mu} \cdot k$$

The properties of water at ambient temperature are given by (Incropera and DeWitt 1996 [DIRS 108184], p. 846). The water density (ρ) equals 1000 kg/m^3 and the absolute viscosity (μ) equals $8.935 \cdot 10^{-4}$ N•s/(m^2). The values for the unsaturated hydraulic conductivity are then determined by scaling the saturated hydraulic conductivity relationship by the relative permeability relationship presented in Equation IV.11 for a given moisture potential.

X.6   SUMMARY OF HYDROLOGIC PROPERTIES BASED ON THE NON-DIMENSIONALIZED MOISTURE POTENTIAL RETENTION RELATIONS

The van Genuchten retention parameters as well as other hydrologic properties are summarized in Table X-7 over a range of particle sizes. These analyses show that the finer crushed tuff would have a greater tendency to retain water over the range of the moisture potentials in the repository.

Table X-7.   Summary of Hydrologic Properties Based on the Non-Dimensionalized Moisture Potential Retention Relation

Parameter	Particle Size (d_m)			
	0.317 mm	3 mm	10 mm	20 mm
Saturated Volumetric Moisture Content (θ_s)[a]	0.450	0.450	0.450	0.450
Residual Volumetric Moisture Content (θ_r)	0.050	0.050	0.050	0.050
van Genuchten Air-entry Parameter (bars^{-1}) (α)[b]	65.9	624.	2080.	4160.
van Genuchten Air-entry Parameter (cm^{-1}) (α)	0.0647	0.612	2.04	4.08
van Genuchten n Value (n)	8.013	8.013	8.013	8.013
van Genuchten m Value (m)[c]	0.875	0.875	0.875	0.875
Saturated Intrinsic Permeability(m^2) (k)[d]	1.68E-10	1.51E-08	1.67E-07	6.69E-07
Saturated Hydraulic Conductivity (cm/sec) (K_s)[e]	0.184	16.48	183.1	732.5

DTN:MO0307SPAVGSUM.000

[b] See text and Table X-1 for the calculation of the van Genuchten Air-Entry Parameter (α)

[a] The saturated volumetric moisture (θs) content equals the porosity (ϕ) .

[c] The value of n is given by 1/(1-m) (Fetter 1993 [DIRS 102009], p. 172).

[d] The intrinsic permeability (k) is calculated from Equation X.62.

[e] The value of the saturated hydraulic conductivity (Ks) is obtained by the equation that converts an unsaturated intrinsic permeability (k) to a saturated hydraulic conductivity (Ks) (Freeze and Cherry 1979 [DIRS 101173], p. 27):

$$K_s = \frac{\rho \cdot g}{\mu} \cdot k$$

The properties of water at ambient temperature are given by (Incropera and DeWitt 1996 [DIRS 108184], p. 846). The water density (ρ) equals 997 kg/m3 and the absolute viscosity (μ) equals 8.935 x10-4 N•s/(m2). Note that these values compare well with the values for sands and gravels from Freeze and Cherry (1979 [DIRS 101173], p. 29).

INTENTIONALLY LEFT BLANK

APPENDIX XI

THERMAL CONDUCTIVITY OF THE COLLAPSED DRIFT ZONE

This appendix presents two EXCEL workbooks used to corroborate the thermal conductivity of the collapsed drift as a function of the void fraction within this zone. Section XI.1 presents the calculation of the void fraction determination from the bulking factor as determined in *Drift Degradation Analysis* (BSC 2004 [DIRS 166107], Section 6.4.2 and Appendix V). Section XI.2 presents the thermal conductivity calculation based upon the Kunii and Smith relationship (Kunii and Smith 1960 [DIRS 153166]).

XI.1   ASSESSMENT OF THE VOID FRACTION WITHIN THE COLLAPSED DRIFT

The intergranular porosity of collapsed drift material is a function of the bulking factor and lithophysal porosity. The lithophysal porosity is assumed to be added to the void volume after collapse. Consider that one cubic meter of drift collapses with a lithophysal porosity of ϕ, and the bulking factor (a fraction) is B. Then the total void volume is $\phi + B$, and the total volume of the one cubic meter is $1 + B$ as presented in the derivation below.

Derive the expression for the void fraction. Using the fundamental definition of lithophysal porosity:

$$\phi_L = \frac{V_{voids}}{V_{solids} + V_{voids}}$$

(Eq. XI-1)

Where V_{voids} is equal to the volume of the voids, and V_{solids} is equal to the volume of the solids.

Note the following relationship:

$$V_{Total} = V_{solids} + V_{voids}$$

(Eq. XI-2)

Where V_{total} is equal to the total volume.

Now consider the new total volume is V'_{Total} after bulking has occurred. Let V_{solids} be equal to one, following the soil mechanics convention. Expressing the lithophysal porosity in terms of the volume of the voids:

$$\phi_L = \frac{V_{voids}}{1 + V_{voids}}$$

(Eq. XI-3)

Now expressing the change in total volume in terms of the bulking factor:

$$V'_{Total} = (1 + B)V_{Total}$$

(Eq. XI-4)

Derive an expression for the volume of the voids before and after bulking. The volume of the voids after bulking:

$$V'_{voids} = (1 + B) \cdot V_{Total} - V_{solids}$$

$$V'_{voids} = (1 + B) \cdot V_{Total} - 1$$

(Eq. XI-5)

Solving for the volume of the voids in terms of the lithophysal porosity:

$$V_{voids} = \frac{\phi_L}{1 - \phi_L}$$

(Eq. XI-6)

Expressing the total volume in terms of the lithophysal porosity, with the volume of solids set to one:

$$V_{Total} = 1 + \frac{\phi_L}{1 - \phi_L}$$

(Eq. XI-7)

The void fraction after bulking is defined as:

$$Void\_Fraction = \frac{V'_{voids}}{V'_{Total}}$$

(Eq. XI-8)

Substituting in the relationships for the void volume and the total volume:

$$Void\_Fraction = \frac{(1 + B) \cdot V_{Total} - 1}{(1 + B) V_{Total}}$$

(Eq. XI-9)

$$Void\_Fraction = \frac{(1+B)\cdot\left(1 + \dfrac{\phi_L}{1-\phi_L}\right) - 1}{(1+B)\cdot\left(1 + \dfrac{\phi_L}{1-\phi_L}\right)}$$

(Eq. XI-10)

$$Void\_Fraction = \frac{B + \phi_L}{1 + B}$$

(Eq. XI-11)

The calculations of the void fraction as a function of the lithophysal porosity, and of the bulking factor as given by Equation XI.11 are presented in the EXCEL workbook in Table XI-1. A range of lithophysal porosities are considered, 10% to 30%, and a range of bulking factors, 0.1 to 0.4. The lithophysal porosity of interest is 35% for a lithophysal rock mass category of 1 (BSC 2004 [DIRS 166107], Table 6-33). Category 1 and a bulking factor of 0.19 are chosen for analysis in *Drift Degradation Analysis* (BSC 2004 [DIRS 166107], Section 6.4.2.5).

XI.2 SUMMARY OF THE EFFECTIVE THERMAL CONDUCTIVITY OF DRIFT-COLLAPSE MATERIAL

Kunii and Smith (1960 [DIRS 153166]) describe a method for calculating the thermal conductivity of a porous medium with radiant heat transfer. The effective thermal conductivity is expressed by Kunii and Smith (1960 [DIRS 153166], Equation 8):

$$k_e = k_g \cdot \left[\varepsilon \cdot \left(1 + \beta \cdot \frac{h_{rv} \cdot D_p}{k_g}\right) + \frac{\beta \cdot (1-\varepsilon)}{\dfrac{1}{\dfrac{1}{\phi} + \dfrac{D_p \cdot h_{rs}}{k_g}} + \gamma \cdot \dfrac{k_g}{k_s}} \right]$$

(Eq. XI- 12)

where

D_p Nominal or average diameter of packing (m)
h_{rv} Heat transfer coefficient for radiation, void to void
h_{rs} Heat transfer coefficient for radiation, solid to solid
k_s Thermal conductivity of the solids (W/(m•K))
k_g Thermal conductivity of the fluid (W/(m•K))
ε Void fraction

β l_p/D_p which equals 1 as presented by Kunii and Smith (1960 [DIRS 153166], p. 72).

γ l_s/D_p which equals 2/3 as presented by Kunii and Smith (1960 [DIRS 153166], p. 72).

κ   Ratio of the solids thermal conductivity to the thermal conductivity of air.

The function $\phi(\kappa = k_s/k_g)$ is defined in Kunni and Smith (1960 [DIRS 153166], Equation 13) as:

$$\phi(\kappa) = \phi(k_s / k_g) = \frac{1}{2} \cdot \left[\frac{\left(\frac{\kappa-1}{\kappa}\right)^2 \cdot \sin(\theta)^2}{\ln(\kappa - (\kappa-1)\cdot\cos(\theta)) - \frac{\kappa-1}{\kappa}\cdot(1-\cos(\theta))} \right] - \frac{2}{3}\cdot\frac{1}{\kappa}$$

(Eq. XI-13)

where $\sin(\theta^2) = 1/n$, and n is associated with the fraction of the total heat transfer associated with one contact point (of the solids). Kunii and Smith (1960 [DIRS 153166], p. 74) define n ≈ 1.5 for loose solids.

The radiant heat transfer coefficients need to be estimated. The radiant heat-transfer coefficients (h_{rs} and h_{rv}) are given by Yagi and Kunii (1957 [DIRS 170330], Equations 7 and 8):

$$h_{rs} = 0.1952 \cdot \{p/(2-p)\} \cdot \{(t+273)/100\}^3$$

(Eq. XI- 14)

$$h_{rv} = \left[0.1952 / \left\{ 1 + \frac{\varepsilon}{2\cdot(1-\varepsilon)} \cdot \frac{1-p}{p} \right\} \right] \cdot (t+273/100)^3$$

(Eq. XI-15)

The lead coefficient of 0.1952 is derived from four times the Stephan Boltzmann constant in units of kcal/(m^2 h K^4) (Perry et al. 1984 [DIRS 125806], p. 10-53).

The calculations are presented in Table XI-2. The calculations involve inputting the thermal parameters; estimating the thermal conductivity of the air as a function of absolute temperature using the relationship from Irvine (1998 [DIRS 170361]); estimating the φ function using the equation presented above; estimating the radiant heat transfer coefficients using the relationships presented above; and then substituting these values into the effective thermal conductivity relationship presented by Kunii and Smith (1960 [DIRS 153166], Equation 8).

The effective thermal conductivity of dry drift-collapse material is calculated to be 0.82 W/(m·K), ±30%, or ranges from 0.57 to 1.05 W/(m·K). The 0.82 W/(m·K) value cited here is based on the following independent variables: a temperature of 75°C (with radiant heat transfer being temperature dependent); a lithophysal porosity of 35% and a bulking factor of 0.19, as noted previously; a dry rock thermal conductivity of 1.3998 W/(m·K) for stratigraphic unit Tptpll (DTN: SN0404T0503102.011 [DIRS 169129], Table 7-11); drift-collapse material

(rock size) of 10 centimeters (BSC 2004 [DIRS 166107], Section 6.4.2.5); and a rock emissivity of 0.92, which is the midpoint of the range in Table 4.1-1.

The uncertainty of ±30% is based on a review of the literature by Crane et al. (1977 [DIRS 113426]). An estimate of a wet effective thermal conductivity is not provided because there has been no analysis to show that the flux of water vapor down the thermal gradient is resupplied at the energy source by an equal or greater amount of liquid water. If there is no resupply of liquid water to the energy source, the collapse material will be dry.

The effective thermal conductivity that contains a radiation component is a function of temperature. Consider that the base case described above at 75°C has an effective thermal conductivity of 0.76 W/(m·K) at 65°C, and at 85°C this becomes 0.86 W/(m·K).

Table XI-1. Workbook for Determining the Void Fraction in the Collapsed Drift

file: voidbulk.xls; 7/8/2004b

Purpose: Calculate the void fraction after drift collapse as a function of the bulking factor and lithophysal porosity. The lithophysal porosity is added to the void volume. Therefore the void volume in 1 cubic meter of rock becomes the bulking factor + the lithophysal porosity %/100.

Lithophysal Porosity	Bulking Factor			
%	0.1	0.19	0.4	0.2
10	0.18	0.24	0.36	0.25
15	0.23	0.29	0.39	0.29
20	0.27	0.33	0.43	0.33
25	0.32	0.37	0.46	0.38
27.5	0.34	0.39	0.48	0.40
30	0.36	0.41	0.50	0.42
35	0.41	0.45	0.54	0.46

Intergranular Void Fraction

Obtain the lithophysal porosity from the drift degradation analysis, use 35% (BSC 2004 [DIRS 166107], Table 6-33) for Category 1, (BSC 2004 [DIRS 166107], Sect. 6.4.2.5), and a bulking factor of of 19% (BSC 2004 [DIRS 166107], Sec. 6.4.2.5).

Table XI-2.   Workbook for Calculation of the Collapsed Drift Thermal Conductivity

file: thermalk.xls; 7/8/2004b							
Purpose: Calculate the effective thermal conductivity for loose solids, includes a contribution							
from radiant heat transfer. Refer to line 96 in this xls file for keff.							
Reference: S. Yagi & D. Kunii, AIChE J., 3(3), 373-381, 1957; refer to as Y&K [DIRS 170330].							
Reference: D. Kunii & J.M. Smith, AIChE J., 6(1), 71-77, 1960; refer to as K&S [DIRS 153166].							
ENTER THE FOLLOWING:							
Air thermal k =		0.030	W(m*K), calculated from temperature entered below.				
Rock thermal k =		1.3998	W/(m*K), wet = 2.0707, or dry = 1.3998.				
Void fraction =		0.45	from the bulking factor and lithophysal porosity.				
Rock size =		10	cm				
Rock emissivity =		0.92	Ranges from 0.88 to 0.95.				
Temperature =		75	deg C, see note at end of this file.				
Temperature =		348	deg K				
Stephan-Boltzmann=		5.67E-08	W/(m^2 K^4)				
Beta =		1.00	see page 72, right column K&S				
Gamma =		0.67	see page 72, right column K&S				
Uncertainty, % =		30	see notes				
Air thermal k from Irvine (1998 [DIRS 170361], p. 2.4).							
Void fraction from bulking factor & lithophysal porosity, see spreadsheet voidbulk.xls in Table XI-1.							
Rock thermal k from SN0404T0503102.011 ([DIRS 169129], file: Readme.doc).							
Rock size from Drift Degradation Analysis (BSC 2004 [DIRS 166107], Sec. 6.1.4.1).							
Rock emissivity is from Incropera & DeWitt (2002 [DIRS 163337], Table A.11).							
Stephan-Boltzmann constant from Cho, et al. (1998 [DIRS 160802], p.1.3).							
Calculate phi1 and phi2 in K&S, verify Figure 5, see plot on sheet2.							
phi1 is for loose packing, phi2 is for close packing.							
See K&S, page 74, left column for n1 and n2.							
n1 =	1.5	theta1 =	54.73	degrees, =	0.955	radian	
n2 =	6.928	theta2 =	22.3	degrees, =	0.389	radian	
sin^2(t1) =	0.666	cos(t1) =	0.577				
sin^2(t2) =	0.144	cos(t2) =	0.925				
Calculate phi1 & phi2 versus ks/kg using equation 13, K&S, page 73.							
kappa =	**Denom.**	**Denom.**	**Denom.**	**Numerator**			
ks/kg	**log term**	**cos term**		**term**	**phi1 =**		
0.01	-0.542470853	-41.877	41.33453	3263.733	12.29233		
0.02	-0.53522138	-20.727	20.19178	799.533	6.263624		
0.05	-0.513783134	-8.037	7.523217	120.213	2.645603		
0.1	-0.479043714	-3.807	3.327956	26.973	1.438308		
0.2	-0.412989167	-1.692	1.279011	5.328	0.832386		
0.5	-0.237562492	-0.423	0.185438	0.333	0.46242		

Table XI-2. Workbook for Calculation of the Collapsed Drift Thermal Conductivity (Continued)

2	0.35267768	0.2115	0.141178	0.08325	0.256349			
5	0.990032778	0.3384	0.651633	0.21312	0.193722			
10	1.569674229	0.3807	1.188974	0.26973	0.160193			
20	2.200767898	0.40185	1.798918	0.300533	0.13373			
50	3.077773458	0.41454	2.663233	0.319813	0.106751			
100	3.757380549	0.41877	3.338611	0.326373	0.091091			
200	4.443602026	0.420885	4.022717	0.329678	0.078621			
500	5.355588201	0.422154	4.933434	0.331669	0.065896			
1000	6.047198316	0.422577	5.624621	0.332334	0.058419			
2000	6.739488203	0.422789	6.3167	0.332667	0.052331			
5000	7.655137182	0.422915	7.232222	0.332867	0.045892			
10000	8.347971888	0.422958	7.925014	0.332933	0.041944			
Calculate phi1 here in the next line for the given entries above.								
47.45	3.026864954	0.414085	2.61278	0.319112	0.108085			
phi2 is not used, it is calculated and plotted for further verification.								
					phi2 =			
0.01	-0.077131455	-7.425	7.347869	705.672	29.37098			
0.02	-0.076321835	-3.675	3.598678	172.872	14.7043			
0.05	-0.073896901	-1.425	1.351103	25.992	5.904281			
0.1	-0.069868369	-0.675	0.605132	5.832	2.970906			
0.2	-0.061859681	-0.3	0.23814	1.152	1.504151			
0.5	-0.038211501	-0.075	0.036788	0.072	0.6238			
2	0.072302285	0.0375	0.034802	0.018	0.183874			
5	0.262297597	0.06	0.202298	0.04608	0.09445			
10	0.515682096	0.0675	0.448182	0.05832	0.063459			
20	0.885606432	0.07125	0.814356	0.06498	0.04646			
50	1.541837278	0.0735	1.468337	0.069149	0.03376			
100	2.130661932	0.07425	2.056412	0.070567	0.027649			
200	2.767186873	0.074625	2.692562	0.071282	0.02314			
500	3.647781143	0.07485	3.572931	0.071712	0.018738			
1000	4.328645811	0.074925	4.253721	0.071856	0.016226			
2000	5.015508247	0.074963	4.940546	0.071928	0.014225			
5000	5.927882982	0.074985	5.852898	0.071971	0.012163			
10000	6.619623289	0.074993	6.544631	0.071986	0.010933			
Calculate the radiation heat transfer coefficients from Y&K for solid-to-solid (hrs),								
equation (7), and void-to-void (hrv), equation (8):								
hrs =	8.14	W/(m^2 K)		Note: division of temperature by 100 is not included				
hrv =	9.23	W/(m^2 K)		because the Stephan-Boltzmann constant is used				
				with its 10^-8.				
Calculate the effective conductivity from equation (8) from K&S for the given independent								
variables.								
term1 =	14.53	is the first term in equation (8) from K&S.						
term2 =	13.35	is the second term in equation (8) from K&S.						

Table XI-2. Workbook for Calculation of the Collapsed Drift Thermal Conductivity (Continued)

keff =	0.82	W/(m*K), is the effective thermal conductivity, equation (8), K&S.					
keff range based on input uncertainty =			0.58	to	1.07	W/(m*K)	
End of file note: The radiant heat transfer coefficients are temperature dependent. Therefore, the use of any heat transfer coefficient with a radiant contribution becomes a trial-and-error heat transfer calculation. It is necessary to choose a temperature at which to perform the heat transfer calculation and this temperature should be in the range of temperatures subsequently calculated.							

APPENDIX XII

COMPARISON OF PERCOLATION FLUXES

This appendix compares percolation fluxes from *UZ Flow Models and Submodels* (BSC 2004 [DIRS 169861]) models with the corresponding fluxes implemented in the discretization used for calculations with the multiscale thermohydrologic model (MSTHM). The detailed comparisons are for the three climates (present-day, monsoonal and glacial) and for the lower, mean and upper-bound infiltration flux cases. The input DTNs are discussed and input to the analysis in Section XII.1 through XII.2. The sampling points are presented. Sections XII.3 through XII.7 develop the cumulative distribution functions. The cumulative distribution functions are developed for the respective cases and compared between the input DTN and its implementation in the MSTHM grid.

Figure XII-1 presents a flowchart showing how information for making the comparison is obtained from the Technical Data Management System (TDMS). The upper portion of the flowchart shows DTN: MO0406CDFINSMT.000 for the UZ flow model. This DTN contains a summary EXCEL workbook file T2_perc_data_and CDF.xls. The workbook contains nine worksheets that correspond to three climates and three cases. These represent cumulative distribution functions that are weighted according to grid areas. Each of these worksheets are used to define MathCad Column vectors that represent nine individual cumulative distribution functions (CDFs).

The lower portion of the flow chart shows the three output DTNs for the MSTHM model. These are DTNs: LL030608723122.028, LL030610323122.029, LL030602723122.027 for the lower, mean, and upper bounds respectively.   These DTNs contain the following text files, all of which are used to define EXCEL components that are read into MathCad column vectors for purposes of plotting the distribution functions:

- Nevada_SMT_percolation_BIN_la.txt
- Nevada_SMT_percolation_BIN_ma.txt
- Nevada_SMT_percolation_BIN_ua.txt.

The calculations presented in this appendix are performed in the MathCad File Cumulative Distribution Plots of Percolation.mcd. The data from the DTNs are input as EXCEL components in MathCad Professional 11.   These DTNs are output from the multiscale thermohydrologic model.

EXCEL components in MathCad represent an efficient method for inputting the data from the input DTNs into MathCad. The EXCEL components presented below are input from EXCEL files that in turn are compiled from text files as discussed below. The inputs are generally column vectors from the EXCEL spreadsheet component as defined by the output property for each EXCEL component in MathCad.

Cumulative Distribution Functions for the UZ Flow Model

TDMS **EXCEL Workbook** **EXCEL Worksheets**

| DTN MO0406CDFINSMT.000 | → | Workbook T2_perc_data_and_CDF.xls | → | Worksheets glac_l glac_m glas_u mon_l mon_m mon_u pre_l pre_m pre_u |

| MathCad EXCELComponents for each Individual Worksheets | → | MathCad Column Vectors pre_l,pre_l_CDF pre_m,pre_m_CDF pre_u,pre_u_CDF mon_l,mon_l_CDF mon_m,mon_m_CDF mon_u,mon_u_CDF gla_l,gla_l_CDF gla_m,gla_m_CDF gla_u,gla_u_CDF | → | MathCad Comparison Plots CDFs for Present Day CDFs for Monsson CDFs for Glacial for the two models. |

Cumulative Distribution Functions for the MSTHM Model

TDMS **Textfile**

| DTNs LL030608723122.028, LL030610323122.027, LL030602723122.029 | → | Nevada_SMT_percolation _BIN_la.txt, Nevada_SMT_percolation _BIN_ma.txt Nevada_SMT_percolation _BIN_ua.txt | → | MathCad EXCEL Components from the Text File | → | MathCad Column Vectors Modern or Present Day Monsoon Glacial |
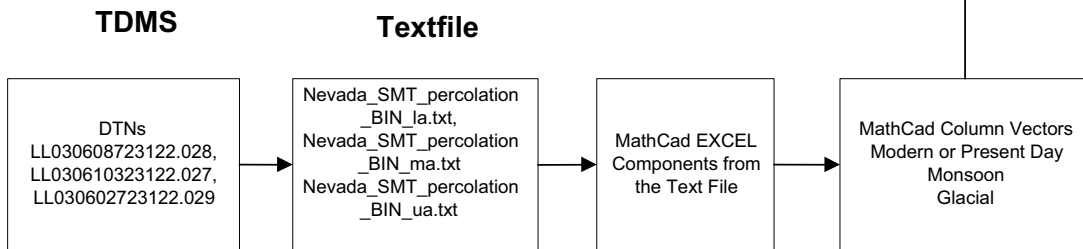
Figure XII-1. Flow Chart for Comparing Cumulative Distribution Functions

XII.1   INPUT DATA FROM THE 3-D SITE-SCALE UZ FLOW MODEL

The DTN LB0302PTNTSW9I.001 [DIRS 162277] entitled "PTN/TSW Interface Percolation Flux Maps for 9 Infiltration Scenarios" and   DTN LB03023DSSCP9I.001[DIRS 163044] entitled "3-D Site Scale UZ Flow Field Simulations for 9 Infiltration Scenarios" were   used   to   develop   the   cumulative   distribution   function   for   the   nine cases   in   DTN: MO0406CDFINSMT.000.   Input   the   coordinate   data   from DTN: LB03023DSSCP9I.001[DIRS 163044] for purposes of developing a plot of sampling points of percolation for the UZ flow model. Note that any of the text files can be used since the coordinates are included in each file. Use the file monq_ma_ptn.q.

$$\begin{pmatrix} EPTn_{perc} \\ NPTn_{perc} \end{pmatrix} :=$$

168251	229650
168551	229650
170181	229720
170951	229650
171551	229650
172451	229650
172750	229650
168301	229890
168551	229950
170201	230010

In the above EXCEL MathCad assignment, $EPTN_{perc}$ represents the Easting coordinate (m) vector, and $NPTN_{perc}$ represents the Northing coordinate (m) vector.

Determine the number of points using the row function:

$$rows\left(EPTn_{perc}\right) = 2.042 \times 10^3$$

Rescale the data:

$$j := 1 .. 2042$$

$$EPTn'_{perc_j} := \frac{EPTn_{perc_j}}{1000} - \frac{1.701 \times 10^5}{1000}$$

$$NPTn'_{perc_j} := \frac{NPTn_{perc_j}}{1000} - \frac{2.319 \times 10^5}{1000}$$

Figure XII-2 shows the sampling points for the 3-D Site-Scale UZ Flow Model.
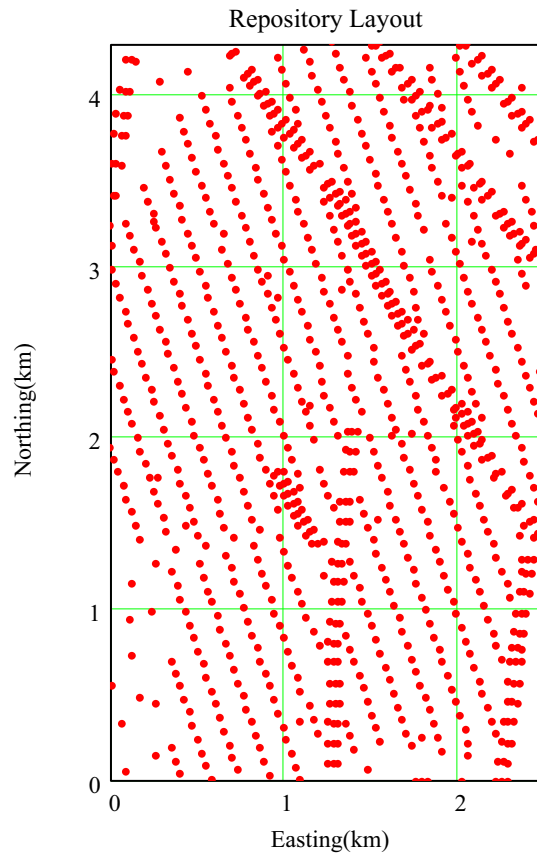
Figure XII-2.   Sampling Points for the Tough2 PTn/TSw Model

Input the cumulative distribution functions from the EXCEL spreadsheet summarizing the results from DTN: MO0406CDFINSMT.000. In this DTN, there is an EXCEL workbook entitled T2_perc_data_and_CDF.xls. This EXCEL workbook has 10 worksheets. The first worksheet is the combined data, and is not used in the analysis presented below. The next nine worksheets present cumulative distribution functions for the three climates and the three bounds as listed in Table XII-2. These are input to the MathCad program through the use of vectors using the properties tab for the EXCEL component.

Table XII-1. Summary of EXCEL Worksheets in T2_perc_data_and_CDF.xls for
DTN: MO0406CDFINSMT.000

Climate	Bound	Worksheet Name
Glacial	Lower	glac_l
Glacial	Mean	glac_m
Glacial	Upper	glac_u
Monsoon	Lower	mon_l
Monsoon	Mean	mon_m
Monsoon	Upper	mon_u
Present-Day	Lower	pre_l
Present-Day	Mean	pre_m
Present-Day	Upper	pre_u

Input the values for the present day climate for the lower case. These values are obtained from the worksheet pre_l of T2_perc_data_and_CDF.xls. Note that only the first few rows are shown.

$$\begin{pmatrix} pre\_l \\ pre\_l\_CDF \end{pmatrix} :=$$

pre_l	pre_l_CDF
0.00	2.358330E-03
0.00	4.716688E-03
0.00	7.139175E-03
0.00	9.718286E-03
0.00	1.208377E-02
0.00	1.416974E-02
0.00	1.644986E-02

pre_l represents the percolation flux in mm per year. pre_l_CDF represents the cumulative distribution pertaining to the percolation flux (dimensionless).

Input the values for the present day climate for the mean case. These values are obtained from the worksheet pre_m of T2_perc_data_and_CDF.xls

$$\begin{pmatrix} pre\_m \\ pre\_m\_CDF \end{pmatrix} :=$$

pre_m	pre_m_CDF
0.203114	0.00257911
0.20648	0.00523494
0.298709	0.0075933
0.337577	0.00987342
0.363078	0.01223175
0.440667	0.01445095
0.445001	0.01691418
0.466575	0.01900016
0.561075	0.02154509

pre_m represents the percolation flux in mm per year. pre_m_CDF represents the cumulative distribution pertaining to the percolation flux (dimensionless).

Input the values for the present day climate for the upper case. These values are obtained from the worksheet pre_u of T2_perc_data_and_CDF.xls.

$$\begin{pmatrix} pre\_u \\ pre\_u\_CDF \end{pmatrix} :=$$

pre_u	pre_u_CDF
0.872483	0.0022801
1.014349	0.0049359
1.275882	0.0063444
1.460394	0.0084303
1.486113	0.0110095
1.573294	0.0114768
1.634857	0.0126458
1.69199	0.0138239
1.827775	0.0144066
1.9445	0.0153848

pre_u represents the percolation flux in mm per year. pre_u_CDF represents the cumulative distribution pertaining to the percolation flux (dimensionless).

Input the values for the monsoon climate for the lower case. These values are obtained from the worksheet mon_l of T2_perc_data_and_CDF.xls.

$$\begin{pmatrix} mon\_l \\ mon\_l\_CDF \end{pmatrix} :=$$

mon_l	mon_l_CDF
0.1104	0.00265583
0.113641	0.00304332
0.149631	0.00562243
0.201519	0.00790255
0.315411	0.01026091
0.339742	0.01234688
0.460166	0.01269943
0.49525	0.01387761
0.496857	0.01504657

mon_l represents the percolation flux in mm per year. mon_l_CDF represents the cumulative distribution pertaining to the percolation flux (dimensionless).

Input the values for the monsoon climate for the mean case. These values are obtained from the worksheet mon_m of T2_perc_data_and_CDF.xls.

$$\begin{pmatrix} mon\_m \\ mon\_m\_CDF \end{pmatrix} :=$$

mon_m	mon_m_CDF
0.317967	0.00228012
0.339869	0.00493595
0.464943	0.00751506
0.668382	0.00960103
0.865489	0.01195939
0.914458	0.01442262
0.935272	0.01678095
0.937129	0.01900016
1.567351	0.02089934

mon_m represents the percolation flux in mm per year. mon_m_CDF represents the cumulative distribution pertaining to the percolation flux (dimensionless).

Input the values for the monsoon climate for the upper case. These values are obtained from the worksheet mon_u of T2_perc_data_and_CDF.xls.

$$\begin{pmatrix} mon\_u \\ mon\_u\_CDF \end{pmatrix} :=$$

mon_u	mon_u_CDF
0.615142	0.00228012
1.213646	0.00493595
1.302603	0.00702192
2.1896	0.00960103
2.466724	0.01100946
2.505965	0.0114768
2.721702	0.01205944
2.949617	0.01273885
3.309009	0.01391703
3.37513	0.015086

mon_u represents the percolation flux in mm per year. mon_u_CDF represents the cumulative distribution pertaining to the percolation flux (dimensionless).

Input the values for the glacial climate for the lower case. These values are obtained from the worksheet glac_l of T2_perc_data_and_CDF.xls.

$$\begin{pmatrix} glac\_l \\ glac\_l\_CDF \end{pmatrix} :=$$

glac_l	glac_l_CDF
0.002101	0.00236548
0.007418	0.00502132
0.007655	0.00710729
0.010456	0.00938741
0.017005	0.0097749
0.017178	0.01235401
0.021309	0.01270911
0.0608	0.01306165
0.067621	0.01552488

glac_l represents the percolation flux in mm per year. glac_l_CDF represents the cumulative distribution pertaining to the percolation flux (dimensionless).

Input the values for the glacial climate for the mean case. These values are obtained from the worksheet glac_m of T2_perc_data_and_CDF.xls.

$$\begin{pmatrix} glac\_m \\ glac\_m\_CDF \end{pmatrix} :=$$

glac_m	glac_m_CDF
0.604386	0.00265583
0.772607	0.00493595
0.827256	0.00751506
1.086087	0.00997829
1.222658	0.01219749
1.312919	0.01428347
1.757234	0.0166418
1.942364	0.01900016
2.488503	0.02136434

glac_m represents the percolation flux in mm per year. glac_m_CDF represents the cumulative distribution pertaining to the percolation flux (dimensionless).

Input the values for the glacial climate for the upper case. These values are obtained from the worksheet glac_u of T2_perc_data_and_CDF.xls.

$$\begin{pmatrix} glac\_u \\ glac\_u\_CDF \end{pmatrix} :=$$

glac_u	glac_u_CDF
1.533968	0.002280115
2.549426	0.004935948
2.83767	0.007021922
4.015425	0.00748926
4.621348	0.010068371
4.734478	0.011476797
5.203607	0.012059437
5.413422	0.012738851
5.888617	0.013907817

glac_u represents the percolation flux in mm per year. glac_u_CDF represents the cumulative distribution pertaining to the percolation flux (dimensionless).

XII.2   INPUT DATA FROM THE MSTHM

Consider the output DTNs containing the percolation flux boundary conditions for the MSTHM.

These DTNs are summarized below:

Table XII-1   Output DTNs for MSTHM model

Lower Percolation Rate	DTN: LL030608723122.028
Mean Percolation Rate	DTN: LL030610323122.029
Upper Percolation Rate	DTN: LL030602723122.027

Input the properties for the mean case. Note that the data are organized for the three climates for the lower, mean, and upper percolation rates presented above. The data are obtained from the text file Nevada_SMT_percolation_BIN_ma.txt of DTN: LL030610323122.029. Note that only the first few rows of the EXCEL component derived from the textfile are shown below.

$$
\begin{pmatrix}
E_{perc} \\
N_{perc} \\
Modern_{mean} \\
Monsoon_{mean} \\
Glacial_{mean}
\end{pmatrix} :=
$$

easting	northing	Modern	Monsoon	Glacial
171132.8	236151.3	2.220288	7.246367	10.20758
171151.8	236157.5	2.265795	7.410341	10.59777
171170.8	236163.7	2.311301	7.574315	10.98797
171189.8	236169.9	2.356808	7.738289	11.37816
171208.8	236176.1	2.402314	7.902264	11.76835
171227.9	236182.3	2.447821	8.066237	12.15854
171246.9	236188.5	2.493327	8.230211	12.54874
171265.9	236194.7	2.538834	8.394186	12.93893
171284.9	236200.8	2.58434	8.558161	13.32912
171303.9	236207	2.629847	8.722135	13.71932

$Modern_{mean}$ represents the percolation flux vector (mm/yr) for the mean bound for the present day climate. $Monsoon_{mean}$ represents the percolation flux vector (mm/yr) for the for mean bound for the monsoon climate. $Glacial_{mean}$ represents the percolation flux vector (mm/yr) for the for mean bound for the glacial climate. E_{perc} represents the easting coordinate vector (m). N_{perc} represents the northing coordinate vector.

Input the percolation fluxes for the lower bound case. The data that are read into the EXCEL component presented below are obtained from the text file Nevada_SMT_percolation_BIN_la.txt of from DTN: LL030608723122.028.

$$
\begin{pmatrix}
Modern_{lower} \\
Monsoon_{lower} \\
Glacial_{lower}
\end{pmatrix} :=
$$

Modern	Monsoon	Glacial
0.555732	4.865694	2.496985
0.576192	4.890319	2.519521
0.596651	4.914944	2.542056
0.617111	4.939568	2.564592
0.637571	4.964193	2.587128
0.658031	4.988817	2.609663
0.678491	5.013442	2.632199
0.698951	5.038067	2.654735
0.719411	5.062692	2.677271
0.739871	5.087317	2.699807
0.76033	5.111941	2.722343
0.78079	5.136565	2.744878

Modern$_{lower}$ represents the percolation flux vector (mm/yr) for the lower bound for the present day climate. Monsoon$_{lower}$ represents the percolation flux vector (mm/yr) for the for lower bound for the monsoon climate. Glacial$_{lower}$ represents the percolation flux vector (mm/yr) for the for lower bound for the glacial climate.

Input the percolation fluxes for the upper bound case. The data that are read into the EXCEL component presented below are obtained from the text file Nevada_SMT_percolation_BIN_ua.txt of from DTN: LL030602723122.027.

$$\begin{pmatrix} Modern_{upper} \\ Monsoon_{upper} \\ Glacial_{upper} \end{pmatrix} :=$$

Modern	Monsoon	Glacial
11.33837	20.15363	29.32075
11.27895	19.90239	29.25167
11.21954	19.65115	29.18258
11.16013	19.39991	29.11349
11.10072	19.14868	29.04441
11.04131	18.89744	28.97532
10.9819	18.6462	28.90624
10.92249	18.39497	28.83715
10.86308	18.14373	28.76806
10.80367	17.89249	28.69898
10.74425	17.64126	28.62989
10.68484	17.39002	28.5608

Modern$_{upper}$ represents the percolation flux vector (mm/yr) for the upper bound for the present day climate. Monsoon$_{upper}$ represents the percolation flux vector (mm/yr) for the for upper bound for the monsoon climate. Glacial$_{upper}$ represents the percolation flux vector (mm/yr) for the for upper bound for the glacial climate.

Rescale the plots to km.

$$j := 1 .. rows(E_{perc})$$

$$min(E_{perc}) = 1.701 \times 10^5$$

$$E'_{perc_j} := \frac{E_{perc_j}}{1000} - \frac{min(E_{perc})}{1000}$$

$$min(N_{perc}) = 2.319 \times 10^5$$

$$N'_{perc_j} := \frac{N_{perc_j}}{1000} - \frac{min(N_{perc})}{1000}$$

Figure XII-2 shows the SMT sampling locations.
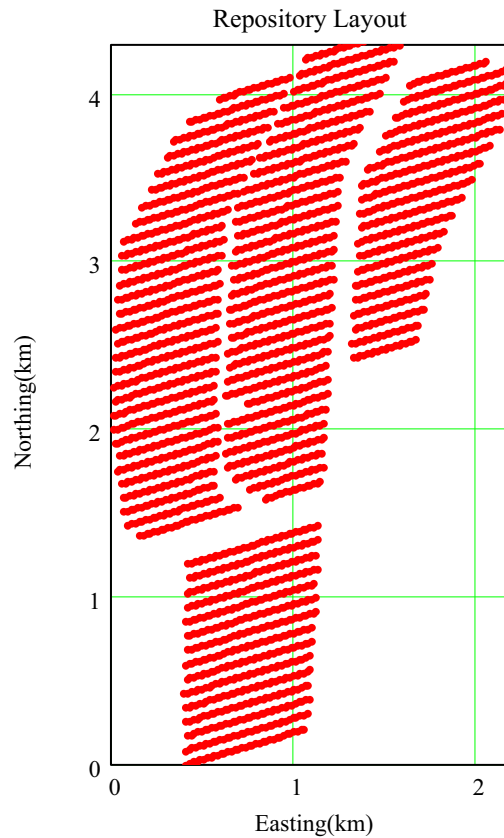
Figure XII-3.   Sampling Points for the MSTHM Model

XII.3   COMPARISONS FOR THE PRESENT-DAY CLIMATE

The data for the present-day climate from the MSTHM calculations have equal weightings. In order to develop the CDF for the MSTHM model, sort the data in ascending order. Note that since the percolation values are for areas that are equal weighting, the CDF is determined directly by sorting the data in MathCad, and plotting the sorted data against the rank order expressed as a percentile. Output the first 16 values in mm/yr Modern$_{lower}$ for purposes of illustration:

$$Modern_{lower} =$$

	1
1	0.556
2	0.576
3	0.597
4	0.617
5	0.638
6	0.658
7	0.678
8	0.699
9	0.719
10	0.74
11	0.76
12	0.781
13	0.801
14	0.822
15	0.892
16	0.961

Determine the number of rows in the column vector:

$$rows\left(Modern_{lower}\right) = 2.874 \times 10^3$$

Now use the sort function in MathCad to sort the values in ascending order:

$$Modern_{lower} := sort\left(Modern_{lower}\right)$$

Output the first values to show that MathCad sorted the values in ascending order:

$$Modern_{lower} =$$

	1
1	$2.8 \cdot 10^{-5}$
2	$3.8 \cdot 10^{-5}$
3	$4.4 \cdot 10^{-5}$
4	$4.7 \cdot 10^{-5}$
5	$4.9 \cdot 10^{-5}$
6	$5 \cdot 10^{-5}$
7	$5.6 \cdot 10^{-5}$
8	$5.9 \cdot 10^{-5}$
9	$6 \cdot 10^{-5}$
10	$6.1 \cdot 10^{-5}$
11	$6.2 \cdot 10^{-5}$
12	$6.3 \cdot 10^{-5}$
13	$6.4 \cdot 10^{-5}$
14	$6.6 \cdot 10^{-5}$
15	$6.7 \cdot 10^{-5}$
16	$7 \cdot 10^{-5}$

Now sort the other cases having demonstrating the results for the lower case:

$$Modern_{mean} := sort\left(Modern_{mean}\right)$$

$$Modern_{upper} := sort\left(Modern_{upper}\right)$$

Develop the CDF by plotting the rank order against the sorted values for mean, lower and upper percolation cases. The results are shown in Figure XII-3 for the modern or present case. The figure shows the .05, 0.30, 0.70, and 0.95 percentiles for the CDF.

Perform the analysis for the other cases. These are presented in Figures XII-4 through XII-6.

$$jj := 1..rows\left(Modern_{lower}\right)$$

$$mm := 1..rows(pre\_l)$$
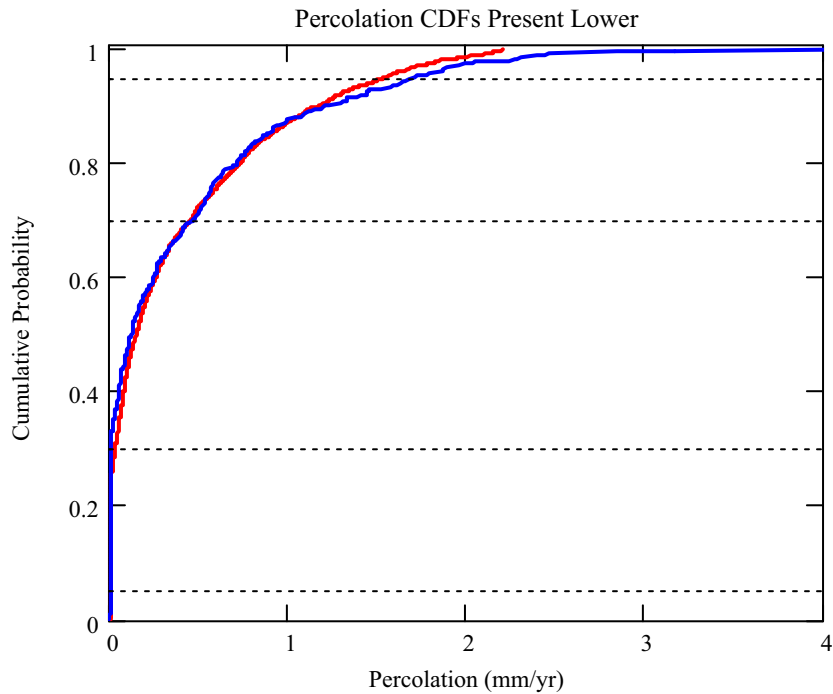
NOTE: Red line = MSTHM model; blue line = UZ flow model.

Figure XII-4.   Cumulative Distribution Function Comparison for the Present Day Lower Case

$$jj := 1..\,rows\left(Modern_{mean}\right)$$
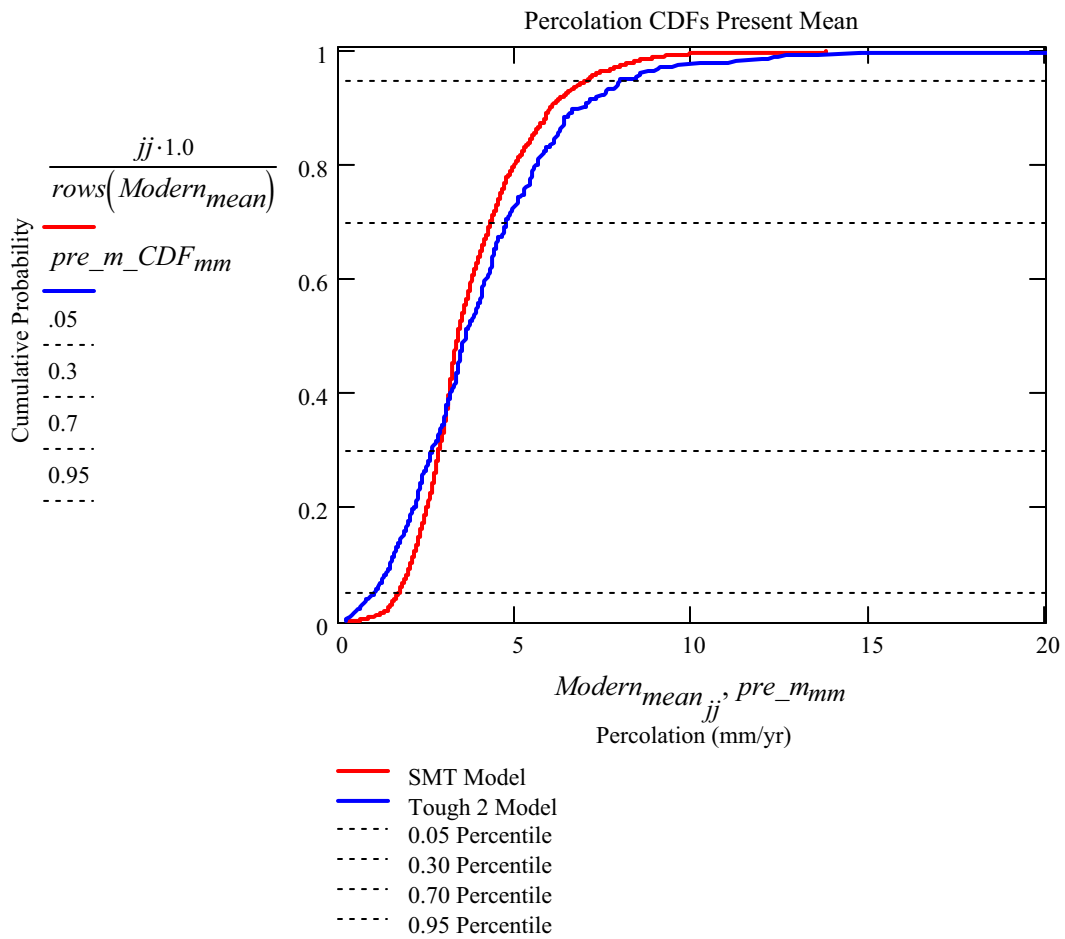
NOTE: Red line = MSTHM model; blue line = UZ flow model.

Figure XII-5.   Cumulative Distribution Function Comparison for the Present-Day Mean Infiltration-Flux
          Case

Percolation CDFs PresentUpper
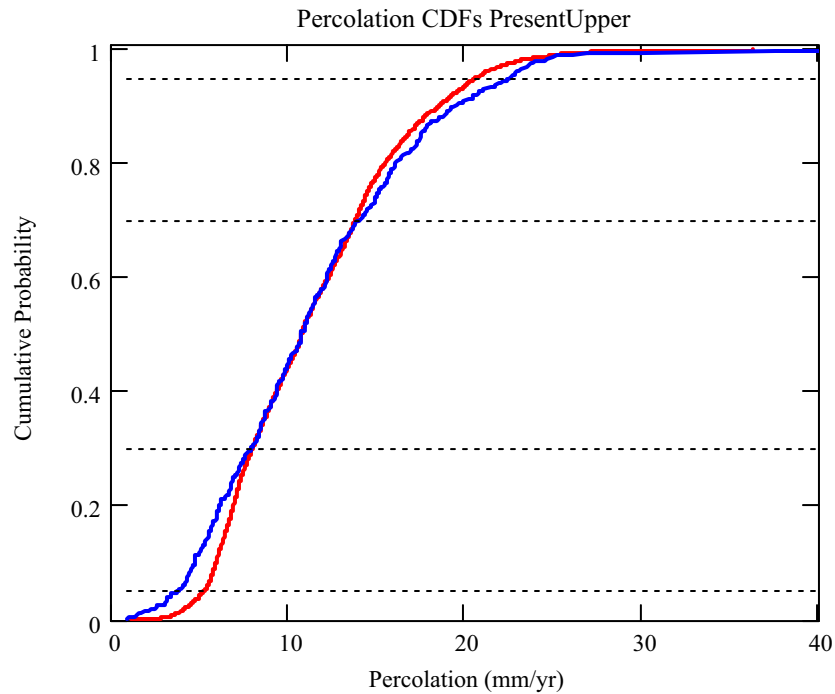
NOTE: Red line = MSTHM model; blue line = UZ flow model.

Figure XII-6.   Cumulative Distribution Function Comparison for the Present Day Upper Case

XII.4   COMPARISONS FOR THE MONSOONAL CLIMATE

The data for the monsoonal climate from the MSTHM calculations have equal weightings. In order to develop the CDF for the MSTHM, sort the data in ascending order.

$$Monsoon_{lower} := sort\left(Monsoon_{lower}\right)$$

$$Monsoon_{mean} := sort\left(Monsoon_{mean}\right)$$

$$Monsoon_{upper} := sort\left(Monsoon_{upper}\right)$$

Develop the CDF by plotting the rank order against the sorted values for lower-, mean, and upper-bound infiltration-flux cases. Figures XII-7 through XII-9 show these cases for the monsoonal climate.

$$jj := 1 .. rows\left(Monsoon_{lower}\right)$$

Percolation CDFs Monsoon Lower
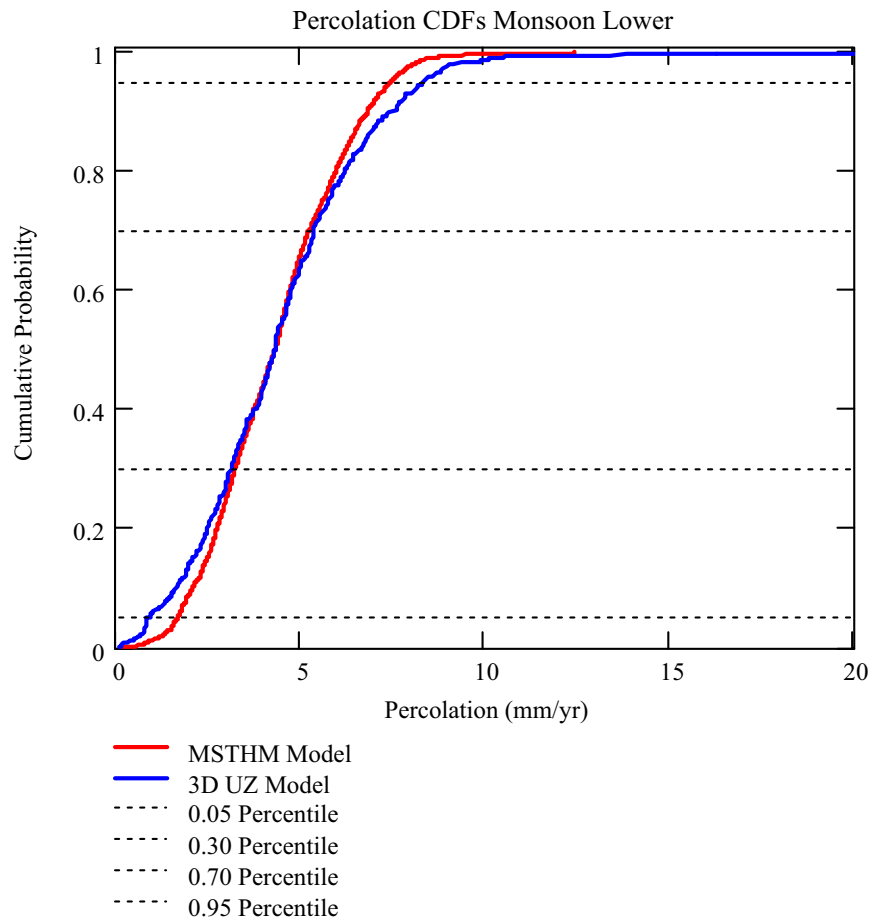
NOTE: Red line = MSTHM model; blue line = UZ flow model.

Figure XII-7. Cumulative Distribution Function Comparison for the Monsoonal-Climate Lower-Bound Infiltration-Flux Case

$$jj := 1 .. rows\left(Monsoon_{mean} \right)$$

$$mm := 1 .. rows(mon\_m)$$

Percolation CDFs Monsoon Mean
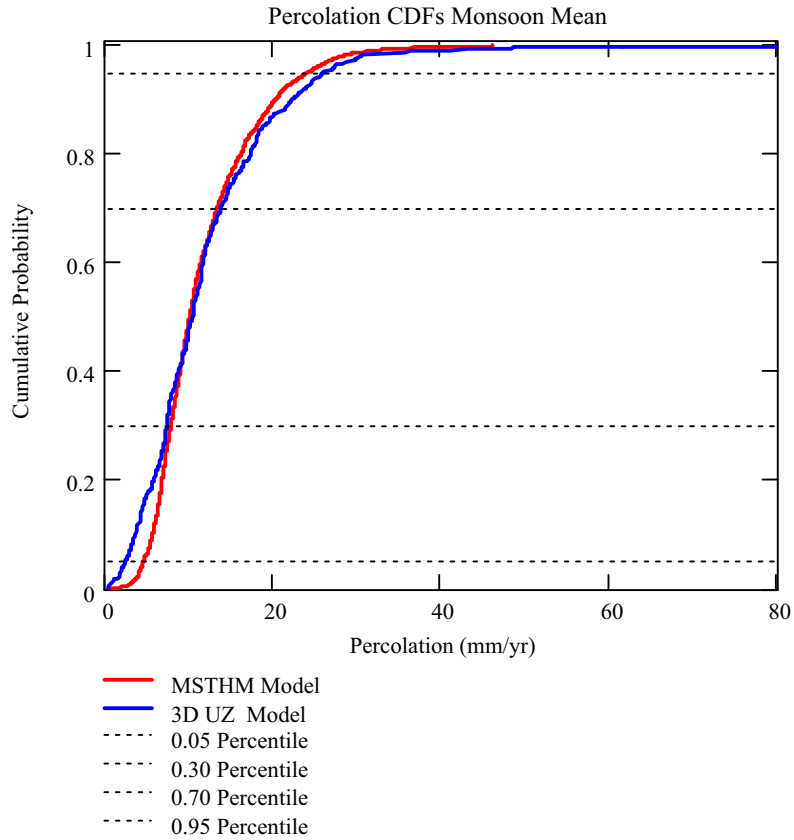
NOTE: Red line = MSTHM model; blue line = UZ flow model.

Figure XII-8.   Cumulative Distribution Function Comparison for the Monsoonal-Climate Mean
        Infiltration-Flux Case
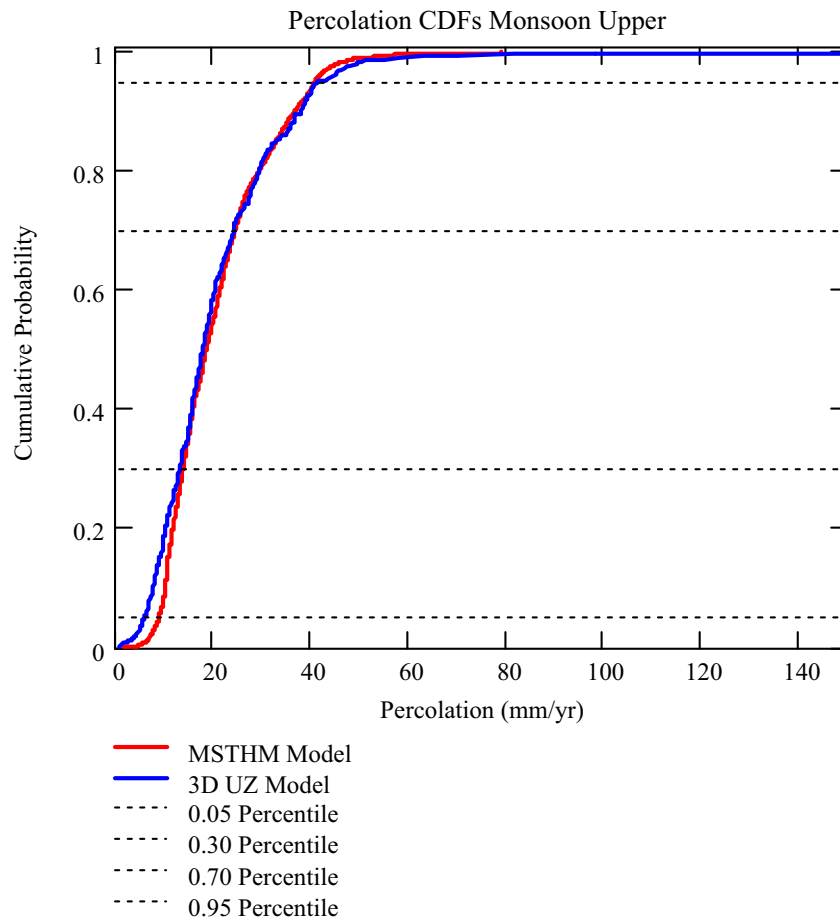
NOTE: Red line = MSTHM model; blue line = UZ flow model.

Figure XII-9. Cumulative Distribution Function Comparison for the Monsoonal-Climate Upper-Bound Infiltration-Flux Case

XII.5   COMPARISONS FOR THE GLACIAL CLIMATE

The data for the glacial climate from the MSTHM calculations have equal weightings. In order to develop the CDF for the MSTHM, sort the data in ascending order.

$$Glacial_{lower} := sort\left(Glacial_{lower}\right)$$

$$Glacial_{mean} := sort\left(Glacial_{mean}\right)$$

$$Glacial_{upper} := sort\left(Glacial_{upper}\right)$$

Develop the CDF by plotting the rank order against the sorted values for lower-, mean, and upper-bound infiltration-flux cases. Figures XII-10 through XII-12 show these cases for the glacial climate.

$$jj := 1..rows\left(Glacial_{lower}\right)$$
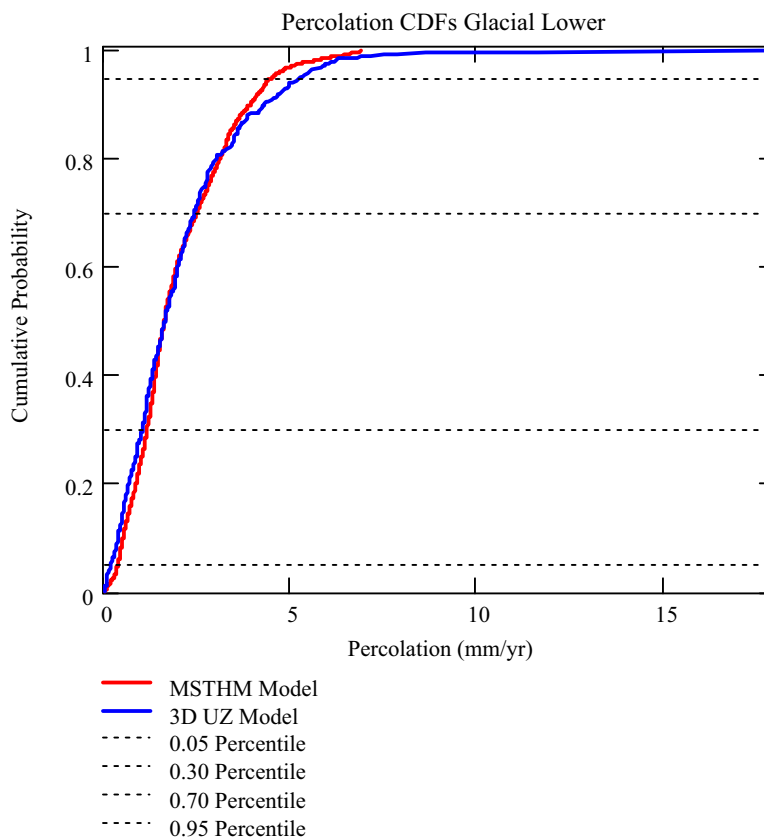
NOTE: Red line = MSTHM model; blue line = UZ flow model.

Figure XII-10. Cumulative Distribution Function Comparison for the Glacial-Climate Lower-Bound Infiltration-Flux Case

$$jj := 1 .. rows\left(Glacial_{mean}\right)$$

$$mm := 1 .. rows(glac\_m)$$

Percolation CDFs Glacial Mean
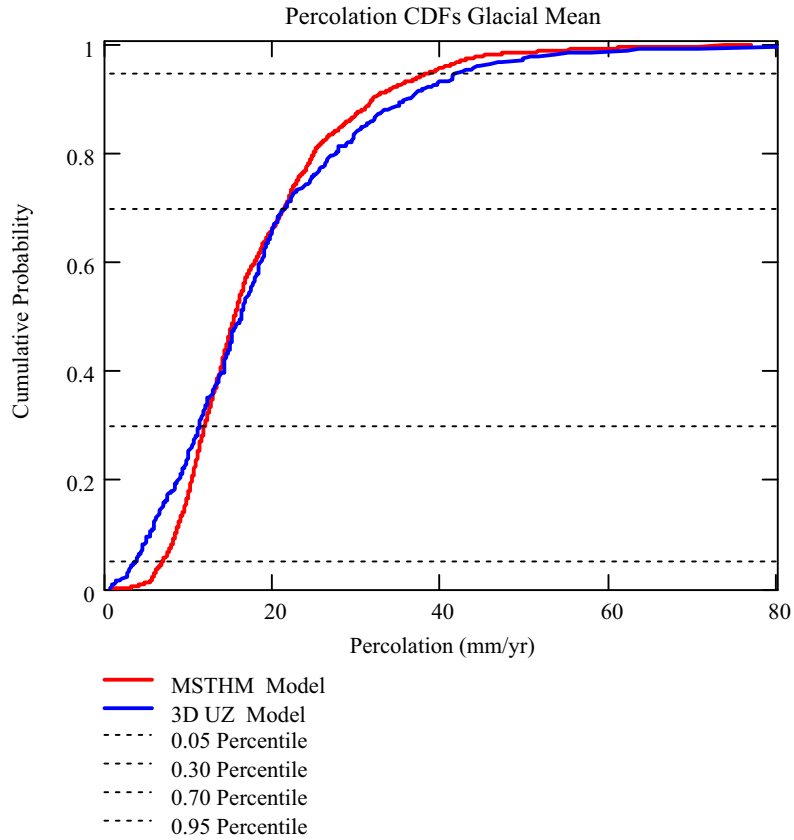
NOTE: Red line = MSTHM model; blue line = UZ flow model.

Figure XII-11. Cumulative Distribution Function Comparison for the Glacial-Climate Mean Infiltration-Flux Case
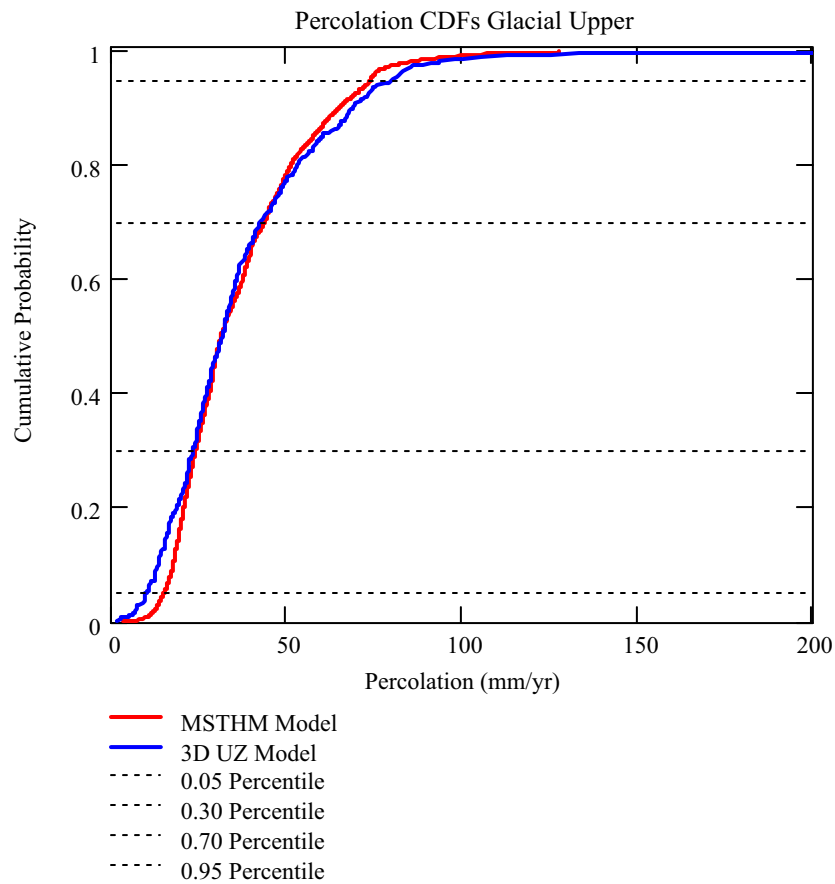
NOTE: Red line = MSTHM model; blue line = UZ flow model.

Figure XII-12. Cumulative Distribution Function Comparison for the Glacial-Climate Upper-Bound Infiltration-Flux Case

XII.8   SUMMARY OF RESULTS

Comparisons between the two models have been conducted. The comparisons of the cumulative distribution functions (CDF) show good agreement for the nine cases considered in the analysis with minor differences attributable to differences in gridding, sampling locations, and the areas tributary to sampling locations.

APPENDIX XIII

LIST OF DATA SOURCES FOR FIGURES AND TABLES

Table XIII-1.   List of Data Sources for Figures

Figure No.	Data Source	File Name	Plotting Software	Notes
4-1	LL030808623122.036	INPUT/main_runs/SMT/tspa03.mesh03-150w	MATLAB v6.1.0.450 (R12.1)	
4-2	LL040703123122.049	percolation_flux_files/ccdf_modern_perc_new-old-layouts.pltsc percolation_flux_files/ccdf_monsoonal_perc_new-old-layouts.pltsc percolation_flux_files/ccdf_glacial_perc_new-old-layouts.pltsc	XTOOL v10.1	
6.1-2	Buscheck et al. 2002 [DIRS 160749], Figure 2		XTOOL v10.1	
6.2-3	LL030808623122.036	INPUT/main_runs/SMT/tspa03.mesh03-150w	MATLAB v6.1.0.450 (R12.1)	
6.2-6	LL030808623122.036	INPUT/main_runs/LDTH/mi/LDTH55/P2WR5C10-LDTH55-1Dds_mc-mi-01.in	RADPRO v4.0	
6.2-7	LL030808623122.036	INPUT/initialization_runs/DDT/DDT55/P2WR5C10-DDT55-01v.in	RADPRO v4.0	
6.2-8	LL030808623122.036	INPUT/main_runs/DDT/DDT55/P2WR5C10-DDT55-03.in	RADPRO v4.0	
6.2-9	LL030808623122.036	INPUT/initialization_runs/DDT/DDT55/P2WR5C10-DDT55-01v.in	RADPRO v4.0	
6.2-10	LL030808623122.036	INPUT/main_runs/DDT/DDT55/P2WR5C10-DDT55-03.in	RADPRO v4.0	
6.2-11	LL040310323122.044	Submodel_input_files_listing/P2WR5C10-LDTH55-mi-mkt-14.in	RADPRO v4.0	
6.2-12	LL040310323122.044	Submodel_input_files/P2WR5C10-DDT55_nat-bkfl-11.in	RADPRO v4.0	
6.3-1	LL030808623122.036	INPUT/main_runs/SMT/tspa03.mesh03-150w	MATLAB v6.1.0.450 (R12.1)	
6.3-2	LL030808523122.035	MSTHAC/li_abstractions/OUTPUT/li_P1@/#*:*:1.ext.gz MSTHAC/li_abstractions/OUTPUT/li_P2e@/#*:*:1.ext.gz MSTHAC/li_abstractions/OUTPUT/li_P2w@/#*:*:1.ext.gz MSTHAC/li_abstractions/OUTPUT/li_P3@/#*:*:1.ext.gz MSTHAC/li_abstractions/OUTPUT/li_P5@/#*:*:1.ext.gz MSTHAC/mi_abstractions/OUTPUT/mi_P1@/#*:*:1.ext.gz MSTHAC/mi_abstractions/OUTPUT/mi_P2e@/#*:*:1.ext.gz	XTOOL v10.1	

Table XIII-1. List of Data Sources for Figures (Continued)

Figure No.	Data Source	File Name	Plotting Software	Notes
		MSTHAC/mi_abstractions/OUTPUT/mi_P2w@r#*:*:1.ext.gz		
		MSTHAC/mi_abstractions/OUTPUT/mi_P3@r#*:*:1.ext.gz		
		MSTHAC/mi_abstractions/OUTPUT/mi_P5@r#*:*:1.ext.gz		
		MSTHAC/ui_abstractions/OUTPUT/ui_P1@r#*:*:1.ext.gz		
		MSTHAC/ui_abstractions/OUTPUT/ui_P2e@r#*:*:1.ext.gz		
		MSTHAC/ui_abstractions/OUTPUT/ui_P2w@r#*:*:1.ext.gz		
		MSTHAC/ui_abstractions/OUTPUT/ui_P3@r#*:*:1.ext.gz		
		MSTHAC/ui_abstractions/OUTPUT/ui_P5@r#*:*:1.ext.gz		
6.3-3	LL030808523122.035	MSTHAC/mi_abstractions/OUTPUT/mi_P1@r#*:*:1.ext.gz	Tecplot v9.2-0-3 (09-16-2002)	
		MSTHAC/mi_abstractions/OUTPUT/mi_P2e@r#*:*:1.ext.gz		
		MSTHAC/mi_abstractions/OUTPUT/mi_P2w@r#*:*:1.ext.gz		
		MSTHAC/mi_abstractions/OUTPUT/mi_P3@r#*:*:1.ext.gz		
		MSTHAC/mi_abstractions/OUTPUT/mi_P5@r#*:*:1.ext.gz		
6.3-4	LL030808523122.035	MSTHAC/li_abstractions/OUTPUT/li_P1@r#*:*:1.ext.gz (a)	XTOOL v10.1	
		MSTHAC/li_abstractions/OUTPUT/li_P2e@r#*:*:1.ext.gz (a)		
		MSTHAC/li_abstractions/OUTPUT/li_P2w@r#*:*:1.ext.gz (a)		
		MSTHAC/li_abstractions/OUTPUT/li_P3@r#*:*:1.ext.gz (a)		
		MSTHAC/li_abstractions/OUTPUT/li_P5@r#*:*:1.ext.gz (a)		
		MSTHAC/mi_abstractions/OUTPUT/mi_P1@r#*:*:1.ext.gz (a)		
		MSTHAC/mi_abstractions/OUTPUT/mi_P2e@r#*:*:1.ext.gz (a)		
		MSTHAC/mi_abstractions/OUTPUT/mi_P2w@r#*:*:1.ext.gz (a)		
		MSTHAC/mi_abstractions/OUTPUT/mi_P3@r#*:*:1.ext.gz (a)		
		MSTHAC/mi_abstractions/OUTPUT/mi_P5@r#*:*:1.ext.gz (a)		
		MSTHAC/ui_abstractions/OUTPUT/ui_P1@r#*:*:1.ext.gz (a)		
		MSTHAC/ui_abstractions/OUTPUT/ui_P2e@r#*:*:1.ext.gz (a)		
		MSTHAC/ui_abstractions/OUTPUT/ui_P2w@r#*:*:1.ext.gz (a)		
		MSTHAC/ui_abstractions/OUTPUT/ui_P3@r#*:*:1.ext.gz (a)		
		MSTHAC/ui_abstractions/OUTPUT/ui_P5@r#*:*:1.ext.gz (a)		
		MSTHAC/li_abstractions/OUTPUT/li_P1@r#*:*:1_T_horizontalPillar_Xdist.ext.gz (b)		

Table XIII-1. List of Data Sources for Figures (Continued)

Figure No.	Data Source	File Name	Plotting Software	Notes
		MSTHAC/li_abstractions/OUTPUT/li_P2e@/#*:*:1_T_horizontalPillar_Xdist.ext.gz (b) MSTHAC/li_abstractions/OUTPUT/li_P2w@/#*:*:1_T_horizontalPillar_Xdist.ext.gz (b) MSTHAC/li_abstractions/OUTPUT/li_P3@/#*:*:1_T_horizontalPillar_Xdist.ext.gz (b) MSTHAC/li_abstractions/OUTPUT/li_P5@/#*:*:1_T_horizontalPillar_Xdist.ext.gz (b) MSTHAC/mi_abstractions/OUTPUT/mi_P1@/#*:*:1_T_horizontalPillar_Xdist.ext.gz (b) MSTHAC/mi_abstractions/OUTPUT/mi_P2e@/#*:*:1_T_horizontalPillar_Xdist.ext.gz (b) MSTHAC/mi_abstractions/OUTPUT/mi_P2w@/#*:*:1_T_horizontalPillar_Xdist.ext.gz (b) MSTHAC/mi_abstractions/OUTPUT/mi_P3@/#*:*:1_T_horizontalPillar_Xdist.ext.gz (b) MSTHAC/mi_abstractions/OUTPUT/mi_P5@/#*:*:1_T_horizontalPillar_Xdist.ext.gz (b) MSTHAC/ui_abstractions/OUTPUT/ui_P1@/#*:*:1_T_horizontalPillar_Xdist.ext.gz (b) MSTHAC/ui_abstractions/OUTPUT/ui_P2e@/#*:*:1_T_horizontalPillar_Xdist.ext.gz (b) MSTHAC/ui_abstractions/OUTPUT/ui_P2w@/#*:*:1_T_horizontalPillar_Xdist.ext.gz (b) MSTHAC/ui_abstractions/OUTPUT/ui_P3@/#*:*:1_T_horizontalPillar_Xdist.ext.gz (b) MSTHAC/ui_abstractions/OUTPUT/ui_P5@/#*:*:1_T_horizontalPillar_Xdist.ext.gz (b)		
6.3-5	LL030808523122.035	MSTHAC/mi_abstractions/OUTPUT/mi_P1@/#*:*:1.ext.gz MSTHAC/mi_abstractions/OUTPUT/mi_P2e@/#*:*:1.ext.gz MSTHAC/mi_abstractions/OUTPUT/mi_P2w@/#*:*:1.ext.gz MSTHAC/mi_abstractions/OUTPUT/mi_P3@/#*:*:1.ext.gz MSTHAC/mi_abstractions/OUTPUT/mi_P5@/#*:*:1.ext.gz	Tecplot v9.2-0-3 (09-16-2002)	
6.3-6	LL030808523122.035	MSTHAC/mi_abstractions/OUTPUT/mi_P1@/#*:*:1_T_horizontalPillar_Xdist.ext.gz MSTHAC/mi_abstractions/OUTPUT/mi_P2e@/#*:*:1_T_horizontalPillar_Xdist.ext.gz MSTHAC/mi_abstractions/OUTPUT/mi_P2w@/#*:*:1_T_horizontalPillar_Xdist.ext.gz MSTHAC/mi_abstractions/OUTPUT/mi_P3@/#*:*:1_T_horizontalPillar_Xdist.ext.gz MSTHAC/mi_abstractions/OUTPUT/mi_P5@/#*:*:1_T_horizontalPillar_Xdist.ext.gz	Tecplot v9.2-0-3 (09-16-2002)	
6.3-7	LL030808523122.035	MSTHAC/li_abstractions/OUTPUT/li_P2e@/#111:46:1.ext.gz MSTHAC/mi_abstractions/OUTPUT/mi_P2e@/#111:46:1.ext.gz MSTHAC/ui_abstractions/OUTPUT/ui_P2e@/#111:46:1.ext.gz	XTOOL v10.1	

Table XIII-1. List of Data Sources for Figures (Continued)

Figure No.	Data Source	File Name	Plotting Software	Notes
6.3-8	LL030808523122.035	MSTHAC/li_abstractions/OUTPUT/li_P2w@r#94:46:1.ext.gz MSTHAC/mi_abstractions/OUTPUT/mi_P2w@r#94:46:1.ext.gz MSTHAC/ui_abstractions/OUTPUT/ui_P2w@r#94:46:1.ext.gz	XTOOL v10.1	
6.3-9	LL030808523122.035	MSTHAC/li_abstractions/OUTPUT/li_P2w@r#79:55:1.ext.gz MSTHAC/mi_abstractions/OUTPUT/mi_P2w@r#79:55:1.ext.gz MSTHAC/ui_abstractions/OUTPUT/ui_P2w@r#79:55:1.ext.gz	XTOOL v10.1	
6.3-10	LL030808523122.035	MSTHAC/li_abstractions/OUTPUT/li_P3@r#51:49:1.ext.gz MSTHAC/mi_abstractions/OUTPUT/mi_P3@r#51:49:1.ext.gz MSTHAC/ui_abstractions/OUTPUT/ui_P3@r#51:49:1.ext.gz	XTOOL v10.1	
6.3-11	LL030808523122.035	MSTHAC/li_abstractions/OUTPUT/li_P3@r#33:46:1.ext.gz MSTHAC/mi_abstractions/OUTPUT/mi_P3@r#33:46:1.ext.gz MSTHAC/ui_abstractions/OUTPUT/ui_P3@r#33:46:1.ext.gz	XTOOL v10.1	
6.3-12	LL030808523122.035	MSTHAC/mi_abstractions/OUTPUT/mi_P2e@r#111:46:1.ext.gz	XTOOL v10.1	
6.3-13	LL030808523122.035	MSTHAC/mi_abstractions/OUTPUT/mi_P2w@r#94:46:1.ext.gz	XTOOL v10.1	
6.3-14	LL030808523122.035	MSTHAC/mi_abstractions/OUTPUT/mi_P2w@r#79:55:1.ext.gz	XTOOL v10.1	
6.3-15	LL030808523122.035	MSTHAC/mi_abstractions/OUTPUT/mi_P3@r#51:49:1.ext.gz	XTOOL v10.1	
6.3-16	LL030808523122.035	MSTHAC/mi_abstractions/OUTPUT/mi_P3@r#33:46:1.ext.gz	XTOOL v10.1	
6.3-17	LL030804023122.034	mi-mkt/P2ER8C6/mi-mkt-P2ER8C6.ext.gz mi-mkt/P2ER8C6_EXT/mi-mkt-P2ER8C6.ext.gz	XTOOL v10.1	
6.3-18	LL030804023122.034	mi-mkt/P2WR8C8/mi-mkt-P2WR8C8.ext.gz mi-mkt/P2WR8C8_EXT/mi-mkt-P2WR8C8.ext.gz	XTOOL v10.1	
6.3-19	LL030804023122.034	mi-mkt/P2WR5C10/mi-mkt-P2WR5C10.ext.gz mi-mkt/P2WR5C10_EXT/mi-mkt-P2WR5C10.ext.gz	XTOOL v10.1	
6.3-20	LL030804023122.034	mi-mkt/P3R8C13/mi-mkt-P3R8C13.ext.gz mi-mkt/P3R8C13_EXT/mi-mkt-P3R8C13.ext.gz	XTOOL v10.1	

Table XIII-1.   List of Data Sources for Figures (Continued)

Figure No.	Data Source	File Name	Plotting Software	Notes
6.3-21	LL030804023122.034	dp-mkt/P2ER8C6/dp-mkt-P2ER8C6.ext.gz mi-mkt/P2ER8C6/mi-mkt-P2ER8C6.ext.gz fp-mkt/ P2ER8C6/fp-mkt-P2ER8C6.ext.gz	XTOOL v10.1	
6.3-22	LL030804023122.034	dp-mkt/P2WR8C8/dp-mkt-P2WR8C8.ext.gz mi-mkt/P2WR8C8/mi-mkt-P2WR8C8.ext.gz fp-mkt/ P2WR8C8/fp-mkt-P2WR8C8.ext.gz	XTOOL v10.1	
6.3-23	LL030804023122.034	dp-mkt/P2WR5C10/dp-mkt-P2WR5C10.ext.gz mi-mkt/P2WR5C10/mi-mkt-P2WR5C10.ext.gz fp-mkt/ P2WR5C10/fp-mkt-P2WR5C10.ext.gz	XTOOL v10.1	
6.3-24	LL030804023122.034	dp-mkt/P3R8C13/dp-mkt-P3R8C13.ext.gz mi-mkt/P3R8C13/mi-mkt-P3R8C13.ext.gz fp-mkt/ P3R8C13/fp-mkt-P3R8C13.ext.gz	XTOOL v10.1	
6.3-25	LL030804023122.034	mi-1lkt/P2ER8C6/mi-1lkt-P2ER8C6.ext.gz mi-mkt/P2ER8C6/mi-mkt-P2ER8C6.ext.gz mi-1hkt/P2ER8C6/mi-1hkt-P2ER8C6.ext.gz	XTOOL v10.1	
6.3-26	LL030804023122.034	mi-1lkt/P2WR8C8/mi-1lkt-P2WR8C8.ext.gz mi-mkt/P2WR8C8/mi-mkt-P2WR8C8.ext.gz mi-1hkt/P2WR8C8/mi-1hkt-P2WR8C8.ext.gz	XTOOL v10.1	
6.3-27	LL030804023122.034	mi-1lkt/P2WR5C10/mi-1lkt-P2WR5C10.ext.gz mi-mkt/P2WR5C10/mi-mkt-P2WR5C10.ext.gz mi-1hkt/P2WR5C10/mi-1hkt-P2WR5C10.ext.gz	XTOOL v10.1	
6.3-28	LL030804023122.034	mi-1lkt/P3R8C13/mi-1lkt-P3R8C13.ext.gz mi-mkt/P3R8C13/mi-mkt-P3R8C13.ext.gz mi-1hkt/P3R8C13/mi-1hkt-P3R8C13.ext.gz	XTOOL v10.1	
6.3-29	LL030804023122.034	dp-1lkt/P2ER8C6/dp-1lkt-P2ER8C6.ext.gz mi-mkt/P2ER8C6/mi-mkt-P2ER8C6.ext.gz fp-1hkt/ P2ER8C6/fp-1hkt-P2ER8C6.ext.gz	XTOOL v10.1	

Table XIII-1.   List of Data Sources for Figures (Continued)

Figure No.	Data Source	File Name	Plotting Software	Notes
6.3-30	LL030804023122.034	dp-1lkt/P2WR8C8/dp-1lkt-P2WR8C8.ext.gz mi-mkt/P2WR8C8/mi-mkt-P2WR8C8.ext.gz fp-1hkt/ P2WR8C8/fp-1hkt-P2WR8C8.ext.gz	XTOOL v10.1	
6.3-31	LL030804023122.034	dp-1lkt/P2WR5C10/dp-1lkt-P2WR5C10.ext.gz mi-mkt/P2WR5C10/mi-mkt-P2WR5C10.ext.gz fp-1hkt/ P2WR5C10/fp-1hkt-P2WR5C10.ext.gz	XTOOL v10.1	
6.3-32	LL030804023122.034	dp-1lkt/P3R8C13/dp-1lkt-P3R8C13.ext.gz mi-mkt/P3R8C13/mi-mkt-P3R8C13.ext.gz fp-1hkt/ P3R8C13/fp-1hkt-P3R8C13.ext.gz	XTOOL v10.1	
6.3-33	LL040102223122.042	01/P2ER8C6-LDTH55-1Dds_mc-li-01.m.EBS.ext (a) 01/P2ER8C6-LDTH55-1Dds_mc-li-01.f.EBS.ext (c) 02/P2ER8C6-LDTH55-1Dds_mc-li-02.m.EBS.ext (a) 02/P2ER8C6-LDTH55-1Dds_mc-li-02.f.EBS.ext (c) 01/P2ER8C6-LDTH55-1Dds_mc-ui-01.m.EBS.ext (b) 01/P2ER8C6-LDTH55-1Dds_mc-ui-01.f.EBS.ext (d) 02/P2ER8C6-LDTH55-1Dds_mc-ui-02.m.EBS.ext (b) 02/P2ER8C6-LDTH55-1Dds_mc-ui-02.f.EBS.ext (d)	XTOOL v10.1	T_{ds} at upper drip-shield gridblock RH_{ds} at drift block above upper drip-shield block
6.3-34	LL040102223122.042	01/P2WR8C8-LDTH55-1Dds_mc-li-01.m.EBS.ext (a) 01/P2WR8C8-LDTH55-1Dds_mc-li-01.f.EBS.ext (c) 02/P2WR8C8-LDTH55-1Dds_mc-li-02.m.EBS.ext (a) 02/P2WR8C8-LDTH55-1Dds_mc-li-02.f.EBS.ext (c) 01/P2WR8C8-LDTH55-1Dds_mc-ui-01.m.EBS.ext (b) 01/P2WR8C8-LDTH55-1Dds_mc-ui-01.f.EBS.ext (d) 02/P2WR8C8-LDTH55-1Dds_mc-li-02.m.EBS.ext (b) 02/P2WR8C8-LDTH55-1Dds_mc-li-02.f.EBS.ext (d)	XTOOL v10.1	T_{ds} at upper drip-shield gridblock RH_{ds} at drift block above upper drip-shield block

Table XIII-1. List of Data Sources for Figures (Continued)

Figure No.	Data Source	File Name	Plotting Software	Notes
6.3-35	LL040102223122.042	01/P2WR5C10-LDTH55-1Dds_mc-li-01.m.EBS.ext (a) 01/P2WR5C10-LDTH55-1Dds_mc-li-01.f.EBS.ext (c) 02/P2WR5C10-LDTH55-1Dds_mc-li-02.m.EBS.ext (a) 02/P2WR5C10-LDTH55-1Dds_mc-li-02.f.EBS.ext (c) 01/P2WR5C10-LDTH55-1Dds_mc-ui-01.m.EBS.ext (b) 01/P2WR5C10-LDTH55-1Dds_mc-ui-01.f.EBS.ext (d) 02/P2WR5C10-LDTH55-1Dds_mc-ui-02.m.EBS.ext (b) 02/P2WR5C10-LDTH55-1Dds_mc-ui-02.f.EBS.ext (d)	XTOOL v10.1	T_{ds} at upper drip-shield gridblock RH_{ds} at drift block above upper drip-shield block
6.3-36	LL040102223122.042	01/P3R8C13-LDTH55-1Dds_mc-li-01.m.EBS.ext (a) 01/P3R8C13-LDTH55-1Dds_mc-li-01.f.EBS.ext (c) 02/P3R8C13-LDTH55-1Dds_mc-li-02.m.EBS.ext (a) 02/P3R8C13-LDTH55-1Dds_mc-li-02.f.EBS.ext (c) 01/P3R8C13-LDTH55-1Dds_mc-ui-01.m.EBS.ext (b) 01/P3R8C13-LDTH55-1Dds_mc-ui-01.f.EBS.ext (d) 02/P3R8C13-LDTH55-1Dds_mc-ui-02.m.EBS.ext (b) 02/P3R8C13-LDTH55-1Dds_mc-ui-02.f.EBS.ext (d)	XTOOL v10.1	T_{ds} at upper drip-shield gridblock RH_{ds} at drift block above upper drip-shield block
6.3-37	LL040703123122.049	base-case_output/P2ER8C6-LDTH55-mi-mkt-02Q.m.EBS.ex.gz (matrix) base-case_output/P2ER8C6-LDTH55-mi-mkt-02Q.f.EBS.ext.gz (fracture)	MATLAB v6.1.0.450 (R12.1)	
6.3-38	LL040703123122.049	base-case_output/P2ER8C6-LDTH55-mi-mkt-02Q.m.EBS.ext.gz (matrix) base-case_output/P2ER8C6-LDTH55-mi-mkt-02Q.f.EBS.ext.gz (fracture)	MATLAB v6.1.0.450 (R12.1)	
6.3-39	LL040703123122.049	base-case_output/P2WR8C8-LDTH55-mi-mkt-02Q.m.EBS.ext.gz (matrix) base-case_output/P2WR8C8-LDTH55-mi-mkt-02Q.f.EBS.ext.gz (fracture)	MATLAB v6.1.0.450 (R12.1)	
6.3-40	LL040703123122.049	base-case_output/P2WR8C8-LDTH55-mi-mkt-02Q.m.EBS.ext.gz (matrix) base-case_output/P2WR8C8-LDTH55-mi-mkt-02Q.f.EBS.ext.gz (fracture)	MATLAB v6.1.0.450 (R12.1)	

Table XIII-1.   List of Data Sources for Figures (Continued)

Figure No.	Data Source	File Name	Plotting Software	Notes
6.3-41	LL040703123122.049	base-case_output/P2WR5C10-LDTH55-mi-mkt-02Q.m.EBS.ext.gz (matrix) base-case_output/P2WR5C10-LDTH55-mi-mkt-02Q.f.EBS.ext.gz (fracture)	MATLAB v6.1.0.450 (R12.1)	
6.3-42	LL040703123122.049	base-case_output/P2WR5C10-LDTH55-mi-mkt-02Q.m.EBS.ext.gz (matrix) base-case_output/P2WR5C10-LDTH55-mi-mkt-02Q.f.EBS.ext.gz (fracture)	MATLAB v6.1.0.450 (R12.1)	
6.3-43	LL040703123122.049	base-case_output/P3R8C13-LDTH55-mi-mkt-02Q.m.EBS.ext.gz (matrix) base-case_output/P3R8C13-LDTH55-mi-mkt-02Q.f.EBS.ext.gz (fracture)	MATLAB v6.1.0.450 (R12.1)	
6.3-44	LL040703123122.049	base-case_output/P3R8C13-LDTH55-mi-mkt-02Q.m.EBS.ext.gz (matrix) base-case_output/P3R8C13-LDTH55-mi-mkt-02Q.f.EBS.ext.gz (fracture)	MATLAB v6.1.0.450 (R12.1)	
6.3-45	LL040703123122.049	base-case_output/P2ER8C6-LDTH55-mi-mkt-02Q.m.EBS.ext.gz (matrix) base-case_output/P2ER8C6-LDTH55-mi-mkt-02Q.f.EBS.ext.gz (fracture) base-case_output/P2WR8C8-LDTH55-mi-mkt-02Q.m.EBS.ext.gz (matrix) base-case_output/P2WR8C8-LDTH55-mi-mkt-02Q.f.EBS.ext.gz (fracture) base-case_output/P2WR5C10-LDTH55-mi-mkt-02Q.m.EBS.ext.gz (matrix) base-case_output/P2WR5C10-LDTH55-mi-mkt-02Q.f.EBS.ext.gz (fracture) base-case_output/P3R8C13-LDTH55-mi-mkt-02Q.m.EBS.ext.gz (matrix) base-case_output/P3R8C13-LDTH55-mi-mkt-02Q.f.EBS.ext.gz (fracture)	MATLAB v6.1.0.450 (R12.1)	
6.3-46	LL040703123122.049	base-case_output/P2ER8C6-LDTH55-mi-mkt-02Q.m.EBS.ext.gz (matrix) base-case_output/P2ER8C6-LDTH55-mi-mkt-02Q.f.EBS.ext.gz (fracture)	MATLAB v6.1.0.450 (R12.1)	
6.3-47	LL040703123122.049	base-case_output/P2WR8C8-LDTH55-mi-mkt-02Q.m.EBS.ext.gz (matrix) base-case_output/P2WR8C8-LDTH55-mi-mkt-02Q.f.EBS.ext.gz (fracture)	MATLAB v6.1.0.450 (R12.1)	
6.3-48	LL040703123122.049	base-case_output/P2WR5C10-LDTH55-mi-mkt-02Q.m.EBS.ext.gz (matrix) base-case_output/P2WR5C10-LDTH55-mi-mkt-02Q.f.EBS.ext.gz (fracture)	MATLAB v6.1.0.450 (R12.1)	
6.3-49	LL040703123122.049	base-case_output/P3R8C13-LDTH55-mi-mkt-02Q.m.EBS.ext.gz (matrix) base-case_output/P3R8C13-LDTH55-mi-mkt-02Q.f.EBS.ext.gz (fracture)	MATLAB v6.1.0.450 (R12.1)	

Table XIII-1. List of Data Sources for Figures (Continued)

Figure No.	Data Source	File Name	Plotting Software	Notes
6.3-51	LL030808523122.035 LL030905931032.001 LL030906331032.004	From LL030808523122.035: MSTHAC/li_abstractions/OUTPUT/li_P1@/#*:*:.1.ext.gz MSTHAC/li_abstractions/OUTPUT/li_P2e@/#*:*:.1.ext.gz MSTHAC/li_abstractions/OUTPUT/li_P2w@/#*:*:.1.ext.gz MSTHAC/li_abstractions/OUTPUT/li_P3@/#*:*:.1.ext.gz MSTHAC/li_abstractions/OUTPUT/li_P5@/#*:*:.1.ext.gz MSTHAC/mi_abstractions/OUTPUT/mi_P1@/#*:*:.1.ext.gz MSTHAC/mi_abstractions/OUTPUT/mi_P2e@/#*:*:.1.ext.gz MSTHAC/mi_abstractions/OUTPUT/mi_P2w@/#*:*:.1.ext.gz MSTHAC/mi_abstractions/OUTPUT/mi_P3@/#*:*:.1.ext.gz MSTHAC/mi_abstractions/OUTPUT/mi_P5@/#*:*:.1.ext.gz MSTHAC/ui_abstractions/OUTPUT/ui_P1@/#*:*:.1.ext.gz MSTHAC/ui_abstractions/OUTPUT/ui_P2e@/#*:*:.1.ext.gz MSTHAC/ui_abstractions/OUTPUT/ui_P2w@/#*:*:.1.ext.gz MSTHAC/ui_abstractions/OUTPUT/ui_P3@/#*:*:.1.ext.gz MSTHAC/ui_abstractions/OUTPUT/ui_P5@/#*:*:.1.ext.gz From LL030905931032.001: /post_process/createCCDFS/LI-lkt_CCDF.txt MSTHAC_abstraction/MSTHAC_output/LI-lkt_P1@/#*:*:.1.ext.gz MSTHAC_abstraction/MSTHAC_output/LI-lkt_P2e@/#*:*:.1.ext.gz MSTHAC_abstraction/MSTHAC_output/LI-lkt_P2w@/#*:*:.1.ext.gz MSTHAC_abstraction/MSTHAC_output/LI-lkt_P3@/#*:*:.1.ext.gz MSTHAC_abstraction/MSTHAC_output/LI-lkt_P5@/#*:*:.1.ext.gz From LL030906331032.004: /post_process/createCCDFS/UI-hkt_CCDF.txt MSTHAC_abstraction/MSTHAC_output/UI-hkt_P1@/#*:*:.1.ext.gz	XTOOL v10.1	

Table XIII-1. List of Data Sources for Figures (Continued)

Figure No.	Data Source	File Name	Plotting Software	Notes
		MSTHAC_abstraction/MSTHAC_output/UI-hkt_P2e@r#*:*:1.ext.gz		
		MSTHAC_abstraction/MSTHAC_output/UI-hkt_P2w@r#*:*:1.ext.gz		
		MSTHAC_abstraction/MSTHAC_output/UI-hkt_P3@r#*:*:1.ext.gz		
		MSTHAC_abstraction/MSTHAC_output/UI-hkt_P5@r#*:*:1.ext.gz		
6.3-52	LL030808523122.035 LL030905931032.001 LL030906331032.004	From LL030808523122.035:	XTOOL v10.1	
		MSTHAC/li_abstractions/OUTPUT/li_P1@r#*:*:1.ext.gz (a)		
		MSTHAC/li_abstractions/OUTPUT/li_P2e@r#*:*:1.ext.gz (a)		
		MSTHAC/li_abstractions/OUTPUT/li_P2w@r#*:*:1.ext.gz (a)		
		MSTHAC/li_abstractions/OUTPUT/li_P3@r#*:*:1.ext.gz (a)		
		MSTHAC/li_abstractions/OUTPUT/li_P5@r#*:*:1.ext.gz (a)		
		MSTHAC/mi_abstractions/OUTPUT/mi_P1@r#*:*:1.ext.gz (a)		
		MSTHAC/mi_abstractions/OUTPUT/mi_P2e@r#*:*:1.ext.gz (a)		
		MSTHAC/mi_abstractions/OUTPUT/mi_P2w@r#*:*:1.ext.gz (a)		
		MSTHAC/mi_abstractions/OUTPUT/mi_P3@r#*:*:1.ext.gz (a)		
		MSTHAC/mi_abstractions/OUTPUT/mi_P5@r#*:*:1.ext.gz (a)		
		MSTHAC/ui_abstractions/OUTPUT/ui_P1@r#*:*:1.ext.gz (a)		
		MSTHAC/ui_abstractions/OUTPUT/ui_P2e@r#*:*:1.ext.gz (a)		
		MSTHAC/ui_abstractions/OUTPUT/ui_P2w@r#*:*:1.ext.gz (a)		
		MSTHAC/ui_abstractions/OUTPUT/ui_P3@r#*:*:1.ext.gz (a)		
		MSTHAC/ui_abstractions/OUTPUT/ui_P5@r#*:*:1.ext.gz (a)		
		From LL030905931032.001:		
		/post_process/createCCDFS/LI-lkt_CCDF.txt		
		MSTHAC_abstraction/MSTHAC_output/LI-lkt_P1@r#*:*:1.ext.gz (a)		
		MSTHAC_abstraction/MSTHAC_output/LI-lkt_P2e@r#*:*:1.ext.gz (a)		
		MSTHAC_abstraction/MSTHAC_output/LI-lkt_P2w@r#*:*:1.ext.gz (a)		
		MSTHAC_abstraction/MSTHAC_output/LI-lkt_P3@r#*:*:1.ext.gz (a)		
		MSTHAC_abstraction/MSTHAC_output/LI-lkt_P5@r#*:*:1.ext.gz (a)		

Table XIII-1.   List of Data Sources for Figures (Continued)

Figure No.	Data Source	File Name	Plotting Software	Notes
		From LL030906331032.004: /post_process/createCCDFS/UI-hkt_CCDF.txt MSTHAC_abstraction/MSTHAC_output/UI-hkt_P1@#*:*:1.ext.gz (a) MSTHAC_abstraction/MSTHAC_output/UI-hkt_P2e@#*:*:1.ext.gz (a) MSTHAC_abstraction/MSTHAC_output/UI-hkt_P2w@#*:*:1.ext.gz (a) MSTHAC_abstraction/MSTHAC_output/UI-hkt_P3@#*:*:1.ext.gz (a) MSTHAC_abstraction/MSTHAC_output/UI-hkt_P5@#*:*:1.ext.gz (a) From LL030808523122.035: MSTHAC/li_abstractions/OUTPUT/li_P1@#*:*:1_T_horizontalPillar_Xdist.ext.gz (b) MSTHAC/li_abstractions/OUTPUT/li_P2e@#*:*:1_T_horizontalPillar_Xdist.ext.gz (b) MSTHAC/li_abstractions/OUTPUT/li_P2w@#*:*:1_T_horizontalPillar_Xdist.ext.gz (b) MSTHAC/li_abstractions/OUTPUT/li_P3@#*:*:1_T_horizontalPillar_Xdist.ext.gz (b) MSTHAC/li_abstractions/OUTPUT/li_P5@#*:*:1_T_horizontalPillar_Xdist.ext.gz (b) MSTHAC/mi_abstractions/OUTPUT/mi_P1@#*:*:1_T_horizontalPillar_Xdist.ext.gz (b) MSTHAC/mi_abstractions/OUTPUT/mi_P2e@#*:*:1_T_horizontalPillar_Xdist.ext.gz (b) MSTHAC/mi_abstractions/OUTPUT/mi_P2w@#*:*:1_T_horizontalPillar_Xdist.ext.gz (b) MSTHAC/mi_abstractions/OUTPUT/mi_P3@#*:*:1_T_horizontalPillar_Xdist.ext.gz (b) MSTHAC/mi_abstractions/OUTPUT/mi_P5@#*:*:1_T_horizontalPillar_Xdist.ext.gz (b) MSTHAC/ui_abstractions/OUTPUT/ui_P1@#*:*:1_T_horizontalPillar_Xdist.ext.gz (b) MSTHAC/ui_abstractions/OUTPUT/ui_P2e@#*:*:1_T_horizontalPillar_Xdist.ext.gz (b) MSTHAC/ui_abstractions/OUTPUT/ui_P2w@#*:*:1_T_horizontalPillar_Xdist.ext.gz (b) MSTHAC/ui_abstractions/OUTPUT/ui_P3@#*:*:1_T_horizontalPillar_Xdist.ext.gz (b) MSTHAC/ui_abstractions/OUTPUT/ui_P5@#*:*:1_T_horizontalPillar_Xdist.ext.gz (b) From LL030905931032.001: /post_process/createCCDFS/LI-lkt_CCDF_pillar.txt MSTHAC_abstraction/MSTHAC_output/LI-lkt_P1@#*:*:1_T_horizontalPillar_Xdist.ext.gz (b)		

Table XIII-1. List of Data Sources for Figures (Continued)

Figure No.	Data Source	File Name	Plotting Software	Notes
		MSTHAC_abstraction/MSTHAC_output/LI-lkt_P2e@r#*:*::1_T_horizontalPillar_Xdist.ext.gz (b) MSTHAC_abstraction/MSTHAC_output/LI-lkt_P2w@r#*:*::1_T_horizontalPillar_Xdist.ext.gz (b) MSTHAC_abstraction/MSTHAC_output/LI-lkt_P3@#*:*::1_T_horizontalPillar_Xdist.ext.gz (b) MSTHAC_abstraction/MSTHAC_output/LI-lkt_P5@#*:*::1_T_horizontalPillar_Xdist.ext.gz (b) From LL030906331032.004: /post_process/createCCDFS/UI-hkt_CCDF_pillar.txt MSTHAC_abstraction/MSTHAC_output/UI-hkt_P1@#*:*::1_T_horizontalPillar_Xdist.ext.gz (b) MSTHAC_abstraction/MSTHAC_output/UI-hkt_P2e@#*:*::1_T_horizontalPillar_Xdist.ext.gz (b) MSTHAC_abstraction/MSTHAC_output/UI-hkt_P2w@#*:*::1_T_horizontalPillar_Xdist.ext.gz (b) MSTHAC_abstraction/MSTHAC_output/UI-hkt_P3@#*:*::1_T_horizontalPillar_Xdist.ext.gz (b) MSTHAC_abstraction/MSTHAC_output/UI-hkt_P5@#*:*::1_T_horizontalPillar_Xdist.ext.gz (b)		
6.3-53	LL030808523122.035 LL030905931032.001 LL030906331032.004	From LL030808523122.035: MSTHAC/li_abstractions/OUTPUT/li_P1@#*:*::1.ext.gz MSTHAC/li_abstractions/OUTPUT/li_P2e@#*:*::1.ext.gz MSTHAC/li_abstractions/OUTPUT/li_P2w@#*:*::1.ext.gz MSTHAC/li_abstractions/OUTPUT/li_P3@#*:*::1.ext.gz MSTHAC/li_abstractions/OUTPUT/li_P5@#*:*::1.ext.gz MSTHAC/mi_abstractions/OUTPUT/mi_P1@r#*:*::1.ext.gz MSTHAC/mi_abstractions/OUTPUT/mi_P2e@#*:*::1.ext.gz MSTHAC/mi_abstractions/OUTPUT/mi_P2w@r#*:*::1.ext.gz MSTHAC/mi_abstractions/OUTPUT/mi_P3@#*:*::1.ext.gz	XTOOL v10.1	

Table XIII-1. List of Data Sources for Figures (Continued)

Figure No.	Data Source	File Name	Plotting Software	Notes
		MSTHAC/mi_abstractions/OUTPUT/mi_P5@r#*:*:1.ext.gz		
		MSTHAC/ui_abstractions/OUTPUT/ui_P1@r#*:*:1.ext.gz		
		MSTHAC/ui_abstractions/OUTPUT/ui_P2e@r#*:*:1.ext.gz		
		MSTHAC/ui_abstractions/OUTPUT/ui_P2w@r#*:*:1.ext.gz		
		MSTHAC/ui_abstractions/OUTPUT/ui_P3@r#*:*:1.ext.gz		
		MSTHAC/ui_abstractions/OUTPUT/ui_P5@r#*:*:1.ext.gz		
		From LL030905931032.001:		
		/post_process/createCCDFS/LI-lkt_CCDF.txt		
		MSTHAC_abstraction/MSTHAC_output/LI-lkt_P1@r#*:*:1.ext.gz		
		MSTHAC_abstraction/MSTHAC_output/LI-lkt_P2e@r#*:*:1.ext.gz		
		MSTHAC_abstraction/MSTHAC_output/LI-lkt_P2w@r#*:*:1.ext.gz		
		MSTHAC_abstraction/MSTHAC_output/LI-lkt_P3@r#*:*:1.ext.gz		
		MSTHAC_abstraction/MSTHAC_output/LI-lkt_P5@r#*:*:1.ext.gz		
		From LL030906331032.004:		
		/post_process/createCCDFS/UI-hkt_CCDF.txt		
		MSTHAC_abstraction/MSTHAC_output/UI-hkt_P1@r#*:*:1.ext.gz		
		MSTHAC_abstraction/MSTHAC_output/UI-hkt_P2e@r#*:*:1.ext.gz		
		MSTHAC_abstraction/MSTHAC_output/UI-hkt_P2w@r#*:*:1.ext.gz		
		MSTHAC_abstraction/MSTHAC_output/UI-hkt_P3@r#*:*:1.ext.gz		
		MSTHAC_abstraction/MSTHAC_output/UI-hkt_P5@r#*:*:1.ext.gz		
6.3-54	LL030808523122.035 LL030905931032.001 LL030906331032.004	From LL030808523122.035:	XTOOL v10.1	
		MSTHAC/li_abstractions/OUTPUT/li_P1@r#*:*:1.ext.gz		
		MSTHAC/li_abstractions/OUTPUT/li_P2e@r#*:*:1.ext.gz		
		MSTHAC/li_abstractions/OUTPUT/li_P2w@r#*:*:1.ext.gz		
		MSTHAC/li_abstractions/OUTPUT/li_P3@r#*:*:1.ext.gz		
		MSTHAC/li_abstractions/OUTPUT/li_P5@r#*:*:1.ext.gz		
		MSTHAC/mi_abstractions/OUTPUT/mi_P1@r#*:*:1.ext.gz		

Table XIII-1. List of Data Sources for Figures (Continued)

Figure No.	Data Source	File Name	Plotting Software	Notes
		MSTHAC/mi_abstractions/OUTPUT/mi_P2e@r#*:*:1.ext.gz MSTHAC/mi_abstractions/OUTPUT/mi_P2w@r#*:*:1.ext.gz MSTHAC/mi_abstractions/OUTPUT/mi_P3@r#*:*:1.ext.gz MSTHAC/mi_abstractions/OUTPUT/mi_P5@r#*:*:1.ext.gz MSTHAC/ui_abstractions/OUTPUT/ui_P1@r#*:*:1.ext.gz MSTHAC/ui_abstractions/OUTPUT/ui_P2e@r#*:*:1.ext.gz MSTHAC/ui_abstractions/OUTPUT/ui_P2w@r#*:*:1.ext.gz MSTHAC/ui_abstractions/OUTPUT/ui_P3@r#*:*:1.ext.gz MSTHAC/ui_abstractions/OUTPUT/ui_P5@r#*:*:1.ext.gz From LL030905931032.001: /post_process/createCCDFS/LI-lkt_CCDF.txt MSTHAC_abstraction/MSTHAC_output/LI-lkt_P1@r#*:*:1.ext.gz MSTHAC_abstraction/MSTHAC_output/LI-lkt_P2e@r#*:*:1.ext.gz MSTHAC_abstraction/MSTHAC_output/LI-lkt_P2w@r#*:*:1.ext.gz MSTHAC_abstraction/MSTHAC_output/LI-lkt_P3@r#*:*:1.ext.gz MSTHAC_abstraction/MSTHAC_output/LI-lkt_P5@r#*:*:1.ext.gz From LL030906331032.004: /post_process/createCCDFS/UI-hkt_CCDF.txt MSTHAC_abstraction/MSTHAC_output/UI-hkt_P1@r#*:*:1.ext.gz MSTHAC_abstraction/MSTHAC_output/UI-hkt_P2e@r#*:*:1.ext.gz MSTHAC_abstraction/MSTHAC_output/UI-hkt_P2w@r#*:*:1.ext.gz MSTHAC_abstraction/MSTHAC_output/UI-hkt_P3@r#*:*:1.ext.gz MSTHAC_abstraction/MSTHAC_output/UI-hkt_P5@r#*:*:1.ext.gz		
6.3-55	LL040310323122.044 LL030804023122.034	From LL040310323122.044: MSTHAC_output/P2WR5C10-mi-mkt_nat-bkfl-11-15.ext (low K_{th}) MSTHAC_output/P2WR5C10-mi-mkt_nat-bkfl-10-14.ext (high K_{th})	XTOOL v10.1	

Table XIII-1.   List of Data Sources for Figures (Continued)

Figure No.	Data Source	File Name	Plotting Software	Notes
6.3-56	LL040310323122.044 LL030804023122.034	From LL030804023122.034 mi-mkt/P2WR5C10/mi-mkt-P2WR5C10.ext.gz (Intact drift) From LL040310323122.044: MSTHAC_output/P2WR5C10-mi-mkt_nat-bkfl-11-15.ext (low K_{th}) MSTHAC_output/P2WR5C10-mi-mkt_nat-bkfl-10-14.ext (high K_{th}) From LL030804023122.034: mi-mkt/P2WR5C10/mi-mkt-P2WR5C10.ext.gz (Intact drift)	XTOOL v10.1	
6.3-57	LL040310323122.044 LL030804023122.034	From LL040310323122.044: MSTHAC_output/P2WR5C10-mi-mkt_nat-bkfl-11-15.ext (low K_{th}) MSTHAC_output/P2WR5C10-mi-mkt_nat-bkfl-10-14.ext (high K_{th}) From LL030804023122.034: mi-mkt/P2WR5C10/mi-mkt-P2WR5C10.ext.gz (Intact drift)	XTOOL v10.1	
6.3-58	LL040501323122.046	The following files are found in file: rubble_heat-capacity output files.zip: P2WR5C10-LDTH55-mi-mkt-15.m.EBS.ext (a) P2WR5C10-LDTH55-mi-mkt-17.m.EBS.ext (a) P2WR5C10-LDTH55-mi-mkt-15.f.EBS.ext (b) P2WR5C10-LDTH55-mi-mkt-17.f.EBS.ext (b)	XTOOL v10.1	
6.3-59	LL030808523122.035	MSTHAC/mi_abstractions/OUTPUT/mi_P3@/#51:49:1.ext.gz	XTOOL v10.1	
6.3-60	LL040501323122.046	host-rock_study output_files/P2WR5C10-LDTH55-mi-tsw33-e2-09.m.EBS.ext (a,b) host-rock_study output_files/P2WR5C10-LDTH55-mi-tsw34-e2-09.m.EBS.ext (a,b) host-rock_study output_files/P2WR5C10-LDTH55-mi-tsw35-e2-09.m.EBS.ext (a,b) host-rock_study output_files/P2WR5C10-LDTH55-mi-tsw36-e2-09.m.EBS.ext (a,b) host-rock_study output_files/P2WR5C10-LDTH55-mi-tsw33-e1-09.m.EBS.ext (c,d) host-rock_study output_files/P2WR5C10-LDTH55-mi-tsw34-e1-09.m.EBS.ext (c,d) host-rock_study output_files/P2WR5C10-LDTH55-mi-tsw35-e1-09.m.EBS.ext (c,d) host-rock_study output_files/P2WR5C10-LDTH55-mi-tsw36-e1-09.m.EBS.ext (c,d) host-rock_study output_files/P2WR5C10-LDTH55-mi-tsw33-e-1-09.m.EBS.ext (e,f) host-rock_study output_files/P2WR5C10-LDTH55-mi-tsw34-e-1-09.m.EBS.ext (e,f)	MATLAB v6.1.0.450 (R12.1)	T_{dw} is the grid-block-volume-weighted average for host-rock gridblocks around drift perimeter T_{ds} is the grid-block-volume-weighted average around drip-shield perimeter

Table XIII-1. List of Data Sources for Figures (Continued)

Figure No.	Data Source	File Name	Plotting Software	Notes
6.3-61	LL040501323122.046	host-rock_study output_files/P2WR5C10-LDTH55-mi-tsw35-e-1-09.m.EBS.ext (e,f) host-rock_study output_files/P2WR5C10-LDTH55-mi-tsw36-e-1-09.m.EBS.ext (e,f) host-rock_study output_files/P2WR5C10-LDTH55-mi-tsw33-e-2-09.m.EBS.ext (g,h) host-rock_study output_files/P2WR5C10-LDTH55-mi-tsw34-e-2-09.m.EBS.ext (g,h) host-rock_study output_files/P2WR5C10-LDTH55-mi-tsw35-e-2-09.m.EBS.ext (g,h) host-rock_study output_files/P2WR5C10-LDTH55-mi-tsw36-e-2-09.m.EBS.ext (g,h) host-rock_study output_files/P2WR5C10-LDTH55-mi-tsw33-e2-09.f.EBS.ext (a,b) host-rock_study output_files/P2WR5C10-LDTH55-mi-tsw34-e2-09.f.EBS.ext (a,b) host-rock_study output_files/P2WR5C10-LDTH55-mi-tsw35-e2-09.f.EBS.ext (a,b) host-rock_study output_files/P2WR5C10-LDTH55-mi-tsw36-e2-09.f.EBS.ext (a,b) host-rock_study output_files/P2WR5C10-LDTH55-mi-tsw33-e1-09.f.EBS.ext (c,d) host-rock_study output_files/P2WR5C10-LDTH55-mi-tsw34-e1-09.f.EBS.ext (c,d) host-rock_study output_files/P2WR5C10-LDTH55-mi-tsw35-e1-09.f.EBS.ext (c,d) host-rock_study output_files/P2WR5C10-LDTH55-mi-tsw36-e1-09.f.EBS.ext (c,d) host-rock_study output_files/P2WR5C10-LDTH55-mi-tsw33-e-1-09.f.EBS.ext (e,f) host-rock_study output_files/P2WR5C10-LDTH55-mi-tsw34-e-1-09.f.EBS.ext (e,f) host-rock_study output_files/P2WR5C10-LDTH55-mi-tsw35-e-1-09.f.EBS.ext (e,f) host-rock_study output_files/P2WR5C10-LDTH55-mi-tsw36-e-1-09.f.EBS.ext (e,f) host-rock_study output_files/P2WR5C10-LDTH55-mi-tsw33-e-2-09.f.EBS.ext (g,h) host-rock_study output_files/P2WR5C10-LDTH55-mi-tsw34-e-2-09.f.EBS.ext (g,h) host-rock_study output_files/P2WR5C10-LDTH55-mi-tsw35-e-2-09.f.EBS.ext (g,h) host-rock_study output_files/P2WR5C10-LDTH55-mi-tsw36-e-2-09.f.EBS.ext (g,h)	MATLAB v6.1.0.450 (R12.1)	RH_{dw} is the grid-block-volume-weighted average for host-rock gridblocks around drift perimeter RH_{ds} is the grid-block-volume-weighted average for drift gridblocks around drip-shield perimeter
6.3-62	LL040703123122.049	base-case_output/P2WR5C10-LDTH55-mi-mkt-02Q.m.EBS.ext.gz (a) base-case_output/P2WR5C10-LDTH55-mi-mkt-02Q.f.EBS.ext.gz (b) pseudo-kb_ouput/P2WR5C10-LDTH55-mi-mkt-kbe-12-02.m.EBS.ext.gz (a) pseudo-kb_output/P2WR5C10-LDTH55-mi-mkt-kbe-12-02.f.EBS.ext.gz (b) pseudo-kb_output/P2WR5C10-LDTH55-mi-mkt-kbe-10-02.m.EBS.ext.gz (a) pseudo-kb_output/P2WR5C10-LDTH55-mi-mkt-kbe-10-02.f.EBS.ext.gz (b) pseudo-kb_output/P2WR5C10-LDTH55-mi-mkt-kbe-9-02.m.EBS.ext.gz (a)	XTOOL v10.1	T_{ds} at upper drip-shield gridblock RH_{ds} at drift block above upper drip-shield block

Table XIII-1. List of Data Sources for Figures (Continued)

Figure No.	Data Source	File Name	Plotting Software	Notes
		pseudo-kb_output/P2WR5C10-LDTH55-mi-mkt-kbe-9-02.f.EBS.ext.gz (b) pseudo-kb_output/P2WR5C10-LDTH55-mi-mkt-kbe-7-02.m.EBS.ext.gz (a) pseudo-kb_output/P2WR5C10-LDTH55-mi-mkt-kbe-7-02.f.EBS.ext.gz (b) pseudo-kb_output/P2WR5C10-LDTH55-mi-mkt-kbe-6-02.m.EBS.ext.gz (a) pseudo-kb_output/P2WR5C10-LDTH55-mi-mkt-kbe-6-02.f.EBS.ext.gz (b)		
6.3-63	LL040501323122.046	invert_study output_files/P2WR5C10-LDTH55-mi-mkt_tsw33inv-02.f.EBS.ext (a) invert_study output_files/P2WR5C10-LDTH55-mi-mkt_tsw33inv-02.m.EBS.ext (b) invert_study output_files/P2WR5C10-LDTH55-mi-mkt_tsw34inv-02.f.EBS.ext (a) invert_study output_files/P2WR5C10-LDTH55-mi-mkt_tsw34inv-02.m.EBS.ext (b) invert_study output_files/P2WR5C10-LDTH55-mi-mkt_tsw35inv-02.f.EBS.ext (a) invert_study output_files/P2WR5C10-LDTH55-mi-mkt_tsw35inv-02.m.EBS.ext (b) invert_study output_files/P2WR5C10-LDTH55-mi-mkt_tsw36inv-02.f.EBS.ext (a) invert_study output_files/P2WR5C10-LDTH55-mi-mkt_tsw36inv-02.m.EBS.ext (b)	XTOOL v10.1	$S_{liq,inv}$ is the grid-block-volume-weighted average for the invert gridblocks T_{inv} is the grid-block-volume-weighted average for the invert gridblocks
6.3-64	LL040703123122.049	invert_study_output/P2WR5C10-LDTH55-mi-mkt_tsw33inv-02fninv.m.EBS.ext.gz (a) invert_study_output/P2WR5C10-LDTH55-mi-mkt_tsw33inv-02fninv.f.EBS.ext.gz (b) invert_study_output/P2WR5C10-LDTH55-mi-mkt_tsw34inv-02fninv.m.EBS.ext.gz (c) invert_study_output/P2WR5C10-LDTH55-mi-mkt_tsw34inv-02fninv.f.EBS.ext.gz (d) invert_study_output/P2WR5C10-LDTH55-mi-mkt_tsw35inv-02fninv.m.EBS.ext.gz (e) invert_study_output/P2WR5C10-LDTH55-mi-mkt_tsw35inv-02fninv.f.EBS.ext.gz (f) invert_study_output/P2WR5C10-LDTH55-mi-mkt_tsw36inv-02fninv.m.EBS.ext.gz (g) invert_study_output/P2WR5C10-LDTH55-mi-mkt_tsw36inv-02fninv.f.EBS.ext.gz (h)	XTOOL v10.1	T and RH obtained for center gridblock at upper invert layer below drip shield
6.3-65	LL040703123122.049	invert_study_output/P2WR5C10-LDTH55-mi-mkt_tsw35inv-02fninv.m.EBS.ext.gz (a,b; base case) invert_study_output/P2WR5C10-LDTH55-mi-mkt_case1-02.m.EBS.ext.gz (a,b) invert_study_output/P2WR5C10-LDTH55-mi-mkt_case2-02.m.EBS.ext.gz (a,b) invert_study_output/P2WR5C10-LDTH55-mi-mkt_case3-02.m.EBS.ext.gz (a,b) invert_study_output/P2WR5C10-LDTH55-mi-mkt_case4-02.m.EBS.ext.gz (a,b) invert_study_output/P2WR5C10-LDTH55-mi-mkt_tsw35inv-02fninv.f.EBS.ext.gz (c; base case)	XTOOL v10.1	T and RH obtained for center gridblock at indicated locations

Table XIII-1. List of Data Sources for Figures (Continued)

Figure No.	Data Source	File Name	Plotting Software	Notes
		invert_study_output/P2WR5C10-LDTH55-mi-mkt_case1-02.f.EBS.ext.gz (c) invert_study_output/P2WR5C10-LDTH55-mi-mkt_case2-02.f.EBS.ext.gz (c) invert_study_output/P2WR5C10-LDTH55-mi-mkt_case3-02.f.EBS.ext.gz (c) invert_study_output/P2WR5C10-LDTH55-mi-mkt_case4-02.f.EBS.ext.gz (c)		
6.3-66	LL040703123122.049	base-case_output/P2WR5C10-LDTH55-mi-mkt-02Q.m.EBS.ext.gz (a) base-case_output/P2WR5C10-LDTH55-mi-mkt-02Q.f.EBS.ext.gz (b) vent_study_output/P2WR5C10-LDTH55-mi-mkt-02.in-70p.m.EBS.ext.gz (a) vent_study_output/P2WR5C10-LDTH55-mi-mkt-02.in-70p.f.EBS.ext.gz (b) vent_study_output/P2WR5C10-LDTH55-mi-mkt-02.in-80p.m.EBS.ext.gz (a) vent_study_output/P2WR5C10-LDTH55-mi-mkt-02.in-80p.f.EBS.ext.gz (b) vent_study_output/P2WR5C10-LDTH55-mi-mkt-02.in-90p.m.EBS.ext.gz (a) vent_study_output/P2WR5C10-LDTH55-mi-mkt-02.in-90p.f.EBS.ext.gz (b) vent_study_output/P2WR5C10-LDTH55-mi-mkt-02.in-100p.m.EBS.ext.gz (a) vent_study_output/P2WR5C10-LDTH55-mi-mkt-02.in-100p.f.EBS.ext.gz (b)	XTOOL v10.1	T_{ds} at upper drip-shield gridblock RH_{ds} at drift block above upper drip-shield block
6.3-67	LL030808523122.035 LL030905931032.001 LL030906331032.004	From LL030808523122.035: MSTHAC/li_abstractions/OUTPUT/li_P1@r#*.*:1.ext.gz MSTHAC/li_abstractions/OUTPUT/li_P2e@r#*.*:1.ext.gz MSTHAC/li_abstractions/OUTPUT/li_P2w@r#*.*:1.ext.gz MSTHAC/li_abstractions/OUTPUT/li_P3@r#*.*:1.ext.gz MSTHAC/li_abstractions/OUTPUT/li_P5@r#*.*:1.ext.gz MSTHAC/mi_abstractions/OUTPUT/mi_P1@r#*.*:1.ext.gz MSTHAC/mi_abstractions/OUTPUT/mi_P2e@r#*.*:1.ext.gz MSTHAC/mi_abstractions/OUTPUT/mi_P2w@r#*.*:1.ext.gz MSTHAC/mi_abstractions/OUTPUT/mi_P3@r#*.*:1.ext.gz MSTHAC/mi_abstractions/OUTPUT/mi_P5@r#*.*:1.ext.gz MSTHAC/ui_abstractions/OUTPUT/ui_P1@r#*.*:1.ext.gz MSTHAC/ui_abstractions/OUTPUT/ui_P2e@r#*.*:1.ext.gz MSTHAC/ui_abstractions/OUTPUT/ui_P2w@r#*.*:1.ext.gz MSTHAC/ui_abstractions/OUTPUT/ui_P3@r#*.*:1.ext.gz	MATLAB v6.1.0.450 (R12.1)	

Table XIII-1.   List of Data Sources for Figures (Continued)

Figure No.	Data Source	File Name	Plotting Software	Notes
		MSTHAC/ui_abstractions/OUTPUT/ui_P5@r#*:*:1.ext.gz From LL030905931032.001: /post_process/createCCDFS/LI-lkt_CCDF.txt MSTHAC_abstraction/MSTHAC_output/LI-lkt_P1@r#*:*:1.ext.gz MSTHAC_abstraction/MSTHAC_output/LI-lkt_P2e@r#*:*:1.ext.gz MSTHAC_abstraction/MSTHAC_output/LI-lkt_P2w@r#*:*:1.ext.gz MSTHAC_abstraction/MSTHAC_output/LI-lkt_P3@r#*:*:1.ext.gz MSTHAC_abstraction/MSTHAC_output/LI-lkt_P5@r#*:*:1.ext.gz From LL030906331032.004: /post_process/createCCDFS/UI-hkt_CCDF.txt MSTHAC_abstraction/MSTHAC_output/UI-hkt_P1@r#*:*:1.ext.gz MSTHAC_abstraction/MSTHAC_output/UI-hkt_P2e@r#*:*:1.ext.gz MSTHAC_abstraction/MSTHAC_output/UI-hkt_P2w@r#*:*:1.ext.gz MSTHAC_abstraction/MSTHAC_output/UI-hkt_P3@r#*:*:1.ext.gz MSTHAC_abstraction/MSTHAC_output/UI-hkt_P5@r#*:*:1.ext.gz		
6.3-68	LL030808523122.035 LL030905931032.001 LL030906331032.004	From LL030808523122.035: MSTHAC/li_abstractions/OUTPUT/li_P1@r#*:*:1.ext.gz MSTHAC/li_abstractions/OUTPUT/li_P2e@r#*:*:1.ext.gz MSTHAC/li_abstractions/OUTPUT/li_P2w@r#*:*:1.ext.gz MSTHAC/li_abstractions/OUTPUT/li_P3@r#*:*:1.ext.gz MSTHAC/li_abstractions/OUTPUT/li_P5@r#*:*:1.ext.gz MSTHAC/mi_abstractions/OUTPUT/mi_P1@r#*:*:1.ext.gz MSTHAC/mi_abstractions/OUTPUT/mi_P2e@r#*:*:1.ext.gz MSTHAC/mi_abstractions/OUTPUT/mi_P2w@r#*:*:1.ext.gz MSTHAC/mi_abstractions/OUTPUT/mi_P3@r#*:*:1.ext.gz MSTHAC/mi_abstractions/OUTPUT/mi_P5@r#*:*:1.ext.gz MSTHAC/ui_abstractions/OUTPUT/ui_P1@r#*:*:1.ext.gz	MATLAB v6.1.0.450 (R12.1)	

Table XIII-1. List of Data Sources for Figures (Continued)

Figure No.	Data Source	File Name	Plotting Software	Notes
		MSTHAC/ui_abstractions/OUTPUT/ui_P2e@r#*:*:1.ext.gz MSTHAC/ui_abstractions/OUTPUT/ui_P2w@r#*:*:1.ext.gz MSTHAC/ui_abstractions/OUTPUT/ui_P3@r#*:*:1.ext.gz MSTHAC/ui_abstractions/OUTPUT/ui_P5@r#*:*:1.ext.gz From LL030905931032.001: /post_process/createCCDFS/LI-lkt_CCDF.txt MSTHAC_abstraction/MSTHAC_output/LI-lkt_P1@r#*:*:1.ext.gz MSTHAC_abstraction/MSTHAC_output/LI-lkt_P2e@r#*:*:1.ext.gz MSTHAC_abstraction/MSTHAC_output/LI-lkt_P2w@r#*:*:1.ext.gz MSTHAC_abstraction/MSTHAC_output/LI-lkt_P3@r#*:*:1.ext.gz MSTHAC_abstraction/MSTHAC_output/LI-lkt_P5@r#*:*:1.ext.gz From LL030906331032.004: /post_process/createCCDFS/UI-hkt_CCDF.txt MSTHAC_abstraction/MSTHAC_output/UI-hkt_P1@r#*:*:1.ext.gz MSTHAC_abstraction/MSTHAC_output/UI-hkt_P2e@r#*:*:1.ext.gz MSTHAC_abstraction/MSTHAC_output/UI-hkt_P2w@r#*:*:1.ext.gz MSTHAC_abstraction/MSTHAC_output/UI-hkt_P3@r#*:*:1.ext.gz MSTHAC_abstraction/MSTHAC_output/UI-hkt_P5@r#*:*:1.ext.gz		
6.3-69	LL030808523122.035 LL030905931032.001 LL030906331032.004	From LL030808523122.035: MSTHAC/li_abstractions/OUTPUT/li_P1@r#*:*:1.ext.gz MSTHAC/li_abstractions/OUTPUT/li_P2e@r#*:*:1.ext.gz MSTHAC/li_abstractions/OUTPUT/li_P2w@r#*:*:1.ext.gz MSTHAC/li_abstractions/OUTPUT/li_P3@r#*:*:1.ext.gz MSTHAC/li_abstractions/OUTPUT/li_P5@r#*:*:1.ext.gz MSTHAC/mi_abstractions/OUTPUT/mi_P1@r#*:*:1.ext.gz MSTHAC/mi_abstractions/OUTPUT/mi_P2e@r#*:*:1.ext.gz MSTHAC/mi_abstractions/OUTPUT/mi_P2w@r#*:*:1.ext.gz	MATLAB v6.1.0.450 (R12.1)	

Table XIII-1. List of Data Sources for Figures (Continued)

Figure No.	Data Source	File Name	Plotting Software	Notes
		MSTHAC/mi_abstractions/OUTPUT/mi_P3@r#*:*:1.ext.gz MSTHAC/mi_abstractions/OUTPUT/mi_P5@r#*:*:1.ext.gz MSTHAC/ui_abstractions/OUTPUT/ui_P1@r#*:*:1.ext.gz MSTHAC/ui_abstractions/OUTPUT/ui_P2e@r#*:*:1.ext.gz MSTHAC/ui_abstractions/OUTPUT/ui_P2w@r#*:*:1.ext.gz MSTHAC/ui_abstractions/OUTPUT/ui_P3@r#*:*:1.ext.gz MSTHAC/ui_abstractions/OUTPUT/ui_P5@r#*:*:1.ext.gz From LL030905931032.001: /post_process/createCCDFS/LI-lkt_CCDF.txt MSTHAC_abstraction/MSTHAC_output/LI-lkt_P1@r#*:*:1.ext.gz MSTHAC_abstraction/MSTHAC_output/LI-lkt_P2e@r#*:*:1.ext.gz MSTHAC_abstraction/MSTHAC_output/LI-lkt_P2w@r#*:*:1.ext.gz MSTHAC_abstraction/MSTHAC_output/LI-lkt_P3@r#*:*:1.ext.gz MSTHAC_abstraction/MSTHAC_output/LI-lkt_P5@r#*:*:1.ext.gz From LL030906331032.004: /post_process/createCCDFS/UI-hkt_CCDF.txt MSTHAC_abstraction/MSTHAC_output/UI-hkt_P1@r#*:*:1.ext.gz MSTHAC_abstraction/MSTHAC_output/UI-hkt_P2e@r#*:*:1.ext.gz MSTHAC_abstraction/MSTHAC_output/UI-hkt_P2w@r#*:*:1.ext.gz MSTHAC_abstraction/MSTHAC_output/UI-hkt_P3@r#*:*:1.ext.gz MSTHAC_abstraction/MSTHAC_output/UI-hkt_P5@r#*:*:1.ext.gz		
7.3-1	LL040703023122.048	OUTPUTS/ms-valid-LBT-02.ST.m.ext.gz	XTOOL v10.1	
7.3-2	LL040703023122.048	OUTPUTS/ms-valid-LBT-02.ST.m.ext.gz OUTPUTS/ms-valid-LBT-02.m.P.ext.gz	XTOOL v10.1	
7.4-2	LL030808923122.039	MSTHM_large_block/DST/MAIN_RUN/OUTPUTS/ ms-valid-DST-03.m.ext (base case)	XTOOL v10.1	
7.4-3	LL030808923122.039	MSTHM_large_block/DST/MAIN_RUN/OUTPUTS/ ms-valid-DST-03.m.xyz.T (base case) MSTHM_large_block/DST/BH_SEAL/OUTPUTS/ ms-valid-DST-03-bhSeal.m.xyz.T	XTOOL v10.1	

Table XIII-1. List of Data Sources for Figures (Continued)

Figure No.	Data Source	File Name	Plotting Software	Notes
		(sealed bulkhead) MSTHM_large_block/DST/SENSITIV/OUTPUTS/ ms-valid-DST-sensit-1htk.m.xyz.T (high K_{th}) MSTHM_large_block/DST/SENSITIV_R/OUTPUTS/ ms-valid-DST-sensit-1htkr.m.xyz.T (high K_{th}, restart run)		
7.4-4	LL030808923122.039	MSTHM_large_block/DST/MAIN_RUN/OUTPUTS/ ms-valid-DST-03.m.xyz.T (base case) MSTHM_large_block/DST/BH__SEAL/OUTPUTS/ ms-valid-DST-03-bhSeal.m.xyz.T (sealed bulkhead) MSTHM_large_block/DST/SENSITIV/OUTPUTS/ ms-valid-DST-sensit-1htk.m.xyz.T (high K_{th}) MSTHM_large_block/DST/SENSITIV_R/OUTPUTS/ ms-valid-DST-sensit-1htkr.m.xyz.T (high K_{th}, restart run)	XTOOL v10.1	
7.4-5	LL030808923122.039	MSTHM_large_block/DST/MAIN_RUN/OUTPUTS/ ms-valid-DST-03.m.xyz.T (base case) MSTHM_large_block/DST/BH__SEAL/OUTPUTS/ ms-valid-DST-03-bhSeal.m.xyz.T (sealed bulkhead) MSTHM_large_block/DST/SENSITIV/OUTPUTS/ ms-valid-DST-sensit-1htk.m.xyz.T (high K_{th}) MSTHM_large_block/DST/SENSITIV_R/OUTPUTS/ ms-valid-DST-sensit-1htkr.m.xyz.T (high K_{th}, restart run)	XTOOL v10.1	
7.4-6	LL030808923122.039	MSTHM_large_block/DST/MAIN_RUN/OUTPUTS/ ms-valid-DST-03.m.xyz.T (base case) MSTHM_large_block/DST/BH__SEAL/OUTPUTS/ ms-valid-DST-03-bhSeal.m.xyz.T (sealed bulkhead) MSTHM_large_block/DST/SENSITIV/OUTPUTS/ ms-valid-DST-sensit-1htk.m.xyz.T (high K_{th}) MSTHM_large_block/DST/SENSITIV_R/OUTPUTS/ ms-valid-DST-sensit-1htkr.m.xyz.T (high K_{th}, restart run)	XTOOL v10.1	
7.4-7	LL030808923122.039	MSTHM_large_block/DST/MAIN_RUN/OUTPUTS/ ms-valid-DST-03.m.xyz.T (base case) MSTHM_large_block/DST/BH__SEAL/OUTPUTS/ ms-valid-DST-03-bhSeal.m.xyz.T (sealed bulkhead) MSTHM_large_block/DST/SENSITIV/OUTPUTS/ ms-valid-DST-sensit-1htk.m.xyz.T (high K_{th}) MSTHM_large_block/DST/SENSITIV_R/OUTPUTS/ ms-valid-DST-sensit-1htkr.m.xyz.T (high K_{th}, restart run)	XTOOL v10.1	

Table XIII-1.   List of Data Sources for Figures (Continued)

Figure No.	Data Source	File Name	Plotting Software	Notes
7.4-8	LL030808923122.039	MSTHM_large_block/DST/MAIN_RUN/OUTPUTS/ ms-valid-DST-03.m.xyz.T (base case) MSTHM_large_block/DST/BH__SEAL/OUTPUTS/ ms-valid-DST-03-bhSeal.m.xyz.T (sealed bulkhead) MSTHM_large_block/DST/SENSITIV/OUTPUTS/ ms-valid-DST-sensit-1htk.m.xyz.T (high K_{th}) MSTHM_large_block/DST/SENSITIV_R/OUTPUTS/ ms-valid-DST-sensit-1htkr.m.xyz.T (high K_{th}, restart run)	XTOOL v10.1	
7.4-9	LL030808923122.039	MSTHM_large_block/DST/MAIN_RUN/OUTPUTS/ ms-valid-DST-03.m.xyz.T (base case) MSTHM_large_block/DST/BH__SEAL/OUTPUTS/ ms-valid-DST-03-bhSeal.m.xyz.T (sealed bulkhead) MSTHM_large_block/DST/SENSITIV/OUTPUTS/ ms-valid-DST-sensit-1htk.m.xyz.T (high K_{th}) MSTHM_large_block/DST/SENSITIV_R/OUTPUTS/ ms-valid-DST-sensit-1htkr.m.xyz.T (high K_{th}, restart run)	XTOOL v10.1	
7.4-10	LL030808923122.039	MSTHM_large_block/DST/MAIN_RUN/OUTPUTS/ ms-valid-DST-03.m.xyz.T (base case) MSTHM_large_block/DST/BH__SEAL/OUTPUTS/ ms-valid-DST-03-bhSeal.m.xyz.T (sealed bulkhead) MSTHM_large_block/DST/SENSITIV/OUTPUTS/ ms-valid-DST-sensit-1htk.m.xyz.T (high K_{th}) MSTHM_large_block/DST/SENSITIV_R/OUTPUTS/ ms-valid-DST-sensit-1htkr.m.xyz.T (high K_{th}, restart run)	XTOOL v10.1	
7.4-11	LL030808923122.039	MSTHM_large_block/DST/MAIN_RUN/OUTPUTS/ ms-valid-DST-03.m.xyz.T (base case) MSTHM_large_block/DST/BH__SEAL/OUTPUTS/ ms-valid-DST-03-bhSeal.m.xyz.T (sealed bulkhead) MSTHM_large_block/DST/SENSITIV/OUTPUTS/ ms-valid-DST-sensit-1htk.m.xyz.T (high K_{th}) MSTHM_large_block/DST/SENSITIV_R/OUTPUTS/ ms-valid-DST-sensit-1htkr.m.xyz.T (high K_{th}, restart run)	XTOOL v10.1	
7.4-12	LL030808923122.039	MSTHM_large_block/DST/MAIN_RUN/OUTPUTS/ ms-valid-DST-03.m.xyz.T (base case) MSTHM_large_block/DST/BH__SEAL/OUTPUTS/ ms-valid-DST-03-bhSeal.m.xyz.T (sealed bulkhead) MSTHM_large_block/DST/SENSITIV/OUTPUTS/ ms-valid-DST-sensit-1htk.m.xyz.T (high	XTOOL v10.1	

Table XIII-1. List of Data Sources for Figures (Continued)

Figure No.	Data Source	File Name	Plotting Software	Notes
		K_{th})		
7.4-13	LL030808923122.039	MSTHM_large_block/DST/MAIN_RUN/OUTPUTS/ ms-valid-DST-03.m.xyz.T (base case)	XTOOL v10.1	
		MSTHM_large_block/DST/BH__SEAL/OUTPUTS/ ms-valid-DST-03-bhSeal.m.xyz.T (sealed bulkhead)		
		MSTHM_large_block/DST/SENSITIV/OUTPUTS/ ms-valid-DST-sensit-1htk.m.xyz.T (high K_{th})		
		MSTHM_large_block/DST/SENSITIV_R/OUTPUTS/ ms-valid-DST-sensit-1htkr.m.xyz.T (high K_{th}, restart run)		
7.4-14	LL030808923122.039	MSTHM_large_block/DST/MAIN_RUN/OUTPUTS/ ms-valid-DST-03.m.xyz.T (base case)	XTOOL v10.1	
		MSTHM_large_block/DST/BH__SEAL/OUTPUTS/ ms-valid-DST-03-bhSeal.m.xyz.T (sealed bulkhead)		
		MSTHM_large_block/DST/SENSITIV/OUTPUTS/ ms-valid-DST-sensit-1htk.m.xyz.T (high K_{th})		
		MSTHM_large_block/DST/SENSITIV_R/OUTPUTS/ ms-valid-DST-sensit-1htkr.m.xyz.T (high K_{th}, restart run)		
7.4-15	LL030808923122.039	MSTHM_large_block/DST/MAIN_RUN/OUTPUTS/ ms-valid-DST-03.m.xyz.T (base case)	XTOOL v10.1	
		MSTHM_large_block/DST/BH__SEAL/OUTPUTS/ ms-valid-DST-03-bhSeal.m.xyz.T (sealed bulkhead)		
		MSTHM_large_block/DST/SENSITIV/OUTPUTS/ ms-valid-DST-sensit-1htk.m.xyz.T (high K_{th})		
		MSTHM_large_block/DST/SENSITIV_R/OUTPUTS/ ms-valid-DST-sensit-1htkr.m.xyz.T (high K_{th}, restart run)		
7.4-16	LL030808923122.039	MSTHM_large_block/DST/MAIN_RUN/OUTPUTS/ ms-valid-DST-03.m.ext (base case)	XTOOL v10.1	
7.4-17	LL030808923122.039	MSTHM_large_block/DST/MAIN_RUN/OUTPUTS/ ms-valid-DST-03.m.xyz.S (base case)	XTOOL v10.1	
		MSTHM_large_block/DST/BH__SEAL/OUTPUTS/ ms-valid-DST-03-bhSeal.m.xyz.S (sealed bulkhead)		
		MSTHM_large_block/DST/SENSITIV/OUTPUTS/ ms-valid-DST-sensit-1htk.m.xyz.S (high K_{th})		
		MSTHM_large_block/DST/SENSITIV_R/OUTPUTS/ ms-valid-DST-sensit-1htkr.m.xyz.S (high K_{th}, restart run)		

Table XIII-1. List of Data Sources for Figures (Continued)

Figure No.	Data Source	File Name	Plotting Software	Notes
7.4-18	LL030808923122.039	MSTHM_large_block/DST/MAIN_RUN/OUTPUTS/ ms-valid-DST-03.m.xyz.S (base case) MSTHM_large_block/DST/BH__SEAL/OUTPUTS/ ms-valid-DST-03-bhSeal.m.xyz.S (sealed bulkhead) MSTHM_large_block/DST/SENSITIV/OUTPUTS/ ms-valid-DST-sensit-1htk.m.xyz.S (high K_{th}) MSTHM_large_block/DST/SENSITIV_R/OUTPUTS/ ms-valid-DST-sensit-1htkr.m.xyz.S (high K_{th}, restart run)	XTOOL v10.1	
7.4-19	LL030808923122.039	MSTHM_large_block/DST/MAIN_RUN/OUTPUTS/ ms-valid-DST-03.m.xyz.S (base case) MSTHM_large_block/DST/BH__SEAL/OUTPUTS/ ms-valid-DST-03-bhSeal.m.xyz.S (sealed bulkhead) MSTHM_large_block/DST/SENSITIV/OUTPUTS/ ms-valid-DST-sensit-1htk.m.xyz.S (high K_{th}) MSTHM_large_block/DST/SENSITIV_R/OUTPUTS/ ms-valid-DST-sensit-1htkr.m.xyz.S (high K_{th}, restart run)	XTOOL v10.1	
7.4-20	LL030808923122.039	MSTHM_large_block/DST/MAIN_RUN/OUTPUTS/ ms-valid-DST-03.m.ext (base case)	XTOOL v10.1	
7.5-2	LL040703223122.050 LL050500323122.060	From LL040703223122.050: MSTHAC_center_output: center_MSTHAC7_T_ds.ext.gz center_MSTHAC7_T_dw.ext.gz DLMTH_center_output: ms-valid-anisot-cen-01r.m.T.EBS.ext.gz (no gas transport along drift) ms-valid-anisot-cen-01rb.m.T.EBS.ext.gz (no gas transport along drift, restart) ms-valid-anisot-cen-01rc.m.T.EBS.ext.gz (no gas transport along drift, restart) ms-valid-anisot-cen-01rd.m.T.EBS.ext.gz (no gas transport along drift, restart) ms-valid-anisot-cen-01re.m.T.EBS.ext.gz (no gas transport along drift, restart) ms-valid-anisot-cen-01rf.m.T.EBS.ext.gz (no gas transport along drift, restart) ms-valid-mixed-cen-01r.m.T.EBS.ext.gz (with sealed bulkhead) From LL050500323122.060: See README file, Table 1	MATLAB v6.1.0.450 (R12.1) XTOOL v10.1	D/LMTH model: T_{dw} is the grid-block-volume-weighted average for host-rock gridblocks around drift perimeter T_{ds} is the grid-block-volume-weighted average around drip-shield perimeter

Table XIII-1. List of Data Sources for Figures (Continued)

Figure No.	Data Source	File Name	Plotting Software	Notes
7.5-3	LL040703223122.050 LL050500323122.060	From LL040703223122.050: MSTHAC_center_output: center_MSTHAC7_RH_ds.ext.gz center_MSTHAC7_RH_dw.ext.gz DLMTH_center_output: ms-valid-anisot-cen-01r.f.RH.EBS.ext.gz (no gas transport along drift) ms-valid-anisot-cen-01rb.f.RH.EBS.ext.gz (no gas transport along drift, restart) ms-valid-anisot-cen-01rc.f.RH.EBS.ext.gz (no gas transport along drift, restart) ms-valid-anisot-cen-01rd.f.RH.EBS.ext.gz (no gas transport along drift, restart) ms-valid-anisot-cen-01re.f.RH.EBS.ext.gz (no gas transport along drift, restart) ms-valid-anisot-cen-01rf.f.RH.EBS.ext.gz (no gas transport along drift, restart) ms-valid-mixed-cen-01r.f.RH.EBS.ext.gz (with sealed bulkhead) From LL050500323122.060: See README file, Table 1	MATLAB v6.1.0.450 (R12.1) XTOOL v10.1	D/LMTH model: RH_{dw} is the grid-block-volume-weighted average for host-rock gridblocks around drift perimeter RH_{ds} is the grid-block-volume-weighted average for drift gridblocks around drip-shield perimeter
7.5-4	LL040703223122.050 LL050500323122.060	From LL040703223122.050: MSTHAC_center_output: center_MSTHAC7_S.liq_dw.ext.gz center_MSTHAC7_S.liq_invert.ext.gz DLMTH_center_output: ms-valid-anisot-cen-01r.m.S.EBS.ext.gz (no gas transport along drift) ms-valid-anisot-cen-01rb.m.S.EBS.ext.gz (no gas transport along drift, restart) ms-valid-anisot-cen-01rc.m.S.EBS.ext.gz (no gas transport along drift, restart) ms-valid-anisot-cen-01rd.m.S.EBS.ext.gz (no gas transport along drift, restart) ms-valid-anisot-cen-01re.m.S.EBS.ext.gz (no gas transport along drift, restart) ms-valid-anisot-cen-01rf.m.S.EBS.ext.gz (no gas transport along drift, restart) ms-valid-mixed-cen-01r.m.S.EBS.ext.gz (with sealed bulkhead) From LL050500323122.060: See README file, Table 1	MATLAB v6.1.0.450 (R12.1) XTOOL v10.1	D/LMTH model: $S_{liq,dw}$ is the grid-block-volume-weighted average for host-rock gridblocks around drift perimeter $S_{liq,inv}$ is the grid-block-volume-weighted average for the invert gridblocks

Table XIII-1.   List of Data Sources for Figures (Continued)

Figure No.	Data Source	File Name	Plotting Software	Notes
7.5-5	LL040703223122.050 LL050500323122.060	From LL040703223122.050: MSTHAC_edge_output: edge_MSTHAC7_T_ds.ext.gz edge_MSTHAC7_T_dw.ext.gz DLMTH_edge_output: ms-valid-anisot-edge-01r.m.T.EBS.ext.gz (no gas transport along drift) ms-valid-mixed-edge-01r.m.T.EBS.ext.gz (with sealed bulkhead) ms-valid-mixed-edge-01rb.m.EBS.T.ext.gz (with sealed bulkhead, restart) ms-valid-mixed-edge-19.m.T.ext.gz (no bulkhead) ms-valid-mixed-edge-19b.m.T.ext.gz (no bulkhead, restart) From LL050500323122.060: See README file, Table 1	MATLAB v6.1.0.450 (R12.1) XTOOL v10.1	D/LMTH model: T_{dw} is the grid-block-volume-weighted average for host-rock gridblocks around drift perimeter T_{ds} is the grid-block-volume-weighted average around drip-shield perimeter
7.5-6	LL040703223122.050 LL050500323122.060	From LL040703223122.050: MSTHAC_edge_output: edge_MSTHAC7_RH_ds.ext.gz edge_MSTHAC7_RH_dw.ext.gz DLMTH_edge_output: ms-valid-anisot-edge-01r.f.RH.EBS.ext.gz (no gas transport along drift) ms-valid-mixed-edge-01r.f.RH.EBS.ext.gz (with sealed bulkhead) ms-valid-mixed-edge-01rb.f.RH.EBS.ext.gz (with sealed bulkhead, restart) ms-valid-mixed-edge-19.f.RH.EBS.EBS.ext.gz (no bulkhead) ms-valid-mixed-edge-19b.f.RH.EBS.EBS.ext.gz (no bulkhead, restart) From LL050500323122.060: See README file, Table 1	MATLAB v6.1.0.450 (R12.1) XTOOL v10.1	D/LMTH model: RH_{dw} is the grid-block-volume-weighted average for host-rock gridblocks around drift perimeter RH_{ds} is the grid-block-volume-weighted average for drift gridblocks around drip-shield perimeter
7.5-7	LL040703223122.050 LL050500323122.060	From LL040703223122.050: MSTHAC_edge_output: edge_MSTHAC7_S.liq_dw.ext.gz edge_MSTHAC7_S.liq_invert.ext.gz DLMTH_edge_output:	MATLAB v6.1.0.450 (R12.1) XTOOL v10.1	D/LMTH model: $S_{liq,dw}$ is the grid-block-volume-weighted average for host-rock gridblocks around

Table XIII-1.   List of Data Sources for Figures (Continued)

Figure No.	Data Source	File Name	Plotting Software	Notes
		ms-valid-anisot-edge-01r.m.S.ext.gz (no gas transport along drift) ms-valid-mixed-edge-01r.m.S.ext.gz (with sealed bulkhead) ms-valid-mixed-edge-01rb.m.S.ext.gz (with sealed bulkhead, restart) ms-valid-mixed-edge-19.m.S.ext.gz (no bulkhead) ms-valid-mixed-edge-19b.m.S.ext.gz (no bulkhead, restart) From LL050500323122.060: See README file, Table 1		drift perimeter $S_{liq,inv}$ is the grid-block-volume-weighted average for the invert gridblocks
7.5-8	LL040703223122.050 LL050500323122.060	From LL040703223122.050: ms-valid-mixed-edge-19.m.q.water.gas.EBS.ext.gz ms-valid-mixed-edge-19.f.q.water.gas.EBS.ext.gz	MATLAB v6.1.0.450 (R12.1) XTOOL v10.1	D/LMTH model: Axial vapor flux is grid-block-area-weighted average for drift and invert gridblocks
7.5-9	LL040703223122.050 LL030905931032.001 LL030906331032.004 LL050500323122.060	From LL040703223122.050: MSTHAC_center_output: center_MSTHAC7_T_ds.ext.gz center_MSTHAC7_T_dw.ext.gz DLMTH_center_output: ms-valid-mixed-cen-01r.m.T.EBS.ext.gz (with sealed bulkhead) From LL030905931032.001: MSTHAC_abstraction/MSTHAC_output/Ll-lkt_P2w@r#79:55:1.ext.gz From LL030906331032.004: MSTHAC_abstraction/MSTHAC_output/Ul-hkt_P2w@r#79:55:1.ext.gz From LL050500323122.060: See README file, Table 1	MATLAB v6.1.0.450 (R12.1)	D/LMTH model: Temperature differences are based on Figure 7.5-2 Full repository MSTHM: Temperature range is equal to Li-lkt minus Ui-hkt
7.5-10	LL040703223122.050 LL030905931032.001 LL030906331032.004 LL050500323122.060	From LL040703223122.050: MSTHAC_center_output: center_MSTHAC7_RH_ds.ext.gz center_MSTHAC7_RH_dw.ext.gz DLMTH_center_output:	MATLAB v6.1.0.450 (R12.1)	D/LMTH model: Relative humidity differences are based on Figure 7.5-3 Full repository

Table XIII-1.   List of Data Sources for Figures (Continued)

Figure No.	Data Source	File Name	Plotting Software	Notes
				MSTHM: Relative humidity range is equal to Ui-hkt minus Li-lkt
		ms-valid-mixed-cen-01r.f.RH.EBS.ext.gz (with sealed bulkhead) From LL030905931032.001: MSTHAC_abstraction/MSTHAC_output/LI-lkt_P2w@r#79:55:1.ext.gz From LL030906331032.004: MSTHAC_abstraction/MSTHAC_output/UI-hkt_P2w@r#79:55:1.ext.gz From LL050500323122.060: See README file, Table 1		
7.5-11	LL040703223122.050 LL030905931032.001 LL030906331032.004 LL050500323122.060	From LL040703223122.050: MSTHAC_center_output: center_MSTHAC7_S.liq_dw.ext.gz center_MSTHAC7_S.liq_invert.ext.gz DLMTH_center_output: ms-valid-mixed-cen-01r.m.S.EBS.ext.gz (with sealed bulkhead) From LL030905931032.001: MSTHAC_abstraction/MSTHAC_output/LI-lkt_P2w@r#79:55:1.ext.gz From LL030906331032.004: MSTHAC_abstraction/MSTHAC_output/UI-hkt_P2w@r#79:55:1.ext.gz From LL050500323122.060: See README file, Table 1	MATLAB v6.1.0.450 (R12.1)	D/LMTH model: Liquid-phase saturation differences are based on Figure 7.5-4 Full repository MSTHM: Liquid-phase saturation range is equal to Ui-hkt minus Li-lkt
7.5-12	LL040703223122.050 LL030905931032.001 LL030906331032.004 LL050500323122.060	From LL040703223122.050: MSTHAC_edge_output: edge_MSTHAC7_T_ds.ext.gz edge_MSTHAC7_T_dw.ext.gz DLMTH_edge_output: ms-valid-mixed-edge-19.m.T.ext.gz (no bulkhead) ms-valid-mixed-edge-19b.m.T.ext.gz (no bulkhead, restart) From LL030905931032.001: MSTHAC_abstraction/MSTHAC_output/LI-lkt_P2e@r#111:46:1.ext.gz From LL030906331032.004:	MATLAB v6.1.0.450 (R12.1)	D/LMTH model: Temperature differences are based on Figure 7.5-5 Full repository MSTHM: Temperature range is equal to Li-lkt minus Ui-hkt

Table XIII-1.   List of Data Sources for Figures (Continued)

Figure No.	Data Source	File Name	Plotting Software	Notes
7.5-13	LL040703223122.050 LL030905931032.001 LL030906331032.004 LL050500323122.060	MSTHAC_abstraction/MSTHAC_output/UI-hkt_P2e@r#11:46:1.ext.gz From LL050500323122.060: See README file, Table 1 From LL040703223122.050: MSTHAC_edge_output: edge_MSTHAC7_RH_ds.ext.gz edge_MSTHAC7_RH_dw.ext.gz DLMTH_edge_output: ms-valid-mixed-edge-19.f.RH.EBS.EBS.ext.gz (no bulkhead) ms-valid-mixed-edge-19b.f.RH.EBS.EBS.ext.gz (no bulkhead, restart) From LL030905931032.001: MSTHAC_abstraction/MSTHAC_output/LI-lkt_P2e@r#111:46:1.ext.gz From LL030906331032.004: MSTHAC_abstraction/MSTHAC_output/UI-hkt_P2e@r#111:46:1.ext.gz From LL050500323122.060: See README file, Table 1	MATLAB v6.1.0.450 (R12.1)	D/LMTH model: Relative humidity differences are based on Figure 7.5-6 Full repository MSTHM: Relative humidity range is equal to UI-hkt minus Li-lkt
7.5-14	LL040703223122.050 LL030905931032.001 LL030906331032.004 LL050500323122.060	From LL040703223122.050: MSTHAC_edge_output: edge_MSTHAC7_S.liq_dw.ext.gz edge_MSTHAC7_S.liq_invert.ext.gz DLMTH_edge_output: ms-valid-mixed-edge-19.m.S.ext.gz (no bulkhead) ms-valid-mixed-edge-19b.m.S.ext.gz (no bulkhead, restart) From LL030905931032.001: MSTHAC_abstraction/MSTHAC_output/LI-lkt_P2e@r#111:46:1.ext.gz From LL030906331032.004: MSTHAC_abstraction/MSTHAC_output/UI-hkt_P2e@r#111:46:1.ext.gz From LL050500323122.060: See README file, Table 1	MATLAB v6.1.0.450 (R12.1)	D/LMTH model: Liquid-phase saturation differences are based on Figure 7.5-7 Full repository MSTHM: Liquid-phase saturation range is equal to UI-hkt minus Li-lkt

Table XIII-1. List of Data Sources for Figures (Continued)

Figure No.	Data Source	File Name	Plotting Software	Notes
7.5-15	LL040703223122.050 LL050500323122.060	From LL040703223122.050: DLMTH_center_output: ms-valid-mixed-cen-01r.f.RH.EBS.ext.gz (with sealed bulkhead) ms-valid-mixed-cen-01r.m.S.EBS.ext.gz (with sealed bulkhead) From LL050500323122.060: See README file, Table 1		

Table XIII-2. List of Data Sources for Tables

Table No.	Data Source	File Name	Software	Notes
6.3-1	LL040704323122.051	li-02/output:		
		P2ER4C4-LDTH66-1Dds_mc-li-02i.m.ext		
		P2ER5C5-LDTH66-1Dds_mc-li-02i.m.ext		
		P2ER6C6-LDTH66-1Dds_mc-li-02i.m.ext		
		P2ER8C7-LDTH66-1Dds_mc-li-02i.m.ext		
		P2ER8C6-LDTH66-1Dds_mc-li-02i.m.ext		
		P2ER8C5-LDTH66-1Dds_mc-li-02i.m.ext		
		P2ER7C6-LDTH66-1Dds_mc-li-02i.m.ext		
		P2ER7C5-LDTH66-1Dds_mc-li-02i.m.ext		
		P2ER6C5-LDTH66-1Dds_mc-li-02i.m.ext		
		P2ER3C4-LDTH66-1Dds_mc-li-02i.m.ext		
		P2ER2C5-LDTH66-1Dds_mc-li-02i.m.ext		
		P2WR1C8-LDTH66-1Dds_mc-li-02i.m.ext		
		P3R1C11-LDTH66-1Dds_mc-li-02i.m.ext		
		P3R8C13-LDTH66-1Dds_mc-li-02i.m.ext		
		mi-02/output:		
		P2ER4C4-LDTH66-1Dds_mc-mi-02i.m.ext		
		P2ER5C5-LDTH66-1Dds_mc-mi-02i.m.ext		
		P2ER6C6-LDTH66-1Dds_mc-mi-02i.m.ext		
		P2ER8C7-LDTH66-1Dds_mc-mi-02i.m.ext		
		P2ER8C6-LDTH66-1Dds_mc-mi-02i.m.ext		
		P2ER8C5-LDTH66-1Dds_mc-mi-02i.m.ext		
		P2ER7C6-LDTH66-1Dds_mc-mi-02i.m.ext		
		P2ER7C5-LDTH66-1Dds_mc-mi-02i.m.ext		
		P2ER6C5-LDTH66-1Dds_mc-mi-02i.m.ext		
		P2ER3C4-LDTH66-1Dds_mc-mi-02i.m.ext		
		P2ER2C5-LDTH66-1Dds_mc-mi-02i.m.ext		
		P2WR1C8-LDTH66-1Dds_mc-mi-02i.m.ext		
		P3R1C11-LDTH66-1Dds_mc-mi-02i.m.ext		
		P3R8C13-LDTH66-1Dds_mc-mi-02i.m.ext		
		ui-02/output:		
		P2ER4C4-LDTH66-1Dds_mc-ui-02i.m.ext		
		P2ER5C5-LDTH66-1Dds_mc-ui-02i.m.ext		
		P2ER6C6-LDTH66-1Dds_mc-ui-02i.m.ext		
		P2ER8C7-LDTH66-1Dds_mc-ui-02i.m.ext		
		P2ER8C6-LDTH66-1Dds_mc-ui-02i.m.ext		
		P2ER8C5-LDTH66-1Dds_mc-ui-02i.m.ext		
		P2ER7C6-LDTH66-1Dds_mc-ui-02i.m.ext		
		P2ER7C5-LDTH66-1Dds_mc-ui-02i.m.ext		
		P2ER6C5-LDTH66-1Dds_mc-ui-02i.m.ext		
		P2ER3C4-LDTH66-1Dds_mc-ui-02i.m.ext		
		P2ER2C5-LDTH66-1Dds_mc-ui-02i.m.ext		
		P2WR1C8-LDTH66-1Dds_mc-ui-02i.m.ext		
		P3R1C11-LDTH66-1Dds_mc-ui-02i.m.ext		
		P3R8C13-LDTH66-1Dds_mc-ui-02i.m.ext		

Table XIII-2.   List of Data Sources for Tables (Continued)

Table No.	Data Source	File Name	Software	Notes
6.3-2	LL040704323122.051	mi-02/output:		
		P2ER4C4-LDTH66-1Dds_mc-mi-02i.f.ext		
		P2ER4C4-LDTH66-1Dds_mc-mi-02i.m.ext		
		P2ER5C5-LDTH66-1Dds_mc-mi-02i.f.ext		
		P2ER5C5-LDTH66-1Dds_mc-mi-02i.m.ext		
		P2ER6C6-LDTH66-1Dds_mc-mi-02i.f.ext		
		P2ER6C6-LDTH66-1Dds_mc-mi-02i.m.ext		
		P2ER8C7-LDTH66-1Dds_mc-mi-02i.f.ext		
		P2ER8C7-LDTH66-1Dds_mc-mi-02i.m.ext		
		P2ER8C6-LDTH66-1Dds_mc-mi-02i.f.ext		
		P2ER8C6-LDTH66-1Dds_mc-mi-02i.m.ext		
		P2ER8C5-LDTH66-1Dds_mc-mi-02i.f.ext		
		P2ER8C5-LDTH66-1Dds_mc-mi-02i.m.ext		
		P2ER7C6-LDTH66-1Dds_mc-mi-02i.f.ext		
		P2ER7C6-LDTH66-1Dds_mc-mi-02i.m.ext		
		P2ER7C5-LDTH66-1Dds_mc-mi-02i.f.ext		
		P2ER7C5-LDTH66-1Dds_mc-mi-02i.m.ext		
		P2ER6C5-LDTH66-1Dds_mc-mi-02i.f.ext		
		P2ER6C5-LDTH66-1Dds_mc-mi-02i.m.ext		
		P2ER3C4-LDTH66-1Dds_mc-mi-02i.f.ext		
		P2ER3C4-LDTH66-1Dds_mc-mi-02i.m.ext		
		P2ER2C5-LDTH66-1Dds_mc-mi-02i.f.ext		
		P2ER2C5-LDTH66-1Dds_mc-mi-02i.m.ext		
		P2WR1C8-LDTH66-1Dds_mc-mi-02i.f.ext		
		P2WR1C8-LDTH66-1Dds_mc-mi-02i.m.ext		
		P3R1C11-LDTH66-1Dds_mc-mi-02i.f.ext		
		P3R1C11-LDTH66-1Dds_mc-mi-02i.m.ext		
		P3R8C13-LDTH66-1Dds_mc-mi-02i.f.ext		
		P3R8C13-LDTH66-1Dds_mc-mi-02i.m.ext		
		mi-01/ouput:		
		P2ER4C4-LDTH66-1Dds_mc-mi-01i.f.ext		
		P2ER4C4-LDTH66-1Dds_mc-mi-01i.m.ext		
		P2ER5C5-LDTH66-1Dds_mc-mi-01i.f.ext		
		P2ER5C5-LDTH66-1Dds_mc-mi-01i.m.ext		
		P2ER6C6-LDTH66-1Dds_mc-mi-01i.f.ext		
		P2ER6C6-LDTH66-1Dds_mc-mi-01i.m.ext		
		P2ER8C7-LDTH66-1Dds_mc-mi-01i.f.ext		
		P2ER8C7-LDTH66-1Dds_mc-mi-01i.m.ext		
		P2ER8C6-LDTH66-1Dds_mc-mi-01i.f.ext		
		P2ER8C6-LDTH66-1Dds_mc-mi-01i.m.ext		
		P2ER8C5-LDTH66-1Dds_mc-mi-01i.f.ext		
		P2ER8C5-LDTH66-1Dds_mc-mi-01i.m.ext		
		P2ER7C6-LDTH66-1Dds_mc-mi-01i.f.ext		
		P2ER7C6-LDTH66-1Dds_mc-mi-01i.m.ext		

Table XIII-2. List of Data Sources for Tables (Continued)

Table No.	Data Source	File Name	Software	Notes
		P2ER7C5-LDTH66-1Dds_mc-mi-01i.f.ext		
		P2ER7C5-LDTH66-1Dds_mc-mi-01i.m.ext		
		P2ER6C5-LDTH66-1Dds_mc-mi-01i.f.ext		
		P2ER6C5-LDTH66-1Dds_mc-mi-01i.m.ext		
		P2ER3C4-LDTH66-1Dds_mc-mi-01i.f.ext		
		P2ER3C4-LDTH66-1Dds_mc-mi-01i.m.ext		
		P2ER2C5-LDTH66-1Dds_mc-mi-01i.f.ext		
		P2ER2C5-LDTH66-1Dds_mc-mi-01i.m.ext		
		P2WR1C8-LDTH66-1Dds_mc-mi-01i.f.ext		
		P2WR1C8-LDTH66-1Dds_mc-mi-01i.m.ext		
		P3R1C11-LDTH66-1Dds_mc-mi-01i.f.ext		
		P3R1C11-LDTH66-1Dds_mc-mi-01i.m.ext		
		P3R8C13-LDTH66-1Dds_mc-mi-01i.f.ext		
		P3R8C13-LDTH66-1Dds_mc-mi-01i.m.ext		
7.6-1	SN0408T0509903.007 LL030808523122.035	From SN0408T0509903.007: TOC.mcd; hyperlink 6.3.10, Verification of 2-D Heat Transfer Model for Structures within the Drift (Condensation Model) From LL030808523122.035: MSTHAC/mi_abstractions/OUTPUT/mi_P2w@r#79:55:1.ext.gz	Mathcad 11.2a	Temperature differences from FLUENT model are obtained from the arithmetic averages of the waste-package, drip-shield, and drift-wall temperatures Temperature differences from the MSTHM are obtained from the waste-package, drip-shield, and drift-wall temperatures
7.6-2	LL030808523122.035	MSTHAC/mi_abstractions/OUTPUT/mi_P2w@r#79:55:1.ext.gz		Temperature differences from the MSTHM are obtained from the waste-package, drip-shield, and drift-wall temperatures

APPENDIX XIV

QUALIFICATION OF UNQUALIFIED PROJECT DATA

This appendix presents the results of the documentation of a data qualification task. The checking, reviewing, and documentation of the results of the data qualification activity are performed according to LP-SIII.2Q-BSC. The following discussion addresses point by point the data qualification:

Data Set for Qualification:

The data set for qualification is DTN: MO0304MWDALACV.000 [DIRS 164551].

Methods of Qualification Selected:

The method selected for qualification is through the use of corroborating data. The data sets for ventilation efficiencies or heat generation fractions from the qualified source are compared to the source requiring qualification both spatially and temporally to determine if the comparisons satisfy the quantitative evaluation criteria. The rationale for this method is that if the heat mass fractions are in agreement to within the range of uncertainty, then the temperatures predicted at the drift wall from the average waste package line loading will be in agreement over the postclosure period that is analyzed in the multiscale thermohydrologic model.

Evaluation Criteria:

Appendix III presents the heat generation fractions derived from ventilation efficiencies for the various submodels used in this report. The DTN for ventilation efficiency (DTN: MO0304MWDALACV.000 [DIRS 164551]) requires qualification according to the data qualification plan (BSC 2005 [DIRS 173404]). This plan requires a comparison of the heat generation fraction (ventilation efficiencies) at times of 10, 20, 30, and 50 years at distances of 100, 200, 300, 400, 500, 600, 700, and 800 meters from the ventilation inlet from DTN: MO0304MWDALACV.000 [DIRS 164551] with the qualified source from DTN: MO0306MWDASLCV.001 [DIRS 165695]. The criterion for data qualification is that the difference in heat generation fraction or ventilation efficiency from these two sources is less than 0.02, or 2%. This difference represents an estimate in the uncertainty in the data.

Evaluation of the Technical Correctness of the Data, as Applicable:

As documented in *Ventilation Model and Analysis Report* (BSC 2004 [DIRS 169862]), both analytical and finite element methods were developed for assessing spatial and temporal variations in ventilation efficiencies for use in repository preclosure analysis. These calculations show that for the selected repository design parameters, and existing thermal properties of the rock mass surrounding the emplacement drift at the repository horizon, a high ventilation efficiency is achievable over a range of conditions as predicted by either analytical or finite-element methods and that the ventilation efficiency is insensitive to variations in rock thermal properties. The ventilation model was validated against measured data in *Ventilation Model and Analysis Report* (BSC 2004 [DIRS 169862]). Therefore, since the ventilation model is validated, correct ventilation efficiencies or heat mass fractions are calculated from the qualified source.

Data Generated by the Evaluation

Table XIV-1 presents the heat generation fraction or ventilation efficiencies (rounded to three decimal places) at the times and locations from the source DTNs reproduced from Table III-1 and III-2, and the absolute value of the differences in these values that constitutes the data generated by this evaluation. The difference in heat generation fraction is equal to the difference in ventilation efficiency. The table shows that the criterion for data qualification from the plan is satisfied, with the maximum difference being 0.006 or 0.6%.

Table XIV-1 Qualification of Heat Removal Fraction or Ventilation Efficiency

Time (yr)	Distance from Ventilation Inlet (m)							
	100	200	300	400	500	600	700	800
Net Available Heat Generation Fraction used in this Report from Table III-1.								
10	0.072	0.099	0.125	0.152	0.178	0.204	0.230	0.254
20	0.043	0.069	0.094	0.118	0.143	0.167	0.192	0.213
30	0.039	0.061	0.083	0.104	0.125	0.145	0.166	0.187
50	0.009	0.027	0.045	0.064	0.081	0.100	0.117	0.135
Net Available Heat Generation Fraction from the Updated Data Source from Table III-2.								
10	0.071	0.098	0.123	0.149	0.175	0.200	0.225	0.248
20	0.043	0.068	0.093	0.117	0.141	0.164	0.188	0.210
30	0.040	0.062	0.083	0.104	0.125	0.146	0.166	0.186
50	0.010	0.029	0.048	0.067	0.086	0.103	0.121	0.139
Difference between the Sources								
10	0.001	0.001	0.002	0.003	0.003	0.004	0.005	0.006
20	0.000	0.001	0.001	0.001	0.002	0.003	0.004	0.003
30	0.001	0.001	0.000	0.000	0.000	0.001	0.000	0.001
50	0.001	0.002	0.003	0.003	0.005	0.003	0.004	0.004

NOTE: Values presented in this table from Tables III-1 and III-2 are rounded to the third decimal place.

EVALUATION RESULTS:

Based upon the comparisons made above, and based upon the experience of the data qualification team, the data are qualified for use in the calculations reported in Section 6.3.

Rationale for Abandoning any Qualification Methods, if Appropriate:

Note that a single method was specified in the data qualification plan, and that there were no deviations from this plan. Therefore this item does not apply to the data qualification effort.

Limits or Caveats Considered by Potential Users of the Data:

The ventilation efficiency or heat mass fraction as presented in DTN: MO0304MWDALACV.000 [DIRS 164551] is based upon the current repository design involving an emplacement drift diameter of 5.5 m; an emplacement drift spacing of 81 m; an emplacement drift length varying from 600 m to 800 m; a ventilation air flow rate of 15 m^3/sec; and a ventilation preclosure period of 50 years. The heat mass fraction from these DTNs is

limited to this repository design. Any change in these design parameters would require a new analysis of heat mass fraction with the technical method of analysis presented in *Ventilation Model and Analysis Report* (BSC 2004 [DIRS 169862]).

Identification of Any Supporting Information Used in the Qualification Effort:

Note that the qualification is a direct comparison, and requires no supporting information other than the source DTN, and the method of analysis as presented in *Ventilation Model and Analysis Report* (BSC 2004 [DIRS 169862]).

Data Qualification Plan:

The data are qualified according to *Data Qualification Plan – Qualification of DTN: MO0304MWDALACV.000 for Use in the Multiscale Thermohydrologic Model* (BSC 2005 [DIRS 173404]).

INTENTIONALLY LEFT BLANK

APPENDIX XV

PREDICTION OF RH IN THE INVERT

This appendix presents a method for the calculation of the relative humidity in the invert from the temperature and saturation time histories obtained from the multiscale thermohydrologic analysis. The method is being implemented in the total system performance assessment because of a problem in the method that MSTHAC Version 7.0 uses to calculate the invert relative humidity. The calculation presented in this appendix can be used to verify the calculation method used in the total system performance assessment. The saturation and temperature histories are obtained for P2WR5C10 as discussed below. The data for this prediction are obtained from DTN: LL040703123122.049, entitled *Input and Output Files for the Sensitivity Studies for (1) Invert Intergranular Hydrologic Properties, (2) Pseudo Permeability of the Gas-Filled Drift Cavity, and (3) Ventilation Heat-Removal Efficiency*, dated 14 July 2004.

Section XV.1 presents a partial list of basic thermophysical properties of water in Table XV-1 as obtained from Incropera and DeWitt (2002 [DIRS 163337], Table A.6 , pp. 924-925). Section XV.2 then defines three column vectors for the time, temperature, and matrix saturation histories over the time period from emplacement to 20,000 years after emplacement (from DTN: LL040703123122.049, PZWR5C10-LDTH55-mi-mkt-02Q.m.ebs.ext). A partial list of these column vectors is presented in Table XV-2. Section XV.3 then presents the governing relationships and Van Genuchten retention properties for the lower lithophysal unit. Also, this section defines the retention properties for the governing relationships. Section XV.4 then presents hand calculations that verify the MathCad 11 capillary pressure functions. Section XV.5 presents the governing relationships for the relative humidity calculation in the invert. Section XV.6 then presents the hand calculation for verification of the invert relative humidity calculation. Section XV.7 presents the MathCad 11 functions and the verification of these functions for relative humidity. Section XV.8 presents the comparison of relative humidity predictions from the MathCad 11 calculation with the multiscale thermohydrologic model. Section XV.9 presents the conclusions to the analysis.

The analyses presented in this appendix use MathCad 11 and EXCEL 97 for performing calculations and illustrating graphical output. The calculations have been performed using standard functions for this software, and the results illustrated are not dependent on the use of this software as evidenced by the independent verification of MathCad 11 functions by independent hand calculation in Section XV.4 and XV.6. The software does not need to follow LP-SI.11Q-BSC, *Software Management*, under Sections 2.1.2, and 2.1.6 of that procedure, because this standard industrial software is exempt.

The translation of information from DTN: LL040703123122.049 is shown in Figure XV-1. Note that in this figure an EXCEL workbook refers to the EXCEL file. The EXCEL workbook consists of several worksheets that refer to individual spreadsheets. The saturation, temperature, capillary pressure, and relative humidity information is downloaded through the following steps:

1. Access the technical data management system (TDMS) and locate DTN: LL040703123122.049 in the trace window. The trace type is "Get TDIF." In this window, click on the link on the upper right hand of the web page that you use to access the Model Warehouse Datatset.

2. Click button to download files. Note that at this stage, the address is ftp://sol.ymp.gov/pub11/LL040703123122.049/LDTH_Sensitivity_Studies/.

3.   Open the zip file **LL040703123122_049.zip** with Winzip and specify a directory for receipt of the data. Note that the zip file that is downloaded from the above site is large (over 200 megabytes). Now after downloading to the personal computer, Winzip can be used to extract (uncompress) the files. The extraction process generates a subfolder that contains other subfolders.

4.   Locate directory **base-case_output** folder.

5.   Locate and extract the file **P2WR5C10-LDTH55-mi-mkt-02Q.m.ebs.ext**. Note that the file is again a compressed file that needs to be extracted. This file represents the file datafile that is used by XTOOL Version 10.1.

6.   Note that XTOOL v10.1 works on a Sun workstation. The file then needs to be sent to a workstation with the current version of XTOOL v10.1.

7.   Open the .ext file with File/Open.

8.   Press "extraction" from the data menu.

9.   Input the element name (in#1:1:58) where the history data will be plotted.

10.   Highlight T to save the temperature history into the buffer window. Highlight S to save the saturation history into the buffer window. The other variables are placed into the buffer window accordingly. Each of these histories is exported as text files entitled **S_vs_t_P2WRC10_55_58.PLTSC**, and **T_vs_t_P2WR5C10_55_58.PLTSC** to the EXCEL **Inputs to the Prediction of the Invert.xls** workbook; and **Pcap_vs_t_P2WR5C10_55_58.PLTSC**; and **RH_vs_t_P2WR5C10_55_58.PLTSC** to the EXCEL **Outputs to the Prediction of the Invert.xls** accordingly.

11.   These files are placed in the workbook entitled **Inputs to the Prediction of the Invert.xls** in worksheets with the titles for the files respectively. The saturation, and temperature time histories are input to MathCad 11 as column vectors as Time, Temperature, and Saturation. The predicted capillary pressure and relative humidity is then exported with the **Preout.prn** textfile to EXCEL for comparison with the capillary pressure and relative humidity predicted by NUFT. Note that MathCad 11 uses a function entitled WRITEPRN(filename):= array to export data (capillary pressure and relative humidity time histories) that are then read on the worksheet MathCad in the **Outputs to the Prediction of the Invert.xls.**

12.   The completion of steps 10 and 11 then allow for a comparison of the MathCad 11 calculation to data in the DTN.

Prediction of Relative Humidity(RH) in the Invert
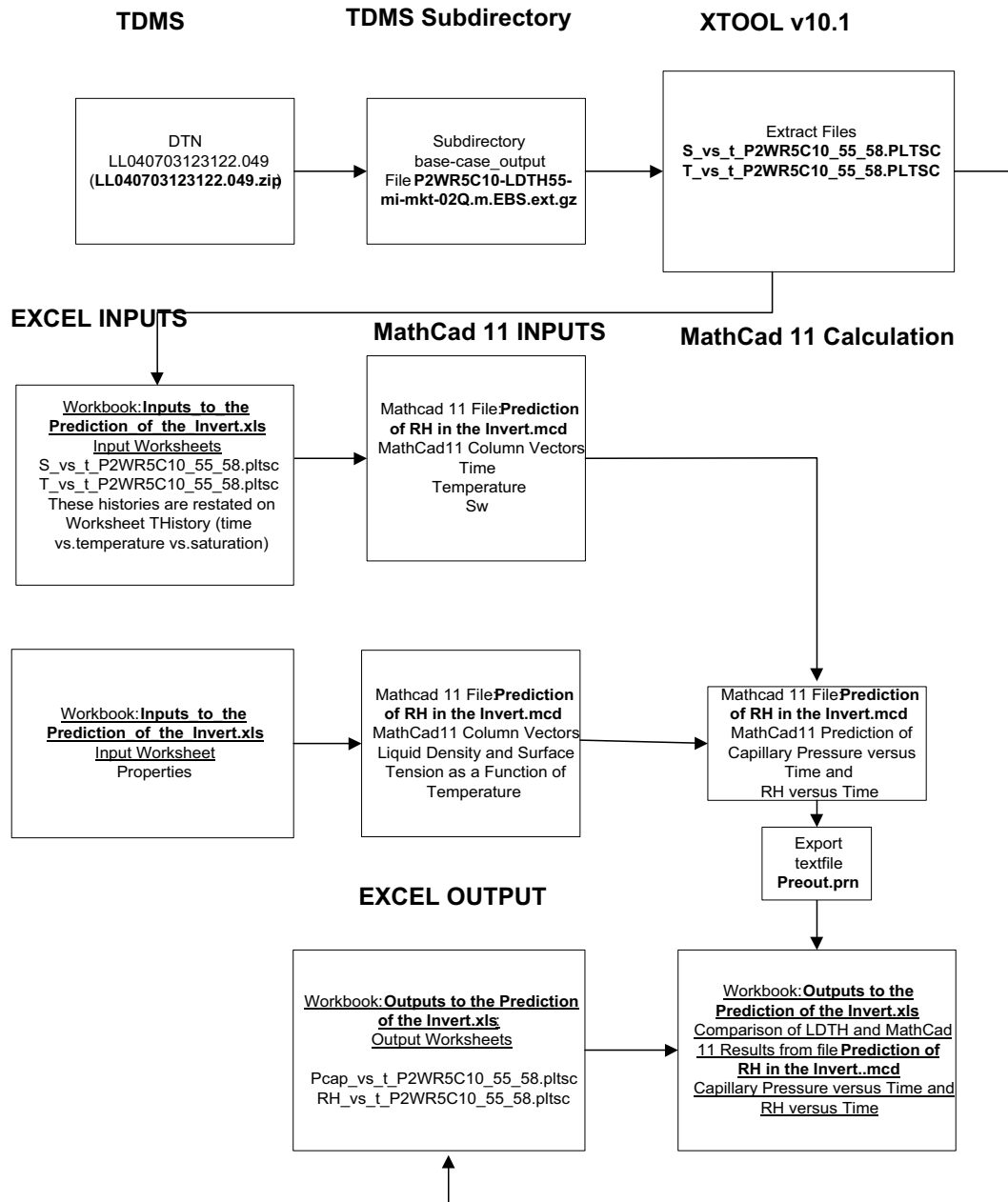
Note: Files shown in Bold.

Figure XV-1.   Flow of Information for Extracting Invert Data

As shown in the figure, after the input and output histories are downloaded from the TDMS, the data are placed on the EXCEL worksheets in the workbook entitled Inputs_to_the_Prediction_of_the_Invert.xls. The thermophysical properties of water are also placed on the "Properties" worksheet. MathCad 11 then references these inputs as EXCEL

components. After the calculations are processed in MathCad 11, the calculations are output to the EXCEL file Outputs_to_the_Prediction_of_the_Invert.xls on the "MathCad 11" worksheet for plotting purposes and for comparison to the NUFT calculations.

XV.1 THERMOPHYSICAL PROPERTIES OF WATER

Read in the properties of water vapor used to estimate the vapor pressure, the mass density, and the surface tension properties of the water as a function of temperature (Incropera and DeWitt 2002 [DIRS 163337], pp. 924-925, Table A.6). The properties are used in the capillary pressure and relative humidity calculations from invert saturation. Table XV-1 is a partial list of these properties used in the calculations in subsequent sections.

Table XV-1.   Thermophysical Properties of Water

$B :=$

Temperature (K)	Saturated Vapor Pressure (Bars)	Specific Volume (m3/kg)*10^3	Surface Tension (N/m) *10^3
273.15	0.00611	1	75.5
275	0.00697	1	75.3
280	0.0099	1	74.8
285	0.01387	1	74.3
290	0.01917	1.001	73.7
295	0.02617	1.002	72.7
300	0.03531	1.003	71.7
305	0.04712	1.005	70.9
310	0.06221	1.007	70
315	0.08132	1.009	69.2
320	0.1053	1.011	68.3
325	0.1351	1.013	67.5
330	0.1719	1.016	66.6
335	0.2167	1.018	65.8
340	0.2713	1.021	64.9
345	0.3372	1.024	64.1
350	0.4163	1.027	63.2
355	0.51	1.03	62.3
360	0.6209	1.034	61.4
365	0.7514	1.038	60.5
370	0.904	1.041	59.5
373.15	1.0133	1.044	58.9
375	1.0815	1.045	58.6
380	1.2869	1.049	57.6
385	1.5233	1.053	56.6
390	1.794	1.058	55.6
400	2.455	1.067	53.6
410	3.302	1.077	51.5
420	4.37	1.088	49.4
430	5.699	1.099	47.2
440	7.333	1.11	45.1
450	9.319	1.123	42.9
460	11.71	1.137	40.7
470	14.55	1.152	38.5
480	17.9	1.167	36.2
490	21.83	1.184	33.9
500	26.4	1.203	31.6
510	31.66	1.222	29.3
520	37.7	1.244	26.9

These properties are read from the workbook **Inputs_to_the_Prediction_of_the_Invert.xls** from worksheet Properties. Note that not all values are shown for the EXCEL component. The underlying worksheet does show all the values in the interpolation table.

Define the unit bar for expressing pressure results.

$$bar := 10^5 \cdot Pa$$

$$P_{sat}(T) := linterp\left[\left(B^{\langle 0 \rangle}\right), B^{\langle 1 \rangle}, \frac{T}{K}\right] \cdot bar$$

$$P_{sat}(342 \cdot K) = 0.298 \, bar$$

$$P_{sat}(342 \cdot K) = 0.294 \, atm$$

(Eq. XV-1)

Define an interpolation function for the surface tension of the liquid water.

$$\sigma_f(T) := linterp\left[\left(B^{\langle 0 \rangle}\right), B^{\langle 3 \rangle}, \frac{T}{K}\right] \cdot 10^{-3} \cdot \frac{N}{m}$$

$$\sigma_f(342 \cdot K) = 0.06458 \frac{N}{m}$$

(Eq. XV-2)

Define the specific volume and density functions.

$$spev(T) := \left[linterp\left[\left(B^{\langle 0 \rangle}\right), B^{\langle 2 \rangle}, \frac{T}{K}\right]\right] \cdot \frac{cm^3}{gm}$$

$$\rho(T) := \frac{1}{spev(T)}$$

$$\rho(300 \cdot K) = 997.009 \frac{kg}{m^3}$$

(Eq. XV-3)

Note that these MathCad linear interpolation functions are verified in Section XV.4.

XV.2 TEMPERATURE HISTORIES FROM THERMOHYDROLOGIC MODELING AND ANALYSIS

Input the temperature and saturation (Sw) histories for P2WR5C10. The data for this prediction are obtained from DTN: LL040703123122.049, entitled *Input and Output Files for the Sensitivity Studies for (1) Invert Intergranular Hydrologic Properties, (2) Pseudo Permeability of the Gas-Filled Drift Cavity, and (3) Ventilation Heat-Removal Efficiency*, dated 14 July 2004.
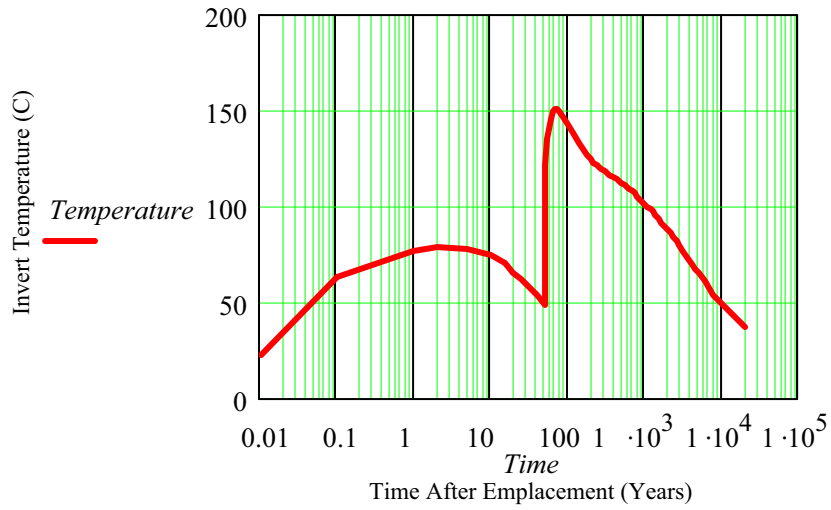
Table XV-2. Invert Temperature and Saturation Time Histories for the P2WR5C10 Column

$$\begin{pmatrix} Time \\ Temperature \\ Sw \end{pmatrix} :=$$

| Time (yrs)	Temperature C	Saturation (-)
0.01	22.43	0.94
0.10	63.37	0.96
1.00	76.23	0.27
2.00	78.72	0.27
5.00	77.85	0.28
10.00	74.32	0.29
15.00	70.61	0.29
20.00	65.54	0.30
25.00	62.21	0.31
30.00	58.80	0.33
40.00	53.46	0.35
50.00	48.86	0.39
50.10	76.66	0.27
51.00	107.83	0.24
52.00	120.89	0.23
55.00	135.04	0.21
60.00	145.78	0.21
65.00	149.81	0.21
70.00	150.94	0.21
75.00	150.55	0.21
80.00	149.40	0.21
90.00	146.55	0.21
100.00	143.43	0.21
120.00	137.94	0.21
140.00	133.15	0.21
160.00	129.41	0.22
180.00	126.61	0.22
200.00	124.27	0.22
220.00	122.89	0.22
240.00	121.47	0.22
260.00	120.28	0.23

These time histories are read from the workbook **Inputs_to_the_Prediction_of_the_Invert.xls** from worksheet THistory. Note that not all values are shown for the EXCEL component. Note that the Temperature and Saturation Histories are restated from the worksheets **T_vs_t_P2WR5C10_55_58.pltsc** and **S_vs_t_P2WR5C10_55_58.pltsc**, respectively. Note also that not all the data are shown in MathCad 11 for this EXCEL component. These time histories are restated on a single worksheet THistory that is derived from data on worksheets **T_vs_t_P2WR5C10_55_58.pltsc** and **S_vs_t_P2WR5C10_55_58.pltsc**. The data on THistory is then read into MathCad as an EXCEL component.

Figures XV-2 and XV-3 present the temperature and saturation (Sw) relationships as a function of time. Note that data plotting in these figures is performed in MathCad 11 and is considered qualified for graphical display of information.

DTN: LL040703123122.049.

Figure XV-2. Invert Temperature History as a Function of Time (from Time versus Temperature on the Worksheet Thistory)
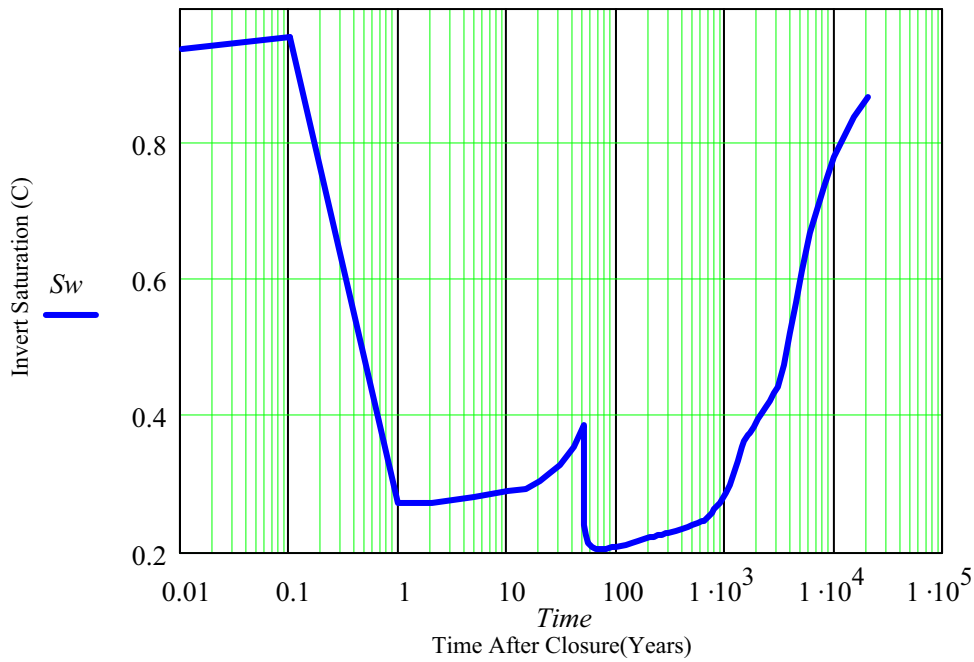
DTN: LL040703123122.049.

Figure XV-3. Invert Matrix Saturation History as a Function of Time (from Time versus Saturation on the Worksheet Thistory)

XV.3 GOVERNING RELATIONSHIPS AND VAN GENUCHTEN RETENTION PROPERTIES FOR THE LOWER LITHOPHYSAL UNIT

This section presents the governing relationships and then presents the van Genuchten retention properties for the lower lithophysal unit used in the analysis.

The prediction of the moisture potential can be performed through the van Genuchten retention relationship for the tuff matrix (Fetter 1993 [DIRS 102009], p. 172):

$$\theta(\psi_m) = \theta_r + \frac{(\theta_s - \theta_r)}{\left[1 + \left|\alpha \psi_m^{\,n}\right|\right]^m}$$

(Eq. XV-4)

where

θ Volumetric moisture content (-)

θ_r Residual volumetric moisture content (-)

θ_s Saturated volumetric moisture content (-)

ψ_m Moisture potential (bars or Pa))

α Van Genuchten air entry parameter (bar^{-1} or Pa^{-1})

n   Van Genuchten curve-fit parameter (-), and

m   Van Genuchten curve-fit parameter (-)

Note that in NUFT, the moisture potential is expressed as a capillary pressure in which it is understood that the air entry parameter α is expressed in (Pa)$^{-1}$. Also, Fetter (1993 [DIRS 102009], p. 172) designates the (m) parameter for the van Genuchten relationship as: m = 1−1/n. This value of "m" can be substituted into Equation XV-4 to derive the volumetric moisture content (θ) along with the notation:

$$\theta(P_c) = \theta_r + \frac{(\theta_s - \theta_r)}{\left[1 + \left(|P_c \alpha|\right)^n\right]^{(1-\frac{1}{n})}}$$

(Eq. XV-5)

where

P_c (Capillary Pressure expressed in bars) = ψ_m (expressed in bars)

In Equation XV-5, the moisture potential can be solved for in terms of the volumetric moisture content:

$$P_c(\theta) = \frac{\left[\left[\frac{\theta_s - \theta_r}{\theta - \theta_r}\right]^{\frac{1}{m}} - 1\right]^{\frac{1}{n}}}{\alpha}$$

(Eq. XV-6)

The van Genuchten capillary pressure relationship for the tuff matrix (Fetter 1993 [DIRS 102009], p. 172) is for ambient temperature. Note that a correction for surface tension effects is necessary since surface tension is a function of temperature. Note that, as discussed by Hillel (1998 [DIRS 165404], pp38-44), the height of capillary rise or capillary pressure is a function of surface tension that in turn is a function of temperature. Therefore to calculate the correct capillary pressure, multiply the ambient capillary pressure by the ratio of the surface tension at elevated temperature to that at ambient temperature (set at 25 degrees Centigrade). The following calculation is performed in MathCad 11:

$$P'_c(\theta, T) = P_c(\theta) \cdot \frac{\sigma_f(T + 273.15 \cdot K)}{\sigma_f(25 \cdot K + 273.15 \cdot K)}$$

(Eq. XV-7)

where

P′c (θ,T) is the capillary pressure corrected for surface tension effects

The moisture retention properties for the tuff matrix from the Tptpll unit (TSw35) are taken from Table IV-4 under the row heading tswM5 that corresponds to the material name m-tsw35 in the LDTH submodel. It should also be noted that the ratio $(\theta_s-\theta_r)/(\theta-\theta_r)$ is equivalent to the ratio $(1-S_r)/(S-S_r)$ that is used in NUFT.

$$\theta_s := 0.131 \qquad \theta_r := 0.12 \cdot \theta_s \qquad \alpha := 1.08 \cdot {}^{-5} \cdot Pa^{-1} \qquad m' := 0.216$$

$$n := \frac{1}{1 - m'}$$

Input the universal gas constant and the molecular weight of water.

$$M := 18.016 \cdot \frac{gm}{mole} \qquad\qquad R := 8.315 \cdot \frac{J}{mole \cdot K}$$

$$\frac{\theta_r}{\theta_s} = 0.12 \qquad\qquad \theta_r = 0.01572$$

(Eq. XV-8)

$$\alpha = 1.08 \times 10^{-5} \frac{1}{Pa}$$

Solve for θ as a function of Sw. Note that in the following equation, index notation is used to define the corresponding volumetric moisture content (Θ) for the saturation (Sw). The index range is established by the statement *i:= 0...rows(Sw)-1*.

$$i := 0 .. rows(Sw) - 1 \qquad \Theta_i := \theta_s \cdot Sw_i$$

(Eq. XV-9)

Output the results of the calculation. The following table shows the relationship of volumetric moisture content as a function of time as derived from Equation XV-9.

$Time_i =$	$\Theta_i =$
	0.123
0.01	0.125
0.1	0.036
1	0.035
2	0.037
5	0.038
10	0.038
15	0.04
20	0.041
25	0.043
30	0.046
40	0.051
50	0.035
50.1	0.031
51	0.03
52	0.028
55	0.027
60	0.027
65	0.027
70	0.027
75	0.027
80	0.027
90	0.027
100	0.027
120	0.028
	0.028

Note that this is a partial listing of the data. The complete listing of the data are presented on Worksheet "Thistory" of the workbook **Input to the Prediction of the Invert.xls**.

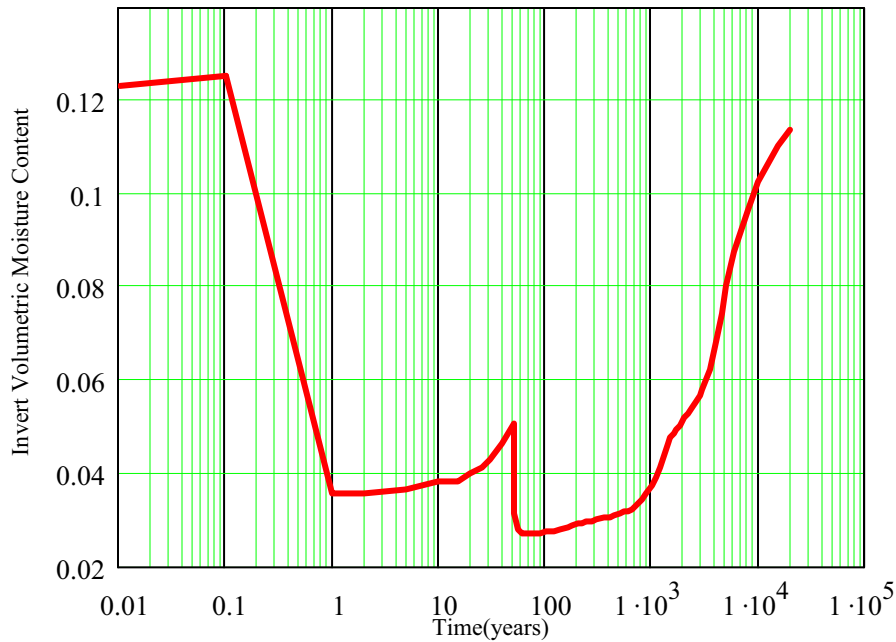Plot the invert volumetric moisture content as a function of time.

Figure XV-4. Invert Volumetric Moisture Content as a Function of Time

XV.4 HAND CALCULATIONS FOR VERIFICATION OF MATHCAD FUNCTIONS

Develop a hand calculation for verification of the relative humidity function. At 4,000 years the temperature of the invert is 70.5 degrees centigrade with a saturation of 0.52163. Calculate the moisture potential in bars. From Equation XV-4:

$$\theta = \theta_r + \frac{\left(\theta_s - \theta_r\right)}{\left[1 + \left(\alpha \cdot \psi\right)^n\right]^m}$$ (Eq. XV-10)

$$S_r := 0.12 \qquad S_s := 1$$

Rewriting Equation XV-10:

$$\frac{\theta - \theta_r}{\theta_s - \theta_r} = \frac{1}{\left[1 + \left(\alpha \cdot \psi\right)^n\right]^m}$$ (Eq. XV-11)

or rewriting in terms of saturation:

$$\frac{S - S_r}{1 - S_r} = \frac{1}{\left[1 + \left(\alpha \cdot P_c \right)^n \right]^m}$$

(Eq. XV-12)

Substituting in the saturation:

$$\frac{0.5216 - 0.12}{1 - 0.12} = \frac{1}{\left[1 + \left(\alpha \cdot P_c \right)^n \right]^m}$$

(Eq. XV-13)

$$.4563 = \frac{1}{\left[1 + \left(\alpha \cdot P_c \right)^n \right]^m}$$

(Eq. XV-14)

$$\left[1 + \left(\alpha \cdot P_c \right)^n \right]^m = \frac{1}{.4563}$$

(Eq. XV-15)

$$\left[1 + \left(\alpha \cdot P_c \right)^n \right]^m = 2.191$$

(Eq. XV-16)

$$1 + \left(\alpha \cdot P_c \right)^n = 2.191^{\left(\frac{1}{0.216} \right)}$$

(Eq. XV-17)

$$1 + \left(\alpha \cdot P_c \right)^n = 2.191^{4.6296}$$

(Eq. XV-18)

$$1 + \left(\alpha \cdot P_c \right)^n = 37.760$$

(Eq. XV-19)

$$\left(\alpha \cdot P_c \right)^n = 37.760 - 1$$

(Eq. XV-20)

$$\left(\alpha \cdot P_c \right)^n = 36.760$$

(Eq. XV-21)

$$\alpha \cdot P_c = 36.760^{\frac{1}{1.276}}$$

(Eq. XV-22)

$$\alpha \cdot P_c = 16.857$$

(Eq. XV-23)

$$P_c = \frac{16.857}{1.08 \cdot 10^{-5} \cdot \dfrac{1}{Pa}}$$

(Eq. XV-24)

$$P_c = 1560833. \cdot Pa$$

(Eq. XV-25)

or 15.60 Bars at a temperature of 70.5 degrees C at 4,000 yrs and a saturation of 0.5216.

Now consider the surface tension effects (σ_f) and correct the capillary pressure function for surface tension effects. From Incropera and DeWitt (2002 [DIRS 163337], p. 924, Table A.6) and as reproduced in Table XV-1:

340 64.9 *10⁻³
345 64.1 *10⁻³ $70.5 \cdot K + 273.15 \cdot K = 343.65\,K$

(Eq. XV-26)

$$\sigma f = \left[\frac{343.65 - 340}{345 - 340} \cdot (64.1 - 64.9) + 64.9 \right] \cdot 10^{-3} \cdot \frac{N}{m}$$

(Eq. XV-27)

$$\sigma f = 64.3 \cdot 10^{-3} \cdot \frac{N}{m} \qquad \text{for a temperature of 70.5 C.}$$

(Eq. XV-28)

Now calculate the surface tension at ambient temperature (25 degrees C):

$$273.15 \cdot K + 25 \cdot K = 298.15\,K$$

295 72.7*10-3
300 71.7 *10-3

(Eq. XV-29)

$$\sigma f = \left[\frac{298.15 - 295}{300 - 295} \cdot (71.7 - 72.7) + 72.7 \right] \cdot 10^{-3} \cdot \frac{N}{m}$$

(Eq. XV-30)

$$\sigma f = 72.07 \cdot 10^{-3} \cdot \frac{N}{m}$$

(Eq. XV-31)

for a temperature of 25 C.

Provide a capillary pressure correction based upon the ratio of the surface tension (0.07207 N/m) at 25 degrees C and 70.5 degrees C:

$$P'_c = \left[1560833. \cdot Pa \cdot \frac{\left(64.3 \cdot 10^{-3} \cdot \frac{N}{m} \right)}{\left(72.07 \cdot 10^{-3} \cdot \frac{N}{m} \right)} \right]$$

(Eq. XV-32)

$$P'_c = 1392556. \cdot Pa$$

(Eq. XV-33)

Now calculate the density of water at this temperature. From Incropera and DeWitt (2002 [DIRS 163337], p. 924, Table A.6) and as reproduced in Table XV-1:

340   $1.021*10^{-3}$
345   $1.024*10^{-3}$

$$\left[\frac{343.65 - 340}{345 - 340} \cdot \left(1.024 \cdot 10^{-3} - 1.021 \cdot 10^{-3} \right) + 1.021 \cdot 10^{-3} \right] \cdot \frac{m^3}{kg}$$

$$977.3 \cdot \frac{kg}{m^3}$$

(Eq. XV-34)

XV.5   GOVERNING RELATIONSHIPS FOR RELATIVE HUMIDITY CALCULATION IN THE INVERT

The relative humidity, RH (P_c), in the invert can be expressed as a function of the moisture potential expressed as the capillary pressure through the soil-psychrometer relation (Kelvin equation) presented by Jury et al. (1991 [DIRS 102010], p. 60):

$$RH(P_c) = P_v / P_v^* = \exp\left(\frac{M_w \cdot P'_c}{\rho_w \cdot R \cdot T_w} \right)$$

(Eq. XV-35)

where

P'_c	Capillary Pressure (Pa) with surface tension correction
M_w	Molecular weight of water (kg/mole),
ρ_w	Mass Density of Water (kg/m3)
T_w	Absolute temperature (K)
P_v	Partial pressure of water (Pa)
P_v^*	Saturated vapor pressure of water (Pa)
R	Universal Gas Constant (8.315 J/(mole*K))

XV.6 HAND CALCULATIONS FOR VERIFICATION OF THE MATHCAD FUNCTION FOR INVERT RELATIVE HUMIDITY

The hand calculation for the corrected capillary pressure in Equation XV-32 is $1.393*10^6$ Pa. Now substitute values into the Kelvin equation (Equation XV-35) to calculate the relative humidity. The hand calculation produces:

$$exp\left(M \cdot \psi \cdot \frac{1}{\rho(343.65 \cdot K) \cdot R \cdot T} \right) \quad R = 8.315 \frac{\text{kgm}^2}{\text{s}^2 \text{K mol}} \quad M = 0.018016 \frac{\text{kg}}{\text{mol}}$$

(Eq. XV-36)

$$exp\left[18.016 \cdot \frac{gm}{mole} \cdot \left[-\left(1.395 \times 10^6 \text{Pa} \right) \right] \cdot \frac{1}{977.3 \frac{\text{kg}}{\text{m}^3} \cdot \left(8.315 \frac{\text{kgm}^2}{\text{s}^2 \text{K mol}} \right) \cdot 343.65 \cdot K} \right]$$

$$= 0.99104$$

(Eq. XV-37)

Note that before the adjustment for surface tension, the capillary pressure was $1.56 *10^6$ Pa as presented above. Therefore the capillary tension correction is about 11 percent.

XV.7 MATHCAD FUNCTIONS AND VERIFICATION

Note that in the relative humidity function presented below requires the moisture potential as a function of the volumetric moisture content. Define the inverse van Genuchten Moisture Retention Function. Note that in MathCad a := is equivalent to an assignment statement. Note also that the MathCad calculations in this Appendix are found in file **Prediction of the RH in the Invert.mcd**.

$$P_c(\theta) := \frac{\left[\left[\left[\frac{(\theta_s - \theta_r)}{(\theta - \theta_r)} \right]^{\frac{1}{m'}} \right]^{\frac{1}{n}} - 1 \right]}{\alpha}$$

(Eq. XV-38)

$$P'_c(T, \theta) := P_c(\theta) \cdot \frac{\sigma_f(T + 273.15 \cdot K)}{\sigma_f(25 \cdot K + 273.15 \cdot K)}$$

(Eq. XV-39)

Define the relative humidity function on the basis of temperature, and volumetric moisture content.

$$REL2(T, \theta) := exp\left[\frac{-P'_c(T, \theta)}{\rho(T + 273.15 \cdot K)} \cdot \frac{1 \cdot M}{R \cdot (T + 273.15 \cdot K)} \right]$$

(Eq. XV-40)

The MathCad 11 functions presented above produce the following results that are in agreement with the hand calculations presented in Sections XV.4 and XV.6. The functions are therefore verified.

$$P_c(0.5216 \cdot \theta_S) = 1.56321 \times 10^6 \, Pa$$

(Eq. XV-41)

$$\sigma_f(343.65 \cdot K) = 0.064 \frac{N}{m}$$

(Eq. XV-42)

$$\rho(343.65 \cdot K) = 977.336 \frac{kg}{m^3}$$

(Eq. XV-43)

$$-P_c(0.52163 \cdot \theta_S) \cdot \frac{\sigma_f(70.5 \cdot K + 273.15 \cdot K)}{\sigma_f(25 \cdot K + 273.15 \cdot K)} = -1.395 \times 10^6 \, Pa$$

(Eq. XV-44)

$$REL2(70.5 \cdot K, 0.52163 \cdot \theta_S) = 0.99104$$

(Eq. XV-45)

Now develop the capillary pressure relationship (after surface tension correction) as a function of time. The data are output in the following arrays and Figure XV-5 presents a plot of the data.

$Time_i =$	$\dfrac{P_c(\Theta_i)}{bar} =$	$\dfrac{P'_c\big(Temperature_i \cdot K, \Theta_i\big)}{bar}$
0.01		
0.1		
1	0.435	0.438
2	0.329	0.299
5	532.092	467.423
10	559.908	488.379
15	450.19	393.654
20	358.257	316.43
25	341.592	304.757
30	269.585	243.646
40	220.765	201.36
50	172.438	158.604
50.1	111.629	104.103
51	69.987	66.014
52	594.822	521.903
55	$1.308 \cdot 10^3$	$1.042 \cdot 10^3$
60	$2.054 \cdot 10^3$	$1.561 \cdot 10^3$
65	$3.047 \cdot 10^3$	$2.193 \cdot 10^3$
70		$2.742 \cdot 10^3$
75		$2.946 \cdot 10^3$
80		$3.007 \cdot 10^3$
90		$2.993 \cdot 10^3$
100		$2.944 \cdot 10^3$
120		$2.828 \cdot 10^3$
140		$2.682 \cdot 10^3$
160		$2.432 \cdot 10^3$
180		$2.204 \cdot 10^3$
200		$2.019 \cdot 10^3$
		$1.874 \cdot 10^3$
		$1.748 \cdot 10^3$

Note that MathCad 11 illustrates a portion of the results. The results are exported to the EXCEL workbook entitled **Output_to_the_Prediction_of_Invert.xls** on the MathCad 11 worksheet.
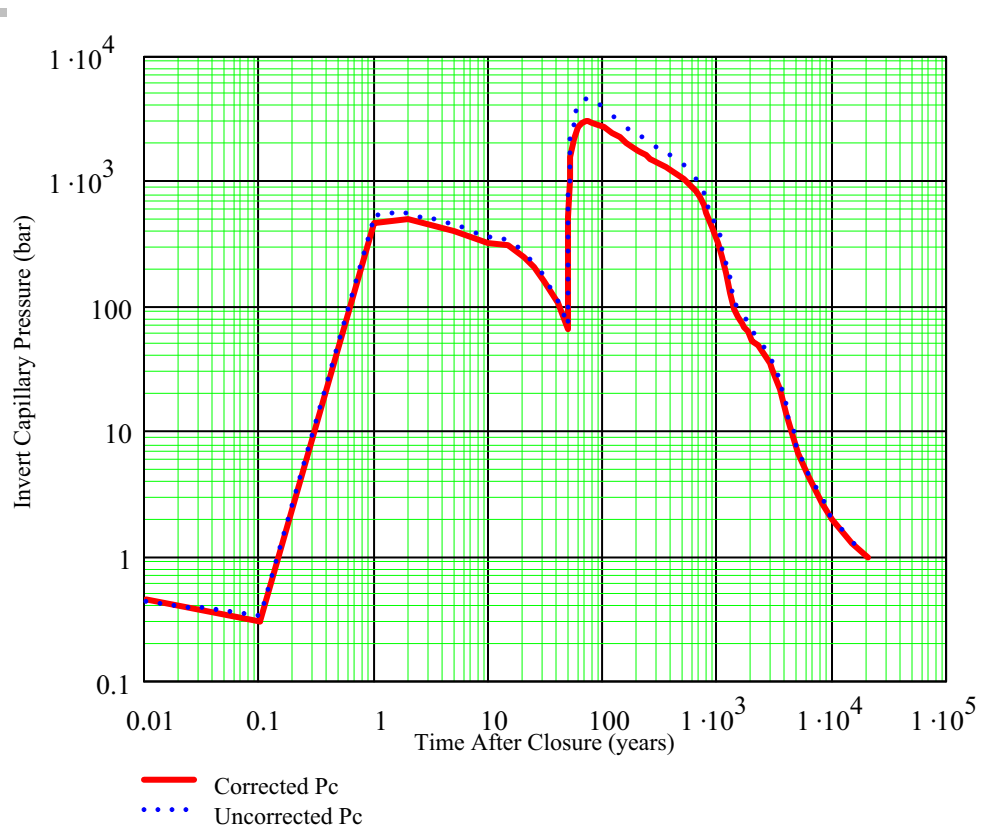
Figure XV-5.   Invert Capillary Pressure and Corrected Capillary Pressure as a Function of Time

Note that MathCad 11 illustrates a portion of the results. The results are exported to the EXCEL workbook entitled **Output_to_the_Prediction_of_Invert.xls** on the MathCad 11 worksheet.

$Time_i =$	$REL2\left(Temperature_i \cdot K, \Theta_i\right)$
0.01	0.99968
0.1	0.9998
1	0.74261
2	0.73405
5	0.77903
10	0.81682
15	0.82156
20	0.85298
25	0.87593
30	0.90009
40	0.93237
50	0.95605
50.1	0.71752
51	0.53676
52	0.40195
55	0.286
60	0.21409
65	0.19263
70	0.18668
75	0.18797
80	0.19268
90	0.20436
100	0.22038
120	0.25106
140	0.2832
160	0.31273
180	0.33837
200	0.36249
220	0.37956
240	0.39727

Note that MathCad 11 plots presented in Figures XV-6 and XV-7 are exported to the EXCEL workbook entitled **Output_to_the_Prediction_of_Invert.xls** on the MathCad 11 worksheet. A complete listing of the data is presented.
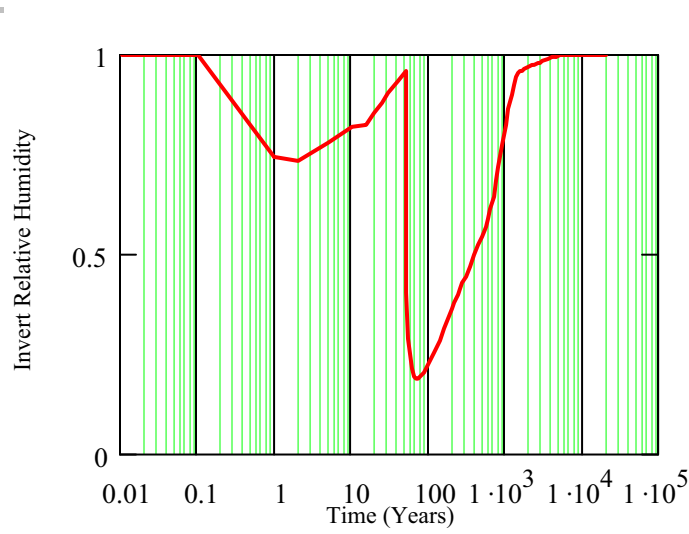
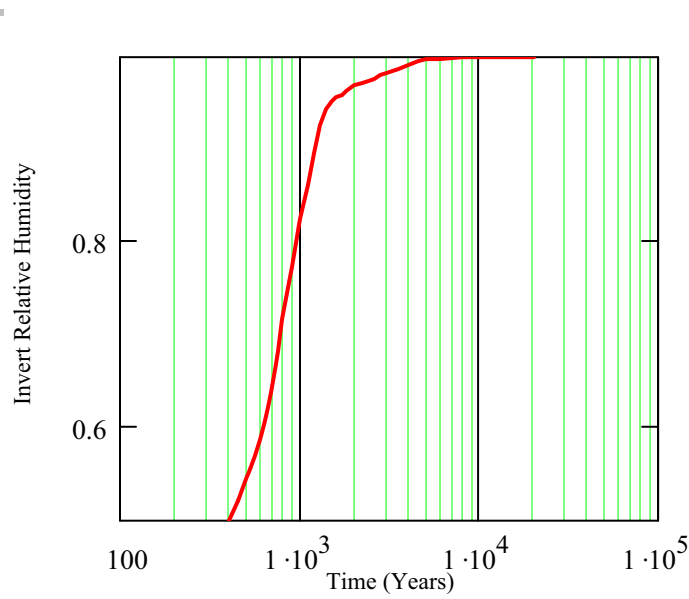Figure XV-6. Relationship of Invert Relative Humidity to Time

Figure XV-7. Relationship of Invert Relative Humidity over the Range from 0.50 to 1.0 After 100 Years

Write the MathCad 11 results to an output file for comparing results to the LDTH model. These results are then placed on the worksheet MathCad 11 of the workbook **Output_to_the_Prediction_of_Invert.xls**. The EXCEL worksheet presents a complete listing of the output.

$$ARH_{i,0} := Time_i$$

$$ARH_{i,1} := REL2\left(Temperature_i \cdot K, \Theta_i\right)$$

$$ARH_{i,2} := \frac{P'_c\left(Temperature_i \cdot K, \Theta_i\right)}{bar}$$

$$WRITEPRN(\text{"Preout"}) := ARH$$

XV.8   COMPARISON OF RELATIVE HUMIDITY PREDICTIONS FROM THE MATHCAD 11 CALCULATION WITH THE MULTISCALE THERMOHYDROLOGIC MODEL

The tabulated relative humidity and capillary pressure results along with the results generated from the MathCad 11 File **Prediction of the RH in the Invert Rev01** for P2WR5C10 are presented in the EXCEL workbook **Output_to_the_Prediction_of_Invert.xls**. Figures XV-8 through XV-9 present the comparisons between the two calculations. The calculations are in close agreement.
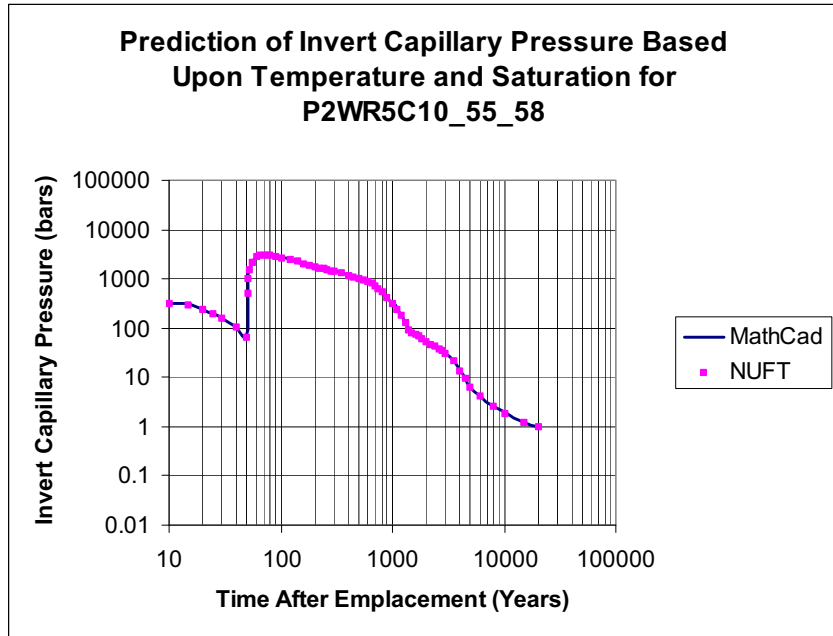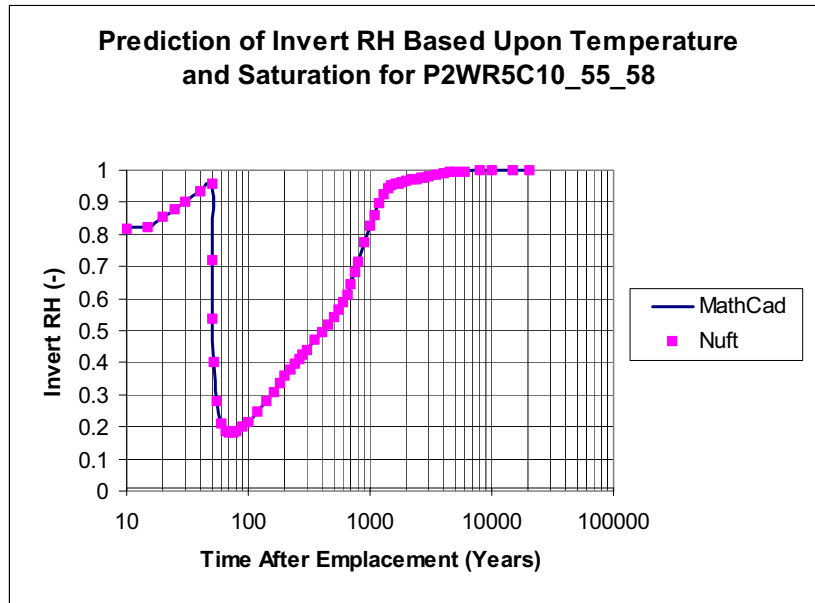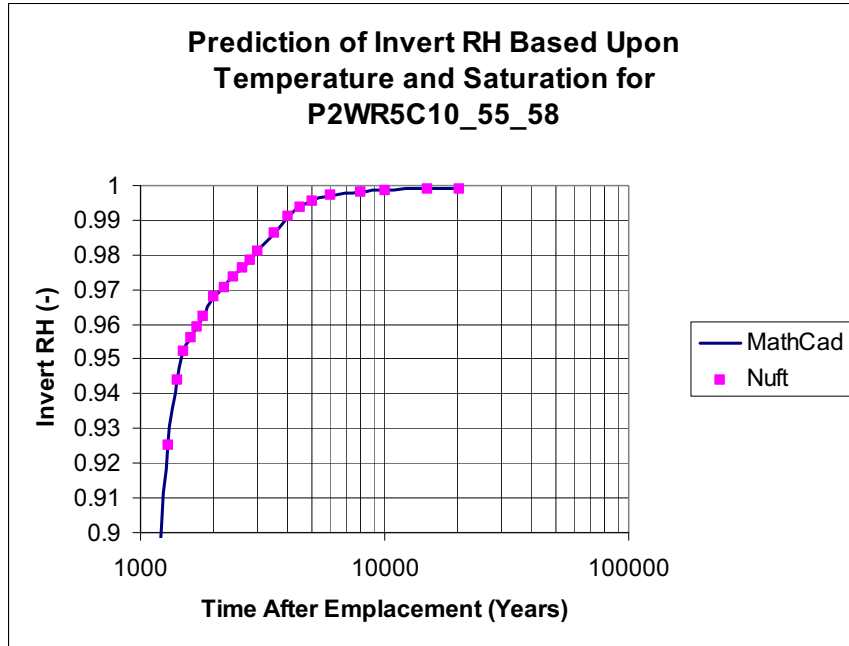
Figure XV-8. Comparison of Invert Capillary Pressure Between the MathCad 11 and Multiscale Calculations

NOTE: The data for this plot are presented in the Workbook Outputs to the Prediction of the Invert.xls on worksheet RH_vs_t_P2WR5C10_55_58.pltsc and worksheet Math11. A complete listing of the data is presented on that worksheet.

Figure XV-9. Comparison of Invert Relative Humidity Between the MathCad 11 and Multiscale LDTH Calculations

Prediction of Invert RH Based Upon Temperature and Saturation for P2WR5C10_55_58

NOTE: the data for this plot are presented in the Workbook Outputs to the Prediction of the Invert.xls on
          worksheet RH_vs_t_P2WR5C10_55_58.pltsc and worksheet Math11. A complete listing of the data are
          presented on that worksheet.

Figure XV-10. Comparison of Invert Relative Humidity Between the MathCad 11 and Multiscale Calculations Near 100 Percent Relative Humidity

XV.9   CONCLUSIONS

The relative humidity is a smooth function based upon the Kelvin equation, the van Genuchten equation, and the temperature saturation from the multiscale thermohydrologic model.   The results of the two calculations are in agreement.